



Kyoji Sassa · Paolo Canuti · Yueping Yin *Editors*

Landslide Science for a Safer Geoenvironment

Volume 2
Methods of Landslide Studies



 Springer

Landslide Science for a Safer Geoenvironment

Kyoji Sassa • Paolo Canuti • Yueping Yin
Editors

Landslide Science for a Safer Geoenvironment

Volume 2: Methods of Landslide Studies

 Springer



Editors

Kyoji Sassa
UNITWIN Headquarters Building
Kyoto University Uji-Campus
Uji, Kyoto, Japan

Paolo Canuti
ICL - International Consortium on Landslides
Florence, Italy

Yueping Yin
Center of Geo-Hazards Emergency Technology, MLR
Beijing, China

ISBN 978-3-319-05049-2 ISBN 978-3-319-05050-8 (eBook)
DOI 10.1007/978-3-319-05050-8
Springer Cham Heidelberg New York Dordrecht London

Library of Congress Control Number: 2014938097

© Springer International Publishing Switzerland 2014

This work is subject to copyright. All rights are reserved by the Publisher, whether the whole or part of the material is concerned, specifically the rights of translation, reprinting, reuse of illustrations, recitation, broadcasting, reproduction on microfilms or in any other physical way, and transmission or information storage and retrieval, electronic adaptation, computer software, or by similar or dissimilar methodology now known or hereafter developed. Exempted from this legal reservation are brief excerpts in connection with reviews or scholarly analysis or material supplied specifically for the purpose of being entered and executed on a computer system, for exclusive use by the purchaser of the work. Duplication of this publication or parts thereof is permitted only under the provisions of the Copyright Law of the Publisher's location, in its current version, and permission for use must always be obtained from Springer. Permissions for use may be obtained through RightsLink at the Copyright Clearance Center. Violations are liable to prosecution under the respective Copyright Law.

The use of general descriptive names, registered names, trademarks, service marks, etc. in this publication does not imply, even in the absence of a specific statement, that such names are exempt from the relevant protective laws and regulations and therefore free for general use.

While the advice and information in this book are believed to be true and accurate at the date of publication, neither the authors nor the editors nor the publisher can accept any legal responsibility for any errors or omissions that may be made. The publisher makes no warranty, express or implied, with respect to the material contained herein.

Cover Illustration: The Loess landslide, 100 m long, 70 m wide, with a volume of 180,000 m³, occurred in Dongxiang town, Gansu Province, China, in March 2011. The landslide destroyed major roads and tens of houses, but 760 people were evacuated successfully due to early warning.

Printed on acid-free paper

Springer is part of Springer Science+Business Media (www.springer.com)

Foreword for *International Consortium on Landslides*



United Nations
Educational, Scientific and
Cultural Organization

Organisation
des Nations Unies
pour l'éducation,
la science et la culture

Organización
de las Naciones Unidas
para la Educación,
la Ciencia y la Cultura

Организация
Объединенных Наций по
вопросам образования,
науки и культуры

منظمة الأمم المتحدة
للتربية والعلم والثقافة

联合国教育、
科学及文化组织

More than 200 million people are affected every year by natural hazards, and the impact is deepening—especially in developing countries, where they can set back healthy growth for years. Globally, an estimated one trillion United States dollars have been lost in the last decade alone.

We may not be able to stop disasters, but we can reduce their risks and their consequences. Mitigating the effects of natural hazards requires education, training, and capacity building at all levels. Fundamentally, it calls for new thinking—to move from reaction after disasters to action before.

Landslides are important in this regard, given the tragic loss of life and the economic disruption they cause. More than ever, we need to address landslides in ways that are integrated and coordinated internationally. This is the goal guiding the *International Consortium on Landslides* and its International Programme on Landslides, focusing on research, education, and capacity building in landslide risk reduction, working with international, governmental, and non-governmental actors.

Associated with the *International Consortium on Landslides*, UNESCO has accompanied the International Programme on Landslides from its inception, as an innovative initiative for cooperative research and capacity building in landslide risk mitigation. In the same spirit, UNESCO and Kyoto University established a University Twinning and Networking Cooperation Programme on landslide risk mitigation for society and the environment in March 2003, in order to deepen cooperation in this vital area.

This publication is an essential tool for both organizations and individuals to deepen understanding of landslide phenomena and to reduce their risks. Drawing on latest scientific developments, this volume presents a range of initiatives under way across the world and puts forward recommendations on risk mitigation. At a time when the consequences of climate change are deepening, this work provides a benchmark reference to strengthen the resilience of societies under pressure. I wish to thank all participants in the *International Consortium on Landslides* and all involved in this important work. Let me highlight especially Professor Kyoji Sassa, Chairperson of the

Consortium, for his tireless efforts. In this spirit, I look forward to further strengthening UNESCO's cooperation with the *International Consortium on Landslides*.



A handwritten signature in blue ink that reads "Irina Bokova". The signature is written in a cursive, flowing style.

Ms. Irina Bokova
Director-General of UNESCO

Foreword

Landslide, floods, drought, wildfire, storms, tsunami, earthquakes, and other types of natural hazards are increasingly affecting the world. For the first time in history the world has experienced 3 consecutive years (2010–2012) where annual economic losses have exceeded \$100 billion due to an enormous increase in exposure of industrial assets and private property to extreme disaster events. During the period of 2000–2012, 2.9 billion people were affected by disasters, economic damage is equivalent of USD 1.7 trillion, and 1.2 million people were killed by disasters.¹

The Global Assessment Report (GAR), a regular publication by the United Nations on disaster risk levels, trends, and analysis of the underlying causes, found that most of the small-scale recurrent disasters such as landslides are not effectively accounted for by authorities. The same report also found that while landslides and other recurrent natural hazards are responsible for only a small proportion of global disaster mortality, they account for a very significant proportion of damage to public assets, such as health and educational facilities and infrastructure, as well as to the livelihoods, houses, and assets of low-income groups.

Extensive risk associated with localized, mainly weather-related hazards with short return periods. These highly localized yet frequent hazards include surface water and flash flooding, landslides, fires, and both agricultural and hydrological drought. They are exacerbated by badly managed urban development, environment degradation, and poverty.²

The *Hyogo Framework for Action 2005–2015: Building the Resilience of Nations and Communities to Disasters (HFA)*, adopted at the 2nd World Conference on Disaster Reduction (WCDR, Kobe, Hyogo, Japan, in January 2005), represents the most comprehensive action-oriented policy guidance in universal understanding of disasters induced by vulnerability to natural hazards and reflects a solid commitment to implementation of an effective disaster reduction agenda. In order to ensure effective implementation of HFA at all levels, tangible and coordinated activities must be carried out. Since 2005, we have seen many activities and initiatives developed to implement HFA in various areas. As a concrete activity in the area of landslide risk reduction, the International Programme on Landslides has maintained the momentum created in 2005 through organizing the two World Landslide Forums in 2008 in Tokyo and in 2011 in Rome, being led by the International Consortium on Landslides. It is my great pleasure to see the valuable development for the last 8 years.

There is a growing evidence of the need for a strong science basis to understand the causes and impacts of landslides as well as the most effective measures to reduce landslide risk. This book includes a number of substantive articles on landslide risk reduction. Applying science into practice is one of the key words for the global endeavour. I expect this book as well as the Third World Landslide Forum to make a substantive contribution for that purpose in the area

¹ Disasters refers to drought, earthquake (seismic activity), epidemic, extreme temperature, flood, insect infestation, mass movement (dry and wet), storm, volcano, and wildfire/Data source: EM-DAT: The OFDA/CRED International Disaster Database/Data version: 12 March 2013 - v12.07.

² Global Assessment Report on Disaster Risk Reduction 2013: http://www.preventionweb.net/english/hyogo/gar/2013/en/home/GAR_2013/GAR_2013_2.html

of landslide risk reduction by the promotion of exchange of experience and achievements in science and facilitating discussion on sustainable disaster risk management.

Recognizing that disaster reduction needs interdisciplinary and multi-sectoral action, we build on partnerships and take a global approach to disaster reduction. Therefore, we welcome better cooperation between government authorities and the international community including scientific community that play a critical role in helping people make life-changing decisions about where and how they live before the disaster strikes, in particular high-risk urban areas.

Once the ten-year mark has been passed in 2015, the world will have a new disaster risk reduction framework. Consultations on elements for the post-2015 framework (“HFA2”) are currently ongoing. Multi-stakeholders, including academic and scientific institutions, are encouraged to be engaged in the ongoing consultation towards HFA2, which is expected to be adopted at the Third World Conference on Disaster Risk Reduction in March 2015 in Sendai, Japan.

Scientist, international, and regional institutions have a responsibility to assist with the tools, knowledge, and capacity to understand their risk and take the most effective measures to reduce them. The knowledge on landslides is a key part of the equation and the work and outcome of The Third World Landslide Forum in June 2014 in Beijing will be important contribution to these efforts and ongoing consultation towards 2015. UNISDR is fully behind the community of practice working on landslide risk.



A handwritten signature in black ink, appearing to read 'Margareta Wahlström'.

Ms. Margareta Wahlström
Special Representative of the UN Secretary-
General for Disaster Risk Reduction, Chief
of UNISDR

Preface: Landslide Science for a Safer Geoenvironment

The Third World Landslide Forum (**WLF3**) was held at the China National Convention Center, Beijing, China, on 2–6 June 2014. WLF is the triennial conference of the International Consortium on Landslides (**ICL**) and the International Programme on Landslides (**IPL**).

ICL (The International Consortium on Landslides) launched at the Kyoto Symposium in January 2002 is an international non-governmental and non-profit scientific organization promoting landslide research and capacity building for the benefit of society and the environment. Major activities of the ICL are the publication of a bimonthly full-colour journal “Landslides: Journal of the International Consortium on Landslides”, the International Programme on Landslides including IPL Projects in many countries/regions, and the Triennial World Landslide Forum and promotion of ICL regional and thematic networks and the World Centres of Excellence on Landslide Risk Reduction (WCoE). All activities involve cooperation by ICL-supporting organizations and other various stakeholders (national and local governments, civil society, and private sectors) contributing to landslide risk reduction.

The IPL is a programme of the ICL. It is developed in partnership with ICL-supporting organizations. The programme is managed by the IPL Global Promotion Committee including ICL and ICL-supporting organizations: the United Nations Educational, Scientific and Cultural Organization (UNESCO), the World Meteorological Organization (WMO), the Food and Agriculture Organization of the United Nations (FAO), the United Nations International Strategy for Disaster Risk Reduction (UNISDR), the United Nations University (UNU), the International Council for Science (ICSU), the World Federation of Engineering Organizations (WFEO), and the International Union of Geological Sciences (IUGS). The IPL contributes to the United Nations International Strategy for Disaster Reduction.

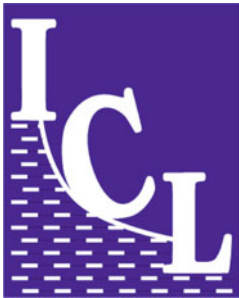
ICL-IPL invites relevant organizations and programmers to promote Landslide Science for a Safer Geoenvironment.

The International Consortium on Landslides (ICL)

- ICL was established by adopting its statutes in January 2002. The headquarters was registered as a legal body under the Japanese law for non-profit-making organizations (NPO) in the Kyoto Prefectural Government, Japan, in August 2002.
- ICL established the UNITWIN (University Twinning and Networking) Cooperation Programme on Landslide Risk Mitigation for Society and the Environment with UNESCO and Kyoto University in March 2003. The UNITWIN Headquarters Building was constructed by ICL and Kyoto University at the Kyoto University Uji Campus in September 2004. The programme was developed to promote landslide and water-related disaster risk management for society and the environment in November 2010.
- ICL founded “*Landslides*”: *Journal of the International Consortium on Landslides* in 2004. It was established as a quarterly journal published by Springer Verlag. It was approved as an ISI journal in 2005 and moved to a bimonthly journal from Vol. 10 in 2013.
- ICL founded the International Programme on Landslides (IPL) in partnership with seven global stakeholders by adopting the 2006 Tokyo Action Plan. It exchanged MoU to

promote IPL with the United Nations Educational, Scientific and Cultural Organization (UNESCO), the World Meteorological Organization (WMO), the Food and Agricultural Organization of the United Nations (FAO), the United Nations International Strategy for Disaster Reduction (UNISDR), the United Nations University (UNU), the International Council for Science (ICSU), and the World Federation of Engineering Organizations (WFEO) in 2006.

- The IPL Global Promotion Committee (IPL-GPC) was established following the 2006 Tokyo Action Plan to manage IPL activities including IPL projects, the World Landslide Forum (WLF) every 3 years, and the World Centres of Excellence for Landslide Risk Reduction (WCoEs) to be identified at WLFs.
- ICL headquarters in Kyoto, Japan, was approved as a scientific research organization (No. 94307) which can receive scientific grants from the Ministry of Education, Culture, Sports, Science and Technology (MEXT), Japan, in March 2007 and registered in the cross-ministerial research and development management system of all ministries of Japan in May 2008.
- ICL was approved as an NGO having operational relations with UNESCO in April 2007. It was reclassified as an NGO with consultative partnership with UNESCO in March 2012.
- ICL-IPL organized the First World Landslide Forum (WLF1) at the United Nations University, Tokyo, in November 2008.
- ICL-IPL organized the Second World Landslide Forum (WLF2) at the Food and Agriculture Organization of the United Nations, Rome, in October 2011.
- ICL-IPL is organizing the Third World Landslide Forum (WLF3) at the China National Convention Center, Beijing, in June 2014.
- ICL-IPL will organize the Fourth World Landslide Forum (WLF4) in Ljubljana, Slovenia, in May 29–June 2, 2017.



The symbol of ICL was designed as below.

I is a symbol of cultural heritage at landslide risk

C symbolizes the moving landslide mass

L is a symbol of retaining wall to stop landslides for its risk reduction.

The greatest discussion on C whether the Consortium should stand still or might be inclined during dynamic motion.

The International Programme on Landslides (IPL)

- The United Nations World Conference on Disaster Reduction was held on 18–22 January 2005 in Kobe, Japan. At this conference, the ICL proposed the organization of a thematic session to develop the IPL within the WCDR, and it was approved by the United Nations Secretariat for the International Strategy for Disaster Risk Reduction. With financial support from the Cabinet Office of Japan, the Ministry of Education, Culture, Sports, Science and Technology of the Government of Japan (MEXT), and the Disaster Prevention Research Institute of Kyoto University, the thematic conference Session 3.8 “New International Initiatives for Research and Risk Mitigation of Floods (IFI) and Landslides (IPL)” was organized together with ICL-supporting organizations and also the flood group.
- The thematic session 3.8 was opened with the addresses by Koichiro Matsuura (Director-General of UNESCO), Michel Jarraud (Secretary-General of WMO), and others. The session was chaired by Hans van Ginkel (Rector of UNU). The ICL proposed a **Letter of**

- Intent** to promote further joint global activities in disaster reduction and risk prevention through “Strengthening research and learning on ‘Earth system risk analysis and sustainable disaster management’ within the framework of the ‘United Nations International Strategy for Disaster Reduction’ (ISDR)”. This Letter of Intent was agreed and signed by heads of seven global stakeholders of UNESCO, WMO, FAO, UNISDR, UNU, ICSU, and WFEO.
- Based on this Letter of Intent, ICL, UNESCO, WMO, FAO, UNISDR, UNEP, UNU, and Kyoto University jointly organized the Round Table Discussion (RTD) “Strengthening research and learning on earth system risk analysis and sustainable disaster management within UN-ISDR as regards landslides—towards a dynamic global network of International Programme on Landslides (IPL)” on 18–20 January 2006 at Elizabeth Rose Hall of the United Nations University, Tokyo, Japan. The RTD was cosponsored by Japanese and international governmental and non-governmental organizations. The 2006 Tokyo Action Plan was adopted as the result of RTD.
 - The 2006 Tokyo Action Plan decided to develop the International Programme on Landslides (IPL) which is managed by IPL Global Promotion Committee. It is formed by ICL member organizations, ICL-supporting organizations which have exchanged the Memorandum of Understanding with ICL to promote ICL, and organizations which provide Subvention to IPL.
 - The ICL exchanged the Memoranda of Understanding with each of seven global stakeholders: UNESCO, WMO, FAO, UNISDR, UNU, ICSU, and WFEO to promote the 2006 Tokyo Action Plan within 2006. Then, IPL was formally launched as a programme of the ICL in partnership with ICL-supporting organizations aiming at organizing work in response to the ICL goals.
 - The logo of IPL in Fig. 1 is a simple design of ICL and ICL-supporting organizations which have exchanged MOU with ICL to promote ICL-IPL.



Fig. 1 Logo of the International Programme on Landslides (IPL)

The World Landslide Forum

The First World Landslide Forum: Implementing the 2006 Tokyo Action Plan on the International Programme on Landslides (IPL)

WLF1 was organized at the United Nations University, Tokyo, in November 2008. It was a global cross-cutting information and cooperation platform for all types of organizations from academia, United Nations, governments, private sectors, and individuals that are contributing to landslide research and education and who are willing to strengthen landslide and other related earth system risk reduction.

- Plenary sessions were (1) Open forum “Progress of IPL Activities”, (2) Plenary symposium “Global Landslide Risk Reduction”: A special Report and four keynote lectures, (3) Public Forum on “Protection of Society and Cultural and Natural Heritage, (4) “Landslides for Children”, (5) High-level panel discussion “Landslides in Global Change—How to mitigate risk? Toward the Second World Landslide Forum in 2011”.
- Parallel sessions were (1) A look from space, (2) Case Studies and National Experiences, (3) Catastrophic slides and avalanches, (4) Climate change and slope instability, (5) Landslides threatening heritage sites, (6) Economic and Social Impact of Landslides, (7) Education, Capacity Building and Public Awareness for Disaster Reduction, (8) Environmental Impact of Landslides, (9) Landslides in General, (10) Landslides and multi-hazards, (11) Mapping: inventories, susceptibility, hazard and risk, (12) Monitoring, prediction and early warning, (13) Policy and Institutional framework for Disaster Reduction, (14) Rainfall, debris flows, and wildfires, (15) Landslide Disaster Mitigation Engineering Measures, (16) Watershed and Forest Management for Risk Reduction, (17) Landslides in Dam Reservoirs.
- One full-colour book—Landslides-Disaster Risk Reduction—including all papers in plenary sessions and introduction of all parallel sessions was published, two monocolour proceedings for full papers were accepted for parallel sessions, and papers accepted for poster papers were printed and also are uploaded in the ICL web in full colour.
- 430 people from 48 countries and several other international organizations participated (175 from Japan, and 255 from abroad).

The Second World Landslide Forum: Putting Science into Practice

WLF2 was organized at the Headquarters of the Food and Agriculture Organization of the United Nations (FAO) on 3–9 October 2011. It was jointly organized by the IPL Global Promotion Committee (ICL, UNESCO, WMO, FAO, UNISDR, UNU, ICSU, WFEO) and two ICL members in Italy: the Italian Institute for Environmental Protection and Research (ISPRA) and the Earth Science Department of the University of Florence with support from the Government of Italy and many Italian landslide-related organizations.

- 864 people from 63 countries and several international organizations participated. Attendance was larger than expected, and twice the attendance at the First World Landslide Forum 2008 in Tokyo.
- 25 Technical sessions were held, and 465 full papers were submitted. All accepted papers were edited in seven full-colour volumes titled as “**Landslide Science and Practice**” as below.
 - Vol. 1 Landslide inventory and susceptibility and hazard zoning
 - Vol. 2 Early warning, instrumentation and monitoring
 - Vol. 3 Spatial analysis and modelling
 - Vol. 4 Global environmental change (420 pages)
 - Vol. 5 Complex environment (520 pages)
 - Vol. 6 Risk assessment, management and mitigation (430 pages)
 - Vol. 7 Social and Economic Impact and Policies (430 pages)

The Third World Landslide Forum: Landslide Risk Mitigation Toward a Safer Environment

WLF3 will be organized on 2–6 June 2014 in Beijing, China.

Three full-colour volumes (Vol. 1–Vol. 3) will be published by Springer, titled as Landslide Science for a Safer Geoenvironment. 303 papers will be published in three full color volumes. One monocolour proceedings which contains 123 full papers and an abstract volume will be published by the Chinese Organizing Committee. Volume 1 includes Plenary lectures, and selected papers from the side events. Volume 2 includes papers accepted in sessions for methods of landslide studies. Volume 3 includes papers accepted for methods of landslide studies. Front matters include two Forewords from Ms. Irena Bokova, Director-General of UNESCO and Ms. Margareta Wahlström, Special Representative of the UN Secretary General for Disaster Risk Reduction, Chief of UNISDR, and Preface by Kyoji Sassa (Executive Director), Paolo Canuti (President) and Yueping Yin (Incoming President) of ICL. Back matters include “Landslide Technology and Engineering in Support of Landslide Science” and “ICL Structure”.

Plenary sessions are:

1. High-Level Panel Discussion toward a Safer Geoenvironment
2. Plenary Lectures “Progress in Landslide Science”
 - Runqiu HUANG: Progress in Large-Scale Landslide Studies in China
 - Farrokh NADIM: Progress in Living with landslide risk in Europe
 - Rex BAUM: Progress in Regional landslide hazard assessment
 - Kyoji SASSA: Progress in Landslide Dynamics
3. Round Table Discussion “Major achievement in WLF3 and development toward WLF4”

Parallel sessions are:

Special Sessions

A1 International Programme on Landslides, A2 Thematic and Regional Networks on Landslides, A3 Policy, Legislation and Guidelines on Landslides, A4 Climate & Landuse Change Impacts on Landslides, A5 Recognition and Mechanics of Landslide, A6 General Landslide Studies

Sessions for Methods of Landslide Studies

B1 Physical Modeling and Material Testing, B2 Application of Numerical Modeling Techniques to Landslides, B3 Remote Sensing Techniques for Landslide Mapping and Monitoring, B4 Hazard Mapping, B5 Monitoring, Prediction and Warning of Landslides, B6 Risk Assessment, B7 Remedial Measures & Prevention Works, B8 Risk Reduction Strategy, B9 Inventory and Database

Sessions for Targeted Landslides

C1 Debris Flows, C2 Rock-Slope Instability and Failure, C3 Earthquake-Induced Landslides, C4 Rain-Induced Landslides, C5 Landslides in Cultural/Natural Heritage Sites, C6 Urban Landslides, C7 Landslides in Cold Regions, C8 Landslide in Coastal and Submarine Environments, C9 Natural Dams and Landslides in Reservoirs

Side Events

D1 Student Session, D2 Landslide Teaching tools, D3 Dialogues on Country Landslide Issues

Other ICL-IPL Activities

Other ICL-IPL activities include (1) IPL Projects, (2) ICL Regional and thematic networks, (3) World Centre of Excellence on Landslide Risk Reduction, (4) ICL Landslide Teaching Tools.

Landslides: Journal of the International Consortium on Landslides

The ICL decided to create a new international journal on landslides “Landslides: Journal of the International Consortium on Landslides” at the First Board of Representatives of ICL held at the UNESCO Headquarters, Paris on 19-21 November 2002. The ICL planned to publish full color journal presenting full color photos and colored maps & figures to attract policy makers, government officers and citizens as well as scientists and engineers in many fields.

The first issue of the journal *Landslides* was published from Springer Verlag in April 2004 as the core project of the International Programme on Landslides (IPL). This journal was the first full-colour scientific journal without a full-colour printing fee. The field of landslides is very wide in the related basic science fields. Common information source which all readers may understand is a full-colour photo of landslides. Landslide researchers from geology, geomorphology, geotechnology, geophysics, and landslide dynamics may obtain various aspects of information from the colour photos. The journal “Landslides” aims to promote landslide research and investigation in the developing countries as well as in developed countries. Published papers of most international journals are shared by researchers in the developed countries. *Landslides* have made the following five categories to promote contribution from developing countries and young researchers.

Within these categories, “Original articles” will deal with the frontiers of landslide science and technology. “Recent landslides” will accept recent landslide reports from developing countries where many landslide disasters will occur and “Technical note” will accept case studies of landslides in the less reported countries. “ICL-IPL activities” will report for international information dissemination and cooperation. As a central tool of the global landslide community, the journal is planned to provide different functions.

1. Original paper (6–12 pages): original research and investigation results.
2. Review paper (6–12 pages): review of current research and development of technology in a thematic area of landslides.
3. Recent landslide (less than 6 pages): reports of recent landslides including location (latitude/longitude), plan, section, geology, volume, movement, mechanism, and associated disasters.
4. Technical note (less than 6 pages): research notes, review notes, case studies, progress of technology, and best practice in monitoring, testing, investigation, and mitigation measures.
5. ICL-IPL activities: progress of IPL projects and ICL committee activities.



Fig. 2 Cover of “Landslides”, Vol.11, No.2, 2014

“Landslides” have published 513 articles in 42 issues in Volume 1–Volume 10 since 2004. Volumes 1–9 were 4 issues per year. The total pages in Vol. 9 were 569 pages containing 47 papers. Vol. 10 from 2013 was 6 issues per year. The total pages in Vol. 10 are 851 pages containing 68 papers. Figure 2 presents the front and back cover of Vol.11, No.2, 2014. The design of the cover is the same from the founding issue in 2004.

“Landslides” was identified as an SCI journal by Thomson Reuters in 2005. The impact factor was 2.216 in the 2011 Journal Citation Report, and it was 2.093 in 2012 Journal Citation Report. This journal is the core activity of ICL-IPL to share information on scientific and technological development and to develop “Landslide Science” toward a Safer Geoenvironment.

IPL Projects

IPL Projects are proposed by one or more ICL members or by IPL-Global Promotion Committee (IPL-GPC) by submitting the [IPL project proposal form](#) by 30 March every year. Proposal form will be evaluated by IPL Evaluation Committee. The proposer or a member of the project is requested to orally explain the project in the IPL-GPC which will be organized together with the Board of Representatives (BOR) of ICL each year. IPL-GPC will decide the approval of proposed project based on the evaluation committee report, oral presentation, and discussion. Each IPL Project leader with ongoing status is requested to submit an annual report of the project by 30 March each year.

The IPL project may authorize the leader and the accepted project by the IPL Global Promotion Committee. The project, leaders, and the annual report are uploaded in IPL WEB <http://www.iplhq.org/>. The progress and the research results are invited to contribute to **Landslides: Journal of the International Consortium on Landslides**. The achievements of IPL Projects are evaluated every 3 years. Three successful IPL projects will be identified at the World Landslide Forum. The leaders will receive US\$3,000 per project together with a certificate.

ICL Regional and Thematic Networks

Establishment of ICL networks was proposed at the 10th Session of Board of Representatives of ICL held at the headquarters of the Food and Agriculture Organization of the United Nations (FAO) in Rome, Italy, on 5 October 2011. The networks were approved at the 10th anniversary meeting of ICL held on 17–20 January 2012 in Kyoto, Japan. The regional and thematic networks are platforms for cooperation within ICL member organizations and non-ICL member organizations in each region and each thematic field.

Current networks are:

ICL Regional Networks

- (1) Adriatic-Balkan Network, (2) Latin America Network, (3) North-East Asia Network, (4) South-East Asian Network for Landslide Risk Management

ICL Thematic Networks

- (1) Landslides Risk Management Network, (2) Capacity Development Network, (3) Landslides in Cold Regions Network, (4) Landslides and Cultural & Natural Heritage Network, (5) Landslide Monitoring and Warning Network

World Centre of Excellence on Landslide Risk Reduction

The Global Promotion Committee (GPC) of the International Programme on Landslides (IPL) will identify World Centres of Excellence on Landslide Risk Reduction at the World Landslide Forum organized every 3 years within eligible organizations, such as universities,

institutes, NGOs, government ministries, and local governments, contributing to “Risk Reduction for Landslides and Related Earth System Disasters”. An independent Panel of Experts, set up by the Global Promotion Committee of International Programme on Landslides (IPL-GPC), endorses the WCoEs.

Objectives of WCoE:

To strengthen the International Programme on Landslides (IPL) and IPL Global Promotion Committee

To create “A Global Network of entities contributing to landslide risk reduction”; and

To improve the global recognition of “Landslide Risk Reduction” and its social-economic relevance, and entities contributing to this field

Twelve World Centres of Excellence (WCoEs) 2008–2011 were identified at the First World Landslide Forum in November 2008 at UNU in Tokyo, Japan. Fifteen WCoEs for 2011–2014 were identified at the Second World Landslide Forum in October 2011 at FAO, Rome, Italy. New WCoEs for 2014–2017 will be identified and announced at WLF3. WCoEs are cores of ICL regional and thematic networks.

ICL Landslide Teaching Tools

ICL Landslide Teaching Tools aim to provide various teaching materials to ICL members and other landslide institutions and entities for their efforts to educate university students, local government officers, people in non-governmental organizations, and local communities. Tools include text including figures and full-colour photos, PDFs of published papers, guidelines and laws, and PPTs for lectures.

Copyright and Responsibility for Each Teaching Tool

ICL called for contributions and compiled the accepted teaching tools. Copyright and responsibility for the content of each tool lie with its contributing organization. Each tool may be updated by the contributing organization.

The Teaching Toolbox contains five parts:

1. Mapping and Site Prediction
2. Monitoring and Early warning
3. Testing and Numerical Simulation
4. Risk Management and Others
5. Country Practices and Case Studies

The Teaching Toolbox contains three types of tools:

1. The first type are TXT-tools consisting of original texts with figures.
2. The second type are PDF-tools consisting of already published reference papers, manuals, guidelines, laws, codes, and others. They are on the accompanying CD as pdf files.
3. The third type are PPT-tools consisting of Powerpoint[®] files made for lectures. They are on the accompanying CD as ppt files.

ICL invites landslide research organizations and their experts to jointly develop effective and practical Landslide Teaching Tools. The copyright and the updating responsibility belong to the contributing organization.

A Call for ICL-IPL Partners

The International Consortium on Landslides (ICL) and partners of the International Programme on Landslides (IPL), including the United Nations Educational, Scientific and Cultural Organization (UNESCO), the World Meteorological Organization (WMO), the Food

and Agricultural Organization of the United Nations (FAO), the United Nations Office for Disaster Risk Reduction (UNISDR), the United Nations University (UNU), the International Council for Science (ICSU), the World Federation of Engineering Organizations (WFEO), and the International Union of Geological Sciences (IUGS), invite related international programmes and initiatives from natural sciences (earth sciences and water sciences), engineering sciences, human and social sciences, and governmental and non-governmental programmes to promote science and technology and their applications for landslide risk mitigation and to support this initiative by joining the International Networking and Partnerships aimed at enhancing capacities, in particular in the developing world, to reduce risk and vulnerabilities and build resilience related with landslides, and contribute to a safer Geoenvironment in support of UNISDR.

The “Third World Conference on Disaster Risk Reduction of the United Nations (3rd WCDRR)” will be organized in Sendai, Japan, on 14–18 March 2015, succeeding the 2nd WCDR (Kobe, 18–22 January 2005). ICL-IPL is examining an activity for 3rd WCDRR to enhance partnerships and agree with relevant organizations and programmes on ICL-IPL SENDAI PARTNERSHIPS 2015–2024 for Landslide Disaster Risk Reduction for a Safer Geoenvironment.

Kyoji Sassa
Executive Director of ICL



Paolo Canuti
President of ICL



Yueping Yin
Incoming President of ICL



ICL-IPL Secretariat

ICL office: The International Consortium on Landslides
138-1 Tanaka Asukai-cho, Sakyo-ku, Kyoto 606-8226, Japan
IPL office: UNESCO-KU-ICL UNITWIN Headquarters
Kyoto University Uji Campus, Uji Kyoto 611-0011, Japan
Email: secretariat@iclhq.org
URL: <http://icl-iplhq.org/> and <http://www.iplhq.org/>

List of Editors

Editors

Kyoji Sassa
International Consortium on Landslides
Kyoto, Japan

Yueping Yin
Center of Geo-Hazards Emergency Technology, MLR
Beijing, China

Associate Editors

Eileen and Mauri McSaveney
GNS Science,
Lower Hutt, New Zealand

Vol.1 Part Editors

Part 2
Matjaž Mikoš
University of Ljubljana,
Ljubljana, Slovenia

Part 4
Sálvano Briceño
International Consortium on Landslides
Kyoto, Japan

Part 6
Luciano Picarelli
Seconda Univ. di Napoli
Aversa, Italy

Part 8
Bin He
Nanjing Institute of Geography & Limnology, CAS
Nanjing, China

Vol.2 Part Editors

Part 1
Binod Tiwari
California State University, Fullerton
Fullerton, California, USA

Part 3
Vern Singhroy
Canada Centre for Remote Sensing
Ottawa, Ontario, Canada

Part 5
Željko Arbanas
University of Rijeka
Rijeka, Croatia

Paolo Canuti
International Consortium on Landslides
Florence, Italy

Lynn Highland
U.S. Geological Survey
Denver, Colorado, USA

Part 3
Snjezana Mihalić Arbanas
University of Zagreb
Zagreb, Croatia

Part 5
Vit Vilimek
Charles University
Prague, Czech Republic

Part 7
Peter Bobrowsky
Geological Survey of Canada
Ottawa, Ontario, Canada

Part 2
Marc-Andre Brideau
BGC Engineering Inc.
Vancouver, British Columbia, Canada

Part 4
Rex Baum
U.S. Geological Survey
Denver, Colorado, USA

Part 6
Huabin Wang
Huazhong University of Science and Technology
Wuhan, Hubei, China

Part 7
Sebastian Fischer
Technische Universität Darmstadt
Darmstadt, Germany

Part 9
Snježana Mihalić Arbanas
University of Zagreb
Zagreb, Croatia

Vol.3 Part Editors

Part 1
Giovanni Crosta
Università degli Studi di Milano Bicocca
Milano, Italy

Ko-Fei Liu
National Taiwan University
Taipei, Taiwan

Part 3
Kazuo Konagai
Yokohama University
Tokyo, Japan

Fawu Wang
Shimane University
Matsue, Shimane, Japan

Part 5
Jan Vlcko
Comenius University, Bratislava
Bratislava, Slovakia

Part 7
Ying Guo
Northeast Forestry University
Harbin, China

Part 9
Alexander Strom
JSC “Hydroproject Institute”
Moscow, Russian Federation

Part 8
Farrokh Nadim
International Centre for Geohazards at NGI
Oslo, Norway

Part 2
Jan Klimeš
Institute of Rock Structure and Mechanics, CAS
Praha, Czech Republic

Part 4
Binod Tiwari
California State University, Fullerton
Fullerton, California, USA

Part 6
José Chacón
University of Granada
Granada, Spain

Part 8
Michael Strasser
ETH Zurich
Zurich, Switzerland

Contents

Part I Physical Modeling and Material Testing

| | |
|--|-----------|
| Introduction: Physical Modeling and Material Testing | 3 |
| Binod Tiwari, Baoping Wen, Yasuhiko Okada, and A.A. Virajh Dias | |
| Laser Scanner Application in Monitoring Short-Term Slope Deformation | 5 |
| Kiminori Araiba and Naoki Sakai | |
| Experimental Research of Risk Parameters in the Process of Bedding Rock Landslide Motion | 13 |
| Bo Chai, Huanying Pan, and Xiang Li | |
| Calculation of Permeability of Clay Mineral in Natural Slope by Using Numerical Analysis | 21 |
| Junghae Choi, Byung-gon Chae, Katsuyuki Kawamura, and Yasuaki Ichikawa | |
| Study on the Microscopic Structure Characteristics of the Gray Matter Slate . . . | 27 |
| Maolin Deng, Qiang Xu, Xing Zhu, Guojun Cai, and Guang Zheng | |
| Effect of Vertical Load on Shear Characteristics of Micro-Piles in Landslide | 33 |
| ShuFeng Wang and YuePing Yin | |
| Geotechnical Centrifuge Modelling for Rock Slope Failure: A Brief Overview . . . | 39 |
| Zhen Feng and Yueping Yin | |
| Physical Model of the Mechanism for Thermal Wedging Failure in Rocks | 45 |
| Vladimir Greif, Ivana Simkova, and Jan Vlcko | |
| Shallow Modes of Slope Failure in Road Earth Cuttings in Sri Lanka | 51 |
| H.M. Janaki M.K. Herath, Sudheera S.I. Kodagoda, and A.A. Virajh Dias | |
| Discussion on the Method of Intact Loess Humidification Considering Water Content Uniformity | 59 |
| Kai He and Bin Li | |
| Undrained Shear-Strength Variation of Salt-Rich Clay: Implications for Fast-Moving Clay Landslides | 63 |
| Lei He, Bao-ping Wen, and Xiu-juan Xu | |
| Analysis of Engineering Geological Properties of Sliding-Zone Soil in Large-Scale Landslides in the Weibei Loess Tableland Area | 69 |
| Bin Li, Shuren Wu, Jusong Shi, and Zhen Feng | |
| Dynamic Centrifuge Modelling Tests for Sliding Rock Slopes | 75 |
| Xianglong Li, Joseph Wartman, Huiming Tang, Jinkai Yan, Hongming Luo, and Wei Hu | |

| | |
|---|-----|
| Changes in Shear Strain and Subsurface Flow Prior to Rainfall-Induced Landslide in Flume Experiments | 81 |
| Yasuhiko Okada | |
| Geotechnical Properties of Landslide Sites in Korea with Differing Geology | 87 |
| Young-Suk Song and Kyeong-Su Kim | |
| Modelling Fragmentation in Rock Avalanches | 93 |
| Øystein Thordén Haug, Matthias Rosenau, Karen Leever, and Onno Oncken | |
| Experimental Modelling for the Effect of Rainfall and Earthquake on Slope Stability of Engineered Fill | 101 |
| Binod Tiwari, Santiago Caballero, and Wissam Zalzali | |
| Experimental Modelling of Seepage in a Sandy Slope | 109 |
| Binod Tiwari and Adam Lewis | |
| Curvature of Failure Envelopes for Normally Consolidated Clays | 117 |
| Binod Tiwari and Beena Ajmera | |
| Experimental and Numerical Studies on the Effect of Rainfall on Triggering Shallow Landslides | 123 |
| Binod Tiwari, Katsuyuki Kawai, Adam Lewis, and Phommachanh Viradeth | |
| Feasibility Analysis of Loess Slope Improved by Lime Pile | 129 |
| Wanjiong Wu, Shouyun Liang, Fanyu Zhang, Xude Yan, and Jianji Zhou | |
| Effect of Soaking on Shear Strength of Weathered Argillaceous Rocks Susceptible to Landsliding in the Three Gorges Area of China | 135 |
| Baoping Wen, Hui Li, and Kaihao Ke | |
| Creep Behavior of the Slip Zone of a Giant Slow-Moving Landslide in Northwest China: The Suoertou Landslide as an Example | 141 |
| Xiu-zi Jiang and Bao-ping Wen | |
| Data Collection and Processing for Measurement of Time-Variable Gravity Erosion in the Laboratory Study | 147 |
| Xiang-Zhou Xu, Song Zhan, Qiao Yan, and Ming-Dong Zhu | |
| Study on the Effect of Plant Roots for Stability of Slopes | 153 |
| Udeni P. Nawagamuwa, S. Sarangan, B. Janagan, and S. Neerajapriya | |
| The Dynamic Process and Sensitivity Analysis for Debris Flow | 159 |
| Guoqiang Yu, Maosheng Zhang, and Hong Chen | |
| Evaluation of Sensitivity of the WAA and SINMAP Models (Static) for Landslide Susceptibility Risk Mapping in Sri Lanka | 167 |
| A.A. Virajh Dias and A.A.J.K. Gunathilake | |
| The Method for In-situ Large Scale Shear Test of Saturated Soils and Its Application | 175 |
| Maosheng Zhang, Wei Hu, Lifeng Zhu, Ying Pei, and Junbo Bi | |
| Microstructural Characteristics of Qinyu Landslide Slip Soil, NW China | 181 |
| Xuemei Jia, Shouyun Liang, and Chenyi Fan | |
| An In-situ Darcy Method for Measuring Soil Permeability of Shallow Vadose Zone | 189 |
| Pingping Sun, Maosheng Zhang, Lifeng Zhu, Ying Pei, and Xiujuan Cheng | |

| | |
|---|-----|
| Discussion on Assessment in the Collapse of Loess: A Case Study of the Heifangtai Terrace, Gansu, China | 195 |
| Pingping Sun, Maosheng Zhang, Lifeng Zhu, Qiang Xue, and Wei Hu | |
| Quantitative Deformation Analysis of Landslides Based on Multi-period DEM Data | 201 |
| Qiang Xue, Maosheng Zhang, Lifeng Zhu, Xiujuan Cheng, Ying Pei, and Junbo Bi | |
| Research on Prediction Methods of Surges Induced by Landslides in the Three Gorges Reservoir Area of the Yellow River | 209 |
| Wei Hu, Maosheng Zhang, Lifeng Zhu, Pingping Sun, Xiujuan Cheng, and Jun Jia | |
| Analyses of the Changes of Loess Engineering Properties Induced by Irrigation | 215 |
| Wei Hu, Lifeng Zhu, Maosheng Zhang, Ying Pei, and Junbo Bi | |
| Deformation Behavior of Mechanically Stabilized Earth Walls with Geocomposite Drainage Under Seepage Condition | 221 |
| Avirut Chinkulkijniwat and Somjai Yubonchit | |
| Loess Landslides Respond to Groundwater Level Change in Heifangtai, Gansu Province | 227 |
| Ying Dong, MaoSheng Zhang, Jie Liu, Pingping Sun, and Jun Jia | |
| Part II Application of Numerical Modeling Techniques to Landslides | |
| Introduction: Application of Numerical Modelling Techniques to Landslides | 235 |
| Marc-André Brideau | |
| Numerical Simulation on the Deformation and Failure of the Slope Treated by Building by Cave Dwellings | 237 |
| Chunli Chen, Kai He, and Tonglu Li | |
| Long- and Short-term Controls on the Spriana Rockslide (Central Alps, Italy) | 243 |
| Federico Agliardi and Giovanni B. Crosta | |
| Engineering Geology and Numerical Modelling of a Steep Rock Slope for the Ensi-Qianjiang Expressway, China | 251 |
| Xiuwen Hu, Doug Stead, Longxiang Zhai, Hongyan Jin, and Dezhi Kong | |
| Determination of the Effective Computing Region for Rock Slope Stability Based on Seismic Wave Theory | 259 |
| Chen Zhenlin and Hu Xiao | |
| Factors Controlling Kinematic Behaviour of a Huge Slow-Moving Landslide in China | 267 |
| Shu Jiang, Baoping Wen, Cheng Zhao, and Ruidong Li | |
| Finite Element Simulation for an Earthquake-Induced Catastrophic Landslide Considering Strain-Softening Characteristics of Sensitive Clays | 275 |
| Akihiko Wakai, Fei Cai, Keizo Ugai, and Tsutomu Soda | |
| Numerical Modelling of Deformation for Partially Saturated Slopes Subjected to Rainfall | 281 |
| Binod Tiwari, Katsuyuki Kawai, and Phommachanh Viradeth | |
| Feasibility Study of Dumping Area on Bearing Capacity and Slope Stability Analysis | 287 |
| Twin Hosea W. Kristyanto, Iskandar, Dicky Muslim, and Febri Hirnawan | |

| | |
|--|------------|
| Modelling Rockslide Displacements with Delayed Plasticity | 291 |
| Gabriele Frigerio, Riccardo Castellanza, Giovanni Battista Crosta, and Claudio di Prisco | |
| Part III Remote Sensing Techniques for Landslide Mapping and Monitoring | |
| Introduction: Remote Sensing Techniques for Landslide Mapping and Monitoring | 301 |
| Veronica Tofani, Yang Hong, and Vern Singhroy | |
| Landslide Susceptibility Assessment Based on Remote Sensing and GIS in Lombok Island of Indonesia | 305 |
| Arifianti Yukni, Teerarungsigul Suree, Cita Akbar, Kuehn Friedrich, and Fuchs Michael | |
| Application of Remote Sensing and GIS Techniques in Landslide Hazard Zonation of Hilly Terrain | 313 |
| Rajeshwar Singh Banshtu and Chander Prakash | |
| Mapping the Deformation of Shuping Landslide Using DInSAR and Offset Tracking Methods | 319 |
| Jinghui Fan, Hao Lin, Ye Xia, Hongli Zhao, Xiaofang Guo, and Man Li | |
| Rainfall-Triggered Shallow Landslides Mapping Through Pleiades Images | 325 |
| Davide Zizioli, Claudia Meisina, Massimiliano Bordoni, and Francesco Zucca | |
| Monitoring the Activity of Landslides in the Coastal Zones of Reservoirs with SAR Interferometry | 331 |
| Zbigniew Perski, Guang Liu, Tomasz Wojciechowski, Fan Jinhui, and Antoni Wójcik | |
| Relative Age Estimation at Landslide Mapping on LiDAR Derivatives: Revealing the Applicability of Land Cover Data in Statistical Susceptibility Modelling | 337 |
| Helene Petschko, Rainer Bell, and Thomas Glade | |
| Automated Remote Sensing Based Landslide Detection for Dynamic Landslide Inventories | 345 |
| Sigrid Roessner, Robert Behling, Karl Segl, Darya Golovko, Hans-Ulrich Wetzel, and Hermann Kaufmann | |
| Persistent Scatterer Interferometry (PSI) Technique for Landslide Characterization and Monitoring | 351 |
| Veronica Tofani, Federico Raspini, Filippo Catani, and Nicola Casagli | |
| Persistent Scatterers Interferometry Provides Insight on Slope Deformations and Landslide Activity in the Mountains of Zhouqu, Gansu, China | 359 |
| Janusz Wasowski, Fabio Bovenga, Tom Dijkstra, Xingmin Meng, Raffaele Nutricato, and Maria Teresa Chiaradia | |
| Landslide Hazard Investigation and Assessment Using Remote Sensing in the Three Gorges Reservoir Area | 365 |
| Runqing Ye, Wenming Cheng, Xiaolin Fu, Runze Wu, Jianying Yang, and Ruiqing Niu | |
| Landslides Susceptibility Mapping in Oklahoma State Using GIS-Based Weighted Linear Combination Method | 371 |
| Xiaogang He, Yang Hong, Xiaodi Yu, Amy B. Cerato, Xinhua Zhang, and Marko Komac | |
| InSAR-Based Landslide Location and Monitoring in Alpine Valley Region | 379 |
| Guijie Wang, Yueping Yin, Mowen Xie, and Weilun Wu | |

| | |
|--|-----|
| Use of Satellite and Ground Based InSAR in Hazard Classification of Unstable Rock Slopes | 389 |
| John F. Dehls, Tom Rune Lauknes, Reginald L. Hermanns, Halvor Bunkholt, Tom Grydeland, Yngvar Larsen, Harald Ø. Eriksen, and Trond Eiken | |
| Part IV Hazard Mapping | |
| Introduction: Hazard Mapping | 395 |
| Rex L. Baum, Toyohiko Miyagi, Saro Lee, and Oleksandr M. Trofymchuk | |
| Landslide Hazard Evaluation Using Artificial Neural Networks and GIS | 397 |
| Alok Bhardwaj and G. Venkatachalam | |
| Landslide Susceptibility Mapping Using Remote Sensing and GIS: Nueva Colombia, Chiapas, Mexico | 405 |
| Ixtlitzin Bravo-Carvajal, Ricardo J. Garnica-Peña, Luis C. López-Bravo, and Irasema Alcántara-Ayala | |
| Landslide Susceptibility Model Validation: A Routine Starting from Landslide Inventory to Susceptibility | 413 |
| Gulseren Dagdelenler, Hakan A. Nefeslioglu, and Candan Gokceoglu | |
| GIS-Based Landslide Susceptibility Mapping Using a Certainty Factor Model and Its Validation in the Chuetsu Area, Central Japan | 419 |
| Jie Dou, Takashi Oguchi, Yuichi S. Hayakawa, Shoichiro Uchiyama, Hitoshi Saito, and Uttam Paudel | |
| Landslide Susceptibility Mapping Using a Grid-based Infiltration Transient Model in Mountainous Regions | 425 |
| Dongyeob Kim, Eun Jai Lee, Byungkyu Ahn, and Sangjun Im | |
| Evaluating a Slope-Stability Model for Shallow Rain-Induced Landslides Using Gage and Satellite Data | 431 |
| Soni Yatheendradas, Dalia Kirschbaum, Rex L. Baum, and Jonathan W. Godt | |
| Landslide Susceptibility Modeling on Regional Scales: The Case of Lower Saxony, NW Germany | 437 |
| Martin Klose, Daniel Gruber, Bodo Damm, and Gerhard Gerold | |
| Regional Scale Landslide Susceptibility Mapping in Emilia Romagna (Italy) as a Tool for Early Warning | 443 |
| Daniela Lagomarsino, Samuele Segoni, Riccardo Fanti, Filippo Catani, and Nicola Casagli | |
| GIS-Based Probabilistic Analysis of Shallow Landslide Susceptibility Using a Transient Hydrogeological Model and Monte Carlo Simulation | 451 |
| Jung-Hyun Lee and Hyuck-Jin Park | |
| Collapse Landslide and Mudslides Hazard Zonation | 457 |
| Mingxue Liu, Xiang Chen, and Shanni Yang | |
| Mapping and Management of Landslide Risk in the City of Azazga (Algeria) | 463 |
| Lynda Djerbal, Nassima Alimrina, Bachir Melbouci, and Ramdane Bahar | |
| Landslide Susceptibility Analysis of Belgrade City Area | 469 |
| Miloš Marjanović, Uroš Đurić, Biljana Abolmasov, and Snežana Bogdanović | |
| Study on Earthquake-Triggered Landslide Hazard Assessment Under Rainfall Condition | 475 |
| Meng Wang, Jianping Qiao, and Lili Shi | |

| | |
|---|------------|
| A GIS Approach to Analysis of Deep-Seated Slope Stability in Complex Geology . . . | 483 |
| Ivan Marchesini, Martin Mergili, Mauro Rossi, Michele Santangelo, Mauro Cardinali, Francesca Ardizzone, Federica Fiorucci, Barbara Schneider-Muntau, Wolfgang Fellin, and Fausto Guzzetti | |
| Risk Evaluation of Landslide Topographic Area by Aerial Photointerpretation . . . | 491 |
| Toyohiko Miyagi and Eisaku Hamasaki | |
| Accounting for Variability in Rain-Event Intensity and Initial Conditions in Landslide Triggering Return Period Mapping via a Monte Carlo Approach . . . | 499 |
| David J. Peres and Antonino Cancelliere | |
| Predictive Capability of Deterministic and Statistical Models in Weathered Granite Soil Watershed | 507 |
| Ananta Man Singh Pradhan, Jeong-Rim Oh, Min-Su Jung, and Yun-Tae Kim | |
| Area Based Landslide Hazard and Risk Assessment for Penang Island Malaysia . . . | 513 |
| Shabri Shaharom, Low Tian Huat, and Mohd Asbi Othman | |
| Landslide Hazard Mapping Using a Poisson Distribution: A Case Study in Penang Island, Malaysia | 521 |
| Lea Tien Tay, Habibah Lateh, Md Kamrul Hossain, and Anton Abdulbasah Kamil | |
| Shallow Landslide Susceptibility Mapping for Zagreb Hilly Area, Croatia | 527 |
| Chunxiang Wang, Snjezana Mihalić Arbanas, Hideaki Marui, Naoki Watanabe, and Gen Furuya | |
| Hazardous Activation of Landslides Within Western Carpathian Region (Ukraine) | 533 |
| Olexandr Trofymchuk, Olexandr Kolodyazhnyy, and Evgeniy Yakovlev | |
| Part V Monitoring, Prediction and Warning of Landslides | |
| Introduction: Monitoring, Prediction and Warning of Landslides | 539 |
| Željko Arbanas, Teuku Faisal Fathani, Ziaoddin Shoaie, Byung-Gon Chae, and Paolo Tommasi | |
| Suggestion of a Landslide Early Warning Method Using a Gradient of Volumetric Water Content | 545 |
| Byung-Gon Chae, Junghae Choi, and Yong-Seok Seo | |
| RADAR Images Supporting Rescue and Recovery Actions for Landslide and Flood Disasters: A Rio de Janeiro State Case Study | 551 |
| Francisco Dourado, Aline Freitas, and Nelson Fernandes | |
| Application of Low-Cost Tools and Techniques for Landslide Monitoring | 557 |
| Etim Eyo, Tajul Musa, Kamaludin Omar, Khairulnizam M. Idris, Temel Bayrak, and Ifeanyi Onuigbo | |
| An Adaptive and Sustained Landslide Monitoring and Early Warning System . . . | 563 |
| Teuku Faisal Fathani, Dwikorita Karnawati, and Wahyu Wilopo | |
| Early Warning and Real-Time Slope Monitoring Systems in West and East Malaysia | 569 |
| William H.T. Fung, Richard J. Kinsil, Suhaimi Jamaludin, and Sashi Krishnan | |
| A National Warning System for Rainfall-Induced Landslides in Slovenia | 577 |
| Marko Komac, Jasna Šinigoj, and Mateja Jemec Auflič | |

| | |
|--|-----|
| Monitoring of Critical Himalayan Landslides and Design of Preventive Measures | 583 |
| Kishor Kumar, Pulikanti Subramanya Prasad, Anil Kathait, and Indervir Negi | |
| Geotechnologies for Surveys and Catastrophic Events of Rio de Janeiro Geological Survey: A Case Study | 589 |
| Tiago Marino, Francisco Dourado, Claudio Amaral, and Jorge Xavier-da-Silva | |
| Automated Inclinometer Monitoring Based on Micro Electro-Mechanical System Technology: Applications and Verification | 595 |
| Andrea Segalini, Luca Chiapponi, Benedetta Pastarini, and Corrado Carini | |
| Energy Demodulation-Based All-Fiber Warning System for Landslides | 601 |
| Xing Wang, Guangqing Wei, Bin Shi, Fenggao Xu, and Hengjin Tong | |
| Evaluation of ‘Wig-Wag’ Landslide Warning Signs | 607 |
| Mike G. Winter, Neale Kinnear, Barbara Shearer, Louise Lloyd, and Shaun Helman | |
| Latest Developments of Hong Kong’s Landslip Warning System | 613 |
| A.C.W. Wong, S.M. Ting, Y.K. Shiu, and K.K.S. Ho | |
| A Multi-Scaled Early Warning Method for Rainfall-Induced Mountain Hazards | 619 |
| Zong-ji Yang, Jian-ping Qiao, Dong Huang, Hong-ling Tian, Yuan-jun Jiang, and Lili Shi | |
| Laboratory Studies on Slope Stability Monitoring Using Distributed Fiber-Optic Sensing Technologies | 625 |
| Hong-Hu Zhu, Bin Shi, Jun-Fan Yan, Cheng-Cheng Zhang, Jie Zhang, and Zhan-Pu Song | |
| A Landslide Monitoring and Early Warning System Using Integration of GPS, TPS and Conventional Geotechnical Monitoring Methods | 631 |
| Željko Arbanas, Kyoji Sassa, Osamu Nagai, Vedran Jagodnik, Martina Vivoda, Sanja Dugonjić Jovančević, Josip Peranić, and Kristijan Ljutić | |
| Review of Monitoring Parameters of the Kostanjek Landslide (Zagreb, Croatia) | 637 |
| Martin Krkač, Snježana Mihalić Arbanas, Željko Arbanas, Sanja Bernat, Kristijan Špehar, Naoki Watanabe, Osamu Nagai, Kyoji Sassa, Hideaki Marui, Gen Furuya, Chunxiang Wang, Josip Rubinić, and Koyi Matsunami | |
| Part VI Risk Assessment | |
| Introduction: Risk Assessment | 647 |
| Huabin Wang, Rejean Couture, and Cees Van Westen | |
| Site Selection Study for Hazardous Waste Based on Fuzzy Comprehensive Evaluation Method | 649 |
| Jiang Bing, Wei Yunjie, Xu Mo, and Han Caiyi | |
| Research of Stability of an Fossil Landslide on the Urban Fringe of Metropolitan Region in Beijing, China | 655 |
| Dong-hao Liu and Cheng Sun | |
| Estimation of Direct Landslide Costs in Industrialized Countries: Challenges, Concepts, and Case Study | 661 |
| Martin Klose, Lynn Highland, Bodo Damm, and Birgit Terhorst | |
| Estimation of Landslide Impact Disaster by Discrete Element Method: Jiangping Hydropower Station, Hubei, China | 669 |
| S.N. Wang, Chong Shi, Weiya Xu, Yulong Zhang, and Hailong Zhang | |

| | |
|---|-----|
| Assessing the Effect of Mitigation Measures on Landslide Hazard Using 2D Numerical Runout Modelling | 679 |
| Haydar Y. Hussin, Roxana Ciurean, Simone Frigerio, Gianluca Marcato, Chiara Calligaris, Paola Reichenbach, Cees van Westen, and Thomas Glade | |
| Part VII Remedial Measures and Prevention Works | |
| Introduction: Remedial Measures and Prevention Works | 687 |
| Rolf Katzenbach and Sebastian Fischer | |
| Study of a Landslide in Dafnoula Village, Epirus Region, Greece | 689 |
| Michael Bellas and Georgios Voulgaridis | |
| Seismic Damage Assessment of Gravity Retaining Walls Based on Grey Correlation and Fuzzy Mathematics | 701 |
| Zheng Da and Liang Lidan | |
| Effectiveness of Hybrid Anchor Soil Nails in Stabilizing Slopes and Stability Assessment Based on Mechanics | 707 |
| M.J. Md. Noor, M.A. Saidin, and S.M. Tahir | |
| A Vigorous Debris-Flow Incident at Al-Hada Descent and Remedial Measures . . . | 715 |
| Bahaaeldin Sadagah | |
| Application of Reinforced Concrete Retaining Walls for the Rehabilitation of Landslides on Roads | 719 |
| Nedim Suljić | |
| A Simplified Analytical Model for the Design of Flexible Barriers Against Debris Flows | 725 |
| Andrea Segalini, Roberto Brighenti, and Gessica Umili | |
| Engineering Solutions for Elimination of the Risk of Destruction of Moraine | 731 |
| Eduard Zaporozhchenko and Aleksandr Butenko | |
| Part VIII Risk Reduction Strategy | |
| Introduction: Risk Reduction Strategy | 743 |
| Farrokh Nadim | |
| Place-Conscious Education for Disaster Prevention in Risk-Prone Areas of Sao Paulo | 745 |
| Erica Akemi Goto and Jefferson de Lima Picanço | |
| Landslide Community Mapping and Public Awareness in the Region of Chichonal Volcano, Chiapas, Mexico | 751 |
| Guadalupe Hernández-Moreno, Ricardo J. Garnica-Peña, and Irasema Alcántara-Ayala | |
| Community-Based Rainfall Observation for Landslide Monitoring in Western Nepal | 757 |
| Yuwan Malakar | |
| Landslide Risk Reduction in Poland: From Landslide Inventory to Improved Mitigation and Landuse Practice in Endangered Areas | 765 |
| Teresa Mrozek and Izabela Laskowicz | |
| Quantitative Multi-risk Modelling and Management Using Bayesian Networks . . . | 773 |
| Zhongqiang Liu, Farrokh Nadim, Bjørn Vidar Vangelsten, Unni Eidsvig, and Bjørn Kalsnes | |

Part IX Landslide Inventories and Databases

| | |
|---|-----|
| Introduction: Landslide Inventories and Databases | 783 |
| Snježana Mihalić Arbanas, Marko Komac, Candan Gokceoglu, and Legorreta Paulin | |
| Landslide Database for the Federal Republic of Germany: A Tool for Analysis of Mass Movement Processes | 787 |
| Bodo Damm and Martin Klose | |
| Landslide Inventory of the Eastern Part of the Gallipoli Peninsula (Canakkale, Turkey) | 793 |
| Gulseren Dagdelenler, Hakan A. Nefeslioglu, and Candan Gokceoglu | |
| GIS-Based Integration of Heterogeneous Data for a Multi-temporal Landslide Inventory | 799 |
| Darya Golovko, Sigrid Roessner, Robert Behling, Hans-Ulrich Wetzel, and Hermann Kaufmann | |
| Investigating and Managing Shallow Landslides in Switzerland | 805 |
| Josef Hess, Christian Rickli, Brian McArdeall, and Manfred Stähli | |
| Global Catalog of Rainfall-Triggered Landslides for Spatial and Temporal Hazard Characterization | 809 |
| Dalia Kirschbaum | |
| Landslide Counteracting System (SOPO): Inventory Database of Landslides in Poland | 815 |
| Teresa Mrozek, Marcin Kułak, Dariusz Grabowski, and Antoni Wójcik | |
| Development of a Landslide Inventory for a Region in Mexico Using Very High Resolution Satellite Stereo-Images | 821 |
| Franny G. Murillo-García, Federica Fiorucci, and Irasema Alcántara-Ayala | |
| Inventory of Precipitation Triggered Landslides in the Winter of 2013 in Zagreb (Croatia, Europe) | 829 |
| Sanja Bernat, Snježana Mihalić Arbanas, and Martin Krkač | |
| Landslide Inventory in the Area of Dubračina River Basin (Croatia) | 837 |
| Petra Đomlija, Sanja Bernat, Snježana Arbanas Mihalić, and Čedomir Benac | |
| Landslide Technology and Engineering in Support of Landslide Science | 843 |
| Kyoji Sassa | |

Part I

Physical Modeling and Material Testing



Introduction: Physical Modeling and Material Testing

Binod Tiwari, Baoping Wen, Yasuhiko Okada, and A.A. Virajh Dias

Abstract

Physical modeling and material testing play important roles for investigation, analysis, design and countermeasure planning of landslides. This introductory article briefly describes the nature of the diversified range of papers included in Section B1, Volume 2 of the Proceedings of the World Landslide Forum 3.

Keywords

Physical modeling • Landslides • Shear strength • Unsaturated soil • Rainfall

Significant advancements have been made in recent years in the area of physical modeling and material testing pertinent to investigation, analysis, design, and prevention of landslides. Results of research and studies related to the advancement of methodologies and standards for physical modeling and material testing are available in recent literature including journal articles, conference proceedings, and research reports. The objective of session B1: Physical modeling and material testing in the World Landslide Forum 3 (WLF3) was to provide opportunities to international researchers to publish and present their recent research findings in an international venue where thousands of

professionals who are working towards landslide hazard mitigation through different approaches, meet and discuss.

Section B1 of volume 2 of this proceeding includes the research findings pertinent to a wide theme—physical modeling and material testing. High quality papers were submitted to the conference secretariat for possible publication in the proceedings of the WLF3. Those papers went through a rigorous review process. Each paper was reviewed by at least two reviewers. Among the papers submitted for possible publication, 35 papers were accepted for publication in this section of the proceeding. After peer reviewing, all of these papers were further edited by the editorial board of the conference for technical contents and English language usage.

Papers included in this section cover a wide area of physical modeling and material testing pertinent to landslide hazard mitigation. Nine papers include the results of physical modeling for sand (1 paper), clay (2 papers) and rock materials (6 papers). Five papers included in this section cover the results regarding permeability and seepage behavior of geo-materials. One paper includes the findings pertaining to the geotechnical properties of clay. Likewise, five papers included in this section deal with the causes and stability of shallow landslides in general, whereas other five papers describe the behavior of slopes on loess soil. Out of 35 accepted papers, 4 papers cover mechanism of large scale landslides, whereas one paper each covers the mechanism of earthquake induced landslides and debris flows. Moreover,

B. Tiwari (✉)
Civil and Environmental Engineering Department, California State University, Fullerton, 800 N State College Blvd., Fullerton, CA 92831, USA
e-mail: tiwari@fullerton.edu

B. Wen
School of Water Resources and Environment, China University of Geosciences (Beijing), Beijing 100083, China

Y. Okada
Department of Soil and Water Conservation, Forestry and Forest Products Research Institute, Matsunosato 1, Tsukuba 305-8687, Japan

A.A.V. Dias
CECB Laboratory, Central Engineering Consultancy Bureau, Center for Research and Development, No. 11, Jawatta Road, Colombo 5, Sri Lanka

this section also includes papers, one each, on risk mapping and behavior of unsaturated soils.

Thirty five papers included in this section were co-authored by 127 researchers all over the world including Asia, North

America, and Europe. Among the included papers, 21, 4, 4, 2, 2, 1, and 1 papers were submitted from China, USA, Sri Lanka, Japan, Korea, Germany, and Thailand, respectively, through the lead authors of the papers.



Laser Scanner Application in Monitoring Short-Term Slope Deformation

Kiminori Araiba and Naoki Sakai

Abstract

In order to develop a method to estimate the risk of secondary disaster during rescue activities at a site suffering from slope failure, a method for using repeated surveying by means of laser scanner installed on the ground is proposed. Eight experiments of slope failure including one carried in a natural slope were done. To improve the accuracy in the deformation, spatial stacking of data was adopted. Availability and reliability of the method, characteristics of deformation measured are discussed.

Keywords

Laser scanner • Precursor • Delayed collapse

Introduction

Assessing and controlling the risk of a secondary disaster during a search and rescue (S&R) operation at a disaster site are difficult because both the quantity and quality of information regarding the disaster are usually inadequate due to the limited time and space available for investigation. As an example, 60 fire-fighting volunteers were killed during an S&R activity because of a secondary failure of a slope that occurred approximately 4 h after the initial slope failure, which had buried 1 person in Shigeto, Kochi prefecture, Japan, in 1972 (Nakagawa and Okunishi 1977). Figure 1 is a picture of a landslide caused by an earthquake in Fukushima Prefecture on 11 April, 2011. Fire fighters conducted S&R activity in the deposit. They recognized that the slope was still moving. The activity was finished on the next day, recovering a body.

Extensometers are frequently used to monitor movement in the slope failure site. Saito and Uezawa (1961) first discussed the prediction of failure using extensometer data; related studies have been carried out (e.g., Varnes 1982; Fukuzono 1985; Hayashi and Yamamori 1991). An extensometer is easy to set up, and it provides one-dimensional data; therefore, it is easy to handle. On the other hand, it has the following drawbacks:

1. It measures the variation in the distance between two posts. One post must be located on the stable ground and the other on the potential failure mass. However, it is difficult to recognize the failure part and stable part before failure actually occurs, especially in cases where numerous cracks exist on the slope.
2. The installation must be carried out in an unstable area.
3. The direction of movement of the sliding mass is not always parallel to the direction of the extensometer's sensitivity.

By means of repeated surveying, it is possible to monitor the spatial distribution of the deformation on a certain extent of the slope; therefore, shortcomings 1 and 3 of the extensometers can be overcome. With regard to shortcoming 2, some survey methods, such as, use of laser scanners, photographic measurements, and fringe analyses require no targets. These methods can reveal three-dimensional deformations that can provide information for understanding the mechanism of a potential failure. The application of such

K. Araiba (✉)
National Research Institute of Fire and Disaster, Jindaiji-Higashimachi
4-35-3, Chofu, Tokyo, Japan
e-mail: araiba@fri.go.jp

N. Sakai
National Institute of Earth Science and Disaster Prevention, Tennoudai
3-1, Tsukuba, Ibaraki, Japan
e-mail: sakai@bosai.go.jp



Fig. 1 A S&R activity was done in the deposit of a landslide where mass of up-slope was still sliding during activity

a method to monitoring of a slope failure can allow the monitoring to start quickly and safely, which are the desirable aspects of an emergency response.

In this study, availability and reliability of repeated surveying using a laser scanner installed on the ground for monitoring pre-failure deformation of slope was investigated by means of model slope experiments and a model slope failure experiment, and the characteristics of measured surface deformation are discussed.

Method

Method for Deformation Measurement

The laser scanner measures distance to a part of a target that lies within the angular width of the laser pulse beam divergence, and it automatically scans the designated vertical and horizontal angle widths by using designated angle intervals. The accuracy of the laser scanner is not as good as that of conventional total stations; however, it can quickly measure wide areas. The survey technique was applied to seven model tests to verify the possibility of detecting pre-failure deformation.

Specifications of the laser scanner used in this study are listed in Table 1. Result of accuracy check and method of data process were described in Araiba (2006). Definition of coordinate system is shown in Fig. 2.

Shape of slope was measured by each scan and representative Y value was calculated for 20 cm mesh by averaging data in each mesh. Deformation of slope can be detected as variations in the representative values.

Method of Experiments

Seven experiments (No. 1–7 in Table 2) involving model slope failure induced by artificial rainfall were performed in

Table 1 Specifications of laser scanner used in this study

| Precision in distance | Resolution in angle | Beam divergence | Scan rate |
|-----------------------|---------------------|-----------------|----------------|
| 8 mm | 0.009° | 1.2 m rad. | 1,000 points/s |

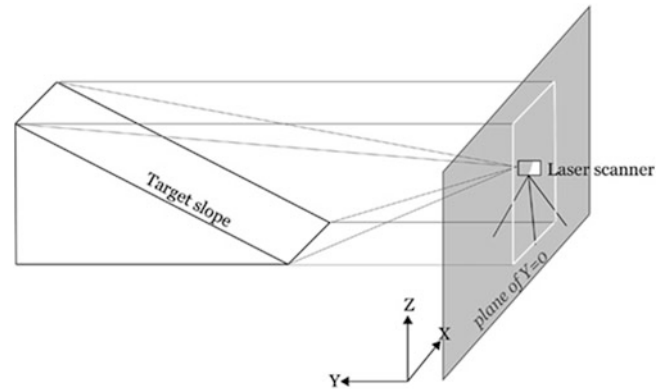


Fig. 2 Definition of coordinate system

the large-scale rainfall simulator at the National Research Institute for Earth Science and Disaster Prevention (Fukuzono and Terashima 1985).

A model slope covered by a soil layer with a height of 5 m, width of 4 m, depth of 1 m and an inclination of 30° was constructed using material listed in Table 2. Water was sprayed from nozzles that were set at a 6-m-high ceiling. A series of preparatory sprays were applied to the model slope for about 10 days. Each preparatory spray application was done for 8 h per day; its intensity was increased on a daily basis from 15 to 45 mm/h. On the final day, the intensity was increased to the value in Table 2, and water was sprayed until the model slope eventually failed. Figure 3 shows photographs of the model slope before and after the failure.

One experiment (No. 8 in Table 2) involving slope failure induced by artificial rainfall was performed in a natural slope mainly consists of decomposed granite soil. The detailed conditions of this experiment were reported in Ochiai et al. (2004). A section of the natural hill slope was isolated by driving steel plates into the ground. The isolated segment was 5 m wide, about 30 m long and had an average surface gradient of about 33°. The topsoil comprised weathered decomposed granite. The original vegetation was removed and the ground surface was covered by straw mats in order to prevent surface erosion and to improve the infiltration of water into the ground.

Water was sprayed from nozzles attached to steel pipes at a height of 2 m above the ground. The intensity of the spray was 78 mm/h. The lower half of the segmented slope failed approximately 6 h after the start of spraying. The maximum depth of the failed mass was about 1.2 m. Figure 4 shows the photographs of the slope before and after failure. The pair of white arrows indicates the location of the head of the failure.

Table 2 Experiment conditions

| No. | Material | Water spray intensity (mm/h) | Slope angle (degree) | Scanner—slope distance (m) | Horizontal scan angle (degree) | Horizontal scan step (degree) | Vertical scan angle (degree) | Vertical scan step (degree) | Time for one scan (min) | No. of data (approx.) |
|-----|-------------------------|------------------------------|----------------------|----------------------------|--------------------------------|-------------------------------|------------------------------|-----------------------------|-------------------------|-----------------------|
| 1 | River sand | 100 | 30 | 12 | 21.6 | 0.108 | 18.0 | 0.054 | 4.0 | 35,000 |
| 2 | River sand | 50 | 30 | 10.5 | 20.6 | 0.200 | 17.0 | 0.1 | 1.5 | 13,500 |
| 3 | River sand | 50 | 30 | 16.5 | 26.2 | 0.153 | 17.0 | 0.099 | 2.4 | 14,000 |
| 4 | River sand | 50 | 30 | 10.5 | 23.0 | 0.297 | 20.2 | 0.126 | 1.4 | 6,400 |
| 5 | River sand | 50 | 30 | 10.5 | 19.4 | 0.243 | 16.2 | 0.081 | 1.2 | 12,000 |
| 6 | Decomposed granite soil | 50 | 30 | 8.8 | 24.4 | 0.216 | 21.2 | 0.054 | 1.8 | 21,000 |
| 7 | Decomposed granite soil | 30 | 40 | 13.3 | 22.4 | 0.216 | 15.9 | 0.054 | 1.5 | 12,400 |
| 8 | Natural slope | 78 | 33 | 40 | 7.0 | 0.054 | 27.0 | 0.054 | 1.5 | 20,000 |

Fig. 3 Model slope used in experiments No. 1–7. (a) Before failure; (b) after failure



Fig. 4 Slope after the experiment No. 8

Result and Discussion

Characteristics of Deformation

Figure 5 shows the deformation of slope prior to failure measured in experiment No. 4. Blue colour indicates progressive deformation and red colour indicates retrogressive deformation. Distinct deformation can be observed about 880 s before the failure and the amount of deformation became larger with time.

Figure 6 shows changes in the cross section of model slope with time in experiment No. 2 where the amount of deformation is magnified by 20 times. The amount of retrogressive deformation in the upper region of slope has positive correlation with height and, on the other hand, that of progressive deformation in the lower part does not show correlation with position.

Figure 7 is a picture of slope about 1 min before failure, captured from video in experiment No. 4. Two clear lines

(compression cracks) can be seen in the lower part of slope and one tension crack can be seen on the top of the slope.

Retrogressive deformation was observed in the region below the tension crack and its amount has a positive correlation with height, which indicates that the deformation accompanied rotation. On the other hand, progressive deformation does not show such tendency. Slope seems to have dislocated at the compression cracks with slight changes in the angle of slope surface.

Reliability of Measurement

Figure 8 shows time series of specific meshes where large deformation was observed. Remarkable deformation was observed in all of tests. We can conclude that deformation prior to failure can be detected with high possibility in slopes that consists of the sandy material.

Retrogressive deformation shows acceleration with time; on the other hand, slight acceleration can be seen in progressive deformation.

Figure 9 shows result of test No. 8, which is done with natural slope. Although the surface of slope was covered by straw mats, which must have disturbed measurement, the deformation prior to the failure can be detected about 20 m away from slope. The amount of deformation is large and acceleration can be observed in Fig. 9.

The reason that acceleration can be observed in some cases and cannot in the other cases is considered due to the noise in the measurement and resolution. In order to improve the accuracy in the deformation, all laser spots within 10 cm mesh are averaged in this method, thus spatial resolution is compromised.

The dislocation at the compression is spatially sharp as shown in Fig. 7 and 10 cm mesh is larger than the area of dislocation, thus deformation values at meshes involving compression cracks must be smaller than values of dislocation. Furthermore, laser beam have a certain divergence therefore shape of laser-spot at the slope is in the shape of an ellipse. To measure more accurate value of dislocation, it is necessary to make the size of mesh smaller and area of laser-spot smaller. Further research in optimizing resolution of measurement, robustness of measurement, scan rate and scan position is necessary.

Conclusions

In order to develop a method to estimate the risk of secondary disaster during rescue activities at a site suffering from slope failure, a method for using repeated surveying by means of laser scanner installed on the ground is proposed.

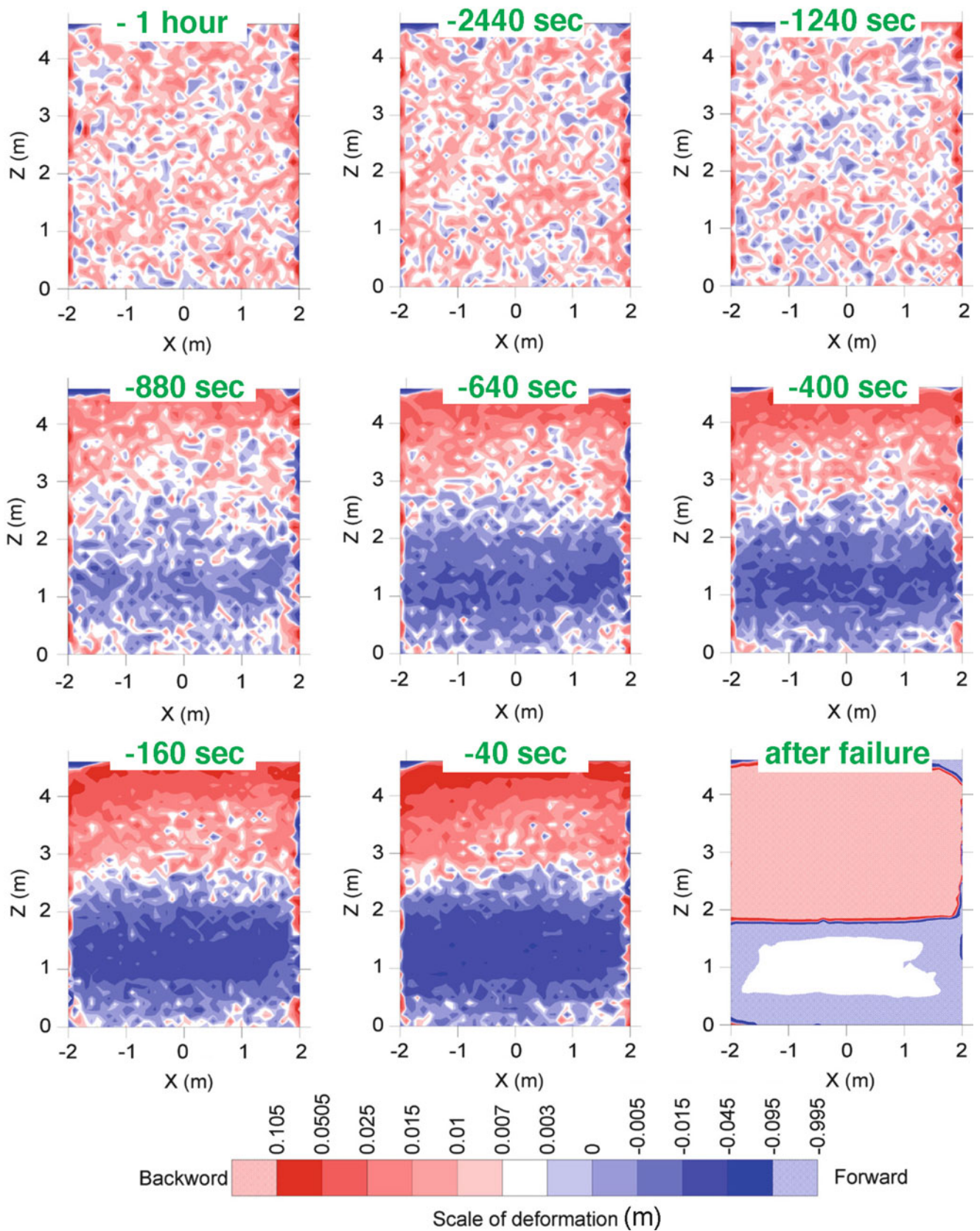


Fig. 5 Deformation measured in the experiment No. 4 projected to the X-Z plane

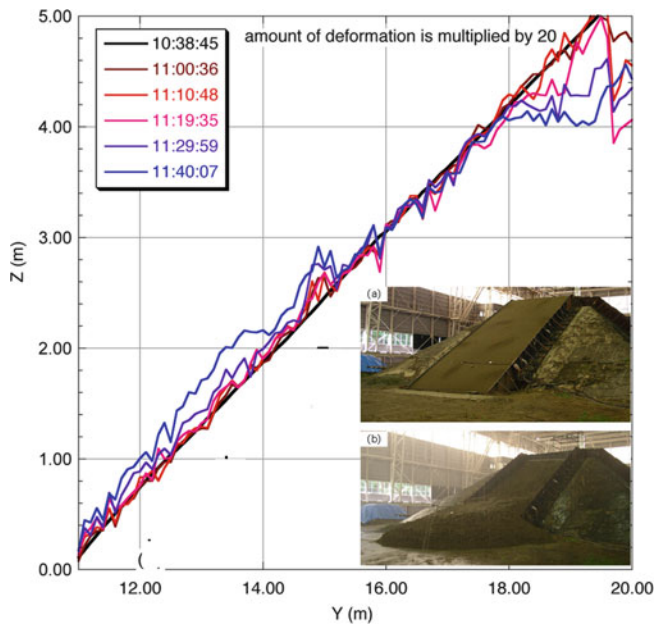


Fig. 6 Change in the cross section of slope with time. The amount of deformation is multiplied by 20



Fig. 7 Picture of model slope about 1 min before failure in experiment No. 4

Eight slope failure experiments including one carried out in a natural slope were performed. To improve the accuracy in the deformation, spatial stacking of data was adopted. Availability and reliability of the method was verified.

Progressive deformation in the upper part of slope and retrogressive one in the lower part were detected. Acceleration of deformation was observed clearly in retrogressive deformation and was not clear in progressive one.

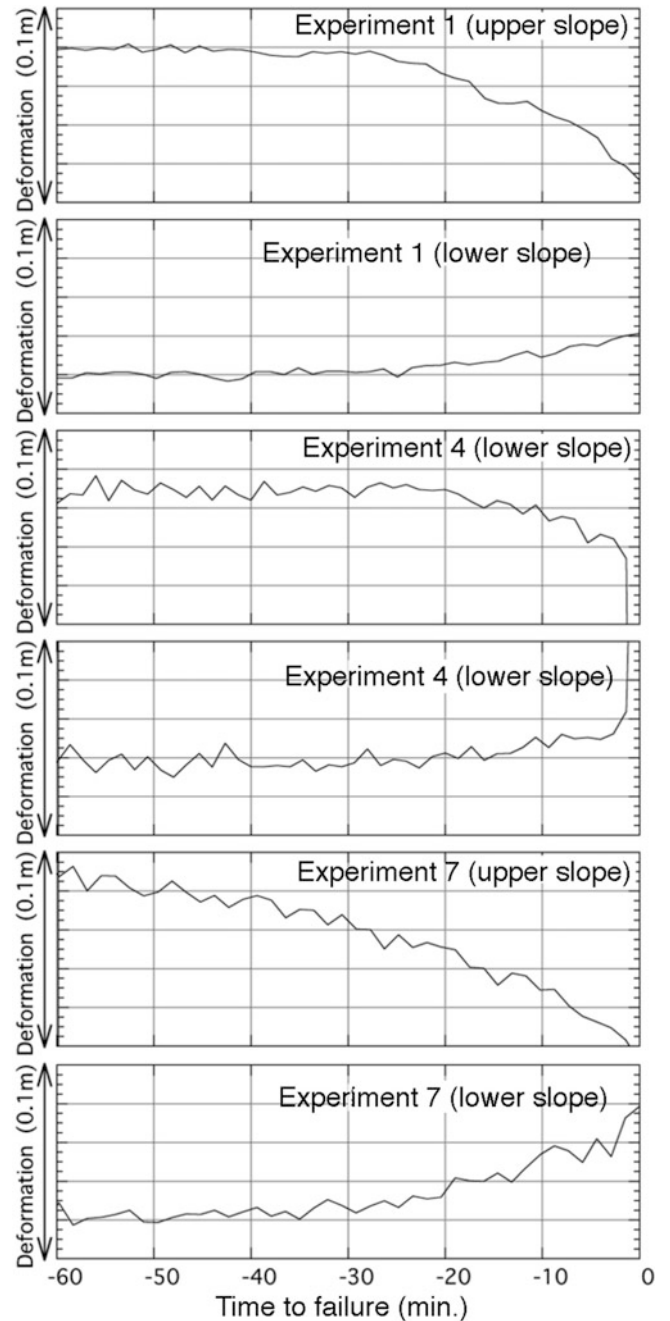


Fig. 8 Time series of deformations

One possible reason for this difference is considered to be the spatial extent of progressive deformation is limited in a small region. To make more accurate measurements for such spatially sharp deformation, it is necessary to optimize resolution of measurement, robustness of measurement, scan rate and scan position.

Acknowledgments The authors express their sincere gratitude to late Mr. Hiroshi Nagura of the Mathematical Assist Design Lab. Co. Ltd.

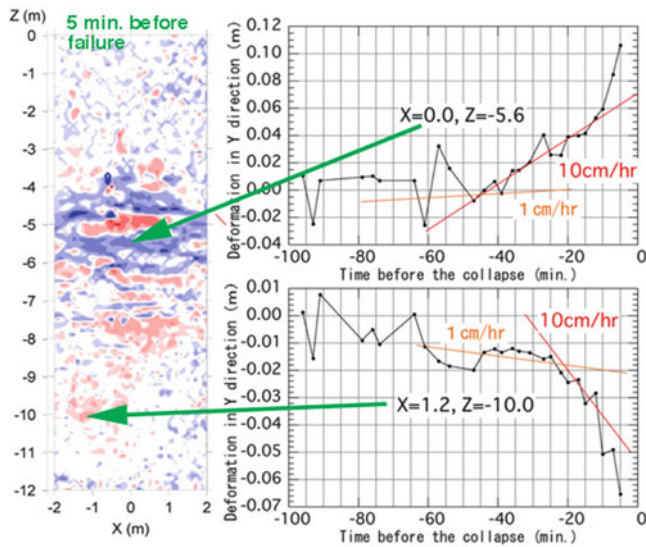


Fig. 9 Measured deformations in test No. 8

for his active cooperation throughout this study. The authors are also grateful to Mr. Teruki Fukuzono of NIED, and Hirota Ochai of FFPRI, who provided the opportunity to conduct the model and natural slope experiments. The authors appreciate, with respect, the firefighters who informed us the actual conditions and problems in rescue activities in landslides.

References

- Araiba K (2006) Study on the method for detecting and monitoring of pre-failure deformation in slope. In: Proceedings of interpret, Tokyo, pp 581–589
- Fukuzono T (1985) A new method for predicting the failure time of a slope. In: Proceedings of 9th international conference and field workshop on landslides, Tokyo, pp 145–150
- Fukuzono T, Terashima H (1985) Experimental study of slope failure in cohesive soils caused by rainfall. In: Proceedings of international symposium on erosion, debris flow and disaster prevention, Tsukuba, pp 346–349
- Hayashi S, Yamamori T (1991) Basic equation of slide in tertiary creep and features of its parameters. *Landslide (J Jpn Landsl Soc)* 28 (1):17–22
- Nakagawa A, Okunishi K (1977) A large-scale landslide at Shigeto, Kochi prefecture - part 1. Characteristics of ground structure on the landslide. Departmental bulletin paper, Bulletin of Disaster Prevention Research Institute of Kyoto University 20(B-1):209–236 (in Japanese)
- Ochiai H, Okada Y, Furuya G, Okura Y, Matsui T, Sannori T, Terajima T, Sassa K (2004) A fluidized landslide on a natural slope by artificial rainfall. *Landslides* 1(3):211–219
- Saito M, Uezawa H (1961) Failure of soil due to creep. In: Proceedings of 5th international conference on soil mechanics and foundation engineering, vol 1, Paris, pp 315–318
- Varnes DJ (1982) Time-deformation relations in creep to failure of earth materials. In: Proceedings of 7th Southeast Asian geotechnical conference, Hong Kong, pp 107–130



Experimental Research of Risk Parameters in the Process of Bedding Rock Landslide Motion

Bo Chai, Huanying Pan, and Xiang Li

Abstract

Bedding rock landslide is a common slope failure. The intensity of landslide is closely related to rock structure and terrain. It is important to assess landslide risk based on the geological structure. Firstly, the geological structure model of landslide was set up based on the affecting factors pertinent to the analysis of landslide motion. Then, a physical experimental set up was built to measure the kinematics parameters of bedding rock landslide with different geological structures. Lastly, intensity parameters of bedding rock landslides were proposed by applying test data based on risk theories. It indicates that: (1) bedding rock landslide can be divided into three structures, i.e. similar granular, layer and blocky structure. Layer structure could be divided into three subcategory considering terrain, rock structure and slip surface; (2) Three dynamic parameters of final velocity on active-slide segment (v_f), accumulation range (L1) and impact strength (ϕ) are sorted as follows: layer rock (α) > blocky rock (χ) > similar granular rock (ϕ); (3) The blocky rock (χ) has the largest of accumulation range L1, but the multilayer rock (α) has the largest of impact strength ϕ . (4) The intensities within sliding mass are sorted as follows: blocky rock (χ and δ) > multilayer rock (α and β) > granular landslide (ϕ) > single layer rock (I). Intensities in the beginning of landslide deposit area are (α , β and δ) > χ > I > ϕ ; Intensities on the top edge of deposit area are α > δ > χ > β > I.

Keywords

Bedding rock landslide • Movement process • Physical experiment • Risk

Introduction

Bedding rock slopes can easily form giant landslides which have high potential to risk and are difficult to control through present technology. Studying kinematics parameters of bedding rock landslide is of great significance to guide risk mitigation and management. Numerical modelling and

physical experiment are often used to simulate the movement of landslides. The main available numerical methods of landslides movement simulation are DDA, DEM, DAN and the FEM (Stead et al. 2006; Crosta et al. 2009; Hung and McDougall 2009). Physical experiments can be used to study the landslide motion process directly and obtain main parameters of risk assessment such as impact, run-out distance and velocity (Chen et al. 2010; Wu et al. 2011).

The run-out distance and intensity of landslide movement is highly influenced by the geological conditions, especially rock structure and topography of landslide (Margielewski 2006; McSaveney and Davies 2009; Manzella and Labiouse 2009). In order to assess the risk of the bedding rock landslide motion, a physical experiment based on common geological models is conducted to get kinematic parameters of landslide process. Moreover, semi-quantitative parameters of risk

B. Chai (✉) • H. Pan
School of Environmental Studies, China University of Geosciences,
Wuhan, Hubei 430074, China
e-mail: chai1998@126.com; phy75@163.com

X. Li
Hubei Province geological Environment Terminus, Wuhan 430034,
China
e-mail: 83263809@qq.com

assessment are proposed, considering different rock structures of landslides.

Risk Theory of Landslide Movement

The UNESCO defined the landslide risk as follow (Leroi 1996; Lee and Jones 2004).

$$\text{Risk} = \sum (H \sum (VA)) \quad (1)$$

Where, H is the hazard of landslide; V is a number between 0 and 1 that express the vulnerability of element in the risk for a specific intensity landslide; A is the quantity or economic value for elements. Among them, the hazard and vulnerability analysis are two keys of the risk assessment.

The hazard H of landslide is a probability of landslide appeared in certain period, which includes two probabilities of space and time. On the process of landslide movement, time probability is 1 and space probability can be calculated by runout distance. The vulnerabilities of elements (life and building) are related to landslide's velocity, disintegration and impact. Thus, the landslide risk is expressed by the following equation.

$$\text{Risk} = \sum P_H(x, y) \sum (f_V(v, E, D)A) \quad (2)$$

Where P_H is probability of sliding mass to reach the position (x, y) ; f_V is the vulnerability of element, which is a function of velocity v , impact energy E and disintegration mode D .

Space Probability P_H

The process of landslide motion can be divided into three zones, sliding mass (S_0), main sliding zone (S_1), accumulation zone (S_2). The space probability is the function as follow:

$$P_H = \begin{cases} 1 & (x, y) \subset (S_0 \text{ or } S_1) \\ P(L, W) & (x, y) \subset S_2 \end{cases} \quad (3)$$

Where P is the probability of runout length L and width W in accumulation zone. If the position (x, y) is located in the area of (L, W) , the probability is 1 or else is 0.

Vulnerability of Element

Li et al. (2010) proposed the vulnerability model.

$$V = f(I, R) = \begin{cases} 2 \frac{I^2}{R^2} & \frac{I}{R} \leq 0.5 \\ 1.0 - \frac{2(R - I)^2}{R^2} & 0.5 < \frac{I}{R} \leq 1.0 \\ 1.0 & \frac{I}{R} > 1.0 \end{cases} \quad (4)$$

Where I is landslide intensity, R is resistance of element to landslide. V is a value between 0 and 1.0.

The resistance to landslide is related to its own attribute, such as building structure, basic types, human's health, etc. Landslide intensity I is closely related to the sliding process. The intensity within sliding mass is mainly affected by slide acceleration a and disintegration mode D . While, the intensity outside sliding mass (in the path of sliding) is related to sliding mass thickness th , velocity v and impact E . The total intensity I can be expressed by this equation.

$$I = \begin{cases} 1 - (1 - I_a)(1 - I_D) & (x, y) \subset S_0 \\ 1 - (1 - I_{th})(1 - I_v)(1 - I_E) & (x, y) \subset (S_1 \text{ or } S_2) \end{cases} \quad (5)$$

Where I_a , I_D , I_{th} , I_v and I_E are intensities of acceleration, disintegration mode, thickness, velocity and impact. They are related to the geological structure of bedding rock landslide. A physical experiment is employed to analyse these intensities parameters.

Physical Experiment

Geological Model of Rock Landslide

Geological model of landslides contains geological mechanics model and geological structure model. In this study, the physical experiment compliers with similar structural model, but without considering the influence of groundwater and other environments.

Geological model of bedding rock landslide is proposed by considering three main factors, i.e. (1) slope dip and free face of sliding, (2) rock structure of sliding mass, and (3) slip surface (Cheng and Wang 2011; Qiao 2002). Common geological models of bedding rock landslide are shown in Table 1.

Experimental Design

The physical experiment considers the geological structure similarity and physical parameters of sliding mass. The model consisted of 2.4 m × 1.8 m tilting plane with an inclination (α) between 10° and 45°, which could be regarded as the slope of landslide. A fixed horizontal plane (3.0 m × 2.4 cm) serve as the accumulation area of landslide (Fig. 1).

The tested material of sliding mass was made from cement, sand, gravel and water, with a density of 2.10 g/cm³. Sliding masses were put into a box with the size of 20 cm × 35 cm × 15 cm. Sliding masses consisted of blocks with three sizes (19 cm × 32.5 cm × 3 cm; 6.5 cm × 11.2 cm × 3 cm; 4.5 cm × 2.5 cm × 3 cm) to simulate the rock structures of thick layer (platy), large block and small block, respectively. Seven types of sliding mass

Table 1 Geological model of common bedding rock landslide

| Geological Model | | Slip surface | Slope inclination and rock structure | Deformation and motion |
|----------------------------|------------|--|--|--|
| Similar granular landslide | | Bottom of weathered rock | Slope dip is less than 40°; Cataclastic structure of rock formed through the process of tectonics or weathering | Slope failure begins at the bottom and develops to top of slope with slow velocity |
| Layer rock landslide | Gently dip | Weak interlayer, bedding layer and joint | Slope dip is 20°–40° and bedding dip is 15°–25°; Thick layer (platy) structure of hard rock with soft underlay or layer rock with soft and hard alternating sequence | Translation slide often occurred along the weak interlayer with slow velocity |
| | Medium dip | | Slope dip is 30°–40° and bedding dip is 25°–35°; Platy, layered or block structure of rock; Slip surface is weak interlayers | Various failure modes with fast velocity |
| | Steep dip | Slope and rock layers dips are >40°; Platy structure of rock; Slip surface is bedding layer and Shear-out face | Slide with fast velocity | |
| Blocky rock landslide | | Combined by bedding and joints | Slope dip is >30°; Blocky and thick layer structure of hard rock; Slip surface is the bedding layer | Block slide with fast velocity |

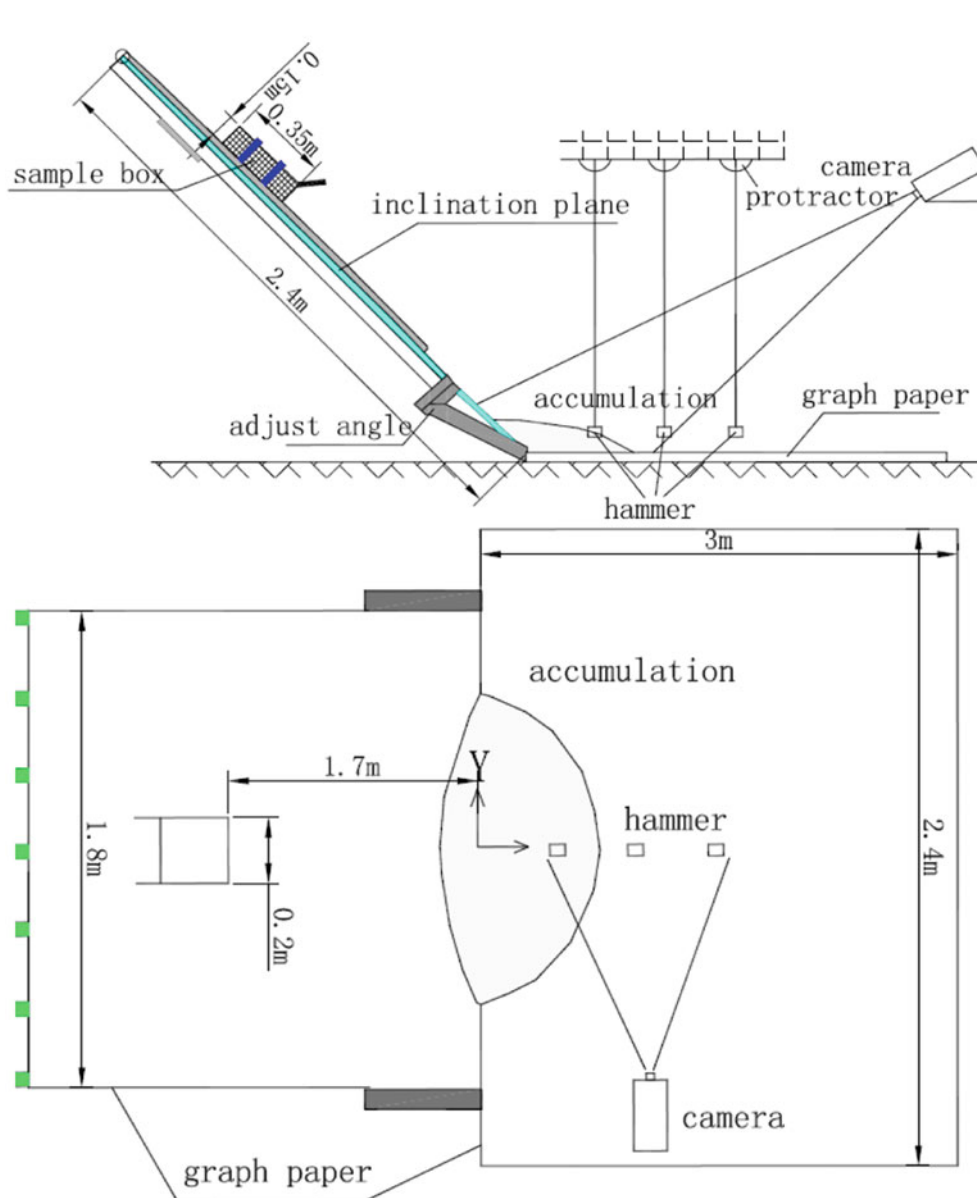

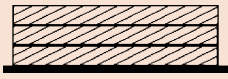

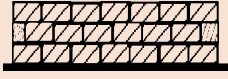
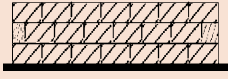



Fig. 1 Design of experimental device

Table 2 Slide body structure and character

| No. | Slide body structure | Sketch map | Slide body characteristics |
|-----|--------------------------------------|---|---|
| I | Single layer |  | Joints and cleavages are small number, sliding mass is less thickness than 10 m which is composed of intact platy or layer rock |
| II | Multilayer |  | Joints and cleavages are small number, sliding mass is 15 m to 30 m thickness and is composed of thick layer rock, e. g. limestone or sandstone |
| III | Multilayer rock with weak interlayer |  | Sliding mass is 15 m to 20 m thickness and is composed of intact platy or layer rock. Moreover, the slip surface is a thick weak interlayer |
| IV | Blocky |  | Sliding mass is 15 m to 30 m thickness and is composed of blocky rock that is from layer hard rock developing orthogonal joints |
| V | Blocky with discontinuous joints |  | Sliding mass is blocky rock with discontinuous joints and rock bridge |
| VI | Granular rock |  | Sliding mass is composed of cataclastic rock and granular rock in tectonic fracture zone |

structures were tested in the experiment (see Table 2). The smooth slip surface was simulated by the contact surface of the sliding mass and transparent resin plate upon the planes. The slip surface along weak interlayer was simulated by the contact of sands and transparent plate.

Three small hammers hanged over the horizontal plane were employed to measure landslide impact in different positions through their swing angles. The slide distance (d) was fixed on 1.7 m along the tilting plane. The movements of sliding mass were captured by two cameras. Otherwise, deposition features on horizontal plane were measured by tape, including run-out distance, width and distribution of blocks.

Data Collection Method

1. Initial velocity (v_0) and final velocity (v_t) along inclined plane: The 'Freevideo' software made the movies (camera at 33 fps) into pictures with time interval of 0.03 s. The mass's movement within 0.06 s was taken as a uniformly accelerated linear motion. Velocities between v_0 and v_t were calculated by principle of dot timer.
2. The position parameters of deposition: The parameters for whole deposition area, front edge ($L1$), back edge ($L2$), length (L) and width (W); and for main deposition area, front (l_1), back edge (l_2), length (l), width (w), maximum

thickness (th), were measured by the graph paper and steel tape.

3. Landslide impact: was measured with heavy hammer swing angle.

Results

Experimental results are listed in Table 3. The initial velocities were the velocity of the sliding mass getting away from the box; the final velocities were the velocity at the toe of the inclined plane. Landslide deposition was shown in Fig. 3, and the distances were measured from the horizontal section.

Discussions

Landslide Movement of the Different Rock Structures

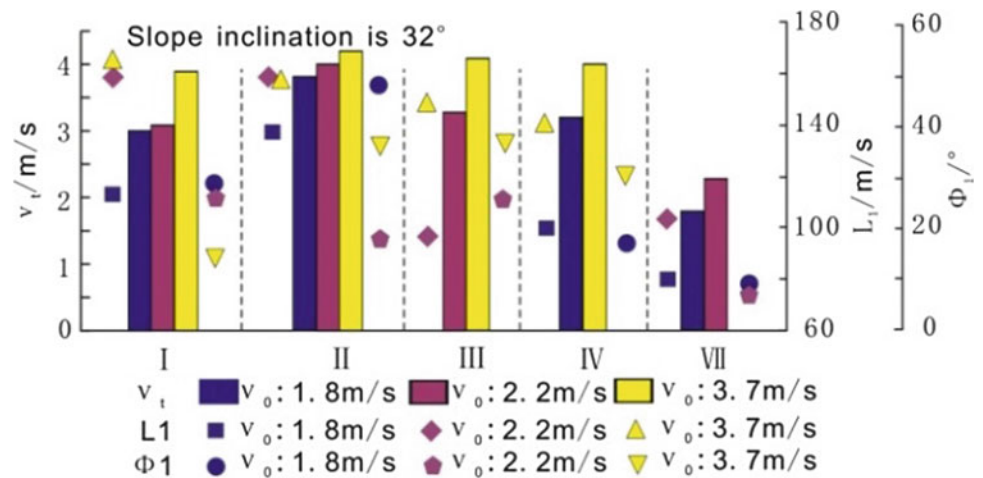
1. For same dip slope and initial velocity, the final velocities are ranked as follow: layer rock (II) > blocky rock (IV) > granular rock (VI), and the slide range ($L1$) and impact ($\phi1$) have same rank as the final velocity (Fig. 2).

Layer rock slides along slope with little fracture, energy dissipation mainly happen to slip surface for dynamic friction. Blocky rocks move along slope with

Table 3 Experimental date table

| No. | Slope dip (°) | Sliding mass structure | ν_0 (m/s) | ν_t (m/s) | L_1 (cm) | L (cm) | W (cm) | l_1 (cm) | l (cm) | w (cm) | th (cm) | $\phi_1/\phi_2/\phi_2$ (°) |
|-----|---------------|------------------------|---------------|---------------|------------|----------|----------|------------|----------|----------|-----------|----------------------------|
| 1 | 26 | I | 1 | 2.4 | 59 | 59 | 49 | 40 | 30 | / | 3 | 10/0/0 |
| 2 | 26 | I | 2.2 | 2.7 | 81 | 87 | 27 | 46 | 31 | / | 3 | 32/0/0 |
| 3 | 26 | I | 3.7 | 4.3 | 64 | 71 | 77 | 50 | 31 | 43 | 3 | 21/0/0 |
| 4 | 26 | II | 1.8 | 3.2 | 105 | 105 | 64 | 71 | 50 | 43 | 9 | 13/0/0 |
| 5 | 26 | II | 2.2 | 3.7 | 110 | 110 | 72 | 83 | 55 | 49 | 9 | 20/0/0 |
| 6 | 26 | II | 3.7 | 4 | 154 | 154 | 90 | 125 | 68 | 64 | 9 | 33/20/0 |
| 7 | 26 | III | 3.7 | 3.9 | 85 | 85 | 55 | 60 | 60 | 55 | 6.5 | 33/18/0 |
| 8 | 26 | IV | 1.8 | 3 | 100 | 79 | 67 | 83 | 58 | 37 | 9 | 40/10/0 |
| 9 | 26 | IV | 2.2 | 3.8 | 117 | 91 | 55 | 104 | 78 | 43 | 9 | 32/0/0 |
| 10 | 26 | IV | 3.7 | 4.1 | 104 | 80 | 55 | 89 | 65 | 29 | 6 | 30/10/0 |
| 11 | 26 | VI | 2.2 | 2.1 | 63 | 69 | 62 | 63 | 69 | 62 | 3 | 29/8/0 |
| 12 | 32 | I | 1.8 | 3 | 113 | 113 | 51 | 86 | 23 | / | 3 | 29/7/0 |
| 13 | 32 | I | 2.2 | 3.1 | 159 | 80 | 65 | 156 | 48 | / | 3 | 26/10/0 |
| 14 | 32 | I | 3.7 | 3.9 | 166 | 166 | 68 | 146 | 57 | / | 3 | 15/12/0 |
| 15 | 32 | II | 1.8 | 3.8 | 137 | 137 | 52 | 77 | 49 | / | 9 | 48/12/0 |
| 16 | 32 | II | 2.2 | 4 | 156 | 156 | 132 | 119 | 89 | / | 9 | 18/8/0 |
| 17 | 32 | II | 3.7 | 4.2 | 158 | 158 | 98 | 112 | 59 | / | 6 | 37/30/0 |
| 18 | 32 | III | 2.2 | 3.3 | 97 | 103 | 59 | 63 | 43 | / | 3.2 | 26/16/0 |
| 19 | 32 | III | 3.7 | 4.1 | 149 | 149 | 67 | 149 | 122 | / | 3.5 | 37/12/7 |
| 20 | 32 | IV | 1.8 | 3.2 | 100 | 61 | 54 | 86 | 47 | 42 | 6 | 17/9/5 |
| 21 | 32 | IV | 3.7 | 4 | 141 | 118 | 71 | 95 | 72 | 59 | 6 | 31/11/3 |
| 22 | 32 | VI | 1.8 | 1.8 | 80 | 85 | 59 | 68 | 68 | | 2.4 | 9/0/0 |
| 23 | 32 | VI | 2.2 | 2.3 | 104 | 115 | 72 | / | / | / | / | 7/0/0 |
| 24 | 40 | II | 1.8 | 3.5 | 115 | 105 | 27 | 110 | 31 | / | 7 | 55/40/11 |
| 25 | 40 | II | 2.2 | 3.8 | 136 | 136 | 54 | 79 | 45 | 54 | / | 60/38/0 |
| 26 | 40 | IV | 1.8 | 2.8 | 198 | 188 | 177 | 99 | 81 | 83 | 4.6 | 32/25/0 |
| 27 | 40 | IV | 2.2 | 3.2 | 265 | 247 | 156 | 96 | 78 | 94 | 5.6 | 38/16/0 |
| 28 | 40 | V | 1.7 | 3.8 | 141 | 146 | 64 | 117 | 95 | 48 | 5 | 40/25/0 |
| 29 | 40 | V | 2.2 | 4 | 175 | 207 | 45 | 143 | 96 | 45 | 6 | 43/21/5 |

Fig. 2 Comparison of movement parameter in different structure sliding body model



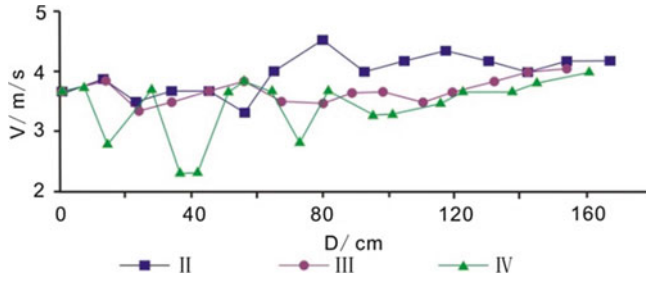


Fig. 3 Relationship of Velocity (V)—Slip distance (D) of active slide

sliding and dispersing, and energy dissipates by slip surface friction and blocks collision. Granular landslide disperses continuously when it slid along slope, so the energy dissipation is mainly from slip surface friction and mass inside which would increase with extending area. Manzella and Labiouse (2009) proposed that friction and rock collision result in energy loss during landslide movement. High-speed landslide must have a whole sliding. Speed of landslide would slow down when sliding mass were breaking up.

- For layer rock, final velocity are sorted as follows: multilayer rock (II) > multilayer rock with weak interlayer (III) > single layer rock (I). In general, acceleration and final velocity of landslide is greater with increasing number of layers and layer's thickness. In this experiment, the weak interlayer extends in sliding process and increases frictional energy dissipation, which cause its velocity to be slower than the multilayer rock. Otherwise, the landslide of I and II break partly, so their areas of accumulation are greater than III.
- Compared with Multilayer (II), blocky (IV) and blocky rock with discontinuous joints (V), they have an obvious acceleration in sliding process. Their final velocity of along slope is $V > II > IV$. McSaveney and Davies (2009) proposed that the elastic energy of slip mass almost transform into kinetic energy, there is no crushing grain contact surface energy consumption. Therefore, the rock mass of δ showed high velocity. In the steep slope, the maximum accumulation area is χ , but with the minimum impact. The impact force of α is the largest, followed by rock mass δ .
- According to the relationship between velocity and distance along inclined slope, the volatility variation of blocky rock (V) is more obvious than layer rock (II and

III). Blocky rock is easy to collide and disintegrate, which can change the instantaneous volatility of sliding (Fig. 3).

Risk Parameters in Bedding Rock Landslide Motion

The intensities parameters I_i is proposed based on experiment data. Because no real building and human is applied in the experiment, the I_i is given by a relative value as below

$$I_{ij} = \frac{X_{ij}}{\max(X_i)} \quad (6)$$

Where I_{ij} is the relative intensities of landslide with rock structure j and the index i ; X_{ij} is the kinematics parameters of landslide j with index i ; $\max(X_i)$ is the maximum of index i .

- Acceleration index I_a in sliding mass S_0 : Ratio of $(v_t - v_0)/v_0$ is a value between 0 and 1.1 according to relationship curve of velocity and distance (Fig. 3). The acceleration index I_a is positively correlated with the ratio. Figure 3 shows different variation degrees with $VII < II < IV$. Acceleration indices are determined by the ratio multiplying different coefficients, 1.0, 1.1 and 1.2.
- Disintegration index I_D in sliding mass S_0 : It is suggested by the equation, $I_D = L \times W/S_b + 2 \times L \times W/S_b$, where S_b is the area of the horizontal plane.
- Thickness index I_{th} in the zone of S2: It is the maximum thickness th of accumulation.
- Velocity index I_v in the zone of S2: It is calculated assuming the mass have a deceleration process with negative exponent.
- Impact energy index I_E in the zone of S2: It is determined by the maximum hammer swing angle.

We analysed the risk assessment parameters through Eqs. (3), (5) and (6). Risk parameters in bedding rock landslide motion are shown Table 4.

Among all bedding rock landslides, the intensities in the slide body ranks as blocky rock (IV and V) > multilayer rock (II and III) > granular rock landslide (VI) > single rock (I). But, the intensities in accumulation zone is different. At the one time zones of the initial length L_s of sliding mass, intensities are (II, III and V) > IV > I > VI. At the 2 L_s and 3 L_s of accumulation zone, the intensities show II > V > IV > III > I > VI.

Table 4 Suggested value of intensity of bedding rock landslide with different structure

| Str. | In $S_0, P_H = 1$ | | | | | | At Ls of S_2 | | | | | | At 2Ls of S_2 | | | | | | At 3Ls of S_2 | | | | | | | | | |
|------|-------------------|-------|------|-------|----------|-------|----------------|------|-------|----------|-------|-------|-----------------|-------|----------|-------|-------|------|-----------------|----------|-------|-------|------|-------|----------|-------|-------|------|
| | I_a | I_D | I | P_H | I_{th} | I_v | I_E | I | P_H | I_{th} | I_v | I_E | I | P_H | I_{th} | I_v | I_E | I | P_H | I_{th} | I_v | I_E | I | P_H | I_{th} | I_v | I_E | I |
| I | 0.27 | 0.38 | 0.55 | 1 | 0.37 | 0.83 | 0.53 | 0.95 | 0.67 | 0.37 | 0.17 | 0.12 | 0.54 | 0.50 | 0.37 | 0.00 | 0.00 | 0.00 | 0.50 | 0.37 | 0.00 | 0.00 | 0.00 | 0.50 | 0.37 | 0.00 | 0.00 | 0.37 |
| II | 0.59 | 0.71 | 0.88 | 1 | 1.00 | 0.97 | 0.86 | 1.00 | 1.00 | 1.00 | 0.35 | 0.45 | 1.00 | 1.00 | 1.00 | 0.15 | 0.03 | 0.03 | 1.00 | 1.00 | 0.15 | 0.03 | 1.00 | 1.00 | 1.00 | 0.15 | 0.03 | 1.00 |
| III | 0.20 | 0.68 | 0.74 | 1 | 0.54 | 0.97 | 0.77 | 1.00 | 1.00 | 0.54 | 0.27 | 0.37 | 0.79 | 0.33 | 0.43 | 0.10 | 0.05 | 0.05 | 0.79 | 0.33 | 0.10 | 0.05 | 0.51 | 0.37 | 0.28 | 0.03 | 0.03 | 0.56 |
| IV | 0.47 | 1.00 | 1 | 1 | 0.81 | 0.88 | 0.76 | 0.99 | 1.00 | 0.81 | 0.28 | 0.28 | 0.90 | 0.71 | 0.37 | 0.28 | 0.03 | 0.03 | 0.90 | 0.71 | 0.28 | 0.03 | 0.56 | 0.37 | 0.28 | 0.03 | 0.03 | 0.72 |
| V | 1.00 | 0.83 | 1 | 1 | 0.68 | 1.00 | 1.00 | 1.00 | 1.00 | 0.68 | 0.44 | 0.55 | 0.92 | 1.00 | 0.68 | 0.08 | 0.06 | 0.06 | 1.00 | 1.00 | 0.08 | 0.06 | 0.72 | 0.37 | 0.28 | 0.03 | 0.03 | 0.56 |
| VI | 0.00 | 0.67 | 0.67 | 1 | 0.35 | 0.53 | 0.36 | 0.80 | 0.67 | 0.35 | 0.08 | 0.06 | 0.44 | 0.00 | 0.00 | 0.00 | 0.00 | 0.00 | 0.00 | 0.00 | 0.00 | 0.00 | 0.00 | 0.00 | 0.00 | 0.00 | 0.00 | 0.00 |

Note: in the table, L_s is slide body initial length, $2L_s$ is accumulation zone distance which is two times of sliding body initial length

Conclusion

For bedding rock landslide, the geological structure is very important to its' motion and intensity. It is necessary to consider topography, rock structure and slip surface in common geological model for risk assessment.

By building the model, risk can be analyzed by suggested parameters of intensity. Moreover, it is necessary to get abundant risk samples to transform the relative parameters into absolute values in special region.

Acknowledgments The research was funded by the National Natural Science Foundation of China (No. 41202247) and the Fundamental Research Funds for the Central Universities, China University of Geosciences(Wuhan)(No. CUGL110218).

References

- Chen HK, Tang HM, Xian XF, Zhang YP (2010) Experimental model of debris flow impact features. *J Chongqing Univ* 33:114–119 (In Chinese)
- Cheng YG, Wang YF (2011) Research on contribution rate for dip angle of bedding landslide. *Rock Soil Mech* 12:3708–3712 (In Chinese)
- Crosta GB, Imposimato S, Roddeman D (2009) Numerical modelling of entrainment/deposition in rock and debris-avalanches. *Eng Geol* 109:135–145
- Hungr O, McDougall S (2009) Two numerical models for landslide dynamic analysis. *Comput Geosci* 35:978–992
- Lee EM, Jones D (2004) *Landslide risk assessment*. Thomas Telford, London, 454
- Leroi E (1996) Landslide hazard-risk maps at different scales: objectives, tools and development. In: Senneset K (eds) *Landslides-Glissements de Terrain*. 7th International symposium on landslides, 17–21 June 1996. Balkema, Trondheim, Norway. pp 35–51
- Li Z, Nadim F, Huang H, Uzielli M, Lacasse S (2010) Quantitative vulnerability estimation for scenario-based landslide hazards. *Landslides* 7:125–134
- Manzella I, Labiouse V (2009) Flow experiments with gravel and blocks at small scale to investigate parameters and mechanisms involved in rock avalanches. *Eng Geol* 109:146–158
- Margielewski W (2006) Structural control and types of movements of rock mass in anisotropic rocks: case studies in the Polish Flysch Carpathians. *Geomorphology* 77:47–68
- McSaveney MJ, Davies TR (2009) Surface energy is not one of the energy losses in rock comminution. *Eng Geol* 109:109–113
- Qiao JP (2002) Structure and shape of landslide. *Chin J Rock Mech Eng* 21:1355–1358 (In Chinese)
- Stead D, Eberhardt E, Coggan JS (2006) Developments in the characterization of complex rock slope deformation and failure using numerical modelling techniques. *Eng Geol* 83:217–235
- Wu Y, Liu DS, Li MJ (2011) Impact energy calculation for rock slope and quantitative assessment of vulnerability for emement at risk. *Chin J Rock Mech Eng* 30(5):901–909 (In Chinese)



Calculation of Permeability of Clay Mineral in Natural Slope by Using Numerical Analysis

Junghae Choi, Byung-gon Chae, Katsuyuki Kawamura, and Yasuaki Ichikawa

Abstract

A natural landslide is mainly occurred by rainfall, snowmelt, earthquakes and construction works. Especially, the role of rainfall or snowmelt in slope stability is very important because it causes a decrease in shear strength by reducing the soil cohesion. If clay exists in the weathered soil, the physical characteristics such as viscosity and permeability are generally different from the condition without the clay. In this case, changes of permeability or viscosity due to the rainfall or snowmelt are dependent on the content of clay in soil. In order to calculate the variation in permeability according to the content of clay in soil, many researchers have conducted laboratory experiments or in-situ tests in the field. However, it is difficult to determine the property of the clay such as a viscosity because of its poor crystalline property. In order to solve this problem and to calculate permeability of clay under various dry densities, we used molecular dynamic (MD) simulation to examine the viscosity of micro scale and homogenization analysis (HA) method to expand micro material property to macro scale. In this research, we determined the permeability of clay with various dry densities due to the rainfall or snowmelt conditions by using MD/HA method.

Keywords

Molecular dynamics • Homogenization analysis • Viscosity • Permeability • Clay

Molecular Structure of Kaolinite

Radioactive waste disposal facilities have been planned in formations containing kaolinite, for example in the Opalinus Clay of Switzerland, because of their low permeability and resultant diffusion-dominant characteristics. For safely isolating radioactive substances for a long time, it is essential to fully understand the physical and chemical properties of the host rock. For this purpose, authors here present a unified

procedure of molecular dynamics (MD) simulation and homogenization analysis (HA) for water-saturated kaolinite clay. This MD/HA procedure was originally developed for analyzing seepage, diffusion and consolidation phenomena of bentonite clay. In the current research, a series of MD calculations were performed for kaolinite and kaolinite-water systems, appropriate to a saturated deep geological setting. Then, by using HA, the seepage behavior is determined for conditions of the spatial distribution of the water viscosity associated with some configuration of clay minerals. The seepage behavior is calculated for different void ratios and dry densities.

Kaolinite is a 1:1 clay mineral; composed of alternating silica tetrahedral and aluminum octahedral sheets. To achieve charge balance, the apical oxygens of the silica tetrahedra are incorporated into the octahedral sheet. In the plane of atoms common to both sheets, two-thirds of the

J. Choi (✉) • B.-g. Chae
Korea Institute of Geoscience and Mineral Resources, 124 Gwahangno, Yuseong-gu, Daejeon 305-350, South Korea
e-mail: jhchoi@kigam.re.kr

K. Kawamura • Y. Ichikawa
Department of Urban Environmental Development, Okayama University, Okayama, Japan

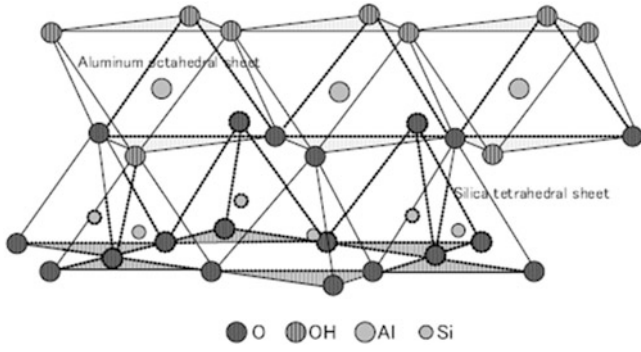


Fig. 1 Diagrammatic sketch of the structure of kaolinite

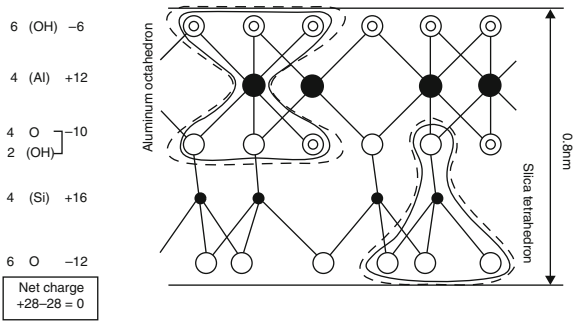


Fig. 2 Charge distribution in kaolinite

atoms are oxygens and are shared by both silicon and the octahedral aluminum cations. The remaining atoms in this plane comprise hydroxyl molecules (OH), located in such a way that each sheet is directly below the base of a silica tetrahedron. A diagrammatic sketch of the kaolinite structure is shown in Fig. 1. The structural formula is $\text{Si}_4\text{Al}_4\text{O}_{10}(\text{OH})_8$, and the charge distribution is indicated in Fig. 2. Mineral particles of the kaolinite subgroup consist of these basic units, stacked in the c -direction. The bonding between successive layers is by both van der Waals forces and hydrogen bonds. The extensive hydrogen bonding, in particular, is sufficiently strong that there is no interlayer swelling. Because of a slight difference of oxygen-to-oxygen distance in the tetrahedral and octahedral layers there is some distortion of the ideal tetrahedral network. As a result, kaolinite is triclinic instead of monoclinic.

Homogenization Analysis for the Seepage

Seepage Problem by HA

A two-scale HA is introduced for a macro-domain Ω^0 using the coordinate system x^0 and a micro-domain Ω^1 using the coordinate system x^1 . Both coordinates are related as $x = x^0/\varepsilon$ by the scale factor ε .

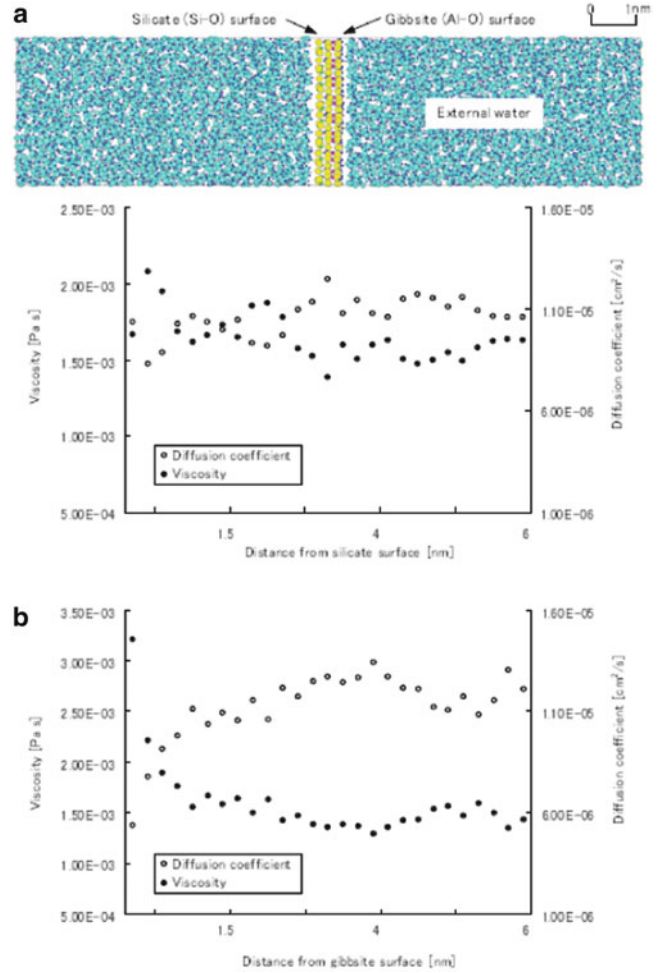


Fig. 3 Diffusivity and viscosity of water in the neighbourhood of a silicate surface (a) and gibbsite surface (b)

To represent incompressible flow, the following Stokes equation is introduced:

$$\rho \left(\frac{\partial V_i^e}{\partial t} + V_j^e \frac{\partial V_i^e}{\partial x_j} \right) = - \frac{\partial P^e}{\partial x_i} + \frac{\partial}{\partial x_j} \left(\eta \frac{\partial V_i^e}{\partial x_j} \right) + f_i \quad \text{in } \Omega_f \quad (1)$$

$$\frac{\partial V_i^e}{\partial x_i} = 0 \quad \text{in } \Omega_f \quad (2)$$

where ρ is the density of water, V^e is the water velocity in the fluid domain Ω_f , P^e is the pressure, f_i is the body force, and η is the water viscosity. Note that we consider a steady state, and hence the convective term $V_j \partial V_i / \partial x_j$ of the left-hand side (LHS) of (1) vanishes in the perturbation procedure, and we can ignore the LHS terms from the beginning. The superscript e implies a variable which varies rapidly in the microscale domain. The viscosity distribution calculated by MD is shown in Fig. 3 for an isolated kaolinite layer.

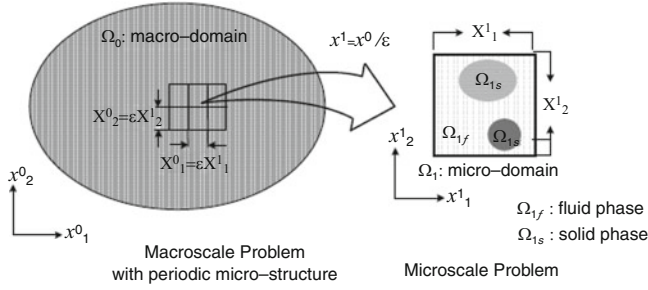


Fig. 4 Two-scale domains for homogenization analysis

Naturally the velocity vanishes on the fluid-solid interface Γ :

$$V_i^\varepsilon = 0 \quad \text{on } \Gamma \quad (3)$$

Now we introduce ‘two-scale domains’ for homogenization analysis (Fig. 4); that is, the macro-domain Ω_0 and micro-domain Ω_1 . Coordinate systems that were set x^0 in Ω_0 and x^1 in Ω_1 which are related by

$$x^1 = \frac{x^0}{\varepsilon} \quad (4)$$

Since the two-scale coordinates are employed, the differentiation is changed to

$$\frac{\partial}{\partial x_i} = \frac{\partial}{\partial x_i^0} + \frac{1}{\varepsilon} \frac{\partial}{\partial x_i^1} \quad (5)$$

By using the parameter ε we introduce the following perturbations:

$$\begin{aligned} V_i^\varepsilon(x) &= \varepsilon^2 V_i^0(x^0, x^1) + \varepsilon^3 V_i^1(x^0, x^1) + \dots \\ P^\varepsilon(x) &= P^0(x^0, x^1) + \varepsilon P^1(x^0, x^1) + \dots \end{aligned} \quad (6)$$

The perturbed terms of the right-hand sides (RHS) of (6) are assumed to be periodic:

$$\begin{aligned} V_i^\alpha(x^0, x^1) &= V_i^\alpha(x^0, x^1 + X^1) \\ P^\alpha(x^0, x^1) &= P^\alpha(x^0, x^1 + X^1) \end{aligned} \quad (7)$$

where X^1 is the size of a microscale unit cell.

Equations (5) and (6) were substituted into (1) and (2) to get a set of perturbation equations. Due to the ε^{-1} -term resulting from (1) we understand that p^0 is a function of only the macro-coordinates x^0 . The ε^0 -term resulted from (1) is given by

$$-\frac{\partial P^1}{\partial x_i^1} + \frac{\partial}{\partial x_j^1} \left(\eta \frac{\partial V_i^0}{\partial x_j^1} \right) = \frac{\partial P^0}{\partial x_i^0} - f_i \quad (8)$$

The body force f usually works in the macro-domain Ω_0 ($f = f(x^0)$), and the RHS terms of (8) are functions only of

x^0 . Thus we can introduce the separation of variables into $P^1(x^0, x^1)$ and $V^0(x, x^1)$ as

$$\begin{aligned} V_i^0(x^0, x^1) &= - \left| \frac{\partial P^0(x^0)}{\partial x_j^0} - f_j(x^0) \right| v_i^j(x^1) \\ P^1(x^0, x^1) &= - \left| \frac{\partial P^0(x^0)}{\partial x_j^0} - f_j(x^0) \right| p^j(x^1) \end{aligned} \quad (9)$$

These are substituted into (8), and we get the following *microscale incompressible Stokes' equations*:

$$\begin{aligned} -\frac{\partial P^k}{\partial x_i^1} + \frac{\partial}{\partial x_j^1} \left(\eta \frac{\partial v_i^k}{\partial x_j^1} \right) + \delta_{ik} &= 0 \quad \text{in } \Omega_{1f} \\ \frac{\partial v_i^k}{\partial x_j^1} &= 0 \quad \text{in } \Omega_{1f} \end{aligned} \quad (10)$$

where $v(x^1)$ and $p^k(x^1)$ are characteristic functions for velocity and pressure, respectively (δ_{ik} is Kronecker's delta). By solving (10) under periodic conditions the characteristic functions, which reflect a complex geometry of the micro-scale domain, were obtained. Let us operate an integral average of (9) in the micro-domain, producing Darcy's law as,

$$\begin{aligned} \tilde{V}_i^0(x^0) &= \langle V_i^0(x^0, x^1) \rangle = -K_{ji} \left| \frac{\partial P^0(x^0)}{\partial x_j^0} - f_j(x^0) \right| \\ K_{ij} &\equiv \langle V_j^i(x^1) \rangle = \frac{1}{|\Omega_{1f}|} \int_{\Omega_{1f}} V_j^i(x^1) dx^1 \end{aligned} \quad (11)$$

where $|\Omega_{1f}|$ is the volume of the micro-domain Ω_1 and represents an averaging operation in the micro-domain. We call K_{ij} the HA-permeability.

Equation (8) gives a mass conservation relationship between the micro-domain and the macro-domain. When averaging this in the micro-domain, the second term of LHS vanishes due to the periodicity; then substituting Darcy's law (9) yields the *macroscale incompressible permeability equation*:

$$\frac{\partial \tilde{V}_i^0}{\partial x_i^0} = 0 \Rightarrow -\frac{\partial}{\partial x_i^0} \left[-K_{ji} \left\{ \frac{\partial P^0(x^0)}{\partial x_j^0} - f_j(x^0) \right\} \right] = 0 \quad (12)$$

The water velocity and pressure are approximated as

$$V_i^\varepsilon(x^0) \simeq \varepsilon^2 V_i^0(x^0, x^1), \quad P^\varepsilon(x^0) \simeq P^0(x^0) \quad (13)$$

It should be remembered that, in HA, the distribution of velocity and pressure are calculated in the micro-domain. The procedure to solve the total HA-seepage problem is

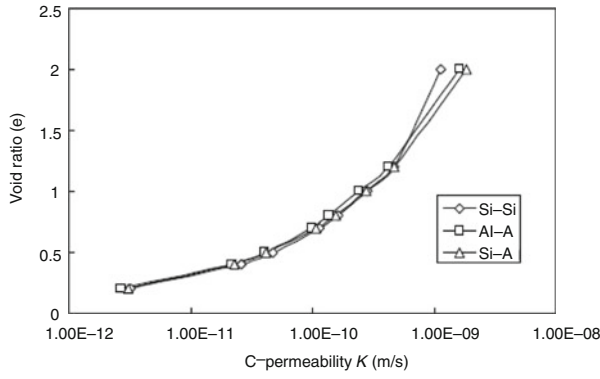


Fig. 5 Relationship between C-permeability (K^*) and void ratio (e)

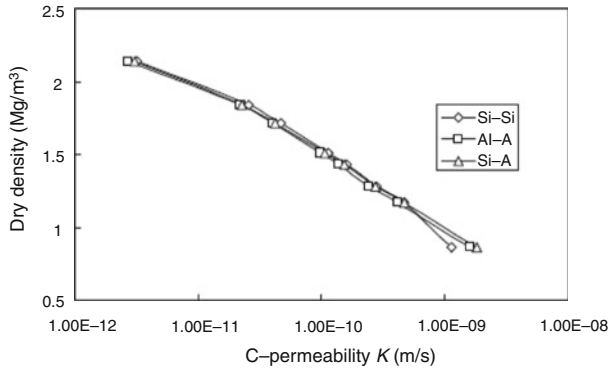


Fig. 6 Relationship between C-permeability (K^*) and dry density (ρ_d)

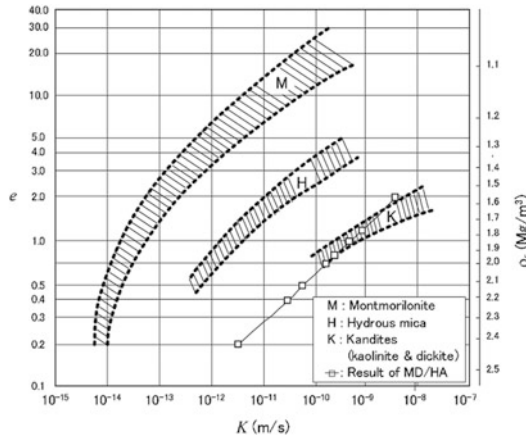


Fig. 7 Permeabilities given by HA and by Pusch

summarized as follows: first, we solve micro-scale equation (10) and get V_i^k and P^k , then determine Darcy's coefficient K_{ij} from (11). Next by solving macro-scale equation (12), we get the macro-pressure and velocity fields. In classical geomechanics, Darcy's law is written as

$$\hat{V}_i^* = -K_{ij}^* \frac{\partial \phi}{\partial x_j^0}, \quad \phi = \frac{p}{\rho g} + \xi \quad (14)$$

Where ϕ is the total head, $p/\rho g$ is the pressure head, ξ is the elevation head, and g is the gravity constant. K_{ij}^* is called C-permeability and is defined as

$$K_{ij}^* = \varepsilon^2 \rho g K_{ij} \quad (15)$$

Conclusions

Macroscale and microscale models of the kaolinite-water permeability system analyzed here are shown in Fig. 7. The number of mineral layers in one stack is assumed to be eight. It is known that one layer is connected to others by hydrogen bond, and the separation distance is calculated as 0.8 nm by the MD simulation. The density of solid part of the mineral is also calculated by MD as 2.56 g/cm³. A distribution of viscosity calculated by MD is shown in Fig. 3. The distance between two stacks is determined by the overall dry density of clay. We assume that the kaolinite stacks are randomly distributed; then the averaged permeability K^* is estimated as $K^* = K_{11}^*/3$. The relationships between the C-permeability (K^*), the void ratio (e) and the dry density (ρ_d) are plotted in Figs. 5 and 6. These relations can curve fit as

$$\begin{aligned} \log K^* &= 1 \times 10^{-9} \rho_d^{-6.709} \\ \log K^* &= 3 \times 10^{-10} e^{2.775} \end{aligned} \quad (16)$$

where the unit of K^* is in m/s.

In this paper, a unified MD/HA method for analyzing the seepage problem in kaolinite was presented. The results obtained by this method are similar to the experimental data, which supports the validity of the method (Fig. 7).

Acknowledgments This research was supported by the Public Welfare & Safety Research Program through the National Research Foundation of Korea (NRF) funded by the Ministry of Science, ICT & Future Planning (2012M3A2A1050983).

References

- Delville A (1995) Monte Carlo simulations of surface hydration: an application to clay wetting. *J Phys Chem* 99:2033–2037
- Delville A, Sokolowski A (1993) Adsorption of vapor at a solid interface: a molecular model of clay wetting. *J Phys Chem* 97:6261–6271
- Du J, Cormack AN (2004) The medium range structure of sodium silicate glasses: a molecular dynamics simulation. *J Non-Cryst Solids* 349:66–79
- Ichikawa Y, Kawamura K, Nakano M, Kitayama K, Kawamura H (1999) Unified molecular dynamics and homogenization analysis

- for bentonite behaviour: current results and the future possibility. *Eng Geol* 54:21–31
- Ichikawa Y, Kawamura K, Nakano M, Kitayama K, Seiki T, Theramast N (2001) Seepage and consolidation of bentonite saturated with pure-or salt-water by the method of unified molecular dynamics and homogenization analysis. *Eng Geol* 60:127–138
- Kawamura K, Ichikawa Y (2001) Physical properties of clay minerals and water -By means of molecular dynamics simulations. *Bull Earthq Res Inst Univ Tokyo* 76:311–320
- Kawamura K, Ichikawa Y, Nakano M, Kitayama K, Kawamura H (1999) Swelling properties of smectite up to 90C: In situ X-ray diffraction experiments and molecular dynamics simulations. *Eng Geol* 54:75–79
- Salles J, Thovert JF, Delannay R, Prevors L, Auriault JL, Adler PM (1993) Taylor dispersion in porous media. Determination of the dispersion tensor. *Phys Fluids A* 5(10):2348–2376
- Skipper NT, Sposito G, Chang FRC (1995) Monte Carlo simulation of interlayer molecular structure in swelling clay minerals: 2. Monolayer hydrates. *Clays Clay Miner* 43(3):294–303



Study on the Microscopic Structure Characteristics of the Gray Matter Slate

Maolin Deng, Qiang Xu, Xing Zhu, Guojun Cai, and Guang Zheng

Abstract

The changes of the stress state and strength of the slip zone in a landslide are determined by the material composition, micro-structural feature, and formation mechanism of the slip zone. It affects the activities of the landslide. In this paper, the mineral composition of the slip zone, which is composed of soft rock of the gray matter slate, is identified by DMAX-3C X-ray diffractometer, polarizing microscope, and scanning electron microscope (SEM). Results show that the content of calcite reaches up to 68 %. There are no changes in the slickensides composition of the sliding surface material. The microscopic structure has been analyzed by different experiments. The results show that the weak zone is composed of the banded calcareous tuffaceous slate, and its structure is characterized by gray black striped fine grains, heterogranular and irregular, and cryptocrystal texture. There is clay on these surfaces, and can be cut into pieces, so it is easy to track and accommodate the shear failure surfaces.

Keywords

The gray matter slate • The slip zone soft rock • Microscopic structure • Mineral composition

Introduction

The tilted mountain constructed with thick limestone is widely distributed in the limestone territory of the south-western China, including cities of Chongqing, Hubei, Guizhou, Yunnan and Sichuan. Most of the landslides occurred in those mountains caused large number of casualties and great loss of property. Liu et al. (1995), researched the dangerous rock mass whose weak zone was carbonaceous shale and mudstone took place in Lianzi cliff of Zigui county, Hubei province in 1964. Man (1991) studied the Zhongyang landslide that occurred on January 10,

1988, in Wuxi, Chongqing. The landslide volume was $7.65 \times 10^6 \text{ m}^3$ and weak zone was on coal. The landslides caused the death of 26. The Jiguanling landslide is located in Wulong, Chongqing. Volume of landslide was 4.24 million m^3 and weak zone was located on shale. This landslide blocked the Yangtze River. Huang (2008) mentioned that the Yankou landslide, located in Yinjiang, Guizhou, killed five people and caused economic losses of 150 million Yuan. The slip zone was made of a thin layer of shale. Xu et al. (2009, 2010) described that the Jiweishan landslide, located in Wulong, Chongqing, produced a volume of 5 million m^3 and killed 74 people.

Liu et al. (2004) argued that the type, material composition, microstructural features, formation mechanism etc. of the slip zone determine the changes in its stress state and strength, which would affect the activities of a landslide. So, the research on the slip zone provides an in-depth knowledge pertinent to the development of landslide. The study on the mechanism of slip zone clay cracks presented were similar to the

M. Deng • Q. Xu (✉) • X. Zhu • G. Cai • G. Zheng
State Key Laboratory of Geohazard Prevention and Geoenvironment
Protection, Chengdu University of Technology, Chengdu 610059,
China
e-mail: dmltop@163.com; xuqiang_68@126.com; zhuxing330@163.com; 33531278@qq.com; 306956070@qq.com

research of slip soil performed by Wang (2006). Li (2007) made in-depth studies on the formation, evolution process and mode of slip zone of the large bedrock bedding landslide. Gibo (2002) and others performed systematic and in-depth research about the strength properties of sliding zone soil. After the Jiweishan landslide in Wulong and Deng (2012), Feng et al. (2012a, b), Liu (2010), Xu et al. (2009, 2010), Yin (2010, 2011), Zhang et al. (2010), Zou et al. (2012) have rushed to the scene, carried out a detailed geological disaster research work and obtained a wealth of research information. Liu (2010), Xu et al. (2010), Yin (2010, 2011) made in-depth study on the formation mechanism of the landslide, and Zhang et al. (2010) analyzed the high-speed remote motion characteristics of the landslide. However, Deng et al. (2009) studied the microscopic structure of soft rock located in the slip zone, which is rare. In recent years, with the improvement of science and technology, the equipment in rock mechanics and the test technique have been greatly advanced, so the achievements in this regard are also increasingly high.

The research about the microscopic structure of soft rock of slip zone is of great significance to the disaster prevention and mitigation of geological disasters in the thick limestone regions of the southwestern China, where the mining, river, road and cities have been or are planned to be constructed. In the present paper, on the basis of the field macro geological survey of the Jiweishan landslide, the mineral composition, microscopic structure of soft rock of slip zone were studied by using DMAX-3C diffractometer (light filtering by CuK α , Ni), polarizing microscope, scanning electron microscope (SEM), and some valuable conclusions have been drawn.

Overview of the Jiweishan Landslide

At 3 pm on June 5, 2009, a tremendous landslide occurred at the Jiweishan in Tiekuang Township, Wulong County, Chongqing City. The thick limestone slipped down along a low angle dip inter-bedded shale plane from 1,300 m cliffs (the height difference of about 200 m). Blocked by the opposite steep creek wall, the sliding rock mass changed its direction and travelled further along the 22,000 m along Tiejiang ditch (Fig. 1). The landslide body was mainly constituted by the Permian off-white thick-bedded micritic limestone, dark gray medium to thick bedded asphaltene-containing limestone, argillaceous limestone and limy-slate mezzanine etc. The area was about 84,000 m², and its volume was about 5×10^6 m³.

The slip zone generally developed along the rock strata, with the occurrence of $30 \sim 355^\circ \angle 22 \sim 30^\circ$. There are a large number of scratches on the slip surface along the sliding direction and a large number of white slickensides were developed on the slip surface, as can be seen in Fig. 2. The Jiweishan landslide with a dual structure in Wulong is a



Fig. 1 Image of the Jiweishan landslide



Fig. 2 Destruction of the samples and the observed slickensides

typical landslide located in tilted thick limestone territory. The soft rock of slip zone is the gray matter slate of 5 ~ 20 cm thickness. Under the combined effect of long-term mining activity in the lower part of the landslide and blocked sliding in the leading edge, the slope slowly crept. This status has lasted for half a century, and therefore the structure of the soft rock of slip zone changed. The field landslide survey results show that microscopic structure of soft rock of slip zone plays an important role in accelerating the creep and eventually rapid starting of the landslide.

Test Equipment and Samples Preparation

The mineral composition is analyzed by the DMAX-3C diffractometer (light filtering by CuK α , Ni). Samples used in the micro tests of the rock were prepared according to the standard of the polarizing microscope and scanning electron microscope (SEM) powdered sample preparation. The powdered samples were then tested according to the polarizing microscope and scanning electron microscope (SEM) standards. To observe its microscopic characteristics, the micro testing of the sample was done with the polarizing microscope (OLYMPUS CX21P) and scanning electron microscope (SEM) S-3000 N/H manufactured by Hitachi. The test program was conducted in College of Materials

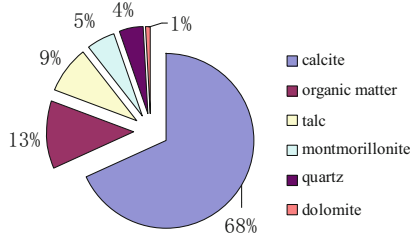


Fig. 3 Proportions of various minerals in the sliding zone materials

and Chemistry Engineering and State Key Laboratory of Geohazard Prevention and Geoenvironment Protection, Chengdu University of Technology.

Mineral Compositions

The mineral composition of the soft rock sample is analyzed by the DMAX-3C diffractometer (light filtering by CuK α , Ni). X-ray diffraction pattern is shown in Fig. 3. The identification result of the mineral compositions shows that the content of calcite reaches up to 68 %, whereas the proportion of the organic matter was 13 %, talcum was 9 %, montmorillonite was 5 %, quartz was 4 % and dolomite was 1 % (Fig. 4). With water dissolution and transportation, the calcite permeated and then stagnated in the striped calcareous gray matter slate. The high organic matter content reduces the compressive strength and shear strength of the layer of striped calcareous gray matter slate. The talcum is soft, delicate and smooth. It provides the conditions for the long creeping and rapid movement of the landslide after its initiation. There is a layer of slickensides covering the sliding surface, observed during the field investigation of soft rock of slip zone and shearing specimens. No changes were observed in the slickensides composition when they were analyzed by the DMAX-3C diffractometer (The red is X-ray diffraction of the slip zone slickensides, the light blue is X-ray diffraction of the slip zone soft rock) (Fig. 4).

Microstructure Features

The test results of the polarizing microscope structure show that the lithology of the weak zone is the striped calcareous gray matter slate, the structure is granular and aphanitic structure is gray-black inclusion off-white stripe fine-grained irregular inequi-granular. The slaty cleavage of the rock in weak zone is more significantly developed. The main rock components are off-white fine-grained carbonate and black carbonaceous mudstone.

The rock body is the dust-color inclusion of white stripes fine-grained lepidoblastic texture and a semi-directed bands-striped structure. The main rock components are carbonate, a lot of scaly calcite and a little fine-grained quartz, mainly calcite. The microstructure shows scaly aggregates often form in irregular pellet-group porphyritic. There is a little fine-grained irregular granular quartz between the particles, and sometimes there is fine-grained irregular granular or pellet carbonate, which is interpenetration symbiosis (Figs. 5 and 6).

Due to the effect of small granularity and impurities, the interference color tends to be less distinctive. The structural impact may lead to the slaty cleavage development along the bands or the edge of the group porphyritic. The organic gray matter is recrystallized and has formed the black aphanitic carbonaceous (Aphanitic graphite), and it can make hands dirty. The quartz disorderly intersperses between the calcite intergranular particles, and its distribution is ordinary, but its content is less. The slice is colorless. The interference color is gray, and it has much more developed wavy extinction. The quartz-carbonate veins in the rock is well developed. It macroly shows white zone and synchronous folding with the surrounding rock. Its locals contain black surrounding rock xenoliths, which are mainly constituted by band aggregates consisting of medium-grained irregular granular carbonate, and sometimes containing a relatively small amount of medium-grained irregular granular quartz, which are interpenetration symbiosis. The locals cut through the surrounding rock structure, but they are not affected by metamorphism structures. It may indicate that the formation of carbonate veins is mainly through the same structural development (Fig. 6). The structure and mineral composition of the gray matter slate are more complex. They experienced multi-phase deformation and metamorphic processes.

On the basis of the field macro geological survey of the Jiweishan landslide, the typical samples from 10 landslide sliding surfaces are tested by the scanning electron microscope (SEM). The samples at natural state and samples with 10-day water saturation were analyzed, and then the microstructure features of the landslide sliding surface were obtained. The lithology of the test's sliding surfaces is gray matter slate, dried naturally and plated, when the samples were observed by SEM. There are a large number of linear scratches, micropore, microfissure and the clay mineral directional arrangement (Figs. 7 and 8).

Under the rainfall condition, the situation where the water flowed into the interiors of the slip zone were simulated, and then the saturated-water tests were done. Five samples which were immersed in distilled water for 10 days were selected. They were soaked and then dried, and the microstructure were then examined by the SEM. The result shows that the micro-cracks expand, the porosity increases significantly, and new micro-cracks occur (Figs. 9 and 10). The water

Fig. 4 X-ray diffraction of the Soft rock and specular materials

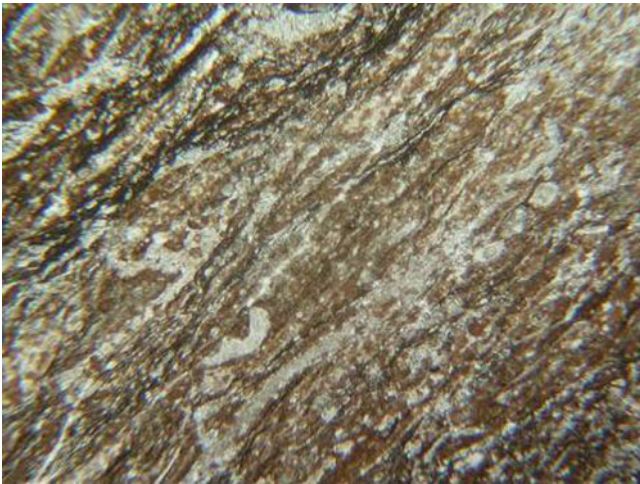
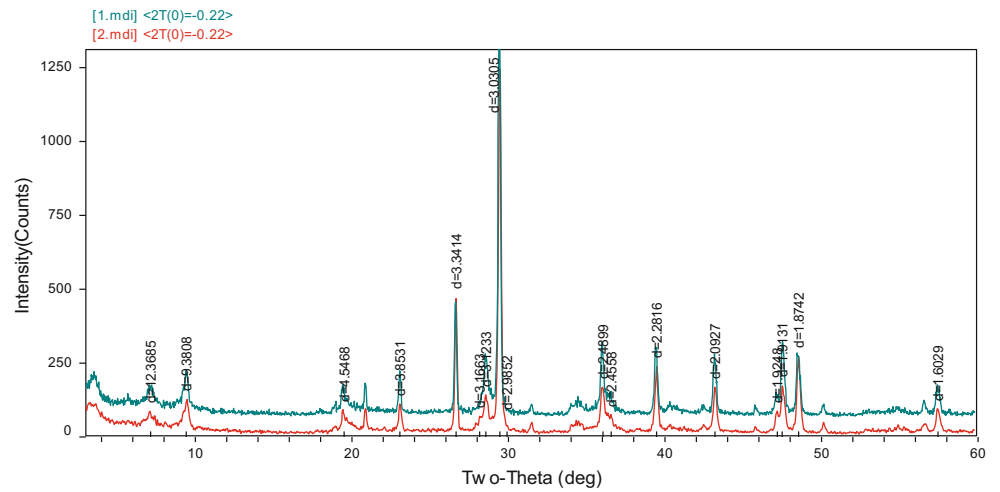


Fig. 5 Banded and perthitic structure (visual field diameter: 5.2 mm, parallelling to the polarization)

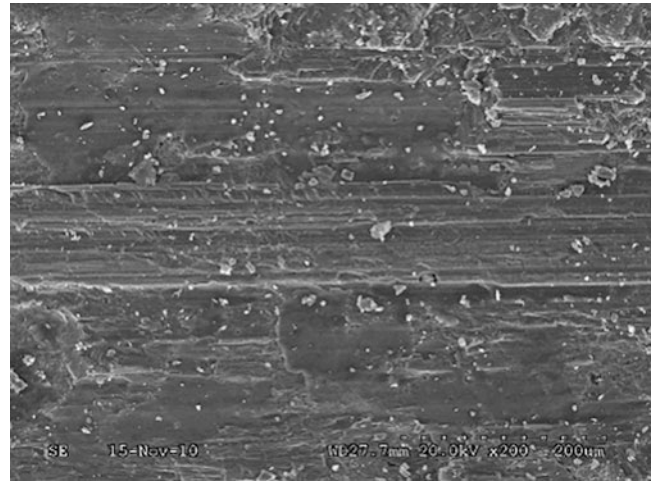


Fig. 7 Linear scratches in low magnification $\times 200$ times

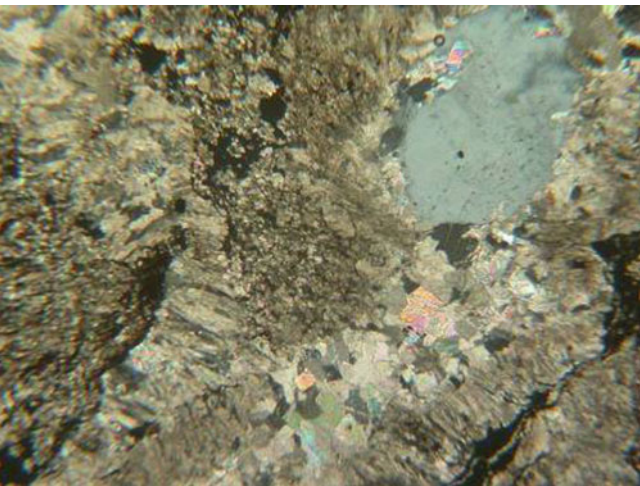


Fig. 6 Contact relationship between the carbonate aggregate and surrounding rock (visual field diameter: 1.0 mm, parallelling to the polarization)

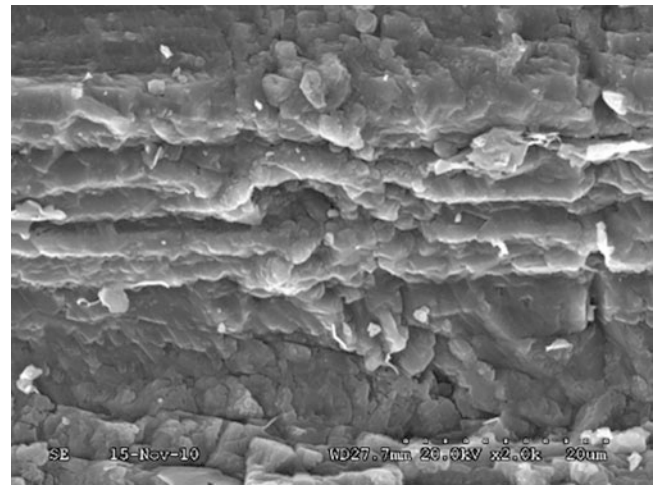


Fig. 8 Microcosmic linear scratches at high magnification $\times 2,000$ times

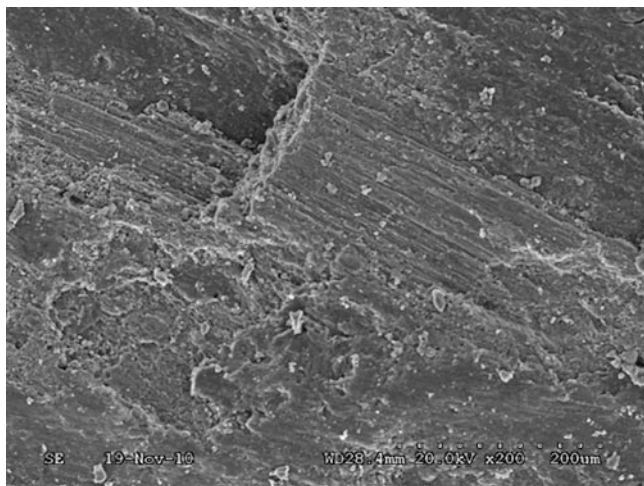


Fig. 9 Microporosity increases $\times 200$ times

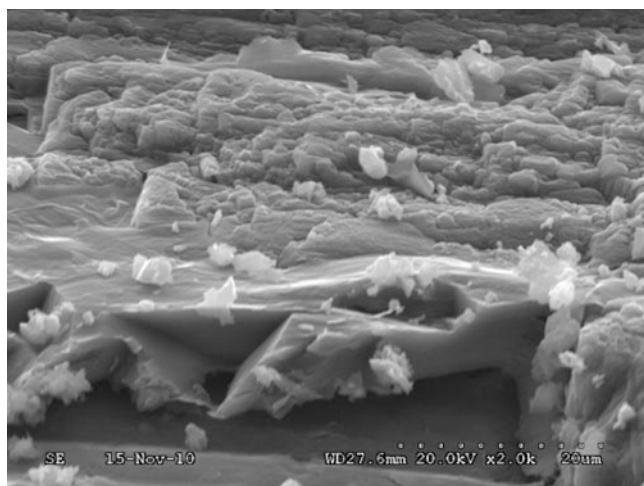


Fig. 10 Microporosity exists $\times 2,000$ times

can lead to new micro-cracks of the soft zone, which become the main sources of continuous sliding cracks. The test results of the microstructure show that the structure and mineral composition of the gray matter slate are more complex. They have experienced multi-phase deformation and metamorphic processes. Some microscopic structures above the weak zone play an important role in the slow chain-styled catastrophe processes after the fast development, during which several stages have been experienced: the formation of landslide boundary in a long period \rightarrow creeping along the weak surface \rightarrow stress concentration and then shear collapse \rightarrow disintegration impact \rightarrow catastrophic failure occurrence. All these stages also coincide with the basic characteristics of the landslide movement.

Conclusion

The typical material composition, microstructural features, formation mechanism etc. of the landslide weak zone determine the changes in its stress state and strength, and these changes would affect the activities of a landslide. On the basis of the field geological survey of Jiweishan landslide (especially the slip zone), the slip zone characteristics of the Jiweishan landslide obtained much more detailed research through a series of laboratory tests.

1. The content of calcite reaches up to 68 %, whereas the organic matter about 13 %, talcum about 9 %, montmorillonite 5 %, quartz 4 % and dolomite 1 %. With water dissolution and transportation, the calcite permeated, and then stagnated in the striped calcareous gray matter slate. The high organic matter content reduces the compressive strength and shear strength of the layer of striped calcareous gray matter slate. The talcum is soft, delicate and smooth. There is a layer of slickensides covering the sliding surface in the investigation scene of the slip zone soft rock and shearing specimens. There are no changes in the slickensides composition when it is analyzed by the DMAX-3C diffractometer.
2. There are a variety of irregular granular or pellet minerals, and they are interpenetration symbiosis. The main rock components are off-white fine-grained carbonate and black carbonaceous mudstone. The former rock will produce bubbles when it meets cold HCl. The latter rock is soft and flexible, and it is mainly composed by mud, and it can make hands dirty. It hardly forms bubbles when it meets acid. Results before and after water saturation of the weak zone show that there are a large number of linear scratches, micropore, microfissure, and the clay mineral demonstrates directional arrangement in the natural dried samples in the scanning electron microscope. Besides, some micro-cracks and expansions occur in the fully water-saturated samples from the slip surfaces, the porosity increases significantly, and new micro-cracks emerge. These micro-cracks become the main sources of continuous sliding cracks. Some microscopic structures above the weak zone play an important role in the slow chain-styled catastrophe processes after the fast development.

Acknowledgments The research has been supported by the National Basic Research Program “973” Project of the Ministry of Science and Technology of the People’s Republic of China (2013CB733200), by China National Science Fund for Distinguished Young Scholars (41225011), and by State Key Laboratory of Geodesy and Earth’s Dynamics(SKLGED2013-1-1-EZ).

References

- Deng ML, Xu Q, Cai GJ (2009) Micro-characteristics of weak-soft zone of Jiweishan Rockslide in Wulong County, Chongqing, June 5, 2009. *Geotech Inves Surv* 4:5–10 (in Chinese)
- Feng Z, Yin YP, Li B (2012a) Centrifuge modeling of apparent dip slide from oblique thick bedding rock landslide. *Chin J Rock Mech Eng* 31(5):890–897 (in Chinese)
- Feng Z, Yin YP, Li B (2012b) Mechanism analysis of apparent dip landslide of Jiweishan in Wulong Chongqing. *Rock Soil Mech* 33(9):2704–2712 (in Chinese)
- Gibo S (2002) Strength recovery from residual state in reactivated landslides. *Geotechnique* 52(9):683–686
- Huang RQ (2008) *Catastrophic landslide in China*. Science Press, Beijing
- Li SD, LU X, Wu J (2007) Evolution process and pattern of sliding zone in large consequent bedding rock landslide. *Chin J Rock Mech Eng* 26(12):2473–2480
- Liu CZ (2010) Mechanism analysis on the jiweishan rockfall disaster happened in Wulong, Chongqing, June 5, 2009. *J Eng Geol* 18(3):297–304
- Liu CZ, Shi T, Zhang MX (1995) On the mechanism of deforming-cracking on the segment of cracks T_8 - T_{12} of Lianzi Cliff dangerous rock body. *J Eng Geol* 3(2):29–41
- Liu XL, Deng JH, Li GT (2004) Shear streng properties of slip soils of landslides: an overview. *Rock Soil Mech* 25(11):1849–1854
- Man ZW (1991) Analysis of the mechanism of landslide Tanken Place Zhongyang Village, Wuxi district, Sichuan Province. *J Geol Haz Control* 2(1):71–77
- Wang J (2006) Experimental study on engineering properties of slip soils of landslides along G212 high way in long-nan. Lanzhou University, Lanzhou
- Xu Q, Huang RQ, Yin YP (2009) The Jiweishan landslide of June 5, 2009 in Wulong, Chongqing: characteristics and failure mechanism. *J Eng Geol* 17(4):433–444
- Xu Q et al. (2010) A catastrophic rockslide-debris flow in Wulong, Chongqing, China in 2009: background, characterization, and causes. *Landslides* 7(1):75–87
- Yin YP (2010) Mechanism on apparent dip sliding of inclined bedding rockslide—a case study of Jiweishan Rockslide in Wulong, Chongqing. *Chin J Rock Mech Eng* 29(2):217–226 (in Chinese)
- Yin YP (2011) Mechanism on apparent dip sliding of oblique inclined bedding rockslide at Jiweishan, Chongqing. *Chin Landsl* 8(1):49–65
- Zhang L, Tang HM, Xiong CR (2010) Movement process simulation of high-speed long-distance Jiweishan landslide with PFC^{3D}. *Chin J Rock Mech Eng* 31(Supp.1):2601–2611, in Chinese
- Zou ZX, Tang HM, Xiong CR (2012) Geomechanical model of progressive failure for large consequent bedding rockslide and its stability analysis. *Chin J Rock Mech Eng* 31(11):2222–2231



Effect of Vertical Load on Shear Characteristics of Micro-Piles in Landslide

ShuFeng Wang and YuePing Yin

Abstract

In recent years, micro-pile has been widely applied to landslide treatment engineering due to its advantages in application and construction. Its engineering effect is quite evident. At present, some researchers focus on studying the effects and failure mode of micro-pile in landslide reinforcement. However, only few of them discussed how the pile works with shearing force and vertical load. By numerical simulations, a part of which were compared with the results from large-scale physical model tests, effects of vertical load on shear characteristics of micro-piles in landslide were analyzed. Each row of piles simultaneously sheared with vertical loads, which played an active role in increasing anti-sliding force. According to the analysis, the four rows of piles, installed close to trailing edge, were mainly affected by compression, comparing to the rows installed in front, which are affected with tension.

Keywords

Micro-pile • Vertical load • Physical model test • Numerical simulation • Shearing force

Background

Installation of micro-piles to improve stability of slopes has been highly effective in recent decades, and it is widely used in landslide remediation projects because of its advantages, such as requiring small equipment, adaptability to various soils, low noise, minimal disturbance on slope during construction, flexible forms to pile location, etc.

At present, many researches in the world have been studying the shearing characteristics of micro-piles. Thompson (2004) and Su (2010) used of the shearing box model to study the mechanism of micro-piles under lateral

load. Sun et al. (2010), Xiao (2008) and Andrew (2006) conducted model tests to investigate sliding mechanism of the micro-piles in landslide. Yan (2010) and Wang et al. (2010) also made large-scale model tests to study failure mode and sliding mechanism of the micro-piles in landslide.

These authors focused on stress situation, failure mode and the sliding mechanism of micro-piles, rather than the relationship between shear properties and the vertical load. Impact of vertical load on shear properties for micro-pile was discussed based on results from numerical simulations, and parts of the results were compared with results obtained from large-scale physical model tests.

Numerical Simulation Model

Numerical simulation model test adopted geometric similarity ratio $C_g = 3$, elastic modulus ratio $C_E = 1$ as basic similarity ratio, and listed similar criterion equation as of π type according to the similarity principle. Accordingly, the physical quantities were calculated as follows: $C_q = 3$,

S. Wang (✉)

Department of Geological Disasters, Wuhan Institute of Geology and Minerals Resources, No. 69, Guanggu Road, Wuhan 420305, China
e-mail: wshufeng2010@163.com

Y. Yin

China Institute of Geological Environment Monitoring, No. 20, Da Huisi Road, Beijing 100081, China
e-mail: 506358410@qq.com

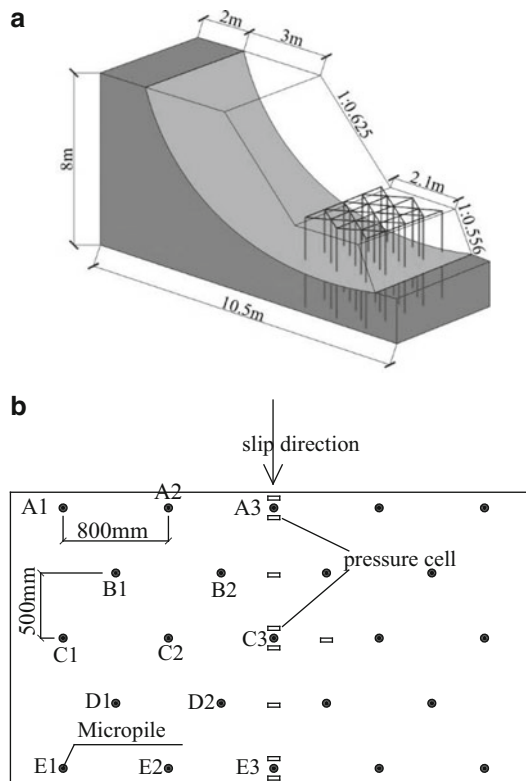


Fig. 1 Model for test and numerical simulation and the serial number of piles. (a) Model size, (b) Serial number of piles

$C_p = 9, C_\sigma = 1, C_\varepsilon = 1, C_{Ac} = 9, C_{As} = 9, C_{\sigma s} = 1$. Here, the subscripts q is the linear load, p is the force the piles are subjected to, σ is the stress, ε is the strain in the pile, Ac is the cross-sectional area, As is the reinforcement cross-sectional area of the piles, and σs is stress in the soil (Yan 2010).

Numerical Model Design

Numerical model was assumed to be homogeneous body with weak surface between the slide and the slide bed as slip surface.

The piles were 4 m in length and 60 mm in diameter, corresponding to prototype pile with length of 12 m and diameter of 180 mm, respectively.

The piles were circular in shape and laid as quincunx by 5, 4, 5, 4, 5 (sign row A, B, C, D, E) pattern along the pile load transfer direction with coupling rigid beam connection on the top. The strength of pile was at the grade of C25. Multi-stage loading approach was utilized with the corresponding pressure value of 8, 16, 24, 32, 40, and 48 kPa. The size of the test model and the chosen monitoring pile are shown in Fig. 1. Likewise, the model for numerical simulation is shown in Fig. 2. Monitoring nodes are shown in Fig. 3. Physical and mechanical parameters are: loess

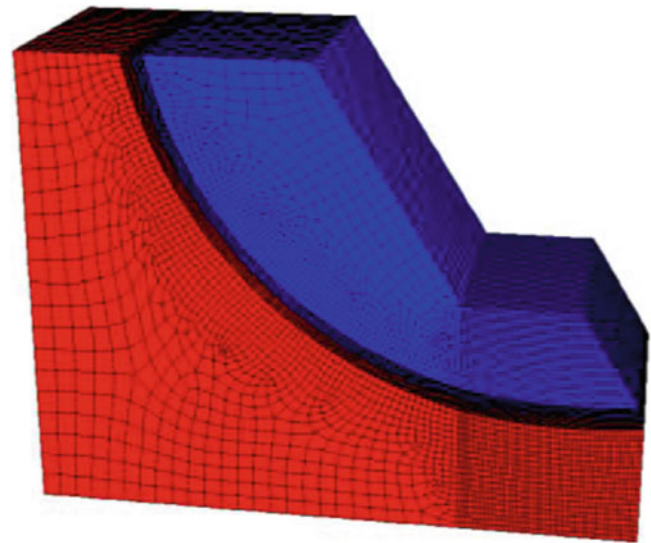


Fig. 2 Model for numerical simulation

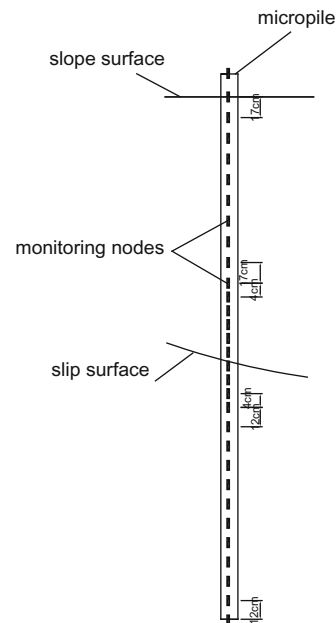


Fig. 3 Schematic diagram of monitoring nodes

friction angle $\phi = 11.7^\circ$, cohesion $c = 24.6$ kPa, density $d = 1,400$ kg/m³; sliding surface friction angle $\phi = 15^\circ$, cohesion $c = 3.5$ kPa.

Results and Analyses

Shearing forces at each stage of pile A1 from numerical simulation are shown in Fig. 4. Comparisons of this result with that of the monitoring piles with vertical load are presented in Figs. 5, 6, 7, and 8.

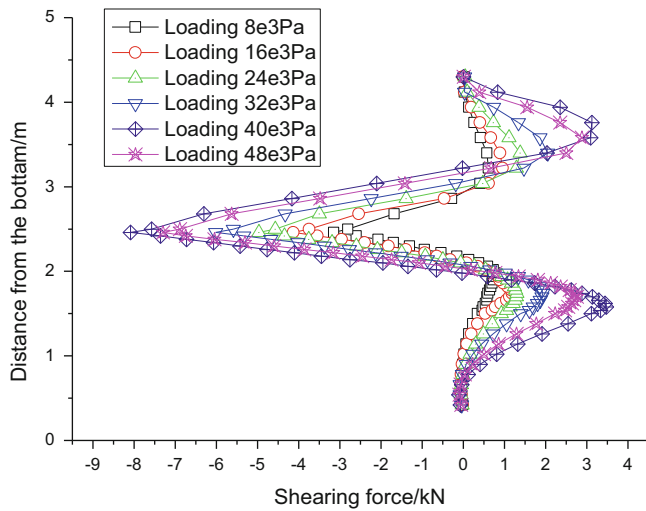


Fig. 4 Shearing force at each stage

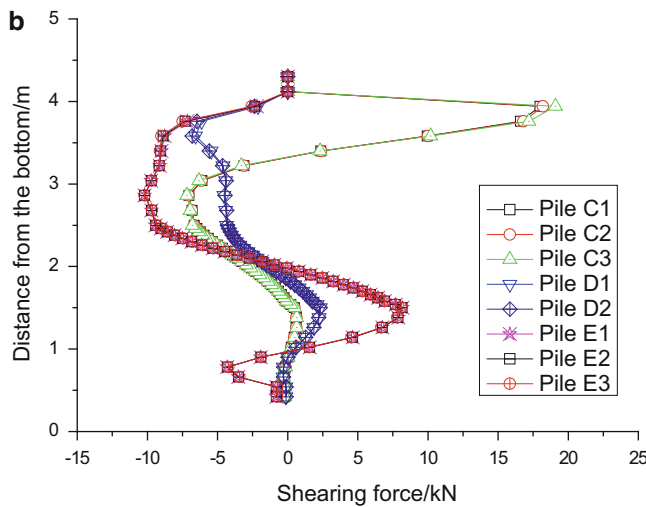
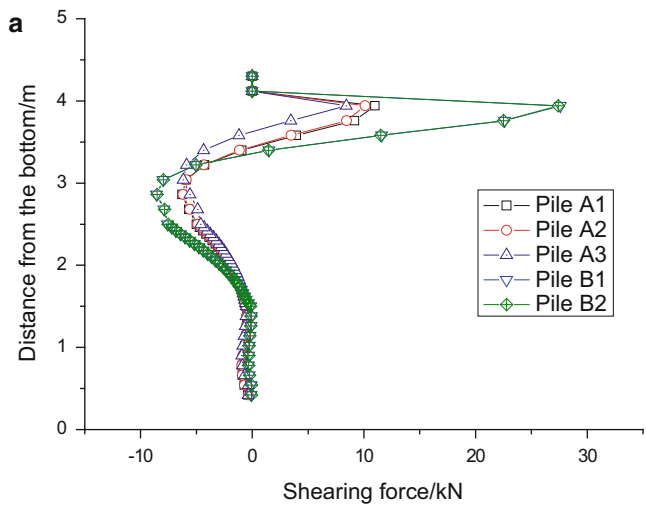


Fig. 5 Shearing force distributed in piles with 50 Pa vertical load. (a) Shearing force distributed in rows A and B. (b) Shearing force distributed in rows C-E

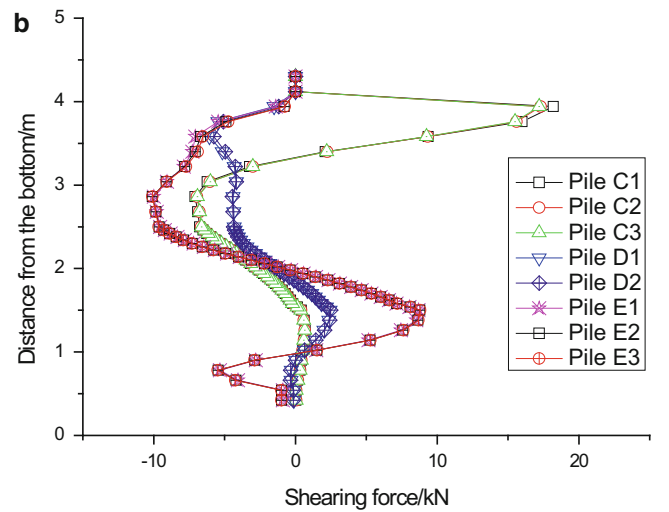
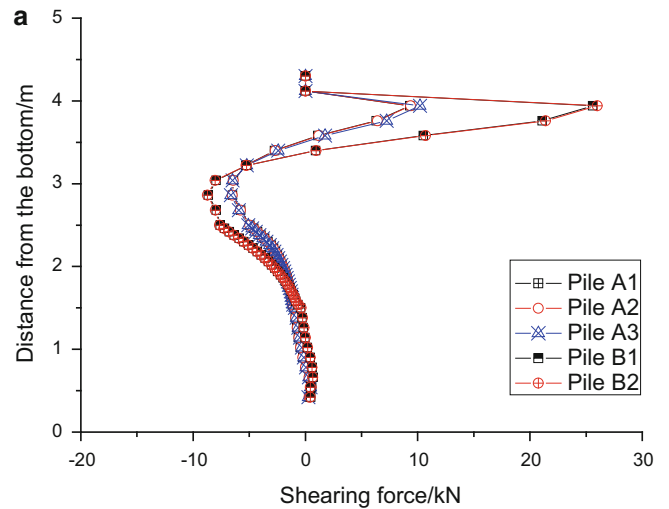


Fig. 6 Shearing force distributed in piles with 100 Pa vertical load. (a) Shearing force distributed in rows A and B. (b) Shearing force distributed in rows C-E

As can be observed in Fig. 4, with no vertical loads on top of piles, we can see that the form of shearing force distributed along the pile is like a shape of “M”, turned perpendicular on left; each shear curve has three peaks, and the peak near the slip surface is in the same direction as in the sliding mass, comparing with the ones close to the top and bottom of the micro-pile in the opposite direction. Shearing curves on and under the slip surface are approximately symmetrical about the surface. The maximum value of shearing force is located near the sliding surface, which moves closer to the top of pile with an increase in loading on the slope surface, reaching close to 2–3 cm. Likewise, the two peaks close to top and bottom move slightly to the tips of the micro-pile with the maximum distance of 50 cm. Shearing force of each row of piles decreases in turn along the direction of load transfer.

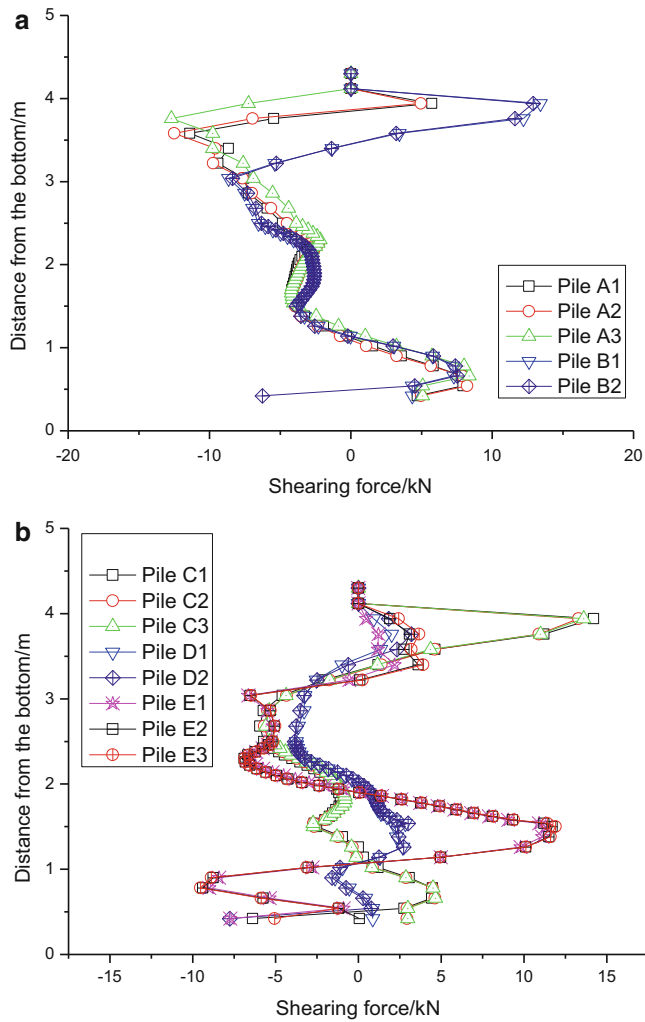


Fig. 7 Shearing force distributed in piles with 400 Pa vertical load. (a) Shearing force distributed in rows A and B. (b) Shearing force distributed in rows C–E

As can be observe in Figs. 5, 6, 7, and 8, vertical load plays a significant role on the shear force in the piles; and each row of piles charges the shearing force simultaneously.

Existing data showed that the landslide thrust distributed triangularly along the pile with the maximum near the slip surface, which means that the landslide thrust of the third monitoring node is close to 0. Results from numerical simulation show that its value is larger than 0, which relates to the small lateral confinement because of its position of close to the slope surface. Let's take Fig. 9 as an example; nodes near the slope surface firstly break because of excessive deformation when loading to 1,200 Pa.

Shearing force in each pile of row A is less than that of row B, which may be related to the number of piles between row A and B. The “zero” points near the slip surface usually exists when vertical loads are added on micro-piles, and their position usually do not change concomitantly with the

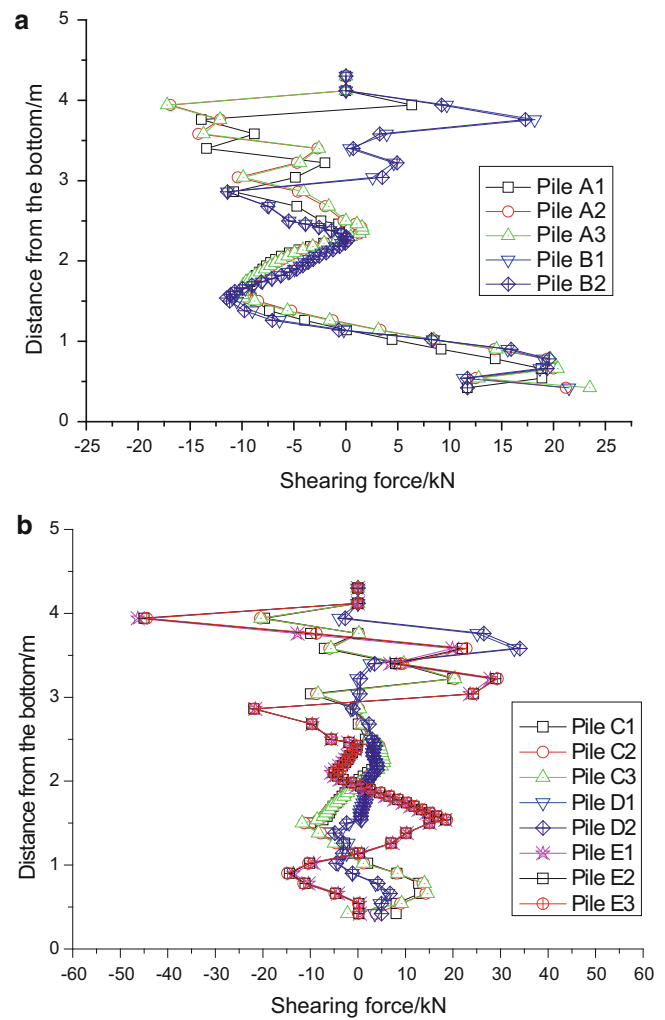
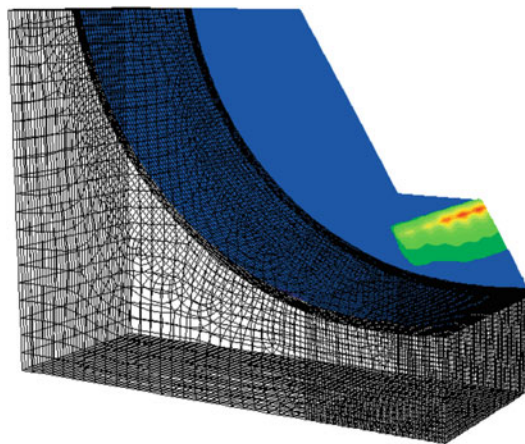


Fig. 8 Shearing force distributed in piles with 800 Pa vertical load. (a) Shearing force distributed in rows A and B. (b) Shearing force distributed in row C–E

increase of the vertical load. When the vertical loads are small (such as 50 Pa, 100 Pa), the maximum values of shearing force in the pile are less than 10kN. Moreover, each pile has different values. At the same time, there are no shearing forces at the bottom of the piles. So, we can conclude that smaller vertical load has little effect on enhancing the shear force capability of the pile. However, for the higher vertical loads (such as 400, 800 Pa), a great variations in the shearing forces appear at the bottom of each pile. Although the values are opposite, they also have an uniform distribution around the zero value, which are helpful to strengthen the shearing capacity of micro-piles.

Existing research data (Zhou et al. 2009) shows that the piles can take tensile loads of the landslide thrust when the piles reach the yield condition.

A very interesting phenomenon is that the maximum value of shearing force and the maximum range of variation



Contour of X-Displacement

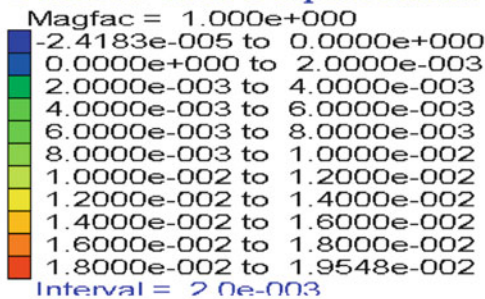


Fig. 9 Contour of x-displacement for landslide

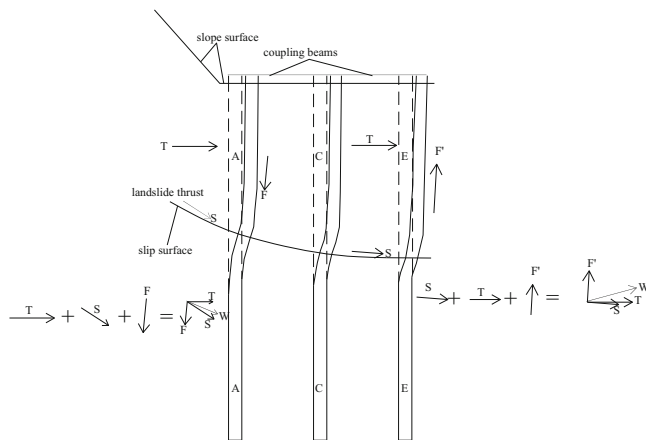


Fig. 10 Schematic diagram for force distributed on piles

were observed in row E, among the rows C, D, and E. Analyzing its force process (Fig. 10), we can see that rows A and E mainly undertake extrusion (T) from soil between piles, landslide thrust (S) at the slip surface, tensile force

after broken (F or F'), the difference in value of which and direction of resultant leads to different shearing force. According to the analysis presented above, row A is mainly affected by compression, compared to row E, which is affected with tension.

Discussion

The shearing force along the pile mentioned in the text are instantaneous among of the process of iterative calculation, which means that it can not represent the whole process of loading, and the value is only with regular statistical significance.

Conclusions and Recommendations

Each row of piles shears simultaneously with the vertical loads on the top of piles. When the vertical load increases to a certain value, shearing forces appear at the bottom of the pile, and at the same time, longer piles are needed in the anchored segment. Vertical loads play an active role in increasing anti-sliding force for micro-piles. The “zero” points near the slip surface usually exist when adding vertical loads on micro-piles. The four rows close to trailing edge are mainly affected by compression, compared to the row in front, which is affected with tension.

References

- Andrew ZB (2006) Load transfer in micropiles for slope stabilization from tests of large-scale physical models. MS thesis, University of Missouri, Columbia, Columbia, MO, p 69
- Sun SW, Zhu BZ, Ma HM (2010) Model experimental research on anti-sliding characteristics of micropiles with cap beam. *Chin J Rock Mech Eng* 29(Supp. 1):30
- Su YY (2010) Model tests on grouted micro-steel-tube pile in earth slope. MS thesis, Ocean University of China, Qing Dao, China, p 16
- Thompson MJ (2004) Experimental load transfer of piles subject to lateral soil movement. In: *Transportation scholars conference*, Ames, IA, pp 18
- Wang SF, Yin YP, Men YM (2010) In-situ test and numerical analysis of skid resistance for micropile to loess landslide. *Hydrogeol Eng Geol* 37(6):22–26
- Xiao WM (2008) Study on anti-sliding mechanism of micro-pile structure. MS thesis, Southwest Jiaotong University, ChengDu, China, p 16
- Yan JK (2010) Model test study on micropiles in landslide reinforcement. DR thesis, Chang'an University, Xi'an, China, pp 71–98
- Zhou DP, Wang HL, Sun SW (2009) Micro-pile composite structure and its design theory. *Chin J Rock Mech Eng* 28(7):1354–1356



Geotechnical Centrifuge Modelling for Rock Slope Failure: A Brief Overview

Zhen Feng and Yueping Yin

Abstract

Geotechnical centrifuges are used widely worldwide for rock mechanics. This paper gives a brief overview of rock slope failure modeling using geotechnical centrifuges. Several cases involving centrifuge modeling for rockslide mechanisms have been recorded. Two methods of small-scale geotechnical centrifuge modeling for large scale problems, such as landslide form massive rock slope failure, are presented. Furthermore, model materials for structures are introduced considering the structures dominating rock slope stability. Finally, a short discussion regarding difficulties in rock slope failure modeling is given.

Keywords

Geotechnical centrifuge • Rock slope • Failure mechanism • Small-scale modeling • Model materials

A Brief History of Geological Geotechnical Centrifuge Testing in Rock Mechanics

Philip Bucky of Columbia University was the first researcher who made Edouard Phillips' idea a reality by undertaking geotechnical centrifuge modeling for mine roof collapses in 1931 (Taylor 1994). Since then, researchers worldwide have adopted the methodology from Bucky's tests and have gained a good understanding of the mechanical properties that apply to mining engineering design. Panek (McWilliams 1989) performed notable works on underground excavation in rocks and conducted several sets of geotechnical centrifuge tests regarding the bolting of bedded

mine roofs, and several publications were published from 1952 to 1962. Ramberg agreed with Stephansson (1965) with respect to the centrifuge modeling of underground openings. Simplified models collapsed in a high acceleration field, and thus, replicated the unstable behavior of natural mines. Based on theoretical stability analysis and geotechnical centrifuge modeling test, Stephansson (1971) performed a more detailed finite element analysis on the stability of excavations in layered rocks. Mathematical solutions of strain and stress for mining roof were proposed. Subsequently, synthetic analyses consisting of theories, numerical simulations, and physical modeling have been accepted as the most effective method in engineering disciplines.

In the early 1980s, Sutherland and his collaborators conducted a series of tests on subsidence above mine structures in a 25-ft radius centrifuge. Since then, large-scale geotechnical centrifuges have emerged in the field and have become widely accepted. Joseph et al. (1988) and Einstein et al (1990) performed an extensive study of scaled modeling on arching in granular and jointed media. They compared the behavior of differently scaled models of the same prototype through a so-called "modeling the model" approach and concluded that discontinuities can only be modeled to a limited extent. Tsessarsky and Talesnick (2007) modeled

Z. Feng (✉)

Key Laboratory of Neotectonic movement and Geohazards of MLR in Institute of Geomechanics, Chinese Academy of Geological Sciences, No.11 Minzudaxue South Street, Haidian District, Beijing 100081, China
e-mail: fengzhengcs@126.com

Y. Yin

China Geological Environmental Monitoring Institute, Beijing 100080, China
e-mail: yyueping@mail.cgs.gov.cn

multiple vertically-joined Voussior beams to calibrate and validate numerical methods employed in the kinematic analysis of underground openings in horizontal bedded and discontinuous rock masses. A distinctive set of tests to determine the shear stress-shear displacement features of interfaces between rock blocks was also conducted in geotechnical centrifuge, and the results were compared with the theories proposed by Barton and Bandis. They suggest that the scaling of shear displacement along the interface surface should not be done in the context of the model/prototype analysis.

In the early years, fields related to tectonic movements, as well as mining engineering, were the main areas in which geotechnical centrifuge modeling was performed. Due to the high scale contrast, the tasks were performed in much higher-speed drum centrifuges. Ramberg (1963, 1964) and Ramberg and Stephansson (1965) conducted an extensive series of tests to study gravity tectonics and the folding of moraines using geotechnical centrifuges. His work was very influential during the early days of plate tectonics. The work continues at the Hans Ramberg Tectonic Laboratory, which is the forerunner of numerous tectonic laboratories that are situated throughout the world (Soula 1982; Harris et al. 2002; Harris and Koyi 2003; Corti et al. 2004).

Dixon (1975), Talbot (1974, 1977), Schwerdtner and Troeng (1978), and Langenberg and Ramsden (1980) respectively performed studies on diapiric domes and gneiss, or plutonic diapirs, employing geotechnical centrifuges. In the early 1990s (Liu and Dixon 1990; Dixon and Liu 1992) studied the structural evolution of foreland fold and thrust belts. The centrifuge models were constructed out of silicon putty modeling rocks and plasticine modeling clay and were confined to a 2,000-g drum centrifuge at Queen's University. It should be noted that Lebedev and Kadik (2000) employed a high-temperature centrifuge to simulate the probing of liquid and crystal separation in the evolution of partially molten zones involving a multiphase flow.

However, it should be stated that all of the tectonic modeling tests were performed in drum centrifuges. The tectonic centrifuge modeling not only improves our understanding of tectonic processes, but to an extent, it assists in exploration performed by the petroleum industry. By clarifying the structural geometry and sequence trap formation, assessments of reservoir potential can be made. In analogue materials research, tectonic experts make use of low density and viscosity materials to model large-scale natural rock masses in high-acceleration-running geotechnical centrifuges. This kind of method merits application for large-scale prototype modeling in other fields.

Geotechnical Centrifuge Modeling Tests in Rock Slope Engineering

Generally, self-weight and gravity-induced hydraulic stress may be the dominant force causing the failure of slopes. The movement of pore fluid, also known as self-weight-induced

seepage, can only be modeled in a geotechnical centrifuge. Therefore, the realization of slope stability was inevitable among the initial applications of geotechnical centrifuges. Thus, one of the main areas requiring the use of geotechnical centrifuges in rock mechanics is rock slope stability. However, one issue is that in the early stages, most studies focus on soil slopes, which are easily understood. Rock slopes always involve joints, foliations, and faults, which produce the anisotropy and discontinuity, and this is the key difference in the geotechnical centrifuge modeling of rock mechanics.

To determine the stability of flysch rock slopes, Goldstein et al. (1966) tested some models in a large-scale geotechnical centrifuge. The influence of the joints on the rock slope was observed, and the outcomes validated the field and theoretical methods. Likewise, Sugawara et al. (1984), carried out a series of centrifuge tests using homogeneous models to interpret the progressive failure of rock slopes and the influence of a single discontinuity.

Until now, most geotechnical centrifuge analysis of rock slope stability has focused on toppling failures and the University of Western Australia foreruns in the area. Fahey et al. (1990) conducted a series of centrifuge modeling tests on foliated rock slopes, and developed several model preparation techniques in the laboratory. Following on the idea from Fahey, Adhikary et al. (1997), Adhikary and Dyskin (2007) investigated the mechanism of flexural toppling failure of jointed rock slopes without cross-joints by performing centrifuge experiments. Some significant results were obtained, and the modeling tests were also used to validate and calibrate the limit equilibrium method and numerical analysis. As a pioneer in centrifuge modeling, the China Institute of Water Resource and Hydroelectric Power Research (IWHR) did extensive and impressive work on topples (Wang et al. 1996). Gypsum column models, aluminum models and plastic cubic models (Chen et al. 2006) with a defined basal plane were used to validate the basic frame of extensions proposed for the Goodman-Bray method. Furthermore, artificial rock models comprising cement, sand, magnet powder, and water were tested to represent the failure modes (Zhang et al. 2007). Deep-seated biplanar slip breaking out through the toe of the slope was observed. Studies suggested that the tensile strength of rock mass should be amended if numerical models are employed to analyze centrifugal modeling tests, due to the existence of joints. To the author's knowledge, this is the first centrifugal experiment on a rock slope using more than one set of joints.

When there are joints dipping along the slope, landslides parallel to the rock layer can occur very easily. Bedding rock slopes have also been investigated in geotechnical centrifuges. Stacey (1973) conducted both jointed and intact rock slope tests. The centrifuge model studies illustrated that failures occurred when sliding along the pre-existing joints. In contrast, failure through the intact model was not observed. "The tests also revealed that the failure mechanism was progressive and coherent sliding of one large block could not be observed"

(Sjöberg 1996). Another innovator at the Yangtze River Scientific Research Center, China analyzed the mechanics of rock masses with joints and faults. Han and Wang (1991, 1994) released example models involving the deeply excavated rock slope of the Three Gorges Project and underground extraction to illustrate the stability problem on the Lianziya rock cliff. They developed some new techniques and instruments for dynamic problems, water pressure and anchoring. The results provided valuable references for both the assessment and design of high rock slopes and thick bedding rock slopes.

Studies of cold climate slope processes have been carried out since 1969, and they have focused mainly on massive movements. Davies et al. (2003) has led centrifuge-based research of warming permafrost within jointed bedrock to study the effects of global warming on alpine slope stability. Experiments involving simplified thick-bedded rock slope models with two sets of ice-bonded discontinuities were conducted. The plane strain models were constructed using four blocks and had a dimensional scale of 1:120. Günzel and Davies (2006) performed extensive work with pre-stressed rock bolts and reinforced the model slopes during tests. There is a significant feature in model construction that the slide surface was cast against profiled steel in a sawtooth shape.

Some peculiar geotechnical centrifuge modeling tests on rock mechanics have been carried out. Xing et al. (2005) performed modeling of wedge failure in rock slopes and the tests were analyzed using the Hook and movable mechanism methods. The results of the centrifuge model tests also showed reasonable evidence to support Pam's principle of maximum.

The use of geotechnical centrifuges could significantly enhance the understanding of not only nondestructive deformation, but also post-failure behaviors for rock slope failure. In an attempt to determine the mechanism behind this behavior, Imre et al. (2010) carried out centrifugal model experiments and represented the process of Sturzstrom, which involves a highly dynamic collisional granular regime. Rock fragmentation is the main concern of the centrifugal model tests. Through observation and model studies, they concluded that the run out is controlled by the initial size, intact strength, and intact elastic properties of the rocks involved. Feng (2012, 2013) has carried out experiments on oblique thick-bedded rock slope failure by centrifuge to replicate rockslide initiation. A four-blocks model and a more discrete model were used and apparent dip slide was observed during the tests, which validated the previously proposed "key block resisting" theory.

Similarity and Scaling Laws for Massive Rock Slope Failure

Most of the geotechnical centrifuge modeling tests adopt an N_g acceleration, where N is the dimensional ratio. By doing this, it is easy to realize an equal stress between the prototype

and model. Sometimes, like massive rock slope failure problems on a very large scale, being subject to a fixed model container size and a maximum acceleration of the centrifuge, a compromise has to be made where the dimensional ratio (C_L) is larger than the gravity ratio (N), which implies a small-scale centrifuge modeling. There are two different small-scale modeling methods that deal with large scale problems, the unequal stress modeling and the equal strain modeling.

The unequal stress modeling means that the stress field is unequal between the model and prototype. Models possessing the same characteristics as the prototype are put into a centrifugal box being spun under an N_g acceleration which is smaller than C_L . The prototype can easily be deduced from obtained data either under a specific low acceleration via a similar linear relationship, or under several low accelerations via linear fitting. However, nonlinear and elastic plastic problems dominate in practice and cannot be simply treated as linear-elastic (Zhang and Hu 1990). The rock mass shows elasticity under a low stress load, while the plasticity in a high stress field and modulus changes with stress variation. Thus, the similarity criterion derived from a mathematical physical equation analysis is a better and more effective method. However, most of the time, quantitative difficulties result in incomplete analytical solutions or approximate solutions, which is contrary to the core meaning of equation analysis.

Because the unequal stress modeling is a non-destructive test and the equation analysis is tedious, scientists have developed an equal strain modeling that is based on dimensional analysis and have made progress with it in the area of rock mechanical modeling. To satisfy the strain and deformation similarity, not all parameters of the model materials are similar to those of the prototype, and low modulus materials characterizing greater plasticity and lower cohesion than prototype rocks are used. Therefore, although the equal strain modeling cannot generate an original gravitational field as well as can the unequal stress modeling, a progressive or instantaneous failure process can be reproduced. The destructive equal strain modeling helps us to better understand the initiation mechanism and behavior of rockslides, in particular massive rock slope failure.

Materials for Rock Slope Geotechnical Centrifuge Test

Structures, including sliding surface, faults, and fissures, are distinctive features for rock slope failure modeling, and they play the most important role in the destabilization of rock slopes. Researchers have developed many modeling materials for structures in the rock mechanical centrifuge test. Structures are usually simulated by inserting a medium

Table 1 Materials used for joints in rock slope failure geotechnical centrifuge modeling

| References | Material | Angle of friction | Cohesion |
|--|-----------------------------------|-------------------|----------------------------------|
| Fahey et al. (1990) | Paper | Unknown | 22 kPa |
| | Sand–cement layers in contact | Unknown | 40 kPa |
| | Fiber-cement layers in contact | Unknown | 17 kPa |
| Wang et al. (1991) | Plastic film | 21.8°–26.6° | 0 |
| | Polyester | 16.7° | 0 |
| Wang et al. (1996) | Latex | Unknown | $\sigma_T = 0.3\text{--}0.4$ MPa |
| | Butter | 37° | 65 kPa |
| | Vaseline | 31.4° | 5 kPa |
| Adhikary et al. (1996, 1997), Adhikary and Dyskin (2007) | Silica glass sheets in contact | 8.25°–8.5° | Unknown |
| | Limonite–gypsum layers in contact | 22°–26° | Unknown |
| Xing et al. (2005) | Sandpaper | 27°–27.5° | 0 |
| | Geotextile | 17.1° | 0 |
| Davies et al. (2001, 2003) | Sawtooth surfaces | Unknown | 0 |
| | Ice-filled sawtooth surfaces | Unknown | 0 |
| Feng (2011, 2012) | Grease smeared on geotextile | 18° | 1.7 |
| | Geomembrane | 12° | 2 |

between two opposing surfaces, such as sheets, viscous coatings, and sometimes just a bare contact of blocks (Stephansson 1971). Different types of glue, lubricants, and mixtures of mineral powder and glue or lubricants, paper, clay, etc. have been used (Sjöberg 1996; Stimpson 1970). Davies et al. (2003) performed a distinctive simulation on ice-filled joints and produced an interlocking or imbricate slide surface with small steps to produce friction angle values that are dependent on normal stress. Table 1 presents some of the materials used in previous tests. It should be noted that the thickness of the slide surface has a significant influence on the stability of the rock slope, but it is difficult to control the compressive deformation of thick and weak intercalated layers due to increase in the g-level.

Discussion and Conclusions

Geotechnical centrifuge modeling tests can replicate the failure processes of rock slopes, helping to reveal rockslide mechanisms through direct observation and data analysis. This brief overview simply recorded several cases of rock slope failure modeling and modeling techniques, which can be used as references for researchers in the study of rock slopes.

However, there remain difficult and unsettled problems regarding data acquisition, material determination, model preparation, and modeling techniques, etc. One important reason why the failure mechanism of the jointed rock slope is not well understood is that it is very difficult to monitor the interior reactions of the rock slope during flight. In the future, wireless, delicate, and tiny conductors are expected to play a significant role as they can be buried in advance to measure inner, minor, and simultaneous responses. Furthermore, seismic responses have become a hot issue in recent years, whereas the dynamical instability failure of rock slopes is not

frequently mentioned in literature. Vibration tables and boxes, as well as dynamic theory in geotechnical centrifuge modeling involving boundary effects and inertia, etc. require further studies. Finally, the construction effects including excavation and building slopes are particularly difficult in the rock mass, not to mention the heavy and the need of small light strong instruments. Nowadays, most of the parts, such as excavation and bolt, are installed before the tests are performed. The use of liquid bags may be a good choice that can be introduced into rock mechanical centrifuge modeling considering incompressibility.

Scientists and engineers are developing new devices and techniques to resolve conflicting difficulties in centrifuge modeling of rock slope failures. It is believed that a greater understanding of the rock slope failure mechanism will be obtained from geotechnical centrifuge modeling.

Acknowledgments This work is sponsored by the National Key Technology R&D Programme for the 12th Five-years Plan (No. 2012BAK10B01), the National Geological Survey (No.1212011220140), the National Natural Science Foundation of China (No.41302246) and the Basic Science Foundation of Institute of Geomechanics (No. DZLXJK201307). The author appreciates the help of Dr. Li B. and He K. in literature retrieval.

References

- Adhikary DP, Dyskin AV, Jewell RJ (1996) Numerical modelling of the flexural deformation of foliated rock slopes. *Int J Rock Mech Mining Sci Geomech Abstr* 33(6):595–606
- Adhikary DP, Dyskin AV, Jewell RJ (1997) A study of the mechanism of flexural toppling failure of rock slopes. *Rock Mech Rock Eng* 30 (2):75–93

- Adhikary DP, Dyskin AV (2007) Modelling of progressive and instantaneous failures of foliated rock slopes. *Rock Mech Rock Eng* 40 (4):349–362
- Chen ZY, Zhang JH, Wang WX (2006) Centrifuge modeling for rock slopes. In: *Proceeding of the 6th international conference on physical modeling in geotechnics, 6th ICPMG '06, 4–6 Aug 2006, Hong Kong*, pp 19–28
- Corti G, Bonini M, Sokoutis D et al (2004) Continental rift architecture and patterns of magma migration: a dynamic analysis based on centrifuge models. *Tectonics* 23(2):1–20
- Davies MCR, Hamza O, Harris C (2001) The effect of rise in mean annual temperature on the stability of rock slopes containing ice filled discontinuities. *Permafrost Periglacial Process* 12(1):137–144
- Davies MCR, Hamza O, Harris C (2003) Physical modelling of permafrost warming in rock slopes. In: Springman P, Arenson (eds) *Permafrost*. Swets & Zeitlinger, Lisse, pp 169–174
- Dixon JM (1975) Finite strain and progressive deformation in models of diapiric structures. *Tectonophysics* 28(1–2):89–124
- Dixon JM, Liu S (1992) Centrifuge modelling of the propagation of thrust faults. In: *Thrust tectonics*. Chapman & Hall, London, pp 53–70
- Einstein HH, Li V, Whiteman RV (1990) Stochastic and centrifuge modelling of jointed rock executive summary. Department of Civil Engineering, Massachusetts Institute of Technology, Massachusetts (MIT CE R-90-22), 95 pp
- Fahey M, Finnie I, Hensley P (1990) Geotechnical centrifuge modeling at the University of Western Australia. Department of civil engineering, University of Western Australia, Perth, Australia (Geo:90092), 34 p
- Feng Z (2011) State-of-the-art: review of geotechnical centrifuge modeling test in China. *J Eng Geol* 19(3):323–331 (In Chinese with English abstract)
- Feng Z (2012) Centrifuge modeling of apparent dip slide from oblique thick bedding rock landslide. *Chin J Rock Mech Eng* 31(5):890–897 (In Chinese with English abstract)
- Feng Z (2013) Physical modeling of landslide mechanism in oblique thick-bedded rock slope: a case study. *Acta Geol Sinica (English Edition)* 87(4):1129–1136
- Goldstein M, Berman M, Goosev B (1966). Stability investigation of fissured rock slopes. In: *Proceedings of 1st congress international society of rock mechanics, 25 Sep–1 Oct 1966, Lisbon, Portugal*, pp 175–178
- Günzel FK, Davies MCR (2006) Influence of warming permafrost on the stability of ice filled rock joints. In: *Proceeding of the 6th international conference on physical modeling in geotechnics, 6th ICPMG '06, 4–6 Aug 2006, Hong Kong*, pp 343–348
- Han SH, Wang HH (1991) Application of centrifugal modeling technique to the research of rock slopes in the Thress Gorges Project. *J Yangtze River Sci Res Inst* 26:32–38 (in Chinese with English abstract)
- Harris LB, Koyi HA, Fossen H (2002) Mechanisms for folding of high-grade rocks in extensional tectonic settings. *Earth-Sci Rev* 59 (1–4):163–210
- Harris LB, Koyi HA (2003) Centrifuge modelling of folding in high-grade rocks during rifting. *J Struct Geol* 25(2):291–305
- Imre B, Laue J, Springman S (2010) Fractal fragmentation of rocks within sturzstroms: insight derived from physical experiments within the ETH geotechnical drum centrifuge. *Granul Matter* 12 (3):267–285
- Joseph PG, Einstein HH, Whitman RV (1988) A literature review of geotechnical centrifuge modeling with particular emphasis on rock mechanics. Defense Technical Information Center, Belvoir (ADA213793), 119 pp
- Lebedev EB, Kadik AA (2000) High-temperature centrifuge simulation- new method to study multiphase flow of partially molten zones. *Phys Chem Earth Solid Earth Geod* 25(6–7):591–595
- Liu S, Dixon JM (1990) Centrifuge modelling of thrust faulting: strain partitioning and the sequence of thrusting in duplex structures. In: *Deformation mechanisms, rheology and tectonics*. Geological Society of London, Special Publication, 54(1):431–444
- McWilliams PC (1989). Bureau of mines geotechnical centrifuge research: a review. U.S. Department of the Interior, Bureau of Mines, Washington, DC (IC9218), 19 pp
- Ramberg H (1963) Experimental study of gravity tectonics by means of centrifuged models. *Bull Geol Inst Univ Uppsala New Ser* 42 (1):369–370
- Ramberg H (1964) Note on model studies of folding of moraines in piedmont glaciers. *J Glaciol* 5(38):207–218
- Ramberg H, Stephansson O (1965) Note on centrifuged models of excavations in rocks. *Tectonophysics* 2(4):281–298
- Schwerdtner WM, Troeng B (1978) Strain distribution within arcuate diapiric ridges of silicone putty. *Tectonophysics* 50:13–28
- Sjöberg J (1996) Large scale of slope stability in open pit mining-a review. University of Technology, Lulea (0349-3571), 229 pp
- Soula JC (1982) Characteristics and mode of emplacement of gneiss domes and plutonic domes in central-eastern Pyrenees. *J Struct Geol* 4(3):313–337, 339–342
- Stacey TR (1973) Stability of rock slope in mining and civil engineering situations. National Mechanical Engineering Research Institute. Council for Scientific and Industrial Research, Pretoria, South Africa (CSIR Report ME 1202), 217 p
- Stephansson O (1971) Stability of single openings in horizontally bedded rock. *Eng Geol* 5(1):5–71
- Stimpson B (1970) Modelling materials for engineering rock mechanics. *Int J Rock Mech Min Sci* 7(1):77–121
- Sugawara K, Akimoto M, Kaneko K (1984) Experimental study on rock slope stability by the use of a centrifuge. In: *Proceeding 5th congress of the international society for rock mechanics, Melbourne, 10–15 Apr 1983*, pp 152
- Talbot CJ (1974) Fold nappes as asymmetric mantled gneiss domes and ensialic orogeny. *Tectonophysics* 24(3):259–276
- Talbot CJ (1977) Inclined and asymmetric upward-moving gravity structures. *Tectonophysics* 42(2–4):159–181
- Taylor RN (1994) Geotechnical centrifuges: past, present and future. In: Taylor RN (ed) *Geotechnical centrifuge technology*. Blackie Academic & Professional, London, pp 1–19
- Tsesarsky M, Talesnick ML (2007) Mechanical response of a jointed rock beam; numerical study of centrifuge models. *Int J Numer Anal Methods Geomech* 31(8):977–1006
- Wang HH, Han SH, Zhou XY (1991) Experiment study of dangerous rock mass at Lianzi cliff in the Thress Gorges by centrifuge. *Construct Des Res* 4:27–31 (in Chinese)
- Wang XG, Zhang JH, Zhao YZ (1996) Investigations on mechanism of slope toppling failure by centrifuge model testing. *Chin J Geotech Eng* 18(5):14–21 (in Chinese with English abstract)
- Willem Langenberg C, Ramsden J (1980) The geometry of folds in granitoid rocks of northeastern Alberta. *Tectonophysics* 66 (1–3):269–285
- Xing JY, Xing YC, Chen ZY (2005) Method research of centrifuge modeling of wedge failure in rock slope. *Bull Soil Water Conserv* 25(3):15–19 (in Chinese)
- Zhang JH, Chen ZY, Wang XG (2007) Centrifuge modeling of rock slopes susceptible to block toppling. *Rock Mech Rock Eng* 40 (4):363–382
- Zhang LM, Hu D (1990) Yielding and failure behavior of small scale centrifuge models. *J Chengdu Univ Sci Technol* 2:7–12



Physical Model of the Mechanism for Thermal Wedging Failure in Rocks

Vladimir Greif, Ivana Simkova, and Jan Vlcko

Abstract

Cyclic diurnal and annual temperature variations acting upon rocks are rarely considered among triggers of slope movements. The importance of temperature change is viewed mainly as a precursor of failures, where the triggers are rainfall or seismic activity. This paper aims to determine the limit conditions in which plastic deformation develops in a situation where one or more blocks fallen into an open crack create a wedge, causing non-elastic displacement of a block resting on an inclined plane. A physical model was prepared to study this phenomenon in a thermal dilatometer, in which the displacements were measured using linear variable differential transformer (LVDT) sensors for blocks with different block/wedge ratios, while temperature was varied in a controlled manner. Nine physical models of sandstone blocks were tested over a cyclic temperature change of $\Delta T = 35^\circ\text{C}$ while measuring the permanent displacements of a block in order to confirm the existence of this type of failure mechanism. Further, a series of cyclic tests were performed on all nine physical models to determine the threshold temperature change at which plastic deformation occurs for different block/wedge ratios. Results showed plastic deformation resulting from a cyclic wedging mechanism for a block/wedge ratio 0.5 and total model size of 50 mm, reaching a permanent displacement of 4.23×10^{-3} mm for a block resting on an inclined plane with a slope of 7° . For these conditions, a temperature change which caused permanent block displacement by thermal wedging was as low as 6°C . The results of the physical model are in agreement with a proposed analytical solution by Pasten (2013) and measurements of Bakun-Mazor et al. (2013) at a site at Masada, Israel.

Keywords

Thermal wedging • Rock stability • Failure mechanism • Cyclic temperature change

Introduction

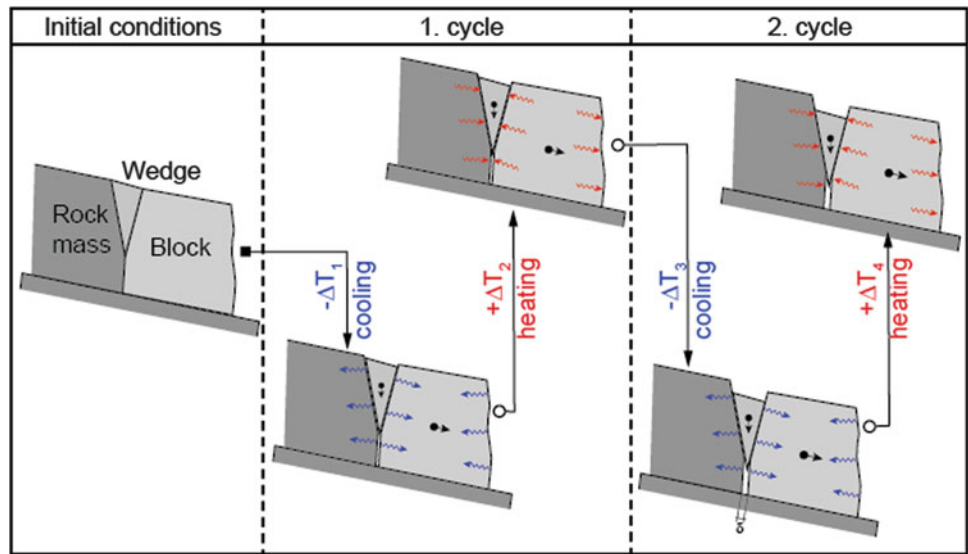
Knowledge of slope movements due to cyclic temperature change is not new. Davison (1888) describes rock-block displacement on an inclined plane triggered by temperature

variations. Further ideas that slope movements can be triggered by cyclic temperature changes are found in Redlich et al. (1929) and Záruba (1932).

The occurrence of slope movement as a consequence of thermal stress generation inside a rock slope is at present not well understood. Many authors (Gunzburger et al. 2005; Watson et al. 2004; Vlcko et al. 2005, 2009; Jezný et al. 2007; Brcek 2010; Brcek et al. 2010; Gischig et al. 2011a, b; Mufundirwa et al. 2011; Vargas et al. 2013) dealing with these problems acknowledge the thermo-mechanical effect affecting the rock slopes, but

V. Greif (✉) • I. Simkova • J. Vlcko
Department of Engineering Geology, Comenius University in Bratislava,
Mlynska dolina G, Bratislava 84215, Slovakia
e-mail: greif@fns.uniba.sk; simkova@fns.uniba.sk; vlcko@fns.uniba.sk

Fig. 1 Principle of the mechanism of thermally-induced wedging



quantification has proven to be difficult. Pasten (2013) attempted to quantify the amount of thermal sliding in a simplified conceptual analytical model shown in Fig. 1, where several blocks fall into an open crack, simplified as a wedge block of the same rock material, act on the block resting on a sliding surface, forcing it to move due to the wedging/ratcheting mechanism.

This led to a series of equations allowing the calculation of the plastic deformation of this rock block. Recently, Bakun-Mazor et al. (2013) applied this conceptual model to the rock slope at Masada (Israel) to distinguish between seismically- and thermally-induced displacements of a monitored rock block. In this work a series of physical models was carried out in order to understand the wedging mechanism and measure the plastic deformation for blocks with different wedge/block size ratios.

Model Preparation and Set-Up

The modeling experiment was prepared as a block of sandstone reacting against an inclined base made of the same material. The model was in the shape of cylinder core drilled from a sandstone rock block, with a diameter of 3.5 cm and length of 5 cm. The wedge acting in the open discontinuity was created by sawing the cylindrical sample at angle of $\chi = 15^\circ$ in order to obtain a wedge, as shown in Fig. 2. Nine model variations were prepared, differing by the ratio between the wedge width L_W and block width L_B (L_W/L_B). The dimensions of all model variations are summarized in Table 1. The base of the model was sawn to create a flat surface inclined at angle $\eta = 7^\circ$ from the horizontal. The model material properties are shown in Table 2.

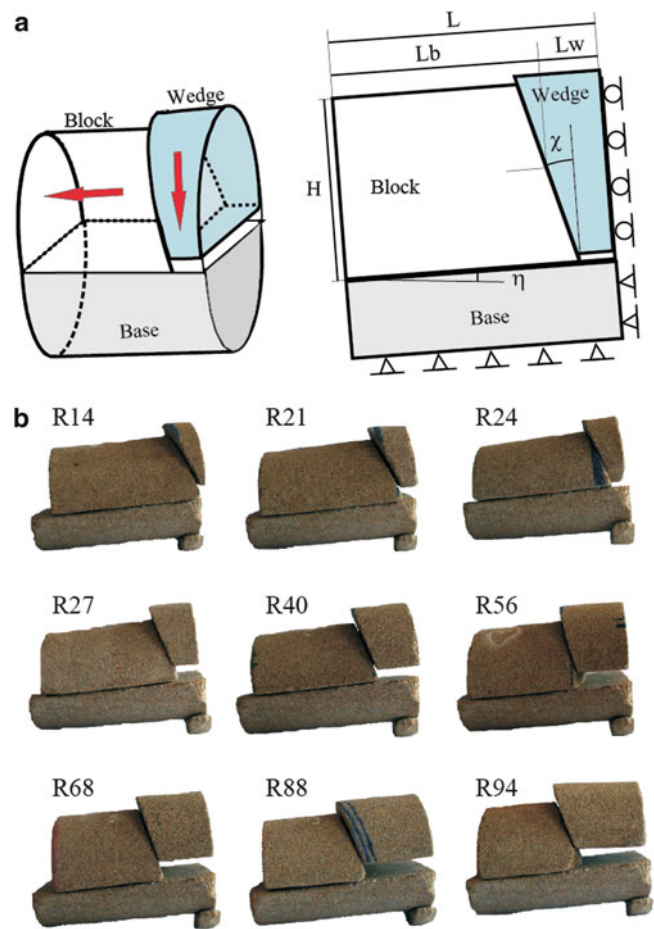


Fig. 2 (a) Geometry of the models and (b) the nine models prepared with various wedge/block ratios named in Table 1

All prepared model variations were tested in the thermo dilatometer VLAP04, which consists of a frame made of borosilicate glass enclosed in a thermally controlled

Table 1 Model dimensions and geometry

| Model dimensions/model | R14 | R21 | R24 | R27 | R40 | R56 | R68 | R88 | R94 |
|------------------------|-------------|-------------|-------------|-------------|------------|-------------|-------------|-------------|-------------|
| $L = L_b + L_w$ [cm] | 4.45 | 4.48 | 4.49 | 4.43 | 4.51 | 4.51 | 4.24 | 4.50 | 4.54 |
| L_b [cm] | 3.90 | 3.70 | 3.62 | 3.48 | 3.13 | 2.88 | 2.52 | 2.39 | 2.34 |
| L_w [cm] | 0.55 | 0.78 | 0.87 | 0.95 | 1.38 | 1.63 | 1.72 | 2.12 | 2.20 |
| L_w/L_b [–] | 0.14 | 0.21 | 0.24 | 0.27 | 0.4 | 0.56 | 0.68 | 0.88 | 0.94 |
| H [cm] | 1.94 | 1.88 | 1.94 | 1.76 | 1.74 | 1.81 | 1.88 | 1.75 | 1.84 |
| χ [°] | 15 | 18 | 17 | 15 | 15 | 13 | 12 | 11 | 17 |
| η [°] | 7 | 7 | 7 | 7 | 7 | 7 | 7 | 7 | 7 |

Table 2 Model properties

| Model material properties | |
|--|-----------------------|
| Joint friction angle ϕ_j [°] | 23.7 |
| Mass density ρ [kg/m ³] | 2,410 |
| Thermal expansion coefficient α [°C ⁻¹] | 1.09×10^{-5} |
| Thermal diffusivity χ [m ² s ⁻¹] | 8.44×10^{-7} |
| Specific heat C [J.Kg ⁻¹ °C ⁻¹] | 1.01×10^3 |
| Thermal conductivity λ [Wm°C ⁻¹] | 2.09 |
| Young's modulus [GPa] | 8.82 |
| Shear joint stiffness [MPa/m] | 18.7 |

chamber. The temperature is controlled by a computer and could be adjusted in the range from -17 to $+60$ °C. The temperature was measured on the surface of the rock model and in the center of a dummy sample prepared from the same material as the model. Figure 3 shows the scheme of the dilatometric device, with a close-up of the model set-up prepared for testing.

In order to measure the block displacements caused by the wedging action due to the cyclic thermal loading, a push rod made from fused silica was attached to the free side of the block with a cyanoacrylate adhesive to prevent unwanted slippage. This rod transferred the block movement to a linear variable differential transformer (LVDT) transducer, which measured the displacement with a resolution of 1×10^{-4} mm.

Thermal Testing Procedure

The relatively small size of the physical model was chosen intentionally in order to allow for complete equalization of the temperature inside the model.

This was documented by comparison of the temperature curves measured inside the model and at the model surface (Fig. 4). This situation corresponds to an exposure time long enough to reach temperature homogenization inside the model according to Pasten (2013).

Each model was inserted in the thermal chamber, where the temperature was controlled by a thermocouple inserted inside a dummy sample composed of the same material as the model. The testing procedures were designed to determine two characteristic values.

The first was the amount of plastic displacement of the block due to the wedging action created during one thermal cycle with $\Delta T = 35$ °C. For this procedure the model was inserted inside the dilatometric device VLAP04 according to Fig. 2. Testing started after 1 h to allow for temperature equalization.

The temperature was then decreased from an initial 20 to -15 °C and then back to the initial temperature. The rate of the temperature change was nonlinear, with higher rates in initial stages of cooling and heating and slower rates during equalization (Fig. 4). The testing procedure with the cooling/heating rates was kept similar for all model tests. The plastic deformation of the block was calculated by measuring the value of the displacement after one thermal cycle by the LVDT sensor.

The second characteristic value was the limit temperature change ΔT_{\max} causing a permanent displacement of the block. The testing procedure consisted of repeating the thermal cycles while increasing the temperature difference ΔT by 1 °C at each step. The displacement of the block was measured after completion of each cycle and the procedure was stopped when the displacement reached 10^{-3} mm. The corresponding temperature difference ΔT was then declared the limit temperature change ΔT_{\max} causing a permanent displacement of the block for that particular model.

Analytical Model

An analytical model for the wedging failure mechanism was developed by Pasten (2013) and subsequently used by Bakun-Mazor et al. (2013) for assessing the possibility of block displacements at the rock slopes of Masada (Israel).

The model is based on an assumption of rock fragments fallen in an open crack of average aperture L_w , simplified into a wedge block in the conceptual model. The sliding block dimensions are L_B (length) and H (height). Pasten assumes the rock block is a homogenous body subjected to a temperature change from T_0 in the center to a new boundary temperature T_1 . The time required for the temperature to equalize in the entire rock block t^* is defined as $t^* = L_B^2/D_T$, where L is the sliding block length and D_T is the

Fig. 3 Scheme of the dilatometric device VLAP04, with the detail of the testing configuration and thermocouple placement

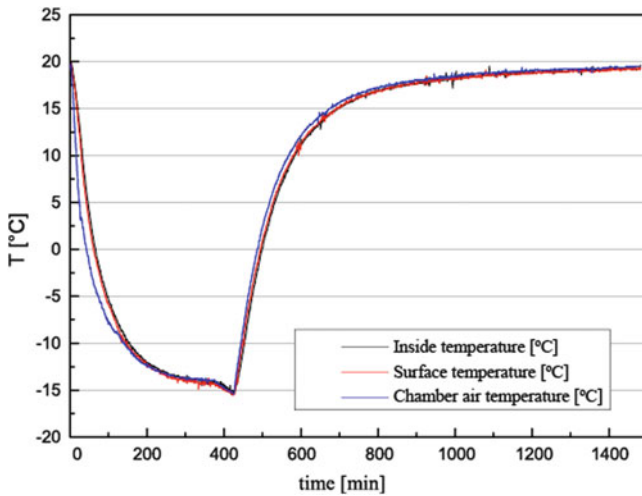
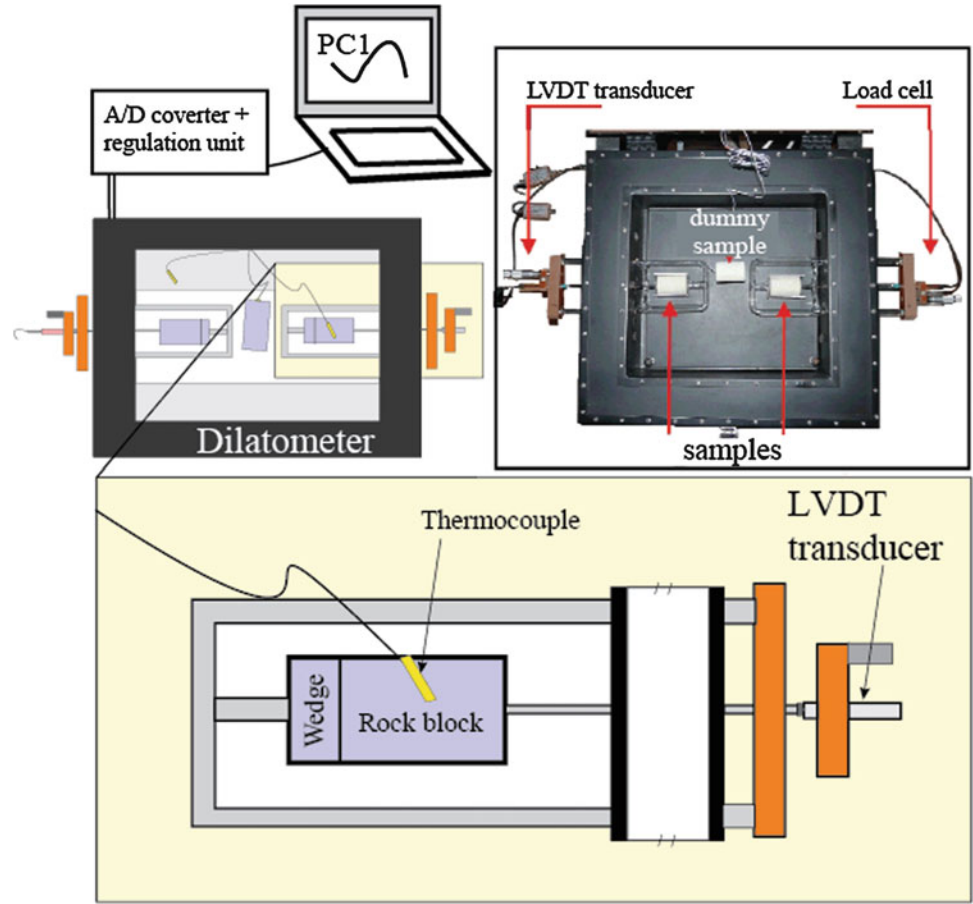


Fig. 4 Records of the temperature measurements at the model surface, center and chamber temperature during the test

thermal diffusivity of the rock, which is proportional to the rock thermal conductivity (λ), and inversely proportional to its mass density (ρ) and specific heat capacity (C_p). Following Pasten (2013), the depth of penetration of the heating

front during an annual cycle, referred to here as the “thermal skin depth” (S_d), may be estimated as

$$S_d \approx L/2 \quad \text{for } t_{\text{exp}} > 2L^2/D_T, \quad (1)$$

where t_{exp} is the exposure time, which is in the case of physical models longer than the homogenization time required to equalize the temperature inside the rock block, as documented in Fig. 4.

Pasten (2013) further suggests three displacement components that are involved in the thermal expansion process: the thermal expansion (δ_T), the elastic compression of the rock material (δ_σ), and the elastic shear response along the sliding interface (δ_j). The unconstrained seasonal thermal expansion (δ_T) of both sides of the tension crack as well as the wedge fragments inside the tension crack may be expressed by

$$\delta_T = \alpha \cdot \Delta T \cdot (L_w + \xi \cdot L_B + \beta \cdot S_d) \quad (2)$$

where α is the thermal linear expansion coefficient of the rock material, ΔT is the seasonal temperature change, and β is a coefficient accounting for non-uniform diffusive temperature distribution inside the sliding block and the rock mass

with values ranging from 0 to 1. The coefficient β is only introduced when the skin depth S_d is smaller than the half-length of the rock block. The dimensionless coefficient $\xi \leq 1.0$ accounts for the free thermal expansion of the right portion of the block that does not contribute to constraining the system thermal expansion.

During block heating, an elastic force develops, acting along the crack and leading to the block displacement. The maximum force per unit length parallel to the base F_{\max} [N/m] that the block frictional resistance can sustain is

$$F_{\max} = \gamma L_B \cdot \left(H - \frac{1}{2} L_B \tan \eta \right) \cdot (\tan \phi \cos \eta - \sin \eta) \quad (3)$$

where γ is the unit weight of the rock ($\gamma = \rho \cdot g$), ϕ is the friction angle of the sliding plane, and η is the inclination of the sliding plane.

The resulting elastic displacement (δ_σ) generated in the block and wedge due to the action of F_{\max} is

$$\delta_\sigma = \frac{F_{\max} \cdot \cos \eta}{H \cdot E} \cdot \left(L_W + \frac{L_B}{2} \right) \quad (4)$$

where E is the modulus of elasticity of the rock material.

The final component for the calculation of plastic displacement (δ_p) is the joint elastic displacement (δ_j)

$$\delta_j = \frac{1}{k_j} \cdot \frac{F_{\max}}{L_B} \cdot \cos \eta \quad (5)$$

The term k_j is the shear stiffness coefficient for the sliding surface. Knowing these components, one can determine the plastic displacement generated by an annual temperature cycle as follows

$$\delta_p = \delta_T - \delta_\sigma - \delta_j \text{ for } (\delta_T - \delta_\sigma - \delta_j) > 0 \text{ else } \delta_p = 0 \quad (6)$$

In order to calculate the plastic displacement, an estimation of joint shear stiffness was carried out using several tests conducted on a micro shear frame custom made for the purpose of testing shear resistance of the sawn model surface under low normal stress. The linear expansion coefficient was determined in the dilatometer VLAPO4 and the resulting value is shown in Table 2, together with the result of the tilting test focused on measuring the joint friction of the saw-cut shear surface of the sliding block.

The maximum temperature that the system can sustain without plastic displacement is calculated from

$$\Delta T_{\max} = \frac{F_{\max}}{\alpha \cdot (L_w + \xi \cdot L_B + \beta \cdot S_d) \cdot E} \cdot \left[\frac{E}{k_j \cdot L_B} + \frac{L_w}{H} + \frac{L_B}{2H} \right] \quad (7)$$

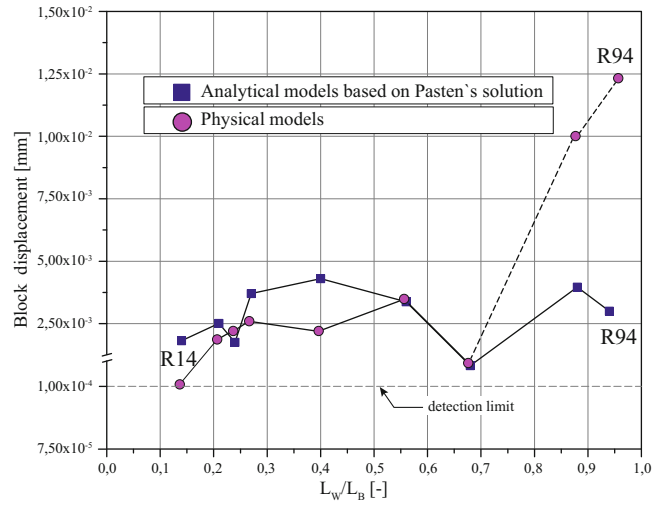


Fig. 5 Comparison of plastic displacements of sandstone blocks measured on physical models and calculated based on the analytical conceptual model of Pasten (2013)

which for typical field conditions can be simplified to

$$\Delta T_{\max} = \frac{1}{\alpha} \cdot \left(1 + \frac{L_w}{L_b} \right) (\mu \cdot \cos \eta - \sin \eta) \frac{H}{d(t_{\text{exp}})} \cdot \frac{\gamma_r}{k_j} \quad (8)$$

where length subjected to expansion $d(t_{\text{exp}})$ is a function of the exposure time for the physical models equals to

$$d(t_{\text{exp}}) = L_w + \xi \cdot L_B + \beta \cdot S_D \quad (9)$$

Comparison of Results to Analytical Model

Calculated values of the plastic displacement of the sliding sandstone block for nine models with different wedge-block ratios are presented in a graph shown in Fig. 5. For all the model scenarios the measured displacements by the LVDT sensors on equivalent wedge-block ratios obtained from physical models are presented on the same figure.

By comparing the result it might be concluded that displacements curves for both analytical and physical models have a similar tendency, despite some differences in the amplitude of displacements. More importantly, the existence of the wedging mechanism in rock blocks has been confirmed. As for the maximum temperature change the system can sustain (Fig. 6) without observing plastic displacement, it can be noted, that the values of ΔT_{\max} for analytical prediction and physical models were very similar for the model with smaller wedges, while with the increase of the wedge size (L_B) the ΔT_{\max} values decreased for the physical models.

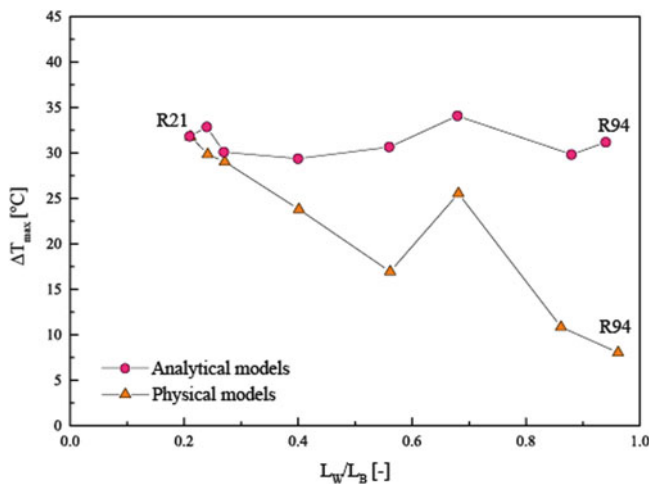


Fig. 6 Comparison of maximum temperature change the model can withstand without plastic deformation of sandstone blocks measured on physical models and calculated based on analytical conceptual model of Pasten (2013)

This decrease is possibly attributable to a non-linear trend of shear-stiffness coefficient k_j . This coefficient was estimated from tests with R21 (a large sliding block and thus a smaller wedge).

Conclusions

A set of physical models was prepared to study thermal wedging mechanism in a thermal dilatometer, where the displacements were measured using LVDT sensors for blocks with different block/wedge ratios, while changing the temperature in a controlled manner. Nine physical models of sandstone blocks were tested for an annual temperature change of $\Delta T = 35$ °C while measuring the permanent displacements of a block, in order to confirm the existence of this type of failure mechanism. Further, a series of cyclic tests were performed on all 9 physical models in order to determine the threshold temperature change ΔT_{max} at which the plastic deformation occurs for different block/wedge ratios.

The results confirmed the existence of plastic deformation resulting from a cyclic wedging mechanism for a block/wedge ratio 0.5 and total model size of 50 mm, reaching permanent displacement of 4.23×10^{-3} mm for a block resting on an inclined plane with slope of 7°. For the same conditions, a temperature change which causes a permanent displacement of the block by the wedging mechanism was found to be as low as 6 °C for a wedge/block ratio 0.94. The results of the physical model support the proposed analytical solution by Pasten (2013) and measurements of Bakun-Mazor et al. (2013) at the Masada site in Israel.

Acknowledgments This work was supported by the Slovak Research and Development Agency under the contract No. APVV-0641-10, Study of rocks properties and investigation of structural and textural characteristics in correlation with thermophysical and physico-mechanical properties, further under contract No. APVV –0330–10 Development of Remote System of Stability Monitoring of High Voltage Pylons Located in Landslide Risk Areas and APVV SK-CN-0017-12 Landslide hazard and risk assessment for UNESCO World Heritage Site, Danxia, China.

References

- Bakun-Mazor D, Hatzor YH, Glaser SD, Santamarina JC (2013) Thermally vs. seismically induced block displacements in Masada rock slopes. *Int J Rock Mech Min Sci* 61:196–211
- Breck M (2010) Vplyv teplotných cyklov na zvetrávanie hornín. Ph.D. thesis, Prírodovedecká fakulta Univerzity Komenského v Bratislave, Bratislava, 127 p (in Slovak)
- Breck M, Varilova Z, Greif V, Vlcko J (2010) Stanovenie teplotného pola pieskovcového masívu Pravčickej brány (ČR) na základe zhodnotenia denných a ročných teplotných cyklov. *Mineralia Slovaca* 42(2):205–216 (in Slovak)
- Davison CH (1888) Note on the movement of screen-material. *Q J Geol Soc Lond* 44(1–4):232–238
- Gischig V, Moore J, Evans K, Amann F, Loew S (2011a) Thermomechanical forcing of deep rock slope deformation. 1. Conceptual study of a simplified slope. *J Geophys Res* 116(F4), F04010
- Gischig V, Moore J, Evans K, Amann F, Loew S (2011b) Thermomechanical forcing of deep rock slope deformation. 2. The Randa rock slope instability. *J Geophys Res* 116(F4), F04011
- Gunzburger Y, Merrien-Soukatchoff V, Senfaute G, Piguet JP (2005) Influence of daily surface temperature fluctuations on rock slope stability: case study of the Rochers de Valabres slope (France). *Int J Rock Mech Min Sci* 42(3):331–349
- Jezný M, Vlcko J, Hvozďara M (2007) Teplota ako faktor štruktúrneho oslabenia horninových masívov. *Geotechnika* 10(3):8–15 (in Slovak)
- Mufundirwa A, Fujii Y, Kodama N, Kodama J (2011) Analysis of natural rock slope deformations under temperature variation: a case from a cool temperate region in Japan. *Cold Reg Sci Technol* 65:488–500
- Pasten C (2013) Geomaterials subjected to repetitive loading: implications on energy systems. Ph.D. thesis, Georgia Institute of Technology, Atlanta, GA
- Redlich K, Terzaghi K, Kampe R (1929) *Ingenieurgeologie*. Springer, Wien, p 708
- Vargas JE, Velloso R, Chávez L, Gusmão L, Amaral C (2013) On the effect of thermally induced stresses in failures of some rock slopes in Rio de Janeiro Brazil. *Rock Mech Rock Eng* 46:123–134
- Vlcko J, Greif V, Grof V, Jezny M, Petro L, Breck M (2009) Rock displacement and thermal expansion study at historic heritage sites in Slovakia. *Environ Geol* 58(8):1727–1740
- Vlcko J, Jezny M, Pagacova Z (2005) Influence of thermal expansion on slope displacements. In: Sassa K, Fukuoka H, Wang F, Wang G (eds) *Landslides: risk analysis and sustainable disaster management*, Proceedings of the first general assembly of the international consortium on landslides. Springer, Washington, DC, pp 1–74
- Watson AD, Moore DP, Stewart TW (2004) Temperature influence on rock slope movements at checkerboard creek. In: Lacerda W, Ehrlich M, Fontoura S, Amaral CP (eds) *International symposium on landslides (ISL)*, Rio de Janeiro, pp 1293–1298
- Záruba Q (1932) O stabilite svahů nad povltavskou silnicí u Štěchovic a Vraného. *Časopis československých inženýrů Technický obzor* (16) (in Czech)



Shallow Modes of Slope Failure in Road Earth Cuttings in Sri Lanka

H.M. Janaki M.K. Herath, Sudheera S.I. Kodagoda, and A.A. Virajh Dias

Abstract

Road associated failures in Sri Lankan landslides that have been investigated to date were highly dependent on geological setting of the cut slope. Numbers of cut slopes and their failure modes were studied in order to understand the influence of factors: slope height and angle, bed rock geology, seepage, overburden geology and geometry of the cut slope on the slope failure. Shallow failure mode (height of failed mass less than 4 m) is a very common feature in these cut slopes when exposed to intense rainfall due to extensive saturation. Slope stability can be evaluated with the use of geometry, shear strength characteristics and geological setting. Importance of geological setting and characteristics of failure modes must be considered when designing structural measures to improve the stability. An understanding of combined effect of geomorphology and overburden geology, which sets stability of a road cutting, is an essential parameter and helps in understanding sliding potential of the immediate upper slope. This study emphasises importance of geological setting, which determines the characteristics of failure modes when designing structural measures to improve the stability. Combined effect of geomorphology and overburden geology, which sets stability of a road cutting, is an essential parameter for designing of remedial measures by reducing sliding potential of the immediate upper slope.

Keywords

Morphology • Geology • Shallow sliding mode • Infinite slope • Factor of safety

Introduction

Sri Lanka has a tropical climate and the mean annual rainfall varies throughout the island with the wet zone receiving over 2,500 mm (maximum of 5,500 mm in Watawala), while the intermediate zone receiving between 1,750 and 2,500 mm and the dry zone receiving less than 1,750 mm of rainfall in a year. A distinct dry season is existent in the dry zone from May to September (Jayasena et al. 2007).

In ancient times, almost total hill country regions consisted of virgin forests with indications of slope stability. With the increase of population and developments, hill slopes of the upcountry of the Sri Lanka have been occupied for settlements and this activity rapidly increased after the British era. An effort was made to avoid soil slopes and use somewhat denser formations (meta-sedimentary rocks) in eroded slopes for the infrastructure developments (Fig. 1).

Good road location can often avoid landslide areas and reduce slope failures. Further, it is necessary not to create instability when cuts are made. It is reasonable to update and define failures in road earth cutting as shown in Table 1.

Other than overburden soil conditions and morphology, road based earth cutting failures are influenced considerably by underlying bedrock conditions (geology, genesis, dip, rock orientation, degree of weathering, inter-planer material)

H.M.J.M.K. Herath (✉) • S.S.I. Kodagoda • A.A.V. Dias
Centre for Research and Development (CRD), Central Engineering
Consultancy Bureau (CECB), No. 11, Jawatta Road, Colombo 05,
Sri Lanka
e-mail: jmkherath@yahoo.com; sudheeraik@gmail.com;
aavirajhd@yahoo.com



Fig. 1 Construction of Colombo—Kandy Railway in Sri Lanka during, British era 1796–1948 (Source: <http://lankapura.com>)

and environmental conditions. General physical setting of road section and surrounding factors of importance in the environment are shown in Figs. 2 and 3 below.

Geology and Topography of Hill Country, Sri Lanka

The topography of the island shows three distinguished geographical peneplains named as “Up-country” with an average elevation above 900 m, “Mid-country” with an elevation of 300–900 m and “Low-country” below 300 m in elevation (Cooray 1984). Mid and high peneplains are made of landforms such as mountains, escarpments, valleys, hills and ridges (Panabokke 1996). Precambrian crystalline hard rock is spread over 90 % of the land area in Sri Lanka. The rest is covered by Jurassic, Miocene, Holocene sedimentary formation and very few igneous rocks (Cooray 1984).

These Precambrian rocks which metamorphose under granulite facies and amphibolite facies are sub divided in to three groups based on the lithology, structures and age of the rocks. They are Highland complex (HC), Vijayan complex (VC) and Wannan complex (WC) with the Kadugannawa complex as a subordinate unit (Cooray 1984). The Highland complex rocks comprises mainly of granulite grade charnockitic rocks, and meta-sediments. The Highland Complex is bound on the east by the amphibolite

grade Vijayan Complex. The Wannan Complex consists mainly of granitic gneisses, charnockitic gneisses, and migmatites, and the metamorphic grade ranges from amphibolite to granulite (Mathavan et al. 1999).

Slope failures typically occur: where a slope is very steep, where cuts in natural soils encounter more saturation, groundwater or zones of weak material. Geology plays major role in stability of an earth cut, especially in different soil—rock stratification patterns set at sites, as shown in Fig. 4.

Common Modes of Slope Failures

The road associated soil and rock slope failure mechanisms can be classified as (1) soil and rock slump, rotational slides in homogeneous clayey soil, (2) translational slides and slip along plane of weakness and (3) complex form due to geological setting (rock–soil). Driving force is the component of soil weight and the resisting force is the soil strength acting in the opposite direction. Slope failure occurs when driving force exceed the resisting force. Factor of safety (FS) is defined as the ratio of resisting forces (or moments) to the driving forces (or moments). If $FS < 1$, the slope will fail, if $FS > 1$, the slope is theoretically stable. The minimum FS requirement for the design of slope is between 1.3 and 1.5 (Geotechnical manual for slopes, Hong Kong 1997).

Circular Soil Slumps and Soil Falling Mode

In principle-, circular mode of failure is very difficult to distinguish in natural soil slopes, but geometry of relatively small landslides show this in circular pattern. This is usually observed in homogeneous residual form of soils as shown in the Figs. 5, 6, 7, 8 and 9.

A series of statistical interpretations were performed from the direct field data of earth cutting behaviour which is associated with various geological conditions at site. The falling of soil or soil slump mode are very common features if height of slope exceeds 3.4 m as indicated in Fig. 10.

Table 1 Defining road associated types of failures

| Type of movement | Type of material in fall, flow or deposited | | |
|----------------------|---|--------------------------------|------------------------------------|
| | Bed rock | Debris (coarse soil particles) | Earth-(fine soil) |
| Fall | Rock fall | Debris fall during rain | Earth fall—immediate after the cut |
| Rotational slides | | Debris slump- Colluvium | Earth slump—residual soil |
| Translational slides | Rock block slide | Debris slide - | Earth slide |
| | Rock slide | | Composit landslide |
| Complex | Composite failures in rock and soil etc. | Slump and earth flow | Composite failures in soils |

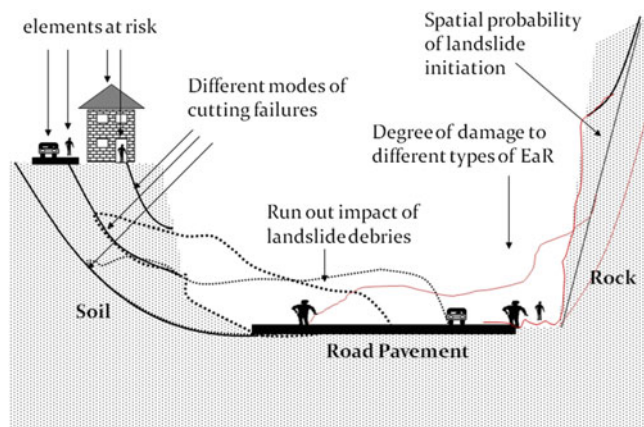


Fig. 2 Road based morphological patterns, land use and different modes of failures

Infinite Slope Failure Mode

Infinite slope failure is significant in dip slope with highly foliated, jointed and stratified rocks as shown in Figs. 11 and 12. Detachment of passive wedge, removal of earth cover and exposure of foliated rock to temperature has triggered slope failures. That means, negligence of geological detachments along interfaces, and inability to accommodate appropriate design requirements adversely affect the stability of these slopes. Therefore, it is important to consider outcrops, shear veins, quartz veins, secondary graphite and other indicators of brittleness in the weathered rock outcrops during the design of cut slopes. Above geometrical similarities and rock slope infinite modes of failures were observed in field as shown in Figs. 11 and 12.

It is well known that rocks may undergo degradation when they are exposed to atmospheric weathering and/or hydrothermal fluid transition through foliated joints, and

other rock joints during saturation. It is also noted that, top surface foliated faces tend to initiate hairline opening of joints during construction of road cut sections, and finally those slopes will subject to wetting and drying over a period of time. The infinite slope failures may create unexpected failure patterns even at 0.8–1.2 m open cut section as shown in the field (Fig. 12). In deterministic approach; interface friction of foliated layers, joint density and effect of seepage pressures are important for the evaluation of FS. In such situations, minimum FS for the design of slope section is considered to be $FS > 1.5$ (Geotechnical manual for slopes, Hong Kong 1997). In addition to it, if the evaluation is considered under seismic acceleration, minimum FS should be greater than 1.2. When using the infinite slope method, if the FS is near or below 1.0–1.15, severe erosion or shallow slumping is likely. However, vegetation on the slope can help to reduce this problem because roots add cohesion to the surficial soil which improves stability.

The rock slope failures are statistically represented in Fig. 13. Typically, if the slope height exceeds 5 m, rock slope failures are highly significant. In addition, the infinite slope failures are significant in dip slopes even at the cutting height exceeds 0.8 m as indicated in Figs. 12 and 13.

Composite Mode of Slope Failure

Composite failure allows the failure surface to intersect the subsoil and then to follow the rock interface. Stability is critical, if the slope is geologically unsuitable either due to soil overlaying under-dipping rock slopes or a saturated layer at the interface which can form a composite failure as shown in Fig. 14.



Fig. 3 An example of negligence during the construction stage to evaluate and design for stability of rock slope, geological setting, overburden parameters and land use during road widening works

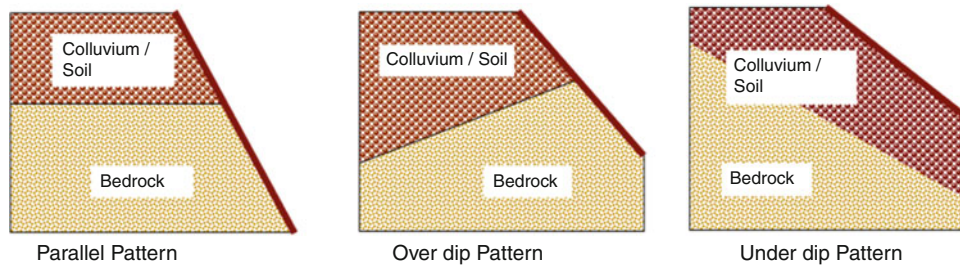


Fig. 4 Surface slope and stratification patterns of soil and rock

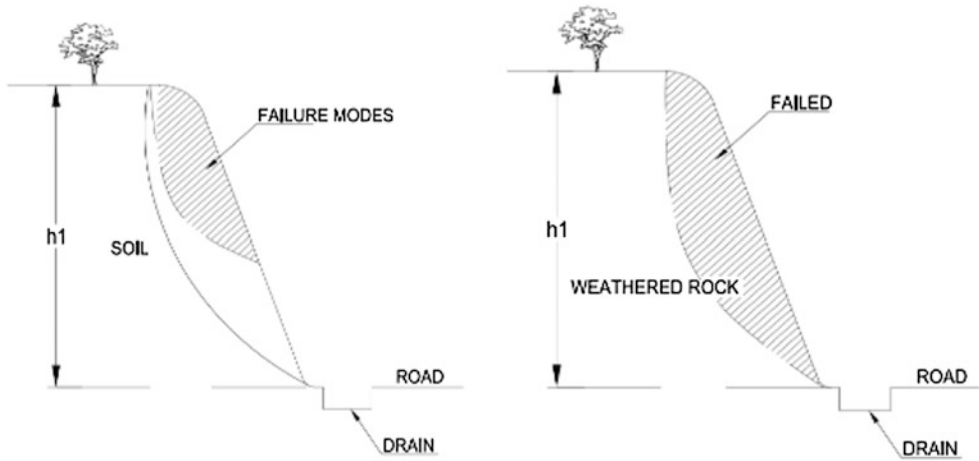


Fig. 5 Typical pattern of the circular soil slump and circular failure modes in soil and weathered rock faces

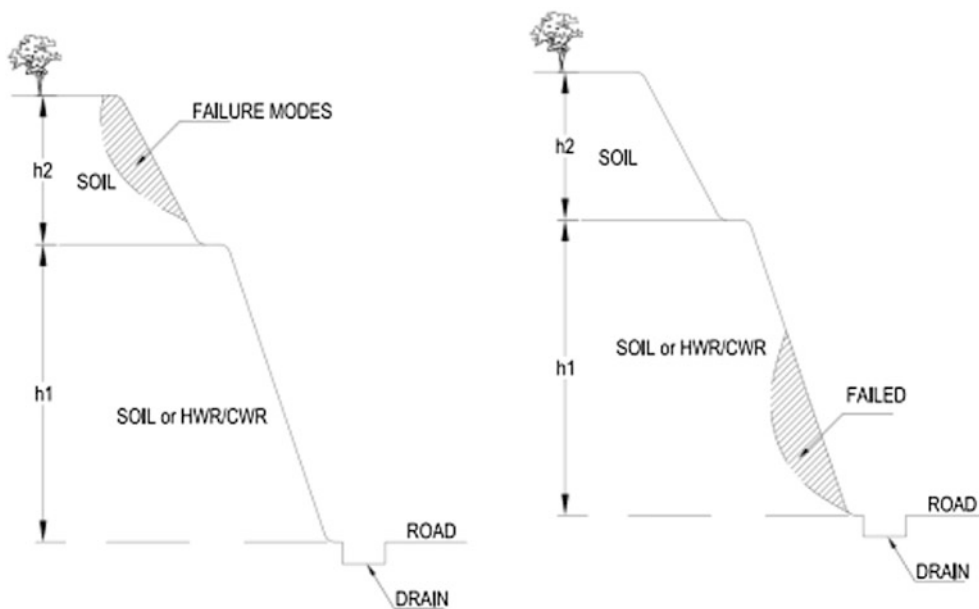


Fig. 6 Typical observations of relatively circular modes of failure in high earth cuts with soil-rock site



Fig. 7 Relatively large soil slump feature in residual soil due to lack of appropriate remedial measures

Weathering transforms hard rocks into soft rocks, which maintains structure of the parent rock, but the weathering increases void ratio and reduces material strength. The physical and chemical weathering impacts can be a predominant fact in controlling the modes of soil failure at the interfaces.

Stable Rock Slopes in Weathered Rock

It is interesting to note that number of earth cuts that were observed along roads have fully resisted to weathering even under severe weathering conditions prevailed in recent past as presented in Figs. 15 and 16.



Fig. 8 Some typical examples of unsupported soil slump failures in residual soil exposed to surface saturation during rain



Fig. 9 An observation of relatively circular modes of failure in colluvium formation

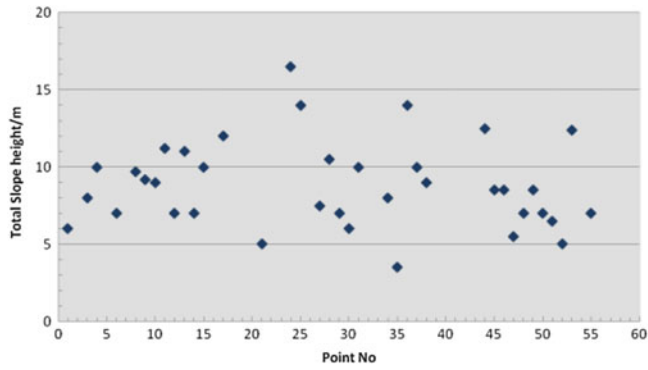


Fig. 10 Statistical representation of the soil failure of the non-engineered construction of earth cut sections

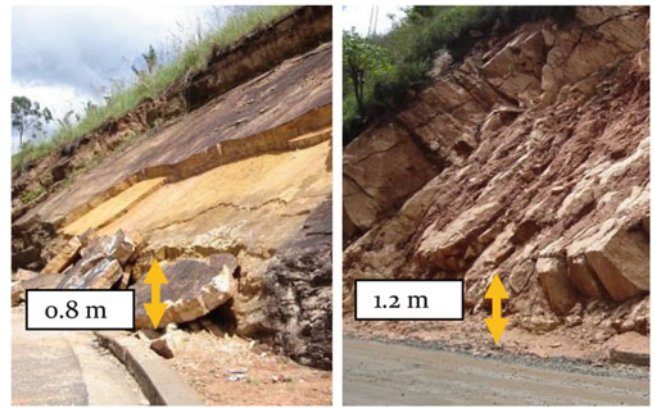


Fig. 12 Field example of failure of cut slopes in a foliated rock due to lack of passive support

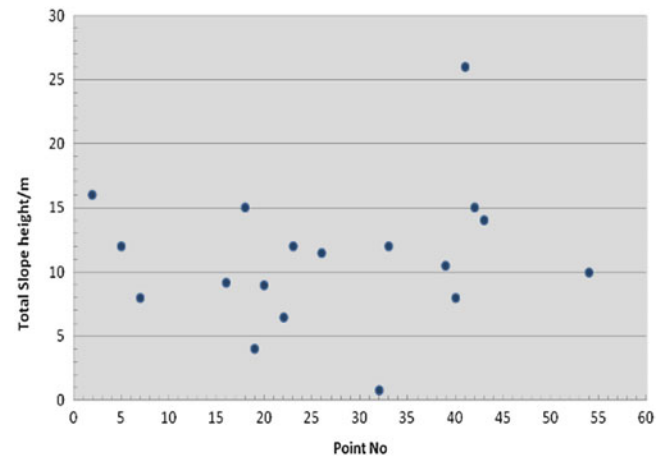


Fig. 13 Statistical representation of foliated rock slope failures

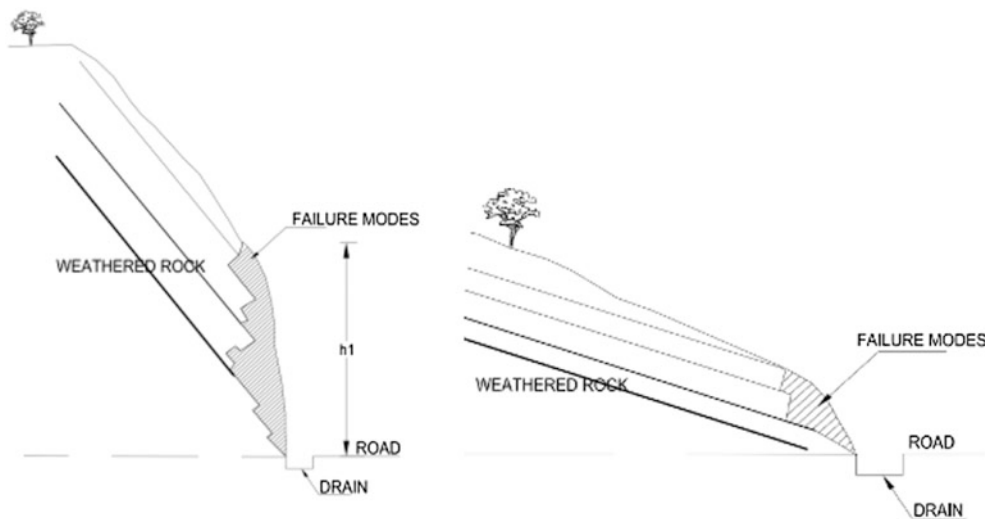


Fig. 11 Typical geometry of infinite—rock slope failure mode



Fig. 14 Geologically unstable rock-soil slope condition



Fig. 16 Highly foliated under dip conditions at cutting with long term standstill section at tropical weather conditions



Fig. 15 Typical field showing completely weathered rock cutting, which remains as stable even after subjected to periodic wetting and drying in last 20–30 years

Conclusion

It appears that, in above cases, a prominent pattern of failure can be noticed along a road trace if the tropical weather conditions prevail at site. Under such circumstances, the minimum factor of safety was observed in the composite failure mode, involving a circular failure that intersects softer soils resulting in a slip surface in the lower portion of the cut. This evaluation has implied that a second set of parameters deemed necessary for sub-soils on the upper, and steeper, slope areas. The shallow sliding mode is very common in

slopes with a 2–6 m wide wet strip along the road beneath the slope surface, and, in general, the circular sliding mode occurs in slopes with strong groundwater influence within the uniform residual soil strata. For the shallow sliding mode, the safety factor could be smaller, if the slope height is more than 3.4 m.

A hypothesis suggests that besides the secondary failure such as debris flow in the erosion trenches, there are two major failure modes significant in those slopes, i.e., shallow planer failure in the rock-soil formation and circular sliding in residual soil slopes. By conducting the above mentioned assessment, the authors make the following conclusions, as presented in Table 2.

After some review of the data, and the overall objective, following observation were made: significant cohesion values were detected only in soils with somewhat higher densities, and average friction angles in completely weathered rocks. A review of the data found that these were noted in slopes with clayey soils.

The study of relationship between safe heights, geology, geometry and land use are important in designing safe cut slope section in residual form soil regions under tropical weather conditions. It is noted that, limited field observations on shear strength, pore water pressure and their correlations with the above modes of failures need to be studied further in order to draw a scientific explanations to the design of engineering slopes in roads.

Table 2 Sensitivity of open cuttings in roads

| Shallow modes of failure | Description | Limiting cutting height |
|--|--|---------------------------------|
| Circular failures, soil slumps and soil falling mode | Residual soil and compacted transported soil | 3.4 m |
| Infinite slope failure mode | Critical in under dipping rock | 0.8 m |
| Composite mode of slope failure | soil overlaying under-dipping rock slopes | Very low |
| Long-term stable slope in weathered rock | Over-dipping rock slopes and moderately to highly weathered rock slopes only | 5 m single cut, 15 m with berms |

Acknowledgments This paper forms an integral part of the research on “Evaluation of Modes of Failures of the Road Base Landslide in Hill Country, Sri Lanka” being implemented by the Centre for Research & Development, Central Engineering Consultancy Bureau (CECB) of the Ministry of Irrigation and Water Resources Management. It is published with their permissions. The views expressed in the paper are however those of the authors only. Our grateful thanks are due to Eng. N. Rupasinghe, Chairman and Eng. K. L. S. Sahabandu, General Manager, Central Engineering Consultancy Bureau for the permission and encouragements.

References

- Cooray PG (1984) An introduction to geology of Sri Lanka, 2 (revised) th edn. National Museum of Sri Lanka Publication, Colombo
- Geotechnical Control Office, Engineering Development Department, Hong Kong (1997) Geotechnical manual for slopes. Government Publication Centre, Hong Kong
- Jayasena HA, Chandrajith R, Dissanayake CB (2007) Hydrogeochemistry of the groundwater flow system in a crystalline terrain: a study from the Kurunegala district. Springer, Sri Lanka
- Mathavan V, Prame WKBN, Cooray PG (1999) Geology of the high grade Proterozoic terrains of Sri Lanka, and the assembly of Gondwana: an update on recent developments. *Gondwana Res* 2:237–250
- Panabokke R (1996) Soils and agro-ecological environments of Sri Lanka. Natural Resources, Energy and Science Authority of Sri Lanka, Colombo



Discussion on the Method of Intact Loess Humidification Considering Water Content Uniformity

Kai He and Bin Li

Abstract

Soil mass strength has a direct correlation with soil mass water content. The shearing test for soil under different water contents is the most important method of analyzing landslide (sliding belt) soil mass strength. According to the humidification requirements on the intact loess for indoor test, we should pay attention to the uniformity of humidification for the intact loess. Through comparative studies on three humidification methods, it is considered that when the same loess samples have reached the same preset humidity, the loess sample with the pre-wetting method for 24 h can reach the uniform water distribution; the loess sample using the burying method can reach to the uniform water distribution after 10 days and the loess sample using the steaming method can reach the uniform water distribution after 8 h. The burying method can get the large water content range for humidification and saturated loess samples can be obtained through humidification, whereas the saturated loess samples cannot be obtained through the pre-wetting and steaming method.

Keywords

Water content • Humidification method • Pre-wetting method • Burying method • Steaming method

Introduction

Loess landslide is one of the most common geo-hazards in the Northwest of China and the landslide disaster has become a major hazard for human settlements and urban construction. The triggers of loess landslide is the decrease in the strength of soil mass in the slope. The strength of the soil mass is closely related to its water content: when the water content in the slope reaches a certain value, the pore pressure in the loess is sharply increases and the shearing

strength significantly decreases (Miao et al. 1999), thereby causing landslides.

The loess in China is mostly distributed in arid or semi-arid regions. In general, shallow layer loess is in the unsaturated state. The unsaturated loess has high strength and low compressibility when its water content is low, but its strength is greatly decreased and its compressibility is evidently increased when it has high water content. For loess slopes, precipitation, irrigation, temperature changes will cause changes in the water content of the unsaturated loess, which leads to changes in the strength of loess and thereby causing the landslide disasters (Chen 1997; Chen 1999; Chen et al. 2006; Li et al. 2012; Xiong and Hu 2007; Yin et al. 2004). Therefore, when analysing the stability of loess landslide, physical and mechanical parameters of intact loess at different water ratios should be obtained by tests (Li and Miao 2006; Xie 2001; Zhang and Li 2011). As controlled by sampling conditions or test requirements, humidification processing is often carried out for the intact loess samples

K. He (✉)
School of Geological Engineering and Surveying, Chang'an University, YanTa Road, Xi'an 710054, China
e-mail: hekai2005@163.com

B. Li
Institute of Geomechanics, Chinese Academy of Geological Science, Beijing 100081, China
e-mail: libin1102@163.com

Table 1 Pre-wetting method water content uniformity test

| Initial dry density ($\text{g} \cdot \text{cm}^{-3}$) | Dry density after humidification ($\text{g} \cdot \text{cm}^{-3}$) | Average water content after humidification (%) | Water content (%) | | | | Differential water content (%) |
|---|--|--|-------------------|-------------|----------------|----------------|--------------------------------|
| | | | Soil surface | In the soil | The lower part | The upper part | |
| 1.28 | 1.28 | 21.2 | 21.4 | 20.6 | 21.3 | 21.6 | 1.0 |
| 1.27 | 1.27 | 21.3 | 21.4 | 20.9 | 21.4 | 21.7 | 0.8 |
| 1.29 | 1.29 | 21.3 | 21.5 | 20.8 | 21.4 | 21.7 | 0.9 |
| 1.28 | 1.28 | 21.6 | 21.8 | 21.2 | 21.8 | 21.7 | 0.6 |

Table 2 Burying method for water content uniformity test

| Test sample | Water content (%) | | Differential water content (%) |
|--------------------------|-------------------|-------------|--------------------------------|
| | Soil surface | In the soil | |
| Cutting ring test sample | 17.1 | 16.1 | 1.0 |
| | 20.6 | 20.4 | 0.2 |
| | 31.1 | 30.3 | 0.8 |
| | 30.2 | 29.7 | 0.5 |
| Triaxial test sample | 17.3 | 16.8 | 0.5 |
| | 28.0 | 28.0 | 0.0 |
| | 29.8 | 29.5 | 0.3 |
| | 31.4 | 31.3 | 0.1 |

during testing in order to get loess samples with different water contents. For the special structure of the loess, how to change the water content in the intact loess samples uniformly without changing the structure of soil is the key to carry out pretreatment under the precondition. By introducing a contrastive analysis method on the prevailing humidification methods, it is hoped that it will be helpful for selecting the humidification method so that the physical and mechanical parameters of the intact soil mass can be better obtained during the follow-up tests.

Contrastive Study on Humidification Tests

Pre-wetting Method

The pre-wetting method is a widely used humidification method for testing. Firstly, we drip water on the surface of the loess samples directly, and then put the loess samples into the humidifier to stand still and let the water dropped on the surface of the soil layer penetrate into the soil mass to obtain a uniform water content.

Taking a triaxial shear test sample, as an example, the author used the pre-wetting method to carry out humidification for the intact loess samples. We dry the triaxial test samples, and drip water from upper and lower ends as well as sides using a dropper. After humidification, we let the samples stand still in the humidifier for 24 h to

make the water distributed uniformly (Table 1). According to the soil test regulations (China Code for standard for soil test method 1999), this humidification method can meet the requirement of uniform water distribution in the test samples. However, as the triaxial test samples have large volumes, a large quantity of dripping water is needed. To prevent damaging the soil structure for excessive water, we select different positions for dripping and circulating for a certain time interval when dripping.

Burying Method

The burying method was rarely used in previous experimental studies. The specific approach is to bury the loess samples into the soil with basically the same target water content. Under the diffusion, it makes the loess samples reaching to the target water content. This is a humidification method under the natural conditions. This method realizes the humidification only through water migration using the humidification process under the natural state but without changing the structure of the loess samples during the humidification process.

To simplify the test operation, the authors attempted to make the following improvement: wrap the loess samples with filter paper and bury them into the sawdust with proper water content for humidification. We buried the intact loess samples with initial water content of 13.9 %, in-situ void

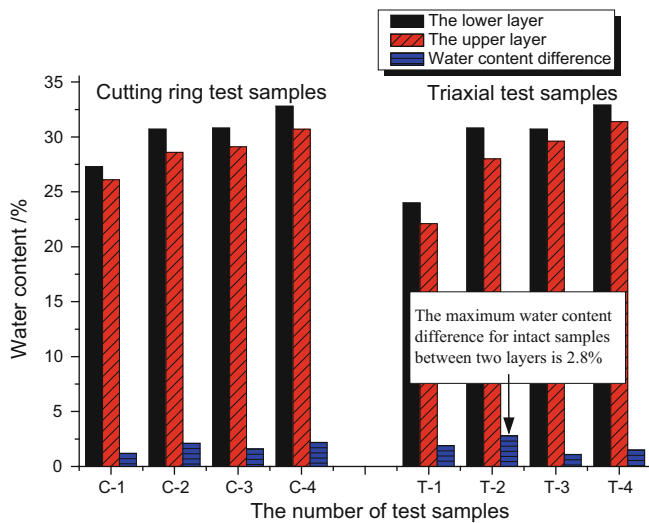


Fig. 1 Water content difference between samples in upper and lower layer

ratio of 0.895, specific gravity of soil particles of 2.69 into two layers of sawdust with the same water contents with a vertical elevation difference of 15 cm between the upper layer and the low layer. We measured water contents from the surface of the test samples and the soil core respectively after the samples are buried and carried out water content comparison for the upper layer and the lower layer soil samples (Table 2). The results indicate that the uniformity of water contents in the two layers of loess samples meet the requirement, however, because the samples are buried for a long period, under the gravity, water is transferred, resulting in dry sawdust in the upper layer and humid sawdust in the lower layer in the humidifier. The water content of the loess samples buried in the upper layer is less than that in the lower layer. The maximum water content difference for samples in two layers is 2.8 % (Fig. 1), which is beyond the regulation requirement (China Code for standard for soil test method 1999). As a result, two layers of loess samples cannot be used for carrying out experiment as the test

samples with the same water content. Therefore, it is required that the loess samples should be buried in the same level height for the burying humidification method to ensure that each loess sample have the same water content. During the burying method tests, the maximum water content of the triaxial test samples is 32.9 % and the saturation is 96.5 %. Therefore, the burying method can humidify the intact loess samples into the saturated state.

Steaming Method

The steam humidification method is a new method that was suggested in recent years but it is rarely used at present. The basic idea of the steam humidification method is to carry out even pre-wetting through the uniformity of the steam. We cut the loess samples first, carry out steam humidification, and then use preservative film to wrap the loess samples after humidification and put them into the humidifier to stand still until the water content inside the loess samples is uniformly distributed.

In case there is no special equipment such as the steam tank, the steam can also be provided by a pressure cooker. When testing, we put the loess samples into a pressure cooker and open the pressure valve of the pressure cooker to make the vapour in a non-pressure state (with respect to atmosphere). The length of time for providing the steam has no major impact on the effect of humidification, as it generally takes 10 min. After humidification the samples are set on standing for 8 h to ensure that the water ratio is evenly distributed in the loess samples (Wang et al. 2010).

Taking the 10 min non-pressure humidification as an example (Table 3), the test results indicate that when carrying out humidification for the unsaturated loess using the non-pressure steam the humidification rate is about 20 % of the initial water content and there is almost no change in dry density before and after loess sample humidification (Wang et al. 2010), therefore the non-pressure state humidification does not have impact on the soil structure.

Table 3 Steam humidification method effect test (according to Wang et al. 2010)

| Initial water content (%) | Initial dry density ($\text{g}\cdot\text{cm}^{-3}$) | Dry density after humidification ($\text{g}\cdot\text{cm}^{-3}$) | Water content (%) | | Differential water content (%) | Average water content after humidification (%) | Increased water content (%) |
|---------------------------|---|--|-------------------|-------------|--------------------------------|--|-----------------------------|
| | | | Soil surface | In the soil | | | |
| 14.5 | 1.25 | 1.25 | 17.3 | 17.1 | 0.2 | 17.2 | 2.7 |
| 15.0 | 1.25 | 1.25 | 17.7 | 17.5 | 0.2 | 17.6 | 2.6 |
| 21.4 | 1.35 | 1.34 | 25.6 | 25.2 | 0.3 | 25.4 | 4.0 |
| 21.6 | 1.34 | 1.34 | 25.7 | 25.2 | 0.5 | 25.5 | 3.9 |
| 25.9 | 1.28 | 1.28 | 31.9 | 31.4 | 0.5 | 31.7 | 5.8 |
| 25.8 | 1.28 | 1.29 | 31.6 | 31.2 | 0.4 | 31.4 | 5.6 |

Conclusions

1. For using the same test samples to achieve the same pre-set humidity, setting the loess samples on standing for 24 h for the pre-wetting method can make the water distributed uniformly in the samples, while setting the loess samples on standing for 10 days in the burying method can make water distributed uniformly. Likewise, setting the loess samples on standing for 8 h using the steaming method can make water distributed uniformly in the samples.
2. The idea of the pre-wetting method is simple, but it requires repeated dripping for humidification, and a frequent manual operation.
3. The burying method can carry out humidification for a large range of water contents. The saturated soil samples can be obtained by humidification but not using the pre-wetting method and the steaming method. However burying method requires longer time for water to be distributed uniformly and in-situ humidification. It also requires that the loess samples with the same water content be buried in the same level/height.
4. The operation of the steam humidification method is the most simple and convenient, it requires the shortest time for humidification but the volume of loess samples for humidification is limited. It is fitting for cutting ring test samples but not for loess samples with large volume. When the target water content is large, steam should be used repeatedly for humidification.

When carrying out the tests, we select an appropriate humidification method according to the type of test

samples, requirements on the humidification speed as well as the specific test conditions.

Acknowledgments We are grateful to Chun-li Chen for her help about humidification tests and data collection, which improved this paper.

References

- Chen S (1997) A method of stability analysis taken effects of infiltration and evaporation into consideration for soil slopes. *Rock Soil Mech* 18(2):8–12
- Chen Z (1999) Deformation, strength, yield and moisture change of a remolded unsaturated loess. *Chin J Geotech Eng* 21(1):82–90
- Chen C, Gao P, Tang J (2006) Structural quantitative parameter of intact loess with different water contents under triaxial stress condition. *Chin J Rock Mech Eng* 25(11):2313–2319
- China Code for standard for soil test method (GB/T50123-1999) (1999) China Planning Press, Beijing
- Li B, Miao T (2006) Research on water sensitivity of loess shear strength. *Chin J Rock Mech Eng* 25(5):1003–1008
- Li B, Yin Y-p, Wu S-r et al (2012) Failure mode and formation mechanism of multiple rotational loess landslides. *J Jilin Univ (Earth Sci Ed)* 42(3):760–769
- Miao T, Liu Z, Ren J (1999) Deformation mechanism and constitutive relation of collapsible loess. *Chin J Geotech Eng* 21(4):383–387
- Wang T-h, Luo S-f, Liu X-j (2010) Testing study of freezing-thawing strength of unsaturated undisturbed loess considering influence of moisture content. *Rock Soil Mech* 31(8):2378–2382
- Xie D-y (2001) Exploration of some new tendencies in research of loess soil mechanics. *Chin J Geotech Eng* 23(1):3–13
- Xiong B, Hu X-m (2007) The triaxial test study of loess wetting properties. *J Railw Eng Soc* 105:23–27
- Yin Y, Zhang Z et al (2004) Occurrence and hazard assessment on loess landslide of gaolanshan in Lanzhou. *Quat Sci* 24(3):302–310
- Zhang M, Li T (2011) Triggering factors and forming mechanism of loess landslides. *J Eng Geol* 19(4):530–540



Undrained Shear-Strength Variation of Salt-Rich Clay: Implications for Fast-Moving Clay Landslides

Lei He, Bao-ping Wen, and Xiu-juan Xu

Abstract

It is well recognized that the shear strength of salt-rich clay is reduced after leaching and under drained conditions, as commonly occurs in reactivated landslides or in slow-moving landslides of such clay. This is due to loss of the physical and/or chemical bonds provided by the salt, demonstrating the physico-chemical effect of pore water on the shear strength of the clay. However, is there a similar effect when such clay is subjected to undrained conditions after leaching, as in fast-moving landslides in the clay following rainstorms or irrigation? To gain better understanding of the mechanisms of fast-moving landslides of salt-rich clay, the shear strength of a salt-rich clay under undrained conditions was investigated after being leached repeatedly. The clay was weathered mudstone from Heifangtai, Gansu, China. Test results showed that the clay's undrained shear strength was remarkably reduced after leaching, mainly through water-soil physical-chemical interactions. The effective friction angle and cohesion of the clay may be reduced due to loss of the bonding salts, similar to the variation of its strength parameter under drained conditions. In addition, higher pore water pressure could build up during shearing due to an increase in the clay fraction caused by disaggregation of silt-size particles, leading to a decrease in effective normal stress and then shear strength.

Keywords

Salt-rich clay • Salt-leaching • Shear strength • Pore water pressure • Water-soil physical-chemical interactions • Disaggregation

Introduction

The shear strength of clay is one of the key parameters for evaluating slope stability or landslides, and it is affected by both the composition of the soil skeleton and its interactions with pore water. In arid or semi-arid or coastal areas, clays normally contain significant amount of soluble salts, and the salts could be leached by flood irrigation or long-term

rainfall. Leaching salt from the clay should greatly reduce the clay's shear strength under drained conditions, especially the clay's residual shear strength (e.g., Moore 1991; Tiwari et al. 2005; Wen and He 2012). Moore (1991), Tiwari et al. (2005), and Wen and He (2012) attributed this phenomenon to loss of physical or chemical bonds or both provided by the salt, namely a physical-chemical effect, and thought that this explained the reactivation mechanism of some salt-rich clay landslides.

However, when the soluble salts are leached and the clay is subjected to undrained conditions, as in fast-moving clay landslides following a rainstorm or irrigation, does the physical-chemical effect of pore water still influence the shear strength of the clay, apart from pore water pressure?

L. He (✉) • B.-p. Wen • X.-j. Xu
School of Water Resources and Environment, China University of Geosciences (Beijing), No. 29 Xueyuan Road, Haidian District, Beijing 100083, China
e-mail: helei06@126.com; wenbp@cugb.edu.cn;
twttevkexuxiujuan@163.com

Table 1 Chemical compositions of the clay, groundwater and the Yellow River water

| Ion type | Clay (mg/100 g) | Groundwater (mg/L) | Yellow River water (mg/L) |
|-------------------------------|-----------------|--------------------|---------------------------|
| K ⁺ | 6.18 | 37.63 | 1.1 |
| Na ⁺ | 201.95 | 8,827 | 26.36 |
| Ca ²⁺ | 14.57 | 562.4 | 67.93 |
| Mg ²⁺ | 2.46 | 1,090 | 18.78 |
| Cl ⁻ | 192.41 | 9,560 | 18 |
| NO ₃ ⁻ | 0 | 847 | 2.94 |
| SO ₄ ²⁻ | 70.33 | 10,591.6 | 52.48 |
| HCO ₃ ⁻ | 180.1 | 5.21 | 271.72 |
| Total | 668.86 | 31,520.84 | 459.31 |

Table 2 Physical properties of the clay

| Particle density (KN/m ³) | Particle size fraction (mm, %) | | Liquid limit (%) | Plastic limit (%) | Plasticity index |
|---------------------------------------|--------------------------------|--------------------|------------------|-------------------|------------------|
| | Clay (<0.002) | Silt (0.002–0.075) | | | |
| 27.7 | 37 | 63 | 33 | 16 | 17 |

Table 3 Mineralogical compositions of the clay

| Whole soil (%) | | | | | | Clay portion (%) | | | |
|----------------|----------------------|---------|----------|----------|---------------|------------------|----|---|---|
| Quartz | Plagioclase feldspar | Calcite | Dolomite | Hematite | Clay in total | I/S | I | K | C |
| 27 | 5 | 16 | 3 | 4 | 46 | 50 | 32 | 9 | 9 |

Note: I/S Inter layered illite/smectite, K kaolinite, C Chlorite

This paper aims at better understanding the mechanisms of fast moving landslides of salt-rich clay. The shear strength of a salt-rich clay under undrained conditions was investigated after the clay was leached a number of times, and the effect of pore water was analyzed in terms of both pore-water pressure and water-soil physical-chemical interactions.

Samples and Methods

Samples

The salt-rich clay used in this study was collected from highly weathered Cretaceous red mudstone close to the Huangci Landslide at Heifangtai, Yongjing county of Gansu. At the sampling site, the weathered Cretaceous red mudstone appeared to be a loose, very wet and soft red clay. The Huangci landslide was a large, fast-moving landslide with a volume of 6×10^6 m³. It occurred following irrigation in January 30, 1995, with a sliding distance of 40 m in 90 min. Extensive investigation has proved that the landslide developed along bedding planes of the weathered Cretaceous mudstone and that reduction of shear strength in the slip surface induced by irrigation was one of the primary factors leading to the sliding. A salt deposit could be observed at the toe of the landslide, indicating that desalination of the slip zone occurs along with irrigation.

The soluble salts within the clay and groundwater in Huangci Landslide and the nearby Yellow River water which was used for irrigation are presented in Table 1. The

salt content in the sample was determined following Chinese National Standards CNS GB/T50123-1999 (Standardization Administration of China et al. 1999). Nearly 0.7 % of the sample was composed of soluble salts, with NaCl as the most common, forming up to 47.4 %. A high salinity of 31.5 g/L was found in the ground water, with an abundance of Na⁺, Cl⁻, and SO₄²⁻. In contrast, the Yellow River water has a salinity of only 0.5 g/L.

Basic physical properties of the clay are presented in Table 2. The grain size distribution and Atterberg limits of the sample were obtained in compliance with CNS GB/T50123-1999. Results showed that the sample was 37 % clay and 63 % silt. The liquid limit and plasticity indices were 33 and 17. X-ray diffraction analysis showed that the sample had primary massive minerals of quartz and calcite, and primary clay minerals of interlayered illite/smectite and illite with a minor amount of kaolinite and chlorite (Table 3).

Since the clay is very loose and soft, it was very difficult to collect enough good quality undisturbed soil in the field. Remolded samples were used in the study. To simulate various degrees of salt leaching of the clay, the soil saturated with groundwater was used to represent an unleached clay sample in the field, i.e., the “natural condition”. Salt leaching was carried out by leaching the sample with deionized water for different numbers of times, which is similar to the conditions when irrigation water has infiltrated into the clay several times. In this study, deionized water substituted for irrigation water (Yellow River water has an extremely low salinity, Table 1). Therefore, five groups of samples were used: samples saturated with groundwater, with

Table 4 Ionic concentrations of the pore fluids and the remaining soluble salts

| Sample | Ion concentration (mg/L) in pore fluid | | | | | | | Soluble salts in soil | |
|-----------------|--|-----------------|------------------|------------------|-----------------|-------------------------------|-------------------------------|-----------------------|----------------|
| | K ⁺ | Na ⁺ | Ca ²⁺ | Mg ²⁺ | Cl ⁻ | SO ₄ ²⁻ | HCO ₃ ⁻ | Remaining (mg/g) | % of remaining |
| S _G | | | | | | | | 12.36 | 100 |
| S _D | | | | | | | | 6.69 | 54 |
| S _{L2} | 2.6 | 159.0 | 4.0 | 0.8 | 135.0 | 85.5 | 125.0 | 4.33 | 35 |
| S _{L4} | 2.4 | 91.9 | 2.5 | 0.8 | 8.6 | 9.2 | 237.0 | 2.96 | 24 |
| S _{L6} | 1.5 | 46.2 | 2.2 | 0.6 | 1.2 | 1.4 | 131.0 | 2.09 | 17 |

deionized water, and those leached 2 times, 4 times and 6 times, which were labeled as S_G, S_D, S_{L2}, S_{L4} and S_{L6}.

The leached samples were prepared following Tiwari et al. (2005) and Wen and He (2012). Chemical analyses for post-leaching fluid and the remaining salt within the soil sample are presented in Table 4. Soluble salts within the “natural condition” sample from both the groundwater and dry soil samples was 12.36 mg/g. During the leaching process, soluble salts were dissolved and leached away, and Na⁺, Cl⁻ and SO₄²⁻ were the main type of ion compositions, consistent with the chemical composition in the soil mass (Table 1). The sample saturated with deionized water contained 54 % of the soluble salts in the “natural condition”. After leaching 2, 4 and 6 times, 35, 24 and 17 % of salts remained within the sample respectively. After leaching, the obtained slurry was air-dried and powdered for triaxial specimen preparation.

Testing Method and Specimen Preparation

A triaxial consolidated undrained (CD) test was adopted to determine the sample's shear strength. The triaxial specimens were prepared following British Standard Institution (BSI) BS 1377–8 (British Standard Institution 1990). The soil powder was thoroughly mixed with groundwater and deionized water to a water content of 5 % and stored in a sealed container for at least 24 h. The specimens were prepared by compacting the humid soil in six layers to an initial length of 76 mm, a diameter of 38 mm and a desired dry density of 1.76 g/cm³, which was obtained from an undisturbed sample. A vacuum saturation method was used to saturate the specimens. The pore pressure parameter B in all the specimens reached more than 95 %, indicating adequate saturation.

In the consolidation stage, filter-paper strips are used to decrease the time required for consolidation, as suggested by BSI BS 1377–8. At least 95 % of pore pressure was dissipated. For each group of samples, four specimens were consolidated at four confining pressures to define strength envelopes, which were 100, 200, 300, and 400 kPa.

The rate of axial strain was estimated as 0.036 mm/min based on the 100 % consolidation time according to BSI BS 1377–8. At this deformation speed, the pore pressure could be equalized throughout the specimen at failure. And each specimen was compressed to the maximum axial strain of 25 %.

Results

Shear Behavior

For the measured deviator stress, correction for filter-paper strips and rubber membranes were applied in accordance with BSI BS 1377–8. Figure 1 illustrates variation of the deviator stress, pore pressure and the effective principal stress ratio σ_1'/σ_3' with the axial strain of different specimens when the confining stress was 400 kPa. It could be seen that: (1) all samples did not show a distinct peak deviator stress or post-peak softening behavior, (2) the built-up pore pressure first rose then decreased as shearing proceeded, with the peak value occurring at an axial strain of 6–10 %, and (3) the effective principal stress ratio σ_1'/σ_3' presented a weak post-peak decrease, with the peak value at an axial strain of 11–14 %. It should be stressed that the specimens under confining stresses of 100, 200 and 300 kPa also presented similar shear behaviors to those under 400 kPa.

Under the same confining stress, S_G had the highest deviator stress, which was gradually reduced in the specimens in the order of S_D, S_{L2}, S_{L4} and S_{L6} (Fig. 1a), and also in the order of loss of soluble salts. Moreover, the value of σ_1'/σ_3' was also highest in S_G and gradually decreased in S_D, S_{L2}, S_{L4} and S_{L6} (Fig. 1c). However, the excess pore water pressure seemed to become greater as more soluble salts were lost (Fig. 1b).

Variation of Deviator Stress and Pore Water Pressure at Failure with Soil Salinity

As no peak deviator stress could be located in the stress–strain curves, the failure was defined by the maximum effective principal stress ratio, as suggested in BSI BS 1377–8. The deviator stress and pore water pressure at failure were plotted with the percentage of salts remaining within the clay, as in Fig. 2.

At four levels of confining stress, the deviator stress of the sample at failure significantly decreased as the soluble salts reduced (Fig. 2a). The decrement of deviator stress was 7–10 % in S_D, compared with S_G, which were 19–21, 27–30 and 31–33 % in S_{L2}, S_{L4} and S_{L6} respectively.

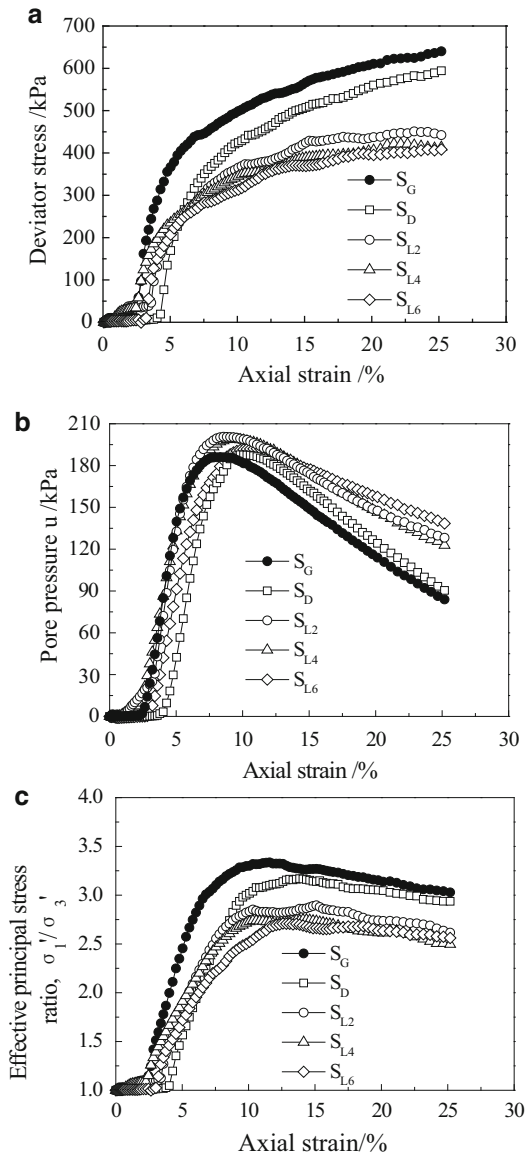


Fig. 1 Undrained triaxial test on specimens (a) deviator stress (b) pore water pressure (c) effective principal stress ratio σ_1'/σ_3' against axial strain

The pore water pressure at failure seems slightly increased with decreased soil salinity (Fig. 2b). An increment of 1–9 % in pore pressure between S_G and S_D was observed, which were 3–10, 4–16 and 6–18 % in S_{L2} , S_{L4} and S_{L6} respectively compared with S_G .

Effective Shear Strength Parameters

The effective shear strength parameters, effective friction angle (φ') and effective cohesion (c') of the sample were determined by Mohr stress circles based on effective stresses at failure. The effective strength envelopes are presented in

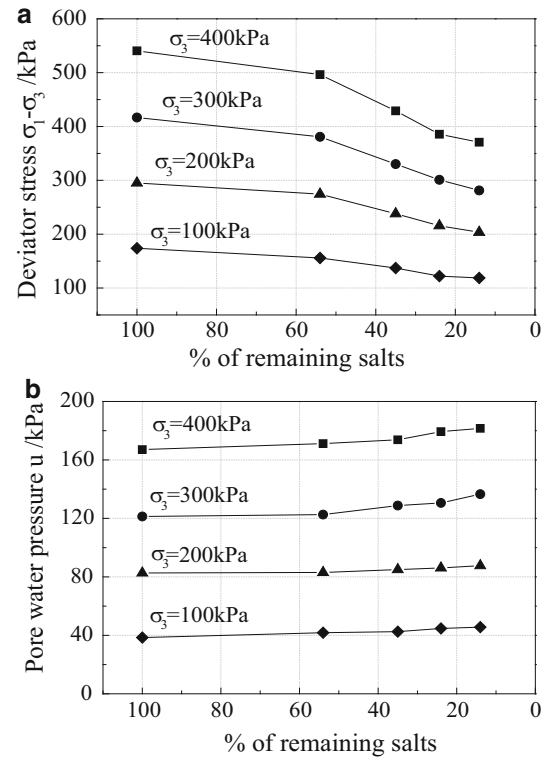


Fig. 2 Variation in (a) deviator stress (b) pore water pressure at failure with percentage of remaining salts within the clay

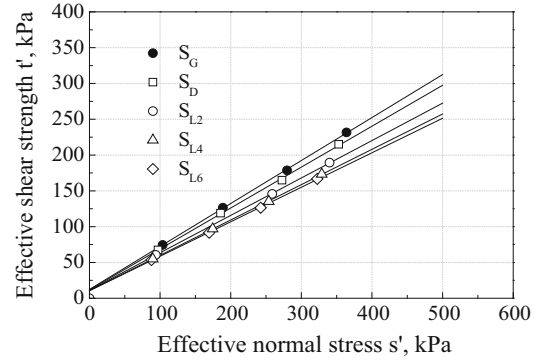


Fig. 3 Effective strength envelopes of the clay

Fig. 3, and the estimated effective shear strength parameters are summarized in Table 5 and plotted with the percentage of remaining salts in Fig. 4.

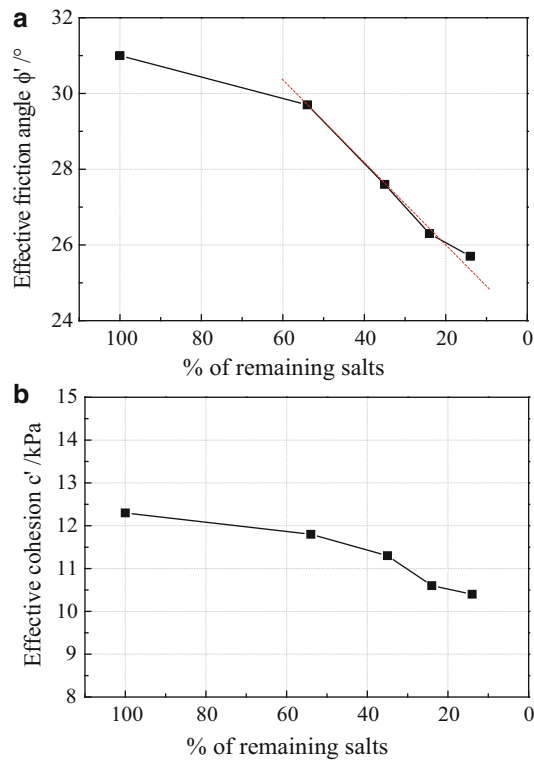
Sample S_G presented the highest value of φ' , 31° . S_D gave 29.7° , which was 4 % reduced from S_G . Then with leaching process repeated and the remaining salts within the sample reduced, the value of φ' continuously decreased, by 11 % in S_{L2} , 15 % and 17 % in S_{L4} and S_{L6} respectively, compared with the natural condition. In Fig. 4a, the value of φ' decreased almost linearly as the soluble salts content was reduced from 54 to 24 %.

Table 5 Effective strength parameters of the samples

| Sample | ϕ' (°) | c' (kPa) |
|----------|-------------|------------|
| S_G | 31.0 | 12.3 |
| S_D | 29.7 | 11.8 |
| S_{L2} | 27.6 | 11.3 |
| S_{L4} | 26.3 | 10.6 |
| S_{L6} | 25.7 | 10.4 |

Table 6 Physical properties of the leached samples

| Sample | Particle size fraction (mm, %) | |
|----------|--------------------------------|--------------------|
| | Clay (<0.002) | Silt (0.002–0.075) |
| S_{L2} | 44 | 56 |
| S_{L4} | 49 | 51 |
| S_{L6} | 51 | 49 |

**Fig. 4** Variation in effective strength parameters ϕ' (a) and c' (b) with percentage of remaining salts within the clay

The effective cohesion c' also tended to decrease in the order of soluble salts reduction (Fig. 4b). The reduction was 4, 8, 14 and 16 % in S_D , S_{L2} , S_{L4} and S_{L6} , compared with S_G respectively. However, as the value of c' varied between 10.4 and 12.3 kPa, the greatest variation in c' from S_G to S_{L6} was no more than 2 kPa.

Discussions

As all the samples were subjected to the same test conditions, and salinity was the only difference among them, the variation in effective strength parameters as well as pore water pressure and the deviator stress could be fully attributed to the discrepancy in soluble salt content within the samples.

Previous researches have proved soluble salts played a crucial role in cementing clayey soil particles, and loss of soluble salts would lead to disaggregation of coarse particles (Di Maio and Fenelli 1994; Tiwari et al. 2005; Wen and He 2012). Particle size analysis reveals that the sample had its initial clay fraction of 37 % increase to 44, 49 and 51 % after 65, 76 and 83 % of its soluble salts were lost in S_{L2} , S_{L4} and S_{L6} respectively (Table 6). As discussed by Di Maio (1996), Moore and Brunsten (1996) and Sridharan and Prakash (1999), due to loss of soluble salts, the pore water with high salinity is diluted, and weakening the salt bonding among individual clay particles causes an increase in the thickness of their diffuse double layers, leading to increased repulsive force and reduced Van der Waal's attraction force among clay particles.

Thus reduction in the effective friction angle ϕ' would result from an increased fine fraction and weakening of inter-particle forces, as illustrated in Fig. 4a. And reduced c' should arise from weakening inter-particle or inter-aggregate bonding. However, as reconstituted specimens were used, the origin soil fabric and bonding between particles could not be fully reconstructed, and the estimated c' should not represent the real cohesion between soil particles in situ. And the reduction in c' could only partly reflect the weakening inter-particle forces resulting from loss of bonding salts. Only 1.9 kPa of reduction in c' was observed in S_{L6} compared with S_G , which could be neglected in high normal stress.

On the other hand, since an increased clay fraction has been produced as a result of disaggregation of coarse particles when the bonding salts were leached, larger inter-aggregate pores would be replaced by smaller ones due to the averagely finer aggregates or clay clusters. Similar variation in soil after desalinization has been observed using a SEM technique by Zhang et al. (2013). They found that the void space within loess was smaller when saturated with diluted NaCl solution than in one saturated with higher concentration fluid. Consequently, the smaller voids would lead to higher pore water pressures built under the same level of confining pressure, and then reduction in overall shear strength too. This illustrates that the pore water pressure under undrained conditions was also influenced by water-soil physical-chemical interactions.

According to the principle of Terzaghi's effective stress, under undrained shear conditions, the shear strength of clays is defined as:

$$\tau_f = c' + (\sigma - u) \tan \varphi' \quad (1)$$

in which τ_f is the shear stress on the plane, σ the stress normal to that plane, u the pore water pressure, c' the effective cohesion, and φ' the effective friction angle.

As discussed above, for the salt-rich clay under undrained conditions, both its effective shear parameters (c' and φ') and pore water pressure (u) are influenced by the soluble salts content of the clay, or in pore water. After leaching, reduction in shear strength of the clay should be a combination of decrement in both its effective shear parameters (c' and φ') and an increase in pore water pressure.

The above discussion indicates that fast-moving landslides in hilly areas with salt-rich clay may be prone to movement where the salts of the clay have been leached by infiltration of long-term rainfall or irrigation water, or where the clay has a lower quantity of soluble salts, similar to slow-moving landslides in clay or reactivation of such clay landslides, as mentioned by many researchers (e.g., Moore and Brunsden 1996; Tiwari et al. 2005; Wen and He 2012).

Conclusions

A series of triaxial CU tests was conducted on a salt-rich clay collected from Huangci landslide after being leached various times. The following could be concluded:

1. Under undrained shear conditions, the clay's shear strength decreased significantly with loss of salts.
2. The reduction in the clay's shear strength could be attributed to water-soil physical-chemical interactions in two ways. One is that the effective friction angle and cohesion of the clay were reduced due to loss of bonding salts. The other is that higher pore water pressure was built up during the shear process due to increased clay fraction, leading to reduced effective normal stress.

3. Fast-moving landslides with salt-rich clay may be prone to movement where salts in the clay have been leached by long-term rainfall or irrigation, or where the clay has a lower quantity of soluble salts.

Acknowledgement This research was funded by the National Natural Science Foundation of China (No. 40872182). The authors are thankful to Ms Ya-jing Yan, Mr. Shu Jiang and Mr. Jing-fang Yan for sampling in the field.

References

- British Standard Institution (BSI) (1990) Methods of test for soil for civil engineering purposes-part 8 (BS 1377-8): shear strength tests (Effective Stress)
- Di Maio C (1996) Exposure of bentonite to salt solution: osmotic and mechanical effects. *Geotechnique* 46(4):695-707
- Di Maio C, Fenelli GB (1994) Residual strength of kaolin and bentonite: the influence of their constituent pore fluid. *Geotechnique* 44(4): 217-226
- Moore R (1991) The chemical and mineralogical controls upon the residual strength of pure and natural clays. *Geotechnique* 41(1): 35-47
- Moore R, Brunsden D (1996) Physicochemical effects on the behavior of a coastal mudslide. *Geotechnique* 46(2):259-278
- Sridharan A, Prakash K (1999) Influence of clay mineralogy and pore-medium chemistry on clay sediment formation. *Can Geotech J* 36 (5):961-966
- Standardization Administration of China (SAC), Ministry of Construction, Ministry of Water Resources (1999) China national standards GB/T50123-1999: standard for soil test method. China Planning Press, Beijing (In Chinese)
- Tiwari B, Tuladhar GR, Marui H (2005) Variation in residual shear strength of the soil with salinity of pore fluid. *J Geotech Geoenviron Eng* 131(12):1445-1456
- Wen BP, He L (2012) Influence of lixiviation by irrigation water on residual shear strength of weathered red mudstone in northwest China: implication for its role in landslides' reactivation. *Eng Geol* 151:56-63
- Zhang FY, Wang GH, Kamai T (2013) Undrained shear behaviour of loess saturated with different concentrations of sodium chloride solution. *Eng Geol* 155:69-79



Analysis of Engineering Geological Properties of Sliding-Zone Soil in Large-Scale Landslides in the Weibei Loess Tableland Area

Bin Li, Shuren Wu, Jusong Shi, and Zhen Feng

Abstract

Hipparion laterite exists extensively below the thick loess units on the northern bank of the Weihe River in Shaanxi, and its engineering geological properties control the occurrence of landslide hazards. Through hipparion laterite tests, this study shows the following: (1) the clay content of hipparion laterite is high including expansive clay minerals, such as ascanite or illite-smectite. The specific surface area values are as high as 262.9 m²/g. This property is due to the expansive clay, and this indicates that the material is physically and chemically active; (2) the hipparion laterite is characterized by micro-fissures, poor cementation, and disintegration. Its natural gumbo-like state changes to a plastic or soft plastic state when saturated and exhibits significant expansibility; (3) the natural intensity of hipparion laterite is relatively high. Its cohesion and internal friction angle are greatly reduced when saturated, and reduction from peak to residual shear strength is 47–63 %. Therefore, for a slope structure of thick loess, hipparion laterite, and bedrock, the strength of hipparion laterite greatly decreases under the effect of underground water. It then becomes a weak layer in high and steep slopes, forming shear zones that control the development and distribution of landslides in the Weibei loess tableland area.

Keywords

Hipparion laterite • Sliding zone • Engineering geological properties • Landslide

Introduction

There are two sets of strata under the thick loess layer of the Weibei tableland in Shaanxi Province. One set consists of red clay sediments in which hipparion fauna have been discovered; thus, it is also called “hipparion red clay” (Liu et al. 1985; Yue 1996; Peng and Guo 2007). The other set is a lacustrine facies sedimentary strata of grayish yellow, grayish green, and red clays, sandy clay and gravel. They are referred to as ancient Sanmen Lake deposits

(Wang et al. 1959; Sun 1986; Wang et al. 1999; Wang et al. 2001). There are some disputes about the ages and origins of these two sets of strata; however, in general, they are thought to be transitional from the end of the Pliocene Epoch to the Early Pleistocene (Pei and Huang 1959; Liu and Zhu 1959; Xue 1981). He et al. (1984) and Yue (1996) concluded that there were no monsoons during the Pliocene Epoch and that the climate was relatively moist. Thus, lacustrine facies materials were deposited in the basin of ancient Sanmen Lake and hipparion red clay accumulated outside the basin; thus, contemporaneous sediments with different facies were formed. At the initial stage of the Early Pleistocene, the global climate became cold and the modern pattern of the East Asian monsoon was formed. Because of these events, suitable formation conditions for widely distributed hipparion red clay ceased to exist. Sanmen Lake Basin shrank and the dust material carried

B. Li (✉) • S. Wu • J. Shi • Z. Feng

Key Laboratory of Neotectonic movement and Geohazards of MLR in Institute of Geomechanics, Chinese Academy of Geological Sciences, Beijing 100081, China
e-mail: libin1102@163.com; shrwu@cags.ac.cn; shijusong@126.com; fengzhencgs@126.com

Table 1 Test results of material composition and physicochemical properties of hipparion laterite

| Sample | Particle size fraction (mm) (%) | | | | Activity index (%) | Montmorillonite content (%) | Specific surface area (m ² /g) |
|--------------------|-----------------------------------|-------------------------------------|-------------------------------------|-------------------------------------|-----------------------------------|-------------------------------------|---|
| | >0.075 | 0.075–0.005 | <0.005 | <0.002 | | | |
| Hipparion laterite | 0.08–3.41 (1.54) ₁₀ | 45.02–62.71 (55.2) ₁₀ | 37.12–54.40 (43.3) ₁₀ | 30.24–48.04 (37.1) ₁₀ | 0.43–0.79 (0.65) ₁₀ | 18.61–27.56 (21.7) ₁₀ | 151.2–262.9 (205) ₁₀ |

Note: Data in parentheses are average values, while the subscript outside the parentheses is the number of analyses

Table 2 Quantitative analysis results of minerals in hipparion laterite

| Sample | Clay content <2 μm (%) | Clay mineral relative content (%) | | | | I/S mixed-layer ratio (%) | Clay mineral absolute content (%) | | | |
|--------|------------------------|-----------------------------------|-----|---|----|---------------------------|-----------------------------------|-------|------|------|
| | | I | I/S | C | K | | I | I/S | C | K |
| 1 | 38.19 | 26 | 67 | – | 7 | 40 | 9.93 | 25.59 | – | 2.67 |
| 2 | 37.90 | 15 | 75 | 3 | 7 | 55 | 5.69 | 28.43 | 1.14 | 2.65 |
| 3 | 32.99 | 17 | 72 | 4 | 7 | 45 | 5.61 | 23.75 | 1.32 | 2.31 |
| 4 | 36.08 | 19 | 72 | 3 | 6 | 45 | 6.86 | 25.98 | 1.08 | 2.17 |
| 5 | 38.48 | 18 | 76 | 2 | 4 | 55 | 6.93 | 29.25 | 0.77 | 1.54 |
| 6 | 31.87 | 21 | 69 | 4 | 6 | 40 | 6.69 | 21.99 | 1.28 | 1.92 |
| 7 | 35.04 | 22 | 63 | 7 | 8 | 40 | 7.71 | 22.08 | 2.45 | 2.80 |
| 8 | 42.48 | 31 | 55 | – | 14 | 70 | 5.22 | 33.98 | – | 2.55 |

Note: I/S illite–montmorillonite mixed-layer minerals, I illite, K kaolinite, C chlorite

by the monsoons (loess) was deposited extensively over northern China. It accumulated toward the middle of the lake in a chasing form along the edge of Sanmen Lake Basin. When Sanmen Lake disappeared, loess fully covered the tableland. Due to the limited Quaternary sediment coverage and geographic restrictions, limited research has been conducted on these two sets of strata.

In recent years, through detailed surveys on the geologic hazards in the loess area in the Guanzhong western region of Shaanxi Province, the authors found slip bands of large-scale landslides in the strata of the hipparion red clays and determined that its physical and mechanical properties directly controlled landslide occurrence (Qu et al. 1999; Li et al. 2011, 2012). Therefore, this paper analyzes the material composition, microstructure, physical and mechanical properties of hipparion red clays on the north bank of the Weihe River in Baoji, Shaanxi, to report its engineering geological properties and its influence on geological hazards.

Material Composition and Structural Features of Hipparion Red Clay

Particle size distribution and clay mineral and cement compositions of hipparion red clay determine its engineering geological properties. Different compositions of clay minerals, especially differences in the montmorillonite content, directly determine the physicochemical properties of this clay and thus its corresponding engineering properties.

Material Composition

1. Particle-size distribution of stiff clay

Particle-size analysis results via the pipette dispersion method show that the hipparion red clay of Baoji is generally characterized by high clay content (Table 1). Samples from different spots in the research area (<0.005 mm) show the clay content to range from 37 to 55 %, with the lowest clay content being 37.12 %. The average colloidal grain (<0.002 mm) content ranges from 30 to 48 %. The clay's specific surface area was measured by using the ethylene glycol monoethyl ether polar organic molecules adsorption method. The results show the specific surface area mean values to be 205 m²/g with a minimum value of 151.2 m²/g and the highest value is 262.9 m²/g. The variations in clay content correlate with the montmorillonite content and specific surface area of the clay.

Mineral Composition

Using X-ray diffraction analysis, quantitative tests for clay minerals were completed via the following three treatment methods: (1) orientation of sample pieces in a <2 μm clay particle suspension; (2) orientation of sample pieces in a <2 μm clay particle suspension treated in ethylene glycol; (3) orientation of sample pieces in a <2 μm clay particle suspension heated at 550 °C for 2 h (Środoń et al. 2001; Kahle et al. 2002; Zhang and Qu 2004). The mineral test results (Table 2) show that hipparion red clay has a characteristic mineral assemblage dominated by Ca-montmorillonite

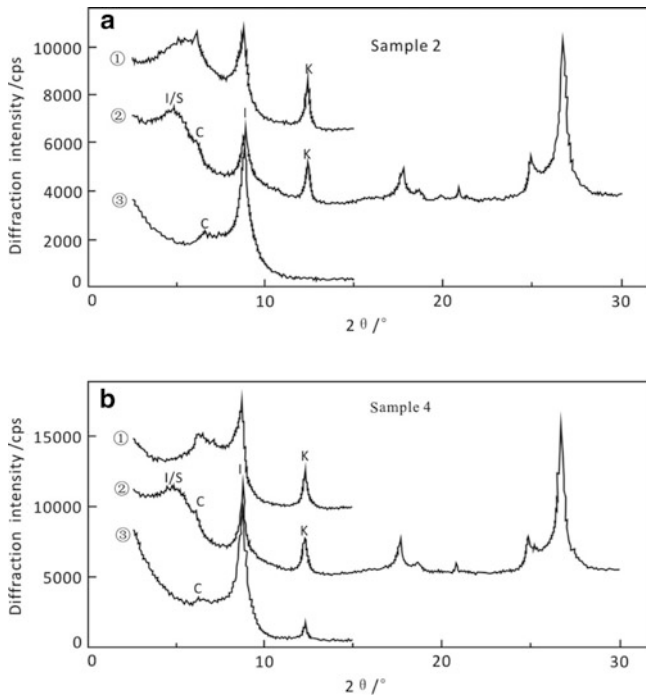


Fig. 1 X-ray diffraction curves of hipparion laterite. ① Natural sample; ② sample after treatment with ethylene glycol; ③ sample after heat treatment at 550 °C (a) Sample 2—hipparion laterite in the Xiashi gully. (b) Sample 4—hipparion laterite in the Hulu gully

with clay particles consisting of illite and kaolinite (Fig. 1). Montmorillonite mainly exists in a mixed layer form with medium and high illite/montmorillonite ratios. The mixed layer ratio ranges from 40 to 70 %, the relative content ranges from 55 to 75 %, and the absolute content ranges from 21.99 to 33.98 %. The relative content of the auxiliary mineral illite ranges from 15 to 31 % and the relative content of the concomitant kaolinite ranges from 4 to 14 %. A small amount of chlorite also exists in the clay.

Montmorillonite and mixed-layer illite/montmorillonite belong to the swelling clay minerals category, which have high internal and external specific surface areas and exhibit strong physical and chemical activity. The test results show that the effective montmorillonite content in the hipparion red clay ranges from 18.61 to 27.56 %, with an average content of 21.70 %, a mean value of the specific surface area of 204.7 m²/g, and the highest value reaching 262.9 m²/g. These results are consistent with those for swelling clay. The relationship between the montmorillonite content and specific surface area shows a weakly positive correlation (Fig. 2).

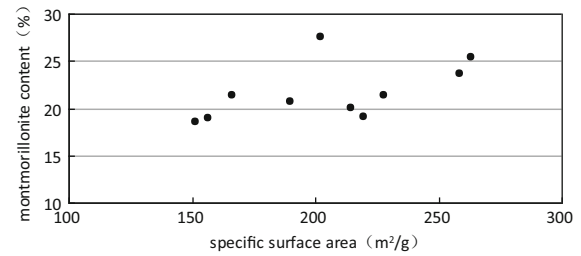


Fig. 2 Relation between smectite content and specific surface area in hipparion laterite

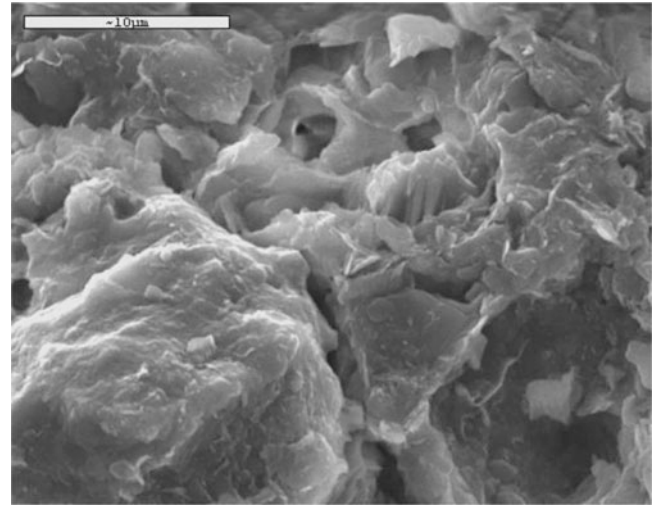


Fig. 3 Microstructural features of hipparion laterite

Microstructure

The clay mineral content in hipparion red clay is high with the clay minerals dominated by montmorillonite or mixed-layer minerals of medium and high illite/montmorillonite ratios. The kaolinite content is low and has few granular accumulation structures. Scanning electron microscopy results (Fig. 3) show that the microstructure types are mainly flocculent, cementation, and turbulent flow structures. In the structural grillwork, micropores or microcracks are relatively well developed and can provide channels for water infiltration. When water infiltrates, montmorillonite and illite clay tablets that are closely superimposed in “side-surface” and “surface-surface” forms will absorb water and the hydration shell will thicken and swell. Conversely, when water evaporates and is lost, the clay tablets will reduce and shrink. Therefore, hipparion red clay is

Table 3 Test results of physical properties of hipparion laterite

| Sample | Water content (%) | Bulk density (g/cm ³) | Dry bulk density (g/cm ³) | Void ratio | Liquid limit (%) | Plastic limit (%) | Plasticity index | Liquidity index | Free swelling ratio (%) |
|--------------------|-------------------|-----------------------------------|---------------------------------------|----------------|------------------|-------------------|------------------|-----------------|-------------------------|
| Hipparion laterite | 12.10 | 1.98 | 1.64 | 0.40 | 36.70 | 17.7 | 17.83 | -0.50 | 58 |
| | – | – | – | – | – | – | – | – | – |
| | 20.46 (16.0) | 2.13 (2.07) | 1.90 (1.77) | 0.59 (0.50) | 57.30 (44.1) | 24.30 (20.8) | 33.00 (23.3) | 0.10 (-0.21) | 77 (65) |

Note: Data in parentheses is the average value

characterized by dilatation and easily forms microcracks or micropores.

Engineering Geological Properties of Hipparion Red Clays

Physical Properties

1. Physical properties

Table 3 shows test results pertinent to the physical properties of hipparion red clays. The natural water content of hipparion red clays ranges from 12.10 to 20.46 % with a mean value of 16 %, so it may be classified as having medium water content. The natural density ranges from 1.98 g/cm³ to 2.13 g/cm³ having a mean value of 2.07 g/cm³. The dry density ranges from 1.64 g/cm³ to 1.90 g/cm³ having a mean value of 1.77 g/cm³. The void ratio ranges from 0.40 to 0.59 having a mean value of 0.50. Compared to mudstone from the Miocene Epoch, the density is lower, which indicates that solidification is poorer. The high water content and low density imply that hipparion red clays have low strength. The liquid limit of hipparion red clays ranges from 36.70 to 57.30 % with a mean value of 44.10. The plasticity index ranges from 17.83 to 33.00 having a mean value of 23.30 and the liquidity index ranges from -0.50 to 0.10, with a mean value of -0.21. This indicates that in their natural state, hipparion red clays behave like gumbo clays but change to a plastic or soft plastic state after saturation with water.

2. Swelling properties

Williams' internationally-adopted diagramming method for determining swelling power divides swelling power into low, medium, strong, and extremely strong swelling. It is a generally accepted measure of clay swelling and is appropriate for practical applications. Using the William's diagramming method, we show in Fig. 4 that the Pliocene clay of the Sanmen Formation has medium to strong swelling power.

3. Disintegration properties

Samples were either dried under a constant temperature of 105 °C or left with their natural water content and then

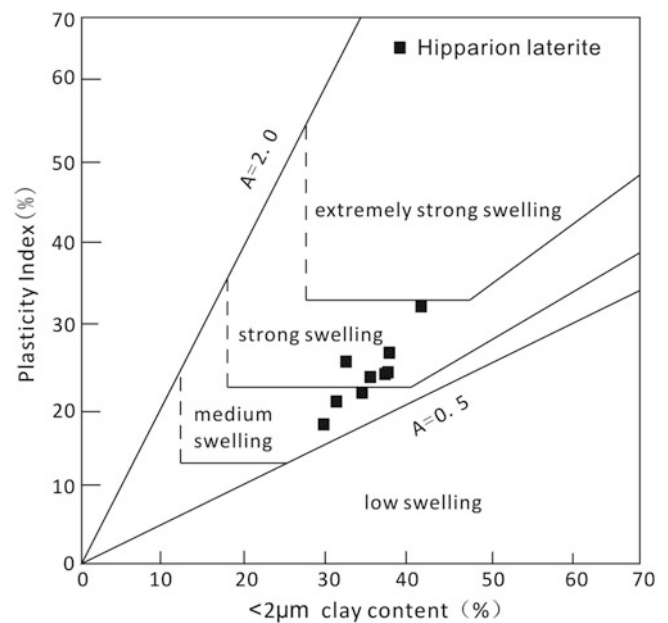


Fig. 4 Differentiation diagram for the expansion trend of hipparion laterite

put into containers filled with clear water for testing. The process by which the test blocks fragmented in water is then observed and we show that the disintegration properties of hipparion red clays are extremely strong in both its dry and natural states. The disintegration speed in the dry state is faster, and its disintegration durability is quite low. All dry samples of hipparion red clay disintegrated within 1 h and the natural samples disintegrated within 6 h. From previous tests, we know that the clay minerals of hipparion red clays are dominated by minerals characterized by strong hydrophilism and swelling power, such as montmorillonite or mixed layer illite/montmorillonite, as well as paragenetic associations of illite, kaolinite, and chlorite. As a result, its degree of cementation is low and fractures and microcracks are often present. Therefore, when water infiltrates these pores or cracks, a capillary film of fine particles will thicken and cause swelling of the soil mass. Thus, nonhomogeneous stress will develop in the soil

Table 4 Major shearing strength indexes of hipparion laterite

| Test conditions | Peak strength | | Residual strength | |
|------------------|---------------|------------------|-------------------|------------------|
| | C/kPa | $\phi(^{\circ})$ | C/kPa | $\phi(^{\circ})$ |
| Natural state | 115.1 | 34.3 | 48.9 | 21.2 |
| Saturation state | 75.6 | 26.4 | 29.4 | 15.6 |

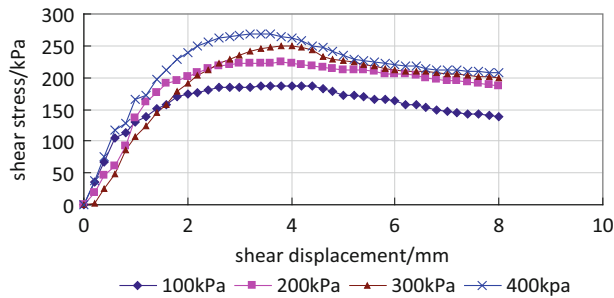


Fig. 5 Shear strength-shear displacement curve for hipparion laterite (saturated state)

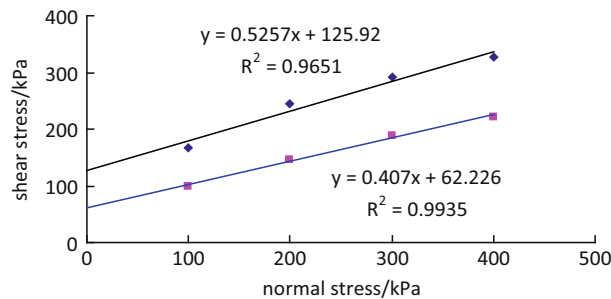


Fig. 6 Shear strength-normal stress curve for hipparion laterite (saturated state)

mass and some cements will be diluted, softened, or dissolved and then the soil mass will disintegrate.

Mechanical Properties

Next, we performed direct shear tests for hipparion red clays under both natural and saturated states using the slow shearing rate of 0.02 mm/min. The effective normal stresses were 100, 200, 300, and 400 kPa. Each soil sample was sheared five times with a shear displacement of 8 mm each time. The first peak value was selected as the peak strength of slow shearing and the 5th stable value was chosen as the residual strength. Table 4 presents the test result for the shear strengths of hipparion red clays. Figure 5 shows the shear strength-shear displacement curve of the test sample, and Fig. 6 shows the shear strength-normal stress curves for hipparion laterite.

The analysis explained earlier shows:

1. The shear strength- displacement curves of hipparion red clays under natural and saturated states exhibit the behaviour of soft clay. After the peak point, there is no obvious reduction in stress.
2. According to the direct shear test results, under natural water content conditions, the strength of hipparion red clays are relatively high but after saturation both the cohesion and the internal friction angle greatly decrease. The residual strength under both states is low and the cohesion decreases by two-thirds. For a sequence of thick loess, hipparion red clay, and sloped bedrock under a long-term effect of underground water, the strength of hipparion red clay will reduce rapidly, weak strata will appear in the slope and finally slip bands will form by a long-term creep deformation.

Discussion

1. Relationship between engineering geological properties of hipparion red clays and weak strata development
According to the material composition and physical test results on hipparion red clay, hipparion red clay has high clay content, and the clay mineral composition is dominated by montmorillonite and illite. As a result, its specific surface area and cation exchange capacity are high. When the clay is affected by water, the surface of clay minerals characterized by strong hydrophilism will absorb water to form an adsorption layer and will attract cations and hydration cations to form a diffused double layer. Thus, hipparion red clays have strong swelling properties. In terms of the microstructure, clay minerals are often superimposed in “side-surface” and “surface-surface” arrangements, which allow micropores to develop in the structure. This creates favorable microstructure conditions for clay swelling. Therefore, the clay swells easily when absorbing water and shrinks after losing water. Under the effects of long-term dilatation, the clay macrostructure will develop fractures and reduce in strength. Thick loess layers will press and shear these strata, and thus weak strata will form in the slope. Finally, interlayer shear zones will appear.

2. Strength attenuation of hipparion red clays and landslide evolution

According to mechanical analyses of hipparion red clays, the clay has peak strength, τ_p , and residual strength, τ_r , before and after destruction, respectively. When the natural slope is in an equilibrium state, the hipparion red clay containing slip bands is at its peak strength. During slope instability, its strength will reduce rapidly until reaching its residual strength. There is a value of difference, S_h , between the peak and residual strength (Hu 1995), which

can be expressed as

$$S_h = \frac{\tau_p - \tau_r}{\tau_p} = \frac{\Delta\tau}{\tau_p}.$$

According to the shear envelopes of peak and residual shear strengths of hipparion red clays, the difference between the peak and residual strengths under natural and saturated states is large. According to the formula for S_h , the difference in values between the peak and residual strength of hipparion red clays under its natural state ranges from 32 to 40 %, while under a saturated state, S_h ranges from 47 to 63 %. The reduction in strength is apparent. Under long-term irrigation or rainfall infiltration, hipparion red clays may be located below the water table. As a result, thin hipparion red clay layers will gradually saturate and their strength will reduce. From the squeezing action of thick loess layers, creep and shear deformation will occur and interlayer shear zones will form gradually. When its shear strength reduces to a certain level, sudden large-scale deformation of the slope will occur and landslides will take place. Therefore, the strata location and strength of hipparion red clays directly affects the deformation and instability of the slope.

Conclusion

This study primarily analyzed the relationship between the engineering geological properties of hipparion red clays in Baoji of Shaanxi and landslide occurrence.

1. The test analyses show that the hipparion red clays with developed cracks have high clay content and contain a large amount of montmorillonite and other swelling clay minerals. They are characterized by strong physical and chemical activity, a low degree of cementation, low strength, and swelling power. These characteristics provide the material basis for characterizing its engineering geological properties, and they also determine its low mechanical strength.
2. The strength test shows that there is a large difference between the peak value and residual strength in hipparion red clays. Under the effect of underground water, its strength parameters greatly decrease. Therefore, during irrigation periods or rainy seasons, surface water seeped through infiltration in the loess causes a decrease in the strength of the underlying hipparion red clay. Thick sloped loess layers presses and shears the thin hipparion red clay layers at the bottom and the slope slides. This is the main cause of landslides in the

loess hill and edge areas of the Guanzhong western region.

Acknowledgments This research received support from National Science Foundation of China (41102164) and National Technology Support grants (2006BAC04B02, 2012BAK10B01).

References

- He P, Liu L, Yu Q (1984) The age of the "Sanmen Series" and the evolution of its depositional environment discussed in the light of the Dongpogou section in the Sanmen Gorge area. *Geol Rev* 30 (2):161–169
- Hu G (1995) *Landslide dynamics*. Geological Publishing House, Beijing
- Kahle M, Kleber M, Jahn R (2002) Review of XRD-based quantitative analyses of clay minerals in soils: the suitability of mineral intensity factors. *Geoderma* 109:191–205
- Li B, Wu S, Shi J (2011) Research and analysis on large-scale loess landslides in loess tableland area of Weihei. *Res Soil Water Conserv* 19(1):206–211
- Li B, Yin Y, Wu S, Shi J (2012) Failure mode and formation mechanism of multiple rotational loess landslides. *J Jilin Univ (Earth Sci Ed)* 42(3):760–769
- Liu D, Zhu Z, (1959) Some opinions on Sanmen Stratigraphic division. In: *Sanmenxia quaternary geology conference proceedings, the Chinese quaternary research committee*. Science Press, Beijing, pp 63–68
- Liu T et al (1985) *Loess and the environment*. Science Press, Beijing
- Pei W, Huang W (1959) Some opinions on Sanmen series. *Sanmenxia quaternary geology conference proceedings, the Chinese quaternary research committee*. Science Press, Beijing, pp 3–20
- Peng S, Guo Z (2007) Clay mineral composition of the tertiary red clay and the quaternary loess-paleosols as well as its environmental implication. *Quat Sci* 27(2):277–285
- Qu Y, Zhang Y, Qin Z (1999) Hipparion laterite and landslide hazards on loess plateau of Northwestern China. *J Eng Geol* 7(3): 257–265
- Środoń J, Drits VA, McCarty DK, Hsieh JCC, Eber DD (2001) Quantitative X-ray diffraction analysis of clay-bearing rocks from random preparations. *Clays Clay Miner* 49(6):514–528
- Sun J (1986) On yellow Sanmen and green Sanmen. *J Xi'an Geol Coll* 8 (4):42–45
- Wang Y, Hu H, Li S (1959) Some ideas on Sanmen stratigraphic age and causes. *Acta Geol Sin* 39(2):167–186
- Wang S, Jiang F, Wu X et al (1999) A study on the age of Sanmen group in Sanmenxia area. *J Geomech* 5(4):57–65
- Wang S, Wu X, Zhang Z et al (2001) Environmental changes of Sanmen Lacustrine deposits and the yellow river flows eastwards. *Sci China (Ser D)* 31(9):760–768
- Xue X (1981) An early pleistocene mammalian fauna and its stratigraphy of the River You, Weinan, Shaanxi. *Vert Palas* 19(1):35–44
- Yue L (1996) Depositional relation between the loess, red clay and sedimentation of the Lakebasin in the Loess Plateau. *Acta Sedimentol Sin* 14(4):148–153
- Zhang Y, Qu Y (2004) Quantitative research on clay mineral composition of the Malan Loess from the Loess Plateau in China. *Geol Rev* 50(5):530–537



Dynamic Centrifuge Modelling Tests for Sliding Rock Slopes

Xianglong Li, Joseph Wartman, Huiming Tang, Jinkai Yan, Hongming Luo, and Wei Hu

Abstract

Sliding rock slope models with intermittent rock planes and secondary rock joints are built of synthetic material, and tested in a centrifuge testing system to study the failure process of rock slopes during an earthquake. The models are made of synthetic material containing gypsum, sand and pure water with certain mix ratio through strictly controlled casting procedure. New methods are invented to build the bedding planes with full contact and no gaps; special casting method is invented to add unbroken bedding plane parts inside each bedding plane. The results of the dynamic centrifuge tests reveal that the secondary rock joints inside the rock slope serve to weaken the dynamic stability of the sliding rock slope significantly, and could affect the dynamic failure mechanism of the slopes, making the rock layers collapse into smaller rock masses during sliding along the bedding planes.

Keywords

Rock slope • Bedding plane • Secondary rock joints • Dynamic • Centrifuge modelling test

X. Li (✉) • J. Yan
China Institute of Geo-Environment Monitoring, Beijing 100081,
China
e-mail: lixianglong1986@gmail.com; yanjinkaisw@163.com

J. Wartman
Department of Civil and Environmental Engineering, University of
Washington, Seattle, WA 98105, USA
e-mail: wartman@uw.edu

H. Tang
China University of Geosciences (Wuhan), Wuhan 430074, China
e-mail: hmtang@cug.edu.cn

H. Luo
State Key Laboratory of Geomechanics and Geotechnical Engineering,
Institute of Rock and Soil Mechanics, Chinese Academy of Sciences,
Wuhan 430071, China
e-mail: luohm1980@126.com

W. Hu
Three Gorges Geotechnical Consultants Co., Ltd., Wuhan 430074,
China
e-mail: huwei_cumt@163.com

Introduction

Seismic-induced rock slope failure is one of the most common and dangerous seismic-induced geo-hazard all over the world. Among them the sliding rock slope failure is the most common type. Sliding rock slope, whose safety is mainly controlled by its rock bedding planes and secondary rock joints inside, could generate dynamic sliding failure along the bedding planes inside the rock slope during earthquake and other seismic events. Numerous researches involving the failure mechanism of sliding rock slope under seismic load were carried out; however, most of them were post-event site investigations, and the research conclusions and results are made based on the site characteristics of some certain rock slope failure scenes. Theories were brought out based on simple sliding mechanism with barely any considerations of rock joint structure properties, which happen to control rock slope stability. An earthquake event usually happens suddenly, and is not predictable, so it is nearly impossible to witness or monitor the whole process of the rock slope failure during the earthquake. Therefore, data for rock slope dynamic failure process is very rare and

Table 1 Comparison of the synthetic material properties to natural sandstone

| Material properties | Synthetic material | Natural sandstone |
|--|--------------------|-------------------|
| Density (kg/m ³) | 1,900 | 2,200 |
| UCS (MPa) | 68.99 | 70 |
| UTS (MPa) | 4.33 | 5 |
| Elastic Modulus (GPa) | 13.29 | 30 |
| Poisson's Ratio (1) | 0.25 | 0.30 |
| Shear wave velocity (km/s) | 2.00 | 2.30 |
| Mode I Fracture Toughness (MPa/m ^{-0.5}) | 0.95 | 0.68 |

could not meet the research requirement. Physical modelling tests can make up for this deficiency, and dynamic centrifuge modelling is one of the potential testing methods for rock slope dynamic failure mechanism research (Hoek 1965; Joseph et al. 1988).

Sliding rock slope contains both rock bedding planes and a large number of secondary rock joints inside the rock masses. The secondary rock joints are usually orthogonal to the bedding planes. These two major groups of rock joints are usually not completely penetrating, but are intermitted many unbroken parts inside. These unbroken parts play an important role in maintaining the slope stability, but have not been studied properly. Most of the research works neglect the existence of these unbroken parts inside rock joints and the effect of the secondary rock joints on slope stability (Dong et al. 2011; Li et al. 2007). Zhang et al. (2007) added secondary rock joints in the toppling layered rock slope physical model, and studied the failure process of the slope under static condition, but considered no seismic loads.

In this paper, a new method is invented to build the bedding planes with full contact and no gap. A special casting process is used to add unbroken parts inside each bedding plane. Two different rock slope physical models containing intermittent rock planes and secondary rock joints are built of synthetic material, and are tested in a centrifuge testing system under dynamic loads, to study the dynamic failure behaviour of the sliding rock slope, and the effect of the secondary rock joints on the dynamic stability of the rock slope.

Sliding Rock Slope Physical Model Building

Synthetic Rock Material

The synthetic rock material used in this series of test is made of gypsum, fined grained sand, and pure water, with a mass ratio of 1:0.6:0.4. Through proper casting process, the material can reach its steady condition and is ready to be cut and tested.

In order to obtain the properties of this synthetic material, basic mechanical tests are carried out, including uniaxial compression test, Brazilian test, and Mode I fracture

toughness test. The material properties are listed in Table 1. Noticeably, the synthetic material is comparable to natural sandstone, except that the elastic modulus is lower than natural sandstone, while the Mode I fracture toughness is higher.

Fully Contacted Rock Bedding Plane

The synthetic rock bedding plane should be able to simulate two major properties of the natural plane: the broken parts of the bedding plane should be in full contact with no gaps and the unbroken parts of the bedding plane should maintain tensile and shear strength that are comparable with the natural unbroken bedding plane. In order to meet such requirements, a brand new casting method is designed and tested to make a synthetic rock bedding plane with 'closed' broken parts and unbroken parts whose strength is about 15 ~ 20 % of the intact synthetic rock material. The basic concept of this new casting method is to mould one piece of the rock bedding plane first, then smear some special painting material as a shield to cover the plane surface where the broken part is designed to be located, in order to prevent cementing on these parts of plane surface in the next casting process; finally, the other piece of the plane is moulded together with the first piece to form one fully contacted rock bedding plane with no gap between each piece. Lard refined from pork is used as the shield during casting. The lard behaves as solid fat in temperatures under 20 °C, and melts when the temperature rises beyond, creating the rock plane with no gap after setting.

Through this casting process, the parts with lard shield will have no gaps, no tensile strength, but only a controllable surface roughness and frictional function, and the parts with no lard shield will cement together, with low tensile and shear strengths.

Figure 1a shows the synthetic rock brick sample with one single rock bedding plane across the body. The center of the plane contains one part of the fully contacted broken plane, and the rest of the plane on each side is unbroken. In order to test the applicability of the rock bedding plane casting method, a group of such rock brick sample are cast and tested to fail under uniaxial compressive load, and one of the failed sample is shown in Fig. 1b. As depicted in the

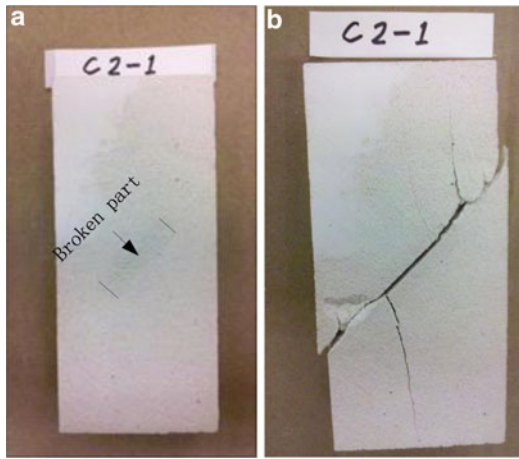


Fig. 1 Experimental test of the synthetic rock brick sample with bedding planes inside (a) Synthetic rock brick with fully contacted rock plane inside (b) Synthetic rock brick after compressive failure

figure, the central broken bedding part generated two wing fractures from two tips, and propagated toward the direction of the maximum stress (compressive); the original unbroken parts of the rock plane failed in shear afterwards. This test prove that the synthetic bedding plane behaves properly. The basic mechanical properties of the synthetic rock bedding plane are tested and listed in Table 2.

Sliding Rock Slope Physical Model

Two different types of sliding rock slope physical models were made by using the casting method described above. Both slopes share the same profile, with a height of 20 cm, a thickness of 5 cm, and a bottom length of 25 cm. The slope surface dipping angle is 75°. Both slopes contain five rock layers with a uniform thickness of 2 cm, and a dipping angle of 45° (Figs. 2 and 3). The slope named as Slide_1 has

Table 2 Basic mechanical properties of the synthetic rock bedding plane

| Bedding plane type | Frictional angle (°) | Cohesion (kPa) | Mode I fracture toughness (Mpa/m ^{-0.5}) |
|--------------------|----------------------|----------------|--|
| Broken parts | 32 | 2.0 | N/A |
| Unbroken parts | 41 | 85 | 0.67 |

Fig. 2 Schematic diagram of the sliding slope models Slide_1 and Slide_2

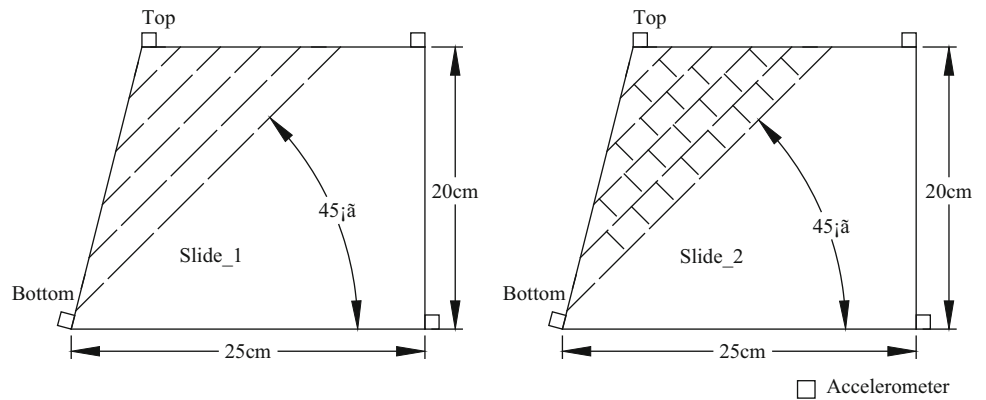


Fig. 3 Two types of sliding rock slope Physical model (a) Slide_1 slope (b) Slide_2 slope

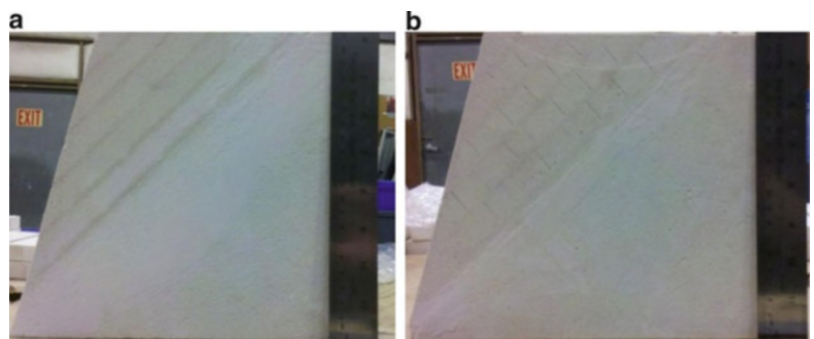
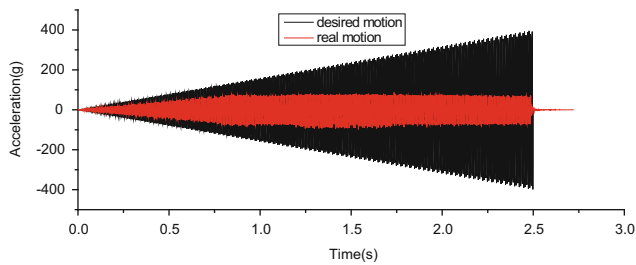


Table 3 Input dynamic wave parameters for slope dynamic tests

| Scale | Amplitude (g) | Frequency (Hz) | Time duration (s) |
|-----------|---------------|----------------|-------------------|
| Model | 0 ~ 400 | 120 | 2.5 |
| Prototype | 0 ~ 10 | 3 | 100 |

**Fig. 4** Comparison between the designed input motion and the real input motion for slope dynamic tests

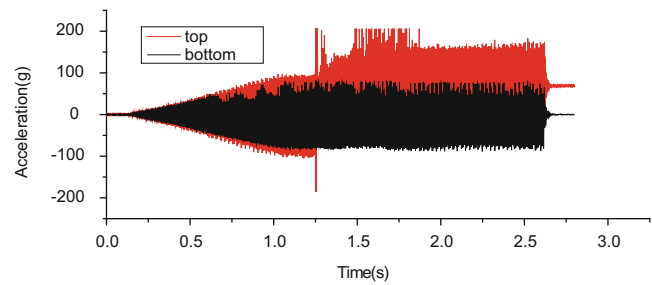
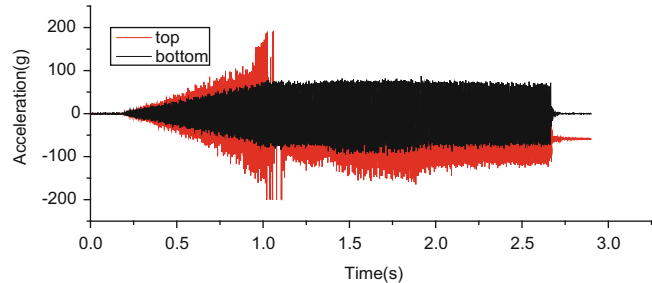
intermittent rock bedding planes inside, but with no secondary rock joints; while the slope named as Slide_2 has intermittent rock bedding planes exactly the same as Slide_1, and orthogonal secondary rock joints inside. The secondary rock joints are made 17 mm long, a little shorter than the thickness of each rock layer, leaving a 3 mm of rock linkage.

Dynamic Centrifuge Test

The centrifuge testing system called Schaevitz in the University of California Davis is used to test the two slope models. The testing gravity is 40 g. According to the parameter scaling rules of centrifuge test, the prototype shape of the two slopes are 40 times larger than the model shape, that is, 8 m tall and 10 m long.

Monitoring system is installed into the testing system, including high speed cameras, accelerometers on the slope and the model holding box.

In order simulate the seismically induced failure of the slope models, a harmonic sine wave motion with constant frequency and ramping amplitude is introduced to the testing system. The parameters of the input wave are shown in Table 3. According to the scaling rules, the maximum amplitude of the input wave reaches 10 g in prototype scale, which is high enough to fail both physical models. However, the real input motion loaded to the models is not always the same as designed, due to the limitation of the motion actuator capacity of the centrifuge system. The actuator, driven by high pressure gas, has certain limits on shaking frequency and amplitude. The higher the gravity utilized, the narrower capacity the actuator has. Therefore, motion adjustment must be done before carrying out the tests. Figure 4 shows the designed input motion (black curve) and the real input motion (red curve) for the two slope tests under 40 g environment. As it is shown, the real input motion is

**Fig. 5** Acceleration time history of Slide_1 slope under Wave3**Fig. 6** Acceleration time history of Slide_2 slope under Wave3

very different from the designed motion. In spite of this, the real input motion is still high enough to fail both slope models, and it would be unnecessary to adjust the designed input motion.

Results Analysis

The acceleration time history recorded by the accelerometers on the top and bottom of each slope is drawn in Fig. 5 (for Slide_1) and Fig. 6 (for Slide_2), in which the black curves represents the acceleration time history on the bottom, and the red curves represents the acceleration time history on the top.

As shown in these two figures, the acceleration on the top of the slopes is larger than on the bottom, which proves obvious topographic amplification effect. Moreover, the amplification effect tends to magnify as the amplitude of input motion ramps.

In Figs. 5 and 6, both acceleration records on the top of slope change aggressively at certain time point, which indicate the occurrence of the slope failure events; the Slide_1 slope failed at 1.25 s, with the acceleration of 177 g (in model scale) on the slope top; the Slide_2 slope failed at 1.08 s with the acceleration of 118 g (in model scale) on the slope top. This difference between the two models shows that the presence of secondary rock joints inside sliding rock slope could weaken the dynamic stability of the slope significantly.

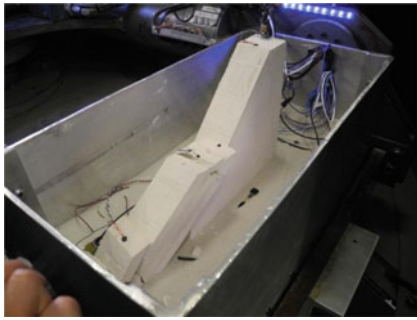


Fig. 7 Failure condition of Slide_1 slope

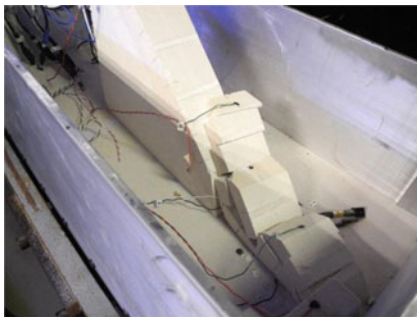


Fig. 8 Failure condition of Slide_2 slope

The slope failure process, recorded by high speed cameras, also shows obvious differences between Slide_1 and Slide_2. The Slide_1 slope generally failed along the lowest (the fifth) bedding plane, and the body slid down as one intact rock piece. After the slipping rock brick hit the bottom of the model holding box, it collapsed along rock bedding planes inside and separated into five rock layers, but each the rock layer still remained in one piece (Fig. 7).

The Slide_2 Slope failed along the fourth bedding plane, leaving the bottom rock layer unbroken and still attached to the slope base. Moreover, before the fourth bedding plane started to slide, multiple secondary rock joints inside rock layers had propagated and caused internal damage to the rock mass. During sliding along the fourth bedding plane and before the collision to the loading box, the upper rock mass had already collapsed into smaller rock bricks due to the cutting through of multiple secondary rock joints (Fig. 8).

The two tested sliding rock slope models share identical shape of slope, material properties, bedding plane characteristics, and dynamic test procedure. The only difference between the two tests lies on whether the model has secondary rock joints inside. Therefore, we can conclude that the existence of secondary rock joints is the cause for the difference in the failure process of the two tested models. The existence of the secondary rock joints makes the rock

mass structure more complex, and weakens the rock mass strength as a whole, which results in the decrease of the rock slope dynamic stability. Moreover, the increased complexity of the rock mass structure can significantly change the dynamic property of the rock mass, including the elastic/plastic deformation properties, the stress wave propagation characteristics, and the dynamic damping characteristics, all of which would then effect the dynamic response of the rock slope, including the failure process. In addition, the existence of secondary rock joints can serve as potential rock mass failure path, changing the sliding rock slope failure mode from pure bedding plane failure to step path failure with the interconnected of secondary rock joints and rock bedding planes in different rock layers. The conclusions above could be the reason Slide-1 slope (with no secondary rock joints) failed along the lowest bedding plane, while the Slide-2 slope (with secondary rock joints) broke into rock bricks during the failure process and slid along the fourth rock layer.

Conclusions

Sliding rock slope models with intermittent rock planes and secondary rock joints are built from synthetic material, and tested in the centrifuge. The results of the centrifuge dynamic tests reveal that: the unbroken parts inside rock bedding planes contribute greatly to the stability of sliding rock slope; the secondary rock joints inside the rock slope serve to decrease the dynamic stability of the rock slope significantly and could affect the dynamic failure mechanism of the slopes, making the rock layers collapse into smaller rock masses before and during sliding along the bedding planes.

Acknowledgments This research work is funded by the National Science Foundation No. 1156413 of United States Government, with Joseph Wartman as principal investigator.

References

- Dong JY, Yang GX, Wu FQ et al (2011) The large-scale shaking table test study of dynamic response and failure mode of bedding rock slope under earthquake. *Rock Soil Mech* 32(10):2977–2983
- Hoek E (1965) The design of a centrifuge for the simulation of gravitational force fields in mine models. *J S Afr Inst Min Metall* 65 (9):445–487
- Joseph PG, Einstein HH, Whitman RV (1988) A literature review of geotechnical centrifuge modeling with particular emphasis on rock mechanics. DTIC Document
- Li HB, Xiao KQ, Liu YQ (2007) Factor of safety analysis of bedding rock slope under seismic load. *Chin J Rock Mech Eng* 26 (12):2385–2394
- Zhang G, Zhao Y, Shi GH et al (2007) Toppling failure simulation of rock slopes by numerical manifold method. *Chin J Geotech Eng* 29 (6):800–805



Changes in Shear Strain and Subsurface Flow Prior to Rainfall-Induced Landslide in Flume Experiments

Yasuhiko Okada

Abstract

Two shallow landslides were induced in a large-scale model slope by artificial heavy rainfall, in which the heights of sand layers were set at 0.7 and 0.5 m. A total of 2,931 s of rainfall produced a relatively large landslide in a whole steep slope section in the 0.5 m high sand layer. On the contrary, only a small landslide was produced by a total of 4,000 s of rainfall in the lower half of a steep slope section in a sand layer that was 0.7 m high. Changes in shear deformation and subsurface flow were monitored in the experiments. By tracing the movements of markers imbedded inside the sand layers, the changes in shear strain were analysed and expressed in a form of Mohr's circle. In addition, by approximating the equi-potential lines from the observed data of pore-water pressure, the changes in subsurface flow directions were calculated. It has been shown that, although the sand layers were packed to be uniform, the observed shear deformation and subsurface flow conditions were not homogeneous; just before the landslide initiation, water tables were formed in almost all slope sections, but a sliding surface was not necessarily formed below the water table. Directions of maximum shear strain and subsurface flow were more in general agreement with the direction of slope base in the parts inside the landslide, indicating their possible influence on the landslide initiation.

Keywords

Rainfall-induced landslide • Shear strain • Subsurface flow

Introduction

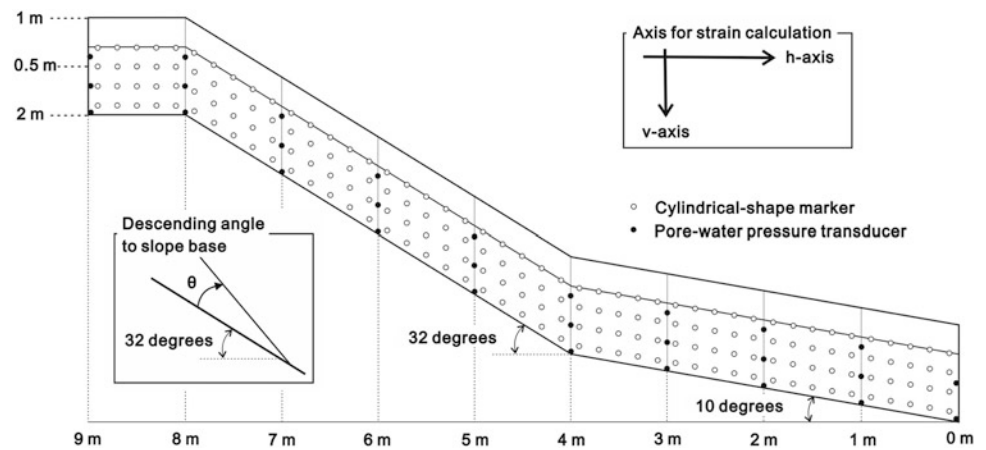
In order to investigate the mechanisms of rainfall-induced landslides, large-scale model slopes have been used to induce shallow landslides. Fukuzono (1978) used a 10-m long, 4-m wide model slope and proposed a prediction model indicating that the initiation time of rainfall-induced landslides was a function of inverse shear velocity. Iverson and LaHusen (1989) pointed out that pore-water pressures were dynamically fluctuating during the rapid shearing at failure. Okura et al.

(2002) explained that the excess pore-water pressure generation was induced by the negative dilatancy followed by the fast shearing. Those studies focussed on the behaviour during failure. Details of shear strain and subsurface flow prior to failure were not as well examined and clarified. Because it is difficult to adequately scale the cohesive stresses and the stresses associated with deformation within the continua, in this study a large-scale model slope was used, in which attention was paid to the subsurface flow conditions and shear deformation before failure initiation.

Y. Okada (✉)

Department of Soil and Water Conservation, Forestry and Forest Products Research Institute, Matsunosato 1, Tsukuba 305-8687, Japan
e-mail: okada10@ffpri.affrc.go.jp

Fig. 1 Schematic illustration of a large-scale model slope showing pore-water pressure transducer and marker positions, axes to calculate the strain, and the descending angle to the slope base



Experiments on Rainfall-Induced Landslides

Sample and the Model Slope

River sand was used. This material was excavated from the Sakuragawa River in Tsukuba city, Ibaraki prefecture, Japan. The density of sand particles was $2,620 \text{ kg/m}^3$, the mean diameter (D_{50}) was 0.50 mm , the uniformity coefficient (U_c) was 4.31 , and the coefficient of curvature (U_c') was 0.93 . Two experiments were conducted, in which Experiment 1 was in a sand layer 0.7 m high (void ratio, $e_0 = 0.79$) and Experiment 2 in a layer 0.5 m high ($e_0 = 0.76$).

A schematic illustration of the large-scale model slope is shown in Fig. 1. In Fig. 1, the positions of pore-water pressure transducers and markers, axes to calculate the strain, and the angle of descent to the slope base are also shown. The model-slope is 1 m wide, and consists of three parts, a gentle slope (10°) section that was 4 m long, a steep slope (32°) of 4 m , and a horizontal section of 1 m , in total 9 m long. The sample was loosely placed in the model slope by gently dropping sands through a mobile hopper. The sand layers were packed as uniform as possible. The rain simulator, which was equipped with nozzles at five locations all 6.4 m above the floor along the model slope, produced uniform rainfall at an hourly intensity of 100 mm in the experiments. One side of the model slope is made of reinforced glass, making it possible to film the landslide movement using digital video cameras.

Monitoring and Data Acquisition

The changes in pore-water pressure were measured by pressure transducers (strain-gauge type, 18 mm in diameter, 83 mm long, range 70 kPa , accuracy = 0.015%). These transducers were configured to measure positive and negative pore-water pressure by using a water-filled gap between the sensor and a glass filter cap ported to the sand. A calibration to

check the linearity of the pressure was conducted by sinking the transducers to depths of 0.1 , 0.5 , and 1 m in water before situating them in the sand-layer in each experiment. During the landslide experiments, the transducers moved together with the sand until final deposition. The data were logged by a PC at 100 Hz .

In addition, the shear deformation was monitored by digital video cameras that traced the movement of markers imbedded in the sand layers. The markers were of cylindrical shape (30 mm long, 16 mm in diameter). One bottom side of each marker was adjacent and visible through the reinforced glass. Five time-code indicators were set around the model-slope to show the elapsed time, with a resolution of one hundredth of a second. The digital video cameras were situated so that they could film the time-code indicators. Using this system, the pore-water pressure and filmed images could be synchronised in the analysis.

Results and Discussion

Subsurface Flow Conditions

The changes in equi-potential lines before failure initiation are shown in Fig. 2, at (a) 500 s , (b) 300 s , (c) 60 s , and (d) 1 s before slope failure in Experiment 1, and (e) 1 s before slope failure in Experiment 2. In Fig. 2d and (e), approximate sliding surfaces of the first landslide are also shown by dotted lines.

The equi-potential lines were generally horizontal in (a), then the lines changed in shape and crossed the slope base at larger angles with the increase in precipitation time. Water tables firstly formed around the connection between steep and gentle slope sections and the horizontal section, and they enlarged as precipitation time went on. Just before the failure, the water tables formed in almost the whole slope sections in (d) and (e).

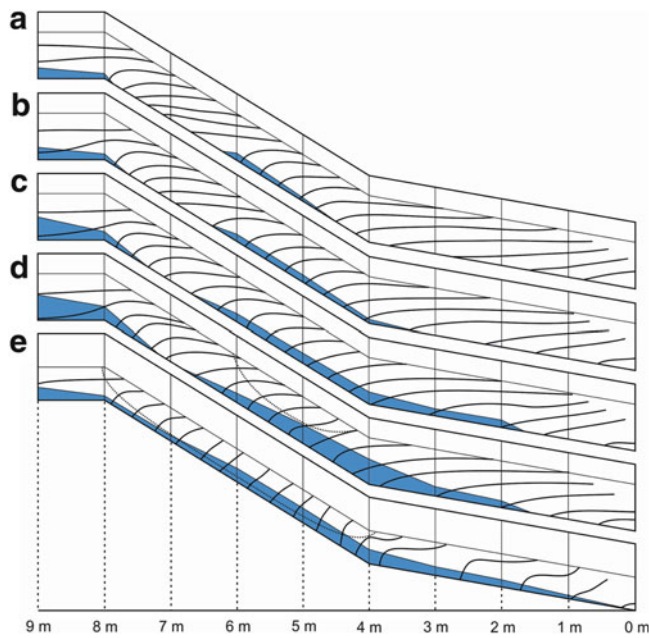


Fig. 2 Changes in equi-potential lines (every 0.2 m of pressure head) and water table formation: (a) 500 s; (b) 300 s; (c) 60 s; (d) 1 s before the first landslide in Experiment 1 respectively; and (e) 1 s before the landslide in Experiment 2. (approximate sliding surfaces of the first landslides are also shown in (d) and (e) by dotted lines)

Shear Deformation in Sand Layer

Strain was calculated assuming the plane strain conditions, in which shear strain ($\gamma_{hv}/2$), normal strain in v -direction (ε_v), and normal strain in h -direction (ε_h) were as follows:

$$\Delta V_i = \frac{\partial V}{\partial v} \times V_i + \frac{\partial V}{\partial h} \times H_i \quad (i = 1, 2) \quad (1)$$

$$\Delta H_i = \frac{\partial H}{\partial v} \times V_i + \frac{\partial H}{\partial h} \times H_i \quad (i = 1, 2) \quad (2)$$

$$\varepsilon_v = -\frac{\partial V}{\partial v}, \quad \varepsilon_h = -\frac{\partial H}{\partial h}, \quad \frac{\gamma_{hv}}{2} = -\frac{1}{2} \left(\frac{\partial H}{\partial v} + \frac{\partial V}{\partial h} \right) \quad (3)$$

where normal strain is positive in contraction and shear strain is positive in an anti-clockwise direction.

Since landslides occurred in steep slope sections, strain was analysed at longitudinal positions of 4.6, 5.6, 6.6, and 7.6 m. Figure 3a, b and c shows changes in strain in the form of a Mohr's circle at a 6.6 m longitudinal position just upslope of the head scarp of the first landslide in Experiment 1. In the same way, strain at 5.6 m just down slope of the landslide is shown in Fig. 3d, e and f. In the figures, the measured shear strain ($\gamma_{hv}/2$) is also shown as a dot.

In 6.6 m longitudinal positions, strain was similar in the shallow and middle parts and it was smaller in the deep part.

Conversely, strain was getting larger from the shallow part to the deep part in 5.6 m longitudinal positions. Strain in the shallow and middle parts at 6.6 m was larger than that at 5.6 m, whilst strain at the deep part at 6.6 m was smaller than that at 5.6 m. Although the sand layer was uniformly packed, strain at the 5.6 and 6.6 m longitudinal positions was quite different. A point to note is that the strain was larger in the shallow and middle parts at 6.6 m longitudinal position where the landslide did not occur than that at 5.6 m where the landslide took place.

Regarding Experiment 2, in which the landslide occurred along the whole steep slope section, strain at 6.6 m and that at 5.6 m longitudinal positions were similar and the deep parts had a larger strain.

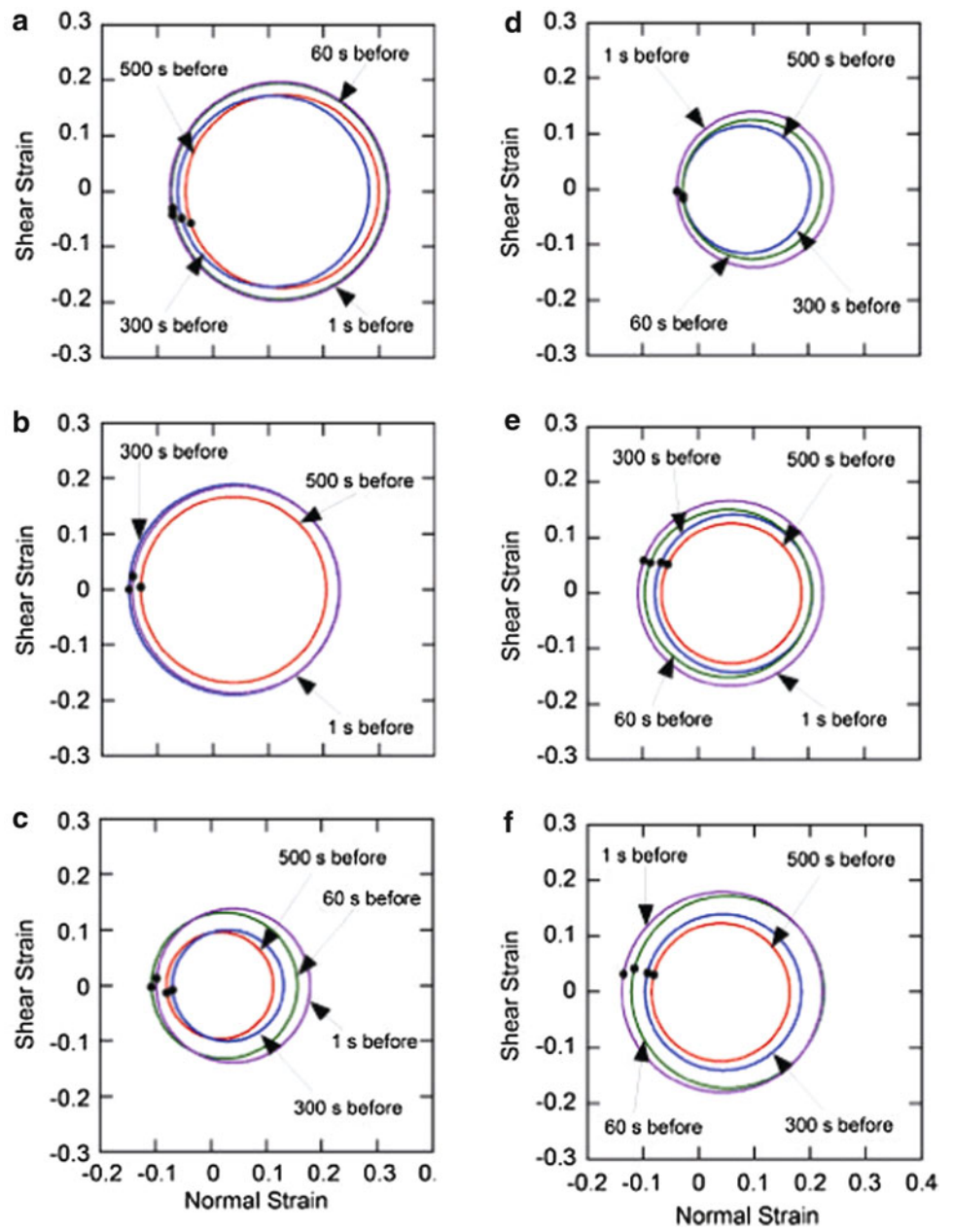
Correlation with Directions of Maximum Shear Strain and Subsurface Flow

The changes in descending angle between directions of maximum shear strain and steep slope base in Experiment 1 are shown in Fig. 4. The descending angle between directions of maximum shear strain and the steep slope base was rather larger in shallow parts than in the middle and deep parts. The descending angle at 6.6 m longitudinal position was larger in all shallow, middle, and deep parts than that at 5.6 m, indicating the angle of maximum shear strain at 5.6 m was in better agreement with the direction of the steep slope base. It was also shown that the descending angle at 7.6 m was between that of 5.6 and 6.6 m, the angle at 4.6 m was smallest and showed negative values at some points, indicating the direction of maximum shear strain went towards the sand layer surface.

The changes in descending angle between directions of subsurface flow at 0.4 m deep and that of the steep slope base in Experiment 1 are shown in Fig. 5. The descending angle between directions of subsurface flow and the steep slope base was large at the 6.6 m longitudinal position and the angles ranged between 52 and 68°, while those at 5.6 m were between 40° and 45° and they were smaller than at 6.6 m. Those at 4.6 and 7.6 m were smaller than at 6.6 m and they converged to about 40° just before the landslide.

It was pointed out that the generation and enlargement of subsurface flow played quite an important role in rainfall-induced landslides (Fukuzono 1978). Since the seepage force is, in fact, applied to the soil particles, it would be most dangerous when subsurface flow moved along the direction of the slope base. Although the Mohr's circles in shallow and middle parts at the 6.6 m longitudinal position outside the landslide were larger than those at 5.6 m inside the landslide, the descending angle between maximum shear strain and steep slope base was also larger. Likewise the descending angle between subsurface flow and steep slope

Fig. 3 Changes in strain in the form of a Mohr's circle in Experiment 1. (a) shallow; (b) middle; and (c) deep parts at the 6.6 m longitudinal positions, and (d) shallow; (e) middle; and (f) deep parts at the 5.6 m longitudinal positions



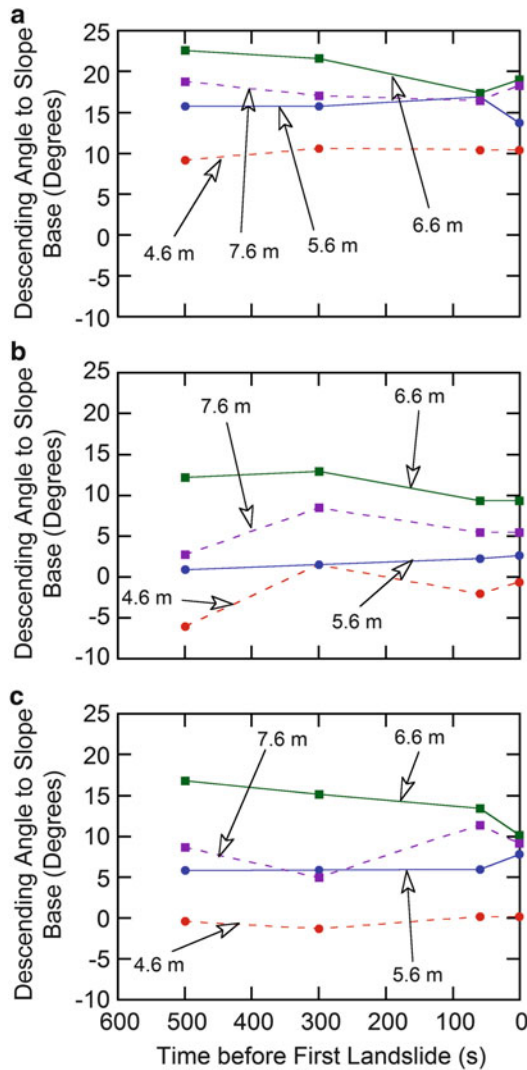


Fig. 4 Changes in descending angle between directions of maximum shear strain and steep slope base in Experiment 1: (a) shallow; (b) middle; (c) deep parts

base was larger at 6.6 m than that at the 5.6 m longitudinal position. These indicated that directions of maximum shear strain and subsurface flow correlated to the slope-base direction in the parts inside the landslide.

The changes in descending angles of maximum shear strain and subsurface flow to steep slope base at 0.4 m depth in Experiment 2 are shown in Fig. 6. The descending angle of maximum shear strain ranged narrowly between 7° and 12°. Although the descending angle of subsurface flow ranged widely, it decreased to be smaller than 20° 1 s before the landslide took place. A water table was formed along the whole steep slope section, and the landslide appeared to occur in the whole steep slope in Experiment 2.

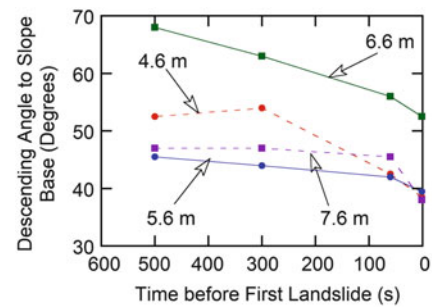


Fig. 5 Changes in descending angle between directions of subsurface flow and steep slope base in Experiment 1

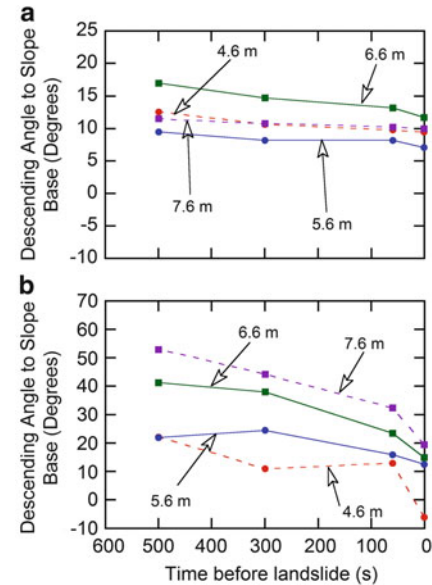


Fig. 6 Changes in descending angle to slope base in Experiment 2: (a) maximum shear strain, and (b) subsurface flow

Concluding Remarks

Two landslides were induced in a large scale model by artificial rainfall. Shear strain and subsurface flow before the landslide took place were analysed. The side sections of landslides are invisible on a natural slope and it is impossible to conduct the strain analyses examined in this study for natural landslides. The number of the flume experiments is somewhat restricted, but the following conclusions could be drawn regarding the rainfall-induced landslides:

1. Although the sand layers were uniformly packed, shear strain and subsurface flow behaviour were not homogeneous.
2. Just before the landslide was triggered, water tables formed in almost all steep slope sections. However, a

sliding surface was not necessarily formed below the water table.

3. Directions of maximum shear strain and subsurface flow generally correlated to the slope-base direction in the parts inside the landslide, indicating their possible influence on landslide initiation.

Acknowledgments The author would like to thank Mr Teruki Fukuzono (former National Research Institute for Earth Science and Disaster Prevention) for his valuable advice, suggestions, and encouragements.

References

- Fukuzono T (1978) On the state of internal stress at slope failure caused by rainfall. Rep Natl Res Cent Disaster Prev 20:101–122 (in Japanese with English abstract)
- Iverson RM, LaHusen RG (1989) Dynamic pore-pressure fluctuations in rapidly shearing granular materials. Science 246:796–799
- Okura Y, Kitahara H, Ochiai H, Sammori T, Kawanami A (2002) Landslide fluidization process by flume experiments. Eng Geol 66:65–78



Geotechnical Properties of Landslide Sites in Korea with Differing Geology

Young-Suk Song and Kyeong-Su Kim

Abstract

The goal of this study is to find out the relationship between geotechnical properties and landslide occurrence in areas with differing geology in Korea. The soil properties were measured in three study areas (Jangheung, Sangju and Pohang) which are underlain by gneiss, granite and sedimentary rock, respectively. Many landslides occurred in these areas during the rainy season. To investigate the factors that influence the landslides, a landslide survey was made, and a series of laboratory soil tests were carried out. The results of soil tests show that the average porosity of the soils originated from the gneiss of Jangheung and the granite of Sangju is greater than that of soils originated from the sedimentary rocks of Pohang. The average coefficient of permeability of the soils originating from the granite of Sangju is higher than that of soils from the gneiss of Jangheung and the sedimentary rocks of Pohang. The average coefficient of permeability of soils obtained from the landslide sites is greater than that of soils obtained from landslide-free sites in the same geology. The average shear strengths of soils obtained from the landslide sites are smaller than those of soils obtained from the landslide-free sites. It is confirmed that soils with low shear strength and high permeability are especially vulnerable to landslide occurrence.

Keywords

Landslides • Geology • Porosity • Permeability • Shear strength

Introduction

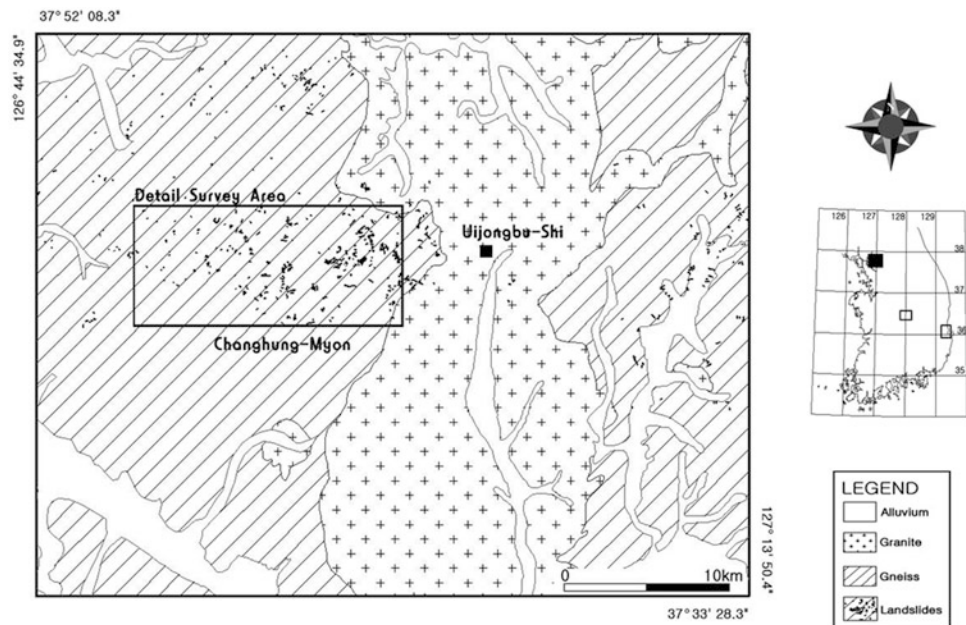
In Korea, about 70 % of the total area is mountainous, and the annual precipitation ranges from 1,100 to 1,400 mm. Most of this precipitation is concentrated in the rainy season from June through September. Most landslides occur due to heavy rainfall in this season. Previous studies have found that the occurrence of landslides is mainly influenced by the topography and precipitation (Lumb 1975; Caine 1980; Kim et al. 1991; Van Asch et al. 1996; Iverson 2000; Onda et al. 2004).

The geotechnical properties are very important, because most landslides occur in the soil layer or at the interface between the soil and the rock. The geotechnical properties depend on the weathering grade and the geology (Lumb 1975; Hutchinson 1988; Wakatsuki et al. 2005; Matsushi et al. 2006; Yalcin 2007). Topsoils consist of weathered residual soils, debris material, and coarse rock fragments. The soil properties are related to geological process and the soils retain the characteristics of the parent rocks (Wolle and Hachich 1989; Dykes 2002; Ahrendt and Zuquette 2003). Soils deposited on the parent rocks are called residual soils.

To investigate the factors influencing landslides, the properties of the topsoils that covered the slopes were measured. Three study areas are selected to include different geologies: granite, gneiss and sedimentary rocks. A landslide survey was carried out, and soil samples were obtained from both the landslide sites and landslide-free sites in each

Y.-S. Song (✉) • K.-S. Kim
Korea Institute of Geoscience and Mineral Resources, Geologic Environment Division, 124 Gwahang-no Yuseong-gu, Daejeon 305-350, South Korea
e-mail: yssong@kigam.re.kr; kks@kigam.re.kr

Fig. 1 Landslide distribution and the detailed survey section on a geological map of the Jangheung area (Lee et al. 1999)



study area. Then, a series of laboratory soil tests were carried out to measure the properties of the soils. Based on these results, the relationship between landslide occurrence and soil properties was analyzed and evaluated.

Landslide Occurrence Sites

Jangheung Area (Gneiss)

Many landslides occurred in the Jangheung area as a result of 588 mm of rainfall over 4 days from August 4 through 7, 1998. A general field survey found that about 511 landslides occurred in this area during that time. Based on the results of the general field survey, a zone with a high frequency of landslide occurrence was selected for a more detailed survey. A detailed field survey was performed for 77 landslides.

Figure 1 shows the landslide distribution map and the detailed survey section on the geological map of Jangheung (Lee et al. 1999). According to the geological map, granite is distributed on the center part to the south and north, and banded gneiss and porphyroblastic gneiss occur on both sides of the granite zone. Landslides occur widely throughout Jangheung, and an especially high frequency zone is located in Jangheung-Myeon and its surroundings. The landslides mainly occur on the gneiss zone of this area, so a detailed field survey was performed there (Fig. 1), as a representative section of gneiss in this study.

Sangju Area (Granite)

Many landslides occurred in Sangju as a result of 522 mm of rainfall over 3 days from August 10 through 12, 1998. The

general field survey found that about 788 landslides occurred in this area during that time. A detailed field survey was performed for 99 landslides in the zone with a high frequency of landslide occurrence.

Figure 2 shows the landslide distribution map and the detailed survey section on the geological map of the Sangju area (Kim and Lee 1986). According to the geological map, granite covers most of the area, with some areas of metamorphic and sedimentary rocks. Landslides occurred widely throughout Sangju. A zone with an especially high frequency of landslides is located in Hwaseo-Myeon and its surroundings. Therefore, a detailed field survey was performed in the granite zone, which is shown in Fig. 2, as a representative section of granite.

Pohang Area (Sedimentary Rock)

Many landslides occurred in Pohang as a result of 150 mm of rainfall over 2 days from July 25 through 26, 1998. The general field survey found that about 283 landslides occurred in this area during that time.

Figure 3 shows the landslide distribution map and the detailed survey area on the geological map of the Pohang area (Um et al. 1964). According to the geological map, granites widely cover the area, and metamorphic and sedimentary rocks are also distributed throughout the area.

Several landslides occurred in two small zones. These zones are mainly covered with Tertiary sedimentary rocks. Therefore, a detailed field survey was performed at the two zones, which are shown in Fig. 3, as representative sections for sedimentary rocks.

Fig. 2 Landslide distribution and a detailed survey section on the geological map of the Sangju area (Kim and Lee 1986)

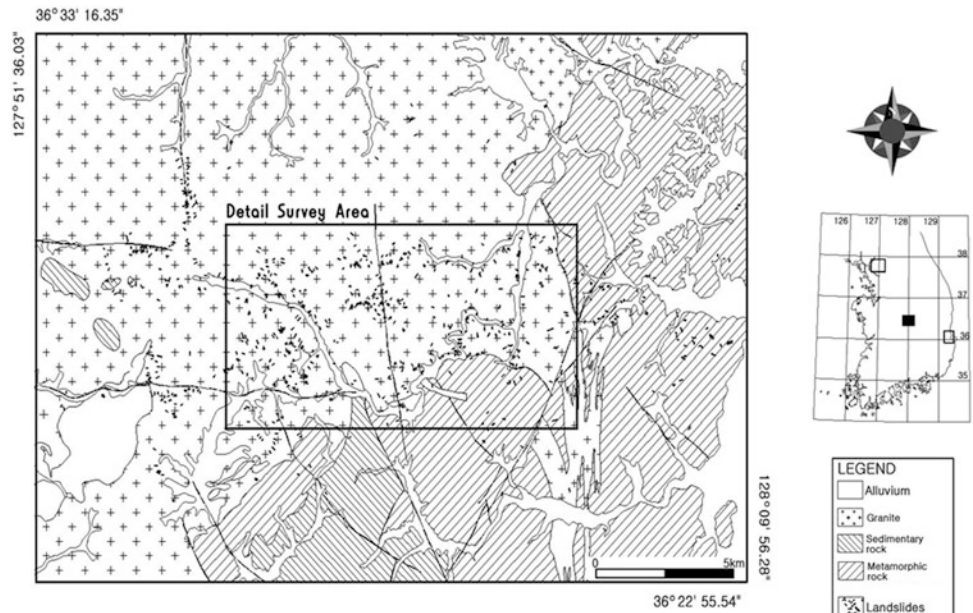
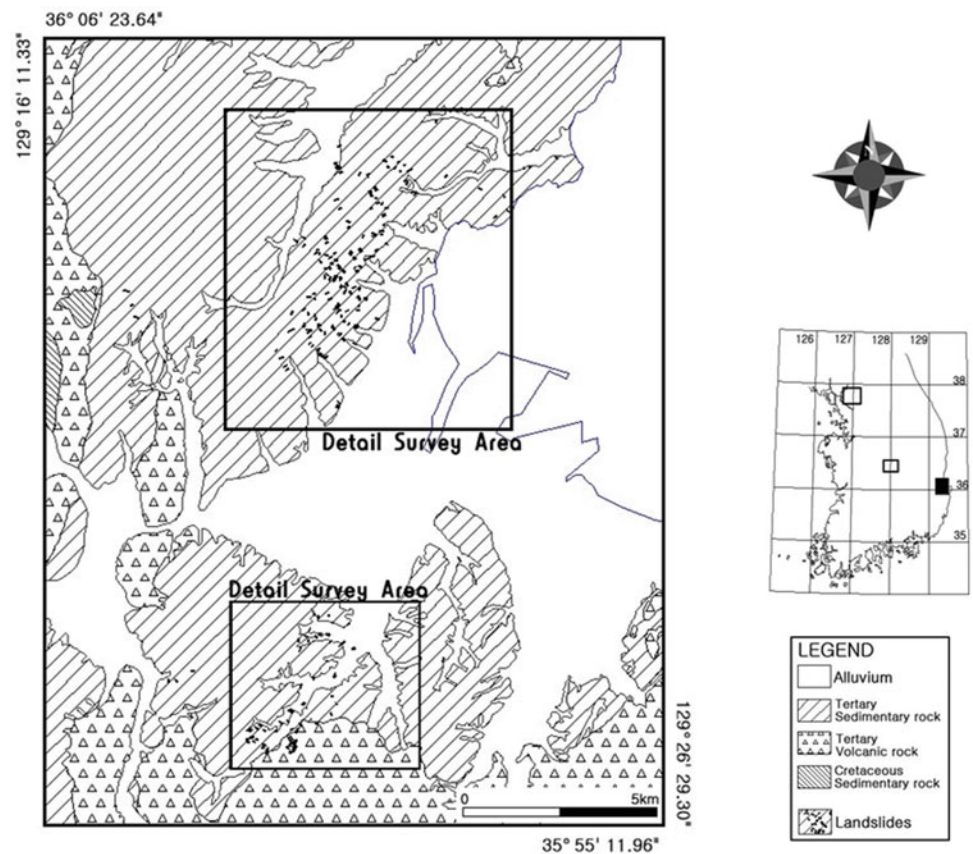


Fig. 3 Landslide distribution and a detailed survey section on a geological map of the Pohang area (Um et al. 1964)



Soil Sample and Laboratory Tests

The topsoils on the bedrock mainly consist of weathered residual soils, sedimentary materials and weathered rock fragments. The properties of these materials may be related

to the geology of the parent rocks because the mineral components of the soils are still present in the residual soils on the rocks.

The undisturbed and disturbed soil samples were obtained at depths of 40–60 cm from the ground surface after removing the surface soils. To take the unsaturated

soil samples on a site, the stainless ring sampler with 10 cm diameter and 6 cm height was used. All soil samples were packed in the field and then conveyed to the soil laboratory to maintain the field conditions.

A series of the soil laboratory tests, including particle size distribution tests (KS F 2302), particle density tests (KS F 2308), variable head permeability tests (KS F 2322), and direct shear tests (KS F 2343) were carried out in accordance with the procedures specified by the Korean Standard Association. The soil properties such as shear strength, permeability, dry unit weight, and void ratio were measured and calculated using the result of these tests.

In this study, a total of 60 soil samples were obtained from the three study areas, i.e., 20 soil samples in each area were collected for soil laboratory test. In particular ten soil samples were collected at the landslide sites and another ten soil samples were collected at the landslide-free site.

Geotechnical Properties

Void Ratio and Dry Unit Weight

Figure 4 shows the porosity and dry unit weight of soils obtained from the three study areas. The average porosity of soils obtained from the landslide sites is greater than that of soils from the landslide-free sites. In addition, the average dry unit weight of soils from the landslide sites is smaller than that of soils from the landslide-free sites, indicating that the soils from the landslide sites are more poorly graded or looser than those from the landslide-free sites. In general, poorly-graded soils and loose soils have large void spaces and a small dry unit weight. Soils with high porosity or low dry unit weight are particularly vulnerable to landslide occurrence. In addition, the porosity and the dry unit weight influence the occurrence of landslides in these areas. According to the analyses, the porosities of soils that originated from gneiss and granite are greater than that of soils that originated from sedimentary rocks.

Permeability

Variable head permeability tests (KS F 2322) were performed to measure the coefficient of permeability. Figure 5 shows the average permeability coefficients of soils obtained from sites in each area. In Jangheung, the average coefficient of permeability at the landslide sites is 5.43×10^{-3} cm/s, and that at the landslide-free sites is 4.33×10^{-3} cm/s. In Sangju, the average coefficient of permeability at the landslide sites is 6.00×10^{-3} cm/s, and that at the landslide-free sites is 5.14×10^{-3} cm/s. In Pohang, the average coefficient of permeability at the

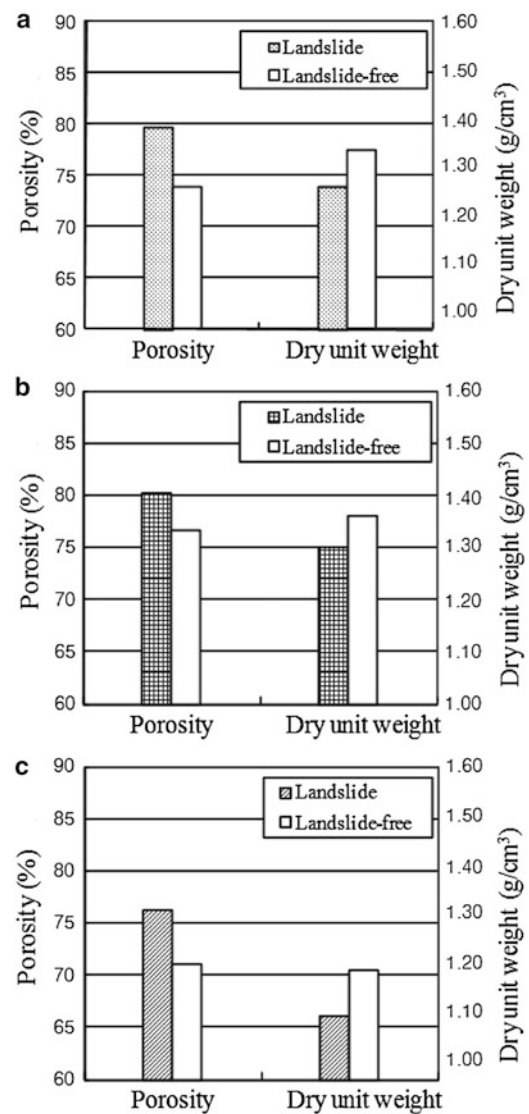


Fig. 4 Average porosity and average dry unit weight of soils in the study areas (a) Gneiss (Jangheung area); (b) Granite (Sangju area); (c) Sedimentary rock (Pohang area)

landslide sites is 4.78×10^{-3} cm/s, and that at the landslide-free sites is 3.90×10^{-3} cm/s.

As shown in Fig. 5, the permeability of soils obtained from the landslide sites was greater than that of soils from the landslide-free sites in the same geology. The distinction of the coefficient of permeability between the landslide sites and the landslide-free sites can be seen in these figures, even though the difference value is small.

The soils of Sangju are mainly composed of sands with coarse particles originating from the granite. However, the soils of Jangheung and Pohang are mainly composed of sands with some fine particles originating from the gneiss and sedimentary rocks, respectively. The coefficients of permeability in Sangju are higher than those in Jangheung and Pohang. This result might be caused by the particle size

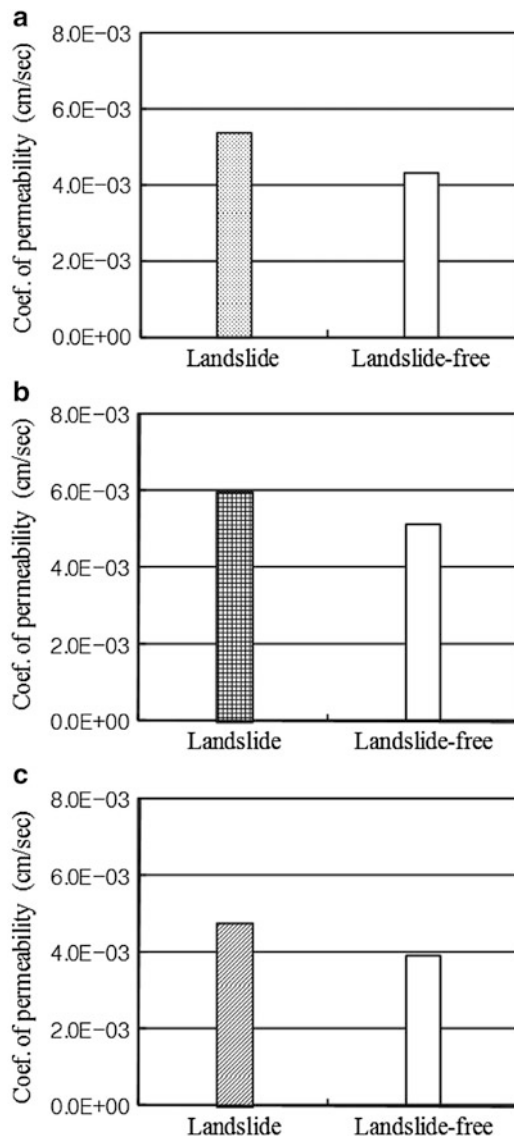


Fig. 5 Average coefficient of permeability of soils in the study areas (a) Gneiss (Jangheung area); (b) Granite (Sangju area); (c) Sedimentary rock (Pohang area)

and porosity of the soils. These soil properties originate from the geologic properties of the parent rocks.

Shear Strength

The shear strength is one of the most important properties of soil for determining whether a landslide will occur. This property is strongly related to the ability to resist sliding along internal surfaces within a soil mass. In a slope stability problem, sliding and resisting forces are calculated using the Mohr-Coulomb failure criterion. The shear strength is usually expressed as the cohesion and the internal friction angle.

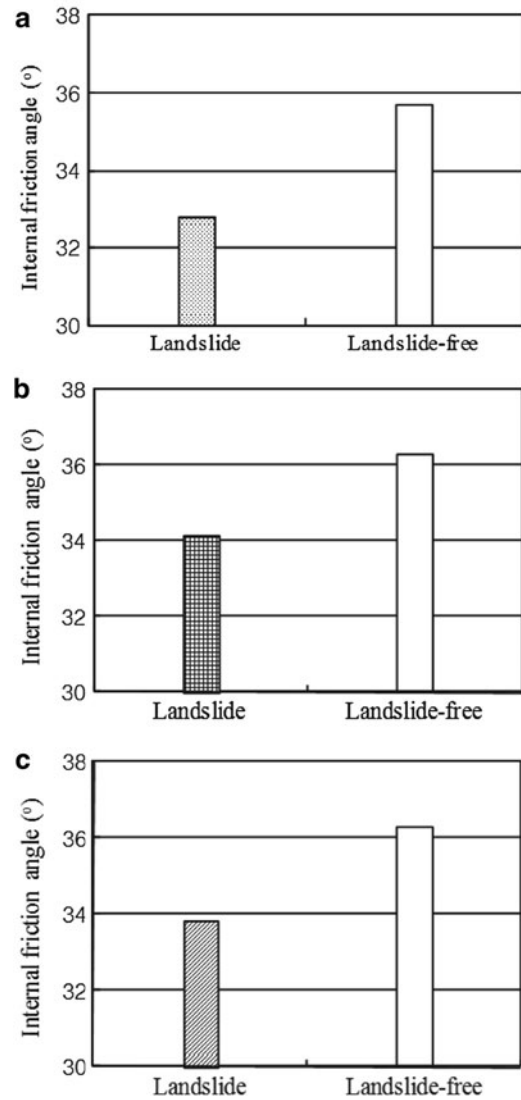


Fig. 6 Average internal friction angle of soils in the study areas. (a) Gneiss (Jangheung area); (b) Granite (Sangju area); (c) Sedimentary rock (Pohang area)

These values are measured by the direct shear test (KS F 2343), considering field conditions.

Figure 6 shows the internal friction angles of the soils obtained from the three study areas. Only the internal friction angles between the landslide sites and the landslide-free sites are compared, because the cohesions of soils from the landslide sites are very similar to those of the landslide-free sites. In addition, the cohesions of the soils are very small because the soils are sands.

In Jangheung, the average internal friction angle of the soils from the landslide sites is 33°, and that of soils from the landslide-free sites is 36°. In Sangju and Pohang, the average internal friction angle of soils from the landslide sites is 34°, and that of soils from the landslide-free sites is 36°.

The average internal friction angles of soils from the landslide sites are smaller than those of soils from the landslide-free sites. It is confirmed that soils with low shear strength are more vulnerable to landslide occurrence.

Conclusions

Most landslides in the natural terrain of Korea occur as transitional failures at shallow soil depths during the rainy season. Therefore, the geotechnical properties of the soils and precipitation records should be investigated to know the reasons for landslide occurrence. In this study, three study areas (Jangheung, Sangju and Pohang) were selected to find the relationship between geotechnical properties and landslide occurrence, considering geology and precipitation. Many landslides occurred in these three areas during the rainy season. To investigate the factors that influence landslides in more detail, a landslide survey was performed and soil samples were obtained from both the landslide sites and the landslide-free sites for laboratory soil tests.

According to the analysis results, the average porosity of the soils obtained from the landslide sites is greater than that of soils obtained from the landslide-free sites. The average dry unit weight of soils from the landslide sites is smaller than that of soils obtained from the landslide-free sites. The average coefficient of permeability of the soils from the landslide sites is greater than that of soils from the landslide-free sites with the same geology. The average shear strength of soils from the landslide sites is smaller than that of soils from the landslide-free sites. This result indicates that the soils from the landslide sites are more poorly-graded or looser than the soils from the landslide-free sites. Also, it is confirmed that soils with low shear strength and high permeability are especially vulnerable to landslide occurrence.

Acknowledgments This research was supported by the Public Welfare & Safety Research Program through the National Research Foundation of Korea (NRF) funded by the Ministry of Science, ICT & Future Planning (Grant No. 2012M3A2A1050983).

References

- Ahrendt A, Zuquette LV (2003) Triggering factors of landslides in Compos do Jordao city, Brazil. *Bull Eng Geol Environ* 62:231–244
- Caine N (1980) The rainfall intensity-duration control of shallow landslides and debris flows. *Geografiska Annaler* 62A:23–27
- Dykes AP (2002) Weathered-limited rainfall triggered shallow mass movement in undisturbed tropic rainforest. *Geomorphology* 46:73–93
- Hutchinson JN (1988) Morphological parameters of landslides in relation to geology and hydrogeology. In: Bonnard C (ed), *Proc 5th International Symposium on Landslides*, vol 1. Rotterdam, Netherlands, pp 3–35
- Iverson RM (2000) Landslides triggering by rain infiltration. *Water Resour Res* 36:1897–1910
- Kim DH, Lee BJ (1986) Explanatory text of the geological map of the Chungsan sheet, Scale 1:50,000, Korea Institute of Energy and Resources
- Kim SK, Hong WP, Kim YM (1991) Prediction of rainfall triggered landslides in Korea. In: Bell DH (ed), *Proc 6th International Symposium on Landslides*, vol 2. Christchurch, New Zealand, pp 989–999
- Lee BJ, Kim YB, Lee SR, Kim JC, Kang PJ, Choi HI, Jin MS (1999) Explanatory text of the geological map of the Seoul—Namcheonjeom sheet, Scale 1:250,000. Korea Institute of Geology, Mining and Materials
- Lumb P (1975) Slope failures in Hong Kong. *Q J Eng Geol* 8:31–65
- Matsushi Y, Hattanji T, Matsukura Y (2006) Mechanisms of shallow landslides on soil-mantled hillslopes with permeable and impermeable bedrocks in the Boso peninsula, Japan. *Geomorphology* 76:92–108
- Onda Y, Tsujimura M, Tabuchi H (2004) The role of subsurface water flow paths on hillslope hydrological processes, landslides and landform development in steep mountains of Japan. *Hydrol Process* 18:637–650
- Um SH, Lee DW, Park, BS (1964) Explanatory text of the geological map of the Sangju sheet, Scale 1:50,000. Geological Survey of Korea
- Van Asch TWJ, Hendriks MR, Hessel R, Rappage FE (1996) Hydrological triggering conditions of landslides in varved clays in the French Alps. *Eng Geol* 42:239–251
- Wakatsuki T, Tanaka Y, Matsukura Y (2005) Soil slips on weathering limited slopes underlain by coarse-grained granite or fine-grained gneiss near Seoul, Republic of Korea. *Catena* 60:181–203
- Wolle CM, Hachich W (1989) Rain-induced landslides in southern Brazil. *Proc 12th International conference on soil mechanics and foundation engineering*. Rio de Janeiro, Brazil, pp1639–1642
- Yalcin A (2007) The effects of clay on landslides: a case study. *Appl Clay Sci* 38:77–85



Modelling Fragmentation in Rock Avalanches

Øystein Thordén Haug, Matthias Rosenau, Karen Leever, and Onno Oncken

Abstract

The physical description of rock masses travelling down a slope is a complex problem, involving bouncing, rolling, sliding, flowing, fracturing and/or combinations of these. Modelling serves as a valuable tool to study these systems which are rarely monitored at high resolution in nature. Often, granular models (e.g. loose sand) are used to study rock avalanches in experimental simulations. For such granular models, one has to assume that the rock mass disintegrates instantaneously after detachment and that fragment size does not reduce further during the movement. We present a new method that overcomes this limitation by simulating dynamically fragmenting gravitational mass movements.

We have developed a material that fails in a brittle manner at lab scale conditions. The material is produced by cementing sand with gypsum (anhydrite) or potato starch, which allows controlling the shear strength over a wide range. Experiments are performed by releasing the material down a slope and monitoring with a digital camera at frequencies of 50 or 250 Hz. Two techniques are used to quantify the experimental results: particle image velocimetry which quantifies the surface velocity field, and optical image analysis to derive geometric (e.g. fragment size distribution) and mechanical properties (e.g. basal friction) of the model.

Preliminary results from the experiments illustrate the different dynamics of the gravitational mass movement as a function of shear strength.

Keywords

Rock avalanche • Fragmentation • Analogue material • Image analysis

Introduction

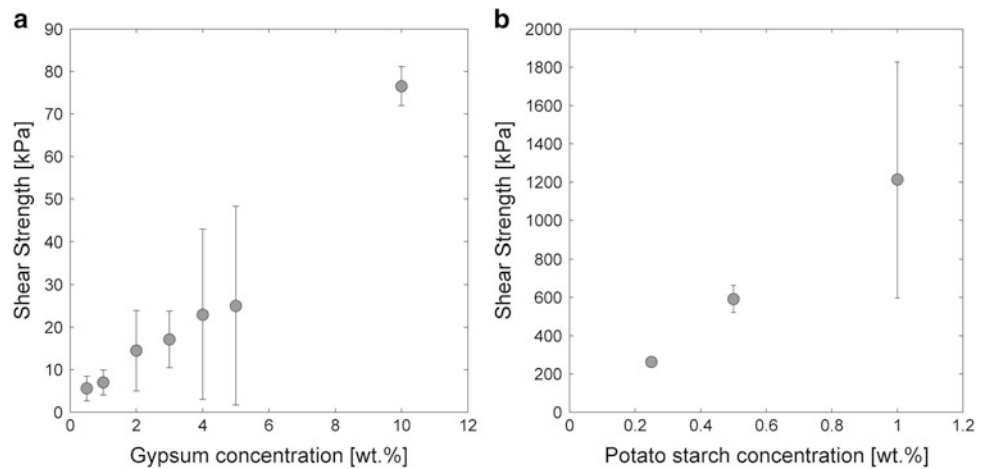
Rock avalanches are large (volume $>10^6$ m³) rapid gravitational movements of rocks (Hsü 1975; Davies and McSaveney 1999). Rock-avalanche deposits are often made up of granular material with fragment sizes ranging from meter sized boulders down to dust on a micro-meter scale (Crosta et al. 2007; McSaveney and Davies 2007). The rock

mass prior to the detachment can be assumed to have been more or less intact (Locat et al. 2006), suggesting that the deposits are the products of fragmentation processes occurring during detachment (static fragmentation) and during the travel (dynamic fragmentation).

Likely due to the shape and the granular nature of the deposits, rock avalanches are often modelled as granular flows both in analogue (Davies and McSaveney 1999; Iverson et al. 2004; Shea and van Wyk de Vries 2008; Dufresne 2012; Manzella and Labiouse 2012) and numerical (Campbell et al. 1995; Mollon et al. 2012) experiments. However, using granular material to model rock avalanches means assuming that dynamic fragmentation is negligible, i.e., one assumes that the rocks instantaneously disintegrate

Ø.T. Haug (✉) • M. Rosenau • K. Leever • O. Oncken
Section 3.1—Lithosphere Dynamics, GFZ—Potsdam, Telegrafenberg,
14473 Potsdam, Germany
e-mail: thorden@gfz-potsdam.de; rosen@gfz-potsdam.de; karen.
leever@gfz-potsdam.de; oncken@gfz-potsdam.de

Fig. 1 Shear strength as a function of gypsum (a) and starch (b) concentrations. Each point is the mean value of 15 AT-tests and the error bars are given by the standard deviation around this mean



after detachment and that no further fragmentation occurs during the travel.

Few models have taken dynamic fragmentation during rock avalanches into consideration (Imre et al. 2010; Bowman et al. 2012) and these were performed in centrifuges, which pose restrictions on the possible scales that can be studied. Nevertheless, Bowman et al. (2012) showed that material that fragmented dynamically caused a longer runout than that of pre-fragmented material, suggesting that dynamic fragmentation is an important agent in rock-avalanche dynamics.

We study the effect of dynamic fragmentation in rock avalanches at lab scale under normal gravity conditions. To do this, a new rock-analogue material, and a method to quantitatively analyse the dynamics of fragmenting model avalanches have been developed. Compared to experiments performed in a centrifuge, this approach has the advantage that a wider range of scales can be studied and the potential to simulate more realistically the full process from detachment to deposition.

Analogue Material and Experimental Setup

According to the principle of model similarity (Hubbert 1937), the analogue material must behave in a dynamically similar way to the rocks in natural rock avalanches. Ideally, the material should therefore deform in a brittle manner with limited elastic and ductile strains up to a certain critical stress, beyond which the material breaks and deforms irreversibly.

The material is created by cementing together well-rounded fluvial quartz sand (average size $\sim 300 \mu\text{m}$) with a cementing agent. In the tests reported here, the cementing agents are gypsum (anhydrite) and potato starch (carbohydrate).

The material properties are tested using a ring shear tester (RST) and a uniaxial tester (AT).

Material Preparation and Properties

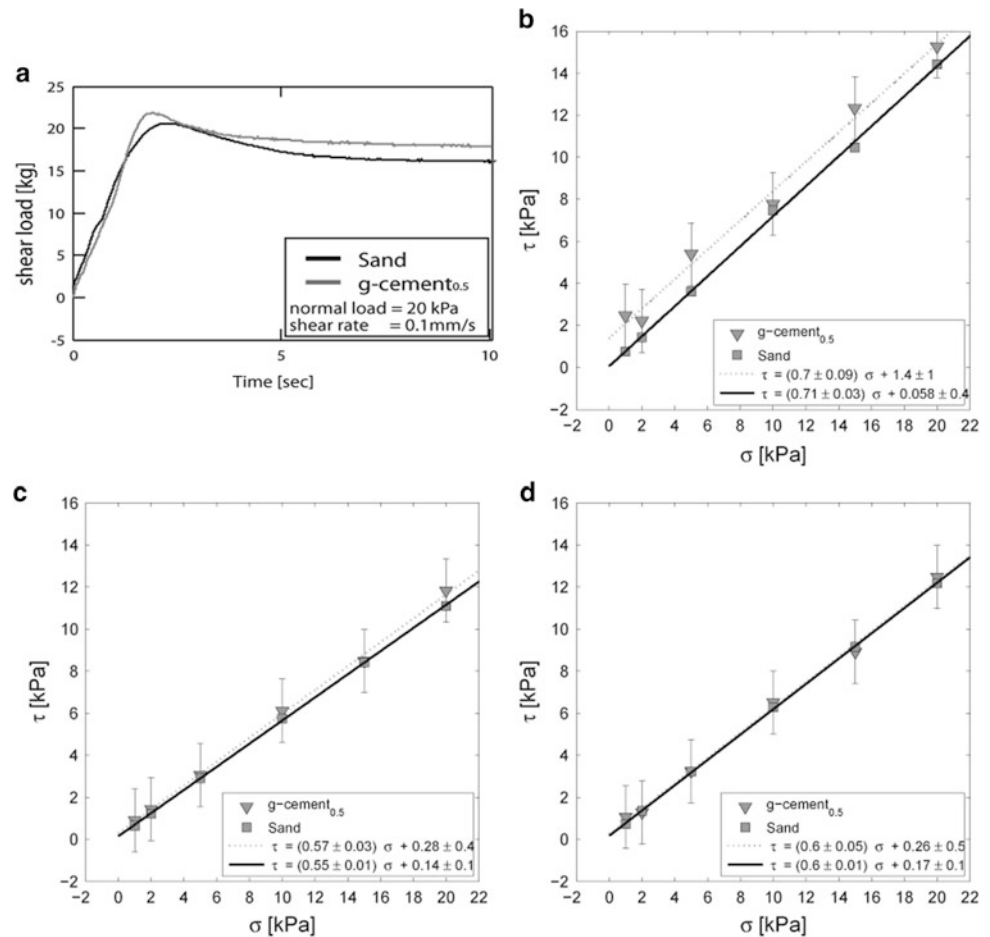
The sand and the cement are first mixed while dry, afterwards a small amount of water ($\sim 10 \text{ wt}\%$) is added and everything is thoroughly mixed to yield a homogeneous mass. The material is then placed inside a mould, and compacted by hammering by hand.

The material hardens by either setting for 48 h at room temperature (in the case of gypsum cement) or heating in a 900 W microwave oven for 15 min (in the case of potato starch cement).

The shear strength of the material can be controlled by the concentration of cementing agent. Systematic AT-tests of the effect of concentration shows that the shear strength can be varied between 1 and 10^3 kPa (Fig. 1). As seen in Fig. 1, the shear strength achieved using gypsum cement (hereafter called “g-cement”, Fig. 1a) varies from 1 to 10^2 kPa and scales approximately linearly with the concentration. A stronger material can be achieved using potato starch cement (hereafter called “s-cement”). The correlation between the shear strength and the concentration of potato starch is also approximately linear and the shear strength of s-cement varies between 10^2 and 10^3 kPa (Fig. 1b). The two data sets (Fig. 1a, b) are seen to complement each other, allowing us to vary the shear strength over six orders of magnitude.

The frictional properties of a low strength material, g-cement_{0.5} (lower case number referring to concentration, here 0.5 wt%), in comparison with loose sand, were tested using the RST (Fig. 2). Typical shear stress curves obtained from the RST are shown in Fig. 2a. In general, the shear

Fig. 2 Data from the ring shear tester (RST). (a) Raw data of sand and g-cement_{0.5}. (b)–(d) Comparisons of peak, kinetic and static friction between loose sand and g-cement_{0.5}



stress curves show an increase of shear stress until it reaches a peak (peak friction) when a shear fracture forms, followed by a decrease to a constant shear stress level (kinetic friction). A similar curve to that presented in 2a, but with a lower peak value, is obtained if a sample with an existing shear fracture is sheared (static friction).

In Fig. 2b, c, d, the results of a series of RST tests are presented. In these plots, the frictional strengths of g-cement_{0.5} is compared with that of loose sand for normal stresses ranging from 0.5 to 20 kPa. The resulting linear relationships can be modelled as a Mohr-Coulomb failure envelope, the slope of which is the coefficient of friction and the y-axis intercept is the cohesion. Accordingly, the cohesion of undeformed loose sand is in the order of 10 Pa, while the cohesion of the g-cement_{0.5} is in the order of 10^3 Pa (Fig. 2b). Importantly, the friction coefficients are not influenced by cementing, nor is there any residual cohesion once a fracture has been created (Fig. 2c, d). The peak static and kinetic coefficients of friction for both loose sand and the cemented sand are 0.7, 0.6 and 0.55, respectively.

We conclude that increasing concentration of cementing agent in the mix increases its primary cohesion, while the other frictional properties remain constant. Due to the small amount of cementing material, this is assumed for all concentrations.

Experimental Setup

In our setup, rock avalanches can be modelled at lab scale by a sudden release of material down a slope of 1–2 m length and at an angle of 30°–60°. Past the slope, the angle changes suddenly to 0° (Fig. 3). The experiments are monitored with a digital camera at frequencies of 50 and 250 Hz and image resolutions of 8.29 and 0.23 MPx, respectively.

Here we report the first series of experiments, consisting of three runs on a 45° dipping slope, where only the shear strength of the material is varied while all other parameters are kept constant. Materials used in this series are 1.5 kg samples of loose sand, g-cement_{0.5} and s-cement₁. The shear strength thus varies from 10, 10^3 to 10^6 Pa (assuming shear

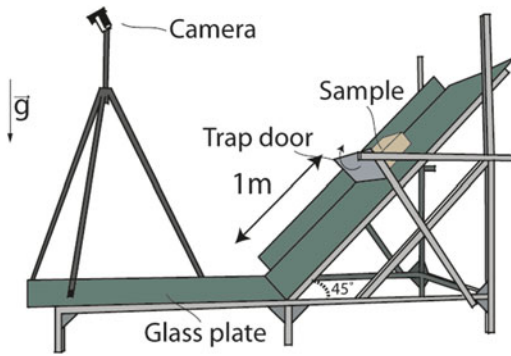


Fig. 3 Experimental setup

strength of sand \approx cohesion of sand). The camera frequency during these experiments was 50 Hz at 8.29 MPx resolution.

The initial geometry of the released material is a rectangular cube of dimension $0.15 \times 0.15 \times 0.04 \text{ m}^3$ lying on its widest side. Additionally, a thin layer of red sand is added on top of the samples (not to the loose sand) to increase contrast for image analysis. The sliding base consists of glass plates.

Image Analysis

To quantify the experiments we use two types of image analysis: Particle Image Velocimetry (PIV) and Optical Image Analysis (OIA).

The goal of the image analysis is to measure deformation, velocity and fragmentation through time. The first two parameters are found using PIV, while the last point is found using OIA.

Before any analysis, the images are calibrated, i.e., corrected for distortions and the differences in distances between the different objects in the images and the camera. This is done using the PIV software (PIV Strainmaster by LaVision).

Particle Image Velocimetry

Particle Image Velocimetry (PIV) is used to monitor the velocity and deformation of the surface of the sliding material (Fig. 4a). The basic concept of the PIV method is to use cross-correlation of patterns in sequential images to detect the displacement of the pattern between the images (see Adam et al. (2005) for a comprehensive description).

The patterns in question are, in fact, a specific distribution of grayscale-intensities within a given interrogation window (a smaller part of the image). For the analysis given here the PIV-algorithm uses interrogation window sizes decreased from 256×256 to 128×128 pixels with 75 % overlap.

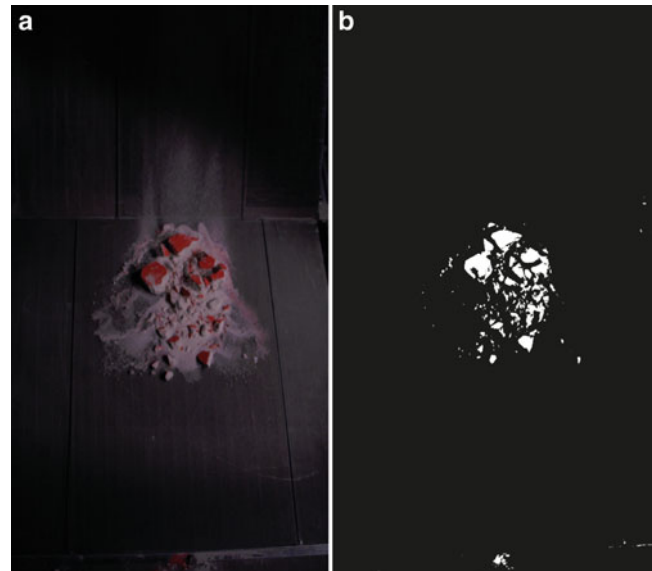


Fig. 4 (a) Example of an experimental image showing a fragmented block spreading on a horizontal plane. (b) Binary image of (a)

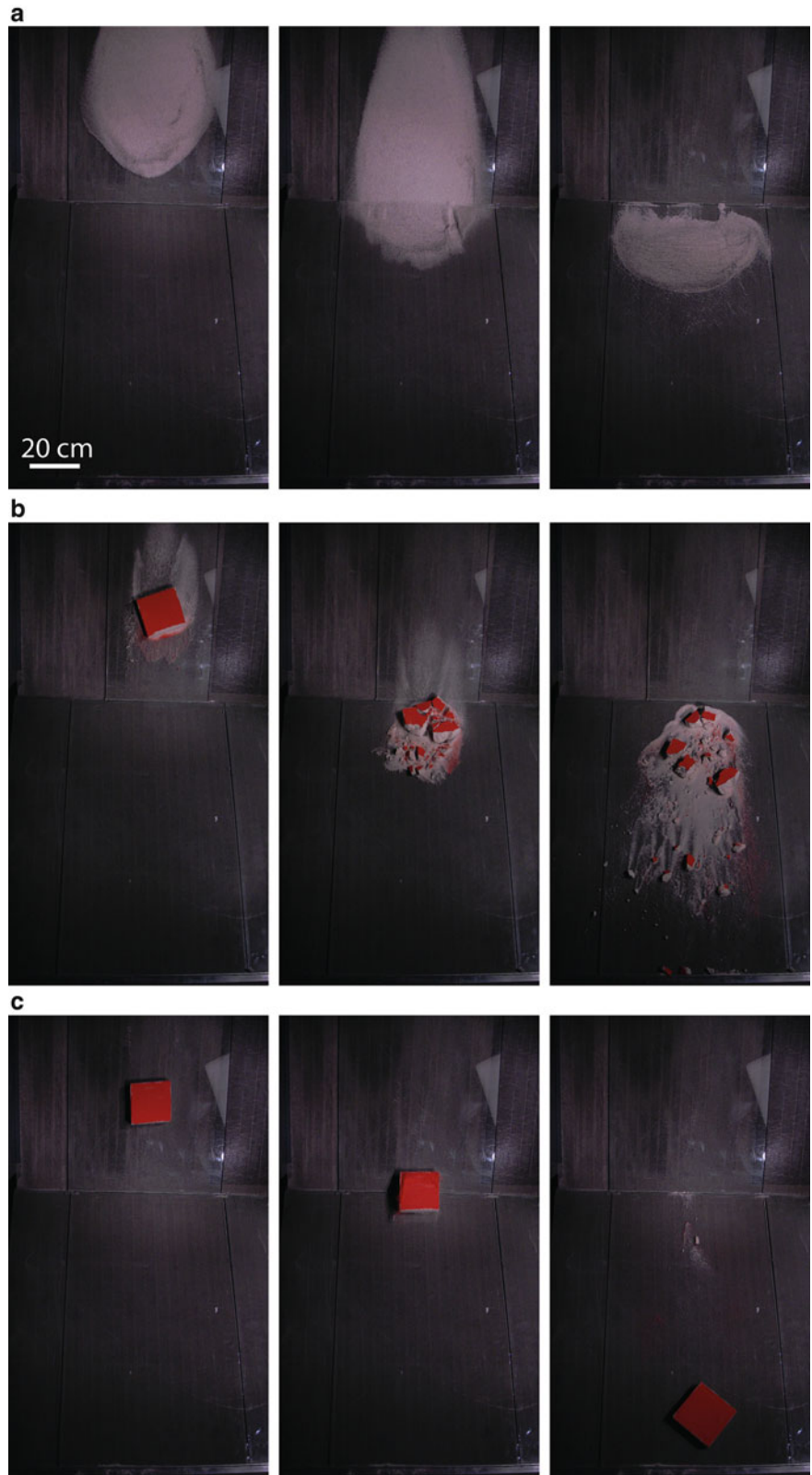
This results in velocity field resolution of 0.0563 m, at a precision of 0.03 m/s.

Optical Image Analysis

Optical Image Analysis (OIA) is used here to quantify the fragmentation process. The general strategy of OIA in our approach is to convert the original image (Fig. 4a) to a binary image (Fig. 4b) where the fragments are of value 1 (white) and everything else is of value 0 (black). In this process, all fragments below a size of 10 pixels are considered background. The binary image is created in three steps. In each step a binary image is produced, and in the end all these are combined into one final binary image (Fig. 4b).

The first binary image is produced by considering only the red contribution to the RGB image. The image is binarized by setting all pixels with intensity above a certain limit to 1 and all below to 0. This process is called thresholding. Since the top of the samples have a thin layer of red sand (see Fig. 4a), this procedure captures most of the larger fragments which have not rotated. The second binary image is produced by converting the RGB image to grayscale and thresholding it. This method is most appropriate to find the largest fragments. The third binary image is found by differentiating in both directions across the grayscale image, subtracting this from the original grayscale image, and thresholding the resulting image. This procedure finds the small fragments, and is also capable of extracting fragments which are resting on top of sand (which is considered background).

Fig. 5 Images of experiments with different cohesion **(a)** loose sand ($SS = 10^1$ Pa), **(b)** g-cement_{0.5} ($SS = 10^3$ Pa), and **(c)** s-cement₁ ($SS = 10^6$ Pa)



The sizes of the fragments are approximated by the areas they project on the images and are given in equivalent diameters.

$$L = \sqrt{\frac{Area}{\pi}}$$

Additional to the fragmentation process, OIA is used to monitor the area covered by the slide through time. In this calculation, the area is found by considering all fragment sizes. In practice, this is done by thresholding so that all the sand and blocks are 1's while the rest is 0.

Preliminary Observations and Interpretation

Figure 5 shows snapshots of three different experiments, where the shear strength (SS) is varied from 10 (Fig. 5a), 10^3 Pa (Fig. 5b) to 10^6 Pa (Fig. 5c). All other parameters are kept constant. The sand, in Fig. 5a, can be described as flowing, in contrast, the block in Fig. 5c is sliding. The fragmenting block (Fig. 5b) is at first seen to slide, until it hits the knickpoint, at which point it breaks and spreads across the horizontal plane. The longest runout is seen for the intact block, and the second longest for the fragmenting block, while the loose sand shows the shortest runout. This may reflect the difference in energy consumption due to internal deformation which is lowest for the intact block.

PIV-derived velocity fields of the experiments from Fig. 5a, b is presented in Fig. 6. These show that the behaviour of the two experiments is kinematically different on the horizontal plane: While the loose sand avalanche has higher displacement in the rear than in the front of the pile, the cement slide-avalanche has higher displacement in the front than in the rear. This suggests that the material in the sand avalanche actively contracts while the g-cement_{0.5} avalanche expands, in the direction of travelling.

The evolutions of areas of the slides are presented in Fig. 7a and shed light on the role of basal contact area on runout. The vertical line represents the time when the material reaches the horizontal plane. For the experiment with $SS = 10^1$ Pa (Fig. 5a) the area is seen to increase until ca. 0.2 s after reaching the plane, after which the area decreases again. This behaviour reflects the active spreading and contraction during movement of the avalanche. For the experiment shown in Fig. 5b ($SS = 10^3$ Pa) an initial increase is seen, until a plateau is reached, the area increases again directly after impact. The first increase is due to the sample moving into the field of view, while the second reflects the

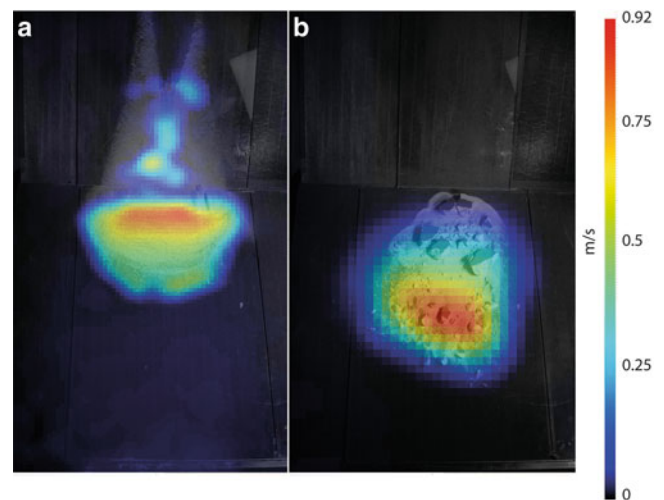


Fig. 6 Snapshots of the velocity field calculated from the PIV for experiments shown in Fig. 5a (a) and 5b (b)

spreading after fragmentation. For the experiment shown in Fig. 5c ($SS = 10^6$ Pa) the area is seen to be more or less constant, reflecting the rigid block-like behaviour of the slide. Considering the differences in runout, one might argue that the frictional energy dissipation is more pronounced for low-cohesive material due to (a) the increase of basal sliding area during acceleration in combination with (b) frictional dissipation by compressive internal deformation during deceleration.

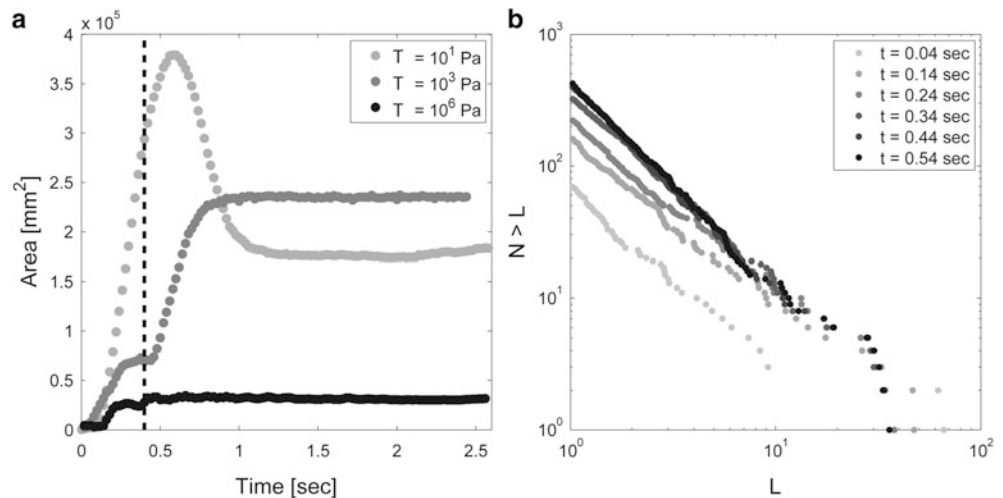
In Fig. 7b snapshots of the fragment size distribution (FSD) are presented. The approximately linear trends of the fragment size distributions suggest that they can be described by power-laws where the exponent is given by the slope. Interestingly, the slopes of the fragment size distributions appear more or less constant through time, while the distribution is shifted towards higher numbers in time. This suggests that the fragmentation is a self-organized (fractal) process.

Discussion

Limitations of the Approach

From Fig. 1, it is observed that the uncertainty of the shear strength (SS) increases with the strength, reflecting the variability of the sample material under otherwise identical preparation conditions. Most likely, this variability in shear strength arises because the material is not completely homogenous. One might therefore expect the fragmentation to be affected by the variability of the material and should not

Fig. 7 (a) Basal area during slide for the three experiments shown in Fig. 5. Vertical line displays time of impact. (b) Fragment size distribution (FSD) at different time steps for the experiment presented in Fig. 5b. Time given in legend is after impact



over-interpret single experiments. Instead, a large number of experiments are needed to constrain uncertainty of experimental results.

Even though the OIA finds fragments and their sizes, there are some problems related to this approach. One is that sometimes piles of sand may be interpreted as fragments, even though they should not be. This error is minimized by removing fragments with very elongated shapes. A second problem is that shadows can cause separation of larger fragments into several smaller ones. This effect is dealt with by averaging over time. The OIA only takes into account fragments larger than 10 pixels, equivalent to a 4.4 mm long fragment. A rough estimate of how much material is below this level can be found by comparing the total area of all fragments registered and the total area of the entire slide. Such an estimate for the experiment presented in Fig. 5a suggests that the latter is as much as 1 order of magnitude larger. This can cause a bias of the fragment size distribution to the coarser end of the distribution. However, if the fragment size distributions truly are scale-invariant power laws, the exponent should remain the same regardless of the resolution.

Comparison with Centrifuge Models

Similar to what Bowman et al. (2012) showed, we also see that a fragmenting material travels further than a pre-fragmented one (Fig. 5a, b), corroborating their interpretation that fragmentation can be viewed as an energy source. Our results show, however, that an even longer runout is achieved for an intact block. This may suggest that dynamic fragmentation causes loss of cohesion, which causes higher energy dissipation due to increased internal deformation and larger basal friction (due to increased basal area).

Imre et al. (2010) found that their experimental fragment size distribution was given by power laws and interprets this

to be due to a fractal process. Our experimental fragment size distributions are also well approximated by power laws. However, a linear regression of the data in Fig. 7b reveals a power law exponent of $\sim 1 \pm 0.2$, this is steeper than the ~ 0.4 exponent found by Imre et al. (2010). Such a discrepancy might be caused by our bias toward larger fragments. Imre et al. also report a steeper slope for the larger fragments.

Conclusion and Outlook

We have developed a tool for studying fragmentation in rock avalanches. Rock avalanches are modelled at lab scale by releasing an analogue material down a slope. The shear strength of the material can be controlled by the amount of cementing agent added to the sand. Our image analysis tool allows us to quantify the fragmentation process and the following dynamics of the slide.

With this new tool, we plan to perform a parameter study, to better understand the changes in dynamics and energetics of a system of varying shear strength.

Acknowledgments Thanks to Frank Neumann and Thomas Ziegenhagen for construction and technical assistance. The work is supported by GEOSIM and BMBF.

References

- Adam J, Urai JL, Wieneke B, Oncken O, Pfeiffer K, Kukowski N, Lohrmann J et al (2005) Shear localisation and strain distribution during tectonic faulting—new insights from granular-flow experiments and high-resolution optical image correlation techniques. *J Struct Geol* 27(2):283–301
- Bowman ET, Take WA, Rait KL, Hann C (2012) Physical models of rock avalanche spreading behaviour with dynamic fragmentation. *Can Geotech J* 49(4):460–476
- Campbell CS, Cleary PW, Hopkins M (1995) Large-scale landslide simulations: global deformation, velocities and basal friction. *J Geophys Res* 100(B5):8267–8283
- Crosta GB, Frattini P, Fusi N (2007) Fragmentation in the Val Pola rock avalanche, Italian Alps. *J Geophys Res* 112:F01006

- Davies TR, McSaveney M (1999) Runout of dry granular avalanches. *Can Geotech J* 36(2):313–320
- Dufresne A (2012) Granular flow experiments on the interaction with stationary runout path materials and comparison to rock avalanche events. *Earth Surf Proc Land* 37(14):1527–1541
- Hubbert M (1937) Theory of scale models as applied to the study of geologic structures. *Geol Soc Am Bull* 48(October): 1459–1520
- Hsü KJ (1975) Catastrophic debris streams (sturzstroms) generated by rockfalls. *Geol Soc Am Bull* 86(50117):129–140
- Imre B, Laue J, Springman SM (2010) Fractal fragmentation of rocks within sturzstroms: insight derived from physical experiments within the ETH geotechnical drum centrifuge. *Granul Matter* 12(3):267–285
- Iverson RM, Logan M, Denlinger RP (2004) Granular avalanches across irregular three-dimensional terrain: 2 experimental tests. *J Geophys Res* 109, F01015
- Locat P, Couture R, Leroueil S, Locat J, Jaboyedoff M (2006) Fragmentation energy in rock avalanches. *Can Geotech J* 43(8)
- Manzella I, Labiouse V (2012) Empirical and analytical analyses of laboratory granular flows to investigate rock avalanche propagation. *Landslides* 10(1):23–36
- McSaveney MJ, Davies T (2007) Rockslides and their motion. In: Sassa K, Fukuoka F, Wang F, Wang G (eds) *Progress in landslide science*. Springer, Berlin, pp 113–133
- Mollon G, Richefeu V, Villard P, Daudon D (2012) Numerical simulation of rock avalanches: influence of a local dissipative contact model on the collective behavior of granular flows. *J Geophys Res* 117(F2): 1–19
- Shea T, van Wyk de Vries B (2008) Structural analysis and analogue modeling of the kinematics and dynamics of rockslide avalanches. *Geosphere* 4:657–686



Experimental Modelling for the Effect of Rainfall and Earthquake on Slope Stability of Engineered Fill

Binod Tiwari, Santiago Caballero, and Wissam Zalzali

Abstract

The collapse of several houses in some residential developments in Sendai during the M9 Tohoku earthquake warranted the health monitoring of several slopes in southern California. Majority of the houses developed in southern California are in engineered fill and the qualities of compaction may not be sufficiently checked. Due to recent trend of unpredictable rainfall and being located in the high seismic activity area, houses constructed on slopes in southern CA have strong potential to slide during earthquake or heavy rainfall. This study involves a systematic study of an engineered fill at Mission Viejo, California for potential slide activities. The materials borrowed from the site were compacted in a Plexiglass container at the field density, moisture content, and field slope angle. The slope was poured with the 100 year return period rainfall expected in the area using, a rain simulator. Variation in suction in the soil mass was recorded with duration of rainfall. Slope stability analyses were performed to evaluate the effect of earthquake in those slopes in reducing the factor of safety. The study result shows that the combined effect of antecedent rainfall and seismic shaking has significantly high effect on slope stability, compared to strong magnitudes of either rainfall or seismic acceleration acting separately.

Keywords

Clay • Antecedent rainfall • Seismic shaking • Slope stability • Soil suction

Background

Landslides cause an annual loss of \$1–2 billion (USGS). Heavy rainfall, earthquake and associated hazards related to these events such as typhoon, tsunami, hurricane etc. are considered to be the major triggers of landslides. However,

combined effects of earthquakes and rainfall were ignored in the past. We have evidenced several high magnitude earthquakes in recent years; many of them were either during or slightly prior to or after the rainy season. These earthquakes triggered several landslides. Therefore, the current research works pertinent to landslides are focusing on the combined effect of rainfall and earthquake. Several large scale landslides occurred after the M9.0 Tohoku Earthquake (Tiwari et al. 2013). More than 50 houses were damaged in a built-in area that was developed on embankment slopes. The area did not have much rainfall prior to the earthquake. However, it is believed that the soil lost suction during the heavy shaking that could have triggered the landslide.

With a desire to have a beautiful view, there is a growing tendency in southern California to construct houses on slopes. Majority of these houses are constructed on

B. Tiwari (✉) • S. Caballero
Department of Civil and Environmental Engineering, California State University Fullerton, 800N State College Blvd, Fullerton, CA 92831, USA
e-mail: btiwari@fullerton.edu; scaballero@csu.fullerton.edu

W. Zalzali
Zalzali & Associates, 2070 Business Center Dr. Suite 200, Irvine, CA 92612, USA
e-mail: wissam@zalzali.com

engineered fills. As the houses are mainly developed by the real estate developers, the construction quality control may not be as severe as required for the public infrastructures. Therefore, stability of the slopes where these houses are constructed should be checked for possible combined effect of rainfall and earthquake. In this study, we considered a case study of a site located in the city of Mission Viejo, 50 miles south of Los Angeles, California. The housing community was developed around 1998, mostly on the engineered fills. A total of 209 single family homes were constructed. The landslide investigation that took place from 2005 to 2010 concluded that there is no slope movement. However, some of the home owners were concerned that if the area gets a good amount of rainfall for a long period during an earthquake event, the slope may not remain stable.

The authors conducted field investigation and collected soil samples from the slope. Soil samples collected from the site were utilized to prepare slopes at various angles of inclination in a model container, which were later subjected to a rainfall of 21 mm/h for several days. The depth of water front and values of suction at various locations were measured during the rainfall event. The data obtained during the experimental modelling was utilized to conduct slope stability analysis and evaluate the stability of slope during various magnitudes of ground shaking.

Results of Field Investigation

Site Condition

Presented in Fig. 1 is the google earth image of the study area. As can be observed in Fig. 1, the property is located at the corner of the filling and both east and south sides of the building have slopes. During the field investigation, the authors noticed that the area, especially at both banks of the river, had several existing landslides. Two of those landslides are presented in Fig. 2. The meandering pattern of the river shows possible landslide events in the past on the opposite bank of the river as well.

Close view of the south side of the slope, which will be considered during this study is presented in Fig. 3. The area is currently covered with grass. A good drainage network has been constructed in the area. The authors didn't detect any cracks in those drains during the field investigation. However, as presented in Figs. 4, 5, 6, and 7, cracks were identified on stuccos, swimming pools, drive ways, and the compound walls.

Field Investigation Result

Cross-section survey was conducted with a total station to measure the details of the slope (Fig. 8). Likewise, position



Fig. 1 Google earth image of the study area



Fig. 2 Google earth image of the study area—two existing landslides are clearly visible in the area

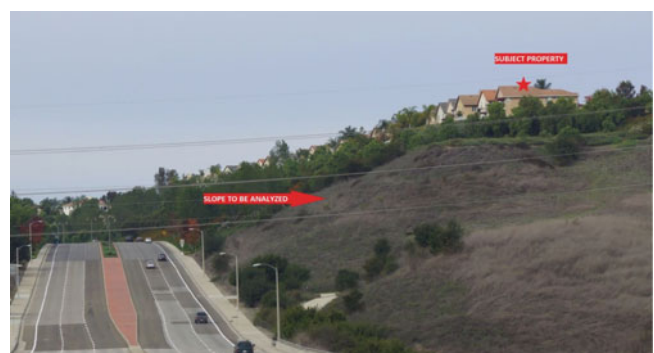


Fig. 3 Close view of the south side of the slope

of water table during the field investigation was measured at an inclinometer located at the backyard of the building (Fig. 9). At the time of survey i.e. December 2012, the depth of water table was much lower than 21 m (limit of the inclinometer) below the ground level. Soil samples were collected from an excavation area, which is located near the



Fig. 4 Cracks on the stucco of the building



Fig. 5 Separation of compound wall from the main building—identified during the field visit



Fig. 6 Separation of pool walls from the floor slab—identified during the field visit



Fig. 7 Separation of garage slab from the driveway—identified during the field visit



Fig. 8 Field surveying to prepare the cross-section of the slope

swimming pool (Fig. 10). Profile of the soil at the excavation area is presented in Fig. 11. Plan and sections of the study area are presented in Figs. 12 and 13, respectively.



Fig. 9 Location of inclinometer in the study area



Fig. 10 Location of soil sampling point

As presented in Fig. 13, the embankment slope was approximately 23.4° . This slope was utilized to prepare experimental model of the slope in the laboratory.

Soil Test Result

The soil samples collected from the site is used to measure geotechnical properties of soil. Grain size distribution analysis with both sieve and hydrometer analysis, Atterberg limit tests, specific gravity test, falling head permeability tests, Proctor compaction tests, and direct shear tests were performed in the laboratory following the pertinent ASTM standards. The field moisture content was 26.8 %. This moisture content was slightly higher because the sprinkler system was on a day prior to excavation. Field dry density was 15.3 kN/m^3 . Liquid limit and plasticity indices of the



Fig. 11 Close view of the compacted soil profile

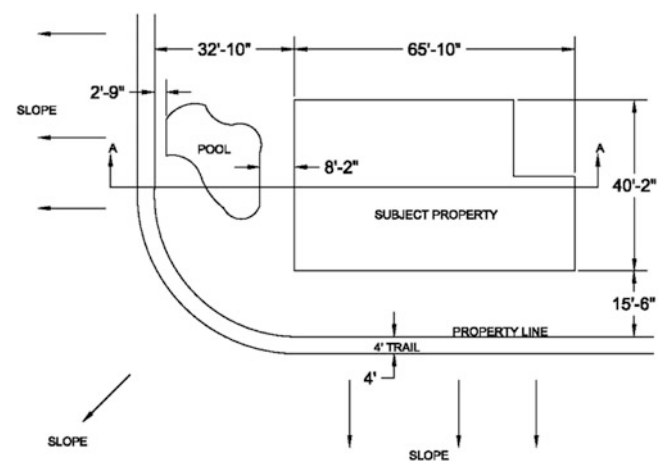


Fig. 12 Plan of the study area

soil were 44.1 and 10.8, respectively. Specific gravity of the soil was 2.69. Proportions of sand, silt and clay were 10 %, 75 %, and 15 %, respectively. The maximum dry unit weight and optimum moisture contents were 17.0 kN/m^3 and 15.0 %, respectively. The direct shear test that was conducted on the saturated soil sample showed the fully

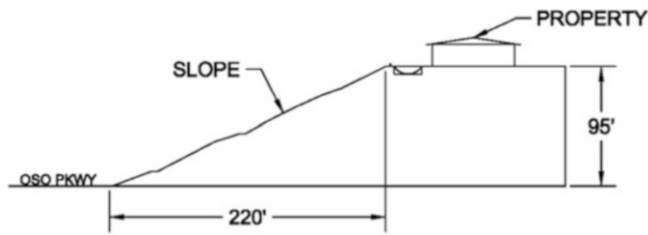


Fig. 13 Cross-section of the study slope



Fig. 15 Photograph of the slope model after its completion

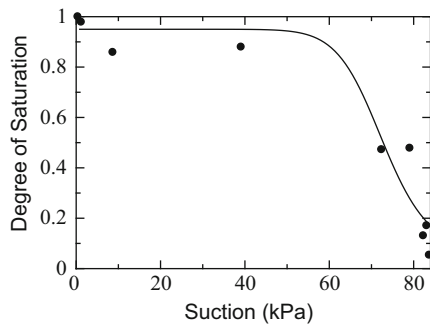


Fig. 14 SWRCC prepared for the tested soil sample

softened shear strength of 23° with no cohesion. However, the peak shear strength parameters (c and ϕ) when the soil was compacted at the field density were 11 kPa and 22° , respectively. Soil Water Retention Characteristics Curve (SWRCC) was prepared by measuring suction of soil prepared at various degrees of saturation. Presented in Fig. 14 is the SWRCC prepared for the tested soil sample. The result presented in Fig. 14 was for the dry to wet cycle. The data for the wet to dry cycle to complete the hysteresis is not presented here. The SWRCC presented in Fig. 14 was used to estimate the values of suction at different degrees of saturation.

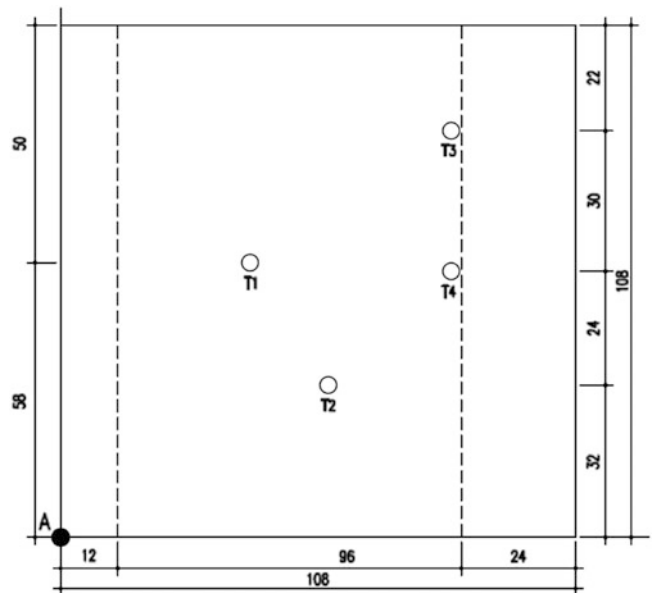


Fig. 16 Location of tensiometers shown in plan

Experimental Modeling

Experimental modelling of slopes were performed by many researchers to evaluate the stability of slope during rainfall (Orense et al. 2004; Tohari et al. 2007). Many of these studies involved externally applied seepage. However, the objective of this study was to evaluate the effect of rainfall and seismic ground motion on the stability of the proposed slope. Therefore, the soil samples collected from the site were utilized to prepare the model slope at the dry unit weight of 14.3 kN/m^3 and moisture content of 15 %. The soils were compacted at the relative density of approximately 84 % to keep the model in a conservative side. Slope of the model was kept close to the field slope. Presented in Figs. 15, 16 and 17 are the photographs and sketches of the experimental model.

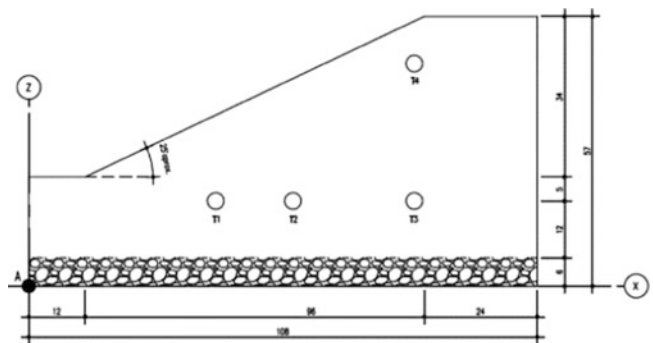


Fig. 17 Location of tensiometers shown in section

The locations of four tensiometers that were used to measure the suction during rainfall are shown in Figs. 16 and 17. The internal dimension of the box was

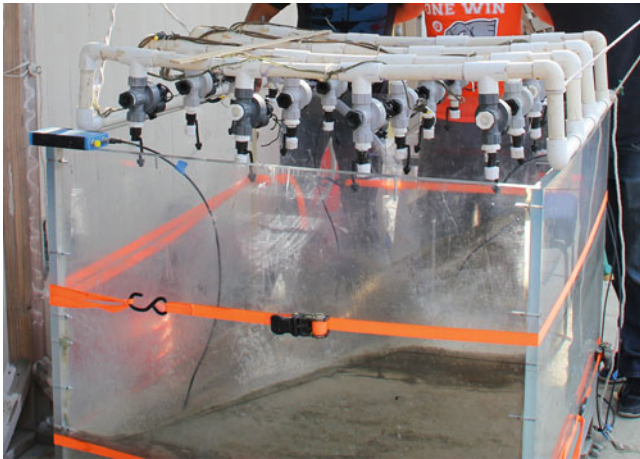


Fig. 18 Photograph of the sprinkler system

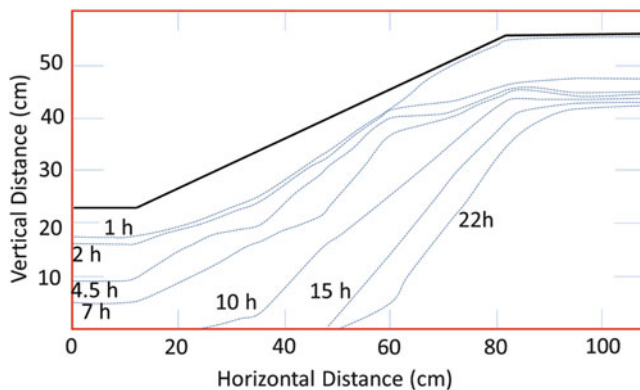


Fig. 19 Depth of water front with duration of rainfall

1.08 × 1.08 m. Likewise, height of the model above 6 cm thick gravel bed was 51 cm. Photograph of the sprinkler system is presented in Fig. 18. A rainfall of 21 mm/h was applied to the slope for different periods of rainfall and the depths of water front were measured with time. Presented in Fig. 19 is the depth of water front recorded with time. Please note that amount of run-off was also recorded during the experimental modeling. Average run-off was 7 mm/h. This shows the net rainfall responsible for infiltration was 14 mm/h. As can be observed in Fig. 19, water could infiltrate 12 cm depth in 7 h. The seepage profile was steeper than the slope. The average infiltration rate was 17 mm/h. Likewise, suction values were measured during the application of rainfall. Recorded values of suction with time for the four tensiometer locations presented in Figs. 16 and 17 are presented in Fig. 20. As can be observed in Fig. 20, tensiometer T4 took 154 min to have suction reduced to 0, i.e. have the water front reach T4. Likewise, it took 500 min for the water front to reach T1. Water front never reached to T2 and T3.

Slope stability analyses were performed prior to rainfall and for the measured values of suction after the completion

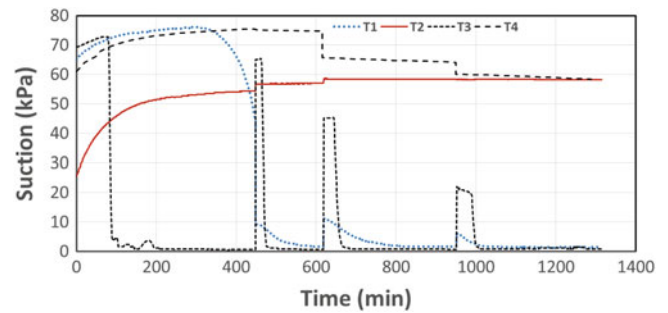


Fig. 20 Variation of suction with duration of rainfall

Table 1 Calculated factors of safety for various conditions of seepage and seismic coefficients

| Prior to rainfall | After 4 days of rainfall | Rainfall with k of 0.1 | Rainfall with k of 0.3 | Rainfall with k of 0.5 |
|-------------------|--------------------------|------------------------|------------------------|------------------------|
| 1.85 | 1.56 | 1.22 | 1.10 | 0.98 |

of the test i.e. 4 days of rainfall. Please note that the rainfall lasted for 450 min and was stopped for 18 h on the first day; continued for 166 min and stopped for 20 h on the second day; continued for 330 min and stopped for 17 h on the third day; and continued for 360 min on the fourth day. This was done to simulate the real situation. The slope stability analysis was performed with Spencer's method using "RocScience, Slide 6.0". The total calculated building load of 12.8 kPa was added on top of the slope as a uniformly distributed load. Apparent cohesion and friction angles measured at different suction levels were used to divide the entire soil mass into different zones based on suction values. At the end, factors of safety were also calculated for the slope using seismic coefficients ranging from 0.1 through 0.5. The calculated factors of safety are presented in Table 1. Based on the data presented in Table 1, the slope should be stable when the seismic shaking is less than 0.3 g when 4 days of rainfall is applied as used in the experimental study. However, a detailed study is underway to evaluate the stability of slope when the slope subjected to rainfall is shaken on the shake table at different magnitudes of shaking.

Summary and Conclusion

Field investigation and laboratory tests were performed to evaluate the effect of rainfall and seismic shaking on the stability of an engineered slope. A case of a house that was constructed near existing landslide was used for this study. Experimental modelling was performed by applying different amount (but same intensity) of rainfall with durations ranging from 166 to 450 h for 4 days. The values of suction recorded with the tensiometers and water fronts marked during the modeling process

were utilized to assign different soil boundaries for slope stability analysis. The experimental result shows that the slope will have safety factor higher than 1 under normal amount of rainfall and at the seismic shaking of 0.3 g. As this result is preliminary, detailed study is underway. It should be noted that the results presented in this study are mainly for academic purpose and should not be used for any type of interpretation pertinent to the safety of the houses in the study area. The actual situation in the field depends on many factors and this result does not cover those factors.

References

- Orense RP, Shimoma S, Maeda K, Towhata I (2004) Instrumented model slope failure due to water seepage. *J Nat Disaster Sci* 26 (1):15–26
- Tiwari B, Wartman D, Pradel D (2013) Slope stability issues after Mw 9 Tohoku earthquake. *Geotech Spec Pub* 231(1):1594–1601
- Tohari A, Nishigaki M, Komatsu M (2007) Laboratory rainfall induced slope failure with moisture content measurement. *J Geotech Geoenviron Eng* 133(5):575–587
- US Geological Survey, <http://www.usgs.gov>



Experimental Modelling of Seepage in a Sandy Slope

Binod Tiwari and Adam Lewis

Abstract

Rainfall-induced shallow landslides cause significant damage to infrastructure every year. Among the major causes of shallow landslides is an increase in degree of saturation with rainfall. Partially saturated slopes have high factors of safety due to the apparent cohesion induced by soil suction. In this study, sandy soil was used to prepare slopes with four different angles of inclination and two different void ratios. Utilizing a rain simulator, the slopes were provided with different intensities and durations of rainfall, ranging from 30 mm/h to 240 mm/h. The movement of the water front was recorded during the rainfall at an interval of 5 min. The experimentally recorded values for the depth of water front with time was used to develop relationships between the velocity of seepage, void ratio and angle of inclination of the sandy slope. The proposed equations can be utilized to evaluate the stability of sandy slopes during rainfall.

Keywords

Partially saturated soil • Suction • Water front • Finite element analysis • Rainfall intensity • Slope stability

Background

During rainy seasons, damage done by shallow landslides is reported frequently in newspapers and television channels all over the world. Potential of occurrence and possible damage by these landslides are high in areas: (a) having mountainous terrain, (b) subject to high intensity rainfall for a prolonged duration, and (c) consisting of highly

weathered and loose residual soils to a significant depth. Statistical data on the distribution of such shallow landslides, their associated factors, and losses due to those landslides are periodically reported in the literature. Although shallow landslides are caused by many factors such as rainfall, earthquakes, anthropogenic disturbances, etc., rainfall is reported to be among the major causes. Rainfall-induced shallow landslides often occur in marginally stable slopes, and due to their proximity to various important infrastructure such as roads and irrigation channels, they are considered one of the most significant geo-environmental hazards that need immediate attention (Orense et al. 2004). Several countries have therefore implemented significant monitoring systems to observe the real-time change in rainfall amounts and implement warning systems based on an estimated threshold rainfall amount. The increase in the number of landslides during and slightly after heavy precipitation can be attributed to the saturation of the ground and an increase in the unit weight, as well as to

B. Tiwari (✉)

Department of Civil and Environmental Engineering, California State University Fullerton, 800N State College Blvd, Fullerton, CA 92831, USA

e-mail: btiwari@fullerton.edu

A. Lewis

GeoStabilization International, P.O. Box 4709, Grand Junction, CO 81502, USA

e-mail: adam@gsi.us

pore water pressure in the potential sliding zone. Decoupling these triggering factors requires a detailed investigation on the behavior of slopes during seepage under both partially saturated and fully saturated conditions. However, there is little systematic research on the mechanisms associated with the infiltration of water into saturated and/or partially saturated soil and its effect on the stability of slopes.

Results of numerical and experimental studies of the seepage of rainwater into sloping ground and its effect on slope stability have been frequently reported in the literature. Orense et al. (2004) prepared slope models of silty sand material in a 2.2 m long and 0.8 m wide container and measured deformation and failure modes of soil for nine different seepage conditions, ranging from artificially prepared seepage from a side of the model tank to artificially simulated rainfall through nozzles. Intensity of rainfall varied from 80 to 262 mm/h across the model soil mass. Model tests were performed on soils having relative densities of 50 and 70 % and slope angles of 30° and 40°. They reported that slope failure occurs when the soil around the toe region becomes saturated, even though the remaining part of the slope is still in just a partially saturated condition. They also reported that water infiltration alone doesn't cause a failure of the slope if there is no seepage flow to raise the pore water pressure at the toe. They argued that prediction of slope failure is possible by monitoring the soil moisture content. Please note that, in this study, pore pressure was generated by supplying water from a side of the container using a water tank. The rainfall intensity was not uniformly applied in the model—rainfall intensity in one end was higher than four times the intensity in the other end.

Similarly, Huat et al. (2006) performed an experimental study of the mechanisms of water infiltration in unsaturated soil slopes and evaluated the stability of the slope based on the water infiltration behavior. Using a sandy soil sample, they prepared inclined soil models at different slope angles—0°, 15°, 30° and 45° (with the help of hydraulic jack) and applied a rainfall of 756 mm/h through a sprinkler-type rain simulator. They also measured soil suction at various depths. Although the presented data did not fully support the conclusion, the authors concluded that water infiltration rate in a soil mass becomes constant after some length of time of rainfall. They observed that the infiltration rate decreases with an increase in the inclination of the slope. They argued that the infiltration rate is higher on a covered slope compared to a bare slope. Some of the major issues we observed in this study were—the test results pertinent to suction were not consistent, and the rainfall that was applied in the inclined direction might have caused a non-uniform distribution of rainfall intensity throughout the model.

In addition to the above mentioned experimental model testing, Tohari et al. (2007) performed experimental studies

on a 2.0 × 1.0 × 1.5 m size metal tank to understand the mechanism of slope failure on river sand as well as residual granite at angles of inclination of 45° and 32°. This research utilized three different relative densities of soil; a rainfall intensity of 100 mm/h was utilized throughout the study. They also studied the effect of seepage on slope stability by supplying water from the head of the slope using a constant head water tank. The variation in the degrees of saturation with time was measured with moisture sensors. They concluded that the permeability of the soil and antecedent soil moisture conditions control the slope stability. In this study, time to initiate the failure was observed experimentally without measuring the soil suction and the depth of the water front with time. Moreover, analysis of partially saturated condition was loosely described.

Among the studies available in the literature, none of the studies incorporated the combined effect of soil suction, rainfall intensity, and angle of inclination of slopes in triggering shallow landslides. Moreover, either the rainfall intensities were non-uniform throughout the slope or were much higher than the reported rainfall intensities in various parts of the world. In our study, experimental studies were performed in a systematic manner to observe the infiltration of water in sandy soil, variation in suction with intensity and duration of rainfall and the effect of water infiltration as well as change in suction on slope stability.

Materials and Methods

Experimental Modeling

Experimental models were prepared with double washed sand. The proportion of sand was approximately 90 %, with approximately 5 % fines. The soil was classified as SW material according to USCS. Specific gravity of the sand was 2.65. Horizontal and vertical coefficients of permeability of the sand were 8.0×10^{-3} cm/s and 4.3×10^{-3} cm/s, respectively. A 1.22 × 1.22 × 1.22 m sized Plexiglas container was used to prepare the models. The Plexiglas container provides visibility to mark the depth of water front at various durations of rainfall. The rain simulator that was used in this study was made of 16 special sprinkler heads arranged in such a way that flow of water could be controlled in the sprinkler system in order to vary the intensity of rainfall from 18 to 360 mm/h. Separate slope models were prepared at angles of inclination of 0°, 30°, 40°, 45° and 50° by compacting soil in the container at the void ratio of 0.6 (40° slope) and 0.7. The experimental set-up is presented in Fig. 1. Four tensiometers were installed in the slopes, as presented in Fig. 2, in order to measure the spatial variation in suction with the duration of rainfall. The

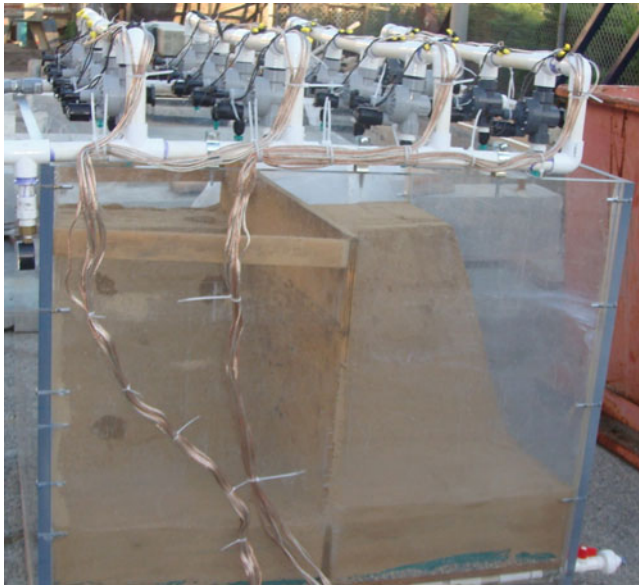


Fig. 1 Plexiglas container with slope made of the double washed sand at 45 and 50° inclinations, and rain simulator used in this study

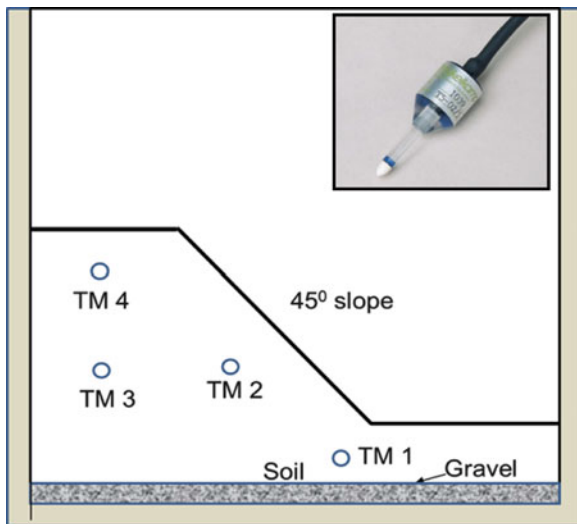


Fig. 2 Location of tensiometers within slope. A tensiometer is shown on the top right corner

tensiometers used in this study were miniature tensiometers with a 0.5 cm² surface area and 5 mm tip size (T5 type), supplied by the Decagon Devices. The tensiometer can measure pore pressures ranging from -100 to +85 kPa with an accuracy of ±0.5 kPa. Slopes with angles of inclination of 0°, 40°, and 45° were first subjected to a rainfall with an intensity of 240 mm/h. Then, slopes with angles of inclination of 30, 45, and 50 were subjected to the rainfall with an intensity of 30 mm/h for 3 h. The movement of the water front was marked at the boundary of slope around the Plexiglas container every 15 min and the values of suctions were recorded every minute.

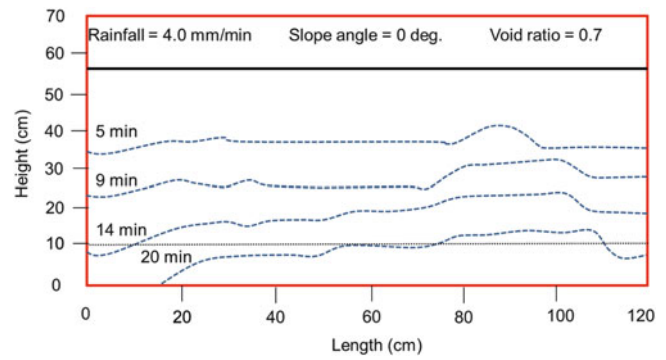


Fig. 3 Depth of water front on a flat slope subjected to 240 mm/h of rainfall, recorded at different periods

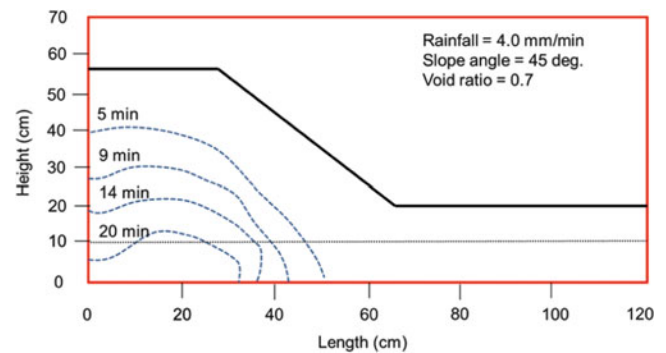


Fig. 4 Depth of water front on 45° slope having 240 mm/h of rainfall, recorded at different periods

Results of the Study

The depth of water front with time can approximately reveal the rate of infiltration of water into the soil mass. Depth of the water front is an approximate indicator that illustrates nearly saturation of soil as the soil above the water front (in case of rain water percolating downwards) is considered to be close to saturation, although it may not be fully saturated. Presented in Figs. 3, 4, and 5 are the depth of water front in those models prepared at 0°, 45° and 40° slopes, respectively with a void ratio of 0.7. As could be observed in Fig. 3, the water front reached a 10 cm height (equivalent to 46 cm depth) in 20 min. As the slope was flat, the depth of the water front was expected to be uniform throughout the model. However, there were small spatial variations in the depth of the water front at different locations. This can be attributed to several factors, including a slight spatial variation in compaction densities of soil and in rainfall amount. As the variation was not unacceptably high, the experimental results were considered reasonable. As observed in these figures, the water front traveled an approximately 46 cm vertical distance in 20 min in all slopes. In slopes (Figs. 4 and 5), the advance of the water front was approximately

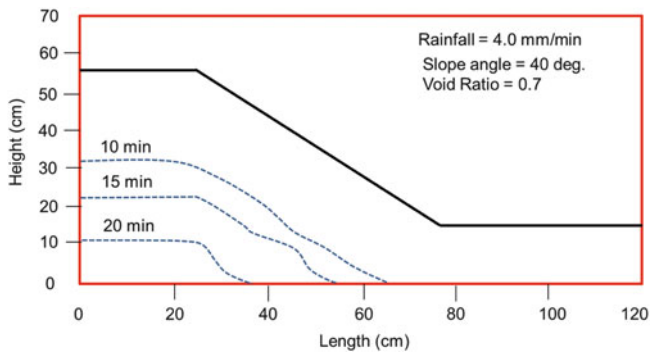


Fig. 5 Depth of water front on 40° slope having 240 mm/h of rainfall, recorded at different periods

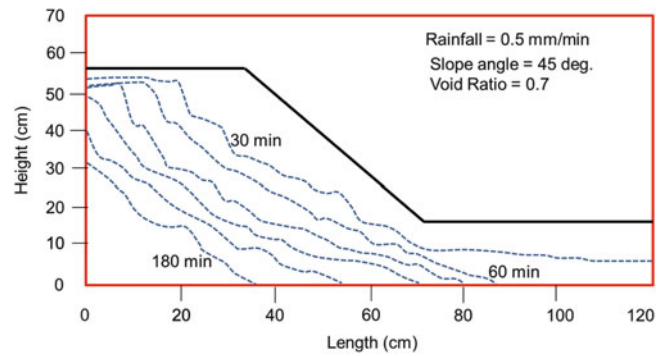


Fig. 7 Depth of water front on 45° slope having 30 mm/h of rainfall, recorded at different periods

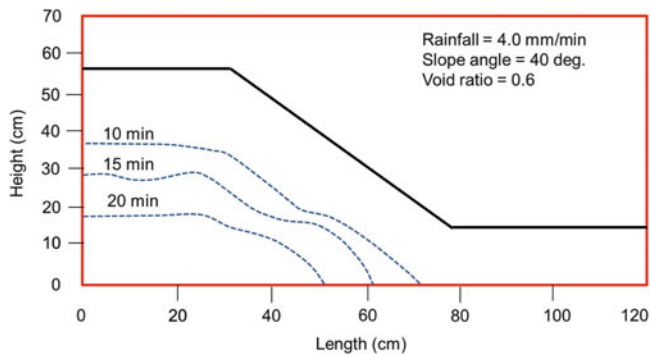


Fig. 6 Depth of water front on 40° slope and void ratio of 0.6 having 240 mm/h of rainfall, recorded at different periods

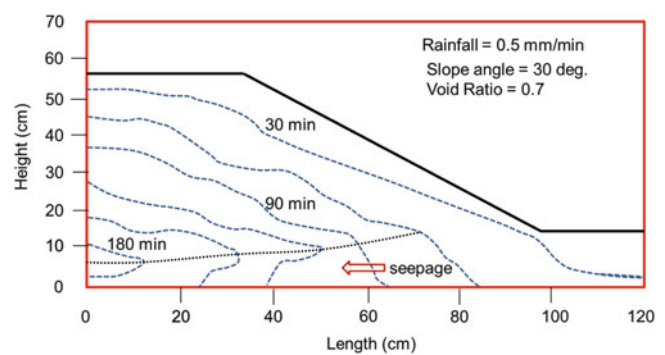


Fig. 8 Depth of water front on 30° slope having 30 mm/h of rainfall, recorded at different periods

parallel to the slope. This is inconsistent with the reports available in the literature (Pradel and Raad 1993). Figure 6 also illustrates the depth of water front in the 40° slope model prepared at the void ratio of 0.6. Figure 6 shows that although the depth of the water front was parallel to the slope, the rate of infiltration (i.e., the rate of movement of the water front) is lower in the soil compacted at the void ratio of 0.6 (denser soil) compared to the soil compacted at the void ratio of 0.7 (looser soil). This is reasonable as the hydraulic conductivity of soil decreases with the decrease in void ratio.

Presented in Figs. 7 and 8 are the depths of water fronts at different periods on 45° and 30° slopes, respectively when those slopes were subjected to 30 mm/h of rainfall. The rate of movement of water front was much slower than that with 4 mm/min of rainfall. As it can be observed in Figs. 7 and 8, the rate of movement of the water front within the slope (location b) is much faster than the rate of movement of the water front in the flat portion on top of the slope (location a). This can be attributed to the movement of water in an inclined direction, especially for the saturated soil above the water front. However, the angle of inclination of the water front was less than the angle of inclination of the slopes. In the case of the slope with a 30° angle of

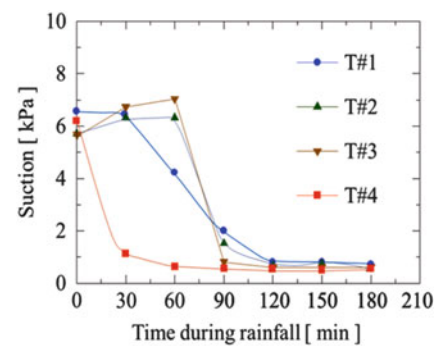


Fig. 9 Variation in suction with duration of rainfall at locations described in Fig. 2 for a 45° slope

inclination, it was observed that once the flat portion near the toe (location c) became saturated, it completely filled the drainage layer and started to supply water in the horizontal direction as well. Therefore, the data below the dotted line (indicated as seepage) is not considered for further analysis.

Figure 9 illustrates the values of suction observed at four locations, described in Fig. 2. The initial suction at four locations prior to rainfall ranged from 5.5 to 6.5 kPa. The soil at the top (near tensiometer #4) required approximately 60 min to reduce the suction close to 0 kPa, whereas the soil near the

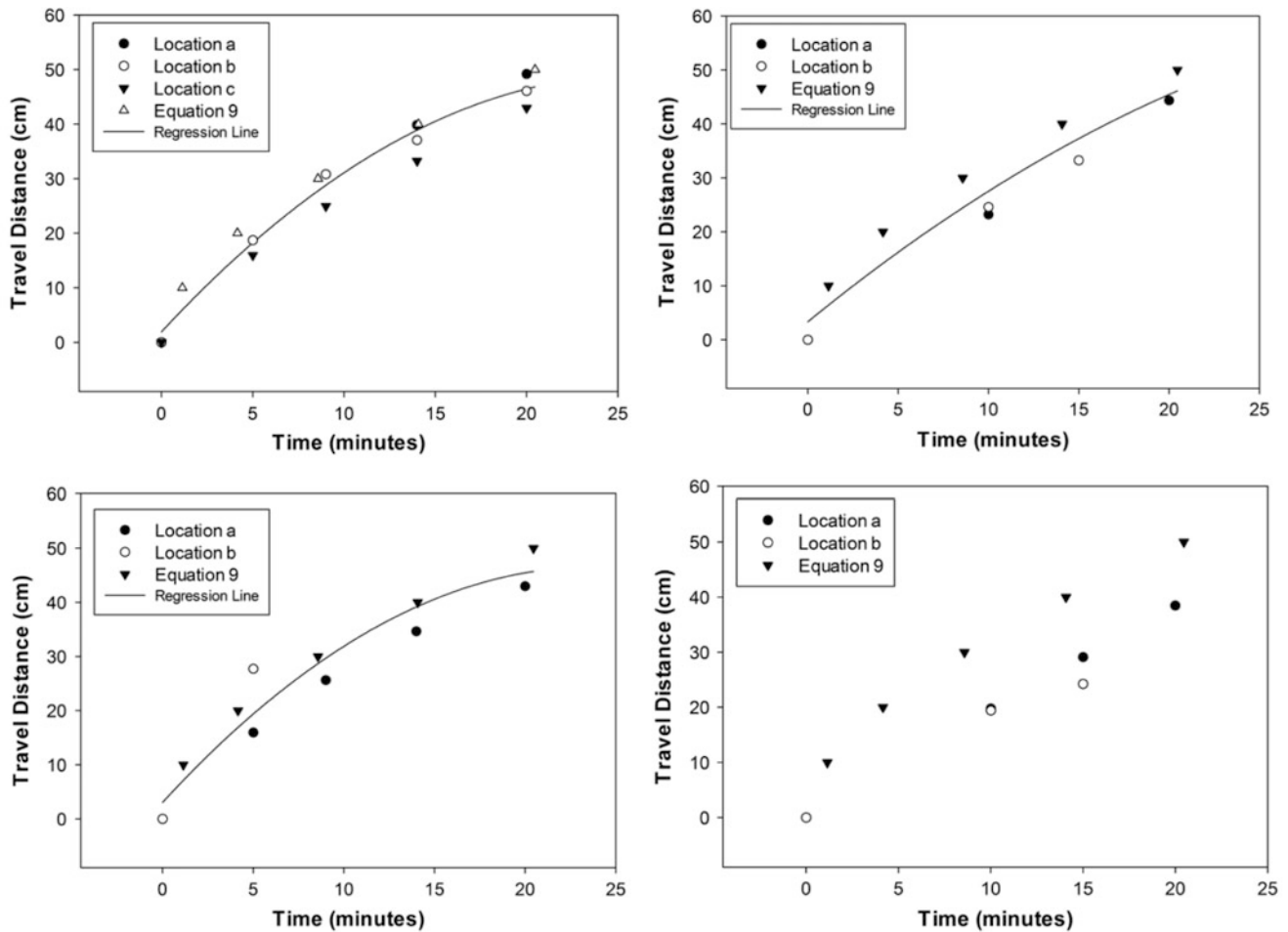


Fig. 10 Variation in travel distance of water front with duration of rainfall at locations a, b, and c in slopes with inclinations of 0, 40 (void ratio of 0.7), 45, and 40 (void ratio of 0.6) degrees, respectively

bottom of the slope (near tensiometer #1) required almost 120 min to drop the suction to 0 kPa. Please note that due to the sensitivity of the tensiometer used in this study (i.e. ± 0.5 kPa), measured suction may give an error of up to 0.5 kPa. The tensiometers installed at other two locations within the slope also needed more than 60 min to become saturated. The rates of change in suction with time at all four locations were different. Locations near tensiometers 2 and 3 showed similar pattern in the reduction of suction with time. Results presented in Fig. 9 show that the water fronts were not able to progress to tensiometer #1 in 30 min and to tensiometers #s 2 and 3 in 60 min, after the initiation of rainfall.

Analysis of Test Results and Discussion

The main objective of this study was to identify a method that can be used to calculate the velocity of the movement of the water front in a sandy slope based on the intensity of

rainfall. Such relationships are beneficial in predicting the movement of water front at different intensities and durations of rainfall and evaluating the stability of slopes. Presented in Fig. 10 are the travel distances of the water front plotted with time at locations a, b, and c, for 0°, 40° and 45° slopes, respectively when they were subjected to a rainfall of 240 mm/h. The movement of the water front showed a parabolic correlation with time, as presented in (1), (2), and (3). These equations are utilized later to develop the relationships between velocity of movement of the water front with the intensity of rainfall. As can be observed in Fig. 10, the movements of the water front at location b were faster than that at location a, although they are not significantly different for such a high intensity of rainfall. The velocity of the water front for a saturated soil mass can be calculated theoretically with (4) (Pradel and Raad 1993). The depth of the water front with time was also calculated using (4). For durations larger than 5 min of rainfall, the values calculated with the Eq. (4) were similar to the values

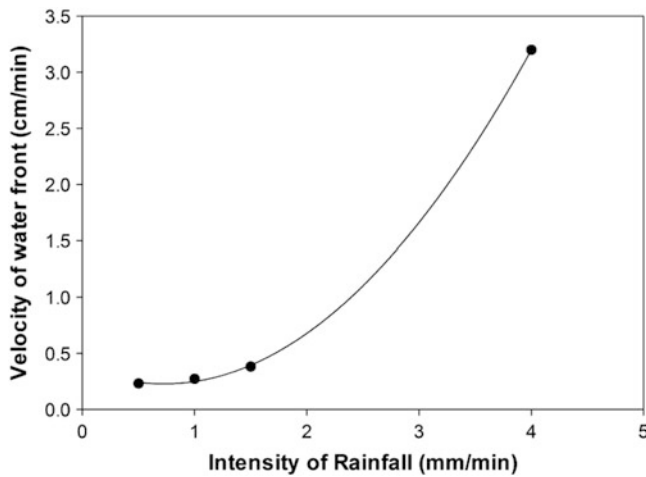


Fig. 11 Change in the velocity of the water front with the intensity of rainfall for a shorter duration of rainfall

obtained from the experimental modeling on the flat surface. Calculated values using (4) were slightly higher than the experimentally observed values at location a in the sloped models. However, the calculated values were similar to the observed values at location b, irrespective of the angle of inclination of the slope. As can be observed in Fig. 10, the rate of movement of the water front in soil with a void ratio of 0.6 was approximately 15 % slower than the movement in soil with a void ratio of 0.7.

$$Z_w = -0.091T^2 + 4.079T \quad (1)$$

Where, Z_w = Depth of water front in cm.; T = Time duration in minutes.

$$Z_w = -0.008T^2 + 2.366T \quad (2)$$

$$Z_w = -0.063T^2 + 3.406T \quad (3)$$

$$T_w = \frac{\mu}{K_w} \left[Z_w - S \cdot \ln \left(\frac{S + Z_w}{S} \right) \right] \quad (4)$$

where T_w = Time required for water front to move a distance Z_w ; μ = difference in volumetric water content before and after wetting; K_w = Saturated hydraulic conductivity; and S = Suction head at the water front.

Among the various objectives of this study was developing a relationship between the velocity of movement of the water front in a slope with the intensity of rainfall. The relationship was exponential for durations of rainfall shorter than 10 min. For durations of rainfall longer than 20 min, a second-order parabolic correlation was observed between the velocity of movement of the water front with the intensity of rainfall, as presented in Fig. 11. The corresponding

regression equation is presented in (5). Please note that the velocity of the water front remains constant when the intensity of rainfall is higher than the rate of infiltration in a soil mass. The rate of infiltration (V_{is}) for saturated flow can be calculated using the Green and Ampt (1911) model, as presented in (6). For the soil slopes presented in this study, the calculated rate of infiltration for saturated soil is approximately 5 mm/min. However, it should be noted that the hydraulic conductivity of the soil changes with the degree of saturation. The seepage velocity calculated with (6) applies to saturated soil. For partially saturated soil, the velocity of flow could be as low as 10 % of this velocity. This is the subject of separate research.

$$V_i = 0.191I^2 + 0.033I \quad (5)$$

$$V_{is} = K_w \frac{Z_w + S}{Z_w} \quad (6)$$

The experimentally observed values showed that the velocities of movement of water front were higher when the angle of inclination of slope was higher at locations b and c. This justifies that once gets close to saturation, water moves in an inclined direction as well.

Summary and Conclusion

Experimental modelling was conducted in order to investigate the variation in the depth of the water front and spatial distribution of suction in sandy slopes for slopes ranging from 0° to 50° and intensities of rainfall of 30 and 240 mm/h. The results obtained from the experimental studies show that infiltration velocity increases with the intensity of rainfall. The infiltration velocity depends on the angle of inclination of the slope and initial degree of saturation. For soils with a high degree of saturation and a high intensity of rainfall, the movement of the water front is parallel to the slope.

Acknowledgments

The authors would like to thank the Associated Student Inc. (ASI), California State University, Fullerton, for providing financial support to purchase materials.

References

- Green WH, Ampt C (1911) Studies on soil physics I. Flow of air and water through soils. *J Agric Sci* 1:1–24
- Huat BBK, Ali FH, Low TH (2006) Water infiltration characteristics of unsaturated soil slope and its effect on suction and stability. *Geotech Geol Eng* 24:1293–1306

- Orense RP, Shimoma S, Maeda K, Towhata I (2004) Instrumented model slope failure due to water seepage. *J Nat Disaster Sci* 26 (1):15–26
- Pradel D, Raad G (1993) Effect of permeability on surficial stability of homogeneous slopes. *J Geotech Eng Div ASCE* 119(2):315–332
- Tohari A, Nishigaki M, Komatsu M (2007) Laboratory rainfall induced slope failure with moisture content measurement. *J Geotech Geoenviron Eng* 133(5):575–587



Curvature of Failure Envelopes for Normally Consolidated Clays

Binod Tiwari and Beena Ajmera

Abstract

Shear strength parameters play an important role in the stability of slopes. Accuracy of the analysis result depends on the nature of the failure envelopes used, especially in the case of shallow landslides, where the shear strength is mobilized at low effective vertical stresses (σ_n'). Ten normally consolidated samples prepared from mixtures of montmorillonite, kaolinite and quartz were sheared in a constant volume simple shear device at the normal stresses ranging from 25 to 800 kPa. From the results, it was noted that correlations for undrained shear strength should be selected with respect to the anticipated failure mechanism. The power function can be used to represent the curvature in failure envelopes. Direct shear results suggests a lack of curvature in the effective failure envelopes for normally consolidated clays. However, results from the simple shear testing show that failure envelopes are curved for low effective normal stresses and thus, the use of a linear $c' - \phi'$ envelope can be unconservative for shallow landslides.

Keywords

Undrained shear strength • Failure envelope • Curvature • Simple shear • Soil minerals • Slope stability

Background

Shallow landslides and underground excavations pose some of the most challenging problems in geotechnical engineering. In these situations, there is a redistribution of stresses occurring under very low confining stresses. Therefore, an overestimation of the shear strengths may result when linear failure envelopes are assumed. Studies such as Baker (2004),

Pradel (1994) and Maksimovic (1989) have shown that failure envelopes are not linear at low effective vertical stresses. However, all three studies focused on coarse-grained materials or compacted clays. Furthermore, the strength of these materials was studied when the soils were isotropically consolidated in the triaxial device at effective stresses greater than 50 kPa. Bishop et al. (1965) also conducted CU triaxial tests on London clay for effective vertical stresses between 0.2 to 1,100 psi. They noted that the failure envelope has a very distinct curvature. Ponce and Bell (1971) used triaxial testing to apply effective stresses of 0.14–0.22 psi on sand. The failure envelope was also noted to be curved at low effective stresses.

Since field conditions are anisotropic and the curvature is most significant at low effective stresses, there is still a lack of thorough understanding of the curvature at effective normal stresses lower than 50 kPa for normally consolidated clays. In part, this can be attributed to the difficulty associated with maintaining low stresses in the drained ring

B. Tiwari (✉)
Department of Civil and Environmental Engineering, California State University Fullerton, 800N State College Blvd, Fullerton, CA 92831, USA
e-mail: btiwari@fullerton.edu

B. Ajmera
Department of Civil and Environmental Engineering, Virginia Polytechnic Institute and State University, Blacksburg VA, 24061, USA
e-mail: bajmera@vt.edu

shear and direct shear tests. Possible alternatives are to conduct constant volume simple shear tests or CU triaxial tests so that for the same total normal stress, a lower effective normal stress can be measured as a result of pore pressure generation during the shearing process. In fact, the first simple shear device probably introduced by Taylor (1952) as a modification to the conventional direct shear device to allow drainage control in order to reduce the time required to obtain effective shear strength measurements. In his paper, he concluded by stating that “direct shear data obtained under properly controlled conditions are probably sufficient for the great majority of investigation and they can be obtained in much less time than required for triaxial data.” Airey et al. (1985), Airey and Wood (1987), Ladd (1991), and Baxter et al. (2010) stated that the simple shear device has many advantages over the triaxial device including the following: (a) The sample preparation is easier; (b) The failure mechanism of the direct shear device is better resembled by the simple shear device than the triaxial device; Simple shear requires the use of significantly smaller samples, which are less susceptible to disturbance during preparation; (c) The samples are consolidated under anisotropic (K_0) conditions, which resembles the in-situ conditions better than isotropically consolidated samples from the triaxial apparatus; (d) Simple shear device requires shorter consolidation times; and (e) Principal stress rotation is allowed.

Evans (1972) stated a very common geotechnical concern in Southern California is surficial failures that occur in compacted clay slopes after extended periods of rain. In particular, Gill (1967) estimated that for developed properties that the surficial slope failures account for 95 % of the problems associated with land movements. These failures are a result of swelling of the clays that have desiccated and shrunken during the hot and dry summers. The swelling is caused by the water seeping through the cracks within the soil mass resulting in saturations, which is associated with a loss of strength and a reduction in effective vertical stress (Day and Axten 1989). Day and Axten (1989) as well as Zaruba and Mencl (1976) found that at low normal stresses the cohesion is very small. Moreover, they stated that the cohesion approaches zero, thus, suggesting curvature of the failure envelope. Day and Axten (1989) concluded that as a result of the decreasing cohesion as the effective stress reduces, the factor of safety estimated is dependent in the normal stresses used to determine the strength parameters. Moreover, when the high normal stress parameters are used for shallow landslides, the factor of safety can be overestimated leading to failures.

Penman (1953) tested dry powder silt from Braehead Power Station, Scotland. The silt has a liquid limit of 24.6 and the plastic limit could not be determined. The silt was tested under drained conditions for normal stresses of 15, 30,

60, and 100 psi. Undrained testing was conducted for a normal stress of 5 psi. It should be noted that the failure envelopes presented in the paper were linear. However, Penman (1953) stated that the failure envelope of the silt under undrained conditions varied with the confining pressure applied. In particular, the silt was stated to have a failure envelope with a cohesion intercept and non-zero friction angle until a limiting cell pressure beyond which the failure envelope is horizontal (zero friction angle). In the case of the silt tested, the limited cell pressure was found to be approximately 65 psi.

Materials and Methods

Commercially available minerals were used to prepare ten different proportions of montmorillonite with quartz and kaolinite with quartz. The liquid limit of these specimens ranged from 8 to 61 and plasticity indices ranged from 4 to 21. A soil-water mixture for each sample was prepared by mixing the appropriate amounts of the dry mixtures by weight with an initial moisture content equal to the corresponding liquid limit. The initial moisture content was set equal to the liquid limit based on the recommendations by Burland (1990). Furthermore, this initial moisture content is consistent with that selected by Tiwari and Ajmera (2011) for direct shear testing and thus, allows for comparison between the results. Each sample was then allowed to hydrate for a period of 24 h in an air tight container with special attention to ensure that there was no loss of moisture during this time. After the hydration period, the soil-water mixture was stirred in a batch-mixer to form a slurry. The slurry was then placed into the simple shear device, laterally confined by a rubber membrane and stacked Teflon rings. The sample was then consolidated with an effective vertical stress of 25 kPa. The completion of the primary consolidation was determined via the use of the real-time log of time versus vertical deformation curves generated by the fully automated data acquisition and reporting system connected to the simple shear device. Upon the completion of the primary consolidation phase, shearing rate was calculated based on the ASTM procedure. The calculated shearing rates for all of the specimens were faster than 0.01 mm/min. Therefore, the consolidated samples were sheared at a rate of 0.01 mm/min, to be in a conservative side. At the end of the test, the entire sample was removed from the apparatus and oven dried for 24 h in order to determine the dry weight. Separate samples from the same batch were consolidated to vertical stresses of 50, 100, 200, 400, and 800 kPa and sheared. In this study, the pore water pressure was back-calculated from the change in the effective vertical stress in order to maintain constant volume of the sample (Airey and Wood 1987; Bjerrum and Landva 1966; Dyvik et al. 1987).

The resistance of the membrane and the stacked Teflon rings was determined by shearing a sample full of water at a rate of 1 mm/min. A regression curve between shearing resistance and shear deformation was determined and used to subtract the shearing resistance obtained for the corresponding shear displacements for all the soil samples.

Results of the Study

A typical shear stress versus strain plot is shown in Fig. 1 for the entire range of normal stresses for one sample. A typical pore pressure versus strain plot is shown in Fig. 2 and the stress paths are shown in Fig. 3. As expected the shear stress and the pore pressure increases as the consolidation pressure increases. Moreover, as the consolidation pressure increases, more significant strain softening was observed. Similar trends were observed for the remaining samples.

Undrained Strength Ratios

There are two well-known and commonly used trends for estimating the undrained strength ratios. The first was proposed by Skempton (1957) and the second by Ladd (1991). Both of these correlations are applicable for use when dealing with low plasticity soils. The results obtained in this study were compared to the trends proposed by Skempton (1957) and Ladd (1991) as shown in Fig. 4. As seen from Fig. 4, Ladd's equation accurately estimates the undrained strength ratio for the majority of the data. Although there appears to be a large amount of scatter, the relationship presented by Ladd (1991) contained approximately the same amount of scatter.

Accuracy of Simple Shear Results for Drained Conditions

As a result of the conclusions in Budhu (1984), it seems that the suitability of the simple shear device for strength measurements be evaluated in terms of the results obtained on real soils rather than theoretical simulations. In fact, many researchers have compared the results obtained from the simple shear device to those obtained with more conventional techniques. One such study was completed by Bjerrum and Landva (1966), which tested undisturbed samples using the vane shear, triaxial and simple shear apparatuses. They found that the results from the simple shear device were closer to those obtained in the field with the use of the vane shear device as well as those back-calculated in slope failures in comparison to those from the triaxial device. In fact, the triaxial test results were

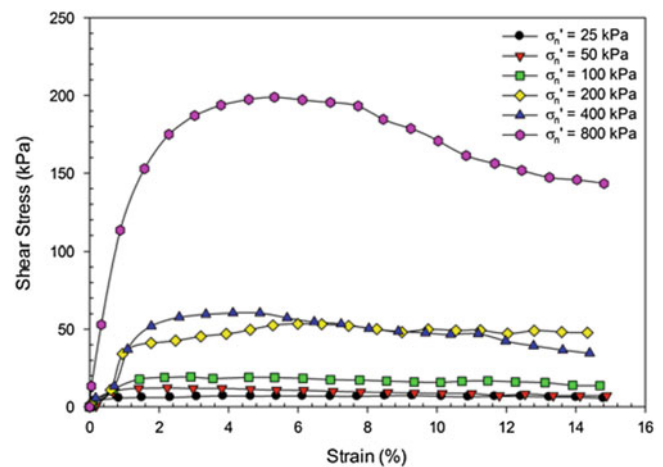


Fig. 1 Typical stress versus shear strain curves

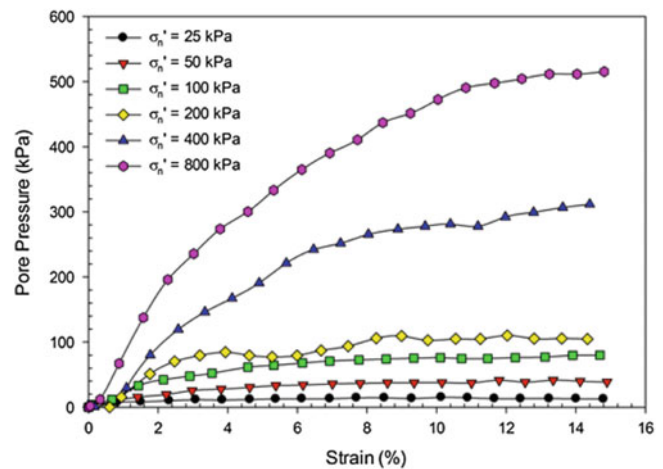


Fig. 2 Typical pore pressure versus shear strain curve

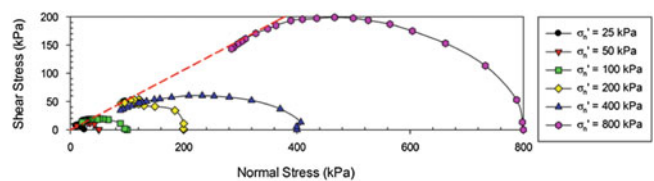


Fig. 3 A typical stress path

considerably higher than those measured in the field and therefore, leading to failures. Similar results were found by Ladd and Edgers (1972) when simple shear results were compared to those obtained from the back-analysis of failed embankments. The results obtained in this study from the simple shear device were compared to those presented by Tiwari and Ajmera (2011) for the same samples obtained with the use of the direct shear device. A comparison of the

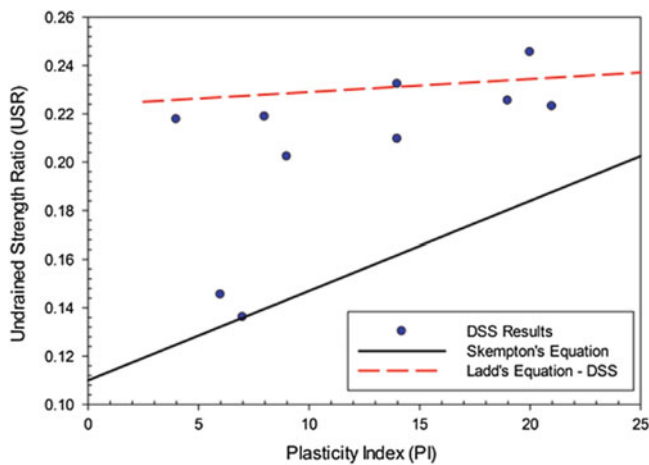


Fig. 4 Comparison with previously proposed undrained strength ratio correlations

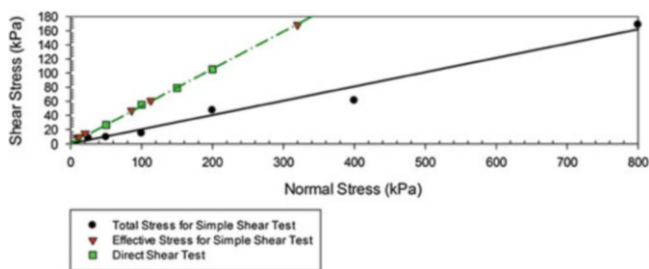


Fig. 5 Typical total and effective stress shear envelopes

failure envelopes is shown in Fig. 5. As expected, the undrained shear strength is less than that of the effective shear strength. However, it can be seen that the results from the simple shear match very well with the results from the direct shear device. The trends obtained for other samples were similar. Figure 6 shows a comparison of the friction angles measured from the simple shear device to those measured from the direct shear device. It can be seen that the simple shear results were within $\pm 8\%$ of the direct shear results.

Curvature of the Failure Envelopes

Tiwari and Ajmera (2011) tested normally mineral mixtures in the direct shear device at effective normal stresses of 50, 100, 150, and 200 kPa. From their results, they suggested that failure envelopes are linear based on visual inspection. In order to numerically determine the lack of curvature, the power function, shown in (1), was fitted to the data provided. In (1), τ is the shear stress, p_a is the atmospheric pressure, σ_n' is the effective normal stress, while A and B are correlation

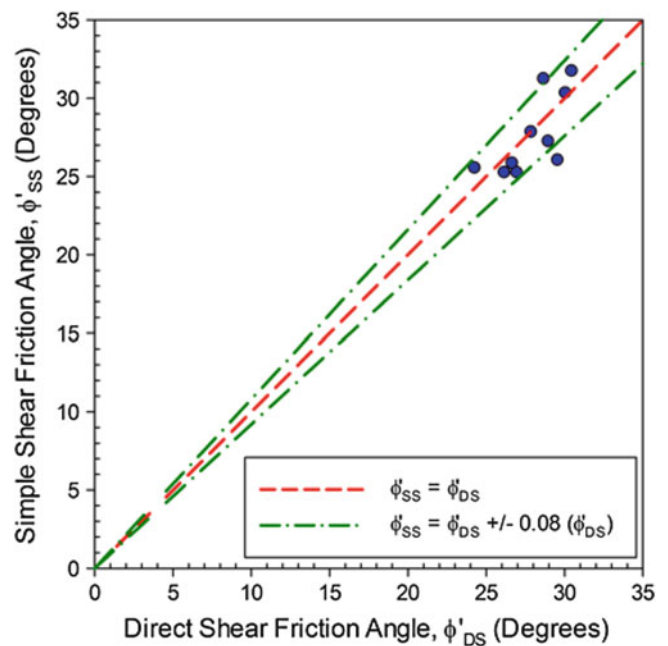


Fig. 6 Comparison of effective friction angles obtained with direct and simple shear tests

parameters. Furthermore, note that B represents the curvature of the graph. Note that a property of the power function is that it will always pass through the origin of the graph regardless of the values of A and B.

$$\tau/p_a = A(\sigma_n'/p_a)^B \quad (1)$$

The correlation coefficients for A and B were calculated for the direct shear data. It was observed that the value of B is approximately one for all of the samples except for one. Therefore, the failure envelopes obtained from the direct shear device are linear with zero cohesion.

Visually inspecting the failure envelopes over the entire range of normal stresses tested, through figures similar to that in Fig. 5, suggests that the failure envelopes are linear. However, examination of the failure envelope for the range of effective vertical stresses less than 100 kPa reveals curvature. For Sample #5, the failure envelope for effective vertical stresses less than 100 kPa is shown in Fig. 7. Although similar figures were prepared for the remaining nine samples, the results are not presented here due to the space limitations. However, similar trends were observed for all of the samples. As Fig. 7 shows, the best-fit linear envelope would have some cohesion. However, the data presented is for a normally consolidated sample that has not aged and therefore, there should be no cohesion. Thus, the failure envelope must be curved.

Curvature is also noted when the secant friction angle is plotted against the effective normal stress. As the effective

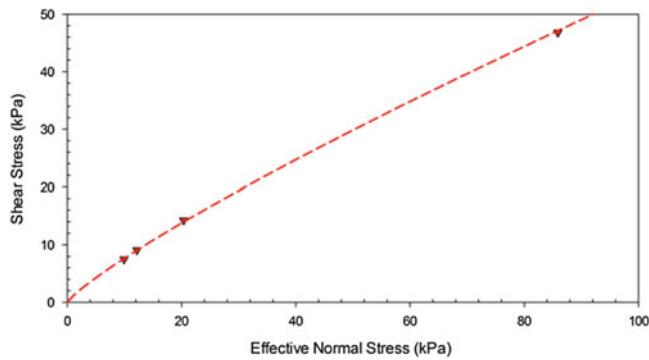


Fig. 7 Typical failure envelope for effective normal stress less than 100 kPa

normal stress increases, the effective secant friction angle reduces with a greater sensitivity at lower effective vertical stresses. The sensitivity advocates that the curvature is greater at lower effective stresses. This is necessary in order for the failure envelope to pass through the origin. As with the direct shear data, the A and B parameters were calculated for the simple shear measurement. Except for one sample, B was significantly less than 1. Therefore, using the properties of the power function, the failure envelopes were indeed curved.

Influence of the Curved Failure Envelopes on Slope Stability Analysis

Day and Axten (1989) analyzed a fictional slope with sides at 1.5 horizontal to 1 vertical using the strength parameters obtained at high effective stress and those obtained at low effective stresses. Specifically, for the high effective stress parameters, the material was said to have a higher cohesion and a lower friction angle than those obtained for low effective stresses. They found that the slope had an acceptable factor of safety of 2.0 with high effective stress parameters and an unacceptable factor of safety of 0.8 with the strength parameters obtained low effective stresses.

In this study, a shallow slope in Nepal was analyzed using RocScience Slide 6.0. The cross-section of the slope along with the location ground water table and the sliding surface that caused failure is shown in Fig. 8. The material in the slope is assumed to be homogenous and anisotropically consolidated for K_0 conditions. Moreover, the material in the slope was similar to that presented in the above figures. The slope was analyzed for four different failure conditions. The envelopes used are as follows: (a) Linear $c' - \phi'$ Envelope; (b) Linear $c' = 0$ Envelope; (c) Curved Effective Envelope; (d) Undrained Linear Envelope. Spencer's

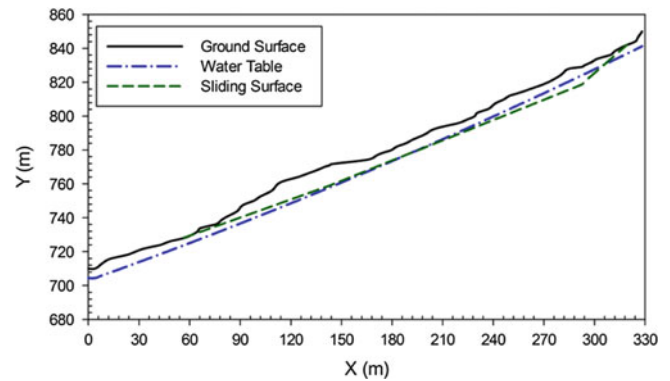


Fig. 8 Cross section of the shallow landslide

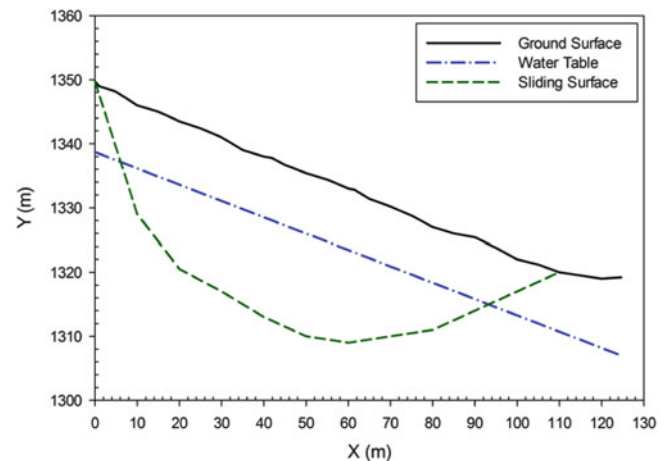


Fig. 9 Cross section of the deep seated landslide

method was used for the analysis. It should be noted the undrained failure envelopes for all of the samples were linear with zero cohesion. The results for all of the envelopes show the factors of safety of 1.2, 1.0, 0.9, and 0.4 for the cases a, b, c, and d, respectively. Using traditional linear $c' - \phi'$ envelope would predict a factor of safety about 22 % higher, and therefore, a safe slope as a result of the cohesion. However, the curved envelope suggests that that the slope will fail.

Another slope in Nepal with the same material properties was analyzed. However, the sliding surface for this landslide is deep and the cross section with the water table is shown in Fig. 9. The factor of safety was calculated for this sliding surface using the four envelopes described above and the results were 1.5, 1.5, 1.4, and 0.5, respectively.

These analyses explain that the curvature of the failure has little effect on the calculated factor of safety for a deep seated failure. It can be seen that the use of a linear $c' - \phi'$ envelope can be unconservative for shallow landslides.

Summary and Conclusion

The undrained shear tests conducted on ten mineral mixtures prepared from montmorillonite, kaolinite and quartz were useful to make following conclusions: (a) Correlations for undrained shear strength should be selected with respect to the anticipated failure mechanism, (b) The power function parameter B can be used as a check for curvature, (c) Simple shear accurately predicts drained shear strengths, (d) The failure envelopes are curved for low effective normal stresses and thus, the use of a linear $c' - \phi'$ envelope can be unconservative for shallow landslides.

Acknowledgments The authors would like to thank the National Science Foundation Graduate Research Fellowship Program for their generous support to conduct this research.

References

- Airey DW, Wood DM (1987) An evaluation of direct simple shear tests on clay. *Géotechnique* 37(1):25–35
- Airey DW, Budhu M, Wood DM (1985) Some aspects of the behavior of soils in simple shear. *Dev Soil Mech Found Eng* 2:185–215
- Baker R (2004) Nonlinear Mohr envelopes based on triaxial data. *J Geotech Geoenviron Eng* 130(5):498–506
- Baxter CDP, Bradshaw AS, Ochoa-Lavergne M, Hankour R (2010) DSS test results using wire-reinforced membranes and stacked rings, vol 199. *Proceedings of GeoFlorida 2010*, pp 600–607
- Bishop AW, Wedd DL, Lewin PI (1965) Undisturbed samples of London clay from the ashford common shaft: strength-effective normal stress relationship. *Géotechnique* 15(1):1–31
- Bjerrum L, Landva A (1966) Direct simple-shear tests on a Norwegian quick clay. *Géotechnique* 16(1):1–20
- Budhu M (1984) Nonuniformities imposed by simple shear apparatus. *Can Geotech J* 20:125–137
- Burland JB (1990) On the compressibility and shear strength of natural clays. *Géotechnique* 40(3):329–378
- Day RW, Axten GW (1989) Surficial stability of compacted clay slopes. *J Geotech Eng* 115(4):577–580
- Dyvik R, Berre T, Lacasse S, Raadim B (1987) Comparison of truly undrained and constant drained simple shear tests. *Géotechnique* 37:3–10
- Evans DA (1972) Slope stability report. Slope stability committee. Department of Building and Safety, Los Angeles
- Gill LD (1967) Landslides and attendant problems. Mayor's Ad Hoc Landslide committee report, Los Angeles, CA
- Ladd CC (1991) Stability evaluation for staged construction. *J Geotech Eng* 117(4):540–615
- Ladd CC, Edgers L (1972) Consolidated-undrained direct simple shear tests on saturated clays. Research Report R 72–82, Department of Civil Engineering, Massachusetts Institute of Technology
- Maksimovic M (1989) Nonlinear failure envelope for soils. *J Geotech Eng* 115(4):581–586
- Penman ADM (1953) Shear characteristics of a saturated silt, measured in triaxial compression. *Géotechnique* 15(1):79–93
- Ponce VM, Bell JM (1971) Shear strength of sand at extremely low pressures. *J Geotech Eng* 9(4):625–638
- Pradel D (1994) Active pressure distribution in cohesive soils. In: *Proceedings of 13th international conference on soil mechanics and foundation engineering*, pp 795–798
- Skempton AW (1957) Discussion on the planning and design of the New Hong Kong Airport, vol 7. In: *Proceedings of the institution of civil engineers*, pp 305–307
- Taylor DW (1952) A direct shear test with drainage control. *Symposium on direct shear testing of soils*, STP 131, pp 63–74
- Tiwari B, Ajmera B (2011) A new correlation relating the shear strength of reconstituted soil to the proportions of clay minerals and plasticity characteristics. *Appl Clay Sci* 53:48–57
- Zaruba Q, Mencl V (1976) *Engineering geology*. Developments in geotechnical engineering 10. Elsevier, New York



Experimental and Numerical Studies on the Effect of Rainfall on Triggering Shallow Landslides

Binod Tiwari, Katsuyuki Kawai, Adam Lewis, and Phommachanh Viradeth

Abstract

Rainfall is considered one of the major triggering factors for shallow landslides. The effect of rainfall in causing landslides depends on the intensity and duration of rainfall, the type of soil, the inclination of the slope, and ground water conditions. The majority of slope stability problems in shallow slides involve partially saturated soils. Although experimental modelling of slopes subjected to various intensities and durations of rainfall are ideal to evaluate the effect of rainfall on slope stability, it is time consuming and expensive. Numerical simulation of such experimental modelling can save a great deal of time and cost. In this study, slope models were prepared at angles of inclination of 30° and 45° with double washed construction sand, at a void ratio of 0.7. The slopes were subjected to 30 mm/h of rainfall for 3 h. Spatial variation of suction during the rainfall and depth of water front with time were measured for the entire rainfall period. The depth of water front and spatial variation of suction were also calculated through the finite element model (FEM) that was developed based on a hydro-mechanical model developed for the partially saturated soil. The numerical and experimental results provided identical results. The numerical result was extended to predict the spatial variation of suction, depth of water front and deformation of slope subjected to higher intensity of rainfall.

Keywords

Partially saturated soil • Suction • Water front • Finite element analysis • Rainfall intensity • Slope stability

Background

Damage caused by rainfall-triggered shallow landslides is well documented in the literature. Although shallow landslides are caused by various factors such as rainfall, earthquakes, and anthropogenic causes, statistics show that rainfall-induced shallow landslides are much frequent than landslides triggered by other factors. Fukuoka (1980) reported that the annual number of documented landslides in Japan exceed 10,000, and could reach 100,000, if documented properly. Similar numbers of shallow landslides are reported all over the world. The depth and steepness of shallow landslides are reported to be 0.5–2 m and 30–50°, respectively. Significant monitoring and warning systems

B. Tiwari (✉)
Department of Civil and Environmental Engineering, California State University Fullerton, 800 N State College Blvd., Fullerton, CA 92831, USA
e-mail: btiwari@fullerton.edu

K. Kawai • P. Viradeth
Department of Civil Engineering, Kobe University, 1-1 Rokkoudaicho Nadaku, Kobe 657-0013, Japan
e-mail: kkawai@kobe-u.ac.jp; pviradeth@gmail.com

A. Lewis
GeoStabilization International, P.O. Box 4709, Grand Junction, CO 81502, USA
e-mail: adam@gsi.us

have been implemented in various countries including USA, Japan, and Italy, in order to predict potential shallow sliding based on the calculated threshold rainfall amounts.

Various studies that have been conducted to evaluate the effect of rainfall on the stability of shallow slides loosely incorporate seepage conditions for partially saturated soils. Moreover, the numerical simulation results have not been verified with the experimental or field data. In this study, we conducted experimental studies on the change in the depth of water front and suction in soil with time and verified the results with the results obtained from the fully coupled hydro-mechanical model that was developed for partially saturated soils. The numerical results were further utilized to predict the velocity of movement of the water front based on the intensity and duration of rainfall at different inclinations of slopes. In this paper, the experimental modelling results are described briefly, but the numerical modelling results are described in more detail.

Materials and Methods

Experimental Modeling

Experimental models were prepared with double washed sand. The proportion of sand was approximately 95 %, with approximately 5 % fines. The soil was classified as SW material according to USCS. Specific gravity of the sand was 2.65. The horizontal and vertical coefficients of permeability of the sand were 8.0×10^{-3} and 4.3×10^{-3} cm/s, respectively. Soil water retention characteristic curves were prepared by measuring suctions in soil samples that were prepared in a 30 cm \times 30 cm \times 30 cm containers at different degrees of saturation, both for dry to wet and wet to dry cycles. A 1.22 m \times 1.22 m \times 1.22 m sized Plexiglas container was used to prepare the models. The Plexiglas container provides visibility to observe the depth of the water front at various durations of rainfall. The rain simulator used in this study was made of 16 special sprinkler heads arranged in such a way that the flow of water could be controlled in the sprinkler system in order to vary the intensity of rainfall from 18 to 360 mm/h. Separate slope models were prepared at angles of inclination of 30° and 45° by compacting soil in the container at the void ratio of 0.7 (corresponding relative density of 30 %). The experimental set-up is shown in Fig. 1. Four tensiometers were installed in the slopes, as shown in Fig. 2, in order to measure the spatial variation in suction with the duration of rainfall. The tensiometers used in this study were miniature tensiometers with a 0.5 cm² surface area and 5 mm tip size (T5 type), supplied by Decagon Devices. The tensiometer can measure pore pressures ranging from -100 kPa to $+85$ kPa with an accuracy of -0.5 kPa. Each slope was subjected to a rainfall



Fig. 1 Plexiglas container, slope made of double washed sand at a 30° inclination, and the rain simulator used in this study

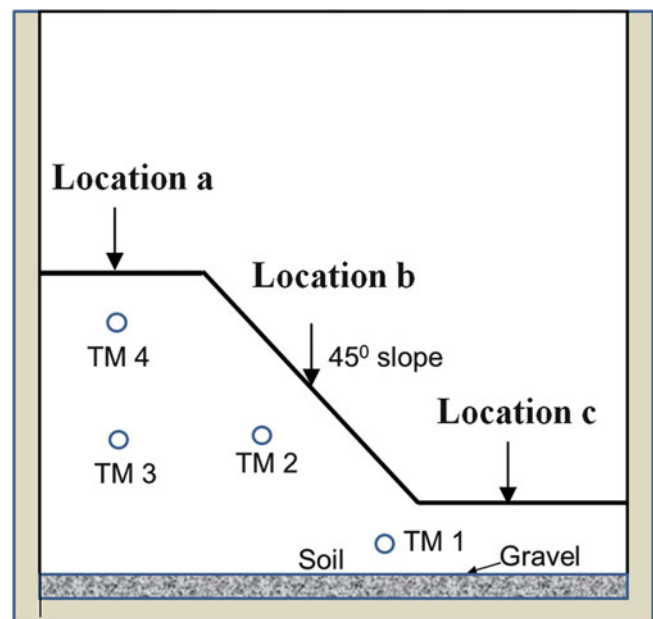


Fig. 2 Location of tensiometers within the slope

having an intensity of 30 mm/h for 3 h. The movement of the water front was marked at the boundary of the slope around the Plexiglas container every 15 min and the values of suction were recorded every minute.

Numerical Modeling

The soil-water-air coupled hydro-mechanical model developed by Kawai et al. (2007) was used in this study. Soil water retention characteristics curves were used to calculate the relationship between moisture content and suction.

The procedure proposed by Kawai et al. (2009), based on the approach recommended by Sugii and Uno (1996), was utilized to evaluate the parameters of the soil water retention characteristics of the tested soil sample. The equation utilized for the shape of drying and wetting cycles, i.e., the hysteresis of the soil water retention characteristics curves are presented in Eq. (1).

$$\frac{S_r - S_{rc}}{S_{rf} - S_{rc}} = \frac{1}{1 + \exp(A + B \log_e s)} \quad (1)$$

where,

S_r is degree of saturation; S_{rf} is degree of saturation at $s \rightarrow 0$; S_{rc} is degree of saturation at $s \rightarrow \infty$; s is initial suction; and A and B are curve-fitting parameters.

In this study, a soil/water/air coupled finite element analysis program was developed to evaluate the effect of rainfall on the variation in suction. Darcy's law applies for coefficients of permeability of both water and air. The relationships developed, as presented in Eqs. 2 and 3, were utilized in this study.

Darcy's law for water permeability is calculated as:

$$\mathbf{v}_w = -\mathbf{K}_w \cdot \text{grad } h = -k_{rw} \mathbf{k}_w \cdot \text{grad } h \quad (2)$$

$$\text{Here, } \text{grad } h = \frac{\partial h}{\partial x} + \frac{\partial h}{\partial y}$$

Darcy's law for air permeability is calculated as:

$$\mathbf{v}_a = -\mathbf{K}_a \cdot \text{grad} \left(\frac{P_a}{\rho_w g} \right) = -k_{ra} \mathbf{k}_a \cdot \text{grad} \left(\frac{P_a}{\rho_w g} \right) \quad (3)$$

$$\text{Here, } \text{grad} \left(\frac{P_a}{\rho_w g} \right) = \frac{\partial \left(\frac{P_a}{\rho_w g} \right)}{\partial x} + \frac{\partial \left(\frac{P_a}{\rho_w g} \right)}{\partial y}$$

Several functions of water and air permeability have been proposed in the literature. In this study, the equation proposed by Mualem (1974) for water permeability and the equation proposed by Van Genuchten (1980) for air permeability of unsaturated soil were used. The equations for the ratios of water and air permeability with the permeability of saturated soil (K_{rw} and K_{ra} respectively, herein after referred as the relative coefficient of permeability) are presented in Eqs. 4 and 5, respectively. Water permeability of soil is:

$$k_{rw} = S_e^{\frac{1}{2}} \left[1 - \left(1 - S_e^{\frac{1}{m}} \right)^m \right]^2 \quad (4)$$

Air permeability is calculated as:

$$k_{ra} = (1 - S_e)^\gamma \left(1 - S_e^{\frac{1}{m}} \right)^{2m} \quad (5)$$

where, m is Mualem's coefficient, which is taken as 0.8 in this study; γ is a shape parameter, which ranges between 0.33 and 0.50, and S_e is effective degree of saturation.

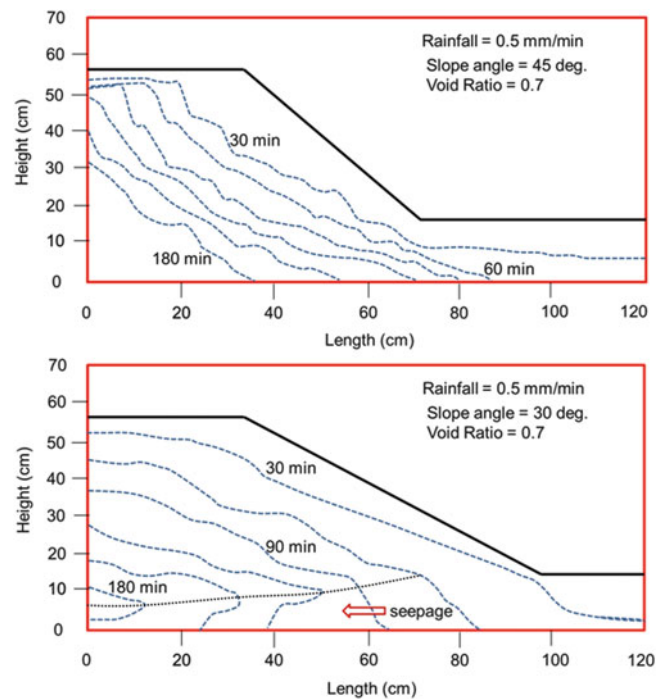


Fig. 3 Depth of water front at different durations of rainfall in model numbers 8 (top) and 7 (bottom)

Results of the Study

Experimental Modeling

The variation in the depth of water front that was recorded at 30 min intervals in slopes having angles of inclinations of 45° and 30° are presented in Fig. 3. As it can be seen in Fig. 3, the rate of movement of the water front within the slope is much faster than the rate of movement of water front in the flat portion at the top of the slope. This can be attributed to the movement of water in an inclined direction, especially for the saturated soil above the water front. However, the angle of inclination of the water front was less than the angle of inclination of the slopes. In the case of the slope with a 30° angle of inclination, it was observed that once the flat portion near the toe became saturated, it completely filled the drainage layer and started to supply water in the horizontal direction as well. Therefore, the data below the dotted line (indicated as seepage) is not considered for further analysis.

Figure 4 illustrates the values of suction observed at four locations, as described in Fig. 2. The initial suction at the four locations prior to rainfall ranged from 5.5 to 6.5 kPa. The soil at the top (near tensiometer #4) required approximately 60 min to reduce the suction close to 0 kPa, whereas the soil near the bottom of the slope (near tensiometer #1) required almost 120 min to drop the suction to 0 kPa. Please

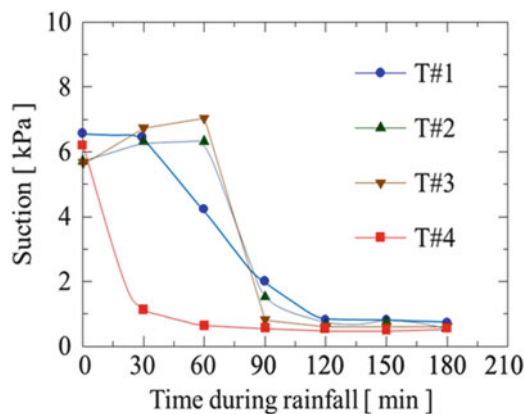


Fig. 4 Variation in suction with the duration of rainfall at locations described in Fig. 2 for a 45° slope

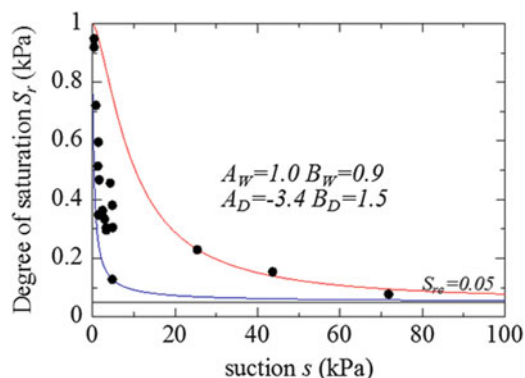


Fig. 5 Soil water retention characteristics curves of tested sample, derived from lab test

note that due to the sensitivity of the tensiometer used in this study (i.e. ± 0.5 kPa), measured suction may give an error of up to 0.5 kPa. The tensiometers installed at the other two locations within the slope also needed more than 60 min to become saturated. The rates of change in suction with time at all four locations were different. Locations near tensiometers 2 and 3 showed a similar pattern in the reduction of suction with time. The results presented in Fig. 4 show that the water fronts were not able to progress to tensiometer # 1 in 30 min and to tensiometers #s 2 and 3 in 60 min after the initiation of rainfall.

Numerical Modeling

Shown in Fig. 5 is the soil water retention characteristics curves prepared for both wetting and drying cycles of the degree of saturation–suction relationship curve. Equation 1 represents the regression curves for both dry and wet cycles. The suction parameters A and B (Eq. 1) were calculated for both drying and wetting cycles using the experimentally

derived values, as presented in Fig. 5. These parameters were used to calculate the values of suction in soil at different degrees of saturation during the numerical simulation.

Equations 1 through 5 were combined to calculate the depth of the water front during rainfall, and corresponding values of the degree of saturation and suction. Presented in Fig. 6 are the spatial distributions of suction in slopes with angles of inclination of 45° and 30°, compacted at a void ratio of 0.7, prior to rainfall. Suction ranged from 5.5 to 6.5 kPa in both slopes. Presented in Fig. 7 are the values of suction in those slopes after the application of 30 mm/h of rainfall for 3 h. The depth of water front, depicted by zero suction, can be seen in both figures. As expected, the depth of water front was higher in the steeper slope. Once the water saturates the toe of the slope, water starts to flow towards the slope in a horizontal direction as a result of a significantly high coefficient of permeability of gravel (drainage layer). Based on the numerical simulation result, the movement of the water front appeared to be parallel to the slope until the soil at the right side of the toe was fully saturated with rain water. After that, the soil close to the toe received water from rainfall as well as the seepage water from the saturated soil mass below the toe. This caused a slight deviation in the shape of the water front from the shape before the toe became saturated. The effect, right after 3 h of rainfall, is more pronounced in the slope with an inclination of 45° compared to the slope having an inclination of 30°.

Comparison between the numerically computed and experimentally observed values of the depths of the water front for a 45° slope after 30, 60, 90, and 180 min of rainfall are presented in Fig. 8a–d, respectively. Figure 8 also includes the numerically simulated values of the depths of the water front for the intensities of rainfall of 1.0 mm/min and 1.5 mm/min, whichever are applicable. The calculated and observed locations of the depth of the water front were very close near the flat portions on top of the slope (location a, Fig. 2) and bottom of the slope (location c, Fig. 2). However, the actual location of water front was lower than the front predicted by the numerical simulation within the inclined portion of the slope (location b, Fig. 2). Similarly, the location of the water front was slightly higher than the numerically simulated position in the case of location a, but was lower than the numerically simulated positions at location b for the durations of 60, 90, and 180 min of rainfall. The experimentally observed and numerically simulated positions of water front were close at location c for 60, 90 and 180 min of rainfall. Similar results were obtained for the 30° slope.

Comparison between the suctions obtained with the numerical simulation and model experiments for four different locations T1, T2, T3, and T4, described in Fig. 2, are presented in Fig. 9a–d, respectively. The numerical values differed from the observed values by less than 0.5 kPa. In the

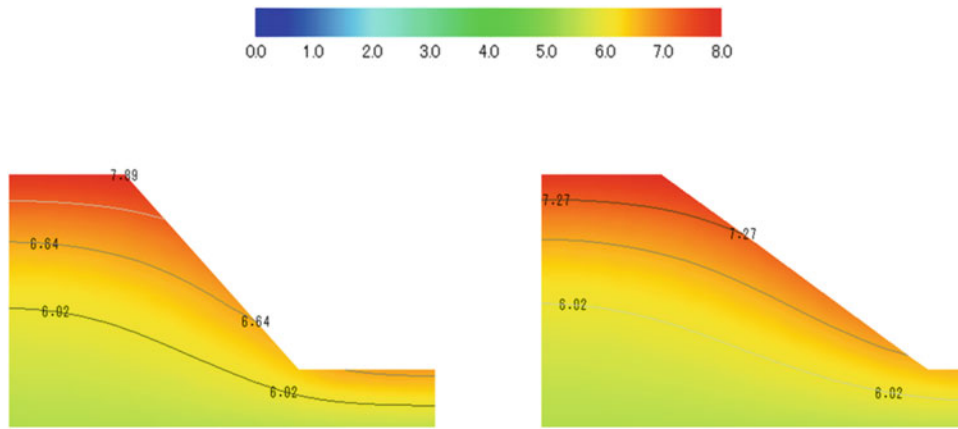


Fig. 6 Variation of suction in slopes prior to rainfall—(left) 45° slope, (right) 30° slope

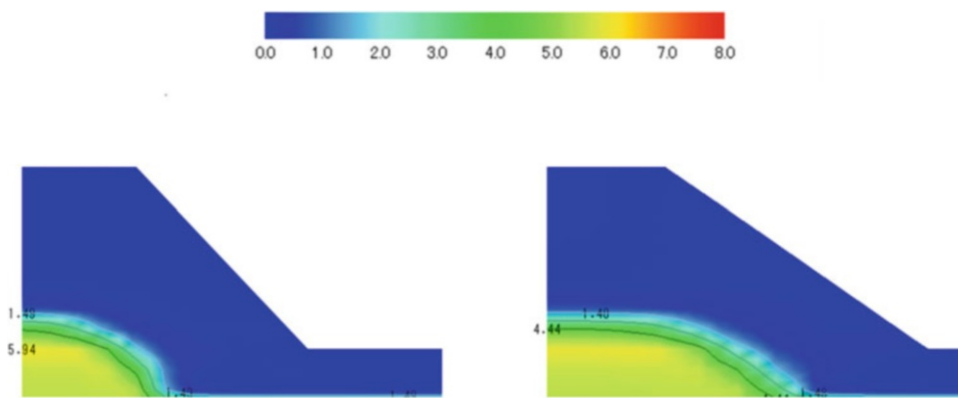


Fig. 7 Variation of suction in slopes after 3 h of rainfall—(left) 45° slope, (right) 30° slope

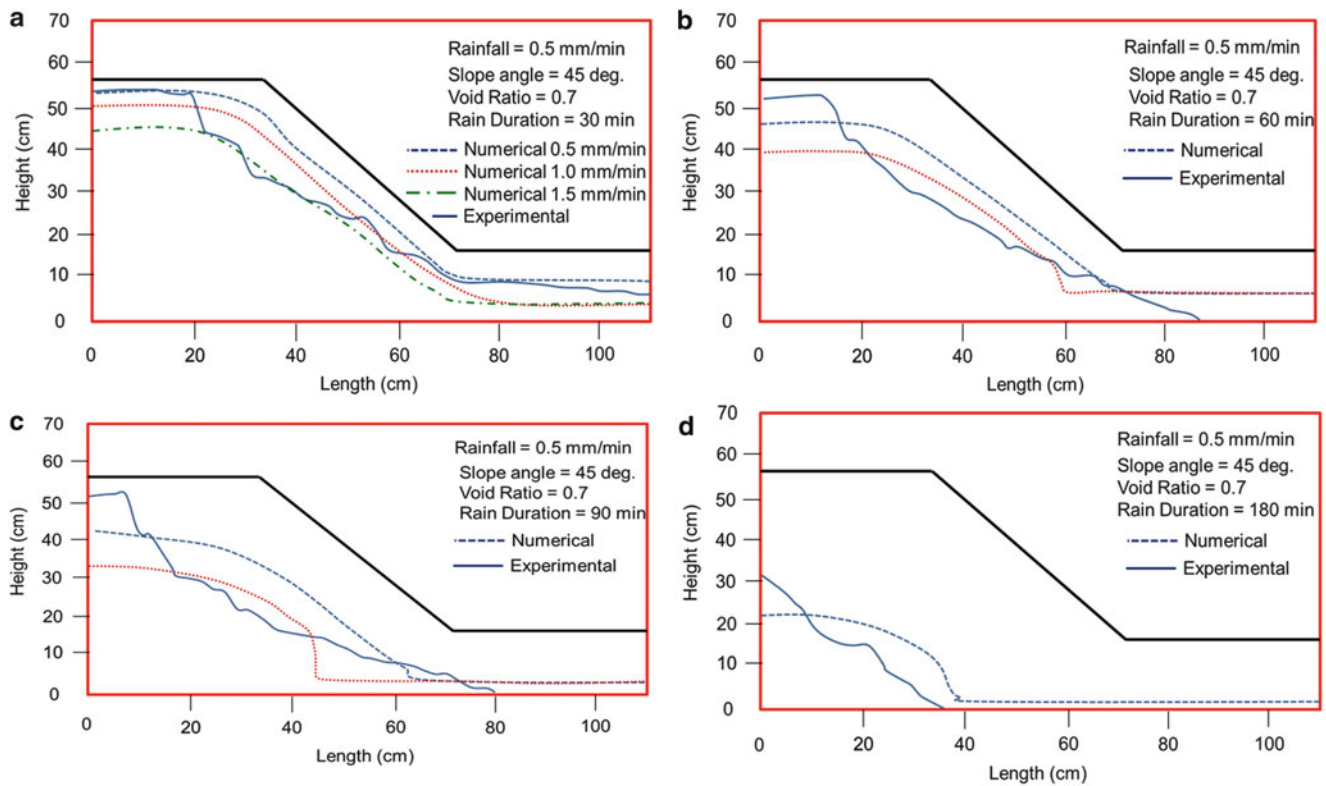
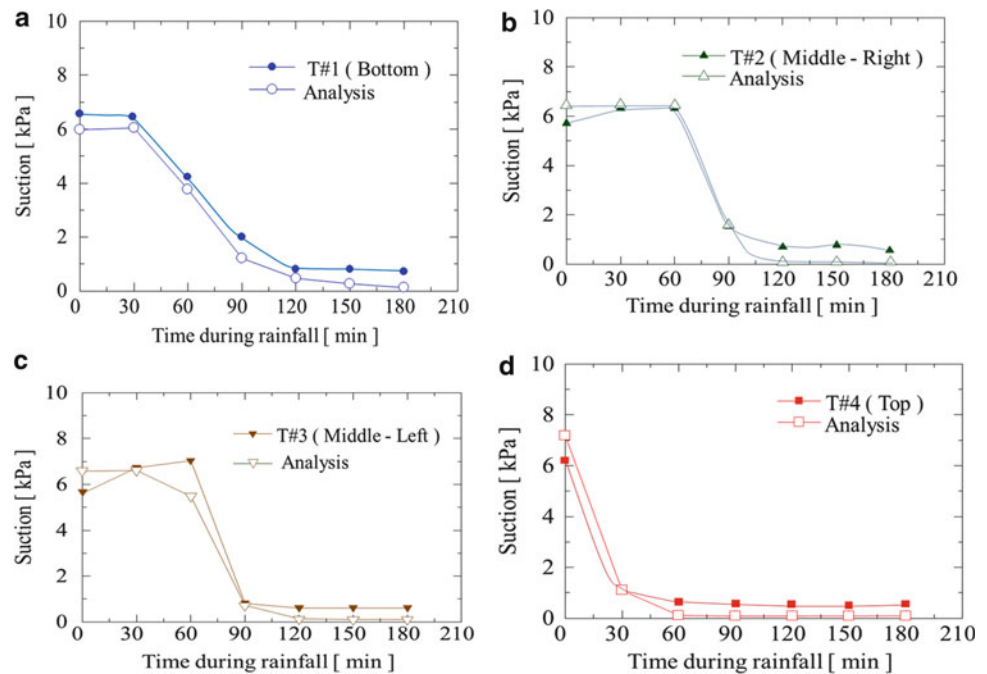


Fig. 8 Experimentally observed and numerically simulated positions of water front for different durations of rainfall

Fig. 9 Comparison between the experimental and numerical values of the suction at different locations (see Fig. 2)



majority of the cases, the numerical calculations showed lower suction values. Considering the precision of the tensiometer (i.e. ± 0.5 kPa), the numerically calculated values are considered to be reasonably accurate. This shows that the proposed numerical modeling technique can be utilized with reasonable accuracy to calculate the spatial distribution of suction in slopes during rainfall on partially saturated slopes.

Summary and Conclusions

Experimental and numerical modelling were conducted in order to investigate the variation in the depth of the water front and spatial distribution of suction in sandy slopes with two different inclinations during a rain event that produced 30 mm/h of rainfall for 3 h. The model developed by the authors that incorporated a hydro-mechanical coupled analysis for partially saturated soil with a finite element modelling technique was able to predict the depth of the water front and variation in suction with reasonable accuracy. This model was also utilized to evaluate the depth of the water front and variation in suction as well as a deformation analysis of slope for various intensities and durations of rainfall.

Acknowledgments The authors would like to thank the Associated Student Inc. (ASD), California State University, Fullerton, for providing financial support to purchase materials.

References

- Fukuoka M (1980) Landslides associated with rainfall. *Geotech Eng J Southeast Asia Soc Soil Eng* 11:1–29
- Kawai K, Iizuka A, Hayakawa E, Wang W (2007) Non-uniform settlement of compacted earth structures caused by the deformation characteristics of unsaturated soil on wetting. *Soils Found* 47 (2):195–205
- Kawai K, Iizuka A, Tachibana S, Ohno S (2009) Impacts of plant induced uptake on the stability of earth structure. In: *Proceedings of international conference on soil mechanics and geotechnical engineering*, Alexandria, Egypt, pp 526–529
- Mualem Y (1974) A conceptual model of hysteresis. *Water Resour Res* 10(3):514–520
- Sugii T, Uno T (1996) Modeling of hydraulic properties for unsaturated soils. In: *Proceedings of symposium on permeability of unsaturated ground*, pp 179–184 (in Japanese)
- Van Genuchten M (1980) A closed form equation for predicting hydraulic conductivity of unsaturated soils. *J Soil Sci Soc Am* 44:892–898



Feasibility Analysis of Loess Slope Improved by Lime Pile

Wanjiong Wu, Shouyun Liang, Fanyu Zhang, Xude Yan, and Jianji Zhou

Abstract

Lime has powerful characteristics of hygroscopicity, expansibility and gelation with soil, so a slope can be strengthened by placement of lime piles. In this paper, experiments have been performed to investigate the diffusion characteristic of lime in loess, and the influence of lime to the physical and mechanical properties of loess also have been examined, in order to verify the feasibility of using pile to improve the stability of slope. The results show that it is feasible to improve stability of slope by lime piles. Pile spacing should be set about 8.5 times as many as the diameter of the pile when the pile holes arranged according to the plum flower form from this test. Moreover, lime piles strengthen the loess slope mainly by gathering and cementing the clay grains in loess.

Keywords

Lime piles • Loess slop • Diffusion • Landslide prevention

Introduction

Loess is widely distributed in the northwest of China. It has stable structure, affluent vertical joints and obvious collapsibility (Wang and Gao 2012). The loess landscape such as loess tablelands, loess ridges, loess hills and loess gullies are shaped due to the dual function of accumulation and erosion, and always form high and craggy natural slopes (Liu 2007). However, a lot of loess slopes have been generated during the construction of infrastructures, like highways or railways etc. posing a threat to people's lives and properties (Yang et al. 2000). So, it is very important to improve the stability of loess slope in loess area. Statistics show that loess landslides and debris flow are major geohazards in Lanzhou City, accounting for more than 60 % of its total geohazards (Ding and Li 2009).

Lime has used to strengthen soft soil foundation (Mathew and Narasimha 1997), owing to its strong water-absorbing capacity, expansibility and physical absorption reaction between lime and soil grains. Specifically, it increases the soil strength and water stability by improving the engineering properties through physical and chemical reactions. Later, lime piles were used to solidify foundations by punching into the foundation soil, and then injecting lime powder to form lime piles (Wang and Cheng 1994). Because of lime hydration expansion of compaction, exothermic dehydration, ion exchange, gelling effect and the effect of displacement of a pile group or compaction due to punching, it greatly improves the foundation bearing capacity. At present, using lime to strengthen loess has been studied, and is mainly used as embankment and foundation treatment (Metelková et al. 2012; Lin et al. 2007). Lime added in loess produces a series of physical and chemical reactions with clay soil grains (Lin and Liu 2003). As a result, loess is solidified by changing its engineering properties. Loess landslides occurred frequently in the northwest of China (Zhang et al. 2013). If we use the idea that lime piles solidify loess, it can emerge as a new method to prevent and mitigate landslides. At the same time, lime piles can function as anti-slide piles.

W. Wu • S. Liang (✉) • F. Zhang • X. Yan • J. Zhou
Department of Geological Engineering, Lanzhou University, Lanzhou
730000, China
e-mail: wuwj2012@lzu.edu.cn; liangsy@lzu.edu.cn; zhangfy@lzu.
edu.cn; 517679408@qq.com; 742024323@qq.com

Physical experiment is performed to simulate the diffusion process of lime pile in loess. The physical, chemical and mechanical properties of loess are tested to illustrate the solidification phenomenon of loess surrounding the lime pile. The characteristics of solidified loess are analyzed, as well. Moreover, the primary reasons that lime pile solidifies loess from the perspective of diffusion have been discussed. This study provides guidance for further application of lime piles to improve stability of loess slope successfully.

Materials and Methods

Materials

Loess tested in lab is part of the Malan loess stratum at Jiuzhou platform, Lanzhou city, Gansu province. The Malan loess stratum is the main place of living and production activities. Its thickness is over 30 m (Li et al. 2007). The physical and chemical properties are shown in Table 1. Lime used in this study is produced by Tianjin Guangfu Exquisite Chemical Research Institute. The content of CaO was over 90 % and weight loss after ignition was about 2 %. In addition, it contains a small amount of insoluble acetic acid, chloride, sulfate, nitrate, iron, lead, alkali metal and magnesium and other impurities. It satisfies the requirements of JC/T479-92 standard for building quick lime.

The home-made square steel box is used (450 × 450 × 300 mm) to maintain the soil sample (Fig. 1a). In the middle of box a movable rigid plastic tube (External diameter, $D = 40$ mm) is arranged in order to form a lime pile (Fig. 1b).

Methods and Procedure

The loess was dried at 105 °C for 24 h to remove the elastic impurities by sieving through 0.5 mm size sieve after the loess cooled down to room temperature. According to the design, dry density (ρ_d) was 1.5 g/cm³ and optimum moisture content (ω_{opt}) was 15 %. The soil was divided into 15 equal portions and placed into black plastic bag and sealed for 24 h after evenly mixing with the corresponding distilled water. The plastic tube was installed and surrounded with the mixed soil to fill up the maintain box. The plastic box was slowly rotated out of the maintain box while packing the pile hole with lime at a moisture content of 15 %. The box was sealed for 22 days.

After completion of the maintenance, the 50 mm thick surface soil layer was scrapped off in order to reduce the influence of boundary conditions. Then the surface was flattened to conduct miniature vane shear test and hardness test. Once again, 30 mm thick disturbed soil layer was

Table 1 Physical and chemical properties of loess

| Physical properties | | Chemical properties | |
|---------------------|------------------------|---------------------|-------------------------|
| G_s | 2.73 g/cm ³ | SSA | 29.97 m ² /g |
| I_p | 11.79 | CEC | 4.01 cmol/kg |
| LL | 28.25 | | |

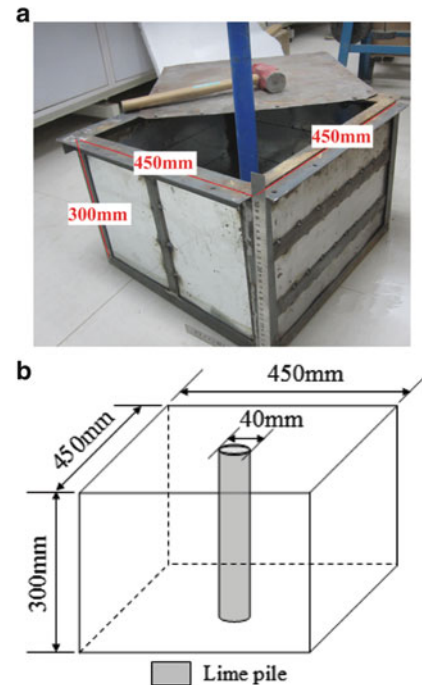


Fig. 1 Schematics of testing equipment. (a) Maintain box. (b) Sketch map of equipment

scrapped off, and four concentric rings spacing was carved at 50 mm centered on pile axis (Fig. 2a). Then with a small ring knives (inner diameter $d = 28$ mm) take samples as shown in Fig. 2b. Physical properties were measured based on GB/T50123-1999. The specific surface area (SSA) and cation exchange capacity (CEC) were measured with methylene blue adsorption method (Santamarina et al 2002; Savant 1994).

Results and Discussion

The soil samples are marked as Rx ($x = 50, 100, 150$ and 200) in order to collect data and perform the analysis easily. Soil in box is assumed to be homogeneous and share same physical and mechanical properties before test. Lime can absorb moisture and diffuses into loess because of its tiny particles, and strong water imbibition. As a result, the physical and mechanical properties of loess will changed due to changes in the structure. So, we can speculate the effect of improvement by testing the physical and mechanical properties of samples that are located around the lime pile.

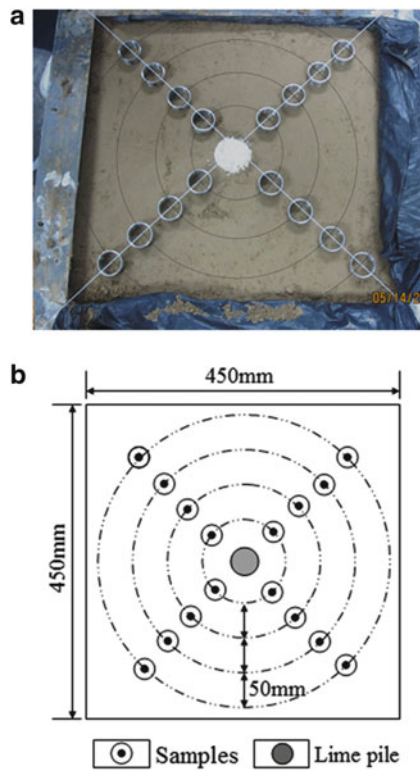


Fig. 2 Location of sample. (a) Physical map. (b) Sketch map

The Effect on Physical Properties of Loess from Lime Pile

Water content will greatly influence the stability of slope, due to the strong collapsibility and disintegrative of loess. Void ratio is the crucial physical index that represents the compaction of loess. Figure 3 shows the maximum, minimum and average values of water content and void ratio change along with radius. From the chart, it is clearly shown that water content (ω) and void ratio (e) decreased in comparison to the original soil samples ($\omega = 15\%$ and $e = 0.82$). In particular, every physical properties of improved soil samples located in $R = 50\text{ mm}$ change significantly. The average moisture content is 13.47% and average void ratio is 0.63 . Meanwhile, the moisture content and

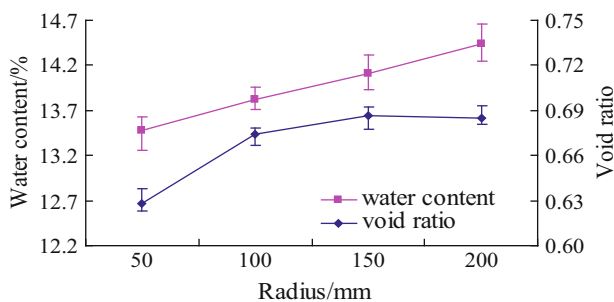


Fig. 3 Change of water content and void ratio along with radius

void ratio, when $R = 200\text{ mm}$, are close to the corresponding value of original soil sample. It is revealed that lime piles only improve the soil within a certain radius in this test, and with the increase of radius the improvement gradually decreases.

Loess belongs is a clay with low liquid limit, and the content of clay in loess is very important to its engineering geological properties (Lin and Liu 2003). An increase in plasticity index causes an increase in the content of clay and reduction in the stability. Figure 4 shows the change in liquid and plastic properties with radius. We can find some regular changes from the chart, that plastic index (I_p) of soil sample the one located close to lime pile is minimum. As lime diffuses into loess and reacts with the clay grains, I_p is increases along with the radius. When $R = 50\text{ mm}$, $I_p = 9.6$, when $R = 200\text{ mm}$, $I_p = 11.1$, and the I_p of original soil sample is 11.8 . It indicates that the content of clay grain in loess decreases, but within the range of influence of lime pile, the content of clay grain is increases along with radius. Plasticity index decreased due to a reduction in liquid limit and an increase in plastic limit. It is show that lime improves loess mainly by gathering and cementing the clay grains in loess and at the same time decreasing the plastic index increasing the water stability.

In order to further explore the influence of clay on the engineering properties of loess, specific surface area (SSA) and cation exchange capability (CEC) tests were conducted. Results of the tests (Fig. 5) indicate that SSA values and

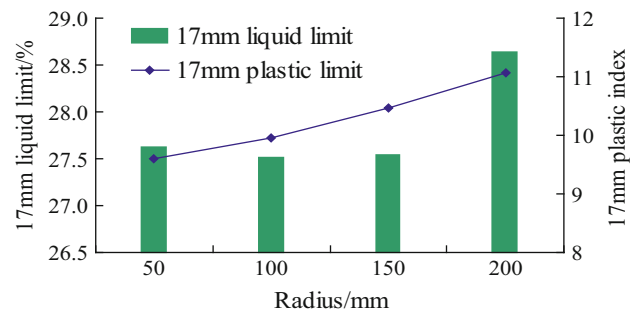


Fig. 4 Change of liquid and plastic properties along the radius

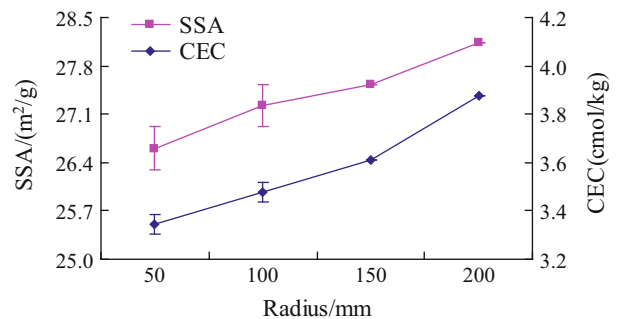
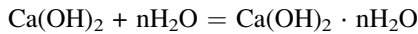


Fig. 5 Change of SSA and CEC along with radius

CEC values increase along with the radius, but are lower than the values of original soil sample, which mainly due to $\text{Ca}(\text{OH})_2$ generated in the nitration reaction after lime absorbed water, and released Ca^{2+} . Then Ca^{2+} was exchanged with the low charged ions absorbed on soil particle surface such as Na^+ , K^+ , H^+ etc. As a consequence, a reduction in the diffused double layer, gathering and cementing clay grains. Furthermore, there is a decrease in the dispersivity of the soil and an increase in its adhesiveness then forming a stable coherence structure. Afterwards recrystallization of lime reaction produces crystallization of calcium hydroxide:



Crystal products combined with each other then integrate the clay grains form eutectic, resulting in a decrease in the SSA and CEC values.

The Effect on Mechanical Properties of Loess by Lime Pile

The mechanical strength of loess is the outward manifestation of loess improvement effect. It is also one of the most concentrated engineering properties in the landslide prophylaxis and treatment projects. Micro cross section shear apparatus and Piccolo hardness tests are innovatively used to test shear strength and tensile strength of soil indirectly. The test results are shown as Fig. 6. Shear and tensile strength have a consistent trend, similar to the change of physical and chemical properties. Compared with original sample, the values of mechanical strength increase and display a rising trend along with radius. Because of the expansion of the lime pile, which absorbs water afterward, it leads to forming the expansion of cracks and circular cracks, etc. within 50 mm (Fig. 7). So, the mechanical strength of soil samples named R50 decrease to the minimum. It is easily found that lime piles should be mixed with some cement, fly ash or SH additive when they are used to improve loess (Wang et al. 2005; Guo et al. 2004), instead of using only lime. It will weaken the expansion of lime pile, enhance the mechanical strength of pile

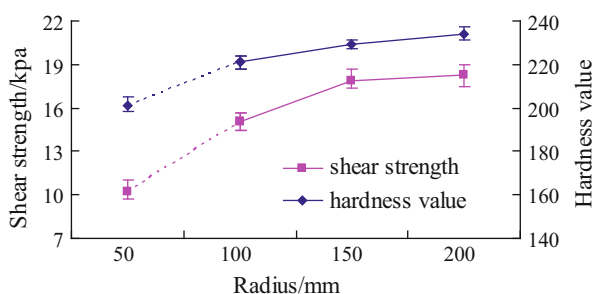


Fig. 6 Change of shear strength and hardness along with radius

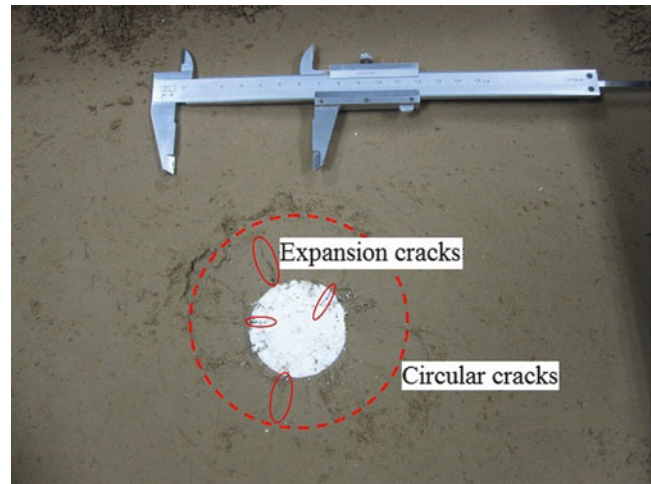


Fig. 7 Map of cracks reduced by lime expansion

itself and amplify the effect of anti-slide pile in the landslide prophylaxis and treatment project.

Feasibility Analysis of Loess Slope Improved by Lime Pile

Lime piles to improve the stability of loess slope mainly involves imbedding lime piles into loess in the slope toe and slope weak interlayer or shear zone of potential sliding surface, and to make sure that the lime piles are perpendicular to the slope (Fig. 8a). The water absorption and lime

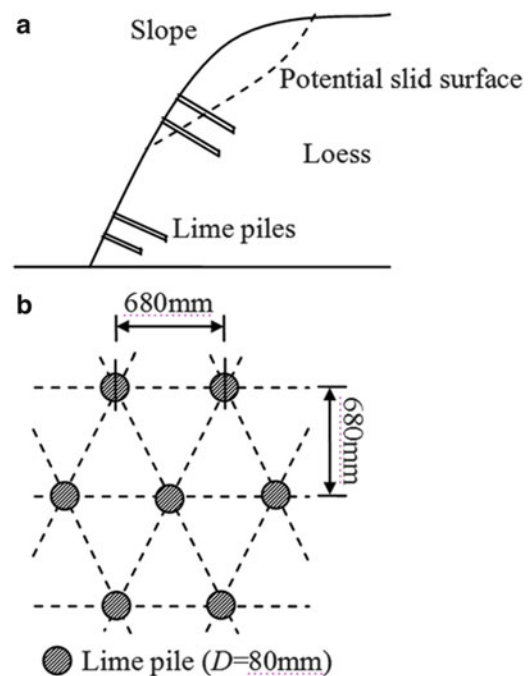


Fig. 8 Sketch map of lime piles in loess slope. (a) Location of lime piles. (b) Arrangement of lime piles

diffusion into surrounding loess will increase its strength, so that the stability of loess slope will be improved. Based on the physical and mechanical strength characteristics of improved loess, the space between piles can be determined. From the test results, when the diameter of pile is 40 mm ($D = 40$ mm), the influence radius is about 200 mm. The influence radius is about five times of pile diameter. If the pile holes are arranged in the plum flower form, the pile spacing can be calculated to be approximately 8.5 times the diameter of the pile based on the geometric relationships of a triangle and the edges. For example, if the diameter of pile is 80 mm, then the pile spacing will be 680 mm (Fig. 8b).

Conclusions

- (a) It is preliminary demonstrated that lime piles can be used to improve the stability of loess slope, but more physical experiment or field test are needed to verify this fact. In addition, lime piles should be mixed with some additives instead of pure lime in practical engineering to make the loess slope more stable.
- (b) Under similar conditions to this test, the influence radius of lime pile in loess is about five times of pile diameter. If the pile holes are arranged according to the plum flower form, pile spacing can be calculated to be about 8.5 times the diameter of the pile.
- (c) Lime piles improve loess mainly depends on the water absorption, ion exchange reaction and recrystallization reaction. All of them cement clay grains in loess forming a stable coherence structure, so that the loess is improved.

Acknowledgments This study was supported by the National Natural Science Foundation of china (No.41072213). The valuable comments by Binod, an Associate Professor and earnest modification by Wengui Huang are greatly appreciated.

References

- Ding ZQ, Li ZH (2009) Geological hazard and control in Lan Zhou. Gansu Science and Technology Press, Lanzhou, p 472. ISBN 978-7-5424-1198-3
- Guo TT, Zhang BP, Tian ZG (2004) Study on engineering characteristic of lime-fly ash loess. *Chin J Geot Eng* 26(5):719–721
- Li BX, Niu YH, Miao TD (2007) Water sensitivity of Malan loess in Lanzhou. *Chin J Geot Eng* 29(2):294–298
- Lin T, Liu ZD (2003) Study on indoor tests of fly ash and quick lime improving soft soils. *Rock Soil Mech* 24(16):1049–1052
- Lin DF, Lin KL, Hung MJ (2007) Sludge ash/hydrated lime on the geotechnical properties of soft soil. *Hazard Mater* 145(1–2):58–64
- Liu YH (2007) Experimental study on properties of lime-stabilized loess embankment. MS thesis, Southwest Jiaotong University, Chengdu, China
- Mathew PK, Narasimha RS (1997) Effect of lime on cation exchange capacity of marine clay. *J Geot Geoenviron Eng* 123(2):183–185
- Metelková Z, Boháč J, Přikryl R (2012) Maturation of loess treated with variable lime admixture: pore space textural evolution and related phase changes. *Appl Clay Sci* 61:37–43
- Santamarina JC, Klein KA, Wang YH (2002) Specific surface: determination and relevance. *Can Geotech J* 39(1):233–241
- Savant NK (1994) Simplified methylene blue method for rapid determination of cation exchange capacity of mineral soils. *Commun Soil Sci Plant Anal* 25(19–20):3357–3364
- Wang R, Cheng SX (1994) Stabilizing soft foundation with quicklime piles. *Rock Soil Mech* 15(3):19–25
- Wang YM, Gao LC (2012) Experimental research on chemical improvement of loess. *J Eng Geol* 20(6):1071–1077
- Wang YM, Yang ZC, Chen WW (2005) Strength characteristics and mechanism of loess solidified with new polymer material SH. *Chin J Rock Mech Eng* 24(14):2554–2559
- Yang XT, Dong HY, Huang YR (2000) Study on slop stability of expressway in loess region. *J Soil Water Conserv* 14(1):77–81
- Zhang F, Wang G, Kamai T (2013) Undrained shear behavior of loess saturated with different concentrations of sodium chloride solution. *Eng Geol* 155:69–79



Effect of Soaking on Shear Strength of Weathered Argillaceous Rocks Susceptible to Landsliding in the Three Gorges Area of China

Baoping Wen, Hui Li, and Kaihao Ke

Abstract

Slope stability in the Three Gorges reservoir has been one of the greatest concerns for both researchers and officials in China since inundation of the Three Gorges reservoir area. Shear-strength reduction of the inundated slope materials may be one of the major causes leading to slope failures. In this study, the shear strength of three kinds of weathered argillaceous rocks that are most susceptible to landsliding was experimentally investigated after soaking the material for different periods. It was found that reduction in shear strength of all the three weathered argillaceous rocks and their strength parameters occurred significantly after soaking for about 35 days, and that a very minor reduction was observed after soaking for a longer period. The weathered argillaceous rocks with more particles coarser than silt showed a greater reduction in internal friction angle, while those with more clay and silt displayed a greater decrease in cohesion. Particle analysis of the weathered argillaceous rocks after soaking, the compositions of their clay minerals and chemical analysis of the soak water suggested that shear strength reduction of the weathered argillaceous rocks may be attributed to a combination of slaking of rock fragments coarser than silt, hydration of clay minerals, and dissolution of calcite, as well as hydrolysis of feldspar due to soaking.

Keywords

Weathered argillaceous rock • Shear strength • Soaking • Slaking • Hydrations • Dissolution • Hydrolysis

Introduction

Landsliding is one of the geological hazards that poses the greatest risk to the Three Gorges area due to its steep hilly terrain and complex geology. It has been commonly believed that construction of the Three Gorges dam will

raise the landslide risk in the area as a result of either inundation or drawdown of the reservoir water, or both. One well-known case induced by reservoir inundation was the Qianjiangping landslide, which occurred on July 13, 2003 when the reservoir was impounded to an elevation of 135 m for 43 days (Wang et al. 2004; Wen et al. 2009). It has been extensively investigated, and shown that among the rock types predisposed to landsliding in the Three Gorges area, the argillaceous rock and its weathered materials are landslide-prone because of their low shear strength, particularly when wetted (Qi et al. 2009). Previous investigations found that more than 92 % of the landslides in the area were composed of a variety of the argillaceous rocks, mainly their weathered materials (MGMR 1988). Of the landslides in the

B. Wen (✉) • K. Ke
School of Water Resources and Environment, China University of Geosciences (Beijing), Beijing 100083, China
e-mail: wenbp@cugb.edu.cn; 806549778@qq.com

H. Li
Beijing Geological Engineering Corp. Ltd, Beijing 100143, China
e-mail: shiyao03lihui@163.com

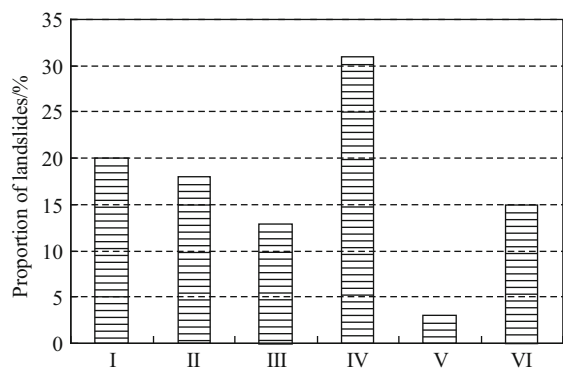


Fig. 1 Argillaceous rocks and their weathered materials predisposed to landslides in the Three Gorges area (after Li et al. 2008) (I: mudstone of the middle Jurassic and its weathered material; II: mudstone of the middle Tertiary; III: marls of the middle Tertiary and its weathered material; IV: other argillaceous rocks of the Jurassic and their weathered materials; V: other argillaceous rocks of the Tertiary and their weathered materials; VI: other argillaceous rocks and their weathered materials.)

area, more 50 % of them were related to three kinds of argillaceous rocks and their weathered materials, namely the mudstone of the middle Jurassic, and the mudstone and marl of the middle Tertiary (Li et al. 2008) (Fig. 1).

Since impoundment of the Three Gorges reservoir a much larger portion of the Yangtze River's bank slope has been submerged than before. Soaking may thus have a significant influence on the shear strength of the argillaceous rocks and their weathered materials in the reservoir area, resulting in or being a major factor leading to more slope failures. It has been widely recognized that landslides induced by reservoir inundation are largely related to shear strength reduction of the materials of its bank slopes (e.g., Stark and Duncan 1991; Singh et al. 2012). To explore the effect of soaking on shear strength of the weathered argillaceous rocks in the Three Gorges area and thus the effects on slope stability there, an experimental study was carried out using samples collected from three kinds of weathered argillaceous rocks, specifically the weathered material of the mudstone of the middle Jurassic, and the mudstone and marl of the middle Tertiary. These are the materials that are the most susceptible to landsliding in the reservoir area (MGMR 1988; Li et al. 2008).

Samples and Testing Method

Samples

In this study, samples of the weathered materials of the mudstone of the middle Jurassic, and those of the mudstone and marls of the middle Tertiary were collected from the reservoir bank at Zigui and Badong counties of Hubei

province, respectively. These samples are numbered as samples I, II and III, respectively. At the sampling sites, the mudstone of the middle Jurassic, and the mudstone and marls of the middle Tertiary are highly weathered. The former two form very loose, wet and soft purplish red clayey soils, whilst the third forms very loose, wet and soft brownish yellow clayey soils. Physical properties of the samples are shown in Table 1, which were determined following CNS GB/T50123-1999 standards (SAC et al. 1999). Sample II had the least clay (24 %) and silt (28 %) with the most gravel (20 %) and sand (28 %), whilst sample III had the most clay (60 %) and silt (35 %) with no gravel, and the abundance of each size fraction in sample I was in between (Table 1). Bulk and clay mineralogy of the samples measured using an X-ray diffractometer are given in Table 2. Quartz and clay minerals were predominant in all three samples, followed by calcite and feldspar (Table 2). In terms of clay mineralogy, samples I and III had primarily interlayered illite/smectite with some illite, interlayered kaolinite/chlorite and minor kaolinite and chlorite, whereas sample II had the most illite, with some interlayered illite/smectite and chlorite and minor kaolinite. Analysis of water samples from the Yangtze River near the sampling sites showed that the water was slightly alkaline with a very low salinity (Table 3).

Testing Method and Sample Preparation

The shear strengths of the samples were determined using direct shear testing. Since there is an increase in pore water pressure inside the bank slopes following reservoir impoundment, a direct shear test was conducted under consolidated and undrained conditions. ShearTrac II, a fully automated direct shear test apparatus (by Geocomp Corporation) was employed. The apparatus is capable of applying a horizontal displacement to the specimen of up to 15 mm and has two shear boxes. One is circular with a diameter of 10 cm and height of 2.5 cm, and the other is square with a side length of 15 cm and height of 7 cm, the latter which was customized for the soils with significant amount of particles coarser than 2 mm but finer than 7 mm. Based on the size of particles and their abundance in the three samples, samples I and III were sheared using the circular shear box, and sample II was sheared using the square shear box.

To investigate the effect of soaking on the shear strength of the samples, six groups of specimens were prepared for each sample, each of which included four specimens. The samples were first air-dried and powdered with a rubber hammer, followed by thoroughly mixing and wetting with deionized water. The wetted soil was then kept in airtight containers for at least 24 h before being remolded.

Table 1 Basic physical properties of the weathered argillaceous rock samples

| Sample | Dry unit weight (KN/cm ³) | Particle size fraction (mm, %) | | | |
|--------|---------------------------------------|--------------------------------|--------------------|----------------|-------------|
| | | Clay (>0.005) | Silt (0.005–0.075) | Sand (0.075–2) | Gravel (>2) |
| I | 18.6 | 33 | 35 | 28 | 4 |
| II | 19.6 | 24 | 28 | 28 | 20 |
| III | 12.4 | 60 | 35 | 5 | / |

Note: *LL* liquid limit, *PL* plastic limit

Table 2 Mineralogical compositions of the weathered argillaceous rock samples

| Sample | Whole rock (%) | | | | | Clay portion (%) | | | | |
|--------|----------------|----------|---------|----------|---------------|------------------|----|---|----|-----|
| | Quartz | Feldspar | Calcite | Hematite | Clay in total | I/S | I | K | C | K/C |
| I | 38 | 5 | 24 | / | 33 | 60 | 18 | 3 | 4 | 15 |
| II | 37 | 2 | 8 | 9 | 44 | 15 | 68 | 3 | 14 | / |
| III | 18 | 1 | 29 | / | 52 | 58 | 30 | 1 | 1 | 10 |

Note: *I/S* Interlayered illite/smectite, *I* Illite, *K* Kaolinite, *C* Chlorite, *K/C* Interlayered kaolinite/chlorite

Table 3 Chemical compositions of the Yangtze River water near the sampling sites (ion concentration in mmol/L)

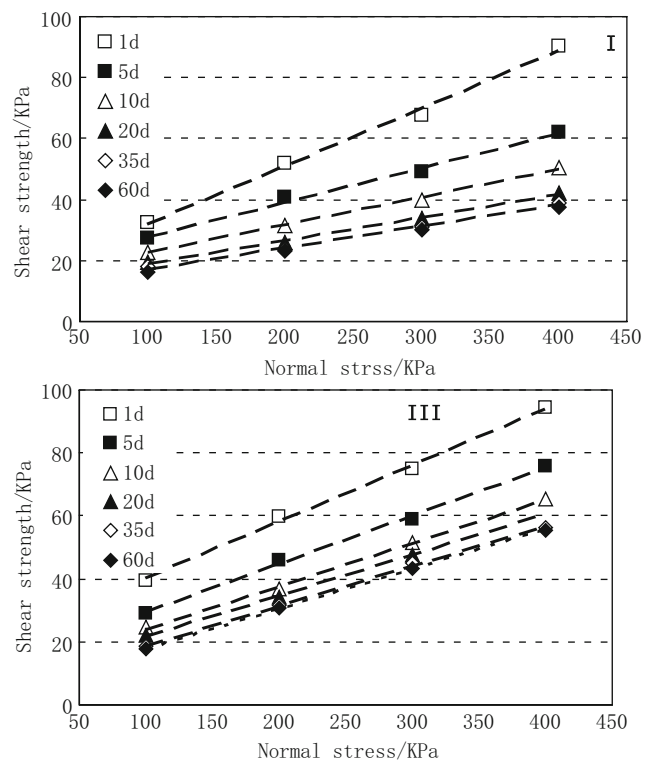
| Site | F ⁻ | Cl ⁻ | NO ₃ ⁻ | SO ₄ ²⁻ | HCO ₃ ⁻ | K ⁺ | Na ⁺ | Ca ²⁺ | Mg ²⁺ | pH |
|-------------|----------------|-----------------|------------------------------|-------------------------------|-------------------------------|----------------|-----------------|------------------|------------------|------|
| Near Zigui | 0.01 | 0.59 | 0.09 | 0.45 | 3.04 | 0.03 | 1.00 | 1.21 | 0.60 | 8.11 |
| Near Badong | 0.01 | 0.55 | 0.09 | 0.45 | 2.81 | 0.03 | 0.90 | 1.16 | 0.56 | 8.19 |

Subsequently the remolded samples were produced by pressing the wet soil to a prescribed unit weight using a customized pressure molder. The prescribed unit weight of each sample was calculated based on its unit dry weight and water content. For each sample, the specimens were trimmed from their remolded samples to fit the size of the desired shear boxes using sample cutters. The specimens confined by the cutters and fixed with a customized saturator were saturated using a vacuum saturation method following CNS GB/T50123-1999 (SAC et al. 1999). The saturated specimens of each group of the samples were then submerged in containers for 1, 5, 10, 20, 35 and 60 days respectively. Four specimens of each group were fully consolidated under normal stress of 100, 200, 300 and 400 KPa respectively before being sheared. A fast shear rate of 14 mm/min was set to simulate the undrained condition. Peak shear strength of the samples was determined for analysis.

Results

Variation of Shear Strength of the Weathered Argillaceous Rocks with Soaking Time

Test results showed that the shear strength of the three samples under each normal stress decreased markedly with soaking time (Fig. 2). It should be mentioned that the data for sample II is not shown due to this paper's limited space. This indicates that soaking resulted in shear strength reduction of the weathered argillaceous rocks. Notably, for the

**Fig. 2** Shear strength envelope of samples I and III after soaking for different times

three samples, their shear strength reduction under each normal stress occurred largely when soaking time was less than 35 days, and mostly in a period shorter than 20 days, whereas there was very little further reduction after soaking

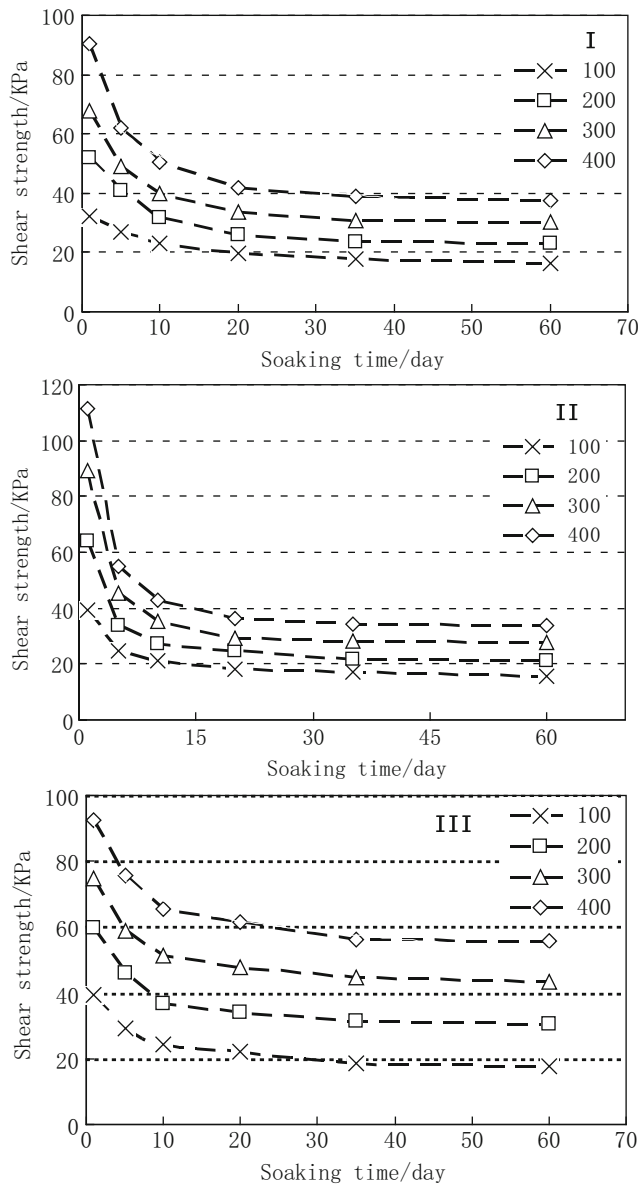


Fig. 3 Variation of shear strength of the three samples with soaking time

another 25 days, i.e., soaking 60 days in total (Fig. 3). This implies that shear strength reduction of the three weathered argillaceous rocks may be significant after reservoir impoundment for less than 60 days.

Variation of Strength Parameters of the Weathered Argillaceous Rocks with Time

For the three samples, their shear strength parameters of cohesion (C) and internal friction angle (ϕ), the stress parameters measured in this study, also display a pronounced reduction with soaking time (Fig. 4a, b). Again,

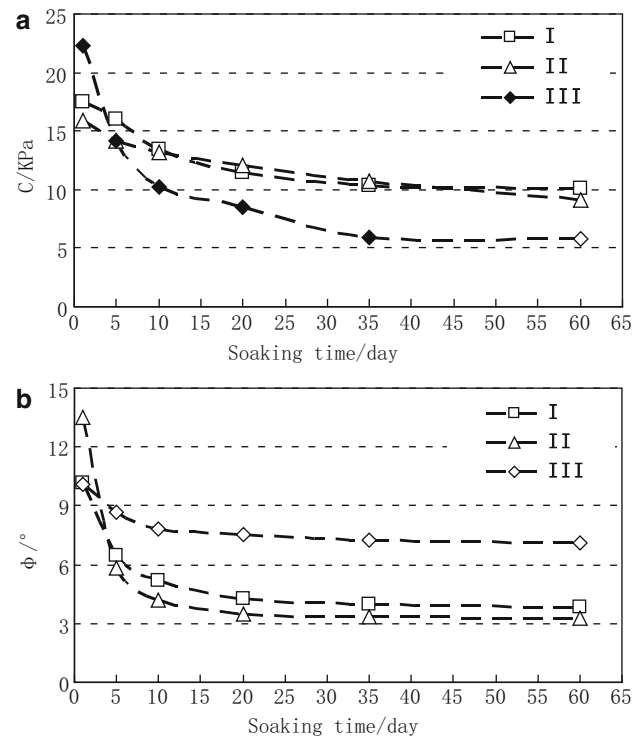


Fig. 4 Variation of strength parameters of the three samples with soaking time

significant reduction in these stress parameters also occurred when the soaking time was less than 35 days, and for most in a period shorter than 20 days (Fig. 4a, b). Among the three samples, for the same soaking time, the cohesion of sample III showed the greatest reduction and the internal friction angle was reduced the least, whereas the cohesion of sample II decreased the least and the internal friction angle was reduced the most. Those values of sample I were in between (Fig. 4a, b).

Discussion

Obviously reduction in shear strength of the three weathered argillaceous rocks after soaking should be attributed to either physical or chemical interactions between the weathered rocks and water, or both.

Particle size analysis of part of the soaked specimens revealed that the longer the soaking time, the more particles finer than silt and the fewer coarser particles they had (Fig. 5). This was more striking after the weathered argillaceous rocks were soaked for a shorter period rather than for a longer one, as the data after soaking for 10 days and 35 days versus that for 60 days shows in Fig. 5. Such phenomenon suggests that slaking or disaggregation of particles coarser than silts occurred when the weathered rocks were soaked, which could be referred to as a kind of physical interaction

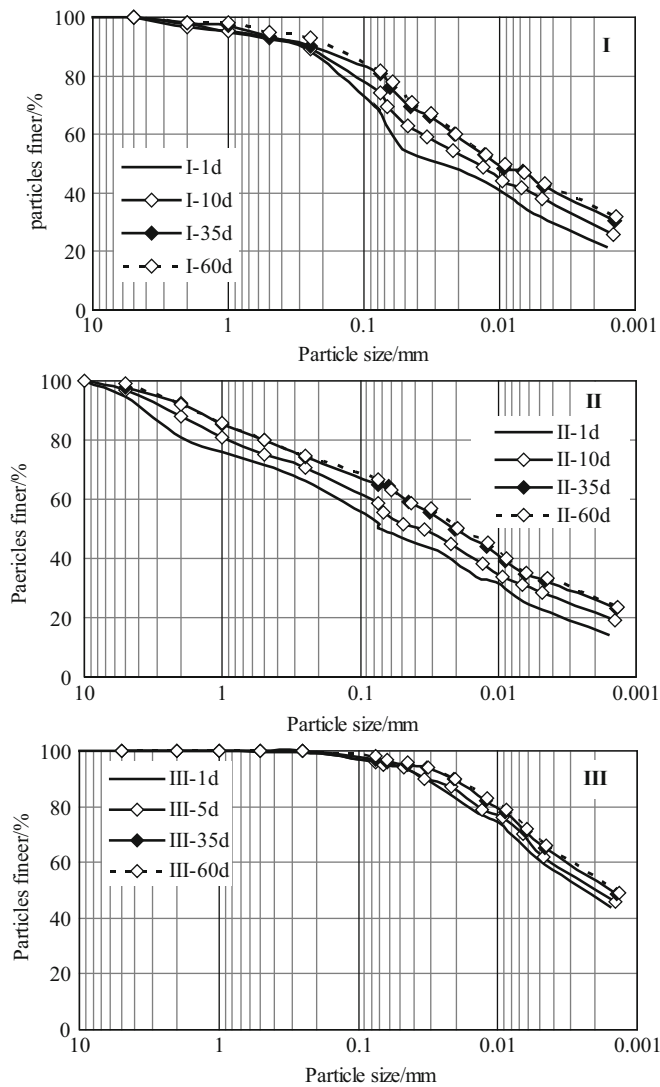


Fig. 5 Particle size distribution of the three samples after soaking for different times

between the weathered argillaceous rocks and water. Slaking of coarse particles then contributed to shear strength reduction of the weathered rocks after soaking. It is believed that particles coarser than silt in these weathered argillaceous rocks may be mainly rock fragments which have not fully decomposed yet. The rock fragments may be those mainly cemented by clay, thus being readily slaked after soaking for a short period. The internal friction angle of soil-like materials is known to be essentially governed by the size of their particles (Terzaghi et al. 1996), and the reduction in friction angles of the three weathered argillaceous rocks after soaking may thus be mostly associated with slaking of coarse particles. It is noted that, after soaking, the change of particle size distribution of sample II was the greatest, that of sample III was the least, and that of sample I was in between. This could explain why the reduction in internal

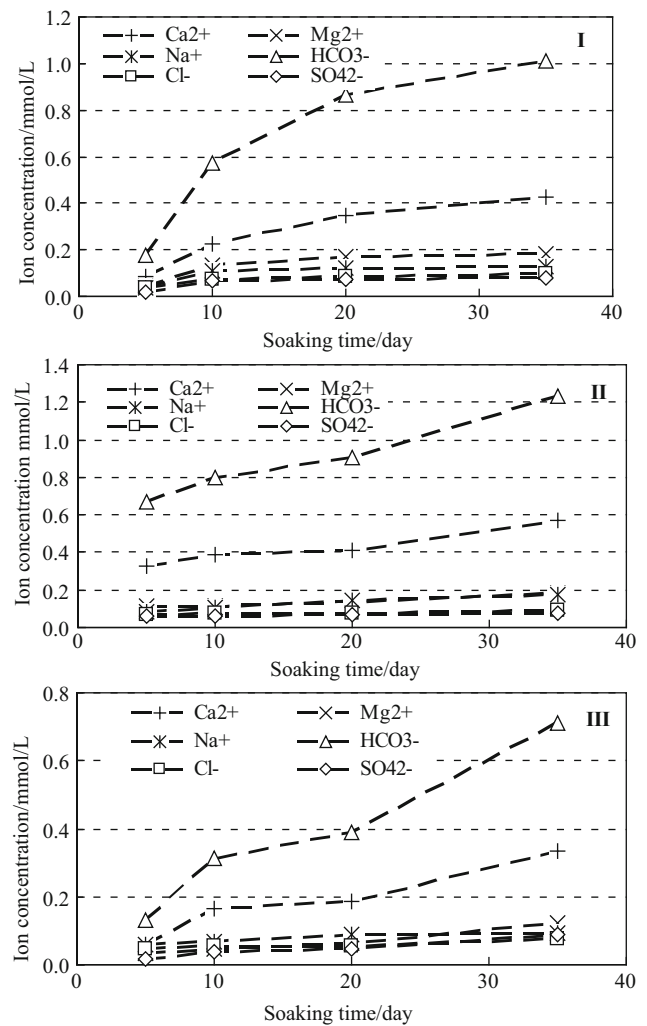


Fig. 6 Ion concentrations in sample soak water

friction angle of sample II was the greatest, followed by sample I and then sample III, after soaking for same period.

On the other hand, hydration of clay minerals, most likely interlayered illite/smectite and illite, may occur too during soaking of weathered rocks because these clay minerals swell when they encounter water. This may contribute to reduction in cohesion of the weathered argillaceous rocks. Such an effect may be more prevalent within the weathered rock with more clay, hence leading to a greater reduction in its cohesion. This may be the reason why cohesion of sample III was reduced the most, and that of sample II the least, as these samples had the most and least clay respectively among the three weathered argillaceous rocks. It is inferred that hydration of clay minerals within the weathered rocks may be complete soon after soaking. This may be why reduction in cohesion of the weathered argillaceous rocks occurred largely after soaking for less than 35 days.

Moreover, chemical analysis of water from the soaked weathered argillaceous rocks showed that there were various

ions with low concentrations, including cations of Na^+ , Ca^{2+} and Mg^{2+} and anions of HCO_3^- , Cl^- and SO_4^{2-} (Fig. 6a–c). The concentration of these ions in the water seems to increase with soaking time. Since deionized water was used for soaking the weathered rocks, occurrence of these ions in the soak water indicates that chemical interactions also occurred during soaking. Consistently for the three weathered argillaceous rocks Ca^{2+} and HCO_3^- were the most abundant among the cations and anions respectively in the soak water, followed by Mg^{2+} , Na^+ and Cl^- , SO_4^{2-} respectively. From the constituent minerals of the weathered argillaceous rocks (Table 2), it is deduced that two kinds of chemical interactions between the weathered rocks and water may occur: dissolution of some calcites (Ca^{2+} and HCO_3^-); hydrolysis of some feldspars (cations of Ca^{2+} , Mg^{2+} and Na^+), including albite and anorthite. Although calcite is generally recognized to be insoluble, it is known that dissolution of calcite may occur in an open system with circulation of chemical nutrients, such as carbon, oxygen and nitrogen. The inundated weathered argillaceous rocks in the Three Gorges area were indeed in such an open system. Such system could also accelerate hydrolysis of feldspar, which usually occurs very slowly. Dissolution of calcite and hydrolysis of feldspar may contribute to the slaking of rock fragments within the weathered rocks during soaking. The trend of variation in the ions' concentration in the soak water suggests that dissolution of calcites and hydrolysis of feldspar in the soaked weathered rocks may continue. Nevertheless their contribution to the slaking of rock fragments, and in turn to reduction in shear strength of the weathered argillaceous rocks may be very minor because of the very low concentration of the ions.

As a result of a combination of those effects discussed above, significant reduction in shear strength of the weathered argillaceous rocks and their parameters occurred after soaking. Variation of their shear strength implies that failures of the slopes composed of the weathered argillaceous rocks occurred after the Three Gorges reservoir impoundment for a short period, probably shorter than 2 months, and may be mainly related to reduction in shear strength of the weathered argillaceous rocks.

Conclusions

These experiments clarified that soaking significantly reduces shear strength of weathered argillaceous rocks in the Three Gorges reservoir area. This supports the view that reservoir inundation lowered slope stability there, and induced slope failures. The following specific conclusions can be drawn from this study:

1. Shear strength of the three types of weathered argillaceous rocks and their strength parameters were significant reduced after soaking for 35 days, with very minor further reduction after longer soaking
2. After soaking, weathered argillaceous rock with more particles coarser than silt experienced greater reduction in its friction angle, whereas that containing more clay displayed greater reduction in its cohesion.
3. Reduction in shear strength of weathered argillaceous rocks and their strength parameters due to soaking may be associated with four kinds of effects: slaking of rock fragments coarser than silt, clay-mineral hydration, calcite dissolution and feldspar hydrolysis.
4. Shear-strength variation of weathered argillaceous rocks after soaking implies that failures of slopes composed of such materials occurred after the Three Gorges reservoir was inundated for a short period, probably less than 2 months, and may be mainly led by this shear-strength.

Acknowledgments This research was funded by National Natural Science Foundation of China (No. 40872182).

References

- Li Y, Yin K, Cai B, Zhang G (2008) Statistical correlation between shear strength parameters and strata susceptible to landsliding. *Rock Soil Mech* 29(5):1419–1429 (In Chinese)
- Ministry of Geology and Mineral Resources (MGMR) (1988) Slope stability of the Three Gorges area. Geological Publishing House, Beijing, p 112. ISBN 7116003630
- Qi S, Yue Z, Wu F, Chang Z (2009) Deep weathering of a group of thick argillaceous limestone rocks near Three Gorges Reservoir, Central China. *Int J Rock Mech Min Sci* 46(5):929–939
- Singh Y, Bhat GM, Sharma V, Pandita SK, Thakur KK (2012) Reservoir induced landslide at Assar, Jammu and Kashmir: a case study. *J Geol Soc India* 80(3):435–439
- Standardization Administration of China (SAC), Ministry of Construction, Ministry of Water Resources (1999) China National Standards (CNS) GB/T50123-1999: standard for soil test method. China Planning Press, Beijing, p 323 (In Chinese). ISBN 9158005841607
- Stark TD, Duncan JM (1991) Mechanism of strength loss in stiff clay. *J Geotech Eng* 117:139–154
- Terzaghi K, Peck RB, Mesri G (1996) Soil mechanics in engineering practice, 3rd edn. Wiley, New York, p 549
- Wang FW, Zhang YM, Huo ZT, Matsumoto T, Huang BL (2004) The July 14, 2003 Qianjiangping landslide, Three Gorges Reservoir, China. *Landslides* 1(2):157–162
- Wen B, Shen J, Tan J (2009) Evaluation of the roles of reservoir impoundment and rainfall for the Qianjiangping landslide in Zigui County. In: Wang FW, Li TL (eds) Landslide disaster mitigation in Three Gorges Reservoir, China. Springer, Berlin, p 606. ISBN 1863–5520



Creep Behavior of the Slip Zone of a Giant Slow-Moving Landslide in Northwest China: The Suoertou Landslide as an Example

Xiu-zi Jiang and Bao-ping Wen

Abstract

The Suoertou landslide, a giant landslide with a volume of $72.85 \times 10^6 \text{ m}^3$ in Zhouqu County, Gansu province of China, has been reactivated with a rate ranging from 300 to 600 mm/year since 1990s. The slow-moving dynamic nature indicates that the creep nature of its slip zone may play one of the predominant roles in the reactivation of the landslide. To clarify this, creep behavior of the saturated soil collected from the landslide's slip zone was investigated via a series of direct shear creep tests. It was found that the creep behavior of the landslide's slip soil was strongly dependent on the stress-level for both normal and shear stresses. It was also found that the accelerated creep stage could not be reached until the shear stress exceeded 125, 187.5 and 300 kPa and the initial strain rate at 3.141, 3.688 and 4.5 min^{-1} , under the normal stresses of 100, 200 and 400 kPa, respectively. Moreover, both the critical shear stresses and the initial strain rates at which the accelerated creep stage begins seem to have a linear correlation with the normal stress.

Keywords

Slip zone • Direct shear creeping test • Creep behavior • Critical shear stress • Initial strain rate

Introduction

Slow-moving landslides are generally known to undergo time-dependent deformation, namely creep (Di Maio et al. 2013; Huvaj-Sarihan 2010; Macfarlane 2009; Mansour et al. 2011; Van Asch et al. 2009). The Suoertou landslide, a giant slow-moving landslide with a volume of $72.85 \times 10^6 \text{ m}^3$ in Zhouqu County, Gansu province of China, has been observed reactivating slowly since 1990s. The slide has caused severe damage to a road and local communities, and is moving at a rate ranging from 300 to 600 mm/year (Gansu Geological Disaster Survey and Design Institute 2012). Since a landslide's behavior is largely controlled by mechanical

characters of its slip zone, it is of great significance to study the creep behavior of the slip zone to understand the mechanism of the sliding and to forecast the landslide's moving dynamic. The creep behavior of landslides is normally studied via two approaches: displacement monitoring in field (Corominas et al. 2005; Macfarlane 2009; Mansour et al. 2011; Van Asch et al. 2009) and laboratory testing of creep behavior of landslides' slip zones (Bhat et al. 2011; Di Maio et al. 2013; Huvaj-Sarihan 2010). Due to absence of systematic monitoring data, the creep behavior of the Suoertou landslide's slip zone was investigated experimentally.

The Suoertou Landslide and Its Slip Zone

The Suoertou landslide was located on the north bank of the Bailongjiang river, about 1 km upstream of Zhouqu County, Gansu province of China (Fig. 1). The landslide fully developed within a regional active fault zone, namely the

X.-z. Jiang (✉) • B.-p. Wen
School of Water Resources and Environment, China University of Geosciences (Beijing), No.29 Xueyuan Road, Haidian District, Beijing 100083, China
e-mail: jyz5671@163.com; wenbp@cugb.edu.cn



Fig. 1 View of the Suoertou landslide



Fig. 2 Slip zone of Suoertou landslide from borehole ZK3

Pingding-Huama fault zone. The landslide is 3,300 m long with a width of 80–700 m. The elevations at front and back of the landslide are 1,300 and 1,970 m, respectively, with a height difference of 670 m. Boreholes revealed that the maximum and minimum of thickness of the landslide body is 100 and 20 m, with an average thickness of 60 m. Its sliding body consists of grey clayey soil with abundant carbonate rock fragments in the upper part and dark grey clayey soil with carbonaceous slate rock fragments in the lower part. The latter was wet, soft and sludged. The bed of the landslide is carbonaceous slate cataclasite. The slip zone of the landslide is a dark clayey seam, with a thickness of 1.3–4.3 m (Fig. 2), developed along the interface between carbonaceous slate cataclasites and clayey soil. The slip soil was very wet and highly soft. Groundwater level in the slide was observed to be 5–26.5 m under the ground surface.

The test soil sample in the study was collected from borehole ZK3, in the middle portion of the landslide (Figs. 1 and 2). The sampling depth was 60–64 m. Basic physical properties of the sample were presented in Table 1. Grain size distribution and Atterberg limits of the sample were obtained in compliance with CNS GB/T50123-1999 (SAC 1999). Results showed that there was 10 % clay fraction with 52 % silt, 8 % sand and 30 % gravel. The liquid limit and plasticity indices were 35 and 19, respectively. X-ray diffraction analysis showed that the sample had primarily quartz, pyrophyllite and clay minerals, which primarily consisted of illite, kaolinite and pyrophyllite with some interlayered illite/smectite and chlorite (Table 2).

Testing Program

Consolidated and drained direct shear creep test was adopted to investigate the creep behavior of the sample. A triple set direct shear creep test apparatus was employed in this study.

Table 1 Physical properties of the sample

| Particle density (g/cm^3) | Particle size fraction (mm, %) | | | | Liquid limit (%) | Plasticity index |
|---|--------------------------------|--------------------|----------------|-------------|------------------|------------------|
| | Clay (<0.005) | Silt (0.005–0.075) | Sand (0.075–2) | Gravel (>2) | | |
| 2.73 | 10 | 52 | 8 | 30 | 35 | 19 |

Table 2 Mineralogical compositions of the sample

| Quartz | Whole soil (%) | | | | | | Clay portion (%) | | | | |
|--------|--------------------|----------|----------|---------|--------------|---------------|------------------|----|----|----|---|
| | Potassium feldspar | Siderite | Dolomite | Plaster | Pyrophyllite | Clay in total | I/S | Py | I | K | C |
| 7.5 | 0.7 | 2.5 | 1 | 0.3 | 41.3 | 46.7 | 7 | 33 | 25 | 29 | 6 |

Note: I/S Interlayered illite/smectite, I illite, K kaolinite, C Chlorite, Py pyrophyllite

Normal and shear stresses were loaded through weights. The creep test was carried out following MT/T 895–1998 (State Bureau of Coal Industry 1998). Shear stresses were applied in increment. Each level of increment was estimated to be a fraction of the peak shear stress, which was obtained through a series of direct shear test under normal stresses of 100, 200, 300 and 400 kPa. The number of fractions was 6–8 in this study. The next level of increment was applied when the deformation of the specimen was observed less than 0.01 mm in 24 h. In this study, each shear stress increment was maintained for at least 1 week.

Since the slip zone was basically below the groundwater table and had primary particles finer than 2 mm, remoulded specimens with particles <2 mm were used with a water content about its liquid limit.

Results

Strain-Time Behavior

Figure 3 shows the strain versus time (γ -log t) behavior under different levels of normal stresses. It could be seen that the instantaneous deformation ($t = 0$) occurred once a shear load was applied, and these deformations became greater with the increment of shear stress. When the shear stress was less than 50, 75 and 125 kPa under the normal stresses of 100, 200 and 400 kPa, respectively, only attenuating creep was observed, during which shear strain became constant and the strain rate became nearly zero. When the shear stress was greater than the value mentioned above, steady-state flow was observed, during which the creep rate reached a constant value. When the shear stresses reached 125, 187.5, and 300 kPa respectively, the specimens underwent transient attenuating creep, steady creep and then went into accelerating creep until the specimens failed. These shear stresses 125, 187.5 and 300 kPa could be defined as critical stresses corresponding to the normal stresses of 100, 200, and 400 kPa.

The creep behavior of the landslide's slip zone illustrated above indicates that it is strongly dependent on the stress level. Interestingly, the values of shear stress leading to failure of specimens in creeping shear seem to have an approximately linear correlation with the normal stress (Fig. 4). Such correlation could be used to estimate the creep state of the Suoertou landslide given the sliding mass thickness, density of its materials and the occurrence of its slip zone is known. For example, at the sampling site (ZK3), dip of the slip zone was about 10° , given the slide materials' bulk gravity is 18 kN/m^3 , the normal stress and shear stress

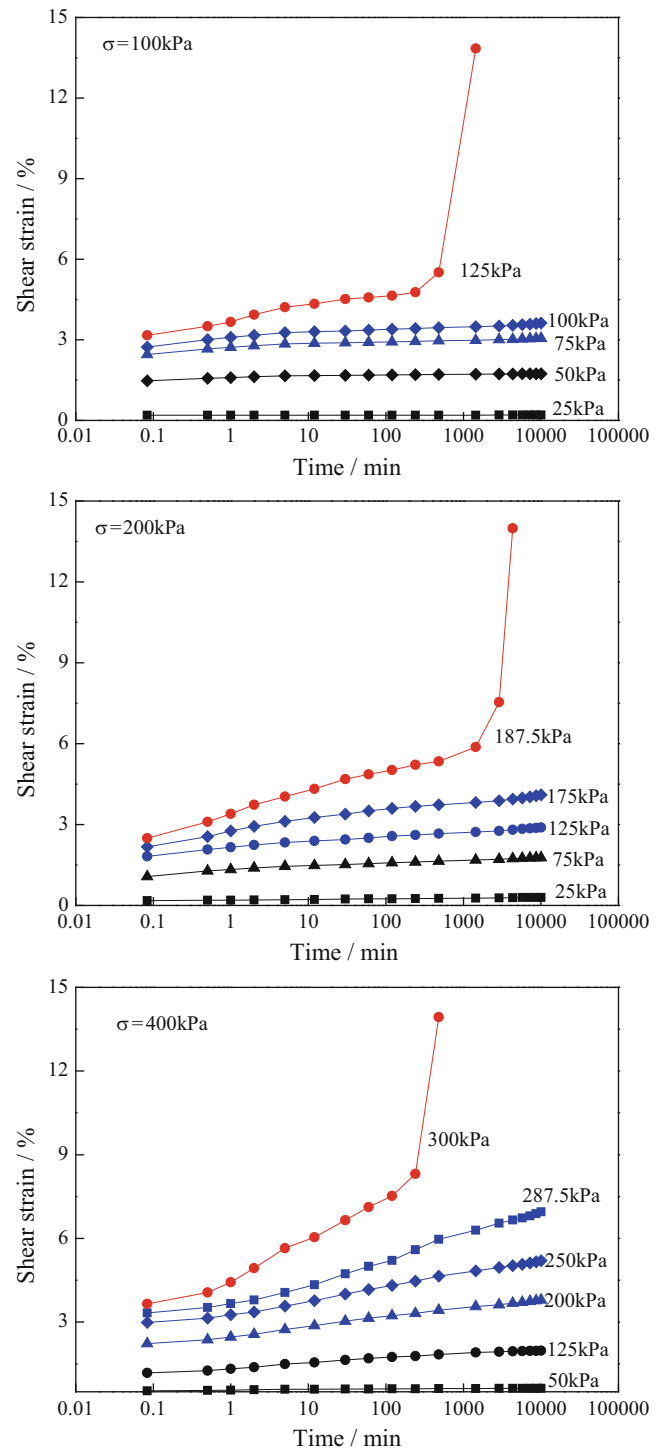


Fig. 3 Creep curves under normal stress of 100, 200 and 400 kPa

are about 1,134 and 200 kPa, respectively. According to the relationship shown in Fig. 4, shear stress calculated was less than the critical stress (726 kPa) leading to failure of the slip

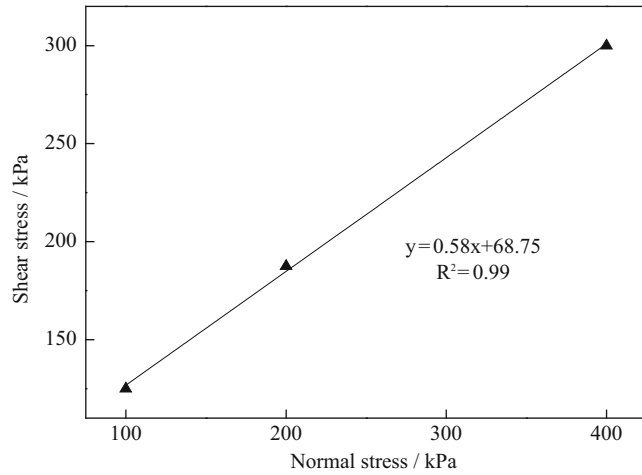


Fig. 4 Relationship between shear stress at failure and normal stress

zone. Therefore, the landslide at ZK3 has not reach the accelerated creep state yet, but it is already under a steady creep state.

Strain Rate-Time Behavior

Figure 5 shows the creep rate (shear strain rate) versus time (log-log scale) under different levels of normal stress. The results show that the initial shear strain rate increased with the shear stress. When the initial strain rate was less than 0.653 , 1.023 and 1.529 min^{-1} at normal stresses of 100, 200 and 400 kPa, respectively, the specimens were under attenuating creep and the relationship between strain rate and time could be described using Eq. (1) ($A < 0$). When the initial strain rate was higher than the rate mentioned above, creep of the specimens occurred in steady-state flow, the relationship between strain rate and time is found from Eq. (2). When the initial strain rate reached 3.141 , 3.688 and 4.5 min^{-1} , the specimens illustrated accelerated creep, and the curves had a point of inflection (minimum strain rate) when the strain rate changed from a decreasing to an increasing trend, and the relation between the strain rate and time could be described by Eq. (1) ($A > 0$). Clearly greater initial strain rates were needed for the sample to experience creep from attenuating state to steady state and to accelerated state. Notably the initial shear strain rates leading to accelerated creep also had an approximately linear correlation with the normal stress similar to those of shear stresses (Fig. 6). On the other hand, the minimum strain rate (e.g. $2.67 \times 10^{-3} \text{ min}^{-1}$ at 240 min in Fig. 5a, $0.52 \times 10^{-3} \text{ min}^{-1}$ at 480 min in Fig. 5b, $6.58 \times 10^{-3} \text{ min}^{-1}$ at 240 min in Fig. 5c) and the time to failure were almost linearly related as well (Fig. 7). If the displacement of the landslide is monitored, the slide's creep state could also be estimated based on the correlation shown in Fig. 6. Unfortunately, for the landslide no systematic monitoring data has

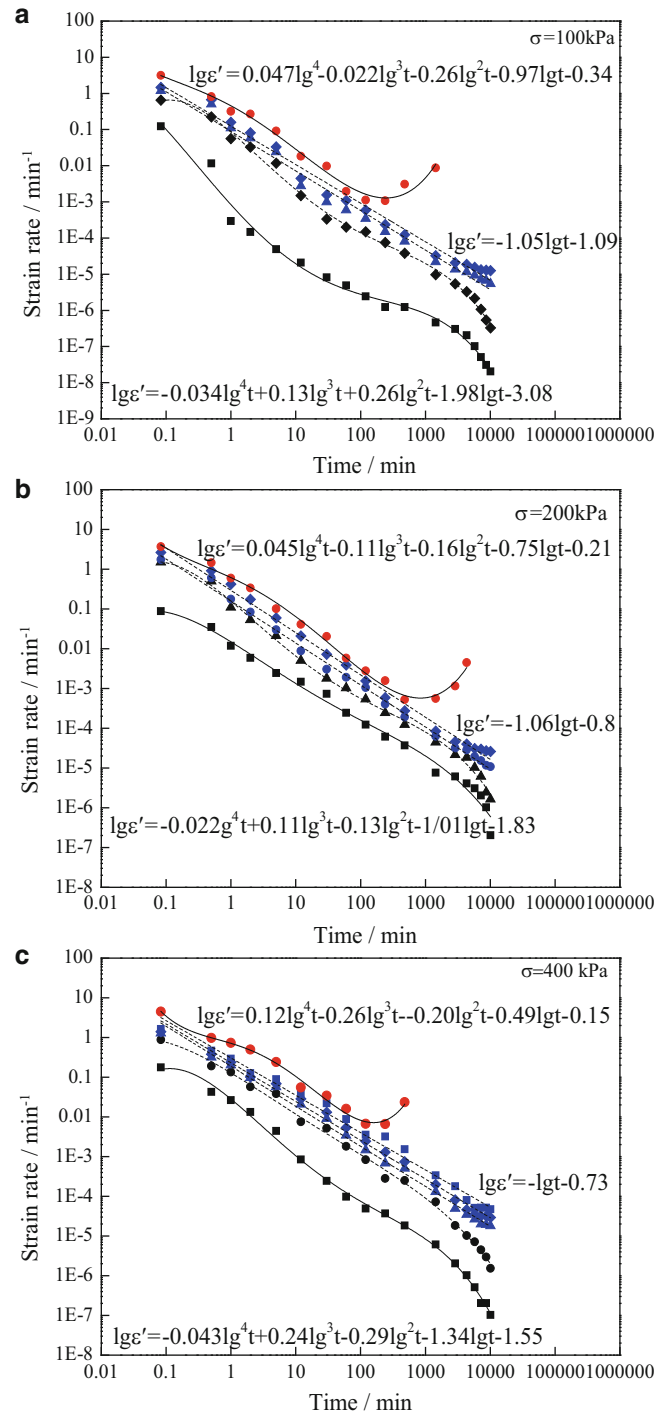


Fig. 5 Creep rate behavior of slip soil

been recorded at present. However, in any case, such correlation revealed another criteria that could be used to estimate the creep state of the landslide.

$$\lg \dot{\epsilon} = A \times \lg^4 t + B \times \lg^3 t + C \times \lg^2 t + D \times \lg t + E \quad (1)$$

$$\lg \dot{\epsilon} = A \times \lg t + B \quad (2)$$

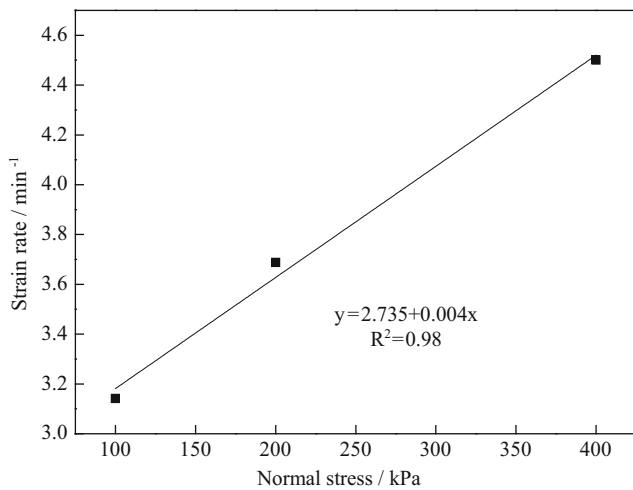


Fig. 6 Relationship between initial strain rates and normal stress at accelerated creep stage

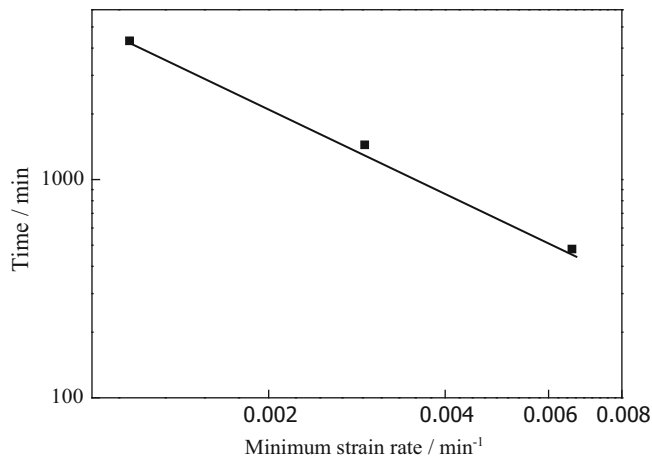


Fig. 7 Relationship between minimum strain rate and failure time during accelerating creep

in which, A, B, C, D, E are undetermined coefficients; $\dot{\epsilon}$ the strain rate and t the time.

Conclusion

This experimental study revealed that the creep behavior of the Suoertou landslide's slip zone varies with both the stress level and the initial shear strain rate. Specifically, the following could be concluded:

1. Creep behavior of the Suoertou landslide's slip zone was strongly dependent on the stress level, including both the normal and shear stresses. When the shear stress less than 50, 75 and 125 kPa under normal stress of 100, 200 and 400 kPa, respectively, the slip zone underwent an attenuating creep. Otherwise, it reached steady-state creep. The slip zone did not reach accelerating creep until the shear stress were 125, 187.5, and 300 kPa under normal stresses of 100, 200, and 400 kPa,

respectively. Such critical shear stresses had an approximately linear relationship with the normal stress. Based on this relationship, the Suoertou landslide has not reached accelerated creep yet.

2. Initial strain rate also had a significant control on the slip zone's creep behavior. When the initial strain rate was less than 0.653, 1.023 and 1.529 min^{-1} under normal stresses of 100, 200, and 400 kPa respectively, the slip zone was in attenuating creep; otherwise the slip zone reached steady-state creep. When the initial strain rate reached 3.141, 3.688, and 4.5 min^{-1} , respectively, the slip zone went into accelerating creep. The initial shear strain rates leading to accelerated creep also had an approximately linear correlation with the normal stress. This could be another criteria to estimate creep state of the landslide.
3. Creep characteristics of the slip zone revealed in this study should be just part of its behavior as only one group of tests has been completed currently. To get more information about the creep behavior of the landslide's slip zone more tests are needed, which are in progress.

Acknowledgments This research was funded by the National Natural Science Foundation of China (No. 41372305). The authors are thankful to Mr. Shu Jiang for sampling in the field.

References

- Bhat DR, Bhandari NP, Yatabe R, Tiwari RC (2011) Residual-state creep test in modified torsional ring shear machine: methods and implications. *Int J Geomate* 1(1):39–43
- Corominas J, Moya J, Ledesma A, Lloret A, Gili JA (2005) Prediction of ground displacements and velocities from groundwater level changes at the Vallcebre landslide (Eastern Pyrenees, Spain). *Landslides* 2(2):83–96
- Di Maio C, Vassallo R, Vallario M (2013) Plastic and viscous shear displacements of a deep and very slow landslide in stiff clay formation. *Eng Geol* 162:53–66
- Gansu Geological Disaster Survey and Design Institute (2012) Investigation report for Suoertou landslide prevention and control engineering, Lanzhou (In Chinese)
- Huvaj-Sarihan N (2010) Experimental investigation of failure time prediction in landslides. In: Paper presented at the EGU general assembly conference abstracts, Vienna.
- Macfarlane DF (2009) Observations and predictions of the behaviour of large, slow-moving landslides in schist, Clyde Dam reservoir, New Zealand. *Eng Geol* 109(1–2):5–15
- Mansour MF, Martin CD, Morgenstern NR (2011) Movement behaviour of the little chief slide. *Can Geotech J* 48(4):655–670
- Standardization Administration of China (SAC), Ministry of Construction, Ministry of Water Resources (1999) China national standards (CNS) GB/T50123-1999: standard for soil test method. China Planning Press, Beijing, p 323, In Chinese. ISBN 9158005841607
- State Bureau of Coal Industry (1998) MT/T 795–1998: testing method of rheologic characteristic for direct shear of rock and soil. China Coal Industry Publishing House, Beijing, p 12, In Chinese
- Van Asch TWJ, Malet JP, Bogaard TA (2009) The effect of groundwater fluctuations on the velocity pattern of slow-moving landslides. *Nat Hazards Earth Syst Sci* 9:739–749



Data Collection and Processing for Measurement of Time-Variable Gravity Erosion in the Laboratory Study

Xiang-Zhou Xu, Song Zhan, Qiao Yan, and Ming-Dong Zhu

Abstract

Researchers face great difficulties that few measurable data of gravity erosion on the Loess Plateau are found due to a lack in observation techniques. A problem common to all of the existing methods is that the data were observed after the failure events, and the gravity erosion was not separated from other forms of erosion. This study presents a novel experimental technique and a reliable data processing method that quantitatively measures the time-variable gravity erosion on the steep loess slope in the laboratory test. A structure with laser based gauge and the Topography Meter was designed and fabricated to monitor the dynamic variation of the steep slope topography under rainfall simulation. As the slope landform deforms over time, the process will be recorded in the video, and then imported into the computer to acquire a snapshot image at particular time instance. Given depth in ArcGIS, the 3D geometric shape of the target surface can be computed accurately. All erosion data in every rainfall event, including the amount of each failure mass, the total amount of soil loss, the total amount of hydraulic erosion, etc., could be calculated according to the videos caught by the Topography Meter. It is recommended to make 3D surface together with R2V and ArcGIS, although ArcGIS is sufficient for 3D surface modelling, because contour tracing in R2V is implemented on the undistorted original image, and R2V is also in much smaller size and easy to operate.

Keywords

Gravity erosion • Structure laser • Topography meter • ArcGIS • R2V

X.-Z. Xu (✉) • Q. Yan
School of Hydraulic Engineering, Dalian University of Technology,
Dalian 116024, China
e-mail: xz xu@dlut.edu.cn

S. Zhan
State Key Laboratory of Soil Erosion and Dryland Farming on the
Loess Plateau, Institute of Soil and Water Conservation, Chinese
Academy of Science and Ministry of Water Resources, Yangling,
Shaanxi 712100, China

M.-D. Zhu
State Key Laboratory of Hydrosience and Engineering, Tsinghua
University, Beijing 100084, China

Introduction

Gravity erosion, also referred as gravitational erosion or mass erosion, is the mass failure on steep slope, and is triggered by self-weight in contrast to the physical movement of wind and water required for other types of soil erosion. On the Loess Plateau of China, forms of gravity erosion include landslides, earth flow, creep etc. (Tang 2004). Although gravity erosion generally takes place together with hydraulic erosion in the rainfall event, the mechanism and dynamics of them are different. Hence the measures to control hydraulic erosion and gravity erosion are different, and it is essential to quantitatively distinguish the amount of them during a same event of rainfall. Yet predicting just where and when a mass failure will occur

continues to be a complex process. No direct observation of the soil geotechnical parameters at the moment of failure at any of the specific sites was recorded in the data set from existing literature (Darby and Thorne 1996).

The volume of individual failure mass was normally calculated by the slide area and the thickness of the slide mass (depth to the failure plane). Sattar et al. (2011) determined the dimensions of an eroded gully by laser scanning, and then showed a soil volume and a change in the body of the landslide dam. Papers presented individual measurements of landslide area and volume for multiple slope failures in an area were studied (e.g., Whitehouse 1983; Derbyshire et al. 1995; Larsen and Torres-Sanchez 1998; Martin et al. 2002; Hafidason et al. 2005; Guzzetti et al. 2009; Jaiswal et al. 2011). Nevertheless, a problem common to all of the above techniques is that the data were observed after the failure events, and the gravity erosion was not separated from other forms of erosion. The assessment of failure mass in the process of gravity erosion is hardly possible to achieve for several reasons. First, site-specific observation is almost impossible due to randomness of the gravity erosion, and nobody knows when and where the failure will occur. Second, gully erosion usually occurs by a combination of soil transportation with water and mass failure under gravity. Thus the amount of gravity erosion is hard to be distinguished from other forms of soil loss. A third trouble arises because, in general, the properties of earth materials and slope conditions vary greatly over short distances, and the timing, location, and intensity of triggering events, such as storm precipitation or earthquake shaking, are difficult to forecast (Keefer and Larsen 2007).

Presently 3D shape measurement based on structured light technique has been developed, which provides a great opportunity to overcome the above problems. Employing a digital projector and camera, the structured light 3D surface imaging technique is able to extract the 3D surface shape based on the information from the distortion of the projected structured light pattern (e.g., Wang et al. 2010; Peng 2007; Zhang 2005). However, no record has still been found in the existing literature to acquire the 3D object in dynamic motion using the above techniques (Geng 2011).

In order to represent the real complex geological objects in mining, oil industries and geological research, it is important to develop novel data models and algorithms to use real measurement data for the re-construction of bodies (Xue et al. 2004). Creating surfaces and 3D data can harness information from GIS data that was not readily apparent in its 2D form. The process involves identifying a series of ground control points, known x and y coordinates, which link locations on the raster dataset with locations in the spatially referenced data (target data). However, georeferencing in ArcGIS modifies the shape of the original pixels and makes the background image deformed. Contours

will become unclear and uneasy to be portrayed. In contrast, for R2V, counterdrawing is implemented on the original image and georeferenced only after it output in *.shp or *.dxf style.

This study presents a method of data collection and processing that could quantitatively measure the time-variable gravity erosion in the whole process of a rainfall event. The focus of this research is to develop and verify such a system and to demonstrate its practical value for the failure process on the steep slope.

Experimental Setup

The hardware used by the Topography Meter consists of regular devices: a camera, a laser source, and a position device. Figure 1 shows a representative scheme for quantitative monitoring of gravity erosion using a structured light based gauge. A stripe pattern with equidistant horizontal lines is generated by a laser source, and is recorded by a camera with sighting direction perpendicular to the light pattern. Positioning marks are placed on the fixed position with same height.

As the slope terrain deforms over time, the process video will be recorded, and then imported into the computer to acquire a snapshot image at particular time instance. Given depth in ArcGIS, the 3D geometric shape of the target surface can be computed accurately. In the Topography Meter we used a laser source with a monitoring range of 3.0×2.0 m and a SONYHDR-XR550E video camera with a resolution of 6.63 Megapixel. The laboratory calibration tests on the wooden brae show that the relative errors of the observed volumes were all within 10 % for the five landform models with the volume of about $24,000 \text{ cm}^3$ and slope gradients from 35° to 75° (Zhao et al. 2011).

Then we applied the Topography Meter on the real landslide experiments. In 2010 and 2012 at the Joint Laboratory for Soil Erosion of Dalian University of Technology and Tsinghua University, we have conducted a series of gully bank collapse experiments under closely controlled conditions. The landscape simulator consisted of a rainfall simulator suspended above a flume containing the slope model, as shown in Fig. 1. Six lines of five sprayer-styled rainfall simulators were utilized to simulate rainfall in the experimental plot covering 4.0×3.0 m. A short and intense downpour, with an intensity of 0.8 mm/min and the duration of 60 min, was applied. The landscape was constructed using matrix loess collected from the Shunyi District, Beijing. The 50 % diameter of soil particles, D_{50} , was $52.2 \mu\text{m}$, and specific gravity, γ_s , was 2.56. An experimental model landscape, with the steep slope of $60\text{--}80^\circ$ and a gentle slope of 4° , was developed. Soil was prepared by hand patting to generate a 'smooth' roughness to ensure a regular and

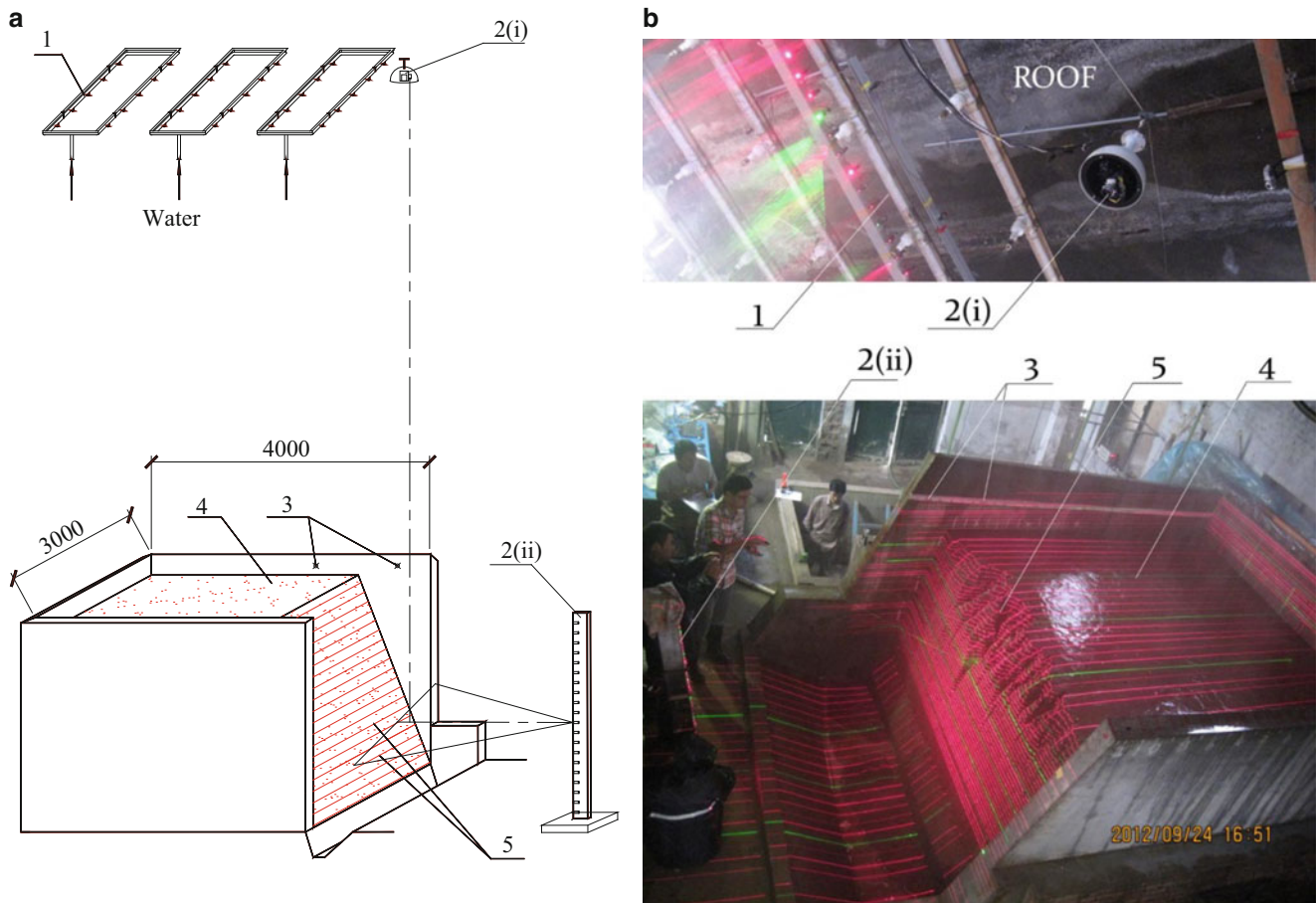


Fig. 1 A representative scheme for quantitative monitoring of gravity erosion using a structured light based gauge. *1*: Rainfall simulator; *2*: Topography Meter (*i*: Camera with a collimator; *ii*: Laser source); *3*:

Positioning marks; *4*: Model slope; *5*: Equidistant horizontal projections. (a) Schematics of the topography meter measurement system. (b) Picture of the experimental site

original microrelief. Five rainfall events were applied on the slope in turn. An equal period, 24 h, was kept after each rainfall. The Topography Meter was used to monitor the dynamic variation of the steep slope topography under rainfall simulation.

Data Processing

Based on the contour map obtained by the Topography Meter, we formed a 3D stereogram in ArcGIS software, and then provided the slope parameters such as volume, projection area and point coordinates. The calculation method is as follows: (1) the volume of each individual failure mass was calculated by comparing the failure block geometries in the moments before and after the incident; (2) the total amount of soil loss T in a rainfall event was that the slope volume at the beginning of the rainfall subtracts that at the end of the rainfall; and (3) the amount of hydraulic erosion W in a rainfall event equaled that the total amount

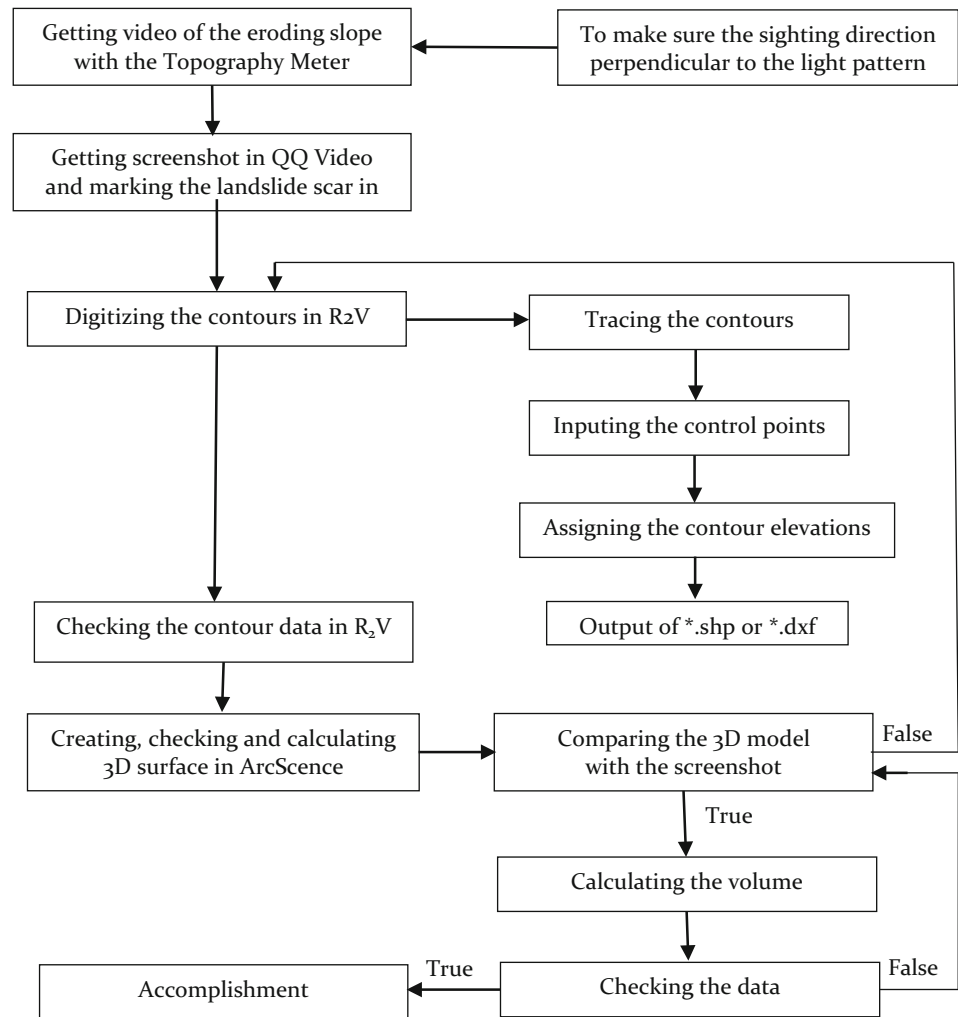
of soil loss T minus the sum of the volume of every individual failure mass in the rainfall event.

In the following text, a method is introduced to investigate the slope volume. Involved software includes the Chinese versions of QQ Video 2013 v4, Photoshop 6.0, R2V 5.5 and ArcGIS 10.0. The technical route is shown in Fig. 2.

Getting the Screenshot in QQ Video and Marking the Landslide Scar in Photoshop

Case no. 1—Dealing with the individual collapse. WE use the software QQ Video to open the test video, and tap the keyboard shortcuts Alt + A to get the screenshots seconds before the failure starts and soon after the incident finishes. Then we add the virtual boundaries in the screenshots in Photoshop. The boundaries should enclose the scar causing the individual collapse. Surely, the frames in the two images should be in same location and with same size.

Fig. 2 Data processing method of MX-2010-G topography meter



Case no. 2—Dealing with the total erosion during a rainfall. We use the software QQ Video to open the test video, and get the screenshot before the start of sprinkling. Then we go to the scene as the rainfall stops, and get the screenshot too. We open the screenshots in Photoshop, and add the virtual boundaries in the screenshots including the scope of all soil erosion during the rainfall.

Digitizing the Topographic Map in R2V

WE load the picture with virtual boundary in R2V, and then portray the contours, set the contour heights and input the control points. Finally, we output the above file as format *.shp or *.dxf. Since measurement accuracy of the failure volume is influenced by the tracing precision of the contours, more attentions should be paid to make sure the contour matches the laser line in the screenshot.

Creating a TIN Surface and Calculating the Volume in ArcGIS

We open ArcScene of the ArcGIS, input the vector file *.shp or *.dxf, and form the TIN surface of the slope. Comparing to the screenshot, we can check the surface and make sure it is all right, and then calculate the volume of the given surface with the command Surface Volume. Otherwise, we inspect and revise the file *.prj in R2V once more.

Calculation Results and Discussion

The Topography Meter has completed observation for more than 120 events of rainfall simulation of the experiments in 2010 and 2012, and has been proved to be reliable and easy to use. All erosion data in every rainfall event, including the amount of each failure mass, the total amount of soil loss, the

Table 1 Calculated amounts of gravity erosions: a sample

| Experiment | Rainfall event | Events of gravity erosion | Soil loss during rainfall (cm ³) | | | G1/T(%) |
|-------------|----------------|---------------------------|--|----------------------|-----------------------|---------|
| | | | Total (T) | Gravity erosion (G1) | Hydraulic erosion (H) | |
| L60-1.5-80d | 120924-1 | 3 | 1.31E + 04 | 8.51E + 02 | 1.22E + 04 | 6.50 |
| | 120924-2 | 21 | 2.60E + 05 | 2.40E + 05 | 2.05E + 04 | 92.14 |
| | 120925-3 | 2 | 1.09E + 04 | 6.21E + 03 | 4.64E + 03 | 57.21 |
| | 120925-4 | 8 | 5.38E + 05 | 3.58E + 05 | 1.80E + 05 | 66.46 |
| | 120926-5 | 0 | 2.24E + 04 | 0.00E + 00 | 2.24E + 04 | 0.00 |
| | 120926-6 | 13 | 2.41E + 05 | 1.20E + 05 | 1.20E + 05 | 49.96 |

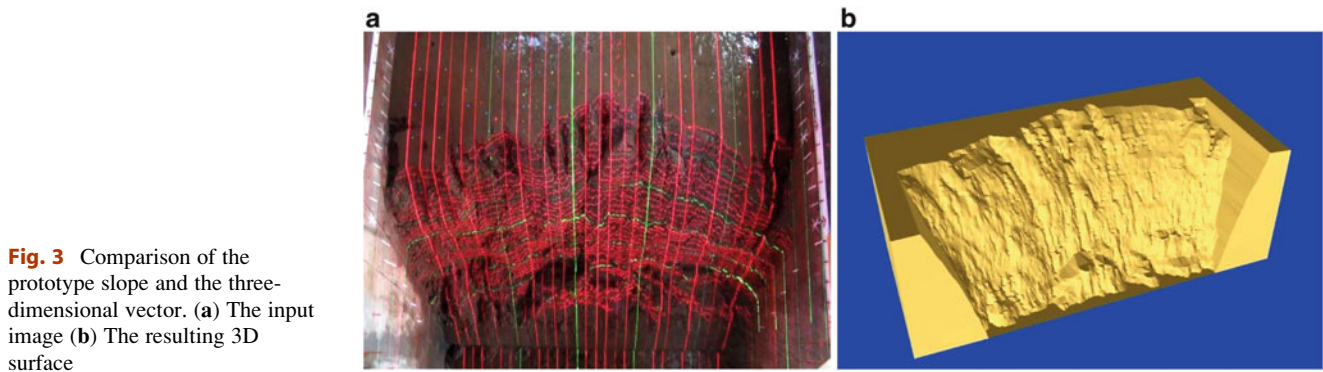


Fig. 3 Comparison of the prototype slope and the three-dimensional vector. (a) The input image (b) The resulting 3D surface

total amount of hydraulic erosion, etc., have been calculated according to the videos caught by the Topography Meter.

Table 1 illustrates the calculated amounts of gravity erosions in Experiment L60-1.5-80d we performed in 2012. The slope height was 1.5 m and gradient was 80° of the initial landscape in this experiment. Any collapses with volume more than 100 cm³ were accurately metered. In the third event, landslides with amount more than 100 cm³ occurred two times, and the total amount of gravity erosion reached 6,210 cm³, all of which completed in a very short time. Simultaneously, the amount of hydraulic erosion was 4,640 cm³, which lasted for the whole term of rainfall simulation. Hence gravity erosion was undoubtedly more dangerous than hydraulic erosion.

In Fig. 3, we show a typical scenario and the resulting 3D digital model on the failure surface. High resolution is achieved by only labeling the grid surface, and results obtained by the Topography Meter keep quite constant to the real in-situ phenomena. Different to any other monitoring devices, the Topography Meter only settles the landslip areas just before and after the failure incident. Consequently it could evaluate the failure mass bulk more quickly and precisely. Then the volume of “pure” gravity erosion will be also calculated due to the distinction of hydraulic erosion and gravity erosion.

Making 3D surfaces together with R2V and ArcGIS is preferable. In this research, contours were traced with the undistorted original image in advance and then the coordinates of control points were set in R2V. Thus the laser projection was clear and easy to be traced. Furthermore, R2V is in much smaller size than ArcGIS and easy to

operate. On the other hand, it is important to improve the regulation on the intermediate data checking and calibration. In order to increase work efficiency, popularizing the data processing method and working on a document by multiple people is needed, for onerous data processing.

Conclusions

The experiments presented here demonstrate the possibility of quantitatively measuring time-variable gravity erosion on the steep loess slope. All erosion data in every rainfall event, including the amount of each failure mass, the total amount of soil loss, the total amount of hydraulic erosion, etc., could be calculated according to the videos caught by the Topography Meter.

It is recommendable to make 3D surface together with R2V and ArcGIS although ArcGIS is sufficient for 3D surface modelling, because contour tracing in R2V is implemented on the undistorted original image, and R2V is also in much smaller size and easy to operate.

Acknowledgements This study is supported by the National Natural Science Foundation of China (51079016; 51179021).

References

- Darby SE, Thorne CR (1996) Development and testing of riverbank-stability analysis. *Hydraul Eng* 122:443
- Derbyshire E, Asch TV, Billard A, Meng X (1995) Modelling the erosional susceptibility of landslide catchments in thick loess: Chinese variations on a theme by Jan de Ploey. *Catena* 25:315–331

- Geng J (2011) Structured-light 3D surface imaging: a tutorial. *Adv Opt Photon* 3:128–160
- Guzzetti F, Ardizzone F, Cardinali M, Rossi M, Valigi D (2009) Landslide volumes and landslide mobilization rates in Umbria, central Italy. *Earth Planet Sci Lett* 279:222–229
- Hafidason H, Lien R, Sejrup HP, Forsberg CF, Bryn P (2005) The dating and morphometry of the Storrega Slide. *Mar Petrol Geol* 22:187–194
- Jaiswal P, Westen CJ, Jetten V (2011) Quantitative assessment of landslide hazard along transportation lines using historical records. *Landslides* 8:279–291
- Keefer DK, Larsen MC (2007) Assessing landslide hazards. *Science* 316:1136–1137
- Larsen MC, Torres-Sanchez AJ (1998) The frequency and distribution of recent landslides in three montane tropical regions of Puerto Rico. *Geomorphology* 24:309–331
- Martin Y, Rood K, Schwab JW, Church M (2002) Sediment transfer by shallow landsliding in the Queen Charlotte Islands, British Columbia Canadian. *J Earth Sci* 39:189–205
- Peng T (2007) Algorithms and models for 3-D shape measurement using digital fringe projections. Thesis, University of Maryland
- Sattar A, Konagai K, Kiyota T, Ikeda T, Johansson J (2011) Measurement of debris mass changes and assessment of the dam-break flood potential of earthquake-triggered Hattian landslide dam. *Landslides* 8:171–182
- Tang KL (2004) Soil and water conservation in China. Science Press, Beijing (in Chinese)
- Wang Y, Liu K, Lau D, Hao Q, Hassebrook LG (2010) Maximum SNR pattern strategy for phase shifting methods in structured light illumination. *J Opt Soc Am A* 27:1962–1971
- Whitehouse IE (1983) Distribution of large rock avalanche deposits in the Central Southern Alps, New Zealand. *J Geol Geop* 26:271–279
- Xue Y, Sun M, Ma A (2004) On the reconstruction of three-dimensional complex geological objects using Delaunay triangulation. *Futur Gener Comput Syst* 20:1227–1234
- Zhang S (2005) Real-time 3-D shape measurement. Thesis, Stony Brook University
- Zhao C, Xu XZ, Xu FL, Wang SF (2011) A device to measure dynamic process of slope erosion. *Sci Soil Water Conserv* 10:65–69 (in Chinese)



Study on the Effect of Plant Roots for Stability of Slopes

Udeni P. Nawagamuwa, S. Sarangan, B. Janagan, and S. Neerajapriya

Abstract

There have been several studies on the properties of plants, which are beneficial to critical slopes in preventing failures. However, the impacts of the tensile properties of the plant roots have to be studied in detail. In this study, three different situations were addressed: completely dry, saturated and unsaturated. Under these three situations, stability of different slopes with different soil conditions was studied. Some roots were tested through the tensile testing machine normally used for yarn testing and some were tested with the traditional tensometer. Variation of root diameter was established by measuring the roots of tea plants available at cut slopes. Literature was found on the variation of tensile strength of tea roots with its diameter. Slopes of the tea estates were modeled considering the number of tea plants available in a particular slope. This was later converted to a percentage cover and values of factor of safety (FOS) were compared by changing different soil properties with the percentage of cover. It was found that the FOS tends to increase with the percentage cover under completely dry, saturated and unsaturated situations. However, it was learnt that the impact of tensile capacity of roots had not been so high under dry and saturated cases for cohesionless soils compared to the same situation under unsaturated condition which had high FOS values due to the plant properties.

Keywords

Slope stability • Tensile strength of plant roots • Percentage cover

Introduction

Slope instability has been a major problem faced by the geotechnical engineers. This causes heavy damages and losses, such as loss of lives and property and which will have a significant impact on the country's economy. It is therefore, necessary to stabilize the slopes in an effective and economical way. There are lots of solutions, such as retaining structures and other different mechanical ways of improving. They effectively provide immediate stabilization

and erosion control on the slopes. However, the adverse effects on the environment and their costs are major drawbacks. There are many internal causes for slope failures such as gravity, weak material and structures, triggering events and water table. Removal of vegetation is a common external factor which will lead to landslide vulnerability in slopes. Loss of vegetative cover often initiates soil degradation causing the site to become less productive. Conventional erosion control and re-vegetation efforts subsequent to construction are often ineffective and fail to adequately protect bare soil from incidental surface erosion and adjacent slope impacts (Menashe 2001). Therefore, it is necessary to have an alternative which is more cost effective and aesthetically pleasing than traditional methods. The reinforcement of soil by vegetation is a preferred solution for the stabilization of both natural and man-made slopes.

U.P. Nawagamuwa (✉) • S. Sarangan • B. Janagan • S. Neerajapriya
Department of Civil Engineering, University of Moratuwa, Moratuwa,
Sri Lanka
e-mail: udeni@uom.lk

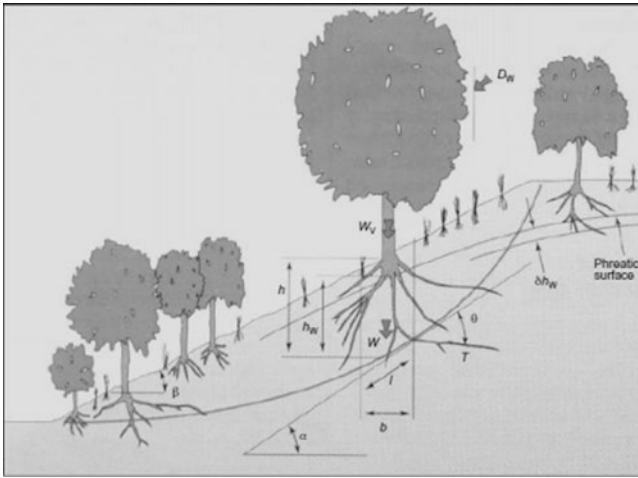


Fig. 1 Role of vegetation in slope stability (Greenwood et al. 2004)

A Bio-Structural approach (by vegetation) to stabilize slopes can be treated as less expensive, more effective, environmental friendly, more adaptable over the long term than purely structural solutions. The vegetation influences the slope stability in following ways:

- By mechanically reinforcing the slopes through plant roots;
- By increasing soil suction or reducing the pore water pressure, hence, increasing the soil shear strength through the removal of water by evaporation through vegetation;
- By the surcharge from the weight of trees; and
- By “wind throwing” or “root wedging”.

Role of vegetation, as presented by Greenwood et al. (2004), is depicted in Fig. 1.

Scope of the Study

The main objective of this research is to study the positive effects of tree roots in reducing landslide vulnerability by conducting laboratory experiments and analysis. Sample collections, carrying out of tensile tests on root samples, developing equations incorporating tensile strength of roots, obtaining FOS for different soil conditions and slope characteristics and analysis of the results are considered as the basic steps of executing this study.

Three scenarios were considered in the analysis:

1. Dry soil condition,
2. Saturated soil condition, and
3. Unsaturated soil condition.

However, only the unsaturated condition is discussed in this paper because the impact of having roots in the system in the other two scenarios is not significant.

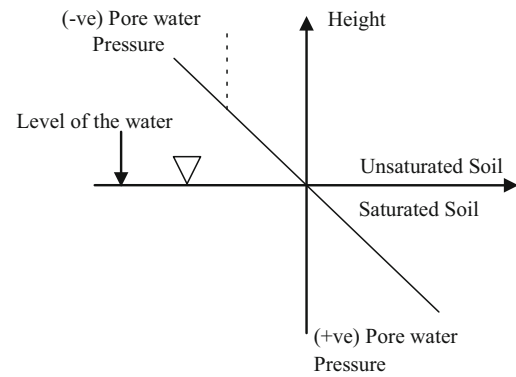


Fig. 2 Variation of matric suction (Sujeewan and Kulathilaka 2010)

Unsaturated Condition and Matric Suction

When the soil is considered as a porous material above the ground water table with some voids filled with air. The soil is in an unsaturated state and three phase system exists with solids, water, and air. Consequently, both pore water pressure (u_w) and pore air pressure (u_a) should be considered in the analysis. The pore air pressure is usually equal to the atmospheric pressure. The pore water pressure above ground water table is less than atmospheric pressure and the variation is presented in a simplified form by Sujeewan and Kulathilaka (2010). Providing a limit to the practically possible maximum matric suction, a more realistic distribution is presented by the broken lines in Fig. 2. Two stress variables $\sigma - u_a$ termed net normal stress and $u_a - u_w$ termed matric suction have been considered.

Further variations of the pore water pressure with depth is presented by Sujeewan and Kulathilaka (2010) as shown in Fig. 3. The different curves in Fig. 3 refer to prolonged rainfall as given in the legend. The shear strength of the unsaturated soils is enhanced by the presence of matric suction. With the infiltration of rainwater, the matric suction will be depleted upto some depth. As the rain event progresses, the depth of depletion increases.

Tensile Capacity of Tea Roots

Tensile force was tested for different root diameters and the results showed that the tensile force of the tea plant increased significantly with increasing root diameter. The vertical roots penetrate the slip surface to work against failure. This situation assumes that the tensile strength of roots becomes fully mobilized for the roots that are deeply embedded into the soil. The following equation represents the relationship between tensile force and root diameter of tea plant (Lateh et al. 2011).

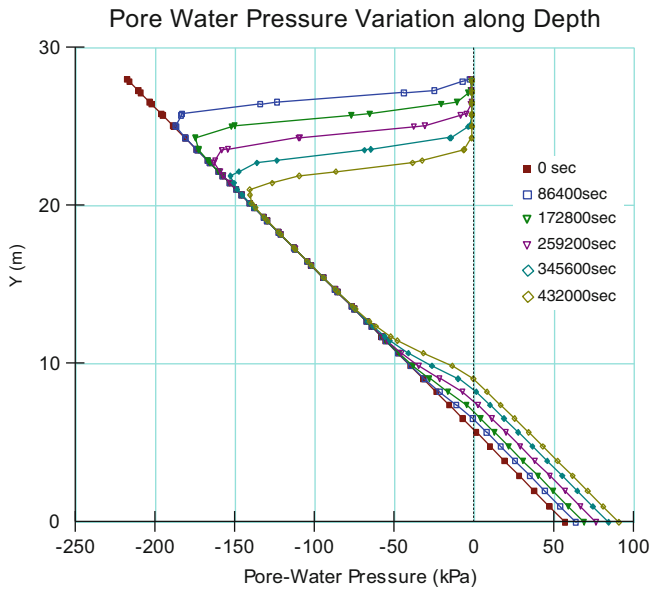


Fig. 3 Pore water pressure variation along depth (Sujeewan and Kulathilaka 2010)

$$TFr = 0.023d^2 + 0.051d + 0.069 \quad (1)$$

TFr had been defined as the root tensile force of a tea plant and d is the diameter of the root (Lateh et al. 2011). This result is shown in Fig. 4. The results obtained for the considered plants have been checked and proved to be in agreement with many other authors (Bischetti et al. 2005; Genet et al. 2005) confirming the validity of the general power law equation for the relationship between root tensile strength and root diameter.

The following equations were developed using Bishop’s method after incorporating tensile strength of roots. It should be noted that the effective internal friction angle φ' is unaffected by root reinforcement (as confirmed by Genet et al. 2006).

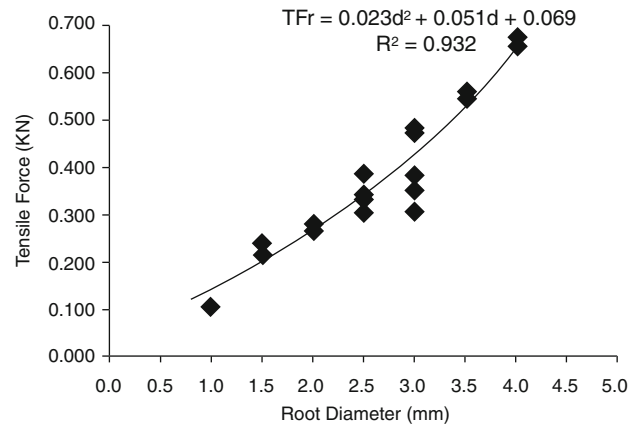


Fig. 4 Tensile capacity vs root diameter (Lateh et al. 2011)

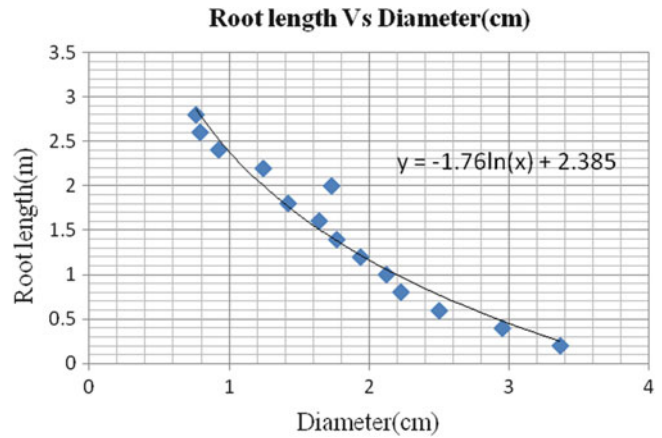


Fig. 5 Root length vs. diameter relationship for Sri Lankan tea plants

$$F = \frac{\sum \frac{c' \Delta x_i}{M_i(\theta)} + T_r \sin \theta_i + \frac{\{w_i - u_m \Delta x_i\} \tan \varphi'}{M_i(\theta)} - [u_m \tan \varphi^b \Delta x_i \tan \theta_i] \left[\frac{1}{\cos \theta_i} - \frac{1}{M_i(\theta)} \right]}{\sum w_i \sin \theta_i} \quad (2)$$

For the case, without tree roots

$$F = \frac{\sum \frac{c' \Delta x_i}{M_i(\theta)} + \frac{\{w_i - u_m \Delta x_i\} \tan \varphi'}{M_i(\theta)} - [u_m \tan \varphi^b \Delta x_i \tan \theta_i] \left[\frac{1}{\cos \theta_i} - \frac{1}{M_i(\theta)} \right]}{\sum w_i \sin \theta_i} \quad (3)$$

Fig. 6 Roots were visible near cut slopes in the estate sector

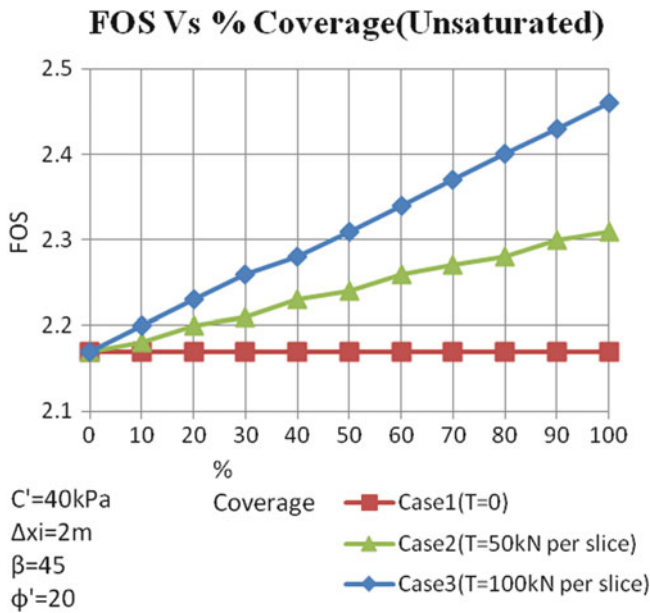
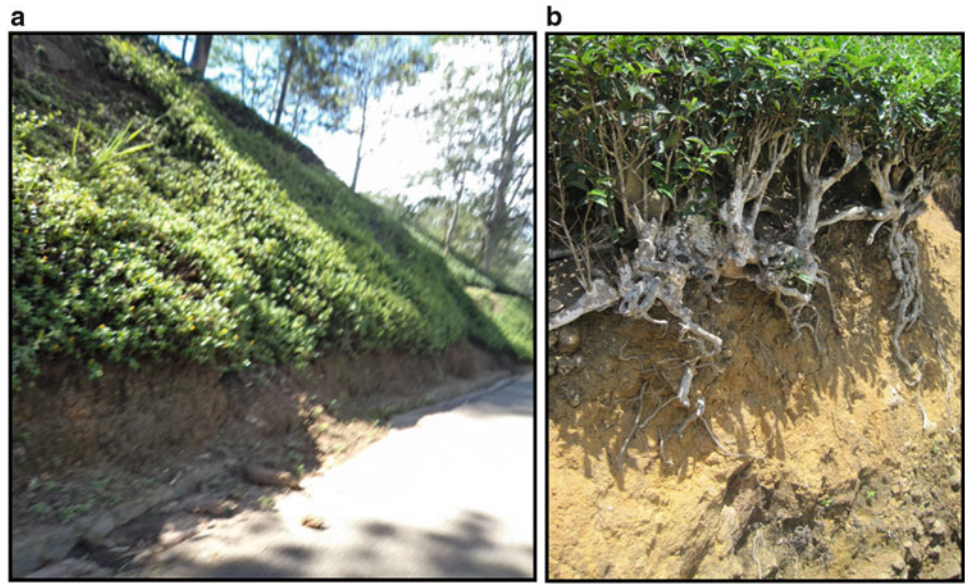


Fig. 7 Obtained graphs for above specified soil and slope characteristics

To develop equations (2) and (3), following relationship was used, considering the shear strength properties of unsaturated soils.

$$\tau = \frac{1}{F} [c' + (\sigma_n - u_a) \tan \varphi' + (u_a - u_w) \tan \varphi^b] \quad (4)$$

Following key notations are used in this study:

- F—Factor of Safety
- c'—Cohesion
- w_i—Weight of the ith soil slice

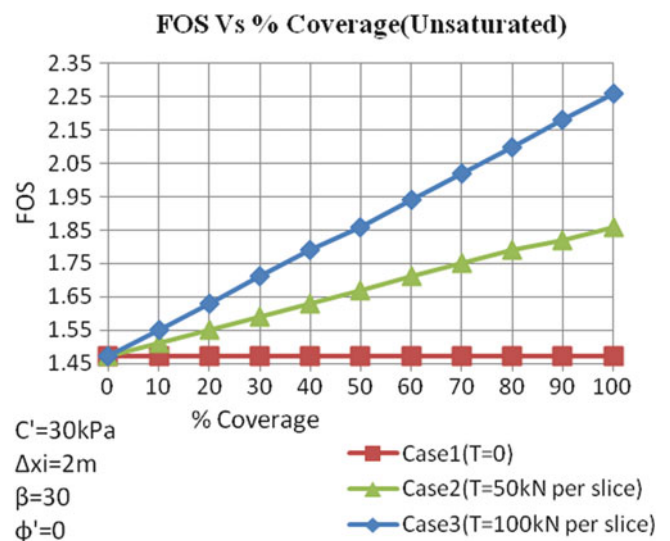
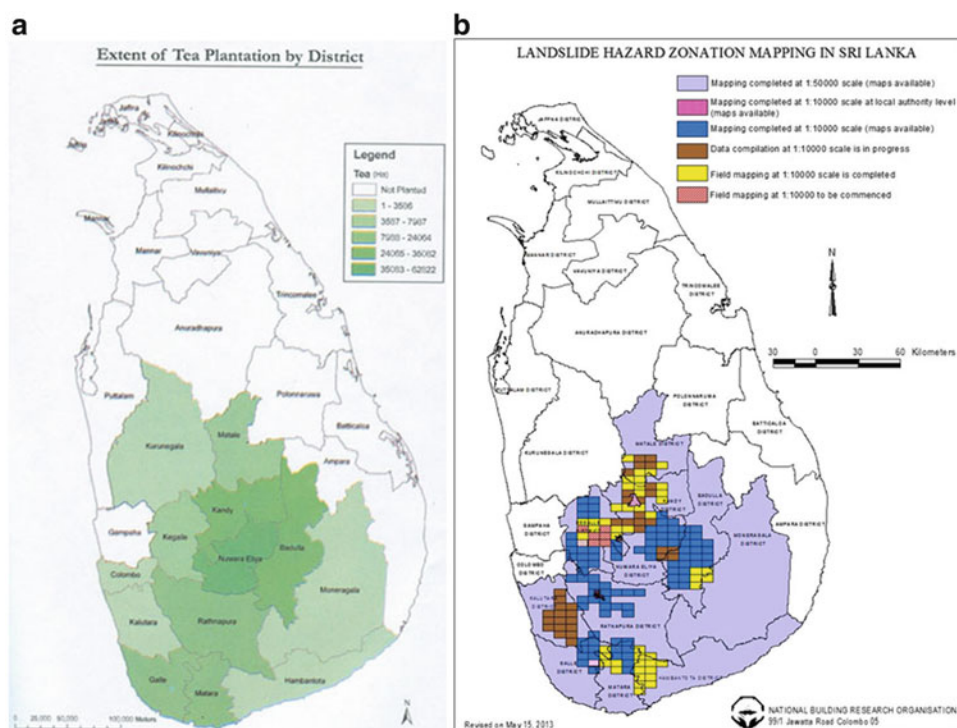


Fig. 8 Obtained graphs for a specified soil and slope characteristics (details are given in the figure itself)

- β—Slope angle
- u_i—Pore water pressure on the ith slice
- φ'—Friction angle
- T_r—Tensile capacity root
- Δx_i—Horizontal width of slice
- φ^b—Angle indicating the rate of increase in shear strength relative to the matric suction
- (u_a—u_w)—matric suction

Shear strength parameters could be measured using drained triaxial shear tests. However, this research study assumed several possible variations in strength parameters and numerically evaluated different factor of safety values.

Fig. 9 (a) Tea plantation map of Sri Lanka and (b) Landslide hazard zonation map of Sri Lanka (courtesy of NBRO, Sri Lanka)



Values of Matric Suction

The above equations contain the term matric suction. This means that for evaluating the factor of safety, matric suction should be readily available at the failure surface. The matric suction pressures can be achieved by directly measuring the pore water and air pressures of a specimen. However, in this research, values for matric suction were obtained from the study carried out by Sujeevan and Kulathilaka (2010).

The tensile strength of the tree roots against their root diameter was obtained from Lateh et al. (2011). Required samples were collected from tea estates and subsequently, the root length vs root diameter relationship was developed. For the calculations, expected root length was estimated and with that possible root diameter, the corresponding tensile capacity were obtained. Those results are shown in Fig. 5. Data was collected to obtain a relationship between root diameter and root length from Sri Lankan tea estates where roots are visible at near cut slopes in the estate sector. Few such examples are shown in Fig. 6a, b.

Percentage Cover

Percentage cover is defined in this research as the fraction between the available number of trees in a slope and the maximum number of trees that can occupy the slope. For example, if a 100 kN (representing all the roots) tensile

capacity is considered for a slice that means this 100 kN is the maximum tensile capacity that can be mobilised with the fully covered vegetation. Then, for the 50 % coverage, 50 kN (representing all the roots) tensile capacity is used for calculations.

Discussion of Results

Different values for factor of safety were numerically evaluated by varying the shear strength parameters. Figures 7 and 8 show some selected results for different conditions. These results clearly indicate that there is a high influence of plant roots (due to coverage) towards the factor of safety. The tea plants in Sri Lankan estate sector were chosen for the study because most of the critical slopes in the central province (land slide prone area) are occupied by tea plants. This can be clearly observed in the Fig. 9a, b, which contain a Tea Plantation map of Sri Lanka and a Hazard Zonation map of Sri Lanka, respectively.

It was further learnt that due to proper management of surface water and practice of tea plants in the tea estate sector, the vulnerability to landslides is noticeably low. Through the literature review, a relationship between the root tensile capacities of tree roots with its diameter was obtained. Developed equation required the tensile capacity of the roots in the failure plane. Therefore, tea root samples were collected and the root lengths were measured with its diameter where the roots are exposed in the visible slopes.

However, it should be noted that the root tensile capacity graph obtained from the literature review is not from Sri Lanka and it was assumed that the tensile capacity of the tree roots would not change significantly.

It was considered that the tensile forces will not contribute to equilibrium of the soil wedge when it is in equilibrium. The tensile force will be mobilized when the soil wedge exceeds limit equilibrium condition.

Conclusions

Following conclusions could be made with the findings of this study:

- Factor of safety (FOS) plots clearly show that the FOS linearly increases with the percentage coverage of tree roots.
- Steeper slopes without cohesion, cannot be considered as suitable even with the full vegetation coverage.
- Matric suction enhances the FOS values of the slopes, but as the rainfall increases, matric suction depletes and this will cause a reduction in FOS and slope instability.
- The results were obtained by considering only the effects of tree roots and surcharge from the plants but transpiration and wind effects are not considered.
- The surcharge from the tree roots increases the slope instability but the plants in the toes of the slopes contribute to the stability of slopes.

Acknowledgments Authors would like to acknowledge the Department of Civil Engineering and the Department of Textile and Technology, University of Moratuwa, Sri Lanka for their help in laboratory studies.

References

- Bischetti GB, Chiaradia EA, Simonato T (2005) Root strength and root area ratio of forest species in Lombardy (Northern Italy). *Plant Soil* 278:11–22
- Genet M, Stokes A, Salin F, Mickovski SB, Fourcaud T, Dumail J-F, van Beek R (2005) The influence of cellulose content on tensile strength in tree roots. *Plant Soil* 278:1–9
- Genet M, Stokes A, Fourcaud T, Cai X, Lu Y et al (2006) Soil fixation by tree roots: changes in root reinforcement parameters with age in *Cryptomeria Japonica* D. Don. plantations. In: Marui H (ed) Disaster mitigation of debris flows, slope failures and landslides. Universal Academy Press, Tokyo, pp 535–542
- Greenwood J, Norris J, Wint J (2004) Assessing the contribution of vegetation to slope stability. *Proc Inst Civ Eng* 157(4):199–207
- Lathe H, Baker MB, Khan YA, Abustan I (2011) Influence of tensile force of agave and tea plants roots on experimental prototype slopes. *Int J Phys Sci* 6:4435–4440
- Menashe E (2001) Bio-structural erosion control: incorporating vegetation in engineering designs to protect puget sound shorelines. Puget Sound Research 2001, Bellevue, WA
- Sujeewan V, Kulathilaka SAS (2010) Rainfall infiltration analysis in unsaturated residual slopes, UG research study. Department of civil Engineering, University of Moratuwa, Sri Lanka



The Dynamic Process and Sensitivity Analysis for Debris Flow

Guoqiang Yu, Maosheng Zhang, and Hong Chen

Abstract

The dynamic process and sensitivity in the debris transportation process are important topics in the study of rapid landslides and debris flows. The motion process of debris flow is recognised as a dynamic interaction between the original moving material and the entrained basal topsoil shearing along their non-slip contact surface. In this paper, we employed numerical modelling to clarify the erosional effects, and use statistical method to compare the influence degree of rheological parameters on the runout behavior. The simulated results show that unconfined flows typically exhibit a wide range of entrainment and deposition volume, whereas confined flows yield moderate volumes of entrainment and small volumes of deposition. The basal topography is an important factor in influencing the debris transportation and deposition processes. The velocity, runout distance, and deposition area and volume are more sensitive to underlying surface conditions, particles of debris, pore water pressure; and can affect the debris intensity, disaster area and scale to a large extent. Conversely, the velocity, runout distance, and deposition area and volume, are less sensitive to the source volume of debris flows, and can only affect the velocity to a little extent. The proposed suggestions can be utilized conveniently in general geotechnical engineering practices.

Keywords

Debris flow • Rheological modelling • Dynamic process • Sensitivity

G. Yu (✉) • M. Zhang
Key Laboratory for Geo-hazards in Loess area, MLR, Xi'an 710054,
People's Republic of China

Xi'an Regional Center, China Geological Survey, Xi'an 710054,
People's Republic of China
e-mail: yuguoqiang23@163.com; xazms@126.com

H. Chen
Department of Civil and Environmental Engineering, University of
Alberta, Edmonton, AB, Canada

Klohn Crippen Berger, 500 - 2618 Hopewell Place NE, Calgary, AB
T1Y 7J7, Canada

Introduction

Debris flows are rapid, gravity-induced mass movements of granular solids, water, and air (Varnes 1978). They usually occur in regions with steep relief and at least occasional rainfall (Jakob 2005; Schuster et al. 2002; Takahashi 1981). Because of their high mobility, velocity, and density, debris flows can be very destructive and damaging when they encounter infrastructures such as buildings, roads, bridges, pipelines, and hydropower facilities, and they may lead to loss of human life (Chen and Lee 2000, 2003). Debris flows are widespread and common in many steeply sloping areas. In mountain areas, intense and localised storms may cause flash floods with significant sediment transport. In steep torrents, the sediment discharge may increase so that the solid volumetric concentration often exceeds 40–50 %. Such events are

called debris flows and transport huge volumes of sediments that are then deposited on alluvial fans, which are often densely populated. In recent years, debris flows have been recognized as one of the major natural risks.

The mechanism of mass changes in a debris transportation process is an interesting but sometimes controversial topic. Based on the equation of motion, Cannon and Savage (1988) developed a lumped-mass model to consider the entrainment or subtracting material lost during debris movement, in which the existence of action–reaction pairs of forces propelling the slide mass along the runout surface was implied. Similarly, van Gassen and Cruden (1989) explained the momentum transfer of debris deposition, and calculated runout distances of rockslides. However, Hungr (1990a, b) pointed out that there were no such forces to propel the slide mass along the runout path; the velocity of mass expelled from the flow must be equal to zero. Erlichson (1991) also indicated that the depositing material slowed by interaction with the bed rather than with the material that continues to move. The cited author further concluded that the equation of motion is unsuitable to apply directly to the debris flow system.

Basal erosion and surficial material entrainment are frequently observed in the field on debris flows during runouts. It embodies the process by which the underlying material is incorporated into the original moving material, resulting in a material volume enlargement of the moving system. Gully erosion and soil slip through the removal of topsoil carve out a low-relief erosional topography. Material can also be lost from the flow by deposition in the form of detached tails or lateral levees during runout. Therefore, mass changes in debris runout affect the behaviour of the flow system and the areal extents of debris. However, few researchers have focused on the impacts of rheological parameters of debris flow on the mass changes, erosion and entrainment of mass, and dynamic process of debris flow.

The aims of the present study were: (1) to analyze the mobility of debris flow using the quasi-three-dimensional finite-element method in the Lagrangian frame of reference; (2) to evaluate the influence degree of the basal friction and the turbulent coefficient of debris on the behaviour of erosion and entrainment, and to quantitatively assess the sensitivity of rheological parameters in terms of the Voellmy model of the rheological formulae, by employing the One-way and Two-way analysis of variance (ANOVA) methods.

Numerical Modelling

In the present study, mobility analyses are conducted using the quasi-three-dimensional finite element method of Chen and Lee (2000) in the Lagrangian frame of reference. We calibrate the model parameters through soil test and back-

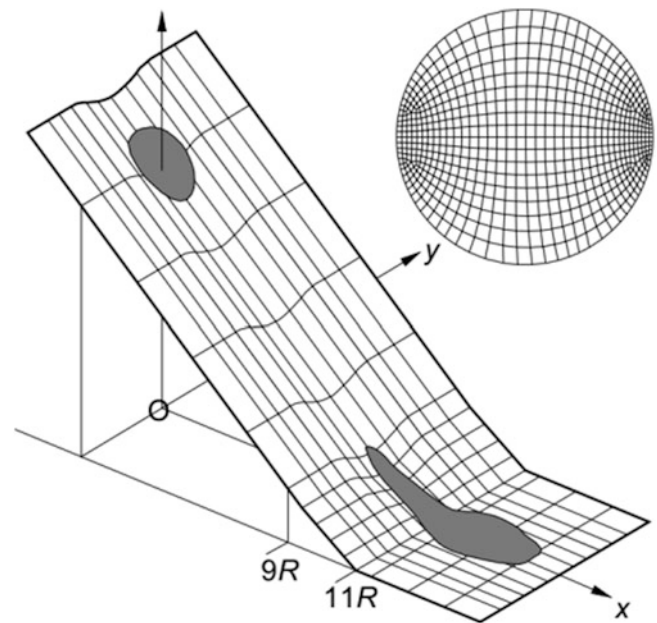


Fig. 1 Set-up of the numerical experiments

analyses of the past slope failures. We then assign series of rheological parameters to numerically model those scenarios analogous to different basal and scale conditions and use them to predict the runout, with different turbulence coefficients and dynamic basal friction angles. Validations and applications of the adopted numerical method can also be found in Chen and Lee (2002, 2003) and Crosta et al. (2004) with various rheologic kernels.

In order to evaluate the erosional effects on debris runout behaviour, we set up the series of numerical modelling with concave basal topographies, rheologic formulae (Voellmy model) and yield rates (0.007) (Chen et al. 2006). The geometric configurations are designed as an inclined slope (40°) and a horizontal runout zone connected with a linear transition zone. The x – y plane of the Cartesian coordinate sits on the horizontal zone with the origin coinciding with the projection of the centre of mass of the initial material. The x -axis is aligned with the steepest descent of the slope surface (Fig. 1). Two basal topographies are considered for the slope: an inclined plane (series A), and one on which a shallow channel is superposed with a concave cross-slope profile (series B) that laterally constrains the material movement. All tests begin with the same amount of material resting on the upper section of the inclined zone. The initial mass is a spherical cap whose projection on the x – y plane is a circle with radius $R = 1$ m. The maximum height of the initial mass is $H = 1/4 R = 0.25$ m, which gives an initial volume $V_0 = \frac{1}{6} \pi H (3R^2 + H^2) = 1.58 \text{ m}^3$. The slope projected on the x -axis lies in the range $x < 9$ m, and the horizontal runout zone is $x > 11R$, and the slope width is 8 m ($-4 \text{ m} \sim +4 \text{ m}$). The concave channel projected on the y -

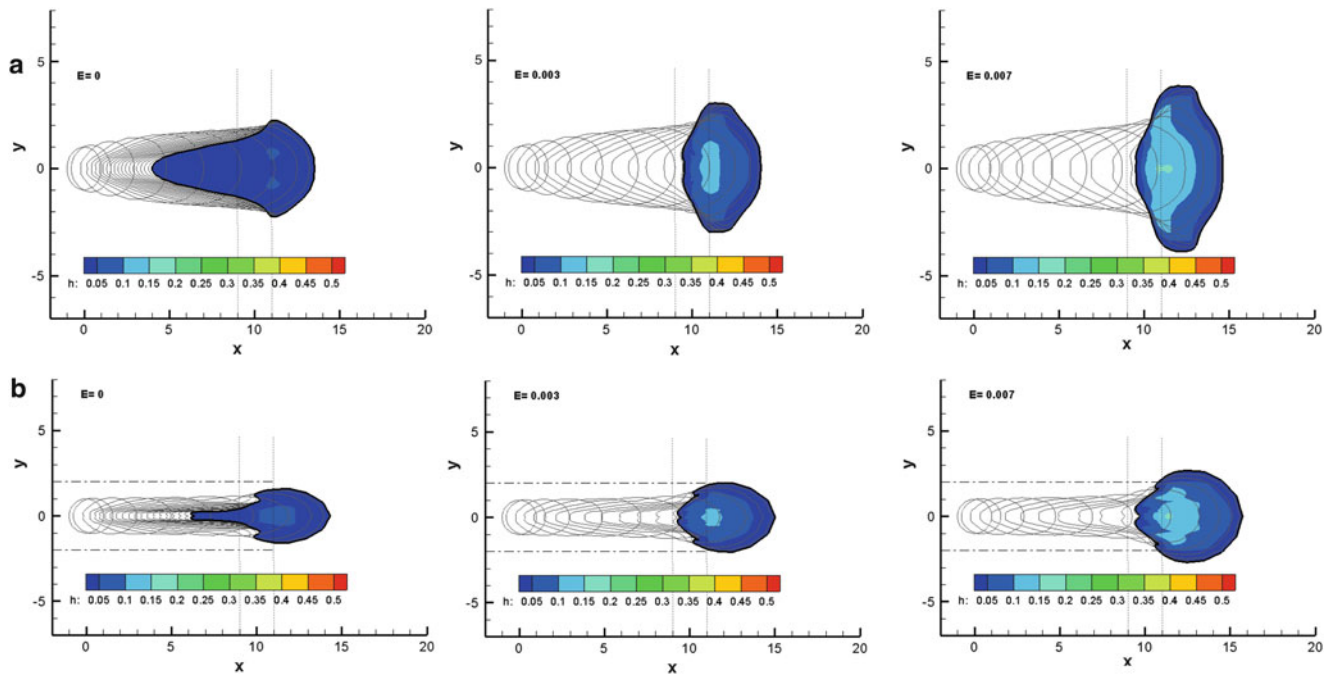


Fig. 2 Projection of debris profiles on horizontal plane (Voellmy model). (a) unconfined flows, (b) partially confined flows

axis lies in the range $-2 \text{ m} < y < 2 \text{ m}$, the deepest part located at $x = 0$, at the depth of 0.25 m .

The granular material is assumed to have an internal friction angle $\phi = 30^\circ$. In Voellmy rheology, the effective dynamic friction coefficient $\mu = 0.1$, and the dimensionless turbulent coefficient $\xi = 1,000 \text{ m/s}^2$. The unstructured mesh of the initial mass is shown in the inset in Fig. 1, where the front and rear are intentionally refined. The convergence tests conducted ensure that the resolution of discretisation is sufficient to reveal the most relevant flow features.

Results of Dynamic Process for Debris Flow

Figure 2a gives the time sequence of the margins of the unconfined flows (series A). The margin changes from initially a circle to a teardrop shape with a wider, blunt front but a concave, narrow end, which may be caused by the turbulent effect from the Voellmy rheology. Lateral spreading is significant. A higher yield rate results in a flatter rear. For channelized flows (series B), longitudinal stretching is dominant but lateral spreading is trivial because of side confinement, as shown in Fig. 2b. The convex front deposits in the horizontal zone while the narrow concave rear is still up in the transition zone that is partially confined. Entrainment with a higher yield rate produces a blunter, less pointed front.

The deposit profiles and thickness distributions are also included in Fig. 2, showing a blunt concave front

(unconfined flow, series A) and a tongue-shaped front (channelized flow, series B) respectively. A higher yield rate always corresponds to a wider front and a longer propagation. For the same yield rate, the front of the channelized flow (series B) displaces further than that of the unconfined flow (series A). It is also noted that the maximum deposit thickness locates largely in the mid-deposit, or slightly towards the front, although the front and the tail are thinly distributed. The centre of mass of the deposit is almost around its maximum thickness. The mass profiles are cut longitudinally along the centre of the descending axis of the flow, shaping from a relatively thick tail and a thin front to a thick body and a thin proximal end in the deposition zone. A higher erosion rate corresponds to a thicker deposit depth. In comparison, the entrainment and runout geometry strongly influences the variations of mean velocity. Generally, the entire body of the debris moves faster, but it also halts faster owing to the increase of system inertia through erosion. Under the same yield rate, the mean velocity of the channelized flow has a higher peak value but decreases faster than that of the unconfined flow. Again, for the same yield rates, the unconfined flows remove more material from the bed during runout than the channelized ones. The front velocity during runout shows a similar trend regardless of yield rate or runout geometry conditions. Under the same runout geometry, a larger value of front velocity corresponds to a higher yield rate. Under the same yield rate, the fronts of unconfined flows move slower than those of channelized ones when they travel the same distance.

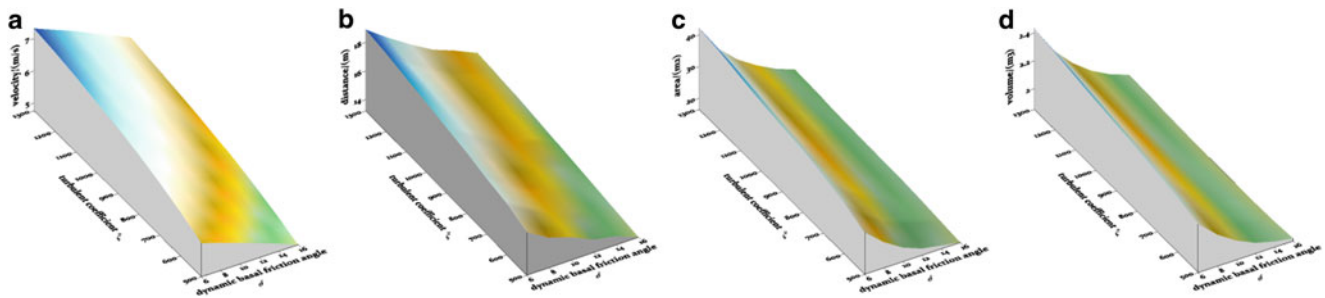


Fig. 3 Three-dimensional surface map of each index. (a) The maximum velocity, (b) movement distance, (c) deposition area, (d) deposition volume

Results of Sensitivity Analysis for Rheological Parameters

Numerical Simulation Analysis on Debris Mobility with Different Rheological Parameters

In order to evaluate the sensitivity of rheological parameters to debris runout behaviour, we consider the influence of basal friction and the turbulence coefficient on the debris mobility. The numerical experiments involve a total of 54 working conditions, including six dynamic basal friction angles (6–16°, with increment $\Delta\delta = 2^\circ$) and nine turbulence coefficient (500–1,300 m/s², with increment $\Delta\xi = 100$ m/s²).

The three-dimensional surface maps of maximum velocity, movement distance, deposition area and deposition volume under different dynamic basal friction angle and turbulent coefficient are shown in Fig. 3. It shows that the variation tendency of maximum velocity is the same as the other three indices; however, the tendency of maximum velocity is closer to the plane (see Fig. 3a). Under the same turbulence coefficient, maximum velocity decrease linearly with the gradual increase of basal friction angle, under different turbulence coefficient, the decreasing trend and extent of maximum velocity are consistent. On the other hand, under the same basal friction angle, maximum velocity increases linearly with the increase of the turbulence coefficients, under the different basal friction angle, the increasing trend and extent of maximum velocity are consistent.

The variation tendencies of other three indices are similar to that with velocity; the three-dimensional surface maps are of curved shape. Under the same turbulence coefficient, movement distance, deposition area and volume are concave decreasing trend in the increase of basal friction angle. Under different turbulence coefficient, the decreasing trend of three indices is consistent; however, the extent of reduction is greater than the change in velocity. Under the same basal friction angle, movement distance, deposition area and

volume are linearly increasing; the extent of reduction is little. The extent of the increase gradually decreases with the increase of basal friction angle.

One-Way ANOVA on Intensity and Scale of Debris Flow

A One-Way ANOVA (Analysis of Variance) is a statistical technique by which we can test if three or more means are equal. It tests if the value of a single variable differs significantly among three or more levels of a factor. In this paper, we respectively tested the means of the single variable such as maximum velocity, movement distance, and deposition area, deposition volume among six levels of dynamic basal friction angles and nine levels turbulence coefficients. The results are shown in Tables 1 and 2.

In terms of the details of the ANOVA test (see Table 1), note that the number of degrees of freedom (DF) for the between groups (8) is less than the number of DF within groups (45) and the overall F test is significant ($F \gg 1$, $P \ll 0.001$) in four cases; showing that the variance between groups is greater than the variance within groups, due to the differences by grouping is far beyond the differences by sampling. Therefore, we can reject the original hypothesis, and conclude that there are significant mean differences of each single variable under different dynamic basal friction angles.

In terms of the details of the ANOVA test (see Table 2), note that the number of degrees of freedom (DF) for the between groups (8) is less than the number of DF within groups (45) and the overall F test is significant ($F = 6.772$, $P < 0.001$) in only case of maximum velocity, indicating there are significant mean differences of maximum velocity under different turbulence coefficients. However, the overall F test is insignificant ($F \approx 1$ or < 1 , $P > 0.05$) in other cases of movement distance, and deposition area and deposition volume, showing there are insignificant mean differences of these variables under different turbulence coefficients.

Table 1 One-way ANOVA results under the different dynamic basal friction angle

| Dynamic basal friction angle δ | | Sum of squares | DF | Mean square | F value | Sig. |
|---------------------------------------|----------------|----------------|----|-------------|---------|-------|
| V_{\max} (m/s) | Between groups | 9.018 | 5 | 1.804 | 7.912 | 0.000 |
| | Within groups | 10.943 | 48 | 0.228 | | |
| | Total | 19.961 | 53 | | | |
| Movement distance (m) | Between groups | 85.778 | 5 | 17.156 | 36.835 | 0.000 |
| | Within groups | 22.356 | 48 | 0.466 | | |
| | Total | 108.133 | 53 | | | |
| Deposition area (m ²) | Between groups | 1.376 | 5 | 0.275 | 156.087 | 0.000 |
| | Within groups | 0.085 | 48 | 0.002 | | |
| | Total | 1.461 | 53 | | | |
| Deposition volume (m ³) | Between groups | 2,238.721 | 5 | 447.744 | 73.011 | 0.000 |
| | Within groups | 294.364 | 48 | 6.133 | | |
| | Total | 2,533.086 | 53 | | | |

Table 2 One-way ANOVA results under different turbulence coefficient

| Turbulent coefficient ξ | | Sum of squares | DF | Mean square | F value | Sig. |
|-------------------------------------|----------------|----------------|----|-------------|---------|-------|
| V_{\max} (m/s) | Between groups | 10.904 | 8 | 1.363 | 6.772 | 0.000 |
| | Within groups | 9.057 | 45 | 0.201 | | |
| | Total | 19.961 | 53 | | | |
| Movement distance (m) | Between groups | 21.160 | 8 | 2.645 | 1.369 | 0.236 |
| | Within groups | 86.973 | 45 | 1.933 | | |
| | Total | 108.133 | 53 | | | |
| Deposition area (m ²) | Between groups | 0.054 | 8 | 0.007 | 0.215 | 0.987 |
| | Within groups | 1.407 | 45 | 0.031 | | |
| | Total | 1.461 | 53 | | | |
| Deposition volume (m ³) | Between groups | 237.646 | 8 | 29.706 | 0.582 | 0.787 |
| | Within groups | 2,295.440 | 45 | 51.010 | | |
| | Total | 2,533.086 | 53 | | | |

The ANOVA results therefore show that the dynamic basal friction angle can affect maximum velocity, movement distance, and deposition area and deposition volume of debris flows. Conversely, the turbulence coefficient can only affect maximum velocity.

Two-Way ANOVA on Velocity of Debris Flow

Based on the above analysis, the turbulence coefficients and dynamic basal friction angles can both impact on the velocity of debris flow. Which among the rheological parameters or the interaction between parameters greater impact on the velocity? We employed a two-way ANOVA to solve it.

The profile plot is a line plot in which each point indicates the estimated marginal mean of a dependent variable (velocity) at one level of a factor. The levels of a second factor can be used to make separate lines (see Fig. 4a, b). As can be seen from these figures, profile plots of each factor are parallel, is not convergent. It shows that the effect of basal friction angle, and the effect of turbulence coefficient are independent of the maximum flow rate, and there is no interaction between two parameters, which means that

there is only the effect of main factors. Therefore, we employed a Two-Way ANOVA without interaction to compare the effect of multiple levels of two factors (turbulence coefficient and dynamic basal friction angle). The results are shown in Table 3.

In terms of the details of the ANOVA test (see Table 3), the overall F test is significant ($F \gg 1$, $P \ll 0.001$) of two factors; indicating that there are significant mean differences of velocity under different dynamic basal friction angles and turbulent coefficient. On the other hand, the F value of dynamic basal friction angle is bigger than F value of dynamic basal friction angle, showing that the influence of dynamic basal friction angle on debris is greater than the impact of the turbulent coefficients.

Conclusions

The front of the channelized flows propagates further than that of the unconfined flows, as confinement strongly influences the overall displacement and the thickness distribution in the deposition zone. Moreover, the volumetric accumulation processes demonstrate that unconfined flows erode more materials than their channelized counterparts owing to the lateral spreading. The computational results

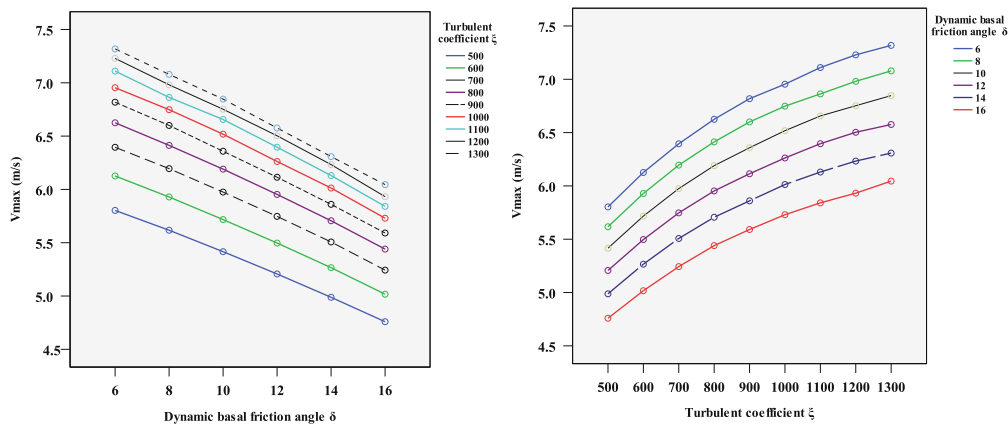


Fig. 4 The profile plot of marginal mean of the velocity

Table 3 Two-way ANOVA results of the maximum velocity without interaction

| Source | Type III sum of squares | df | Mean square | F value | Sig. |
|------------------------------|-------------------------|----|-------------|---------------|-------|
| Corrected model | 19.923 ^a | 13 | 1.533 | 1,584.389 | 0.000 |
| Intercept | 2,030.084 | 1 | 2,030.084 | 2,098,816.831 | 0.000 |
| Dynamic basal friction angle | 9.018 | 5 | 1.804 | 1,864.758 | 0.000 |
| Turbulent coefficient | 10.904 | 8 | 1.363 | 1,409.158 | 0.000 |
| Error | 0.039 | 40 | 0.001 | | |
| Total | 2,050.046 | 54 | | | |
| Corrected total | 19.961 | 53 | | | |

^aR squared = 0.998 (adjusted R squared = 0.997)

coincide with some field observations that unconfined flows typically exhibit a wide range of entrainment and deposition volume, whereas confined flows yield moderate volumes of entrainment and small volumes of deposition. The calculations also suggest that basal topography is an important factor influencing the debris transportation and deposition processes.

A higher friction angle can lead to greater energy dissipation, and a higher turbulent coefficient can sweep more material of the surrounding medium. The basal condition and turbulent item both influence the velocity, and the effect of basal condition is greater than the turbulent item on the velocity, and there is no interaction effect between the two parameters on the velocity.

The velocity, runout distance, and deposition area and volume are more sensitive to underlying surface conditions, particles of debris, pore water pressure; it shows that these factors have very close connection with debris intensity and disaster area and scale, and can affect the debris intensity and disaster area and scale to a large extent. Conversely, the velocity, runout distance, and deposition area and volume, are less sensitive to the source volume of debris flows, and can only affect the velocity to a little extent.

Acknowledgements This research was funded and supported by the National Natural Science Foundation of China (No: 41330858,

41302224, 41071182), the National Basic Research Program of China (2011CB403302), China Postdoctoral Science Foundation (No: 2012 T50797, 2011M501445) and Natural Science Foundation of Shanxi Province, China (No: 2012JQ5001). We are grateful to the anonymous reviewers for their valuable suggestions in improving the manuscript.

References

- Cannon SH, Savage WZ (1988) A mass change model for the estimation of debris flow runout. *J Geol* 96:221–227
- Chen H, Lee CF (2000) Numerical simulation of debris flows. *Can Geotech J* 37:146–160
- Chen H, Lee CF (2002) Runout analysis of slurry flows with Bingham model. *ASCE J Geotech Geoenviron Eng* 128:1032–1042
- Chen H, Lee CF (2003) A dynamic model for rainfall-induced landslides on natural slopes. *Geomorphology* 51:269–288
- Chen H, Crosta GB, Lee CF (2006) Erosional effects on runout of fast landslides, debris flows and avalanches: a numerical investigation. *Geotechnique* 56(5):305–322
- Crosta GB, Chen H, Lee CF (2004) Replay of the 1987 Val Pola Landslide, Italian Alps. *Geomorphology* 60(1–2):127–146
- Erlischon H (1991) A mass-change model for the estimation of debris-flow runout, a second discussion: conditions for the application of the rocket equation. *J Geol* 99:633–634
- Hungr O (1990a) A mass-change model for the estimation of debris-flow runout: a discussion. *J Geol* 98:791
- Hungr O (1990b) Momentum transfer and friction in the debris of rock avalanche: discussion. *Can Geotech J* 27:697
- Jakob M (2005) Debris-flow hazard analysis. In: Jakob M, Hungr O (eds) *Debris-flow hazards and related phenomena*. Praxis-Springer, Berlin, pp 411–443

- Schuster RL, Salcedo DA, Valenzuela L (2002) Overview of catastrophic landslides of South America in the twentieth century. In: Evans SG, DeGraff JV (eds) Catastrophic landslides: effects, occurrence, and mechanisms. Geological Society of America, Boulder, pp 1–34
- Takahashi T (1981) Estimation of potential debris flows and their hazardous zones. *J Nat Disas Sci* 3(1):57–89
- Van Gassen W, Cruden DM (1989) Momentum transfer and friction in the debris of rock avalanche. *Can Geotech J* 26:623–628
- Varnes DJ (1978) Slope movement types and processes. In: Schuster RL, Krizek RJ (eds) Landslides analysis and control, vol 176, Transportation Research Board Special Report. National Research Council, Washington, pp 11–33



Evaluation of Sensitivity of the WAA and SINMAP Models (Static) for Landslide Susceptibility Risk Mapping in Sri Lanka

A.A. Virajh Dias and A.A.J.K. Gunathilake

Abstract

Shallow landslides are one of the most common types of failures occurring frequently in steep slopes, overburden soil and landscapes in different climatic zones. The effect of topography, slope angle, slope drainage, vicinity of road and infrastructure, overburden soil depth and geology are important factors for the interpretation of the recurrence of shallow landslides. Data, although insufficient in number, has stimulated the debate about the effect of geology and topography on the susceptibility of shallow landsliding. An Analytical Hierarchical Process is applied in order to derive the weights associated with attribute map layers. Based on these weights, GIS datasets are combined by weighted Average Analysis (WAA) and the landslide susceptibility map of the study area is created. The resulting information was compared with the landslide susceptibility map derived through the Stability Index Mapping (SINMAP) model. Both outputs are useful for a better understanding of landslide susceptibility and their origins and prioritization of efforts for the reduction and mitigation of future landslide hazards. Sensitivity of both approaches was fine tuned with the overburden soil strength parameters, geomorphological evidences and field verification techniques.

Keywords

Landslides • AHP • Susceptibility • SINMAP

Introduction

Natural instabilities and movement of material on hill slopes have induced researchers to model and predict the behavior of landslide movements. The most common slope instabilities in Sri Lanka represented by an initial shallow rotational or translational slides followed by a flowage mass (Cooray 1994). The infiltration of heavy downpours within

relatively short periods of time creates the development of excessive pore water pressure at shallow depths of the slope almost parallel to the morphology. Contact with less permeable bedrock tends to increase the pore water pressure and cause significant reduction of shear strength or causes the soil to reach a maximum permissible strain leading to downward and outward movement of the slope (Bhandari et al. 1992). Such regional scale destabilisations are, therefore, necessary to evaluate the landslide susceptibility through an appropriate spatial analysis model to interpret the potentially hazardous conditions.

A.A.V. Dias (✉)

Central Engineering Consultancy Bureau, Centre for Research and Development, Colombo 7, Sri Lanka
e-mail: aavirajhd@yahoo.com

A.A.J.K. Gunathilake

Department of Geology, Post Graduate Institute of Science, University of Peradeniya, Peradeniya, Sri Lanka
e-mail: aajkg@yahoo.com

Slope Dynamics

Landslides result from independent or combined effect of spatio-temporal intrinsic and extrinsic variables, including hydrology (rainfall, evapotranspiration and ground water), topography (slopes and ground setting), geology (soil and rock), land use (vegetation surcharge, and root strength) and human activities including excavation, trenching and backfilling (Van Westen 1993). Relatively static environmental factors (i.e. elevation, slope, aspect and topographic curvatures) exhibit negligible changes in their state through time and differ from dynamic factors such as climatic or human activities which tend to alter landslide susceptibility through time (Varnes 1984). However, the spatio-temporal differences do exist in both environments. To predict the spatial and temporal pattern of the areas susceptible to landslide, a distribution approach is needed that incorporates varying precipitation intensity, soil depth, vegetation (species, age, density) and root strength. Some of the difficulties arise in the modeling of the unsaturated boundary condition and the flow through the unsaturated soil (Dias et al. 2001).

Understanding factors which influence slope stability should be firmly based on the principles of effective stress and the influence of strains and deformations on shear strength. Moreover, the importance of geology, geological history and geological modeling can hardly be overstated (Fookes 1997; Fookes et al. 2000; Hutchinson 1988). Conventional stability analyses play a useful but limited role in assessing and managing slopes. For a discussion of the merits and limitations of conventional deterministic and probabilistic analyses, refer to the explanations given in Chowdhury and Flentje (1998).

Landslide dynamics get remarkably modulated by interplay of several factors. Therefore, all related scientific studies must necessarily attempt to correlate cause-effect relationship (Bhandari and Dias 1996). Since the advantage of slope movement and piezometric measurements may not always be available, it may often be helpful to correlate rainfall intensities with possible initiation of Riedel shears and other slope surface features particularly in landslide susceptible areas (Bhandari and Dias 1996).

Study Area

The selected study area is in the Kalawana Administrative Division which belongs to Rathnapura District, Sabaragamuwa Province in Sri Lanka. It runs from 6°35'30" to 6°22'20" northern latitude and from 80°38'25" to 80°17'23" eastern longitude. It is in the Kalawana main watershed drained by three major tributaries namely

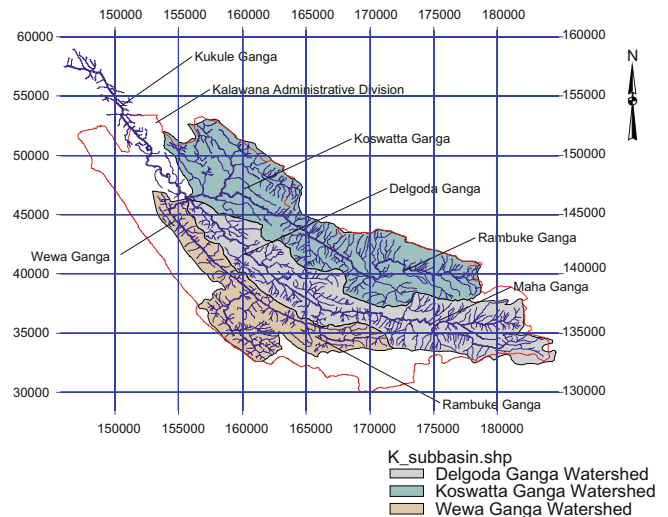


Fig. 1 Overall sanction of the study which includes major sub watersheds of the Kukule Ganga main watershed. Three major tributaries are situated within the Kalawana Administrative Division of the Rathnapura District

Delgoda Ganga, Koswatta Ganga and the Wewa Ganga, as shown in Fig. 1.

SINMAP Model Approach

The shallow landslide usually obeys the infinite slope failure condition. The mathematical models developed by Montgomery and Dietrich (1994), Dietrich et al. (1993) are used to study shallow landslides. The model takes into account the infinite plane slope stability coupled with a steady state topographic hydrologic model.

The stability index (SI) is defined as the probability that a location is stable and is calculated by considering the most and least favourable situations (i.e. lower or upper bounds) and the probability that a certain factor of safety may be attained. The factor of safety calculation (FS) in SINMAP is based on the infinite slope form of the Mohr-Coulomb failure law as expressed by the ratio of stabilizing forces (shear strength) to destabilizing forces (shear stress) on a failure plane parallel to the ground surface (Hammond et al. 1992), shown in Eq. (1).

$$FS = \frac{C_r + C_s + \cos^2 \alpha [\gamma_s (D - D_w) + (\gamma_s - \gamma_w) D_w] \tan \phi}{\sin \alpha \cos \alpha [\gamma_s D]} \quad (1)$$

The specific catchment area is defined by the ratio of the area that drains into the grid cell to the contour length across the grid cell. For steady saturated flow, lateral subsurface flow may be expressed by the transmissivity (T) along the

slope (Pack et al. 1999) using Eq. (2).

$$T \sin \alpha b = K_s D_w \cos \alpha \sin \alpha b \tag{2}$$

where, T is assumed to be constant with depth, b is the flow length, and K_s is saturated hydraulic conductivity. The capacity for subsurface lateral flow is defined by the product of recharge and contributing area in Eq. (3).

$$Ra = K_s D \cos \alpha \sin \alpha b \tag{3}$$

where, D is the vertical thickness of soil. Combining the above equations, an expression (Eq. 4) for the thickness of the water table could be obtained.

$$D_w = D \frac{R}{T} \frac{a}{b \sin \alpha} \tag{4}$$

where $C = (C_r + C_s)/(h r_s g)$ is the combined (root and soil) cohesion made dimensionless relative to the perpendicular soil thickness; $h = D \cos \alpha$ soil thickness, perpendicular to the slope; C_r —root cohesion [N/m^2]; C_s —soil cohesion [N/m^2]; D—the vertical soil depth [m]; α - slope angle; r_s —wet soil density [Kg/m^3]; g—the gravitational acceleration ($9.81 m/s^2$); R—recharge rate (m/h); T—transmissivity (m^2/h); a—specific catchment area (m^2); r_w —the density of the water [Kg/m^3]; ϕ —the internal friction angle of the soil [degree]

Model uses the following assumptions:

- Shallow lateral subsurface flow follows topographic gradients.
- Lateral discharge at each point is in equilibrium with steady state recharge R [m/h].
- The capacity for lateral flux at each point is $T \cdot h$, where T is the soil transmissivity [m^2/h], i.e. hydraulic conductivity [m/h] times soil thickness, h [m].

In Eq. (1), terrain stability model SINMAP can compute all the variables from the topography, except for combined cohesion (C), tan of effective angle of internal friction of soil ($\tan(\phi)$) and wetness index (T/R). The digital elevation model (DEM) and appropriate soil parameters were the fundamental input parameters for the model. For the purpose of detailed calibration of the model, Kalawana Division was initially divided into 10 sub watersheds using the hydrology extension of the ArcView 3.2. The analysis was further extended by sub-dividing to more sub watersheds in old landslide proven areas. The evaluation of the T/R ratio and the combined cohesion (i.e. soil cohesion and the root cohesion) was determined by considering the supportive landuse pattern of the particular watershed. The uncertainty of these parameters is incorporated through the use of uniform probability distributions with lower and upper bounds. The

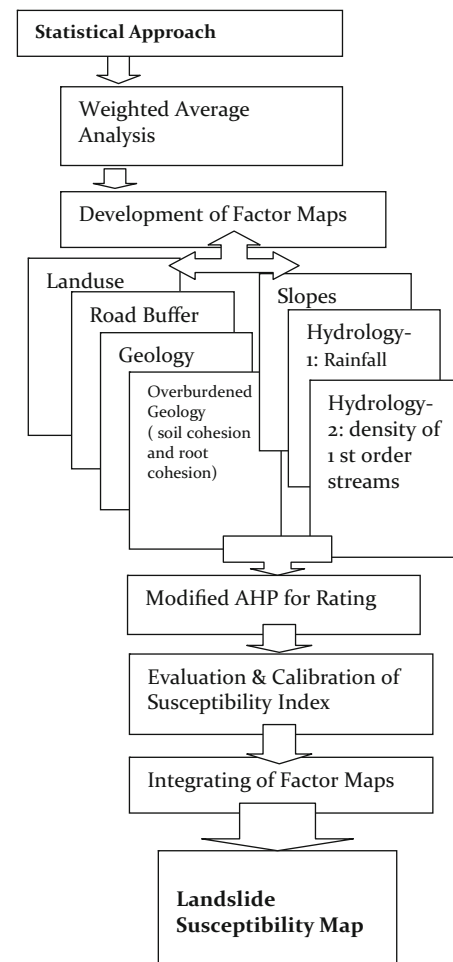


Fig. 2 Method 1: SINMAP model approach for the Landslide Susceptibility Assessment

SINMAP model approach of evaluation of susceptibility coefficient is shown in Fig. 2.

Weighted Average Analysis (Factor Overlay Model) Approach

In the second method of approach, a number of factor maps were used for the study. These were slope maps derived from the DEM, bedrock geology map, landuse map derived from the aerial photos, soil map derived from the average combined cohesion concept (i.e. root cohesion and soil cohesion), derived map of road buffer from slopes, rainfall map and stream density map. Rainfall is a major triggering factor in most slope instability problems on hill slopes. Therefore, hydrological parameters (rainfall and stream density) were considered to obtain a reasonably accurate weight for the analysis. Three days cumulative rainfall distribution pattern in a particular watershed and the total number of 1st order

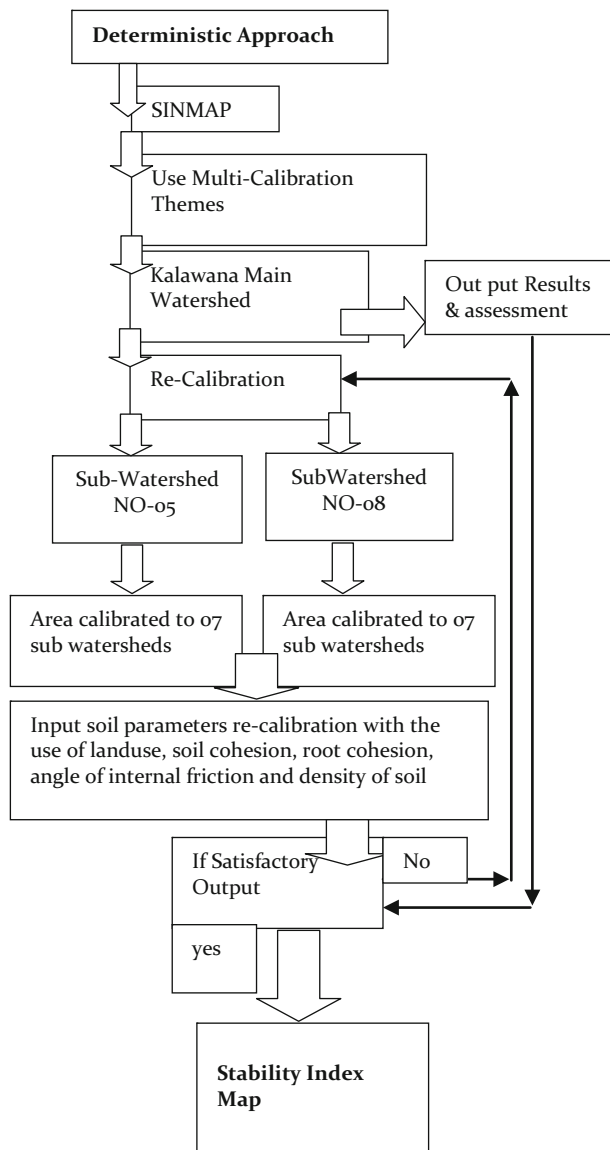


Fig. 3 Method 2: weighted average analysis (factor overlay approach) model approach for the Landslide Susceptibility Assessment

streams in the watershed were considered. The evaluation of weighted average was made through the Analytical Hierarchy Process (AHP). The model approach for the evaluation of the susceptibility coefficient using WAA approach is shown in Fig. 3.

After evaluation of the area with regard to seven factors, at present, the values of seven factors classes X are multiplied by derived individual weights for each factor ($w_1 \dots w_7$) and then are summed together. Then, the total value (M_1) for each pixel and the regional model will be derived in Eq. (5).

$$M_1 = w_1X_1 + w_2X_2 + w_3X_3 + w_4X_4 + w_5X_5 + w_6X_6 + w_7X_7 \quad (5)$$

Table 1 Cohesion parameters for the different landuses

| Landuse pattern as at 2003 | Soil cohesion (kPa) | Root cohesion with soil moisture (kPa) |
|----------------------------|---------------------|--|
| Dense forest | 15.5 | 12 |
| Forest | 12 | 10 |
| Homestead and Barren | 2 | 2 |
| Paddy | 2 | 0 |
| Plantations | 6.5 | 4 |
| Scrub and Grass | 5 | 4 |
| Water Features | 0 | 0 |

Table 2 Laboratory measured value of K (saturated hydraulic conductivity) for various residual soils

| Type of residual formations | Category | Saturated hydraulic conductivity, K (10^3 m/year) |
|-----------------------------|----------|--|
| Clay | Type 5 | <0.0001 |
| Silt, clayey | Type 3 | 0.1–0.4 |
| Silt, slightly sandy clay | Type 2 | 0.5 |
| Silt, moderately sandy | Type 2 | 0.8–0.9 |
| Silt, very sandy | Type 4 | 1.0–1.3 |
| Sandy silt | Type 1 | 1.3 |
| Silty sand | Type 1 | 1.4 |

By replacing the combined weights ($w_1 \dots w_7$) that had been derived previously, the final model was formulated (Eq. 6).

$$M = w_1X_1 + w_2X_2 + w_3X_3 + w_4X_4 + w_5X_5 + w_6X_6 + w_7X_7 \quad (6)$$

Where: M = Susceptibility coefficient.

$X_1 \dots X_7$ = in order, are related to slope, soil, geology, landuse, hydrology 1(rainfall), hydrology 2(1st order streams) and road buffer and, $w_1 \dots w_7$ = are the weights related to each $X_1 \dots X_7$ factors. M varies from 0 to 1; thereafter five number of susceptibility classes were assigned, considering higher values for higher susceptibility of landslides (Dias et al. 2005).

Parameters for Analysis

The relevant parameters for the evaluation of Table 4 derived from various combinations of analysis are shown in Tables 1, 2 and 3 below.

The specific gravity of the soils average from 2.6 to 2.9. Laboratory test for shear strength showed an average effective cohesion (C'), of 6.5 kPa to 15.5 kPa with effective angle of internal friction (ϕ') from 26° to 35° . At the shear boundary, the effective cohesion (C') and effective angle of internal friction (ϕ') were 0 kPa and 22° , respectively.

Table 3 Recommended effective shear strength parameters for the evaluation of landslide Susceptibility using SINMAP

| Soil type | Moist unit weight (kN/m ³) | Saturated unit weight (kN/m ³) | Cohesion intercept (kPa) | Angle of internal friction (°) |
|--------------|--|--|--------------------------|--------------------------------|
| Type 1 SM | 16.5 | 18.5 | 5.0 | 34.0 |
| Type 2 SM | 18.5 | 20.0 | 6.5 | 26.0 |
| Type 3 SM | 18.5 | 20.0 | 0.0 | 21.0 |
| Type 4 SM | 16.5 | 18.5 | 15.5 | 29.2 |
| Type 5 SM/CL | 18.5 | 20.0 | 6.5 | 26.0 |

Results and Discussion

The analysis defines the areas that intuitively appear to be susceptible to landslides. It was noted that few landslides occurred on slopes that would not normally be recognized as susceptible to landslides. This indicates that methodology mis-classified several of these sites as being landslide-prone due to the site-specific conditions and inaccurate input parameters. The wetness index was identified to cause inaccuracy during preliminary modelling of the area, therefore, re-calibration was done by further subdividing the landslide proven watershed areas of the main Kalawana watershed.

Results from the factor of safety calculations are expressed by a stability index based on values of FS ranging from 0 to >1.5. The stability index (SI) is defined as the probability that a location is stable assuming uniform distribution of the soil parameters over their range of values. The classification is divided into six classes. Classes 1–3 are for regions that should not fail according to the model with the most conservative parameters in the specified range. These areas have SI >1.5 and FS >1.0. For classes 4–5, the calculated FS is <1.0, yet the probability of failure is less than and greater than 50 %, respectively. These two classes define a lower and upper limit for ground failure and have SI values 1.0–1.5 and 0–1.0, respectively. Class 6 is unconditionally unstable meaning that the probability of failure

within the specified range of parameters is greatest (assumed >90 % probability). In this case, FS is <1.0 and SI = 0.

In WAA, the state-of-nature attribute maps are well defined under the weighted average technique which explores sensitivity of the geomorphological input parameters such as road buffer, rainfall zones, stream order and overburden geology for the overall assessment. From the resulting weights in Table 4, the most important influential types of factor maps related to the landslide were recognized. Based on the weights assignment, landslide susceptibility was categorised between no-susceptibility to very-high susceptibility. The final weights of the resulting map ranged from 0.036 to 0.585 or 1. The hazard map was grouped into five simplified categories as shown in below based on the histogram of the final weighted values.

| | | |
|---|---------------------|---------------------------|
| 1 | $0 < M < 0.146$ | No susceptibility |
| 2 | $0.146 < M < 0.256$ | Low susceptibility |
| 3 | $0.256 < M < 0.365$ | Moderately susceptibility |
| 4 | $0.365 < M < 0.475$ | High susceptibility |
| 5 | $0.475 < M < 1$ | Very high susceptibility |

The final output is shown in Table 4 before and after recalibration. The overall map output and evaluation of sensitivity is shown in Fig. 4.

Conclusion and Recommendations

The above findings indicate the variability of the conceptual models and their relative importance with the input databases. The detailed and comprehensive geographical information databases are required to obtain the statistical interpretation and calibration of the model. Similarly, soil saturation conditions and the validity of wetness indices within a watershed is another avenue to calibrate the analytical model with the inputs of other soil parameters.

Space technology using satellite and aerial remote sensing plays a very important role in terrain mapping and the scientific assessment of the ground conditions. This technology is ideally suitable for inaccessible mountainous regions where the majority of old landslides were

Table 4 Overall results of the landslide susceptibility analysis of Kalawana division

| RESULTS WAA—use of weighted average analysis method of assessment model SINMAP- use of terrain stability model of stability index mapping (SINMAP) | % Area fall in the equivalent stability class according to the susceptibility criteria | | | | | |
|--|--|--------|---|--------|--|--------|
| | Sub-watershed number 05 of main watershed | | Sub-watershed number 08 of main watershed | | Overall results of the Kalawana main watershed | |
| | WAA | SINMAP | WAA | SINMAP | WAA | SINMAP |
| No susceptibility | 46.45 | 45.6 | 22.07 | 40.1 | 38.67 | 52.49 |
| Low susceptibility | 8.09 | 6.4 | 25.53 | 7.4 | 18.99 | 8.90 |
| Moderately susceptibility | 26.29 | 10.4 | 25.44 | 11.2 | 22.80 | 12.11 |
| High susceptibility | 15.78 | 35.0 | 21.04 | 35.4 | 16.30 | 24.11 |
| Very high susceptibility | 3.39 | 2.8 | 5.91 | 5.0 | 3.24 | 2.19 |

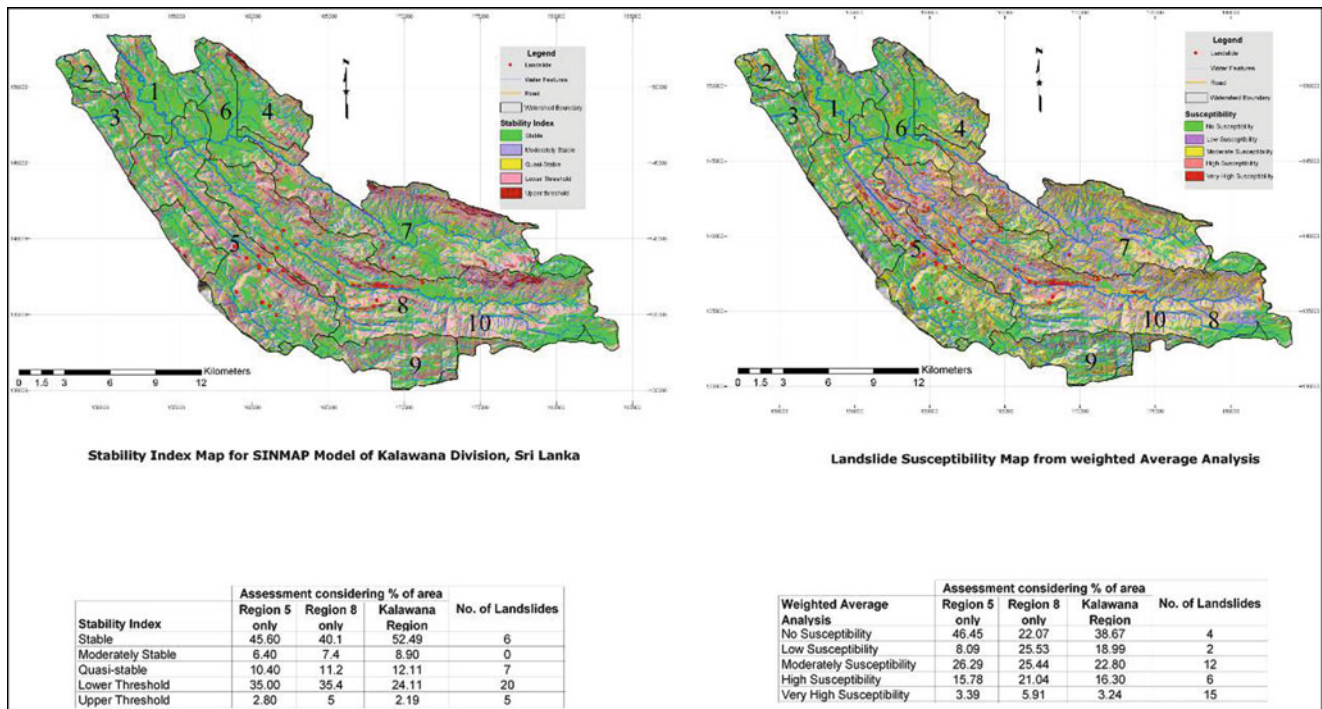


Fig. 4 Overall evaluation of results of the landslide susceptibility analysis of the Kalawana Division, Ratnapura District, Sri Lanka

identified. One of the critical observations of the study is the lack of a complete data base of recent occurrences of old landslides on May 2003. Only 39 landslides were used out of 78 case records at Kalawana to calibrate models due to inaccessibility at field. Therefore, multi-temporal satellite data may be the only solution to overcome such problems and acquire more geographical information. In landslide study high spatial resolution satellite photo images are recommended.

The satellite imagery data allowed generation of high-resolution Digital Elevation Models (DEM). The derived relief parameters can be analyzed in GIS together with other information obtained from remote sensing data, thematic maps and field observations for a spatially differentiated terrain as a basis for further assessment of landslide hazard.

Acknowledgments This paper forms an integral part of the IPL research (IPL 143) on "Evaluation of Sensitivity of the Combined Hydrological Model for Landslide Susceptibility Risk Mapping in Sri Lanka" being implemented by the Centre for Research & Development, Central Engineering Consultancy Bureau (CECB) of the Ministry of Irrigation and Water Resources Management. Authors would like to acknowledge the financial and technical support provided by the Japan Aerospace Exploration Agency (JAXA) and the Dr. L Samarakoon, Director, Geo Informatics Center (GIC) of the Asian Institute of Technology (AIT) in executing this study and extensive support provided in collecting necessary data by the Survey Department of Sri Lanka. Also it is a part of the research leading to MPhil which has been registered at the Post Graduate Institute of Science, University of Peradeniya,

Sri Lanka. It is being published with their permissions. The views expressed in the paper are however those of the authors only. Our grateful thanks are due to Eng. N Rupasinghe, Chairman and Eng. K L S Sahabandu General Manager, Central Engineering Consultancy Bureau for the permission and encouragements.

References

- Bhandari RK, Dias AAV (1996) Rain triggered slope movement as indicators of landslide dynamics. In: Proceedings of 7th international symposium on landslides. Balkema, Trondheim, 17-21 June 1996
- Bhandari RK, Jeyatharan K, Raviskanthan A (1992) Dynamics of rockfalls in Sri Lanka and landslide hazards. In: Proceeding of the international conference on case histories in geotechnical engineering, St Louis
- Chowdhury R, Flentje P (1998) A landslide database for landslide hazard assessment. In: Proceedings second international conference on environmental management (ICEM2), 10-13 Feb 1998, Wollongong, Australia, vol 2. Elsevier, Oxford, pp 1229-1237
- Cooray (1994) Geological factors affecting landslides in Sri Lanka. In: Proceedings of national symposium of landslides in Sri Lanka, Colombo, 17-19th Mar 1994
- Dias AAV, Goonasekara U, Rupasinghe N (2001) Natural slope instability measures of roads in hill country, Sri Lanka. In: Proceedings of 8th world emergency management conference, Oslo, Norway, 19-21 June 2001 (TIEMS)
- Dias AAV, Jayasumana DTN, Fonseka HJS (2005/2006) Application of remotesensing and GIS technology for landslide susceptibility analysis, JAXA Mini Project, 2005/2006
- Dietrich WE, Wilson CJ, Montgomery DR, McKean J (1993) Analysis of erosion thresholds, channel networks and landscape morphology using a digital terrain model. *J Geol* 101:161-180

- Fookes PG (1997) The first Glossop lecture, geology for engineers: the geological model, prediction and performance. *Q J Eng Geol* 30:293–424
- Fookes PG, Baynes FJ, Hutchinson JN (2000) Total geological history: a model approach to the anticipation, observation and understanding of site conditions, invited Paper, *Geoen 2000 Conference*. Technomic Publishing, Melbourne, pp 370–460
- Hammond C, Hall D, Miller S, Swetik P (1992) Level I stability analysis (LISA) documentation for Version 2, General Technical Report INT-285. USDA Forest Service Intermountain Research Station, Fort Collins, CO, 121p
- Hutchinson JN (1988) Morphological and geotechnical parameters of landslides in relation to geology and hydrology. In: *Proceedings of 5th international symposium on landslides, Lausanne*, pp 3–36
- Montgomery DR, Dietrich WE (1994) A physically based model for topographic control on shallow landsliding. *Water Resour Res* 30 (4):1153–1171
- Pack RT, Tarboton DG, Goodwin CN (1999) GIS-based landslide susceptibility mapping with SINMAP. In: Bay JA (ed) *Proceedings of the 34th symposium on engineering geology and geotechnical engineering*, vol 34, pp 219–231
- Van Westen CJ (1993) Application of geographic information systems to landslide hazard zonation. Ph.D. dissertation, Technical University Delft. ITC Publication Number 15, ITC, Enschede, The Netherlands, p 245
- Varnes DJ (1984) *Landslide hazard zonation: a review of principles and practice*. United Nations International, Paris



The Method for In-situ Large Scale Shear Test of Saturated Soils and Its Application

Maosheng Zhang, Wei Hu, Lifeng Zhu, Ying Pei, and Junbo Bi

Abstract

Due to inherent uncertainties associated with laboratory testing, such as sampling disturbance and size effect, and the limitation that conventional in-situ large scale shear tests are generally carried out for soil masses of natural water content, soil mass strength parameters determined by back analysis instead of testing are, mostly, used for geotechnical stability analyses and engineering designs. In this study, based on conventional in-situ large scale shear test apparatus, two modes of apparatus, the vertical soaking mode and the lateral soaking mode, were developed to accommodate testing techniques for saturated soil. With the apparatus, seven in-situ large scale shear tests were carried out on saturated loess masses in Heifangtai, Gansu province. The results show that the loess masses could be saturated by both modes. Compared with the lateral soaking technique, vertical soaking often causes more sample disturbance, even failure, although it takes less time to saturate. Compared with parameters from in-situ large scale shear tests of the loess masses with natural water content, cohesion from in-situ large scale shear tests of the saturated loess masses decreased sharply from 44.65 to 17.35 kPa, while internal friction angle decreased marginally from 14.18° to 11.95°. Compared with parameters obtained through consolidated quick direct shear tests on the saturated loess, the increments of cohesion and the internal friction angle from in-situ large scale shear tests of the saturated loess masses were about 4 kPa and 3° respectively. To improve the method, it is necessary to carry out comparative tests in order to improve the uniformity of water distribution and degree of saturation, as well as select more pervious materials.

Keywords

Saturated loess • In-situ large scale shear tests • Cohesion • Internal friction angle

Introduction

Equation of shear envelope to evaluate the shear strength of soils with cohesion and internal friction angle was developed by C. A. Coulomb in 1776, laying the theoretical foundation for classical soil mechanics. Since the establishment of soil mechanics by K. Terzaghi in the early twentieth century, various tests have been done to acquire shear strength parameters of soil (Bishop 1954; Seed and Lee 1966; Bishop et al. 1971; Fredlund et al. 1978; Fredlund and Rahardjo 1993; Chen 1999; Vallejo and Roger 2000; Li et al. 2007;

M. Zhang • W. Hu (✉) • L. Zhu • Y. Pei • J. Bi
Key Laboratory for Geo-hazards in Loess area, MLR, Xi'an 710054,
People's Republic of China

Xi'an Regional Center, China Geological Survey, Xi'an 710054,
People's Republic of China
e-mail: xazms@126.com; whwhuw@hotmail.com; sx-zhulf@163.com

Zhang et al. 2006; Cao et al. 2010). Besides, some indirect methods have also been developed.

Laboratory tests are the most common techniques to obtain shear strength parameters. Boundary conditions of laboratory testing can be controlled easily. Moreover, various laboratory tests are available including direct shear, triaxial shear, ring shear and torsional shear. However, laboratory tests also have obvious shortcomings: firstly, after a series of procedures of exploration, site sampling, wrapping, transportation, safekeeping, laboratory sampling and testing, the structures of laboratory samples are often disturbed or even damaged; secondly, because laboratory samples are often small in dimensions, the representativeness of test results is greatly reduced; thirdly, soil masses are composed of both soil particles and structural planes which cannot be included by laboratory samples. Hence, shear strength parameters obtained from laboratory tests are rarely used directly in stability analysis and design of geotechnical structures.

Vane shear tests, borehole shear tests and in-situ large scale shear tests are the main in-situ methods to directly test shear strength of soil masses, among which in-situ large scale shear tests are more widely used for their applicability to almost all types of rock and soil masses (Vallejo and Roger 2000; Li et al. 2005, 2007; Zhang et al. 2006; Cao et al. 2010; Xu et al. 2006; Huang et al. 2008; You and Tang. 2002). Compared with laboratory tests, in-situ tests are advantageous in terms of larger sample dimensions, less disturbance and better representativeness. However, at present, in-situ large scale shear tests of soil masses are generally carried out in soil masses of natural water content, while tests in saturated soil masses are seldom recorded.

For water sensitive loess, the shear strength reduces rapidly after saturation which is one of the main causes of loess slope and foundation failure. Hence, it is both theoretically significant and practically valuable to develop in-situ large scale shear test methods and obtain corresponding parameters of saturated loess masses in the failure analysis of loess slopes and foundations. In this study, two modes of soaking and saturating apparatus, the vertical soaking mode and the lateral soaking mode, were developed. With the apparatus, seven in-situ large scale shear tests of saturated loess masses were carried out in Heifangtai, Gansu province. By analyzing the degree of saturation and the structural disturbance of samples, as well as comparing the parameters with those obtained from in-situ large scale shear tests of loess masses with natural water content and consolidated quick direct shear tests of saturated loess, the in-situ large scale test method and shear strength parameters of saturated soil masses is discussed. Also some improving measures of the test method are proposed.



Fig. 1 Conventional in-situ large scale shear test apparatus

Design of Soaking and Saturating Test Apparatus

Compared with conventional tests of soil masses with natural water content, the principle of in-situ large scale shear tests of saturated soil masses is the same, with the only difference on testing procedures, which is to make saturated soil mass samples by tailor-made devices before starting to consolidate and shear. The in-situ large scale shear test apparatus for saturated soil masses is based on conventional WBJL in-situ large scale shear apparatus, as shown in Fig. 1. The main components and their parameters are as follows: a square-shaped shear box with an area of 2,500 cm², a hydraulic jack providing shearing forces with the peak loading capacity of 500 kN, a strain gauge pressure sensor with the top range of 500 kN, several dial-typed displacement gauges with the range between 0 and 50 mm and a ground anchor beam-typed reaction frame. Data is recorded and computed automatically.

There are two key issues in deciding whether an in-situ large scale shear test of saturated soil masses is successful: firstly, how to make the sample saturated and in the meantime ensure the undisturbed state of the sample; secondly, how to measure degree of saturation to ensure that the sample is saturated. To live up to two constraint conditions of reasonable degree of saturation and limited sample disturbance, two modes of apparatus, the vertical soaking mode and the lateral soaking mode, were designed, as shown in Fig. 2.

The vertical soaking mode includes the use of a soaking ring, 80 cm in diameter and 50 cm in height. The bottom rim of the ring is sharp-edged to help with soil penetration. Once penetrated and in position, the ring serves as a water tight barrier around a cylindrical soil sample 20 mm less in diameter than that of the ring. Water is then injected into

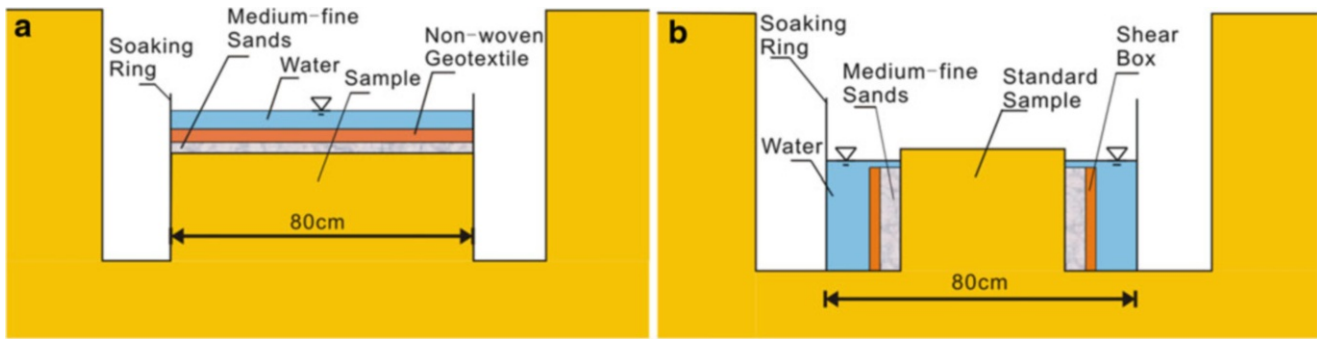


Fig. 2 Schematics of the two soaking modes. (a) Vertical soaking mode, and (b) lateral soaking mode

Table 1 Physical properties of the loess with natural water content

| Specific gravity | Water content (%) | Density ($\text{g} \cdot \text{cm}^{-3}$) | Void ratio | Liquid limit (%) | Plastic limit (%) | Plasticity index | Liquidity index |
|------------------|-------------------|---|------------|------------------|-------------------|------------------|-----------------|
| 2.70 | 9.1 | 1.51 | 0.930 | 25.04 | 17.20 | 7.84 | -1.13 |

the ring until the cylindrical soil is covered and saturated. After that, a standard sample is cut into shape before consolidation and shearing.

The lateral soaking technique is to make a standard sample first, which is 10 mm smaller inside length than that of the shear box. The shear box is gently adjusted to the centre of the standard sample. After that, the gap between the shear box and the sample is densely filled with sieved medium-fine sands, which in turn forms a permeable barrier. Lastly, the soaking ring is installed outside the shear box and water is injected until saturation.

Test Scheme and Key Technical Points

This study focused on the loess from Heifangtai, Gansu province in northwestern China. The basic physical properties of the loess are summarized in Table 1. With the two sets of soaking test apparatus mentioned above, seven loess samples were soaked for a long period until saturation. And then the rest of the apparatus was implemented and shearing started. After shearing, several verification tests were followed: firstly, several water content tests were done at different parts of the saturated samples to test the degree of saturation; secondly, to compare shear strength parameters of loess masses under saturated state with those under natural water content, in-situ large scale shear tests of three loess samples with natural water content were carried out in the vicinity; thirdly, undisturbed loess samples were taken to the laboratory to carry out consolidated quick direct shear tests. The aim is to compare laboratory shear strength parameters of saturated loess with the in-situ test results.

The detailed operation of in-situ large scale shear test follows the guidance of Specification for in-situ direct

shear test (Kunming Prospecting Design Institute of China Nonferrous Metals Industry 2001). The loading conditions, including loading magnitude of each level, loading speed, stable standard, shearing speed, have to be controlled very rigorously.

1. Control of the vertical loading conditions: To not only avoid sudden failure of the samples, but also compare the deformation process of both natural and saturated loess, the vertical loading magnitudes of each level for both water content states were kept as 5 kN. The vertical loading increment would not be applied until the changing rate of the vertical displacement meter reached 0.05 mm/min or less and stayed stable. For the last level of vertical loading, the changing rate would reach 0.05 mm/h or less. Then the vertical deformation would be considered to be stable and shearing could start.
2. Control of the shearing loading conditions: To simulate consolidated undrained conditions, the vertical pressure was kept constant as designed while the lateral pressure was applied quickly step by step. Based on predicted shearing strength, shearing load for each loading level was set to be 1 or 2 kN. In the process of loading, the readings of lateral pressure meters kept increasing. When the readings stopped increasing or even decreased dramatically, the samples were deemed to be failed. Because most of the loess landslides in Heifangtai belong to high-speed long run-out landslides, the shearing durations were kept to be around 10 min.

For in-situ large scale shear test of saturated loess, three sampling techniques should be stated herein.

1. Precise sample preparation

For vertical soaking mode, cylindrical samples 20 mm less in diameter than that of the soaking ring were cut in the loess. The ring was installed around the cylinder.

Water was not injected until the position of the ring was adjusted to make the cylinder centered, as well as the gap between the sample and the ring was filled with sieved medium-fine sands. After finishing saturation, the ring was removed. The cylinder was further modified into a standard square-shaped sample with a side length of 49 cm and a height of 27 cm. The shear box was then installed around the standard sample and gently adjusted to the centre of the sample.

For lateral soaking mode, a standard square-shaped sample with a side length of 49 cm and a height of 27 cm was made in the first step before installation of the shear box and filling of the gap with sieved medium-fine sands. Afterwards, the soaking ring was installed around the shear box and water was injected until saturation occurred.

2. Medium-fine sand filling

Whichever the mode, it was essential to fill the gap between the shear box and the sample with medium-fine sands. Before filling, the sands were sieved to remove large grains to ensure sand uniformity. The 5 mm wide gap with medium-fine sands was then laid at five levels. At each level, a long steel knife was used to vibrate and density the sands before the next level was laid.

3. Soaking mode

According to design for the vertical soaking mode, most water goes into the sample via the upper surface while only a very small amount of water takes the channel between the sample and the soaking ring. For the lateral soaking mode, water goes into the sample only via the side surfaces. To do so, certain test settings should be fulfilled. For the vertical soaking mode, as shown in Fig. 2, two prevention layers, the bottom layer of medium-fine sands with a depth of 3–5 cm and the top layer of non-woven geo-textile, were laid on top of the sample to prevent potential erosion by injection of water. Water was injected until the geo-textile was 5 cm beneath the water surface. For the lateral soaking mode, as shown in Fig. 2, water level was kept between the top of the shear box and the top of the sample, with the optimal level being higher than the top of the shear box around 1 cm. In this way, water could infiltrate into the samples only via the medium-fine sands until saturation.

Table 2 Comparison of the two soaking mode effects

| Sample | Soaking and saturating mode | Soaking duration (day) | Water content (%) | Degree of saturation (%) |
|--------|-----------------------------|------------------------|-------------------|--------------------------|
| 1 | The lateral soaking mode | 3 | 24.0 | 69.7 |
| 2 | The lateral soaking mode | 6 | 32.1 | 93.2 |
| 3 | The vertical soaking mode | 6 | 33.2 | 96.4 |
| 4 | The vertical soaking mode | 6 | 32.9 | 95.5 |
| 5 | The vertical soaking mode | 6 | 33.1 | 96.1 |
| 6 | The vertical soaking mode | 5 | 32.5 | 94.4 |
| 7 | The vertical soaking mode | 7 | 32.9 | 95.5 |

seven in-situ samples were listed in Table 2. Sample 1 was prepared by the lateral soaking mode. It reached a degree of saturation of 69.7 % after 3 days of continuous soaking. This level was far from a satisfactory degree of saturation. Consequently the soaking duration was prolonged to 6 days for sample 2, resulting in an obvious increment of the degree of saturation to 93.2 % which is close to the laboratory standard of 95 %. For comparison, three vertical soaking mode samples, samples 3, 4 and 5, were soaked for 6 days. In the end they reached a degree of saturation of 96.4, 95.5 and 96.1 % respectively, all of which are higher than 95 % and that of sample 2. Moreover, sample 6 and 7 were soaked for 5 days and 7 days, respectively. The results show that the degree of saturation for sample 6 is 94.4 %, a little lower than those saturated for 6 days. For sample 7 the degree of saturation is 95.5 %, basically equal to those saturated for 6 days.

The analyses of saturating effect show that the loess can be saturated by both soaking modes as long as samples undergo enough saturation time. Since loess presents higher permeability in the vertical direction than in the lateral direction (Li et al. 2007), it is understandable that the vertical soaking mode samples have higher degree of saturation than their lateral soaking counterparts within the same soaking duration considering the water flow direction in two soaking modes. In-situ samples which are soaked longer than 5 days by the vertical soaking mode can satisfy the requirements on the degree of saturation for laboratory tests, hence shearing parameters obtained by in-situ large scale shear tests of saturated loess can be compared with those obtained in the laboratory.

Analysis and Discussion of Test Results

Saturating Effect

Two factors, the stable infiltration velocity and water content after soaking, were used to decide whether the samples were saturated. The soaking effects with two soaking modes for

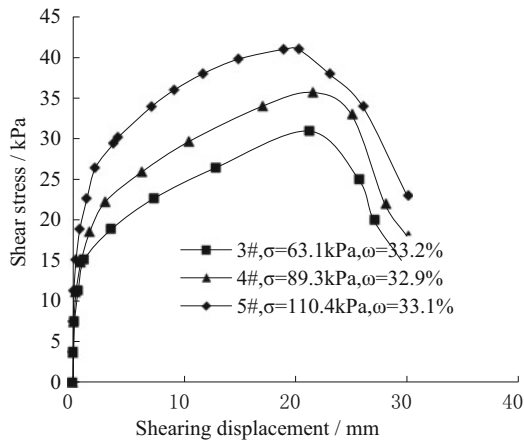


Fig. 3 Shear stress and shearing displacement relationships for in-situ large scale shear tests for saturated loess

Sample Disturbance

The degree of linearity of the strength envelope, together with the rationality of shear strength parameters, can be taken as effective back analysis means for evaluating the degree of sample disturbance. As is known, shear strength of loess is greatly influenced by water content. So the stress-strain relationships (Fig. 3) for sample No.3, 4 and 5 with the same soaking time and the closest water contents were chosen to plot the shear envelope (Fig. 4). Based on the linear regression equation, cohesion and internal friction angle were found to be 17.35 kPa and 11.95°, respectively. The coefficient of correlation is 0.9913 suggesting the effectiveness of the chosen regression method. From this viewpoint, the impact of soaking mode on sample disturbance is not so obvious.

However, according to our experience, loess structure is prone to collapse after soaking in water. Moreover, excessive pore water pressure within the voids of saturated loess will rise sharply when external load is applied suddenly, and result into liquefaction. This understanding was verified on site. When a piece of the saturated loess is put on one's palm and shaken, it easily converts into fluid mud. In the process of making vertical soaking mode samples, several disturbing actions such as removal of the soaking ring and further cutting of samples exist after soaking and saturating. No matter how cautious we are, it was unavoidable to cause sample edge disturbance whose typical indications are either loss of soil or the slumping of a small piece of soil in the edge, making it very inefficient to make vertical soaking mode samples. Relatively speaking, lateral soaking mode can avoid disturbance of saturated loess samples, so tests with lateral soaking mode can better reveal the true strength of the saturated loess as long as the samples reach enough degree of saturation.

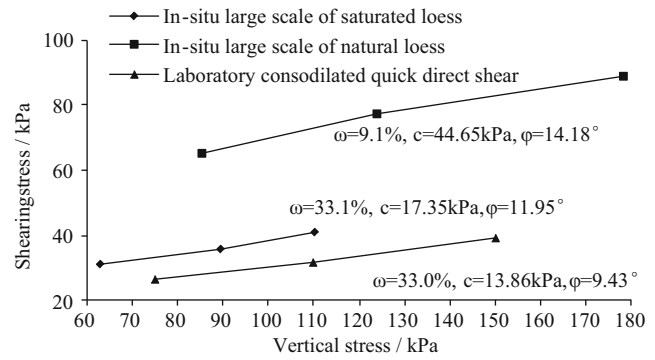


Fig. 4 Shear strength envelope of saturated loess based on vertical soaking mode in-situ large scale shear tests

Comparison of Shear Strength Parameters

The shear strength envelopes, based on in-situ test results of samples No. 3, 4 and 5, are shown in Fig. 4. Then the shear strength parameters for saturated loess were acquired from the strength envelop. Also in Fig. 4, the results for three in-situ large scale shear tests of natural loess, as well as representative laboratory CU tests of saturated loess, are presented. Compared with parameters from in-situ large scale shear tests of the loess masses with natural water content, cohesion from in-situ large scale shear tests of the saturated loess masses decreased sharply from 44.65 to 17.35 kPa, while internal friction angle decreased gently from 14.18° to 11.95°. This demonstrated both cohesion and internal friction would decrease under soaking conditions. Compared with the representative parameters from consolidated quick direct shear tests of saturated loess, the increase in cohesion and the internal friction angle from in-situ large scale shear tests of the saturated loess masses were about 4 kPa and 3°, respectively. This can be attributed to the fact that the in-situ samples that remained intact with the parent loess underwent fewer disturbances than the laboratory samples.

Conclusions

Taking into account in-situ saturation conditions and structural disturbance requirements, the vertical soaking mode and the lateral soaking mode of samples were designed. Together with conventional in-situ large scale shear test apparatus, two sets of in-situ large scale shear test apparatus for saturated soil masses were developed. With the apparatus, seven in-situ large scale shear tests were carried out on the saturated loess in Heifangtai, Gansu province. Three in-situ large scale shear tests done by vertical soaking mode, of which water contents were close, were chosen to plot the shear envelope. The following conclusions are made:

1. Compared with parameters from in-situ large scale shear tests of the loess masses with natural water content, cohesion from in-situ large scale shear tests of the saturated loess samples decreased from 44.65 to 17.35 kPa, while internal friction angle decreased from 14.18° to 11.95°. Compared with parameters from consolidated quick direct shear tests of the saturated loess, the increase in cohesion and the internal friction angle from in-situ large scale shear tests of the saturated loess masses were about 4 kPa and 3°, respectively. Therefore in-situ large scale shear tests of saturated loess masses could obtain more reasonable shear strength parameters for saturated loess masses, which is very valuable for stability analyses of water-sensitive loess slopes and foundations. Hence, it is necessary to carry out in-situ large scale shear tests of saturated loess masses.
2. Samples could be saturated by both vertical soaking mode and lateral soaking mode, demonstrating that it is workable to carry out in-situ large scale shear tests of saturated soils. However, with vertical soaking apparatus, samples were often disturbed leading to inefficient testing. On the contrary, shearing tests with lateral soaking apparatus could obtain better results for shear strength parameters of saturated soil masses.
3. To improve current testing method of in-situ shear strength of saturated soil masses, further detailed studies were deemed to be necessary. The necessary studies include work on the uniformity of water distribution in samples, rate and degree of saturation, evaluation of structural disturbance of samples and determination of most suitable permeable material.

Acknowledgments This research work received support from the Massive Land and Resources Survey project funded by China Geological Survey (Project number 1212011014024). The authors are sincerely thankful to Pingping Sun and Xiujuan Cheng for their efforts in

collecting data in this study. We give our special thanks to Professor Tonglu Li for the careful revision of the manuscript.

References

- Bishop AW (1954) Correspondence on shear characteristics of saturated soil, measured in triaxial compression. *Geotechnique* 4:43–55
- Bishop AW, Green GE, Garga VK, Anderson A, Brown JD (1971) A new ring shear apparatus and its application to the measurement of residual strength. *Geotechnique* 21(4):273–328
- Chen ZH (1999) Deformation, strength, yield and moisture change of a remolded unsaturated loess. *Chin J Geotech Eng* 21(1):82–90
- Cao XP, Li BX, Yan SH (2010) Influence of loess mechanical parameter by different experimentations. *Hydrogeol Eng Geol* 37(1):80–84
- Fredlund DG, Morgenstern NR, Widger RA (1978) The shear strength of unsaturated soils. *Can Geotech J* 15(3):313–321
- Fredlund DG, Rahardjo H (1993) *Soil mechanics for unsaturated soils*. Wiley, New York
- Huang ZQ, Wu LF, Wang AM et al (2008) Stability analysis of expansive soil slope based on in-situ shear test. *Rock Soil Mech* 29(7):1764–1768
- Kunming Prospecting Design Institute of China Nonferrous Metals Industry (2001) Specification for in-situ direct shear test. China Planning Press, Beijing
- Li KG, Xu J, Li SC (2005) Study on property of rock mass discontinuity shear strength in Three Gorges reservoir area. *Rock Soil Mech* 26(7):1063–1067
- Li BX, Niu YH, Miao TD (2007) Water sensitivity of Malan loess in Lanzhou. *Chin J Geotech Eng* 29(2):294–298
- Li X, Liao QL, He JM et al (2007) Study on in-situ tests of mechanical characteristics on soil-rock aggregate. *Chin J Rock Mech Eng* 26(12):2377–2384
- Seed HB, Lee KL (1966) Liquefaction of saturated sands during cyclic loading. *Soil Mech Found Eng Div ASCE* 92:105–134
- Vallejo LE, Roger M (2000) Porosity influence on the shear strength of granular material-clay mixtures. *Eng Geol* 58(2):125–136
- Xu WJ, Hu RL, Zeng RY (2006) Research on horizontal push-shear in-situ test of subwater soil-rock mixture. *Chin J Geotech Eng* 28(7):814–818
- You XH, Tang JS (2002) Research on horizontal push-shear in-situ test of soil and rock mixture. *Chin J Rock Mech Eng* 21(10):1537–1540
- Zhang ZL, Zhao DA, Chen ZM et al (2006) Analysis on in-situ direct shearing tests of grouting loess. *Commun Stand Issue* 5:59–62



Microstructural Characteristics of Qinyu Landslide Slip Soil, NW China

Xuemei Jia, Shouyun Liang, and Chenyi Fan

Abstract

Slip zones are closely related to landslides. The microstructural analysis of slip soil has become one of the important contents on landslide researches. Based on two slip zone profiles of Qinyu landslide, the microstructural characteristics of slip soil and its geological implications were studied by the means of scanning electron microscope (SEM). The results showed that: (1) the microstructures of slip soil are mainly characterized by flocculated-clotted texture, fine and meso-pores; (2) on the slip zone profile in front of the main landslide, the closer to the centre of the slip zone, the greater amount of pores, the narrower and longer shape of pores, as well as the smaller apparent porosity and probability entropy of pores become. Obviously, the amount of pores is negatively related to apparent porosity, while probabilistic entropy is positively related to the shape factor; (3) on the slip zone profile in the upstream side of the secondary landslide, the amount and apparent porosity of pores are smaller as a whole. In addition, higher orientation, especially, near the upper slip surface in the profile has revealed the microscopic mechanism that Qinyu landslide is relative stable on the whole, while the secondary landslide was in a constant active state.

Keywords

Slip soil • SEM • Microstructures • Geological significance

Introduction

As a historical product of landslide development and evolution, a slip zone not only records a wealth of geological information, but also, to a great extent, controls the stability of landslide. Therefore, research of slip zone is an important content in stability prediction and prevention of landslide.

On macroscopic scales, slip zones often have brilliant colours as distinguished from sliding mass and bedrock (Wen et al. 2004; Shuzui 2001), making field identification easy. On microscopic scales, slip soil which formed under certain conditions has certain physical-mechanical properties (Shi et al. 1995). Through study on the microstructures of sheared soil, Skempton (1964) suggested that oriented arrangement of particles was the basic reason for slip soil producing residual strength. The minerals of landslide slip soil in the Three Gorges reservoir showed the microstructural characteristics of oriented arrangement and of being elongated, which were the main causes of the friction coefficient and shearing resistance reduction. Rich micro-pores and micro-fissures result in an increase of the porosity of slip zones. Once destroyed by shearing, it would cause high pore water pressure, and thereby become the important formation mechanism of high-speed landslides

X. Jia • S. Liang (✉)
Department of Geological Engineering, Lanzhou University, Lanzhou
730000, China
e-mail: Jiaxm07@lzu.cn; Liangsy@lzu.edu.cn

C. Fan
Urban & Rural Planning & Design Institute of Yunnan, Kunming
530100, China
e-mail: fanchy923@126.com

(Wen et al. 2007). Wen and Aydin (2005) studied the microstructures of slip soil by OPM and BEM, and then found that the porosity, flat clay particle content and particle arrangement were the three key indicators to control mechanical property of slip soil. Using SEM and XRD, Yan et al. (2001, 2002) studied the microstructures and material components of slip soil, and associated them with the active frequency, phases, and the formation mechanism of landslide. The stage of landslide stability and instability could also be judged by scratches and fluidal structures on slip surfaces. Given the fact that slip soil formed on different periods and conditions has different microstructural characteristics, therefore, the research of slip soil microstructures is an effective way for better understanding of the mechanisms of landslide formation and evolution (Zhang et al. 2008; Li et al. 2010).

Taking two typical slip zone profiles of Qinyu landslide as the research objects, we systematically took samples and attempted to study the microstructural characteristics of slip soil by SEM. Moreover, the study is intended to reveal the evolution information about the landslide development and evolution.

Samples and Methods

Study Area

Qinyu landslide is located at the south bank of Mingjiang River in Tangchang County, Gansu Province of China (Fig. 1). The National Highway No. 212 (K376 + 475~377 + 617) goes through the landslide mass. The main outcrop strata are Middle Devonian, Lower Permian, Triassic series and Quaternary covering layer. The landslide is a multilevel and multiphase talus slide controlled and affected by fault, and in essence it is a large-scale landslide group. The secondary landslide in the upstream side sustains an active state all the time, which has severely restricted the normal operation of the National Highway No. 212 (Chen et al. 2006).

On the slip zone profile Q1 is in leading edge of the main landslide (N33° 47' 03", E104° 32' 17") and Q2 is in a gully close to the highway at secondary landslide along lateral margin in the upstream (N33° 47' 04", E104° 32' 00") (Fig. 2, Table 1). We took samples in each layer from the bottom up and then coded sequentially. The thickness of the well-exposed slip zone in profile Q1 is 90 cm and in profile Q2 reaches more than 180 cm, but its lower slip surface doesn't crop out. Each sample represents a certain sampling site on the slip zone profile, namely, sample Q1-1 in the sliding bed, samples Q1-2 ~ Q1-8 and Q2-1 ~ Q2-5 in the main slip zone, and sample Q1-9 and Q2-6 in the sliding mass, respectively. In addition, sample Q2-7 represents the slip zone involved into sliding mass.



Fig. 1 The satellite image of Qinyu landslide

Methods

All samples of slip soil were observed under low-vacuum scanning electron microscopy JSM-5600Lv with a resolution of 3.5 nm. Apart from direct morphology observation, a computer image-processing system was used to obtain much information about microstructures which can't be observed with the naked eye, including the number of pores (N), apparent porosity (n), the shape factor (F), the distribution of pore radius and probability entropy (Hm) (Shi et al. 1995). These quantitative parameters could properly combine the complex structural morphology with engineering properties of soil. To extract and calculate these parameters, a kind of image processing software, Image J was chosen. The processing steps included contrast, brightness adjustment, noise removal, median, filtering and binarization (Fig. 3). In this paper, the optimum threshold was determined by the method of minimum cumulative difference (Fan and Liang 2012).

As the fact that the force condition of slip soil is different in the direction perpendicular and parallel to slip surfaces during the forming process, so does the microstructures, then all samples were prepared in two directions except for sample Q1-9 for its loose structure. And then all samples were observed by SEM, and the magnification of images we took ranged from 35× to 5,000×. After comparison, we thought that 800× SEM images could clearly reflect the characteristics of particle morphology and porosity, and may be used as the ideal magnification for sample microstructural parameter extraction. In order to increase the measuring accuracy, three 800× SEM images were selected and then the average in each sample was taken.

Fig. 2 The photos of sampling locations of Qinyu landslide slip soil. (a) Profile Q1; (b) Profile Q2

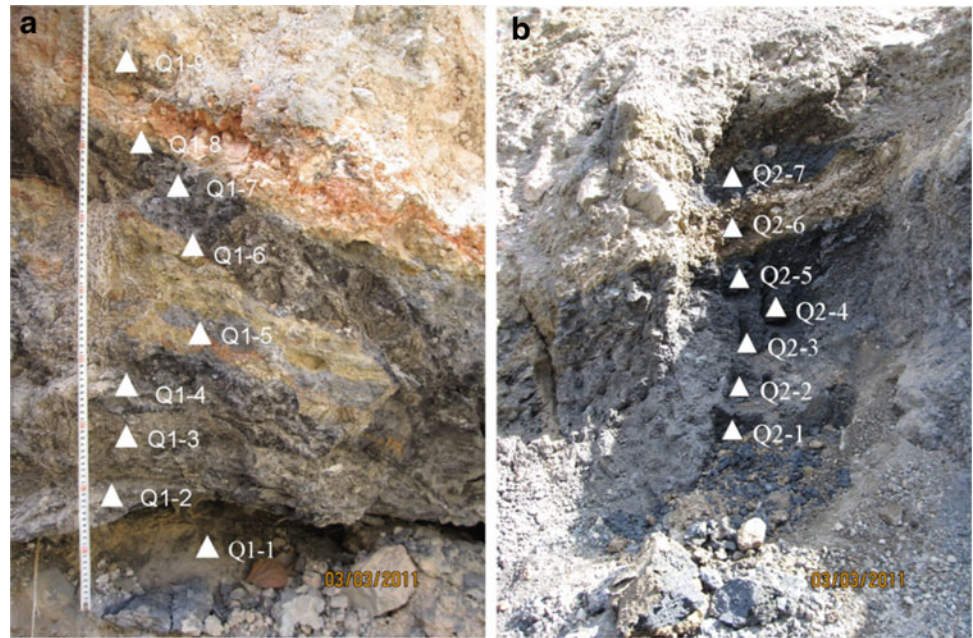
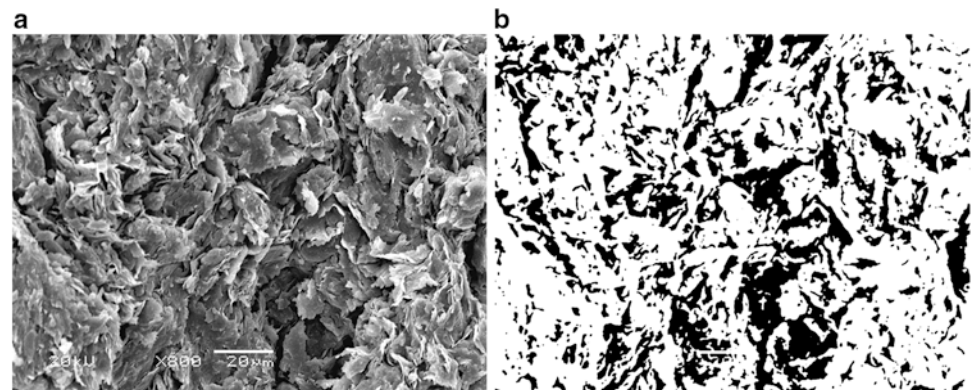


Table 1 Basic feature of samples

| No. | Location (cm) | Characteristics | No. | Location (cm) | Characteristics |
|------|---------------|--|------|---------------|---|
| Q1-9 | 80–90 | Yellow angular pebbles soil containing limestone | Q1-1 | 0–10 | Yellow gravelly soil |
| Q1-8 | 80–90 | | Q2-7 | 170–180 | Black clay mixed into slip body |
| Q1-7 | 60–70 | Black breccia-clay | Q2-6 | 140–150 | Yellow gravelly soil close to the upper sliding surface |
| Q1-6 | 50–60 | Yellow and red breccia silty clay interbedded with grey clay | Q2-5 | 130–140 | Black breccia-clay (main slip zone) |
| Q1-5 | 40–50 | | Q2-4 | 100–110 | |
| Q1-4 | 30–40 | Black breccia-clay | Q2-3 | 80–90 | |
| Q1-3 | 20–30 | Grey and black breccia-clay | Q2-2 | 50–60 | |
| Q1-2 | 10–20 | Black breccia-clay close to the lower sliding surface | Q2-1 | 20–30 | |

Fig. 3 SEM images of slip soil (a) The origin SEM image; (b) the binary SEM image. The white represent particles, while the black represent pores



Results

The Characteristics of Microscopic Structure Morphology

In this paper, H and V represent the horizontal and vertical directions (that is parallel and perpendicular) to slip surfaces respectively. The sample in sliding bed shows pore undeveloped and better cementation in directions H than V. The microscopic structures of slip soil have been collapsed obviously, presenting flocculated structure. For profile Q1, curly and schistic clay minerals widely exist on the surface of slip soil, which makes grain boundary blurry. Additional micro-pores are in large quantities. Roughly speaking, the orientation of pores is better in direction V than H, presenting fluid state. Sample Q1-9 in sliding mass shows macro-porous stents and semi-cementation structure characterized by loose deposition of framework grains, developed macro-pores and good connectivity, and additional calcium deposition on particle surface.

The slip soil of profile Q2 is also a flocculated structure. But it has suffered more intense shear deformation as well as compressed and crumpled. Overall there's no obvious difference in the two directions. Within the main slip zone, reticulate structure with poor orientation is observed. Up to the upper slip surface, micro-fractures increase and orient in directions nearly parallel to the surface. The microstructures of sample Q2-6 in the sliding mass is similar to slip soil, and secondary leached pores can be seen within it.

The Characteristics of Pores

Amount and Apparent Porosity

For profile Q1, apart from sample Q1-1 and Q1-5, amount of pores in direction H was greater than in direction V (Fig. 4a). From the bottom up, the amount of pores firstly increases and then decreases, and the maximal value appeared in the middle of slip zone (Q1-6). On the whole, apparent porosity was more in direction V than in direction H and increased gradually from the middle of slip zone to both sides (Fig. 4b). In direction V, the minimum value appeared at the centre of slip zone (Q1-5). While in direction H, the maximum value appeared at the side of sample Q1-5. Sample Q1-9 in sliding mass with value of 39 % obtained the maximum of apparent porosity in two directions.

For profile Q2, apart from sample Q2-3 and Q2-4, the amount of pores in direction V was greater than in direction H as a whole (Fig. 4c). Compared with the slip zone, the amount of pores in the sliding mass (Q2-6) was much greater

(Fig. 4d). In brief, overall apparent porosity, as well as amount of pores was much smaller than that of samples in profile Q1.

Pore-size Distributions

As mentioned earlier, the number of pores is the maximum at the centre of slip zone, where apparent porosity reaches the minimum. To reveal the underlying mechanism, we analysed the characteristics of pore-size distribution of slip soil and found that micro-spores account for about 70 ~ 80 % of all pore types, while the area rate is very low, about 10 ~ 20 %. According to the dividing criterion of pore types (Lei 1987), the slip soil of Qinyu landslide is mainly predominated by fine and meso-pores. Meanwhile, it illustrates the concept that microstructural changes of slip soil are mainly of soil skeleton and particle breakage in the course of shear deformation. Macro-pores decrease and micro-pores increase owing to fine particles filling, as a result, the total number of pores increase and the area rate decrease. Therefore, there is a negative correlation between the quantity and apparent porosity.

Pore types have effects on soil engineering quality. On the one hand, though the quantity of macro-pores is very low, while the proportion of area is much greater than micro-pores and the influence on soil properties can't be ignored. On the other hand, the effects on soil properties created by micro-pores are still limited, while the influences on pore arrangement characteristics are notable. So when calculating pore parameters of the shape factor and probability entropy in this paper, micro-pores were eliminated.

The Shape Factor and Probability Entropy

The shape factor of pores of samples in profile Q1 shows $F_H > F_V$ (Fig. 5a), that shows the shape of pores in direction H is rounder than V. Within the main slip zone, the shape factor of pores is relatively small, and then increases in both sides. The value of sample Q1-4 is the minimum in both directions, i.e. 0.55 and 0.57 in H and V directions, respectively. It is indicated that the shape of pores within the main slip zone is more irregular than the slip surface and sliding mass.

Similar to the shape factor, probability entropy shows $H_{mH} > H_{mV}$ (Fig. 5b), which means that the ordination of pores in direction H is poorer than V. In direction H, probability entropy varies from 0.95 to 0.98, nearly 1, almost round shape. However, probability entropy shows large variation range in the V direction. Overall samples within the main slip zone have a higher pore ordination than in the slip

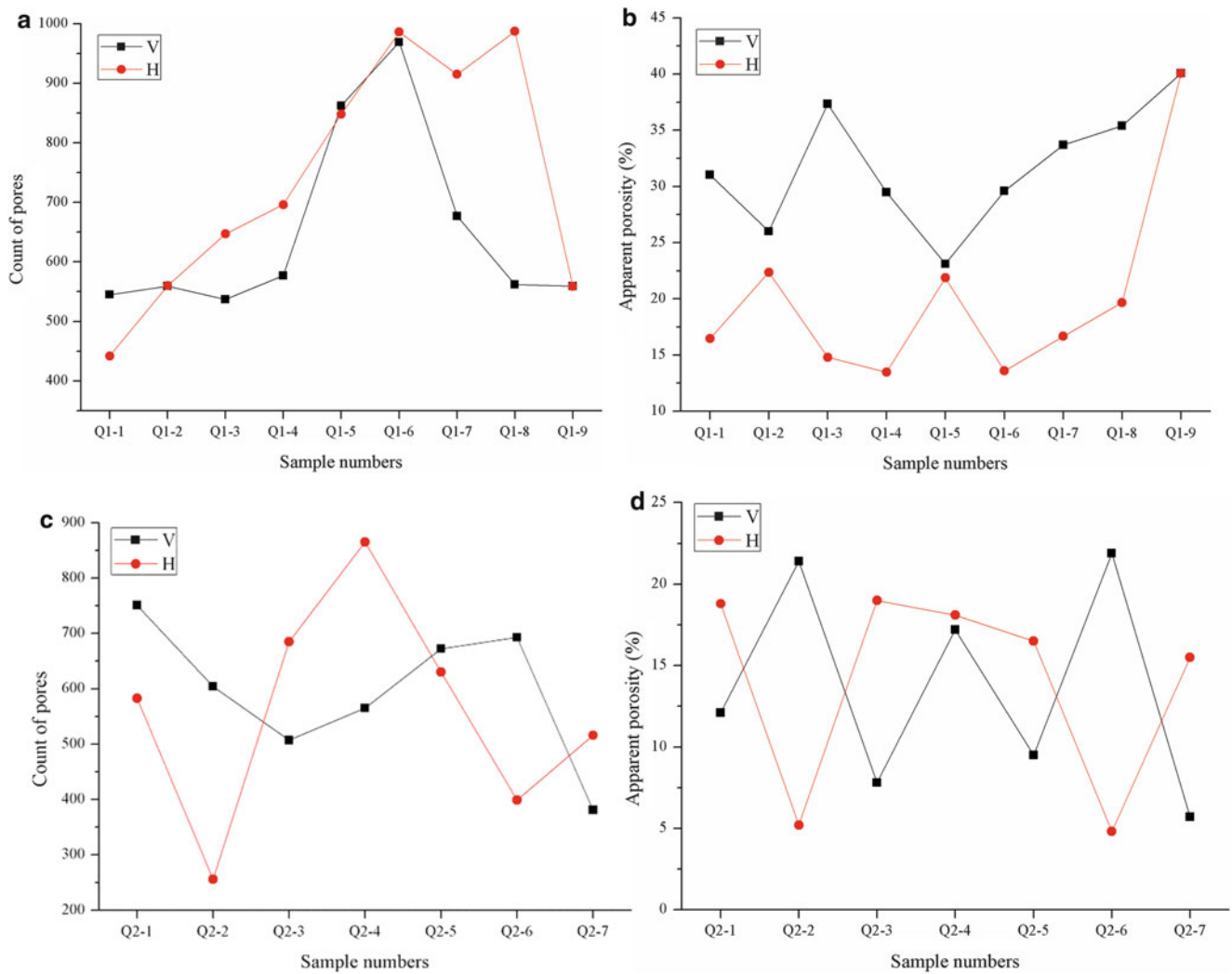


Fig. 4 Curves of pore numbers (a, c) and apparent porosity (b, d) of samples along the profile of Q1 and Q2 in the direction parallel (H) and perpendicular to the sliding surface (V), respectively

surfaces, sliding mass and sliding bed, which reflects that a remarkably positive correlation exists between probability entropy and the shape factor.

For profile Q2, the shape factor of sample Q2-1 ~ Q2-4 within the main slip zone increases in direction H, and then decreases slightly on sample Q2-5 and Q2-6 located near the slip surfaces, to the values of 0.59–0.60 (Fig. 5c). In direction V, the values of shape factor are very close to each other, representing the serrated distribution, except for sample Q2-7H in the sliding mass with the maximum value of 0.69.

Apart from sample Q2-1, probability entropy values of other samples have the same trend in both directions (Fig. 5d). Pore directionality of samples within the main

slip zone is higher than sliding mass. Especially, probability entropy of sample Q2-5 close to the upper slip surface shows the highest orientation.

Compared to profile Q1, pores of samples in profile Q2 are characterized by smaller shape factor, more irregular and higher orientation. As mentioned, the difference of microstructural characteristics may reflect the landslide activity and situation (Yan et al. 2001, 2002). Almost no orientation and disorderly growth of samples on profile Q1 indicates that the slip zone reaches to a stable state. However, samples on profile Q2 with better pore orientation, especially sample Q2-5 close to the upper slip surface, prove that the slip zone has suffered great shear deformation and been in an active state.

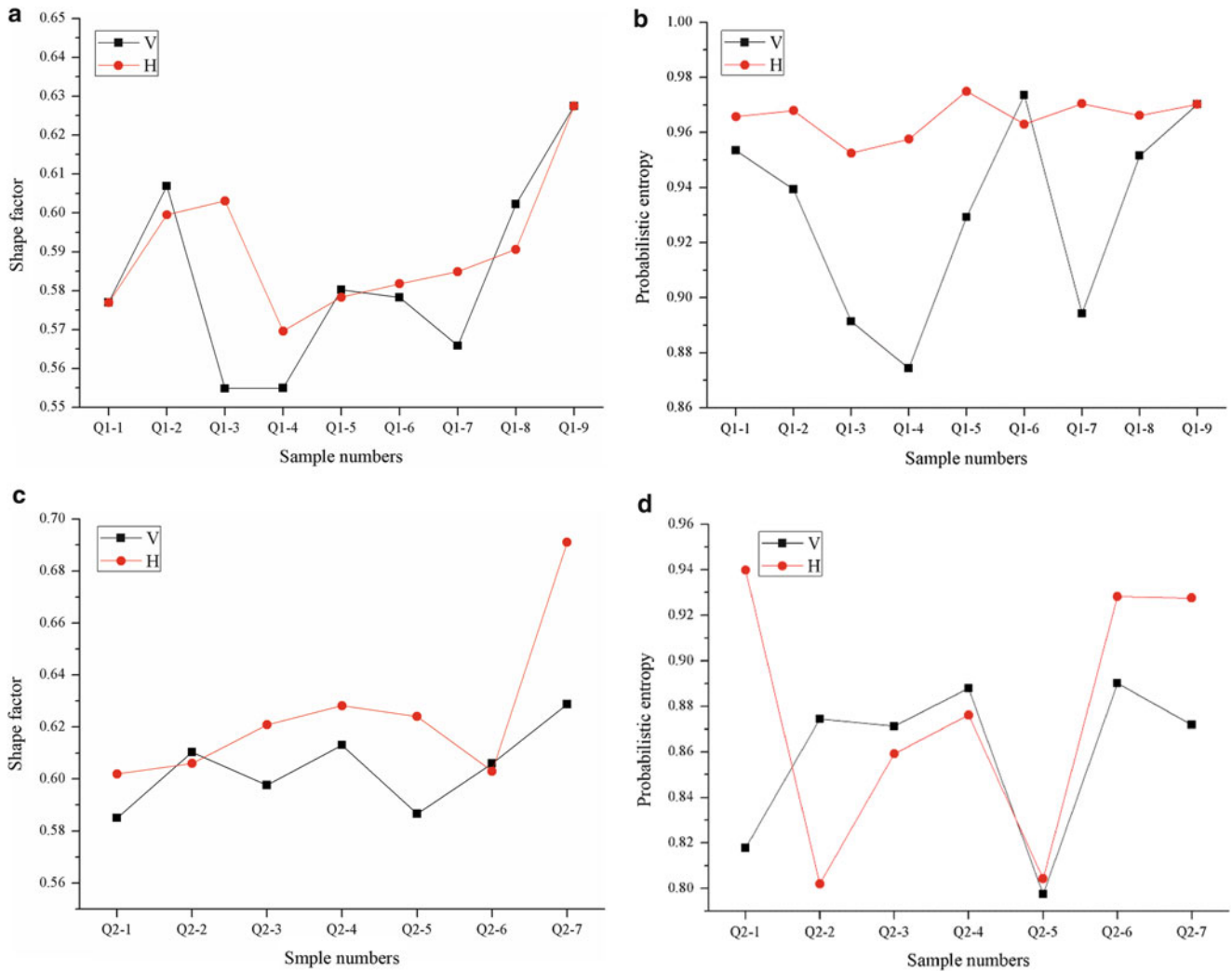


Fig. 5 Curves of the shape factor (a, c) and probability entropy (b, d) of samples along the profile of Q1 and Q2 in the direction parallel (H) and perpendicular to the sliding surface (V), respectively

Conclusions

1. The microstructure morphology features observed by SEM show that the slip soil is mainly predominated by flocculated structure, representing blurry particle boundary, abundant of curly and schistic clay minerals and developed microspores.
2. Microscopic pore characteristics of slip soil are dominated by fine and meso-pores. For profile Q1, the closer to the centre of the slip zone, the greater the amount of pores, the narrower and longer shape of pores, as well as the smaller apparent porosity and probability entropy of pores become. Namely, amount of pores is negatively correlated with apparent porosity, while the shape factor of pores is positively correlated with probability entropy. For profile Q2, the regularity of pores of samples is not as strong as that of profile Q1. Overall amount of pores and apparent porosity are smaller than
3. The microstructural parameters of pores have not obvious differences in two directions. Relatively speaking, the direction V is more sensitive to the shape factor and probability entropy. So sample preparation should consider to choose the direction V (perpendicular to the slip surface) in assessing pore ordination.
4. The differences of microstructural characteristics, to some extent, reflect the shear deformation of slip zone and landslide stability on different profiles. The disordered structure of slip zone of profile Q1 indicates that the main landslide is relatively stable. However, according to high directive property, especially near the upper slip surface of profile Q2, we can deduce that the slip zone of profile Q2 is greatly influenced by constantly active shear deformation, corresponding to the secondary landslide in an active state.

Acknowledgments This study was supported by the National Natural Science Foundation of China (No. 41072213).

References

- Chen WW, Zhao ZF, Liu G, Liang SY, Yang CC, Han WF, Da SD (2006) Research of engineering geological problems at Gansu section of Lanzhou-Haikou Expressway. Lanzhou University Press, Lanzhou. 240p. ISBN: 7-311-0.2898-1/P29
- Fan CY, Liang SY (2012) Selection of the threshold of SEM images in process of studying soil microstructure. *J Eng Geol* 20 (Suppl):719-723
- Lei XY (1987) Pore type and collapsible of Chinese loess. *Sci China Ser B* 17(12):1309-1318
- Li X, Liang SY, Zheng GD (2010) Progresses in sliding zone soil of landslides. *Adv Earth Sci* 25(5):484-491
- Shi B, Li SL, Tolkachev M (1995) Quantitative research of SEM images of cohesive soil microstructure. *Sci China Ser A* 25(6):666-672
- Shuzui H (2001) Process of slip surface development and formation of slip surface clay in landslide in Tertiary volcanic rocks, Japan. *Eng Geol* 61(4):199-220
- Skempton AW (1964) Long-term stability of clay slopes. *Geotechnique* 14(2):77-101
- Wen BP, Aydin A (2005) Mechanism of a rainfall-induced slide-debris flow: constraints from microstructure of its slip zone. *Eng Geol* 78 (1-2):69-88
- Wen BP, Duzgoren-Aydin NS, Aydin A (2004) Geochemical characteristics of the slip zones of a landslide in granitic saprolite, Hong Kong: implications for their development and microenvironments. *Environ Geol* 47:140-154
- Wen BP, Aydin A, Duzgoren-Aydin NS, Li YR, Chen HY, Xiao SD (2007) Residual strength of slip zones of large landslides in the Three Gorges area, China. *Eng Geol* 93:82-98
- Yan CJ, Tang HM, Sun YZ (2001) Study on the soil of slipping zone in landslides and its significance by scanning electron microscope and X-ray diffractometer. *Geol Sci Technol Inform* 20(4):89-92
- Yan CJ, Tang HM, Chen JY (2002) Studies of soil microstructures and compositions of slipping zone in reservoir district of Three Gorges project. *Rock Soil Mech* 23(Suppl):23-26
- Zhang LZ, Hu RL, Li XQ (2008) Soil microstructure quantitative analysis system and its application. *Geol Sci Technol Inform* 27 (1):108-112



An In-situ Darcy Method for Measuring Soil Permeability of Shallow Vadose Zone

Pingping Sun, Maosheng Zhang, Lifeng Zhu, Ying Pei, and Xiujuan Cheng

Abstract

This paper presents an in-situ Darcy test for measuring permeability of soil in shallow vadose zone. The equipments of the test was designed based on the theory of classic *Darcy Test* comprising water infiltration system, water supply system and measuring system. During the experiment, the soil was submerged by water with constant head maintained by a Mariott tube. Volume of water consumed and the corresponding water head in a time series were recorded when the soil was saturated. Then soil permeability was obtained using the Darcy's law. Three groups of the in-situ Darcy tests were conducted at the loess plateau in north western China, and average values of permeability were obtained to range from 0.84 to 2.22 m/d. It is shown that the original structures of soil can be well considered with the in-situ test compared to the classic in-door *Darcy Test*. Furthermore, the data record was more intuitive and the operations are easier compared to the other in-situ tests to measure the soil permeability.

Keywords

In-situ Darcy test • Permeability • Pressure head • Scale effect

Introduction

Water is one of the major triggering factors for landslide occurrences. It behaves more obviously in loess-distributed area for its intensive water sensitivity (Zhang et al. 2012). Quantitative assessment of infiltration is an important issue when analyzing loess slope stability. Soil permeability in shallow vadose zone is a key parameter affecting infiltration. Henry Darcy introduced permeability parameter in 1856. It is an important parameter in hydrology for quantitative calculations; it's also a significant basis when analyzing

various hydrological processes quantitatively (Bear 1972). Then, series of classic calculating methods for aquifer permeability based on pumping (injection) test were developed (Dupuit 1963; Thiem 1906; Theis 1935; Jacob 1940). There are also several methods evaluating soil permeability in vadose zone.

In the field, double and single ring infiltration test are widely used (Gregory et al. 2005; Lai and Ren 2007; ASTM 2001; Bagarello et al. 2009). In these methods, the tested results change with a variation in water head (Schiff 1953). Stand-pipe methods are usually used to measure the infiltration rate of sediments in stream beds (Chen 2000). However, only infiltration rates can be obtained with the above three methods without accurately measuring the hydraulic gradient. Permeability is usually derived assuming the value of hydraulic gradient of 1.0 (Sammis et al. 1982; Stephens and Knowlton 1986; Healy and Mills 1991; Nimmo et al. 1994). However, some errors can result with this assumption only when the tested soil is below the zone of fluctuations related to climate, in uniform or thickly layered porous media

P. Sun (✉) • M. Zhang • L. Zhu • Y. Pei • X. Cheng
Key Laboratory for Geo-hazards in Loess area, MLR, Xi'an 710054, China

Xi'an Regional Center, China Geological Survey, Xi'an 710054, People's Republic of China
e-mail: sunpingping203@gmail.com; xazms@126.com;
sx-zhulf@163.com; peiying@email.jlu.edu.cn;
cugcheng2008@sina.com

(Gardner 1964; Childs 1969; Chong et al. 1981; Sisson 1987); hence, it is not suitable for the soil in shallow vadose zone. Permeability can also be obtained through measuring air-entry pressure with air entry permeameter (Bouwer 1996). However, it is not widely used because air-entry pressure is relatively hard to measure. In addition, several indirect methods can be used to attain permeability, such as empirical formula based on grain-size analysis (Uma et al. 1989; Vukovic and Soro 1992; Kasenow 2002; Song et al. 2009; Thomas and Peter 2011), numerical and analytical calculations (Chen and Lee 1964; Wu et al. 1997; Li et al. 2009). Nevertheless, accuracy of results from empirical formula is affected by uncertainties of parameters chosen. Calculation process is complicated and multi solutions usually occur when using numerical methods.

In laboratory, *Darcy Test* is a classic method for measuring permeability. However, considerable uncertainties can result from the process of sampling, packaging, transportation and sample preparation. Once the samples are disturbed, it is hard or impossible to restore the natural state, especially for the structural soil (Bagarello et al. 2009; Bouma 1982). Moreover, results tested with small size samples are not representative.

Field tests have advantages of well consideration of structures of soil as well as spatial variation in permeability. *Darcy Test* is a classic laboratory method widely used with reliable accuracy. If the classic *Darcy Test* can be improved to conduct in field, accurate and direct measurement of soil permeability in shallow vadose zone can be achieved. Based on the above analysis, a set of equipments for in-situ Darcy test was designed in accordance with the theory of *Darcy Test*. Three designed in-situ Darcy tests were conducted at the loess plateau in north western China. Permeability of loess in the nearby area was also measured with double-ring infiltration, indoor *Darcy Test*, grain-size analysis and pumping test. The differences of permeability among various methods were analyzed. The possible reasons for the differences are discussed.

In-situ Darcy Test Description

Principle of in-situ Darcy test is totally based on the classic *Darcy Test*. It is a transformation of *Darcy Test* from laboratory to field. During the *Darcy test*, test conditions include homogeneous samples, constant water head, and stable physical property of fluid with negligible viscosity and laminar flow. During the in-situ Darcy test, permeability can be obtained only when its test conditions are in accordance with the above mentioned conditions. In addition, two key factors are of great importance regarding the in-situ test. They are (1) saturated samples with air exhausted and (2) hydraulic gradient measurement.

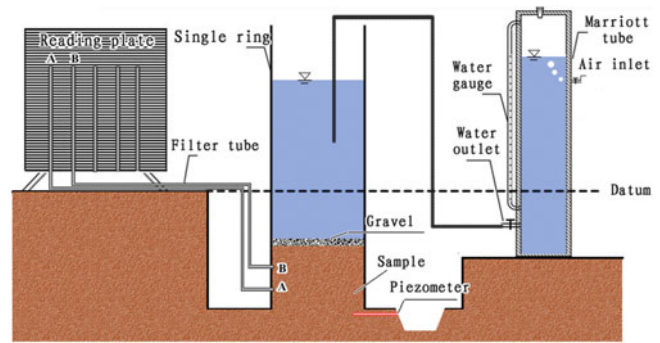


Fig. 1 Schematic of the apparatus for in-situ Darcy test

Equipments Design

Equipments of the in-situ Darcy test were designed as shown in Fig. 1. It contains three systems—infiltration system, water supply system and measuring system.

A single ring is the main component of the infiltration system. It is a steel column with a length of 100 cm, and a diameter of 32 cm. Two vertically distributed circular holes (diameter of 9 mm) were designed to install filter tubes measuring water head, at a vertical distance of 10 cm. Marriott tube act as water supply system used to supply water, maintain constant water head over samples as well as record water consumption volume. The volume of the Marriott tube is 15 l, with 1 cm decrease indicating the consumption of 151.975 m³ of water. The measuring system contains filter tubes, piezometers and reading plate. The filter tube is made from plexiglass with length and diameter of 20 and 8 mm, respectively. Seepage holes are distributed at front 9 cm of the tube. The piezometers (Geonor M-600) used to measure water head are produced by GEONOR Company in Norway. The piezometer has a length of 20 cm and a diameter of 3 cm. The accuracy and resolution of the piezometers are 10 cm and 5 mm, respectively. The reading plate is used to record water head at different depth of the tested samples. In addition, rubber tube, shovels, wooden hammer, water containers, stopwatch, thermometer, sample boxes, PH test strips, glass cement are supplementary instruments.

Test Procedure

The two piezometers (No. 16710 and 16810) needed to be calibrated before the test. During calibration, both of the piezometers were submerged in water until the porous stones were saturated. Then data were recorded when the water head above the porous stones were 30, 25, 20, 15 and 10 cm (Fig. 2).

Figure 2 shows that the piezometer recorded data is negatively proportional to water head. The fitted curves for

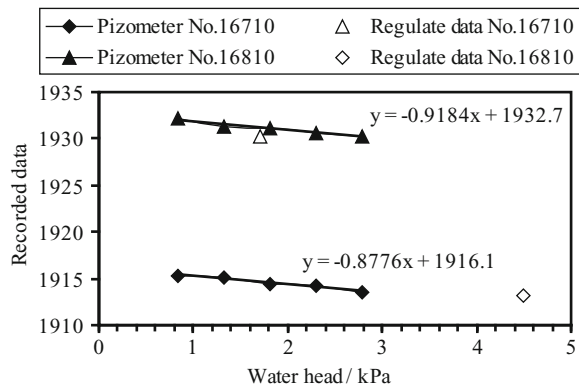


Fig. 2 Water pressure recorded with piezometers

the change in piezometer recorded data with water head fit well for the calibrated points. The fitted formulae of the two piezometers obtained from Fig. 2 are as follows:

$$y = -0.8776x + 1916.1 \quad (1)$$

$$y = -0.9184x + 1932.7 \quad (2)$$

Where, y and x denote the pizometer recorded data and hydraulic head, respectively.

The test procedure comprises the following steps:

1. Sample preparation: the sample is prepared with minimum disturbance before installation of the single ring. The interior chamber wall of the single ring is covered with silicone sealant for easy installation as well as good connection between samples and the single ring. The upper surface of the sample is covered with a layer of sand (thickness of 3 cm) to avoid disturbance of the sample surface during process of water filling.
2. Filter tubes and piezometer installation: tiny holes were drilled before installation to reduce sample disturbance. The connections between the tubes and the ring were sealed avoiding water leakage. Rubber was used to connect reading plate and filter tubes.
3. Water filling: Mariott tubes were used to fill the single ring with water and maintain constant water head over the tested samples.
4. Data recording: data were recorded for water consumption per unit time and water head changes less after long-term submersion of the sample.
5. Water content measurement: water contents of the samples were measured after each in-situ test.

Application Examples

In this section, the in-situ Darcy Test, introduced above, will be used to test loess permeability in shallow vadose zone at Heifangtai, Yongjing county, Gansu province, North

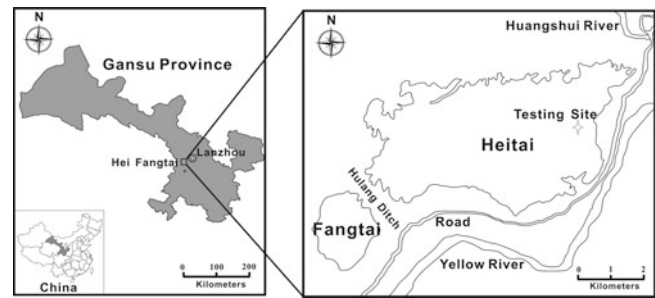


Fig. 3 Location of the study area

western China (Fig. 3). In the study area, large numbers of loess landslides have been triggered for a long-term irrigation since 1963. To mitigate landslides risk and meet water demand for agriculture, it is necessary to quantitatively assess infiltration of irrigation water, in which permeability is a key parameter.

Three sets of in-situ Darcy Test (numbered C1, C2 and C3) were conducted in an abandoned farmland in May, 2010. The three testing sites are close to each other, separated by less than 2 m; and the tested loess samples are windblown deposit (Q_3^{col}) with intensive vertical fractures. To exclude root effect on accuracy of permeability measurement, the upper 50 cm layer of loess was excavated. The tested samples in the in-situ Darcy Test are 32 cm diameter cylinders with a height of 20 cm. As comparative tests, double-ring and pumping tests were also conducted. During the tests, ground temperature was around 10 °C, and the water used was with a temperature of 12.4 °C and a PH value of 7.0. After the in-situ tests, undisturbed loess samples near the tested sites were collected to conduct the *Darcy Test* and grain-size analysis in laboratory.

Data Analysis

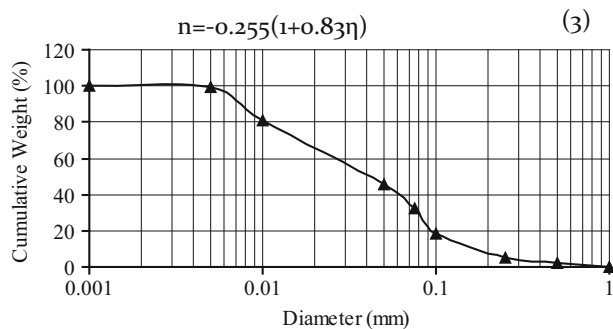
In the in-situ tests, hydraulic gradient was calculated with data recorded by filter tubes and piezometers, respectively, and permeability was calculated according to Darcy's law (Table 1). The averaged values of loess permeability based on data recorded by filter tubes and piezometers are 0.84 and 2.22 m/d, respectively. This difference can be attributed to the difference in positions of installation for the filter tubes and the piezometers. The filter tubes were installed in the middle of the samples, whereas, the piezometers were installed at the bottom as shown in Fig. 1.

Figure 4 is the grain-size distribution of loess based on which parameters d_{10} , d_{17} , d_{20} and d_{60} were obtained. d_{10} , d_{17} , d_{20} and d_{60} are grain sizes corresponding to the percentage finer values of 10, 17, 20 and 60, respectively in Fig. 4. Parameters of n , η and $\varphi(n)$ are used to estimate permeability

Table 1 Recorded data with in-situ Darcy test

| Sample | I_1 | I_2 | V m/d | K_1 m/d | K_2 m/d |
|--------|-------|-------|------------|--------------|--------------|
| C1 | 4.48 | 0.60 | 2.14 | 0.48 | 3.58 |
| C2 | 3.07 | 1.63 | 2.30 | 0.75 | 1.41 |
| C3 | 1.70 | 1.33 | 2.21 | 1.30 | 1.66 |

Note: I_1 and K_1 are hydraulic gradient and permeability measured with filter tubes and I_2 and K_2 are hydraulic gradient and permeability measured with piezometers. V is infiltration rate

**Fig. 4** Grain-size distribution of loess

with empirical formulas (Song et al. 2009). Here, η denotes the ratio of d_{60} to d_{10} , n is porosity calculated with Eq. (3) (Vukovic and Soro 1992; Kasenow 2002). $\varphi(n)$ is a defined parameter based on the changed values with different methods (Table 2). Using a corrected dimensionless coefficient C (Song et al. 2009), three equations developed by Hazen, USBR and Sauerbrei were used to calculate permeability and the results are listed in Table 3.

Permeability was 0.45 m/d when assumed value of hydraulic gradient was 1.0 based on double-ring infiltration test. Permeability was 2.32×10^{-2} m/d when pumping test was conducted in the aquifer at depth of 24 m below ground surface. However, the permeability was 5.96×10^{-4} m/d when tested with indoor *Darcy Test*. Permeability tested with the in-situ Darcy test were then compared to the results measured with the other methods (Table 3).

$$n = -0.255(1 + 0.83\eta) \quad (3)$$

Table 3 shows that the tested results based on in-situ Darcy test is close to the values tested with double-ring infiltration test and grain-size analysis, while differs a lot from the results of pumping test and indoor *Darcy Test*. The difference can be attributed to various factors such as sample-size effects, spatial or direction variation in permeability, and sample disturbance. During the double-ring infiltration test, grain-size analysis, and indoor *Darcy Test*, samples were obtained from shallow vadose zone with smaller size, and the results indicated vertical permeability.

Results of pumping test denoted horizontal permeability of an aquifer at a deep depth.

Compared with the double-ring infiltration tests, hydraulic gradient can be directly obtained (instead of assumption) in the in-situ Darcy test. Compared with three different calculations with grain-size analysis, it differed from the results of Hazen method, while close to the results of USBR and Sauerbrei method, which fit well with the calculations of Song et al. (2009). More than ten samples tested from six sites along Elkhorn River at Nebraska by Song et al. (2009), the results showed that the results from USBR and Sauerbrei method had a better resolution compared to Hazen's method. Compared with the horizontal permeability based on pumping tests, vertical permeability measured with the in-situ Darcy test is 10–100 times of it. This comparison coincides well with the results of Zhang et al. (1996), in which he stated that vertical permeability of loess is approximately 100 times of the horizontal one because of the well-developed vertical fracture in loess. Permeability with the in-situ Darcy Test is about 1,000 times of that with the indoor *Darcy Test*. The possible reason for this large difference is significant disturbance of sample structures during the process of sampling and transportation.

Discussion

All the test conditions of the indoor *Darcy Test* were satisfied in the in-situ Darcy test. Therefore, the design is reasonable:

1. Saturated samples: samples in the in-situ Darcy test were submerged in the single ring with a semi-infinite space at the bottom. They can be exhausted after a long-time vertical infiltration. All the samples were soaked over 10 days during the three groups of tests. After each test, average water contents at the lower part of the samples were measured to be 37.19, 33.23 and 30.57 %, respectively, which can be regarded as saturated loess (Xu and Zhang 1991).
2. Constant water head over samples: Mariott tube used in the in-situ Darcy test guarantees the constant water head condition.
3. Laminar water flow: samples used in the indoor *Darcy Test* are homogeneous sand. In the in-situ Darcy test, samples used are loess with intensive vertical structures, which makes the vertical permeability much bigger than the horizontal ones. However, the single ring used in the test guarantees vertical flow in loess samples which can be regarded as laminar flow, satisfying the Reynolds number less than 10.

In addition, scale effect is another key issue affecting accuracy of the in-situ Darcy Test. Permeability is a parameter indicating how permeable the porous media is, which is

Table 2 Grain-size analysis and the relevant parameters for calculating permeability

| d_{10} | d_{17} | d_{20} | d_{60} | η | n | $\varphi(n)$ | | |
|----------|----------|----------|----------|--------|-----|--------------|------|-----------|
| | | | | | | Hazen | USBR | Sauerbrei |
| 0.18 | 0.14 | 0.09 | 0.027 | 0.15 | 0.5 | 3.4 | 1 | 0.166 |

Table 3 Coefficient of Permeability (in m/d) derived from different methods

| | Double-ring test | Indoor <i>Darcy Test</i> | Pump test | grain-size analysis | | |
|----------|------------------|--------------------------|-----------------------|---------------------|------|-----------|
| | | | | Hazen | USBR | Sauerbrei |
| K' | 0.45 | 5.96×10^{-4} | 2.32×10^{-2} | 11.37 | 0.79 | 2.46 |
| K_1/K' | 1.87 | 1,409.40 | 36.21 | 0.07 | 1.06 | 0.34 |
| K_2/K' | 4.93 | 3,724.83 | 95.69 | 0.20 | 2.81 | 0.90 |

influenced by scale-size of samples and the measurement error (Chowdary et al. 2006). In the future work, it is necessary to study the relationship between permeability and scale effect with the in-situ Darcy Test, and the following research contents can be included: effect of different water head over samples during the test; effect of different diameters of the single ring to test results; different intervals of water head measurement; time of sample immersion.

Conclusion

A set of equipment for the in-situ Darcy test was designed according to the theory of indoor *Darcy Test*. The test conditions of saturated sample, constant water head and laminar flow in the indoor *Darcy Test* were all satisfied in the in-situ test. A comparative analysis showed that the designed in-situ Darcy Test is preferable for permeability measurement of structural soil. In addition, it has advantages of simple devices, easy operation, and intuitive data record. Three sets of the in-situ Darcy Tests were conducted in north western China, with which permeability was obtained for loess in the shallow vadose zone. The obtained permeability is an essential parameter for landslide risk mitigation in the long-term irrigated area. Finally, through the analysis of key issues in the in-situ Darcy Test, it is found that the scale effect on the test results should be studied in the future works. These effects include the different water head effect, different ring diameters, hydraulic head measurement interval, and soil degree of saturation.

Acknowledgments This research was supported by National Land Resources Survey Project (No. 1212011140005 and No. 1212011014024).

References

- ASTM D5126-90 (2001) Standard guide for comparison of field methods for determining hydraulic conductivity in the vadose zone. In: Annual books of ASTM standard, section 4: construction, V.04-08, soil and rock (I): D420–D5779
- Bagarello V, Sferlazza S, Sgroi A (2009) Comparing two methods of analysis of single-ring infiltrometer data for a sandy-loam soil. *Geoderma* 149:415–420
- Bear J (1972) *Dynamics of fluid in porous media*. Dover, Mineola, NY, p 764
- Bouma J (1982) Measuring the hydraulic conductivity of soil horizons with continuous macropores. *Soil Sci Soc Am J* 46: 438–441
- Bouwer H (1996) Rapid field measurement of air entry value and hydraulic conductivity of soil as significant parameters in flow system analysis. *Water Resour Res* 2:729–738
- Chen XH (2000) Measuring of streambed hydraulic conductivity and its anisotropy. *Environ Geol* 12:1317–1324
- Chen S, Lee DT (1964) Estimation of irrigation water demand for paddy rice fields by soil moisture equivalent index. *J Chin Agric Eng* 10(4):15–40
- Childs EC (1969) *An introduction to the physical basis of soil water phenomena*. Wiley, London
- Chong SK, Green RE, Ahuja LR (1981) Simple in-situ determination of hydraulic conductivity by power function descriptions of drainage. *Water Resour Res* 17:1109–1114
- Chowdary VM, Damodhara RM, Jaiswal CS (2006) Study of infiltration process under different experimental conditions. *Agric Water Manag* 83:69–78
- Dupuit J (1963) *Etudes Théoriques et Pratiques sur le mouvement des Eaux dans les canaux découverts et à travers les terrains perméables*, 2nd edn. Dunod, Paris
- Gardner WR (1964) Water movement below the root zone. In: *Proceedings of 8th international congress soil science, Bucharest, 31 Aug–9 Sept, Rompresfilatelia, Bucharest*, pp 317–320
- Gregory JH, Dukes MD, Miller GL, Jones PH (2005) Analysis of double-ring infiltration techniques and development of a simple automatic water deliver system. *Appl Turfgrass Sci*. doi:10.1094/ATS-2005-0531-01-MG
- Healy RW, Mills PC (1991) Variability of an unsaturated sand unit underlying a radioactive-waste trench. *Soil Sci Soc Am J* 55:899–907
- Jacob CE (1940) On the flow of water in an elastic artesian aquifer. *Trans Am Geophys Union* 21(2):574–586
- Kasnow M (2002) Determination of hydraulic conductivity from grain size analysis. *Water Resources Publications*, Littleton, CO
- Lai J, Ren L (2007) Assessing the size dependency of measured hydraulic conductivity using double-ring infiltrometers and numerical simulation. *Soil Sci Soc Am J* 71(6):1667–1675
- Li HL, Sun PP, Chen S et al (2009) A falling-head method for measuring intertidal sediment hydraulic conductivity. *Groundwater*. doi:10.1111/j.1745-6584.2009.00638.x
- Nimmo JR, Stonestrom DA, Akstin KC (1994) The feasibility of recharge rate determinations using the steady-state centrifuge method. *Soil Sci Soc Am J* 58:49–56

- Sammis TW, Evans DD, Warrick AW (1982) Comparison of methods to estimate deep percolation rates. *J Am Water Resour Assoc* 18:465–470
- Schiff L (1953) The effect of surface head on infiltration rates based on the performance of ring infiltrometers and ponds. *Trans Am Geophys Union* 34:256–266
- Sisson JB (1987) Drainage from layered field soils: fixed gradient models. *Water Resour Res* 23:2071–2075
- Song JX, Chen XH, Cheng C, Wang D, Lackey S, Xu ZX (2009) Feasibility of grain-size analysis methods for determination of vertical hydraulic conductivity of streambeds. *J Hydrol* 375:428–437
- Stephens DB, Knowlton RJ (1986) Soil water movement and recharge through sand at a semiarid site in New Mexico. *Water Resour Res* 22:881–889
- Theis CV (1935) The relation between lowering of the piezometric surface and the rate and duration of discharge of a well using ground water storage. *Trans Am Geophys Union* 16(Pt. 2):519–524
- Thiem G (1906) *Hydrologic methods*. J. M. Gebhardt, Leipzig, p 56
- Thomas V, Peter D (2011) Field evaluation of methods for determining hydraulic conductivity from grain size data. *J Hydrol* 400:58–71
- Uma KO, Egboka BCE, Onuoha KM (1989) New statistical grain-size method for evaluating the hydraulic conductivity of sandy aquifers. *J Hydrol* 108:343–366
- Vukovic M, Soro A (1992) Determination of hydraulic conductivity of porous media from grain-size composition. Water Resources Publications, Littleton, CO
- Wu L, Pan L, Roberson M, Shouse PJ (1997) Numerical evaluation of ring-infiltrimeters under various soil conditions. *Soil Sci* 162:771–777
- Xu HA, Zhang L (1991) A discussion about loess water content classification. *J Xi'an Geol Inst* 13(2):65–68 (in Chinese)
- Zhang ZH, Zhai RT, Zhang W et al (1996). Permeability and collapsibility of loess in Dingxi, Gansu Province, China. In: *Proceedings of the Chinese academy of geological sciences, Department of Geology*. China Building Industry Press, China (in Chinese)
- Zhang MS, Dong Y, Sun PP (2012) Impact of reservoir impoundment-caused groundwater level changes on regional slope stability: a case study in the Loess Plateau of Western China. *Environ Earth Sci* 66:1715–1725



Discussion on Assessment in the Collapse of Loess: A Case Study of the Heifangtai Terrace, Gansu, China

Pingping Sun, Maosheng Zhang, Lifeng Zhu, Qiang Xue, and Wei Hu

Abstract

Collapsibility is a unique feature of loess. Besides foundation deformation and subsurface erosion, slope failures can also be resulted from the collapse of loess. Based on analysis of the collapse of loess at the Heifangtai terrace, Gansu, China, a notable difference between the theoretically calculated and actual values of collapse were observed. The theoretical value was less than 50 % of the actual one. Based on this difference, the assessment of the collapse of loess, including definition of collapsible loess and calculation of the collapse are discussed. It is found that collapsible loess is a kind of typical unsaturated soil. Therefore, water content and types of structures were essential factors affecting the collapsibility of loess. Assessment of the collapse of loess, from *why collapse* to *how collapse*, can be achieved by applying parameters representing both water content and types of structure, using the theory of unsaturated soil mechanics.

Keywords

Loess • Collapsibility of loess • Irrigation • Groundwater

Introduction

Loess is a kind of sediment with special physical and mechanical property which is widely distributed in the world (Sun 2005). It covers an area of at least 640,000 km², that is, approximately 6.6 % of the total land area in China, of which three-quarters is collapsible loess (Luo 1998). Loess, especially the collapsible loess, is highly porous sediment which can sustain nearly vertical slopes when dry but subject to catastrophic failure on reaching certain critical moisture contents (Derbyshire et al. 1997, 1999). Collapse of building foundations in collapsible loess

distributed area and consequent cracking of walls is common, and has affected a number of cultural heritage sites (Derbyshire et al. 1997).

Research on the collapse of loess has been conducted by scientists who focus on the engineering properties of loess for more than half a century. From the view of interpreting the reason of the collapse of loess, theories pertinent to hypotheses on soluble salts (Muxart et al. 1995), colloid deficiency and capillary effect (Dudley 1970), under-consolidation of soil and structural effect (Zhang 1964, Zhang et al. 1985; Lei 1987; Gao 1980; Locat 1995), and mechanics of loess (Liu 1997; Chen and Liu 1986; Fredlund et al. 1995) have been proposed. To deal with the practical problems related with the distinctive behaviour of loess, four national standards have been issued in China from 1966 to 2004, where engineering zonation and classifications have been developed for use in regional planning. In the latest one (GB 50025–2004), issues related with types and definition of collapsible loess, and foundation treatments have been improved, with which the engineering projects in collapsible loess distributed areas have been well guided.

P. Sun (✉) • M. Zhang • L. Zhu • Q. Xue • W. Hu
Key Laboratory for Geo-hazards in Loess area, MLR, Xi'an 710054,
Shaanxi, China

Xi'an Regional Center, China Geological Survey, Xi'an 710054,
People's Republic of China
e-mail: sunpingping203@gmail.com; xazms@126.com;
sx-zhulf@163.com; 35225022@qq.com; whwhuhw@hotmail.com

However, most of the previous studies are descriptions of the collapse phenomenon in loess based on the theory of saturated soil. In fact, the collapse of loess in saturated soil is just a special case. It usually occurs at different depth of soil with various water contents (Xie 1999). From the unsaturated soil point of view, Barden et al. (1969) conducted the collapse test of consolidated soil under unsaturated and constant suction condition. Tang (2003) believes that both the synthetic effect of microstructure and uneven suction contribute to the collapse. Yuan et al. (2007) hold the opinion that the collapse of loess is resulted from the decrease of suction stress. Xu and Dai (2009), Xu et al. (2009) introduced a generalized definition of the collapsible loess from the view of unsaturated soil. The theoretical understanding of the collapse of loess is more close to reality from the view of unsaturated soil mechanics theory. However, related studies are usually constrained from the test conditions with complex stress states, which results in great differences between the theoretical and actual values. The Heifangtai terrace was taken as an example in this paper to draw attentions of the related researchers. In this site, the actual value of collapse was more than 5.96 m while a calculated value of collapse is 2.8 m. The related problems when assessing collapsibility of loess were also discussed.

Typical Case Study for the Collapse of Loess

Background of the Study Area

The Heifangtai terrace is located 42 km west of Lanzhou city in Yongjing County, Gansu province, North-West China. The landform comprises windblown loess deposits (Upper Pleistocene), overlying the fourth terrace of the Yellow River, presently forming steep, high cliffs along the river corridor. This used to be an isolated loess platform with a very limited groundwater flow regime. However, following the construction of a major reservoir in 1963, people were resettled onto the platform. In support of this resettlement, most parts of the terrace levels have been reclaimed as farmland with extensive irrigation taking place since 1968.

There are usually five stages of irrigation per year at the Heifangtai platform. The first stage occurs in spring from March to May, the last one occurs in winter from November to December, and the other three stages occur between spring and winter. In the 1980s, the total irrigation volume was 7.22 million m³ per year (about 0.90 m³ per square meter). In the 1990s, this changed into 5.76 million m³ per year (0.64 m³ per square meter). More recently, the total irrigation volume is 5.90 million m³ per year (0.84 m³ per square meter).

Due to the macro-porous fabric of the aeolian loess, widespread soil collapse occurred following the irrigation.

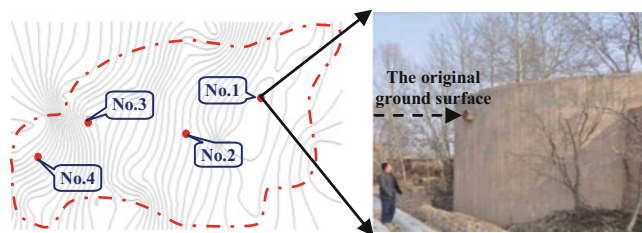


Fig. 1 Location of the water tower

In turn, this resulted in large areas of farmland becoming discarded, most irrigation pipes being destroyed, and the dwellings requiring repair once every 3 or 4 years. Landslides along the plateau edges are also aggravated with the development of the cracks resulting from uneven settlement of the terrace surface.

Actual Value of the Collapse

The phenomenon of conversions of four subsurface cisterns into water tower (Fig. 1) aroused the authors' interest to research on the collapse of loess in the Heifangtai terrace. All the four subsurface cisterns were built at the time of construction in 1968, to meet the need of domestic water supply. Consolidation, tamping, and structural reinforcement were conducted as remedial measures to eliminate collapsibility of loess in the foundation layer. While tremendous collapse occurred to the circumjacent loess of the cisterns. Let us take the No. 1 cistern as an example. It is a cistern with a depth of 9 m, which is built with the top level with the ground surface. However, this top level is now 3.5 m higher than the ground surface due to collapse of the surrounding loess deposits (Fig. 2). This shows that for the top 9 m some 40 % of the original volume has been lost. The other three cisterns (No. 2, 3 and 4) are now in similar situation.

Based on the comparison of topographic maps between 1977 and 1997, obvious differences for the surface elevations at different years were also observed (Fig. 3). The maximum difference for the surface elevation is 5.96 m, with an average difference of 3 m. It shows that the maximum value of land settlement is 5.96 m in the past 20 years. These observations are much greater than the calculations of the collapse of loess in the previous work.

The triggering factors for loess collapse are an increase of groundwater level and infiltration of irrigation water. Based on the tested changes of coefficient of collapsibility with depth (Fig. 4), it shows that the loess layer at the Heifangtai terrace can be divided into four parts on the basis of different mechanism of collapse. Collapse induced by irrigation water occurs between depths of 0–12 m, where the coefficient of collapsibility for loess in the irrigation district differs a lot

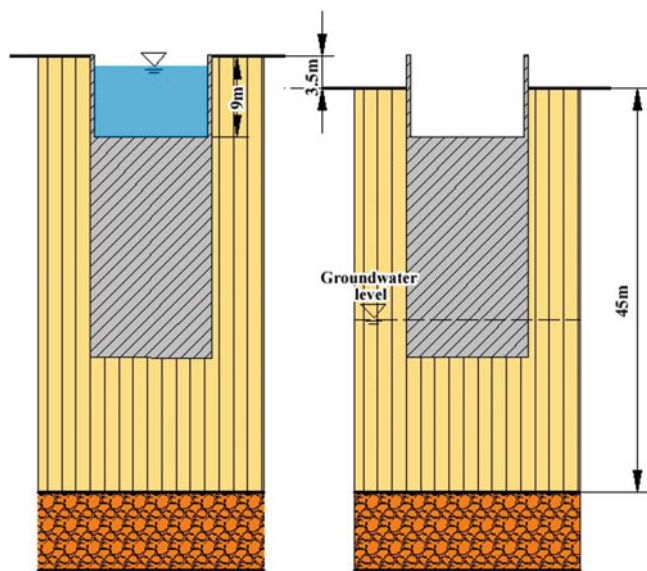


Fig. 2 Conversion of subsurface cistern into water tower

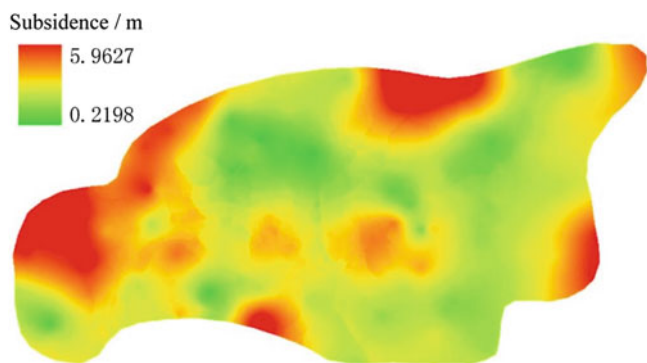


Fig. 3 Comparison of topographic maps between 1977 and 1997

from that in the non-irrigation district. There is no obvious collapse between depths of 12–22 m, where the coefficients are similar in both districts. Collapse induced by capillary water occurs between depths of 22–25 m, and the base of the loess, between 25 and 45 m, is saturated and collapsibility potential can be neglected.

Theoretical Value of the Collapse

The collapse of loess at the study area was self-weight collapse without applied load because most parts of the terrace level have been reclaimed as farmland since 1968. Wells with depth of 15 m were explored in the irrigation and non-irrigation districts. Fifteen samples were collected in each well, with one sample per meter to test the collapsibility of loess, and the averaged values were listed in Table 1.

Table 1 shows that there is still large collapse potential for loess in the upper 15 m, especially for the loess in non-

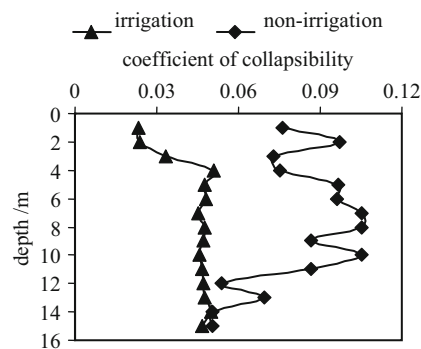


Fig. 4 Changes of coefficient of collapsibility with depth

irrigation district. The average value of the coefficient of collapsibility for loess in the irrigation district is 0.0443, indicating a high potential for collapse, even though it has experienced irrigation for more than 40 years. Based on the information from surrounding wells, loess layer thickness across the irrigation district is approximately 45 m where collapsibility for saturated loess in the lower 20 m is negligible. However, loess layer thickness across the non-irrigation district is 50 m. According to the guide of national standard in China (GB50025-2004), self-weight collapse of loess both in irrigation and non-irrigation districts were calculated with the layer-wise summation method. Assuming that the loess at depth from 0 to 50 m is collapsible, the calculated values of total self-weight collapse in irrigation and non-irrigation districts were 1.68 and 4.48 m, respectively. That is, the collapse of loess in the irrigation district was 2.8 m, which is less than 50 % of the actual collapse of loess.

Discussion on Assessment of Loess Collapsibility

Calculation of the Collapse

The recommended formula in the national standard (GB50025-2004) are based on the mechanism of saturated soil, without considering some essential factors affecting collapsibility of loess, such as changes of water content with depth under long-time irrigation condition, content changes of soluble salts, variations in microstructures of loess, and stress redistribution in loess. In addition, most of the methods testing collapsibility of loess in laboratory are based on lateral confinement condition, which cannot reflect the natural state of the collapse of loess under variable confinement conditions. Multiple factors contribute to the great difference between calculated and actual values of collapse.

Table 1 Coefficients of collapsibility before and after irrigation at different depth

| Depth/m | 1 | 2 | 3 | 4 | 5 | 6 | 7 | 8 | 9 | 10 | 11 | 12 | 13 | 14 | >15 |
|--------------------------------|------|------|------|-----|------|------|------|------|------|------|------|------|------|------|------|
| $\delta_{z1} (\times 10^{-2})$ | 2.43 | 2.40 | 3.34 | 5.1 | 4.75 | 4.83 | 4.52 | 4.74 | 4.73 | 4.57 | 4.66 | 4.72 | 4.77 | 5.01 | 4.68 |
| $\delta_{z2} (\times 10^{-2})$ | 7.63 | 9.73 | 7.30 | 7.5 | 9.67 | 9.63 | 10.5 | 10.5 | 8.69 | 10.5 | 8.65 | 5.36 | 6.93 | 5.03 | 5.04 |

Note: δ_{z1} and δ_{z2} are coefficients of collapsibility of loess in irrigation and non-irrigation district, respectively

Definition of the Collapsible Loess

According to the national standard (GB50025-2004), when the tested value of coefficient of collapsibility under some applied load is more than 0.015, it is defined as collapsible loess; otherwise it is defined as non-collapsible loess. This definition is suitable for loess-distributed area with small-thickness loess. However, for loess with large thickness, the collapse of loess is still not negligible even when the coefficient of collapsibility is less than 0.015 because the value of collapse from accumulation layer by layer is considerable. If the collapsibility of loess with small coefficient is overlooked in practice, tremendous negative effect on stability of buildings will occur.

Further Research Based on the Unsaturated Soil Mechanics Theory

Loess is typical unsaturated soil. Yuan et al. (2007) holds the opinion that the contribution of suction to structure strength is significant, who believes that the collapse of loess is owing to the strength decrease during the process of suction variation. Zhu and Chen (2008) also believes that collapse occur as a result of suction reduction under soaking and applied-load conditions. Based on the above description, one can conclude that water content and types of structures were essential factors affecting the collapsibility of loess. The nature of the collapse of loess can be interpreted applying parameters representing both water content and types of structure. Lu et al. (2010) introduced a parameter representing effective stress in unsaturated soil, which is a combination of water content and structures. With the advanced equipment such as TRIM introduced by Lu et al. (2010) and the combined parameter, assessment of the collapse of loess from why collapse to how collapse may be achieved.

Conclusion

1. The collapse of loess induced by long-time irrigation in the Heifangtai terrace is much greater than empirical values of previous work. The maximum value of collapse is more than 5.9 m, which is two times the calculated value. This fact indicates that assessment of the collapse of loess based on the traditional mechanism of saturated soil cannot satisfy the demands in current engineering.

2. For loess layers with large thickness, the collapse resulted from the loess with coefficient of collapsibility less than 0.015 cannot be negligible.
3. Loess is typical unsaturated soil, and water content and types of structures were essential factors affecting the collapsibility of loess.
4. Tests under complex stress state with advanced equipments are the future trend for studying the mechanism of the collapse of loess.

Acknowledgments This research was supported by National Land Resources Survey Project (No. 1212011140005 and No. 1212011014024).

References

- Barden L, Mador AO, Sides GR (1969) Volume change characteristics of unsaturated clay. *J Soil Mech Found Div* 95 (SM1):33–52
- Chen ZH, Liu ZD (1986) Mechanism of collapsible deformation of loess. *Chin J Geotech Eng* 8(2):1–12
- Code for building construction in collapsible loess regions (GB50025-2004) (2004) China Architecture & Building Press, Beijing
- Derbyshire E, Kemp RA, Meng XM (1997) Climate change, loess and palaeosols: proxy measures and resolution in North China. *J Geol Soc* 154:793–805
- Derbyshire E, Meng XM, Dijkstra TA (1999) Landslides in the thick loess terrain of North-West China. Wiley, England
- Dudley JH (1970) Review of collapsing soil. *J Soil Mech Found Div ASCE* 96(SM3):935–939
- Fredlund DG, et al (1995) The collapse mechanism of a soil subject to one-dimensional loading and wetting. In: Derbyshire E, et al (eds) *Genesis and properties of collapsible soils*, vol 486. Kluwer Academic Publishers, Netherlands, pp 173–206
- Gao GR (1980) Microstructure classification and collapsibility of loess. *Sci Chin* 12:1203–1208
- Lei XY (1987) The relationship between pore types and collapsibility of loess in China. *Sci Chin Ser B* 12:1309–1316
- Liu ZD (1997) *Loess mechanics and engineering*. Shaanxi Science and Technology Press, Xi'an
- Locat J (1995) On the development of microstructure in collapsible soil. In: Derbyshire E, Dijkstra T, Smalley IJ (eds) *Genesis and properties of collapsible soils*. Kluwer Academic, Dordrecht, pp 93–128
- Lu N, Godt JW, Wu DT (2010) A closed-form equation for effective stress in unsaturated soil. *Water Resour Res* 46, W05515. doi:10.1029/2009WR008646
- Luo YS (1998) Assessment of collapsibility of collapsible loess foundation. *Chin J Geotech Eng* 20(4):87–91
- Muxart T et al (1995) Changes in water chemistry and loess porosity with leaching: Implications for collapsibility in the loess of North China. In: Derbyshire E, Dijkstra T, Smalley IJ (eds) *Genesis and properties of collapsible soils*, vol 468. Kluwer Academic, Dordrecht, pp 313–332

- Sun JZ (2005) Loessology, vol 1. Hong Kong archaeological society, Hong Kong
- Tang LS (2003) Synthetic effect of microstructure and uneven suction on loess subsidence. *J Eng Geol* 11(1):30–35
- Xie DY (1999) The past, present and future of the research on mechanical characteristics and application of loess. *Undergr Space* 19(4):273–285
- Xu L, Dai FC (2009) Discussion on the further research in loess hydrocompaction. *J Geomech* 15(1):88–94
- Xu L, Dai FC, Jin YL (2009) Discussion on the mechanism of loess collapsibility from the perspective of unsaturated soil mechanics theory. *Hydrol Eng Geol* 4:62–65
- Yuan ZX, Wang KM, Wang J (2007) Discussion water collapsibility of loess considering unsaturated soil and structure characteristics of loess. *Northw Seismol J* 29(1):12–17
- Zhang ZH (1964) Microstructure of loess in China. *Acta Geol Sinica* 44(3):357–364
- Zhang ZH, Zhang ZY, Zhang P (1985) Microstructure properties and collapsibility evaluation during collapse deformation of loess, vol 6, Geographical paper volume of international exchange. Geography Press, Beijing, pp 67–78
- Zhu YQ, Chen ZH (2008) A new method of studying collapsibility of loess. *Chin J Geotech Eng* 30(4):524–528



Quantitative Deformation Analysis of Landslides Based on Multi-period DEM Data

Qiang Xue, Maosheng Zhang, Lifeng Zhu, Xiujuan Cheng, Ying Pei, and Junbo Bi

Abstract

Quantitative deformation analysis of landslides is a difficult problem in landslide study. The quantitative deformation analysis model of landslide based on multi-period DEM data is established by ArcGIS using four periods of topographic maps obtained in 1977, 1997, 2001, and 2010, in order to reveal the processes of landslide evolution in the Heifangtai Irrigation Area. The deformation amount and deformation rate were calculated in stages for 32 landslides along the margins of Heifangtai platform in Yongjing, Gansu Province. The mean retrograde eroding velocity of landslide scarp was 4.47 m/a from 1977 to 1997, 3.46 m/a from 1997 to 2001, and 1.10 m/a from 2001 to 2010. At the same time, the relational formula between irrigation amount and landslide deformation amount was established, and the landslide evolution tendencies were predicted. The calculation results show that the average retrograde distance of the landslide scarps will be 0.79 m by 2015 and can be reduced to 0.20 m by 2020.

Keywords

Heifangtai platform • Landslide • DEM • Deformation analysis

Introduction

Most of the past landslide deformation analyses were made by dynamic monitoring such as GPS ground surface displacement monitoring, interferometric synthetic aperture radar (InSAR) monitoring, and deep-seated displacement monitoring, etc. Dynamic monitoring is advantageous due to relatively high accuracy, but it is expensive, and very difficult to achieve large area continuous monitoring. Moreover, landslide monitoring data accumulated so far is scarce, which affects comprehensive revelation of occurrence,

dynamic processes and tendencies of landslides over large scale. With development of geographic information system (GIS), geoanalysis based on Digital Elevation Model (DEM) has been increasingly popular (Kawabata and Bandibas 2009; Casalbore et al. 2011; Iwahashi et al. 2012). Guido Ventura et al. (2011) proposed a method of landslide evolution analysis by using multi-period light detection and ranging (LiDAR) data. Dewitte et al. (2008) studied vertical and horizontal displacements of typical landslides at Leupegem Hill in western Belgium from 1952 to 2002 by using multi-period digital terrain model (DTM) coupled with stereophotogrammetry and LiDAR. Although DEM data are very widely applied in landslide research, most of them are based on one set of data or multi-temporal data focusing on landslide displacement analysis only, whereas there are rare studies and applications on deformation amount (e.g., volume) and deformation rate of landslides using multi-period DEM data.

With landslides along the margin of Heifangtai loess platform in the western China as the area of this study, and

Q. Xue (✉) • M. Zhang • L. Zhu • X. Cheng • Y. Pei • J. Bi
Key Laboratory for Geo-Hazards in Loess area, MLR, Xi'an 710054,
People's Republic of China

Xi'an Regional Center, China Geological Survey, Xi'an 710054,
People's Republic of China
e-mail: xueqiang_79@163.com; xazms@126.com; sx-zhulf@163.com;
cugcheng2008@sina.com; 4917895@qq.com;
bijunbo_123@163.com

topographical maps of various periods as data source, we established grid DEMs separately for various periods, stressing on computing ground surface deformation amount and deformation rate of the landslide in different periods, and carried out correlation analysis of landslide-triggering irrigation amount and landslide deformation amount, so as to predict landslide developing tendency in future. Through this study, we explored to develop a kind of technique about quantitative analysis of landslide deformation based on multi-period DEM data, and combined it with irrigation amount to analyze deformation evolution tendency of landslides along the margin of Heifangtai loess platform; this analysis method will be a new thought about landslide deformation analysis.

Outline of Landslides Along the Margins of Heifangtai Loess Platform

Heifangtai platform is situated in Yongjing County, Gansu Province in the western China; it is a loess platform with a total terrace area of 13.44 km² at an altitude about 1,700 m a. s.l. In the Heifangtai platform region, landslides form in late epochs and occur at high frequency with large density, and new landslides take place every year leading to severe deformation of slopes. Most of the landslides are characterized by in-situ tracing and imbricated retrograding sliding; a single landslide exhibits relatively standalone dynamic evolution system with multi-period slip and its deformation is featured in complex nonlinear evolution. Along the about 10-km-long platform margin from Jiaojia in the east to Yanguoxia Town in the west, there are more than 50 landslides varying in size and age, stacking and joining each other to exhibit a banded cluster collectively.

In this paper, only 32 typical landslides along the southern margin of Heifangtai platform were studied, and a multi-period landslide inventory map (Fig. 1) was acquired from multi-period DEM data.

Quantitative Analysis of Deformation of Landslides Along the Margins of Heifangtai Loess Platform

Data Source and Accuracy

Data source of this study includes 1:10,000 topographical maps released by Gansu Administration of Surveying, Mapping and Geoinformation in three periods, i.e., 1977-April, 1997-July, and 2001-July, and the 1:1,000 topographical map made by Xi'an Center of Geological Survey, China Geological Survey through 3D laser scanning in April, 2010.

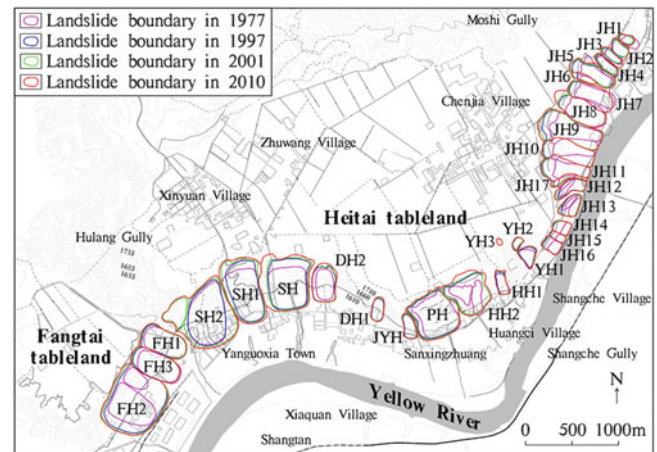


Fig. 1 Multi-period landslide inventory map of the southern margin of Heifangtai platform

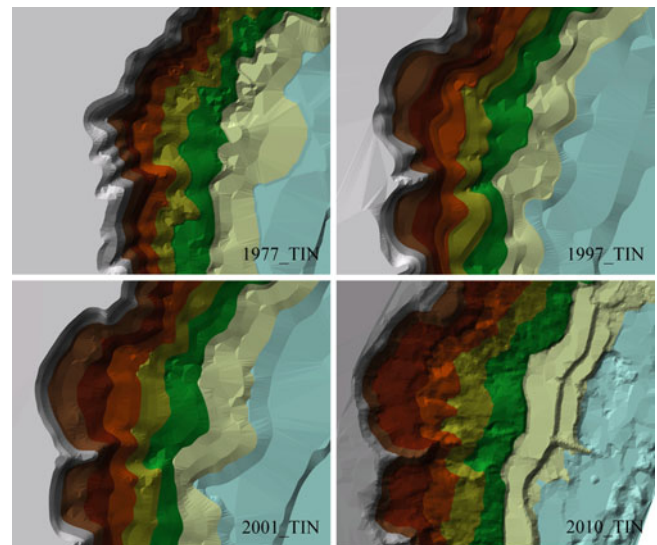


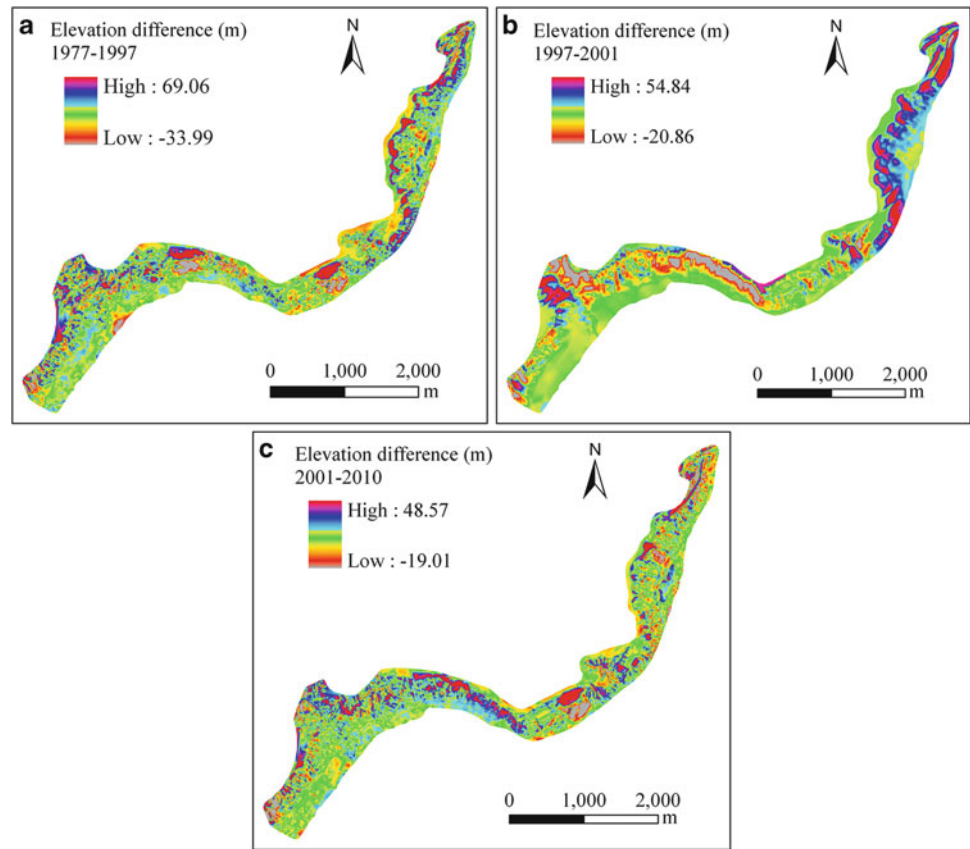
Fig. 2 TIN data of the study area in different periods (local area)

Given a study area covering 5.15 km², based on the data of contour lines and elevation points over the study area obtained through vectorization, we built Triangulated Irregular Networks (TIN) (Fig. 2) in ArcGIS first, and then converted TINs into grid DEMs.

Computation of Landslide Elevation Difference

Subtracting grid DEM data of landslides at Heifangtai platform in 1997 from those in 1977 yields difference values between elevations of landslide bodies in 1977 and in 1997 (Fig. 3a), in which positive values represent decrease in elevation and are attributed to landslide slip zone, whereas

Fig. 3 Changes of elevation differences of Heifangtai landslides in different periods [(a) Elevation difference values during 1977–1997; (b) Elevation difference values during 1997–2001; (c) Elevation difference values during 2001–2010]



negative values represent increase in elevation and are attributed to landslide accumulation zone.

Over two decades from 1977 to 1997, the maximum fall of landslide elevation is 69.06 m. Likewise, subtracting grid DEM data of landslides at Heifangtai platform in 2001 from those in 1997 yields the landslide elevation difference values during this period (Fig. 3b), indicating that the maximum fall of landslide elevation is 54.84 m over 4 years from 1997 to 2001. Subtracting grid DEM data of landslides at Heifangtai platform in 2010 from those in 2001 yields the landslide elevation difference values during this period (Fig. 3c), indicating that the maximum fall of landslide elevation is 48.57 m over 9 years from 2001 to 2010.

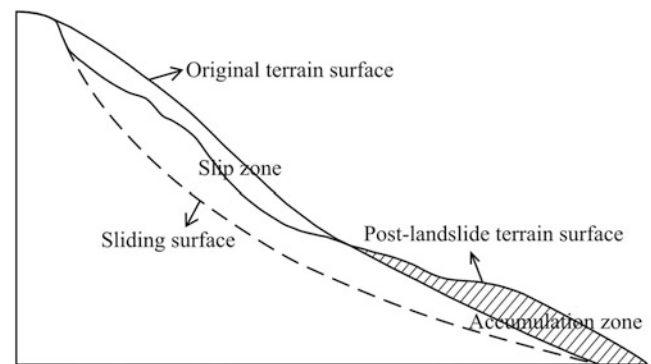


Fig. 4 Slip zone and accumulation zone of a typical landslide

Computation of Landslide Volume

The change in landslide volume can be calculated according to ground surface deformation amount. Suppose that the original curved terrain surface is $H_T = f(x,y)$ and post-landslide curved terrain surface is $H_L = g(x,y)$, within the landslide region L , the volume V (Zhou and Liu 2006) between the original curved terrain surface H_T and the post-landslide curved terrain surface H_L is

$$V = \iint_L [f(x,y) - g(x,y)] dx dy \quad (1)$$

The volume computation result may be positive or negative, depending on the location relationship between original curved terrain surface and post-landslide curved terrain surface. When the post-landslide curved terrain surface is

Table 1 Calculation of frequencies and volumes of landslides at Heifangtai platform

| Landslide No. | Frequency calculation | | | | Volume calculation | | | | | | | |
|---------------|-----------------------|-------------------------|--|-------------------------------|---------------------------------------|-------------------------------|---------------------------------------|-------------------------------|---------------------------------------|-------------------------------|---------------------------------------|--|
| | Number of landslides | Area (km ²) | Frequency (number of landslides/year/km ²) | 1977–1997 | | | 1997–2001 | | | 2001–2010 | | |
| | | | | Slip volume (m ³) | Accumulation volume (m ³) | Slip volume (m ³) | Accumulation volume (m ³) | Slip volume (m ³) | Accumulation volume (m ³) | Slip volume (m ³) | Accumulation volume (m ³) | |
| JH1 | 4 | 0.0157 | 7.74 | 441,487.50 | -4,544.24 | 53,275.81 | -1,656.01 | 16,071.70 | -13,192.88 | | | |
| JH2 | 3 | 0.0285 | 3.19 | 335,847.97 | -11,774.96 | 79,300.41 | -5,371.18 | 73,557.66 | -4,608.25 | | | |
| JH3 | 4 | 0.0264 | 4.60 | 433,748.58 | 0 | 55,093.82 | -9,676.43 | 39,711.93 | -8,462.48 | | | |
| JH4 | 4 | 0.0286 | 4.25 | 480,159.91 | 0 | 46,882.53 | -7,878.95 | 80,849.16 | -7,032.14 | | | |
| JH5 | 4 | 0.0765 | 1.58 | 1,037,765.53 | -15,143.59 | 113,571.17 | -90,792.15 | 227,033.71 | -7,380.47 | | | |
| JH6 | 3 | 0.0164 | 5.55 | 695,176.03 | 0 | 54,748.23 | -21,014.36 | 47,325.26 | -8,929.44 | | | |
| JH7 | 4 | 0.0937 | 1.29 | 1,557,451.37 | 0 | 96,812.89 | -61,668.88 | 136,589.33 | -18,192.09 | | | |
| JH8 | 4 | 0.1168 | 1.04 | 1,427,637.01 | -406.49 | 112,047.99 | -47,150.04 | 394,876.67 | -145,377.24 | | | |
| JH9 | 4 | 0.1759 | 0.69 | 2,516,665.63 | -722.83 | 267,733.06 | -328,878.64 | 493,895.02 | -5,846.82 | | | |
| JH10 | 4 | 0.1092 | 1.11 | 1,644,688.48 | -13.20 | 107,067.75 | -133,970.57 | 248,081.08 | -11,255.99 | | | |
| JH11 | 4 | 0.0908 | 1.33 | 1,682,298.25 | -773.23 | 110,727.55 | -69,000.19 | 184,194.23 | -24,830.42 | | | |
| JH12 | 4 | 0.0421 | 2.88 | 931,814.57 | -9,011.60 | 176,031.69 | -17,184.88 | 113,489.54 | -10,717.95 | | | |
| JH13 | 5 | 0.0413 | 3.67 | 1,842,715.04 | -12,150.35 | 319,965.28 | -6,128.37 | 127,382.16 | -24,504.32 | | | |
| JH14 | 4 | 0.0247 | 4.90 | 802,113.96 | 0 | 82,770.66 | -9,859.29 | 61,780.76 | -14,883.13 | | | |
| JH15 | 4 | 0.0137 | 8.83 | 474,401.71 | 0 | 63,243.70 | -1,927.33 | 44,864.77 | -6,192.37 | | | |
| JH16 | 4 | 0.0278 | 4.36 | 843,399.12 | 0 | 130,852.83 | -2,444.06 | 129,167.85 | -9,295.98 | | | |
| JH17 | 4 | 0.0202 | 6.00 | 593,798.23 | -1,844.82 | 64,543.53 | -44,117.57 | 102,414.92 | -12,138.65 | | | |
| YH1 | 4 | 0.0313 | 3.87 | 159,788.25 | -314,678.10 | 529.60 | -183,225.12 | 192,753.32 | -1,337.29 | | | |
| YH2 | 3 | 0.0111 | 8.16 | 255,857.13 | -5,507.25 | 7,690.81 | -10,904.99 | 48,639.52 | -1,030.86 | | | |
| YH3 | 2 | 0.0035 | 17.55 | 41,031.42 | 0 | 828.91 | -7,576.36 | 11,540.26 | -49.89 | | | |
| HH1 | 4 | 0.0284 | 4.27 | 206,021.75 | -7,504.58 | 5,875.61 | -98,861.76 | 96,483.78 | -3,308.48 | | | |
| HH2 | 5 | 0.1692 | 0.90 | 141,164.51 | -385,891.16 | 141,164.51 | -385,891.16 | 874,703.41 | -417,758.19 | | | |
| PH | 4 | 0.2160 | 0.56 | 2,472,410.74 | -87,500.04 | 7,766.92 | -737,565.23 | 417,660.54 | -7,242.35 | | | |
| JYH | 3 | 0.0326 | 2.79 | 198,622.44 | -56,768.66 | 391,411.28 | -2,287.07 | 115,793.37 | -256.71 | | | |
| DH1 | 3 | 0.0303 | 3.00 | 2,771.79 | -128,788.30 | 385,730.83 | 0 | 126,237.93 | -9.99 | | | |
| DH2 | 4 | 0.0949 | 1.28 | 1,287,438.77 | -68.42 | 1,403,466.30 | 0 | 504,532.54 | -9,681.31 | | | |
| SH | 4 | 0.2923 | 0.41 | 2,415,447.07 | -38,118.21 | 3,848,076.56 | -55,844.27 | 1,246,231.73 | -8,642.67 | | | |
| SH1 | 4 | 0.2656 | 0.46 | 1,927,888.49 | -177,007.38 | 1,926,882.42 | -148,768.08 | 855,545.31 | -34,759.18 | | | |
| SH2 | 5 | 0.3815 | 0.40 | 3,198,417.77 | -136,494.22 | 3,017,146.68 | -142,069.66 | 914,014.38 | -41,262.95 | | | |
| FH1 | 4 | 0.1267 | 0.96 | 1,069,770.13 | -138,131.36 | 533,861.97 | -207,929.80 | 372,526.75 | -10,072.42 | | | |
| FH2 | 5 | 0.3751 | 0.40 | 1,094,677.73 | -91,773.51 | 1,526,427.85 | -89,694.58 | 1,012,812.59 | -52,491.98 | | | |
| FH3 | 4 | 0.1314 | 0.92 | 658,442.95 | -65,300.68 | 561,917.93 | -85,751.53 | 300,751.01 | -9,810.17 | | | |

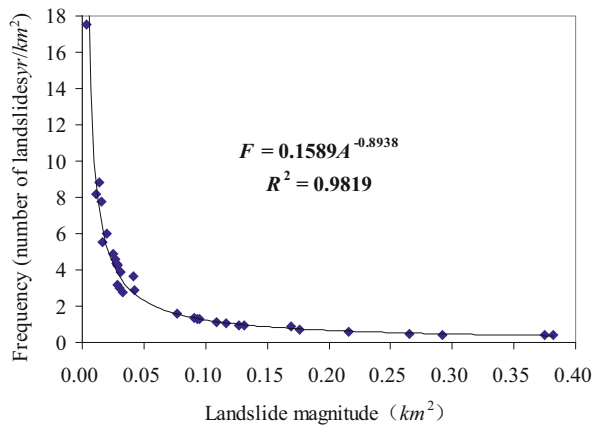


Fig. 5 Magnitude–frequency relationship of landslide

higher than the original curved terrain surface, the volume is negative, representing landslide accumulation zone; in contrast, when the post-landslide curved terrain surface is lower than the original curved terrain surface, the volume is positive, representing landslide slip zone (Fig. 4). Summing up volumes of all slip zones or accumulation zones within a landslide separately yields the total slip volume or total accumulation volume of the landslide.

For the change in landslide volume during a period, we manually delineated landslide boundary based on 3D terrain first, and then calculated landslide volume changes within the boundary using (1) on ArcGIS platform. In this paper, volume changes of 32 typical landslides around Heifangtai loess platform in three time intervals, i.e., 1977–1997, 1997–2001, and 2001–2010, were computed and analyzed respectively to obtain slip volume and accumulation volume of every landslide body during each time interval, as shown in Table 1 below.

Computation of Landslide Frequency

Landslide movement frequency can be expressed as a ratio of number of observed landslide events over unit area, and its unit is number of landslides/year/unit area (Corominas and Moya 2008). The movement frequency of a single landslide is determined by number of landslides occurrence or number of movements identified during observation period, and frequency observation period is 33 years ranging from 1977 to 2010. Landslide frequency F can be computed using the following formula:

$$F = \frac{N}{T \times A} \quad (2)$$

where, F is frequency of landslide occurrence or movement (unit: number of landslides/year/km²), N is number of

landslide occurrence or movement, T is observation period (unit: yr), and A is unit area (unit: km²). See computing result in Table 1 below.

Statistical analysis of 32 landslides along the southern margin of Heifangtai platform yields the magnitude–frequency relationship of landslide (Fig. 5), which exhibits power law distribution and expressed as follows:

$$\begin{aligned} F &= 0.1589A^{-0.8938} \\ R^2 &= 0.9819 \end{aligned} \quad (3)$$

where, A is landslide magnitude (area: km²), F is frequency of landslide events with magnitude greater than or equal to A .

Computation of Landslide Scarp Retrograde Eroding Velocity

Landslide slip displacement during certain time interval can be obtained through continuous aerial photos, satellite photos (or DEMs); then, we divide the total displacement by time interval to get slip velocity of the landslide. This method is able to effectively assess mean slip velocity of a landslide in midterm or long term.

Liquefaction-induced flow occurred in loess after Heifangtai platform landslides slid down, the landslide frontal edges extend underneath terrace scarp composed of Cretaceous sandy mudstone and even enter the Yellow River, so it is difficult to characterize landslide slip velocity with one marker on landslide frontal edge or landslide body. In this study, the retrograde eroding velocity of landslide scarp is used to characterize landslide deformation rate. The retrograding distance of landslide scarp divided by duration is the retrograde eroding velocity of landslide scarp. Meanwhile, the sum of landslide slip volumes of Heifangtai loess platform divided by duration represents the overall deformation rate of Heifangtai platform landslide (Table 2).

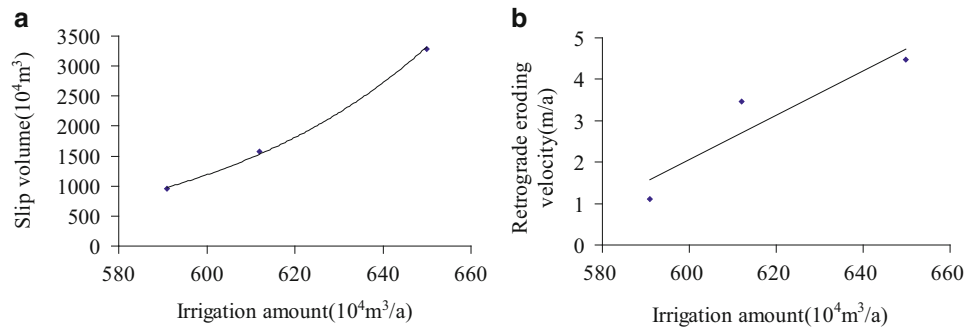
Prediction of Landslide Developing Tendency

Irrigation Amount Versus Landslide Deformation Amount

Long term large area free flooding over Heifangtai platform region makes a great amount of irrigation water seep into the ground to increase groundwater recharge and break the groundwater balance of Heifangtai platform, thereby changing hydrogeological conditions in natural state. Irrigation information of Heifangtai platform irrigation area during various time intervals from 1977 to 2010 is shown in Table 2.

Table 2 Calculation of deformation rates of landslides at Heifangtai platform

| Period | Retrograde distance (m) | | Mean retrograde eroding velocity (m/a) | Total slip volume (m ³) | Overall deformation rate (m ³ /a) | Annual mean irrigation amount (10 ⁴ m ³ /a) |
|-----------|-------------------------|-------|--|-------------------------------------|--|---|
| | Maximum | Mean | | | | |
| 1977–1997 | 136.75 | 89.34 | 4.47 | 32,870,919.83 | 1,643,545.99 | 649.89 |
| 1997–2001 | 47.43 | 13.82 | 3.46 | 15,693,447.08 | 3,923,361.77 | 612.04 |
| 2001–2010 | 35.92 | 9.91 | 1.10 | 9,611,512.19 | 1,067,945.79 | 590.91 |
| Average | | | 3.01 | | 2,211,617.85 | 617.61 |

**Fig. 6** The relationship between irrigation amount and landslide [(a) slip volume; (b) retrograde eroding velocity of landslide scarp]

For each landslide at Heifangtai loess platform, there exists a certain relationship between total slip volume V and annual mean irrigation amount Q (Fig. 6a), that is, the greater the annual mean irrigation amount (unit: 10⁴ m³/a), the larger the landslide slip volume (unit: 10⁴ m³). Statistical analysis shows that they exhibit exponential correlation following the relational expression as follows:

$$\begin{aligned} V &= 2E - 33Q^{12.859} \\ R^2 &= 0.9989. \end{aligned} \quad (4)$$

Certain relationship also exists between mean retrograde eroding velocity S of landslide scarp and annual mean irrigation amount Q (Fig. 6b), that is, the greater the annual mean irrigation amount (unit: 10⁴ m³/a), the higher the mean retrograde eroding velocity (unit: m/a) of landslide scarp. Statistical analysis shows that they exhibit positive correlation following the relational expression as follows:

$$\begin{aligned} S &= 0.0535Q - 30.025 \\ R^2 &= 0.8565. \end{aligned} \quad (5)$$

Prediction of Developing Tendency

It is found from the above calculations that, from 1977 to 2010, the mean retrograde distance of landslide scarp at Heifangtai platform reaches 113.07 m while its mean retrograde eroding velocity is 3.01 m/a. During 9 years since 2001, landslide slip volume, landslide scarp retrograde

Table 3 Predicted developing tendency of landslide scarp retrograde distance at Heifangtai platform

| Time (year) | Retrograde eroding distance (m) |
|-------------|---------------------------------|
| 2013 | 0.90 |
| 2014 | 0.83 |
| 2015 | 0.79 |
| 2016 | 0.72 |
| 2017 | 0.68 |
| 2018 | 0.65 |
| 2019 | 0.47 |
| 2020 | 0.20 |

distance and retrograde eroding velocity decreased significantly, while slope failure exhibits reducing tendency. However, since the landslides at Heifangtai platform are ascribed to high-altitude landslide, with free faces remaining and water table staying high and this loess platform is irrigated by water diverted from the Yellow River, resulting in dense slope cracks, landslides at Heifangtai platform have poor global stability. The loess platform would go on sliding with dislocation, if no effective prevention and control measures are taken.

According to the above analysis on relationship between irrigation amount and landslide deformation amount and the tendency of decreasing overall irrigation amount at Heifangtai platform over these years, it is predicted that landslides will evolve towards a tendency of reduced deformation in future. It is estimated that the mean retrograde distance of landslide scarp will be 0.79 m by 2015 and can be reduced to 0.20 m by 2020 (Table 3).

Conclusions

1. Deformation information of 32 typical landslides along the margin of Heifangtai loess platform during 1977–2010 has been analyzed in stages: from 1977 to 1997, total slip volume is $3,287.09 \times 10^4 \text{ m}^3$ and the mean retrograde eroding velocity of landslide scarp is 4.47 m/a; from 1997 to 2001, total slip volume is $1,569.34 \times 10^4 \text{ m}^3$ and the mean retrograde eroding velocity of landslide scarp is 3.46 m/a; from 2001 to 2010, total slip volume is $961.15 \times 10^4 \text{ m}^3$ and the mean retrograde eroding velocity of landslide scarp is 1.10 m/a.
2. For each landslide at Heifangtai loess platform, both total slip volume and mean retrograde eroding velocity of landslide scarp have certain correlation with annual mean irrigation amount, that is, the greater the annual mean irrigation amount, the larger the landslide slip volume and mean retrograde eroding velocity of landslide scarp; with decreasing irrigation amount at Heifangtai platform each year, the landslide will evolve towards a tendency of decreasing deformation in future. It is estimated that the mean retrograde distance of landslide scarp will be 0.79 m by 2015 and can be reduced to 0.20 m by 2020.
3. Through this study, a new method of landslide deformation analysis has been established and offers scientific basis for prediction, prevention and control of landslides at Heifangtai platform.

Acknowledgments We gratefully thank Gansu Institute of Geo-Environment Monitoring for providing topographical maps in this paper. This study is supported by two projects of China Geological Survey, i.e., Study on Mechanism of Loess Collapses and Landslides Triggered by Irrigation Infiltration (Grant No. 1212011014024) and Detailed Survey of Geological Disasters in Loess Plateau Region in the Northwest China (Grant No. 1212010640330), and one project of National Key Technology R&D Program, i.e., Research and Demonstration of Prevention and Control Technologies for Huge Landslide Disasters in Disturbed Zones of Major Projects (Grant No. 2012BAK10B02).

References

- Casalbore D, Romagnoli C, Bosman A et al (2011) Potential tsunamigenic landslides at Stromboli Volcano (Italy): insight from marine DEM analysis. *Geomorphology* 126:42–50
- Corominas J, Moya J (2008) A review of assessing landslide frequency for hazard zoning purposes. *Eng Geol* 102:193–213
- Dewitte O, Jasselette J-C, Cornet Y et al (2008) Tracking landslide displacements by multi-temporal DTMs: a combined aerial stereophotogrammetric and LIDAR approach in western Belgium. *Eng Geol* 99:11–22
- Iwahashi J, Kamiya I, Yamagishi H (2012) High-resolution DEMs in the study of rainfall- and earthquake-induced landslides: use of a variable window size method in digital terrain analysis. *Geomorphology* 153–154:29–38
- Kawabata D, Bandibas J (2009) Landslide susceptibility mapping using geological data, a DEM from ASTER images and an Artificial Neural Network (ANN). *Geomorphology* 113:97–109
- Ventura G, Vilaro G, Terranova C et al (2011) Tracking and evolution of complex active landslides by multi-temporal airborne LiDAR data: the Montaguto landslide (Southern Italy). *Remote Sens Environ* 115:3237–3248
- Zhou QM, Liu XJ (2006) *Digital terrain analysis*. Science Press, Beijing



Research on Prediction Methods of Surges Induced by Landslides in the Three Gorges Reservoir Area of the Yellow River

Wei Hu, Maosheng Zhang, Lifeng Zhu, Pingping Sun, Xiujuan Cheng, and Jun Jia

Abstract

The risks of surges in the Three Gorges Reservoir area of the Yellow River cannot be neglected. Empirical equations are efficient evaluation methods which should be considered as a priority. Field survey was carried out on the loess landslide and surge which occurred in Jiaojiayatou in the Three Gorges Reservoir area of the Yellow River on 7th February, 2012. Then features of the loess landslide and surge were analyzed. Nine classical equations for landslide-triggered surges were adopted to calculate characteristic parameters of the surge, including initial surge height and run-up height on the opposite bank. Compared with field survey results, characteristic parameters of the surge derived by empirical equations, including ASCE recommended method, method of China Institute of Water Resources and Hydropower Research, Huber and Hager model and Panjiazheng method, are close to those of the real model. The verification coefficients are 2.14, 1.92, 0.6 and 0.66 respectively. After comprehensive comparisons of safety and economical efficiency, Panjiazheng method is recommended to predict similar hazards in the Three Gorges Reservoir area of the Yellow River.

Keywords

Loess • Landslide • Surge • Irrigation • Heifangtai

Introduction

Landslide-induced surges are the important integral parts of landslide disaster chains. Some of historical landslide-induced surges caused even worse disasters than landslides themselves, of which the most well-known case was the surge caused by Vajont rock slope failure in Italy (Muller

1964). Therefore, the assessment of surge risks should be prior to that of mother landslides.

A variety of methods for surge assessment exist which can be summarized in five types, including the theoretical method, the numerical method, the physical modelling method, the field model verification method, as well as empirical method. The theoretical method is rigorous but complex meaning less applicable. The numerical method can calculate featured parameters of surges with high efficiency, with the disadvantage that commercialized software are seldom available. The physical modelling method, mainly referring to the similarity-principle-based laboratory model testing, provides high reference values for surge analysis. The disadvantages include high costs and inconsistency with the real world due to limitations of scale effect. Besides, both numerical modelling and physical modelling have difficulties in deciding reasonable parameters and boundary

W. Hu (✉) • M. Zhang • L. Zhu • P. Sun • X. Cheng • J. Jia
Key Laboratory for Geo-hazards in Loess area, MLR, Xi'an 710054,
People's Republic of China

Xi'an Regional Center, China Geological Survey, Xi'an 710054,
People's Republic of China
e-mail: whuhw@hotmail.com; xazms@126.com; sx-zhulf@163.com; sunpingping203@gmail.com; cugcheng2008@sina.com;
geojia@qq.com

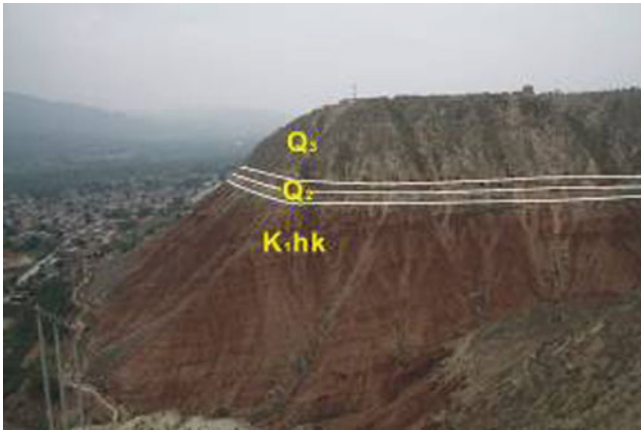


Fig. 1 Typical stratigraphy of Heifangtai

conditions. Hence, the field model verification method which utilizes field observation data to verify calculation equations and further predict similar landslides and surges is a more acceptable method (Zhang et al. 1994). The empirical method is to summarize both theoretical and testing research findings of a type of problems in a summarized and generalized equation. Compared with the former four methods, the empirical method should be considered as a priority for its high efficiency and easy applicability.

The Three Gorges Reservoir of the Yellow River was built in the 1960s. After then, a series of geo-environmental problems including landslide-induced surge disasters were caused. One typical representative slope is the Jiaojiayatou slope of Heifangtai platform, which lies on the north bank of Bapanxia reservoir. Since the 1980s, more than a dozen high-speed loess landslides have occurred. Most of the landslides crushed into the reservoir triggering surges, endangering people and properties along on the river.

This paper studies the latest Jiaojiayatou landslide and subsequent surge occurring on 7th February, 2012. Emergency investigation of the disaster was conducted just a day after obtaining well-recorded field featuring data of the landslide and surge. Then a total of nine equations were utilized to calculate featuring parameters of the surge. By comparing them with field recorded data and obtaining verifying coefficients, the empirical equations were ranked according to their consistencies.

Features of the Landslide and Surge

Heifangtai is a platform of which the bed is the fourth terrace of the Yellow River. The exposed stratigraphic layers, from the youngest to the oldest, are the upper Pleistocene wind-blown loess layer, the mid Pleistocene alluvial silty clay and gravel layer, and the Cretaceous mudstone and sandstone

layer (Fig. 1). The 130 m high Jiaojiayatou slope, locating in the steepest sloping area at the southern edge of Heifangtai, is generally concaved on the top and steep at the toe (Fig. 2). The upper loess slope and the lower bedrock slope have slope gradients of about 32° and 43° , respectively. A provincial road with a width of only 10 m passes by the toe of the slope, while the river reservoir with a width of 200 m and an average depth of 20 m flows just on the outer side of the road. At 16:30 pm on 7th February, 2012, high elevation landslide occurred again, similar to the past several failures, which took place in the same slope. With a total volume of $1.2 \times 10^5 \text{ m}^3$, the landslide is 120 m long, 100 m wide and 10 m thick. The landslide has a clear circle-chair shape and borders (Fig. 3a). After sliding, few sliding masses were left on the sliding bed. Instead, most of the sliding masses disintegrated into powders. Moreover, soils at the bottom of the deposits were in fluid plastic state, demonstrating sharp reduction of soil strength and consequently leading to a high-speed landslide.

When the landslide body reached the toe of the slope, main part of the body with a volume of $1.1 \times 10^5 \text{ m}^3$ almost immediately crushed into the reservoir and triggered surge waves, with only $1.0 \times 10^4 \text{ m}^3$ left at the toe of land. Unfortunately, two cars were just passing and pushed into the water. According to field investigations, the surge pulled out trees with diameters of regular bowls, destroyed the iron roof of a small single house (Fig. 3b). After landing, the surge continued climbing up and further until it reached a run-up height of 6 m and a farthest distance of 270 m (Fig. 3c). In the way, ice blocks with the average thickness of 30 cm were broke apart (Fig. 3d).

Prediction Methods of Surges

Analysis of Factors Influencing Surges

Features of landslide-induced surges are affected by lots of factors, mainly three aspects including landslide factors, hydro-geological factors, and topographic factors (Liu 1987; Carl et al. 2006). The landslide factors refer to size feature including length, width, thickness, etc., material composition and shape of sliding masses, relative positions between landslides and waters, motion modes and tracks of landslides. All these factors mainly influence magnitude and shape of surges. With water depth, width and velocity included, the hydro-geological factors refer to features of waters where surges develop and mainly influence propagation attenuation laws and shapes of surges. Topographic factors refer to angles of river bank slopes, strikes, as well as inshore terrain.

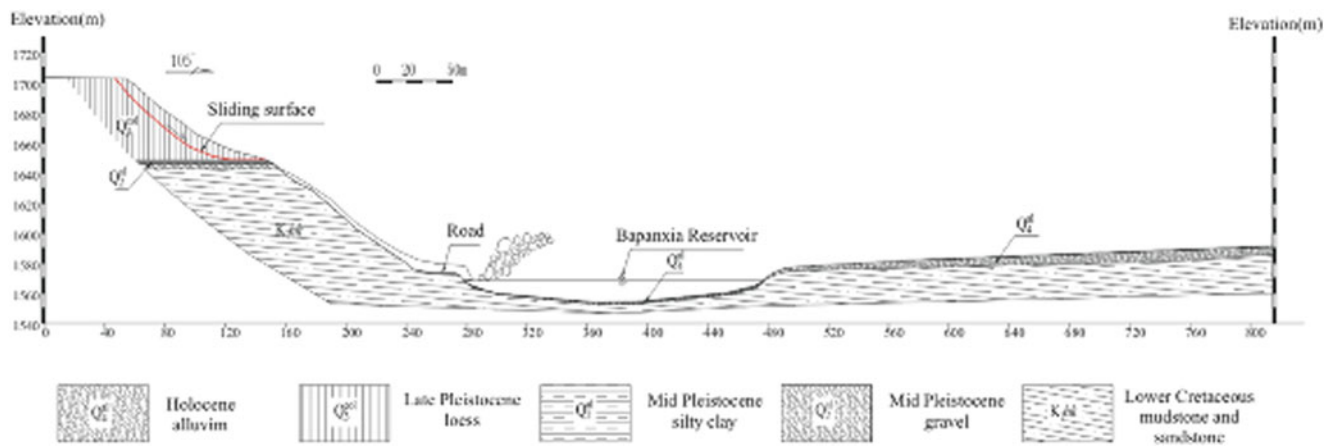
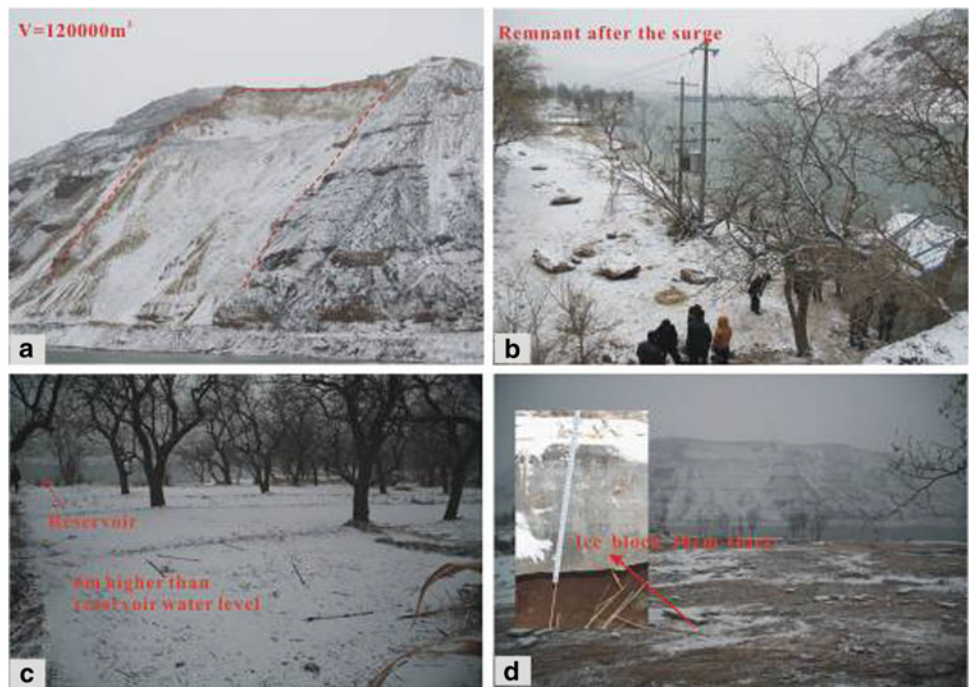


Fig. 2 Schematics of the cross section of Jiaojiayitou and the opposite bank of Yellow River

Fig. 3 Features of the Jiaojiayitou landslide and surge. (a) Overview of landslide, (b) remnants of the opposite bank, (c) maximum run-up height of the surge, and (d) smashed ice blocks



Selection of Calculation Models for Surges

The velocity of a landslide when touching water is one of the parameters prior to surge calculations. For this velocity, several methods already exist, such as Pan’s method, ASCE recommended method, variation method etc. All of these existing methods are based on energy conservation law while considering different assumptions (Hu et al. 2012). Wang’s et al. study (2001) revealed a horizontal projectile motion mode of travelling after a typical Jiaojiayitou landslide breaking away from the mother slope until reaching the boundary between the Yellow River and the road. So if the velocity of a landslide at the shearing outlet is known, then

landslide velocity when touching water could be calculated according to horizontal projectile motion equation.

Huang et al. (2010, 2012) studied and summarized methods for surge calculation. Herein nine most frequently used models, including the ASCE (American Society of Civil Engineers) recommended method (Zhang et al. 1994), the IWHR (China Institute of Water Resources and Hydropower Research) method (Huang and Dong 1983), Pan’s method (1980), as well as models put forward by Hall and Watts (1953), Noda (1970), Slingerland and Voight (1980), Synolakis (1987) Huber and Hager (1997), and Chow (Cited by Huang et al. 2012), were adopted to perform surge calculation.

Table 1 Parameters for surge calculation

| Parameters | Symbol | Value | Unit |
|--|----------|------------------|---------|
| Landslide factors | | | |
| Velocity at shearing outlet via Pan's method | V_1 | 14.9–28 | m/s |
| Velocity at shearing outlet via ASCE method | V_1 | 14.9 | m/s |
| Velocity at shearing outlet via variation method | V_1 | 18.04 | m/s |
| Velocity at shearing outlet via numerical simulation | V_1 | 16.1 | m/s |
| Elevation difference between the centroid of landslide and the water surface | H | 80 | m |
| Tangential obliquity of the sliding track at the shearing outlet | θ | 0 | ° |
| Length of sliding body | L | 120 | m |
| Width of sliding body | W | 100 | m |
| Average thickness of sliding body | H_s | 10 | m |
| Volume of sliding body | V | 12×10^4 | m^3 |
| Density of sliding body | ρ | 1.8 | g/m^3 |
| Hydrological factors | | | |
| Water depth | H_w | 20 | m |
| Width of river | W_w | 200 | m |
| Topographic factors | | | |
| Weighted average slope of the sliding surface | α | 25.7 | ° |
| Slope angle of the opposite bank | β | 35 | ° |
| Empirical coefficients | | | |
| IWHR method coefficient | k | 0.12 | |
| | k_1 | 0.1 | |
| Slingerland and Voight model coefficient | a | -1.25 | |
| | b | 0.71 | |

Determination of Parameters for Models

Parameters for calculation of the Jiaojiayatou landslide and surge occurring on 7th February, 2012, are provided in Table 1. In the table, velocities at shearing outlet are cited from Hu et al. (2012).

$$t = \frac{V_1 \sin \theta + V_1^2 \sin^2 \theta + 2gH}{g} \quad (1)$$

$$S = V_1 \cdot \cos \theta \cdot t \quad (2)$$

$$V_2 = \sqrt{V_1^2 - 2g \sin \theta V_1 t + g^2 t^2} \quad (3)$$

Calculation Results and Discussions

Calculations of Landslide Velocity When Touching Water

Equations (1), (2) and (3) (Cited from Wang et al. 2001) are utilized to calculate horizontal projectile motion features including time t and horizontal motion distance S , as well as landslide velocity when touching water V_2 . The results are presented in Table 2.

Table 2 shows that the horizontal motion distance calculated by variation method is very close to the real situation. However, the distance calculated by Pan's method covers a too wide range to determine an accurate value. While both ASCE recommended method and numerical simulation underestimate the distance. Hence, variation method gives the best calculation results with a landslide velocity of 40.32 m/s.

Calculations of Landslide-Induced Surges

Characteristic parameters of the Jiaojiayatou landslide-induced surge, calculated by nine empirical models, are listed in Table 3. Meanwhile, run-up height was adopted as a verification parameter to compare calculated results and the field survey result which would further acquire field model verification coefficients for the nine methods.

Table 3 shows big differences among the nine methods. Herein, the run-up height of the surge on opposite bank of where landslide touched water is taken as the comparative parameter. The run-up height of field investigation is 6 m. Among the above calculated results, the models put forward by Chow, Noda, Slingerland and Voight, Synolakis, and Hall

Table 2 Comparisons of kinematic parameters for horizontal parabolic motion of the sliding mass

| Method | Time (s) | Motion distance (m) | V ₂ (m/s) |
|----------------------|----------|---------------------|----------------------|
| Pan’s model | 4.04 | 60.20–113.12 | 42.30–48.49 |
| ASCE method | 4.04 | 60.21 | 42.31 |
| Variation method | 4.04 | 72.89 | 40.32 |
| Numerical simulation | 4.04 | 65.05 | 42.75 |

Table 3 Characteristic parameters of the surge calculation by all models

| Method | Initial height of the surge (m) | Calculated run-up height (m) | Verification coefficient |
|--------------------------------|---------------------------------|------------------------------|--------------------------|
| ASCE method | 4.04 | 2.8 | 2.14 |
| IWHR method | 19.8 | 3.13 | 1.92 |
| Chow’s model | – | 82.94 | 0.07 |
| Noda’s model | 28.8 | – | – |
| Slingerland and Voight’s model | 163.32 | – | – |
| Huber and Hager’s model | 12.28 | 10 | 0.60 |
| Synolakis’ model | – | 36.76 | 0.16 |
| Hall and Watts’ model | – | 35.37 | 0.17 |
| Pan’s model | 20 | 9.06 | 0.66 |

overestimate initial height and run-up height. On the contrary, the other four methods, including the ASCE method, the method recommended by Institute of Water Resources and Hydropower Research, Huber and Hager model and Pan’s method, estimate surge features reasonably, with corresponding verification coefficients be 2.14, 1.92, 0.6 and 0.66.

Discussions of Calculation Results

Different assumptions lead to the big contrasts of the calculation results presented above.

The run-up height for Chow model is shown in (4), demonstrating that Chow model is completely relying on transforming relationship between kinetic energy and potential energy. Two assumptions for the model, on the one hand, are no energy loss in the process of wave motion, and immediate transformation of kinetic energy into potential energy once surges reach river banks. According to field investigation data, there was an extra 270 m of motion distance outwards after the surge climbed up to the bank, meaning very considerable kinetic energy. Hence, the calculated run-up height has very big inconsistency compared with the real data.

$$h = \frac{V_2^2}{2g} \tag{4}$$

$$h/H_w = 2.831(\cot \beta)^{0.5}(H_b/H_w)^{1.25} \tag{5}$$

$$h/H_w = 3.1(H_b/H_w)^{1.15} \tag{6}$$

The models of Synolakis and Hall and Watts are listed in (5) and (6), where H_b is surge height at any given time. Since the empirical coefficients in the two models were derived by the researchers’ own model tests whose testing conditions differed greatly from the conditions in Jiaojiaytou, the two models overestimate run-up height.

Relatively speaking, the run-up heights calculated by the ASCE method, the method recommended by Institute of Water Resources and Hydropower Research, Huber and Hager model and Pan’s method, are close to the real recorded data. The consistencies not only reflect similar assuming conditions for those models and Jiaojiaytou landslide and surge, but also confirm broad applicability of these methods. Furthermore, to ensure enough safety and, meanwhile not to overestimate surge risks, Pan’s method is recommended.

Conclusions

1. The results for prediction of velocity, calculated by four methods, including Pan’s method, ASCE recommended method, variation method and numerical simulation, are compared with the real terrain and field investigation. Among them, variation method provides the most reasonable landslide velocity at the shearing outlet to calculate velocity when landslide body touching water. The velocity is 40.32 m/s.
2. The calculated results of the surge with nine empirical models show that four methods, including ASCE recommended method, the method recommended by Institute of Water Resources and Hydropower Research, Huber and Hager model, Pan’s method, provide reasonable surge features. The corresponding verification coefficients are 2.14, 1.92, 0.6 and 0.66, respectively. Taking into account

both safety and economy, Pan's method is recommended for calculation of similar surges in the future.

3. In the past, surge waves and potential disasters have been neglected in geo-hazard prevention in the Three Gorges area of the Yellow River. In the future, it is necessary to incorporate surge risk evaluation into the risk management of entire geo-hazard chains.

Acknowledgments This research work was supported by the National Science and Technology Support Program (Project number 2012BAK10B02) and the Massive Land and Resources Survey project funded by China Geological Survey (Project number 1212011014024). The authors are grateful to the thoughtful comments from Prof. Faquan Wu, Prof. Fuchu Dai and Prof. Xiangjun Pei.

References

- Carl BH, Finn L, Geir P, Doug GM (2006) Mechanisms of tsunami generation by submarine landslides: a short review. *Nor J Geol* 86:255–264
- Hall JV, Watts JW (1953) Laboratory investigation of the vertical rise of solitary waves on impermeable slopes. Beach Erosion Board, Office of the Chief of Engineers, U.S. Army Corps of Engineers
- Hu W, Zhang MS, Zhu LF, Wang FW (2012) Kinetic simulation of irrigation-induced loess landslide in Heifangtai. *J Eng Geol* 20(2):183–188
- Huang ZW, Dong XL (1983) Test study of surges induced by reservoir landslides. China Waterpower Press, Beijing, pp 157–170
- Huang BL, Liu GN, Chen XT, Wang SC (2010) Annual evaluation report on the project 'Mechanism study of steep slope failures in the Three Gorges'. Wuhan Centre of China Geological Survey, Wuhan
- Huang BL, Chen XT, Yin YP, Zhang H (2012) Computing system for impulse wave in reservoir generated by landslide & rockfall. *J Eng Geol* 20(6):909–915
- Huber A, Hager WH (1997) Forecasting impulse waves in reservoirs. Dixneuvième Congress des Grands Barrages C, 22–25 June 2009. Florence, Italy, pp 993–1005
- Liu SK (1987) Preliminary study of the attenuation factors of surge run-up height induced by Xintan landslide in Xinling Gorge of Yangtze River. *Water Resour Hydropower Eng* 9:11–14
- Muller L (1964) The rock slide in the Vajont Valley. *Rock Mech Eng Geol* 2:148–212
- Noda E (1970) Water waves generated by landslides. *J Waterways Harb Coastal Eng Div* 96(4):835–855
- Pan JZ (1980) Anti-sliding stability of structures and landslide analysis. Water Conservancy Press, Beijing
- Slingerland RL, Voight B (1980) Occurrences, properties, and predictive models of landslide-generated water waves. In: Voight B (ed) *Rockslides and avalanches*. Elsevier, Amsterdam, pp 317–397
- Synolakis CE (1987) The runup of solitary waves. *J Fluid Mech* 185:523–545
- Wang JD, Xiao SF, Zhang ZY (2001) The mechanism for movement of irrigation-induced high-speed loess landslides. *J Eng Geol* 20(2):241–246
- Zhang ZY, Wang ST, Wang LS (1994) Principles of engineering geology analysis. Geological Publishing House, Beijing



Analyses of the Changes of Loess Engineering Properties Induced by Irrigation

Wei Hu, Lifeng Zhu, Maosheng Zhang, Ying Pei, and Junbo Bi

Abstract

Irrigation has changed the original environment of loess. In the process of moistening and saturating after irrigation, engineering properties of loess such as microstructure, physical properties, mechanical properties and water-physical properties have been changed, which become important conditions inducing loss due to geo-hazards. Taking Heifangtai of Gansu province as a studied irrigation area, systematic studies were carried out on loess ranging from in-situ tests to laboratory tests, from traditional soil mechanics to mechanics for unsaturated soils, from microstructures to macro properties. Based on the study, the changes of engineering properties of loess due to irrigation were revealed. The results show that irrigation destroys the primary structures of loess with general decrease of the total amount of voids, as well as disappearance of overhead voids. Due to irrigation, natural water content, in-situ density and dry density all increase while natural void ratio decreases. Collapsibility of loess decreases. The shear strength decreases dramatically. In terms of soil mechanics for unsaturated soils, irrigation causes the increase of water content of loess and decrease of matric suction. As a result, the strength parameters for unsaturated loess show decreasing trends.

Keywords

Loess • Engineering geological property • Irrigation • Heifangtai

Introduction

Loess platforms, as the main agricultural areas in the Loess Plateau in China, have little precipitation and intense evaporation. Since the end of the Spring-and-Autumn Period, irrigation in the loess region has lasted for over 2,400 years. Irrigation greatly increases the agricultural yield, but on the other hand, causes loess geo-hazards which range from collapses of platforms to a great amount

of loess landslides at edges of platform slopes. Of these, typical examples include the Hazards in Heifangtai in Gansu province and Jingyang in Shaanxi province. For instance, Heifangtai is an isolated platform which has been cut into two halves right in the middle by Hulang Ditch, as shown in Fig. 1. Originally, few people lived on this platform. Since 1968 when immigrants of the Liujiaxia reservoir project moved here, the platform has endured more than 40 years of continuous broad irrigation. Water infiltrates through the loess layer until it reaches the surface of the underlying silty clay layer of which the saturated permeability K_s is one tenth of that of the loess layer (Fig. 2). Also the loess slopes have low discharging ability. So the groundwater table at the bottom of the loess layer increases gradually causing loess landslides. In general, there are two reasons contributing to the overlapping of loess landslides at the edges of these irrigated platforms.

W. Hu (✉) • L. Zhu • M. Zhang • Y. Pei • J. Bi
Key Laboratory for Geo-hazards in Loess Area, MLR, China Ministry of Land and Resources, Xi'an 710054, People's Republic of China

Xi'an Regional Center, China Geological Survey, Xi'an 710054, Shaanxi, People's Republic of China
e-mail: whwhuhw@hotmail.com; sx-zhulf@163.com; xazms@126.com; peiyang@email.jlu.edu.cn; 85441945@qq.com

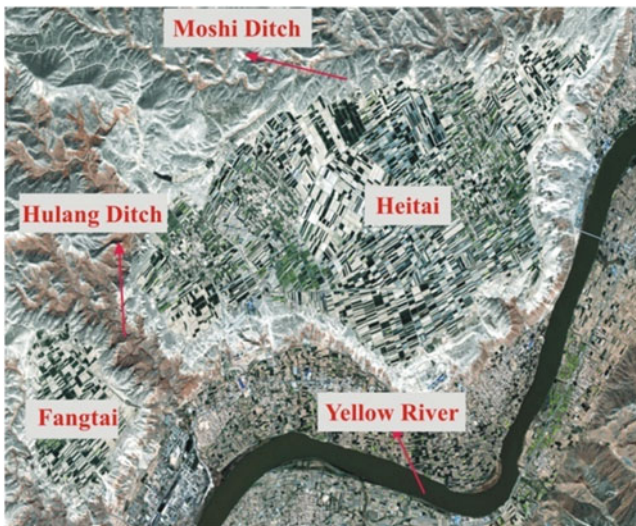


Fig. 1 Remote sensing map of Heifangtai

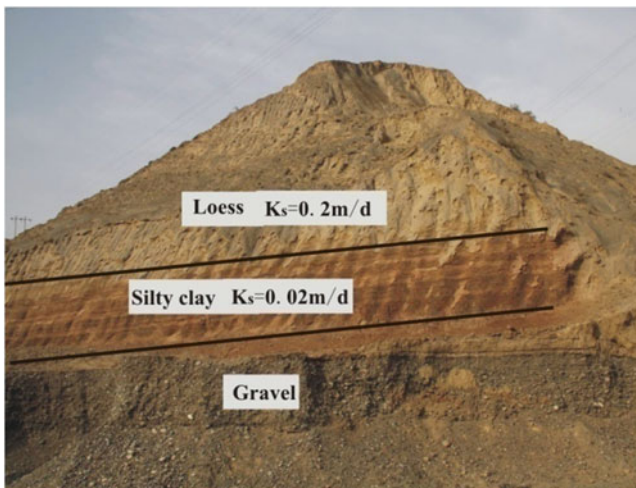


Fig. 2 Typical Quaternary layers of Heifangtai

That is, irrigation not only changes the primitive hydro-geological conditions by raising the groundwater table, but also weakens the engineering properties of loess, leading to the occurrences of loess collapses and loess landslides (Lei 1995; Wang 1992; Wang and Liu 1999; Jin and Dai 2007; Long et al. 2007).

At present, there have been many researches on the changes of hydro-geological conditions due to irrigation. In terms of the impacts of irrigation on loess engineering properties, the existing researches can be grouped into two aspects, including studies concerning the structural changes of loess due to soaking (Hu et al. 1999; Cheng 2002; Guo et al. 2008) and discussions of mechanical properties responses to changes of water contents of loess (Zheng and

Zhang 1989; Ueno et al. 2005; Zhang et al. 2006; Hu et al. 2005). However, the past studies only focused on one certain aspect of the engineering properties responses of loess due to irrigation. Problems still exist in terms of systematic research and quantitative verification. In this paper, Heifangtai in Gansu province is taken as an example to study how engineering properties change due to irrigation. Exploration wells with a depth of 15 m in both irrigated and non-irrigated areas were excavated. In the wells loess undisturbed samples were taken at an interval of 1 m to conduct comparative tests and analyses of loess structures, physical properties and deformation features. Also by artificially controlling water content, loess strength parameters for different water contents were measured. By doing so, the changing mechanisms of loess engineering properties due to irrigation were systematically revealed. Some of the main findings of these tests are presented in this paper.

Changes of Loess Micro-structures

The SEM images magnified for 400 times for both irrigated and non-irrigated loess are presented in Fig. 3. Both samples show the same overall particle shape that is single-grain-based, supplemented by collecting particles. In terms of the contact pattern of particles, both samples are point-contact-based, demonstrating that the loess is highly prone to collapse with big collapsibility even after irrigation. In terms of the voids, both samples are based on inter-granular pores, supplemented by overhead pores. Compared with non-irrigated loess, irrigated loess has much fewer void amounts.

Changes of Loess Physical Properties

Comparisons of physical index properties including specific gravity, plastic limit and particulate component show no evident differences between irrigated and non-irrigated loess samples. However, other physical properties, including natural water content, in-situ density, dry density and natural void ratio, are greatly influenced by irrigation. The comparative results are presented in Figs. 4, 5, 6 and 7. Due to irrigation, the values at different depths are prone to be even with less variation. Specifically, the averaged tested values of natural water content, in-situ density and dry density increase for 7 %, $0.25\text{ g}\cdot\text{cm}^{-3}$ and $0.14\text{ g}\cdot\text{cm}^{-3}$, respectively. On the contrary, the averaged values of natural void ratio decrease for about 0.18.

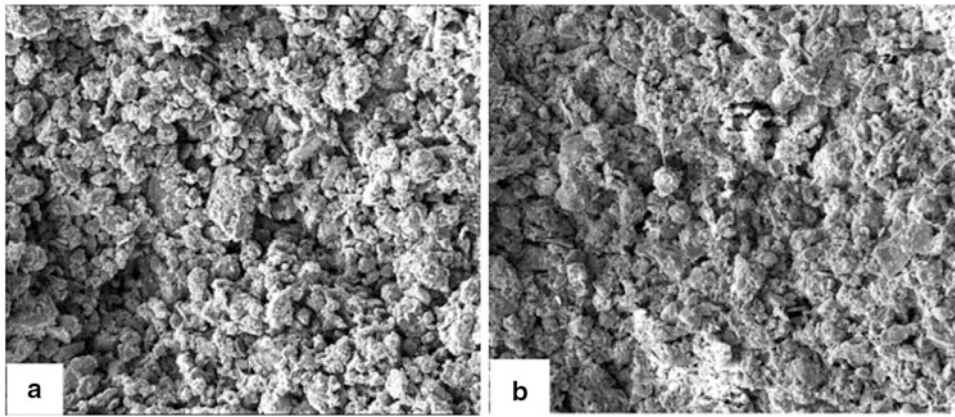


Fig. 3 SEM images ($\times 400$) of (a) non-irrigated loess, and (b) irrigated loess

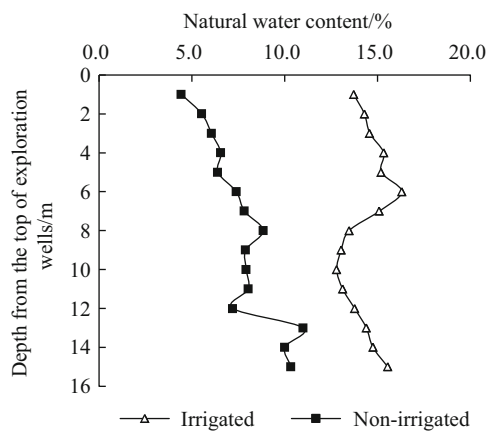


Fig. 4 Comparison of natural water content of loess

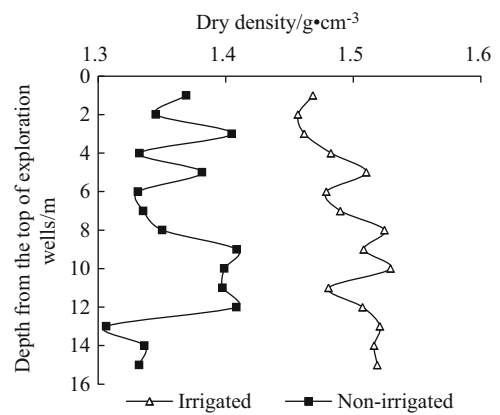


Fig. 6 Comparison of dry density of loess

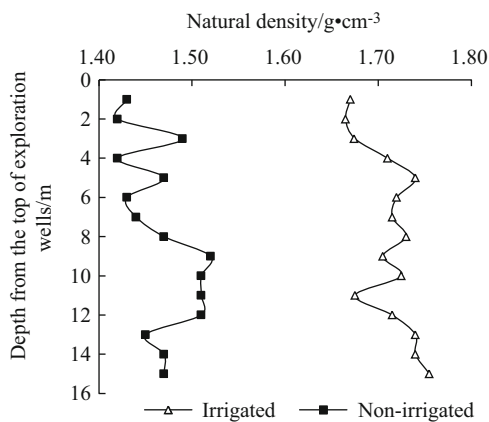


Fig. 5 Comparison of in-situ density of loess

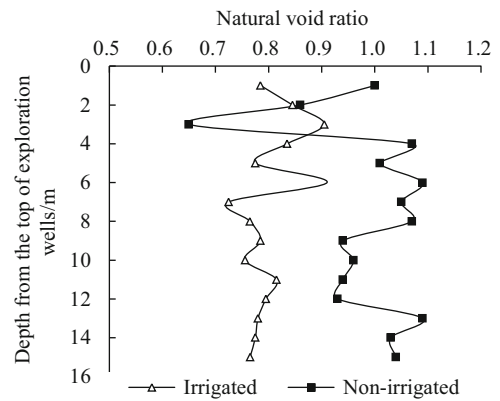


Fig. 7 Comparison of natural void ratio of loess

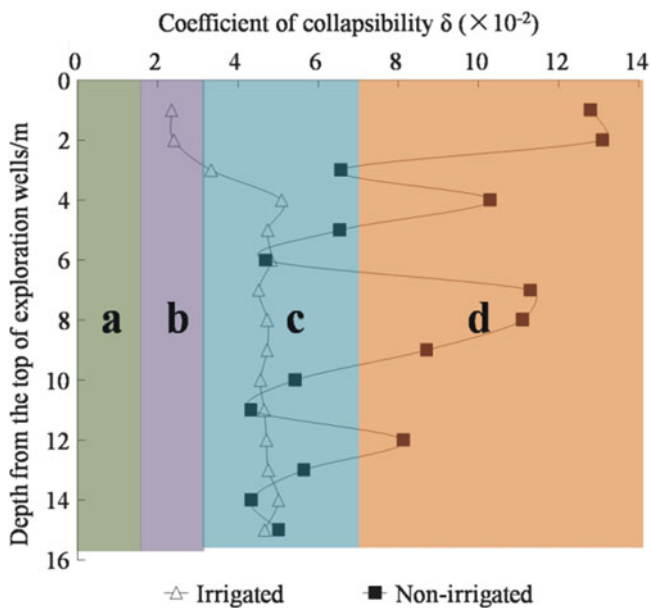


Fig. 8 Comparison of coefficient of collapsibility. (a) non-collapsible zone, (b) slightly collapsible zone, (c) moderately collapsible zone, and (d) intensively collapsible zone

Changes of Loess Collapsibility

Both the absolute values and variations of loess collapsibility are greatly reduced by irrigation, as shown in Fig. 8. According to Code for building construction in collapsible loess regions (China Architecture and Building Press 2004), collapsibility of loess can be divided into four levels, non-collapsible, slightly collapsible, moderately collapsible and intensively collapsible. The four groups are separated by boundary values of 0.015, 0.03 and 0.07. Compared with the above standards, the non-irrigated loess mainly belongs to the intensively collapsible group, while the irrigated loess is moderately collapsible.

Changes of Loess Strength Properties

Strength of loess is mainly controlled by loess structure and physical properties, of which water content is the most decisive factor. Besides, irrigation mainly changes water content of loess. Therefore, both in-situ and laboratory studies of the irrigation impacts on loess strength were carried out at different water contents. For in-situ shear tests, two water contents including natural state and saturated state were conducted. For laboratory shearing tests, more water content levels were carried out.

Comparisons Based on In-situ Shear Tests

The testing schemes of in-situ shear tests are presented in the paper “The method for in-situ large scale shear test of saturated soils and its application” in this proceeding. Herein only the test results are presented (Table 1). Compared with strength parameters of loess in natural state, the cohesion of loess in saturated state reduces from 44.65 kPa to 17.35 kPa, while the internal friction angle drops from 14.18° to 11.98°. This indicates that the main soaking impact on the in-situ shear strength is reflected by the dramatic reduction of cohesion.

Comparisons Based on Conventional Triaxial Shear Tests

Taken from the non-irrigated loess well, undisturbed loess samples were prepared with multiple levels of water contents to carry out consolidated-undrained (CU) triaxial tests. The relationships between shear strength parameters of loess and water content are depicted, as shown in Fig. 9. The results show that shear strength parameters of loess have greater water sensitivity than that of in-situ shear test parameters. With the increase of water content, cohesion decreases in logarithmically, while internal friction angle decreases linearly. Both curves have high fitting degrees.

Comparisons Based on Suction-Controlled Shear Tests

From the perspective of unsaturated soil mechanics, irrigation leads to the increase of water content of loess, or changes of matric suction. Then strength of loess changes accordingly. The multi-functional GDS triaxial apparatus was utilized to carry out suction-controlled shear tests of unsaturated loess. The testing conditions are described in Table 2. The test results are given in Figs. 10, 11, and 12. They show that with matric suction reducing from 100 kPa to 20 kPa, internal friction angle decreases for about 1° and cohesion drops for about 22 kPa. One of the explanations for the cohesion drop is that cohesion actually reflects the comprehensive inter particle actions involving van der Waals attraction, electrical double-layer repulsion, chemical cementation and capillary action (Lu and Likos 2006). All of the above actions are state variables which are closely dependent on water content. With the increase of water content, the overall influence of the above actions on

Table 1 Shear strength parameters of in-situ shear tests of loess

| Testing condition | Water content (%) | Cohesion (kPa) | Internal friction (degree) |
|--|-------------------|----------------|----------------------------|
| In-situ shear test of loess in natural state | 9.1 | 44.65 | 14.18 |
| In-situ shear test of loess in saturated state | 33.1 | 17.35 | 11.95 |

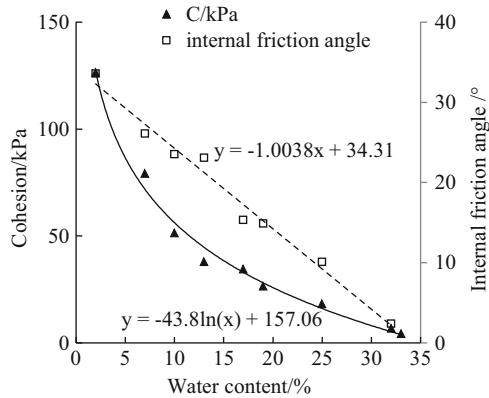


Fig. 9 Relationship between CU strength parameters and water content of loess

Table 2 Testing conditions of triaxial tests of unsaturated loess

| Matric suction (kPa) | Confining pressure (kPa) | Pore air pressure (kPa) | Pore water pressure (kPa) |
|----------------------|--------------------------|-------------------------|---------------------------|
| 20 | 150 | 50 | 30 |
| | 250 | 50 | 30 |
| | 350 | 50 | 30 |
| 50 | 100 | 50 | 0 |
| | 150 | 50 | 0 |
| | 250 | 50 | 0 |
| 100 | 150 | 100 | 0 |
| | 200 | 100 | 0 |
| | 300 | 100 | 0 |

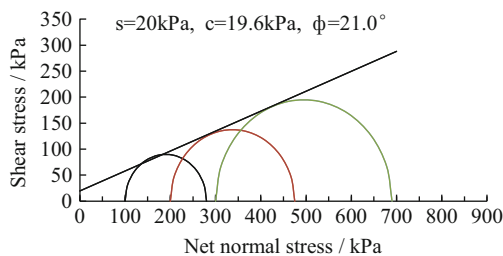


Fig. 10 Mohr circle and shear strength parameters under matric suction of 20 kPa

strength weakens. This weakening effect is particularly obvious in water sensitive loess. On the contrary, internal friction angle represents inherent material behaviour, making it less affected by water content.

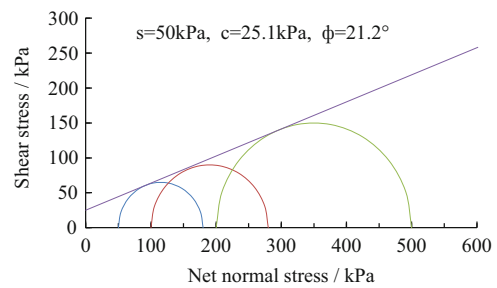


Fig. 11 Mohr circle and shear strength parameters under matric suction of 50 kPa

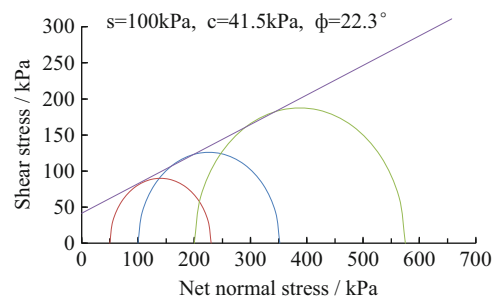


Fig. 12 Mohr circle and shear strength parameters under matric suction of 100 kPa

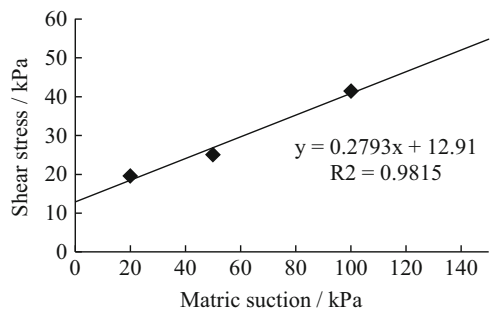


Fig. 13 Relationship between cohesion and matric suction

Furthermore, the relationship between cohesion and matric suction could be drawn on the basis of the above mentioned suction-controlled testing results (Fig. 13). From the linear fitting curve in Fig. 13, both the effective cohesion c' and the additional friction angle contributed by matric suction ϕ^b can be found. The effective cohesion c' is the intercept equalling 12.91 kPa. ϕ^b is the slope equalling 15.6°.

Conclusions

Irrigation has obvious impacts on loess engineering properties, ranging from micro-structure to macro physical indices, from deformation properties to strength parameters. Of these, strength weakening is the most vital factor to cause frequent landslides.

1. In terms of micro-structure, irrigation mainly influences the pore features of loess. The primary structure of loess is destroyed. This leads to the reduction of the total amounts of voids, which is mainly reflected by the dramatic reduction or even disappearance of overhead voids.
2. In terms of physical properties, irrigation has obvious impacts on properties including natural water content, density and void ratio. In contrast, other properties such as specific density, plastic limit and particulate composition are slightly affected.
3. On deformation, irrigation not only increases the averaged values of loess collapsibility, but also reduces the variation of collapsibility values for different depths.
4. Although having different correlations with water content, shear strengths of soils acquired from both in-situ and laboratory tests decreased, revealing evident water sensitivity of loess strength.

Acknowledgments This research work was supported by the National Science and Technology Support Program (Project number 2012BAK10B02) and the Massive Land and Resources Survey project funded by China Geological Survey (Project number 1212011014024). The authors would like to thank Dr. Tianfeng Gu from Northwest University for his great effort in the SEM analyses and suction-controlled shear tests.

References

- Cheng ZY (2002) Soil sink caused by irrigation and the influence on ecological environment of loess platform in middle Gansu province. *J Desert Res* 22(2):172–176
- Guo YW, Zhang YL, Dang XL et al (2008) Behaviors of CaCO₃ in loess collapse caused by irrigation. *ACTA PEDOLOGICA SINICA* 45(6):1034–1039
- Hu RL, Guan GL, Li XQ et al (1999) Micro structure effect on the subsidence of loess. *J Eng Geol* 7(2):161–167
- Hu SX, Zhou YD, Chen ZH (2005) Test study on strength character of unsaturated and undisturbed loess. *Rock Soil Mech* 26(4):660–664
- Jin YL, Dai FC (2007) The mechanism of irrigation-induced landslides of loess. *Chin J Geotech Eng* 29(10):1493–1499
- Lei XY (1995) The hazards of loess landslides in the southern tableland of Jingyang county, Shaanxi and their relationship with the channel water into fields. *J Eng Geol* 3(1):56–64
- Lu N, Likos WJ (2006) Suction stress characteristic curve for unsaturated soils. *Geotechn J Geoenviron Eng* 132(2):131–142
- Long JH, Li TL, Lei XF (2007) Study on physical properties of soil in sliding zone of loess landslip. *Chin J Geotech Eng* 29(2):289–293
- Ministry of Construction & General Administration of Quality Supervision, Inspection and Quarantine (2004) Code for building construction in collapsible loess regions. China Architecture and Building Press, Beijing
- Ueno M, Nishimura T, Kato M et al (2005) Variation of shearing characteristics of loess soil after irrigation. *Northwestern Seismological J* 27(2):128–134
- Wang JD (1992) A mechanism of high-speed loess landslides-saturated loess creeping liquefaction. *Geol Rev* 38(6):532–538
- Wang JD, Liu Y (1999) A further study on the mechanism of high-speed loess landslides in state of creeping and sliding liquefaction. *J Northwest Univ (Nat Sci Edn)* 29(1):79–82
- Zheng JG, Zhang SM (1989) The strength characteristics of collapsible loess during moistening process. *Hydrogeol Eng Geol* 2:6–10
- Zhang MH, Xie YL, Liu BJ (2006) Analysis of shear strength characteristics of loess during moistening process. *Rock Soil Mech* 27(7):1195–1200



Deformation Behavior of Mechanically Stabilized Earth Walls with Geocomposite Drainage Under Seepage Condition

Avirut Chinkulkijniwat and Somjai Yubonchit

Abstract

Both external and internal stabilities are main concerns in design and construction manuals for the mechanically stabilized earth (MSE) wall. Literature showed that the failure of the MSE walls, especially in mountainous areas, is mainly caused by the attack of seasonal heavy rainfall. The seepage through the MSE wall due to the rainfall causes the increase in the lateral stress and the reduction in the effective stress, stiffness and strength of the backfill; hence the reduction in the factors of safety against external and internal failure. This paper investigates the flow and mechanical behaviors of the MSE wall with and without geocomposite grain under seepage condition. The investigation is performed using laboratory physical model tests. It is found that the water pressure significantly controls the performance and the failure of the MSE wall. As the water pressure increases, the settlements in the unreinforced zone increase. The failure of the MSE wall is caused by the piping of the reinforced soil. The geocomposite drainage reduces the water pressure and water content in the reinforced zone, hence the improvement of the stability of the MSE wall. For the same water pressure, the MSE wall with geocomposite drainage sustains lower settlements.

Keywords

Mechanical stabilized earth wall • Geocomposite • Drainage system

Introduction

The MSE wall can be used as an earth retaining structure along the mountainous area. The first project in Thailand was constructed in the Highway route no. 11 (Utaradit-Denchai) in 2011. Several MSE wall projects along the

mountainous area will be released from the Department of Highways, Thailand such as in Khao Pub Pa and Lomsak. For the design of MSE wall in the mountainous areas, the external and internal stabilities must be confirmed. Generally, the examination of the external and internal stabilities can be referred to standard design manuals such as the American Association of State Highway Transportation Officials (AASHTO) and the Federal Highway Administration (FHWA), etc. It is worth noting that the design condition is generally assumed that the drainage system still functions. Shibuya et al. (2007) reported the causes of failure of a MSE wall constructed in a mountain in Yabu, Hyogo prefecture, Japan. The failure occurred in 2004 after the attack of typhoon. One of the causes of failure is the inappropriate installation of the drainage system. Shibuya et al. (2009) recommended that the geocomposite drain with a high coefficient of permeability (10–200 times

A. Chinkulkijniwat (✉)
Center of Excellent in Civil Engineering, School of Civil Engineering,
Institute of Engineering, Suranaree University of Technology, 111
University Ave., Suranaree, Muang, Nakhon Ratchasima 30000,
Thailand
e-mail: avirut@sut.ac.th

S. Yubonchit
School of Civil Engineering, Institute of Engineering, Suranaree
University of Technology, 111 University Ave., Suranaree, Muang,
Nakhon Ratchasima 30000, Thailand

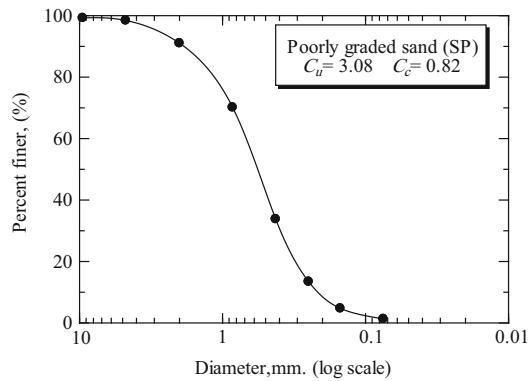


Fig. 1 Particle size distribution of the clean sand

higher than that of the compacted backfill) can be used as a drain in the MSE wall. The advantage of the geocomposite drain over the conventional material (well-graded sand) is the high drainage capacity even under the MSE wall movement caused by dead and live loads. Besides, the geosynthetic drainage system is cheaper and simpler to install than the conventional system.

Presently knowledge on the design of drainage system in MSE wall, using geocomposite, is very limited. Rigorous knowledge on influencing factors to drainage efficiency would enhance the design potential. Understanding flow mechanism in MSE wall is crucial to develop design direction. This paper investigates the flow mechanism in the MSE wall with and without geocomposite. The investigation is performed using laboratory physical model tests. Results from the tests will be useful for further parameter analysis.

Laboratory Investigation

Materials

The soil used in this investigation is a clean sand. It consists of 10 % gravel, 87.3 % sand, and 2.7 % silt. The gradation of the sand is presented in Fig. 1. This sand is classified as poorly graded sand (SP), according to the Unified Soil Classification System (USCS). Its specific gravity is 2.74. The compaction characteristics under standard Proctor energy are optimum water content (OWC) = 5.7 % and maximum dry unit weight, $\gamma_{d,max} = 16.7 \text{ kN/m}^3$. Shear strength parameters of this sand at the optimum point obtained from a large direct shear apparatus with the diameter of 35 cm are $c' = 0 \text{ kN/m}^2$, and $\phi' = 40^\circ$. Generally, well-graded materials are used as backfill due to high efficiency of field compaction. The uniform sand was, however, used in this investigation for the consistency of the laboratory compaction for each test. Even though the tested sand is uniformly graded but its percentages finer than 37,

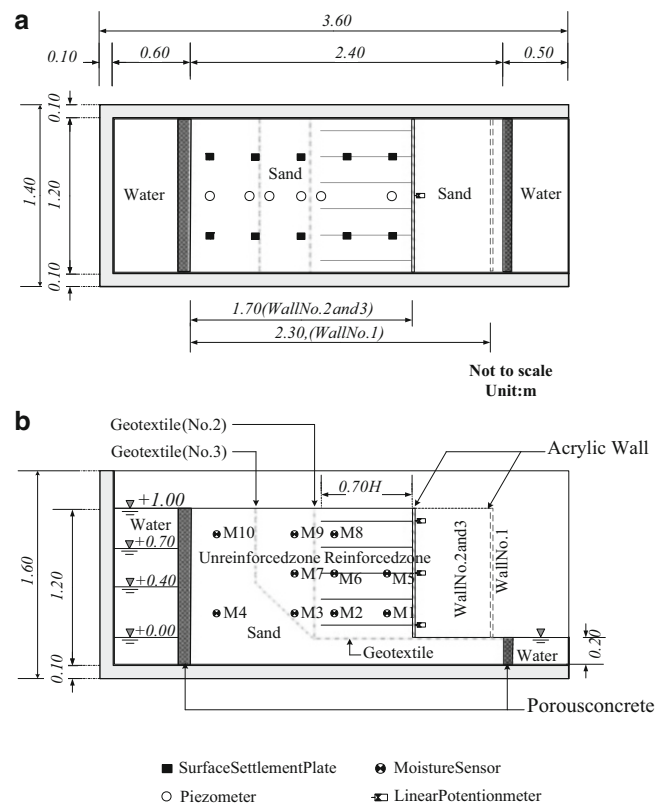


Fig. 2 Dimension of the tank and instrumentations

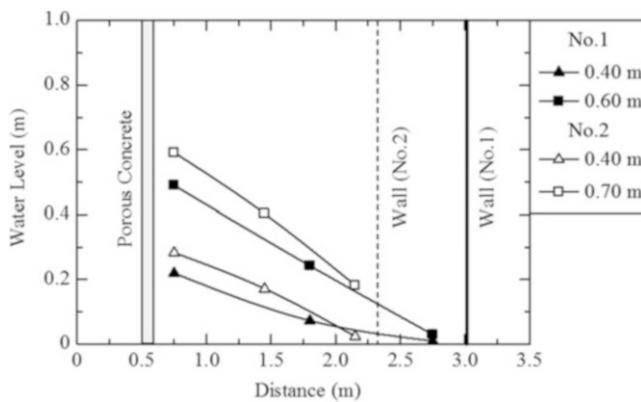
4.75, 0.425, 0.150, and 0.075 mm particle size and its internal friction angle meet the specifications of the Department of highways, Thailand.

Experimental Setup

A large scale tests were conducted in the laboratory of Suranaree University of Technology to simulate MSE wall under a condition of high ground water Table. A reinforce concrete tank was built to carry out the experiment. The Dimensions of the tank is illustrated in Fig. 2. The sand was filled to the tank to a dimension of $1.4 \times 3.6 \times 1.6 \text{ m}$. It was compacted in layers of about 0.15 m thickness to a density of higher than 90 % the standard Proctor density. The compaction was carried out by hand compactors. The degree of compaction and water content were checked regularly at several points by the sand cone method. Wherever the degree of compaction was found to be inadequate, additional compaction was done until the desired standards were met. The wall facing was made of an acrylic plate with five layers of steel reinforcement. The vertical and horizontal spacing between each layer was fixed at 0.20 m and 0.25 m, respectively. The reinforcements for all layers are 3 mm diameter and 0.7 m length (equal to $0.8H$ where H is the wall height). The reinforcement length of larger than $0.7H$ is recommended by AASHTO (2002).

Table 1 Detail of the conducted experiments

| Case | Wall distance (m) | Upstream water level (m) | Geocomposite direction (deg.) |
|------|-------------------|--------------------------|-------------------------------|
| I | 2.4 | 0.2, 0.4, 0.6 | – |
| II | 1.7 | 0.2, 0.4, 0.7, 1.0 | – |
| III | 1.7 | 0.2, 0.4, 0.7, 1.0 | 90 |
| IV | | 0.2, 0.4, 0.7, 1.0 | 45 |

**Fig. 3** Comparison between phreatic lines for cases I and II

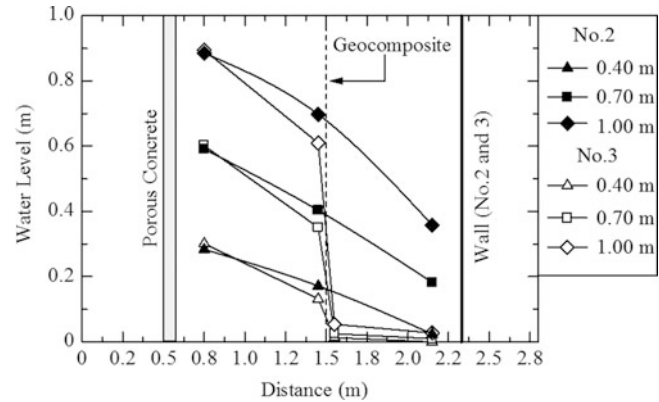
The MSE wall was extensively instrumented within the wall and the wall facing panel. Locations of the instruments are illustrated in Fig. 2. Three piezometers, 10 surface settlement plates and 10 water sensors were installed to measure the change in water levels, settlements and water contents during seepage flow. The surface settlement plates were installed in middle of the backfill. Settlements were measured by a precise leveling with reference to a benchmark. Three linear potentiometers were installed at the wall facing panel to measure the lateral wall movement at different points during seepage.

The ground water table during the tests was controlled by water levels in the upstream and downstream water tanks. The water level in the downstream water tank was kept constant at 0.2 m height by a control weir. The water level in the upstream tank was varied from 0.2 m height to 1.0 m height as indicated in Table 1. Every test was begun with the water level of 0.2 m height in the upstream tank. At every level of upstream water, the upstream water level was kept constant until steady state flow was arrived.

Test Results

Seepage Flow

Figure 3 shows the phreatic drawdown for different water levels for cases I and II. The water heights behind the unreinforced zone were 0.4 m and 0.6 m for the case I and 0.4 m and 0.7 m for the case II. The phreatic level decreases through the wall face due to the head loss in the sandy

**Fig. 4** Comparison between phreatic lines for cases II and III

backfill. The distance of the wall face insignificantly affects the phreatic level. In other word, pore pressure acting on the wall face decreases as the distance from the water source to the wall face increases. The advantage of the geocomposite drainage on the reduction in water pressure in the reinforced zone is illustrated in Fig. 4. The measured data of the water pressure for case II (without geocomposite) are compared with those for case III (with geocomposite). For both cases, the distance from the water source to the wall face is the same. The highly permeable geocomposite can collect the water in the unreinforced zone and drain out at the wall face. This reduces the water pressure acting on the wall face and pore water pressure in the reinforced zone.

It is interesting to mention that the arrangement of the geocomposite plays a significant role on the drainage capacity. The inclined geocomposite drainage is not suitable in terms of workability, economic and engineering points of view. The inclined arrangement is hard in practice and uses more drainage. It is clearly seen from Fig. 5 that the vertical arrangement is more effective than the inclined arrangement.

Deformations

Comparisons among final surface settlements along a longitudinal direction at a specific water level in the upstream tank are presented in Figs. 6 to 8. Figure 6 compares settlements for case I and those for case II. It is clearly shown that the settlements for case I are lower than those for case II. There are two factors that induced the difference; (1) level of water in the upstream tank and (2) distance of the upstream water tank to the wall face. The

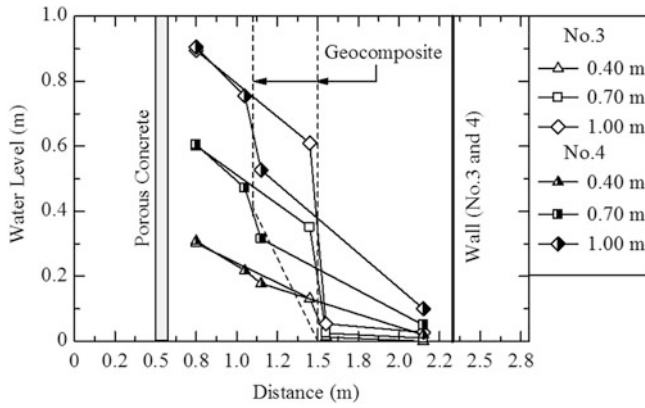


Fig. 5 Comparison between phreatic lines for cases III and IV

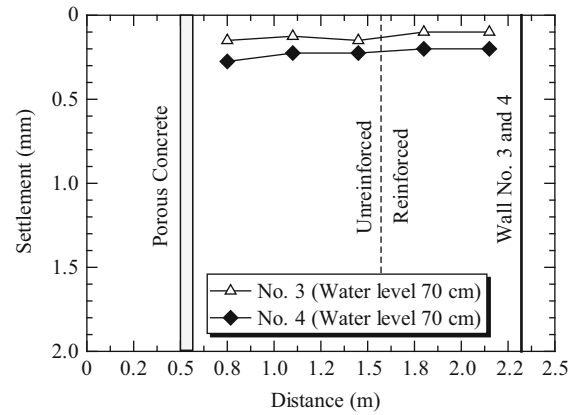


Fig. 8 Comparison between surface settlements for cases III and IV

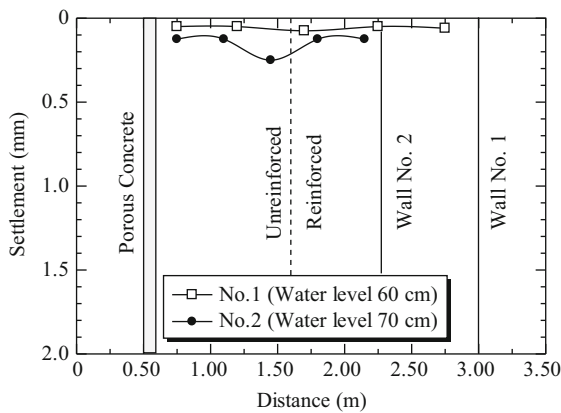


Fig. 6 Comparison between surface settlements for cases I and II

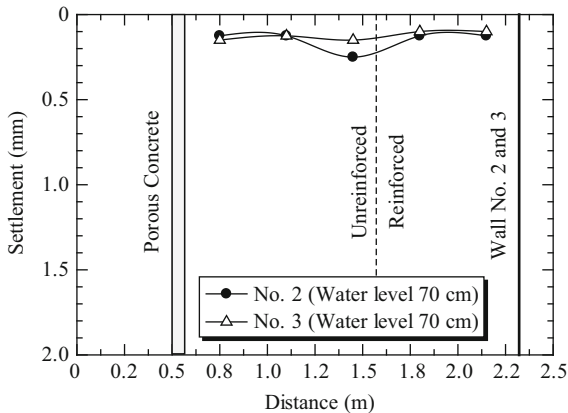


Fig. 7 Comparison between surface settlements for cases II and III

water levels in the upstream water tank for cases I and II are 0.6 m and 0.7 m, respectively. Theoretically, the higher water level provides the greater magnitude of settlement. However, the more important factor is the distance of the upstream water tank to the wall face. As the phreatic level

decreases through the wall face, the shorter distance results the higher phreatic level at the wall face. Figure 3 shows that when the water level in the upstream water tank is 0.7 m, the level of the phreatic line at the wall face remains relatively high at level of 0.3 m. The high phreatic line at the wall face induces piping of the soil at vicinity to the wall face. The piping later induces massive failure in the reinforced zone and hence, there occurs a relatively large settlement in the reinforcement zone as indicted in Fig. 6.

Figure 7 compares the surface settlements for cases II and III. It is shown that the drainage system works well on its function. The surface settlements shown in Fig. 8 show that the inclined geocomposite drainage opposes poor performance comparing with the vertical drainage. Comparing with the vertical drainage, the inclined drainage gives the higher level of phreatic line inside the reinforced zone as shown in Fig. 5 and results in the lower effective stresses inside the reinforced zone. As such the greater magnitude of settlements for the inclined drainage for the vertical drainage is observed as shown in Fig. 8.

Conclusions

A series experiments for multistep flow through the MSE wall were conducted with and without geocomposite drainage in the laboratory of Suranaree University of Technology. Phreatic lines at a specific level of water level in the upstream tank for all studied cases are presented. It is found that geocomposite can be used as drainage material in the drainage system in MSE wall. Regarding to the drainage efficiency, the performance of the vertical drainage is better than that of the inclined drainage. Surface settlements along longitudinal direction at a specific level of water level in the upstream water tank are presented for all cases. The measured settlements are consistent with the measured phreatic lines.

References

- AASHTO (2002) Standard Specifications for Highway and Bridge, 7th edn. American Association of State Highway and Transportation Officials, Washington, DC
- Shibuya S, Kawagushi T, Chae J (2007) Failure of reinforced earth as attacked by typhoon no.23 in 2004. *Soils Found* 47(1):153–160
- Shibuya S, Saito M, Torii N, Hara K (2009) Mitigating embankment failure due to heavy rainfall using L-shaped geosynthetic drain (LGD). In: *Proceedings of prediction and simulation methods for Geohazard mitigation*, Kyoto, Japan. pp 229–306



Loess Landslides Respond to Groundwater Level Change in Heifangtai, Gansu Province

Ying Dong, MaoSheng Zhang, Jie Liu, Pingping Sun, and Jun Jia

Abstract

Change in the ground water level induced by irrigation is a vital factor to geological hazards in Heifangtai areas. Based on the loess water system affecting the stabilities of slopes the most, the evolutionary process of groundwater system induced by irrigation is analyzed, and the relationship of the evolutionary process with occurrence frequency and volume of loess landslides are analyzed comparatively. It indicates that four times sliding have happened since people started irrigation in this area. It shows that groundwater level will continuously go up if present irrigation volume is maintained. Loess landslides may move repeatedly because the volume of shearing-tension plasticity areas enlarges significantly. For this reason controlling the groundwater level can be a significant measure to protect slopes from moving.

Keywords

Heifangtai • Groundwater • Landslide of loess • Couple analysis

Introduction

Groundwater is a vital factor to landslides. Statistics show that 80–90 % landslides are prone to move due to water (Derbyshire et al. 1994). More than 90 landslides are described in detail in the *Landslides in China-selected* (Derbyshire 2001), in which 95 % landslides are susceptible to groundwater. The groundwater level rises continuously because of irrigation, which increases self-weight of slopes and decreases shear strength of loess. Therefore loess slopes may be susceptible to groundwater, even cause to movement (Derbyshire 2001; Dong et al. 2013; Lu et al. 2009; Oda 1986; Sun et al. 2013).

This area has more than four decade irrigation history. It began to irrigate since the year of 1968, diverting water from the Yellow River. The groundwater level goes up continuously because of irrigation, which increases self-weight of slopes and decreases shear strength of loess. Therefore loess slopes are susceptible to groundwater dynamic field and stress field. Based on the loess water system affecting the stabilities of slopes the most, the evolutionary process of groundwater system induced by irrigation is analyzed, and the relationship of the evolutionary process with occurrence frequency and volume of loess landslides are analyzed comparatively. It can provide support for geological hazards forecasting and comprehensive treatment.

Y. Dong • M. Zhang • J. Liu (✉) • P. Sun • J. Jia
Key Laboratory for Geo-hazards in Loess area, China Ministry of Land Resources, Beijing, People's Republic of China

Xi'an Regional Center, China Geological Survey, Xi'an 710054,
Beijing, People's Republic of China
e-mail: dongy329@163.com; xazms@126.com; 32168963@qq.com;
sunpingping203@gmail.com; geojia@qq.com

Irrigation and Groundwater Level

Hydrogeological Condition

In this area 14 hydrogeological drills have been completed successfully, which are located in Chenjia village, Zhuwang village and Jiaojiaya, respectively. The geological structure

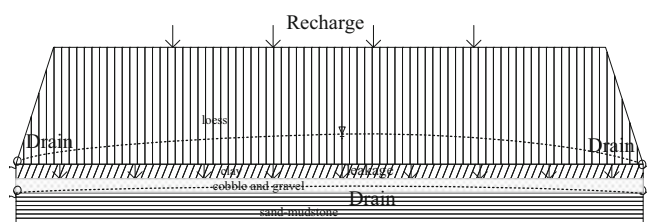


Fig. 1 Schematic diagram of hydro-geological structure

has been identified by combining hydrogeological survey with height measurement of a number of geological outcrops, which consists of loess, silty clay, sand and gravel and cretaceous sand-mud stone from top to bottom. As tectonic structure does not exist in this study area, the hydrogeological structure is made up of three aquifer systems, including holes and fractured unconfined loess aquifer, holes and sand gravel aquifer and fractured rock aquifer (Fig. 1). The unconfined loess aquifer is the predominant research object.

Irrigation History

There were no people lived in the study area. The residents were relocated from Liujiaxia, Bapanxia and Yanguoxia reservoirs from the 1963. At present there are four villages with a population of 4,028, a large proportion of the areas have been reclaimed to farmland to meet the demand of living. From 1966 to 1969, three irrigation projects have been implemented by the local government, diverting water from the Yellow River. The planned extracted water volume is 1.22 m³/s and the actual extracted water volume is 2.115 m³/s. The total irrigation area is 7.0528 km². After the projects, it started to broaden irrigation, which is still using today.

According to statistics, the annual extracted water volume is 722 × 10⁴ m³ in 1980s, it was 576 × 10⁴ m³ in 1990s.

Recently Heifangtai has become a crucial area, focused on planting vegetables and fruits. The demand for irrigation volume has become increasingly large because they have planted not only wheats and corns but also vegetables and fruit trees, which need more water. Based on the recent survey results, there are four main canals with 7.05 km length, and 15 branch canals with 32.84 km length. They irrigate seven times a year, including spring irrigation, winter irrigation and seedling irrigation. The irrigation volume varies with water demand of plants and precipitation.

Groundwater Level Changing

A numerical model has been built up to analyze groundwater dynamic field, which shows precipitation is the only

recharge source before irrigation. According to groundwater dynamic field, simulated with steady flow, unconfined water in loess distributes discontinuously. Groundwater almost does not exist around the terrace except those in the lower parts (Fig. 2).

The groundwater level rises continuously along with irrigation. In 1970, groundwater exists in the bottom of the terrace, and springs were observed around the terrace. The balance model indicates the volume of loess and fracture springs are 230 m³/day and 185 m³/day, respectively, with a total of 415 m³/day.

As the volume of springs becomes larger, obviously, the storage volume becomes smaller than before (Table 1 and Fig. 3).

As Fig. 4 shows, groundwater level increases successively from 1968 when they started to irrigate. Before irrigation, it was lower than the bottom of aquifer, and the groundwater was distributed less and only at terrace center. Few landslides moved. After 2 years, groundwater distributed widely and successively at the terrace. The increased height gradually reduced along with irrigation time and discharge.

Figure 5 shows the groundwater variation curve in the center of the terrace. The accumulated height is about 15 m from 1968 to 1990, with an increasing rate of 0.57 m/a. After 1990, the increasing rate is 0.25 m/a, with an accumulated height of 20 m from 1990 to 2012.

Groundwater Level and Landslides

Since the year of 1980, sliding occurred in Heifangtai approximately 50 times. Those slides were of mainly small and medium size; small ones account for 53 %, medium ones account for 35 % and large ones like cretaceous rock landslides account for 12 %. The maximum volume is up to 400 × 10⁴ m³. Huangci landslides moved many times; the accumulated volume is more than 1,000 × 10⁴ m³. Rockslides are featured by large volume and low speed, so they can be technically monitored. However, loess landslides are featured by small volume, fast speed and long movement which are susceptible to groundwater level and lead to more serious damage. So loess landslides are the main subjects studied by researchers.

As shown in Fig. 6, it has a positive correlation between groundwater level and landslides numbers. After irrigation started in Heifangtai, the groundwater level increased continuously, with an increase of 9 m in 1980 and 20 m in 2012. In the 1980s landslides moved once per year in average, while in the 1990s the frequency increased to 2–3 times per year. Likewise, it increased to 3–4 times per year, in 2007, with the maximum frequency of five times.

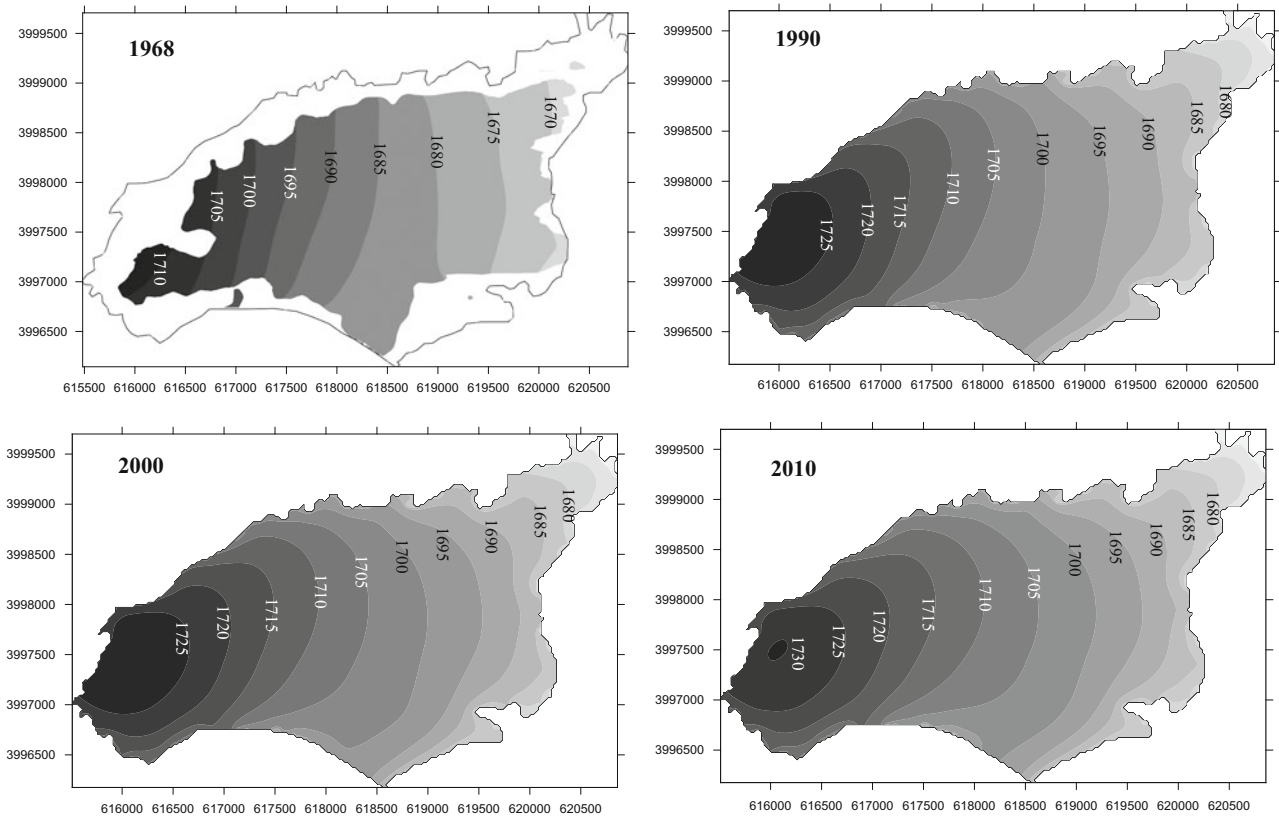


Fig. 2 The development of groundwater flow field in different years

Table 1 Changes of the spring volume and storage volume

| Year | Spring volume (m ³ /day) | Storage volume (m ³ /day) |
|------|-------------------------------------|--------------------------------------|
| 1980 | 1,310.17 | 922.53 |
| 1990 | 1,723.84 | 528.86 |
| 2000 | 1,958.60 | 314.10 |
| 2010 | 2,090.27 | 202.43 |

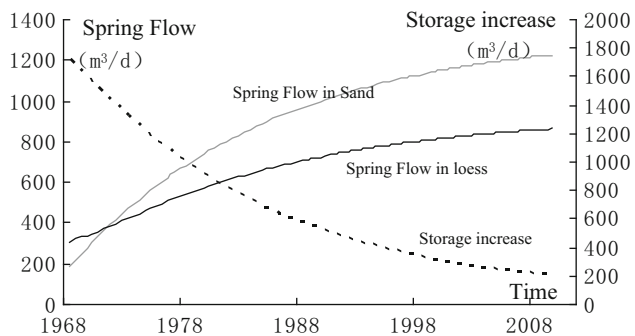


Fig. 3 Changes of water balance

The average volume of landslides decreased with an increase in water level. In 1980s annual average volume of landslides was $90 \times 10^4 \text{ m}^3/\text{a}$, which has decreased to $50 \times 10^4 \text{ m}^3/\text{a}$ in 2000 and $28 \times 10^4 \text{ m}^3/\text{a}$ after 2001. As the increased water level reduced the stability of slopes,

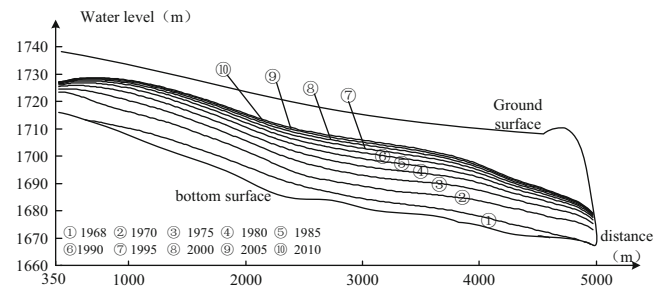


Fig. 4 Changes of ground water level with time

frequency of landslide increased. The slopes became gentler after movement and potential sliding surface gradually moved to backwards, which will be confirmed in the following calculation.

Selecting Jiaojia No.9 landslide as an example, it moved many times after the initiation of irrigation from 1968. It is a typical loess landslide which consists of loess, silty clay, sand and gravel, and cretaceous sand-mud stone from top to bottom. Groundwater discharges at the base of loess and develops a multi-period and long-distance landslide. The stability of this landslide under different water levels is calculated using Geoslope software and Morgenstern and Price calculation method (Fig. 7).

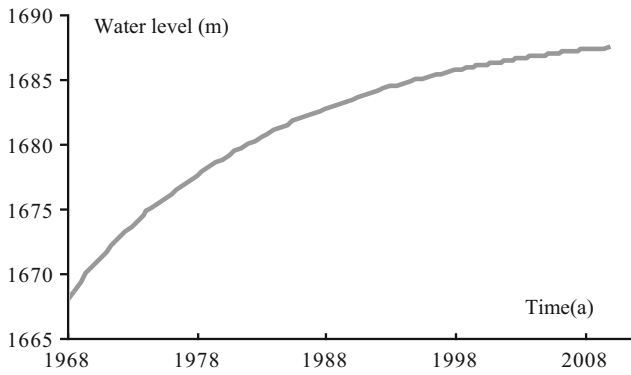


Fig. 5 Changes of ground water level in terrace center

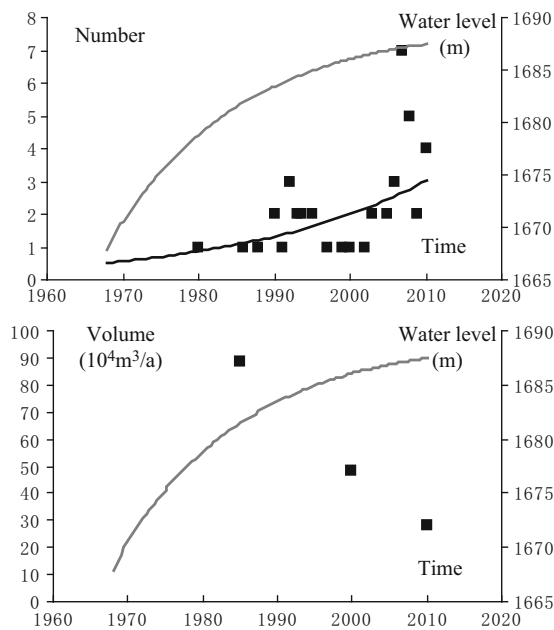


Fig. 6 Statistical data of recorded landslides

During the first period (1968–1983), as irrigation started in 1968, groundwater level went up continuously. The calculated factor of safety of this typical landslide declines from 1.3 to 1.0, showing that it is prone to movement. During the second period (1983–1996), the slope became gentler and stable after previous movement. However water level went up again along with irrigation, it is prone to move again. The back of the slope is vertical and the foot is lower. The sliding surface move backward. The third period (1997–2005) and the fourth period (2006–2012), the sliding surface continue to move backward. Those movements of this typical landslide can be attributed to increased water level (Fig. 8).

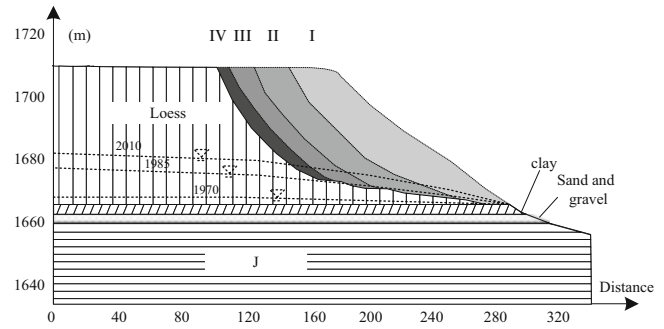


Fig. 7 Sketch of landslides used for calculation of stability of based on changes in water level

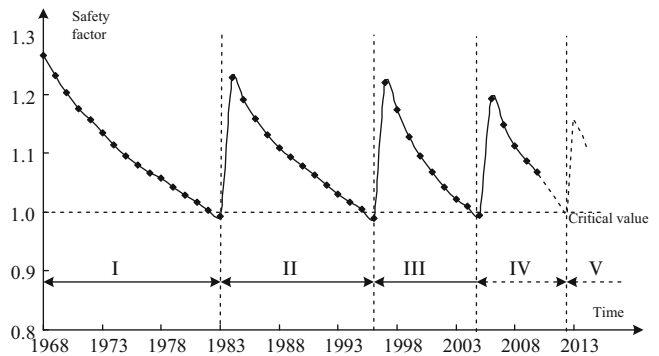


Fig. 8 Stability changes of recorded landslides

Trend Prediction

Under present irrigation condition, groundwater dynamic field has been predicted. The prediction result shows that the ground water level is not stable and the water level increases continuously up to 2020. However the rate of increment rate in different part varied. They are 0.11 m/a, 0.09 m/a, and 0.08 m/a at east, middle and west part, respectively, showing maximum in the east part. The eastern part the recharge source consists of not only precipitation and infiltration water from irrigation but also the side flows.

Changes of the zones for shear and tension failure around the terrace can be obtained by performing coupling model calculations for different times. As Table 2 shows, the volume of shearing-tension plasticity areas enlarges year by year. The volume of shearing plasticity area will increase by 42.46 % in 2015 and 67.36 % in 2020, compare to 2010. The volume of tension plasticity area will increase by 107.11 % in 2015 and 121.11 % in 2020, compare to 2010. Especially, after 2015, the volume of shearing-tension plasticity areas will enlarge seriously. Overall shearing failure can be the main reason for deformation of slopes.

Table 2 Changes of the zones for shear and tension failure around the terrace

| | 2010 | 2015 | 2020 |
|---|------------|------------|------------|
| The volume of shearing plasticity area (10^4 m^3) | 7.23E + 04 | 1.03E + 05 | 1.21E + 05 |
| The volume of tension plasticity area (10^4 m^3) | 4.50E + 03 | 9.32E + 03 | 9.95E + 03 |

Conclusion

1. In the study area, groundwater distributed discontinuously before irrigation; however it overflowed at the bottom of loess aquifer after 2 years. Groundwater level went up successively along with irrigation.
2. The occurrence frequency and volume of landslides are susceptible to groundwater level. The increase in water level reduces the stability of landslides and the backsides of the slopes move backwards continuously.
3. Under present irrigation condition in the study area, water level rises continuously, enlarging the shearing-tension plasticity areas enlarge. Therefore, controlling the groundwater level is a significant measure to protect landslides from moving.

References

- Derbyshire E (2001) Geological hazards in loess terrain with particular reference to the loess regions of China. *Earth-Sci Rev* 54(1):231–260
- Derbyshire E, Dijkstra TA, Smalley IJ, Li YJ (1994) Failure mechanisms in loess and the effects of moisture content changes on remolded strength. *Quaternary Int* 24:5–15
- Derbyshire E, Meng XM, Dijkstra TA (eds) (2000) Landslides in the thick loess terrain of north-west China. Wiley, Chichester
- Dong Y, Jia J, Zhang MS (2013) An analysis of the inducing effects of irrigation and the responses of loess landslides in Heifangtai area. *Geol Bull China* 32(06):893–898
- Lu N, Godt JW, Wu DT (2009) A closed-form equation for effective stress in unsaturated soil. *Water Resour Res* 2010(46), W05515. doi:10.1029/2009WR008646
- Oda M (1986) An equivalent continuum model for coupled stress and fluid flow analysis in jointed rock masses. *Water Resour Res* 22(13):1854–1865
- Sun PP, Zhang MS, Dong Y (2013) The coupled model of seepage-stress at Heifangtai terrace, Gansu province. *Geol Bull China* 32(06):887–892
- Yin YP (2007) Landslides in China-selected. China Land Press, Beijing
- Zhang MS (2013) Formation mechanism as well as prevention and controlling techniques of loess geo-hazards in irrigated areas: a case study of Heifangtai immigration area in the Three Gorges Reservoir of the Yellow. *Geol Bull China* 32(06):833–839
- Zhang DX, Wang GH, Lou C (2009) A rapid loess flow slide triggered by irrigation in China. *Landslide* 6:55–60

Part II

**Application of Numerical Modeling Techniques to
Landslides**



Introduction: Application of Numerical Modelling Techniques to Landslides

Marc-André Brideau

Abstract

Numerical modelling techniques can be used in conjunction with detailed site investigation and slope monitoring to gain a better understanding of the factors controlling the deformation or failure mechanism of a particular slope. A wide range of numerical modelling techniques are also available to assess the post-failure behaviour of mass movements. The numerical modelling techniques for the pre- or post-failure behaviour of a landslide can be based on empirical relationships, continuum mechanics, or discontinuum mechanics. These techniques have been calibrated based on numerous back-analysis of various mass movement types and can now be used as a numerical laboratory to evaluate the mechanical behaviour of landslide for a variety of scenarios.

Keywords

Numerical modelling • Analytical solution • Slope stability • Contributing factors

A wide range of numerical modelling techniques are now available to landslide practitioners. This session focuses on how these tools can be used to increase our knowledge of the processes leading up to slope failures and their travel distance once they have initiated. Numerical modelling provides the opportunity to test competing hypotheses and conceptual models. This session covers applications of numerical modelling techniques to landslides and unstable slopes in rock, soil, and mine waste materials. Nine papers were accepted into the session for oral or poster presentation. They present a wide range of numerical modelling techniques applications, from fundamental research in landslide science, to evaluating mitigation options, in the support of civil and mining engineering design. Case studies demonstrate how field monitoring, detailed mapping and laboratory testing can be used in conjunction with numerical modelling to constrain the failure and emplacement

mechanisms. Four papers investigate the contributing and triggering factors to the development of slope instabilities (Agliardi and Crosta 2014; Jiang et al. 2014; Tiwari et al. 2014; Wakai et al. 2014), three papers assess the influence of anthropogenic modification to the landscape on slope stability conditions (Chen et al. 2014; Hu et al. 2014; Twin et al. 2014), one paper looked at a methodology for optimizing computing resources in seismic dynamic loading analysis (Chen and Hu 2014), while another paper look at advanced constitutive criterion to better understand the progressive natures of two slope failures (Frigerio et al. 2014). The authors applied a range of one-, two- and three-dimensional analytical solutions, limit equilibrium, finite element, and distinct element codes to their respective projects. This collection of papers demonstrates that a wide range of techniques can be used to further our understanding of landslide hazards associated with natural and man-made slopes.

M.-A. Brideau (✉)
BGC Engineering Inc., Vancouver, Canada

Earth Science Department, Simon Fraser University, Burnaby, Canada
e-mail: MBrideau@bgcengineering.ca

References

- Agliardi F, Crosta GB (2014) Long- and short-term controls on the Spriana rockslide (Central Alps, Italy). In: Sassa K et al (eds) *Landslide science for a safer geoenvironment*. Springer, Heidelberg
- Chen Z, Hu X (2014) Determination of the effective computing region for rock slope stability based on seismic wave theory. In: Sassa K et al (eds) *Landslide science for a safer geoenvironment*. Springer, Heidelberg
- Chen C, He K, Li T (2014) Numerical simulation on the deformation and failure of the slope treated by building by cave dwellings. In: Sassa K et al (eds) *Landslide science for a safer geoenvironment*. Springer, Heidelberg
- Frigerio G, Castellanza R, Crosta GB, di Prisco C (2014) Modelling rockslide displacement with delayed plasticity. In: Sassa K et al (eds) *Landslide science for a safer geoenvironment*. Springer, Heidelberg
- Hu X, Stead D, Zhai L, Kong D (2014) Engineering geology and numerical modelling of a steep rock slope for Ensi-Qianjiang expressway, China. In: Sassa K et al (eds) *Landslide science for a safer geoenvironment*. Springer, Heidelberg
- Jiang S, Wen B, Zhao C, Li R (2014) Factors controlling kinematic behavior of a huge slope-moving landslide in China. In: Sassa K et al (eds) *Landslide science for a safer geoenvironment*. Springer, Heidelberg
- Tiwari B, Kawai K, Viradeth P (2014) Numerical modelling deformation for partially saturated slopes subjected to rainfall. In: Sassa K et al (eds) *Landslide science for a safer geoenvironment*. Springer, Heidelberg
- Twin HW, Kristyanto I, Muslim D, Himawan F (2014) Feasibility study of dumping area on bearing capacity and slope stability analysis. In: Sassa K et al (eds) *Landslide science for a safer geoenvironment*. Springer, Heidelberg
- Wakai A, Cai F, Ugai K, Soda T (2014) Finite element simulation for and earthquake-induced catastrophic landslide considering strain-softening characteristics of sensitive clays. In: Sassa K et al (eds) *Landslide science for a safer geoenvironment*. Springer, Heidelberg



Numerical Simulation on the Deformation and Failure of the Slope Treated by Building by Cave Dwellings

Chunli Chen, Kai He, and Tonglu Li

Abstract

There are a large number of cave dwellings existing in the loess area. Building houses at the base of slope by the cave dwellings lead to the instability of numerous slopes, resulting the loss of large number of properties. Building houses by the cave dwellings is quite popular in the loess area, therefore, it is important to conduct stability analysis on this kind of slopes. This article focuses on a typical slope selected in North Shaanxi, the stress and strength variation trend on the critical slip surface for five scenarios such as the natural slope, artificial cut slope, cave dwellings constructed on the foot of the slope, building houses by the cave dwellings for short and long term are studied and the deformation failure mechanism of the slopes are investigated. The result shows that construction by cave dwellings increases the water content of loess, which changes the distribution of stress in the middle and the foot of the slope. And finally the failure of slope occur by the cave dwellings collapse when the sliding force at the bottom of the critical slip surface exceeds the shear resistance.

Keywords

Loess slope • Cave dwelling • Building by cave dwellings • Moisture content changes

Introduction

Ravines are arranged in an intersecting pattern in the loess plateau and most towns are located in the loess gullies. Since ancient times, the local citizens developed the habit and custom to cut slopes to build cave dwellings due to the lack of homestead land (Ren 1989; Hou and Wang 1999; Zhang and Li 2011; Li et al. 2011). Many scholars have carried out studies on aspects of environmental engineering problems of cave dwellings, cave dwelling structural design, cave dwelling collapse mechanism etc. (Chen et al. 1994; Lei and Wei 1998; Wu et al. 2005; Huang et al. 2008). The recent detailed investigation on

geological disasters indicates that with the increase in people's living standard in the loess area, they have begun to abandon the cave dwellings and live in buildings. Due to restriction by the terrain conditions, they often build houses at the foot of slopes neighbouring the old cave dwellings in order to maximize the limited space. Such slopes for building houses by the cave dwellings have extremely high potential slope stability hazard, yet there are many similar working conditions in the loess area region that are severely threatening life and property safety of the households at the foot of slopes. Therefore, it is urgent to carry out stability analysis on the loess slopes with building by cave dwellings. This paper selects a typical slope with buildings by cave dwellings as the focus of the study to carry out analysis and discussion on the deformation and failure of such slope using numerical simulation.

C. Chen • K. He • T. Li (✉)
School of Geological Engineering and Surveying, Chang'an University, YanTa Road, Xi'an 710054, China
e-mail: chen_chunli@126.com; hekai2005@163.com; dcdgx08@chd.edu.cn

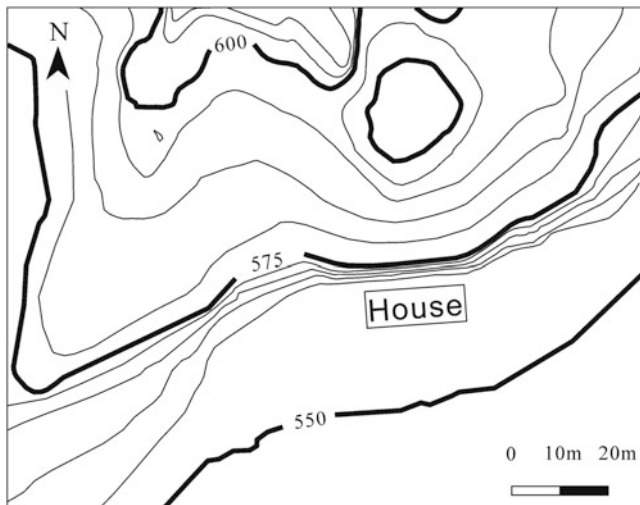


Fig. 1 Topographic map for the slope

Study Area Geometry and Ground Conditions

The height of the slope selected for the paper is 35 m. The upper crest is 45° with height of 15 m and width of 12 m. The height of the lower perpendicular slope is 20 m. There are three cave dwellings built at the foot of the slope. Currently there is a two-storied houses under construction on the front of the slope with a distance from the foot of slope of 3 m. The soil mass of the slope is Q3 loess, and the upper part of the slope body is well covered with vegetation (Fig. 1).

Field investigation of the slope shows that construction of the building has blocked out the sunshine. It is dimmer and damper at the foot of the slope at the rear side of the building than other locations. Furthermore, the cave dwellings at the foot of the slope are mainly used for storing sundries and it is humid inside. There are no reinforcement and drainage measures on the slope.

Modelling and Calculating Parameter Selection

In order to predict the stability under the long-term effect of the buildings on the front of the slope, the in situ original loess is taken to make the soil samples humidified according to the water ratio near the cave dwellings in the shade of the building to measure the physical and mechanical parameters of the loess under the natural state, the slightly wet state and the wet state (Table 1).

In order to analyze the impact of cut slope, constructing cave dwellings and building by cave dwellings on the stability of the slope, three computation scenarios for natural slope, artificial cut slope and cave dwellings constructed on the foot of the slope are investigated based to the terrain of

actual site survey (Fig. 2). The modeling material of the module is Q3 loess. According to field investigation results, strength of loess with different loess moisture contents are considered, such as the natural state, the state of the initial period and a long-term after the building has been present in front of the cave dwelling (Table 1). The finite element software MIDAS/GTS is used for numerical simulation of five working conditions: natural slope, cut slope, slope with cave dwelling, the initial period after the cave dwellings has been built (initial period) and long term period of time since the building of the cave dwellings. Locating the critical failure surface was done using the shear strength reduction method.

Result Analysis

Factors of safety for various states of the slope are obtained using the finite element modelling (Table 2). Results are further analysed based on two typical sections, Section A is in the middle of the cave dwelling and Section B is the area between two cave dwellings. The calculated normal stress, shear stress and shearing strength of the two cross section to get the stress distribution on the critical slip surface for the slope under various working conditions (Figs. 3, 4, 5, 6, 7, where the x-axis indicate the length of the potential slip surface along the profile direction. The length of the most critical slip surface in Section A is as short as 56 m due to the excavation of the cave dwelling).

It is observed from the result of the 3D finite element modeling that the stability factor of the slope gradually decreased with development and length of development. At the beginning of building by cave dwellings, the stability factor drops to 0.99 and the slope is in a critical state. Under the state of long-term shading of the building, the slope stability will be further decreased and tend to be unstable.

Under the natural state, stress distributions in the two cross sections are basically the same. The normal stress and the shear stress from above to below along the slip surface increase constantly and the shear stress is always lower than the shearing strength, so the slope is stable (Fig. 3). After slope cutting, the stress on the two cross sections is 100 kPa lower than that under the natural state. The trends of stress variations on the two cross sections are basically consistent. The normal stress within 10 m from the free face is unchanged but the shear stress is slightly decreased. This is attributed to the unloading of the free face after excavation (Fig. 4). After cave dwelling is excavated at the foot of slope, the normal stress and shear stress in the middle of the critical slip surface in Section A are kept unchanged compared to those before building the cave dwelling. The normal stress and shear stress 15 m from the free face are drastically reduced, indicating that

Table 1 Physical and mechanical parameters of loess

| Soil Sample State | Moisture content ω (%) | Unit weight γ ($\text{kN} \cdot \text{m}^{-3}$) | C (kPa) | Φ ($^\circ$) | Elasticity modulus E_s (Mpa) | Poisson's ratio (μ) |
|---|-------------------------------|--|---------|---------------------|--------------------------------|---------------------------|
| Natural slope | 10.5 | 17 | 64.8 | 34.6 | 100 | 0.3 |
| Slightly wet (The early stages of the building) | 15.3 | 18 | 26.9 | 31.9 | 70 | 0.3 |
| Wet (After building for a long-term) | 27.9 | 19 | 19.0 | 29.5 | 50 | 0.35 |

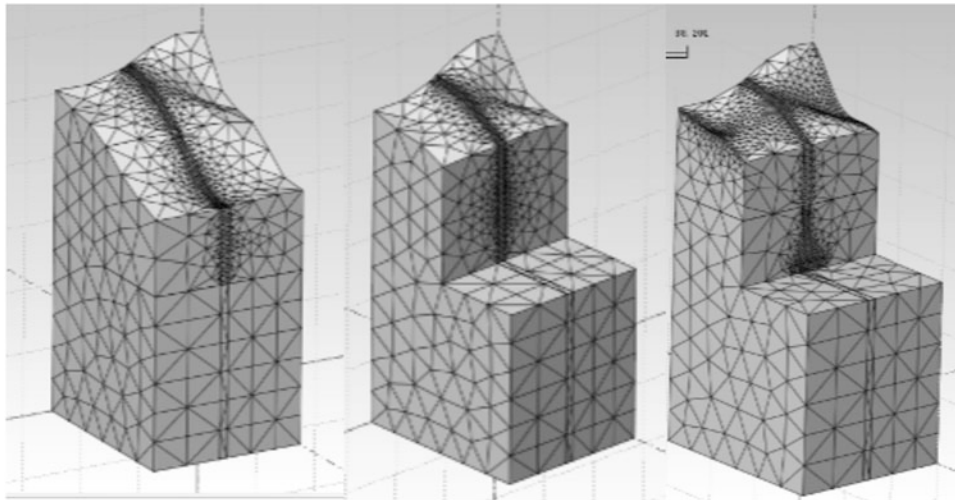


Fig. 2 3D model geometries used in finite element numerical simulations

Table 2 Factors of safety for the various states of the slope

| Slope state | Natural slope | Cut slope | Slope cave dwelling | Building constructed (initial period) | Building constructed (long period) |
|-------------|---------------|-----------|---------------------|---------------------------------------|------------------------------------|
| FOS | 1.71 | 1.16 | 1.01 | 0.99 | 0.94 |

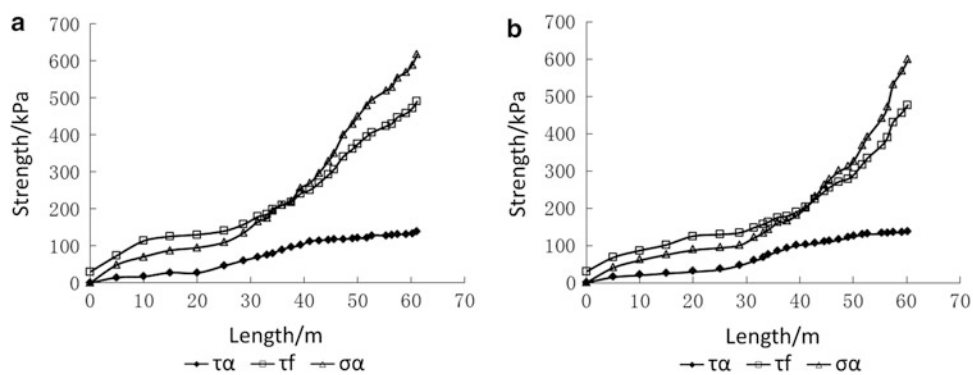


Fig. 3 Stress distribution on the critical slip surface of the natural slope. (a) Section A, (b) Section B

the soil mass is unloaded from the excavation of the cave dwelling (Fig. 5a), whereas the stress on the cross section between two cave dwellings changes greatly. The normal stress and the shear stress values increased sharply some

15 m from the free face and the growth rate is as high as two times, which is related to the stress concentration in the soil mass between two cave dwellings after excavation (Fig. 5b). After constructing the building by cave dwellings,

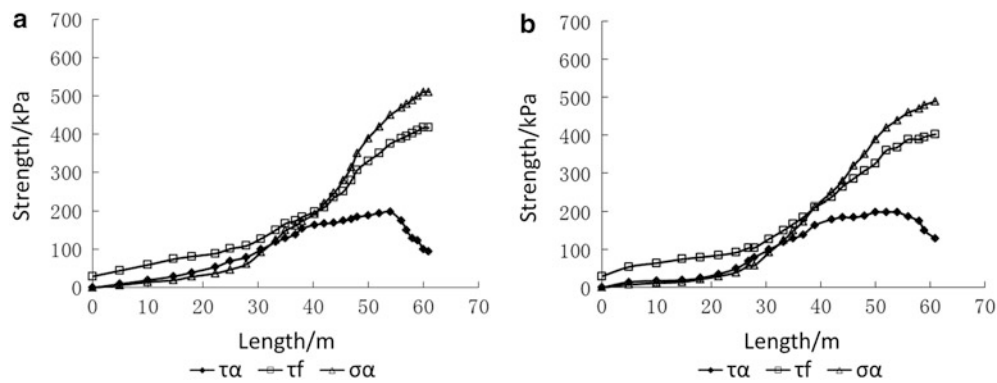


Fig. 4 Stress distribution on the critical slip surface behind the artificial cut slope. (a) Section A, (b) Section B

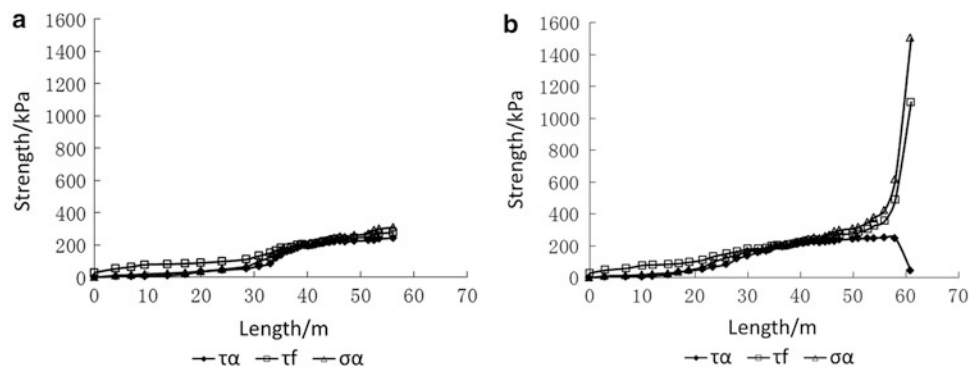


Fig. 5 Stress distribution on the critical slip surface behind the cave dwelling. (a) Section A, (b) Section B

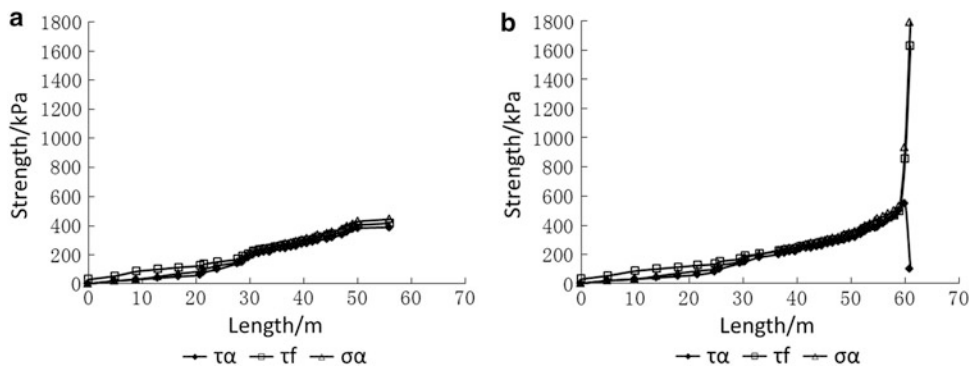


Fig. 6 Stress distribution on the critical slip surface after the cave dwelling is slightly wet. (a) Section A, (b) Section B

it shades the sunshine and blocks the wind, moisture content in the soil mass increases. This increases in moisture content in the 3D model after construction of the cave dwellings uses the mechanical parameters under the slightly wet state (Table 1), owing to the increasing in moisture content and soil mass density, normal stress and shear stress of the soil mass are slightly increased. As a results, the shearing strength is decreased, the shear stress in the lower part of the critical slip surface is closer to the shearing strength

(Fig. 6). The soil is thought to be getting wetter as the time since building increases, the mechanical parameters used for that scenario are under the wet state in Table 1. The results show that the normal stress and shear stress in the cross section between cave dwellings increases markedly, whereas the shearing strength declines sharply, and the shear stress in the middle of the critical slip surface is basically equal to its shear strength. The shear stress on the lower part of the critical slip surface is far higher than its shear strength

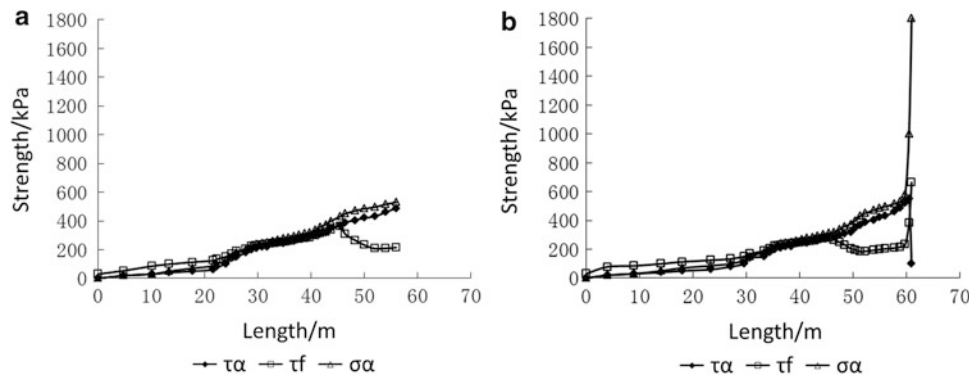


Fig. 7 Stress distribution on the critical slip surface after the cave dwelling is wet. (a) Section A, (b) Section B

(Fig. 7). Then the slope stability factor is 0.94 and the slope will be damaged.

Conclusions and Recommendations

With the progress of manual excavation activities, the stability of the slope is constantly decreasing. After the cave dwellings are constructed, the slope is in a marginally stable condition. Once the dwelling is built, it blocks the sunshine which leads to an increase in moisture content in the soil mass. With the moisture content in the soil of the foot of the slope increasing, slope stability will be gradually decreased and eventually it will cause the entire slope lose stability.

Slope failure can be analysed according to stress-strength relationship analysis for the critical slip surface on the two typical cross-section where the destruction of the cut slope will be started from cave dwelling collapse. As the cave dwelling is located on the foot of the slope, once the cave dwelling collapses, the slope will slide down rapidly which is require personnel evacuation. As such it is necessary to ensure stability of the cave dwellings to in turn ensure the stability of the slope.

Based on field investigation similar slope conditions in the loess area region are common and their stability need great attention. It is recommended to take measures such as proper backfilling or adding reinforcement supports for

the abandoned cave dwellings. Building by cave dwellings shall ensure that the buildings and foot of the slope have reasonable setback distance while taking reasonable precaution to control water discharge and drainage measures to keep the soil mass of the slope dry to promote the stability of this type of slope.

References

- Chen Z, Zhou J, Wang H (1994) Soil mechanics. Tsinghua University Press, Beijing
- Hou J, Wang J (1999) China cave dwellings. Henan Science and Technology Press, Zhengzhou
- Huang Y, Zhang R, Wang J (2008) Geohazards threatening cave dwellings in loess hilly areas of northern Shaanxi, China. *Geol Bull China* 27(8):1223–1229
- Lei X, Wei Q (1998) Study on the origin and counter measure of the casualty loess landfalls in the Northern Shaanxi. *Chin J Geotech Eng* 1:64–69
- Li B, Yin Y, Wu S (2011) Basic types and characteristics of multiple rotational landslides in loess. *J Eng Geol* 19(5):86–96
- Ren Z (1989) The spring of China cave dwelling construction. *Underground Space* 4
- Wu C, Gan Z, Meng C (2005) Stability of cave dwelling of loess hills in north part of Shaanxi province. *J Shaanxi Normal University (Natural Science Edition)* 33(3):119–122
- Zhang M, Li T (2011) Triggering factors and forming mechanism of loess landslides. *J Eng Geol* 19(4):86–96



Long- and Short-term Controls on the Spriana Rockslide (Central Alps, Italy)

Federico Agliardi and Giovanni B. Crosta

Abstract

Deep-seated rockslides in alpine valleys involve huge volumes and evolve over a long time under the action of multiple triggers. Scenario assessment and early warning systems based on monitoring activities are often the only effective ways to mitigate related risks, and require a sound understanding of complex interacting controls. We discuss the Spriana rockslide, affecting the left-hand flank of Val Malenco (Italian Central Alps). Documented rockslide activity dates back to 1912, with major acceleration stages in 1960 and 1977–1978 and later minor reactivations. The rockslide is a compound slide involving up to 50 Mm³ of slope debris and fractured rock, with a basal failure zone up to 90 m deep and two main scarps. Rock mass characterisation based on laboratory and field analyses provided inputs to 2D Finite-Element modelling of long-term slope evolution. The results allowed re-evaluation of the mechanisms of the Spriana rockslide, accounting for both long-term controls related to valley deglaciation and the short-term complexity of groundwater response to rainfall inputs. We suggest that modelling long-term slope evolution may be required to correctly understand large rockslides in changing geomorphic systems.

Keywords

Rockslide • Site investigation • Monitoring • Finite-Element modelling

Introduction

Complex, deep-seated rockslides in formerly glaciated valleys frequently threaten urbanized areas and infrastructures in alpine areas, including hydro-power plants and transportation corridors. These rockslides show peculiar morpho-structural and kinematic features, generally related to their scale, and are often associated with giant, long-lasting deep-seated gravitational slope deformations (Agliardi et al. 2012). These complex rockslides reach up to several tens of millions cubic meters and affect steep slopes up to 1,000 m high. This results in a significant interplay of rock slope instabilities with large-scale geological features (e.g. stratigraphy, folds, faults, master

joints), acting as constraints on rockslide geometry and kinematics.

The long history, large scale, and geometrical and geomechanical complexity of these phenomena result in complex onset and evolutionary mechanisms. They take place over hundreds or thousands of years in changing geomorphic settings under the action of multiple triggers. These include post-glacial debuitressing and associated rock mass strength degradation, fluvial toe erosion, rainfall or snow-melt and related groundwater changes, reservoir level fluctuations, and the onset of progressive failure processes. Forecasting the evolution of these landslides is difficult, due to their nonlinear displacement trends and the complex superposition of seasonal effects. Large rockslides can exhibit accelerating creep-type behaviour, eventually leading to catastrophic failure (Crosta and Agliardi 2003; Rose and Hungr 2007) or show viscous-type relationships (Secondi et al. 2013) between displacement rates and

F. Agliardi (✉) • G.B. Crosta
Earth and Environmental Sciences, University of Milano-Bicocca,
Piazza della Scienza 4, Milano 20126, Italy
e-mail: federico.agliardi@unimib.it; giovannibattista.crosta@unimib.it

seasonal or episodic change in external forcings (e.g. rainfall, snowmelt). The very different observed evolutionary styles of large rockslides (slow vs. catastrophic, continuous vs. episodic) depend on the observation time window, the seasonality of external actions, and whether a critical acceleration stage and/or a critical cumulative displacement or strain level are actually attained in the involved rock masses (Bonzanigo et al. 2007).

Since different rockslide behaviours require different risk management strategies, proper evolution models and monitoring parameters are required to define warning criteria. Nevertheless, any predictive tool (e.g. mathematical models calibrated and updated using field measurements, monitoring-based empirical or analytical alert thresholds) must rely on a sound knowledge of controls and triggers governing rockslide onset and evolution in time. Here we discuss the Spriana rockslide case study, and use Finite-Element numerical modelling to integrate available data and provide an evolutionary model accounting for the complex interplay of long-term and short-term controls on slope evolution.

The Spriana Rockslide

The Spriana rockslide (Fig. 1) affects a steep slope on the left-hand flank of the Val Malenco (Valtellina, Italian Central Alps), a few kilometres north of Sondrio. The slope was carved by glacial erosion in strongly deformed granitic to granodioritic gneisses and epidote-amphibole schists and calcschists, belonging to the “Monte Canale” tectono-metamorphic unit (Austroalpine Bernina nappe). The rocks underwent greenschist facies metamorphism and severe ductile deformation during the Variscan orogeny, with a minor Alpine metamorphic overprint within low-grade shear zones along unit margins (Trommsdorf et al. 2005).

The rockslide extends from 550 m a.s.l. up to 1,400 m a.s.l. over an area of about 0.5 km² (Fig. 2). Although slope instability of the lower slope sector had already been mentioned in 1878, the first well documented evidence of landslide activity dates back to 1912, when a shallow hydroelectric derivation tunnel (Figs. 1 and 2) came into operation and two springs appeared below the village of Cucchi. Between 1912 and 1927, shallow landslides involving scree and glacial deposits were triggered by heavy rainfall, although the southern segment of the tunnel had been moved deeper into the slope. In autumn 1960, during exceptionally long-lasting rainfall, global slope instability retrogressed upslope to 1,160 m a.s.l., causing the evacuation of the villages of Cucchi and Case Piazza. The rockslide underwent further major acceleration stages during the summers of 1977 and 1978, when the upper scarp appeared at

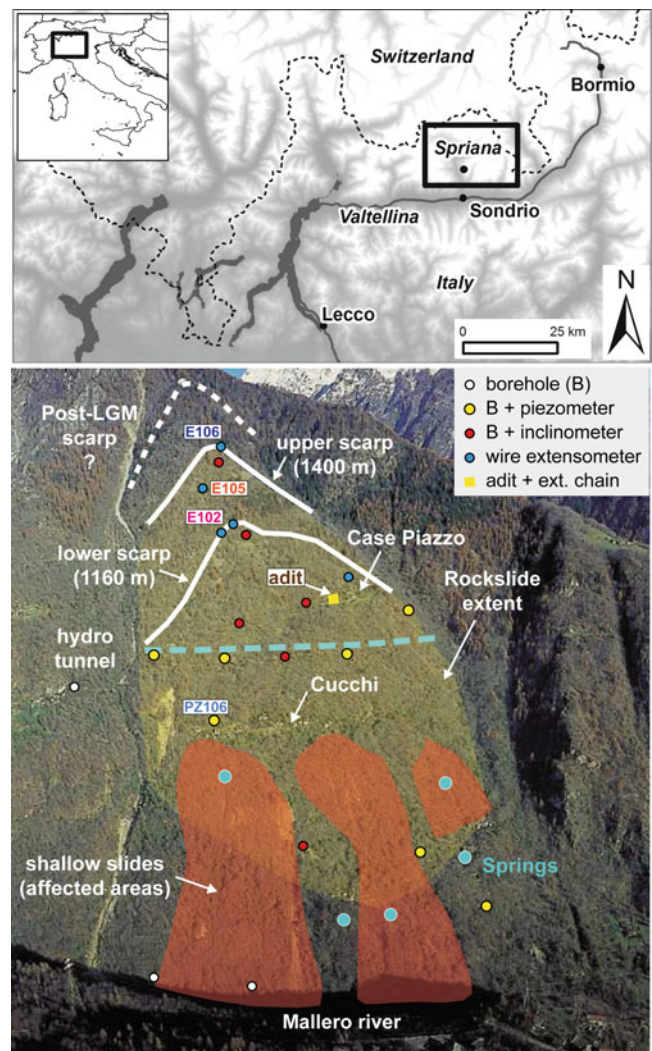


Fig. 1 Rockslide location (top), and view and main features (bottom)

1,400 m a.s.l. (Fig. 1). Then, the possibility of massive catastrophic slope failure threatening the Sondrio urban area motivated extensive geotechnical site investigation and slope monitoring activities, carried out in 1978 (Cancelli 1980) and 1989 (Belloni and Gandolfo 1997). Site investigations included 20 boreholes with complete core logging, a 150 m long horizontal exploratory adit at 1,040 m a.s.l. near the Case Piazza village (Figs. 1 and 2), and 5 refraction seismic lines. A monitoring network was also progressively installed and automated, including piezometers (standpipe and multipoint cells), borehole inclinometers, surface wire extensometers, a topographic network made of optical reflectors, hydro-meteorological stations, and a chain of six wire extensometers installed within the exploratory adit (locations of measuring devices considered in this paper are shown in Figs. 1 and 2).

We re-analysed site investigation and monitoring data collected since 1978 (Fig. 2), previously reviewed by

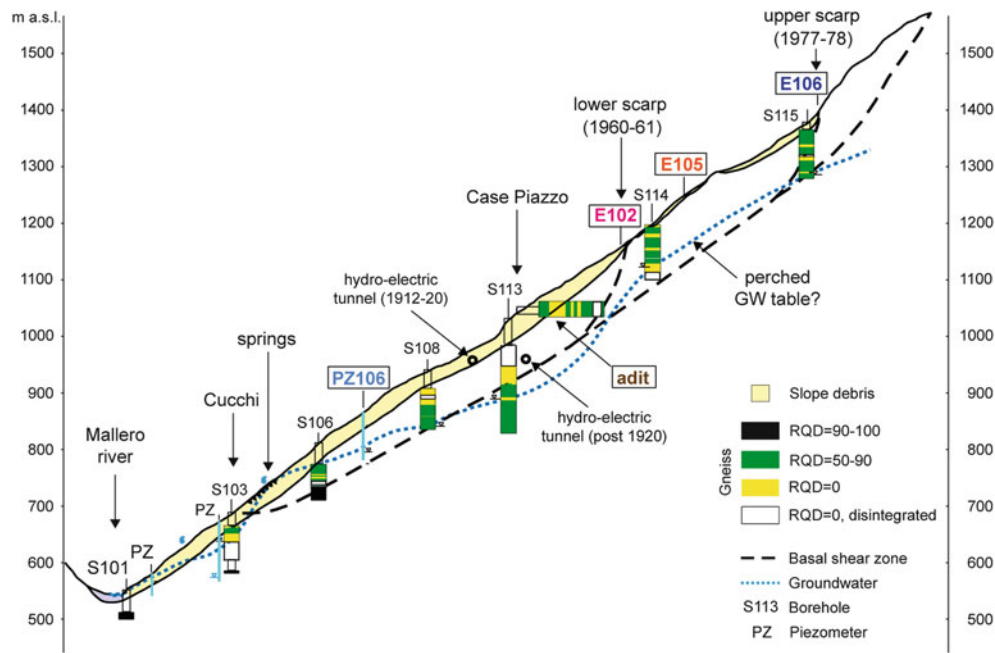


Fig. 2 Geological model of the Spriana rockslide, derived by the integration of available investigation data. The locations of selected monitoring devices providing data in Figs. 5 and 6 are also shown

(E102, E105 and E106 wire extensometers; exploratory adit hosting a chain of six wire extensometers; PZ106 piezometer)

Belloni and Gandolfo (1997). According to available information, the Spriana rockslide has been interpreted as a compound slide (i.e. mixed translational-rotational) involving up to 50 Mm^3 of slope debris and fractured rock with a basal failure zone 60–90 m deep, potentially daylighting at about 700 m a.s.l. (i.e. 150 m above the valley floor). The development of main scarps at 1,160 m and 1,400 m in successive stages (1960 and 1978, respectively) and the discovery of an older (post-Last Glacial Maximum) scarp above 1,600 m (Fig. 1) support the hypothesis of progressive slope failure over a long time.

Below the lower scarp, the instability affects both slope deposits up to 30–40 m thick and the underlying rocks, whereas in the upper part of the slope fractured rock masses are mainly affected. The bedrock is made of gneiss, classified according to the Rock Quality Designation (RQD) rating into “undisturbed” ($\text{RQD} > 90$), “fractured” ($50 < \text{RQD} < 90$), “heavily fractured” (with preserved texture; RQD close to 0), and “disintegrated” (Belloni and Gandolfo 1997).

Correlating disintegrated gneiss layers and surface features allowed us to infer the geometry of the main failure zones (Fig. 2). Borehole inclinometer data revealed minor, shallower sliding zones occurring inside the sliding rock mass and at the slope debris-bedrock interface (12–35 m in depth). Thick bands of disintegrated, highly weathered gneiss and silty-sandy gouge dipping to the WSW were also observed and sampled in the exploratory adit at the inferred location of the rockslide main failure zone

(Fig. 2). These bands roughly follow structural lineaments (i.e. faults, master fractures) observed at the slope scale, and could either represent breccia and gouge materials associated with the gravitational reactivation of pre-existing fractures or the products of severe weathering along major discontinuities, as suggested by the local preservation of pre-existing fabric (i.e. foliation, folds). Heavily fractured gneissic rock masses were found well below the inferred rockslide basal zone up to depths exceeding 120 m, suggesting that weak/disturbed rock masses existed before rockslide onset. Groundwater data derived from borehole drilling records and piezometers suggest that a perched water table, connecting to a deep one near the slope toe and characterised by average annual fluctuations in the range 1–1.5 m, occurs within this near-surface fractured zone (Fig. 2).

While early observations and sparse topographic surveys carried out since 1963 allowed the detection of only major rockslide events, systematic displacement measurements deployed since 1978 (topographic only; low measurement frequency) and 1990 (automatic monitoring network operated by ARPA Lombardia) provided time series for quantitative analysis.

Monitoring data revealed continuing, slow rockslide movements (average rates: 0.4–3 cm/a), with sudden acceleration stages (1977, 300 cm/a; 1993, 9.7 cm/a; 1996, 20 cm/a; 2001, 14 cm/a). This has been confirmed by PS-InSAR satellite interferometry (TRE s.r.l.-Regione Lombardia), providing average displacement rates of 0.5–2.5 cm/a since

1990. Significant rockslide activity continued after the hydroelectric derivation tunnel had been waterproofed in early 1978, suggesting that water leakage may have contributed to, but not dominated global slope instability. Cumulative rockslide displacement had exceeded 2 m in 1977–1978 and reached 5 m in the 1977–2007 period. This correspond to a total deformation ($\Delta L/L$; where L is total landslide length) of about 0.4 %, although morphological evidence (post-Last Glacial Maximum scarp, Fig. 1) suggests that much higher deformation had been accumulated by the slope over the long term. The Spriana slope deformation is thus close to critical conditions, posing significant risk despite a low-rate of activity.

Long-term Slope Evolution: Numerical Modelling

Rock Mass Characterisation

We carried out an extensive geomechanical characterisation of intact rock and rock masses by laboratory testing, core logging, and field surveys, in order to obtain well-constrained inputs to numerical modelling. More than 60 intact rock samples were obtained from rock cores drilled in the rockslide area, and tested under uniaxial compression, triaxial compression, and indirect tension conditions (Brazilian tests). Laboratory tests allowed reconstruction of the stress–strain behaviour and main mechanical properties of the intact rock, as well as the observation of the fracture geometry and patterns of the tested samples. Intact rock revealed quite low and scattered values of unconfined compressive strength and Young’s modulus, and was classified as medium-low strength rock with an average modulus ratio (i.e. E_{t50}/UCS) of about 400.

The rock mass was then characterised by geomechanical logging of available drill cores, allowing classification of the rock masses in terms of Geological Strength Index, from which equivalent Mohr-Coulomb c' and ϕ' and rock mass deformation moduli were derived as inputs for numerical modelling (Table 1).

Finite-Element Modelling: Effects of Deglaciation on Slope Evolution

In order to gain further insights in the factors controlling long-term slope evolution, we performed 2D continuum Finite-Element numerical modelling using the commercial code Phase2TM (Rocscience Inc.). Preliminary simulations showed that considering a two-layer slope model, accounting for the “fractured” gneiss observed in the borehole record below the rockslide basal failure zone (Fig. 2), is required to obtain

Table 1 Rock mass properties used in finite-element modelling

| Rock mass property | Undisturbed rock mass | Damaged rock mass |
|---|-----------------------|-------------------|
| Intact rock UCS (MPa) | 60 | |
| Intact rock E_{t50} (MPa) | 23000 | |
| Geological Strength Index | 58 | 47 |
| Rock mass cohesion (kPa) | 410 | 260 |
| Rock mass friction angle ($^{\circ}$) | 37 | 31 |

model results (i.e. strain localisation and displacement patterns) consistent with observed rockslide features. We attempted to support the hypothesis that a near-surface fractured gneiss layer existed before rockslide onset (and controlled its geometry and mechanism) by setting up a multistage Finite-Element model of the deglaciation sequence following the Last Glacial Maximum. Model results (Fig. 3) suggest that post-Last Glacial Maximum slope debuttressing caused significant tensile and shear rock mass damage, affecting the slope up to 150 m in depth (Fig. 3). This may have resulted in enhanced fracturing, strength degradation and increased hydraulic conductivity in a superficial layer whose extent is fully consistent with available investigation data.

Finite-Element Shear Strength Reduction Stability Analysis: Rockslide Mechanism

We performed 2D slope stability analyses based on the two-layer slope model discussed above, using the Finite-Element-SSR (Shear Strength Reduction) technique. This allows computing a Finite-Element-based “safety factor” of the slope by scaling material properties according to a “Stress Reduction Factor”. Associated stress and displacement fields provide insight on slope failure mechanism (Fig. 4). Results showed that unstable conditions ($SRF = 0.86$) are reached inside the upper slope layer when a perched water table matching critical conditions suggested by monitoring data exists. We validated the results using investigation and field constraints, i.e. rockslide depth, basal shear zone geometry, daylighting location, and displacement patterns. Strain localisation up to the post-Last Glacial Maximum scarp mapped at about 1,700 m supports the idea that the Spriana rockslide is part of a larger, earlier instability started after deglaciation.

Short-term Rockslide Triggering: Monitoring Data

Data provided since 1990 by the monitoring network allowed exploring the rockslide response (Figs. 5 and 6) to external triggers (rainfall, snowmelt).

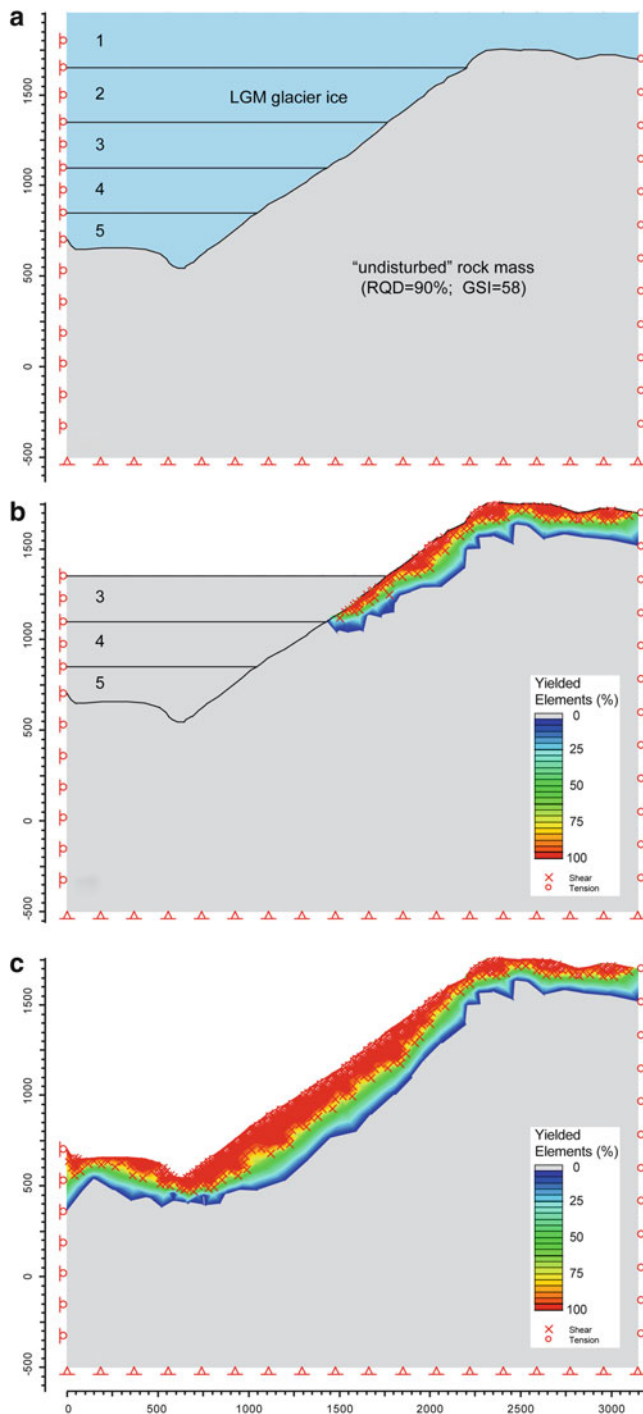


Fig. 3 Multi-stage FEM modelling of post-Last Glacial Maximum deglaciation sequence (a), showing the distribution of failed Finite Elements during (b) and the end of deglaciation (c)

Rockslide acceleration periods show strong seasonality (Fig. 5). They generally start during rainy periods and can last few weeks to several months (Fig. 6). Despite difficulties related to time lags of rockslide response and “noisy” time

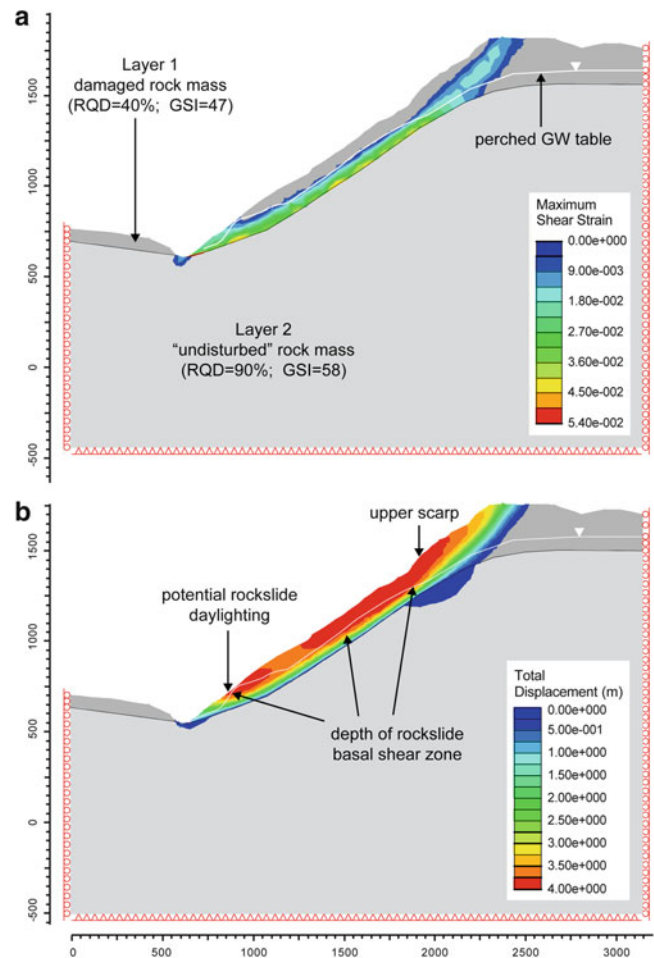


Fig. 4 Stability analysis performed using the FEM shear strength reduction method ($SRF = 0.86$). (a) maximum shear strain, showing the onset of a localised basal shear band; (b) total computed displacements, fitting the geometry of the Spriana rockslide and the magnitude of displacements observed in 2001

series due to low displacement rates, the analysis of rainfall and displacement data since 1990 provided interesting insights. Despite a weak positive correlation between short-term (daily) rainfall and rockslide displacement rates, significant accelerating periods (e.g. 1993, 1996, 2001, 2003) were related to prolonged rainfall, e.g. 7-day rainfall >150 mm or 30-day rainfall >300 mm.

The aforementioned observations suggest that a certain amount of groundwater recharge in the near-surface fractured layer must be attained for significant rockslide accelerations to occur. Figure 6 clearly illustrates this behaviour for the 2000–2001 period. In spring 2000, rainfall and snowmelt caused a water table rise <2 m in the middle-lower slope sector, resulting in a short acceleration period and minor displacements. Instead, intense and prolonged rainfall during the autumn 2000 flooding event resulting in

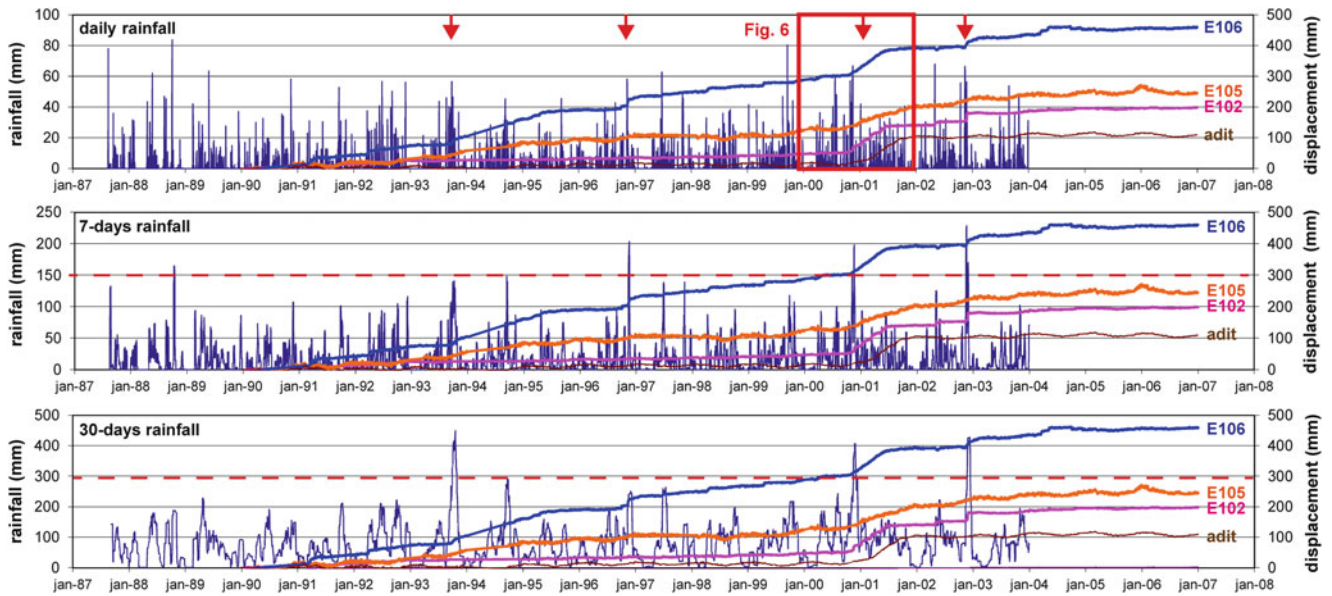


Fig. 5 Cumulative displacements of selected extensometers (see Fig. 2) compared to daily, 7-day and 30-day rainfalls

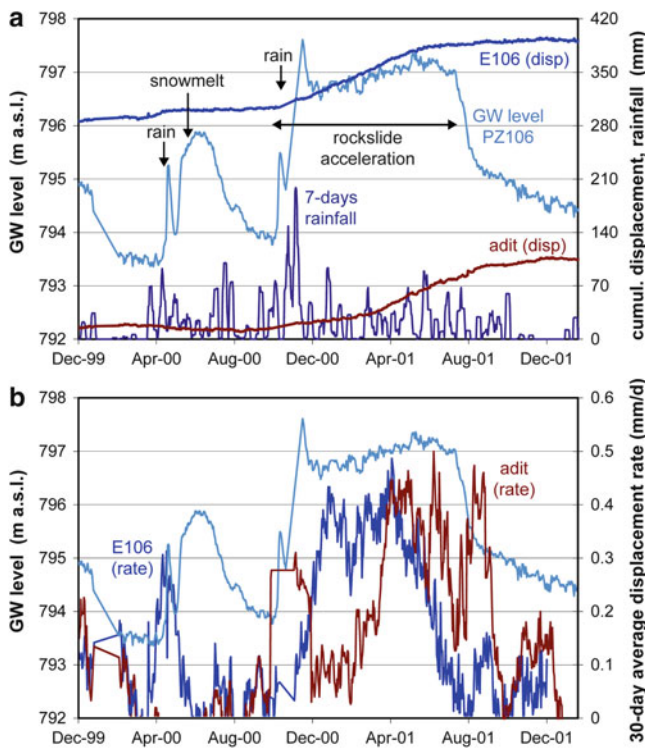


Fig. 6 Response of displacements (a) and displacement rates (b) to groundwater level changes for the 2001 acceleration period (device locations in Fig. 2)

a water table rise exceeding 3 m (probably also sustained by snowmelt during the following spring), leading to 7 months of rockslide velocity increase and cumulative rockslide displacements of up to 100 mm.

Conclusions

We re-interpreted the evolution of the Spriana rockslide, accounting for the role and interplay of different controls, namely: 1) long-term morpho-climatic evolution, including post-Last Glacial Maximum deglaciation and associated rock mass degradation, which possibly led to an embryonic “pre-Spriana” rockslide; 2) short-term response of rockslide activity to complex rainfall patterns, affecting groundwater conditions in fractured bedrock. The combination of these factors introduces significant uncertainties in the analysis of complex rockslides, evolving over timescales of 10^2 – 10^3 years in complex geological settings and in changing geomorphological systems. These need to be taken into account when setting up evolution models for rockslide prediction and early warning systems.

Acknowledgments We thank G. Mannucci and L. Dei Cas (ARPA Lombardia) for data and support, and M. Laini for field and laboratory work. Research was partly supported by PRIN 2010–11 program (2010E89BPY_007).

References

- Agliardi F, Crosta GB, Frattini P (2012) Slow rock slope deformation. In: Clague J, Stead D (eds) Landslides: types, mechanisms and modeling. Cambridge University Press, Cambridge, pp 207–221
- Belloni L, Gandolfo M (1997) La frana di Spriana. *Geologia Tecnica & Ambientale* 3(97):7–36

- Bonzanigo L, Eberhardt E, Loew S (2007) Long-term investigation of a deep-seated creeping landslide in crystalline rock-Part 1: geological and hydromechanical factors controlling the Campo Vallemaggia landslide. *Can Geotech J* 44(10):1157–1180
- Cancelli A (1980) The monitoring of the Spriana landslide. In: *Proceedings international symposium on land-slides*, 7–11 April 1980. New Delhi. 3, pp 216–219
- Crosta GB, Agliardi F (2003) Failure forecast for large rock slides by surface displacement measurements. *Can Geotech J* 40(1): 176–191
- Rose ND, Hungr O (2007) Forecasting potential rock slope failure in open pit mines using the inverse-velocity method. *Int J Rock Mech Min Sci* 44(2):308–320
- Secondi M, Crosta GB, Di Prisco C, Frigerio G, Frattini P, Agliardi F (2013) Landslide motion forecasting by a dynamic visco-plastic model. In: Margottini C, Canuti P, Sassa K (eds) *Landslide science and practice 3: spatial analysis and modelling*. Springer, 151–160
- Trommsdorf V, Montrasio A, Hermann J, Müntenerl O, Spillmann P, Gierè R (2005) The geological map of Val Malenco. *Schweizerische Mineralogische und Petro-graphische Mitteilungen* 85:1–13



Engineering Geology and Numerical Modelling of a Steep Rock Slope for the Ensi-Qianjiang Expressway, China

Xiuwen Hu, Doug Stead, Longxiang Zhai, Hongyan Jin, and Dezhi Kong

Abstract

This paper describes the site investigation and engineering geological characterization of steep engineered rock slopes at the site of a major 280 m single span arch bridge. The rock slopes comprised predominantly carbonaceous limestone with reduced rock mass quality due to the influence of faulting and shearing. The carbonaceous limestone occurs as lenticular bodies with smooth, tectonically disturbed, variably dipping (37° – 57°) bedding planes. The rock slope was excavated to a total height of 90 m, including a bridge foundation excavation depth of 30 m and a final permanent engineered slope height of 60 m. The engineered rock slope was excavated at 60° – 90° and the natural rock slope is between 50° and 70° . Construction of the bridge foundation required the excavation of three rock slopes, two perpendicular to bedding and one parallel to the strike of the bedding. In the two rock slopes excavated perpendicular to bedding, one exhibited potential bedding plane controlled failure and the other potential toppling instability. The intact rock properties were characterized using laboratory testing and selected discontinuities tested in direct shear. Using the derived properties and the results of the engineering geological

X. Hu (✉)

Department of Engineering Geology and Geotechnical Engineering,
China University of Geosciences, No. 388 Lumo Road, Wuhan 430074,
China

Department of Earth Sciences, Simon Fraser University, Vancouver,
Canada, V5A 1S6
e-mail: goodhxw@cug.edu.cn

D. Stead

Department of Earth Sciences, Simon Fraser University, Vancouver,
Canada, V5A 1S6
e-mail: dstead@sfu.ca

L. Zhai • D. Kong

Department of Engineering Geology and Geotechnical Engineering,
China University of Geosciences, No. 388 Lumo Road, Wuhan 430074,
China

China Highway Engineering Consulting Corporation, Wuhan, China

H. Jin

The 5th Engineering Co., Ltd., China Railway Major Bridge
Engineering Group, Jiujiang, China

mapping numerical modelling was undertaken using a discontinuum model, (UDEC). The deformation of the rock mass during the stages of excavation was simulated and the results used to develop plans for safe construction and reinforcement of the rock slopes.

Keywords

Rock slope stability • Engineering geology • Bridge abutment foundation • Discontinuum modelling

Introduction

Rock slope deformation and failure modes in bedded slopes are frequently controlled by the spatial relationship between the bedding planes, joints and faults and the rock slope. From research on natural rock slopes in the Canadian Rockies and in order to evaluate high mountain slope stability Cruden (2000, 2003) divided stratified rock slopes into cataclinal slopes, subdivided into overdip, underdip and dip slopes, and anaclinal slopes.

The rock mass structure of a natural slope is sometimes very complex and subject to a high degree of uncertainty with new rock slope structures often appearing during excavation. The combination of discontinuities in a stratified rock slope and the slope topography determines the mode of deformation, failure mechanism and the degree of instability. A good geological slope model is thus fundamental to accurate assessment of potential slope deformation and failure. As slope excavation can expose many important geological features site investigation during this stage is extremely important in order to collect rock mass geological information and build a reliable geological model with reduced uncertainty.

The construction of an accurate slope geological model is particularly important in order to ensure realistic numerical modelling. There are currently available numerous types of two and three-dimensional numerical codes which can be used to simulate rock slope deformation and failure. The choice of the numerical method is strongly influenced by slope geological model and it is important to realise the limitations and advantages of specific numerical methods. The two-dimensional distinct element code, UDEC is for example well suited to rock slopes controlled by discontinuities (Stead and Coggan 2012; Stead et al. 2006).

Engineering Background

The Longqiao arch bridge is located in Hubei Province, China and was a key project in the construction of Ensi-Qianjiang expressway. It was constructed of steel sections and reinforced concrete with a major 280 m single span and

adjoining spans crossing a 213 m deep valley. The bridge is approximately perpendicular to the valley with an axis of orientation of 236°, Fig. 1. The bridge loading was designed to be transferred to the slope rock mass through an arch abutment foundation. The study area for this paper is the No.5 arch abutment slope on the Qianjiang bank of the valley. The upper-natural slope angle is 25° with mid and lower-slope angles of between 50° to 70°. Due to excavation for the abutment foundation for the No.5 arch abutment, three deep and 60°–90° steep engineered slopes were formed. The SW slope, parallel to the axis of Longqiao Bridge, was excavated to a total height of over 90 m and the SE-NW slopes to a height of 75 m. During slope excavation, the SW rock slope was excavated in five stages in order to reduce stress concentrations in the slope and at same time to allow slope reinforcement by a combination of cable anchors, rock mesh and shotcrete at each excavation level. The arch abutment foundation basement is 22 m long and 6.5 m wide. When it had been excavated to an elevation of 943 m, the SE upper slope slid down along bedding planes. When the excavation reached an elevation of 919.66 m, two cracks of about 11.5 m and 7 m in length occurred in the NW mid- and lower-slopes. In this paper, the SE-NW slope deformation and stability is studied using UDEC models. The analysis of SW rock slope stability is not presented due to the limit of the paper length.

Engineering Geology and Site Investigation

Lithology

The slope rock mass consists predominantly of medium to thickly bedded carbonaceous limestone with abundant carbonaceous content and calcite veining, carbon shale and limestone. The carbonaceous limestone enclosed by the black solid line in Fig. 1 contains significantly more carbonaceous shale. The strength of the carbonaceous limestone and shale are low due to the presence of abundant carbonaceous material. The carbonaceous materials weather rapidly and become weak due to the action of water. Limestone is found to the right of the black solid line near

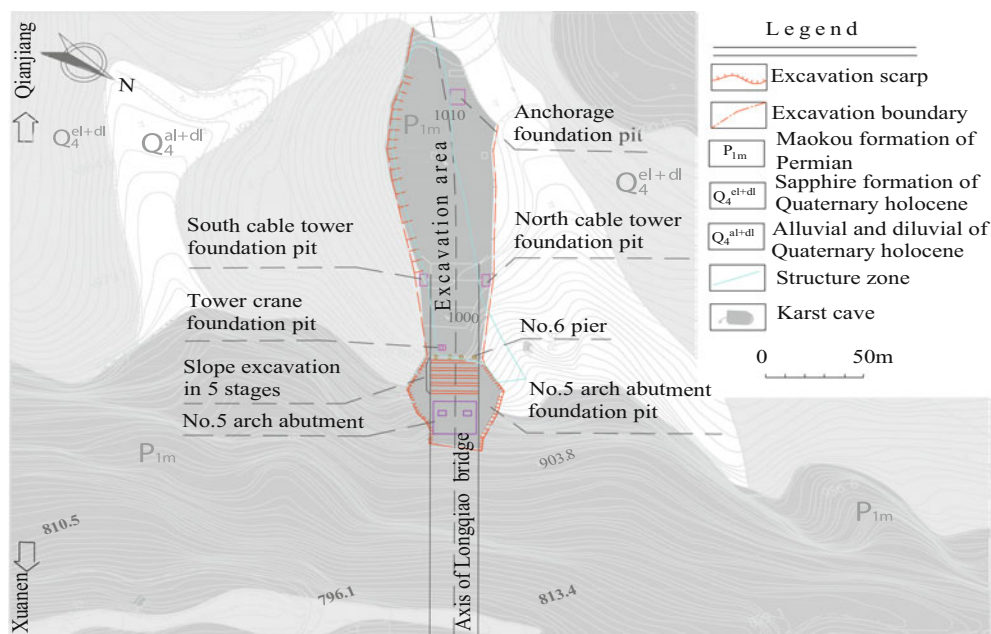


Fig. 1 Engineering geological map of the No.5 arch abutment slope for Longqiao arch bridge, Ensi-Qianjiang expressway, Hubei Province, China

the anchor foundation pit and the north tower crane pit. Highly weathered shale with a high carbonaceous content and calcite veins of 0.10–0.15 m width exist at an elevation of 943 m in the arch abutment foundation pit.

Geological Structures

The rock strata have been deformed due to the folding (Fig. 2). Bedding planes are smooth, striated and coated with calcite veneers due to the strong folding and shearing action. Ground investigation showed that bedding orientations varies with a dip of 37° – 57° and dip directions of 310° – 337° . The bedding plane spacing is 0.30–2.00 m. Two joint sets are present with orientations (dip/dip direction) of $53^{\circ}/135^{\circ}$ and $84^{\circ}/59^{\circ}$ respectively, a persistence of 1–2 m and a spacing of 1–2 m. A set of unloading cracks were observed. When the arch abutment pit had been excavated to an elevation of 943 m, the orientations of the bedding planes were measured with a dip/dip direction of 34° – 70° to 320° – 345° .

A crushed and sheared zone is located within the blue solid line shown in Fig. 1. A smooth and striated fault is exposed in the south tower crane pit shown in Fig. 1 and is infilled with black rocky debris and clay of about 1–10 cm thickness and coated with a veneer of calcite. The layer of black rocky debris and clay disintegrates to a “slimes” consistency in contact with water. Many well developed lens shaped bodies composed of carbonaceous limestone and shale were found in the hanging wall of the fault



Fig. 2 Observed rock mass structures in the natural slope at the location of the No.5 arch abutment of Longqiao Bridge. Bedding planes show varying orientation. Natural slope height is 213 m

indicating that the slope rock mass had been subjected to intense crushing and shearing due to tectonism. These lens shaped bodies (Fig. 3) with strike directions of 227° – 236° are sub-parallel to the strike of the bedding planes, tightly juxtaposed with each other, upright in attitude and coated with a calcite veneer. They exhibit smooth surfaces with vertical striations and contain abundant carbonaceous content. The thickness of each lenticular body is about 0.10–0.30 m (up to 1.00 m) with a height of over 1.6 m. The core of the lens is made of limestone. Fresh carbonaceous limestone lenses of rock are easily broken when disturbed and rapidly become soft in contact with rainfall.



Fig. 3 Cross sectional view of lens-shaped bodies exposed within the southern tower crane pit

Slope Geological Models

The relationship between the bedding planes, joint sets and the two excavated rock slope surfaces are illustrated in Fig. 4, which shows that the SE and NW slopes are an overdip slope and an anaclinal slope.

After consideration of the spatial relationships between the bedding planes, the two joint sets, the unloading cracks and the excavated rock slopes, geological models of the SE and NW rock slopes are developed and the geological sections constructed as shown in Fig. 5. The SE and NW rock slopes are an overdip slope and an anaclinal rock slope respectively according to the terminology of Cruden (2000), Fig. 5. The deformations and stability of these slopes are controlled mainly by the bedding plane properties.

Physical and Mechanical Properties

It is often extremely difficult to obtain representative accurate physical and mechanical properties of discontinuities such as bedding planes, joints and lens surface and the intact rock properties of the carbonaceous

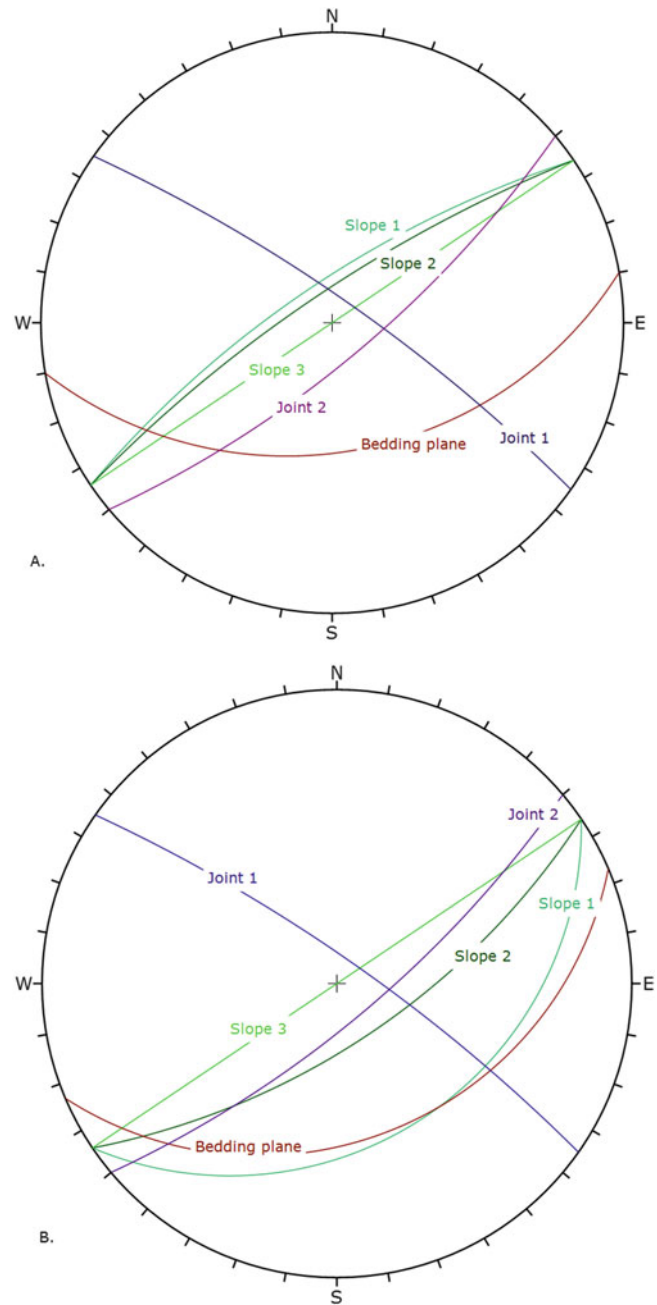


Fig. 4 Spatial relationship between the bedding planes, joints and the rock slope. A is the SE slope and B is the NW slope

limestone, limestone and lens rock. In this paper, uniaxial compression tests were undertaken on 50 mm diameter, 100 mm high samples of intact carbonaceous limestone to determine the physical and mechanical properties. Direct shear tests were conducted on 100 mm × 100 mm samples of the lens rock surface. The cohesion and friction angle of the lens surface are 101 kPa and 24°. Based on the slide failure of the SE upper slope, back-analysis using the method of Ren et al. (2010) produced bedding plane cohesion and friction angles of 40.7 kPa and 22°

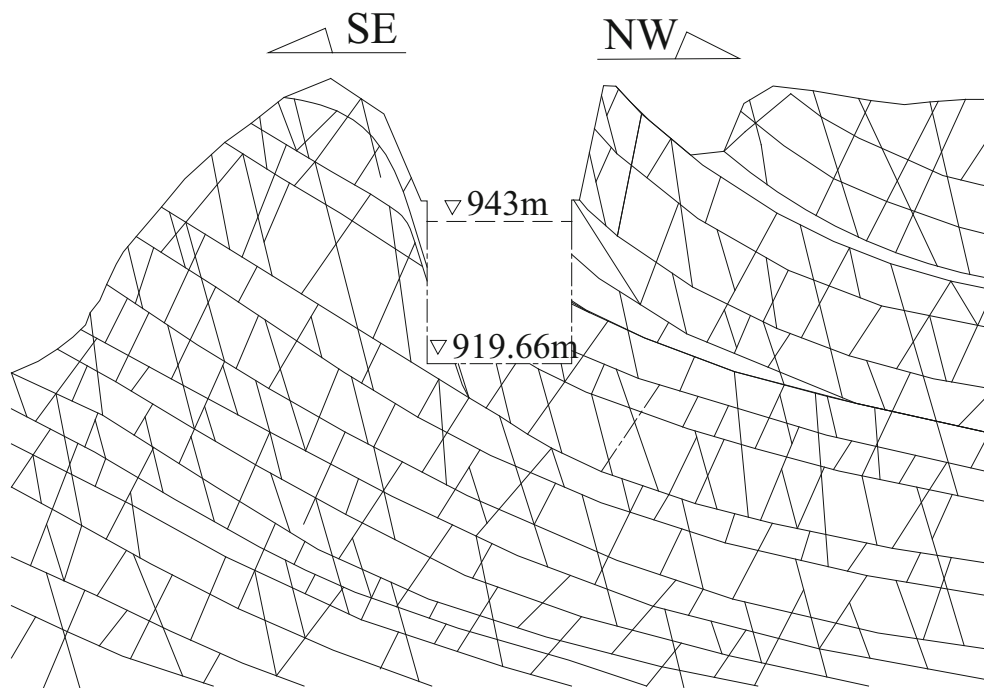


Fig. 5 Rock slope geological model

Table 1 Physical and mechanical parameters of rocks for UDEC modeling

| Rock type | Density (kg/m ³) | Tensile strength (MPa) | Shear strength | | Bulk modulus (GPa) | Shear modulus (GPa) |
|------------------------|------------------------------|------------------------|--------------------|----------------|--------------------|---------------------|
| | | | Friction angle (°) | Cohesion (MPa) | | |
| Limestone | 2,710 | 8.0 | 43 | 16 | 20 | 12 |
| Carbonaceous limestone | 2,645 | 5.3 | 37.1 | 10.6 | 7.81 | 3.46 |
| Lens rock | 2,510 | 2.2 | 28 | 3.5 | 2.81 | 1.3 |

Table 2 Mechanical parameters of discontinuities

| Type | Friction angle (°) | Cohesion (kPa) | Normal stiffness (GPa/m) | Shear stiffness (GPa/m) |
|---------------|--------------------|----------------|--------------------------|-------------------------|
| Bedding plane | 20 | 30 | 1.13 | 0.95 |
| Lens surface | 22 | 41 | 0.713 | 0.498 |
| Joints | 30 | 340 | 2 | 1 |

respectively. The physical and mechanical properties of the limestone and lens rock were determined according to methods outlined in *rock mass mechanics* (Liu and Tang 1999).

Based on the results of laboratory testing, back-analysis and reference to the published literature (Liu and Tang 1999; Xu et al. 1991), the physical and mechanical parameters of the slope rock mass and the discontinuities properties are presented in Tables 1 and 2 and were assumed for UDEC modelling.

Discontinuum Modeling Using UDEC

The slope deformation, failure mechanism and stability of the SE and NW rock slopes including the steep over dip and anacinal slopes shown in Fig. 5 are mainly controlled by bedding planes as the intersection angle between the dip directions of the slope and bedding planes are about 10°. The joints and unloading cracks also have some influence on the slope deformation. The UDEC models are used to

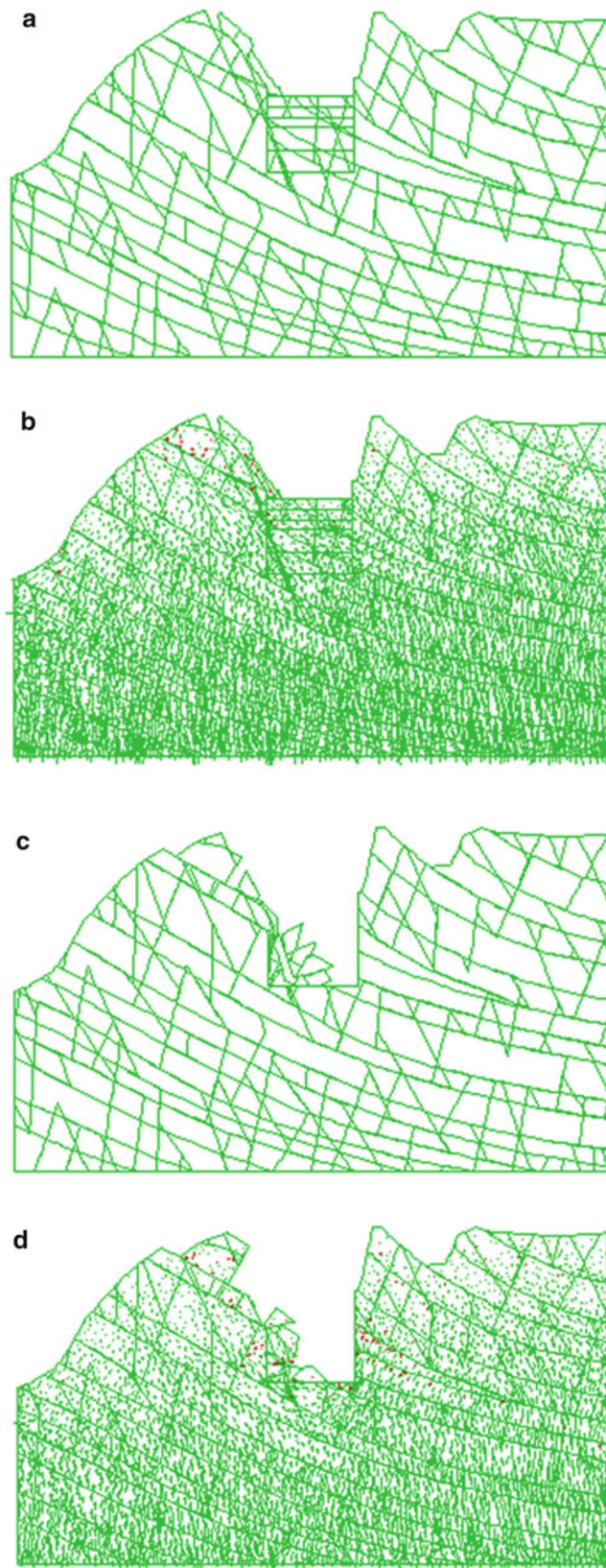


Fig. 6 Instability and stress distributions in the SE and NW slopes of the arch abutment foundation pit at elevation of 943 m (a and b) and 919.66 m (c and d)



Fig. 7 Sliding failure of the SE slope occurred along a bedding plane when the arch abutment foundation pit had been excavated to an elevation level of 943 m.

analyse the slope deformation and changes in stability during the slope and foundation excavation construction, specifically when the excavation depth has reached elevations of 943 m and 919.66 m, respectively.

Figure 6 shows that sliding failure of the overdip slope is simulated along the bedding planes after the slope has been excavated to elevation of 943 m, in agreement with the site observation shown in Fig. 7. If the overdip slope is not reinforced, the zone of failure will increase with increasing pit excavation depth. Figure 6d also clearly shows the tensile stress concentration zone occurring along the bedding plane in the mid and lower sections of the anacinal slope when the excavation has reached an elevation of 919.66 m. This agrees with the field observations of 11.5 m and 7 m long tension cracks along bedding plane in the NW slope at elevations of 925.663 m and 931.663 m, respectively, Fig. 8.



Fig. 8 Rock slope deformation and failure due to excavation of the No.5 arch abutment foundation pit. (a) The SE slope slid along bedding planes and the NW slope showed minor flexural toppling on bedding when the excavation had reached elevations of 943 m and 919.663 m, respectively. Tension cracks 1 and 2 opened along bedding planes at

elevations of 931.663 m and 925.663 m, respectively. (b) Tension crack 1, length along slope over 7 m, maximum width of about 5 cm and trace length over 5 m; separation along a bedding plane. (c) Tension crack 2, length along slope over 11.5 m, maximum width of 10 cm and trace length of over 25 m; separation along a bedding plane

Conclusion

Engineering geological site investigations during excavation of a high and steep slope rock mass for the No.5 arch abutment of Longqiao major arch bridge have been carried out. The engineered slope rock mass was shown to have a complex geological structure including variably oriented bedding planes, a fault, lens shaped bodies, joint sets and unloading cracks. Three different rock slope structures were recognized including an over-dip slope, an anaclinal slope and a transverse slope. Different slope deformational modes occur mainly due to spatial interaction of the discontinuities and the excavated rock slope surfaces.

Discontinuum UDEC numerical modelling was used to analyse the slope deformation and mechanism of the two rock slopes as they were excavated to different elevations. The modelling results showed very good agreement with the actual observed rock slope deformation.

Acknowledgments The authors acknowledge funding received from China Railway Major Bridge Engineering Group, Ltd, in the Ensi-Qianjiang expressway of Hubei, China. We also thank the Construction Project Management Department for assistance with field engineering

geological investigation for the Longqiao arch bridge. The authors also acknowledge China Scholarship Council (CSC) which has supplied funding for us to undertake collaborative research on this paper. The authors also acknowledge the reviewer for his constructive comments.

References

- Cruden DE (2000) Some forms of mountain peaks in the Canadian Rockies controlled by their rock structure. *Quaternary Int* 68–71:59–65
- Cruden DE (2003) The shapes of cold, high mountains in sedimentary rocks. *Geomorphology* 55:249–261
- Liu YR, Tang HM (1999) *Rock mass mechanics*. China University of Geosciences Press, Wuhan. ISBN 7-5625-1429-1
- Ren W, Jin Y, Feng G, Li J (2010) Probing into assessment system of landslide/slope stability. *Rock Soil Mech* 31(7):2129–2134
- Stead D, Coggan J (2012) Numerical modelling of rock slope stability, Chapter 13. In: Clague J, Stead D (eds) *Landslide: types, mechanisms and modelling*. Cambridge University Press, Cambridge, pp 144–158
- Stead D, Eberhardt E, Coggan JS (2006) Developments in the characterization of complex rock slope deformation and failure using numerical modeling techniques. *Eng Geol* 83:217–235
- Xu K, Pan W, Lin J (1991) Engineering geological study on texture of rock mass and weak interrelations in Lianzi Cliff dangerous rock body of Sanxia Gorge on Changjiang (Yangtze) river. *Chin J Geol Hazard Cont* 2(8):43–53



Determination of the Effective Computing Region for Rock Slope Stability Based on Seismic Wave Theory

Chen Zhenlin and Hu Xiao

Abstract

In order to detect the initiation of a rockslide efficiently, FEM and BEM numerical methods are employed to analyze the dynamic response of a slope. The boundary condition (effective computing region) should be selected carefully to maximize both the computational efficiency and precision of the model. The effective computing region can be determined based on the tension damage criterion and the principle of dynamic responses. The seismic wave theory is employed to solve the dynamic response, detect the initialization of cracks and establish the critical sliding zone (comprising all potential sliding surfaces). The relationship between the location of the sliding surface and the excitation frequency, is also investigated. The focus of this study is to identify the effective computing region and to discuss the sliding fracture that occurs in the region based on the seismic theory analysis. The shaking table model results and the time-history analysis of displacement vectors are adopted for investigating the reliability of theoretical analysis.

Keywords

Landslide • Effective computing region • Seismic wave theory

Introduction

The stability analysis of slopes is always an important aspect in slope engineering and seismic prospecting. Normally, the distribution principle of the dynamic response of a complete slope is difficult to determine and the associated computational costs are very high when the seismic wave theory is employed. It is important to choose a suitable computing region in slope stability analysis when a theory analysis method or a numerical simulation method is employed.

The vertical ground motions may have the greatest influence on the displacements induced by seismic activity.

The influence of the shape and slope reinforced measures on seismic response is normally investigated in large-scale shaking table model tests (Wu et al. 2008; Xu et al. 2008; Lin and Wang 2006). These experiments show that the resonance frequency of such a model will decrease after repetitive vibration. At the same time, the seismic acceleration of the soil of the model shows a larger amplification. In general, the acceleration response was employed to analyze the stability of a slope. In some earthquake-induced landslides, especially near-field cases, the vertical acceleration is found to be a relevant factor affecting landslide initiation (Ingles et al. 2006).

In recent years, various procedures (Duncan and Wright 2005) (numerical simulation methods and theoretical analysis methods) have become available for stability analysis, using the magnitude of Peak Ground Acceleration (PGA) at a specific site. The PGA can be included in the deformation analysis using Newmark stick-slip sliding block analysis (Yan et al. 1996), pseudo-static (PS) analysis (Newmark 1965; Hong et al. 2005), or the finite element method

C. Zhenlin (✉)
State Key Laboratory of Geohazard Prevention and Geoenvironment Protection, ChengDu University of Technological, ChengDu 610059, China
e-mail: hustchzl@hotmail.com

H. Xiao
ChengDu University of Technological, ChengDu 610059, China

(FEM) (Tang and Shao 2004). The development of the method-of-slices for identifying the critical failure surface that corresponding to the minimum factor of safety (Malkawi et al. 2001; Zolfaghari et al. 2005). The theory of seismic wave propagation and attenuation has become increasingly popular in solving seismic slope stability problems (Yang et al. 2007; Gulyayev and Ivanchenko 2006).

Later, the research (Li and Ma 2009; Li et al. 2011a, b) employed the principle of conservation of momentum and the discontinuous displacement conditions along a rock joint to investigate the interaction of an obliquely incident P- or S-wave with a rock joint. A fractal damage joint model (Zhao et al. 2008; Li et al. 2011a, b) was developed based on the fractal damage theory, and the analytical solution for the transfer (transmission or reflection) coefficients of stress waves across joints. The interaction between blast waves with arbitrary impinging angles and a rock joint are analyzed in detail in the study by Li and Ma (2010).

The focus of the current research is on getting the dynamic response, not on selecting the effective computing region. If the area of the computing region is too large, the computational cost will be very high, while if the area is small the computational accuracy will be reduced. Hence, after the region is determined, the slope stability characters could be obtained efficiently and accurately by analyzing the dynamic responses of the region in a rock slope. In view of these premises, this paper has been structured around the following objectives:

1. To determine the effective computing region for studying the slope stability based on the theory of seismic wave propagation.
2. To detect the failure initiation and determine the potential sliding surfaces efficiently and accurately by theoretical simulations in the computing region.

Characteristics of Seismic Wave Propagation

The following two assumptions should be considered for our theoretical analyses: (1) The slope is homogeneous and isotropic; (2) The seismic wave is a plane wave.

When a plane wave of either P- or S-type impinges on a free surface, reflection takes place as described in Fig. 1. The positive direction of displacement of the S-wave follows the “right-hand rule”. According to the Snell’s law, we have (see Fig 1):

$$\frac{\sin \alpha_p}{\sin \alpha_s} = \frac{\sin \beta_p}{\sin \beta_s} = \frac{c_p}{c_s} = \sqrt{\frac{2(1-\nu)}{1-2\nu}} \quad (1)$$

where ν is the Poisson’s ratio of the reflecting rock. The reflection coefficients could be obtained by the analysis (Wang 2005).

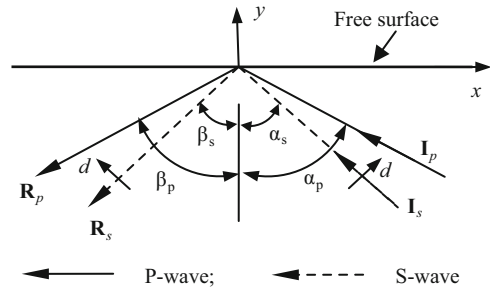


Fig. 1 Seismic wave propagation models on a free surface

Establishment of the Effective Computing Region

In this paper, the method used by Li and Ma (2010) to study the stress on joint elements under seismic waves is extended to analyze the stress state of internal elements of the slope crest. The potentially critical slip surfaces in the effective computing region could be detected based on the theory of seismic wave propagation. More details are given in following subsections.

According to the theory analysis from Li and Ma (2010), when the seismic wave rays run through an infinite small element (ABCD) on a crest as depicted in Fig. 2, the stress state of the element (ABCD) can be portrayed as:

1. Under incident P-Wave

The stresses on the line AB of the element ABCD can be expressed as:

$$\begin{aligned} \sigma &= \rho c_p v_{I_p} \left(\frac{\nu}{1-\nu} + 2 \sin^2 \beta_s \right) \\ &- \rho c_p v_{R_p} \left(\frac{\nu}{1-\nu} + 2 \sin^2 \beta_s \right) - \rho c_s v_{R_s} \sin 2\beta_s \end{aligned} \quad (2)$$

$$\begin{aligned} \tau &= -2\rho c_p v_{I_p} \sin^2 \beta_s \operatorname{ctg} \alpha_p \\ &- 2\rho c_p v_{R_p} \sin^2 \beta_s \operatorname{ctg} \alpha_p - \rho c_s v_{R_s} \cos 2\beta_s \end{aligned} \quad (3)$$

where v_{I_p} , v_{R_p} and v_{R_s} are the particle velocities of the incident P wave, the reflected P-wave and reflected S-wave, respectively, and ρ is the density of the intact rock.

2. Under incident S-Wave

When the S-wave impinges the surface on the line AB of the element ABCD:

$$\begin{aligned} \sigma &= \rho c_s v_{I_s} \sin 2\alpha_s - \rho c_p v_{R_p} \left(\frac{\nu}{1-\nu} + 2 \sin^2 \beta_s \right) \\ &- \rho c_s v_{R_s} \sin 2\beta_s \end{aligned} \quad (4)$$

$$\begin{aligned} \tau &= -\rho c_s v_{I_s} \cos 2\alpha_s - 2\rho c_p v_{R_p} \sin^2 \beta_s \operatorname{ctg} \alpha_p \\ &- \rho c_s v_{R_s} \cos 2\beta_s \end{aligned} \quad (5)$$

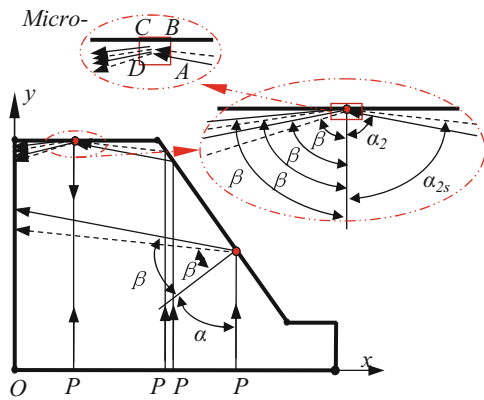


Fig. 2 Access of seismic waves and reflection for a mudstone slope



Fig. 3 The slope model 1 before the test (the left part is the limestone slope and the right part is the mudstone slope)

The initialization of fracturing is controlled by tensile stresses, (2) and (4) could be employed to detect the critical dangerous point on the slope crest.

Validation of the Effective Computing Region

In order to investigate the validity and reliability of the theoretical simulation of the effective computing region, a homogeneous rock slope was considered. The slope geometry is shown in Fig. 3 with a height of 1.7 m, a width of 1.5 m, a length of 1.65 m and a slope angle of 60°. The material properties were obtained from laboratory tests. The modulus, Poisson ratio, frictional angle and cohesive strength of mudstone slope model is 15.2 MPa, 0.3, 35° and 0.3 MPa, respectively. The scaling factor λ ($\lambda = 100$) is the linear ratio between the prototype and the model. A sinusoidal acceleration with a frequency of (5–15 Hz) and a peak acceleration of (0.1 g–0.8 g) were applied to the foundation.

Table 1 The maximal tensile stress at the slope crest for different frequencies

| Frequency (Hz) | Coordinates (x, y) | Maximal tensile stress (Pa) |
|----------------|--------------------|-----------------------------|
| $f = 0.2$ | (0.45, 1.7) | 9.343363E5 |
| $f = 0.5$ | (0.45, 1.7) | 3.737345E5 |
| $f = 1.0$ | (0.45, 1.7) | 1.868673E5 |
| $f = 1.5$ | (0.36, 1.7) | 1.245782E5 |
| $f = 10$ | (0.45, 1.7) | 1.868673E4 |
| $f = 15$ | (0.36, 1.7) | 1.245782E4 |

Localization the ECR

To avoid repetition only a theoretical analysis focused on the dynamic response of the uniform mudstone prototype slope was carried out and compared with the experimental results.

Following the previous discussion and considering a vertical sinusoidal acceleration loading, the principle tensile stresses of the mudstone slope crest were calculated with (2) and (4), for different frequencies. The values are given in Table 1 that the maximum tensile stress on the crest is positioned at $x = 36$ m and $x = 45$ m. So there are two potential dangerous points on the crest. Hence, the boundary point could be $x = 36$ m. The observed amplification effect near the slope crest in experiment could accelerate the development of a failure surface near the point ($x = 0.334$ m, $y = 1.7$ m).

Detecting Potential Sliding Surface in the ECR

From Fig. 4 and Table 2, the explicit seismic motion synthesis functions of the characteristic point H_1 could be obtained as follows:

$$\begin{aligned}
 F_x(t) = & -f(t - t_3)T_3 \sin \beta_{2pp} \\
 & -f(t - t_4)T_4 \cos (\alpha_1 + \beta_{1ps}) \\
 & -f(t - t_5)T_5 \cos \beta_{2ps} - f(t - t_6)T_6 \sin \alpha_{2p}
 \end{aligned} \tag{6}$$

$$\begin{aligned}
 F_y(t) = & f(t - t_1)T_1 - f(t - t_2)T_2 \\
 & -f(t - t_3)T_3 \cos \beta_{2pp} + f(t - t_4)T_4 \sin (\alpha_1 + \beta_{1ps}) \\
 & +f(t - t_5)T_5 \sin \beta_{2ps} + f(t - t_6)T_6 \cos \alpha_{2p}
 \end{aligned} \tag{7}$$

An example for the current slope model, $n = 4$, is considered here. With the stress analysis on the slope point, two orthogonal lines can be drawn: one through the dangerous point of the crest in a vertical direction and one through the toe of the slope along a horizontal direction, respectively. The effective computing region will be the region (abcd) (see Fig. 5) enclosed by these two straight lines and the free surfaces.

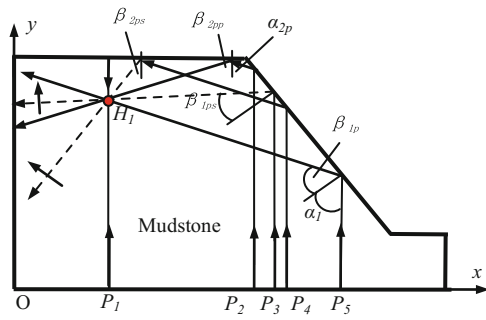


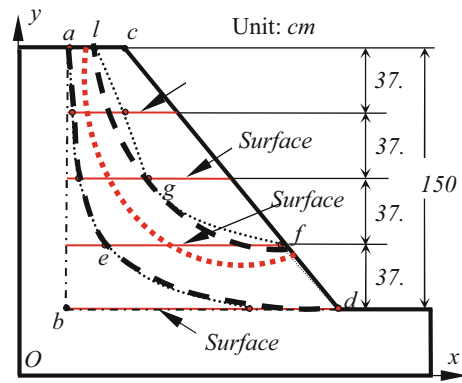
Fig. 4 Assessment of seismic waves for a homogeneous mudstone slope

Table 2 Path, arrival time and transfer coefficients for all the waves through point H_1

| No. | Incident wave | Path | Delay time | Transfer coefficient |
|-----|---------------|------|------------|------------------------|
| 1 | P_1 | P | t_1 | $T_1 = 1$ |
| 2 | P_1 | PP | t_2 | $T_2 = -1$ |
| 3 | P_2 | PPP | t_3 | $T_3 = R_{1PP}R_{2PP}$ |
| 4 | P_3 | PS | t_4 | $T_4 = R_{1PS}$ |
| 5 | P_4 | PPS | t_5 | $T_5 = R_{1PP}R_{2PS}$ |
| 6 | P_5 | PP | t_6 | $T_6 = R_{1PP}$ |

There are four parallel horizontal surfaces for theoretical analysis in the effective computing region. The dangerous points on four analytical surfaces can be obtained by computing the dynamic response. The coefficients of amplification for the PGA of surface 1 are given in Fig.6, which also shows the maximum coefficient of amplification for a PGA at different excitation frequencies. Figure 6 shows that the dangerous point is shifting closer to the free slope surface for larger frequencies. The acceleration amplification factor changes rapidly near the point ($x = 0.63$ m), which points to the possible sliding location of the slope. Hence, the initiation of cracks may occur in the region $x(0.38m, 0.63m)$.

Similarly, the probable dangerous points in other horizontal analytical surfaces can be obtained, as shown in Table 3. All the potential sliding surfaces for different frequencies of excitation are situated within the dangerous region bounded by the polygon ($aedfgl$), as shown in Fig. 5. During the process of shaking table test, the tiny cracks is observed in the middle crest of the slope firstly, Fig. 7 shows cracks at the toe and crest of the homogeneous mudstone slope model induced by an increasing acceleration amplitude and frequency. The results also can be investigated by analyzing the time-history variation of the displacement vector of slope.



- - - - Effective computing region ($aedc$)
- Potential dangerous region obtained from theoretical simulation
- - - Potential sliding surface obtained from theoretical simulation
- Potential sliding surface obtained from experiment

Fig. 5 The potential sliding zone and surfaces obtained from theoretical simulations ($n = 4$) and observed sliding surface after the experiment

Time-History Analysis of Displacement Vector

The time-history variation of displacement vectors can be employed to discuss the potentially unstable region and potential sliding surface of the rock slope under seismic excitation when the effective computing region is determined. The Snell-law could be employed to compute the incident and the reflected angles of seismic waves, the displacement vector function of rock slope.

Considering a sinusoidal acceleration with a frequency of 15 Hz and a peak acceleration of 0.3 g were applied to the foundation. According to the previous analysis, the time-history displacement vector function for uniform rock slope could be evaluated directly. Figure 8 shows the variation of displacement vector of the meshed points at $t = 3$ s, 5 s. The dangerous region (composed of the points with relatively large displacement according to the time-history analysis) is marked with dotted lines. From the time-history analysis, the displacement vectors (horizontal component) of the points in middle crest and the toe of the slope is relatively larger than that of other points (see Fig. 8). Comparing Fig. 5 with Fig. 8, it should be noted that the initializing fracture and the potential sliding surface are located in the effective

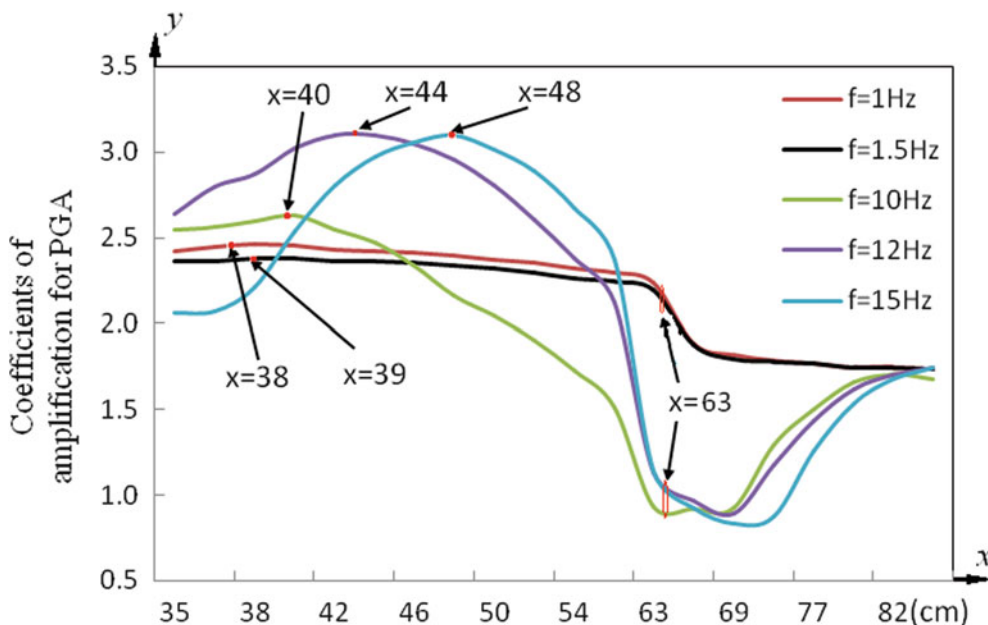


Fig. 6 The vertical coefficients of amplification for PGA at surface 1 for different frequencies

Table 3 The Probable dangerous region of all analytical surfaces for f(1.0Hz, 15Hz)

| | Dangerous region (m) |
|-------------|------------------------------|
| Slope crest | $x(0.36, 0.45), (y = 1.70)$ |
| Surface 1 | $x(0.38, 0.63), (y = 1.325)$ |
| Surface 2 | $x(0.40, 0.70), (y = 0.95)$ |
| Surface 3 | $x(0.52, 1.27), (y = 0.575)$ |
| Surface 4 | $x(1.05, 1.50), (y = 0.20)$ |

computing region proposed in section “Establishment of the effective computing region” previously.

The results obtained by time-history analysis are in accordance with the experimental results and the theoretical simulation results. It is also investigated that the method for determining the effective computing region (boundary) with stress analysis is valid for slope stability analysis based on the seismic wave theory.

Conclusions

Based on the above findings, some conclusions can be made:

1. The effective computing region is determined to help to analyze the dynamic response of a homogenous slope on the impact of seismic waves. It is based on the theory of elastic mechanics and the principle of seismic wave propagation and can save on computation costs.
2. Both the tension damage criterion and the principle of the coefficient of amplification for a PGA are employed to judge the initial failure of the slope crest under seismic loading. The theoretical simulation results are consistent with the experimental results.



Fig. 7 Cracks in the mudstone slope model (a) toe of slope (b) crest of slope

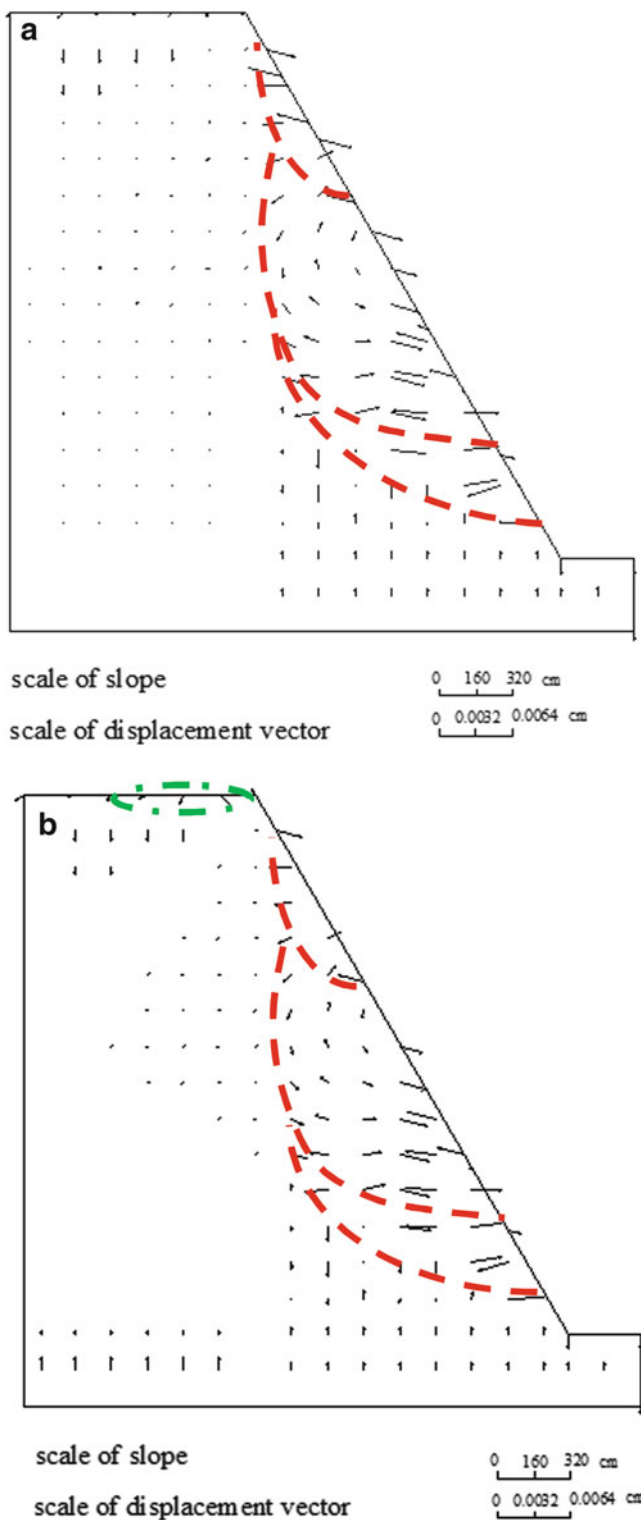


Fig. 8 Distribution of displacement vector in slope at (a) $t = 3$ s, and (b) 5 s

- The critical slip zone could be determined efficiently, making use of the seismic wave theory. The position of the potential sliding surface is closely related to the frequency of the seismic waves. With increasing frequency, the location of the sliding surface will shift closer to the free slope surface and the damaged volume of rock decreases. A decreasing frequency will induce deeper slip surfaces with more damage.
- The preliminary theoretical investigation for the initiation of landslide proposed in this paper is meaningful for landslide prevention and control. The remedial work for a potential landslide must be focused on the initiation stage.

Acknowledgments This research is financially supported by Project of the National Natural Science Foundation of China (No. 41002126); Project of State Key Laboratory of Geohazard Prevention and Geoenvironment Protection (No. SKLGP2009Z010).

References

- Duncan JM, Wright SG (2005) Soil strength and slope stability. Wiley, NJ
- Gulyayev VI, Ivanchenko GM (2006) Discontinuous wave interaction with interfaces between anisotropic elastic media. *Int J Solid Struct* 43:74–90
- Hong YS, Chen RH, Wu CS, Chen JR (2005) Shaking table tests and stability analysis of steep nailed slopes. *Can Geotech J* 42:1264–1279
- Ingles J, Darrozes J, Soula JC (2006) Effects of the vertical component of ground shaking on earthquake-induced landslide displacements using generalized Newmark analysis. *Eng Geol* 86:134–147
- Li JC, Ma GW (2009) Experimental study of stress wave propagation across a filled rock joint. *Int J Rock Mech Min Sci* 46(3):471–478
- Li JC, Ma GW (2010) Analysis of blast wave interaction with a rock joint. *Rock Mech Rock Eng* 43:777–787
- Li JC, Ma GW, Zhao J (2011a) Stress wave interaction with a nonlinear and slippery rock joint. *Int J Rock Mech Min Sci* 44:85–92
- Li YX, Zhu ZM, Li BX, Deng JH, Xie HP (2011b) Study on the transmission and reflection of stress waves across joints. *Int J Rock Mech Min Sci* 1:1–8
- Lin ML, Wang KL (2006) Seismic slope behavior in a large-scale shaking table model test. *Eng Geol* 86:118–133
- Malkawi H, Hassen WF, Sarna SK (2001) A global search method for locating general slip surface using Monte Carlo techniques. *J Geotech Geoenviron Eng* 127(8):688–698
- Newmark NM (1965) Effects of earthquakes on dams and embankments. *Geotechnique* 15(2):139–160
- Tang HX, Shao LT (2004) Finite element analysis on slope stability of earth-rock dam under earthquake. *Chin J Rock Mech Eng* 23(8):1318–1324
- Wang LL (2005) Foundation of stress waves. National Defense Industry Press
- Wu W, Yao LK, Chen Q (2008) Study on influence of shape and reinforced measures on seismic response in large-scale shaking

- table model tests. *J of ChongQing JiaoTong University (Nat Sci)* 27:689–694
- Xu GX, Yao LK, Gao ZN, Li ZH (2008) Large-scale shaking table model test study on dynamic characteristics and dynamic responses of slope. *Chin J Rock Mech Eng* 27(3):624–632
- Yan et al (1996) Seismic response of rigid block on inclined plane to vertical and horizontal ground motions acting simultaneously. In: *Proceedings of the 11th ASCE Engineering Mechanics Conference* 2:1110–1113
- Yang J, Sudak L, Xie H (2007) Study on stress wave propagation in fractured rocks with fractal joint surfaces. *Int J Solid Struct* 44:4256–4271
- Zhao J, Cai JG, Zhao XB, Li HB (2008) Dynamic model of fracture normal behaviors and application to prediction of stress wave attenuation across fractures. *Rock Mech Rock Eng* 41(5):671–693
- Zolfaghari AR, Heath AC, McCombie PF (2005) Simple genetic algorithm search for critical non-circular failure surface in slope stability analysis. *Comput Geotech* 32(3):139–152



Factors Controlling Kinematic Behaviour of a Huge Slow-Moving Landslide in China

Shu Jiang, Baoping Wen, Cheng Zhao, and Ruidong Li

Abstract

Xieliupo landslide, located in the Zhouqu County of northwest China and with volume of $72 \times 10^6 \text{ m}^3$, is a slow-moving landslide for more than 100 years. Several violent slide events have been recorded during its active history. However there has been an argument among professionals about mechanism of the landslide, particularly factors controlling its kinematic behaviour. A detailed investigation found that kinematic behaviour of the landslide may be affected by either an active fault with strike displacement rate of 1.4 mm/a, or river incision at its toe or a combination of those above, apart from its gravity and soft nature of its materials. To understand roles of these factors in slow-moving behaviour of the landslide, a numerical modelling was carried out. Results of the modelling show that gravity of the landslide and visco-plastic nature of its materials may play predominant roles in activity of the landslide followed by the active fault and river incision. The active fault accelerates the landslide velocity by 20–30 %, whereas the lateral incision by the river water may just locally intensify activity of the landslide, mainly in the zone behind the river bank 50–70 m.

Keywords

Slow-moving landslide • Controlling factors • Active fault • River incision • Visco-plastic material

Introduction

Xieliupo landslide has been recorded since 1904 and has been known as one of the largest landslides in China (Scheidegger and Ai 1986; Zhou 2012; Bai et al. 2013). Its latest violent slide event occurred on April 9th, 1981, which blocked the Bailongjiang river channel and flooded roads

and farmlands, causing economic losses over 350 million RMB (Wu 2006). Since then, the landslide has undergone movement at a slow rate, evidenced by cracking of its ground surface and very often deformation of the highway in the front of the landslide, which is the only road to outside of the Zhouqu county, costing a considerable amount of money for its repairing every year.

For a long time there has been an argument among professionals about mechanism of the landslide, particularly factors controlling its kinematic behaviour and their relative importance. Bian (2007) believed that the kinematic of the landslide was largely effected by rainfall. Yu (2007) attributed river incision and rainfall infiltration to be the main controlling factors followed by earthquake, whereas Wang (1985) suggested that river incision couldn't lead to the slow movement of the landslide as a whole. Wu (2006) stressed that behaviour of the landslide is controlled by

S. Jiang (✉) • B. Wen
China University of Geosciences (Beijing), School of Water Resources and Environment, Room 115, Building 1, No.29 Xueyuan Road, Beijing 100083, China
e-mail: jiangshucugb@gmail.com; wenbp@cugb.edu.cn

C. Zhao • R. Li
Gansu Institute of Geo-Environment Monitoring, Lanzhou 730050, China
e-mail: Zhaoc163@163.com; 9608468@gmail.com

active fault, soft strata, slope terrain, underground water and river incision together. The objective of this study is to clarify the importance of the factors controlling the landslide behaviour by numerical simulation under a series of hypothesized scenarios based on its geological settings.

Study Site

The Xieliupo landslide is situated on the left bank of the Bailongjiang River, whose narrow width and steep cliffs indicate strong incision and intensive neotectonic movements have occurred since the Quaternary (Fig. 1). An active fault, namely Pingding-Huama fault passes through the Zhouqu county, which belongs to the Guanggaishan-Dieshan fault zone, a famous regional active fault zone (Yu et al. 2012). Notably the Pingding-Huama fault zone just passes through the place where the Xieliupo

landslide develops, forming a typically trough shape terrain (Fig. 1). The Pingding-Huama fault dips towards 40° with a dip angle 50° to 80° . Recent GPS monitoring data revealed that the fault is being active with a mean slip rates of 1.4 mm/a (Chen and Ren 2012). The fault is more than 90 km long with a width of several hundred meters (Yu et al. 2012). The strata at and in the vicinity of landslide site are mainly Middle Devonian carbonaceous slate, Middle and Late Carboniferous limestone and Quaternary deposits (Fig. 2). At the landslide site, the Pingding-Huama fault zone is about 550 m wide. Its hanging wall and foot wall are composed of Devonian carbonaceous slate and Carboniferous limestone, respectively.

Xieliupo landslide is about $2,600 \text{ m}$ long and 550 m wide with an average slope angle about 19° and a maximum slope angle 38° at the upper portion. Elevation difference reaches to 800 m . Drilling and field survey revealed that thickness of the sliding mass ranges from 15 m to 85 m with 50 m on average. Its volume was estimated to be $72 \times 10^6 \text{ m}^3$. Flank boundaries of the landslide are the fault plane of the Pingding-Huama fault zone (Fig. 1). Detailed investigation found that there are a number of tension cracks, secondary slip scars on the landslide, indicating that the landslide is under deformation.

Three boreholes (Fig. 1) drilled in the summer of 2012 disclosed that bedrocks of the landslide are mainly made up of highly fractured carbonaceous slate of the Middle Devonian. Its sliding mass consists of highly weathered carbonaceous slate and the late Pleistocene loess (Q3), former of which is in presence of rock fragments with loose black clayey soil. Its slip zone developed along the contact between the weathered carbonaceous slate and fractured bedrock, appeared to be a black seam of very soft and clayey soil derived from the carbonaceous slate. No groundwater was found within the slope.



Fig. 1 Overview of the Xieliupo landslide and locations of boreholes (ZK1-ZK3) on the landslide

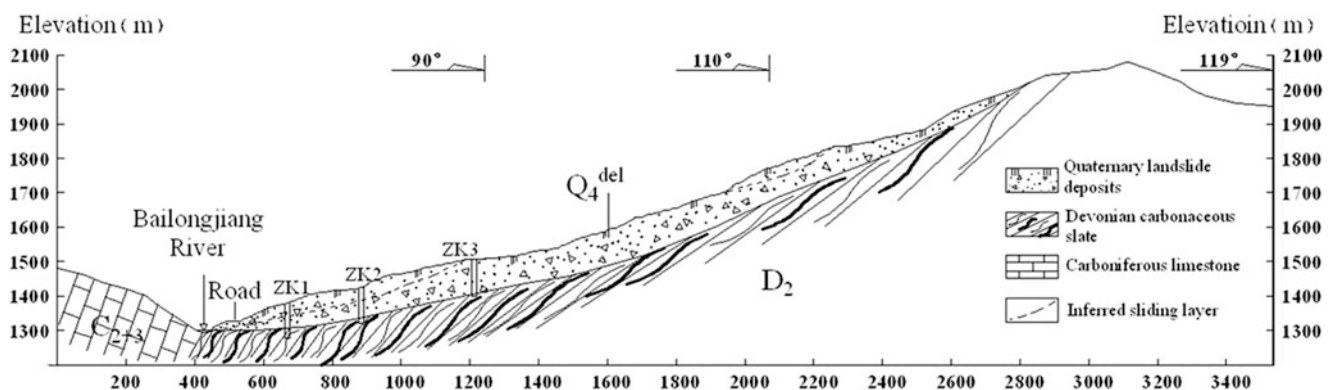
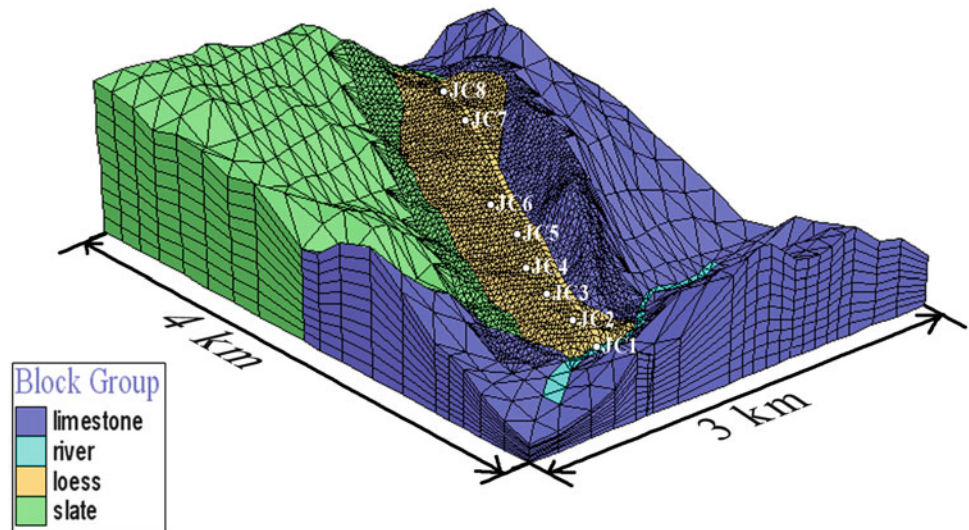


Fig. 2 Geological cross section diagram of the Xieliupo landslide

Fig. 3 3D model of the Xieliupo landslide and locations of virtual monitoring points. (Note that JC1 to JC8 denoted the monitoring points.)



Before the operation of diversion construction for a hydro power station just upstream of the landslide in 2004, the Bailongjiang River flowed quite rapidly, which made a strong lateral incision at the toe of the landslide. Nowadays such incision seems to be much weaker than before.

Numerical Simulation

Setup of a 3D Numerical Model

The finite difference code FLAC3D is widely recognized as one of the advanced codes suitable for simulating large deformation in engineering geology and geotechnical fields (Marcato et al. 2012; Bozzano et al. 2012). It was used for numerical simulation in the study. A 1:1,000 topographic map and a 1:50,000 topographic map were used together to build a DEM of the study area via ArcGIS. These two maps were used for the landslide site and its vicinity, respectively. To construct a 3D numerical model of the landslide, a FISH routine by the first author was called by FLAC3D to generate mesh grids from the DEM. To mitigate boundary effects, the model dimension was designed as 4 km long and 3 km wide, covering the whole landslide and its adjacent area. To improve the calculation accuracy, the mesh grid dimension within and outside the sliding area was set to be 40 m and 100–300 m respectively. The 3D model of the landslide was made up of seven layers, 67,985 grids and 39,311 nodes (Fig. 3). The seven layers were the six geological units of the landslide and its vicinity and plus a river group. The fault was treated as interface elements in the 3D model at the flank boundaries of the landslide. To trace the displacement of the landslide, eight nodes on its surface were marked as virtual monitoring points (Fig. 3).

Scenarios Hypothesized

Settings of the landslide indicate that its kinematics may be controlled by gravity, active fault or river incision. To clarify the relative importance of these factors for the landslide, three scenarios were hypothesized: the landslide driven by gravity only (I) and plus the influence of the fault (II) or the river incision (III), respectively. To examine the effects of the river incision, sub scenarios with different flow rates were further hypothesized. According to the records from the hydrologic station of the Bailongjiang River near the landslide, flow velocities of 1.47 m/s, 5 m/s, 0.5 m/s, were hypothesized in this study, which corresponded to the river water flow rate during dry and rainy seasons before the diversion construction and after its construction.

Since the landslide has been active at a slow rate, creep nature of its materials may be an essential orientating factor of the landslide. The Burger-creep viscoplastic model (Model Cvisc) was employed for describing the nature of landslide materials, which is a built-in constituent model in FLAC3D for the viscoplastic materials complying with Mohr-Coulomb failure criteria. The model is thus a combination of the Burger's model and the Mohr-Coulomb model. Influence of the active fault was considered by imposing an initial displacement rate of 1.4 mm/a on its hanging wall. River incision was conducted by bend shear force of the river water acting along the river bank. In this study, such shear force was calculated using (1) and (2) suggested by Jansen et al. (1979) and Manning and Griffith (1891), respectively.

$$\tau_{0s} = \rho g \frac{V^2}{C^2} \quad (1)$$

Table 1 Geomechanical parameters of the landslide material

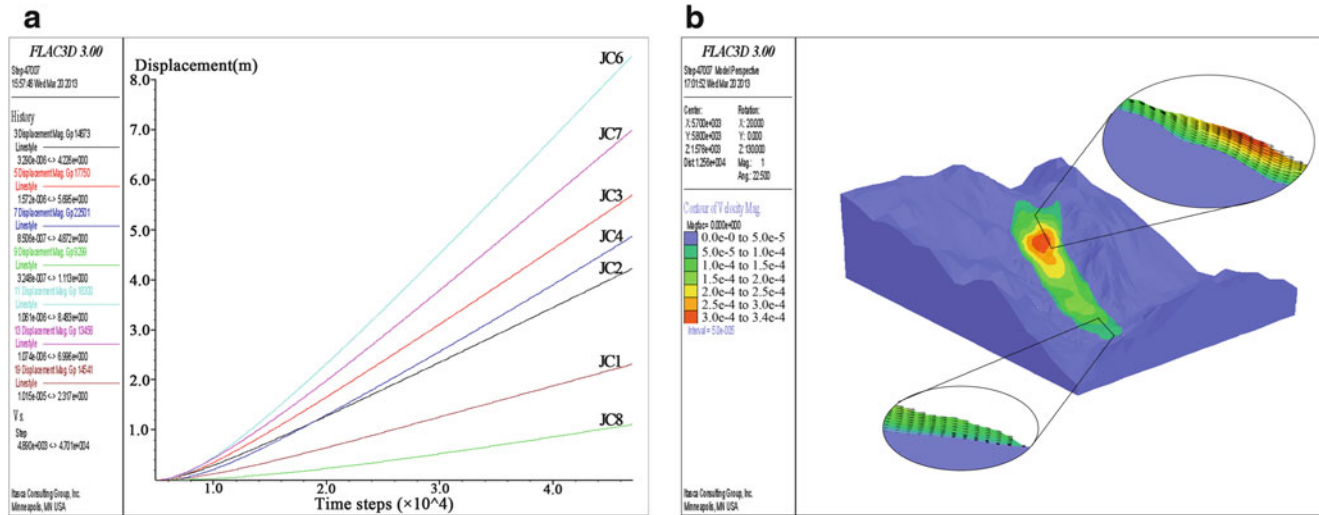
| Material group | ρ (kg/m ³) | c (MPa) | φ (°) | K (MPa) | G (MPa) | G_K (MPa) | η_K (MPa·d) | G_M (MPa) | η_M (MPa·d) |
|-------------------------|-----------------------------|---------|---------------|---------|---------|-------------|------------------|-------------|------------------|
| Loess | 1,720 | 0.01 | 31 | 944 | 461 | 767 | 4,000 | 2,970 | 15,833 |
| Highly weathered slates | 1,800 | 0.02 | 20.5 | 833 | 384 | 384 | 2,500 | 3,370 | 15,627 |
| Slip zone | 1,700 | 0.008 | 10 | 333 | 250 | 71.25 | 103 | 917 | 1,362 |
| River | 1,000 | 0 | 0 | 2,000 | 0 | – | – | – | – |
| Fractured Slate | 2,120 | 0.025 | 25 | 8,800 | 4,297 | – | – | – | – |
| Limestone | 2,090 | 6.72 | 42 | 22,600 | 11,037 | – | – | – | – |

Note: ρ = Density; c = Cohesion; φ =Friction angle; K = Bulk modulus; G = Shear modulus; G_K = Kelvin shear modulus; η_K = Kelvin viscosity coefficient; G_M = Maxwell shear modulus; η_M = Maxwell viscosity coefficient

Table 2 Parameters used for the fault interface

| | c (MPa) | ϕ (°) | φ (°) | K_n (MPa/m) | K_s (MPa/m) | t (MPa) |
|-----------|---------|------------|---------------|---------------|---------------|---------|
| Interface | 0 | 0 | 15 | 8,409 | 8,409 | 0 |

Note: c = Cohesion; ϕ =Dilation angle; φ = Friction angle; K_n = Normal stiffness; K_s = Shear stiffness; t = Tensile strength

**Fig. 4** Displacement curves of the monitoring points with time steps (a) and velocity contour diagram of the landslide (b) under scenario I

$$C = \frac{1}{n} R^{1/6} \quad (2)$$

where τ_{0s} is the bend shear stress, ρ is the density of water, V is flow velocity of the river water, C is Chézy coefficient, n is roughness coefficient and R is the hydraulic radians of the river channel.

Parameters

Parameters of the landslide materials used in the study are shown in Table 1 and Table 2. Geomechanical parameters of the landslide materials were determined by a series of laboratory tests. Rheological parameters of the materials

were estimated based on both an ongoing creep test of the slip zone and empirical values of those materials with similar characteristics to the landslide. Parameters for the interface were mainly from empirical values.

Results and Discussion

When the landslide would be driven by gravity only without influence of active fault and the river incision (Scenario I), the simulation revealed that different portion of the landslide would move slowly with different but constant velocities ranging from 0.03 mm/d to 0.35 mm/d (Fig. 4a). It seemed that the most intense movement would occur in its upper portion, where the steepest terrain just occurs. The velocity

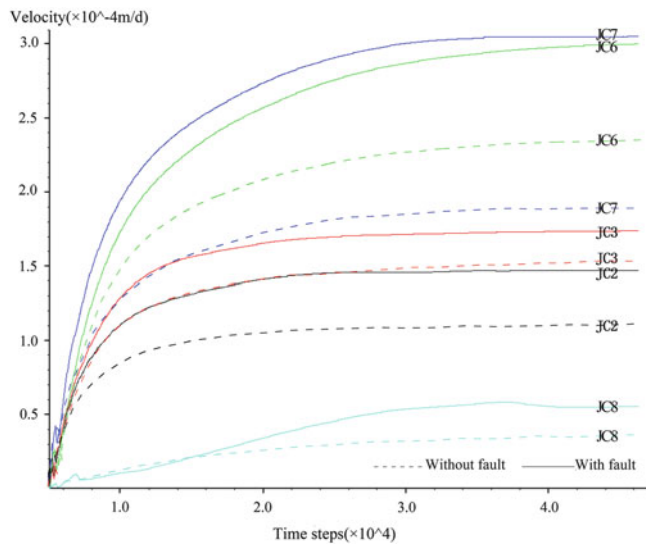


Fig. 5 Velocity curves of the monitoring points with time steps for scenario I and II

distribution (Fig. 4b) indicated that landslide at the most intense portion seemed to behave retrogressively upward slope to its further upper portion and progressively downward slope to lower portion.

When the landslide would be driven by gravity plus the influence of active fault (Scenario II), the result showed that the behaviour pattern of landslide would be generally similar to that under scenario I (Fig. 4b) in terms of kinematics. However, the movement velocity would increase (Fig. 5). Take monitoring point JC2 for example, the steady creep velocity would increase 27 % from 0.11 m/d when gravity was the only driven force to 0.14 mm/d when fault activity was taken into account. Relatively the greatest increase in the movement velocity again occurred in the upper portion of the landslide around JC6 and JC7. Such increase were much less for JC3 and JC8, indicating that the active fault seems to have a weaker influence on the uppermost and lowermost portions of the landslide. When the fault is active, difference in the increase in moving rate of different portions of the landslide seems to be largely associated with the local terrain conditions. Moreover, increased velocity at each portion of the landslide was greater than the applied fault moving rate. This suggests that the active fault greatly stimulated the landslide, rather than drive it uniformly. Generally, the active fault would accelerate the landslide velocity by 20–30 % on average.

When the landslide is assumed to be driven by gravity plus influence of river incision (Scenario III), numerical simulation disclosed that river water incision would increase

velocities of the landslide's frontal portion by comparing Fig. 6a, b. The most intensely affected landslide portion by river water incision concentrated in the southern part of the river bank (Fig. 6a). When flow velocity of the river water increased from 0.0 m/s (Scenario I) to 0.5 m/s, after the same time steps run, the displacement at the toe of the landslide would increase from 1.13 m (Fig. 6b) to 1.26 m (Fig. 6c). When flow velocity was 1.47 m/s (Fig. 6d) and 5 m/s (Fig. 6e), the landslide displacement at the toe reached 2.92 m and 20 m respectively, and displacement contours there turned to be vertical. This implies that the frontal zone might probably collapse in the flood season (Fig 6e). With increase in flow velocity of the river water, kinematic pattern of landslide in its front portion became retrogressive, which was progressive when river incision was not considered, while deformation characteristics behind this portion almost remained the same with scenario I (Fig. 6b). The retrogressive nature is particularly striking in a zone behind the river bank 50–70 m (Fig. 6d, e). The limited retrogressive zone proved that the river incision may just locally intensify the activity of the landslide.

Figure 6 Three dimensional velocity contour diagram with flow velocity 5 m/s (A) and sectional displacement contour diagrams of the frontal portion when the river water incision occurs with different flow velocities (B) $V_{\text{river}} = 0$ (scenario I); (C) $V_{\text{river}} = 0.5\text{m/s}$; (D) $V_{\text{river}} = 1.47\text{m/s}$; (E) $V_{\text{river}} = 5\text{m/s}$ (scenario III).

Conclusions

Factors controlling kinematics of the Xielipu landslide, a giant and slow-moving landslide, were clarified by modelling its behaviour under different scenarios and by comparing their differences. The followings could be drawn from this study:

1. Gravity of the landslide and viscoplastic nature of its material may play primary roles in its kinematic behaviour.
2. The active fault accelerates the landslide moving velocity by 20–30 % and doesn't change the movement pattern of the landslide, suggesting that its role would be weaker than gravity of the landslide and nature of its materials. However the fault should be of much greater significance in the formation of the landslide by producing the trough shape terrain and loose and weak materials.
3. River incision may just locally intensify the activity of the landslide, mainly in the zone behind the river bank 50–70 m.

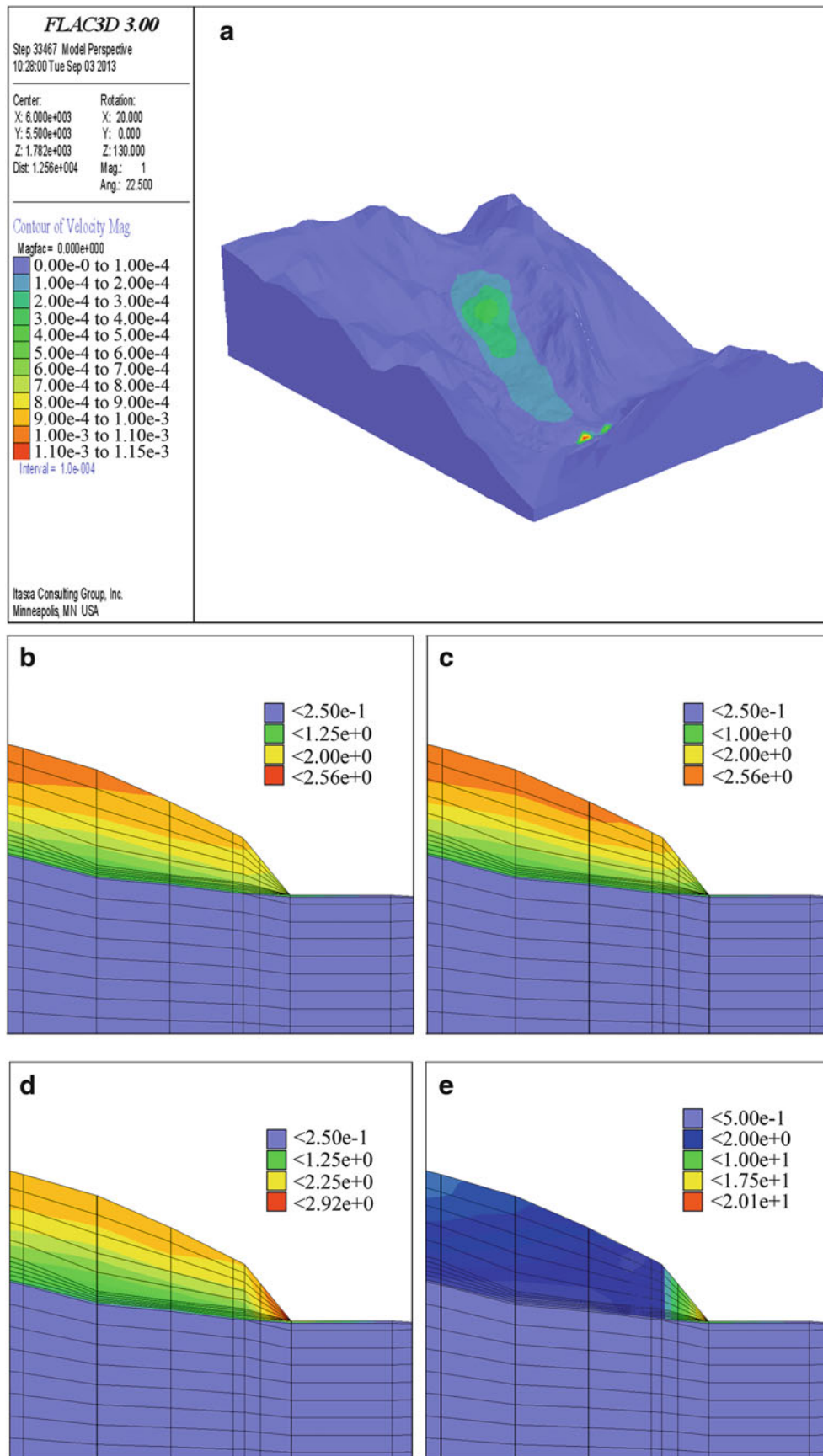


Fig. 6 Three dimensional velocity contour diagram with flow velocity 5 m/s (a) and sectional displacement contour diagrams of the frontal portion when the river water incision occurs with different flow velocities (b) $V_{\text{river}} = 0$ (scenario I); (c) $V_{\text{river}} = 0.5$ m/s; (d) $V_{\text{river}} = 1.47$ m/s; (e) $V_{\text{river}} = 5$ m/s (scenario III)

Acknowledgments This research was funded by National Natural Science Foundation of China (No. 41372305).

References

- Bai S, Wang J, Thiebes B (2013) Analysis of the relationship of landslide occurrence with rainfall: a case study of Wudu County, China. *Arab J Geosci* 1–9
- Bian Y (2007) The influence on Xieliupo landslide by constructing the Hujiaya hydropower station. *Agric Technol Inform* 16:32–33 (in Chinese)
- Bozzano F, Martino S, Montagna A (2012) Back analysis of a rock landslide to infer rheological parameters. *Eng Geol* 131:45–56
- Chen C, Ren J (2012) Analysis of modern activity of major faults in northeast margin of Baryan-Har block. *J Geodesy Geodyn* 32(3):27–30 (in Chinese)
- Jansen P, Van Bendegom L et al (1979) Principles of River engineering: the non-tidal alluvial river. Jansen P (Eds) Pitman (0273011391), 509p
- Manning R, Griffith JP (1891) On the flow of water in open channels and pipes. *Trans Instit Civ Eng Ireland Dublin* 20:160–207
- Marcato G, Mantovani M, Pasuto A (2012) Monitoring, numerical modelling and hazard mitigation of the Moscardo landslide (Eastern Italian Alps). *Eng Geol* 128:95–107
- Scheidegger AE, Ai NS (1986) Tectonic processes and geomorphological design. *Tectonophysics* 126(2):285–300
- Wang J (1985) Cause analysis of the Xieliupo landslide in Zhouqu. *Gansu Environ Res Monit* 1:22–25 (in Chinese)
- Weijiang Wu (2006) Gansu landslide. In: Wei Chunling (Eds) Lanzhou University Publishing House. (7-311-02775-6). 642p (in Chinese)
- Yu Z (2007) Research on the causes and losses of the Xieliupo landslide. *Gansu Sci Technol* 23(12):72–76 (in Chinese)
- Yu J, Zheng W et al (2012) Late quaternary active characteristics and slip-rate of pingding-huama fault, the eastern segment of Guanggaishan-Dieshan fault zone (west Qinling mountain). *Quaternary Sci* 32(5):957–967 (in Chinese)
- Zhou Y (2012) Study on landslides in loess slope due to infiltration. PhD thesis, University of Hong Kong, Hong Kong, China



Finite Element Simulation for an Earthquake-Induced Catastrophic Landslide Considering Strain-Softening Characteristics of Sensitive Clays

Akihiko Wakai, Fei Cai, Keizo Ugai, and Tsutomu Soda

Abstract

In the present study, a strain-softening constitutive model for sensitive clays originating from weathered pumice is applied to simulate an earthquake-induced catastrophic landslide that occurred during the 2011 Great Tohoku and Kanto Earthquake in Japan. The upper part of the slope sliding about 200 m and 13 people were killed. The failure could be related to shear strength degradation of the sensitive clay layers in the slope during the earthquake.

The strain-softening characteristics of the sensitive material in the slope have been investigated in a series of laboratory tests involving undisturbed samples. The observed stress-displacement relationships under cyclic loading are numerically modelled using a proposed elasto-plastic constitutive model, based on the dynamic finite element method. The observed phenomena are appropriately simulated by the proposed model.

Keywords

Earthquake • Strain-softening • Finite element method • Hanokidaira landslide

The Hanokidaira Landslide, Japan

The earthquake-triggered landslide at Hanokidaira in Shirakawa City (Fig. 1) initiated in the upper part of a dip slope and travelled 200 m downslope. The sliding direction changed from NE to E due to local topography. Part of the slide also moved to the NNW, as seen in Fig. 1a. After having moved down the hill surface, the debris covered the adjacent houses and road. This landslide is typical of the landslides that occurred in the hills of Shirakawa City at the time of the earthquake.

From field investigations of the landslide debris, it was determined that some parts of the deposit were strongly disturbed, while others moved as solid blocks with original stratification remaining intact (Fig. 2). This implies that the origin of the landslide might be related to the strain concentration in a certain thin layer in the slope, where the shear strength of the layer has been suddenly decreased due to cyclic loading during the earthquake.

The dip angle of the slope about 15° was measured on several tephra layers observed in the exposed strata of the headscarp, which is about 5 m tall. Figure 3 is a schematic figure for geological structures in the slope. The materials are mainly composed of cohesive volcanic soils with different stiffnesses and particle sizes. Several weaker clay beds are interlayered with scoria, pumice, and tephra, and are thought to have originated from weathered pumice. As can be clearly observed at an exposed section, the sliding surface is located within the clay layers underlying the scoria unit shown in Fig. 3.

The scoria unit above the clay layer has high permeability, and may have acted as an aquifer above the less permeable clay, and the sensitivity of the layer can be promoted by the

A. Wakai (✉) • F. Cai • K. Ugai
Department of Civil Engineering, Gunma University, 1-5-1, Tenjin,
Kiryu, Gunma 376-8515, Japan
e-mail: wakai@gunma-u.ac.jp; feicai@gunma-u.ac.jp; ugai@ce.gunma-u.ac.jp

T. Soda
Institute of Tephrochronology for Nature and History, 2-265-8,
Amagawabara, Maebashi, Gunma 371-0803, Japan
e-mail: inst-tephra@white.plala.or.jp

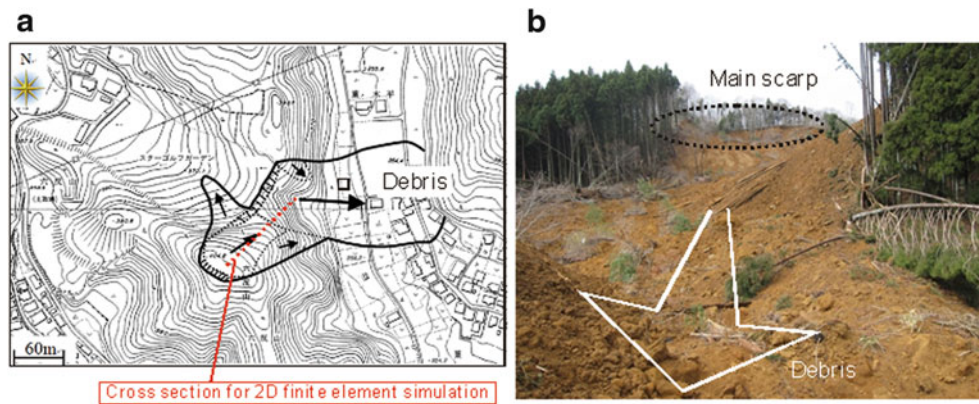


Fig. 1 (a) Case study location at Hanokidaira, Shirakawa City, Japan (map after South Fukushima Prefecture). (b) View looking uphill to the main scarp of the landslide



Fig. 2 Intact stratification in the deposit

water pressure. In addition, it seems very important that the influence of the water-bearing stratum can also be a dominant promotion factor for long-term weathering of the pumice sandwiched in the loam. It should be noted that this slope was located in a buried valley in the hill and it might have increased the amount of ground water in the slope.

Finite Element Simulation

Numerical Models

2D finite element simulations of the investigated landslide were performed to determine the validity of the above hypothesis. The assumed geometry used in the analysis is shown in Fig. 4. The discretized finite element meshes (8-nodes) are also shown in the same figure. The calculated acceleration and displacement histories at Point A in Fig. 4 are shown in detail later on. Two different models were applied to the sensitive clay and under- and overlying

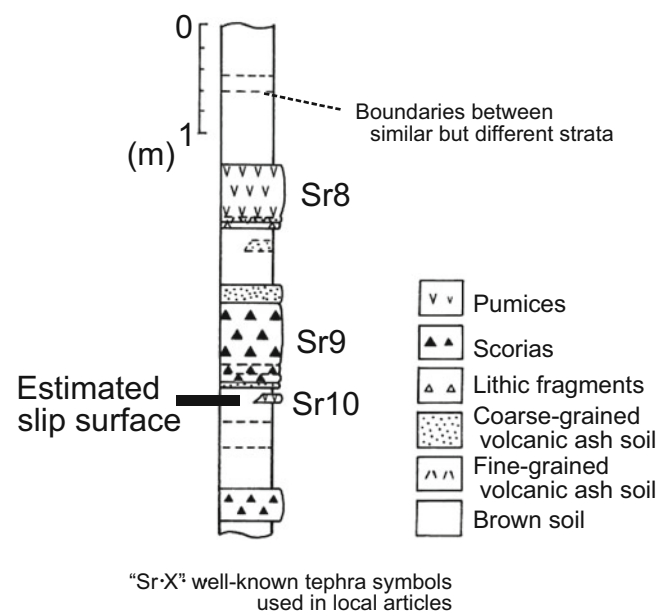


Fig. 3 Stratigraphic section of the units involved in the landslide of 2011 (by Soda)

loamy volcanic materials, namely the UW softening model (Wakai et al. 2010) and the UW model without cyclic softening (Wakai and Ugai 2004), respectively. The parameters for each material are summarized in Table 1.

A series of undrained cyclic direct shear tests using undisturbed specimens of the sensitive clay were performed to derive numerical model properties. Figure 5 shows an example of the observed test results under constant volume conditions, and their numerical simulation using the UW softening model with parameters as shown in Table 1. It can be seen that the apparent shear resistance suddenly decreased, like liquefaction of loose sands under cyclic loading. This may be due to the increase in mobility of each soil particle caused by loss of cohesion in the soil, rather than the increase in excess pore water pressure.

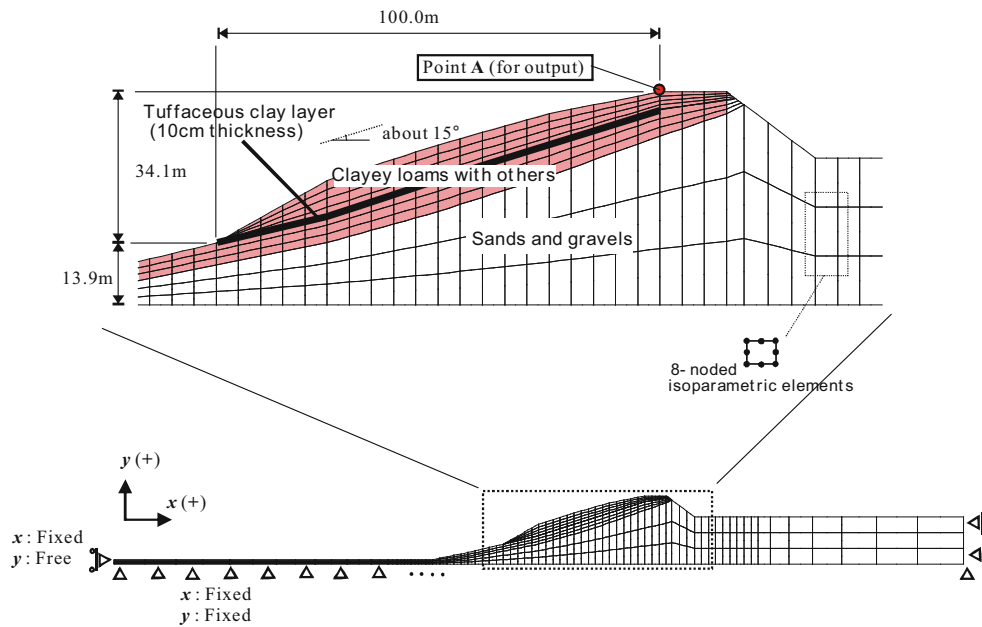


Fig. 4 Finite element meshes used for the numerical simulation

Table 1 Material parameters used in the finite element simulation for the Hanokidaira landslide

| Materials | Clayey loams with others | Tuffaceous clay | Sands and gravels |
|---|--|----------------------------|--------------------|
| Young's modulus $E(\text{kN/m}^2)$ | $13,500 \times \sqrt{p'_0}$ p'_0 : Initial confining pressure (kPa) | $4,530 \times \sqrt{p'_0}$ | 1.00×10^6 |
| Poisson's ratio ν | 0.400 | 0.400 | 0.300 |
| Cohesion $c(\text{kN/m}^2)$ | 49.3 | 56.2(*) | 100. |
| Internal friction angle $\varphi(\text{deg})$ | 45.0 | 41.9(*) | 45.0 |
| Dilatancy angle $\psi(\text{deg})$ | 0 | 0 | 0 |
| Hysteretic damping parameter $b \cdot \gamma_{G_0}$ | 2.50 | 1.30 | 1.10 |
| Hysteretic damping parameter n | 2.20 | 2.50 | 2.80 |
| Unit weight $\gamma(\text{kN/m}^3)$ | 16.0 | 10.8 | 18.0 |
| Residual strength ratio τ_{fi}/τ_{f0} | – | 0.200 | – |
| Softening parameter A | – | 2.00 | – |

(*) Those parameters in this numerical model with softening are a bit different from the physical constants to be observed. They have been slightly adjusted to make the consistency between the simulated and the observed peak strengths in numerical simulations

[Note] Rayleigh damping parameters : $\alpha = 0.0571$, $\beta = 0.000578$ for all materials

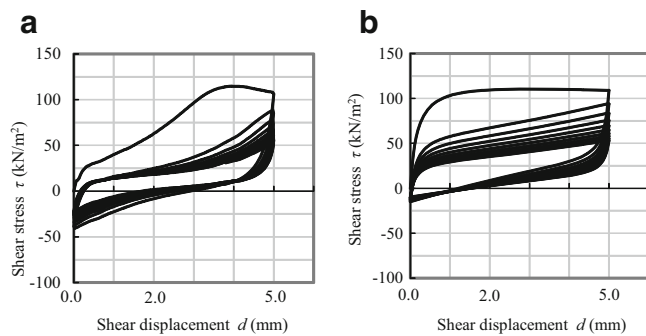


Fig. 5 Example of observed results of cyclic direct shear tests and their numerical simulation using the UW-softening model (under an initial effective confining pressure of 75 kPa) for the sensitive clay (a) Observed, (b) Simulated

Analytical Results

Appropriate earthquake motion data are fundamental for accurate seismic simulations. The amplitude of the input waves at the base has been adjusted so that the corresponding horizontal component of the observed records at K-net Shirakawa by NIED, that is 3 km away from the landslide location, should be realized at the ground level in the finite element meshes. The time history of the input horizontal acceleration for this finite element simulation is shown in Fig. 6.

Figure 7 shows the analytical result of the time histories of horizontal acceleration and displacement at the top of the sliding block, namely, Point A in Fig. 4. The boundless

increase of displacement as shown in the figure indicates that a catastrophic failure of the slope occurred in this case. The horizontal displacement is approximately 5 m at the end of the earthquake. It is very important that the displacement continued to increase even after the earthquake motion

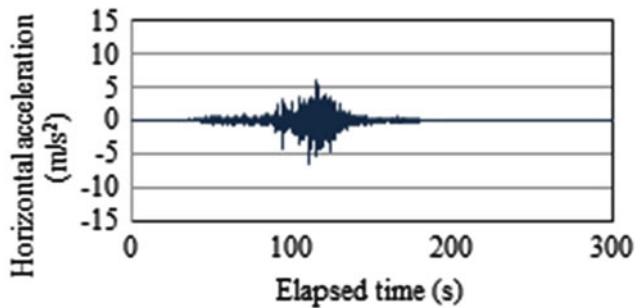


Fig. 6 Input motion used for the numerical simulation

ended. After the simulated earthquake, the acceleration response continues to be variable. It means that the total resistance along the slip surface has become lower than the total of the sliding force of the upper soil block due to its static self-weight, i.e., the slope is still unstable. This was the right reason itself of the long-distance travelling failure of the slope.

The residual deformations and the shear strain distribution at 300 s after the end of the seismic motion are shown in Figs. 8a, b, respectively. The long runout of the sliding block along the stiffer layer is clear. This result is in agreement with the actual phenomenon. However, it should be noted that the predicted velocity of the sliding mass may not be accurate because of the theoretical background of such a solid-based analytical method. In order to simulate precisely the sliding behaviour after having started such high-speed motion, it would be better to improve the numerical model for the friction and damping at the bedding plane, which will

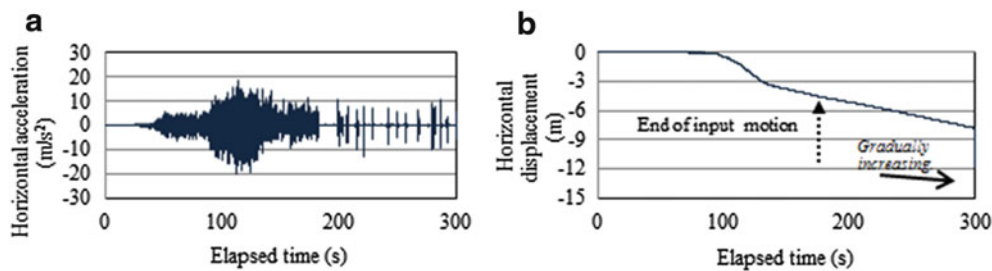


Fig. 7 Calculated time histories of response at the point A shown in Fig. 4. (a) Horizontal acceleration. (b) Horizontal displacement

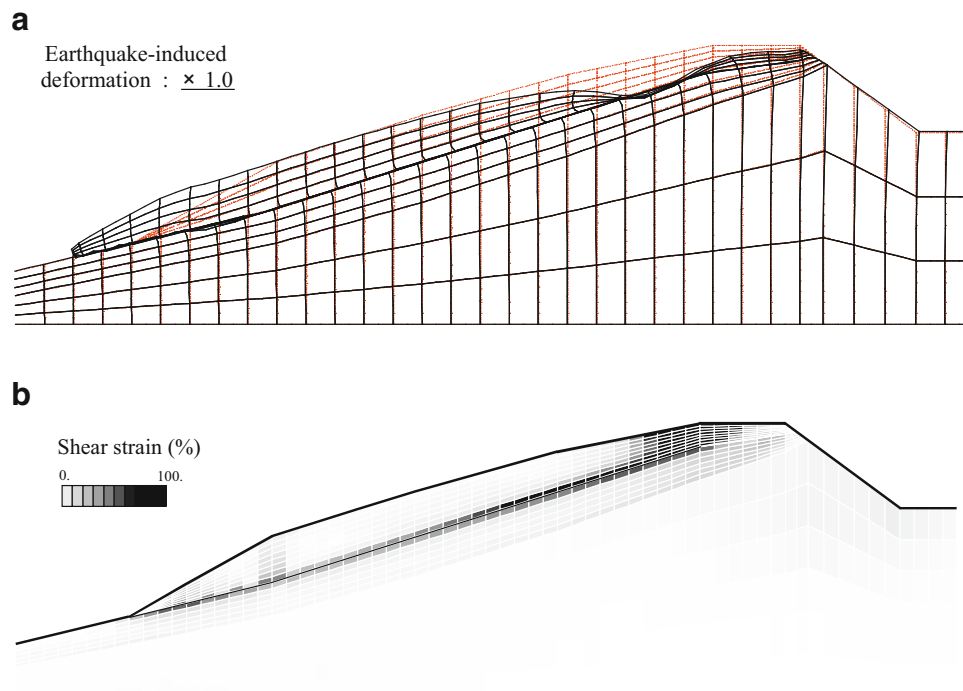


Fig. 8 Calculated residual deformation in the slope after the earthquake. (a) Residual deformation, (b) Residual shear strain distribution

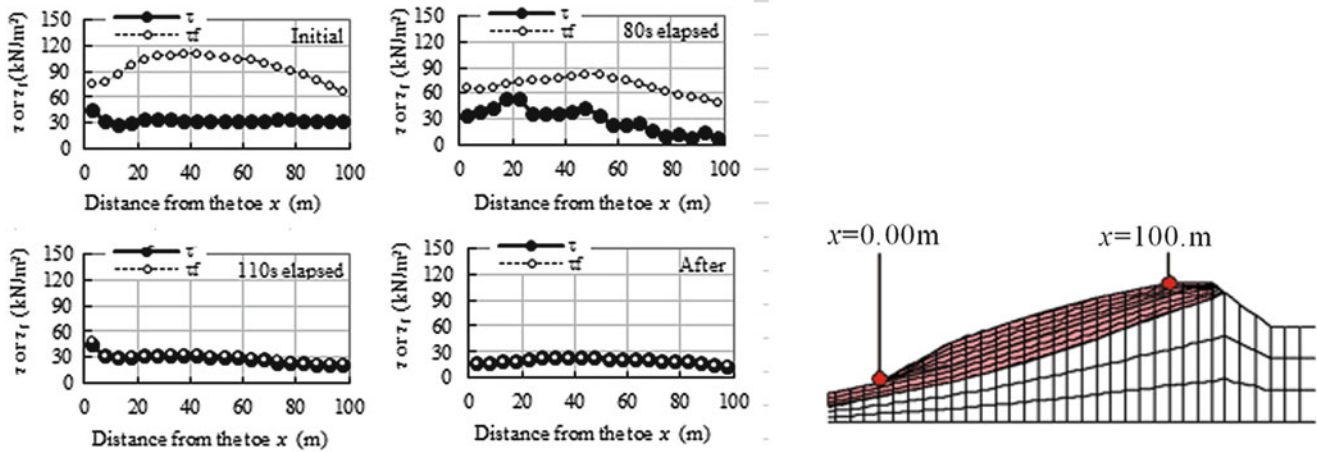


Fig. 9 Distributions of mobilized shear stress and shear strength on the slip surface

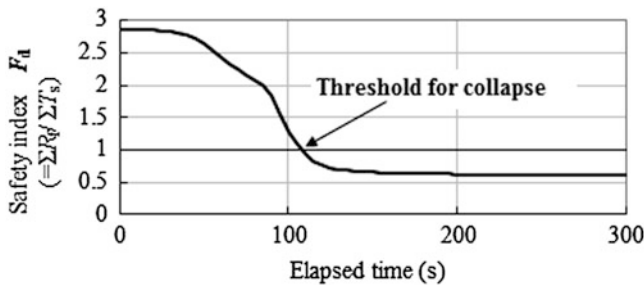


Fig. 10 Time history of the proposed index F_d

be the subject of future studies. Although an exact simulation of the high-speed movement cannot be obtained, this analysis provides information and guidelines for judging the behaviour of such a catastrophic failure.

A Stability Index Refined for Engineering Purposes

Figure 9 shows the distributions of the shear strength τ_f and the mobilized shear stress τ along the slip surface in each time step. These values have been calculated as the average of all Gaussian point values in each element. The horizontal distance x is the distance from the toe. As shown in the figures, before the earthquake, the upper sliding block was safely supported by the shear resistance along the tuffaceous clayey layer. The mobilized shear stress is always equal to or less than the shear strength. The shear strength gradually decreased during the earthquake due to strain softening of

the soils at the slip surface. In addition, the mobilized shear stress decreased along with the decrease in the shear strength. When the total of the shear strength along the slip surface $\sum R_f$ becomes less than the total of the sliding force $\sum T_s$ due to only the static self-weight of the upper sliding mass without the seismic inertia force, a general failure occurs.

Accordingly, a general failure can be evaluated as the balance between $\sum R_f$ and $\sum T_s$, and the following index F_d is introduced to predict catastrophic failures :

$$F_d = \frac{\sum R_f}{\sum T_s} \tag{1}$$

It should be noted that the above definition is a little different from the one of the standard factor of safety which denominator includes the seismic inertia force.

Figure 10 shows the time histories of this index. The moment that this index becomes 1.0 is in agreement with the moment at which catastrophic failure occurs. It is confirmed that the proposed index is useful for prediction of general failures.

Conclusions

In the present study, one of the catastrophic landslides induced by the 2011 Great Tohoku and Kanto Earthquake in Japan was simulated using a dynamic finite element method where stress–strain relationships under cyclic loading for sensitive clay are modelled with an elasto-plastic, strain-softening constitutive model. It was shown

that the shear-strength degradation of the tuffaceous clay in the slope caused a failure and the detailed investigation for such problematic soils in natural slopes would be so important.

Acknowledgments The authors would like to thank Prof. Takehiko Suzuki, Tokyo Metropolitan University, for his great help in the identification of volcanic tephra in the study area.

References

- Wakai A, Ugai K (2004) A simple constitutive model for the seismic analysis of slopes and its applications. *Soils Found* 44(4):83–97
- Wakai A, Ugai K, Onoue A, Kuroda S, Higuchi K (2010) Numerical modeling of an earthquake-induced landslide considering the strain-softening characteristics at the bedding plane. *Soil Found* 50(4):515–527



Numerical Modelling of Deformation for Partially Saturated Slopes Subjected to Rainfall

Binod Tiwari, Katsuyuki Kawai, and Phommachanh Viradeth

Abstract

Rainfall is one among the most common contributing factor and trigger for landslides. In the majority of the cases, slopes are at partially saturated condition when they are subjected to rainfall. While analysing stability of those slopes, deformation analysis is performed in a conservative way assuming the slope to be in a fully saturated condition. In this research, a fully coupled hydro-mechanical finite element model is described based on the constitutive model developed for partially saturated soil condition. A 1.2 m long and 0.6 m high sandy slope was modelled in laboratory and was subjected to 30 mm/h of rainfall for 3 h. Values of suction measured after 3 h were very close to the numerically calculated values based on the finite element method developed by the authors. This model was used to calculate deformation of slope for different intensities of rainfall and at different angles of slopes in order to predict the amount of deformation or failure condition when a slope is subjected to a continuous rainfall of different intensities and durations.

Keywords

Rainfall • Partially saturated soil • Suction • Deformation • Constitutive model • Cam Clay model • Shallow landslides

Background

Rainfall is considered as one among the most common contributing factors and triggers of shallow landslides. While evaluating stability of slopes subjected to rainfall, slopes are generally considered to be saturated. Therefore, shear strength of saturated soil is used for analysis. However, in majority of cases, the slopes remain partially saturated during rainfall. Therefore, analysis that is done for the

assumed saturated condition gives conservative results. In this study a 1.2 m × 1.2 m × 0.6 m sized sandy slope is modelled in laboratory and was subjected to a rainfall of 30 mm/h for 3 h. Values of suction were measured with time for the entire 3 h period. The models were prepared with three different angles of inclinations but at the same void ratio of 0.6. A constitutive model that was developed for the partially saturated condition was utilized for the numerical analysis of the slopes.

B. Tiwari (✉)

Fullerton, Civil and Environmental Engineering Department,
California State University, 800 N State College Blvd., E-419,
Fullerton, CA 92834, USA
e-mail: btiwari@fullerton.edu

K. Kawai • P. Viradeth

Department of Civil Engineering, Kobe University, 1-1 Rokkoudaicho
Nadaku, Kobe 657-0013, Japan
e-mail: kkawai@kobe-u.ac.jp; pviradeth@gmail.com

Experimental and Numerical Modelling

Experimental Modelling

In the experimental setup, a sandy soil was compacted in a Plexiglas container at the void ratio of 0.6. The experimental model is presented in Fig. 1. This model is instrumented with four high-precision tensiometers at different locations under

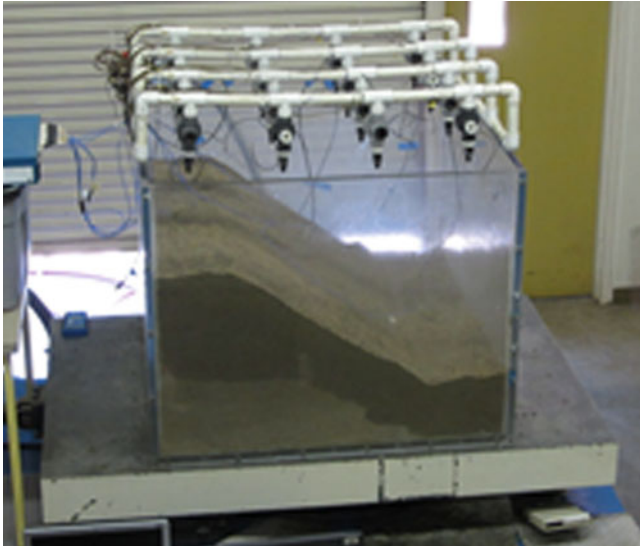


Fig. 1 Overview of the experimental model—change in color shows the water front

the ground. Values of suction were measured at those locations during rainfall. The suction values were recorded in every 15 min interval. Depths of water front were also recorded from outer sides of the Plexiglas container in every 15 min for the entire rainfall period.

Numerical Modelling

Critical state shear strength of soil was obtained by conducting CU triaxial test on the saturated sand following ASTM procedure. Likewise, consolidation and swelling parameters of the saturated soil were obtained through one-dimensional consolidation test as per the ASTM standard. Test results were helpful to obtain critical state friction angle and developing p-q curves to obtain the critical state parameters. The geotechnical properties of the saturated sand obtained from the pertinent soil tests are summarized below.

Compression index = $C_c = 0.2$; Swelling index = $C_s = 0.02$; M : Critical state line = 0.74; Effective Friction Angle = 31.8° ; Effective Cohesion = 0

Deformation analysis of the slope was performed using the modified Cam Clay model based on the approach proposed by Karube and Kawai (2001), which was latter improved by Ohno et al. (2007). Numerous constitutive models for unsaturated soil have been proposed since Bishop (1960) presented the concept of effective stress for unsaturated soils (e.g., Alonso et al. 1990; Karube et al. 1996; 1997). Ohno et al. (2007) developed a relationship between changes in stiffness of unsaturated soil with effective degree of saturation. Kawai et al. (2007) explained the model in

detail. In this model, application of the soil-water retention characteristic curve (SWRCC) model can be used independently in the constitutive model. Kawai et al. (2007, 2009) successfully utilized this model in various geotechnical applications pertinent to unsaturated soils including natural slopes and embankments. According to the proposed model, effective stress is expressed as follows:

$$\boldsymbol{\sigma}' = \boldsymbol{\sigma}^{net} + p_s \mathbf{1} \quad (1)$$

Where,

$$\boldsymbol{\sigma}^{net} = \boldsymbol{\sigma} - p_a \mathbf{1}, \quad p_s = S_e s \quad (2)$$

$$s = p_a - p_w, \quad S_e = \frac{S_r - S_{rc}}{1 - S_{rc}} \quad (3)$$

Here, $\boldsymbol{\sigma}'$ is effective stress tensor for unsaturated soil, $\boldsymbol{\sigma}^{net}$ is the net stress tensor, $\mathbf{1}$ is the second rank unit tensor, $\boldsymbol{\sigma}$ is total stress tensor, s is suction, p_s is suction stress, p_a is pore-air pressure, p_w is pore-water pressure, S_r is degree of saturation, S_e is effective degree of saturation, and S_{rc} is degree of saturation at $s \rightarrow \infty$. Volume change of soil at certain water content levels is expressed as:

$$e = e_0 - \lambda \ln \frac{p'}{\zeta p'_{sat}} \quad (4)$$

Where,

$$\zeta = \exp[(1 - S_e)^n \ln a] \quad (5)$$

Here, a and n are the fitting parameter to express the increase in consolidation yield stress according to de-saturation. Similarly, the plastic volumetric strain is expressed as follows:

$$\varepsilon_v^p = \frac{\lambda - \kappa}{1 + e_0} \ln \frac{p'}{\zeta p'_{sat}} \quad (6)$$

The consolidation yield stress can be obtained as shown in the following equation:

$$p'_c = \zeta p'_{sat} \exp\left(\frac{\varepsilon_v^p}{MD}\right) \quad (7)$$

$$MD = \frac{\lambda - \kappa}{1 + e_0} \quad (8)$$

where, p'_c is the yield stress represented by mean effective principal stress, M is q/p' at the critical state, and D is the dilatancy coefficient. The following yield function can be obtained by applying the equations presented above in the original Cam Clay model.

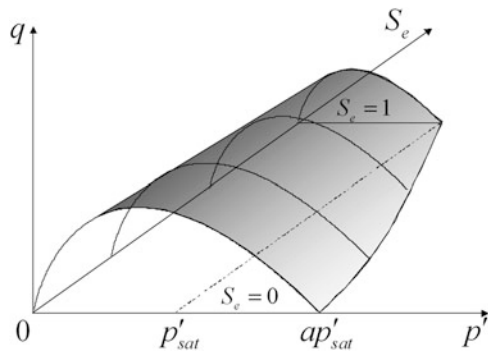


Fig. 2 Yield surface for unsaturated soil based on the proposed constitutive model

$$f(\boldsymbol{\sigma}', \zeta, \varepsilon_v^p) = MD \ln \frac{p'}{\zeta p'_{sat}} + D \frac{q}{p'} - \varepsilon_v^p = 0 \quad (9)$$

where

$$p' = \frac{1}{3} \boldsymbol{\sigma}' : \mathbf{1}, \quad q = \sqrt{\frac{3}{2}} \mathbf{s} : \mathbf{s}, \quad \mathbf{s} = \boldsymbol{\sigma}' - p' \mathbf{1} = \mathbf{A} : \boldsymbol{\sigma}', \quad \mathbf{A} = \mathbf{I} - \frac{1}{3} \mathbf{1} \otimes \mathbf{1}$$

Here, \mathbf{I} is the fourth rank unit tensor. Equation (9) reduces to the original Cam Clay model under saturated condition ($S_e = 1$). Figure 2 shows the concept of yield surface expressed by equations presented above.

A Finite Element Modeling (FEM) program was developed for the constitutive model of the unsaturated soil mechanics based on the equations proposed above. The

values of suction calculated from the Finite Element Analysis program explained in earlier chapter were coupled into the FEM setting of the constitutive model for the unsaturated soil mechanics, presented above.

Results of the Study

Figure 3 presents the values of suction and the velocity of the infiltration within the soil mass after 3 h of rainfall for 30, 45, and 50° slopes. The horizontal and vertical deformation values calculated for slopes with 30, 45 and 50° inclinations after 3 h of rainfall using the FEM analysis are presented in Fig. 4. It shows that the horizontal deformation is maximum near the toe of the slope (Fig. 4). The amount of horizontal deformation is less than 1 mm. The higher the angle of inclination, more the horizontal deformation. The deformation pattern presented in Fig. 4 shows that the slope deformation pattern is more rotational. Likewise, vertical deformation close to 1.5 mm was recorded on top of the slope. The vertical deformation on the ground surface was similar irrespective of the angle of inclination of slopes. Deformations of the slope after the rainfall were measured by redrawing the post-experiment geometry of the slope. Approximately 1.2 mm of settlement was observed on top of the slope and there was less than 1 mm of horizontal deformation. The experimental result was very close to the numerical results presented in Fig. 4.

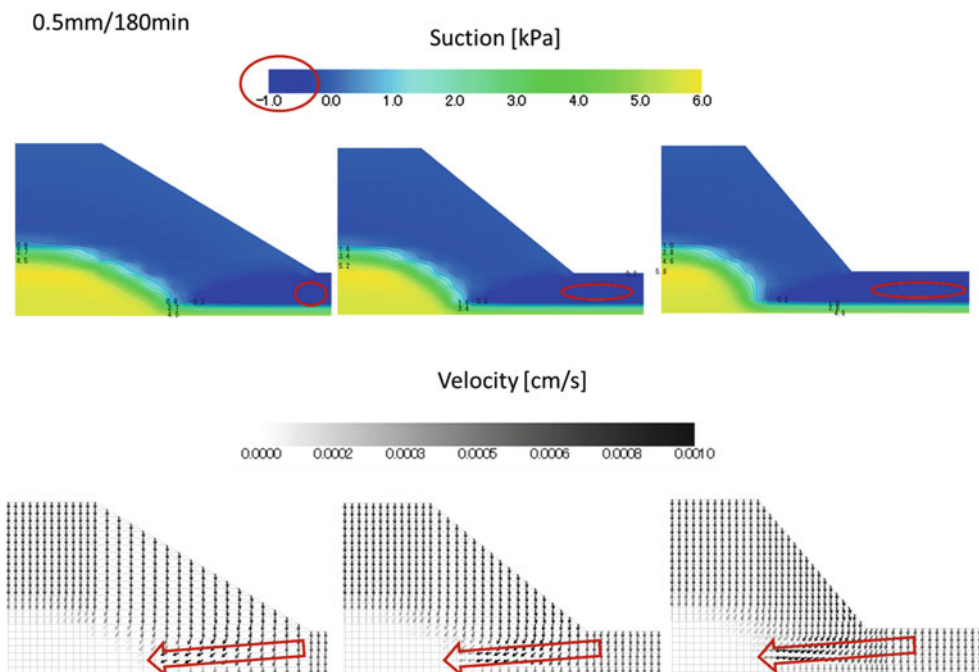


Fig. 3 Numerically calculated values of suction and the velocity of the movement of water front at various locations of the 30, 45, and 50° slopes after 3 h of rainfall—red circles are the points with positive pore water pressure

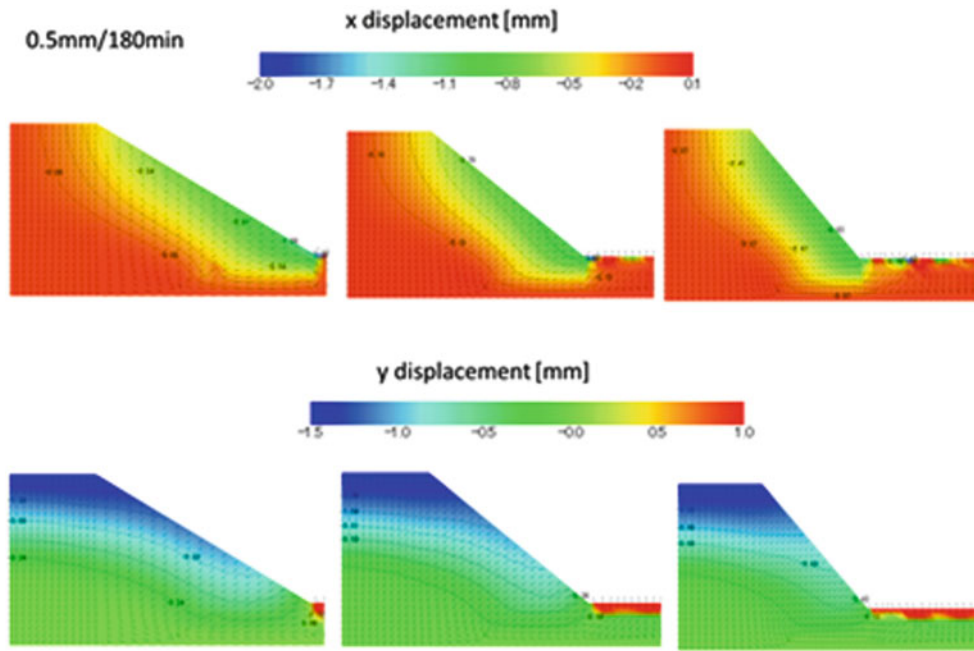


Fig. 4 Numerically calculated values of deformation at various locations of the 30, 45, and 50° slopes after 3 h of rainfall

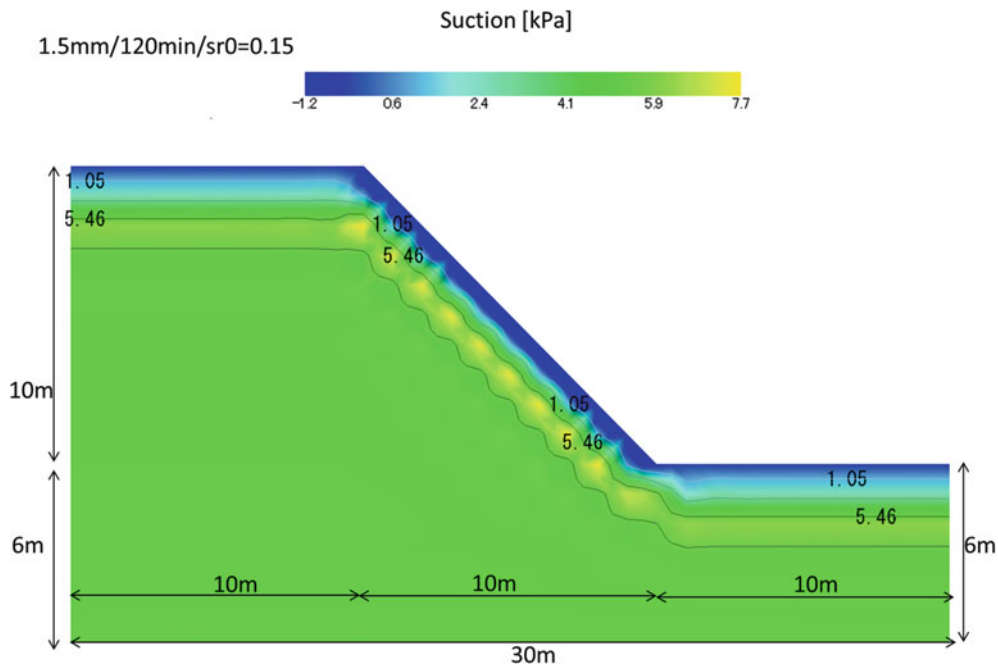


Fig. 5 Numerically calculated values of suction and movement of water front on a conceptual slope after 2 h of rainfall having intensity of rainfall of 90 mm/h

Seepage velocity was estimated using the depth of water-front with time that was calculated using the equations presented earlier and the results presented in Fig. 3. The seepage velocity and the constitutive model was extended to evaluate the temporal change in suction and deformation on a 10 m high slope presented in Fig. 5. Slope presented in Fig. 5 is a conceptual slope prepared for the purpose of

parametric study only. The geotechnical and hydraulic properties of soil obtained for the experimental model slope was used as the geotechnical properties of the conceptual slope. Presented in Fig. 6 are the values of suction recorded after 2 h of rainfall having intensity of 90 mm/h. The pattern of the numerical values of suction and velocity of water front were similar (or proportional) to the small

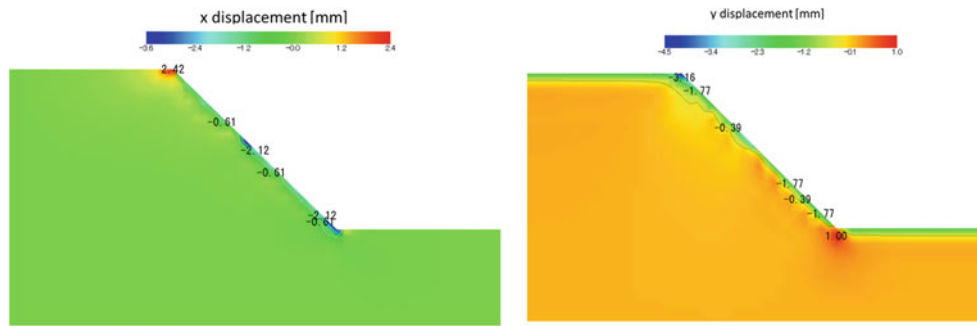


Fig. 6 Numerically calculated values of deformation on a conceptual slope after 2 h of rainfall having intensity of rainfall of 90 mm/h

scale slope used for the experimental modelling. The deformations of slope in x and y axes (i.e. horizontal and vertical direction) are presented in Fig. 6. As observed in Fig. 6, small outward deformation of less than 3 mm (locally) was observed near the head of the slope. The toe of the slope showed an inward deformation i.e. shrinkage. This shows that unless the rainwater percolated downwards along the slope to touch the toe of the slope, the deformation near the toe is negligible.

Summary and Conclusion

In order to study the effect of rainfall on soil-suction and soil deformation, sandy slopes were prepared at three different angles of inclinations. These slopes were subjected to 30 mm/h of rainfall for 3 h, separately, using a rain simulator. The amounts of suction with the duration of rainfall at different locations were measured with tensiometers. A hydro-mechanical model was developed for unsaturated soil condition using the finite element method. Modified Cam Clay model was utilized to prepare the models. The models are capable to couple the unsaturated seepage flow and associate suction into the deformation analysis. The study result shows that the calculated values of suction and deformation were similar to the values observed during the experimental modelling. The numerical analysis for a conceptual 10 m high slope shows that the variations in suction on larger slopes are proportional to the variation in suction in a small scale model. Likewise, the deformation of slope near the toe is negligible if the rainwater is not capable of moving infiltrating to the toe of the slope.

Acknowledgement The authors would like to thank the California State University Fullerton for providing sabbatical leave and the Kobe University, Japan for providing visiting professorship for the first author during the period of this collaborative research. We also would like to thank the graduate students from the research laboratory of the second author for running some numerical models pertinent to this study.

References

- Alonso EE, Gens A, Josa A (1990) A constitutive model for partially saturated soils. *Geotechnique* 40(3):405–430
- Bishop AW (1960) The principle of effective stress. *Norwegian Geotechnical Institute* 32:1–5
- Karube D, Kawai K (2001) The role of pore water in the mechanical behavior of unsaturated soils. *Geotech Geol Eng* 19(3):211–241
- Karube D, Kato S, Hamada K, Honda M (1996) The relationship between the mechanical behavior and the state of pore water in unsaturated soil. *J Jpn Soc Civil Eng* 535(III-34): 83–92 (in Japanese)
- Karube D, Honda M, Kato S, Tsurugasaki K (1997) The relationship between shearing characteristics and the composition of pore water in unsaturated soil. *J Jpn Soc Civil Eng* 575(III-40): 83–92 (in Japanese)
- Kawai K, Iizuka A, Hayakawa E, Wang W (2007) Non-uniform settlement of compacted earth structures caused by the deformation characteristics of unsaturated soil on wetting. *Soils Found* 47 (2):195–205
- Kawai K, Iizuka A, Tachibana S, Ohno S (2009) Impacts of plant induced uptake on the stability of the earth structure. *Proc International Conference on Soil Mechanics and Geotechnical Engineering, Alexandria* 1:526–529
- Ohno S, Kawai K, Tachibana S (2007) Elasto-plastic constitutive model for unsaturated soil applied effective degree of saturation as a parameter expressing stiffness. *J Jpn Soc Civil Eng* 63 (4):1132–1141



Feasibility Study of Dumping Area on Bearing Capacity and Slope Stability Analysis

Twin Hosea W. Kristyanto, Iskandar, Dicky Muslim, and Febri Hirnawan

Abstract

Open pit mining, especially coal mining, needs cleaning and cutting of overburden. It needs an area for dumping overburden material. This area called disposal or dumping area. We need engineering geological mapping, analysis of bearing capacity, and slope stability analysis for preventing the failure of the dumping area. Therefore, this research aims to identify the best location of dumping area and the design of stable dumping area.

Methods that were used in this research are: (1) field engineering geological mapping, soil and rock sampling from either outcrops or three bore holes i.e.: GT01, GT02, and GT03; (2) laboratory analysis method for gaining information about UCS, angle of friction, cohesion, and unit weight, and (3) office method be in the form of analysis of engineering geological map, bearing capacity (Terzhagi's Formula), and slope stability. Then the design of stable dump could be made according to the result of slope stability analysis.

The result shows that value of bearing capacity is different in each borehole. The location that suggested for dumping area is around boreholes GT03 (Engineering Geological Unit of Fine Soil II) because it has highest bearing capacity, among other boreholes, it is about 494.452 t/m² for continuous foundation. The simulation and analysis of slope stability show that safe design of dump is: single slope 25.6°, overall slope 15.5°, and maximum dump height is 50 m.

Keywords

Bearing capacity • Dumping area • Engineering geological map • RMR • Slope stability analysis

T.H.W. Kristyanto (✉)
Graduate Program of Geological Engineering, Padjadjaran University,
Dipati Ukur Street No. 35, Bandung 40132, Indonesia
e-mail: twin.hosea@hotmail.com

Iskandar
Department of Landslide, Indonesian Centre of Volcanology and
Geo-Hazard Mitigation, Bandung 40122, Indonesia
e-mail: iskand96@gmail.com

D. Muslim
Faculty of Geology, Padjadjaran University, Jatinangor 45363,
Indonesia
e-mail: dicky.muslim@unpad.ac.id

F. Hirnawan
Geotechnics Laboratory, Padjadjaran University, Jatinangor 45363,
Indonesia
e-mail: fhirnawan@yahoo.com

Introduction

Open pit mining, especially coal mining, needs cleaning and cutting of overburden. It needs an area for dumping overburden material. This area called disposal or dumping area. We need engineering geological mapping, analysis of bearing capacity, and slope stability analysis for preventing the failure (Sayekti 2007).

The aims of this research include: identifying the location and design of disposal area, in coal mining, based on engineering geological mapping, bearing capacity analysis, and slope stability analysis.

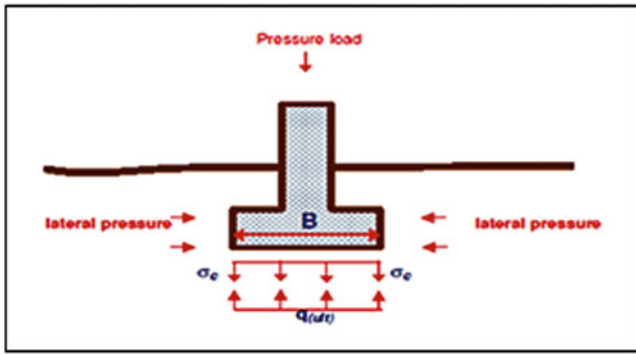


Fig. 1 Bearing capacity (Bowles 1984)

Engineering Geological Mapping

Engineering geological map is the combination of geomorphological map, geological map, and geotechnical properties. Geomorphological map provides information of land shape, drainage pattern, slope gradient, and morphogenetics. Geological map gives information about structural geology and stratigraphy of research area. Geotechnical properties give information about physical and mechanical properties of soil or rocks (Price 2009).

Bearing Capacity

Bearing capacity is ability of soil for holding back pressure or load of building above it without cause shear failure and excessive settlement. The ability is depend on soil shear strength (Bowles 1984) (See Fig. 1).

Terzhagi in Zakaria (2006) discuss the influence of foundation shape toward value of ultimate bearing capacity. The influence is analysed based on continuous foundation that applied for the other shapes of foundation.

Continuous footing also known as general equation of bearing capacity, i.e.:

$$q_u = (c \cdot N_c + \gamma D_f \cdot N_q + 0,5 \gamma \cdot B \cdot N_\gamma).$$

which:

q_u = Ultimate bearing capacity, T/m^2

B = Wide of foundation (m)

D_f = Depth of foundation (m)

γ = Unit weight (T/m^2)

c = Cohesion (T/m^2)

N_c, N_q, N_γ = Bearing capacity factor

ϕ = Angle friction ($^\circ$)

Terzhagi in Zakaria (2006) presented a bearing capacity formula which was calculated in ultimate bearing capacity condition (q_{ult}). It means an equilibrium value that will result in failure or collapse if it is passed over. Therefore the value of allowable bearing capacity (q_a) must be lower than ultimate bearing capacity.

Allowable bearing capacity depends on how great the chosen safety factor (F). In general, value of safety factor that is chosen is in range of 2–5. The formula of allowable bearing capacity is:

$$q_a = \frac{q_u}{F}$$

which:

q_a = allowable bearing capacity ($kg/cm^2, T/m^2$)

q_u = ultimate bearing capacity ($kg/cm^2, T/m^2$)

F = Safety factor.

Slope Stability

A slope has two forces working on it, i.e.: driving force and restraining force. A slope will fail if the driving force is greater than the restraining force. Mathematically the stability of slope can be explained in form of safety factor (F_s), where:

$$F_s = \frac{\text{Restrain Force}}{\text{Driving Force}}$$

According to Bowles (1984) it means:

$F_s < 1.07$ unstable slope

$1.07 < F_s < 1.25$ critical slope

$F_s > 1.25$ stable slope

Methodology

This research used three methods, they are: (1) field sampling of soils and engineering geological mapping; (2) Laboratory analysis method, for getting data cohesion (c), angle of friction (ϕ), and unit weight (γ); and (3) office analysis method for getting engineering geological map, value of bearing capacity, and design of stable disposal area.

The location of the disposal area was determined by analyses of engineering geological map and bearing capacity. Determination of bearing capacity based on Terzhagi formulation. Design of disposal area is determined by simulation of slope stability using software GeoStudio 2004.

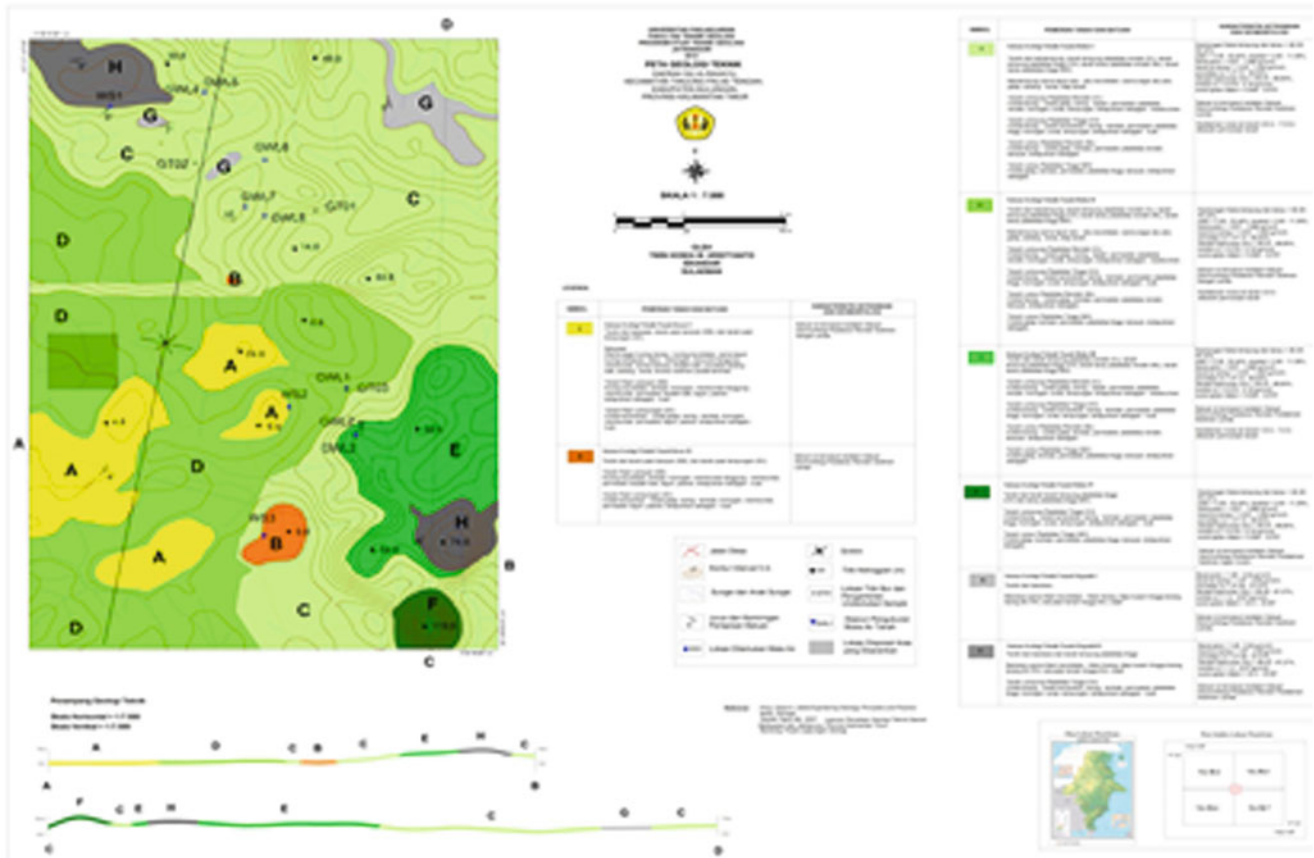


Fig. 2 Engineering geological map of research area

Results and Discussion

Engineering Geological Map

Based on the compilation of geomorphological map, geological map, and geotechnical properties, research area is divided into eight engineering geological units. They are: (i) Engineering geological unit of coarse soil I, (ii) Engineering geological unit of coarse soil II, (iii) Engineering geological unit of fine soil I, (iv) Engineering geological unit of fine soil II, (v) Engineering geological unit of fine soil III, (vi) Engineering geological unit of fine soil IV, (vii) Engineering geological unit of organic soil I, and (viii) Engineering geological unit of organic soil II. Description and distribution of the engineering geological units can be seen Fig. 2.

Bearing Capacity

Calculation of bearing capacity in research area was done based on data of soil mechanics from three boreholes, places of taking undisturbed sample. They are GT01, GT02, and GT03. The type of failure in this research is assumed as general shear failure with wide of foundation and depth of foundation are 1 m. The result of bearing capacity calculation is shown in Table 1.

Disposal Area Location

Based on engineering geological map and bearing capacity the location that is chosen as disposal area is around GT03 that inside of engineering geological units of fine soil II. It



Modelling Rockslide Displacements with Delayed Plasticity

Gabriele Frigerio, Riccardo Castellanza, Giovanni Battista Crosta, and Claudio di Prisco

Abstract

To model the temporal evolution of complex landslides, a 1D pseudo-dynamic visco-plastic approach, based on Perzyna's theory, has been modified. In the original version of the model, the viscous nucleus has been assumed to be bi-linear: where irreversible deformations develop uniquely for positive yield function values whereas, in a more general case, it can also develop for negative values. In this work the model has been enriched by considering: (1) an exponential viscous nucleus, (2) a strain-rate softening to reduce friction angle as the sliding velocity increases and (3) block interaction forces to cope with complex 3D geometries for the sliding mass.

The application of the proposed model to the Vajont slide emphasizes the role played by the strain-rate softening while the application to the La Saxe rockslide (Italy) clearly shows how a relatively simple model can be applied to a complex landslide by considering a spatial discretization of the sliding mass.

Keywords

Delayed plasticity • Visco-plastic model • Time dependent landslide • Displacements prediction • Collapse

Introduction

In order to model complex sliding masses subject to continuous slow movements related to water table fluctuations it is quite convenient to: (i) model the time-dependent mechanical behaviour of the materials by means of a viscous-plastic constitutive law; (ii) assume the water table fluctuation as main input to reproduce time acceleration; (iii) consider the

3D constrains by maintaining a high level of simplicity such to allow implementation into EWS (Early Warning System) for risk management.

In this paper a previously presented 1D pseudo-dynamic visco-plastic model (Secondi et al. 2011), based on Perzyna's theory is applied. The sliding mass is considered as a rigid block subject to its self-weight, inertial forces and seepage forces varying with time. All non-linearities are lumped in a thin layer interface positioned between the rigid block and the bedrock. The mechanical response of this interface is assumed to be visco-plastic. In this paper the viscous nucleus is assumed to be exponential, so that irreversible strains develop for both positive and negative values of the yield function; the friction angle is assumed to reduce with strain rates; the sliding mass is discretized in blocks to cope with complex rockslide geometries.

Two case studies are presented to validate the improvements introduced in this paper. The first relates to the simulation of the displacements of the Vajont rockslide from

G. Frigerio

Department of Earth and Environmental Sciences, University of Milano Bicocca (DISAT), p.za della Scienza 4, 20126 Milan, Italy

DICA, Politecnico di Milano, p.za la da Vinci 32, 20133 Milan, Italy

R. Castellanza (✉) • G.B. Crosta

Department of Earth and Environmental Sciences, University of Milano Bicocca (DISAT), p.za della Scienza 4, 20126 Milan, Italy
e-mail: riccardo.castellanza@unimib.it

C. di Prisco

DICA, Politecnico di Milano, p.za la da Vinci 32, 20133 Milan, Italy

1960 to the failure occurred on October the 9th 1963 (Hendron and Patton 1985; Müller 1964, 1968, 1987; Selli and Trevisan 1964); the second concerns the recent La Saxe rockslide movements (Aosta valley; Italian Western Alps) (Crosta et al. 2013).

It will be shown that, in its modified version, the model satisfactorily fits the Vajont pre-collapse displacements triggered by the fluctuation of the Vajont lake level, while the blocks discretization confirms the model suitability in case of complex 3D slide as in the case of the La Saxe rockslide.

1D Viscous Plastic Model

As is well known, a simple static limit equilibrium analysis is not suitable for modelling and correctly reproducing the time dependent mechanical response of sliding masses triggered by water table fluctuations. A dynamic, or, at least, pseudo-dynamic analysis should be adopted, and a delayed-plastic constitutive approach employed. The first issue can be addressed by evaluating the inertial effects on the soil mass by using a pseudo-dynamic approach, as that introduced by Newmark (Newmark 1965) for dams under seismic actions, whereas, viscous components can be described by employing the visco-plasticity theory introduced by Perzyna (1963).

As was previously suggested, according to this approach, the rockslide is interpreted as a rigid block (Fig. 1), where the active forces taken into account are (i) the weight, (ii) the inertial forces and (iii) the seepage force deriving from the water table level which is a function of time, $\Delta h_w(t)$. All non-linearities are lumped in a shear band of thickness Δs positioned between the rigid block and the bedrock. All the details and the analytical formulation of this model are reported in Crosta et al. (2013). Thus, the main equations controlling this model are.

Visco-Plastic Strain Rate Definition

$$\dot{\gamma}^{vp} = \tilde{\gamma} \cdot \phi(f) \quad (1)$$

Sliding mass displacement rate:

$$\dot{x} = \Delta s \dot{\gamma}^{vp} = \tilde{\gamma} \Delta s \phi(f) \quad (2)$$

Yield function definition

$$f = \frac{\tau - \tau_{res}}{\sigma'_n} \quad (3)$$

shear stress

$$\tau = \tau_{stat} - m^* \ddot{x} \quad (4)$$

$$\tau_{stat} = (W[\Delta h_w(t)] \sin(\alpha) + J)/A \quad (5)$$

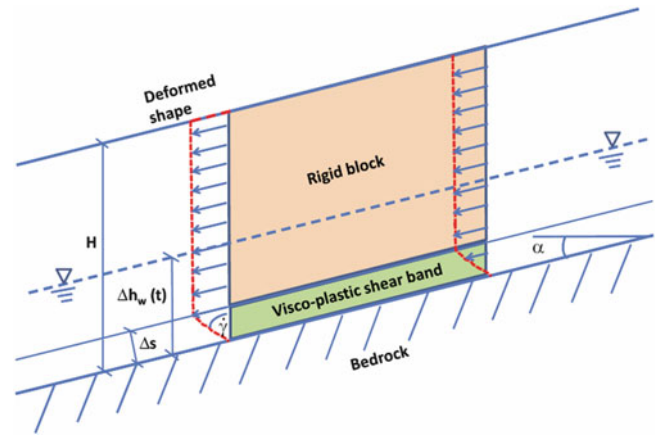


Fig. 1 1D block model with main geometrical elements

Failure criterion

$$\tau_{res} = c' + \sigma'_n \tan \phi'_{res} \quad (6)$$

where f is the yield function, $\tilde{\gamma}$ a constitutive viscous parameter, $\phi(f)$ the viscous nucleus, \dot{x} the sliding displacement rate of the mass m , A the total contact area, W the soil buoyant weight, J the total seepage force, $\Delta h_w(t)$ the groundwater table level varying with time t .

In case f is positive, by substituting (2), (3) and (4) into the expression of the viscous nucleus, and by introducing the geometrical and constitutive parameters, we obtain an equation of the following type:

$$a\ddot{x} + b\dot{x} + c = 0 \quad (7)$$

where coefficients a , b and c depend on time and can be derived from the previous equations. The improvements of the model are presented in the following sections.

Viscous Nucleus

As is sketched in Fig. 2, two different formulations for the viscous nucleus have been considered. The first, proposed in the original version of the model (Secondi et al. 2011), was a bilinear function defined as:

$$\phi(f) = \langle f \rangle \quad (8)$$

where brackets imply the viscous nucleus to coincide with the yield function for $f > 0$ and to be nil for negative values of f (3).

The second expression is an exponential law (Fig. 2b) defined: according to the following equation

$$\phi(f) = e^{\alpha f} \quad (9)$$

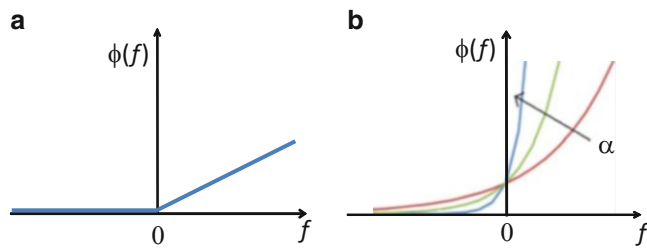


Fig. 2 (a) bilinear viscous nucleus; (b) exponential viscous nucleus

The exponential law is also modified by parameter α , governing the shape of the viscous nucleus (Fig. 2b).

Friction Weakening

As a preliminary way to simulate the transition from the initiation to the propagation of an unstable rock mass, a friction weakening is implemented. An increase in the localized shear strain rate (i.e. slip velocity) is thus assumed to produce a slight reduction in the friction angle:

$$\|\dot{x}\| > \dot{x}_w \quad \tan \phi'(\dot{x}) = \frac{\tan \phi'_0 - \tan \phi'_w}{\|\dot{x}\| - \dot{x}_w} + \tan \phi'_w \quad (10)$$

otherwise,

$$\tan \phi'(\dot{x}) = \tan \phi'_0$$

where ϕ'_0 and ϕ'_w are the static and the weakened friction angles, respectively, and \dot{x}_w is a threshold characteristic velocity for the weakening to occur.

Many authors (e.g. Rice 2006; Beeler et al. 2008; Kuwano and Hatano 2011; Vardoulakis 2000; Veveakis et al. 2007) proposed specific studies and theoretical interpretations to justify the frictional weakening as a consequence of multiple mechanisms. Here the authors introduce (10) only as one possible ways to simulate, within the adopted 1D model, the acceleration usually recorded before the run-out process. No specific theoretical justification are given; (10) should be therefore considered as a macroscopic strength reduction as sliding velocity increases towards catastrophic failure.

3D Discretization

The proposed model can be employed to reproduce the evolution of a non-deformable mass sliding on an inclined rigid plane. A 3D complex landslide a priori does not satisfy

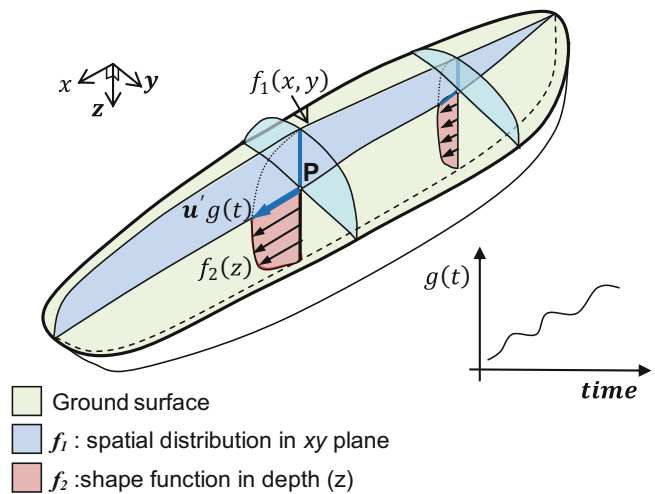


Fig. 3 Suggested elementary functions of $u(x, y, z, t)$ of a rockslide mass

all the hypotheses behind the model. To overcome this limitation and to tentatively apply the proposed model to complex 3D landslide settings, a two steps methodology has been developed.

Step 1: Splitting the Displacement Function

In general, the rockslide displacements can be expressed as a vector function $u(x, y, z, t)$ defined in space and time. At any instant this function should be properly evaluated from the monitoring. As a first order approximation it can be assumed that:

(i) the direction of displacements is constant within the area considered and to be determined by a unit vector u' . This also implies that the dispersion in direction of the velocity within the domain $\hat{u} = u(x, y, z) - u'$ is negligible with respect to u' ;

(ii) the evolution of displacement with time is independent of space

the function $u(x, y, z, t) \in C^0$ can be written as the product of three elementary functions:

$$u(x, y, z, t) = u' \bar{f}_1(x, y) \bar{f}_2(z) g(t) \quad (11)$$

where

$$\bar{f}_1(x, y) = f_1(x, y) / u_P(x_P, y_P, z_P, t_0) \quad (12)$$

$$\bar{f}_2(z) = f_2(z) / u_P(x_P, y_P, z_P, t_0) \quad (13)$$

In particular (see Fig. 3):

- $\bar{f}_1(x, y)$ can be considered as a non-dimensional shape function of the spatial superficial distribution of t displacements. This could be evaluated, for example,

from GB-InSAR measurements divided by the displacement at a selected point, P, and reference time, t_0 ;

- $\bar{f}_2(z)$ is the shape function in depth of the displacement at any point on the ground surface (Fig. 3) of the rockslide assumed to be time independent. This can be obtained from inclinometer data at a chosen point P by dividing it by the ground displacement measured in P. This function is crucial in order to verify the model assumption of a rigid block sliding on a shear band.
- Function $g(t)$ can be considered as the displacement evolution with time of a representative “pivot point” P.

Once shape functions $\bar{f}_1(x, y)$ and $\bar{f}_2(z)$ are known, it becomes possible to provisionally evaluate the displacement of a complex landslide by simulating or predicting the ground movement at a specific representative point P with respect to time by uniquely defining function $g(t)$.

Step 2: Spatial Discretization

If the rockslide movement prevalently slides parallel to the average slope inclination, the outlined model can be employed by assuming for instance both f_1 and f_2 (Heaviside step function) simply describing a rigid block sliding along a plane and variable \hat{z} to coincide with the normal to the average slope inclination (in this case a rotation of the reference frame is suggested, so that $\mathbf{u}^T = [1, 0, 0]$)

For complex 3D rockslides a more refined subdivision of the sliding mass is required. This will be based on a set of criteria employed to identify from monitoring data, geomorphological and geometrical observations, homogeneous displacement zones.

Once the rockslide mass is split into subzones, the same subdivision can be applied to the groundwater table, so that for each zone a time dependent oscillation $\Delta h_{wi}(t)$ can be evaluated.

Each zone is then treated has a rigid block resting on a shear band with a viscoplastic behaviour (Fig.1). In order to take into account the interaction between the blocks, equation (5) becomes

$$\tau_{stat,i} = (W_i[\Delta h_{w,i}(t)] \sin(\alpha_i) + J_i + F_i^{rel})/A_i \quad (14)$$

where F_i^{rel} stands for the resultant of both the forces transmitted by the lateral boundaries of each block and the forces transmitted by the uphill blocks to the downhill ones; index i refers to the current block.

Case Study 1: The Vajont Rockslide

The number of data and simulations available in literature concerning the Vajont rockslide is quite large (see e.g. Hendron and Patton 1985; Müller 1964, 1968, 1987, Selli

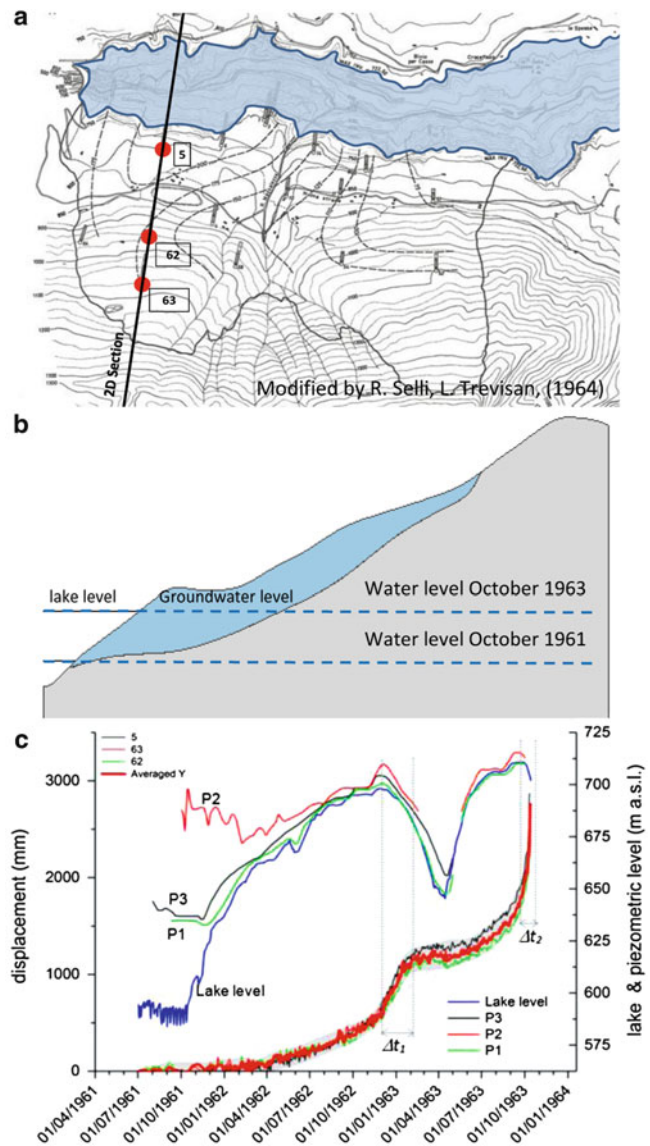


Fig. 4 (a) target position and cross section considered in the analysis; (b) lake and groundwater levels in October 1961 and 1963 (section from Bistacchi et al. 2013); (c) recorded targets displacement, lake and piezometric levels (after Selli and Trevisan 1964)

and Trevisan 1964; Alonso and Pinyol 2010). Our aim is to explore the capability of the proposed 1D viscoplastic model of reproducing the monitoring data in the 1961–1963 period and the collapse triggered by water table and lake level fluctuations.

As shown in Fig. 4 the lake level governs the water table position within the rockslide. The rockslide velocity increased during the impoundment until November 1962 (Δt_1 in Fig. 4c) and the displacements were still increasing during the subsequent drawdown. A similar behavior has been observed when the maximum lake level (712 m a.s.l.) was reached on October 1963 (Δt_2 in Fig. 4c).

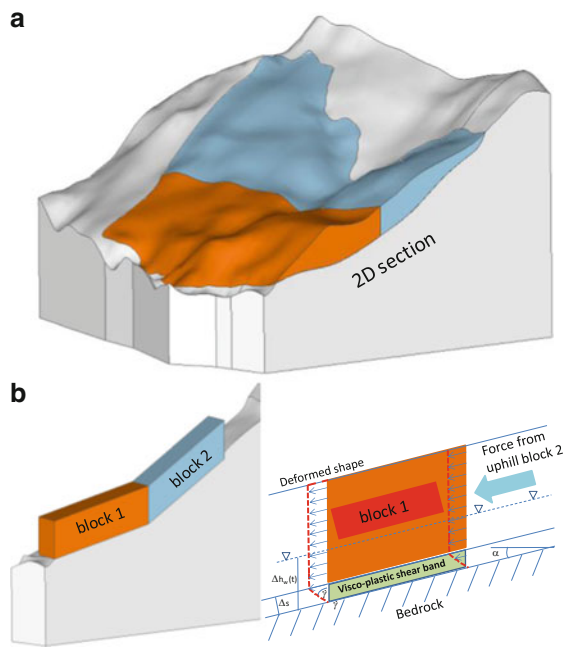
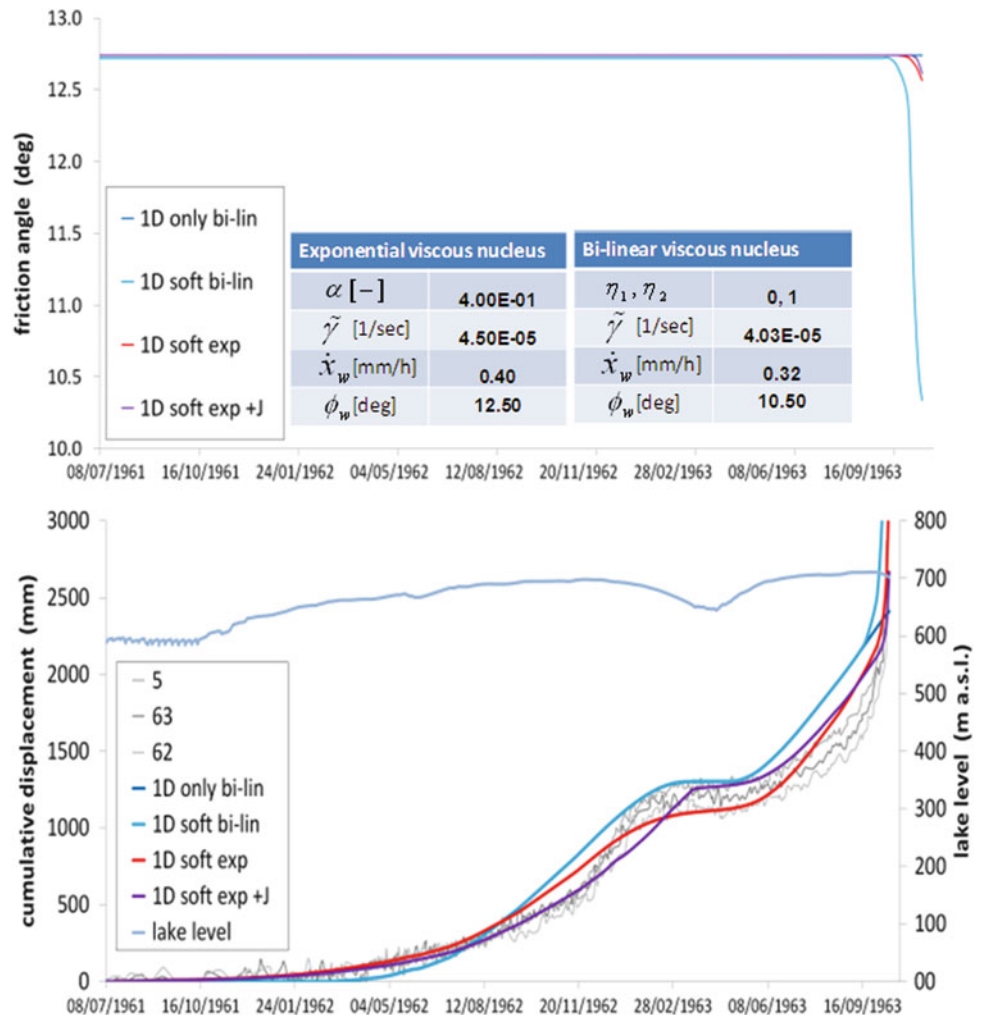


Fig. 5 (a) 3D view of Vajont rockslide sectioned along the same cross section as in Fig. 4a (3D geometrical data from Bistacchi et al. 2013); (b) discretization in two blocks along the cross section; (c) final adopted discretization in one block

Fig. 6 Model simulation ($g(t)$ function for block #1) with bilinear and exponential viscous nucleus and friction weakening



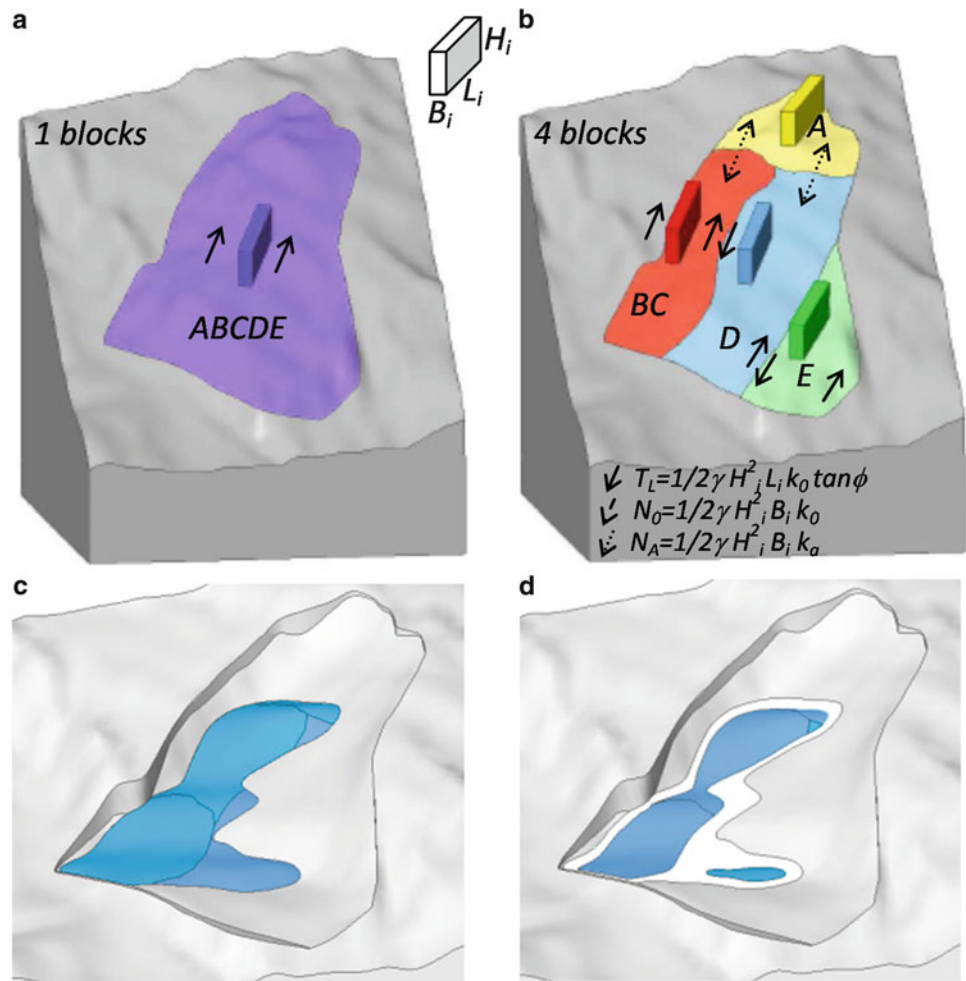
In order to simulate the monitored displacement triggered by the water table fluctuation (Fig. 4) with the described model, a schematization in blocks is required. Starting from an accurate 3D geometrical reconstruction of the unstable mass (Fig. 5a), a cross section along an alignment of monitoring targets (Fig. 4a) is considered. The failure surface is characterized by a bilinear shape suggesting the adoption of a discretization in two blocks (Fig. 5b). Moreover, the mechanism could be further simplified considering that it is dominated by block #1, while block #2 is applying a downward pushing force on block #1 (see Fig. 5c). This force acts parallel to the slope of block #1 and it has been evaluated as (see Crosta et al. 2013):

$$N_{0-2} = 1/2 \cdot k_0 \gamma (H_2)^2 B_2 \quad (15)$$

where H_2 is the depth of failure surface and B_2 the transversal breadth of block #2. This force could be considered as the interaction between the two blocks moving at the same speed (Fig. 4c).

As a consequence of this further assumption, the pre-collapse movements of the Vajont rockslide can be modeled by considering only block #1, so that the problem is reduced to a one dimensional model.

Fig. 7 Landslide discretization in 1 and 4 blocks. The lower panels show the wet and dry season groundwater table (light blue) above the failure surface



For the two blocks, the inclination angles, α , were evaluated with an averaging procedure to be 10.5° and 34° degrees, respectively. The depth of the failure surface, is $H_1 = H_2 = 133$ m; the longitudinal blocks length $L_1 = L_2 = 708$ m and the block breadth is $B_1 = B_2 = 1000$ m. The evolution with time of the water table elevation was considered in two different ways: (i) horizontal at the elevation of the tip of block #1 (568 m a.s.l.), with the water fluctuation converted into a variation with time of the buoyancy force acting on block #1, (ii) including to the buoyancy force, a seepage force resulting from the slight differences between the piezometer and the lake levels.

Both the bi-linear and the exponential viscous kernel were considered to simulate the pre collapse monitoring data (Fig. 4c). The simulation results are reported in Fig. 6. The displacement with time shown in Fig. 6b represents function $g(t)$ of block #1 according to the previously described 3D discretization. It is evident that the 1D viscoplastic model captures satisfactorily the landslide response, in particular when adopting an exponential viscous nucleus. The influence of seepage force (curve *soft exp* + J in

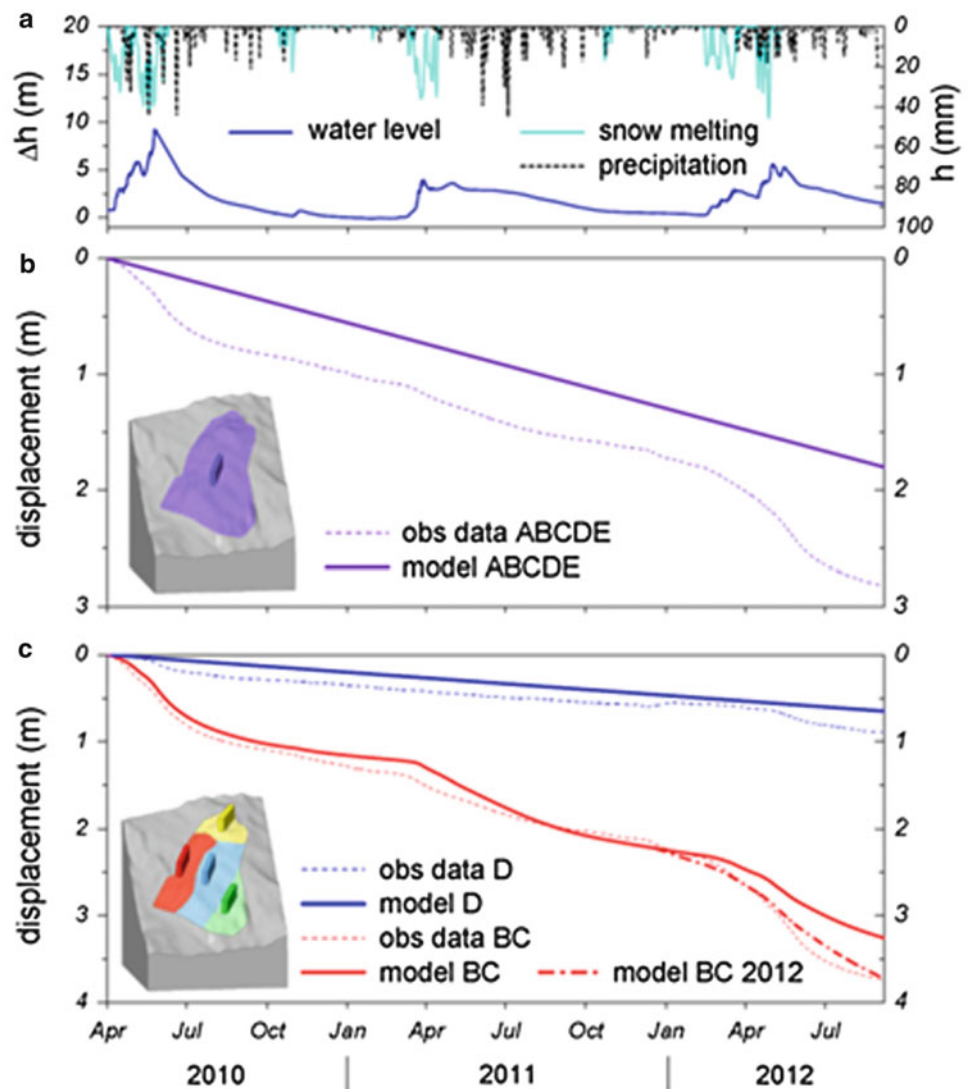
Fig. 6a) is clearly visible when the rockslide still moves during the drawdown phase (winter 1962–1963). The final pre-collapse acceleration of the slope is well captured if a friction weakening, as in (11), is assumed (Fig. 6a, and curves *soft-bi lin* and *soft exp* in Fig. 6b).

Case Study 2: The La Saxe Rockslide

Owing to both the hazard of the event and the vulnerability of the territory, the La Saxe active rockslide in the Aosta Valley, Italy, at present is very high As for the Vajont case, the goal is here to explore the capability of the proposed 1D viscoplastic model of reproducing the monitoring data.

The rockslide is subject to accelerations every spring due to the combined effect of snow melting and rainfall that implies an increase in the groundwater level (Fig. 7). Due to the complexity of the rockslide, this can be subdivided in sub-areas characterized by different geometrical properties (i.e. depth of surface failure, groundwater elevation, Fig. 7). This complexity affects the overall rockslide behavior.

Fig. 8 Model simulations in term of $g(t)$ functions



The four blocks discretization (Fig. 7b) subdivides the overall rockslide into different sub-areas so that each block has its own basal inclination, height, width length and shear band thickness. The interaction between the blocks has been taken into account by assuming lateral and normal forces (Crosta et al. 2013).

In Fig. 8 the results of the 1D viscoplastic model simulations are reported. The results for the single block discretization (Fig. 7a) obtained by assuming averaged geometrical properties for the entire rockslide, are shown in Fig. 8b. From this single block discretization the groundwater level results to always be below the average failure surface with the consequence that the model is unaffected by its oscillation (Fig. 8b). This clearly suggests that the single block discretization is too poor to reproduce the 3D complex behavior. In contrast, the 4 blocks discretization (Fig. 7b) shows the model capability of reproducing the monitored

displacements in different subareas of the rockslide (Fig. 8c).

Conclusion

A 1D rigid-viscoplastic model has been modified for what concerns the expression of the viscous nucleus, the friction strain-rate weakening and extended to simulate the response of systems of multiple interacting blocks to model 3D complex rockslides. Two case studies (Vajont and La Saxe rockslide) were chosen in order to show the capability of the proposed model of reproducing the displacement time series triggered by groundwater table fluctuations. The analysis of the Vajont rockslide has allowed the authors to demonstrate that strain-rate sensitivity is quite useful for fitting the pre-collapse displacement accelerations.

References

- Alonso EE, Pinyol NM (2010) Criteria for rapid sliding I. A review of Vaiont case. *Eng Geol* 114(3–4):198–210
- Bistacchi A, Massironi M, Superchi L, Zorzi L, Francese R, Giorgi M, Chistolini F, Genevois R (2013) A 3d geological model of the 1963 Vaiont landslide. *Ital J Eng Geol Environ* 2013:531–539
- Beeler NM, Tullis TE, Goldsby DL (2008) Constitutive relationships and physical basis of fault strength due to flash heating. *J Geophys Res* 113, B01401,348
- Crosta GB, di Prisco IC, Frattini IP, Frigerio IG, Castellanza IR, Agliardi IF (2013) Chasing a complete understanding of the triggering mechanisms of a large rapidly evolving rockslide. *Landslides*. doi:[10.1007/s10346-013-0433-1](https://doi.org/10.1007/s10346-013-0433-1)
- Hendron AJ, Patton FD (1985) The Vaiont Slide, a geotechnical analysis based on new geologic observations of the failure surface. Technical Report GL-85-5. Department of the Army US Army Corps of Engineers, Washington, DC
- Kuwano O, Hatano T (2011) Flash weakening is limited by granular dynamics. *Geophys Res Lett* 38, L17305. doi:[10.1029/2011GL048530](https://doi.org/10.1029/2011GL048530)
- Müller L (1964) The rock slide in the Vaiont valley. *Rock Mech Eng Geol* 2:148–212
- Müller L (1968) New considerations on the Vaiont slide. *Rock Mech Eng Geol* 6:1–91
- Müller L (1987) The Vaiont catastrophe - A personal review. *Eng Geol* 24:423–444
- Newmark NM (1965) Effects of earthquakes on dams and embankments. *Geotechnique* 15(2):139–160
- Perzyna P (1963) The constitutive equations for rate sensitive plastic materials. *Q Appl Math* 20:321–332
- Rice RJ (2006) Heating and weakening of faults during earthquake slip. *J Geophys Res* 111, B05311
- Secondi M, Crosta G, Di Prisco C, Frigerio G, Frattini P, Agliardi F (2011) Landslide motion forecasting by a dynamic visco-plastic model. *Proc WLF 2*, paper WLF2-2011-0571
- Selli R, Trevisan L (1964) Caratteri e interpretazione della frana del Vaiont. *Giornale di Geologia* 32:8–104
- Vardoulakis I (2000) Catastrophic landslides due to frictional heating of the failure plane. *Mech Cohes-Frict Mater* 5(6):443–467
- Veveakis E, Vardoulakis I, Di Toro G (2007) Thermoporomechanics of creeping landslides: The 1963 Vaiont slide, northern Italy. *J Geophys Res: Earth Surf* (2003–2012) 112(F3)

Part III

**Remote Sensing Techniques for Landslide Mapping
and Monitoring**



Introduction: Remote Sensing Techniques for Landslide Mapping and Monitoring

Veronica Tofani, Yang Hong, and Vern Singhroy

Abstract

Remote sensing is an effective tool for landslide mapping and monitoring. This chapter provides a general overview of the recent applications of optical and radar images for landslide detection, mapping and monitoring with special attention to SAR interferometry that has proved as a promising technique in landslide studies.

Keywords

Landslide • Remote sensing • SAR interferometry • Optical imagery

Remote sensing techniques represent effective tools for landslide detection, mapping, monitoring and hazard analysis. Applications are originating from nearly all types of sensors available today. Rapid developments in this field are fostered by the very high spatial resolution obtained by optical systems (currently in the order of tens of centimeters) and by the launching of SAR (Synthetic Aperture Radar) sensors, purposely built for interferometric applications with revisiting times of few days such as TerraSAR X and COSMO-SkyMed (Tofani et al. 2013a). Also, in the last years satellites have provided accurate measurements of precipitation such as the Tropical Rainfall Measuring Mission (TRMM), which was launched in 1997. Remote rainfall

measurements can be used to predict rainfall-induced landslides in the framework of landslide hazard analysis (Adler et al. 2000; Hong et al. 2006; Baum and Godt 2010).

Landslide detection and mapping benefit from both optical and radar imagery. Recently, a new generation of high resolution satellites as World-View, Geo-eye and the Pleiades constellation provides resolutions ranging from 0.5 to 2 m and offers a very powerful tool for a quick reproduction of regional inventory maps (up to a scale of 1:2,000). In particular the increasingly higher spatial and temporal resolution of optical satellite observations enables (i) more detailed and reliable identification of affected areas, (ii) an immediate response minimizing the risk of omission (due to landslide traces fading away with time), and (iii) repeated observations potentially leading to multi-temporal inventories, which can be easier related to specific events.

There is a large number of studies which proposed, applied and compared automated (both pixel and object-based) techniques for landslide mapping with optical data (Hervás et al. 2003; Cheng et al. 2004; Nichol and Wong 2005; Marcelino et al. 2009; Martha et al. 2010; Lu et al. 2011).

Airborne LiDAR techniques show particular strength for the mapping of old landslides under forest (e.g. Van Den Eeckhaut et al. 2007) but can also be used to support the mapping of newly triggered shallow landslides (Ardizzone et al. 2007; Lu et al. 2011). There seems to be a general agreement that LiDAR based mapping yields more accurate

V. Tofani

Earth Sciences Department, University Firenze, 50121 Florence, Italy
e-mail: veronica.tofani@unifi.it

Y. Hong

Hydrometeorology and Remote Sensing Lab, Department of Civil Engineering, University of Oklahoma, 120 David L. Boren Blvd, Suite 4610, Norman, OK 73072-7303, USA

Environmental Science, University of Oklahoma, Norman, OK 73019, USA

e-mail: yanghong@ou.edu

V. Singhroy (✉)

Canada Centre for Remote Sensing, Natural Resources, Ottawa, ON, Canada

e-mail: Vern.Singhroy@NRCan-RNCan.gc.ca

and complete inventories than field surveys alone (Ardizzone et al. 2007; Schulz 2007; Van Den Eeckhaut et al. 2007). Resulting inventories have been employed for efficient susceptibility models whereby the LiDAR derived terrain model provides also valuable input to extract influential topographic variables (Van Den Eeckhaut et al. 2006, 2009).

The application of the interferometric techniques to radar images is a powerful tool for landslide detection and mapping at large scale. In particular the A-DInSAR technique can contribute to the creation of landslide inventory maps which can be used for susceptibility mapping over large scale. There are a few of examples in literature of the use of landslide inventory maps derived from radar images for landslide hazard assessment (Singhroy et al. 1998; Catani et al. 2005). It's worth noticing that the realization of landslide inventory maps with InSAR technology benefits from the integration with optical imagery, geological and topographic information (Singhroy 2002).

Both Differential SAR interferometry (DInSAR) and multi interferograms SAR Interferometry (A-DInSAR) can be used for landslide monitoring. Though it represents a promising technique for landslide monitoring, the characteristics of the existing satellites put strong constraints on the use of DInSAR as a monitoring instrument. In particular, the spatial resolution of SAR images, the time-interval between two consecutive passages of the satellites and the wavelength of the radiation are unsuitable for a systematic monitoring of landslides that are characterized by relatively rapid movements or that are located on steep slopes or narrow valleys (Rott et al. 2000; Refice et al. 2001). Quantitative information on landslide activity can be acquired in case of extremely slow movements (velocity <16 mm/year according to Cruden and Varnes 1996), affecting large areas with sparse vegetation (Kimura and Yamaguchi 2000; Rizzo and Tesauro 2000). However the availability of deformations time series provided for long period by the radar satellites as ERS and ENVISAT can be used for the definition of the recurrence of landslides. At the same time the comparison of the time series with triggering factors data can define the causes and the deformation thresholds.

An extensive bibliography contains works on the use of DInSAR and A-DinSAR for landslide monitoring (Singhroy and Molch 2004; Strozzi et al. 2005; Meisina et al. 2007; Fornaro et al. 2009; Prati et al. 2010). In many cases the A-DInSAR data have been integrated with in-situ monitoring instrumentation (Strozzi et al. 2010; Tofani et al. 2013b). The joint use of satellite and ground-based data facilitates the geological interpretation of a landslide and allows a better understanding of landslide geometry and kinematics.

Optical imagery can give a great a contribution in the landslide susceptibility assessment especially in the definition of the preparatory factors. In particular the use of optical images is quite common when the analysis is carried out over large areas since these data can be easily collected. As

reported in Metternicht et al. (2005) optical imagery, as well as aerial photographs, have provided the main contribution for the mapping of landslide related factors.

Optical imagery can be used for defining the land cover (Cheng et al. 2004; Catani et al. 2005; Kirschbaum et al. 2009), geology and lithology (Sarkar and Kanungo 2004; Grebby et al. 2011), tectonics lineaments (Ramli et al. 2010) and for the set up of a Digital Elevation Model (DEM) which can be the inputs data for the heuristic and statistical susceptibility approach.

One of the most intriguing applications currently being investigated regarding the use of remote sensing is the temporal prediction of shallow landslides. Drawing on recent advances of satellite remote sensing technology, experimental landslide prediction models are developed to identify the timing for landslides induced by heavy rainfall (Hong et al. 2007; Adler et al. 2000).

Satellites have provided global estimates of precipitation over various temporal and spatial scales since the 1970s. A long history of development in the estimation of precipitation from space has culminated in sophisticated satellite instruments and techniques to combine information from multiple satellites to produce long-term products useful for climate monitoring. In November 1997, the Tropical Rainfall Measuring Mission (TRMM) was launched with the primary objective of making accurate measurements of rainfall and latent heating from space. In particular the Tropical Rainfall Measuring Mission (TRMM) Multi-satellite Precipitation Analysis (TMPA, Huffman et al. 2007) has been used for landslide prediction at global scale (Hong et al. 2006, 2007).

This chapter provides an overview of the application of remote sensing for landslide mapping, monitoring and hazard analysis.

References

- Adler RF, Huffman GJ, Bolvin DT, Curtis S, Nelkin EJ (2000) Tropical rainfall distributions determined using TRMM combined with other satellite and rain gauge information. *J Appl Meteor* 39(12): 2007–2223
- Ardizzone F, Cardinali M, Galli M, Guzzetti F, Reichenbach P (2007) Identification and mapping of recent rainfall-induced landslides using elevation data collected by airborne Lidar. *Nat Hazards Earth Syst Sci* 7(6):637–650
- Baum RL, Godt JW (2010) Early warning of rainfall-induced shallow landslides and debris flows in the USA. *Landslides* 7:259–272
- Catani F, Casagli N, Ermini L, Righini G, Menduni G (2005) Landslide hazard and risk mapping at catchment scale in the Arno River basin. *Landslide* 2(4):329–342
- Cheng K, Wei C, Chang S (2004) Locating landslides using multi-temporal satellite images. *Adv Space Res* 33:296–301
- Cruden DM, Varnes DJ (1996) Landslides types and processes. In: Turner AK, Schuster RL (eds) *Landslides: investigation and mitigation*. Transportation Research Board Special Report 247, National Academy Press, WA, pp 36–75

- Fornaro G, Pauciuolo A, Serafino F (2009) Deformation Monitoring over large areas with multipass differential SAR Interferometry: a new approach based on the use of spatial differences. *Int J Remote Sens* 30(6):1455–1478
- Grebby S, Naden J, Cunningham D, Tansey K (2011) Integrating airborne multispectral imagery and airborne LiDAR data for enhanced lithological mapping in vegetated terrain. *Remote-sens Environ* 115(1):214–226
- Hervás J, Barredo J, Rosin P, Pasuto A, Mantovani F, Silvano S (2003) Monitoring landslides from optical remotely sensed imagery: the case story of Tessina landslide, Italy. *Geomorphology* 54:63–75
- Hong Y, Adler R, Huffman, G (2006) Evaluation of the potential of NASA multi-satellite precipitation analysis in global landslide hazard assessment. *Geophys Res Lett* 33(22), L22402. doi:10.1029/2006GL028010
- Hong Y, Adler R, Huffman G (2007) Use of satellite remote sensing data in the mapping of global landslide susceptibility. *Nat Hazards* 43(2):23–44
- Huffman GJ, Adler RF, Bolvin DT, Gu G, Nelkin EJ, Bowman KP, Hong Y, Stocker EF, Wolff DB (2007) The TRMM multi-satellite precipitation analysis: quasi-global, multi-year, combined-sensor precipitation estimates at fine scale. *J Hydrometeor* 8(1):38–55
- Kimura H, Yamaguchi Y (2000) Detection of landslide areas using radar interferometry. *Photogramm Eng Remote Sens* 66(3):337–344
- Kirschbaum DB, Adler R, Hong Y, Lerner-Lam A (2009) Evaluation of a preliminary satellite-based landslide hazard algorithm using global landslide inventories. *Nat Hazards Earth Syst Sci* 9(3):673–686
- Lu P, Stumpf A, Kerle N, Casagli N (2011) Object-oriented change detection for landslide rapid mapping. *Geosci Remote Sens Lett IEEE* 8(4):701–705
- Marcelino EV, Formaggio AR, Maed E (2009) Landslide inventory using image fusion techniques in Brazil. *Int J Appl Earth Observ Geoinform* 11(3):181–191
- Martha T, Kerle N, van Westen CJ, Kumar K (2010) Characterising spectral, spatial and morphometric properties of landslides for semi-automatic detection using object-oriented methods. *Geomorphology* 116(1–2):24–36
- Meisina C, Zucca F, Conconi F, Verri F, Fossati D, Ceriani M, Allievi J (2007) Use of permanent scatterers technique for large-scale mass movement investigation. *Quatern Int* 171–172:90–107
- Metternicht G, Hurni L, Gogu R (2005) Remote sensing of landslides: an analysis of the potential contribution to geo-spatial systems for hazard assessment in mountainous environments. *Remote Sens Environ* 98:284–303
- Nichol J, Wong MS (2005) Satellite remote sensing for detailed landslide inventories using change detection and image fusion. *Int J Remote Sens* 26(9):1913–1926
- Prati C, Ferretti A, Perissin D (2010) Recent advances on surface ground deformation measurement by means of repeated spaceborne SAR observations. *J Geodyn* 49(3–4):161–170
- Ramli M, Yusof N, Yusoff M, Juahir H, Shafri H (2010) Lineament mapping and its application in landslide hazard assessment: a review. *Bull Eng Geol Environ* 69(2):215–233
- Refice A, Guerriero L, Bovenga F, Wasowski J, Atzori S, Ferrari R, Marsella M (2001) Detecting landslide activity by SAR interferometry. *Proc ERS-ENVISAT Symposium, Goteborg*
- Rizzo V, Tesaro M (2000) SAR interferometry and field data of Randazzo landslide (Eastern Sicily, Italy). *Phys Chem Earth (B)* 25(9):771–780
- Rott H, Mayer C, Siegel A (2000) On the operational potential of SAR interferometry for monitoring mass movements in alpine areas. *Proc of the 3rd European Conf on Synthetic Aperture Radar (EUSAR 2000), Munich, 23–25 May 2000, pp 43–46*
- Sarkar S, Kanungo DP (2004) An integrated approach for landslide susceptibility mapping using remote-sensing and GIS. *Photogramm Eng Remote Sens* 70(5):617–625
- Schulz WH (2007) Landslide susceptibility revealed by LIDAR imagery and historical records, Seattle, Washington. *Eng Geol* 89(1–2):67–87
- Singhroy V (2002) Landslide hazards: CEOS, The use of earth observing satellites for hazard support: Assessments and scenarios. Final report of the CEOS disaster management support group, NOAA, p 98
- Singhroy V, Molch K (2004) Characterizing and monitoring rockslides from SAR techniques. *Adv Space Res* 33(3):290–295
- Singhroy V, Mattar K, Gray A (1998) Landslide characterisation in Canada using interferometric SAR and combined SAR and TM images. *Adv Space Res* 21(3):465–476
- Strozzi T, Farina P, Corsini A, Ambrosi C, Turing M, Zilger J, Wiesmann A, Wegmüller U, Werner C (2005) Survey and monitoring of landslide displacements by means of L-band satellite SAR interferometry. *Landslides* 2(3):193–201
- Strozzi T, Delaloye R, Käab A, Ambrosi C, Perruchoud E, Wegmüller U (2010) Combined observations of rock mass movements using satellite SAR interferometry, differential GPS, airborne digital photogrammetry, and airborne photography interpretation. *J Geophys Res* 115:F01014
- Tofani V, Segoni S, Agostini A, Catani F, Casagli N (2013a) Technical note: use of remote sensing for landslide studies in Europe. *Nat Hazards Earth Syst Sci* 13:299–309
- Tofani V, Raspini F, Catani F, Casagli N (2013b) Persistent scatterer interferometry (PSI) technique for landslide characterization and monitoring. *Remote Sens* 5:1045–1065
- Van Den Eeckhaut M, Vanwalleghem T, Poesen J, Govers G, Verstraeten G, Vandekerckhove L (2006) Prediction of lands slide susceptibility using rare events logistic regression: a case-study in the Flemish Ardennes (Belgium). *Geomorphology* 76:392–410
- Van Den Eeckhaut M, Poesen J, Verstraeten G, Vanacker V, Nyssen J, Moeyersons J, VanBeek LPH, Vandekerckhove L (2007) The use of LIDAR-derived images for mapping old landslides under forest. *Earth Surf Proc Land* 32:754–769
- Van Den Eeckhaut M, Muys B, Van Loy K, Poesen J, Beeckman H (2009) Evidence for repeated re-activation of old landslides under forest. *Earth Surf Proc Land* 34:352–365



Landslide Susceptibility Assessment Based on Remote Sensing and GIS in Lombok Island of Indonesia

Arifianti Yukni, Teerarungsigul Suree, Cita Akbar, Kuehn Friedrich, and Fuchs Michael

Abstract

In many cases, landslide that are causing severe disasters in populated downstream valleys occur in remote mountainous areas of Lombok Island. Those areas are difficult to access and to investigate by conventional ground-based mapping. Remote sensing contributes a way to collect data and information on remote and inaccessible terrain. Statistical approach using probability and weighting methodology has been applied to characterize landslide-prone ground. The methodology combines elements of techniques published by Greenbaum (Project summary report: rapid methods of landslide hazard mapping. Technical Report WC/95/30. International division. British Geological Survey. Key worth, Nottingham, UK, pp 12, 1995) and by Lee and Min (Environ Geol 40:1095–1113, 2001) allowing for increase of reliability of the landslide susceptibility map as the final product. Landslide inventory was supported through, and most of factors data have been derived through GIS processing and interpretation of satellite remote sensing data. Maps of factors weighted for significance in terms of landslide accountability and probability. The landslide susceptibility index (LSI) is the summation of each factors' weight multiplied by the class value of each pixel, pixel by pixel. This produces an interim landslide susceptibility map as the preliminary result. Validation of the results in the field composes the final landslide susceptibility assessment of Lombok Island. The study area was classified into five categories of landslide susceptibility: very low, low, moderate, high and very high.

Keywords

Landslide susceptibility assessment • GIS • Remote sensing • Lombok

A. Yukni (✉) • C. Akbar
Geological Agency of Indonesia, Ministry for Energy and Mineral Resources, Jl. Diponegoro No. 57, Bandung 40122, Indonesia
e-mail: yukni.a@gmail.com; akbarcita@gmail.com

T. Suree
Department of Mineral Resources, Ministry of Natural Resources and Environment, 75/10 Rama VI Road, Ratchatewi, Bangkok 10400, Thailand
e-mail: tee_suree@yahoo.com

K. Friedrich • F. Michael
Federal Institute for Geosciences and Natural Resources (BGR), Stilleweg 2, 30655 Hannover, Germany
e-mail: friedrich.kuehn@bgr.de; michael.fuchs@bgr.de

Introduction

During the period of 25 years in Lombok have occurred several landslides that caused many casualties and properties damage. Landslides in Lombok mostly occurred on the mountainous and hilly areas. The most destructive events with casualties occurred in West Lombok District, a large landslide triggered by 6.5 RS earthquake in Tanjung Sub district, caused 28 people killed, more 100 people injured, destroyed more than 200 buildings and 9,845 houses. On 1994, a landslide at Gerung killed 4 people and destroyed many houses. Following that year, on 4 and 6 November occurred in Aikmel Sub district, killed 31 people and damaged hundreds buildings and houses (Rachmat 2004).

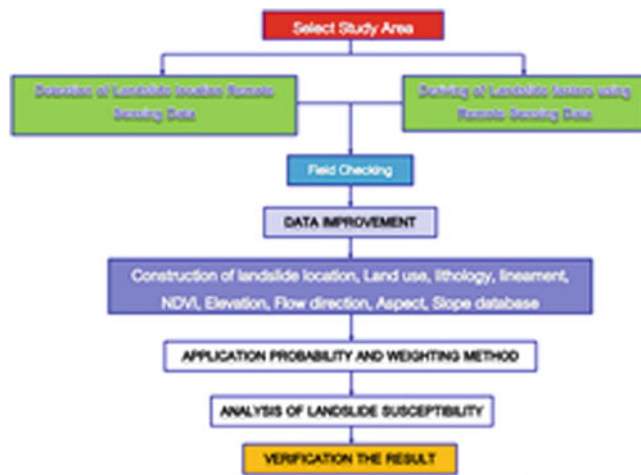


Fig. 1 Workflow

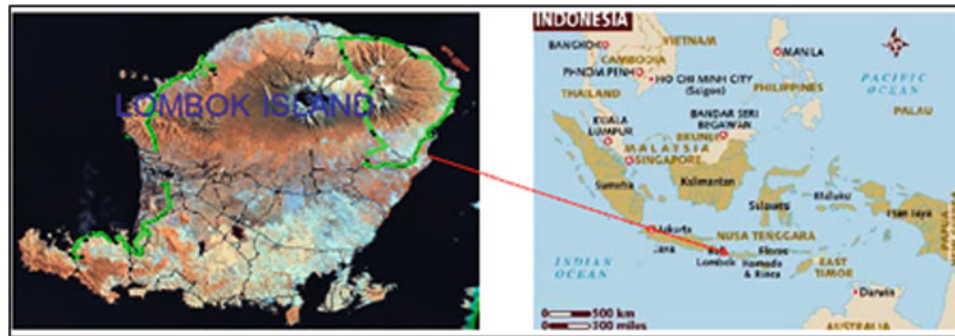


Fig. 2 Lombok Island

Landslide at Cerorong, Central Lombok District occurred prior to 1994 which continues until today, forming a deep and wide valleys (50–75 m), and located <40 m from settlements, roads and schools (Djaja 2011).

Remote sensing is providing a systematic, synoptic framework for advancing scientific knowledge of the Earth as a complex system of geophysical phenomena that, directly and through interacting processes, often lead to natural hazards (Zoran 2008) or in this case geological hazards, such as landslide. Remote sensing processed within a geographical information system (GIS), to derive a landslide susceptibility assessment. GIS are computer based systems with a high potential to archive, manipulate, analyze and display geo-referenced data (Aronoff 1989) and are becoming a major tool for this study.

In many cases, landslides occur in remote areas that are difficult to access. Remote sensing contributes to improving reliability of landslide susceptibility assessment through generalizing perspective provided by sensors in aircrafts and satellites, overall coverage of large areas at one moment, non requirement of entering remote and hazardous ground,

and the availability of new quality of remotely sensed data. A GIS and RS-based method for landslide susceptibility assessment is proposed by using a quantitative assessment of bivariate statistical analysis, in this study, using Frequency Probability Ratio (PR) method. The workflow of this study as shown in Fig 1.

Study Area

Lombok is an island in West Nusa Tenggara Province of Indonesia with an area of 5,435 km² with 3,098,480 inhabitants (BPS 2010). Lombok is located at 115°45'–116°45' E and 8°00'–9°00' S, next to Bali island is shown in Fig. 2. Topography at northern part of the island is mountainous area with Mount Rinjani as the highest peak

of 3,726 m above sea level, in the center is lowland, and the southern part is hilly. This region vulnerable to some naturally hazardous phenomenon such as landslide. There are conflicts of interest, between hazard assessment concerning the preservation of natural resources with the growth of economic activities. Public and private economic losses from landslides include not only the direct costs of replacing and repairing damaged facilities, but also the indirect costs associated with lost productivity, disruption of utility and transportation systems, and reduced property values (Schuster and Fleming 1986).

Geo-Factor Maps

Landslide susceptibility is the likelihood of a landslide occurring in an area on the basis of local terrain conditions (Brabb 1984). The landslide conditioning factor maps (here called Geo-Factor Maps) provide the information which may control the occurrence of areas prone to landslides we would like to predict. The following approved statistical

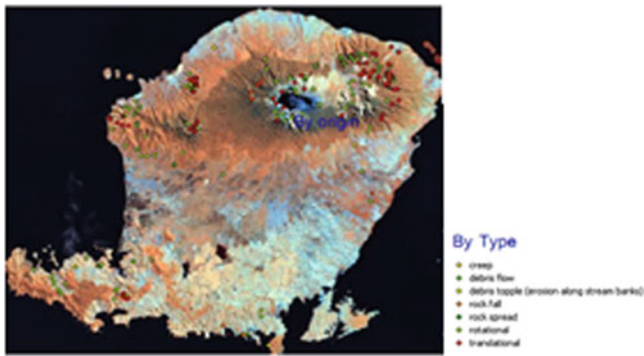


Fig. 3 Landslide distribution

approaches is Frequency Probability Ratio (PR) method will resolve the prediction areas prone to landslides by comparing the interrelation between landslide conditioning factors and the landslide spatial distribution.

Geo-Factor Maps represent a stack of parameter layers containing the input parameters for the statistical approach and provide the information which may control the occurrence of areas prone to landslides. The following Geo-Factor Maps affecting landslides was supported through, and most of have been derived through digital processing and interpretation of satellite remote sensing data. Depending on mapping scale and on general framework, satellite images have been used exclusively. The work with the optical satellite data was made very difficult as no useful up-to-date cloud-free images could be acquired (Kuehn et al. 2011). The results of remote sensing data interpretation had been spot-checked in the field between September 19th to 22, 2011.

Landslide Inventory

The inventory of landslides is indispensable input information for statistical analysis of susceptibility or hazardous areas prone to landslides. Inventory taken in the field is the best prerequisite for successful use of statistical model. However field survey is time consuming in certain pathless areas hard to realize. Therefore a remote sensing driven approach is often used to find landslides (Kuehn et al. 2011). Whereas Carr and Rathje (2008) can identify 94 % of the area affected by landslides using high resolution images from Quickbird, Nichol and Wong (2005) can identify 70 % with images taken from SPOT and IKONOS. Landslide inventory was derived from different sources.

The landslide inventory then stored in a database application called LIDIA, Landslide Inventory Database Indonesia. 147 landslides are of natural origin, 51 landslides are man-made triggered, and 24 events are without information as shown in Fig. 3.

Topographic Features

Topographic features information derived from ASTER GDEM data, a product of METI and NASA. Essential sensitive model parameters will be determined from Digital Elevation Models (DEM) resp. Digital Surface Models (DSM). The DSM is determined from the optical Advanced Spaceborne Thermal Emission and Reflection Radiometer (ASTER). ASTER GDEM is better represents areas with high relief energy, and available on the project area in ground resolution of 30 m. The parameters used in the statistical approach are slope angle and slope aspect, flow direction, streams of first and second order and elevation as shown in Fig. 4.

Geological Map

Information on lithology and lineament were obtained from Geological Map of the Lombok Sheet, West Nusa Tenggara produced by Geological Agency of Indonesia, shown in Fig. 5 (Mangga 1994).

The Lineaments have been mapped through visual interpretation of Landsat TM images, completed by Shaded Relief maps derived from ASTER GDEM.

Master image was the Landsat TM image of path/row 116/066, which was recorded on May 26, 1995. This image is 100 % cloud-free and of excellent radiometric quality. For interpretation, False Color Composite images have been derived from multispectral bands 4, 5 and 7 assigned with colors red, green, and blue (Kuehn et al. 2011), shown in Fig. 5.

Landcover/Landuse

The landcover/landuse classification is based on the spectral bands 1, 2, 3, 4, 5 and 7 which comprise the visual light, the near infrared and the short wave infrared. The unsupervised classification for Lombok was worked-out using the ENVI 4.8 ISO-Data Classification Tool for the Landsat ETM + SLC-Off images path/row 116/066 taken June 11, 2004 and October 15, 2009. Due to the specifics of this data several preprocessing routines have been applied prior to unsupervised classification. Final result of Unsupervised Classification for the Landsat ETM + SLC-Off subset image, taken October 15, 2009, after gap-filling with majority filter; classes: Unclassified, Water, Bare Ground, Urban and Bare Ground, Supposed Area of Fire, Forest 1, Forest 2, Sparse Vegetation 1, Sparse Vegetation 2, Bare Ground partly with Vegetation Coating, shown in Fig. 6 (Kuehn et al. 2011).

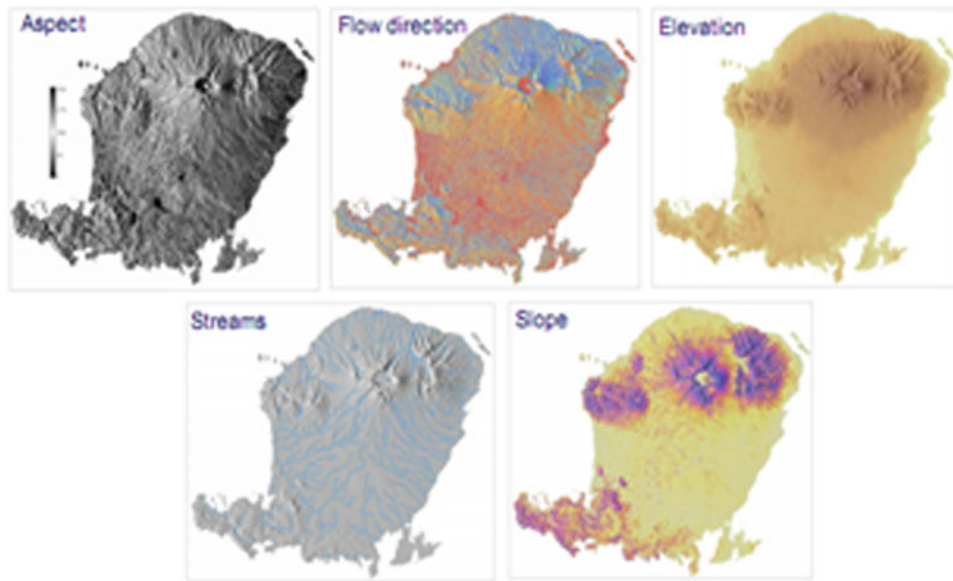


Fig. 4 Topographic feature

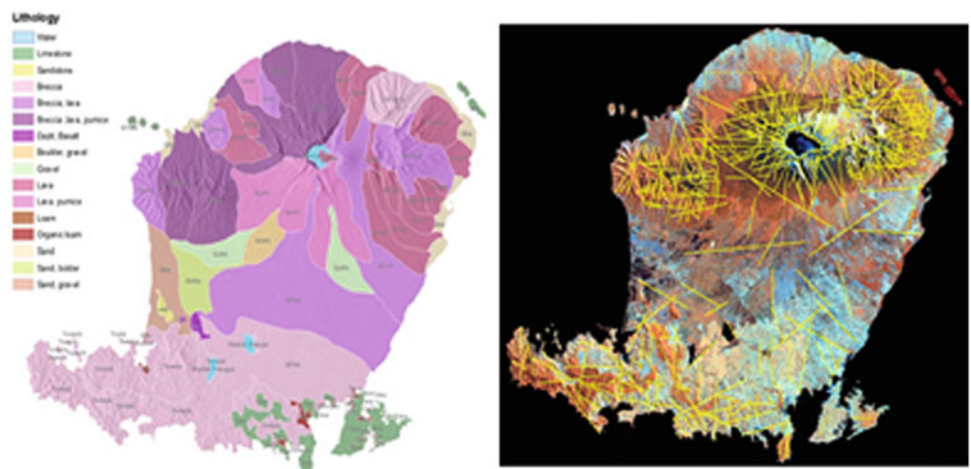


Fig. 5 Lithology and lineament map

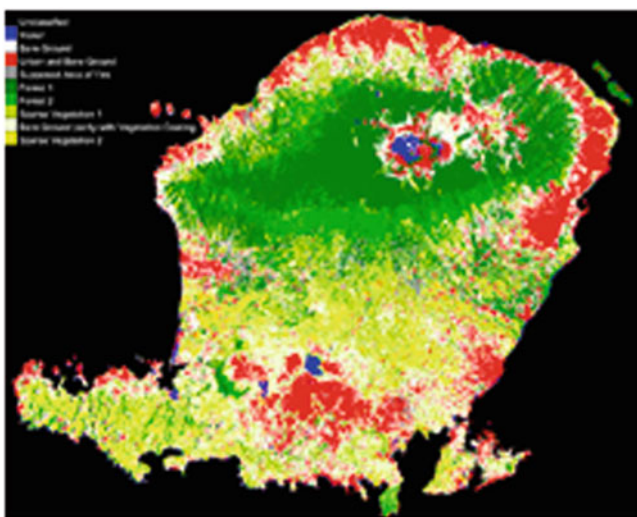


Fig. 6 Landcover map (Kuehn et al. 2011)

Vegetation Indices

The most common Vegetation index calculated from scenes of mentioned sensors is the Normalized Difference Vegetation Index (NDVI). NDVI data were determined from different sources; ASTER and Landsat 5, shown in Fig. 7. However ASTER data from one date doesn't cover the whole Island but two third of the Island are covered by two scenes from the same date. A scene with minimal cloud cover from 21.06.2010 was chosen for the calculation of NDVI Areas uncovered by ASTER data (W-part of Lombok) and gaps caused by clouds were replaced by MODIS NDVI from the date closed to the ASTER scene date. Whereas the differences in the data range have been adjusted by median calculation and subtraction. MODIS data have been adjusted to the ASTER data with an offset of -0.16 (Teerarungsigul 2006).



Fig. 7 NDVI map

Methodology

Image processing was done with the ENVI 4.8 software. All optical imagery has been corrected for the atmosphere using “Flaash Atmospheric Correction Module” running under ENVI as well. Other data layers listed above were processed and added to a Geo-database with ArcGIS 10 software. Then, a statistical approach using probability and weighting methodology was applied to extract standardized weights for the different layers (Fuchs et al. 2011). The methodology uses a combination of components published by Greenbaum (1995) and by Lee and Min (2001) allowing for increase of reliability of the landslide susceptibility map as the final product.

The spatial data analysis and integration for landslide assessment are divided into several steps by using the probability and weighting method, the spatial relationship between landslide occurrence and related factors such as slope, aspect, and so on, were calculated. We assigned probability of landslide occurrences in each factors class as the relationship between landslide location and each factor’s class, that is ratio of landslide occurred cell and total cell. We assigned weight of landslide occurrences in each factors class and factor’s, that is importance of classes and factors effected on landslide occurrence.

The Analysis

A bivariate statistical analysis was applied to this study area, using Frequency Probability Ratio (PR) method. PR analyzes the relation of the landslide occurrence due to the occurrence frequency of the landslide within the parameter

classes (geo-factor maps). All parameter were used, since this method supports additional ranking weighting that allows to reduce the influence of the weak parameters. The calculation of the landslide susceptibility index (LSI) by summation of each factors’ weight multiplied by the class value of each pixel, pixel by pixel.

$$Fr_i = \frac{S_i/N_i = \text{Class_Density}}{S/N = \text{Map_density}} \quad (1)$$

$$LSI = \sum Fr_i \left(\text{Weighting of each factors' type} \right) \quad (2)$$

The first step is to calculate the relationship between landslide location and factors. The result is number of landslide location in each item of factor. Step 2 is using the probability method to calculate probability of landslide occurrence in each class of factor (probability ratio).

The next step is assign weight of factor. Calculation of weights of each factors’ classes (class weight) Calculation of weights of factors (FW) in terms of reliability probability (RP) and accountability probability (AP) (Table 1). Reliability probability (RP) was calculated by the percentage area of factors corresponding to landslides. It was computed for each factor as equation below:

$$RP = \frac{\sum \% \text{ Landslide point in classes having a probability ratio } \geq 1}{\sum \% \text{ Landslide \& non-landslide area in the same classes}} \quad (3)$$

The accountability probability (AP) was calculated by the total landslide population accounted for each factor. It was computed for each factor as equation below:

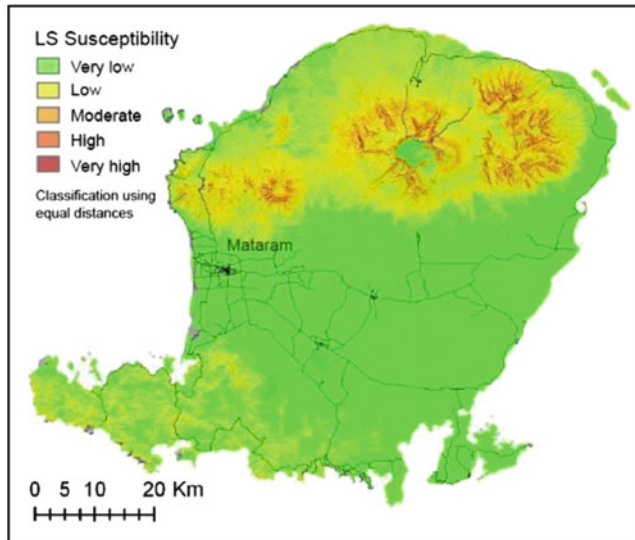
$$AP = \frac{\sum \% \text{ Landslide point in classes having a probability ratio } \geq 1}{\sum \% \text{ Landslide point over the entire study area}} \quad (4)$$

The final result is composition of interim landslide susceptibility map. The level of landslide susceptibility is measured on the ordinal scale based on the equal interval values. Then, five levels of relative landslide occurrence are defined on a landslide susceptibility map: (1) very low; (2) low; (3) moderate; (4) high; and (5) very high hazard, the map shown in Fig. 8.

The verification method is performed by comparison of existing landslide data with landslide susceptibility maps by tabulation area in GIS environment. The validation results show satisfactory agreement between the landslide hazard map based on combination of reliability and accountability (weighted logical weight) and existing landslide location data.

Table 1 Weight of importance of factors

| Factors | Reliability | | Factors | Accountability | | Factors | RP + AP |
|----------------|-------------|--------|----------------|----------------|--------|----------------|---------|
| | RP | Weight | | AP | Weight | | Weight |
| Slope | 3.86 | 22 | NDVI | 91.96 % | 22 | Slope | 18 |
| Elevation | 2.61 | 19 | Lineament | 79.70 % | 19 | NDVI | 18 |
| Landuse | 2.15 | 17 | Lithology | 79.40 % | 17 | Lineament | 17 |
| Lineament | 1.81 | 14 | Slope | 76.65 % | 14 | Elevation | 13 |
| Flow direction | 1.39 | 11 | Aspect | 69.54 % | 11 | Lithology | 12 |
| Aspect | 1.24 | 8 | Flow direction | 63.82 % | 8 | Landuse | 10 |
| Lithology | 1.23 | 6 | Elevation | 54.27 % | 6 | Flow direction | 10 |
| NDVI | 1.18 | 3 | Landuse | 44.72 % | 3 | Aspect | 10 |

**Fig. 8** Landslide susceptibility map

Discussion

GIS and Remote Sensing-based for landslide assessment applies some factors such as slope, elevation, flow direction, aspect, lithology, lineament, landuse and NDVI. The analysis resulted in slope, NDVI and lineament as the most influence factors. The slope factor ranges from 45 to 50 while dense forest is the land-use class that has a high probability of landslides. Landslides in Lombok mostly occurred on the mountainous and hilly areas. The type of landslide is mainly rotational and translational.

Lithology and lineament was examined to find out how geological factor affect the landslides. The analysis demonstrates that lineament is more affected. It creates weak zone that vulnerable to landslides. This shape built by volcanic and fault activities. The presence of pumice as unconsolidated rock proceeds as a weak layer for landslides movement.

The spatial data analysis and integration for landslide assessment can be divided into three steps:

- To overlay the landslide distribution map with the factors.
- To produce the landslide susceptibility map.
- To perform the probability analysis and weighting.

The landslide susceptibility maps can be derived based on:

- Combination of reliability probability and accountability probability (logical weight).
- The accuracy of the result depending on the quality of input data.
- This landslide susceptibility can be predict, where landslide will be occurs.

GIS and Remote Sensing technology can ease landslide hazard assessment. It provides information for immediate planning and operation of disaster relief missions. It also provides a high efficiency and optimizes time resources. The methodology has developed from exclusive technique to standard approach for provision of Geo-information, especially in a remote and inaccessible area. However a field work needs to be done to validate the analysis. The accuracy of the analysis also depends on the quality of input data. This landslide susceptibility can be predicts, where landslide will be occurs. The resulting landslide susceptibility map will be the base for future risk-sensitive land use planning and DRR activities on Lombok Island.

Acknowledgments The authors would like to thank Matthias Dorn, D. Balzer, K. Tissahadi, J. Torizin, Dicky M., and D. Kuhn, for their work and support in the research of Landslide Susceptibility Assessment in Lombok. This research was fully supported by the Geological Agency of Indonesia and Georisk Project (BGR/German Federal Institute for Geosciences and Natural Resources) in 2011. Credits are given to data provider as USGS, USDA, NCDC, NASA and METI.

References

- Aronoff S (1989) Geographic information systems: a management perspective. WDL Publications, Ottawa, p 294
- BPS (Statistical Agency) (2010) Hasil Sensus Penduduk 2010 Nusa Tenggara Barat: data aggregate per Kabupaten/Kota. Lombok. BPS Nusa Tenggara Barat
- Brabb EE (1984) Innovative approaches to landslide hazard and risk mapping. In: Proceedings of the IV international symposium on landslides, vol 1. Toronto, pp 307–323
- Carr LP, Rathje EM (2008) The use of remote sensing to identify landslides caused by the 2004 Niigata-Ken Chuetsu Earthquake in Japan. In: Proceedings of 6th international workshop on remote sensing for disaster management applications, Italy, 11–12 September

- Djaja (2011) Laporan Singkat Peringatan Dini Gerakan Tanah Lombok Tengah. Bandung. Pusat Vulkanologi dan Mitigasi Bencana Geologi
- Fuchs M, Kusnadi M, Mukhlis T, Ghele Radja Z (2011) The geo-factor maps. Mitigation of Georisks. Poster and presentation
- Greenbaum D (1995) Project summary report: rapid methods of landslide hazard mapping. Technical Report WC/95/30. International division. British Geological Survey. Keyworth, Nottingham, UK, p 12
- Kuehn F, Teerarungsigul S, Fuchs M, Arifianti Y, Cita A, Tissahadi K (2011) Draft of technical report: training and implementation of landslide susceptibility assessment methodology using remote sensing. Mitigation of Georisks
- Lee S, Min K (2001) Statistic analysis of landslide susceptibility at Yongin, Korea. *Environ Geol* 40:1095–1113
- Mangga SA (1994) Geological map of the Lombok Sheet, West Nusatenggara. Pusat Penelitian dan Pengembangan Geologi, Bandung
- Nichol J, Wong MS (2005) Detection and interpretation of landslides using satellite images. *Land Degrad Dev* 16:243–255
- Rachmat H (2004) Potensi dan Mitigasi Bencana Geologi di Nusa Tenggara Barat. Mataram. Publikasi Khusus Ikatan Ahli Geologi Indonesia
- Schuster RL, Fleming RW (1986) Economic losses and fatalities due to landslides. *Bull Assoc Eng Geol* 23:11–28
- Teerarungsigul S (2006) Remote sensing for geohazard study in case of landslide and field investigation in northern part of Thailand. PhD thesis SUT, Nakhon Ratchasim
- Zoran MA (2008) Integrated geospatial system for seismic hazard assessment in Vrancea area, Romania. In: *Proceedings of SPIE 7110, Remote Sensing for Environmental Monitoring, GIS Applications, and Geology VIII*, 71100L. doi:[10.1117/12.799939](https://doi.org/10.1117/12.799939)



Application of Remote Sensing and GIS Techniques in Landslide Hazard Zonation of Hilly Terrain

Rajeshwar Singh Banshtu and Chander Prakash

Abstract

Himalayan terrain comprise of rolling mountainous and steep topography. The deep gorges, bank less streams, sprawling catchment area, perennial snow and valley areas form the landscape in Himalayan region. It is well known that the occurrence of landslides is controlled by a lot of morphological, geological, and human factors. Prominent factors include steep slopes, underlying lithology, structure, geomorphology, land use, drainage and vegetation cover. Information on landslides and some of these influencing factors can be extracted from remotely-sensed data products through visual and digital image processing techniques. A comprehensive spatial database can be created in Geographic Information Systems (GIS) incorporating other ancillary information. In this paper a landslide hazard map is prepared using the information value method. Information Values are computed using all the thematic layers. The road network is draped over this hazard map and the road stretch that falls in the highly landslide prone area is identified. Finally an alternate route has been proposed ensuring safety from landslide hazard.

Keywords

Landslides • Deep Seated Slope Gravitational Deformations • Spatial Decision Support System

Introduction

Landslides, like other events such as flood, earthquake and avalanches are natural phenomena which being uncertain are difficult to predict. Landslide is defined as the movement of mass of rock, debris or earth down the slope. The economic loss due to natural hazards in developing countries is about 1–2 % of Gross National Product (GNP), where the contribution from landslide is about 1/4 of the total loss (Hansen 1984). To minimise the damage caused by landslides, information is required about when and where it will occur, about its characteristics, what could be its damaging potential and what are the elements (i.e., human life, roads etc.) at risk and their vulnerability. The characteristics of the landslides

include location, size, mechanics of sliding, composition (i. e. rock, earth or debris), velocity and travel distance. Landslide hazard is commonly shown on maps that display the spatial distribution of landslides and probability of their occurrence. Remotely sensed data products provide most authentic and accurate information on Earth's surface features and processes involved. In most of the studies, remotely sensed data products have been used for mapping of landslides and extraction of information on various geo-environmental parameters such as lithology, structure, landuse, drainage, road excavations and vegetation cover, which directly or indirectly influence slope stability of a region. In the recent past, various methods and techniques have been proposed to analyse these factors and to produce maps portraying the probability of occurrence of similar phenomena in future. Broadly these methods are can be classified as direct and indirect methods (Hansen 1984).

The direct method consists of geomorphological mapping according to which a zonation is made of those sites where

R.S. Banshtu (✉) • C. Prakash
Civil Engineering Department, National Institute of Technology,
Hamirpur, HP 177005, India
e-mail: banshtu.rajeshwar@gmail.com; chandermanali@gmail.com

failures are most likely to occur. The indirect method includes two different approaches, namely the heuristic (knowledge-driven) and statistical (data-driven) techniques (Carrara et al. 1991, 1992). In the heuristic approach, landslide-influencing factors are ranked and weights are assigned according to their assumed or expected importance in causing mass movements. In the statistical approach, the role of each factor is determined based on the relationship with the past/present landslide distribution. With the advancement of computing technology, it has become easier to apply various statistical methods to analyse landslide phenomena and derive hazard zonation maps. In this study we have applied statistical bivariate method for the generation of landslide hazard zone map.

Bivariate Statistical Analysis

In bivariate statistical analysis, each factor map (for example, slope, geology, landuse) is combined with the landslide distribution map and the weight values based on landslide densities are calculated for each parameter class (for example, slope class, lithologic units, land use type). Brabb et.al. (1972) were the first to provide example of such an analysis. They performed a simple combination of a landslide distribution map with a lithologic map and a slope map. Quantitative analysis based on information value serves two purposes: (a) it enables quantification of geologic information, which are otherwise descriptive, hence not suitable for any type of quantitative analysis and (b) it reveals statistical relationship of geoenvironmental parameters and landslide phenomenon (Champati Ray et al. 1995).

Study Area and Data Used

Study area chosen for the present study is the Doon valley in Dehradun district of Uttarakhand, India. The study area is confined between the 30°15' and 30°30' N and 78° and 78° 10' E, covering an area of 440 km² in Dehradun and Tehri-Garhwal districts of Uttarakhand, India. The increased anthropogenic activities such as mining, road excavations, industrialization and deforestation have led to landslides at many places in the region. The area is characterised by a rugged topography with hill ranges rising steeply from about 600 m above mean sea level to over 2,300 m with deep cut valleys. High mountain relief, steep slopes, fractured and jointed rocks constitute a very favourable setting for failure, affecting massive basement rocks. Slope varies almost from level in the plains to very steep in the mountainous regions. The study area includes parts of the Lesser and Sub Himalayan zones and falls in the Zone IV of the seismic zone map of India.

The Lesser Himalaya or Mussoorie mountain range in the northwest and northeastern parts, which is bounded by the Major Boundary Thrust (MBT) in the south, comprises of the Pre-Cambrian shelf. Geological formations in the Lesser Himalaya are rocks of the Jaunsar (Chandpur phyllites and Nagthat quartzites) and Mussoorie group (shales, sandstone, greywacks, calcareous slates, dolomite and lime stone of Blaini-Krol-Tal sequence). Though sedimentary in nature, the rocks have very low inter-granular porosity and are characterised by fissures, fractures and joints.

The Doon valley consists of young sedimentary material over tertiary rocks. Doon gravels consists partly of crushed Siwalik cobbles, angular pebbles of quartzites, slates and shales from the Nagthat, Chandpur and Tal formations and limestone pebbles from the Krol limestone with clay beds.

Siwalik hills which are to the south of Main Boundary Thrust (MBT) consists mainly of tertiary rocks. The area is also characterised by a number of faults, joints and thrusts in the region exhibiting the structural control and tectonic actives in the area. Three broad geomorphic complexes in the area are structural hills, residual hills and plains with a range of drainage patterns from dendritic to parallel and radial.

Quarrying the Mussorie limestone and establishment of limestone-based chemical industries has led to high levels of pollution, slope toe removal due to excavations and deforestation. All these activities have accelerated the rate of soil erosion and other degradation processes in the area.

Data Acquisition and Generation of GIS Data Base

In the present study, most of the data layers or thematic layers are derived from remotely sensed data products in conjunction with the field observations and other ancillary information. Important spatial objects are extracted from these data and the hard copies are converted into digital form so that it can be entered into the system. This requires pre-processing of the data prior to encoding and attributing. For example, image enhancement and classification is done for extracting important spatial objects from satellite data, digitisation to convert hard copy data set into digital form and georeferencing so as to know the geodetic location of a feature.

Image Enhancement

For extracting spatial objects by visual interpretation, image is enhanced by applying various image processing techniques. Using contrast-stretching technique, the slight differences between spatial features are amplified and were

observed readily. By principal component transformation a new set of layers (also called components) are generated which are not correlated with each other. PCT2 image obtained after principal component transformation was found to offer better discrimination capability than the rest. False Colour Composite was generated from bands 4, 3, 2 respectively. In this FCC geomorphological features, vegetation cover and land use pattern can easily be identified. FCC of principal component images highlights landforms, geology and water bodies.

Classification

In the present study supervised classification technique, which identifies object of interest prior to classification is used. Training samples were taken from the features identified in the field and from the inventory information. For classification maximum likelihood classifier is used. The final land use/land cover map is prepared by integrating data. Various land use/land cover classes are barren land, cultivated land, urban area, sparse vegetation land, forest area and rivers.

Visual Interpretation

Landslide scars and escarpments are delineated and mapped using PAN data and FCC. In PAN data change in tone, concave shape, eroded slopes were used as key in demarcating the landslides. In PAN data, the run out surface of the slide on moderate slope can be easily identified and mapped. Vegetation cover, high moisture content and proximity to hills is used as key in demarcating landslides on FCC. Vegetation cover and shape are the potential factors in identifying landslides from multispectral band data. Landslide movement has disrupted vegetation cover and has eroded the soil on rock surfaces. As a result, rock surfaces are exposed on landslide area with different spectral characteristics. Landslide debris forms a concave shape with moisture content higher than the existing surface resulting in different spectral characteristics. Landslides occurred in the area are identified and mapped using FCC of principal component images. All the demarcated landslides are stored in one data layer. Various geomorphological features are identified easily on this FCC and also high pass filter image is used for interpretation of the geomorphic features. Main landforms identified in the region are structural hills, residual hills and plains. Various geological and water bodies are visually interpreted from the FCC of principal component images. Debris with higher moisture content than the surrounding area is readily identified in this FCC. Drainage pattern is mapped from the SOI topographic

maps and band-4 imagery of LISS-II data. Lineaments and structural features are visually interpreted from directional filtered products of contrast stretched band-4 image. Lineaments are also extracted from the first principal component image, which accounts for the maximum spectral variation. Lithological and structural interpretation was carried out with the help of published geological map (Panikkar 1996).

Data Processing

The maps were digitised in line mode (vector format) and were converted into raster format for spatial analysis. Spatial objects identified and delineated on image data were either first traced and then digitised or onscreen digitisation was also carried out. Contours at an interval of 100 m are digitised from SOI topographic maps of the area. From the contour map, Digital Terrain Model (DTM) of the study area is prepared. To create DTM, the digitised contour lines are interpolated using standard procedure in the ILWIS 2.1. From the DTM, slope steepness map giving the inclination at a point is calculated using following function of ILWIS 2.1.

$$\text{Slope} = \text{hyp} ((dx,dy)/\text{pixelsize}) * 100$$

where dx and dy are linear directional filters.

From the DTM, aspect map showing the direction of slope, is calculated using following formula

$$\text{Aspect} = \text{raddeg} (\text{atan2}(dx,dy) + \pi)$$

Three dimensional view is obtained by draping the FCC321 on DTM. Drainage influence zone and lineament influence zones are generated using the neighbourhood operations module available in ILWIS 2.1. First a distance map is generated which is further classified into two zones of influence i.e. high and negligible. It is assumed that lineaments and various streams influence landslide upto a distance of 250 m. Hence the two zones generated comprise area within 250 m and outside 250 m respectively from the corresponding fault or streams.

Georeferencing

Before entering any data into a GIS environment, all the data should share a common coordinate system. This is accomplished by georeferencing all the data with respect to a base map. The base map has been prepared from the SOI topographic maps at 1:50,000 scale with known coordinates. All the data have been georeferenced to the base map by means of an affine transformation. LISS-II data have been georeferenced and resampled using the nearest neighbourhood interpolation method.

Data Analysis and Hazard Zonation

The occurrence of landslide depends generally on complex interactions among the various geo-environmental parameters. Analysis of landslide hazard requires an understanding of the relationship among the parameters. In the present study, spatial statistical modeling technique, i.e. information value method (Yin et al. 1988) is evaluated and used to assess the potential of such methodology for landslide hazard zonation.

Information Value Method

By comparing the different conditional probabilities with the average landslide probability over the entire investigated area, it is possible to know the relative importance of each parameter affecting landslides in the area. With some modifications, this approach has been applied in the present study. The information value equation is expressed as the logarithmic ratio of conditional probability of a thematic feature and the average landslide probability over the entire area, i.e.

$$I_j = \frac{P\left\{\frac{L}{A_j}\right\}}{P\{L\}} \quad (1)$$

where I_j is the predictive information of occurrence of event L if feature A is present under state j . $P\{L/A_j\}$ is the conditional probability of event L to occur under the condition of feature A and state j . This is same as the conditional probability of landslide (L) to occur because of spatial feature (A) present in one of the thematic (j^{th}) layer. $P\{L\}$ is the probability that event L will happen in the selected area irrespective of any evidence. For example, an area with total $N\{\text{Total}\}$ pixels shows landslides in say $N\{L\}$ pixels then the average density of the landslides in the study area is equal to $N\{L\}/N\{\text{Total}\}$. This is same as the probability of a random pixel containing landslide in the study area and this is known as prior probability, i.e. $P\{L\}$. The larger the value I_j , greater the risk of landslide for pixel i .

Calculation of Information Value Using GIS

In the present study, parameter values required to calculate information value are obtained by crossing landslide map with a certain parameter map. Map crossing results in a cross table showing the number of pixels per class occupied by landslides and total number of pixels in each class. The remaining values, necessary to calculate information value,

are obtained from these values. In the present study mapcalc module of ILWIS 2.1 is used to calculate information value

$$i\text{value} = \log(\text{classden}/\text{mapden})$$

where

$$\text{classden} = \text{nsclass}/\text{nclass}$$

$$\text{mapden} = \text{sum}(\text{nsclass})/\text{sum}(\text{nclass}) = \text{nsmap}/\text{nmap}$$

$$\text{nsclass} = \text{number of pixels with landslides in a class}$$

$$\text{nclass} = \text{number of pixels in the class}$$

$$\text{nsmap} = \text{total number of landslide pixels in the map (thematic layer)}$$

$$\text{nmap} = \text{total number of pixels in the map}$$

$$i\text{value} = \text{information value}$$

For calculation of information values, 40 landslides identified using LISS-II data are used.

The information values are calculated for each of the classes in all the thematic layers.

Hazard Zonation

Computed information values are attached to each class by replacing the class attributes by information values. The resulting map was a value map encoded with information value instead of class name. Based on the information values for all the thematic layers, value maps representing information value are generated. All raster files containing the information value for each thematic layer were then added together using simple map combination operation in ILWIS 2.1. The resultant data layer obtained was reclassified into hazard classes by grouping a range of information value into a single class. The criteria for defining the limits of each zone is obtained by plotting a graph between number of landslide pixels taken for the purpose of model developing and information value obtained.

Pixels containing higher information values were classified as very high hazard zones and cells with the least values were classified as very low hazard zones. Rest of the pixels were classified into low, average and high zones depending upon the proximity of their information values from very low and very high hazard zones. Resultant map is hazard zonation map showing the division of land surface into different zones.

Accuracy Analysis

To check the reliability of the method, 21 landslides covering an area around 6,000 m² and 1182 pixels, are taken. These are mapped from IRS-PAN data and from published map (Panikkar 1996) of landslide locations in the area.

Accuracy was calculated in a very simple manner by calculating the percentage of pixels falling in the predicted unstable and potential landslide zones. It was observed that

80 % of the landslide pixels fall in the predicted landslide hazard potential zones.

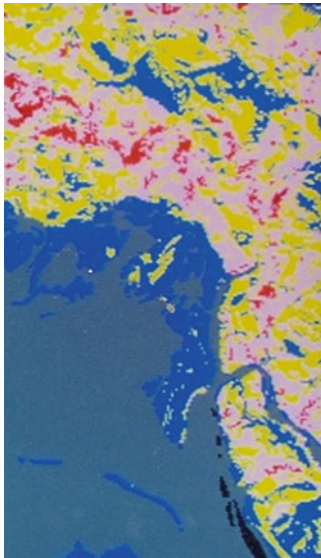
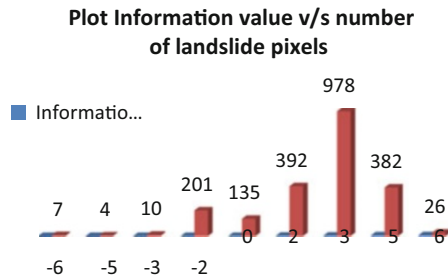


Fig. 1 Landslide hazard zonation map



Fig. 2 Roads draped over hazard zone map

Route Selection

The digitized road network from the SOI topographic maps is draped on to the final hazard map (Fig. 1). The road stretch that is falling on the highly hazardous zone can be easily marked by visual interpretation. The alternative route have been located passing through regions having low and very low hazard zones. Three routes have been identified and are shown in Fig. 2. An extensive survey is required on the above proposed routes to finalize the most optimum route taking care of gradient criterion. While deciding the final route, it should be kept in mind that the already existing small roads are made use of for connecting the origin and destination of our interest.

Conclusion

Planning for the development and to reduce the loss of property and risk to human life in hilly regions with potential landslide occurrence is of primary concern. Such tasks require reliable and up to date information about the area susceptible to landslides, i.e. potential landslide prone zones. Hazard zones draped on to DTM and also draped with road provide very useful and vital information about risk on state highways and also to human settlements. The approach in the study offers a new dimension on hazard preparedness, as the hazard zone map can be updated in a very short time using GIS, as and when required. Whereas, it would take enormous time and cost if conventional technologies are used.

References

- Brabb EE, Pampeyan EH, Bonilla MG (1972) Landslide susceptibility in San Mateo County, California. US Geological Survey Miscellaneous Field Studies Map 360
- Carrara A, Cardinali M, Detti R, Guzzetti F, Pasqui V, Reichenbach P (1991) GIS techniques and statistical models in evaluating landslide hazard. *Earth Surf Process Landform* 2:172–183
- Carrara A, Cardinali M, Detti R, Guzzetti F, Pasqui V, Reichenbach P (1992) Uncertainty in assessing landslide hazard and risk. *ITC Journal* 2:172–183
- Champati Ray PK, Lakhera RC, Prusty BG, Bhan SK (1995) Spatial statistical modelling for landslide hazard zonation in Himalayan terrain using remote sensing and GIS techniques. In: Muralikrishnan II (eds) *GIS applications*. pp 297–304
- Hansen A (1984) In Brunnsden D, Prior DB (eds) *Landslide hazard analysis in slope stability*. Wiley, New York, pp 523–602
- Panikkar SV (1996) A geomorphic evaluation of the landslides around Dehradun and Mussoorie, Uttar Pradesh, India. *Geomorphology* 15:169–181
- Yin KL, Yan TZ (1988) Statistical prediction model for slope instability of metamorphosed rocks. In: Bonnard C (ed) *Proceedings of fifth international symposium on landslides*, vol 2, Lausanne, Balkema, Rotterdam, The Netherlands, pp 1269–1272



Mapping the Deformation of Shuping Landslide Using DInSAR and Offset Tracking Methods

Jinghui Fan, Hao Lin, Ye Xia, Hongli Zhao, Xiaofang Guo, and Man Li

Abstract

Shuping landslide, belonging to Zigui county, Hubei province, is located on a north-inclined slope at the south bank of Yangtze River and about 50 km away from the Three Gorges Dam. The landslide occupies less than 1 km² and is covered by densely vegetations. Since the first impoundment of the Three Gorges Reservoir ended on June 15, 2003, the landslide has suffered obvious deformation. The maximum value of Shuping landslide in special month is up to several decimetres.

Concerning Shuping landslide displacement mapping, both DInSAR and offset tracking methods have been limited by the multi-metric spatial resolution of the previous generation of space-borne SAR sensors (e.g. ENVISAT ASAR or PALSAR).

In this paper we use 4 TerraSAR-X Spotlight images with submetric spatial resolution and apply both DInSAR and offset tracking method to map the deformation field of Shuping landslide. Three images acquired in January, 2012 are processed with DInSAR method. And the other one acquired in January, 2013. As for the offset tracking method, 1 pair with time baseline near 1 year is processed.

After the deformation field mapping, two deformation cones are identified by both DInSAR and offset tracking methods. It is shown by our work that high spatial resolution SAR data can provide an unprecedented level of high density and high precision measurement for recognizing the landslide surface deformation. Simultaneously, the measurement has the guiding function for selecting point location to GPS and leveling.

Keywords

Shuping landslide • terraSAR-X spotlight image • DInSAR • Offset tracking

J. Fan • H. Zhao • X. Guo • M. Li
Remote Sensing department, China Aero Geophysical Survey &
Remote Sensing Centre for Land & Resources, Beijing 100083, China
e-mail: jhfan2004@qq.com; zhaohl@agrs.cn; guoxf@agrs.cn;
lim@agrs.cn

H. Lin (✉)
School Of Land Science and Technology, China University of
Geosciences, Beijing 100083, China
e-mail: 745636087@qq.com

Y. Xia
German Research Centre for Geosciences, PB 1.4, Telegrafenberg A17,
14473 Potsdam, Germany
e-mail: xiaye0803@gmail.com

Introduction

Since the middle of the twentieth century, with the world population continue to grow the space of human's activity gradually expanded and the large scale of the project activity are increasing, together with the influence by global climate change and other factors, landslide occurred frequently and caused increasing economic losses and casualties. The latest 2012 China Land Resources Communique ([China Government 2012](#)) pointed out : in 2012 , a total of 14,322 geological disasters occurred in China, in which there are 10,888 from landslides , accounting for 76 % of all types of

geological disasters, landslides seem to have becoming the most serious natural disasters in China.

Landslide is a geological phenomenon and widely distributed in every province in China, particularly in the Midwest, southwest part, south China and east China. Most of the landslides due to its long development cycle, more unstable, when suffer from external power. It's very easy to fall down and produce powerful destruction, leading to significant damage to people's life and property.

During analysis of the formation mechanism of landslides, how to implement an effective monitoring and early warning becomes particularly important for protecting people's livelihood. Traditional landslide monitoring such as the surface deformation monitoring, the surface crack monitoring, deep displacement monitoring, underground water level monitoring, deep pore-water pressure monitoring and in-situ stress monitoring, etc (Xia et al. 2012), which can't response the overall landslide deformation trend very well because of the sparse monitoring point. Thanks to the development of Synthetic aperture radar (SAR) technology recently years, which can make up for the deficiency of the traditional monitoring methods.

DInSAR technology has become a well-known method in surface deformation, and there are many successful examples in landslide deformation monitoring, its precision can reached to sub-cm level. However, due to the inherent characteristics of DInSAR technology, DInSAR is hardly to obtain the surface displacement in areas with dense vegetation covered, mutation surface deformation because of the easily lead to loss of coherence (Colesanti and Wasowski 2006; Hilley et al. 2004; Xia et al. 2002). Offset tracking technology can make up for the lack of DInSAR technology because of which doesn't rely on the coherence of SAR signal but using backscatter intensity information. However, over-reliance on the resolution of the SAR images, the offset tracking technology deformation monitoring accuracy is just about 1/20 of the SAR image resolution (Strozzi et al. 2002; Raucoules et al. 2012). Although its accuracy cannot be the same as the DInSAR technique which can reached sub-cm, but it's also very useful for detection some areas with larger deformation. The lower resolution SAR satellites launched before 2007 are almost cannot be used in offset tracking technology to detect such a small area with small deformation like landslide, The higher resolution SAR satellite terraSAR-X and cosmo-SkyMed are launched inject new vitality for this technology after 2007, which take offset tracking technology into an practical significance in landslide monitoring with small area.

General Situation of the Study Area

Shuping landslide, belonging to Zigui county, Hubei province, is located on a north-inclined slope at the south bank of Yangtze River and about 50 km away from the Three Gorges Dam (Fan et al. 2010a, b), Geographical coordinates is about E110°37'00", N30°37'59" (shows in Figs. 1 and 2). The landslide occupies less than 1 km² and is covered by densely vegetations all over the year. Since the first impoundment of the Three Gorges Reservoir ended on June 15, 2003, the landslide has suffered obvious deformation. The maximum value of Shuping landslide in special month can reach several decimeters, which bring immeasurable threat to the Yangtze River waterway.

The Data Source

The high-resolution radar satellite TerraSAR-X reliably provides high-resolution SAR imagery with a resolution up to 1 m independent of weather conditions. With its active phased array SAR antenna (frequency 9.6 GHz), TerraSAR-X acquires new high-quality radar images of the entire planet whilst circling Earth in a polar orbit at 514 km altitude (Eineder et al. 2009). Perpendicular baseline is determined by the distance between two observations along the LOS (Line Of Sight) direction and plays an important role in InSAR technique. Long perpendicular baseline tends to cause the geometric decorrelation leading to innegligible phase errors. As for the 6 TerraSAR-X images (whose parameters are listed in Table 1) used in this paper.

At the same time, some CR reflectors were established in some representative point on the landslide for auxiliary DInSAR deformation monitoring. In order to analysis the SAR monitoring accuracy, we also had set level and GPS monitoring point on every CR reflector.

Method and Result Analysis

The particularity of Shuping landslide bring some inconvenience for deformation monitoring by the use of DInSAR method, especially in 4–9 month every year. It can be divided into three main aspects: (1) the landslide is covered by high-density orange trees all the year, especially this period is the season of orange trees growing, the landslide surface vegetation changed largely in every month; (2)

Fig. 1 Location of Shuping landslide

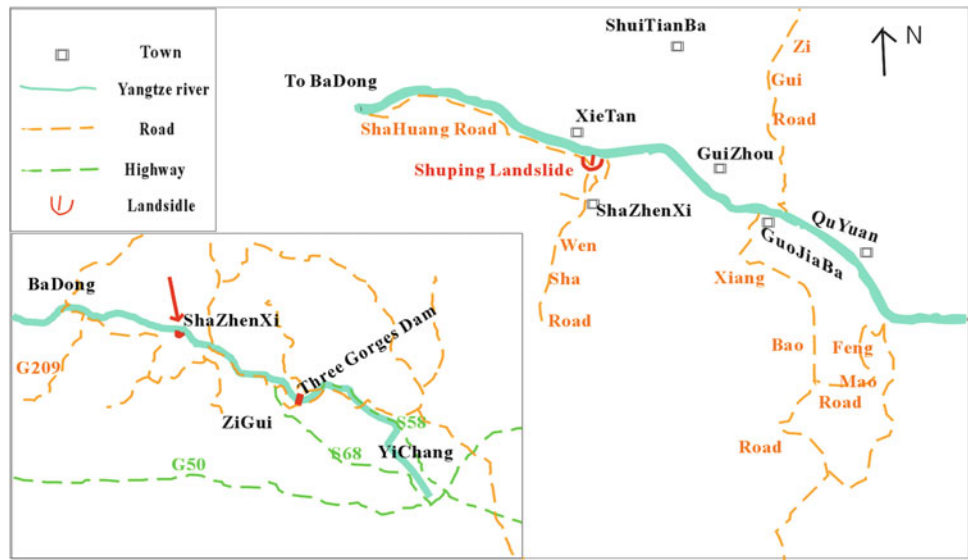


Fig. 2 3D view of the landslide

Table 1 Parameters of the SAR data used in this paper

| Acquired time (YYYYMMDD) | Other parameters |
|--------------------------|----------------------------|
| 20120102 | Polarization: HH |
| 20120113 | Descending |
| 20120124 | Right look |
| 20130110 | Look angle: 43.6° |
| | Range pixel size: 0.45 m |
| | Azimuth pixel size: 0.86 m |
| | Bandwidth: 300 MHz |

before the flood season coming, a large amount of water fall down from Three Gorges Dam, the river water level changing dramatically during this period, and the largest falling is up to 30 m, lead to the one side of landslide lost its backing and the sliding resistance decreases. (3) In the meantime, here is the rainy season, the infiltration of rainwater, leading to an increasing of landslide body’s weight and reducing the shear stress of sliding surface. A lot of factors take the overall Shuping landslide into instability situation in this

period, landslide deformation is about 40 cm to north as a whole, while local variables is added up to 90 cm. The larger surface change is easily lead to the loss of coherence for SAR interferometric and the difficulty for phase unwrapping. Therefore, it’s not conducive to using conventional DInSAR method to monitor the landslide deformation in this period, which directly affects the monitor time series over the year. Offset tracking technology is a well method can make up for the deficiencies in DInSAR technical because of not sensitive with the loss of coherence.

DInSAR Principle

2-pass DInSAR is based on an interferometric image pair and a Digital Elevation Model (Liu et al. 2012), First of all, the Image pairs should have a better coherence, than conjugate multiplication the image pair to obtain interferogram, if the interferometric baseline is not zero, the phase value ϕ_{int} is in fact consists of five components, it can be expressed as the follows:

$$\phi_{int} = \phi_{motion} + \phi_{topo} + \phi_{flat} + \phi_{atmo} + \phi_{noise} \quad (1)$$

where ϕ_{int} is the phase values from the image pair conjugate multiplication; ϕ_{motion} is the phase values form landslide deformation; ϕ_{topo} is the topographic phase, it can be removed through introduce external high precision DEM and known space baseline with the 2-pass DInSAR method; ϕ_{flat} is the ground phase caused by reference ellipsoid, it can be removed through a known accurate space baseline; ϕ_{atmo} is the atmospheric delay phase, it can be modified through averaging multiple interferograms or use external data such as GPS, MODIS, MERIS to correct, if the atmospheric

composition remains unchanged during the two Imaging time, it can be ignored. ϕ_{noise} is the noise phase caused by thermal noise, speckle noise, etc. you can reduce its strength through the filter.

From the (1), remove all kinds of disturb phase, we can get ϕ_{motion} , than unwrap it to absolute phase form twining $[-\pi, +\pi]$. Eventually using the following (2) to calculate surface deformation value ΔR in line of sight direction (LOS).

$$\Delta R = \frac{\lambda}{4\pi} \phi_{motion} \quad (2)$$

in which λ is SAR Sensor wavelength.

Due to the particularity of Shuping landslide and the limitation of the DInSAR method in deformation monitoring, the interferometric image pairs should not separate too long time. Therefore, we select three pairs consist of three SAR images in January 2012 for interferometry, in the end, we have got three deformation diagrams with 11days and 22 days apart. Figure 3 shows a clearer landslide boundaries and overall deformation characteristics of Shuping landslide, the results show that in the stability period, the landslide deformation in LOS direction is about 1 cm/month.

Offset Tracking Principle

The basic idea of Offset tracking technology is:(1) overall registration the two SAR image accurately and calculate the overall offset polynomial; (2) calculate the sub-pixel offset through spatial resampling the image and select appropriately sized of sliding window to analysis the sub-pixel's correlation; (3) Sub-pixel registration offsets minus the overall offset polynomial and remove the system errors caused by the two image in different imaging time with different spatial location; (4) Separate the real part and imaginary part, obtain the deformation in azimuth direction and range direction. Based on pixel coherence and based on pixel intensity are two main methods for offset tracking. In this paper, we select the second method for research, because of the method does not depend on the coherence of the image pair, ant than we can monitor the landslide with a longer time interval, the larger deformation and the serious loss coherence.

The core algorithm of the offset tracking method based on intensity is to find the intensity cross-correlation peak. It learned the traditional optical image matching method which is called normalized cross-correlation by use of SAR image's speckle noise. It will be have a highly coherence if the image pair have similar speckle noise, especially the small baseline image pair. The intensity tracking principle based on normalized cross-correlation is that, select a

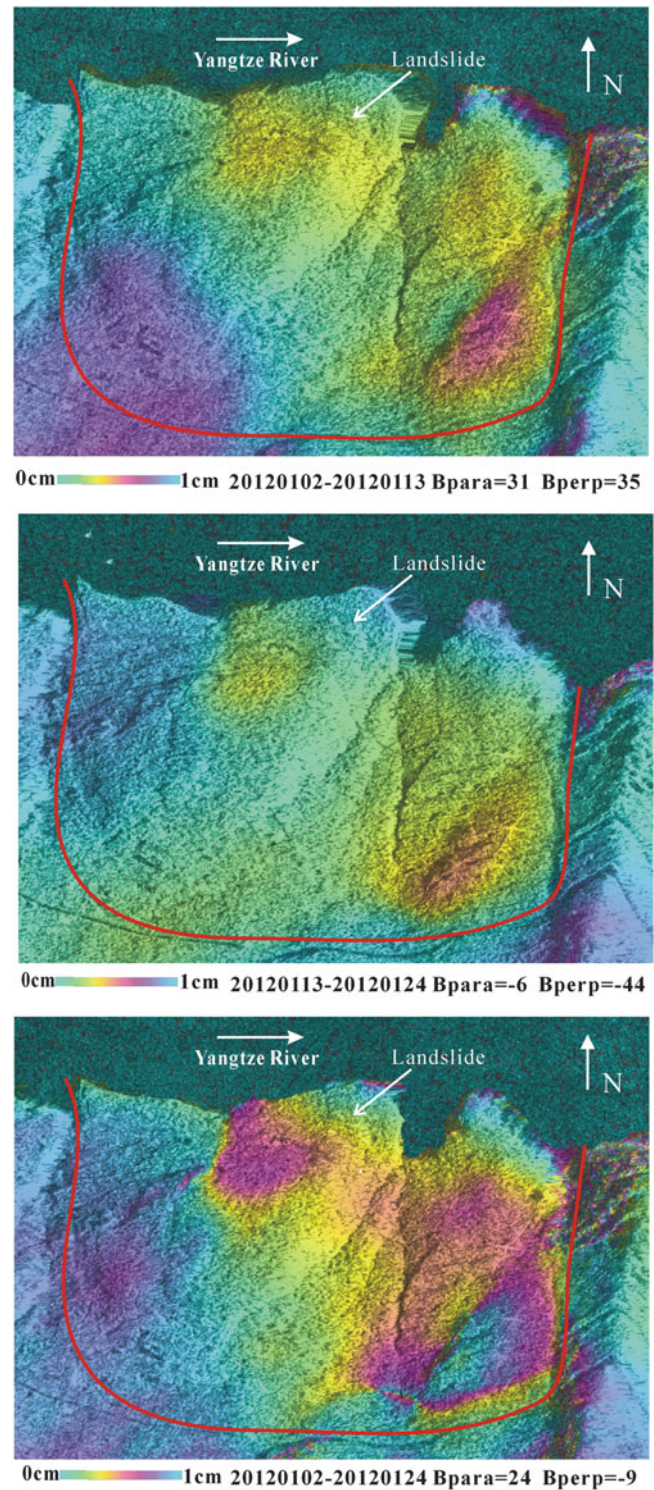


Fig. 3 The DInSAR deformation results

reference window (or called Template window) in the master image, and then moves the reference window according to a certain number of row and column in the slave image, calculate the cross-correlation coefficient through reference window corresponding to slave window

(or called query window), than look the query window with largest cross-correlation coefficient as the best match target window, calculate the displacement between the reference window and target window. The follows is Cross-correlation coefficient calculation equation:

$$NCC(i, j) = \frac{\sum_{k,l} (s(i+k, j+l) - \mu_s)(r(k, l) - \mu_r)}{\sqrt{\sum_{k,l} (s(i+k, j+l) - \mu_s)^2 \sum_{k,l} (r(k, l) - \mu_r)^2}} \quad (3)$$

where (i, j) is the starting point of the query window, (k, l) is the starting point of the reference window, r is the pixel value of the reference window, s is the pixel value of the query window, μ_r is the average pixel value of the reference window, μ_s is the average pixel value of the query window. By (3), we can get the peak value between the reference window and query window, and finally obtain the registration displacement. The registration displacement can be considered as both of orbit offset and the landslide movement displacement (Hu et al. 2008):

$$R_{offset} = R_{orbit} + R_{motion} \quad (4)$$

Because much of the SAR image area is stable, the displacement can be assumed to be zero, the registration offset of these regions approximately equal to the orbit offset. Based on the registration offset, the orbit offset model can be fitted using least-squares method, the following (5) is often used to fit a polynomial function (Strozzi et al. 2002):

$$\begin{aligned} \Delta r &= C_1^r + C_2^r x + C_3^r y + C_4^r xy + C_5^r x^2 + C_6^r y^2 \\ \Delta a &= C_1^a + C_2^a x + C_3^a y + C_4^a xy + C_5^a x^2 + C_6^a y^2 \end{aligned} \quad (5)$$

where Δr and Δa respectively means the range offsets and azimuth offsets for slave image relative to the master image. C_i^r is the fitting coefficients in range direction, C_i^a is the fitting coefficients in azimuth direction. (x, y) is the pixel location in master image.

When we got the R_{offset} and R_{orbit} , connect with formula (4), the actual deformation offset R_{motion} of landslide can be easily figured out.

In this article we select two SAR images in 20120113 and 20130110 to use offset tracking method, which is separated by nearly 1 year. Figures 4 and 5 shows a clearer landslide boundaries and overall deformation characteristics of Shuping landslide. Form the results we can see that the Shuping landslide's overall displace direction is pointing to the Yangtze River, at the same time, there are two small landslides developed on it. The average displacement rate of Shuping landslide is nearly 40 cm/year in the azimuth direction and 50 cm / year in the range direction, even more the

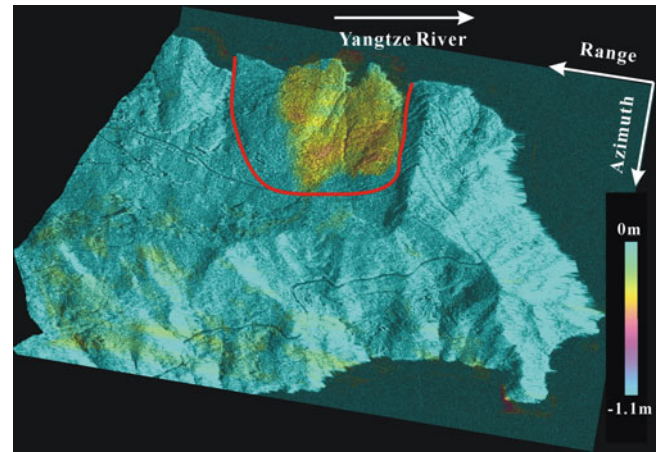


Fig. 4 20120102–20130110(azimuth 374days)

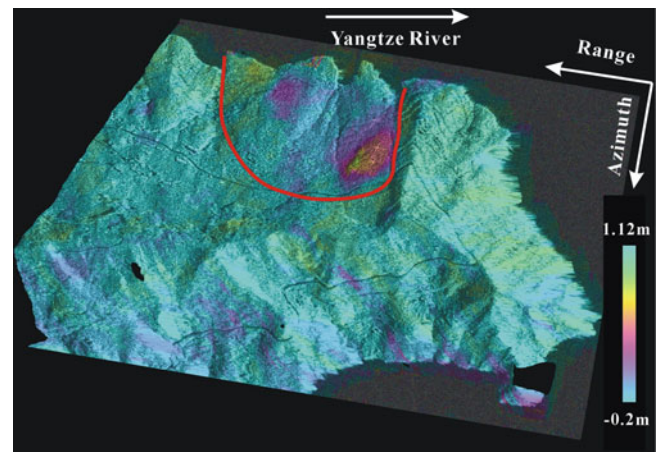


Fig. 5 20120102–20130110(range 374days)

largest displacement is up to 90 cm/year in range direction. The displacement results have a better consistent with the actual measurement results obtained by GPS and Level.

Conclusion and Prospective

So far, the DInSAR technology has been very mature, which has achieved some very good results in landslide deformation monitoring. But the offset tracking technology is rarely used in small areas because of the limitation of lower resolution SAR satellite. Thanks to higher resolution SAR systems such as the German TerraSAR-X, or the Italian COSMO/SkyMed, which provide a guarantee for deformation the large scale, low coherent areas and greatly improved the accuracy of offset tracking method.

InSAR technique in landslide monitoring is unmatched and unique! As more and more higher resolution SAR satellites are launched, InSAR technique will play a much stronger role in the landslide monitoring.

Acknowledgements This work was supported by the International Science & Technology Cooperation Program of China (Project No.2010DFB23380) and the Natural Science Foundation of China (No. 41001264).

References

- Colesanti C, Wasowski J (2006) Investigation landslides with spaceborne Synthetic Aperture Radar (SAR) interferometry. *Eng Geol* 88:173–199
- Eineder M, Adam N, Bamler R, Yague-Martinez N, Breit H (2009) Spaceborne spotlight SAR interferometry with TerraSAR-X. *IEEE Trans Geosci Remote Sens* 47(5):1524–1535
- Fan JH, Tu PF, Guo XF, Wang Y, Ge DQ, Liu G (2010a) Monitoring the deformation of a landslide with differential SAR interferometry using corner reflectors. In: Guo H, Wang C (eds) Sixth international symposium on digital Earth: data processing and applications. *Proc SPIE* 7841; 78411I
- Fan JH, Zhao HL, Tu PF, Wang Y, Guo XF, Ge DQ, Liu G (2010b) CRInSAR for landslide deformation monitoring: a case in three Gorge area. *Proc Int Geosci Remote Sens Symp* 2010:3956–3959
- Hilley GE, Burgmann R, Ferretti A, Novali F, Rocca F (2004) Dynamics of slow-moving landslides from permanent scatterer analysis. *Science* 304:1952–1955
- Hu J, Li ZW, Ding XL et al (2008) Two-dimensional co-seismic surface displacement field of the chi-chi earthquake inferred from SAR image matching. *Sensors* 8:6484–6495
- Liu SW, Guo DH, Chen WT, Zheng XW, Wang SY, Li XJ (2012) The application of airborne lidar technology in landslide investigation and monitoring of Three Gorges Reservoir Area. *Geol China* 39 (02):507–517
- Raucoules D, De Michele M, et al (2012) SAR high resolution image sub-pixel correlation for landslide monitoring. Application to Salazie (La Reunion Island) and La Valette (Alps) landslides. *IGARSS'12 Proceedings*, 2012
- Strozzi T et al (2002) Glacier motion estimation using SAR offset-tracking procedures. *IEEE Trans Geosci Remote Sens* 40 (11):2384–2391
- The Central People's Government of the People's Republic of China. ZHONGGUO GUOTU ZIYUAN GONGBAO. URL: http://www.gov.cn/gzdt/2013-04/20/content_2382978.htm. (in Chinese)
- Xa Y, Fan JH, Li M et al (2012) Monitoring technique of Shuping landslide with high-resolution Radar images in Three Gorges Reservoir area, in China [C]//18th China symposium on Remote Sensing, 2012:161–169
- Xia Y, Kaufmann H, Guo XF (2002) Differential SAR interferometry using corner reflectors. *IGARSS'02*, pp.1243–1246



Rainfall-Triggered Shallow Landslides Mapping Through Pleiades Images

Davide Zizioli, Claudia Meisina, Massimiliano Bordoni, and Francesco Zucca

Abstract

This paper presents the analysis of Pleiades images for the detection and the mapping of rainfall-induced shallow landslides in an area located in the Northern Apennines of Italy. The high resolution of the used images allowed to efficiently recognize also the landslides with small size and to quickly create an inventory map of these phenomena. Field investigations carried up for checking the real presence of the mapped landslides showed a good agreement with the detected through Pleiades images landslides, also in terms of appearance and size of these phenomena. For these reasons Pleiades images can be an useful device for identifying landslides events and to create a complete database of susceptible areas.

Keywords

Landslides • Remote sensing • Pleiades

Introduction

Shallow landslides are triggered by intense rainfalls of short duration. Even though they involve only small portions of hilly and mountainous terrains, they are the cause of heavy damages to people and infrastructures. The identification of shallow landslide prone-areas is, therefore, a necessity to plan mitigation measures.

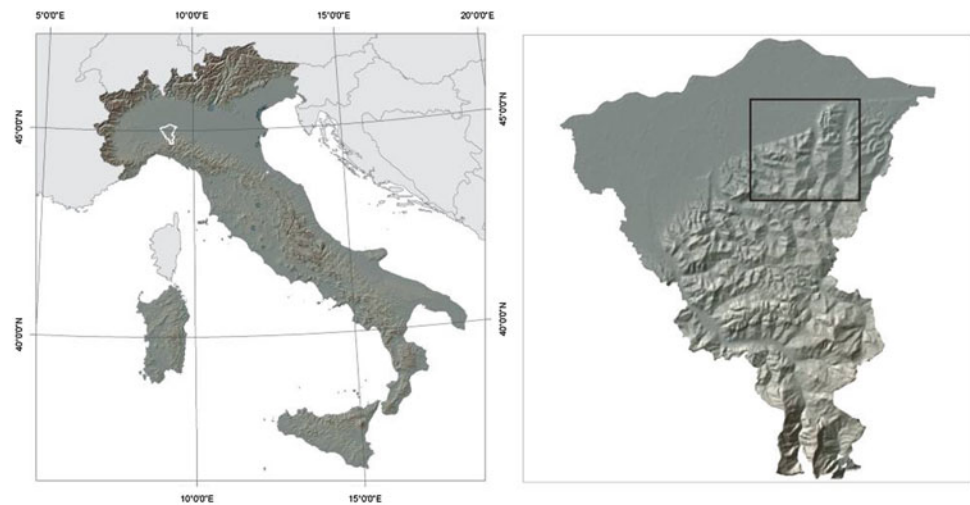
Making an accurate database relative to the phenomena occurred after an event, is an important input to develop and validate shallow landslide susceptibility maps using probabilistic methodologies like logistic regression or generalized additive models. Remote sensing techniques are generally used for the detection and mapping of landslides.

Stereoscopic analysis of photogrammetric products is generally the most used technique for mapping landslides, specially combined with intensive field surveys. Today, landslides detection and mapping benefits from optical imagery (Tofani et al. 2013). The new generation of high resolution satellites presents resolutions ranging from 0.5 to 2 m and offers a tool for a quick reproduction of regional inventory maps. Pleiades is the most recent satellite mission providing optical images at Very High Resolution (VHR) (<1 m for panchromatic and <3 m for multispectral images in the four bands VIR and NIR). Active since 2011, it is composed by a constellation of two satellites, operating in the same sun-synchronous phased orbit with an offset of 180° offering a daily revisit capability over any point on the globe and that is able to capture panchromatic tri-stereo images at very high resolution. The mission is part of the French-Italian ORFEO system (Optical and Radar Federated Earth Observation) and is managed by CNES (Centre National d'Etudes Spatiales) and ASTRIUM Geo-Information Services.

The work aims to present the first results of Pleiades system to implement a database of landslides related to the events of March–April 2013 in Oltrepo Pavese (Northern Italy).

D. Zizioli (✉) • C. Meisina • M. Bordoni • F. Zucca
Department of Earth and Environmental Sciences, University of Pavia,
Pavia 27100, Italy
e-mail: davide.zizioli@unipv.it; claudia.meisina@unipv.it;
massimiliano.bordoni01@universitadipavia.it; francesco.zucca@unipv.it

Fig. 1 Location of the study area covered by the April 2013 tri-stereo Pleiades images



The Study Area

Oltrepo Pavese, which is located in the Northern Apennines of Italy, covers an extension of 1,100 km² and it is characterized by a high density of mass movements and has historically suffered from widespread damage from landslides. More recently extreme rainfall events have triggered shallow landslides in areas which were not yet affected by these types of phenomena. An important event happened subsequently to rapid snowmelt and intense rainfall in April 2009 (150 mm of rain in 48 h, which corresponds to the 20 % of the annual average amount) in the north-eastern sector: several (more than 1,600 shallow landslides) were triggered causing fatal victim and damaging/blocking roads in several places (Zizioli et al. 2013). Other minor events were recorded in 2010.

In the 2013 another important event occurred in the period March-April and was probably caused by the cumulated rainfall amount of this period (till 227.8 mm were measured in Canevino rain gauge in the central sector of Oltrepo Pavese, equal to 28.5 % of the annual average amount) and which affected a more larger area located in the central-northern sector.

Methods

Within a Pleiades evaluation program named Pleiades User Group, kindly organized by ASTRIUM Geo-Information Services, the Department of Earth and Environment Sciences of the University of Pavia received a Pleiades-1A triplet over a portion of Northern Oltrepo Pavese for research purposes. The images composing the triplet were acquired on April 17,

2013. The average viewing angles of the three images are, respectively, -4° , 2° and 8° in along-track direction with respect to the nadir and close to 15° in across-track direction; ground sample distance varies between 0.72 m and 0.78 m, depending on the viewing direction.

The exterior and interior orientation of each image is described by the Rational Polynomial Coefficients (RPCs) available as metadata information. For the evaluation of the orientation accuracy and, eventually, its improvement, the coordinates of 38 Ground Control Points (GCP) clearly visible in the scenes were acquired using static GPS measurements. The accuracy of the initial RPCs, assessed in each image in correspondence of the available GCP, was in the range of 2–4 m. For accurate processing, the given RPCs were improved by estimating six parameters modeling an affine transformation to remove systematic errors (Poli et al. 2009, 2013). The estimation was run simultaneously for the three images in a block adjustment using the well distributed GCPs and, as result, a set of correction parameters was estimated for each image to achieve sub-pixel accuracy; the final RMSE was in fact 0.138 pixel. The DSM was generated with a multi-image least-square matching, as described in Poli et al. 2009, 2013, using a grid space of 2 m and it was used during orthorectification process.

The images covered an area of ~ 290 km² (Figs. 1 and 3). The landslides of the 2013 event were detected though visual interpretation of single and stereoscopic images using the software ERDAS Imagine.

Particularly digital stereoscopic analysis of panchromatic triplet images for the extraction of three-dimensional information related to landslides perimeter, trenches and scarps were used. In the inventory, a single polygon was used to portray a single slope failure or a group of coalescing failures.

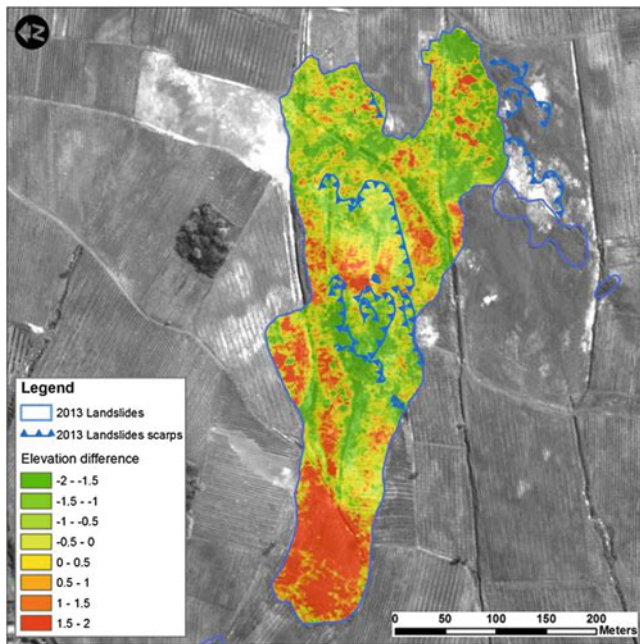


Fig. 2 DoD, DSM of difference showing the accumulation areas and the scarps/detachment areas

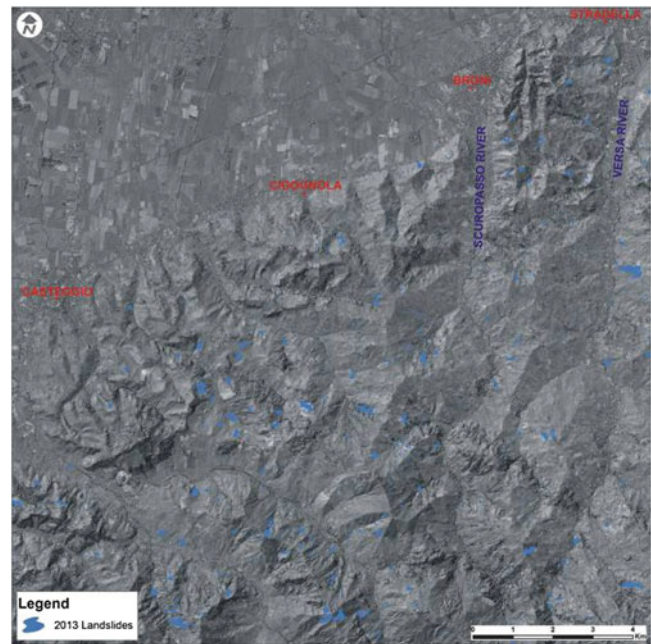


Fig. 3 Landslide inventory of the April 2013 draped over an orthorectified Pleiades panchromatic image

The technique worked where the visual evidence of the slope failures on the image was sufficiently clear. DSM of difference between Pleiades derived DSM and a previous DSM obtained by 2007 photogrammetric aerial survey, allows also to identify the accumulation areas and the scarps/detachment areas (Fig. 2).

The field surveys, carried out in a validation area, were used to check locally the accuracy of the landslide mapping obtained through the analysis of the satellite images. Field work was also carried out in order to check the landslide typology and the depth where the movement occurred. The comparison with previous inventory allowed to distinguish among (a) landslides of new activation triggered by the March–April rainfall event; (b) reactivation of 2009–2010 landslides; (c) reactivation of older landslides.

Results

The collected Pleiades images were used for mapping the landslides triggered by the rainfall events of March and of the first half of April 2013 in Oltrepo Pavese. The landslides database obtained through this device consists in about 440 landslides in an area of about 210 km² (Fig. 3).

The database is essentially constituted by shallow landslides (Figs. 4 and 5). The identified shallow failures

were mainly developed in colluvial soils over bedrock. The depths of shallow landslides slip surface range between 0.4 and 1.2 m from ground surface and are especially located at the contact between soil and weathered bedrock. These movements occurred mainly in correspondence of vineyards and uncultivated terrains (Fig. 4), and, according to what was already seen for the 2009 event (Zizioli et al. 2013), they were often located in correspondence of a slope angle changes, from a gentle to a steep slope, and at the top of the slope. Field work allowed to confirm the real presence of almost all the landslides mapped through Pleiades images, confirming the very high reconnaissance capabilities of Pleiades images despite the small size of these phenomena (Figs. 4 and 5). The analyzed Pleiades images allowed to recognize event 2009 shallow landslides which are still visible, also to evaluate reactivation of some of these phenomena or to border better the bodies of landslides already mapped.

Despite the rainfall-induced shallow landslides, a little number of deep landslides was found (Figs. 6 and 7). These phenomena are characterized by a depth of the slip surface higher than 2 m from ground, and involve a larger hillslope volume interesting in many case also the bedrock materials underlying the colluvial soils. On a preliminary analysis of the typology of these landslides, complex landslides and rotational slides evolving in flows were mainly identified (Figs. 6 and 7).

Fig. 4 Typical examples of shallow translational landslides triggered in vineyard (1) and in a wheat field (2) detected through field work and Pleiades images

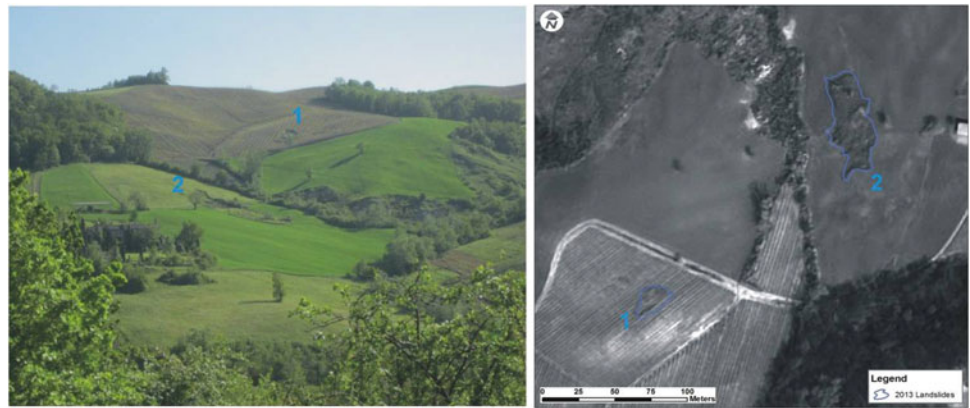


Fig. 5 Examples of shallow translational landslides triggered in uncultivated field detected through field work and Pleiades images



Fig. 6 Complex landslide triggered in the Versa Valley (Eastern Oltrepo Pavese) involving an area of about 7.3 ha and with a scarp height of about 2 m detected through field work and Pleiades images

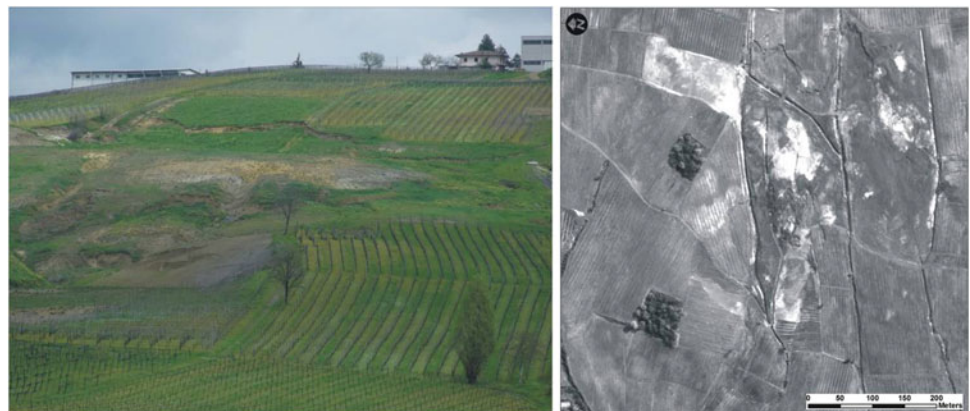
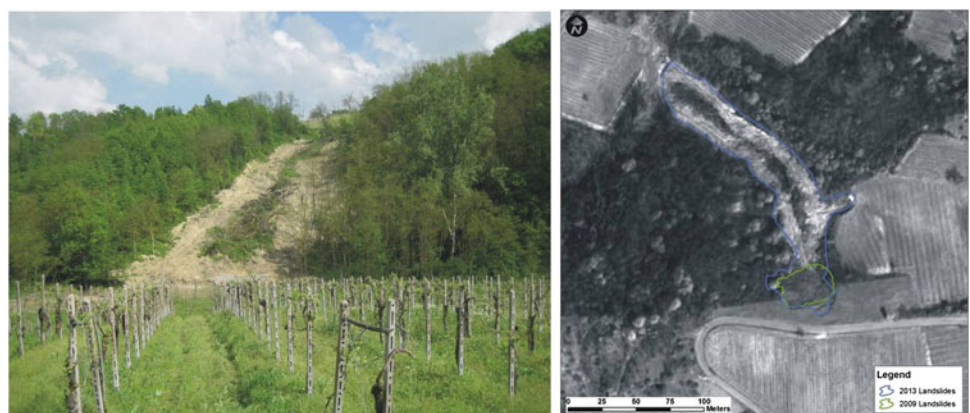


Fig. 7 Michelazza deep landslide (Ruino Municipality, Central Oltrepo Pavese) detected through field work and Pleiades images



Conclusions

The landslides of the 2013 event were detected through the visual interpretation of single and stereoscopic images in the Oltrepo Pavese with Pleiades images. These have a global coverage and the acquisition “on demand” makes the images readily available with a cost/benefit ratio relatively low. Nevertheless, the large coverage of a single image allows for an easier handling of the data rather than how is possible with aerial surveyed images divided into several smaller tiles. This is reflected in every stage of analysis, from the block adjustment to the orthorectification passing through the creation of DSMs.

A good agreement between Pleiades method mapping and field work mapping was founded, suggesting the high potential of use of Pleiades techniques in order to identify landslide events, and also their main features in terms of classification.

The updated landslides database will allow the individuation of critical areas and study of the predisposing factors of the shallow landslides in the Oltrepo Pavese and the development of a susceptibility map dealing with rainfall-triggered shallow landslides, based on historical events. The database will be a useful tool in territory planning, in decision support system during emergency

situations and in the planning of mitigation measures against hydrogeological hazard.

Future work will include a more detailed classification of the 2013 event landslides in relation with movement features and involved soil and bedrock types, and will also be devoted to create an objective automatic detection of occurred phenomena using the pan-sharpened images.

References

- Poli D, Wolff K, Gruen A (2009) Evaluation of Worldview- 1 stereo scenes and related 3D products. *International Archives of the Photogrammetry, Remote Sensing and Spatial Information Sciences*. 38 (1-4-7/W5), Hannover, Germany (on CDROM)
- Poli D, Remondino F, Angiuli E, Agugiaro G (2013) Evaluation of Pleiades-1A triplet on Trento Testfield. *International Archives of the Photogrammetry, Remote Sensing and Spatial Information Sciences, Volume XL-1/W1, ISPRS Hannover Workshop 2013, 21 – 24 May 2013, Hannover, Germany*
- Tofani V, Segoni S, Agostini A, Catani F, Casagli N (2013) Technical note: use of remote sensing for landslide studies in Europe. *Nat Hazard Earth Syst Sci* 13:299–309
- Zizioli D, Meisina C, Valentino R, Montrasio L (2013) Comparison between different approaches to modeling shallow landslide susceptibility: a case history in Oltrepo Pavese, Northern Italy. *Nat Hazards Earth Syst Sci* 13:559–573



Monitoring the Activity of Landslides in the Coastal Zones of Reservoirs with SAR Interferometry

Zbigniew Perski, Guang Liu, Tomasz Wojciechowski, Fan Jinhui, and Antoni Wójcik

Abstract

This work presents the preliminary results of the exploration of Synthetic Aperture Radar (SAR) data archives of Envisat and TerraSAR-X data with multitemporal interferometric techniques like Persistent Scatterers Interferometry (PSI) and Small Baseline Interferometry (SBAS). The analyses were performed on two test areas located in vicinity of Rożnów reservoir in Southern Poland and Three Gorges area in Hubei province in China. Both areas are very challenging for interferometric techniques due to the very rough topography, sparse urbanization, dense vegetation and forest cover. Therefore big part of the work was devoted to improvements of algorithms and data processing chain.

It was found that the number of detected Persistent Scatterers (PS) could be increased by improvements applied to interferograms generation. In terms of PSI processing a multi criteria Persistent Scatterers Candidates selection method was used. The authors noticed that for such problematic areas it is still possible to successfully detect a number of PS but, the interpretation of the associated deformation is difficult and requires further studies.

Keywords

SAR interferometry • Persistent scatterers • Carpathians • Three Georges

Introduction

The current paper is the result of research conducted under the framework of ESA funded Dragon 3 Project ID: 10606 'Landslide identification, movement monitoring and risk

assessment over rugged mountain area using advanced earth observation techniques' that aims to carry out an extensive exploitation of available remote sensing data (mostly Synthetic Aperture Radar—SAR imagery) to evaluate their importance for hazard and risk management. This work includes the detailed documentation of landslides occurrences for the past decades and the analysis of current movement trends which are required to predict future conditions (Fig. 1).

Z. Perski (✉) • T. Wojciechowski • A. Wójcik
Polish Geological Institute, National Research Institute, Carpathian Branch, Skrzatow 1, Krakow, 31-560, Poland
e-mail: zbigniew.perski@pgi.gov.pl; tomasz.wojciechowski@pgi.gov.pl; antoni.wojcik@pgi.gov.pl

G. Liu
Center for Earth Observation and Digital Earth, Chinese Academy of Sciences, No. 9 Dengzhuang South Road Haidian District, Beijing 100094, China
e-mail: liug@ceode.ac.cn

F. Jinhui
China Aero Geophysical Survey and Remote Sensing Center for Land and Resources, No. 31, College Road, Haidian District Beijing, China
e-mail: ghfan2004@gmail.com

Motivation

China and Poland are countries with serious landslide disasters and experiences high economic damage almost every year. According to the information provided by the Chinese Geological Survey Bureau approximately 2/3 areas of China are the mountainous areas with 56 % of population. In Poland however 95 % of the landslides are located on 6 %

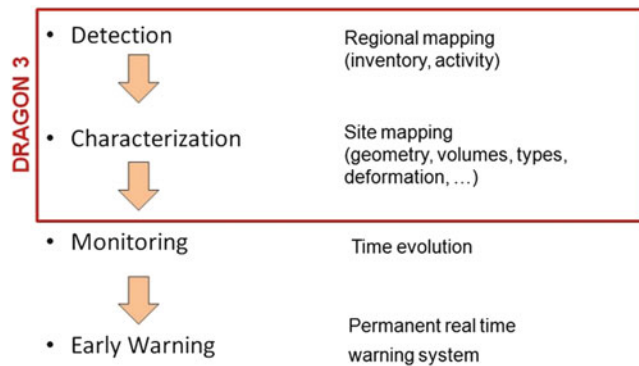


Fig. 1 Typical workflow for landslide investigation and the role of Dragon 3 project (courtesy of M.-H. Derron)

of territory with approximate density of 1–2 landslides per square kilometer.

The traditional techniques like levelling and GPS network are commonly applied to the monitoring of landslides movement but it is labour, financial consuming and not always efficient in mountain area. InSAR has been already recognized as a very effective and relatively low-cost technique for landslide deformation detection and monitoring (Colesanti and Wasowski 2006). However, due to a number of technical and environmental obstacles application of InSAR on rugged terrain is not an easy task (Perski et al. 2011).

Research Areas and SAR Data Exploration

As the test sites for Dragon 3 project purposes three landslide areas: the Three Gorges area, South-East of Gansu Province in Northwest China, and Carpathian mountains in Poland were selected. However, in this paper the results from only two specific areas are presented: Three Gorges area in Hubei province (China) and Rożnów area in Małopolska province (Poland). In both cases the landslides toes are affecting coastal zones of important water reservoirs causing damages to infrastructure and reservoir safety problems.

Three Gorges Area

The Three Gorges area span from the western—upriver cities of Fengjie and Yichang in Chongqing Municipality eastward—downstream to Hubei province. The Three Gorges region has a total length of approximately 200 km. Although it is primarily famous for its scenery, the Three Gorges region is also a historically and culturally important location in China.

The Three Gorges Dam was constructed at a place in the middle of the Xiling Gorge. The reservoir dam was completed in the summer of 2006, and the water level

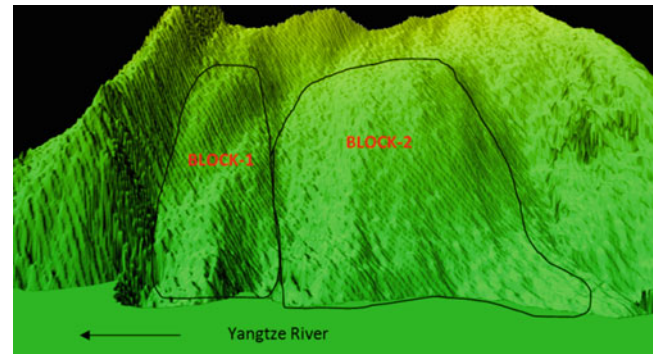


Fig. 2 Shuping landslide overlaid on DEM

quickly reached the maximum level of 110 m above the downstream river. The dam and Three Gorges Reservoir have a substantial impact upon the region's environment and settlement. The higher water level has changed the hydrogeological condition of surrounding slopes and large number of landslides were reactivated.

The study area in the Three Gorges area is Shuping landslide, which lies in the area of Zigui county, and about 50 km to the dam. The landslide belongs to debris landslides, and it is combined by two blocks (Fig. 2). The landslide material is stone and gravel soil with sediments from river terrace. The stones are composed mainly of sandy mudstone, muddy siltstone and brownish gray marl, the size of the stones is generally 0.2 ~ 0.5 m, ratio of soil and gravel debris is from 5:5 to 7:3, gravel particle size is generally 2 to 8 cm; sliding belt is formed under accumulation layer upon the rock bed, mainly with gravelly soil, in the yellow sand road and along the east-west highway across the border the sliding belt is visible; sliding bed material is mainly from Triassic Badong T2b2 ~ T2b4, composed by a set of reddish brown sandy mudstone and muddy siltstone, and brownish gray marl (Wang et al. 2006). The two blocks (Fig. 2) shows different deformation states. According to the in-situ survey, to upper part of block-1 has more serious deformation than that in block-2, and this trend remains active and endanger the inhabitants living there.

For Three Gorges area a set of 20 C-band, archival, Envisat ASAR scenes from descending track have been acquired. These data are currently under processing and the results are not available yet. Additionally for the area of Shuping landslide 10 high resolution X-band TerraSAR-X spotlight mode, descending scenes (Fig. 3.) were used.

Rożnów Area

The study area is located along the eastern bank of Rożnów Lake established on Dunajec river, in the central part of the Outer West Carpathians within the Cieszkowice Foothills

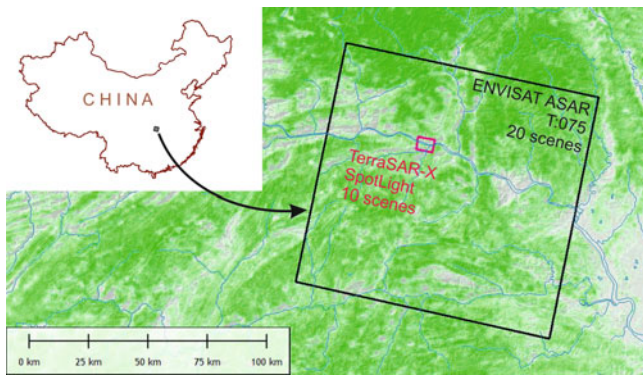


Fig. 3 Location of study area Three Gorges and coverage of available SAR datasets presented on top of MODIS VCF Tree Cover 2005

(Starkel 1972) (Fig. 2). This area is characterized by variable land cover of mixture of meadows, arable lands, forests and sparse urbanization represented mainly by separate houses and individual farms. The relative height differences of the area are up to 315 m and due to the complex geology (Burtan et al. 1992) of the flysh-type rocks (sandstone, sandstone-shale and shale from the Upper Cretaceous to Oligocene), the region is characterized by high landslide susceptibility. Very high activity of the landslides is noted along the banks of Rożnów lake and is related to the variability of the fluctuation of water level in the Rożnów Lake. Flysh-type rock series of the Silesian Nappe, and overthrust Dukla Nappe and Magura Nappe are strongly tectonically disturbed by many local overthrusts and transverse faults, that strongly influencing the location of landslide prone areas. More than 70 landslides are known, in the study area according to PGI's achievements. Most of these landslides are active and causing damages to part of roads and buildings periodically for decades, especially during the seasons of snowmelt and intense rainfall. The particular increase of activity was observed in late spring and early summer of 2010 after heavy rains occurred in April and June. Residents together with local authorities reported damages caused on over 30 landslides. Most of these landslides are very active and causing damages and visible deformations, cracks etc. There are both small, translational landslides and large, complex, rock and shallow landslides covering the entire slopes.

For Rożnów area one Envisat descending dataset and a stack of 20 TerraSAR-X ascending StripMap images have been processed (Perski et al. 2011). The extents of mentioned data are presented on Fig. 4.

Number of landslides remain active within this area. For the purpose of this study we focus on Just landslide located on western bank of Rożnów reservoir. The landslide remains

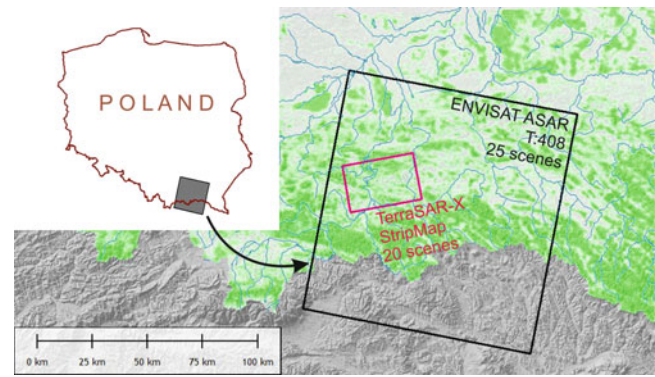


Fig. 4 Location of Rożnów study area and coverage of the datasets used for this study presented on top of MODIS VCF Tree Cover 2005

active since many years causing damages to the houses and the stare road number 75. For the Just landslide, PGI-NRI is carrying out the inclinometer measurements every 6 months.

Methods of Study

SAR Interferometry and Multi Temporal InSAR Methods Description

SAR Interferometry (InSAR) is a method for extracting information related to the topography of the Earth's surface (Goldstein et al. 1988). Differential InSAR (D-InSAR) represents different approach of InSAR that exploits the temporal baseline between subsequent SAR acquisitions to derive phase differences corresponding to displacements of terrain. A good overview of D-InSAR technique and its applications was given by (Bamler and Hartl 1998; Massonnet and Feigl 1998). The main problem associated with D-InSAR is the so-called temporal decorrelation, due to changes in the electromagnetic properties and/or relative positions of scatterers within a resolution cell. Moreover, D-InSAR is very sensitive to atmospheric signal delay. For individual interferograms, this atmospheric phase screen (APS) is impossible to remove and therefore the accuracy of measuring small deformations is significantly reduced. Due to these properties the operational use of D-InSAR is limited to (a) short temporal baselines (b) phenomena with strong deformation gradient in respect to radar wavelength, (c) areas with limited vegetation. Despite these limitations, many successful studies focused on landslides have been performed (Fruneau et al. 1996; Colesanti et al. 2003; Hilley et al. 2004).

To bypass the limitations mentioned different InSAR techniques have been developed. These methods are focusing on stable phase and slowly decorrelating pixels allow to

operate on data stacks (typically more than 20 acquisitions) instead of individual interferograms. The initial method developed by POLIMI (Ferretti et al. 2001) used radar point targets as ‘natural’ corner reflectors that remain coherent phase over time. Other techniques, such as the Small Baseline Subset technique (SBAS) (Berardino et al. 2002) utilize several master images to construct an optimal set of interferograms with the smallest temporal and perpendicular baselines. The crucial element in the point wise analysis is the identification of potentially coherent points. The first selection might be based on amplitude dispersion as in the original PSI algorithm (Ferretti et al. 2001) or coherence as in case of SBAS or spatial correlation of the phase in case of StaMPS (Hooper et al. 2004).

Application of Multitemporal InSAR for Landslide Research

For Carpathian landslides (Perski et al. 2010) and problems related to Three Gorges landslides InSAR applications are limited due to mostly environmental factors like:

- very rough topography (steep slopes causing geometry distortion, and resulting bad coregistration),
- lack of rock outcrops and very sparse urbanization concentrated in the valleys and along the roads (low number of stable phase PS),
- dense vegetation cover (forests in the higher parts of the slopes and meadows and fields in the lower parts), bad weather conditions with high precipitation, long season with thick snow cover (resulting overall coherence reduction).

In our study, the conventional differential SAR Interferometry (DInSAR) technique will be used first to obtain some preliminary results of the research areas, and X-band, TerraSAR-X data are preferred for its short revisit time between subsequent SAR acquisitions. In the next step the DInSAR results of X-band and archival C band SAR data will be compared. After that, the PSI method will be used to estimate the velocity of the landslides. Here we use the software SSDS (SAR Subsidence Demonstration System) developed under the support of the project of International Cooperation Department of the Ministry of Science and Technology of China (Fig. 5).

Results of SAR Data Processing

Three Gorges Area: Shuping Landslide

The SAR data used for Shuping landslide monitoring were obtained from TerraSAR-X satellite, TerraSAR-X SAR is an X band SAR sensor, the satellite is flying at a height of

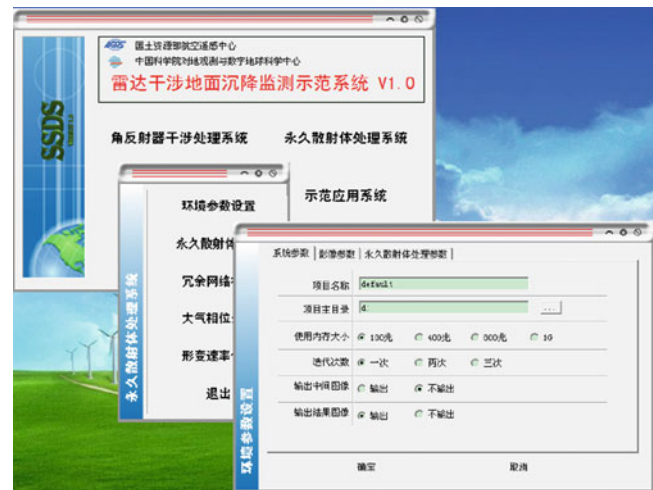


Fig. 5 SAR subsidence demonstration system (SSDS)

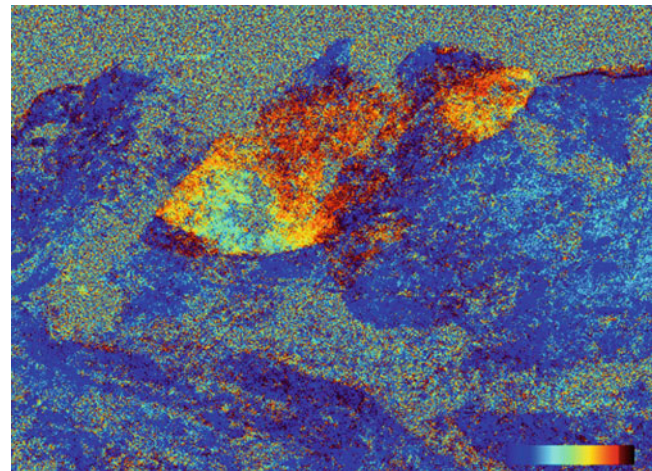


Fig. 6 DInSAR TerraSAR-X interferogram of 2012-02-04 and 2012-02-15 scenes of Shuping landslide

514 km, the revisit time is 11 days. There are three acquisition modes, StripMap, ScanSAR and SpotLight. In this study the SAR data in SpotLight mode of about 1.1 m, and the coverage of about 5×7 km were used (Fig. 2).

The obtained TSX data covering the period between 2012-01-02 and 2012-04-21. The data were acquired in 4 months, and most of perpendicular baselines are small. The maximum baseline is 130 m, that means that the DInSAR data quality is quite good. The Doppler frequency of the TerraSAR-X is controlled very well, so we selected the date 2012-02-15 as the master image.

At the first stage of processing, we computed the differential interferograms. From the interferogram formed with the images acquired in 2012-02-04 and 2012-02-15 (Fig. 6), we can see clearly that the landslide is composed by two parts. Using the color bar, we can estimate roughly the deformation rates for two parts of the landslide. The

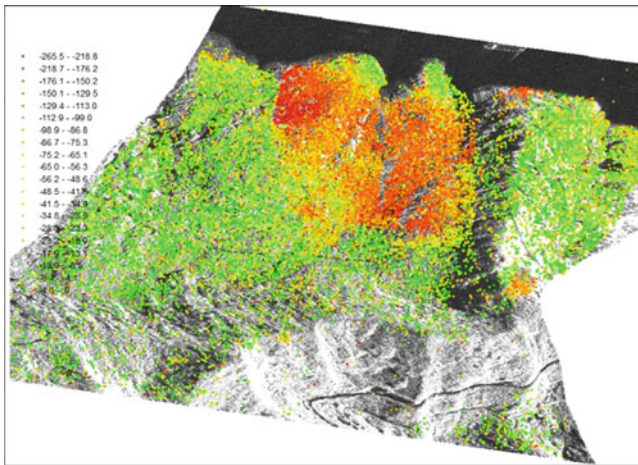


Fig. 7 Time series result of TerraSAR-X of Shuping landslide

deformation of the left part is larger by a half of the color circle, whereas for the right part, the deformation is close to the half of the color circle. The color circle represents half of the wavelength, that means that the maximum deformation of Shuping landslide is close to 250 mm per year.

After obtain the small baseline DInSAR interferograms, all the images were put together and using SSDS processing software, the velocity on the stable points were obtained (Fig. 7).

Since the Shuping landslide is close to the Yangtze river reservoir, lot of points were selected by the use of the dispersion of amplitude criteria in point selection procedure. To avoid false point selections we combined the dispersion of amplitude method with threshold of coherence method for this situation. During the DInSAR processing we obtained the coherence maps for every interferogram. Using that data we can check for every candidate selected with amplitude dispersion, whether the minimum coherence of the candidate point is larger than certain value. Of course in real situation, the combined method could not detect all the stable points due to the complexity of real environment, but it could help a lot to decrease the detection of false points in the river.

We found that the result on the stable points is corresponding with the conventional DInSAR processing. The results shows that the deformation velocity measured with the 4-months data series is larger than 260 mm/year. This founding was somehow amazing since it was estimated

in a range of about few centimeters per year by earlier study (Liao et al. 2011).

Rożnów Area: Just Landslide

For the purpose of Just landslide study 25 ASAR C-band images acquired by Envisat have been processed. The data series cover the period between 2002-12-03 to 2010-04-20. The TerraSAR-X, X-band data series consist of 21 scenes covering 20-months period between 2010-10-06 and 2012-07-13. It should be noted that the highest recent activity of Just landslide occurred in June 2010 after long and heavy rains. The two analysed dataset are not overlapping in time with the gap including main landslide event and therefore should be treated as independent observations of different stages of the same event. Moreover, the SAR datasets represent different geometry: descending in case of ASAR data and ascending in a case of TSX data. Both SAR datasets were processed with StaMPS method but only PSI points were considered.

According to inclinometer data recorded in upper part of the landslide the displacement reached 120 mm from March 2010 to August 2010 at the depth of 12 m. For TSX data it has been detected number of PS points close to inclinometer location that shows 16 mm/year of average surface displacement. The lower part of the landslide appears to be stable in the period of TS acquisitions, however the points located at the coast, outside of landslide show significant subsidence (20 mm/year). It is not clear whether this phenomena has any relation to landslide movement (Fig. 8).

Results obtained for ASAR dataset are complementary but since the dataset represent period prior to landslide event in 2010 the detected movement is much smaller rate. PS points were detected only in the lower part of the landslide (Fig. 8) where the displacement of 1.8 mm/year was detected. It should be noted that the direction of the movement ('uplift' or 'subsidence' depend on direction of SAR observation—LoS) Time series analysis of individual PS points show significant increment of LoS velocity close to the landslide event. For Envisat data, prior to the main event in 2010 we can see the acceleration caused by spring snowmelt. For TerraSAR-X data we observe LoS deformation decrease during the dry period after the main event.

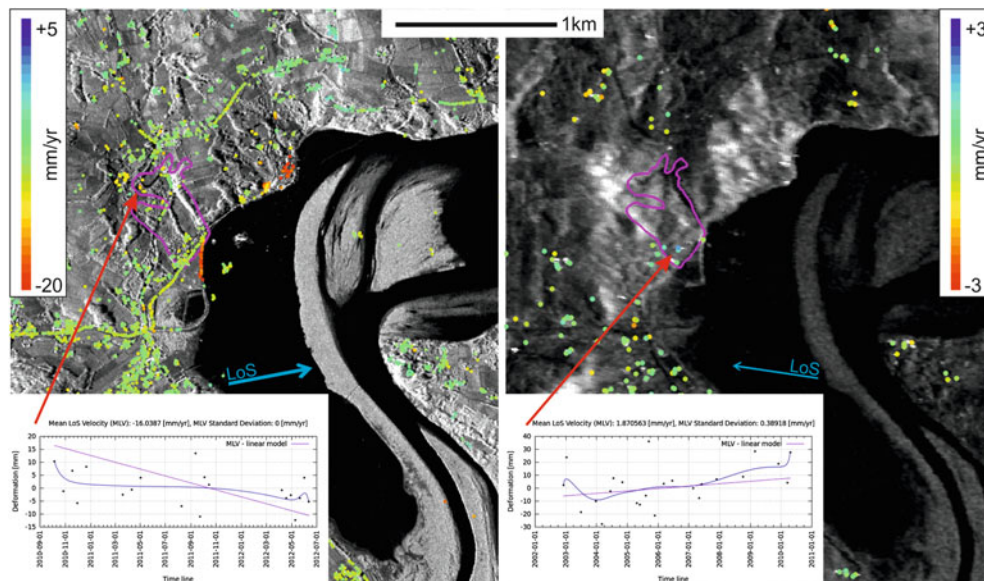


Fig. 8 PSI results of landslide Just in Rożnów area. *Left*: TerraSAR-X data; *right*: Envisat ASAR data; LoS—line of Sight of SAR observation

Conclusions

The results of this work show potential of time series InSAR for landslide deformation monitoring, and the technique has the ability not only for slowly moved landslide, but also quickly moved landslide. During the study the high resolution SAR images show better performance than middle resolution image, especially in detailed deformation pattern required by landslide monitoring.

However, the results show also that the landslide movement measurements with InSAR technique are not easy and requires very careful processing. Further work including algorithmic development, exploration of other datasets is planned. Moreover the interpretation of the results with careful analysis of in-situ data will be performed.

Acknowledgements The research supported by ESA funded Dragon 3 Project ID: 10606 “Landslide identification, movement monitoring and risk assessment over rugged mountain area using advanced earth observation techniques”, Shuping landslide research was also supported by Chinese International Cooperation Department of the Ministry of Science and Technology; Grant: 2010DFB23380. Polish—China collaboration was supported by Inter-Governmental S&T Cooperation Project of Poland and China (3417, 3528). TerraSAR-X data for Rożnów area were supported by research project number NN526146037 funded by Polish Ministry of Science and Higher Education.

References

- Bamler R, Hartl P (1998) Synthetic aperture radar interferometry. *Inverse Probl* 14:R1–R54
- Berardino P, Fornaro G, Lanari R, Sansosti E (2002) A new algorithm for surface deformation monitoring based on small baseline differential SAR interferograms. *IEEE Trans Geosci Remote Sens* 40:2375–2383
- Burtan J, Cieszkowski M, Jawor E, Slaczka (1992) Geology of Kłęczany – Limanowa tectonic window. *Proc. LXIII Meet. PTG Koninki* 171–179
- Colesanti C, Ferretti A, Novali F, Prati C, Rocca F (2003) SAR monitoring of progressive and seasonal ground deformation using the permanent scatterers technique. *IEEE Trans Geosci Remote Sens* 41:1685–1701
- Colesanti C, Wasowski J (2006) Investigating landslides with spaceborne Synthetic Aperture Radar (SAR) interferometry. *Eng Geol* 88:173–199
- Ferretti A, Prati C, Rocca F (2001) Permanent scatterers in SAR interferometry. *IEEE Trans Geosci Remote Sens* 39:8–20
- Fruneau B, Achache J, Delacourt C (1996) Observation and modelling of the Saint-Étienne-de-Tinée landslide using SAR interferometry. *Tectonophysics* 265:181–190
- Goldstein RM, Zebker HA, Werner CL (1988) Satellite radar interferometry: two-dimensional phase unwrapping. *Radio Sci* 23:713–720
- Hilley GE, Burgmann R, Ferretti A, Novali F, Rocca F (2004) Dynamics of slow-moving landslides from permanent scatterer analysis. *Science*
- Hooper A, Zebker H, Segall P, Kampes B (2004) A new method for measuring deformation on volcanoes and other non-urban areas using InSAR persistent scatterers. *Geophys Res Lett* 31, L23611. doi:[10.1029/2004GL021737](https://doi.org/10.1029/2004GL021737)
- Liao M, Tang J, Wang T, Balz T, Zhang L (2011) Landslide monitoring with high-resolution SAR data in the Three Gorges region. *Sci China Earth Sci* 55:590–601
- Massonnet D, Feigl KL (1998) Radar interferometry and its application to changes in the earth’s surface. *Rev Geophys* 36:441–500
- Perski Z, Borkowski A, Wojciechowski T, Wójcik A (2011) Application of persistent scatterers interferometry for landslide monitoring in the vicinity of Rożnów lake in Poland. *Acta Geodyn Geomater* 8:319–323
- Perski Z, Wojciechowski T, Borkowski A (2010) Persistent scatterer SAR Interferometry applications on landslides in Carpathians (Southern Poland). *Acta Geodyn Geomater* 7:1–7
- Starkel L (1972) Characteristics of relief of the Polish Carpathians and their significance for the human economy. *Probl Zagospod Ziem Górskich* 10:15–150
- Wang F, Peng X, Zhang Y, Huo Z, Takeuchi A, Araiba K, Wang G (2006) Landslides and slope deformation caused by water impoundment in the Three Gorges Reservoir, China. *Proc. IAEG2006 Nottm. United Kingd.* 6–10 Sept. 2006 Paper number 137, 1–13



Relative Age Estimation at Landslide Mapping on LiDAR Derivatives: Revealing the Applicability of Land Cover Data in Statistical Susceptibility Modelling

Helene Petschko, Rainer Bell, and Thomas Glade

Abstract

In statistical landslide susceptibility modelling the identification of appropriate explanatory variables describing the predisposing and preparatory factors for the landslides of a given inventory is important. In this context information on the age and the respective land cover at the time of occurrence is beneficiary. The potential of mapping very old (or prehistoric) landslides using LiDAR derivatives has not been analysed yet. Additionally, performing a visual interpretation of derivatives of a single LiDAR DTM it is not possible to assign the accurate age or date of the occurrence of the event to each mapped landslide. Therefore, commonly no information on the land cover at the time of landslide occurrence for these very old landslides (but also for younger ones) is available. The objective of this study is, to estimate the relative age of landslides during the mapping and to explore differences of the recent land cover distribution in the relative ages of the landslides. This is performed to evaluate the sustainability of including recent land cover data into susceptibility modelling. The relative age of the landslides is estimated for each landslide according to its morphological footprint on the LiDAR DTM derivatives and to its appearance on the orthophoto. The different relative ages assigned are “very old”, “old”, “young” and “very young”. The study area is located in three districts of Lower Austria, namely Amstetten, Baden and Waidhofen/Ybbs. The resulting inventory includes 1834 landslides and shows that the “very old” and “old” landslides (60 % of all mapped landslides) are mainly covered by forest (~60 % of all land cover types). We conclude that using this inventory including recent land cover data in the susceptibility model is not appropriate for Lower Austria. There is a potential of mapping “old” or “very old” landslides on the LiDAR derivatives. The absolute age remains unknown.

Keywords

Landslide inventory mapping • LiDAR derivatives • Relative landslide age • Recent land cover map

Introduction

As no detailed information on the date of occurrence of the landslides can be determined from the LiDAR derivatives (or other remote sensing techniques, Van Westen et al. 2005) the age of the landslides can only be estimated relatively in the study area. Whereas the determination of relative landslide age is very common in studies mapping landslides on aerial photographs or orthophotos (e.g. Ardizzone et al. 2002;

H. Petschko (✉) • R. Bell • T. Glade
Department of Geography and Regional Research, University of
Vienna, Universitaetsstrasse 7 1010, Vienna, Austria
e-mail: helene.petschko@univie.ac.at; rainer.bell@univie.ac.at;
thomas.glade@univie.ac.at

Table 1 Land cover evaluated for landslide polygons according their landslide type and relative landslide age

| Land cover unit | Study area (%) | All landslides (%) | Slide (%) | Area with slides (%) | Flow (%) | Complex (%) | Young (%) | Very young (%) | Old (%) | Very old (%) |
|--------------------|----------------|--------------------|-----------|----------------------|----------|-------------|-----------|----------------|---------|--------------|
| Coniferous forest | 12.77 | 19.97 | 25.72 | 16.60 | 11.80 | 16.60 | 5.80 | 0.92 | 16.89 | 23.65 |
| Mixed forest | 13.89 | 20.04 | 20.05 | 19.52 | 24.96 | 10.14 | 13.27 | 7.18 | 26.04 | 17.65 |
| Deciduous forest | 13.65 | 20.19 | 18.08 | 21.86 | 21.74 | 24.46 | 11.91 | 5.19 | 17.90 | 22.91 |
| Arable land | 17.70 | 15.93 | 10.66 | 19.08 | 19.89 | 19.01 | 29.81 | 20.89 | 18.01 | 13.14 |
| Grassland, pasture | 10.14 | 11.25 | 10.21 | 11.85 | 12.10 | 20.66 | 22.03 | 38.08 | 10.05 | 10.10 |
| Rough pasture | 10.48 | 8.21 | 9.96 | 7.09 | 8.85 | 8.37 | 13.58 | 23.45 | 8.47 | 7.16 |
| Snow, Ice | 0.02 | 0.00 | 0.00 | 0.01 | 0.00 | 0.00 | 0.00 | 0.00 | 0.00 | 0.01 |
| Debris | 9.38 | 1.54 | 3.73 | 0.15 | 0.01 | 0.00 | 0.09 | 3.63 | 0.08 | 2.39 |
| Fallow land | 9.76 | 2.49 | 1.41 | 3.36 | 0.54 | 0.63 | 3.35 | 0.53 | 2.25 | 2.58 |
| Housing settlement | 1.66 | 0.31 | 0.20 | 0.39 | 0.10 | 0.13 | 0.15 | 0.11 | 0.32 | 0.32 |
| Water | 0.41 | 0.01 | 0.00 | 0.01 | 0.00 | 0.00 | 0.00 | 0.00 | 0.00 | 0.01 |
| NA | 0.14 | 0.06 | 0.00 | 0.09 | 0.00 | 0.00 | 0.01 | 0.00 | 0.00 | 0.09 |

Cardinali et al. 2002; Guzzetti et al. 2003; Guzzetti 2005; Zanutta et al. 2006), in studies using LiDAR derivatives as mapping basis only few attention is dedicated to this topic so far (e.g. Bell et al. 2012). Therein the potential mapping of “very old” (prehistoric (Schulz 2004)) landslides and its effects on the subsequent application of the inventory are not considered or analysed yet. The quality of the inventory and the information on the landslides stored in it are of importance for any application of the inventory (Ardizzone et al. 2002; Guzzetti et al. 2012; Petschko et al. 2014; Van Westen et al. 2005). Precisely in the context of this study the inventory is a basis for statistical susceptibility modelling in Lower Austria (Petschko et al. 2014) where the resulting susceptibility map is dependent on the model input data and their geomorphological relevance. In this context the landslide age or event date is of importance, as trigger factors or also the land cover is considered as an explanatory variable for landslide susceptibility modelling. However, if the inventory contains “very old” (or prehistoric) landslides, they cannot be related to a trigger event (Van Westen et al. 2005) and the recent land cover information might not match the land cover at the time of the occurrence of the mapped landslides.

This study is aimed to analyse the potential of LiDAR derivatives to map landslides of different age and to assess the landslide age in a relative manner within the study area. Furthermore, the objective is to compare the relative landslide

age with the recent land cover map. This is done to evaluate the sustainability of including recent land cover data into susceptibility modelling using a landslide inventory originating from visual analysis of LiDAR derivatives.

Study Area

The study area is located in the three districts Amstetten (1,187 km²), Baden (754 km²) and Waidhofen/Ybbs (131 km²) in the province of Lower Austria. These districts show a high heterogeneity regarding their land cover, topography and susceptibility to landslides (Petschko et al. 2012). Whereas 40 % of the study area is covered by forest (coniferous, mixed and deciduous forest) 48 % of the area is covered by farmland (arable land, (rough) pasture and fallow land, Table 1). However, the predominant land cover type changes distinctly, as for example in the districts Amstetten and Waidhofen/Ybbs the North is mainly covered by farmland but the South is dominated by forest (Fig. 1).

The main lithological units in the study area are (from North to south) the Bohemian Massif, the Molasse Zone (including the “Schlier”), the Loess and Loam, the Flysch and Klippen Zone and the Austroalpine Unit with dolostone or with limestone and marls.

Landslides are abundant especially in the Flysch and Klippen Zone, as an existing landslide inventory resulting

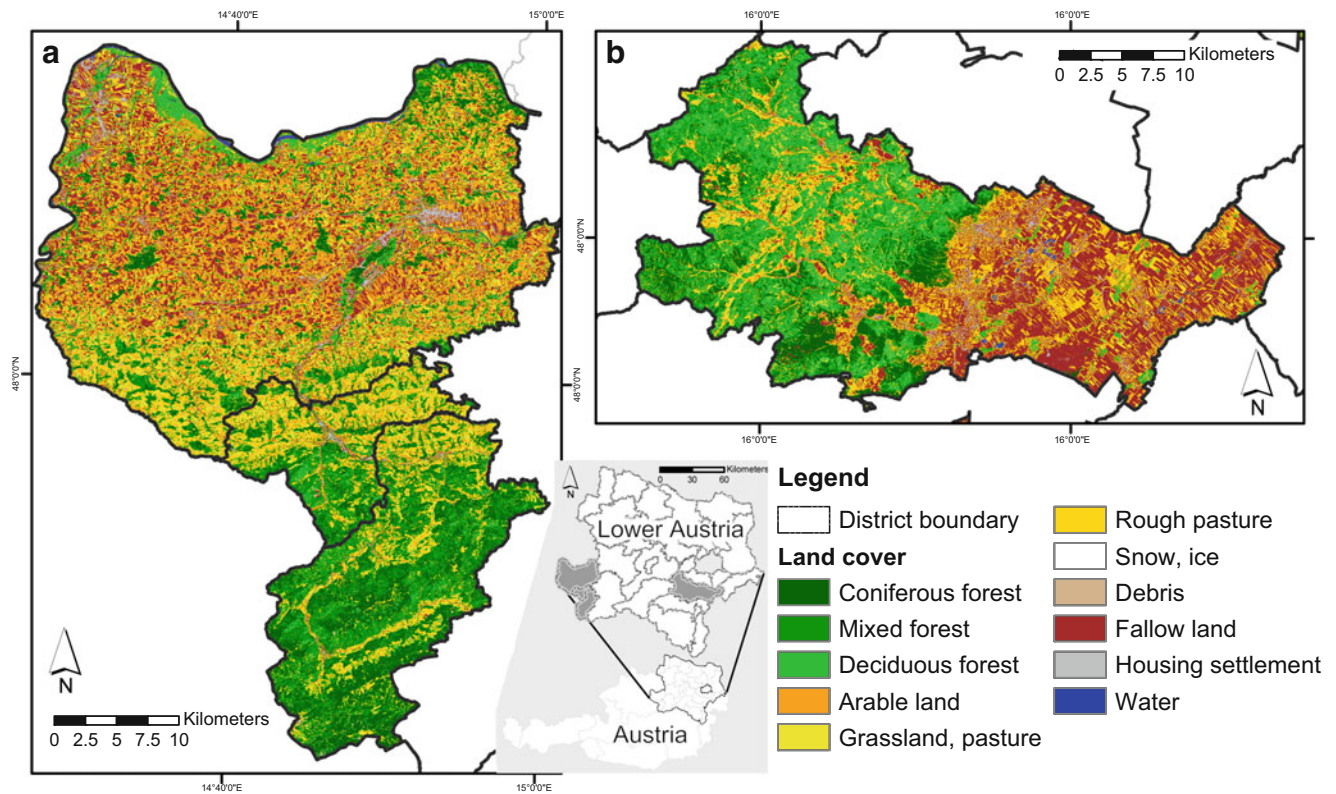


Fig. 1 Land cover in the study area in Lower Austria ((a) Amstetten, Waidhofen/Ybbs, (b) Baden)

from an archive of the Geological Survey of Austria (building ground register (BGR)) shows (Petschko et al. 2013; Schwenk 1992). The landslides mainly occurred under very wet conditions either due to heavy rainfall, rapid snow melt events or a combination of both (Schweigl and Hervás 2009).

Data

Data available in this study include a high resolution LiDAR DTM (1×1 m, acquired in 2006–2009, multiple acquisition years were necessary to cover the entire area), an orthophoto from 2002 (25×25 cm) and a land cover map derived from ASTER data (resampled to 10×10 m; 2007).

Methods

Landslide Inventory Mapping

During the landslide mapping the specific morphological features, which are left after a landslide event occurred, are visually analysed and used to identify landslides, also in forested areas. The landslide inventory mapping was performed in a previous study (Petschko et al. 2013) by visually interpreting hillshade maps of different azimuth

angle (315° , 135° , 45° , (as used by Schulz 2004)), a slope map, contour lines with 4 m elevation difference and an orthophoto to delineate landslide polygons (Petschko et al. 2013). The mapping scale for identifying landslides was 1:2,000, however the polygons have been digitized at a scale of 1:200–1:1,000. During the mapping of the landslides different types were distinguished: “slide” (earth and debris slide), “flow” and “complex” following Cruden and Varnes (1996) (Petschko et al. 2013; Petschko et al. 2010). Areas with many landslides of different generations and where the delineation of single landslides was hardly possible were mapped as an “area of slides” (Petschko et al. 2010). Furthermore, the certainty of the delineation of the polygon was assigned as certain or uncertain for each polygon.

Relative Age Estimation

The relative age estimation is based on an approach proposed by McCalpin (1984) interpreting the morphology and the “freshness” of the morphological features that remain visible after the occurrence of a landslide on LiDAR DTM derivatives and orthophotos.

According to this concept the landslide morphology experiences a transformation starting from a feature showing every landslide detail (e.g. main and minor scarps, landslide

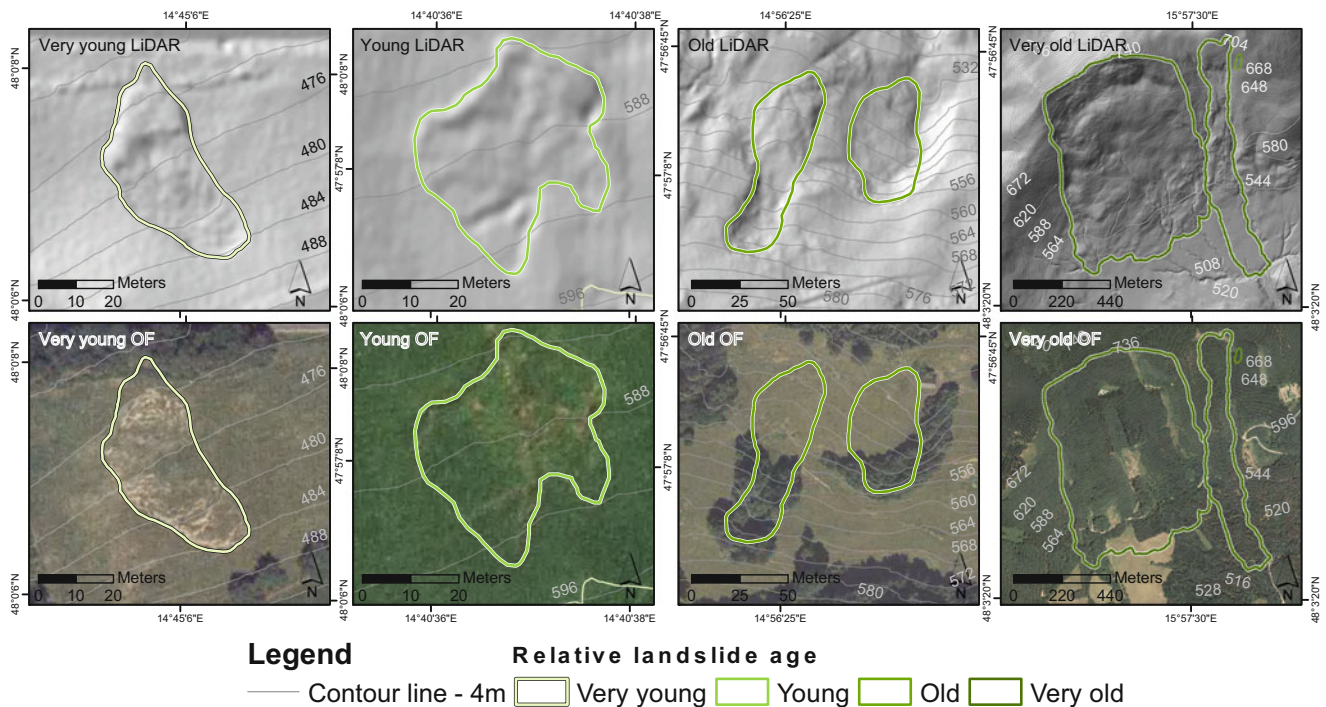


Fig. 2 Relative landslide age as estimated by the morphology visible on the LiDAR derivatives and by the vegetation cover visible on the orthophoto (OF). The relative age classes were defined “very young”,

“young”, “old” and “very old”. Note the different size of the four presented landslides as indicated by the scale bar

toe and fissures) very clear. The older the landslide gets and the longer it is exposed to erosion the more features of erosion will be visible. First the landslide forms will get smoother, later erosion and incision of streams will occur and reshape the morphology (Bell et al. 2012; McCalpin 1984). Furthermore, the vegetation cover is of importance to assess the relative age of the landslides (McCalpin 1984). We assume that in our study area the first occurrence of landslides is mainly on open land (not forested land). In literature this assumption is often related to the reinforcing effect of tree roots on the slope stability (Rickli and Graf 2009). In the field we learned that often after the landslide occurred farming of the land became more difficult and it was abandoned to forest growth.

Adapted after McCalpin (1984) we assign (1) “very young” to landslides which are not vegetated at least at the main scarp and which show a very fresh, rugged morphology (Fig. 2); (2) “young” to landslides which are fully vegetated (grass) and have a smoother morphology, which shows first modifications of the original topography due to erosion and deposition; (3) “old” to landslides which still show a distinct main scarp but a smooth morphology with dense vegetation cover (partly brushes or forest); (4) “very old” to landslides which are characterized by a very smooth morphology, by the re-establishing of the valley drainage pre-slide profile and by a dense vegetation cover. This vegetation cover is of

the same age or density as the surrounding vegetation. This relative age estimation was performed for each landslide and landslide type during the mapping process.

Comparison of Land Cover and Relative Landslide Age

The land cover of the mapped landslides was derived from the available land cover map on a grid cell base. Therefore, only the landslides classified as certain in their delineation and type were analysed further. This landslide inventory was split according to the assigned landslide age in four data sets. Each of this data set was used to mask the land cover map in ArcGIS (Version 9.3). Therewith the amount of pixel in each land cover class per landslide age was determined.

Results and Discussion

Landslide Inventory Mapping

The resulting landslide inventory contains 2,014 landslides of which 1,834 are considered to be of high certainty regarding the delineation and type of process (Petschko et al. 2013). The main mapped landslide type was “slide”

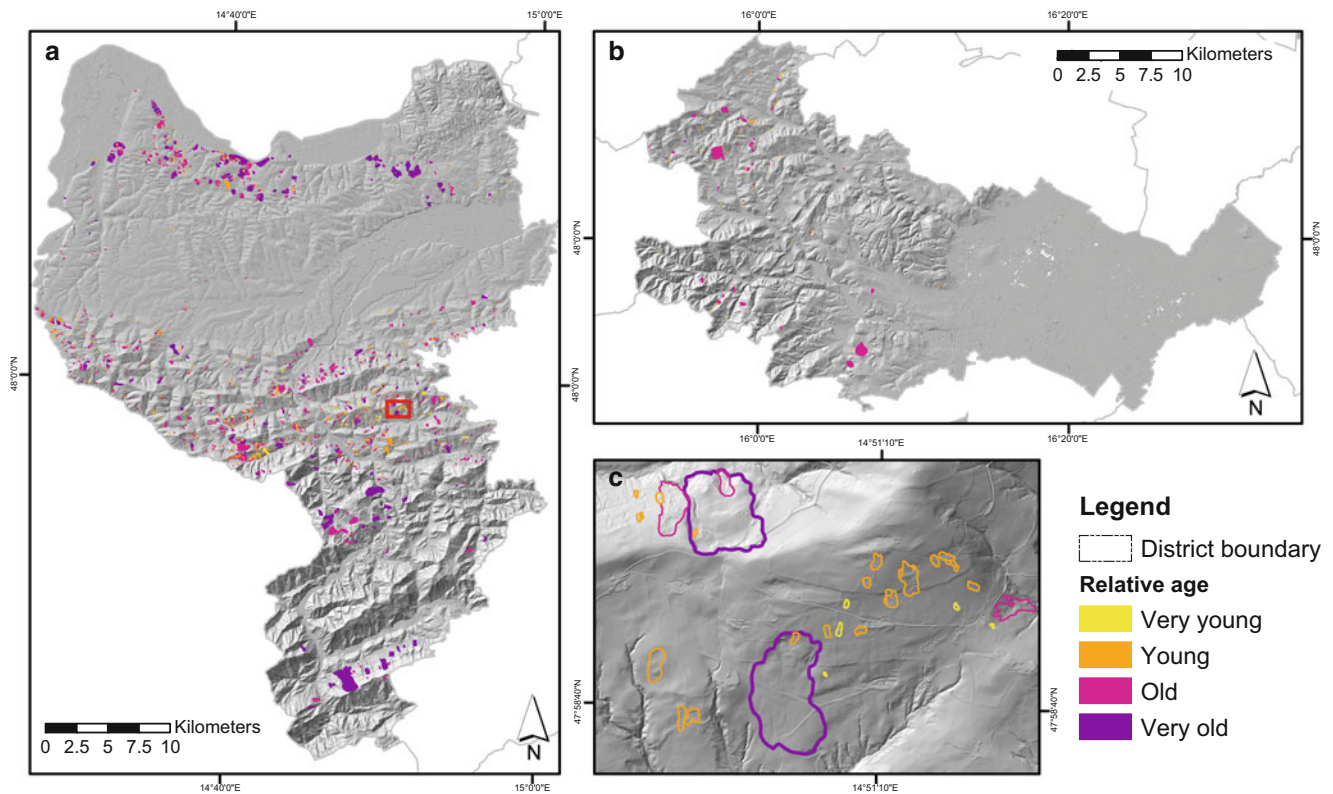


Fig. 3 Results of the relative landslide age estimation for (a) Amstetten and Waidhofen/Ybbs, (b) Baden. (c) Zoom to an example area. The relative age classes were defined “very young”, “young”, “old” and “very old”

(75 %). 20.5 % of the polygons of the landslide inventory were classified as “area with slides”.

Analysing all landslide types we found that these landslides are mainly located in forested areas (20.2 % in deciduous forest, 20 % in mixed forest and 19.9 % in coniferous forest, Table 1). Around 16 % of all landslides are located in arable land and 11 % are covered by grassland or pasture. Within the different landslide types the variation of land cover (forest (coniferous, mixed and deciduous)/no forest (arable land, grassland, pasture, fallow land and rough pasture)) is minor (Table 1). “Slides” (earth and debris slides) show the largest proportion of forested cells (64 %) whereas “complex landslides” only show a forest cover for 51 % of the cells. However, these results show, that more than half of the landslide cells are covered by forest.

Relative Age Estimation

With the relative age estimation we found that 8 % of the landslides were classified as “very young”, 10 % as “very old”, 34 % as “young” and nearly half of the landslides (48 %) were assigned as “old” (Fig. 3). During the mapping of “young” or “very young” landslides the combined interpretation of orthophoto and LiDAR derivatives was found to

be effective. In this way, also landslides with a very short travel distance and a clear but small main scarp could be easily identified. However, for “old” and “very old” landslides the availability of LiDAR derivatives is important. On orthophotos (or aerial photographs) the vegetation cover (mainly forest) does not allow the interpretation of the morphology and therefore the identification of a landslide, as shown in Fig. 2 with the “very old” landslide, is not possible (Brardinoni et al. 2003). Nevertheless, the interpretation of the LiDAR derivatives only might be misleading due to effects of morphological convergence (Antonini et al. 2002) or the conservation effect of forest cover on the landslide morphology. Examples for morphological convergence found in the study area are quarries or artefacts in the DTM due to the removal of single trees, houses and infrastructure. The conservation effect describes morphology that appeared to be fresh and “young” but the type of vegetation (forest), field checks and the starting re-establishing of the valley drainage in the lower part of the landslide revealed the landslide to be “very old” (Fig. 2). Therefore, the comparison with the vegetation cover (grass or forest) during the mapping is of high importance.

Furthermore, regarding the completeness of the inventory it has to be taken into account, that in agriculturally used areas the persistence of the landslide morphology is restricted.

Among the landslides with low persistence mainly “young” or “very young” landslides are not visible on the orthophoto or the LiDAR derivatives anymore (Bell et al. 2012). In these areas, the visibility of landslides is influenced by the activity of local farmers. Immediately after a landslide event smaller landslides are levelled to ensure the harvest or the usability of the area as pasture (Bell et al. 2012; Fiorucci et al. 2011). However, the number of landslides with low persistence and therefore landslides that are potentially missing from the inventory is unknown (Petschko et al. 2014).

In general it has to be pointed out that the relative landslide age estimated in this study is only applicable to the study area and its specific setting (e.g. topography, geology, vegetation, climate (Antonini et al. 2002)). Therefore, comparisons to the relative age of other areas are not possible.

Comparison of Land Cover and Relative Landslide Age

In contrast to the results of the land cover of all mapped landslides the splitting of the data into the different classes of relative age reveals large differences between the classes “very young” to “very old”. In more detail we found that the percentage of the grid cells covered with forest (coniferous, deciduous or mixed) increases the older the landslides were estimated. An exception to this general trend is the mixed forest. Here the “old” landslides show the highest proportion of forested grid cells (26 %, Table 1). All forest types summed up, 13 % of the “very young” landslides, 31 % of the “young” landslides, 61 % of the “old” and 64 % of the “very old” landslides are covered by forest.

With 38 % the land cover class grassland and pasture covers a large area of the “very young” landslides. This land cover class was found for only 10 % of the “very old” landslides. Combining all not forested land cover classes (open land) we found that these cover 83 % of the “very young”, 69 % of the “young”, 39 % of the “old” and 33 % of the “very old” landslides.

These findings match the assumption that landslides mainly occur on open land and the forest grows after abandonment of the land. However, a Swiss study on six event landslide inventories in a lithological similar region showed, that directly after a rainstorm event nearly 50 % of the landslides occurred in forested terrain (Rickli and Graf 2009). Furthermore, a dendrogeomorphology study showed that landslides can reactivate under forest (Van Den Eeckhaut et al. 2009).

Besides, this results show, that also “very young” and “young” landslides are covered by forest (according to the ASTER land cover map). This is clearly contradictory to the age estimation criteria. However, the possible reasons for this misclassified grid cells can be (1) the difference in the

resolution of the land cover data and the mapping scale of the landslides, (2) the algorithm used in the masking of the land cover by the landslides or (3) general problems in the supervised classification of the ASTER data.

Conclusions

The results of this study show that landslides of different relative age can be and are mapped when mapping landslides on the basis of LiDAR derivatives of one acquisition time only. Furthermore it was shown, that the interpretation of the morphology only can be misleading. Therefore, the combined usage of LiDAR and orthophotos is necessary. This potential mapping of very old landslides has to be considered before starting the mapping and might be overcome by restricting the mapping criteria on mapping young landslides only. However, the limited persistence of the landslide morphology of “young” and “very young” landslides in agricultural areas has additional influence on the completeness of the inventory.

At modelling with data on recent land cover the relative landslide age has to be accounted for, as no information on past land cover (at the time of the landslide occurrence) is available. Otherwise, there is a chance of introducing an unwanted bias into the susceptibility modelling. One solution can be the exclusion of “old” and “very old” landslides from the modelling sample. The alternative we propose is to use all landslides but to leave the land cover data out of the modelling. This might be considered, as the range of information on the topographical conditions (which are available in a much better spatial resolution as the land cover data) of the landslides might be better represented including the “old” and “very old” landslides in the analysis as well. Furthermore, leaving out the land cover but having better information on the topography can be of interest in case the land cover changes fast, e.g. by logging, and therefore the susceptibility map is soon not up-to-date anymore.

The absolute age of the landslides remains unknown. With the availability of multi-temporal LiDAR imagery the information on landslide age can be improved. However, this was not analysed in this study.

Acknowledgments The authors are thankful for the fruitful collaboration with the project clients and partners of the project “MoNOE—Method development for landslide susceptibility modelling in Lower Austria”. We are grateful for the funding and provision of data by the Provincial Government of Lower Austria.

References

Antonini G, Ardizzone F, Cardinali M, Galli M, Guzzetti F, Reichenbach P (2002) Surface deposits and landslide inventory

- map of the area affected by the 1997 Umbria-Marche earthquakes. *Boll Soc Geol It Volume speciale n.1*:843–853
- Ardizzone F, Cardinali M, Carrara A, Guzzetti F, Reichenbach P (2002) Impact of mapping errors on the reliability of landslide hazard maps. *Nat Hazards Earth Syst Sci* 2:3–14
- Bell R, Petschko H, Röhrs M, Dix A (2012) Assessment of landslide age, landslide persistence and human impact using airborne laser scanning digital terrain models. *Geografiska Annaler: Series A, Physical Geography* 94:135–156
- Brardinoni F, Slaymaker O, Hassan MA (2003) Landslide inventory in a rugged forested watershed: a comparison between air-photo and field survey data. *Geomorphology* 54:179–196
- Cardinali M, Reichenbach P, Guzzetti F, Ardizzone F, Antonini G, Galli M, Cacciano M, Castellani M, Salvati P (2002) A geomorphological approach to the estimation of landslide hazards and risks in Umbria, Central Italy. *Nat Hazards Earth Syst Sci* 2:57–72
- Cruden DM, Varnes DJ (1996) Landslide types and processes. In: Turner AK, Schuster RL (eds) *Landslides, investigation and mitigation*. Transportation Research Board Special Report 247, Washington DC, pp 36–75
- Fiorucci F, Cardinali M, Carlà R, Rossi M, Mondini AC, Santurri L, Ardizzone F, Guzzetti F (2011) Seasonal landslide mapping and estimation of landslide mobilization rates using aerial and satellite images. *Geomorphology* 129:59–70
- Guzzetti F (2005) *Landslide hazard and risk assessment*. Dissertation, Rheinischen Friedrich-Wilhelms-Universität Bonn
- Guzzetti F, Mondini A, Cardinali M, Fiorucci F, Santangelo M, Chang K-T (2012) Landslide inventory maps: New tools for an old problem. *Earth-Sci Rev* 112:42–66
- Guzzetti F, Reichenbach P, Cardinali M, Ardizzone F, Galli M (2003) The impact of landslides in the Umbria region, central Italy. *Nat Hazards Earth Syst Sci* 3:469–486
- McCalpin J (1984) Preliminary age classification of landslides for inventory mapping. University of Idaho, Moscow, pp 99–120
- Petschko H, Bell R, Leopold P, Heiss G, Glade T (2013) Landslide inventories for reliable susceptibility maps in Lower Austria. In: Margottini C, Canuti P, Sassa K (eds) *Landslide science and practice*. Volume 1: Landslide inventory and susceptibility and hazard zoning. Springer, pp 281–286
- Petschko H, Bell R, Brenning A, Glade T (2012) Landslide susceptibility modeling with generalized additive models - facing the heterogeneity of large regions. In: Eberhardt E, Froese C, Turner AK, Leroueil S (eds) *Landslides and engineered slopes, protecting society through improved understanding*. Taylor & Francis, Banff, Alberta, Canada, pp 769–777
- Petschko H, Brenning A, Bell R, Goetz J, Glade T (2014) Assessing the quality of landslide susceptibility maps – case study Lower Austria. *Nat Hazards Earth Syst Sci* 14:95–118
- Petschko H, Glade T, Bell R, Schweigl J, Pomaroli G (2010) Landslide inventories for regional early warning systems. In: Malet JP, Glade T, Casagli N (eds) *Mountain risks: bringing science to society*. CERIG Editions, Strasbourg
- Rickli C, Graf F (2009) Effects of forests on shallow landslides—case studies in Switzerland. *For Snow Landscape Res* 82:33–44
- Schulz WH (2004) Landslides mapped using LIDAR imagery, Seattle, Washington. US Geological Survey Open-File Report 1396 (11)
- Schweigl J, Hervás J (2009) *Landslide Mapping in Austria*. JRC Scientific and Technical Reports. European Commission Joint Research Centre, Institute for Environment and Sustainability, Italy. 65p
- Schwenk H (1992) Massenbewegungen in Niederösterreich 1953–1990. *Jahrbuch der Geologischen Bundesanstalt*. Geologische Bundesanstalt, Wien, pp 597–660
- Van Den Eeckhaut M, Muys B, Van Loy K, Poesen J, Beeckmann H (2009) Evidence for repeated re-activation of old landslides under forest. *Earth Surf Process Landforms* 34:352–365
- Van Westen CJ, Asch TWJ, Soeters R (2005) Landslide hazard and risk zonation—why is it still so difficult? *Bull Eng Geol Environ* 65: 167–184
- Zanutta A, Baldi P, Bitelli G, Cardinali M, Carrara A (2006) Qualitative and quantitative photogrammetric techniques for multi-temporal landslide analysis. *Ann Geophys* 49:1067–1080



Automated Remote Sensing Based Landslide Detection for Dynamic Landslide Inventories

Sigrid Roessner, Robert Behling, Karl Segl, Darya Golovko, Hans-Ulrich Wetzel, and Hermann Kaufmann

Abstract

Dynamic landslide inventories are important for objective landslide hazard and risk assessment. Multi-temporal satellite remote sensing has the potential for automated landslide detection at a regional scale. For this purpose a new automated approach has been developed based on analysing temporal trajectories of NDVI values derived from a co-registered multi-temporal RapidEye data stack. Specific temporal footprints of vegetation changes enable identification of landslide events. Applying this approach to a 12,000 sqkm study area in Southern Kyrgyzstan, about 250 landslide events could be automatically detected between 2009 and 2012. Subsequent field checks have revealed that the vast majority of these events have been correctly identified. Thus, the developed approach is capable of automatically detecting different kinds of mass movements under diverse natural conditions.

Keywords

Landslide inventory • Multi-temporal • Remote sensing • Change detection • Kyrgyzstan • Central Asia

Introduction

Kyrgyzstan is a mountainous Central Asian country, where 90 % of the country is higher than 1,000 m a.s.l. It is almost completely covered by the W-E trending Tianshan Mountain ranges with peak elevations above 7,000 m a.s.l. Besides earthquakes, floods, and avalanches, gravitational mass movements (landslides) represent one of the major natural hazards to the local population. They are especially concentrated along the Eastern rim of the Fergana Basin (Fig. 1). In this densely populated mountainous region almost

every year large landslides endanger human lives and infrastructure. Therefore local authorities responsible for disaster management and risk reduction have a big need for objective hazard and risk assessment covering large areas in a spatially differentiated way.

Enabling objective hazard assessment requires profound knowledge about spatiotemporal distribution and evolution of landslides in order to improve understanding of regional processes activity in its links to predisposing and triggering factors. In this context, multi-temporal landslide inventories are of special importance (Fell et al. 2008; van Westen et al. 2008). However, their initial generation and subsequent updates represent big challenges especially in case of large areas where they require the combination of different approaches and data sources as well as incorporation of results into common spatial databases within a GIS environment (Guzzetti et al. 2012).

In Kyrgyzstan, landslide inventories have been carried out since the 1950s, whereas approximately 5,000 landslides have been recorded by the local authorities. However, regular

S. Roessner (✉) • R. Behling • K. Segl • D. Golovko • H.-U. Wetzel • H. Kaufmann
Section 1.4 – Remote Sensing, German Research Centre for Geosciences (GFZ) Potsdam, Telegrafenberg 14473, Potsdam, Germany
e-mail: roessner@gfz-potsdam.de; behling@gfz-potsdam.de; segl@gfz-potsdam.de; dgolovko@gfz-potsdam.de; wetzel@gfz-potsdam.de; charly@gfz-potsdam.de

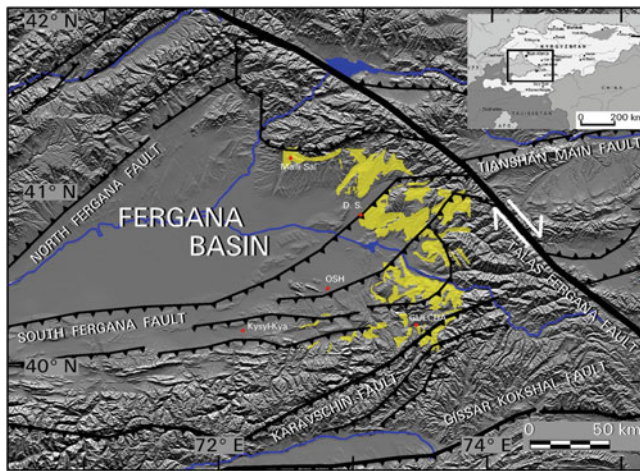


Fig. 1 Study area in Southern Kyrgyzstan. Areas marked in yellow are characterized by high landslide activity

inventories have been limited to the time period between 1968 and 1992 and focused on areas in the vicinity of settlements. Most of the still available documentations comprise verbal descriptions of main events (e.g., Ibatulin 2011) whereas in most of the cases precise geographic locations are missing. Thus, the existing knowledge on landslide events is incomplete in space and time and leaves the need for establishing a systematic multi-temporal landslide inventory.

Because of the limited information base and the large areas which are affected, satellite remote sensing data represent the only consistent, reliable and up-to-date source of spatial information in Kyrgyzstan. Since landslides are a phenomenon which often significantly changes earth surface characteristics, usually they are well detectable in optical imagery which has already been archived for several decades and thus enables longer term analysis required for reliable investigation of landslide occurrence. This situation got further improved by opening the Landsat archive in early 2009 providing free access to a profound data pool of widely available optical multi-temporal data (Wulder et al. 2012) for large parts of the world including Central Asia.

So far, there have been only very few attempts to perform such multi-temporal analysis with the goal of automated landslide detection over longer periods of time (e.g., Martha et al. 2013), whereas most of the landslide related change detection studies have been focused on bi-temporal or mono-temporal analysis of landslide occurrence after well-defined major triggering events, such as earthquakes or intense rainstorms (e.g., Lacroix et al. 2013).

In this paper a new approach for automated landslide detection is presented which has the potential for operational analysis of a multi-sensor multi-temporal satellite remote sensing database at a regional scale. The paper describes the established multi-temporal satellite remote sensing database, the developed approach and its application to the approx.

12,000 sqkm study area in Southern Kyrgyzstan (Fig. 1) based on RapidEye satellite remote sensing data which have been acquired with high temporal resolution between the years 2009 and 2012.

Landslide Situation in Kyrgyzstan

In Kyrgyzstan large deep-seated landslides (up to more than one million cubic meters) represent one of the major natural hazards due to their frequent occurrence within large areas. They are mainly related to active mountain building affecting the Pamir-Tianshan orogenic system in the result of the ongoing collision of the Indian and Eurasian plates (Strecker et al. 2003). These landslides are mostly concentrated along the topographically rising Eastern rim of the Fergana Basin below its transition into the high mountainous terrain. Landslides mostly occur in form of rotational and translational slides within an elevation range between 700 and 2,000 m in weakly consolidated Quaternary and Tertiary sediments consisting of loess, sand- and siltstones, clays, loams and carbonates.

The lithology of the landslides represents the main factor in determining their style of movement. Landslides occurring in massive Quaternary loess units of up to 50 m thickness are characterised by very rapid avalanche-like mass movements which can reach several meters per second (Fig. 2). These landslides are especially dangerous because of their great destructive power and their sudden occurrence after longer periods of sneaky destabilisation which is indicated by cracks developing sub-parallel to hillslope crests. Another form of rotational landslides occurs in Meso- and Cenozoic sediments (Jura up to Paleogene) with intercalated clays (Fig. 2). These environments lead to complex mass movements with long periods of activation and maximum movement rates of several meters per day. Both types of landslides result in devastation of large areas in a region which represents an important human living space in Kyrgyzstan (Roessner et al. 2005).

Multi-temporal Satellite Remote Sensing Database

A multi-temporal database of optical remote sensing data has been established for the study area in Southern Kyrgyzstan. This database consists of 592 multispectral mid- and high-resolution satellite remote sensing images acquired by the Landsat-TM and ETM+, SPOT-1 and 5, ASTER, and RapidEye sensors during the last 25 years. The first image was acquired on the 12th of July 1986 by SPOT-1 followed by a Landsat TM image of 3rd of September 1989, whereas complete annual coverage of the region of interest has been



Field foto taken by S. Roessner in August 1998

Slope failure in quaternary loess – main displacement at night during 15 minutes period in March 1994 (50 victims buried)



Field foto taken by S. Roessner in August 1998

Large complex slope failure in clay-rich tertiary sediments overlaid by loess during a two weeks period in June 1998 (no victims)

Fig. 2 Main landslide types in Southern Kyrgyzstan. Lithological composition weakly consolidated sediments determines style of movement

achieved since 1996. The contributing sensors differ widely in their spatial resolution ranging between 30 m for Landsat and 6.5 m for RapidEye data. They also cover different spectral ranges by varying spectral bands and resolutions. However, all of these sensors represent multispectral instruments comprising the green, red, and NIR spectral bands as lowest common denominator forming the basis for comprehensive multi-sensor analysis of landslide related surface changes.

Remote sensing datasets were mostly acquired in form of orthorectified standard data products in order to minimize geometric preprocessing effort and to facilitate operational suitability of the developed approach independent from local ground truth information, such as GCPs. RapidEye data have been acquired in the frame of the RESA (RapidEye Science Archive) program allowing customized tasking of data acquisition during pre-defined time periods. Due to the five independent satellites of the RapidEye system (Chander et al. 2013), a database of high spatial and temporal resolution could be established containing approx. 20 complete RapidEye coverages for the 4-year period between 2009 and 2012. In total, it comprises of 503 level 3A standard

orthorectified data products resampled to 5 m pixel size. Landsat TM and Landsat ETM + data were obtained from the U.S. Geological Service Global Land Survey (USGS GLS) in form of orthorectified Level 1 T data products. In the result the established multi-temporal and multi-sensor satellite remote sensing database solely contains orthorectified datasets.

Automated Approach for Landslide Identification

The established multi-temporal satellite remote sensing database forms the basis for the development of an automated approach for landslide identification in order to derive a GIS-based multi-temporal landslide inventory in an object-based form including the potential for qualitative and quantitative characterization of the identified landslide events. The main part of the approach (Fig. 3) is represented by multi-temporal change detection allowing separation between changes caused by landslide activity from other land cover changes (e.g. agriculture) as well as from artifact changes caused by geometric mismatches and radiometric differences between image data of different acquisition properties. In order to minimize such artifacts, automated change detection requires adequate pre-processing of the multi-temporal image database. Taking into account the high number of more than 500 datasets, pre-processing has to be carried out in an automated and robust form.

Geometric Correction

Since for this area a continuous and consistent external topographic reference, such as large-scale topographic maps has not been available, the free of charge and widely available terrain corrected Landsat Level 1 T data are used as topographic reference. The Landsat Level 1 T data are characterized by sub-pixel image-to-image registration geolocation accuracy (Kennedy et al. 2010) enabling implementation of multiple reference scenes into the co-registration procedure. Using multiple reference scenes of different acquisition dates is advantageous, because it accommodates multi-temporal effects, such as seasonal and long-term land cover changes which often reduce the accuracy of co-registration (Gao et al. 2009). Moreover, the used Landsat Level 1 T reference enables co-registration independent from the availability of other topographic reference data. Thus, the approach can be applied worldwide under the prerequisite that Landsat Level 1 T data are available.

A special image-to-image co-registration approach has been developed in order to correct for the remaining geometric shifts occurring between the standard orthorectified

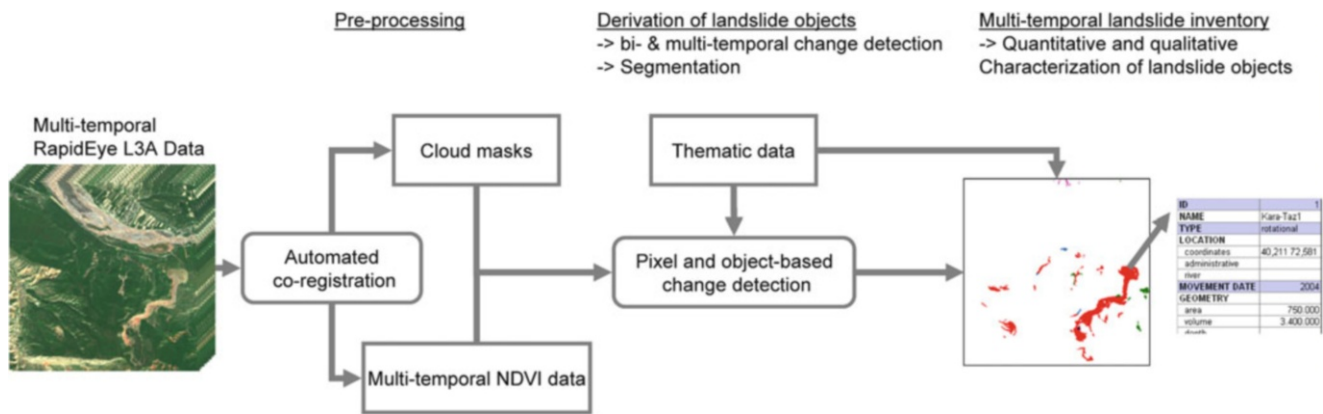


Fig. 3 Overview of developed approach for automated remote sensing based derivation of landslide inventory

datasets contained in the multi-temporal and multi-sensor database. The approach assumes that the orthorectified standard data products of the various sensors only differ by global shifts in x and y direction which are constant for the whole dataset. Checking the fulfillment of this condition for each dataset is part of the developed approach. The final result includes two co-registered images—one adapted to the grid and spatial resolution of the reference data and one maintaining the spatial resolution of the original data with improved map coordinates in the header file.

The co-registration approach builds on an area based cross-correlation algorithm (Dawn et al. 2010) requiring the same spatial resolution for the reference image and the warp image. Resampling of the warp image to the spatial resolution of the reference dataset is a critical step for the performance of the correlation process because different interpolation approaches used for resampling lead to different results. The developed approach simulates realistic Landsat pixels by applying a Gaussian filter kernel taking into account the spatial resolution of both sensors following the approach described in (Mueller and Segl 1999).

The developed co-registration approach has been applied to all of the 592 image datasets resulting in specific shifts for all of them. No image had to be rejected because of the affine criterion in the validation step implying that the previously orthorectified standard image products are characterized by high internal geometric stability. The obtained shifts vary widely between more than 400 m for selected SPOT-1 data and 5 m for the latest RapidEye data. Typically, shifts of several tens of meters had to be applied during co-registration (Behling et al. 2012). Assessment of the relative image-to-image accuracy based on time-invariant check points (CPs) has resulted in an overall accuracy of 17 m (RMSE) and maximum remaining offsets of 20 m to the Landsat reference. Taking into account the 30 m resolution of Landsat, these results show a sub-pixel image-to-image accuracy of the whole multi-sensor database. For the 503 RapidEye data sets

sensor-internal image-to-image accuracies of less than 5 m have been achieved. Absolute accuracy of the co-registered database has been evaluated based at 52 differential GPS (DGPS) points showed an overall accuracy of 23 m (RMSE) and a maximum position error (PE) of 29 m with a systematic shift in western direction. The obtained results have proven the robustness of the developed co-registration approach against variabilities in the image data resulting from various multi-sensor and multi-temporal effects often impeding the applicability of already existing co-registration approaches.

Multi-temporal Change Detection

The developed multi-temporal change detection approach is based on the analysis of temporal trajectories of NDVI time series derived from the pre-processed multi-temporal satellite remote sensing data stack. These temporal trajectories are derived for every pixel across the time span of the entire data archive and thus allow analysis of vegetation cover changes over longer periods of time rather than solely assess the absence of vegetation in a single dataset or the loss of vegetation between two datasets. These specific temporal footprints of vegetation changes enable identification of landslide events due to the temporal characteristics of destruction and regeneration of the vegetation cover caused by the landslide event itself as well as by longer-term processes of (re) activation of landslide-prone slopes. They need to be distinguished from temporal changes of the vegetation cover caused by other processes, such as agricultural land use.

For this purpose a combined pixel- and object-based approach has been developed which is divided into three main steps: (1) bi-temporal change detection, (2) segmentation based on the bi-temporal change result and (3) object-based multi-temporal change detection for final delineation of landslide events (Behling et al. 2013). So far, this approach has been applied to the entire multi-temporal RapidEye image

database containing 20 complete temporal coverages for the whole study area between the years 2009 and 2012. For every analyzed time period a shapefile has been produced containing the image-intrinsic likelihoods for a landslide occurring within this time period.

Visual evaluation of the derived objects resulted in the selection of about 250 objects most likely representing surface changes related to landslides. The size of these objects is ranging between 500 and 250,000 square meters and the total area affected by these landslide-related changes amounts to 5.5 million square meters. About half of these changes happened between 2009 and 2010. For the analyzed time period between 2009 and 2012 the Ministry of Emergency Situations of Kyrgyzstan has only reported 40 events.

The obtained results have been verified during a 4-week field survey which took place in September 2012. During this survey about 100 of the 250 detected landslides have been visited and in almost all of these cases the field checks confirmed recent surface changes related to landslides. Exceptions were primarily caused by the extraction of construction material (e.g., clay and gravel) at the bottom of hillslopes representing artificial mass movements. This field survey has revealed that the developed approach is capable of automatically detecting different kinds of mass movements caused by a variety of slope processes, such as rotational and translational landslides as well as debris flows under diverse natural conditions. Thus, it could be shown that the approach can be used for reliable automated landslide detection at a regional scale.

Discussion and Outlook

Application of the developed automated approach for landslide detection based on a multi-temporal and multi-sensor satellite remote sensing database has shown that in both parts—geometric correction and multi-temporal change detection—meaningful results have been obtained allowing object-based identification of landslides and determination of their periods of occurrence and/or reactivation.

In this context robust spatial co-registration of the large multi-temporal database—comprising almost 600 datasets acquired by five different sensors—has been an important prerequisite for subsequent change detection and could be achieved with sub-pixel accuracy. Due to the high internal stability of the used standard geo-coded data products, it has been possible to apply global shifts to each dataset in order to correct for the spatial image-to-image offsets while maintaining the high internal geometric stability of the initial image database. Due to the use of freely and globally available Landsat Level 1 T data as spatial reference the approach is independent from the existence of local geometric reference information and can be applied to any part of

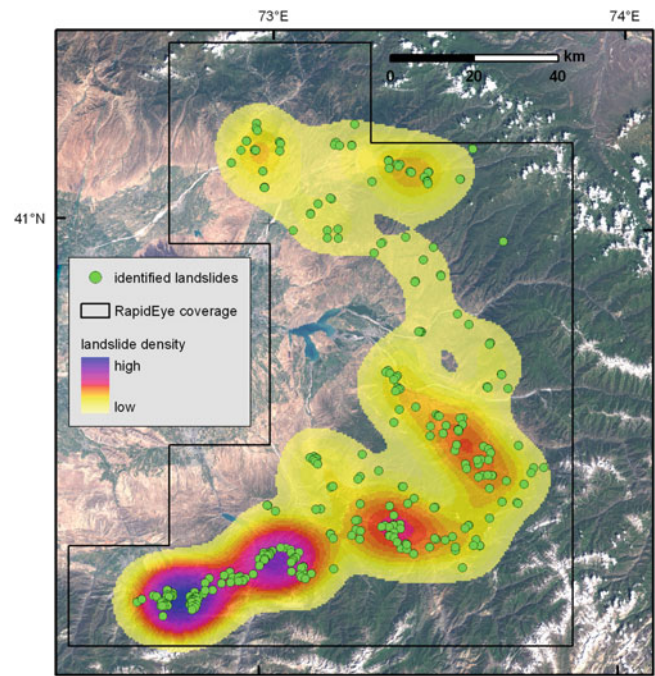


Fig. 4 Automatically identified landslides from multi-temporal RapidEye database between 2009 and 2012

the world covered by suitable Landsat Level 1 T data. In this context, the Landsat-8 Operational Land Imager (OLI) launched on 11 February 2013 will ensure future applicability of the co-registration approach.

The developed change detection approach has been applied to the entire multi-temporal RapidEye database enabling systematic derivation of a multi-temporal landslide inventory for the 12,000 sqkm study area along the Eastern rim of the Fergana Basin (Fig. 4) which is required for objective hazard and risk assessment. Although compared to previous years process activity had been rather low during the analyzed time period between 2009 and 2012 and no specific triggering event has been known, a total of about 250 landslides could be automatically detected. This shows the constant ongoing process activity occurring independently from distinct triggering events in this area. This situation emphasizes the need for systematic multi-temporal landslide inventories in regions dominated by complex slope failures, such as the Eastern rim of the Fergana Basin. In a next step the developed approach will be applied to a longer-term time series containing multi-temporal image data acquired by a variety of optical sensor starting from 1986 whereas annual coverage for the complete study area has been available since 1996.

Acknowledgments This work has been funded by the German Federal Ministry of Research and Technology (BMBF) within the framework of PROGRESS (Potsdam Research Cluster for Georisk Analysis, Environmental Change and Sustainability) and TIPTIMON (Tianshan—Pamir Monitoring program). We also thank the German Aerospace Agency

(DLR) for providing RapidEye data by the RESA (RapidEye Science Archive) program (grant number 424).

References

- Behling R, Roessner S, Segl K, Rogass C, Wetzel HU, Kaufmann H (2012) Automated geometric co-registration of multi-temporal satellite remote sensing data for landslide inventories. In: Proceedings of the 4th RESA workshop, 21–22 March 2012. Neustrelitz, Germany, pp 35–50 (in German)
- Behling R, Roessner S, Segl K, Kaufmann H (2013) Automated landslide detection using multi-temporal RapidEye data. In: Proceedings of the 5th RESA workshop, 20–21 March 2013. Neustrelitz, Germany, pp 241–257
- Chander G, Haque MO, Sampath A, Brunn A, Trosset G, Hoffmann D, Roloff S, Thiele M, Anderson C (2013) Radiometric and geometric assessment of data from the RapidEye constellation of satellites. *Int J Remote Sens* 34:5905–5925
- Dawn S, Saxena V, Sharma B (2010) Remote sensing image registration techniques: a survey, image and signal processing. *Lect Notes Comput Sci* 6134:103–112
- Fell R, Corominas J, Bonnard C, Cascini L, Leroi E, Savage W (2008) Guidelines for landslide susceptibility, hazard and risk zoning for land use planning. *Eng Geol* 102(3–4):85–98
- Gao F, Masek JG, Wolfe RE (2009) Automated registration and orthorectification package for Landsat and Landsat-like data processing. *J Appl Remote Sens* 3(1):033515
- Guzzetti F, Mondini AC, Cardinali M, Fiorucci F, Santangelo M, Chang K (2012) Landslide inventory maps: new tools for an old problem. *Earth Sci Rev* 112(1–2):42–66
- Ibatulin CV (2011) Monitoring of landslides in Kyrgyzstan. Ministry of Emergency Situations of the Kyrgyz Republic, Bishkek. 145 p. (in Russian)
- Kennedy RE, Yang Z, Cohen WB (2010) Detecting trends in forest disturbance and recovery using yearly Landsat time series: 1. LandTrendr — temporal segmentation algorithms. *Remote Sens Environ* 114:2897–2910
- Lacroix P, Zavala B, Berthier E, Audin L (2013) Supervised method of landslide inventory using panchromatic SPOT5 images and application to the earthquake-triggered landslides of Pisco (Peru, 2007, Mw 8.0). *Remote Sens* 5:2590–2616
- Martha TR, van Westen CJ, Kerle N, Jetten V, Kumar KV (2013) Landslide hazard and risk assessment using semi-automatically created landslide inventories. *Geomorphology* 184:139–150
- Mueller M, Segl K (1999) Simulation of high resolution imagery. In: Nieuwenhuis GJ, Vaughan RA, Molenaar M (eds) Operational remote sensing for sustainable development. pp 331–338
- Roessner S, Wetzel HU, Kaufmann H, Sarnagoev A (2005) Potential of satellite remote sensing and GIS for landslide hazard assessment in Southern Kyrgyzstan (Central Asia). *Nat Hazards* 35(3):395–416
- Strecker MR, Hilley GE, Arrowsmith JR, Coutand I (2003) Differential structural and geomorphic mountain-front evolution in an active continental collision zone: The NW Pamir, Southern Kyrgyzstan. *Geol Soc Am Bull* 115:166–181
- Van Westen CJ, Castellanos E, Kuriakose SL (2008) Spatial data for landslide susceptibility, hazard and vulnerability assessment: an overview. *Eng Geol* 102(3–4):112–131
- Wulder MA, Masek JG, Cohen WB, Loveland TR, Woodcock CE (2012) Opening the archive: how free data has enabled the science and monitoring promise of Landsat. *Remote Sens Environ* 122:2–10



Persistent Scatterer Interferometry (PSI) Technique for Landslide Characterization and Monitoring

Veronica Tofani, Federico Raspini, Filippo Catani, and Nicola Casagli

Abstract

Dealing with landslide, the availability of long time series of displacement often represents the most effective method to define its state of activity, to observe relationship with triggering factors and to assess the effectiveness of the mitigation measures. Moreover, the presence of a dense grid of measurements is essential to map correctly the boundary of the mass movements, to reconstruct the actual vector of displacement and to identify the deformation pattern. Persistent Scatterer Interferometry (PSI) represents an effective tool to measure landslide displacement, as it offers a synoptic view that can be repeated at different time intervals and at various scales. In this paper, PSI interferometry and conventional ground-based monitoring techniques have been integrated to characterize and to monitor the earth rotational slide threatening the Santo Stefano d'Aveto village in the Northern Apennines (Italy). On one hand, the in situ information recorded by inclinometers can help in defining the actual location of the sliding surface and the involved volumes of material. On the other hand, PSI measurements have allowed better redefining of the boundaries of the landslide, its state of activity and have allowed a better understanding of landslide geometry and kinematics. The integration of ground-based monitoring data and PSI data have provided sound results for landslide characterization.

Keywords

Landslide • PSI • Monitoring and characterization • Santo Stefano d'Aveto

Introduction

Dealing with landslide, monitoring and characterization means measurement of the superficial displacement induced by a slope movement to define its typology, areal extent, state of activity (Mantovani et al. 1996) and effectiveness of the mitigation measures (Farina et al. 2006).

Retrieval over time of superficial ground displacements related to landslide occurrence is historically based on traditional techniques, including wire extensometers (Corominas

et al. 2000), inclinometers (Angeli et al. 2000), GPS (Gili et al. 2000), levelling (Cotecchia 1996) or, more recently, photogrammetry (Kaab 2000) and terrestrial laser scanning (Fanti et al. 2012). These techniques, despite their robustness and reliability, are time-consuming and resource intensive, since they require a great deal of time and money for timely updates.

In parallel, a number of airborne and satellite remote sensing techniques, became available for the recognition of landslide features (Metternicht et al. 2005). It became clear that availability of new remote sensing technologies, coupling synoptic view that can be repeated at different time intervals, may support the analysis of landslide behaviour. In particular, satellite SAR (Synthetic Aperture Radar) interferometry (Massonnet and Feigl 1998; Tofani et al. 2013) has been proved a sound tool to assess changes on the

V. Tofani (✉) • F. Raspini • F. Catani • N. Casagli
Earth Sciences Department, University Firenze, Via La Pira,
4 Firenze 50121, Italy
e-mail: veronica.tofani@unifi.it; federico.raspini@unifi.it;
filippo.catani@unifi.it; nicola.casagli@unifi.it

Earth's surface. Two different suitable approaches have been implemented over years to exploit information contained in the phase values of SAR images: the single pair Differential SAR Interferometry (DInSAR) and the Persistent Scatterer approach (PSI). The latter relies on the use of a long series of co-registered SAR imagery gathered at different times on the same target area (Zebker and Goldstein 1986).

This work presents the exploitation of PSI approach applied to ERS 1/2 and ENVISAT SAR images to monitor the Santo Stefano d'Aveto landslide (Northern Apennines, Italy), integrating the information deriving from the pre-existing geotechnical monitoring system.

Study Area and Landslide Description

The Santo Stefano d'Aveto village (Fig. 1) is located near the watershed of the Aveto River Basin that sets the limit between the Liguria and the Emilia Romagna regions. From a geomorphological point of view, the study area is located in an ancient glacial valley, ENE-WSW oriented and bordered on the east, north and south by mountain peaks reaching an elevation up to 1,800 m a.s.l. Geologically, the main outcropping lithologies are constituted by sandstones with limestone and marls and ophiolitic rocks, such as basalts and gabbros.

According to the Regional Geological map 1:25,000 scale, the Santo Stefano d'Aveto village is located on unsorted glacial deposits constituted of sandstone and ophiolitic clasts in a sandy-silty matrix. Actually, the village is built on an ancient complex landslide that can be defined according to (Cruden and Varnes 1996) as a complex earth slide-earth flow. The aerial extension of the landslide is 1.3 km², and the estimated volume is around 10 million cubic meters. The slope angle of the landslide area ranges from 0° to 60°, with an average value of 8°. The maximum values are reached in the upper portion of the landslide, where the main scarp is located.

The Santo Stefano landslide is a hold and well-known one and it was already included in the Landslide Inventory Map developed within the PAI (Hydrogeomorphological Setting Plan) of the Po River Basin Authority. The landslide has been classified as active in the upslope portion and dormant in the remaining part, where almost all the villages are located. Despite the velocity of the movement is an extremely slow one (according to the classification given in Cruden and Varnes 1996) and does not represent a high risk to the people, it poses a major threat to the structural elements (buildings and in infrastructure), which are often subjected to repairing and consolidation works.

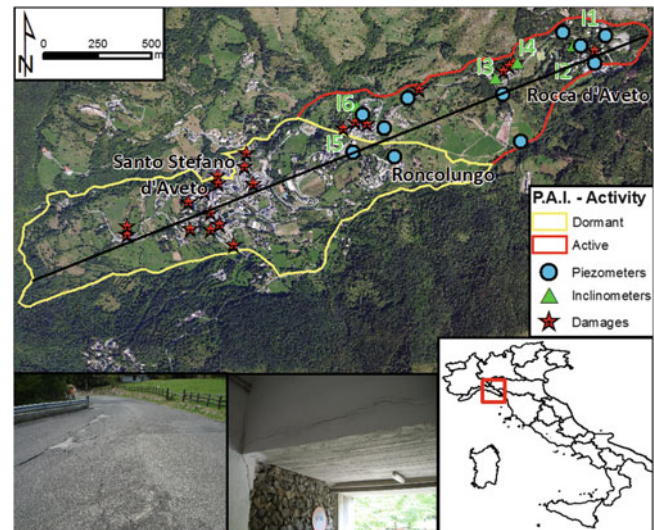


Fig. 1 Landslide map with location of the geotechnical monitoring instrumentation and damage to buildings and infrastructures. The trace of the section is also reported

Data Used and Methodology

Geotechnical and Geological Data

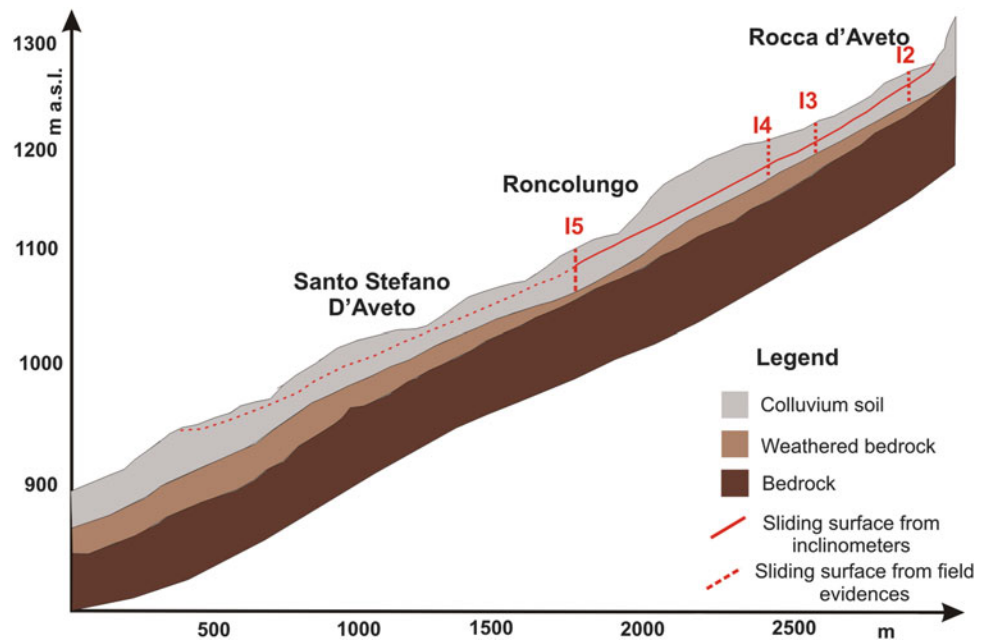
Six inclinometers and eleven piezometers have been installed inside the landslide perimeter (Fig. 1) during a geotechnical campaign carried out from 2000 to 2006.

The I1, I3 and I5 were installed in 2001, with measurements that span the temporal interval from January 2001 to September 2004. In 2004, three more instruments were added, I2, I4 and I6, which have been measured until September 2006. All the inclinometers reached failure. The highest velocities are measured in the I1 inclinometer located in Rocca d'Aveto. The inclinometric measurements have allowed reconstruction of the depth of the sliding surface (Fig. 2), located at about 10 m of depth in the upslope portion of the landslide and at about 20 m of depth near Santo Stefano d'Aveto village. In general, the depth of the slip surface increases from the upper to the lower portion of the landslide.

The landslide affects the first layer of material composed of colluvium soil made of debris in a sandy-silty matrix. Thin layers of clay material are located inside the soil, and they can possibly represent the potentially slip surface.

The piezometric monitoring has been carried out from 2000 to 2006 in eleven piezometers with monthly acquisitions. The monitoring has highlighted that there is a free water table in the debris cover and that the average depth of the piezometric surface ranges from a few meters in the upper portion of the landslide to around 20 m at the toe. The measurements present a seasonal variability with a

Fig. 2 Reconstructed geological section of the Santo Stefano d'Aveto landslide



water table lowering during dry seasons and rising in the wet season.

PSI Data

Characterization and monitoring of the Santo Stefano d'Aveto landslide have been carried out by using four stacks of satellites SAR images. SAR satellite imagery in the C band, acquired by the European Space Agency (ESA) satellites ERS1/2 and ENVISAT, were employed for the reconstruction of the history and spatial patterns of the Santo Stefano landslide (Table 1). These four stacks were processed with the PSInSAR™ approach (Ferretti et al. 2000), the first technique specifically implemented for the processing of multi-temporal radar imagery, finally leading to the generation of deformation velocity maps and a displacement time series of point-wise targets for which a sixteen-year-long displacement history was reconstructed. The reference points of the four stacks—to which displacement measurements are computed—were selected 1.5 km southwest Santo Stefano, over marl formations devoid of ground deformation.

The proper selection of the reference point is a key aspect within the PSI processing chain: the selected point has to be chosen within areas unaffected by ground motions in order to avoid the retrieval of an unreal pattern of deformation. In Fig. 3, the distribution of PS points within the landslide is shown. The highest LOS (Line of Sight) velocities, up to 35 mm/year in ERS descending dataset, have been generally measured in the upslope zone of the landslide, where Rocca d'Aveto is located. A general decrease of deformation rates is observed moving down-slope.

Table 1 Time period, number of Persistent Scatterers (PS) within the landslide area

| Satellite | Orbit | Time period (#scene) | Nr Ps |
|-----------|------------|----------------------------|-------|
| ERS1/2 | Ascending | 09/07/1992–20/08/2000 (27) | 85 |
| | Descending | 16/05/1992–19/12/200 (78) | 403 |
| ENVISAT | Ascending | 06/07/2003–29/06/2008 (30) | 118 |
| | Descending | 15/10/2002–06/05/2008 (33) | 274 |

The measurements recorded during the different time periods (1992–2000 and 2002–2008) and through different acquisition geometries—descending and ascending—are consistent and confirm that the recorded ground movement is related to a slope movement with a NE-SW direction component.

Due to the intrinsic characteristics of the radar sensors, InSAR-based displacements are 1D measurements. SAR sensors are side-looking radar and operate with a LOS direction tilted with respect to the vertical direction. Because of the rather small incidence angle (usually between 23° and 45°), the sensor is much more sensitive to vertical deformation than to horizontal deformation. Hence, the resulting datasets can estimate only the projection along the satellite LOS. Under the assumption of absence of N-S deformation components, combining ascending and descending information permits one to extract the vertical and horizontal (in the east-west direction) components of the movement and, consequently, the real vector of displacement (Raspini et al. 2012). Generally, to combine ascending and descending datasets and extract the vertical and east-west components

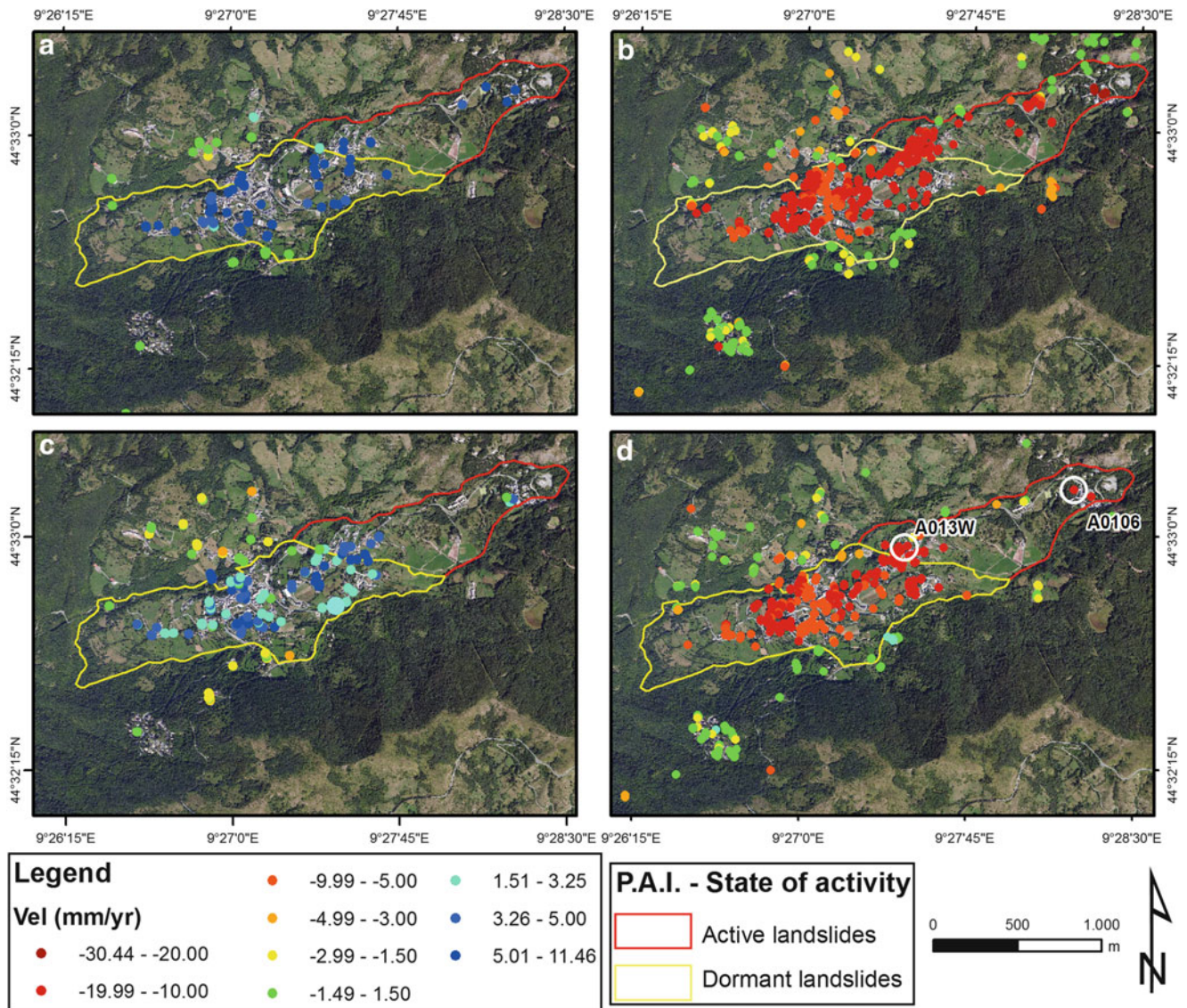


Fig. 3 Input PSI data available for the Santo Stefano d’Aveto landslide: (a) ERS1/2 ascending (1992–2000); (b) ERS1/2 descending (1992–2001); (c) ENVISAT ascending (2003–2008); (d) ENVISAT descending (2002–2008)

of a specific point on the ground, it is necessary to identify a radar target acting as a scatterer in both acquisition geometries.

Practically, identification of the same radar target in both the datasets is often a challenge, due to the low spatial resolution and to the poor geocoding accuracy.

This limitation has been overcome by re-sampling the datasets of PS points by means of a regular grid with 50 m intervals. For each grid cell and for both the ascending and descending geometries, the mean value of the velocities of the radar targets contained within the cell is calculated. Hence, a synthetic Permanent Scatterer is generated, with associated ascending (V_A) and descending (V_D) velocity estimates. Using the synthetic values and taking into account the orientation of the employed LOS, the vertical (V_V) and east-west (V_E) ground velocity components were estimated, by solving—cell by cell—the following formulas (Raspini et al. 2012):

$$V_A = V_V \cos \theta_A + V_E \sin \theta_A \tag{1}$$

$$V_D = V_V \cos \theta_D + V_E \sin \theta_A \tag{2}$$

With θ (incidence angle) = 23° for both geometries.

The results of the combination of ascending and descending data both for ERS and ENVISAT datasets is shown in Fig. 4, where positive velocities indicate surface deformation motion upward and eastward, while negative deformation rates reflect movements downward and westward. Deformation is mainly horizontal, with negative velocity values ranging between 20 mm/year and 30 mm/year with peaks up to 49 mm/year in the ERS dataset and between 10 mm/year and 20 mm/year in the ENVISAT dataset.

The landslide is characterized by low vertical displacements (on the order of a few mm/year), both in ERS and

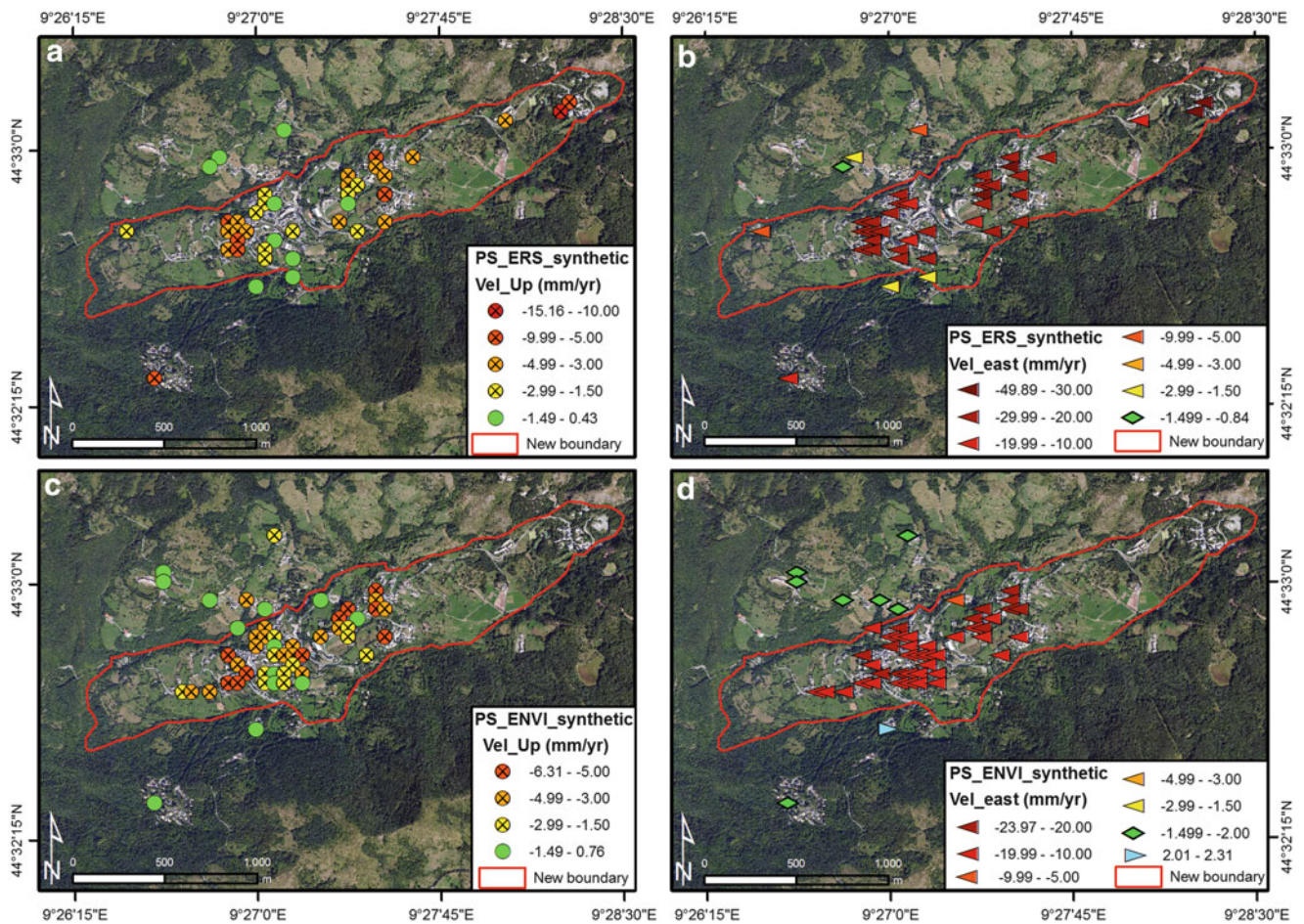


Fig. 4 (a) ERS vertical and (b) horizontal component; (c) ENVISAT vertical and (d) horizontal component

ENVISAT dataset. It is worth noting that in the upslope portion of the landslide, in the ERS time period, higher downward velocities were registered, with a peak up to 15 mm/year.

Landslide Characterization and Comparison of Monitoring Techniques

The re-projection of LOS velocity into its horizontal and vertical components reveals that the Santo Stefano landslide is characterized by predominant horizontal components, consistent with a strong westward movement, just as expected. This pattern of movement is typical of those sliding masses commonly involving two or more of the classes of landslide typologies. In particular, observed displacements in the uppermost part of the landslide body are consistent with a downward movement usually observed in rotational slides: as the mass of material moves down slope along the concave slip surface that is not structurally-controlled, it rotates downward, leaving a large main head scarp. Moving down-slope, the

phenomenon evolves into a translational slide, as the landslide mass moves along a roughly planar surface with little or no internal deformation, as testified by negligible vertical deformation rates. In its lowermost part, the slide further transforms into an earth flow, as the material starts to lose coherence. In sum, the pattern of movement of the Santo Stefano landslide, as observed by InSAR monitoring, supports and constrains the interpretation of the landslide itself and the definition of the style of movement. The landslide is defined as a complex phenomenon, started as a roto-translational slide affecting the source area, which evolves downhill into an earth flow. PSI data allowed the change of the state of activity of the landslide: the whole landslide can be defined as active. According to Cruden and Varnes (1996) and on the basis of the PSI data, landslide velocity can be defined as very slow.

The time series of ENVISAT data, spanning the time period from 2002 to 2008, have been compared with the inclinometers, whose measurements cover a period from 2001 to 2006. The I1 inclinometer has been compared with the PS A0106, whereas the I5 has been compared with the PS A013W (Fig. 3). In order to perform a representative

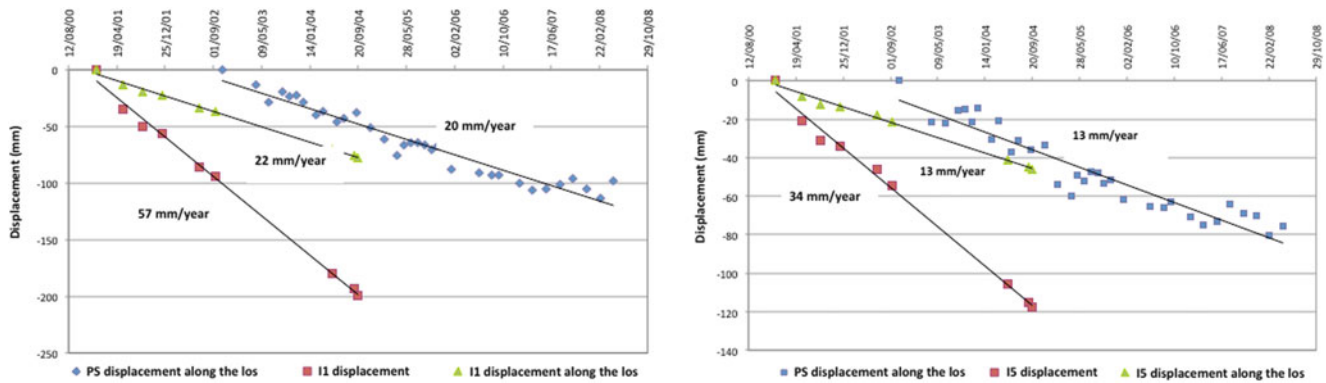


Fig. 5 Comparison of PS[®] and inclinometer time series of displacement

comparison, the displacement vector of the inclinometers has been projected along the LOS using a simple trigonometry equation:

$$I_{los} = I_{slope} \sin \theta \quad (3)$$

where I_{los} is inclinometer displacement along the LOS, I_{slope} is the inclinometer displacement and θ is 23° , the look angle of the SAR sensors. In both cases, the computed velocity values of the inclinometers along the LOS (22 mm/year for I1 and 13 mm/year for I5) show values quite similar to the mean velocities of closest PS (20 mm/year and 23 mm/year) (Fig. 5).

Discussion and Conclusions

In this work, characterization and monitoring of the Santo Stefano d'Aveto landslide have been carried out integrating PSI data and conventional monitoring techniques. The PSI analysis has been performed using SAR scenes from ERS-1/-2 and ENVISAT satellites. Conventional geotechnical monitoring has been carried out from 2000 to 2006 by means of inclinometers.

The analysis of PSI datasets highlights that the velocity within the landslide shows a general decrease from the upper to the lower part of the landslide. PSI analysis for the temporal interval from 1992 to 2008 allowed the changing of the state of activity of the landslide and the defining of the landslide intensity in terms of velocity. The SW portion of the landslide, in correspondence to Santo Stefano d'Aveto village, previously classified as dormant, can be now classified as active.

By combining information on landslide displacements, acquired by ascending and descending geometries, it has been possible to highlight a predominant horizontal component, consistent with a strong westward direction of the movement. Moreover, vertical deformation in the upper part of the landslide body is thought to reflect a rotational movement, evolving downhill into an earth flow.

A comparison between the deformation measured by the PSI techniques and the inclinometric acquisitions has been performed examining the velocity measurements along the same line of sight. The results show that the displacements measured by the two different types of techniques are consistent.

The comparison of the PS results and the in situ monitoring by inclinometers shows that the PS analysis is a valuable technique to monitor landslide deformations, since it can provide plenty of ground measuring points with time-series of deformations.

Based on the above-mentioned results, a couple of guidelines on the applications of PSI to monitor landslides can be derived. Even though PSI analysis is a valuable technique to monitor landslides, some expedients have to take into account to obtain sound results: (i) correct reconstruction of the actual displacement vector, i.e., the vertical component (V_V) and the horizontal E-W component (V_E) and (ii) reconstruction of the link between surface and subsurface displacements combining the PSI results with in situ underground displacements measures.

Acknowledgments The presented work has been carried out in the framework of the Terrafirma project. The authors gratefully acknowledge TeleRilevamento Europa (TRE) for having processed SAR data and the Regione Liguria for providing the geotechnical monitoring data.

References

- Angeli M, Pasuto A, Silvano S (2000) A critical review of landslide monitoring experiences. *Eng Geol* 55:133–147
- Corominas J, Moya J, Lloret A, Gili JA, Angeli MG, Pasuto A, Silvano S (2000) Measurement of landslide displacements using a wire extensometer. *Eng Geol* 55:149–166
- Cotecchia V (1996) La Grande Frana di Ancona: La Stabilità del Suolo in Italia: Zonazione Sismica-Frane. In: *Proceedings of Atti dei Convegni Lincei*, 30–31 May 1996. Roma, Italy. pp. 187–259

- Cruden DM, Varnes DJ (1996) Landslide types and processes. In: Turner AK, Schuster RL (eds) *Landslides: investigation and mitigation*, Special Report-Transportation Research Board, National Research Council; National Academy Press, Washington USA, pp. 36–75
- Fanti R, Gigli G, Lombardi L, Tapete D, Canuti P (2012) Terrestrial laser scanning for rockfall stability analysis in the cultural heritage site of Pitigliano (Italy). *Landslides* 5:1–12
- Farina P, Colombo D, Fumagalli A, Marks F, Moretti S (2006) Permanent scatterers for landslide investigations: outcomes from the ESA-SLAM project. *Eng Geol* 88:200–217
- Ferretti A, Prati C, Rocca F (2000) Nonlinear subsidence rate estimation using permanent scatterers in differential SAR interferometry. *IEEE Trans Geosci Remote Sens* 38:2202–2212
- Gili JA, Corominas J, Rius J (2000) Using global positioning system techniques in landslide monitoring. *Eng Geol* 55:167–192
- Kaab A (2000) Photogrammetry for early recognition of high mountain hazards: new techniques and applications. *Phys Chem Earth* 25:765–770
- Mantovani F, Soeters R, van Westen C (1996) Remote sensing techniques for landslide studies and hazard zonation in Europe. *Geomorphology* 15:213–225
- Massonnet D, Feigl KL (1998) Radar interferometry and its application to changes in the Earth's surface. *Rev Geophys* 36:441–500
- Metternicht G, Hurni L, Gogu R (2005) Remote sensing of landslides: an analysis of the potential contribution to geo-spatial systems for hazard assessment in mountain environments. *Remote Sens Environ* 98:284–303
- Raspini F, Cigna F, Moretti S (2012) Multi-temporal mapping of land subsidence at basin scale exploiting persistent scatterer interferometry: case study of Gioia Tauro plain (Italy). *J Maps* 8: 514–524
- Tofani V, Segoni S, Agostini A, Catani F, Casagli N (2013) Technical note: use of remote sensing for landslide studies in Europe. *NHESS* 13:299–309
- Zebker HA, Goldstein RM (1986) Mapping from interferometric synthetic aperture radar observations. *J Geophys Res* 91:4993–4999



Persistent Scatterers Interferometry Provides Insight on Slope Deformations and Landslide Activity in the Mountains of Zhouqu, Gansu, China

Janusz Wasowski, Fabio Bovenga, Tom Dijkstra, Xingmin Meng, Raffaele Nutricato, and Maria Teresa Chiaradia

Abstract

We present the results of Persistent Scatterers Interferometry (PSI) applied to investigate slope instabilities in a remote high mountain region of Southern Gansu, known to be prone to large magnitude (M7-8) earthquakes and catastrophic slope failures. The PSI processing of high resolution (~3 m) COSMO/SkyMed (CSK) satellite images produced spatially dense information (more than 1,000 PS/km²) on ground surface displacements in the area of Zhouqu, a town located in the Bailong River valley. A substantial portion of the radar targets showed significant displacements (from few to over 50 mm/year), denoting widespread occurrence of slope instabilities. In particular, the PSI results provided valuable information on the activity of some very large, apparently slow landslides that represent a persistent hazard to the local population and infrastructure. Monitoring movements of large long-lived landslides is important especially when, as in the case of the Bailong valley, they are known to undergo periods of increased activity resulting in river damming and disastrous flooding. Given the general lack of monitoring data on large landslides at Zhouqu and on other similar major failures that are common in Southern Gansu, the PSI-derived displacements offer unique information, which, following expert judgment, can be

J. Wasowski (✉) • F. Bovenga
CNR-IRPI, via Amendola 122 I, 70126 Bari, Italy
e-mail: j.wasowski@ba.irpi.cnr.it; bovenga@ba.issia.cnr.it

T. Dijkstra
British Geological Survey, Environmental Science Centre, Keyworth,
Nottingham NG12 5GG, UK
e-mail: tomdij@bgs.ac.uk

X. Meng
Research School of Arid Environment and Climate Change, Lanzhou
University, Lanzhou, China
e-mail: xmmeng@lzu.edu.cn

R. Nutricato
GAP srl, c/o Dipartimento Interateneo di Fisica, Politecnico di Bari,
Via Amendola 173, Bari, Italy
e-mail: raffaele.nutricato@gapsrl.eu

M.T. Chiaradia
Dipartimento Interateneo di Fisica, Politecnico di Bari, Via Amendola
173, Bari, Italy
e-mail: chiaradia@ba.infn.it

used for preliminary wide-area assessments of hazards linked to landslide activity. Furthermore, this study shows that with the high resolution CSK data resulting in high radar target density, PSI can also assist in slope/landslide-specific assessments.

Keywords

SAR interferometry • Persistent scatterers • Landslide monitoring • Gansu • China

Introduction

The space-borne Synthetic Aperture Radar (SAR) Differential Interferometry (DInSAR) can be exploited to measure ground surface deformations with millimeter-centimeter precision. However, the applicability of DInSAR is limited to areas with scarce vegetation cover. The advanced multi-temporal InSAR techniques (MTI) such as Persistent Scatterer Interferometry (PSI) (e.g. Ferretti et al. 2001) mitigate this limitation by using selected, persistent radar targets (PS) that exhibit coherent radar backscattering properties (mostly man-made structures, rocky outcrops and bare ground in general). This offers the possibility of detecting and monitoring with millimeter precision surface displacements that can occur between successive satellite overpasses of the same area. The PSI techniques combine a wide-area coverage (thousands km²) and capability to provide precise, spatially dense measurements (from hundreds to over thousand measurement points/km²), and therefore, can assist in both regional and local scale investigations of landslides (e.g. Bovenga et al. 2006, 2012; Colesanti and Wasowski 2006; Cascini et al. 2010; Herrera et al. 2013).

Importantly, new application opportunities have recently surfaced out thanks to i) the greater data availability offered by the steadily increasing number of radar satellites, and ii) the improved capabilities of the new radar sensors (X-band Cosmo-SkyMed, C-band RADARSAT-2, TerraSAR-X; see Table 1) in terms of spatial resolution (from ~3 to 1 m) and revisit time (dt in Table 1), from 11 to 4 days for X-band acquisitions. The higher resolution of space-based information on ground surface displacements reduces the technical and interpretative limitations of PSI applications to slope instability detection and landslide monitoring (e.g. Bovenga et al. 2012; Wasowski and Bovenga 2014).

However, examples of high resolution PSI applied to landslide investigations are still relatively rare, especially from outside of Europe. More case studies are needed to illustrate and better evaluate the potential, as well as limitations, of this type of applications. This is the main motivation of the work presented here, which describes the

results of catchment-scale (about 40 km²) high resolution X-band PSI investigation of a landslide-prone area located in a high mountain setting of southern Gansu, China.

Environmental Setting of the Study Area

General

The area of interest is located in the southern part of Gansu Province, northwestern China, characterized by steep mountains with elevations ranging from about 1,000 to 4,000 m. The town of Zhouqu (known also as Zhugqu) developed on the northern bank of the Bailong River (Fig. 1) at an altitude of about 1,350 m, whereas the highest nearby peaks reach nearly 3,800 m. The high local relief and deeply incised river valleys are typical of the landscape in southern Gansu. Another characteristic feature of the local slopes is the presence of agricultural terraces in the loess cover materials, often found on steep slopes and at high elevations (exceeding 2,000 m).

The climate is semi-arid to arid, being characterized by modest rainfall with an annual average precipitation of 434 mm (Tang et al. 2011). The rainfall is largely concentrated in the period June–September. On average, 75 % of the annual precipitation falls during this period.

Vegetation cover is limited in the Zhouqu area. The highest elevation areas include some forest and shrub cover, in addition to common presence of grass land. The barren ground is also common on the high steep slopes and corresponds mainly to rock outcrops. The land cover on the middle-lower elevations (valley slopes) is reflects the presence of cultivated ground.

Geology

The Zhouqu area belongs to the seismically active eastern-most Tibetan region. The structural setting is inherited from the ancient and the ongoing Himalayan orogenic phases

Table 1 Selected characteristics of principal SAR sensors, including the upcoming Sentinel-1

| Satellite mission | Wave-length (cm) | Resolution Az/Rg (m) | dt (days) | Max. Vel. (cm/year) |
|-------------------|------------------|-----------------------------|-----------|---------------------|
| ALOS PALSAR | 23.6 | ≈5/8.6 | 46 | 46.8 |
| ALOS PAL SAR-2 | 22.9 | 1/3 3÷10/3÷10 100/100 | 14 | 149.2 |
| ENVISAT | 5.6 | ≈6/24 | 35 | 14.6 |
| RADARSAT-1 | 5.5 | ≈8/30 | 24 | 20.4 |
| RADARSAT-2 | 5.5 | ≈3/3 ≈8/8 ≈26/25 | 24 | 20.4 |
| SENTINEL-1 | 5.6 | ≈5/5÷24 | 12 6 | 42.5 85 |
| COSMO-SkyMED | 3.1 | ≈2.5/2.5 1.0/1.0 | 16 | 17.7 |
| | | | 8 | 35.4 |
| | | | 4 | 70.7 |
| | | | 2 | 141.4 |
| TerraSAR-X | 3.1 | ≈3.3/2.8 | 11 | 25.7 |

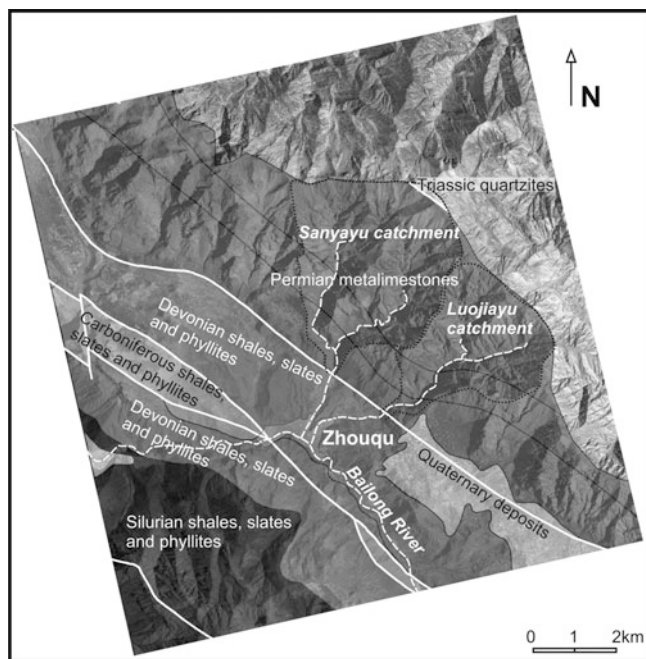


Fig. 1 Geological sketch map on a grey-scale KOMPSAT2 (2010) image, showing the main geological strata in the Zhouqu region

(Dijkstra et al. 1993), with intensely sheared rocks reflecting the long-term tectonic activity.

The surface topography closely reflects the regional geological structure with the major valley system of Bailong River following main NW-SE trending fault systems (Fig. 1). The bedrock geology in the valley mainly

comprises Silurian and Carboniferous slates and phyllites (Fig. 1). The highest mountains are predominantly formed in metamorphosed limestones of Permian and Devonian age. In some portions of the Bailong River valley system significant amounts of Quaternary age deposits are also present (Dijkstra et al. 2012).

The seismic activity of the area is marked by high magnitude events. For example, the 1879 Wenxian/Zhouqu $M_s = 8.0$ earthquake caused extensive landsliding and rockfalls, and the 186 BC $M_s = 7$ to 7.5 earthquake, had an epicentre close to Zhouqu (Dijkstra et al. 1993). The region was also affected by the 12th May 2008 $M_w = 7.9$ Wenchuan earthquake (epicentre located ~250 km away from Zhouqu).

Landslides

Slope failures and erosion are widespread in the Zhouqu mountains, reflecting the fragility of this high relief environment characterized by the presence of tectonically sheared weak rocks, limited vegetation and frequent recurrence of large magnitude earthquakes. Numerous large landslides and debris flows have already been recognized in the region around Zhouqu (Bai et al. 2012; Dijkstra et al. 2012). The most significant of these comprise complex mass movements with large volumes (>1 million m^3) that tend to concentrate along the main river valleys, occasionally resulting in river damming and catastrophic flooding.

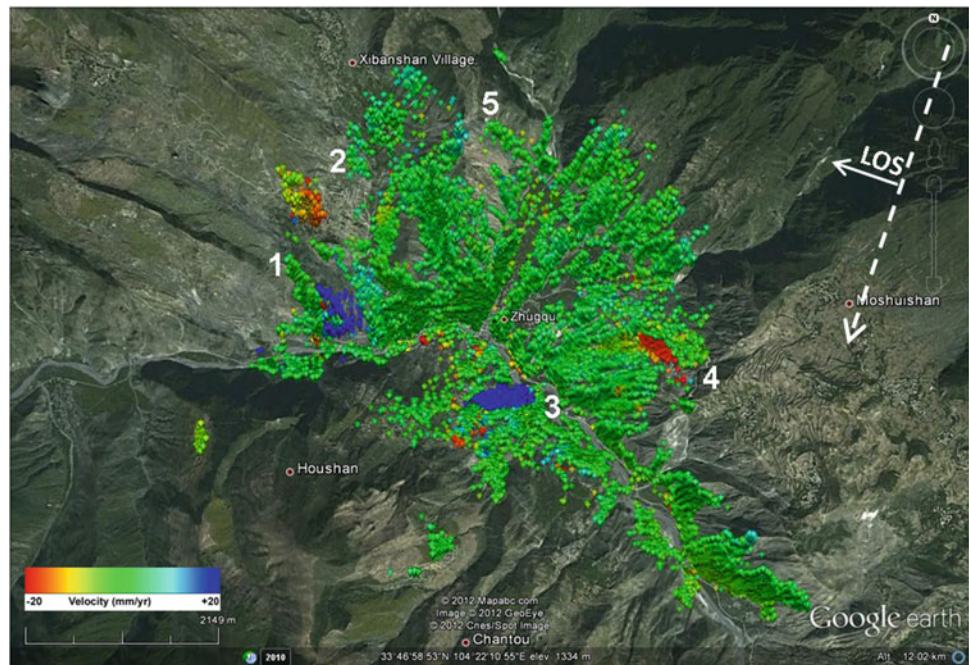
Initiation of many mass movements is thought to have originated during the 1879 AD and 186 BC earthquakes. Furthermore, Bai et al. (2012) reported that the post-earthquake emergency assessment and the remote sensing survey of the area struck by the 2008 Wenchuan event indicated 878 seismically triggered landslides in the Zhouqu-Longnan segment of the Bailong River Basin. However, according to Tang et al. (2011), no significant landslides were triggered by the 2008 Wenchuan earthquake in the Zhouqu area.

Data and Methods

Radar Satellite Data

For PSI processing 22 high resolution (3 m Stripmap mode) X-band images, were used. The images were acquired in descending geometry (incidence angle θ : 40°) by the Italian Space Agency (ASI) satellite constellation COSMO/SkyMed (CSK). They cover the period January 2011–February 2012.

Fig. 2 Distribution of persistent radar targets (over 46,000) in the Zhouqu area. Numbers 1–5 indicate unstable slopes. Bluish and reddish colors mark PS moving, respectively, toward and away from the satellite sensor (LOS = radar line of sight). Background image is from GE (note Bailong River in the center)



PSI Processing

For processing we used SPINUA PSI algorithm (Bovenga et al. 2006). SPINUA adopts a patch-wise approach based on processing of limited portions of radar imagery (usually a few km²), which are selected according to the density and the distribution of initially identified potential PS. This solution enables obtaining fast results by processing small number of SAR images (cf. Bovenga et al. 2012).

Visualization and Interpretation of PSI Results

We had no suitable scale topographic maps or air photos for displaying the outcomes of interferometric processing. Therefore, the visualization of PSI results was done with support of Google Earth (GE) and its optical imagery. The GE images with overlaid PS points were also used during the reconnaissance field checks and the interpretation process.

PSI Results

General Assessment

Figure 2 show that PSI processing produced a large number of persistent radar targets (over 46,000) in the Zhouqu area. The average density of PS is more than 1,000/km². This result is consistent with high resolution of the radar imagery and the environmental characteristics of the area studied (semi-arid setting, limited vegetation).

At Zhouqu many radar targets exhibit the average Line of Sight (LOS) velocities within ± 2 mm/year (Fig. 2). These PS are considered motionless and indicative of stability conditions. This is consistent with our in situ checks and with the presence of hard bedrock commonly cropping out throughout the study area. Nevertheless, the PSI displacement map reveals also many sites with moving PS. Of most interest are large clusters of PS characterized by average velocities typically exceeding 10 mm/year (Fig. 2). These denote significant slope instabilities and are examined in more detail below.

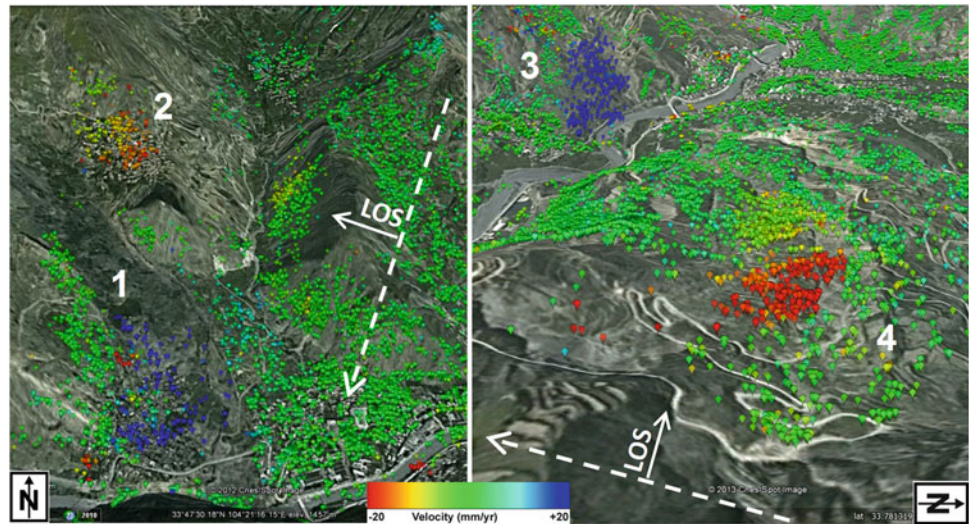
Slope/Landslide Specific Evaluations

The Suoertou Slide (No. 1) and Slope Instability (No. 2)

The Suoertou landslide is a very large (~4 km long, ~0.5 km wide) complex mass movement just to the northwest of Zhouqu, occurring within a narrow (up to 1.5 km wide), NW-SE trending fault-bounded valley (Fig. 2). There are few settlements present on or very close to the landslide, including the Suoertou village situated on the landslide toe, near the Bailong River. The slide involves intensely sheared slates and phyllites and moves into the river valley in approximately SE direction. The average slope gradient of the movement is over 12°.

Figure 3 shows a GE-supported 3D visualization of the PSI results for the middle-lower part of the slide and its surroundings. The displacements in the lower part (toe) are significant, with PS velocities typically exceeding

Fig. 3 (Left) Distribution of PS in the area just east of the town of Zhouqu including the large Suoertou landslide (No. 1) and the ground instabilities at the village of Zhen Yatou (No. 2) interpreted as a collateral slope failure on the left flank of the main landslide. (Right) PS velocity map with No. 3 and No. 4 landslides located south of Zhouqu. Background image is from GE



10–15 mm/year in LOS. The highest displacement rates (over 50 mm/year) were detected in the uppermost part of the landslide toe.

These results are consistent with the presence of damaged retaining structures along the road that traverses the slide toe noticed during the field check in January 2011. At the same time clear evidence of the recent mobility (e.g. fresh, wide open ground fractures) was also observed in the middle-upper part of the landslide.

Figure 3 shows also a cluster of moving PS in the area occupied in part by the village of Zhen Yatou, at the left-lateral flank of the Suoertou landslide. The LOS velocities typically range from about 10 to 15 mm/year. We had no information about the occurrence of ground/slope instabilities there, even though the presence of the disturbed ground and both old and recent landslide features in the upper part of the slope was documented during the 2011 field visit; also small recent failures locally involving the agricultural terraces and signs of erosion were noticed on the slope below the village.

Following the release of the PSI displacement map (2012), a closer examination of the site aided by 3day GE visualizations, suggested that the ground instability at Zhen Yatou could be interpreted as a collateral slope failure caused by the movement of the large Suoertou landslide. The affected slope area is about 450 m wide and 400 m long. Locally the PS movements may also reflect structural instabilities (open cracks on some poorly constructed buildings were noted in the field).

The Mudan Landslide (No. 3)

This landslide, located just to the southeast of Zhouqu, on the NE facing valley slope of the Bailong River (Fig. 2), is about one km long and 500 m wide, and the average slope gradient is around 15°. The slide involves intensely sheared

shales and phyllites and is moving towards the river in an approximately ENE direction.

In spite of some recent stabilization efforts (mainly drainage works), during the field visits in 2011 and 2012 the slide showed clear signs of movement. Its active toe poses a threat to the settlements and infrastructure (e.g. road) along the river.

Figure 3 shows the PSI results for the slope area affected by the Mudan landslide. The PS velocities in the northern segment of the slide typically exceed 15 mm/year, with maximum displacement rates reaching 40 mm/year (in LOS). Parts of the landslide complex show clear evidence (e.g. intensely deformed ground, fractures) indicative of the recent occurrence of significant movement (e.g. the northern part of the slide). These and the associated ground surface disturbance can explain the lack of PS there. The presence of slowly moving PS on the lower slopes of the southern segment of the slide deserves attention, because this area is very close to the village of Henan.

No. 4 Landslide East of Zhouqu

Figure 3 shows the PSI results for the No. 4 landslide located about one km east of Zhouqu. The PS velocities are the highest in the middle-upper portion of the landslide (typically ranging between 15 and 20 mm/year in LOS) and significantly decrease in its middle-lower portion (around 10 mm/year). The movements seem to further diminish in the lower part of the landslide (PS velocities down to few mm/year) and die out in the toe area; the lower-most slope appears to be stable. The local road, which overpasses the upper part of the landslide, is also affected by movements (PS displacements on the order of 20 mm/year).

Before the release of the PSI results very little was known about this landslide. The subsequent interpretation of the GE imagery and field inspection in 2012 showed that the landslide is over 1 km long and up to about 300 m wide. In the

upper and seemingly more active part (marked by the visibly disturbed ground) the movement involves slates or phyllites, whereas the lower part of the landslide appears relatively stable judging from the presence and continuity of cultivated loess terraces observed in situ. The slope failure history is not known, but recent activity (predating the 2010 GE imagery) in the upper part of the landslide can be inferred from the routing of the local road that overpasses that area (Fig. 3).

Conclusion

The PSI processing of high resolution CSK data produced spatially dense information (more than 1,000 PS/km²) on ground surface displacements in the Zhouqu territory. A substantial portion of the radar targets show significant displacements (exceeding few mm/year), denoting widespread occurrence of ground/slope instabilities. This is not surprising considering the high rate of seismotectonic activity of the area.

In particular, when interpreted in the local geomorphological and geological contexts of the study area, the PSI results provide valuable information on the activity of some large landslides that represent a persisting hazard to the local population, buildings and lifelines. In view of the general lack of monitoring data on these and many other large landslides that are also common elsewhere in the Bailong River valley, the PSI-derived displacement results offer unique information, which, following expert judgment, can be used for preliminary wide-area assessments of hazards linked to landslide activity. Importantly, the PSI application also leads to an identification of stable areas, a difficult task in Zhouqu and similar, tectonically active mountainous environments. This information is of much value for the local administrators and planners responsible for the development of the Zhouqu area.

Furthermore, thanks to the high resolution of CSK data resulting in high density of radar targets, the Zhouqu case application shows that PSI can also assist in site-specific or landslide-specific assessments. This, however, implies a close integration of PSI results with good quality/resolution data on local geology, geomorphology and slope history, as well as a good understanding of processes causing ground instability.

Acknowledgements Work supported in part by the Italian Spatial Agency (ASI) - COSMO-SkyMed AO Project ID 1820. COSMO imagery provided by ASI. Special thanks to Dr Jie Gong and Lanzhou University students (Peng Guo, Guan Chen, Yajun Li, Runqiang Zeng, Liang Qiao, Wei Zhou, Haixiao Zhang, Xiaobin Yang) for valuable assistance with fieldwork.

References

- Bai S, Wang J, Zhang Z, Cheng C (2012) Combined landslide susceptibility mapping after the Wenchuan earthquake at the Zhouqu segment in the Bailongjiang Basin, China. *Catena* 99:18–25
- Bovenga F, Nutricato R, Refice A, Wasowski J (2006) Application of multi-temporal differential interferometry to slope instability detection in urban/peri-urban areas. *Eng Geol* 88(3–4):218–239
- Bovenga F, Wasowski J, Nitti DO, Nutricato R, Chiaradia MT (2012) Using COSMO/SkyMed X-band and ENVISAT C-band SAR interferometry for landslides analysis. *Remote Sens Environ* 119:272–285
- Cascini L, Cascini L, Fornaro G, Peduto D (2010) Advanced low- and full-resolution DInSAR map generation for slow-moving landslide analysis at different scales. *Eng Geol* 112:29–42
- Colesanti C, Wasowski J (2006) Investigating landslides with spaceborne Synthetic Aperture Radar (SAR) interferometry. *Eng Geol* 88(3–4):173–199
- Dijkstra TA, Derbyshire E, Meng XM (1993) Neotectonics and mass movements in the loess of North-Central China. In: Owen LA, Stewart I and Vita-Finzi C (eds) *Neotectonics: recent advances. Quaternary Proceedings*, vol 3. Quaternary Research Association, Cambridge, pp 93–110
- Dijkstra TA, Chandler JH, Wackrow R, Meng XM, Ma DT, Gibson A, Whitworth M, Foster C, Lee K, Hobbs PRN, Reeves HJ, Wasowski J (2012) Geomorphic controls and debris flows—the 2010 Zhouqu disaster, China. In: *Proceedings of the 11th ISL and 2nd North American Symposium on Landslides*, 3–8 June, 2012, Banff, Canada
- Ferretti A, Prati C, Rocca F (2001) Permanent scatterers in SAR interferometry. *IEEE Trans Geosci Remote Sens* 39:8–20
- Herrera G, Gutiérrez F, García-Davalillo JC, Guerrero J, Notti D, Galve JP, Fernández-Merodo JA, Cooksley G (2013) Multi-sensor advanced DInSAR monitoring of very slow landslides: the Tena Valley case study (Central Spanish Pyrenees). *Remote Sens Environ* 128:31–43
- Tang C, Rengers N, van Asch TWJ, Yang YH, Wand GF, Luino F (2011) Triggering conditions and depositional characteristic of a disastrous debris flow event in Zhouqu city, Gansu Province, north-western China. *Nat Hazards Earth Syst Sci* 11(11):2903–2912
- Wasowski J, Bovenga F (2014) Investigating landslides and unstable slopes with satellite multi temporal interferometry: current issues and future perspectives. *Eng Geol*. doi:10.1016/j.enggeo.2014.03.003



Landslide Hazard Investigation and Assessment Using Remote Sensing in the Three Gorges Reservoir Area

Runqing Ye, Wenming Cheng, Xiaolin Fu, Runze Wu, Jianying Yang, and Ruiqing Niu

Abstract

Landslides can result in enormous property damages and human casualties in mountainous region, which are controlled and influenced by many temporal and spatial factors. Comprehensive understanding of landslides should be based on multi-source data collection, information extraction and data analysis. In this paper, landslide-prone area from Zigui to Badong in the Three Gorges Project reservoir area is chosen for the study area to landslide information extraction and hazard analysis based on multi-source data, which focused on the integration between remote sensing and non-RS data for landslide investigation and hazard analysis. And ten thematic maps were generated from multi-source data, namely landslides inventory map, slope map, slope structure map, geotechnical map, land cover and its changes map etc. The Support Vector Machine (SVM) model is employed for landslide susceptibility mapping. The results show a convincing success to distinguish the high and low landslide susceptibility regions.

Keywords

Multi-source data • Remote sensing • Landslide susceptibility mapping • The Three Gorges Project reservoir area

Introduction

The Three Gorges Project (TGP) is an unprecedented hydro-power construction in China and even the largest in the world, due to its huge scale, important location, far-reaching influence, combining with many aspects in economic and social benefits like the power generation, flood control and navigation. However, slope instabilities (such as landslides, rockfalls, high cutting slopes) with thousands of recorded

geological hazards, some of those are in state of active deformation (Chen and Cai 1994) contribute to the biggest threaten and obstacle of economic and social development in this area. Landslides are controlled or influenced by multiple factors in TGP reservoir area, not only the landslide-favourable geological and topographical conditions, as well as the triggering factors like rainfall, water storage, human activities. Such as the Qianjiangping landslide occurred shortly after the reservoir water reached to 135 m (Wang et al. 2004). According to the statistics of 1,736 landslides shows that the distribution of landslides are well correlated with the precipitation over time and space, and also strictly controlled by the stratum, geological structure, river valley form, shore types, etc. (He et al. 2008). Hence, comprehensive understanding and assessing landslide hazard in this area should be based on multi-sources data. This work demonstrates the application of remote sensing (RS) and geographic information system (GIS) for landslide interpretation, information extraction and susceptibility analysis

R. Ye (✉) • W. Cheng • X. Fu • R. Wu • J. Yang
China Institute of Geo-Environmental Monitoring, 100081 Beijing, China
e-mail: yerunqing2005@126.com; cwm58@163.com; fxlevan@126.com; wurunze@163.com; 307198446@126.com

R. Niu
Institute of Geophysics and Geomatics, China University of Geosciences, 430074 Wuhan, China
e-mail: rqnium@163.com

based on the fusion of RS imagery and topographic, geological and field investigation data.

Study Area and Multi-Sources Data

Study Area

The study area Zigui to Badong section with an area of 527 km² and the range of 30°47′–31°05′N and 110°00′–110°18′E, lie along the middle reaches of the Yangtze River in Central China. A variety of slope failure types occurred in this area, including simple, rotational slumps in poorly or unconsolidated materials, translational rock and debris slides, debris flows and complex examples involving more than one type of failure mechanism and several types of material (Liu et al. 2004). Such as Qianjiangping landslide occurred on July 13, 2003 and Xintan landslides occurred on June 12, 1985. And also many other slope failures events in the study area. Especially after the TGP completed and reservoir water storage, more unstable areas such as neo-genetic landslides (Luo and Liu 2005).

According to Hubei Province Geology Survey (1984), the strata exposed relatively complete from pre-Sinian to Quaternary, except some formations in Devonian, Carboniferous and Tertiary, and strata chronological time became new gradually from east to west. The strata can be divided into four major engineering rocks group based on lithology and formation characteristics (Ministry of Geology and Mineral Resources 1998), including the pre-Sinian massive crystalline basement, Sinian to Triassic (Z–T1) carbonate rocks, the clastic rocks from middle Triassic (T2) to Jurassic (J), and Quaternary deposits. Fold is the main structural pattern, including Huangling anticline, Zigui syncline and Badong syncline. Several major faults make the rocks fragmented, including Xiannvshan fault, Jiuwanxi fault and Niukou fault (Deng et al. 2000).

Multi-Source Data

In this work, four types of data sources were collected and processed for landslide investigation and assessment, namely, remote sensing images, geological maps, relief maps and field investigation data, which are used to extract the thematic maps for landslide interpretation and landslide susceptibility mapping.

Data Processing and Thematic Information Extraction

There are five major factors that contribute to the occurrences of landslides in the study area, namely rock types and associations, structure/texture combinations, valley slope geometry, hydrogeological conditions, and dynamical factors (Li et al. 2001). Herein ten types of thematic maps were generated from multi-source data (Fig. 1).

Engineering Rocks Map

Lithology is a major controlling factor on the slope stability (Lan et al. 2004). Such as the purplish-red mudstone of the Badong group, which is widely distributed in the Badong, Wushan and Fengjie County in the Three Gorges reservoir area, is often called as “sliding-prone formation” (Yin and Hu 2004; Lu et al. 2010). The strata are divided into three types, namely hard, soft and interbedded rocks, and which characteristics are shown in Table 1.

Slope Structure Map

Slope structure controls the failure mode of slope, such as most of large-scale deep-seated rock landslides developed on the forward slope (Huang 2007), such as Fanjiaping landslide, Qianjiangping landslide, and Huangtupo landslide in the study area. According to the relationship between the slope, aspect and attitude of stratum, slope structure are divided into six types, namely massive rocks, forward slope, oblique slope (i.e. oblique-forward and oblique-reverse), reverse slope, lateral slope (Liu and Yan 2002).

By Geoprocessing functions in ArcGIS software, quantitative model for slope structure division was developed, and the slope structure map was automatically generated by the model after inputting the slope, aspect, and the inclination angle of strata (Li and Niu 2009).

Slope Map

Slope is a measure of the steepness of the terrain or the rate of change in elevation. Slope angle and geometry are controlling factors in slope stability in the TGP reservoir region (Wu et al. 2001). The DEM was generated from the 29 relief maps at the scale of 1:10,000.

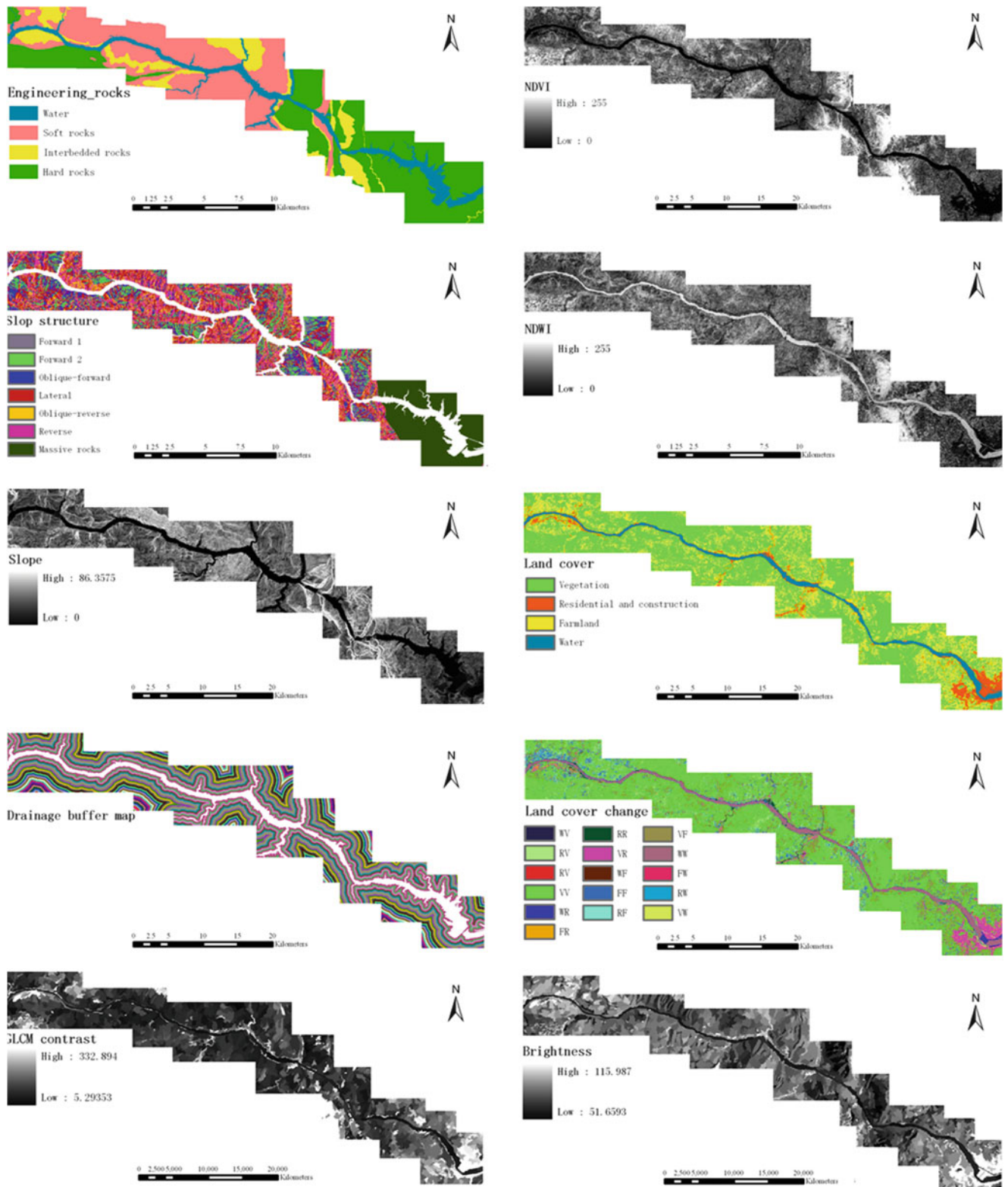


Fig. 1 Thematic maps for landslide susceptibility mapping extracted from multi-source data

Table 1 Engineering rock types in TGP reservoir area

| Engineering rocks | Lithology | Chronological time |
|-------------------|---|--|
| Hard rocks | Igneous rocks, metamorphic c rocks, carbonate, thick to massive sandstone | Pre-Sinian, Permian, Triassic, Cretaceous |
| Interbedded rocks | Sandstone interbedded with siltstone, mudstone or marl | Triassic to Jurassic, Upper Sinian, |
| Soft rocks | Siltstone, shale, mudstone, or siltstone, shale rock | Triassic to Jurassic, Silurian, Quaternary |

Drainage Buffer Map

Drainage buffer analysis is a commonly used evaluation factor in landslide. Many of the large landslides in the Three Gorges region occur in close proximity to water (Wu et al. 2004). Drainage buffers reflect the relevance between reservoir water (or the elevation) and landslides. The farther away from reservoir water, the smaller the impact by reservoir water. Multi-level drainage buffer zones were generated from 135 m water level lines with 200 m intervals.

NDVI and NDWI

Landsat ETM + images capabilities allowed us to understand the feature of land cover in the study area. A Normalized Difference Vegetation Index (NDVI) map was obtained using the infrared (band 4) and red band (band 3) of the Landsat ETM + image.

Water plays an integral role in the formation and evolution in the landslide, the groundwater acts a direct impact on landslide stability. Groundwater monitoring shows the water level and changes are directly related with the landslide. Here the use of Landsat ETM + images of bands 2 and 4 to calculate the Normalized Difference Water Index (NDWI).

In order to facilitate the processing of NDVI and NDWI, here the values normalized to a value of 0 to 255 digital numbers (DN) by the following formula.

Land Cover and Land Cover Change

Land cover and its change maps of 1987 and 2000 were derived from Landsat TM/ETM + images following these steps: Firstly, registration of different images. followed to select the appropriate classification algorithms for land cover classification, here we use maximum likelihood classification (MLC) to access the land cover classification, and generated two land cover maps with four land cover types, namely residential and construction area (R), farmland (F), vegetation (V) and water (W); then land cover change map was derived from two phases of land cover maps.

Object-Oriented Images Features

Image interpretation and field survey, we concluded that landslides, especially large or giant landslides, show a particular combination of several land cover types. Land cover on a large number of landslides are mainly residential area, cultivated land, bare soil and sparse vegetation. In the Landsat images, it shows particular characteristics of texture on the landslides. Beliz and Murat (2012) carried out a data-driven and semiautomatic classification to access landslide prediction from Landsat ETM + satellite images by object-based image analysis and fuzzy logic.

We chosen the Landsat ETM + images for segmentation. After the comparative analysis of spectrol and texture characteristics of objects between landslide areas and non-landslide areas, the object-oriented brightness and GLCM contrast were selected as factors for landslide assessment.

Landslide Interpretation

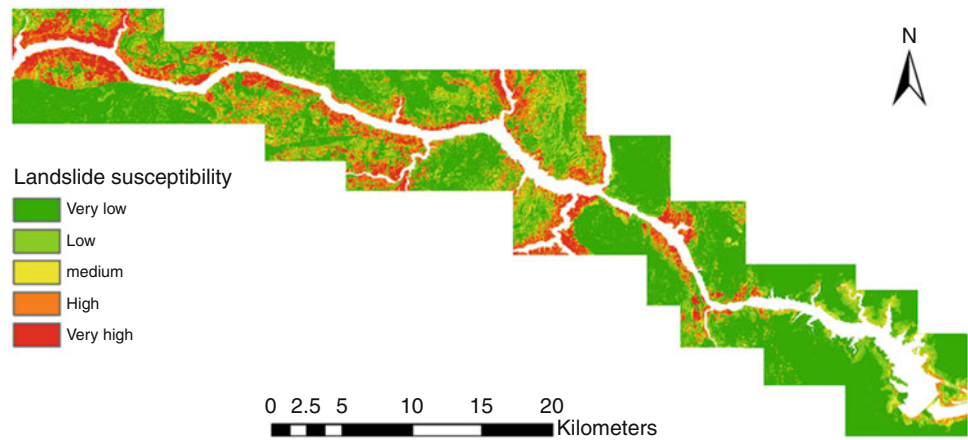
With the continuous improvement of RS imagery resolution, the shape and texture characteristics of the landslide morphological features become more clear and intuitive. The RS technology catches more attention among the landslide investigation, and image interpretation become the first procedure of regional scale landslides investigation.

In this study, we present a approach for landslide investigation based on multi-source data three dimension visualization. The integration and three-dimension visualization of DMC images, DEM, engineering geological maps help us for landslides interpretation and features extraction.

Three Dimension Visualization

We overlaid DMC images and thematic maps (slope, slope structure, geological maps) on the three dimension visual platform for landslide interpretation and features extraction based on multi-source data. It provides a human-computer interactive functions, such as browsing, vector editing, area and volume measurement etc., to facilitate landslide interpretation on it. And slope, slope structure, lithology were added to enhance the capacity of landslide interpretation.

Fig. 2 Landslide susceptibility mapping



Landslides Interpretation

According to the recorded landslides, the diagnostic features of landslide and its development environment are established in this region based on multi-source data. The diagnostic features can be divided into two types, namely new-occured and old landslides. Through 3-D visualization based multi-source data and field investigation, the locations, boundaries, elements at risk and other information of 202 landslides were determined, and the landslide inventory map at the scale of 1:10,000 in this region was generated.

Landslide Susceptibility Mapping

Landslide Susceptibility Mapping

Support Vector Machine (SVM) is applied to landslide susceptibility mapping using multi-sources data. SVMs are particularly appealing in this research due to their ability to generalize well even with limited training samples, a common limitation for landslide susceptibility mapping in a data-sparse environment.

The study area is divided into small units with a size of $28.5 \text{ m} \times 28.5 \text{ m}$. by the samples learning include landslide and non-landslide samples, 10 factors were classified by the SVM model to generate landslide susceptibility map. According to the distribution of landslide susceptibility, the landslide susceptibility of the study area was thresholded into five broad classes with the intervals (0.95, 0.9, 0.85, 0.75), namely, very high, high, medium, low, very low (Fig. 2).

Results Analysis

From the landslide susceptibility map, the area and percentage of very high, high, medium, low, very low hazard regions are 34.40, 39.87, 47.79, 108.10, 297.95 km^2 and

account for 6.51, 7.55, 9.06, 20.48, 56.45 % respectively. Almost all the landslides are located in very high, high landslides susceptibility regions, some are in medium landslides susceptibility regions. The area of very high, high, medium susceptibility regions in the recorded landslides accounted for 86.22 %, indicate that the accuracy of landslide susceptibility analysis is high and the result is reliable.

Field Investigation

Interestingly, during the field survey, thirty one bank collapses triggered by reservoir water storage of 172 m water level in October, 2008 in the study area. All the bank collapses developed in this area with very high, high and medium landslide susceptibility regions. Furthermore, all the bank collapses with large size (more than 10 m wide) occurred in very high, high landslide susceptibility areas.

Conclusions

This work presents a study on the confusion of RS imagery and geology, topography, engineering geology, field investigation data for landslide survey, information extraction and landslide hazard assessment. More than ten thematic maps were extraction from multi-resource data, including landslide inventory map at the scale of 1:10,000 and ten essential factors for landslide susceptibility mapping, namely, slope, drainage buffer, engineering rock group, slope structure, NDVI, NDWI, land cover, land cover change, and object-oriented spectral and texture features. SVM model was employed to landslide assessment based on multi-sources data, and landslide susceptibility map were generated, which shows a convincing success to distinguish the high and low landslide susceptibility regions.

Remote sensing technique plays a key role in this work and enable to acquire abundant detail information

efficiently at regional scale. We obtained the landslide inventory map by images interpretation, field surveys and data collection, and determined the locations, boundaries, elements at risk and other information of 202 landslides. Among ten factors for landslide susceptibility mapping, six thematic maps are extracted from RS images. And land cover change and object-oriented image feature added into landslide assessment which taken the impacts of human activities into consideration, and makes the results of landslide hazard assessment more practical and reasonable. What's more, the three-dimensional visualization and multi-scale segmentation techniques are applied to improve the ability of landslide identification and information extraction.

Acknowledgments This study is funded by Ministry of Land and Resources (No.[2005]13, No. SXKY3-6-2 and No. SXKY3-2-2), National "863 Plan" Projects of Ministry of Science and Technology (No.2007AA12Z160 and No.2009AA122004), National "973 Plan" Projects of Ministry of Science and Technology (No.2011CB710601), and the National Natural Science Foundation of China (No.40672205).

References

- Beliz A, Murat E (2012) Landslide identification and classification by object-based image analysis and fuzzy logic: an example from the Azdavay region (Kastamonu, Turkey). *Comput Geosci* 38:87–98
- Chen DJ, Cai YJ (1994) Monitoring and prediction of landslides and unstable cliffs in the Three-Gorges reservoir region, People's Republic of China. *Int Congress—Int Assoc Eng Geol* 3:1383–1389
- Deng QL, Wang XP, Liu JP, Zhou ZY, Yan CJ (2000) Relations between landslide and liniment in the Three Gorges, Yangtze River. *J Changchun Univ Sci Tech* 30(4):384–387 (In Chinese)
- He KQ, Li XR, Yan XQ, Guo D (2008) The landslides in the Three Gorges Reservoir Region. China and the effects of water storage and rain on their stability. *Environ Geol* 55:55–63
- Huang RQ (2007) Large-scale landslides and their sliding mechanisms in China since the 20th century. *Chin J Rock Mech Eng* 26 (3):433–454 (In Chinese)
- Hubei Province Geology Survey (1984) Geological map of Badong (1:200,000)
- Lan HX, Zhou CH, Wang LJ, Zhang HY, Li RH (2004) Landslide hazard spatial analysis and prediction using GIS in the Xiaojiang watershed, Yunnan, China. *Eng Geol* 76:109–128
- Li JF, Niu RQ (2009) Slope structure automatic mapping based on GIS. *Yangtze R* 40(19):38–40 (In Chinese)
- Li JJ, Xie SY, Kuang MS (2001) Geomorphic evolution of the Yangtze Gorges and the time of their formation. *Geomorphology* 41:125–135
- Liu GR, Yan EC (2002) Discussion on classification of landslides. *J Eng Geol* 10(4):339–342 (In Chinese)
- Liu JG, Mason PJ, Clerici N (2004) Landslide hazard assessment in the Three Gorges area of the Yangtze River using ASTER imagery: Zigui–Badong. *Geomorphology* 61:171–187
- Hf L, Chen CX, Yuan CH, Yu HD, Shen Q (2010) Analysis of failure mechanism of Badong red bed soft rock gently inclined bedding slope. *Chin J Rock Mech Eng* 29(S2):3569–3577
- Luo XQ, Liu DF (2005) Model test study on landslide under rainfall and reservoir water fluctuation. *Chin J Rock Mech Eng* 24 (14):2476–2483 (In Chinese)
- Ministry of Geology and Mineral Resources (1998) Study on the reservoir bank stability of TGP region. Mineral Ministry of Geology and Resources, Beijing, pp 1–24
- Wang FW, Ye MZ, Huo ZT, Matsumoto T, Huang BL (2004) The July 14, 2003 Qianjiangping landslide, Three Gorges Reservoir, China. *Landslides* 1:157–162
- Wu SR, Jin YM, Zhang YS, Shi JS, Dong C, Lei WZ, Shi L, Tan CX, Hu DG (2004) Investigations and assessment of the landslide hazards of Fengdu County in the reservoir region of the Three Gorges project on the Yangtze River. *Environ Geol* 45:560–566
- Wu SR, Shi L, Wang RJ, Tan CX, Hu DG, Mei YT, Xu RC (2001) Zonation of the landslide hazards in the forereservoir region of the Three Gorges Project on the Yangtze River. *Eng Geol* 59:51–58
- Yin YP, Hu RL (2004) Engineering geological characteristics of purplish-red mudstone of middle tertiary formation at the Three Gorges Reservoir. *J Eng Geol* 12(02):124–135 (In Chinese)



Landslides Susceptibility Mapping in Oklahoma State Using GIS-Based Weighted Linear Combination Method

Xiaogang He, Yang Hong, Xiaodi Yu, Amy B. Cerato, Xinhua Zhang, and Marko Komac

Abstract

Oklahoma experiences approximately 20 reported landslides per year, which cause damage to transportation corridors and infrastructure. A refined regional hazard map has the potential ability to assist the state with detecting landslide hotspots and prevent future transportation corridor blockages. Combining the Geographic Information System (GIS) and high resolution satellite images, a first-cut landslide susceptibility map over the state of Oklahoma has been generated through the following two steps. The top four key landslide-controlling factors, including slope, soil texture type, land cover and elevation, were derived from a comprehensive geospatial database. After that, GIS-based weighted linear combination (WLC) method was utilized to assign the factor weight for each controlling parameter to generate the landslide susceptibility values, which are classified into five categories. Our study indicates that the entire state can be divided into five levels of susceptibility, namely very low (7.80 %), low (38.32 %), medium (45.15 %), high (8.09 %) and very high (0.64 %). These results match the historical landslide risk map well, especially in the south eastern and north western corner of the state. Further comparison with the landslide inventory data provided by the Oklahoma Department of Transportation (ODOT) and U.S. Geological Survey (USGS) shows that, 17 out of 19 (ODOT) and 60 out of 86 (USGS) events are located in category “high” or “very high”, which demonstrates the ability of WLC method in predicting landslide prone areas.

Keywords

Landslide susceptibility • Remote Sensing • GIS • Oklahoma

X. He • Y. Hong (✉) • X. Yu
Hydrometeorology and Remote Sensing Lab, Department of Civil Engineering and Environmental Science, University of Oklahoma, Norman, OK 73072, USA
e-mail: hexg@ou.edu; yanghong@ou.edu; xiaodi.yu@ou.edu

A.B. Cerato
Department of Civil Engineering and Environmental Science, University of Oklahoma, Norman, OK 73072, USA
e-mail: acerato@ou.edu

X. Zhang
State Key Laboratory of Hydraulics and Mountain River Engineering, Sichuan University, Chengdu, Sichuan 610065, China
e-mail: xhzhang@scu.edu.cn

M. Komac
Geological Survey of Slovenia, Dimiceva ulica 14, p.p. 2552, Ljubljana SI-1001, Slovenia
e-mail: marko.komac@geo-zs.si

Introduction

Landslides, which are usually described as the large scale gravity driven mass movement over land surface and beneath bodies of water (Lu and Godt 2013), are one of the most common and costly natural hazards in the world. In the U.S., landslides cause huge damages, especially in California, Oregon, and Washington. In fact, Oklahoma experiences approximately 20 reported landslides per year (Reidenbach, Oklahoma Department of Transportation (ODOT) Material Division, 2011, personal communication) that damages home, roadways and infrastructure and quietly cost the taxpayers substantial amounts of money. The landslide problem is even more serious in the south eastern

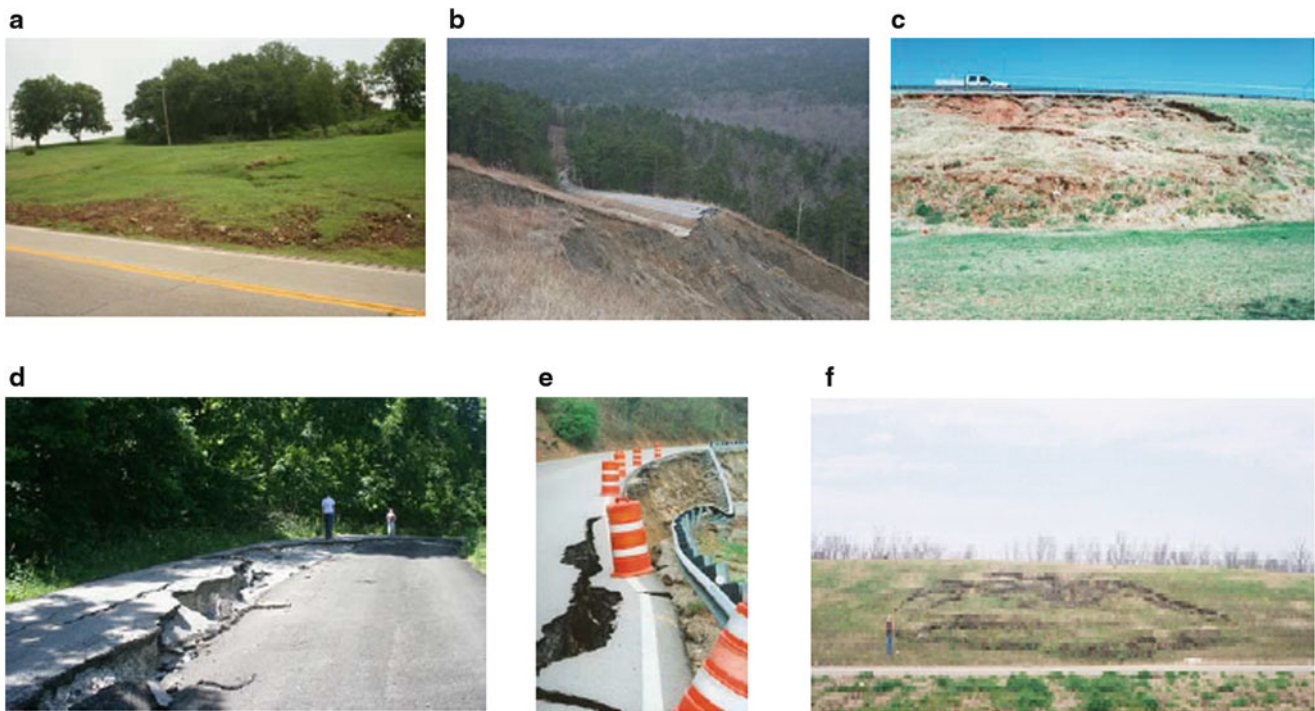


Fig. 1 (a) Pawnee seasonally recurring landslide Route 64; (b) Red Oak Route 82 and abandoned county road; (c) Chickasha, Route 62 (Cerato et al. 2006); (d) Keatonville Road, abandoned; (e) Keatonville

Route 20; (f) Idabel, Route 70 seasonally recurring landslide (Cerato and Nevels 2007)

corner of Oklahoma, where many roads are annually damaged or destroyed (Fig. 1).

It is therefore necessary to generate a refined regional landslide susceptibility map, which will provide guidelines to assess the spatial variability of potential landslides by identifying hot spots in landslide prone areas. Historically, there is one landslide hazard map for Oklahoma (Radbruch-Hall et al. 1982), but it is out of date and created with experiential information as a coarse rendering of historical landslides occurrences. Currently, the development of satellite remote sensing products makes it possible to evaluate the landslide occurrence at an improved spatial resolution, considering the effect of geologic, hydrologic, climatic conditions and human impacts on the triggering of landslide. This study will combine the high-quality satellite images and Geographical Information System (GIS) based weighted linear combination (WLC) method to generate a landslide susceptibility map over the whole Oklahoma state. This would provide clues to the locations and conditions of future slope failures and facilitate the scope and design of site-specific geotechnical investigations and guide slope remediation strategies.

The structure of the manuscript is as follows: section “Geospatial Data Sets” introduces the archived geospatial database, and how comprehensive landslide controlling factors were derived. In section “Methodology”, landslide-controlling factors are classified into numerical categories

with a continuum of increasing susceptibility to landslides. This section further describes how to derive and verify the landslide hazard (i.e. susceptibility) map using multi-thematic geospatial datasets and the Oklahoma landslide inventory database. In-depth analysis and discussion are reported in section “Results and discussion”. The last section concludes the manuscript.

Geospatial Data Sets

Landslide occurrence is determined by complex interactions among large number of factors, such as geologic features, geomorphology, land cover, soil properties and hydrology. All these factors can be classified into two categories: static factors and dynamic factors (Dai and Lee 2002). Static factors include the geologic features, geomorphology, land cover and soil characteristics which remain stable over a relatively long period of time. Dynamic factors refer to the trigger factors of landslides; mainly rainfall and earthquakes (Dai and Lee 2002). When mapping landslide susceptibility, only static factors are considered. Suggested by previous studies (Dai and Lee 2002; Carrara et al. 1991; Anbalagan 1992; Larsen and Torres-Sanchez 1998; Lee and Min 2001; Saha et al. 2002; Fabbri et al. 2003; Sarkar and Kanungo 2004; Coe et al. 2004; Hong et al. 2006, 2007), we considered four dominant factors to generate the Oklahoma

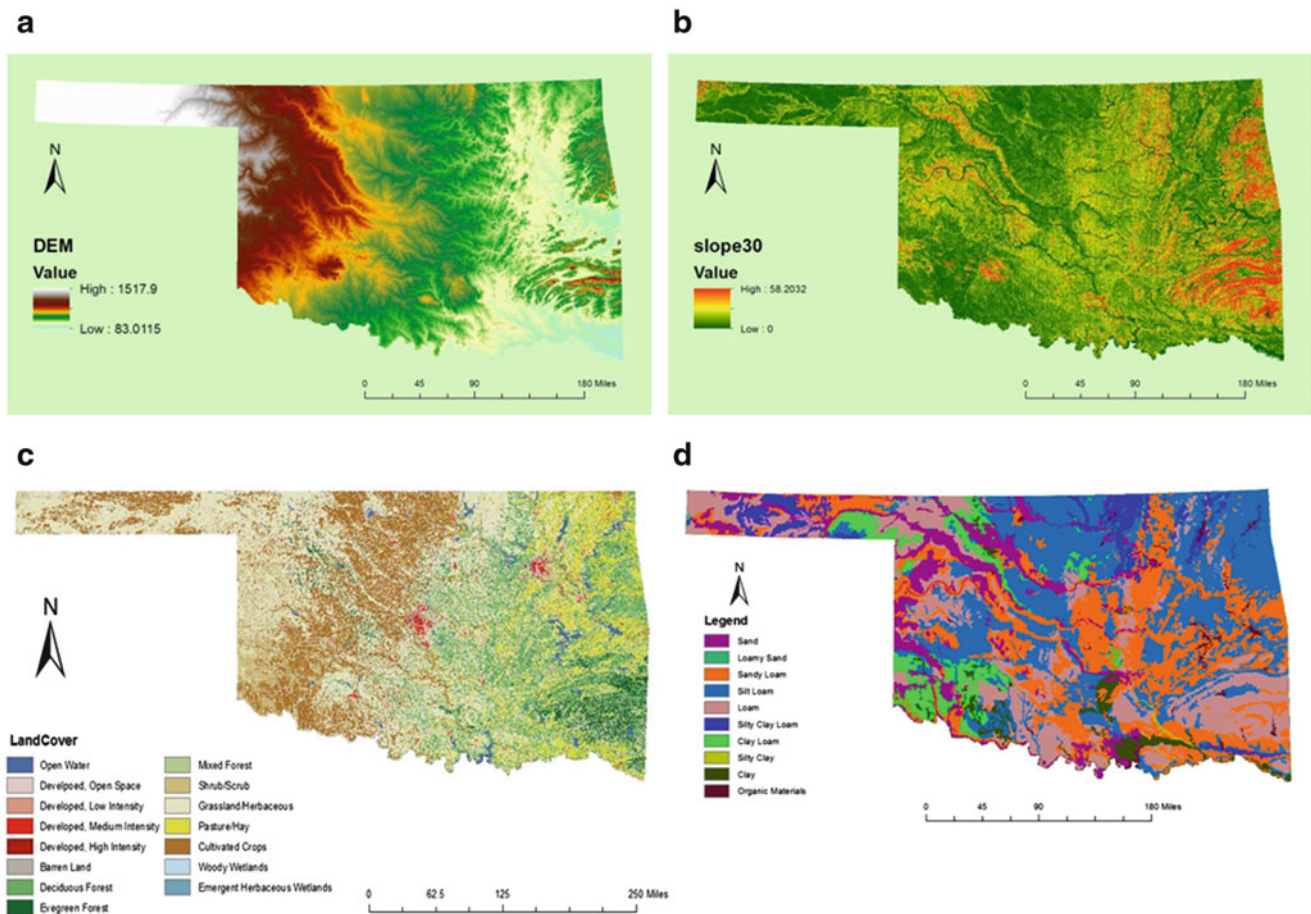


Fig. 2 Geospatial data sets used for landslide susceptibility mapping. (a) 30 m DEM from NED (unit: meter); (b) Slope derived from DEM (unit: degree); (c) 30 m land cover from USGS; (d) Soil texture from STATSGO

landslide susceptibility map, including slope, elevation, land cover type and soil texture type. Parameters related to these controlling factors can be derived from various remote sensing products, as described below in details.

Digital Elevation Model Data

The National Elevation Dataset (NED) (<http://ned.usgs.gov/>) is used in this study, which is the primary elevation data product of U.S. Geological Survey (USGS). The NED is updated bi-monthly by incorporating the best available coverage from other data sources. The resolution of NED is available at 1 arc-second (about 30 m) and 1/3 arc-second (about 10 m) and up to 1/9 arc-second (about 3 m) in limited areas. The absolute error of NED is only 2.44 m according to the root mean square error. Fig. 2a shows the 30 m mosaic DEM of Oklahoma derived from NED. Besides the elevation information which can be directly obtained from DEM, other topographical factors can also be generated by DEM, including slope, slope aspect, hill shading, slope curvature and so

on. In this study, only slope is considered as one of the controlling factors in landslide susceptibility analysis as suggested by previous studies. Fig. 2b shows the slope distribution over the whole state.

Land Cover Data

The land cover data used in this study is National Land Cover Database 2006 (NLCD2006) from USGS. This dataset is generated from Landsat Enhance Thematic Mapper + (ETM+) by using unsupervised classification method. NLCD land cover data has a spatial resolution of 30 m. There exist 15 different types of land cover in Oklahoma, as shown in Fig. 2c.

Soil Type Data

The soil type data adopted in this study is State Soil Geographic Data Base (STATSGO), which is produced by the

United States Department of Agriculture-Natural Resource Conservation Service (USDA-NRCS). It consists of georeferenced digital map data and associated digital tables of attribute data. These vector data cannot be directly used in gridded format. Therefore, they were further developed into the multi-layer datasets with 1 km resolution by Pennsylvania State University. The spatial distribution of soil texture type for Oklahoma State is shown in Fig. 2d. This dataset is resampled to the same horizontal resolution (30 m) as other datasets.

Landslide Inventory Data

The Landslide inventory data was gathered by reviewing existing historical landslides from ODOT Materials Division Archives and USGS, which, in most cases include an as-built and post-slide survey. We also did field surveys of the study areas and believe this is the most direct and exact detection method. However, it can be difficult to get access to the areas where the landslides occur, or detect historical landslides on transportation corridors that may have been repaired. Therefore, the number of available landslide events is limited. Basic characteristics of landslide events, such as location, time, size, extent, cause, geology and climate, are well defined and documented in the inventory database.

Methodology

Assignment of Landslide Susceptibility Values for Controlling Factors

Landslide susceptibility values for each layer were normalized varying from 0 to 1. Higher values indicate higher susceptibility to landslides. For example, pixels whose values were close to 1 had higher potential to induce landslides. For slope and elevation that have continuous values, fuzzy membership functions are applied (Pourghasemi et al. 2012). For discrete values such as soil texture type and land cover type, values from 0 to 1 were assigned to each pixel based on their physical characteristics.

For Elevation

When considering the relationship between elevation and landslides, several studies show that the higher the elevation, the more it is susceptible to landslides (Hong et al. 2007). However, this may not be true in Oklahoma. According to the DEM data (Fig. 2a), the western part of Oklahoma has higher elevation (near 1,200–1,500 m). However, almost no landslide events occurred in this region, which indicates that elevation is not a decisive factor. Considering this, elevation is given much less weight in this study.

For Slope

In terms of the relationship between landslides and slope, Bathrellos et al. (2009) found that steep slopes ($>30^\circ$) had the maximum frequency of landslides, followed by moderately steep slope ($20\text{--}30^\circ$). Gemitzi et al. (2011) also pointed out that maximum frequency was reached in the $35\text{--}40^\circ$ category, followed by a decrease in the $>40^\circ$ category. Based on these previous studies, $30\text{--}40^\circ$ is selected as the most susceptible slope to landslides. Susceptibility values to other slopes will be reclassified using the following condition statement:

$$y_k(i,j,t) = \begin{cases} \frac{\text{slope}(i,j,t)}{30} & \text{slope}(i,j,t) < 30 \\ 1 & 30 \leq \text{slope}(i,j,t) \leq 40 \\ \frac{90 - \text{slope}(i,j,t)}{90 - 40} & \text{slope}(i,j,t) > 40 \end{cases}$$

where $y_k(i,j,t)$ is the value at pixel location (i,j) at time t for k th factor.

For Land Cover

As suggested by Larsen and Torres-Sanchez (1998), landslide vulnerability of different land covers can be defined ranging from 0 to 1 according to the degree of potential to cause erosion. In Hong et al. (2006), numerical values were assigned to different land cover types using MODIS land cover classification map. Even though the land cover classification schemes were different between MODIS and ETM+ images, we can reclassify the NLCD map based on the similarities of these two maps (Table 1).

For Soil Type

The effects of soil on landslide occurrence have been well documented by Dai and Lee (2002) and Lee and Min (2001). Godt et al. (2009) found that a combination of low soil cohesion and a low internal friction angle will greatly increase the probability of landslide occurrence. Thus, silty clay loam is the most vulnerable to landslides. However, according to the field survey, most of the landslides in Oklahoma occurred in clay dominated locations. This is because clay soil has higher water holding capacity, which increases the soil mass and causes more landslides compared to other types of soil. Therefore, clay soil was given a higher weight. In addition, drainage capacity should be considered when assigning values to each soil texture type. Poor drainage increases the downward weight of soil by holding more water than it releases. For example, sands have low landslide susceptibility because of a high drainage capacity. Table 2 shows different weight values for different soil texture types.

Table 1 Numerical values assigned to different land cover types

| Category | Land cover type | Value |
|----------|------------------------------|-------|
| 1 | Open water | 0 |
| 2 | Developed, Open space | 1.0 |
| 3 | Developed, Low intensity | 1.0 |
| 4 | Developed, Medium intensity | 0.7 |
| 5 | Developed, High intensity | 0.7 |
| 6 | Barren land | 0.9 |
| 7 | Deciduous forest | 0.2 |
| 8 | Evergreen forest | 0.1 |
| 9 | Mixed forest | 0.3 |
| 10 | Shrub/Scrub | 0.4 |
| 11 | Grassland/Herbaceous | 0.5 |
| 12 | Pasture/Hay | 0.6 |
| 13 | Cultivated crops | 0.7 |
| 14 | Woody wetlands | 0.1 |
| 15 | Emergent herbaceous wetlands | 0.1 |

Table 2 Numerical values assigned to different soil texture types

| Category | Soil texture type | Value |
|----------|-------------------|-------|
| 1 | Sand | 0.2 |
| 2 | Loamy sand | 0.4 |
| 3 | Sandy loam | 0.8 |
| 4 | Silt loam | 0.6 |
| 5 | Loam | 0.6 |
| 6 | Silt clay loam | 0.8 |
| 7 | Clay loam | 0.8 |
| 8 | Silt clay | 0.2 |
| 9 | Clay | 1.0 |
| 10 | Water | 0 |

GIS-based Weighted Linear Combination Method

A series of thematic maps were created, using the GIS overlay concept of weighted linear combination (WLC). WLC is a method where landslide controlling factors can be combined by applying primary- and second-level weights (Ayalew et al. 2004). In this study, the WLC method was performed to derive the landslide susceptibility values, as shown in the following Equation:

$$Z(i, j, t) = \sum_{k=1}^n w_k y_k(i, j, t)$$

where $Z(i, j, t)$ is the landslide susceptibility value for pixel (i, j) at time t . w_k is the normalized linear combination weight

for k th factor and $\sum_{k=1}^n w_k = 1$.

According to previous studies (Ayalew et al. 2004; Hong et al. 2007), slope and soil texture type are primary-level parameters, while land cover type and elevation are second-level parameters. Therefore, numerical values to assign the weights for these four parameters decrease in the following

order: slope, soil type, land cover and elevation. Following this rule, several WLC susceptibility models were tested to determine the optimal combination of weights through the verification of existing landslide inventory data. Results indicate that the best combination to determine the weight of the four parameters (slope, soil type, land cover and elevation) is (0.5, 0.25, 0.15 and 0.1). Susceptibility values can therefore be calculated for every pixel.

Results and Discussion

A susceptibility map with discrete values would be more direct and useful to indicate the degree of landslide failure for decision making and hazard prevention strategies. This study adopted the natural break method in ArcGIS 10.0 to classify the susceptibility level into five categories: very low, low, medium, high and very high. This method searches the category boundaries at abrupt changes in histogram of the landslide susceptibility values (Sarkar and Kanungo 2004). Fig. 3 shows the landslide susceptibility map of Oklahoma generated from the WLC model with a resolution of 30 m. The highest risk area is at the southeast corner of this state. This region has greater slope and higher clay percentage. The northeast part also has higher potential to induce landslides. Although the soil type (silt loam) does not have high clay percentage, this area does have greater slope, which dominates the final susceptibility values. In contrast, the north western and south western parts of Oklahoma have mild slopes but higher clay fraction in soil types (silt clay and clay loam). This second important factor (soil type) takes a much more important role in the determination of the susceptibility level in these regions.

Histograms are further examined according to the susceptibility map and landslide inventory database (from ODOT and USGS) (Fig. 4) to quantitatively evaluate the performance of WLC method. Statistics show that 89.5 % (17 out of 19) of ODOT and 69.8 % (60 out of 86) of USGS landslide events fall into the high or very high category, which demonstrates the ability of GIS-based WLC model in predicting landslide hotspots. Other sites in low and medium categories are further investigated using the input datasets. Results show that slope is the main factor that contributes to this result. For all these sites, the slope values range from 3° to 8.5° , leading the very low rating in slope layer.

Summary and Future Work

In this paper, a new landslide risk map with 30 m resolution in Oklahoma is generated. Four controlling factors (slope, soil type, land cover and elevation) are selected as the input

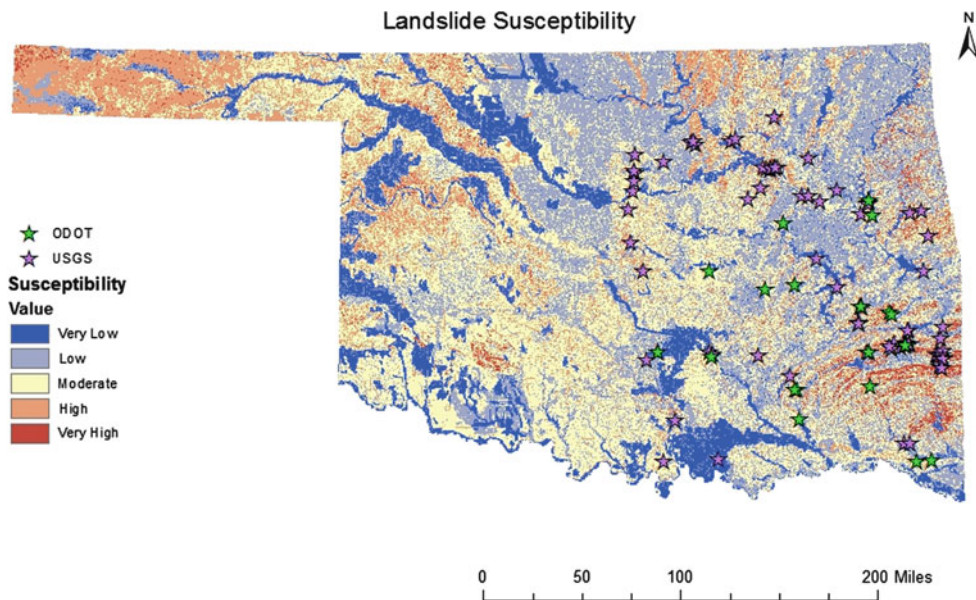


Fig. 3 Landslide susceptibility map for Oklahoma

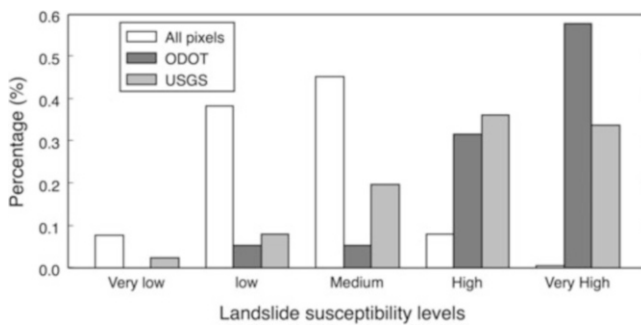


Fig. 4 A histogram indicating the percentage of landslide events/pixels falling into different levels of the susceptibility

of the GIS-based weighted linear combination (WLC) model. A regional landslide susceptibility and hazard index map has been validated and enhanced with existing survey data and the landslide inventory database. Results indicate that the whole state can be divided into five levels of susceptibility, namely very low (7.80%), low (38.32%), medium (45.15%), high (8.09%) and very high (0.64%). Generally speaking, more than 80% of Oklahoma are classified as having a low or moderate susceptible level to landslides. This is reasonable since Oklahoma is flat overall. The highest risk for landslides is located in the south eastern mountainous area. The other two high-risk areas in eastern Oklahoma match the historic landslide hazard map well. Regarding the high plateau elevations in the western part of Oklahoma, our model also indicates high potential of landslide failure, which is solely based on the elevation.

However, this may not be true since this part of state is very flat as can be seen from Fig. 2b.

There still remain some limitations in this research, which merit further consideration. First of all, the best combination of weights for the current controlling factors is determined with comparison to the limited landslide inventory database from ODOT and USGS (in total 105 events). Larger datasets need to be collected, which has the potential to improve current results as well as to make them more reliable. In addition, more geologic, hydrologic and geomorphologic controlling factors should be considered, such as lithology, drainage density, accumulation, flow direction (sliding path), infiltration, slope aspect, curvature, concavity and so on. If possible, site specific, localized properties at focused areas should be measured. They will be invaluable for the development of future real-time monitoring and prediction system in these landslide hot spots.

Acknowledgments This study was supported by “Real-time Monitoring of Slope Stability in Eastern Oklahoma” project funded by the Oklahoma Department of Transportation (ODOT) SPR 2241 and the bilateral project funded by Slovenian Research Agency (BI-US/12-13-048). The authors also acknowledge the partial open fund SKHL1310 support from the State Key Laboratory of Hydraulics and Mountain River Engineering, Sichuan University.

References

- Anbalagan R (1992) Landslide hazard evaluation and zonation mapping in mountainous terrain. *Eng Geol* 32:269–277
- Ayalew L, Yamagishi H, Ugawa N (2004) Landslide susceptibility mapping using GIS-based weighted linear combination, the case

- in Tsugawa area of Agano River, Niigata Prefecture, Japan. *Landslide* 1:73–81
- Bathrellos G, Kavilas D, Skilodimou H (2009) GIS-based landslide susceptibility mapping models applied to natural and urban planning in Trikala, Central Greece. *Estudios Geologicos* 65:49–65
- Carrara A, Cardinali M, Detti R, Guzzetti F, Pasqui V, Reichenbach P (1991) GIS techniques and statistical models in evaluating landslide hazard. *Earth Surf Proc Land* 16:427–445
- Cerato A, Nevels J (2007) Shallow landslide analysis: McCurtain County, Oklahoma. In: *Proceedings of the 1st North American landslide conference: landslides and society*. Integrated Science, Engineering, Management, and Mitigation, June 3–8. Vail, CO, pp 21–30
- Cerato A, Oleski R, Puklin C (2006) Case study: compacted embankment landslide in Grady County, Oklahoma. In: *Proceedings of the 40th annual symposium on engineering geology and geotechnical engineering*. Landslides-investigation, analysis and mitigation. Utah State University, Logan, Utah, May 24–26
- Coe J, Godt J, Baum R, Bucknam R, Michael J (2004) Landslide susceptibility from topography in Guatemala. In: Lacerda WA, Ehrlich M, Fontura SAB, Sayao ASF (eds) *Landslides: evaluation and stabilization*. Taylor & Francis Group, London, pp 69–78
- Dai F, Lee C (2002) Landslide characteristics and slope instability modeling using GIS, Lantau Island, Hong Kong. *Geomorphology* 42:213–238
- Fabbri A, Chung C, Cendrero A, Remondo J (2003) Is prediction of future landslides possible with GIS? *J Nat Hazards* 30:487–499
- Godt J, Baum R, Lu N (2009) Landsliding in partially saturated materials. *Geophys Res Lett* 36: L02403. doi: [10.1029/2008GL035996](https://doi.org/10.1029/2008GL035996)
- Hong Y, Adler R, Huffman G (2006) Evaluation of the potential of NASA multi-satellite precipitation analysis in global landslide hazard assessment. *Geophys Res Lett* 33: L22402. doi: [10.1029/2006GL028010](https://doi.org/10.1029/2006GL028010)
- Hong Y, Adler R, Huffman G (2007) Use of satellite remote sensing data in the mapping of global landslide susceptibility. *J Nat Hazards* 43:245–256
- Larsen M, Torres-Sanchez A (1998) The frequency and distribution of recent landslides in three montane tropical regions of Puerto Rico. *Geomorphology* 24:309–331
- Lee S, Min K (2001) Statistical analysis of landslide susceptibility at Yongin, Korea. *Environ Geol* 40:1095–1113
- Lu N, Godt J (2013) *Hillslope hydrology and stability*. Cambridge University Press, Cambridge, UK and New York
- Pourghasemi HR, Pradhan B, Gokceoglu C (2012) Application of fuzzy logic and analytical hierarchy process (AHP) to landslide susceptibility mapping at Haraz watershed, Iran. *Nat Hazards* 63:965–996
- Radbruch-Hall D, Colton R, Davies W, Luccitta I, Skipp B, Varnes D (1982) *Landslide overview map of the conterminous United States*. US Geological Survey Professional Paper 1183, 25 pp
- Saha A, Gupta R, Arora M (2002) GIS-based landslide hazard zonation in the Bagirathi (Ganga) Valley, Himalayas. *Int J Remote Sens* 23:357–369
- Sarkar S, Kanungo D (2004) An integrated approach for landslide susceptibility mapping using remote sensing and GIS. *Photogramm Eng Remote Sens* 70:617–625



InSAR-Based Landslide Location and Monitoring in Alpine Valley Region

Guijie Wang, Yueping Yin, Mowen Xie, and Weilun Wu

Abstract

Synthetic Aperture Radar Interferometry (InSAR) has become an important technique for monitoring ground movement and it has the advantage that other method cannot compare on the wide area dynamic investigation and monitoring. Thus, InSAR technology has been widely used in the investigation of geologic hazards, such as subsidence, landslide, earthquake, and volcanic activity. But, it is still in the research and practice application stage for the landslide investigation and monitoring of InSAR technology in the complex terrain area. In this paper, based on the rationale and algorithms of InSAR technology, combined with the topography and landform characteristic of landslide disasters, the ground local incidence angle of each point is derived by the geometric model which is established by the satellite Line-of-sight inclination, the slope and aspect of the ground point. And then, the reliable interference areas are determined by the relationship analysis among the local incidence angle, the backward scattering and the coherence of InSAR. Finally, the application example is achieved by using L-band Synthetic Aperture Radar data of the Advanced Land Observing Satellite, potentially moving landslide areas and landslide hazard areas are located, at the same time, the monitoring results of the typical landslide are analyzed in detail.

Keywords

Landslide • InSAR • Local incidence angle • Location • Monitoring

G. Wang (✉)

China Institute of Geo-Environment Monitoring, Dahuisi Lu 20
Haidian District, Beijing 100081, China
e-mail: wanggj@mail.cigem.gov.cn

Y. Yin

China Institute of Geo-Environment Monitoring, Beijing 100082,
China
e-mail: yinyp@mail.cigem.gov.cn

M. Xie

School of Civil and Environmental Engineering Beijing, University of
Science and Technology, Beijing 100083, China
e-mail: mowen@ustb.edu.cn

W. Wu

Geological Exploration Engineering Technology Baodi Yilian Co.,
Ltd, Beijing 100120, China
e-mail: velen.w@hotmail.com

Introduction

Landslide monitoring and early warning have become issues of global concern. However, the conventional geodetic technique is highly inefficient for large-scale landslide monitoring in vast areas (Yao and Mu 2008). With the development of remote sensing, synthetic aperture radar interferometry (InSAR), which enables the monitoring of very small ground movements in continuous large areas, is a high-potential solution to this problem. This technique has the following advantages: high accuracy, high resolution, all-weather adaptability, low cost, and coverage of inaccessible areas. Accordingly, InSAR has been widely applied in the landslide hazard investigation for scientific research and risk assessment (Wang 2011). But, the reliable interference

ranges which locate in the Alpine Valley region still need to be researched.

In this paper, InSAR-based landslide location and monitoring in Alpine Valley region are investigated. The characteristic of topography and landform are analysed by the slope and aspect, the ground local incidence angle of each point is derived by the geometric model which is established by the satellite Line-of-sight inclination, the slope and aspect of the ground point. To further, the local incidence angles are reclassified. And then, the reliable interference areas are determined by the relationship among the local incidence angle, the backward scattering and the coherence of InSAR, at the same time, the regions of layover and shadow are confirmed. Finally, the application example is implemented by using L-band Synthetic Aperture Radar data of the Advanced Land Observing Satellite, the detailed moving displacement maps of two time periods of 368 days (12 July 2007 to 14 July 2008) and 92 days (12 January 2008 to 13 April 2008) are derived in reliable region, the potentially moving landslide areas, as well as the landslide hazard areas are located by the analysis and comparison of the two differential periods. To prove the efficiency, L1R-6 landslide, which is in active state, is examined in detail, the results are compared with those obtained via the high-precision single-point GPS technique, and the same deforming tendency is obtained.

Study Area and Available Data

Study Area

The study area is situated in Wudongde Hydropower Reservoir at the junction of Luquan County in Yunnan Province and Huidong County in Sichuan Province, China. The basin topography and geologic conditions of Wudongde Hydropower Reservoir are unique and complex. The rise in the water level can lead to adverse changes in the geologic and artificial environment, which may result in the occurrence of all scales of landslides on the slope surrounding. Therefore, it is critical and essential for the InSAR monitoring of landslides around the reservoir area.

The study field is shown in Fig. 1. The entire area and the topography surrounding Wudongde reservoir are studied, and one of the landslides, the L1R-6 landslide, is discussed in detail.

Available Data

Five PALSAR acquisitions of the ALOS with a wavelength of 0.23 m (L band) have been applied and their orbital model was ascending and the parameters are shown in Table 1.

The Reliable Regional Analysis of InSAR Investigation

Local Incidence Angle and Its Regionalization

Local Incidence Angle is the intersection angle between the incidence direction of radar electromagnetic wave and the normal direction of slope, and it is determined by the Incidence Angle and Azimuth Angle of the satellite as well as the slope and aspect of the ground point (Xie et al. 2012).

The geometric sketch of the Local Incidence Angle is shown in Fig. 2, where θ is the incidence angle of the satellite; ∂ is the slope angle of the ground; θ_{loc} is the local incidence angle; δ and ω are, respectively, the aspect angle of the ground and the horizontal angles of LOS direction, where they are clockwise rotational horizontal angles and their zero direction is the north; V_s , V_n and V_a are, respectively, the vector of LOS direction, the vector of the surface normal direction, and the combination vector of the V_s , V_a .

Thus, ω is expressed as follows: under the right sight condition, $\omega = azimuthAngle + 90^\circ$; under the left sight condition, $\omega = azimuthAngle - 90^\circ$.

The right sight condition is as an example in Fig. 2.

The three-component of V_s are expressed as follows:

$$X_{V_s} = \left| \vec{V}_s \right| \times \sin \theta \times \cos (90 - \omega) \quad (1)$$

$$Y_{V_s} = \left| \vec{V}_s \right| \times \sin \theta \times \sin (90 - \omega) \quad (2)$$

$$Z_{V_s} = -\left| \vec{V}_s \right| \times \cos \theta \quad (3)$$

The three-component of V_n are expressed as follows:

$$X_{V_n} = \left| \vec{V}_n \right| \times \sin \partial \times \cos (90 - \delta) \quad (4)$$

$$Y_{V_n} = \left| \vec{V}_n \right| \times \sin \partial \times \sin (90 - \delta) \quad (5)$$

$$Z_{V_n} = \left| \vec{V}_n \right| \times \cos \partial \quad (6)$$

Thus, the three-component of V_a are expressed as follows:

$$X_{V_a} = X_{V_n} + X_{V_s} \quad (7)$$

$$Y_{V_a} = Y_{V_n} + Y_{V_s} \quad (8)$$

$$Z_{V_a} = Z_{V_n} + Z_{V_s} \quad (9)$$

Fig. 1 Entire study field surrounding Wudongde Hydropower Reservoir, marked by green square frame in the background and the detailed information (zonation and GPS point arrangement) of L1R landslide is inserted in the lower right

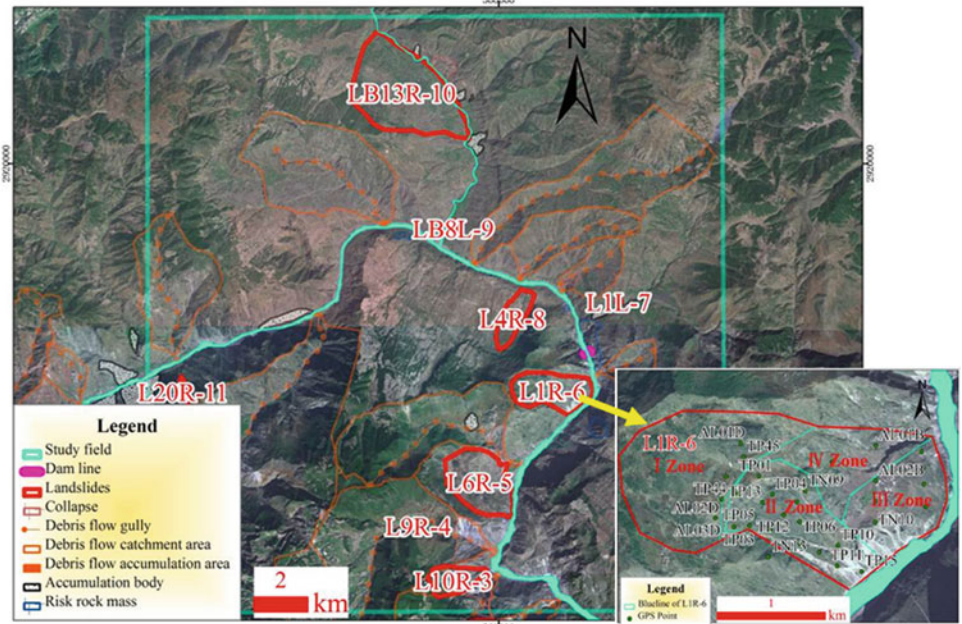


Table 1 Parameters of the available PALSAR data

| Image code | Acquisition number | Date | Polarization mode | Time span/day | Perpendicular baseline/m | Doppler centroid difference | 2PI Ambiguity height/m |
|----------------|--------------------|------------|-------------------|---------------|--------------------------|-----------------------------|------------------------|
| S ₁ | ALPSRP104820510 | 2008-01-12 | FBS/HH | 46 | 438.883 | -14.652 | 131.471 |
| S ₂ | ALPSRP111530510 | 2008-02-27 | FBS/HH | | | | |
| S ₁ | ALPSRP104820510 | 2008-01-12 | FBS/HH | 92 | 813.466 | -33.191 | 70.931 |
| S ₃ | ALPSRP118240510 | 2008-04-13 | FBS/HH | | | | |
| S ₄ | ALPSRP077980510 | 2007-07-12 | FBD/HH | 368 | 832.261 | 2.482 | 69.376 |
| S ₅ | ALPSRP131660510 | 2008-07-14 | FBD/HH | | | | |

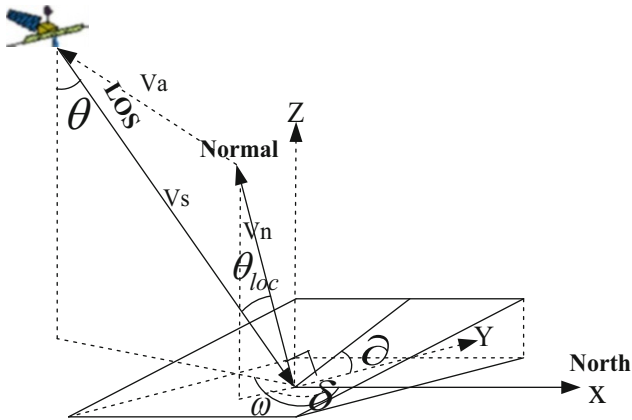


Fig. 2 Geometric sketch of the local incidence angle

The based on cosine law:

$$V_a^2 = V_n^2 + V_s^2 - 2V_nV_s \cos \theta_{loc} \quad (10)$$

Thus,

$$\theta_{los} = \arccos[\cos \vartheta \times \cos \theta - \sin \vartheta \times \sin \theta \times \cos (\omega - \delta)] \quad (11)$$

The ascending data of phased array-type L-band synthetic aperture radar are used in this study. The incidence angle θ is 34.3° , the azimuth angle is 277° , ϑ and δ are obtained by the spatial analysis of the DEM raster data.

According to (11), Local Incidence Angle of the each point in the study area is obtained. As shown in Fig. 3, the range of the Local Incidence Angle values is -26.5787° – 101.961° and the negative values correspond to active layover areas, while values higher than 90° correspond to active shadow areas.

As the each point value of Local Incidence Angles are slightly different, the Local Incidence Angles are reclassified for every 10° period as a group, the negative values and the values higher than 90° are respectively divided into a group. Therefore, the 11 angles groups are divided in the study area as shown in Fig. 4.

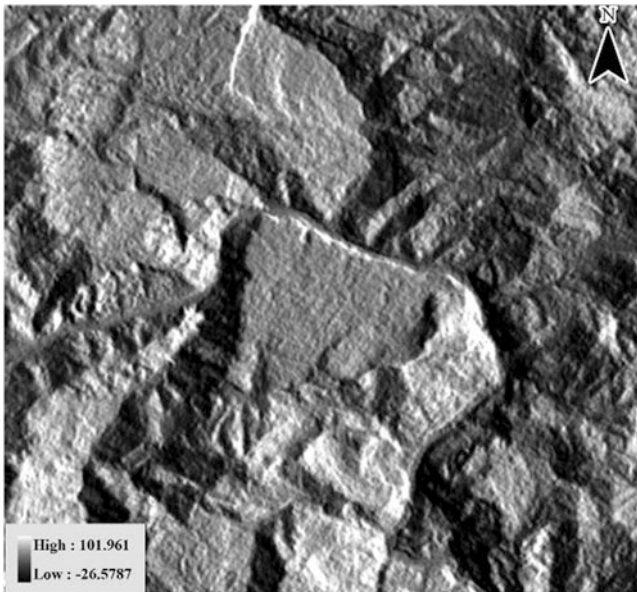


Fig. 3 Distribution map of the local incidence angle

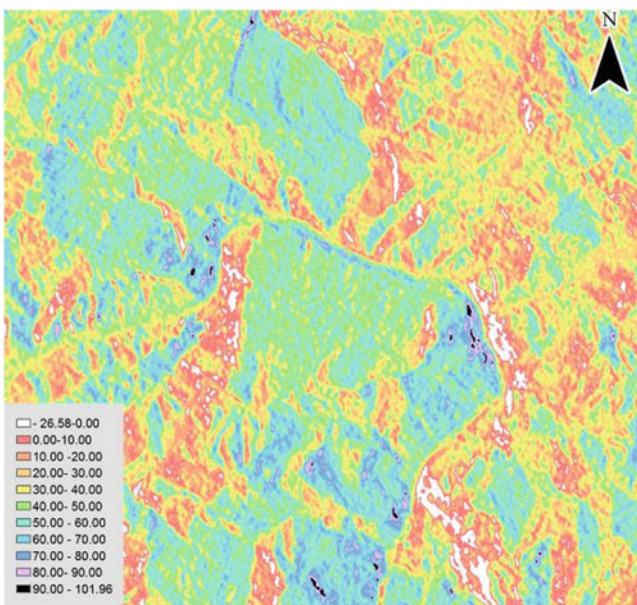


Fig. 4 Reclassify graph of the local incidence angle

The Relationship Between the Local Incidence Angle and the Backward Scattering

To acquire the relationship of the topography and backward scattering element, the backward scattering average value of the every scene data are counted up according to the

reclassify region of the Local Incidence Angle. The regional statistical averages of the backward scattering coefficient are listed in Table 2 and the specific trend diagram is shown in Fig. 5.

That indicate that the backward scattering coefficients are reducing with the increasing of the Local Incidence Angle and the gradient changes are slowing down after 50° – 60° , the backward scattering values of the layover areas are the biggest and the backward scattering values of the shadow areas are the smallest.

The Relationship Between the Local Incidence Angle and the Coherence

In order to investigate the relationship that is the coherence of InSAR image pair and local incidence angle, the coherence coefficients of S_1S_3 image pair and S_1S_3 image pair are computed. The regional statistical averages of the coherence coefficients are counted on the reclassify of local incidence angle in Table 3 and the specific trend diagram is shown in Fig. 6.

That indicate that the coherence coefficients averages are increasing with the increasing of the Local Incidence Angle at first and they are reaching to the largest in the 50° – 60° range. And then, the coherence coefficients are reducing with the increasing of the Local Incidence Angle. But the coherence coefficients averages of the layover area are the smallest and the coherence coefficients averages of the shadow area are the smaller.

The conclusion is drawn that the coherence of the layover and the shadow area is lower than other area.

The Credible Region Analysis

According to the relationship of the local incidence angle and the backward scattering in Table 2 and Fig. 5 as well as the relationship of local incidence angle and coherence in Table 3 and Fig. 6, the conclusion can be drawn that the optimal range of local incidence angle is 50° – 60° for InSAR applying in mountain and it is relatively reliable to 1° – 90° range of local incidence angle for InSAR technology, but the Interferometric result of the layover and the shadow area are incredible for Low coherence. The distribution of credible region in Fig. 7, the red regions for the layover and the shadow are incredible region, the gray region for the 1° – 90° range of the local incidence angle are credible interferometric regions.

Table 2 The correlation table of local incidence angle and backward scattering coefficient

| Angle range (degree) | S1 (20080112) | S2 (20080227) | S3 (20080413) | S4 (20070712) | S5 (20080714) |
|----------------------|---------------|---------------|---------------|---------------|---------------|
| <0 | 0.4068 | 0.4318 | 0.3978 | 0.4981 | 0.4415 |
| 0–10 | 0.2428 | 0.2516 | 0.2251 | 0.3162 | 0.2653 |
| 10–20 | 0.1946 | 0.2008 | 0.1782 | 0.3064 | 0.2602 |
| 20–30 | 0.1665 | 0.1697 | 0.1495 | 0.2918 | 0.2400 |
| 30–40 | 0.1369 | 0.1396 | 0.1234 | 0.2443 | 0.2039 |
| 40–50 | 0.0904 | 0.0920 | 0.0825 | 0.1539 | 0.1298 |
| 50–60 | 0.0694 | 0.0704 | 0.0646 | 0.1021 | 0.0891 |
| 60–70 | 0.0551 | 0.0561 | 0.0529 | 0.0670 | 0.0618 |
| 70–80 | 0.0433 | 0.0447 | 0.0424 | 0.0499 | 0.0449 |
| 80–90 | 0.0304 | 0.0319 | 0.0300 | 0.0354 | 0.0309 |
| 90< | 0.0234 | 0.0247 | 0.0233 | 0.0263 | 0.0243 |

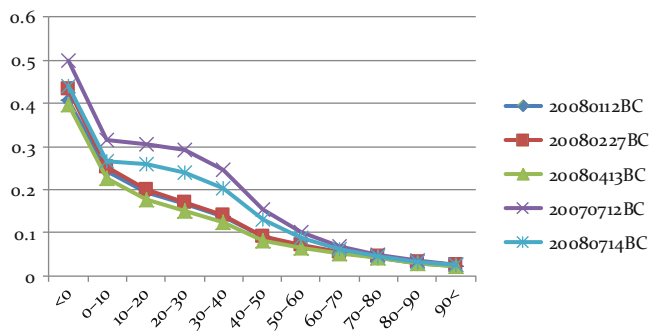


Fig. 5 The trend diagram of the local incidence angle and Backward Scattering coefficient

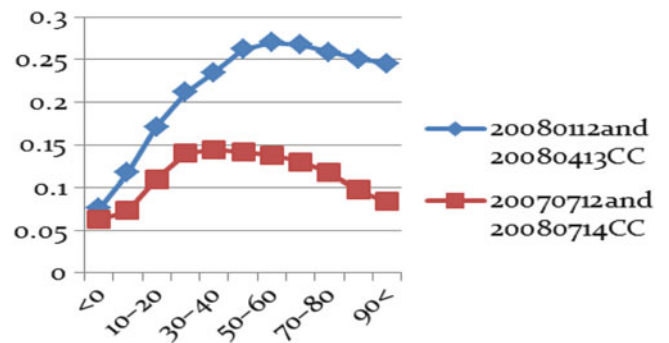


Fig. 6 The trend diagram of local incidence angle and coherence coefficient

Table 3 The correlation table of local incidence angle and coherence coefficient

| Angle range (degree) | S ₁ and S ₃ (20080112 and 20080413) | S ₄ and S ₅ (20070712 and 20080714) |
|----------------------|---|---|
| <0 | 0.4068 | 0.4318 |
| 0–10 | 0.2428 | 0.2516 |
| 10–20 | 0.1946 | 0.2008 |
| 20–30 | 0.1665 | 0.1697 |
| 30–40 | 0.1369 | 0.1396 |
| 40–50 | 0.0904 | 0.0920 |
| 50–60 | 0.0694 | 0.0704 |
| 60–70 | 0.0551 | 0.0561 |
| 70–80 | 0.0433 | 0.0447 |
| 80–90 | 0.0304 | 0.0319 |
| 90< | 0.0234 | 0.0247 |

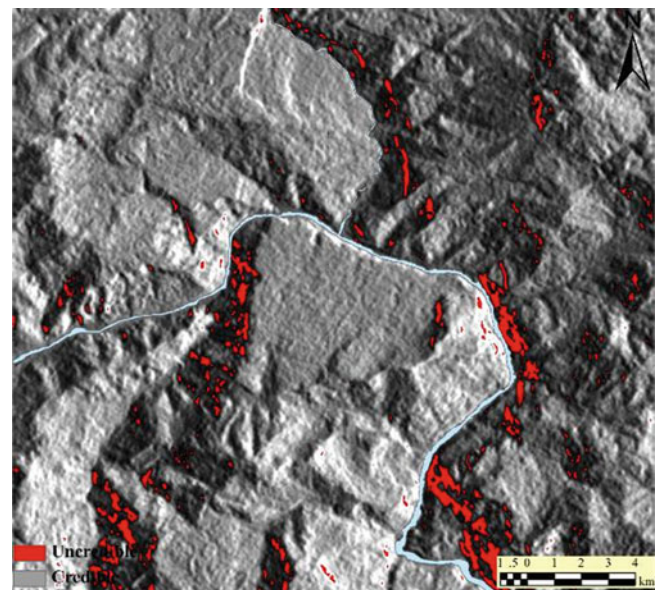


Fig. 7 The distribution map of credible region

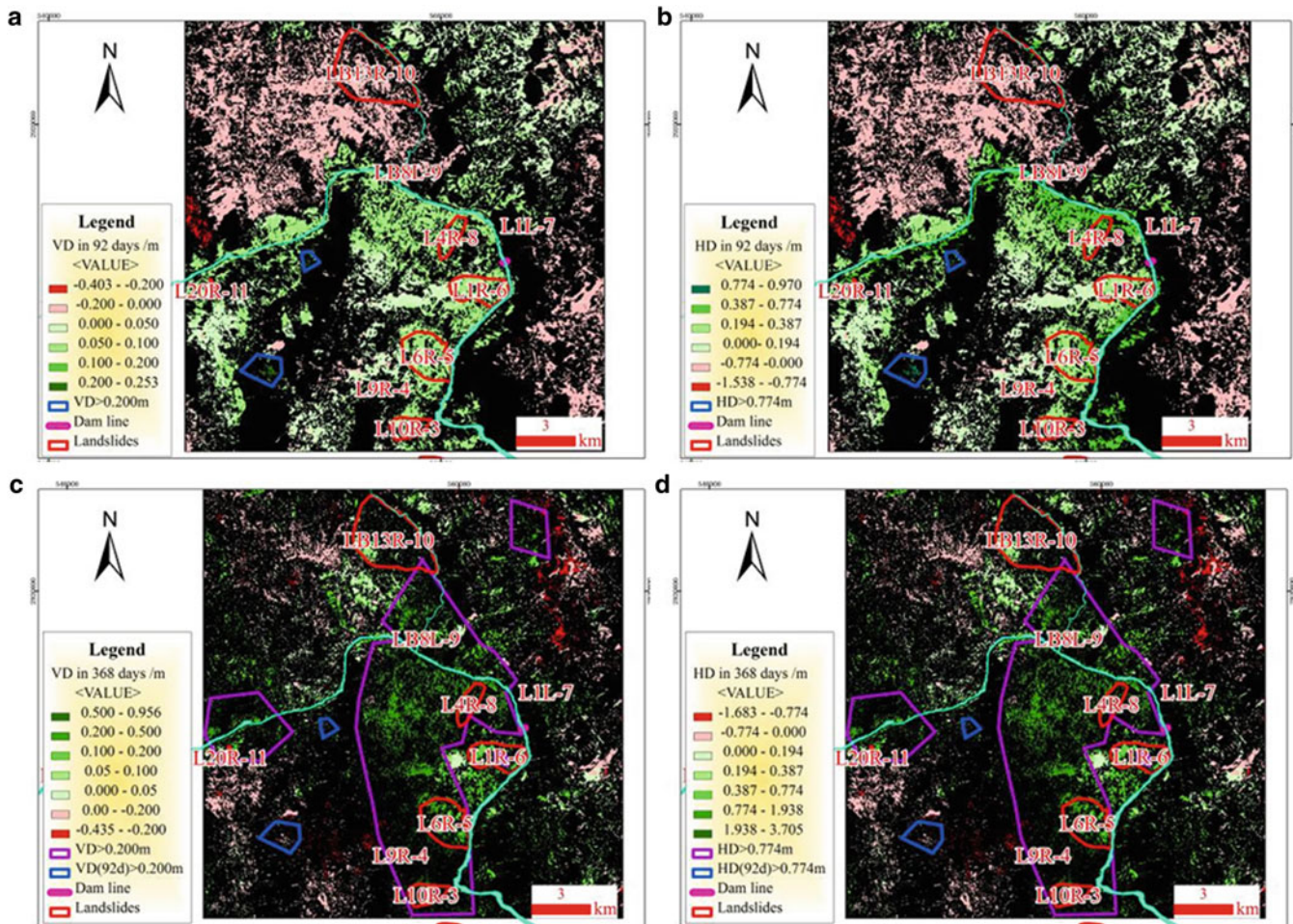


Fig. 8 The displacement state map of the study area in the two time periods. (a) Map of VD in 92 days; (b) Map of HD in 92 days; (c) Map of VD in 368 days; (d) Map of HD in 368 days

The Result of Landslide Monitoring and Precision Analysis

The Results of Landslide Location and Monitoring Incredible Region

The displacement map, which contains the detailed moving displacement information of the credible region in the two time periods, are obtained and then converted into vertical displacement (VD) and horizontal displacement (HD) maps, the HD value is proportional to the VD value because of the same line of sight projection reasons, as shown in Fig. 8 (Wang et al. 2013).

As the landslide movement is always accompanied by subsidence motion, the subsidence area is investigated in the credible area. The rule of signs is given such that in VD maps, the plus sign indicates subsidence, whereas the minus sign indicates uplift; in HD maps, the HD is projected in the north–south direction, and the plus sign indicates a southward movement, whereas the minus sign indicates a

northward movement. From Fig. 8, the deformation states of the various points can be clearly identified in the credible region. The precision of the displacement value obtained via D-InSAR is half of the wavelength (Wang et al. 2010), and the wavelength of the L band employed by PALSAR data is 0.23 m. Considering the effect of all possible errors, the moving areas with $VD > 0.200$ m ($HD > 0.774$ m) are evaluated as potentially moving landslide areas and landslide hazard areas, which are marked by a blue polygon (Fig. 8a, b) and a purple polygon (Fig. 8c, d) in the displacement maps. The red polygons are used to mark the landslides that have occurred or that are in a moving state through ground monitoring.

In the displacement maps of the credible region (Fig. 8), the VD values of the majority uplift area are less than 0.200 m; thus, the uplift displacements of the two time periods are considerably caused by errors. For the subsidence area, the maximum VD value is 0.253 m in the 92-day (12 January 2008 to 13 April 2008) displacement map (Fig. 8a) and 0.956 m in the 368-day (12 July 2007 to 14 July 2008) displacement map (Fig. 8c).

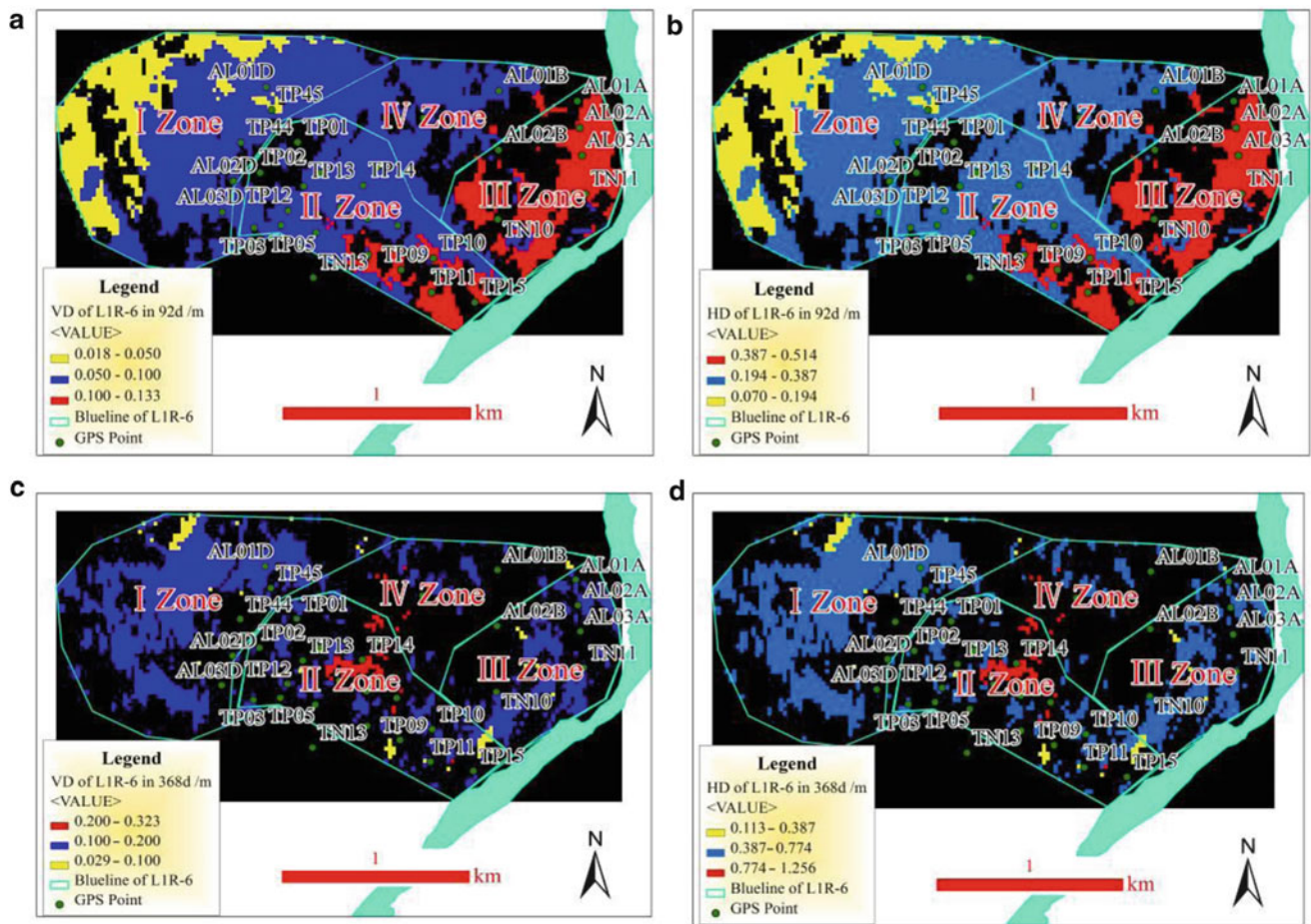


Fig. 9 The displacement state map of the L1R-6 landslide in the two time periods (m). (a) Map of VD in 92 days; (b) Map of HD in 92 days; (c) Map of VD in 368 days; (d) Map of HD in 368 days

As previously mentioned, the areas with $VD > 0.200$ m ($HD > 0.774$ m), which is marked by a blue polygon in Fig. 8a, b of the 92-day displacement map and by a purple polygon in Fig. 8c, d of the 368-day displacement map, are respectively identified as potentially moving landslide areas and landslide hazard areas. The two potential landslide areas in the 92-day period are labeled (blue polygon) in Fig. 8a, b, as well in the 368-day displacement map in Fig. 8c, d, for a clearer comparison. However, the displacement values of the two areas are relatively small in the 368-day displacement map, which indicates that the large displacement of the two areas in the 92-day displacement map can be attributed to seasonal material flow rather than to a potential landslide. This finding is supported by optical images, which demonstrate that these two areas are located at the entrance and at the central catchment area of a large-scale debris flow gully near Wudongde Hydropower Reservoir. Therefore, a possible reason for the displacement variation in these two regions in the 92-day period is that the flowing gully material which is induced by migrating rainwater. Furthermore, in the 368-day displacement map (Fig. 8c, d), the purple polygon in the large deformation area is confirmed as the collective

area of several large-scale debris flows and of three active landslides (L6R-5, L9R-4, and L10R-3). These areas, which are marked by a purple polygon, should be regarded as important research and control areas.

Compared with the D-InSAR results with ground measurement in Fig. 8, almost all landslides measured via ground monitoring (marked by red polygons) are located in the subsided areas (shown by green background), particularly right in the large-subsidence areas with $VD > 0.200$ m (marked by purple polygons) of Fig. 8c, d. Thus, the comparison shows that the D-InSAR monitoring results are consistent with ground measurements.

Precision Analysis

To further verify the precision of the D-InSAR technique for landslide location and monitoring in Alpine Valley, the deformation evolution of the active L1R-6 landslide in the credible region is investigated in detail. The displacement maps of the L1R-6 landslide obtained via D-InSAR monitoring in the two periods are shown in Fig. 9, and the

Table 4 Comparison of D-InSAR and GPS results

| Zone | Point | D-InSAR (92 days) (VD/mm) | GPS (92 days) (VD/mm) | D-InSAR (92 days) (HD/mm) | GPS (92 days) (HD/mm) | D-InSAR (368 days) (VD/mm) | GPS (368 days) (VD/mm) | D-InSAR (368 days) (HD/mm) | GPS (368 days) (HD/mm) |
|------|-------|---------------------------|-----------------------|---------------------------|-----------------------|----------------------------|------------------------|----------------------------|------------------------|
| I | AL01D | 54.42 | 7.57 | 210.51 | 13.00 | 158.52 | 32.89 | 616.17 | 32.36 |
| | AL02D | 73.96 | 2.50 | 285.98 | 3.50 | 130.62 | 2.61 | 507.7 | 1.75 |
| | AL03D | 73.30 | 1.53 | 283.46 | 4.37 | – | 1.03 | – | 2.66 |
| | TP44 | 72.603 | −0.12 | 278.65 | 4.59 | – | −5.36 | – | 3.39 |
| | TP45 | 53.41 | 5.87 | 206.54 | 8.76 | 141.97 | 21.29 | 551.96 | 27.2 |
| II | TP01 | – | 3.98 | – | 1.57 | 126.74 | 10.83 | 492.66 | 27.95 |
| | TP02 | – | 2.78 | – | 0.41 | 110.69 | 12.99 | 430.25 | 15.27 |
| | TP03 | 71.82 | 2.52 | 277.79 | 3.07 | 166.73 | 12.08 | 648.05 | −0.55 |
| | TP04 | 78.65 | 30.75 | 304.25 | 24.78 | 132.44 | 141.72 | 514.93 | 188.51 |
| | TP05 | 71.39 | 13.19 | 276.13 | 22.74 | – | 66.54 | – | 32.54 |
| | TP06 | 90.42 | 42.02 | 349.71 | 53.24 | 295.25 | 204.92 | 1,147.76 | 282.33 |
| | TP07 | 90.98 | 30.05 | 351.90 | 42.25 | 244.24 | 168.3 | 949.55 | 343.99 |
| | TP08 | 105.34 | 38.61 | 407.44 | 56.96 | – | 178.75 | – | 265.27 |
| | TP09 | 112.92 | 40.03 | 436.74 | 62.34 | – | 222.74 | – | 261.2 |
| | TP10 | 103.10 | 29.77 | 398.87 | 48.02 | 176.63 | 171.44 | 686.67 | 269.19 |
| | TP11 | 123.71 | 38.35 | 478.62 | 68.56 | 102.46 | 206.4 | 338.3 | 260.14 |
| | TP12 | 81.63 | 15.82 | 315.66 | 20.45 | 108.9 | 60.78 | 423.28 | 39.95 |
| | TP13 | 81.99 | 13.11 | 317.14 | 22.19 | – | 91.08 | – | 85.94 |
| | TP14 | 83.63 | 42.03 | 323.53 | 43.59 | 261.81 | 220.1 | 1,018.02 | 286.95 |
| | TP15 | 120.12 | 5.74 | 464.68 | 1.99 | 131.46 | −3.27 | 511.18 | 2.51 |
| | AL02C | 88.01 | 22.62 | 340.36 | 49.87 | 205.37 | 141.4 | 798.26 | 203.31 |
| | AL03C | 85.26 | 26.52 | 329.79 | 39.88 | – | 123.28 | – | 131.80 |
| | AL01A | – | 0.45 | – | −1.26 | 123.95 | −9.08 | 482.34 | −0.98 |
| III | AL02A | 119.38 | −1.15 | 462.11 | −1.27 | 131.98 | −2.09 | 513.45 | −1.93 |
| | AL03A | 126.04 | −0.70 | 487.99 | −5.31 | – | −2.58 | – | −1.76 |
| | AL02B | – | 4.55 | – | −0.51 | – | 6.28 | – | −1.86 |
| | AL03B | 108.93 | 3.16 | 421.62 | −1.19 | – | 3.43 | – | −2.45 |
| | TN10 | 102.28 | 3.15 | 395.81 | −1.70 | 121.57 | 2.25 | 472.91 | 0.36 |
| | TN11 | 115.91 | 1.05 | 448.67 | −10.45 | 123.51 | −5.34 | 480.63 | −2.25 |
| IV | AL01B | 89.30 | 3.96 | 345.59 | 1.39 | – | 5.55 | – | 2.31 |
| | AL01C | 83.50 | 5.32 | 323.17 | −5.02 | – | 5.60 | – | 1.72 |

“–” means that the data are not available

displacement value of each point is presented. Considering that the data on the displacement value are enormous, graded maps are employed to present the three displacement intervals in three colors (yellow, blue, and red) in Fig. 9. Thus, the moving displacement of the different regions can be clearly identified by using the displacement map. In Fig. 9, the L1R-6 landslide area is divided into four zones, I, II, III, and IV. In the 92-day displacement map (Fig. 9a, b), the displacement values are smaller in zones I and IV ($VD < 0.100$ m, $HD < 0.387$ m), whereas the values in regions of zones II and III are bigger ($VH = 0.100$ m to 0.133 m, $HD = 0.387$ m to 0.514 m). In the 368-day displacement map (Fig. 9c, d), the displacement values are larger ($VD > 0.200$ m, $HD > 0.774$ m) in a region of zone II and a small region of zone IV, whereas those in the other two zones are smaller ($VD < 0.200$ m, $HD < 0.774$ m).

To summarize, the results of the two periods show that the displacement of zone II is the biggest and that zone II must be regarded as a key disaster area for further investigation. The displacement of the other zones is relatively smaller. It should be noted that the 92-day displacement values in zone III are relatively high. However, the values are smaller than 0.200 m, which indicates that the result is considerably affected by errors and that focusing on monitoring zone III is unnecessary. Therefore, the results obtained via D-InSAR are generally consistent with those obtained via ground monitoring, which shows the occurrence of large displacements in zone II compared with those in other zones.

To test the single-point monitoring precision of the D-InSAR technique, the monitoring displacement values of the GPS monitoring points (green dots with black serial

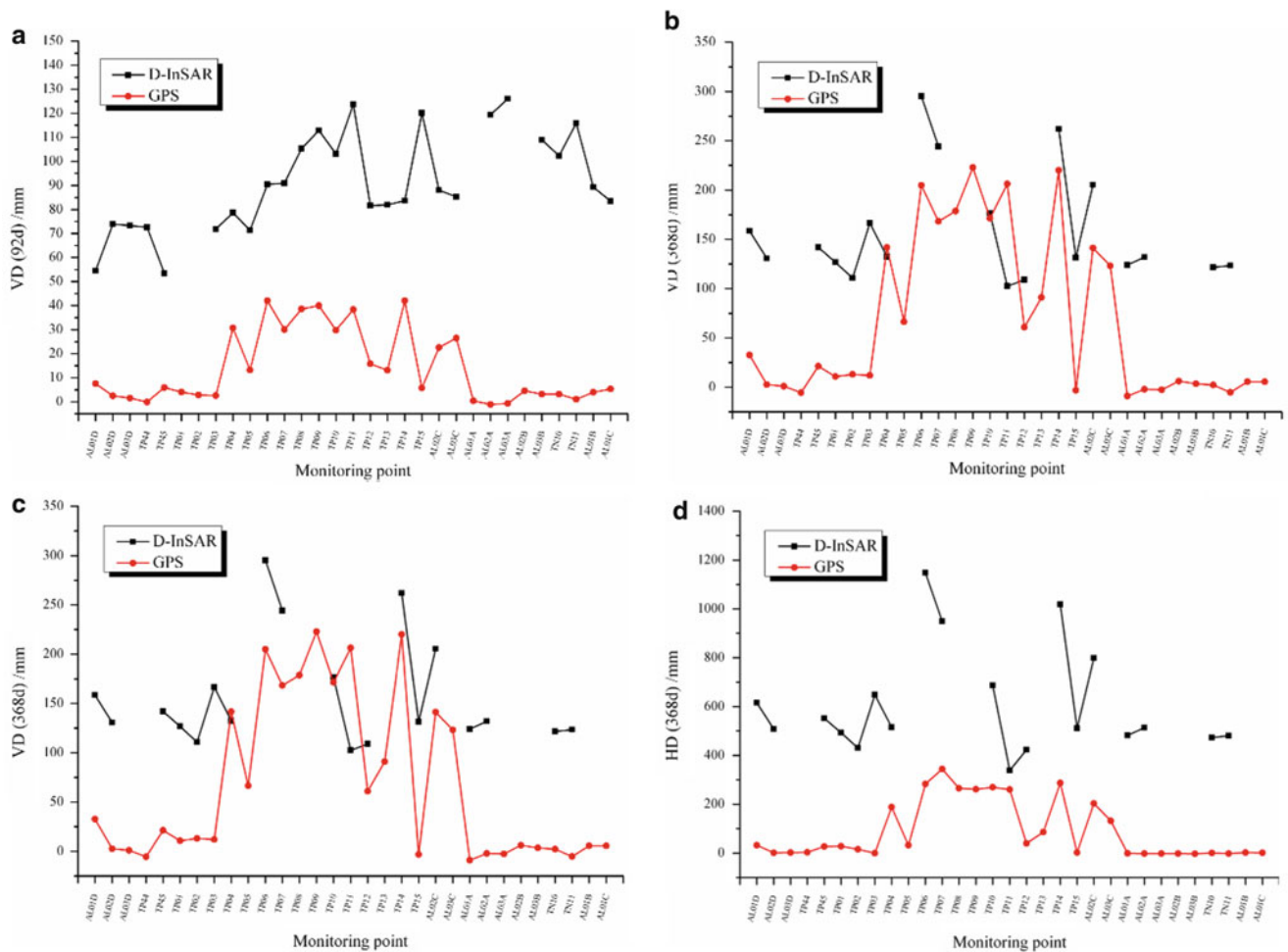


Fig. 10 Comparison of D-InSAR and GPS trend charts (mm). (a) Comparison of 92-day VD trends; (b) Comparison of 92-day HD trends; (c) Comparison of 368-day VD trends; (d) Comparison of 368-day HD trends

numbers on the No. L1R-6 landslide in Fig. 9) obtained via D-InSAR are compared with the GPS investigation results.

Compared with the 92-day (12 January 2008 to 13 April 2008) D-InSAR result, the GPS investigation period is from 11 January 2008 to 19 April 2008 for zone II and from 12 January 2008 to 18 April 2008 for zones I, III, and IV; Compared with the 368-day (12 July 2007 to 14 July 2008) D-InSAR result, the GPS investigation period is from 23 June 2007 to 15 July 2008 for zone II and from 28 June 2007 to 14 July 2008 for zones I, III, and IV. The monitoring results in the two time periods via D-InSAR and GPS are listed in Table 4, and trend charts are compared in Fig. 10.

The comparison in Fig. 10 indicates that although the single-point monitoring accuracy of D-InSAR is not perfect and the displacement trend line is discrete because of unavailable data at certain monitoring points, which is induced by decorrelation, the overall displacement and the moving tendency are basically in agreement with those of

GPS. Therefore, despite the slightly lower single-point monitoring accuracy of the GPS technique, the D-InSAR technique is still an effective approach in landslide monitoring because of its advantage over other methods in that it competently covers a wide and continuous area of hundreds or even thousands of kilometers (e.g., the width of the entire scene in this study is 70 km) in Alpine Valley region.

Conclusion

In this paper, the InSAR technique is used to locate and to monitor the landslides in Alpine Valley area located in Wudongde Hydropower Reservoir of Jinsha River by using five PALSAR data acquisitions. The characteristic of topography and landform are analysed by the slope and aspect, the ground local incidence angle of each point is derived by the geometric model which is established by the satellite Line-of-sight inclination, the slope and aspect. And then, the reliable interference regions are determined.

Finally, the application example is implemented by using L-band PALSAR data and the precision are verified by compared with GPS results. The following conclusions can be drawn:

1. the optimal range of local incidence angle is 50° – 60° for InSAR applying in Alpine Valley and it is relatively reliable to 1° – 90° range of local incidence angle for InSAR technology, but the Interferometric result of the layover and the shadow area are incredible for Low coherence.
2. The potential landslide area can be identified by using the InSAR technique in the Alpine Valley region.
3. The displacement tendencies of the InSAR and GPS monitoring results are basically in agreement.

Therefore, with the development of remote sensing technology and advanced earth-detection and digitization techniques, the InSAR technique is expected to become one of the most important approaches to the identification

and monitoring of early-stage landslides in wide Alpine Valley region.

References

- Wang GJ (2011) Experiment research of D-InSAR technique on identifying landslide moving in a wide area. *J Univ Sci Technol Beijing* 33(2):131–141
- Wang GJ, Xie MW, Qiu C, Esaki T (2010) Application of D-INSAR technique to landslide monitoring. *Rock Soil Mech* 31(4): 1337–1344
- Wang GJ, Xie MW, Chai XQ, Wang LW, Dong CX (2013) D-InSAR-based landslide location and monitoring at Wudongde hydropower reservoir in China. *Environ Earth Sci* 69:2763–2777
- Xie MW, Wang ZF, Hu M, Huang JH (2012) The characteristic analysis of D-InSAR data for landslides monitoring in Alpine and Canyon region. *Bull Surv Mapp* 4:18–21
- Yao GQ, Mu JQ (2008) D-InSAR technique for land subsidence monitoring. *Earth Sci Front* 15(4):239–243



Use of Satellite and Ground Based InSAR in Hazard Classification of Unstable Rock Slopes

John F. Dehls, Tom Rune Lauknes, Reginald L. Hermanns, Halvor Bunkholt, Tom Grydeland, Yngvar Larsen, Harald Ø. Eriksen, and Trond Eiken

Abstract

A newly developed hazard classification system for large unstable rock slopes depends on the evaluation of a number of criteria. These criteria include both displacement rates and the structural development of the unstable slope. Satellite and ground-based interferometric radars have the potential to measure the displacement of active rockslides. By using several complimentary InSAR datasets, with different viewing geometries, we are able to assess both movement criteria and a number of criteria related to structural development of the bounding surfaces.

We have collected five years of high resolution satellite imagery using several viewing geometries for the Gamanjuni 3 rockslide in northern Norway. In addition, we have collected radar using a ground-based radar. The results show a clearly defined block moving as a wedge. However, the decrease in movement velocity and steepness towards the lower part of the slope, along with the lack of visible basal structures, indicates that rock creep acts at the base of the slide body.

Keywords

InSAR • Hazard • Satellite

Introduction

Catastrophic failure of large rock slopes in Norway has occurred several times in the last century, leading to large loss of life. The Geological Survey of Norway (NGU), under the direction of the Norwegian Water and Energy Directorate

(NVE), carries out systematic geological mapping of potentially unstable rock slopes that may fail catastrophically. The large mountainous land area of Norway necessitates a systematic mapping approach. Once a potential unstable slope is identified, a hazard and risk classification is performed in order to prioritize potential mitigation measures, such as periodic or permanent monitoring.

NGU, together with a group of international experts, has developed a systematic hazard classification system for large unstable rock slopes for use in Norway (Hermanns et al. 2012). The hazard analysis is based upon two sets of criteria. The first set involves site investigations, including structural mapping and kinematic analysis. These criteria include the development of bounding surfaces. The second set involves assessment of the current activity level of the slope. This includes evidence of historic or prehistoric events in the area, observations of current rockfall activity, and measurements of current velocity and possible acceleration. These last parameters have historically been provided by periodic GNSS surveys. However, this

J.F. Dehls (✉) • R.L. Hermanns • H. Bunkholt
Geological Survey of Norway, P.O. Box 6315,
Sluppen 7491 Trondheim, Norway
e-mail: john.dehls@ngu.no; reginald.hermanns@ngu.no; halvor.bunkholt@ngu.no

T.R. Lauknes • T. Grydeland • Y. Larsen • H.Ø. Eriksen
Norut, Postboks 6434, Forskningsparken 9294 Tromsø, Norway
e-mail: tom.rune.lauknes@norut.no; tom.grydeland@norut.no;
yngvar.larsen@norut.no; harald.overli.eriksen@norut.no

T. Eiken
Department of Geosciences, University of Oslo, Postboks 107,
Blindern 0316 Oslo, Norway
e-mail: trond.eiken@geo.uio.no

is a very resource intensive method that provides at most one measurement per year on a sparse network of observation points. Increasingly, we have been using first satellite based, and now ground based InSAR measurements to determine deformation rates on a dense network of points.

Study Area

The Lyngen region in Troms County has an unusually high density of large unstable rock slopes (Henderson et al. 2011; Osmundsen et al. 2009). These unstable rock slopes are located in glacially steepened or over-steepened valleys and fjord sides. In this study, we take the example of an unstable rock slope referred to as “Gamanjunni 3”.

The Gamanjunni 3 unstable area consists of a large block, approximately 150 by 160 m, that has been displaced approximately 100 m towards the valley floor. Despite considerable internal fracturing, the upper part has moved together as a cohesive volume. The lower part of the unstable block is highly fractured.

Methods

In 2011, two GNSS benchmarks were installed on the upper block as well as another benchmark in the stable area above. This network was connected to another network on a nearby unstable slope to increase accuracy on both networks. Repeat surveys were carried out in 2012 and 2013. A robust linear regression is usually applied to a time series of dGNSS data to determine yearly average displacement rates (Böhme et al. 2013). Since we only have three measurements so far, this is not yet possible. However the displacements in the two periods are very similar, with both vertical and horizontal velocities of 3–4 cm/year.

We have been acquiring TerraSAR-X stripmap data in both ascending and descending geometries over the Lyngen area since 2009. This radar operates at X-band (9.6 GHz). The satellite has a repeat cycle of 11 days. In addition, we have been acquiring Radarsat-2 data in both Fine mode and Ultrafine mode during the same period. This radar operates at C-band (5.4 GHz), and has a repeat cycle of 24 days. For both satellites, we collected images during each snow-free season. We have process each dataset using both short baseline (SBAS) and persistent scatterer (PSI) algorithms, implemented in the GSAR software package developed by Norut (Larsen et al. 2006).

During six weeks in July and August 2012, we observed the Gamanjunni 3 rockslide using the GPRI radar developed by Gamma Remote Sensing AG. This instrument operates at Ku-band (17.2 GHz) and has measurement sensitivity better than 1 mm. The radar data were acquired with a temporal

sampling as often as every three minutes. Since the instrument was mounted in the valley below the unstable slope, it has a different field of view than the satellites. The shorter wavelength provides a higher sensitivity to motion than the X- and C-band satellites, and the frequent observation interval allows us to measure changes in the velocity during the campaign.

InSAR only provides a measurement of the deformation along the line-of-sight (LOS) between the satellite and the ground, so it cannot measure the absolute deformation magnitude or direction from a single dataset. By using InSAR data from both ascending and descending orbits, as well as the ground based system, we can calculate the horizontal and vertical components and measure changes in the movement direction within the moving area. This is important in assessing the likelihood of proposed deformation mechanisms.

Results

Results from all satellite datasets show a clearly defined area of movement (Fig. 1), constrained by a back scarp, side fractures and a toe area. The average velocity is on the order of 5 cm/year. This is consistent with the results from the dGNSS measurements, that show that the upper block has a horizontal component of movement of about 4 cm/year. The lower part of the slide contains a fast moving lobate shaped landform, visible in the high velocity area in (Fig. 1b). It has the characteristics of a rock glacier with steep front and a rough surface with large blocks floating on top.

The most obvious hazard criteria that the InSAR results can be used in defining are the displacement rate and possible changes in displacement rate over time. We have now establish the average velocity over the last 5 years. Satellite InSAR measurements will be continued long into the future, allowing us to recognise any future acceleration. In addition to displacement, however, there are a number of other criteria that are also much easier to define with the help of InSAR. The presence of both a back scarp and lateral release surfaces are clearly indicated in the velocity maps. While these structures can usually be identified in the field, it is not always clear whether or not such planar surfaces are fully developed, allowing movement.

The presence of a basal rupture surface is a necessary criterion for eventual failure. In this case, there is no morphological expression of a rupture surface in the field. The InSAR data clearly defines an area that is moving and a stable area, but the lower boundary is not as clear as for the lateral surfaces.

By combining InSAR data from three different orientations, we can determine the direction of movement and variations in the direction of movement throughout the surface of the sliding mass. This in turn allows us to infer something about the

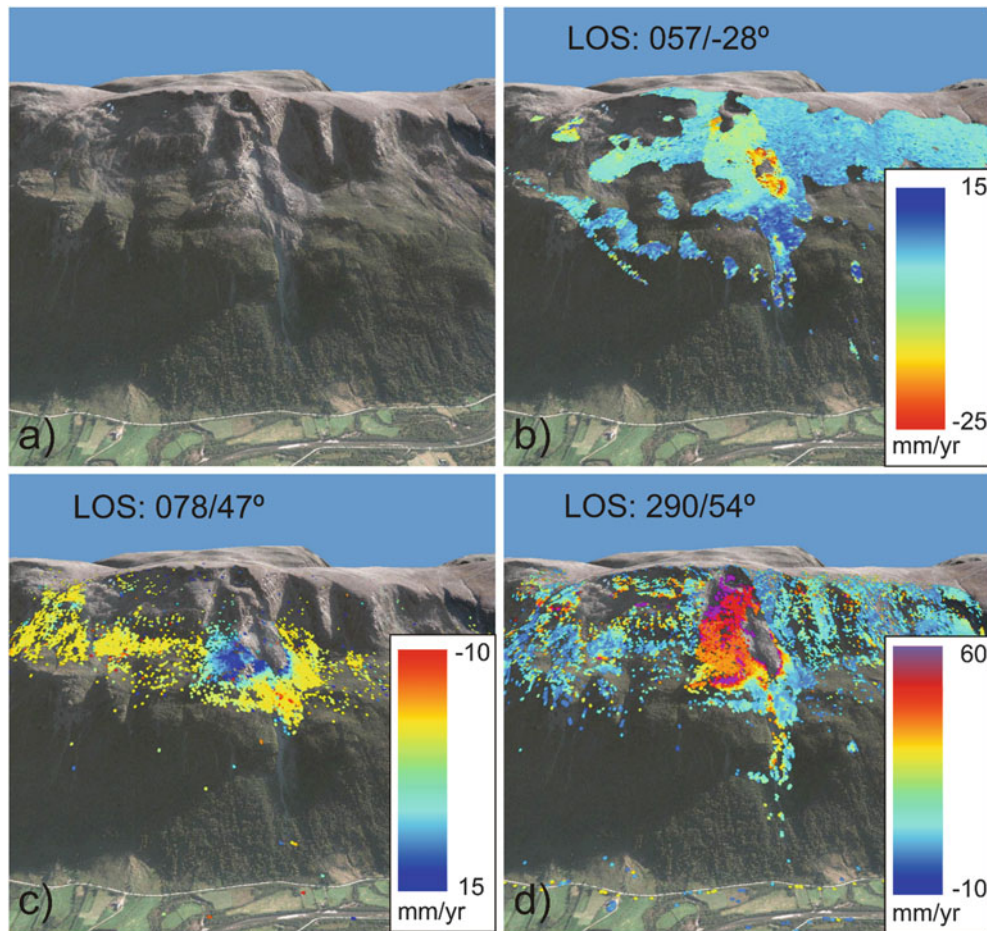


Fig. 1 Gamanjunki 3 rockslide. (a) Area of the rockslide; (b) GPR data from 21-day interferogram. *Red* is towards radar. *Blue* is away from radar; (c) Mean descending TerraSAR-X data (2009–2012). *Red*

is away from radar. *Blue* is towards radar; (d) Mean descending TerraSAR-X data (2009–2012) *Purple* is away from radar. *Blue* is towards radar

sliding mechanism. We have determined that the velocity decreases from the upper block through the fractured area in the toe. In addition, the movement direction becomes shallower near the toe. These observations indicate that we have a clear block slide that develops on an underlying sliding surface and lateral release surfaces, forming a wedge. None of those structures daylight at the slope, and neither does the intersection line. This structural condition makes it necessary that rock creep acts at the base of the slide body. A steady decrease of the velocity from about 5 cm/year to about 2 cm/year in the lower part of the instability supports this interpretation.

Discussion

Satellite-based InSAR has proven invaluable for regional landslide mapping and has led to the discovery of numerous large unstable rock slopes in Norway. In this study, we

show how high resolution ground-based and satellite-based InSAR can also play an important role in hazard classification. Although field mapping of structures still remains a very important part of the process, it is not always possible to determine whether or not structures that are identified actually allow movement. dGNSS surveys allow us to determine whether or not a potentially unstable slope is actually moving. However, it is an expensive and time consuming technique that only provides information on a limited number of points. By using InSAR we are able to obtain tens of thousands of measurements, and delineate areas of movement. This in turn gives us more information about the structures bounding the unstable area. The combination of several look directions gives us the added benefit of being able to determine the actual movement direction for many of these points, potentially giving us further insight into the kinematics. In the case of the Gamanjunki 3 rockslide, it is clear that although there is significant annual displacement, the

basal rupture surface necessary for catastrophic failure has not yet developed.

Acknowledgments The first 3 years of TerraSAR-X data were provided through the German Aerospace Centre (DLR) TerraSAR-X AO projects #GEO0565 and GEO0764.

The use of the ground based radar within this project has been financed by the regional research funds North-Norway.

References

- Böhme M, Hermanns RL, Oppikofer T, Fischer L, Bunkholt H, Eiken T, Pedrazzini A, Derron M-H, Jaboyedoff M, Blikra LH, Nilsen B (2013) Analyzing complex rock slope deformation at Stampa, western Norway, by integrating geomorphology, kinematics and numerical modelling. *Eng Geol* 154:116–130
- Henderson IHC, Lauknes TR, Osmundsen PT, Dehls J, Larsen Y, Redfield TF (2011) A structural, geomorphological and InSAR study of an active rock slope failure development. In: Jaboyedoff M (ed) *Slope tectonics*, vol 351. Geological Society, London, pp 185–199, Special Publications
- Hermanns RL, Oppikofer T, Anda E, Blikra LH, Böhme M, Bunkholt H, Crosta GB, Dahle H, Devoli G, Fischer L, Jaboyedoff M, Loew S, Sætre S, Yugsi Molina F (2012) Recommended hazard and risk classification system for large unstable rock slopes in Norway. NGU-Rapport 2012.029, 53 p
- Larsen Y, Engen G, Lauknes TR, Malnes E, Høgda KA (2006) A generic differential interferometric SAR processing system, with applications to land subsidence and snow-water equivalent retrieval. In: *Fringe 2005 Workshop*, ESA SP-610. Frascati, Italy, p 56
- Osmundsen PT, Henderson IHC, Lauknes TR, Larsen Y, Redfield TF, Dehls J (2009) Active normal fault control on landscape and rock-slope failure in northern Norway. *Geology* 37:135–138

Part IV

Hazard Mapping



Introduction: Hazard Mapping

Rex L. Baum, Toyohiko Miyagi, Saro Lee, and Oleksandr M. Trofymchuk

Abstract

Twenty papers were accepted into the session on landslide hazard mapping for oral presentation. The papers presented susceptibility and hazard analysis based on approaches ranging from field-based assessments to statistically based models to assessments that combined hydromechanical and probabilistic components. Many of the studies have taken advantage of increasing availability of remotely sensed data and nearly all relied on Geographic Information Systems to organize and analyze spatial data. The studies used a range of methods for assessing performance and validating hazard and susceptibility models. A few of the studies presented in this session also included some element of landslide risk assessment. This collection of papers clearly demonstrates that a wide range of approaches can lead to useful assessments of landslide susceptibility and hazard.

Keywords

Landslide hazard assessment • Geographic information systems • Landslide susceptibility maps • Remote sensing

Introduction

Landslide hazard mapping is an essential tool for developing mitigation strategies at local, regional, national, and global scales. The term hazard map has been applied to products ranging from landslide susceptibility maps to maps that indicate the probability of landslides. Determining and mapping landslide probability has proven to be challenging

due to scarcity of historical landslide data in many areas as well as philosophical questions about how such maps are to be validated against landslide inventory data, which often contain subjective uncertainties. Papers in this session (20 in total) addressed the session objectives to survey the range of methods and approaches currently in use for (1) assessing landslide susceptibility and probability and (2) for evaluating the assessments.

About one quarter of the papers presented landslide hazard or susceptibility mapping approaches based on deterministic methods but the majority presented approaches based on statistical or other approaches that compare landslide locations to possible causative factors (slope, geology, land use, and so on). These approaches include several variants that assign weights to the different factors based on landslide density (including a new approach based on the Poisson distribution), one application of logistic regression analysis, and two examples of machine learning techniques (Artificial Neural Networks, Support Vector Machines). Several papers used deterministic models based on limit-equilibrium slope stability concepts to assess landslide susceptibility and two

R.L. Baum (✉)
U.S. Geological Survey, Denver, CO 80225-0046, USA
e-mail: baum@usgs.gov

T. Miyagi
Department of Regional Management, Tohoku-Gakuin University,
Sendai, Japan

S. Lee
Korea Institute of Geoscience and Mineral Resources, Daejeon,
South Korea

O.M. Trofymchuk
Institute of Telecommunication and Global Information Space,
National Academy of Sciences of Ukraine, Kyiv, Ukraine

of them used Monte Carlo approaches to either improve the performance of the deterministic model or to map return periods of slope instability. Another paper used a deterministic method to assess landslide susceptibility followed by the use of statistical weighting to assign hazard levels.

In addition to presenting a variety of methods, most studies made use of widely available remotely-sensed data. Remote sensing data used in the studies were both aerial and satellite based. Remotely-sensed data provided high-resolution imagery for mapping landslides, land cover, and land use as well as high-resolution topography, and rainfall estimates.

Although most papers in this session present methods of assessing landslide susceptibility or qualitative hazard, a few explored methods for qualitatively assessing landslide risk.

These papers incorporated vulnerability into the analysis to illustrate qualitative risk assessment methods for case studies in Algeria, Malaysia, and Japan.

Authors of papers in this session used a variety of methods for evaluating model performance or accuracy of the resulting hazard or susceptibility map. Many of the papers used receiver operating characteristics (ROC) methods for assessing model performance. A few others assessed performance using success rate and prediction rate curves or by simply comparing model predictions to landslide density in the different hazard or susceptibility zones using a random subset of landslide locations not used in calibrating the model. In addition, a few papers compared results of two or more methods to determine which method gave the better prediction.



Landslide Hazard Evaluation Using Artificial Neural Networks and GIS

Alok Bhardwaj and G. Venkatachalam

Abstract

Lantau Island within the territory of Hong Kong has natural and undeveloped terrain (Dai et al. 2001), along with intense and frequent rainfall. It is thus a suitable area for preparation of a landslide susceptibility map of the area. The methods of using Landslide Susceptibility Values (LSV) and artificial neural networks (ANN) were applied in the GIS environment of ArcGIS 9.3 to prepare two landslide susceptibility maps of Lantau Island. The application of LSV and GIS to produce a landslide susceptibility map included the determination of LSV values of causative factors and calculation of a cumulative Landslide Susceptibility Index (LSI) for each pixel which was used to decide zones susceptible to landslides. The application of ANN required initially the preparation of input vectors from causative factors and output vectors of landslide susceptible zones by taking the LSV-produced map as the reference. The neural networks were trained and tested using the Neural Network Toolbox in MATLAB. The best network was obtained and applied further to predict the landslide susceptible zones for the whole study area and a landslide susceptibility map was prepared. These maps were compared with each other and with the landslide susceptibility map produced by Dai et al. (2001) using a logistic regression model. The landslide susceptibility map produced by applying ANN predicted more landslide susceptible regions with high and moderate susceptibility in the study area compared to the map produced using LSV. However, for some regions of the study area the LSV method performed better than the ANN method. Nevertheless, both methods produced quality maps and the performance of ANN was satisfactory, even with a small training dataset.

Keywords

GIS • ANN • LSV • Landslides • Susceptibility

Introduction

Landslides are downward and outward movement of slope materials such as rock debris and earth, under the influence of gravity (NDMA 2009). They usually occur on steep

slopes, in weathered mountainous areas, often with highly fractured rock masses.

To study the landslides of an area, various qualitative and quantitative methods have been proposed in the literature (Aleotti and Chowdury 1999). The qualitative approach incorporates field analysis techniques and/or overlaying of various index maps and applying conventional weight rating systems to arrive at a hazard and/or susceptibility map of the study area. The quantitative approach incorporates artificial intelligence techniques such as artificial neural networks (ANN) and fuzzy systems, statistical techniques and deterministic or probabilistic geotechnical approaches.

A. Bhardwaj (✉)
Department of Geography, FASS, NUS, Singapore, Singapore
e-mail: alokbhardwaj.iitb@gmail.com

G. Venkatachalam
Department of Civil Engineering, IIT Bombay, Powai, Mumbai, India
e-mail: gveccivil@gmail.com

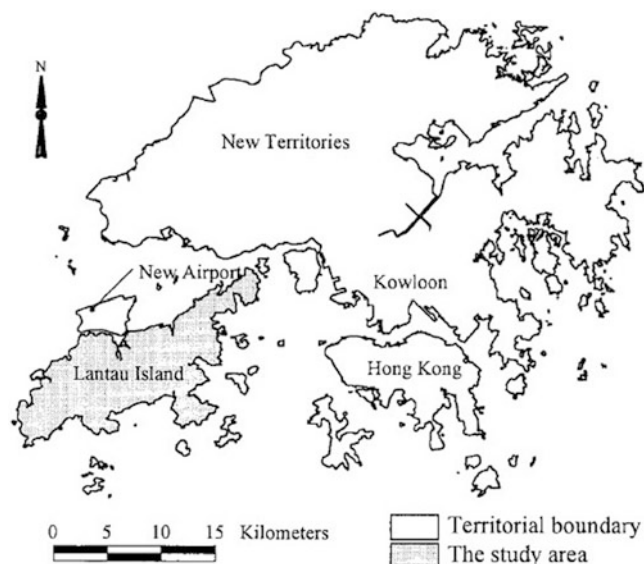


Fig. 1 Location map of Lantau Island (after Dai et al. 2001)

It may be argued that a highly random phenomenon like landslides may not be amenable to rigorous quantification as in artificial intelligence or other deterministic techniques. On the other hand, subjective techniques depend on the experience level of the investigator (Venkatachalam 2003). In this study, an attempt is made to compare ANN and Landslide Susceptibility Value (LSV) methods (Saha et al. 2002) by applying them to the study area of Lantau Island, near Hong Kong. Furthermore, the two maps are compared with a landslide susceptibility map produced by Dai et al. (2001) by applying a step-wise logistic regression model to the same study area.

Description of the Lantau Island Study Area

The study area is Lantau Island, situated in the south-western part of Hong Kong, as shown in Fig. 1. Lantau Island has been selected because data such as topographic maps, geology, vegetation and contour maps (refer Table 1) and the spatial distribution of landslides (Wong et al. 1998) are available. The rainfall is usually high due to the sub-tropical and monsoonal climate of the study area. Also, the terrain of the study area is steep (Dai et al. 2001). The elevations of the rugged terrain reaches to more than 900 m, and more than 70 % of the study area has slope angles greater than 15° . The geology mainly comprises volcanic rocks in the western part and granite rocks in the north-eastern part of the study area. The natural and undeveloped terrain of the island (Dai et al. 2001), along with intense and frequent rainfall, posed the motivation for preparing a landslide susceptibility map of

the area. The Geotechnical Engineering Office (GEO), Hong Kong, have published numerous reports over the past four decades documenting the occurrence of landslides, their causes, and possible solutions for the landslide hazard in various parts of Hong Kong. The present study includes information on the landslides that occurred during one particular rainstorm on November 4 and 5, 1993 (Dai et al. 2001; Wong et al. 1998).

Data Sources

Research papers were studied to obtain thematic maps at a scale 1:20,000 of the geology and vegetation and a contour map of Lantau Island during the year of 1993, as shown in Table 1. The maps of slope, aspect and elevation were produced using the contour map of the study area in ArcGIS 9.3 (Bhardwaj 2013). The information on the number of landslides that occurred in Lantau Island during November 1993 was obtained from Wong et al. (1998).

Preparation of Thematic Maps

Each topographic map (scale 1:20,000) of geology, vegetation and contours (refer Table 1) was geo-referenced in ArcGIS 9.3 and subsequently digitized and stored in vector format. While converting the vector to raster format, cell size was kept at $50\text{ m} \times 50\text{ m}$. The geology raster map (see Fig. 2) was produced with volcanics and granite as the two major rock types in the area. The contour map, boundary layer of Lantau Island and the elevation layer of prominent locations in Lantau Island, all in vector format, were used to generate a Triangulated Irregular_Network (TIN) surface of the study area using ArcGIS 9.3 (Bhardwaj 2013). The inbuilt function of converting TIN to a DEM in ArcGIS 9.3 was applied to obtain a DEM of the study area. The elevation raster map (see Fig. 2) was obtained by categorizing the DEM in 90 m intervals. The DEM was used to obtain a slope raster map (see Fig. 2) with an interval of 10° and an aspect raster map (Fig. 2) with an interval of 45° angles using inbuilt modules in ArcGIS 9.3. The vegetation raster map (refer Fig. 2) was produced using four categories: namely bareland, grassland, woodland and shrubs. Finally, the five raster causative factor maps were prepared: namely geology, elevation, slope, aspect and vegetation. All maps are displayed with the distribution of landslides on Lantau Island superimposed. Moreover, the actual area of Lantau Island is 147.16 km^2 (http://en.wikipedia.org/wiki/Lantau_Island). The area calculated after georeferencing was 146.18 km^2 , giving an error of 0.67 %, which is negligible (Bhardwaj 2013).

Table 1 Research papers used to obtain remote sensing data

| Name of authors | Name of research paper | Data obtained |
|------------------|---|---------------|
| S.W.C Au 1998 | Rain-induced slope instability in Hong Kong | Geology |
| Dai et al. 2001 | Assessment of landslide susceptibility on the natural terrain of Lantau Island, Hong Kong | Contour map |
| Zhou et al. 2002 | On the spatial relationship between landslides and causative factors Lantau Island, Hong Kong | Vegetation |

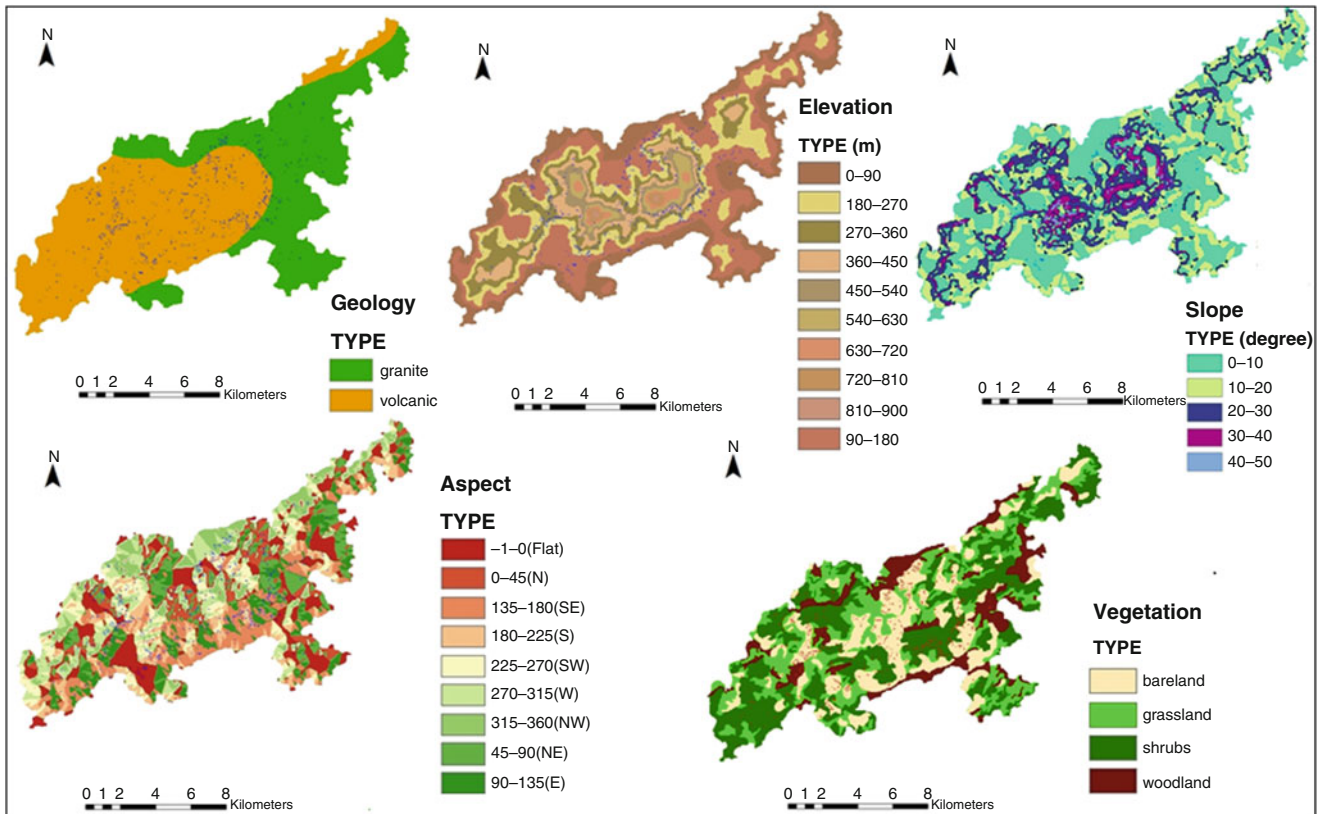


Fig. 2 Landslide causative factor maps derived using GIS

LSV and GIS Methods Used to Derive a Landslide Susceptibility Map

The Landslide Susceptibility Value (LSV) method (Saha et al. 2002) is a subjective method that measures the relative weights of causative factors in causing the landslides to occur. This method not only manages data in a convenient way but also there are no hidden rules involved while processing the remote sensing data, as in artificial neural networks.

Choice of Landslide Susceptibility Values

The subjectivity arises in deciding the LSV values (refer Table 2) of causative factors, as it is based on the experience

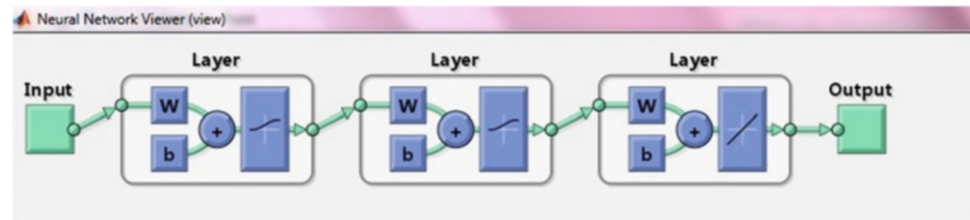
Table 2 Landslide susceptibility values (LSV) of causative factors

| Name of causative factor | LSV |
|--------------------------|-----|
| Slope | 35 |
| Vegetation | 25 |
| Elevation | 20 |
| Aspect | 10 |
| Geology | 10 |
| Total | 100 |

of the investigator and therefore the range of LSV values differ from one investigator to another.

The next step is the computation of a Landslide Susceptibility Index (LSI). LSI is a measure of the relative importance of the sub-categories of a causative factor or a theme. It apportions the LSV of a causative factor amongst its sub-categories in proportion to the past occurrence of landslides. For calculating the area of a sub-category on the ground, information regarding the dimension of a pixel and a count

Fig. 3 ANN network used for training, testing and validation



of pixels in that sub-category is required. Each pixel of the study area is $50 \text{ m} \times 50 \text{ m}$, i.e., 0.0025 km^2 , and the numbers of pixels of each sub-category are obtained from thematic maps of causative factors derived using ArcGIS 9.3. The product of the two quantities is calculated for each sub-category. The number of landslides occurring in each sub-category is also extracted using the thematic maps of causative factors with landslides superimposed. The queries were written in a query builder in ArcGIS 9.3 to find pixels having both landslides and a particular sub-category in a thematic map. The ratio of landslides to area of each subcategory of each causative factor is calculated. The division of landslides per area of a sub-category to the cumulative sum of landslides per area of each sub-category of a causative factor is calculated. The LSI is obtained by taking the product of the last factor and corresponding LSV of the causative factor (refer Eq. 1).

$$LSI = \frac{(Landslide/SqKm)\% \times LSV}{100} \quad (1)$$

ANN and GIS Methods for Deriving a Landslide Susceptibility Map

Artificial Neural Network (ANN) is one of the artificial intelligence techniques and is objective in nature (Arora et al. 2004; Chauhan et al. 2010).

Inputs, Outputs and Training

The class identities were assigned to sub-categories of causative factors and were stored in the attribute tables of causative factor maps in ArcGIS 9.3. This information was extracted in ASCII format from ArcGIS 9.3 and converted to an EXCEL file format and stored in MATLAB. Programs were developed in MATLAB (Bhardwaj 2013) such that the same pixel from each causative factor map had information about class identities of sub-categories in that pixel. This resembles the overlaying operation in GIS wherein five causative factor maps are overlaid and pixels of the resulting layer consist of the same information corresponding to the five factor maps.

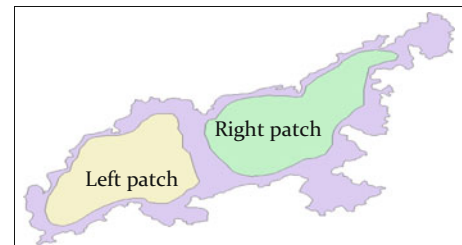


Fig. 4 Dataset selected for ANN

The input layer of ANN consists of five neurons corresponding to five causative factors, and the input data consisting of class identities of sub-categories was fed into ANN pixel-wise. The output layer of ANN has five neurons corresponding to five levels of landslide susceptibility. For each pixel in the input data, one neuron in the output layer is given a value of 1 and the rest are given 0, depending on a priori information on the landslide susceptible zone, obtained from the LSV-based landslide susceptibility map. Two hidden layers are considered in the ANN. The first hidden layer consists of 7–17 neurons and the second hidden layer consists of 7–18 neurons for each neuron of the first hidden layer. The network diagram is shown in Fig. 3. The network diagram depicts three layers. The first and second layers are hidden layers and third layer is the output layer. Each layer has W , which denotes weight on the connections, and b denotes bias weight.

For training, two patches of dataset were considered from the study area (Fig. 4). The first patch, designated as the left patch, had 5115 pixels. 70 % of those pixels, i.e., 3581 pixels were used for training, 15 % of the pixels, i.e., 767 pixels each were considered for the purpose of validation and testing. The data in these pixels were class identities of sub-categories of causative factors. Similarly, the second patch of dataset was designated as the right patch and had the same proportion of pixels as in the left patch. The parameters of the neural network were taken as 0.1 for learning rate, 5000 for epochs, 0.01 for error goal and 0.9 for momentum factor. The MATLAB Neural Network tool was used for training, validating and testing the data. The logarithmic sigmoid function was used as a transfer function in the two hidden layers and a gradient descent back-propagation algorithm was used to train the networks.

Table 3 Best network shown with training validation and testing accuracies

| Network Configuration | Right Patch (%) | | | Left patch (%) | | |
|---------------------------------|-----------------|------|------|----------------|------|------|
| | Tr | Va | Tt | Tr | Va | Tt |
| $5 \times 9 \times 14 \times 5$ | 70.9 | 72.5 | 72.4 | 62.6 | 63.8 | 60.2 |

Tr Training, *Va* Validation, *Tt* Testing

132 ANNs were trained on the left patch and tested on right patch data and vice-versa (Bhardwaj 2013). However, the networks trained on the left patch gave lower training, validation and testing accuracies when tested on the right patch. Finally, the network with a configuration of $5 \times 9 \times 14 \times 5$ was selected, which gave satisfactory accuracies with both data sets, as shown in Table 3.

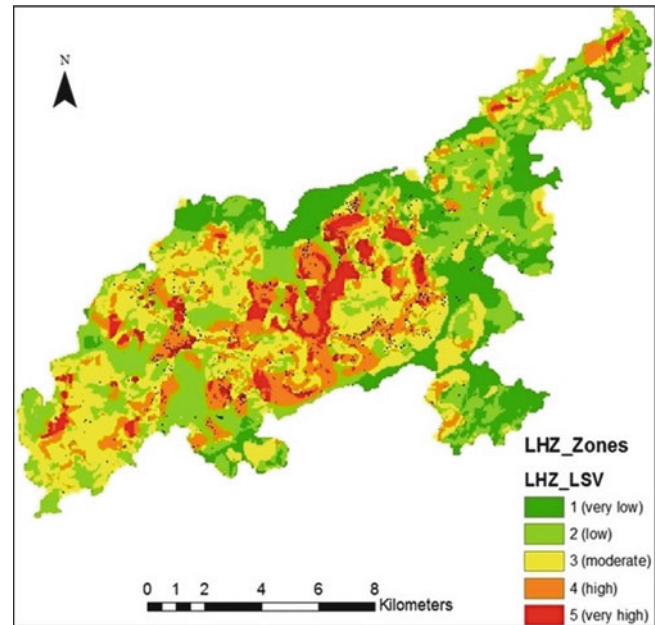
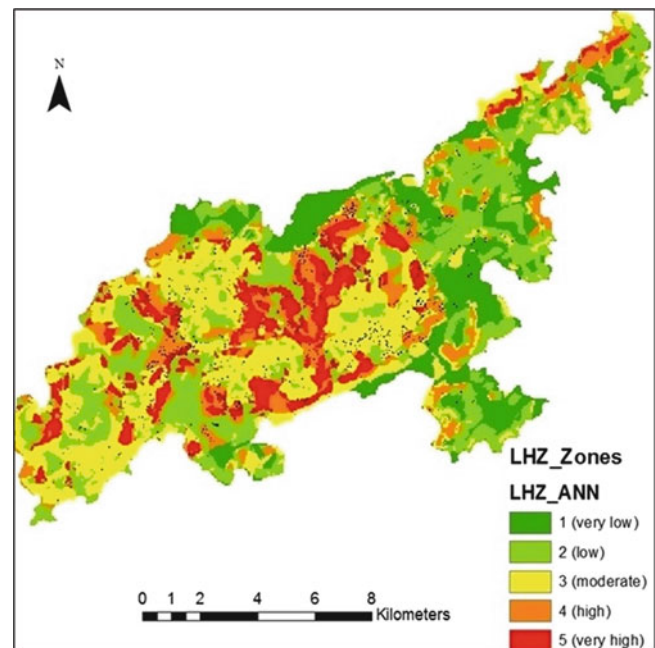
This network was used to predict landslide susceptible zones for the whole of Lantau Island. The output data from ANN was imported in ASCII format in ArcGIS 9.3 and was converted to a landslide susceptibility map. In addition, the accuracy of prediction of landslide susceptible zones was evaluated.

Results

LSI is considered as a measure of instability of the slope. The landslide susceptibility zones are based on the cumulative LSI of all the pixels for the whole study area. Taking LSI as a primary field in ArcGIS 9.3, the factor maps are overlaid to obtain the landslide susceptibility map, as shown in Fig. 5.

In the ANN method, the input data corresponding to the whole study area was prepared in the form of class identities. The output was predicted in the form of landslide susceptible zones ranging from 1 to 5, from the input data using the best network of $5 \times 9 \times 14 \times 5$ in MATLAB. The output data was imported in ASCII format in ArcGIS 9.3 and was converted to the landslide susceptibility map shown in Fig. 6. Further, the accuracy of prediction of landslide susceptible zones by the ANN method was calculated as 60.5% (Bhardwaj 2013).

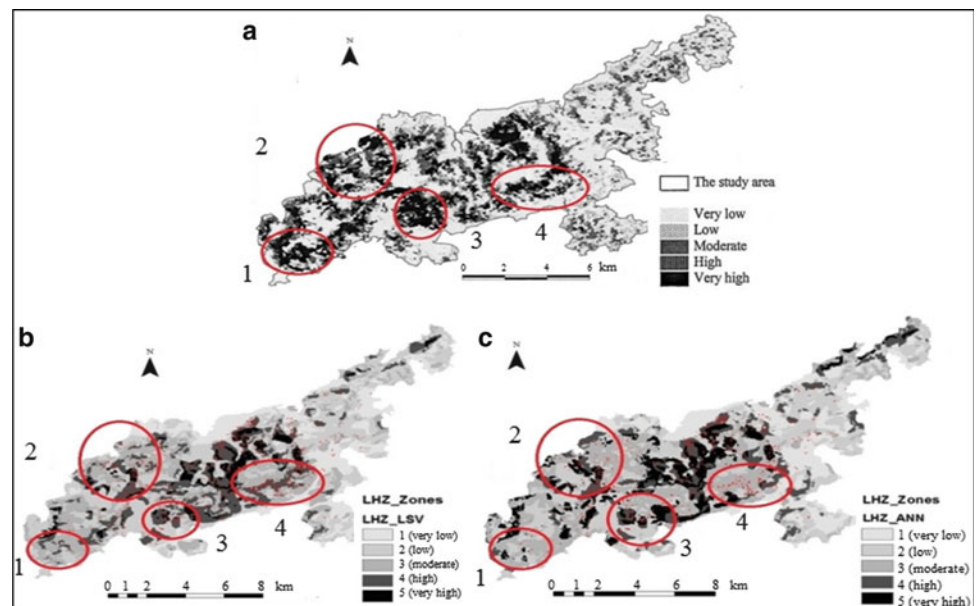
A total of 57527 pixels were predicted by the network to be landslide susceptible zones. Out of this, 6736 were of landslide susceptible zone 1, 11463 were of landslide susceptible zone 2, 9352 were of landslide susceptible zone 3, 4474 were of landslide susceptible zone 4 and 2778 were of landslide susceptible zone 5. All these values were summed and divided by 57527 to obtain the overall accuracy of prediction as 60.5%. The producer's accuracy and user's accuracy for the landslide susceptible zones varies from 44.6% to 84.1% and 40.9% to 69.6%, respectively.

**Fig. 5** Landslide Susceptibility map using LSV and GIS**Fig. 6** Landslide Susceptibility Map using ANN and GIS

Discussion

In Fig. 7, the three landslide susceptibility maps are compared. The color scheme of the two derived maps in this study is changed to meet the color scheme of the map found in the literature (Dai et al. 2001).

Fig. 7 (a) Landslide susceptibility map (after Dai et al. 2001); (b) Landslide hazard evaluation using Artificial Neural Networks and GIS (Bhardwaj 2013); (c) Landslide susceptibility map derived using ANN and GIS (Bhardwaj 2013)



Region 1 of the landslide susceptibility map derived by Dai et al. (2001) shows that it is highly susceptible to landslides, whereas it is shown as moderately susceptible to landslides in both of the derived maps because of the low density of landslides in the region.

Region 2 is very highly susceptible to landslides according to Dai et al. (2001), whereas in both of the derived maps it is highly and moderately susceptible to landslides because of a medium density of landslides.

Region 3 is highly susceptible to landslides as shown by Dai et al. (2001) because of the high density of landslides in the region. This is correctly predicted by ANN.

Region 4 is highly susceptible to landslides as shown by Dai et al. (2001) because of the high density of landslides in the region. This is correctly predicted by LSV method, while the ANN method predicts it as moderate.

The landslide susceptibility maps derived using ANN and LSV qualify to estimate the very high, high and moderate susceptible regions of Lantau Island when compared with Dai et al. (2001).

Scope of Future Work

New methods such as Support Vector Machines could be applied to arrive at more precise maps. The data used in the present study was for 1993. Recently acquired remote sensing data could yield better results, as the information will be updated.

Conclusions

The landslide susceptibility maps derived using ANN and LSV give better estimates of the very high, high and

moderate susceptible regions of Lantau Island when compared with Dai et al. (2001). The ANN-derived map more closely resembles the Dai et al. (2001) derived landslide susceptibility map. ANN estimates more highly susceptible regions when compared to the LSV-derived map. However, in region 4, LSV performs better than ANN. Also, the overall accuracy of prediction of landslide susceptible zones calculated for the ANN-derived landslide susceptibility map was 60.5 % and was not high, but still the results were satisfactory considering the small training dataset.

References

- Aleotti P, Chowdury R (1999) Landslide hazard assessment: summary review and new perspectives. *Bull Eng Geol Environ* 58(1):21–44
- Arora MK, Gupta ASD, Gupta RP (2004) An artificial neural network approach for landslide hazard zonation in the Bhagirathi (Ganga) Valley Himalayas. *Int J Remote Sens* 25(3):559–572, Taylor and Francis Group
- Au SWC (1998) Rain-induced slope instability in Hong Kong. *Eng Geol* 51:1–36
- Bhardwaj A (2013) Landslide hazard evaluation using Artificial Neural Network. M.Tech Thesis, Department Of Civil Engineering, IIT Bombay, India
- Chauhan S, Sharma M, Arora MK, Gupta NK (2010) Landslide susceptibility zonation through ratings derived from Artificial Neural Network. *Int J Appl Earth Observ Geoinform* 12:340–350
- Dai FC, Lee CF, Li J, Xu ZW (2001) Assessment of landslide susceptibility on the natural terrain of Lantau Island, Hong Kong. *Environ Geol* 40(3):381–391
- NDMA (2009) National disaster management guidelines: management of landslides and snow avalanches, National Disaster Management Authority, Government of India
- Saha AK, Gupta RP, Arora MK (2002) GIS-based landslide hazard zonation in the Bhagirathi (Ganga) valley, Himalayas. *Int J Remote Sens* 23(2):357–369

- Venkatachalam G (2003) Remote sensing and GIS techniques in landslide studies. Key note lecture, Proceedings of IGC-2003, IIT Roorkee, India
- Wong HN, Lam KC, Ho KKS (1998) Diagnostic report on the November 1993 natural terrain landslides on Lantau Island. GEO report no. 69. The Government of the Hong Kong Special Administrative Region
- Zhou CH, Lee CF, Li J, Xu ZW (2002) On the spatial relationship between landslides and causative factors on Lantau Island. Hong Kong Geomorphol 43:197–207



Landslide Susceptibility Mapping Using Remote Sensing and GIS: Nueva Colombia, Chiapas, Mexico.

Ixtlitzin Bravo-Carvajal, Ricardo J. Garnica-Peña, Luis C. López-Bravo, and Irasema Alcántara-Ayala

Abstract

In Mexico, landslides are one of the most important natural hazards as they cause considerable human and economic losses. Such phenomena are recurring due to the physical characteristics of the country, characterized by mountain ranges with steep slopes, diverse geology and intensive seasonal rains. The physical environment coupled with the impact of human activities, for example, deforestation and land use change, worsen the conditions of the landscape increasing landslide susceptibility.

The village of Nueva Colombia, situated in the municipality of Angel Albino Corzo in the state of Chiapas, is often affected by the occurrence of landslides. In 2005 and 2010, rainfall triggered landslides seriously damaged crops, destroyed housing and disrupted the main infrastructure.

Located in the southern sector of the state of Chiapas, the town is situated in the mountainous part of the Sierra Madre del Sur. Tropical weather of the area involves a strong rainy season, which combined with the mountainous conditions produces high level of susceptibility to landsliding. This situation is of great importance due to the vulnerability of the exposed population, particularly people of the village of Nueva Colombia.

A landslide inventory using SPOT images was used to generate a susceptibility map by implementing the weights of evidence method. This process relied on remote sensing techniques and geographic information systems (GIS). Preliminary results are presented in this paper.

Keywords

Landslides • Remote sensing • GIS • Weight of evidence

I. Bravo-Carvajal (✉)
Facultad de Filosofía y Letras, Universidad Nacional Autónoma de México, Ciudad Universitaria 04510, Mexico
e-mail: bleufonce.itzy@gmail.com

R.J. Garnica-Peña • I. Alcántara-Ayala
Instituto de Geografía, Universidad Nacional Autónoma de México, Circuito Exterior s/n., México, DF, Mexico
e-mail: garnica@igg.unam.mx; irasema@igg.unam.mx

L.C. López-Bravo
Posgrado en Ciencias de la Tierra, Universidad Nacional Autónoma de México, Circuito Exterior s/n, México, DF, Mexico
e-mail: clemosaurio@gmail.com

Introduction

Landslides are one of the most important phenomena in the generation of disasters. In Mexico there have been important events because of significant human and economic losses. Such phenomena are recurring due to the physical characteristics of the country, characterized by mountain ranges with steep slopes, diverse geology and intensive seasonal rains. The physical environments coupled with the impact of human activities worsen the conditions of the landscape increasing landslide susceptibility.

Some of the main events that have occurred in Mexico were in 1991, in the town of Meztlán, located in Hidalgo

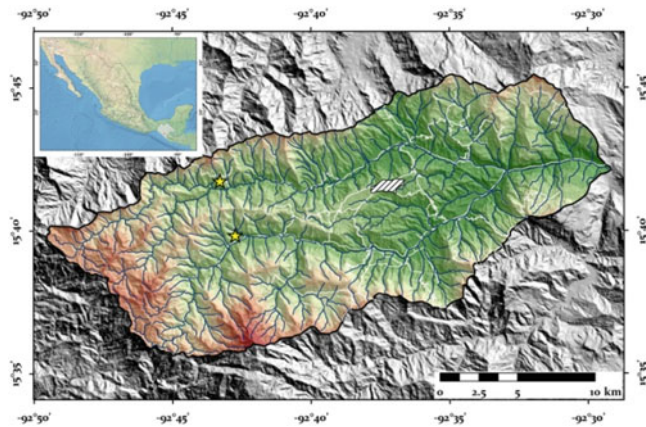


Fig. 1 Location of the basin and landslide inventory

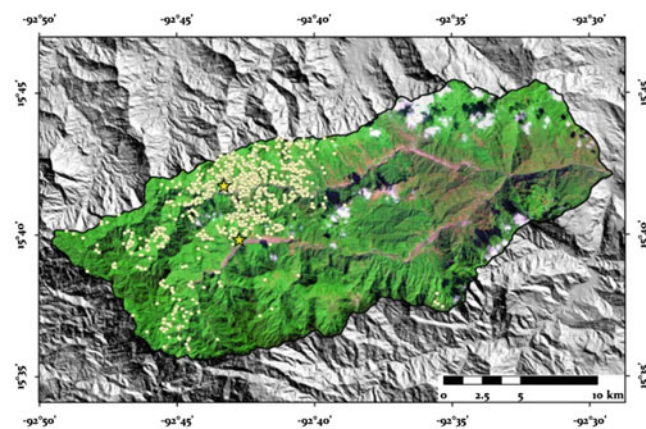


Fig. 2 Spatial distribution of landslides

province, a rotational landslide caused considerable damage to a sixteenth century monastery (Lugo et al. 1996). After Hurricane Pauline in 1997, floods and landslides affected Acapulco's Bay on the Pacific Coast. About 200 municipalities in the States of Puebla, Veracruz and Hidalgo were affected by flooding and mass movement processes that resulted from tropical depression from the Atlantic Ocean in October 1999 (Alcántara-Ayala 2004).

In particular, the State of Chiapas has suffered the worst consequences associated with floods and mass movement processes. These events have occurred in locations with high levels of poverty; a common characteristic in most parts of the State. One such event occurred in 2010, when very heavy rainfall induced a high number of mass movement processes (circa 700) in the mountainous region of Ángel Albino Corzo and Monte Cristo de Guerrero municipalities. For this reason, this study was carried out in the San Nicolas–Independencia River Basin that is located south of the town of Ángel Albino Corzo. Particularly within this basin the town of Nueva Colombia is located; this is the main place where a high number of landslides occurred (Figs. 1 and 2).



Fig. 3 Nueva Colombia Town

The aim of this paper was to generate a susceptibility map using an inventory of mass movements that occurred in October 2010 due to the influence of Hurricane Matthew in the locality of Nueva Colombia that is in Ángel Albino Corzo municipality. The weights of evidence method relied on remote sensing techniques and geographic information systems (GIS) were applied to produce the map.

Nueva Colombia, Chiapas

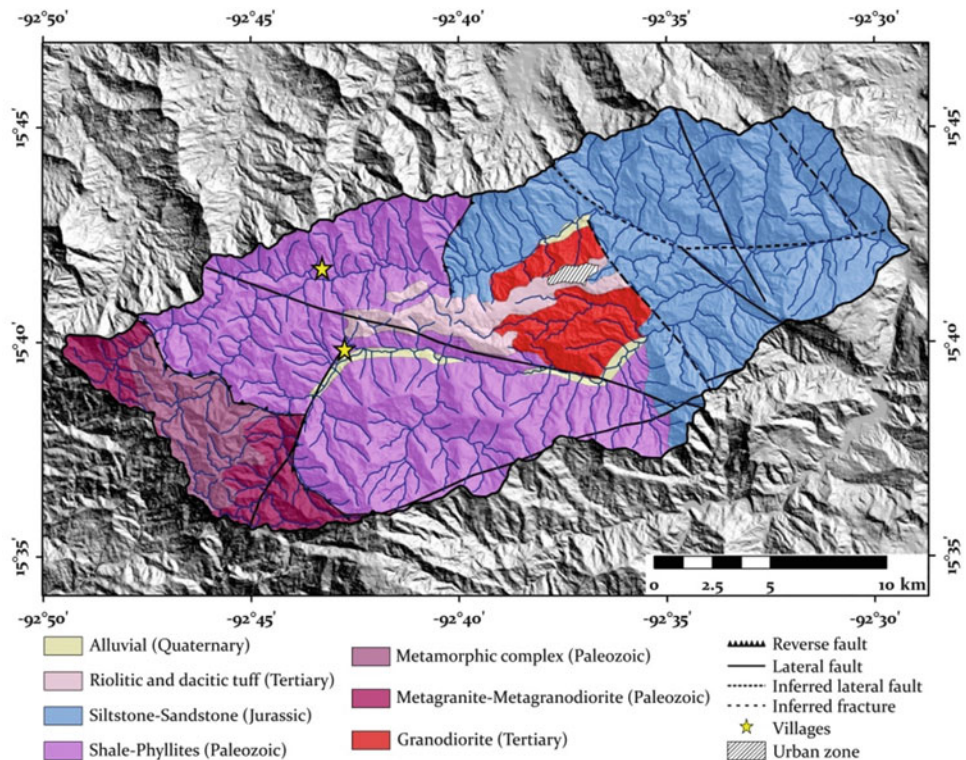
The San Nicolas-Independencia River Basin (watershed) is located in the State of Chiapas within the Sierra Madre de Chiapas. This Basin covers the localities of Nueva Colombia (Fig. 3), Montecristo, Plan de Ayutla and Nueva Independencia.

The Sierra Madre de Chiapas follows a NW-SE orientation. It is extended along the Pacific littoral of Chiapas and reaches the Tehuantepec Isthmus in the NW and the Guatemala's boundary in the SE. It is 360 km long and is formed by a series of stepped mountains ranging between 1,000 and 4,060 ma.s.l. The Tacaná Volcano is the highest elevation of the range, it has about 4,060 ma.s.l. (INEGI 2008). This unit comprises Miocene intrusive igneous rocks, most of which are foliated, strongly deformed and metamorphosed (Weber et al. 2007). It started its deformation during The Laramide Orogeny that formed mountainous series of anticlines and synclines. The last tectonic deformation was developed in the middle Miocene by NW compressional movements caused by clash of North American and Caribbean plates (Servicio Geológico Mexicano 2005).

Geology and Stratigraphy

According to the Huixtla Geological Chart D15-2 Chiapas (Servicio Geológico Mexicano 2005) from the Mexican Geological Service (Fig. 4), the West side of the basin is

Fig. 4 Geology of the study region



dominated by Paleozoic intrusive igneous rocks specifically metagranite and metagranodiorite (490–410 Ma), over these rocks lies a carboniferous layer of slate—phyllite rocks (325 Ma). In the part of Montecristo Town there are some intrusions of granodiorite and some areas with Cenozoic rhyolitic and dacitic tuff (24 Ma). Finally the West-Central part of the basin is formed by Jurassic siltstone and Sandstone (183.5 Ma) (Fig. 4).

Structural Geomorphology

The structural pattern of the study area is rather complex. In the western side of the basin is the N-S Paxtal Thrust that has an East direction and in the central part of the basin there is the N-S San Nicolas Thrust that has a West direction. The main dip direction of the rock layers in the basin is NE-SW.

In the south part of Montecristo Town there is the Nueva Lucha NW-SE left strike-slip fault. The La Pinada NW-SE left strike-slip fault is parallel to the Nueva Lucha Fault; perpendicularly is the Laguna Del Cofre NE-SW left strike-slip fault and in the East side of Montecristo Town is the Montecristo NW-SE left strike-slip fault. The majority of these structures are the limits of the contact between one kind of rock and another (Servicio Geológico Mexicano 2005). This basin is comprised within the physiographic region called “Sierra Madre de Chiapas”.

Materials and Methods

To carry out the analysis, it was decided to divide the research process into different phases. First, we collected the information about the region, by getting Geologic and topographic maps published by the Mexican Geological Service (SGM) and the Statistics, Geography and Informatics National Institute (INEGI). Moreover, information from newspapers, journals and rainfall data from the National Meteorological Service (SMN), was also collected. A database was developed including causal landslide factors, and a landslide susceptibility assessment was carried out.

SPOT images with resolution of 10 m (2005 and 2010) from the study area were used to produce the landslide inventory of the movements that occurred in October 25th 2005 and November 08th 2010; 830 landslides were identified and registered based on the identification of tone, texture, shape and size. All of them were concentrated in the NE portion of the basin. Most of the attributes of the landslides were collected from SPOT images, and the information provided by the SGM and the INEGI (Fig. 5).

ArcMap was used for information processing. In this software the corresponding layers/maps were produced for each causal factor. In total, there were 10 layers, however, the main layers that had more importance in this study were the geologic, the slope, elevation model, aspect, flow accumulation, flow length and distance to rivers (Table 1).

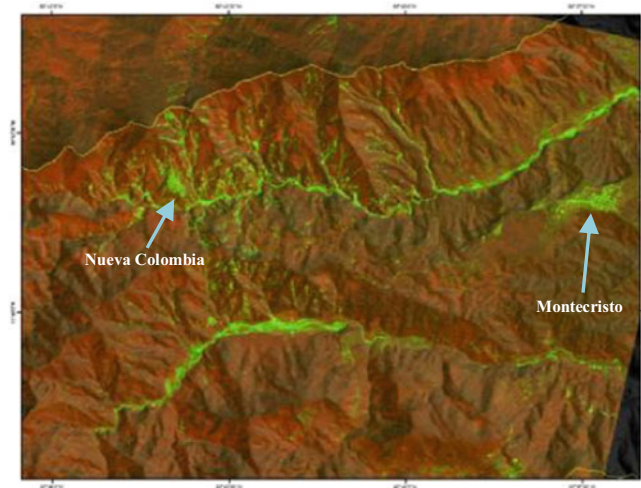


Fig. 5 SPOT image of the NW portion of the basin that shows the Nueva Colombia and Montecristo Towns and some of the landslides that occurred in November 2010

Table 1 Significance of the factors used in the analysis

| Data type | Factors | Significance |
|---------------|---------------------|---|
| Geologic | Geological map | Rock types |
| | Distance to faults | Seismic landslide triggering |
| | Elevation | Vegetation, potential energy and climate |
| Topographic | Slope | Overland and sub-surface flow velocity |
| | Aspect | Solar insolation, evapo-transpiration |
| | Slope shape | Converging, diverging flow, soil water content, flow acceleration, erosion, geomorphology |
| Water-related | FL | Runoff velocity and potential energy |
| | FA | Runoff velocity, runoff volume and potential energy |
| | Distance to rivers | Areas susceptible to river undercutting |
| Human induced | Highways and roads | Areas susceptible due to road cutting and vibration |
| Landslides | Landslide inventory | Spatial pattern of unstable slopes |

Acronyms: *FL* Flow length, *FA* Flow accumulation

The methodology used for the elaboration of the susceptibility map is called “Weights of evidence”. This method has a Bayesian approach in a long-linear form (Spiegelhalter 1986) and uses prior (unconditional) probability and posterior (conditional) probability. The prior probability is the probability of an event, determined by the same types of events that occurred in the past, for a given period of time. The prior probability can be modified using other sources of information or evidence. This revised information

of past events, based on new evidence, is called posterior probability (Regmi et al. 2010).

The total number of registered landslides was 830. To generate the susceptibility map 415 landslides were randomly selected and used, whereas the rest were used to check the effectiveness of the map.

The information contained on each layer was grouped in ranges for easy operation. Once we had the information organized in ranges, a reclassification was carried out where a value was assigned to each class or rank based on the importance or influence that it has for developing landslides. For example, in the slope layer, we generated seven ranges to which they were assigned a weight that ranges from 1 to 7 being the number 1 the minor value and 7 the most important, that is very high susceptibility on slopes greater than 45°.

For each layer the reclassification was made. Once the new layers were obtained and reclassified, the calculation of the weights of evidence and the test for conditional independence (Regmi et al. 2010; Hua Song et al. 2008; Lee and Choi 2004; Neuhäuser and Terhorst 2007) were carried out.

Once evidence weights were calculated the next step involved the preparation of the susceptibility map. As such, a weighted sum of the weights of different factors was also carried out in ArcGIS 9.3 by using spatial analyst tools. This version of the susceptibility map was compared with the landslides that were not subjected to the process.

Results and Conclusions

After having carried out the calculation of weights of evidence, it was observed that the factors that have more influence to increase the instability of the slopes are slope, shape, lithology, and the distance to faults. The rest of the causal factors were not representative for the purposes of this study.

In the case of the slope factor, it was observed that the susceptibility is evident in slopes ranging from 30° to more than 45°. This calculation is consistent with areas where landslides and mudflows occurred. Moreover, most of the landslides have a high probability to occur in the SE slopes of the mountains, presenting a convergent concave geometry, thus favoring the instability of the slopes too.

Landslides were triggered by intense rainfall. Mean annual precipitation and monthly average from 1954 to 2010 were useful to compare the rainfall events of 2005 and 2010. At the regional level, hurricane Mathew involved a greater contribution of rainfall and therefore, not surprisingly the occurrence of mudflows and landslides was higher (Figs. 6, 7 and 8). This causal factor was not included in the weights of evidence calculation because there are not enough rain gauges near the study area that can provide accurate information.

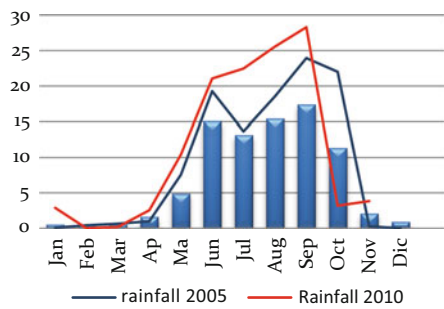


Fig. 6 Monthly mean precipitation (1954–2010)



Fig. 8 Some of the landslides that occurred near Nueva Colombia Town after hurricane Mathew in September 29th 2010

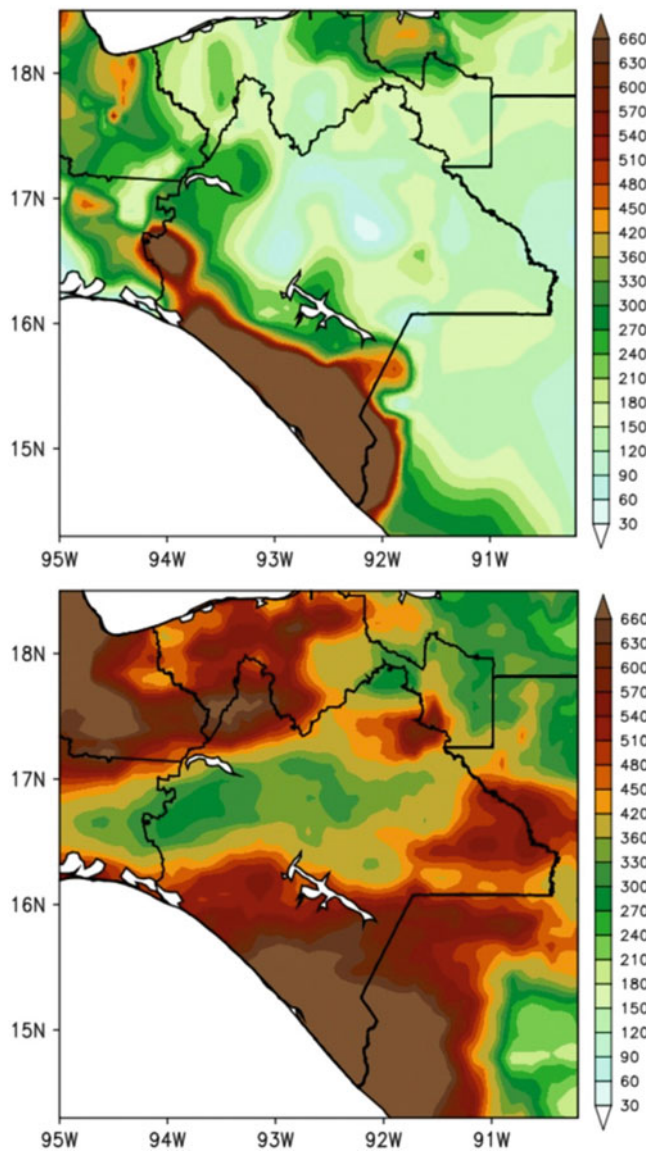


Fig. 7 Cumulative rainfall during October 2005 (upper) and September, 2010 (lower)

Results showed that geologic faults that are 3 km away from the identified landslide points are those that presented more influence in the instability. However, to get a solid argument to this regard, it would be necessary to carry out other kinds of assessment. Slate-phyllite was the lithological unit with a highest weight. That result coincides with areas on which the number of flows and landslides were considered as very high.

The generated landslide susceptibility map (Fig. 9) showed that the eastern part of the basin presents areas ranging from medium to high susceptibility. They correspond to the presence of sandstone and siltstone, which weathers and erodes easily in tropical regions due to moisture.

The central part of the basin ranges from low to medium susceptibility. This is primarily associated with the presence of igneous bedrock (granodiorites); slopes vary from 5° to 20° and in very few places are greater than 45°. The west side of the basin is the region with the highest level of susceptibility and is dominated by phyllites and slates. This type of lithology is easily eroded, and forms highly dissected slopes up to 45°. The presence of Acrisol soils is also an important factor; they result from altered acid rocks, and have high levels of clay. They are characteristic of tropical and warm climates and when wet, they absorb a large amount of water causing the increase of soil weight, which coupled with the high slope gradients, control stability.

According to the landslide classification used, there is a high index of landslide prediction (90 %) for the whole basin. The remaining 10 % represents low susceptibility (Fig. 10). This means that in 61 % of the surface of the basin susceptibility to landslides ranges from high to very high levels (Fig. 10).

Fig. 9 Landslide susceptibility map

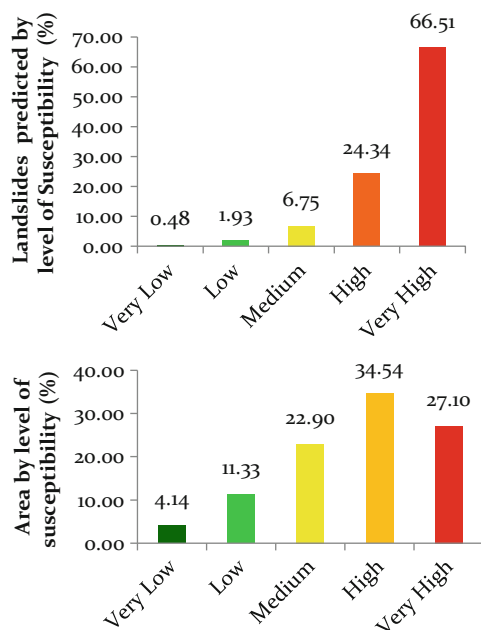
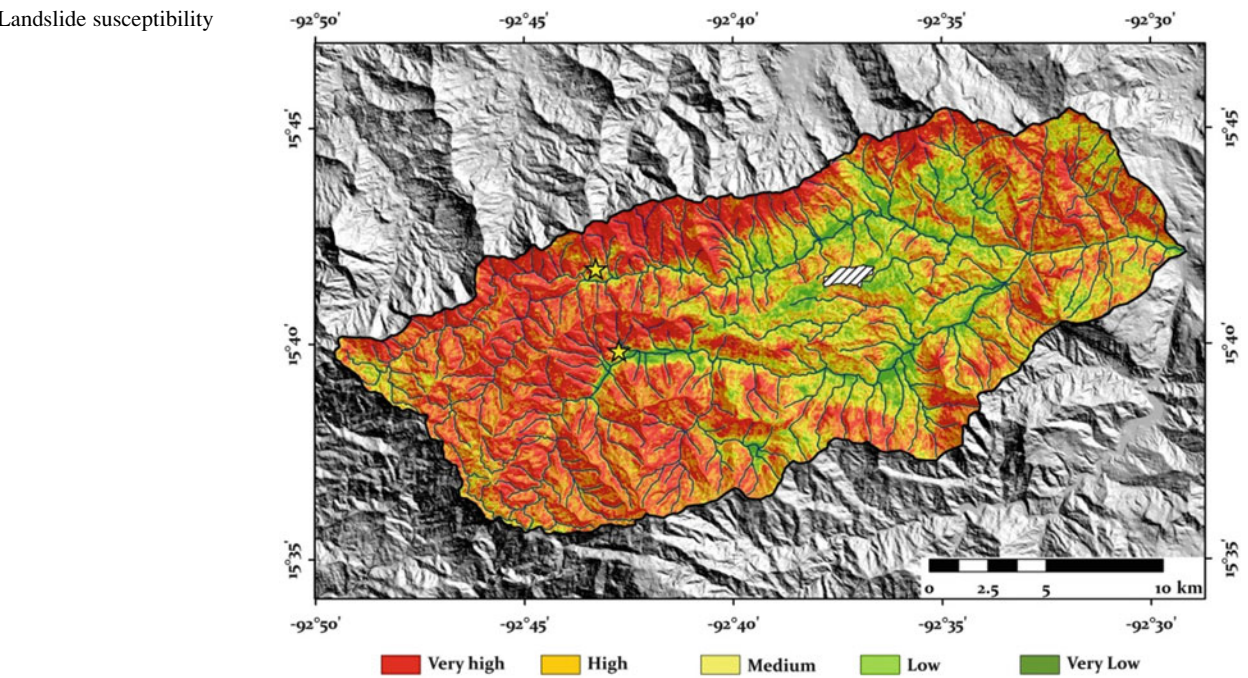


Fig. 10 Predicted landslides according to susceptibility levels (*upper*) and landslide susceptibility areas (*lower*)

The use of Geographic Information Systems and remote sensing techniques is significant to generate landslide susceptibility maps, specifically for regions with difficult access. Results presented here are preliminary.

Acknowledgments Authors are thankful to the Institute of Geography, UNAM for granting a scholarship to I. Bravo-Carvajal. Thanks are also due to CONACYT for financial support for the Project 156242: MISTLI.

References

- Alcántara-Ayala I (2004) Hazard assessment of rainfall-induced landsliding in Mexico. *Geomorphology* 61:19–40, Elsevier
- Hua Song R, Hiromu D, Kazutoki A, Usio K, Sumio M (2008) Modeling the potential distribution of shallow-seated landslides using the weights of evidence method and a logistic regression model: a case study of the Sabae Area. *Jpn Int J Sediment Res* 23:106–118
- Instituto Nacional de Estadística y Geografía (INEGI) (2008) Características Edafológicas, Fisiográficas, Climáticas e Hidrográficas de México, Manual en línea, Available at: http://www.inegi.org.mx/inegi/spc/doc/INTERNET/1GEOGRAFIA-DEMEXICO/MANUAL_CARAC_EDA_FIS_VS_ENERO_29_2008.pdf. date of reference: 2013-08-18
- Lee S, Choi J (2004) Landslide susceptibility mapping using GIS and the weight-of evidence model. *Int J Geogr Inform Sci* 18 (8):789–814
- Lugo J, García-Arizaga T, Zamorano J, Salas O (1996) Landslide in Meztiltan (State of Hidalgo), México – Causes and effects, stability. *Zeitschrift für Geomorphologie*, supplement band 103:323–343
- Neuhäuser B, Terhorst B (2007) Landslide susceptibility assessment using “weights-of-evidence” applied to a study area at the Jurassic escarpment (SW-Germany). *Geomorphology* 83:12–24
- Regmi N, Giardino J, Vitek J (2010) Modeling susceptibility to landslides using the weight of evidence approach: Western Colorado, USA. *Geomorphology* 115:172–187

- Servicio Geológico Mexicano (2005) Carta Geológico- Minera "Huixtla" D15-2 Chiapas, escala 1: 250 000, Mexico
- Spiegelhalter DJ (1986) A statistical view of uncertainty in expert systems. In: Gale W (ed) Artificial intelligence and statistics. Addison-Wesley, Reading, MA, pp 17–55
- Weber B, Iriondo A, Premo W, Hecht L, Schaaf P (2007) New insights into the history and origin of the southern Maya block, SE Mexico: U-Pb-SHRIMP zircon geochronology from metamorphic rocks of the Chiapas massif. *Int J Earth Sci* 96:253–269. doi:[10.1007/s00531-006-0093](https://doi.org/10.1007/s00531-006-0093)



Landslide Susceptibility Model Validation: A Routine Starting from Landslide Inventory to Susceptibility

Gulseren Dagdelenler, Hakan A. Nefeslioglu, and Candan Gokceoglu

Abstract

The main purpose of the present study is to evaluate the model validation stage of a routine landslide susceptibility mapping. For the purpose, model validation is assessed in three stages; (1) during model data production, (2) during model construction, and (3) during the production of model consequences; landslide susceptibility maps. As the results of these evaluations, it is revealed that training and testing data sets should be separated considering an appropriate separation ratio which is about 80 % and 20 % of the presence (1) data after completion of inventory studies. Correct classification percentages, error matrices, and the Kappa index are suggested to be considered for the training data sets during model construction. Additionally, again the correct classification percentage and the Root Mean Square Error (RMSE) should be considered during this stage for the testing data sets as well. In order to evaluate the spatial performance of the produced landslide susceptibility maps, the use of the Receiver Operating Characteristic (ROC) curves and the Area Under Curve (AUC) statistics is recommended. In the present study, the maximum Kappa index (k) value was calculated to be 0.459 for both the random sampling 1 (Rnd1) in the model 1 and for the random sampling 2 (Rnd2) in the model 2 during the model construction stage. The AUC values were calculated for these random samplings to be 0.781 and 0.790 respectively during the production of the model consequence stage in the study.

Keywords

Landslide susceptibility • Model • Testing • Training • Validation

Introduction

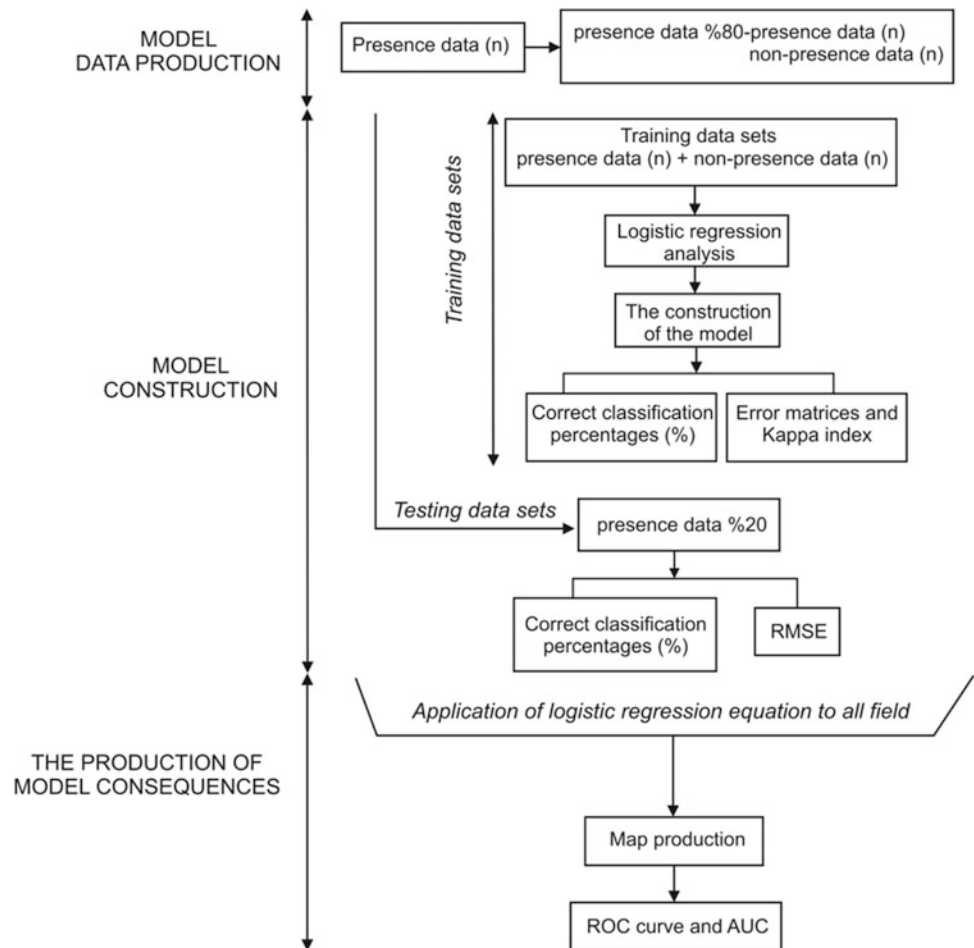
The model validation stage constitutes one of the most important issues in natural hazard modelling studies (Begueria 2006). Obviously, it could be considered that validation of landslide susceptibility models as well as the

maps should also be the most critical topic in landslide susceptibility researches. Although the model validation assessment has a very important role in modelling, many studies in literature do not give necessary importance to model validation, they just allow to be evaluated some basic validation statistics to assess the performance of the models. In landslide susceptibility mapping studies, the performance of the models are checked using different validation statistics by different researchers and that contributes to differences in terms of performance evaluation and the comparisons of the models according to these performances. The main purpose of this study is to represent a procedure for the assessment of the performance of landslide susceptibility mapping. The study proposes a flow chart which evaluates the current validation indices of the models in three stages:

G. Dagdelenler (✉) • C. Gokceoglu
Department of Geological Engineering, Hacettepe University, 06800
Beytepe, Ankara, Turkey
e-mail: gdagdelenler@gmail.com; candan.gokceoglu@gmail.com

H.A. Nefeslioglu
Polatli Technical Sciences Vocational School, Hacettepe University,
06900 Polatli, Ankara, Turkey
e-mail: haneleslioglu@hacettepe.edu.tr

Fig. 1 Procedure for the assessment of the performance of landslide susceptibility mapping



i) the model data production stage, ii) model construction stage and iii) the production of model consequences stage. For the purpose, the landslide susceptibility analyses performed by Dagdelenler (2013) in eastern part of Gallipoli Peninsula (Canakkale, Turkey) were evaluated.

Model Validation

As mentioned, the performance evaluations of the models were performed in three stages given in the flow chart in Fig. 1. These stages are described in detail below.

During Model Data Production

During the landslide susceptibility analyses performed by Dagdelenler (2013), a total of 10 variables (7 continuous and 3 categorical) were used as independent variables and also presence (1) and non-presence (0) data of mapped landslides was used as the dependent variable. 20 % of the presence (1) data was separated as testing and 80 % of the presence (1) data was separated as training data sets for the models

(Nefeslioglu et al. 2011, 2012; Oh and Pradhan 2011; San 2014). This process was carried out three times the models data sets Rnd1, Rnd2 and Rnd3 selected at random were obtained. For each random set, 80 % of the presence (1) data was separated and the training sets were generated by separating also 80 % of non-presence (0) data which equal to 80 % of presence (1) data in number. As it could be clearly realized, this stage constitutes the preparedness for further performance evaluations.

During Model Construction

The landslide susceptibility analyses were performed by applying the logistic regression technique by Dagdelenler (2013). As the results of the logistic regression analyses using training data sets, correct classification percentages (%), error matrices and validation statistics and Kappa index (k) values derived from the error matrices were determined. Correct classification percentages (%) calculated as the results of logistic regression analyses for the models were found to be acceptable and quite similar. They vary between 78 and 79 %.

Table 1 The presentation of true positive

| | | Observed | |
|-----------|--------------------------------|---------------------------|-------------------------------|
| | | X ₁ (presence) | X ₀ (non-presence) |
| Predicted | X' ₁ (presence) | a | b |
| | X' ₀ (non-presence) | c | d |

a; false positive, b; false negative, c; and true negatives, d in an error matrix

An error matrix shows the number of correctly estimated observations for positive and negative cases. In the error matrix in Table 1, the observed and predicted presence (1) and non-presence (0) data sets are represented by a letter (a, b, c, and d). Validation statistics (Table 2) and Kappa index (k) values derived from the error matrices of the models are calculated according to formulations of the validation statistics derived from the error matrix (Begueria 2006). The formula of the Kappa index (k) derived from error matrices was seen in (1,2, and 3). According to the Kappa index classification chart proposed by Landis and Koch (1977), Kappa index value for each model indicates that the model compatibility powers were moderately good.

$$P = \frac{a + d}{N} \quad (1)$$

$$Pe = \frac{(a + b)(a + c) + (c + d)(d + b)}{N^2} \quad (2)$$

$$k = \frac{P - Pe}{1 - Pe} \quad (3)$$

Where,

P = The proportion of observations in agreement; Pe = The proportion in agreement due to chance; k = Kappa index.

RMSE performance index and correct classification percentage (%) values were calculated by using the testing data

sets. Validation indices were derived from the error matrix and Kappa index values (threshold dependent) were specified by using the training data sets. Correct classification percentages for the first, second and third random sets of the landslide body sampling model were calculated as follows: 79.7 %, 80.5 % and 69.8 % respectively. The correct classification percentages for the landslide susceptibility models considered different buffer distances (d = 25 m, d = 50 m, d = 75 m and d = 100 m) in the seed cell samplings (Dagdelenler 2013) vary between 76.6 and 88.5 %. The seed cells obtained by the seed cell sampling strategy (Suzen and Doyuran 2004) are assumed to represent the pre-failure conditions of the landslides for the topographical parameters in particular. The calculated RMSE values for the Model 1 (landslide body samplings) are 0.398, 0.395 and 0.453 respectively and RMSE values vary between 0.334 and 0.422 for the Model 2 (seed cell samplings) at different buffer distances (d = 25 m, d = 50 m, d = 75 m, d = 100 m).

During the Production of Model Consequences

In the third stage of the performance evaluation procedure, the resultant landslide susceptibility maps were analysed by using the ROC curves and the area under ROC curves (AUC). The ROC curve evaluation and the AUC are threshold independent indices which are determined during the production of model consequences. Area under ROC curve value is used as a single threshold independent validation statistics (Begueria 2006). The An AUC value which is close to 1 means the performance of the model is good (Fawcett 2006). The ROC curves of the models were drawn and the AUC values were determined (Table 3). According to the results, the calculated AUC values for the models were found to be close to 1 and were very close to each other (Table 4). These results show that the performances of the models are quite acceptable.

Table 2 The formulation of the validation statistics derived from the error matrix (Begueria 2006)

| Validation statistics | The formulation | Description |
|-------------------------------|-----------------------------|--|
| Efficiency | (a + d)/N | Ratio of correctly classified observations |
| Incorrect classification rate | (b + c)/N | Rate of correct classified observations |
| Odds ratio | (a + d)/(b + c) | Ratio of correct and incorrect classification of cases |
| Positive predictive value | a/(a + b) | Rate of true positives of the total positive estimation values |
| Negative predictive value | d/(c + d) | Rate of true negatives of the total negative estimation values |
| Sensitivity | a/(a + c) | Correctly estimated positive cases ratio |
| Specificity | d/(b + d) | Correctly estimated negative cases ratio |
| False positive rate | b/(b + d) | False positives ratio of total negatives observations |
| False negative rate | c/(a + c) | False negatives ratio of total negative observations |
| Likelihood ratio | Sensitivity/(1-specificity) | The ratio between true positives and false negatives |

Table 3 Validation statistical values derived from error matrices and Kappa index (k) for both displacement + accumulation area (Model 1) and seed cell (Model 2) sampling model

| Model | Efficiency value | Incorrect classification rate | Odds ratio | Positive predictive value | Negative predictive value | Sensitivity | Specificity | False-positive rate | False-negative rate | Likelihood ratio | Kappa index (k) |
|-----------|------------------|-------------------------------|------------|---------------------------|---------------------------|-------------|-------------|---------------------|---------------------|------------------|-----------------|
| Model 1 | | | | | | | | | | | |
| Rnd1 | 0.728 | 0.272 | 2.683 | 0.786 | 0.670 | 0.705 | 0.758 | 0.242 | 0.295 | 2.917 | 0.456 |
| Rnd2 | 0.727 | 0.273 | 2.665 | 0.786 | 0.668 | 0.703 | 0.757 | 0.243 | 0.297 | 2.900 | 0.454 |
| Rnd3 | 0.730 | 0.270 | 2.700 | 0.790 | 0.670 | 0.705 | 0.761 | 0.239 | 0.295 | 2.953 | 0.459 |
| Model 2 | | | | | | | | | | | |
| Rnd1 | | | | | | | | | | | |
| d = 25 m | 0.716 | 0.284 | 2.520 | 0.782 | 0.650 | 0.691 | 0.741 | 0.251 | 0.309 | 2.750 | 0.431 |
| d = 50 m | 0.721 | 0.279 | 2.580 | 0.783 | 0.658 | 0.696 | 0.752 | 0.248 | 0.304 | 2.811 | 0.441 |
| d = 75 m | 0.722 | 0.278 | 2.600 | 0.791 | 0.654 | 0.695 | 0.757 | 0.243 | 0.305 | 2.868 | 0.444 |
| d = 100 m | 0.720 | 0.280 | 2.578 | 0.783 | 0.658 | 0.696 | 0.752 | 0.248 | 0.304 | 2.804 | 0.440 |
| Rnd2 | | | | | | | | | | | |
| d = 25 m | 0.730 | 0.270 | 2.703 | 0.799 | 0.661 | 0.702 | 0.767 | 0.233 | 0.298 | 3.010 | 0.459 |
| d = 50 m | 0.724 | 0.276 | 2.626 | 0.790 | 0.659 | 0.698 | 0.758 | 0.242 | 0.302 | 2.886 | 0.448 |
| d = 75 m | 0.717 | 0.283 | 2.538 | 0.782 | 0.653 | 0.692 | 0.750 | 0.250 | 0.308 | 2.766 | 0.434 |
| d = 100 m | 0.719 | 0.281 | 2.562 | 0.783 | 0.656 | 0.695 | 0.751 | 0.249 | 0.305 | 2.791 | 0.438 |
| Rnd3 | | | | | | | | | | | |
| d = 25 m | 0.720 | 0.280 | 2.575 | 0.793 | 0.647 | 0.692 | 0.758 | 0.242 | 0.308 | 2.859 | 0.440 |
| d = 50 m | 0.720 | 0.280 | 2.575 | 0.785 | 0.656 | 0.695 | 0.753 | 0.247 | 0.305 | 2.811 | 0.440 |
| d = 75 m | 0.721 | 0.279 | 2.583 | 0.785 | 0.657 | 0.696 | 0.753 | 0.247 | 0.304 | 2.821 | 0.441 |
| d = 100 m | 0.718 | 0.282 | 2.551 | 0.781 | 0.656 | 0.694 | 0.749 | 0.251 | 0.306 | 2.771 | 0.436 |

Table 4 Area under ROC curve (AUC) values for the models

| | | Area under curve (AUC) | | |
|---------|-----------|------------------------|-------|-------|
| | | Rnd1 | Rnd2 | Rnd3 |
| Model 1 | | 0.801 | 0.802 | 0.781 |
| Model 2 | d = 25 m | 0.785 | 0.790 | 0.789 |
| | d = 50 m | 0.790 | 0.792 | 0.792 |
| | d = 75 m | 0.787 | 0.788 | 0.789 |
| | d = 100 m | 0.783 | 0.785 | 0.786 |

Results and Conclusions

The validation indices are evaluated in three stages such as during model data production, model construction, and production of model consequences. In addition, a generalized flow chart for the performance evaluation of the landslide susceptibility models is proposed. According to the flow chart, it could be clearly realized that which validation indices are calculated from which data set and in which stage of the model. In recent huge landslide susceptibility literature, there is vagueness about the validation of the models constructed. This uncertainty starts from the model data production and goes up to production of the model consequences. The common way applied for validation is the evaluation of the ROC curves for whole study area (Ayalew and Yamagishi 2005; Mathew et al. 2007; Pradhan 2010). However, the performance evaluation of the model construction stage is commonly ignored particularly in the studies in which the bivariate statistics, artificial intelligence and data mining techniques are applied (Saito et al. 2009; Yilmaz 2009; Oh and Pradhan 2011; Akgun et al. 2012; Bui and Pradhan 2012; Conforti et al. 2014). Obviously, in order to apply this stage, a pre-processing stage including data production for further evaluations is necessary. The performance evaluation of the model construction stage was suggested to be a separate routine step in model validation for landslide susceptibility analyses in the proposed flow chart. It is commonly desired from a landslide susceptibility model to provide both high prediction capacity for the constructed model and high generalization capacity for the application results in whole study area (Can et al. 2005). Assuming that if all probabilities are calculated to be 1 for whole study area, in this case the spatial performance of the model is found to be 100 %. However, the resultant landslide susceptibility texture is irrational and it could be assumed that there is no generalization capacity for the model for this situation. The probabilities will also be calculated to be 1 for whole areas without landslides so that the calculated AUC values will also be low. In other words, the model prediction capacity is maximum while the generalization capacity is minimum. Hence, it could be clearly realized that the validation indices for the model construction and production

model consequences should be evaluated separately. Therefore, it could be concluded that the proposed methodology in this study enables controlling both prediction and generalization capacities for any landslide susceptibility evaluations appropriately.

According to the results obtained from the sample analyses of the models given in this study, the validation indices are quite close and this also shows that model predictive and generalization capacities could be evaluated to be acceptable.

References

- Akgun A, Sezer EA, Nefeslioglu HA, Gokceoglu C, Pradhan B (2012) An easy to use MATLAB program (MamLand) for the assessment of landslide susceptibility using a Mamdani fuzzy algorithm. *Comput Geosci* 38:23–34
- Ayalew L, Yamagishi H (2005) The application of GIS-based logistic regression for landslide susceptibility mapping in the Kakuda-Yahiko Mountains, Central Japan. *Geomorphology* 65:15–31
- Beguieria S (2006) Validation and evaluation of predictive models in hazard assessment and risk management. *Nat Hazards* 37:315–329
- Bui D, Pradhan B (2012) Landslide susceptibility mapping at Hoa Binh province (Vietnam) using an adaptive neuro-fuzzy inference system and GIS. *Comput Geosci* 45:199–211
- Can T, Nefeslioglu HA, Gokceoglu C, Sonmez H, Duman TY (2005) Susceptibility assessment of shallow earthflows triggered by heavy rainfall at three subcatchments by logistic regression analyses. *Geomorphology* 72:250–271
- Conforti M, Pascale S, Robustelli G, Sdao F (2014) Evaluation of prediction capability of the artificial neural networks for mapping landslide susceptibility in the Turbolo River catchment (northern Calabria, Italy). *Catena* 113:236–250
- Dagdelenler G (2013) Assessment of sampling and validation strategies in production of landslide susceptibility Maps (Eastern Part of Gallipoli Peninsula). Hacettepe University, Institute of Science, Ankara, Turkey, 186 p. (unpublished)
- Fawcett T (2006) An introduction to ROC analysis. *Pattern Recogn Lett* 27(8):861–874
- Landis JR, Koch GG (1977) The measurement of observer agreement for categorical data. *Biometrics* 33:159–174
- Mathew J, Jha VK, Rawat GS (2007) Application of binary logistic regression analysis and its validation for landslide susceptibility mapping in part of Garhwal Himalaya, India. *Int J Remote Sens* 28(10):2257–2275
- Nefeslioglu HA, Gokceoglu C, Sonmez H, Gorum T (2011) Medium-scale hazard mapping for shallow landslide initiation: the Buyukkoy catchment area (Cayeli, Rize, Turkey). *Landslides* 8:459–483

- Nefeslioglu HA, San BT, Gokceoglu C, Duman TY (2012) An assessment on the use of Terra ASTER L3A data in landslide susceptibility mapping. *Int J Appl Earth Observ Geoinform* 14:40–60
- Oh HJ, Pradhan B (2011) Application of a neura-fuzzy model to landslide-susceptibility mapping for shallow landslides in a tropical hilly area. *Comput Geosci* 37:1264–1276
- Pradhan B (2010) Remote sensing and GIS-based landslide hazard analysis and cross-validation using multivariate logistic regression model on three test areas in Malaysia. *Adv Space Res* 45:1244–1256
- Saito H, Nakayama D, Matsuyama H (2009) Comparison of landslide susceptibility based on a decision-tree model and actual landslide occurrence: The Akaishi Mountains, Japan. *Geomorphology* 109:108–121
- San BT (2014) An evaluation of SVM using polygon-based random sampling in landslide susceptibility mapping: The Candir catchment area (western Antalya, Turkey). *Int J Appl Earth Observ Geoinform* 26:399–412
- Suzen ML, Doyuran V (2004) Data driven bivariate landslide susceptibility assessment using geographical information systems: a method and application to Asarsuyu catchment, Turkey. *Eng Geol* 71:303–321
- Yilmaz I (2009) Landslide susceptibility mapping using frequency ratio, logistic regression, artificial neural networks and their comparison: A case study from Kat landslides (Tokat-Turkey). *Comput Geosci* 35:1125–1138



GIS-Based Landslide Susceptibility Mapping Using a Certainty Factor Model and Its Validation in the Chuetsu Area, Central Japan

Jie Dou, Takashi Oguchi, Yuichi S. Hayakawa, Shoichiro Uchiyama, Hitoshi Saito, and Uttam Paudel

Abstract

The principal aim of this study is to assess the landslide susceptibility in the Chuetsu area, Niigata Prefecture, Central Japan, using a certainty factor model in a GIS environment. The landslide inventory data used in this study were obtained from the National Research Institute for Earth Science and Disaster Prevention (NIED). The data were divided into two groups: one for training the model and the other for its validation. Seven relative factors, elevation, slope angle, slope aspect, density of geological boundary, density of drainage network, plan curvature, and lithology were utilized for this susceptibility analysis. Based on the aforementioned correlative factors, a landslide susceptibility map was produced and then verified using receiver operating characteristics (ROC). The value of area under the ROC curve (*AUC*) of the constructed CF model is 0.82. A model with such a high *AUC* value is considered good and therefore acceptable in predicting landslides. The landslide susceptibility map prepared in this study can hence be used to mitigate risks associated with landslides in the study area.

Keywords

Landslide susceptibility mapping • GIS • Certainty factor • *AUC* • LiDAR DEM

J. Dou (✉) • U. Paudel

Department of Natural Environmental Studies, Graduate School of Frontier Science, The University of Tokyo, 5-1-5 Kashiwanoha, Kashiwa, Chiba 277-8568, Japan
e-mail: doujie@csis.u-tokyo.ac.jp; uttam@csis.u-tokyo.ac.jp

T. Oguchi • Y. S. Hayakawa

Center for Spatial Information Science, The University of Tokyo, 5-1-5 Kashiwanoha, Kashiwa, Chiba 277-8568, Japan
e-mail: oguchi@csis.u-tokyo.ac.jp; hayakawa@csis.u-tokyo.ac.jp

S. Uchiyama

National Research Institute for Earth Science and Disaster Prevention, 3-1, Tennodai, Tsukuba, Ibaraki 305-0006, Japan
e-mail: uchiyama@bosai.go.jp

H. Saito

College of Economics, Kanto Gakuin University, 1-50-1, Mutsuura-higashi, Kanazawa-ku, Yokohama 236-8501, Japan
e-mail: hsaito@kanto-gakuin.ac.jp

Introduction

Landsliding is one of the natural hazards affecting many parts of the world, especially the mountainous areas. The annual loss of property caused by landslides alone is far greater than that caused by any other single type of natural disaster, such as earthquakes, hurricanes, windstorms and floods (Turner and Schuster 1996; Garcia-Rodriguez et al. 2008). As indicated by Turner and Schuster (1996), this trend will possibly aggravate in the future corresponding to the processes of urbanization, economic development, and increasing regional precipitation in landslide-prone areas because of climate change. It is hence essential to predict landslides so as to mitigate the potential risk.

Landslide susceptibility mapping (LSM) is a primary step to reduce the risk. This involves not only finding where the risk of landslide-related problems is spatially located, but also quantitatively and qualitatively assessing the significance of any such hazards and associated risk factors.

Additionally, LSM could also help to describe the known landslides, make emergency decisions, avoid and mitigate future landslide hazards (Guzzetti et al. 2006). Recently, with the developing accuracy in prediction and positive implications, academic research on regional LSM is gaining momentum.

In recent years, many models for the prediction of landslides have been developed (Chigira et al. 2006; Yilmaz 2009; Dou et al. 2009, 2010; Avinash and Ashamanjari 2010; Devkota et al. 2012). Statistical and probabilistic techniques use multi-bivariate methodology to analyze the spatial data and landslide inventory to predict landslides (Kanungo et al. 2011). Many of these models are complex and time-consuming to build. Here, we have used simpler statistical and probabilistic techniques for the evaluation of landslide susceptibility and its mapping.

This paper investigates the accuracy of LSM using a certainty factor (CF) model as well as the effect of various landslide-conditioning factors. Modeling involves extraction of seven causative factors: elevation, slope angle, slope aspect, density of geological boundary, density of drainage network, plan curvature and lithology with the help of GIS. A landslide susceptibility map was the outcome of the model. We also used the receiver operating characteristic (ROC) method to verify the accuracy of the model.

Study Area and Data

Study Area

The study area is located in a mountainous region of Niigata Prefecture, Japan (Fig. 1). The elevation ranges from 22 m to 734 m with a mean of 206 m. Annual precipitation is around 2,000 mm, mostly delivered by typhoons in the form of heavy snow. The area is underlain by sedimentary and metamorphic rocks from the Paleocene to the Quaternary period (Takeuchi and Yanagisawa 2004). Land-use in the study area is characterized by settlements, small-scale agro-industrial activities such as paddy farming, and deciduous broad-leaved beach forests. According to Oguchi (1996), shallow failures and erosion into bedrock play vital roles in shaping landscapes in mountains of Japan. This area suffered a big earthquake of magnitude 6.8 on October 23, 2004 that triggered many sediment-related disasters, including numerous slope failures and landslides.

Data

Guzzetti et al. (1999) note that landslides in the past are vital to predict those in the future. Therefore, it is important to maintain a landslide inventory. The landslide inventory data for this study

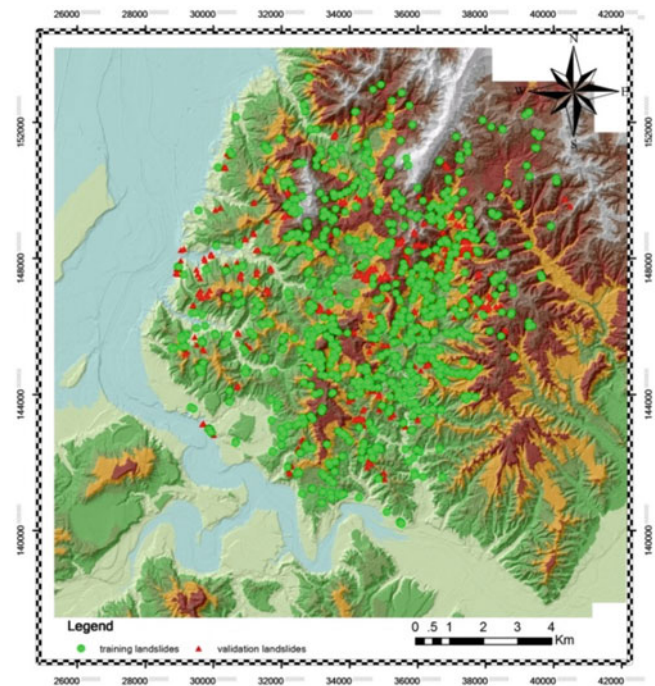


Fig. 1 Location map of landslides in the study area, including the training and testing data

was provided by the National Research Institute for Earth Science and Disaster Prevention (NIED), Japan (Fig. 1). The inventory represented landslides as polygons; the centroids of which were used as landslide points in this study.

Slope angle, aspect, lithology and elevation are the most important parameters affecting landslide occurrences (Caniani et al. 2007). Seven landslide-conditioning parameters were selected in this study: (1) elevation, (2) slope angle, (3) slope aspect, (4) lithology, (5) density of geologic boundaries, (6) density of drainage network, (7) plan curvature. These selections are based on literature (e.g., Guzzetti et al. 2006; Caniani et al. 2007) that discussed spatial relationships between landslide occurrence and conditioning parameters. Slope aspect, slope angle, density of drainage network, and plan curvature were extracted from a 2-m LiDAR DEM obtained from Geospatial Information Authority of Japan (GSI) in 2005. The geology map used in this study was prepared by the Geological Survey of Japan (GSJ).

Methodology

Certainty Factor Model

The certainty factor (CF) model is widely applied in the field of expert system shells, rule-based systems, and landslides (e.g., Shortliffe 1976; Kanungo et al. 2011). The CF approach is one of the probable favorability functions (FF)

to deal with the problem of integrating heterogeneous data (Chung and Fabbri 1993). The general theory function is given by the following equation:

$$CF = \begin{cases} \frac{PP_a - PP_s}{PP_a * (1 - PP_s)} & \text{if } PP_a \geq PP_s \\ \frac{PP_a - PP_s}{PP_s * (1 - PP_a)} & \text{if } PP_a < PP_s \end{cases} \quad (1)$$

where PP_a is the conditional probability of having a number of landslide events occurring in class a and PP_s is the prior probability of having a total number of landslide events in the study area. PP_s for this study area was found to be 0.26.

The CF value is calculated for each class layer using (1). These layers are then integrated pairwise based upon the combination rule given in the following equation (Binaghi et al. 1998):

$$Z = \begin{cases} CF1 + CF2 - CF1 * CF2 & CF1, CF2 \geq 0 \\ CF1 + CF2 + CF1 * CF2 & CF1, CF2 < 0 \\ \frac{CF1 + CF2}{1 - \min(|CF1|, |CF2|)} & CF1, CF2, \text{opposite signs} \end{cases} \quad (2)$$

Equation (2) is also called the parallel-combination function. The pairwise combination is operated until all the CF layers are brought together to produce the landslide susceptibility index (LSI) defined as the sum of the ratio calculated for each relative factor. LSI gives a measure of certainty in predicting landslides.

The CF value ranges from -1 to 1 . Positive values imply an increasing certainty in landslide occurrence, whereas negative values impart a decrease in the certainty. A value close to 0 indicates that the prior probability is very similar to the conditional probability and it is therefore difficult to determine the certainty of landslides occurrence (Pourghasemi et al. 2012).

In the present study, the LSI was classified into six susceptibility classes as shown in Table 1 in order to simplify the results and obtain a landslide susceptibility map. The verification of the LSM was done using receiver-operating characteristics (ROC). The area under the ROC curve (AUC) was utilized as a comparative means to judge the model's performance.

Results and Discussion

Resultant CF Model

The interrelationship between the spatial location of the landslides and landslide conditioning factors was analyzed in GIS (Table 2). The landslide susceptibility map obtained

Table 1 LSI classification according to the range of CF values (Binaghi et al. 1998)

| Code | Range | Description |
|------|--------------|--------------------------|
| 1 | $-1.0-0.09$ | Extremely low certainty |
| 2 | $-0.09-0.09$ | Uncertainty |
| 3 | $0.09-0.2$ | Low certainty |
| 4 | $0.2-0.5$ | Medium certainty |
| 5 | $0.5-0.8$ | High certainty |
| 6 | $0.8-1.0$ | Extremely high certainty |

by the certainty factor model is presented as Fig. 2. In Table 2, the CF values of four elevation classes (131–190, 190–246, 246–301, and 301–357 m) show high positive values, and the percentage of total landslide occurrence in the elevation classes are 19.96 %, 23.37 %, 19.35 % and 15.23 %, respectively. The CF values are greater than 0.5 for the altitude from 190 to 357 m. The results reveal that CF values are high and landslides are frequent in the middle altitudes, because the ratio of the study area in the middle altitudes is greater than that in the higher altitudes, and the lower areas are gentle and thus not prone to landslides.

In the case of slope angle, CF values are strongly positive from 22° to 44° . The percentage of landslide occurrence in the slope classes $28^\circ-33^\circ$, $33^\circ-38^\circ$, and $38^\circ-44^\circ$ are 15.43 %, 19.43 %, and 19.57 %, respectively. The result shows that the occurrence of landslides gradually increases with an increasing slope angle until it drops sharply after 44° slope angle. Gentler slopes have a relatively low frequency of landslide occurrences because of the lower shear stress corresponding to the low gradient; whereas, very steep slope angles lead to outcropped bedrock, which is less susceptible to landslides.

With respect to the slope aspect, most of the landslides occurred along East, South-East, South, South-West and West facing slopes with positive CF values from 0.13 to 0.57. The highest percentage of landslides, 15.76 %, occurred along the Southern slopes, followed by South-West slopes (15.73 %). Landslides triggered by an earthquake are distributed mainly along dip direction of geological formations. The Northern slope aspect with a negative CF value may be related to dipping of bedrock but details are unknown.

In the case of density of geological boundary, the CF values are always positive. The maximum CF value, 0.5, is seen in the class with the most dense geological boundary (15–27) followed by a value of 0.42 in the immediately lower geological density class (10–15). The percentage distribution of landslide occurrences in the above mentioned classes are 25.26 % and 21.73 %, respectively. The negative CF value for the geological-density class lower than 2 indicates that geolocial uniformity affects the stability of the area. Higher density of geological boundaries suggests higher geo-tectonic activity which leads to instability.

Table 2 Part of Spatial relationship between the relative factors and landslides by certainty factor model

| Factors | Class | No. of pixels in domain | Percentage of domain (%) | No. of landslides | Percentage of landslides (%) | PP_a (%) | CF |
|--------------------------------|-----------|-------------------------|--------------------------|-------------------|------------------------------|------------|-------|
| Elevation (m) | 0–73 | 509960 | 18.14 | 75 | 1.01 | 0.01 | −0.96 |
| | 73–131 | 496945 | 17.67 | 507 | 6.86 | 0.1 | −0.68 |
| | 131–190 | 431813 | 15.36 | 1,476 | 19.96 | 0.34 | 0.31 |
| | 190–246 | 379260 | 13.49 | 1,728 | 23.37 | 0.46 | 0.57 |
| | 246–301 | 327443 | 11.65 | 1,431 | 19.35 | 0.44 | 0.54 |
| | 301–357 | 245594 | 8.73 | 1,126 | 15.23 | 0.46 | 0.58 |
| | 357–413 | 184641 | 6.57 | 689 | 9.32 | 0.37 | 0.4 |
| | 413–477 | 137466 | 4.89 | 313 | 4.23 | 0.23 | −0.17 |
| | 477–561 | 75006 | 2.67 | 38 | 0.51 | 0.05 | −0.85 |
| Slope angle (°) | 561–735 | 23670 | 0.84 | 11 | 0.15 | 0.05 | −0.86 |
| | 0–4 | 806102 | 28.67 | 69 | 0.93 | 0.01 | −0.98 |
| | 4–10 | 329623 | 11.72 | 329 | 4.45 | 0.1 | −0.69 |
| | 10–17 | 312941 | 11.13 | 625 | 8.45 | 0.2 | −0.3 |
| | 17–22 | 309831 | 11.02 | 830 | 11.23 | 0.27 | 0.02 |
| | 22–28 | 292849 | 10.42 | 956 | 12.93 | 0.33 | 0.26 |
| | 28–33 | 295299 | 10.5 | 1,141 | 15.43 | 0.39 | 0.43 |
| | 33–38 | 256253 | 9.11 | 1,437 | 19.43 | 0.56 | 0.72 |
| | 38–44 | 162466 | 5.78 | 1,447 | 19.57 | 0.89 | 0.96 |
| Slope aspect | 44–70 | 46434 | 1.65 | 560 | 7.57 | 1.21 | −0.97 |
| | Flat | 505420 | 17.97 | 571 | 7.72 | 0.22 | −0.88 |
| | Northeast | 266989 | 9.5 | 469 | 6.34 | 0.18 | −0.4 |
| | East | 282759 | 10.06 | 822 | 11.12 | 0.29 | 0.13 |
| | Southeast | 272681 | 9.7 | 1,110 | 15.01 | 0.41 | 0.48 |
| | South | 258376 | 9.19 | 1,165 | 15.76 | 0.45 | 0.57 |
| | Southwest | 290646 | 10.34 | 1,163 | 15.73 | 0.4 | 0.47 |
| | West | 337151 | 11.99 | 1,046 | 14.15 | 0.31 | 0.21 |
| | Northwest | 331355 | 11.78 | 664 | 8.98 | 0.2 | −0.3 |
| Density of geological boundary | North | 266421 | 9.48 | 384 | 5.19 | 0.14 | −0.53 |
| | 0–2 | 893627 | 30.82 | 1,153 | 15.59 | 0.13 | −0.58 |
| | 2–5 | 599311 | 20.67 | 1,607 | 21.73 | 0.27 | 0.03 |
| | 5–7 | 602764 | 20.79 | 1,868 | 25.26 | 0.31 | 0.21 |
| | 7–10 | 438573 | 15.13 | 1,345 | 18.19 | 0.31 | 0.19 |
| | 10–15 | 274642 | 9.47 | 1,045 | 14.13 | 0.38 | 0.42 |
| Density of drainage network | 15–27 | 90616 | 3.13 | 376 | 5.09 | 0.41 | 0.5 |
| | 0–2 | 792237 | 27.24 | 1,571 | 21.25 | 0.2 | −0.31 |
| | 2–4 | 792007 | 27.24 | 2,119 | 28.66 | 0.27 | 0.02 |
| | 4–6 | 714523 | 24.57 | 2,210 | 29.89 | 0.31 | 0.2 |
| | 6–9 | 449187 | 15.45 | 1,278 | 17.28 | 0.28 | 0.1 |
| Plan curvature | 9–20 | 159964 | 5.5 | 216 | 2.92 | 0.14 | −0.56 |
| | Concave | 1615639 | 172.76 | 3,659 | 49.49 | 0.23 | −0.18 |
| | Convex | 1196159 | 318.28 | 3,735 | 50.51 | 0.31 | 0.21 |

The density of drainage network (*DR*) shows a positive value for the classes 2–4, 4–6, and 6–9. The positive maximum CF value of 0.2 is observed with the 4–6 *DR* class. The highest percentage of landslide occurrences, 29.89 %, also relates to the same *DR* class followed by 28.66 % of the 2–4 *DR* class. Since the landslides in this study were triggered by an earthquake and the corresponding CF values are comparatively very small, a specific cause-reason relation for the

distribution of landslides in the *DR* class could not be established.

Concave plan curvature corresponds to a negative CF value (−0.18) while convex curvature to a positive value (0.21). Normally convex areas have a lower CF value than concave areas because such slopes retain more water and the increased soil moisture content reduces the stability of the soil. In this study area though, the concavity is not

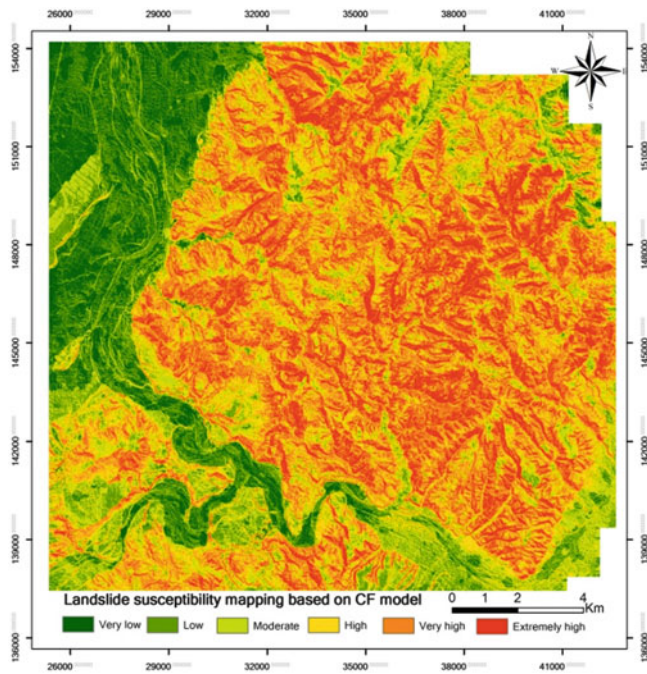


Fig. 2 The landslide susceptibility map showing six susceptible classes from very low to extremely high

responsible for the landslide occurrences, because the landslides are induced by an earthquake, not by rainfall. Ridges tended to collapse because of higher ground acceleration due to the earthquake.

The results of this study also indicate that the eight lithology classes, sandstone and alternation of sandstone and mudstone from Late Miocene–Early Pliocene (As); mudstone interbedded with sandstone (Ku), Andesitic pyroclastic rock (Uv), sandstone (Ks), massive mudstone (Um), sandstone interbedded with mudstone (KI) from Early Pliocene–Late Pliocene; and Massive mudstone (Am) from Late Miocene–Early Pliocene have significantly higher CF values of 1.0, 0.94, 0.89, 0.82, 0.78, 0.75, 0.70, 0.52, respectively. The highest percentage of landslides among the lithology classes, 21.4 %, occurred in Ku, followed by Am (19 %) and Um (13.34 %). The bedrock in the area of major landsliding consists of a folded sequence of sandstone, mudstone and their interbeddings, and the results point to the occurrence of landslides in the weakly cemented lithological groups.

Validation of the CF Model

It is essential to verify the accuracy of any prediction model. We verified the accuracy of the CF model used for this study and the results using *ROC*.

ROC is a very useful indicator to evaluate the quality of deterministic and probabilistic detection and forecast

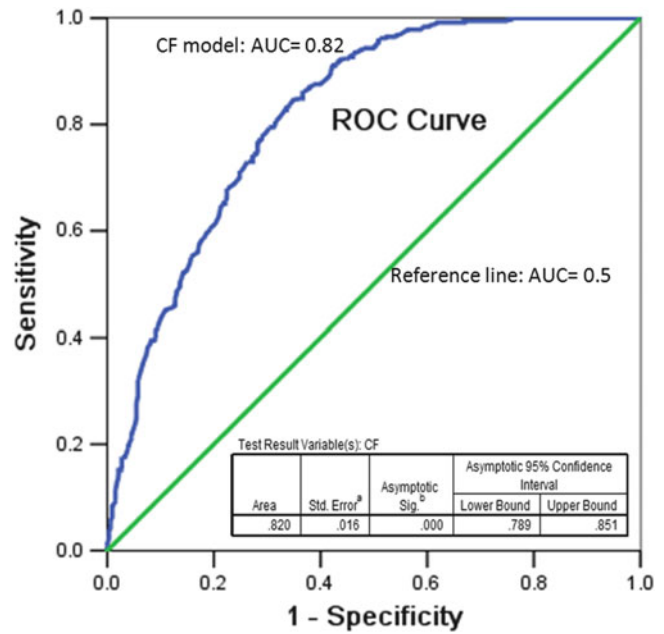


Fig. 3 Evaluation of LSM model performance using ROC

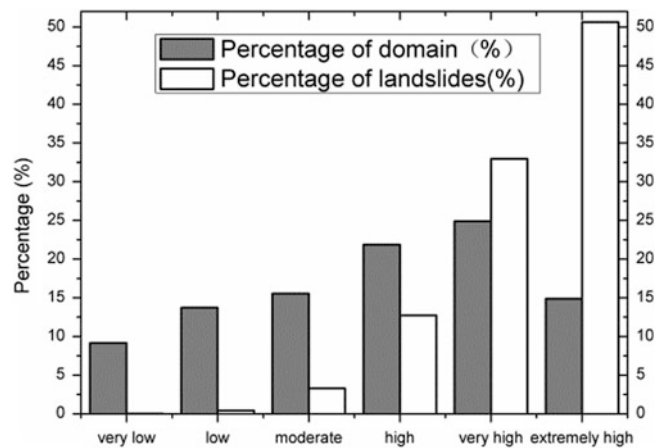


Fig. 4 Distribution of the study area and the occurrence of landslides according to the classification scheme used for LSM

systems (Swets 1988). The area under the *ROC* curve (*AUC*) can characterize the quality of a forecast system by describing the system’s ability to correctly predict the occurrence or non-occurrence of a predefined event.

For the verification, the total landslides were divided into two groups, training data and validation data and an *ROC* plot of sensitivity (true positive rate) and 1-specificity (false positive rate) was made. The *AUC* value varies from 0.5 to 1.0 and only an ideal model has an *AUC* value of 1.0. For our model, the *AUC* value is 0.82 (Fig. 3). According to Yilmaz (2009), a model with an *AUC* value of 0.82 is considered good for use in landslide susceptibility mapping.

Figure 4 shows that 96.28 % of the total landslides occurred in the 61.6 % of the area classified as high (high,

very high and extremely high) according to their CF values. This displays that the modeling result agrees with the real condition.

Conclusions

In this research, an LSM model, namely the CF model was applied to the Chuetsu area in the Niigata Prefecture, Japan, to produce a susceptibility map using GIS. The main trigger for the landslides in this area was the Chuetsu earthquake of 2004. Seven factors (elevation, slope angle, slope aspect, density of geological boundaries, density of drainage network, plan curvature and lithology) were used to predict the susceptible areas. The model was verified using an *AUC* value obtained from ROC plot and it showed a high accuracy.

Landslide susceptibility maps are of great importance for sustainable urban development and thus the local government. The constructed map may be helpful in preliminary decision-making, policy planning and hazard mitigation in the future.

Acknowledgments The authors would like to express their gratitude to the NIED for providing the landslide data. JD is also grateful to Dr. Avinash K.G for his comments.

References

- Avinash KG, Ashamanjari KG (2010) A GIS and frequency ratio based landslide susceptibility mapping: Aghnashini river catchment, Uttara Kannada, India. *Int J Geomatics Geosci* 1:343–354
- Binaghi E, Madella P, Pergalani F et al (1998) Slope instability zonation: a comparison between certainty factor and fuzzy Dempster–Shafer approaches. *Nat Hazards* 17:77–97. doi:10.1023/A:1008001724538
- Caniani D, Pascale S, Sdao F, Sole A (2007) Neural networks and landslide susceptibility: a case study of the urban area of Potenza. *Nat Hazards* 45:55–72. doi:10.1007/s11069-007-9169-3
- Chigira M, Imai C, Hijikata H (2006) Water percolating behavior indicated by the water chemistry within a decomposed granite slope, central Japan. *Eng Geol* 84:84–97. doi:10.1016/j.enggeo.2005.12.002
- Chung CF, Fabbri AG (1993) The representation of geoscience information for data integration. *Nonrenewable Resour* 2:122–139. doi:10.1007/BF02272809
- Devkota KC, Regmi AD, Pourghasemi HR et al (2012) Landslide susceptibility mapping using certainty factor, index of entropy and logistic regression models in GIS and their comparison at Mugling–Narayanghat road section in Nepal Himalaya. *Nat Hazards* 65:135–165
- Dou J, Qian J, Zhang H, et al (2009) Landslides detection: a case study in Conghua city of Pearl River delta. In: Zhang X, Li J, Liu G, Yang X (eds) *Geoinformatics 2008 Jt. Conf. GIS Built Environ. Adv. Spat. Data Model. Anal.* p 74711K–74711K–11
- Dou J, Zheng X, Qian J et al (2010) Object-based and case-based reasoning method for ground collapses detection. *J Image Graph* 15:900–909
- Garcia-Rodriguez MJ, Malpica JA, Benito B et al (2008) Susceptibility assessment of earthquake-triggered landslides in El Salvador using logistic regression. *Geomorphology* 95:172–191. doi:10.1016/j.geomorph.2007.06.001
- Guzzetti F, Carrara A, Cardinali M, Reichenbach P (1999) Landslide hazard evaluation: a review of current techniques and their application in a multi-scale study, Central Italy. *Geomorphology* 31:181–216. doi:10.1016/S0169-555x(99)00078-1
- Guzzetti F, Reichenbach P, Ardizzone F et al (2006) Estimating the quality of landslide susceptibility models. *Geomorphology* 81:166–184. doi:10.1016/j.geomorph.2006.04.007
- Kanungo DP, Sarkar S, Sharma S (2011) Combining neural network with fuzzy, certainty factor and likelihood ratio concepts for spatial prediction of landslides. *Nat Hazards* 59:1491–1512. doi:10.1007/s11069-011-9847-z
- Oguchi T (1996) Factors affecting the magnitude of post-glacial hill-slope incision in Japanese mountains. *Catena* 26:171–186
- Pourghasemi HR, Mohammady M, Pradhan B (2012) Landslide susceptibility mapping using index of entropy and conditional probability models in GIS: Safarood Basin, Iran. *Catena* 97:71–84. doi:10.1016/j.catena.2012.05.005
- Shortliffe EH (1976) Computer-based medical consultations: MYCIN
- Swets JA (1988) Measuring the accuracy of diagnostic systems. *Science* 240:1285–1293. doi:10.1126/science.3287615
- Takeuchi K, Yanagisawa Y (2004) 1:50,000 Digital geological map of the Uonuma Tegion, Niigata Prefecture (Ver. 1), GSJ Open-file Report, 478, Geological Survey of Japan. http://www.gsj.jp/GDB/openfile/index_j.html
- Turner AK, Schuster LR (1996) *Landslides: investigation and mitigation*. National Academy Press, Washington, DC
- Yilmaz I (2009) Comparison of landslide susceptibility mapping methodologies for Koyulhisar, Turkey: conditional probability, logistic regression, artificial neural networks, and support vector machine. *Environ Earth Sci* 61:821–836. doi:10.1007/s12665-009-0394-9



Landslide Susceptibility Mapping Using a Grid-based Infiltration Transient Model in Mountainous Regions

Dongyeob Kim, Eun Jai Lee, Byungkyu Ahn, and Sangjun Im

Abstract

Rainfall-induced landsliding is the major sediment-related disaster in the mountainous regions of Korea. Landslide susceptibility mapping, which is the principal approach to identifying areas prone to landslides, provides decision-makers with the policy priorities for mitigation and prevention measures. A revised TRIGRS (Transient Rainfall Infiltration and Grid-based Regional Slope-stability analysis) model was employed to estimate areas that would be unstable after rainfall occurred. Design rainfall data was statistically derived and input into the model. The influence of trees was considered in terms of tree surcharge and tree root cohesion. A regional estimate of landslide-prone areas was then conducted using the model. Unstable hillslope conditions vary temporally and spatially on a regional scale with soil, topography, and land use/cover.

Keywords

The revised TRIGRS • Tree surcharge • Tree root cohesion • Design rainfall data

Introduction

Damage by landslides is increasing all over the world, with landslides becoming more frequent and severe. In South Korea, the 10-year average of landslide-damaged areas has increased from 231 ha in the 1980s to 349 ha in the 1990s and 713 ha in the 2000s (Korea Forest Service 2013). Since the year 2000, in particular, areas averaging more than 1,000 ha were damaged by landslides due to heavy rainfall

events (Fig. 1). Shallow landslides, typically induced by rainfall, constitute the most dominant type, which is the major sediment-related disaster in the mountainous regions of South Korea.

Assessment of landslide susceptibility in a region is a basic process for landslide risk management. Landslide susceptibility mapping, which is the principal approach to identifying areas prone to landslides, provides decision-makers with the policy priorities for mitigation and prevention measures. Of the methods of assessing landslide susceptibility, the physically-based approach has the advantage of considering changes in landslide-causing factors such as rainfall patterns and land use. These factors have significant impacts on landslide initiation, specifically on rainfall-induced shallow landslides.

In the current study, landslide susceptibility mapping at a regional scale was carried out using a physically-based model. An existing model was modified to consider the effects of trees on landslide initiation, and statistically-derived design rainfall was introduced as input rainfall data for the landslide susceptibility model.

D. Kim (✉) • E.J. Lee • B. Ahn
Department of Forest Sciences, Seoul National University, 1 Gwanak-ro, Gwanak-gu, Seoul 151-921, South Korea
e-mail: dongyeob.kim1@gmail.com

S. Im
Department of Forest Sciences, Seoul National University, 1 Gwanak-ro, Gwanak-gu, Seoul 151-921, South Korea

Research Institute for Agriculture and Life Sciences, Seoul National University, 1 Gwanak-ro, Gwanak-gu, Seoul 151-921, South Korea

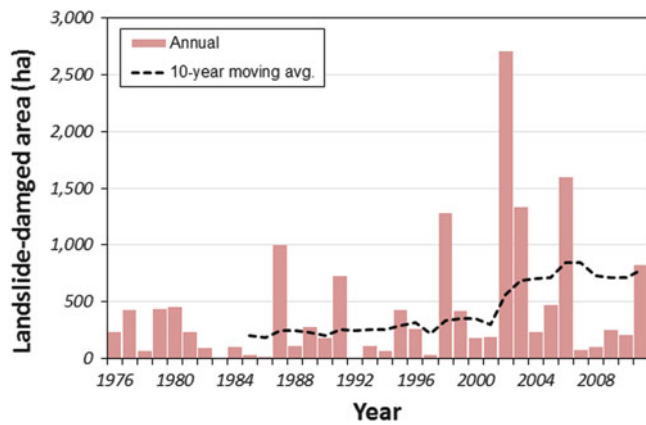


Fig. 1 National statistics on landslide-damaged areas in South Korea

The Revised TRIGRS Program

TRIGRS (Transient Rainfall Infiltration and Grid-Based Regional Slope-Stability Model), developed by the U.S. Geological Survey (Baum et al. 2002), was applied to assess landslide susceptibility in the current study. This grid-based model evaluates the temporal change of slope stability as a Factor of Safety (FS), considering the transient effect of infiltration during rainfall events. The model was revised to consider the effects of trees on landslide initiation, such as rainfall interception, tree surcharge, and tree root cohesion. Figure 2 shows the difference between the original TRIGRS and the revised model in calculating the pressure head of groundwater and Factor of Safety. Specifically, the following equation including terms for tree root cohesion and tree surcharge was used to calculate Factor of Safety in the revised model,

$$FS(Z, t) = \frac{c_r + c' + \{m_t \cos^2 \theta + \gamma_t Z \cos^2 \theta - \psi(Z, t) \gamma_w\} \tan \phi'}{(m_t + \gamma_t Z) \sin \theta \cos \theta}$$

where FS is the factor of safety, Z is soil depth (m), t is time (s), c_r is the root cohesion (kPa), c' is the soil effective cohesion (kPa), m_t is the tree surcharge (kPa), θ is the slope angle ($^\circ$), γ_t is the moist soil unit weight (kN m^{-3}), ψ is the pore water pressure expressed as a head of water (m), γ_w is the water unit weight (kN m^{-3}), and ϕ' is the soil effective internal friction angle ($^\circ$).

Study Site

The study sites were Pyeongchang and Inje in Kangwon province, South Korea (Fig. 3). These two regions have extensive landslide-damaged areas because of steep

topography and heavy annual rainfall. For both of them, more than 80 % of the entire site was covered by forest, and granite was dominant geologically. Table 1 shows some principal environmental characteristics of the study sites.

Parameterization

Rainfall Data

Design rainfall, statistically-derived from rainfall duration and return period, was used as standard rainfall data for the landslide susceptibility assessment. From analysis of the characteristics of landslide-triggering rainfall events in South Korea since the year 2000, 24-h duration and 5-year return period were selected as criteria for standard rainfall. The derived standard rainfall was temporally distributed using the “obs” method suggested by the Ministry of Land, Infrastructure and Transport, South Korea (2011). The obs method, based on the temporal distributions of 297 observed storm events with more than 30 mm h^{-1} of maximum hourly intensity, is thought to represent the characteristic of storm events in South Korea moderately well.

In terms of derived standard rainfall data, 280.7 mm of total rainfall and 47.1 mm of maximum hourly rainfall were used for Pyeongchang, while 205.6 mm of total rainfall and 34.5 mm of maximum hourly rainfall were used for Inje. Figure 4 shows the temporal distribution of the resulting standard rainfall data for each study site.

Topographical Data

GIS data on elevation, slope gradient, and flow direction were generated as input data for the revised TRIGRS model. For the typical landslide size in South Korea, GIS data on slope gradient and flow direction were converted from a 30-m, LiDAR-based DEM. The topographical features of the study sites, based on the generated GIS data, are described in Table 2.

Soil Property Data

Some geotechnical and soil-hydraulic parameters are needed for the simulation using the revised TRIGRS, such as the soil unit weight, the soil cohesion, the soil internal friction angle, and the soil saturated hydraulic conductivity. In the current study, the parameters were estimated for each soil type of the digital forest soil map, Korea Forest Research Institute (KFRI). Table 3 shows the ratio and parameter values of soil types of the study sites. Brown soil (B) was the dominant soil type for both sites, featuring 17.82 kN/m^3 for the soil

Fig. 2 Schematic diagram of the revised TRIGRS (after Kim et al. 2013)

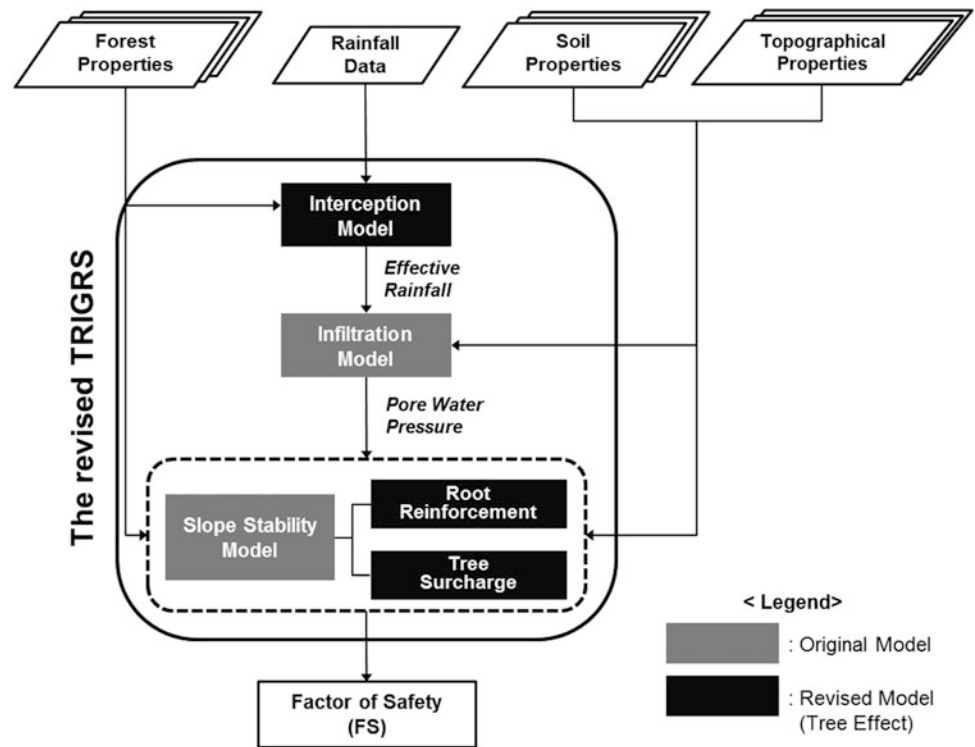


Fig. 3 Location map of the study sites in South Korea

Table 1 The characteristics of the study sites, Pyeongchang and Inje

| | Pyeongchang | Inje |
|-------------------------|-------------------------|---------|
| Area (km ²) | 1,464 | 1,646 |
| Forest Cover (%) | 80 | 88 |
| Geology | Granite/Granitic Gneiss | Granite |
| Temperature (°C) | 6.6 | 10.1 |
| Precipitation (mm) | 1,898 | 1,211 |

based on the typical depth of shallow landslides that have occurred in South Korea.

Forest Property Data

The rainfall interception model of the revised TRIGRS was not employed in the current study because rainfall interception has little impact on landslide initiation during the short duration of a single rainfall event (Kim et al. 2013). The tree surcharge and tree root cohesion were estimated, based on the forest type and crown coverage of the study sites, from the digital forest stock map by KFRI. In terms of forest type, Pyeongchang had 37.1 % of coniferous forest, 39.7 % of deciduous forest, and 23.2 % of mixed forest, while Inje had 22.8 %, 38.1 %, and 39.1 %, respectively. Also, crown coverage value was mostly medium or dense for both sites.

unit weight, 6.80 kPa for the soil cohesion, 26.9° for the soil internal friction angle, and 3.52×10^{-5} m/s for the soil saturated hydraulic conductivity.

For soil thickness, a uniform value was assumed for the entire study sites because there was no reliable existing data on soil thickness distribution. Parametric analyses were conducted for 1.0 m, 1.5 m, and 2.0 m of soil thickness,

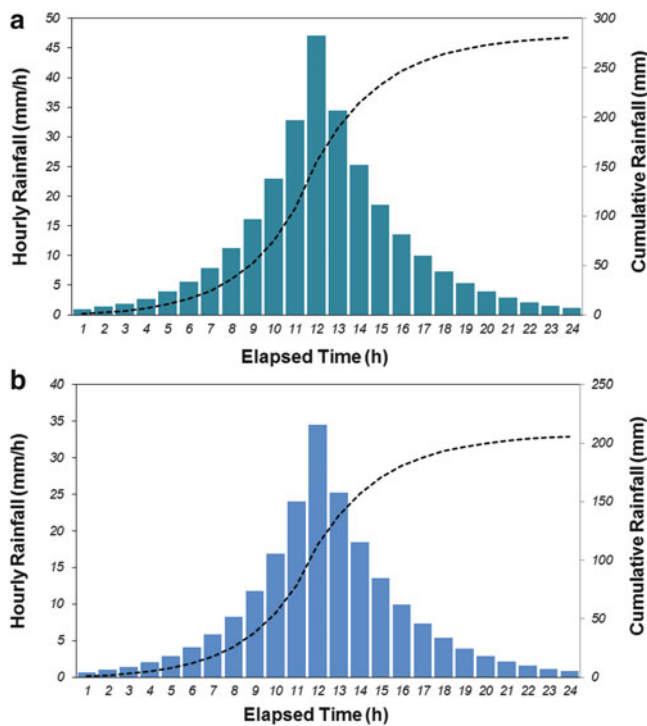


Fig. 4 Input rainfall data of the study sites (a) Pyeongchang, (b) Inje

Table 2 Topographical properties of the study sites based on the generated GIS input data

| | Pyeongchang | Inje |
|--------------------|------------------------------|------------------------------|
| Number of cells | 1,677,003 | 1,798,664 |
| Elevation (m) | 215–1,575 (759) ^a | 180–1,680 (642) ^a |
| Slope gradient (°) | 0–76 (23) ^a | 0–71 (25) ^a |

^aaverage values

For assigned values for the simulation, tree surcharge ranged from 0.177 kPa to 0.465 kPa, and tree root cohesion ranged from 1.00 kPa to 1.67 kPa, respectively.

Initial Conditions and Assumptions of the Revised TRIGRS Simulation

The initial groundwater table was assumed to lie at the boundary of the soil zone and bedrock, namely at the depth to bedrock. In addition, the soil zone above the groundwater table was assumed to be tension-saturated because the saturated-infiltration model of the TRIGRS was applied in

the current study. These soil-hydraulic initial conditions were based on typical topographical and soil-hydraulic properties of South Korea. A series of the revised TRIGRS simulations with the aforementioned initial conditions were conducted for the soil thicknesses of 1.0 m, 1.5 m, and 2.0 m and the final Factors of Safety were calculated from the simulations.

Results and Discussion

As the results of the simulations, the site-averaged Factors of Safety were calculated as 2.09 for 1.0 m of soil thickness, 1.60 for 1.5 m of soil thickness, and 1.35 for 2.0 m of soil thickness in Pyeongchang. The average Factors of Safety of 1.87, 1.44, and 1.23 were calculated for 1.0 m, 1.5 m, and 2.0 m of soil thickness in Inje. For both study sites, the averaged Factor of Safety decreased as soil thickness increased.

In terms of landslide-susceptible areas, areas calculated as having less than a Factor of Safety of 1, Pyeongchang appeared to have 4.7 km², 124.1 km², and 410.3 km² for 1.0 m, 1.5 m, and 2.0 m of soil thickness, while Inje appeared to have 14.0 km², 226.0 km², and 558.1 km², respectively.

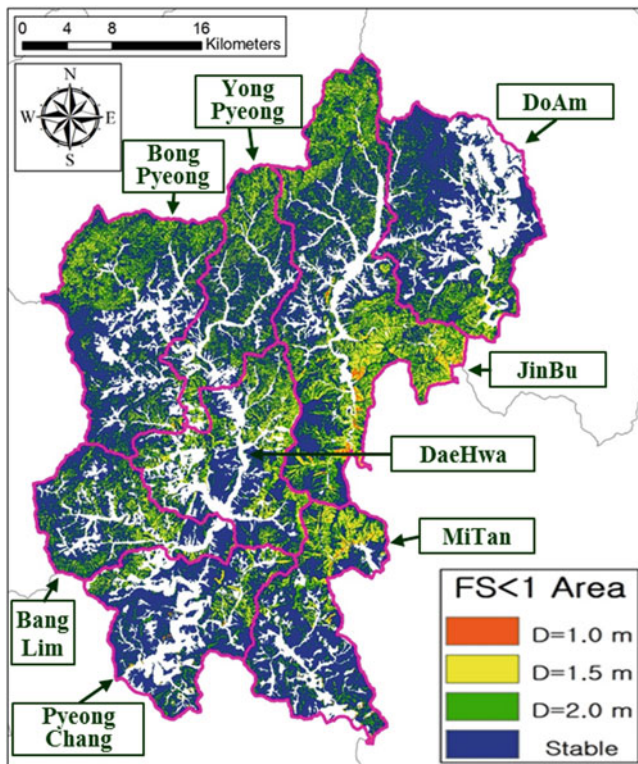
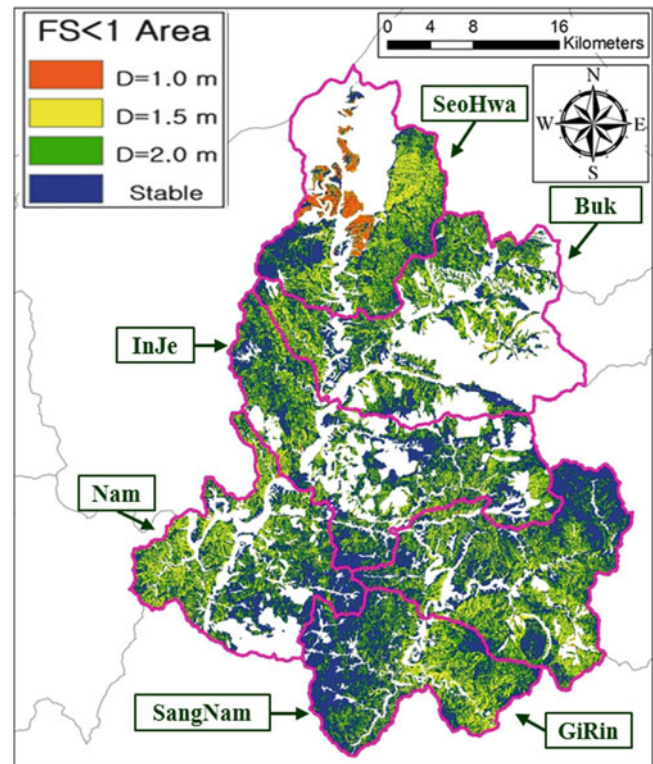
The site-averaged Factors of Safety were calculated as having lower values for all soil thicknesses in Inje than in Pyeongchang. Moreover, Inje had more areas susceptible to landslides than Pyeongchang, not only by area but also by area ratio. With these results, Inje was thought to be more susceptible to landslides than Pyeongchang, although the amount of input rainfall in Pyeongchang was greater than that in Inje. Figures 5 and 6 show the areas with Factors of Safety < 1 by soil thickness for the study sites. According to Figs. 5 and 6, Jinbu in Pyeongchang and Seohwa in Inje were assessed as the areas most susceptible to landslides in each study site.

In the current study, landslide susceptible areas were assessed and mapped for each study site by considering local rainfall characteristics and other landslide-inducing factors. However, landslide-historical data may be needed to evaluate the performance of the approach employed and to analyse the results statistically. Reliable data on landslide-triggering factors are also needed to improve the performance of the physically-based landslide susceptibility model.

Acknowledgments This research is based on a part of the author Dongyeob Kim's doctoral dissertation.

Table 3 Soil properties of the study sites

| | Soil type | Area ratio (%) | Unit weight (kN/m ³) | Cohesion (kPa) | Internal friction angle (°) | Saturated hydraulic conductivity (m/s) |
|-------------|-----------|----------------|----------------------------------|----------------|-----------------------------|--|
| Pyeongchang | B | 66.1 | 17.82 | 6.80 | 26.9 | 3.52×10^{-5} |
| | DR | 11.8 | 16.91 | 11.41 | 22.0 | 1.40×10^{-6} |
| | DRb | 0.2 | 17.77 | 6.87 | 26.8 | 8.55×10^{-6} |
| | Er | 0.0 | 18.95 | 2.44 | 29.0 | 2.26×10^{-5} |
| | Li | 1.7 | 18.51 | 4.76 | 28.0 | 6.43×10^{-6} |
| | No Data | 20.3 | 18.51 | 4.76 | 28.0 | 6.43×10^{-6} |
| Inje | B | 68.5 | 17.82 | 6.80 | 26.9 | 3.52×10^{-5} |
| | rB | 0.3 | 17.08 | 10.42 | 25.8 | 8.85×10^{-7} |
| | Er | 1.8 | 18.95 | 2.44 | 29.0 | 2.26×10^{-5} |
| | Im | 0.0 | 18.07 | 6.67 | 26.5 | 2.92×10^{-6} |
| | Li | 0.4 | 18.51 | 4.76 | 28.0 | 6.43×10^{-6} |
| | No Data | 29.0 | 18.51 | 4.76 | 28.0 | 6.43×10^{-6} |

**Fig. 5** The simulated landslide-susceptible areas of Pyeongchang by soil thickness**Fig. 6** The simulated landslide-susceptible areas of Inje by soil thickness

References

- Baum RL, Savage WZ, Godt JW (2002) TRIGRS - A Fortran program for transient rainfall infiltration and grid-based regional slope-stability analysis. U.S. Geological Survey Open-File Report 2002-424. 61p.
- Kim D, Im S, Lee C, Woo C (2013) Modeling the contribution of trees to shallow landslide development in a steep, forested watershed. *Ecol Eng* 61:658–668
- Korea Forest Service (2013) 2013 Detailed Strategy for Primary Policy. URL:<http://ibook.forest.go.kr/Viewer/R-GSDN3GDGDFX> [Last accessed: Sept. 2, 2013]
- Ministry of Land, Infrastructure and Transport, South Korea (2011) Improvement and Supplement of Probability Rainfall Map. Ministry of Land, Infrastructure and Transport Report No. 11-1611000-001995-01. 237p



Evaluating a Slope-Stability Model for Shallow Rain-Induced Landslides Using Gage and Satellite Data

Soni Yatheendradas, Dalia Kirschbaum, Rex L. Baum, and Jonathan W. Godt

Abstract

Improving prediction of landslide early warning systems requires accurate estimation of the conditions that trigger slope failures. This study tested a slope-stability model for shallow rainfall-induced landslides by utilizing rainfall information from gauge and satellite records. We used the TRIGRS model (Transient Rainfall Infiltration and Grid-based Regional Slope-stability analysis) for simulating the evolution of the factor of safety due to rainfall infiltration. Using a spatial subset of a well-characterized digital landscape from an earlier study, we considered shallow failure on a slope adjoining an urban transportation roadway near the Seattle area in Washington, USA.

We ran the TRIGRS model using high-quality rain gage and satellite-based rainfall data from the Tropical Rainfall Measuring Mission (TRMM). Preliminary results with parameterized soil depth values suggest that the steeper slope values in this spatial domain have factor of safety values that are extremely close to the failure limit within an extremely narrow range of values, providing multiple false alarms. When the soil depths were constrained using a back analysis procedure to ensure that slopes were stable under initial conditions, the model accurately predicted the timing and location of the landslide observation without false alarms over time for gage rain data. The TRMM satellite rainfall data did not show adequately retrieved rainfall peak magnitudes and accumulation over the study period, and as a result failed to predict the landslide event. These preliminary results indicate that more accurate and higher-resolution rain data (e.g., the upcoming Global Precipitation Measurement (GPM) mission) are required to provide accurate and reliable landslide predictions in ungauged basins.

Keywords

Rainfall-triggered • Shallow landslide • Slope-stability model • Satellite products

S. Yatheendradas (✉)
UMD ESSIC and NASA GSFC Hydrological Sciences Laboratory
(Code 617), NASA GSFC, Greenbelt, MD 20771, USA
e-mail: soni.yatheendradas@nasa.gov

D. Kirschbaum
Hydrological Sciences Laboratory (Code 617), NASA GSFC,
Greenbelt, MD 20771, USA
e-mail: dalia.b.kirschbaum@nasa.gov

R.L. Baum • J.W. Godt
U. S. Geological Survey, Golden, CO 80401, USA
e-mail: baum@usgs.gov; jgodt@usgs.gov

Introduction

Shallow landslides are caused by intense or prolonged rainfall that destabilizes slopes (e.g., Crozier 1986), especially on steep topography (e.g., Iverson 2000), and are a hazard to human life and property (e.g., Sidle and Ochiai 2006). Detailed high-resolution landslide modeling is a challenge due to the complex spatiotemporal interaction between the rainfall, the surface soil and the underlying geology. In many areas of the world, absence or sparseness of rain gages further complicates forecasting of the landslide timing.

Satellite-based rainfall estimates are a potential substitute for gage measurements in landslide forecasts for such areas.

In metropolitan areas like Seattle, Wash in the United States, landslides occurring on the hillslopes and bluffs pose a threat to people, property, transportation, utilities and businesses (<http://landslides.usgs.gov/regional/seattle/>). Predicting these landslides is challenging; although rainfall is the predominant cause, additional factors such as snow and human activities sometimes can come into play (Bower 2013, NOAA-NWS, Written Communication). Baum et al. (2010) have shown success in distributed modeling of landslides in the Seattle area on geologic units of glacial origin, such as the transition beds including the Lawton Clay Member of Vashon Drift, and the informally named Advance Outwash Sand. In our study, we build upon the work by Baum et al. (2010) to investigate use of satellite rainfall estimates in making landslide predictions on steep slopes where rain gage data are not available.

Materials and Methods

The Observed Landslides

The observed landslides evaluated in this study occurred on the night of Sunday, March 13, 2011, near and along the 1700 block of Mukilteo Speedway near 19th Drive, north of Seattle, Washington (see Fig. 1a). Multiple small landslides were triggered by excessive rainfall over the weekend, some of which blocked the roadway (Kirschbaum et al. 2009).

Model and Data Used

We used the spatially distributed USGS model called TRIGRS (Transient Rainfall Infiltration and Grid-based Regional Slope-stability analysis) for simulating the evolution of the factor of safety due to rainfall infiltration (Baum et al., 2010). Most of the TRIGRS equations are in linearized form, enabling rapid computation of slope failure over large domains.

The elevation grid used for this study has a horizontal resolution of 1.83 m (6 ft) (Haugerud et al. 2003). These elevations provided the slope grid values, which were further used by Baum et al. (2010) to derive the grid of vertical soil depths, d_{LZ} (L), using the following empirically fitted exponential function of slope for this domain:

$$d_{LZ} = 5.0e^{-0.04\delta} \quad (1)$$

Here, δ is the slope angle in degrees. Such specific exponential or power laws and their associated parameters are site-specific variations of the original DeRose (1996) power

law relation. Soil properties are the same as those used by Baum et al. (2010), and are based on earlier geologic mapping and field studies using slug tests, open-tube capillary rise tests, constant flux permeameters, and direct shear tests (Minard 1982; Lu et al. 2006; Godt and McKenna 2008).

Hourly rain gage observations came from the NOAA NCDC web site (<http://www.ncdc.noaa.gov>) for the Snohomish County Automated Surface Observing System gage that is located ~3 km southeast of the study domain. Satellite rain data were extracted from the Tropical Rainfall Measurement Mission (TRMM) V7 retrospective data and have a 3-hourly, 0.25° resolution. Figure 2a, b compares the TRMM V7 estimates with rain gage data. We also used the same long-term background infiltration rate of 1.5×10^{-7} m/s as Baum et al. (2010), or the equivalent of about 180 mm in 2 weeks. However, we see no difference in the results when using a value of zero for this rate and note the insensitivity to this parameter.

Consistent with Baum et al. (2010), we assumed an initial depth to the water table equal to the soil depth. This is because a few days of no rain existed prior to the start time of the model run during the early morning on the 9th of March, and the corresponding initial Factor of Safety (FS) is slightly above 1, indicating that these initial conditions are just stable enough for the steep slopes associated with the observed landslides.

Constraining the Soil Depth

TRIGRS has a choice of specifying finitely versus infinitely deep impermeable basal boundary. For the finitely deep case applied by Baum et al. (2010), the simulated water table increases monotonically during the entire simulation; whereas for the infinitely deep case the water table decreases during periods of no rain (Fig. 2c). The outwash sand and till at this site are porous and drain rapidly after rainfall. Therefore, for this study we applied the infinitely deep model case to evaluate this landslide event.

Preliminary simulations using rain gage forcing and soil depth based on (1) indicate that steeper slope values fail multiple times during the simulation, including on the days prior to that of the observed landslides. This is because of the extremely narrow range of variation of the Factor of Safety (FS) values during the simulation for high slope values, combined with an extremely close proximity to the failure threshold of 1. Consequently, we used back analysis to constrain soil depth so that simulated time of failure using gage rainfall data would fall within the timing window of the observed landslides. This created a baseline for checking performance of the TRMM data.

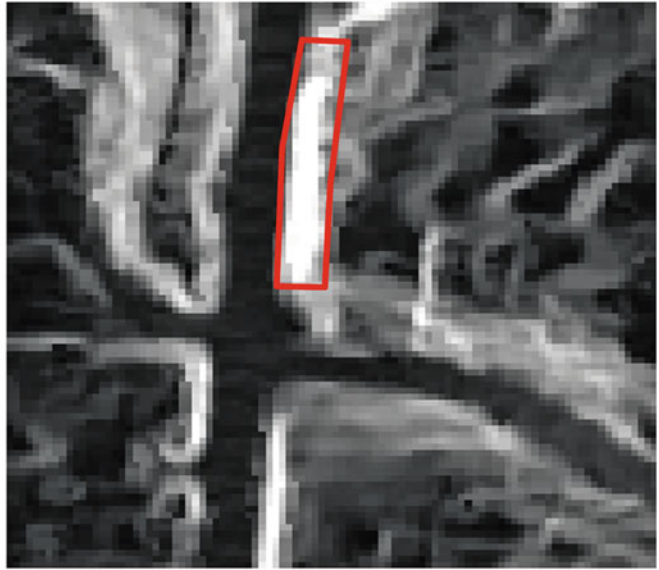
Approximate zone of observed landslide (in red) on Google Maps image:

a Imagery © 2014 Google, Map data © 2014 Google



b

Slope in degrees



High : 52.0237

Low : 0

c

Geologic Units

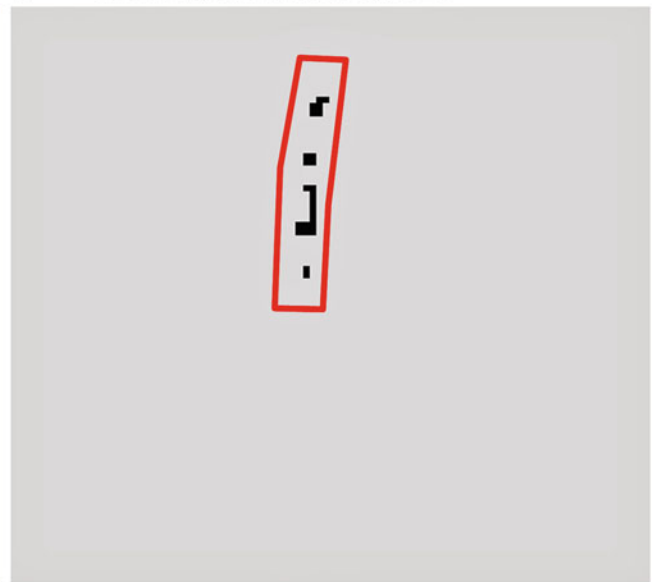


■ Qva: Advance outwash sand

■ Qvt: Till

d

Maximum extent of simulated slope failure on the night of March 13, 2011



■ Failure

■ No failure

Fig. 1 Maps of the considered small domain on Mukilteo Speedway: (a) Google Maps image, (b) Slope, (c) Geology, and (d) maximum modelled failure extent using gage rain forcing

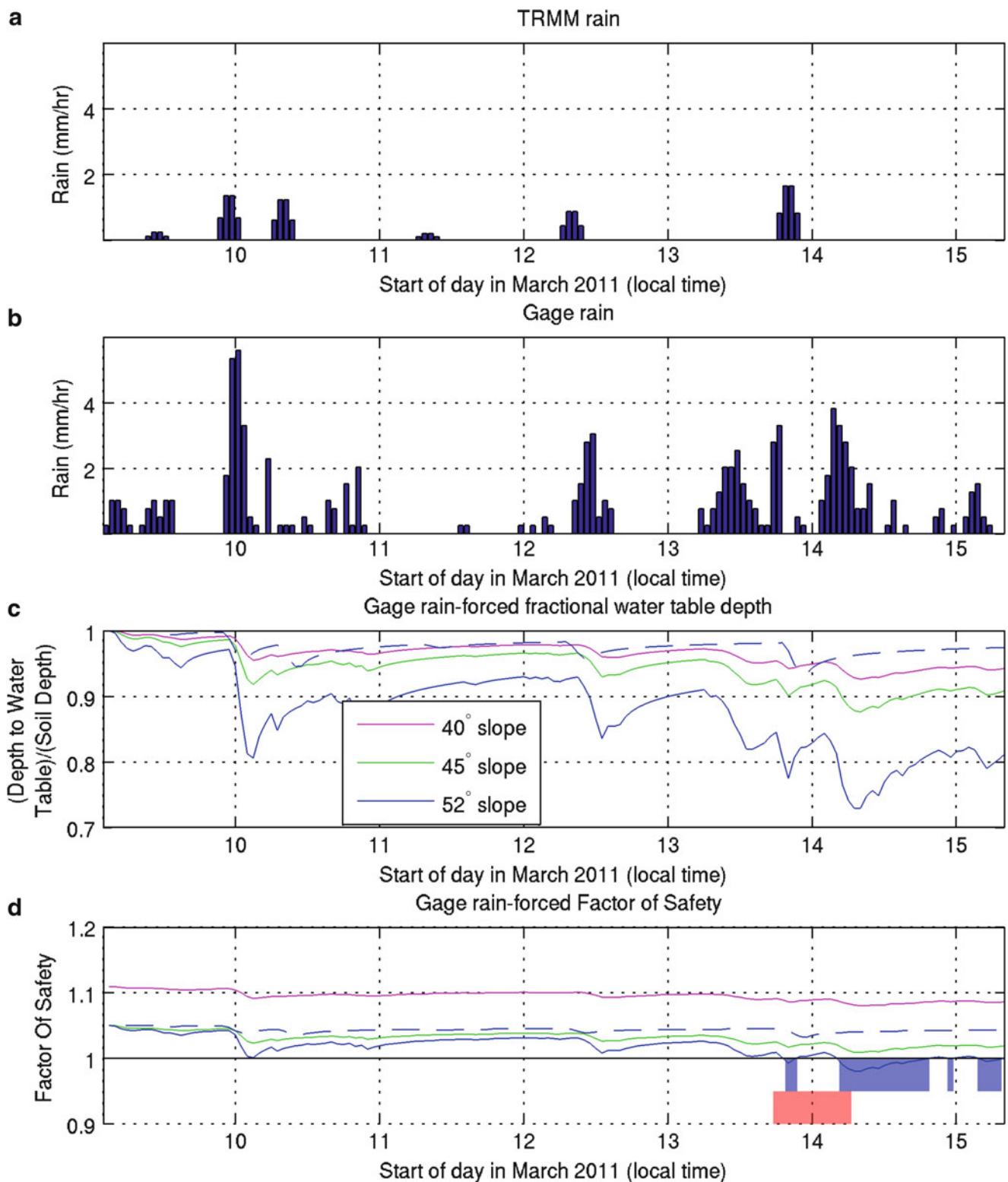


Fig. 2 Rain inputs and TRIGRS outputs for the period of March 9th through 15th, 2011 (maximum domain slope is 52°): (a) TRMM rain, (b) Gage rain (3 km SE of study site), (c) Fractional water table depth on the informally named Advance Outwash Sand or Qva geology type (see Fig. 1c), where *solid lines* are outputs from gage rain on higher slopes, and dashed blue line is output from TRMM rain on the highest

slope of 52°, and (d) same as (c) but showing Factor of Safety instead. Subplot (d) also shows horizontal *black solid* failure threshold line, *red* patch denoting approximate time duration of observed landslides (night of the 13th), and *blue* patches denoting failure times on highest slope of 52° due to gage rain

The 1-D FS used in this study may indicate slope instability prior to the actual landslide event. A 3-D FS that intrinsically has slightly more conservative criteria may better represent reality (Baum et al., 2012). For this preliminary case we assumed that the FS value should reach the failure threshold only during the observed landslide events.

Since the elevational, hydrological and hydromechanical properties are well characterized for this domain based on the study by Baum et al. (2010), the soil depth parameter became the primary candidate to be constrained. Also, since the slope was derived using a high-resolution DEM and the depth was derived from the slope (1) using an empirical “best-fit” model, it is acceptable to slightly constrain or perturb these soil depths using an FS condition while preserving the slopes.

Taylor (1948) characterized failure using the one-dimensional infinite-slope stability equation where the FS (F_s , dimensionless) is the ratio of resisting basal Coulomb friction to the gravitational downslope basal driving force:

$$F_s(Z, t) = \frac{\tan \phi'}{\tan \delta} + \frac{c' - \psi(Z, t)\gamma_w \tan \phi'}{\gamma_s Z \sin \delta \cos \delta} \quad (2)$$

Here, Z is depth (L), t is time (T), ϕ' is the soil friction angle for effective stress (dimensionless), c' is the soil cohesion for effective stress (M/LT^2), ψ is the pressure head (L), γ_w is the unit weight of water (M/L^2T^2), and γ_s is the unit weight of soil (M/L^2T^2). Our study starts with an initial water table at the bottom, thus assigning a zero value to ψ in this equation.

Since the initial FS values for the steepest slopes are just slightly above 1, we used (2) to calculate the soil depths for an FS minimum constraint of 1.05 (or 5 % above 1). This arbitrary choice for the initial factor of safety slightly reduces the soil depths calculated using (1) for slope values greater than $\sim 40^\circ$ (Table 1). This soil depth adjustment is also compatible with our infinitely deep basal boundary choice for the TRIGRS model.

Results

Figure 2d, using constrained soil depths and gage rainfall, shows that the simulated slope failure initiates correctly during the evening of the 13th of March and not before. Figure 1d shows multiple small failed pixel clusters, consistent with reports of the observed landslides.

TRIGRS simulations using the TRMM V7 forcing were unable to initiate slope failures. For the Advance Outwash Sand (Qva, Fig. 1c) informally named geologic unit, the saturated hydraulic conductivity of 5×10^{-5} m/s is much higher than the rain intensities ($< 5 \times 10^{-7}$) during the simulation period. The TRMM rain-forced simulation thus has a lower volume of rain infiltrating and consequently a lower

Table 1 Comparison of estimated soil depth using (1) and (2)

| Slope angle ($^\circ$) | Eq. (1) | Eq. (2) | Difference |
|--------------------------|---------|---------|------------|
| 40 | 1.009 | 1.242 | -0.232 |
| 45 | 0.826 | 0.819 | 0.008 |
| 50 | 0.677 | 0.651 | 0.026 |
| 52 | 0.624 | 0.613 | 0.011 |

water table than the gage rain-forced simulation that leaves the slopes stable.

Discussion and Ongoing Work

Use of a 3-D FS formulation that incorporates the effects of resistance provided by adjacent cells (Baum et al., 2012) instead of the 1-D FS used in this study can potentially provide higher FS and less frequent slope failures using gage rain data. This might also preserve the Baum et al. (2010) characterization of soil depths for this domain, and is part of an ongoing study.

Our results indicate that TRMM rainfall estimates are too low to drive landslide predictions using a spatially distributed model such as TRIGRS. The higher spatiotemporal resolution, accuracy and discrimination between rain and snow in the upcoming Global Precipitation Measurement (GPM; <http://gpm.nasa.gov>) satellite mission holds the promise of better rain fields and improved global landslide predictions using spatially distributed models.

Acknowledgments This work is supported by the NASA New Investigator Proposal Program, 11-NIP11-0039. We also appreciate the review comments and suggestions provided by Jason Kean (USGS) and Diana Salciarini (Università degli Studi di Perugia).

References

- Baum RL, Godt JW, Savage WZ (2010) Estimating the timing and location of shallow rainfall-induced landslides using a model for transient, unsaturated infiltration. *J Geophys Res* 115, F01013. doi:10.1029/2009JF001321
- Baum RL, Godt JW, Coe JA, Reid ME (2012) Assessment of shallow landslide potential using 1-D and 3-D slope stability analysis. In: Eberhardt E, Froese C, Turner K, and Leroueil S (eds) *Landslides and engineered slopes: protecting society through improved understanding*. Taylor & Francis Group, London. ISBN 978-0-415-62123-6
- Bower B (2013) Written Communication. NOAA-NWS. Contacted 20th September 2013.
- Crozier MJ (1986) *Landslides: causes, consequences and environment*. Croom Helm, London, 252 pp
- DeRose RC (1996) Relationships between slope morphology, regolith depth, and the incidence of shallow landslides in eastern Taranaki hill country. *Z Geomorphol* 105:49–60
- Godt JW, McKenna JP (2008) Hydrological response of hillside materials to infiltration: implications for shallow landsliding in the Seattle area. In: Baum R L, Godt J W, and Highland L M (eds) *Landslides and engineering geology of the Seattle, Washington*,

- area, *Reviews in Engineering Geology*. vol XX. Geol Soc Am, Boulder, CO, pp 121–135
- Haugerud RA, Harding DJ, Johnson SY, Harless JL, Weaver CS, Sherrod BL (2003) High-resolution Lidar topography of the Puget Lowland, Washington. *GSA Today* 13:4–10
- Iverson RM (2000) Landslide triggering by rain infiltration. *Water Resour Res* 36:1897–1910
- Kirschbaum DB, Adler R, Hong Y, Hill S, Lerner-Lam A (2009) A global landslide catalog for hazard applications: method, results, and limitations. *Nat Hazards* 52:561–575
- Lu N, Wayllace A, Carrera J, Likos WJ (2006) Constant flow method for concurrently measuring soil-water characteristic curve and hydraulic conductivity function. *Geotech Test J* 29(3):230–241
- Minard J P, (1982) Distribution and description of geologic units in the Mukilteo Quadrangle, Washington, US Geol Surv Misc Field Studies Map, MF-1438, scale 1:24,000
- Sidle RC, Ochiai H (2006) *Landslides: processes, prediction, and land use*. Water Res Monogr Ser 18. AGU, Washington, DC. 312 pp
- Taylor DW (1948) *Fundamentals of soil mechanics*. Wiley, New York, 700



Landslide Susceptibility Modeling on Regional Scales: The Case of Lower Saxony, NW Germany

Martin Klose, Daniel Gruber, Bodo Damm, and Gerhard Gerold

Abstract

This paper presents a regional landslide susceptibility model for the Federal State of Lower Saxony, NW Germany. A modified Information Value approach has been developed, which uses bivariate statistics to identify the spatial probability of landslide occurrence. To optimize the approach for regional applications, several modifications have been made: landslide pixel mapping is replaced by point representation and the weighting function uses landslide densities based on attribute areal coverage. The input data of the landslide susceptibility model include a spatial inventory of about 900 landslides and different data sets of geomorphometry, lithology, and land use.

The model predicts that about 2 % of Lower Saxony shows significant landslide susceptibility. Most of the unstable terrain is concentrated in three key areas in the Lower Saxon Uplands. The spatial patterns of landslide susceptibility are strongly correlated with the regional relief. The most relevant predisposing factors are slope gradients between 21° and 49° as well as different types of Mesozoic sedimentary rock, especially lime- and claystone formations. In conformity with lithology, land use can be of stabilizing or destabilizing influence, but its significance is less important.

The developed approach provides the capability to manage critical problems of regional data processing and proves to be an effective modeling tool for regional applications. Although the model validation indicates good predictive power and high spatial accuracy, the study has shown that regional landslide susceptibility modeling has major data-related and conceptual deficits. Some of these shortcomings are discussed in this paper in detail.

Keywords

Landslide susceptibility modeling • GIS • Large spatial scales • Information Value approach • Regional application • Lower Saxony (NW Germany)

Introduction

The ultimate goal of regional landslide susceptibility modeling is to gain knowledge of the broad spatial patterns of potential slope instability and to support decision makers in the pre-selection and delineation of landslide hazard priority areas. Landslide susceptibility is simply defined as the spatial probability of landslide occurrence and can be modelled by applying a variety of GIS-based approaches (Van Westen et al. 2006). One key assumption says that future landslides will most likely occur in the same

M. Klose (✉) • B. Damm
ISPA, University of Vechta, Universitätsstr. 5, 49377 Vechta, Germany
e-mail: mklose@ispa.uni-vechta.de; bdamm@ispa.uni-vechta.de

D. Gruber • G. Gerold
Institute of Geography, University of Göttingen, Goldschmidtstr. 5,
37077 Göttingen, Germany
e-mail: daniel.gruber@stud.uni-goettingen.de; ggerold@gwdg.de

physiographic setting as in the past. This enables the evaluation of landslide susceptibility on the basis of various geofactors and their past influence on slope instability (Guzzetti et al. 1999).

Most of today's landslide susceptibility assessments use statistical methods. Their core idea is to derive landslide susceptibility on the basis of spatial landslide densities and numerical geofactor weights. Among the most common bivariate methods are the Information Value approach and the Weights-of-Evidence model. A special feature of multivariate techniques is their capability to analyse the correlation and interaction between geofactors. As a result of simple statistical concepts, bivariate methods tend to have lower data requirements, which offers advantages for large spatial scales, because of reduced availability and quality of data (Süzen and Doyuran 2004).

Up until now, landslide susceptibility modeling has mostly concentrated on local to sub-regional levels. True regional perspectives that integrate different physiographic areas or larger territorial units remain exceptional so far. On large spatial scales, landslide susceptibility modeling is faced with special challenges, including data deficits and conceptual limitations (Klose et al. 2014).

In the present study, a modified Information Value approach is developed to model regional landslide susceptibility in the Federal State of Lower Saxony, NW Germany. Using the example of this case study, the paper provides ideas and practical solutions to address some crucial weak points of landslide susceptibility modeling on regional scales.

Study Area

The German Federal State of Lower Saxony is located in the transition between the North European Plain and the Central European Uplands and covers an area of about 47,600 km². In the southern part of this region, the Lower Saxon Uplands form a distinct mountain area with moderate relief intensity (Fig. 1). One major part of the Lower Saxon Uplands constitutes the Palaeozoic basement complex of the Harz Mountains. A typical cuesta landscape of Mesozoic fault-block mountain ranges is developed in the Weser-Leine Uplands, where deep-cut river valleys also characterize the regional relief conditions.

Landslides occur in the Lower Saxon Uplands almost every year. Their types and mechanisms are often complex, but most widespread are shallow slide processes in soil material. Such as landslide volume, which usually is <300 m³, but can reach up to 500,000 m³ in case of large slope movements, landslide velocity varies strongly, ranging from creeping to extremely rapid movement (Klose et al.

2012). In general, landslide activity is controlled by different predisposing factors. Besides mechanical soil properties and structural bedrock parameters, high soil moisture levels and human slope modification play a major role in landslide initiation (Damm et al. 2010).

Methods

General Overview and Limitations on Regional Levels

Landslide susceptibility modeling on the basis of GIS and bivariate statistics usually follows a standardized workflow with several milestones (Aleotti and Chowdhury 1999). Most of them and their different steps find their way into the present research design, but must be partly modified, since the regional focus has a major influence on the investigation process and its efficient organization. In general, input data are, like model formulization, always less than perfect, a fact that is especially on regional levels of key importance (Klose et al. 2014).

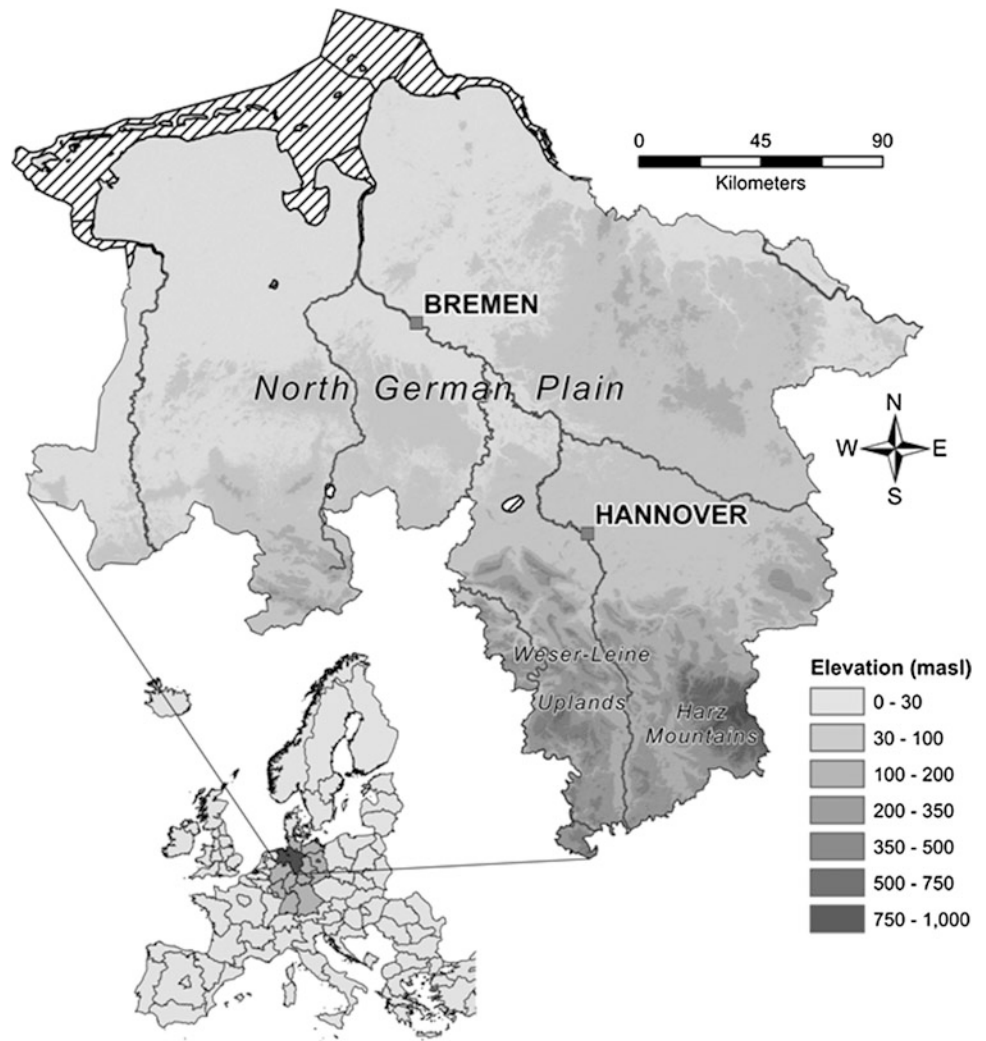
Information Sources and Input Data Generation

This study uses information on landslide occurrence stored in a landslide database (Damm 2013) and extracted from historical landslide distribution maps. The available data sets are compiled in a spatial landslide inventory that includes the geographic coordinates of 889 landslide sites in the Lower Saxon Uplands and adjacent lowland areas. Information on geomorphometry is derived from the ASTER Global Digital Elevation Model (ASTER GDEM), whereby slope gradient, plan curvature, and slope aspect are explicitly considered in the analysis. Lithology is represented in the model on the basis of a generalized geologic map (>1:500,000), which differentiates the major types of Palaeozoic basement and Mesozoic sedimentary rock. Furthermore, the model integrates basic land-use data of five different land-use categories, including forest, grassland, arable land, and urban area.

Geofactor Weighting Using an Information Value Approach

The modeling technique applied for geofactor weighting is known as the Information Value method (Yin and Yan 1988). In this approach, an information value I is calculated as a numerical weight for each geofactor attribute $A(i)$. The value of $I_{A(i)}$ describes the contribution of $A(i)$ to former

Fig. 1 Location and physiographic overview of the Federal State of Lower Saxony, NW Germany (derived from ASTER GDEM, a product of METI and NASA)



landslide occurrence and can be expressed in terms of probability as follows (Wang and Sassa 2005):

$$I_{A(i)} = \frac{P\{B/A(i)\}}{P\{B\}} \quad (i = 1, 2, 3, \dots, n) \quad (1)$$

where $P\{B/A(i)\}$ is the landslide probability in the presence of $A(i)$ and $P\{B\}$ is the overall landslide probability. Since a probability concept is problematic in a data-driven approach, frequency statistics are used to specify this probabilistic relationship. Therefore, (1) is converted to an expression of the following form (modified after Yin and Yan 1988):

$$I_{A(i)} = \ln \frac{N_{A(i)}/S_{A(i)}}{N/S} \quad (i = 1, 2, 3, \dots, n) \quad (2)$$

where $N_{A(i)}$ is the number of landslides in attribute class $A(i)$, N is the number of landslides in the entire territory, $S_{A(i)}$ is

the total area of attribute class $A(i)$, and S is the total area of the entire territory. Thus, (2) derives $I_{A(i)}$ by opposing the landslide density of a certain factor attribute to that of the entire study area. In consequence, attributes having positive values of $I_{A(i)}$ are likely to promote instability, while otherwise their influence can be interpreted as negative. It holds that the higher the value of $I_{A(i)}$ the stronger this relationship (Wang and Sassa 2005).

The geofactor weights are used to calculate the final susceptibility index $SI(x)$ that describes the landslide predisposition of the basic mapping unit. $SI(x)$ is defined as the sum of all values of $I_{A(i)}$ in a defined grid cell x and can be computed as follows (modified after Wang and Sassa 2005):

$$SI(x) = \sum \ln \frac{N_{A(i)}/S_{A(i)}}{N/S} \quad (i = 1, 2, 3, \dots, n) \quad (3)$$

Special Modifications for Regional Applications

The modifications of this modeling approach intend to simplify both data processing and interpretation. To meet the specific requirements on regional levels, the weighting function uses landslide densities based on attribute areal coverage, whereby landslide pixel mapping is replaced by point representation. This concept localizes each landslide site by a single data point, reducing its spatial extent to the area of only one grid cell. The geocoding of large slope movements is based on the spatial reference of the main scarp or the top of the displaced mass. Subsequently, landslide density is derived by putting the number of landslides per attribute class in relation to the areal coverage of the respective attribute. The obtained density values clearly reveal the spatial landslide significance, providing easily interpretable data on the amount of landslides per km².

Results

Landslide Controlling Factors and Susceptibility Classes

This specific model setup leads to the result that slope gradient is identified to be the major controlling factor of slope instability in Lower Saxony (Table 1). A majority of landslides occurs at slope gradients between 0° and 49°, where slopes between 21° and 49° are found to be critical. The analysis reveals that slopes with a high degree of plan curvature show a substantial tendency to landslides. Slope aspect is proven to be a controlling factor of only subordinate relevance. Most landslides are related to Mesozoic sedimentary rock, especially the attribute classes sand-/limestone and clay-/limestone, which have a strong positive effect on landslide occurrence. Alternatively, greywacke/clay shale and Quaternary lowland deposits are ascertained to be negatively associated with slope instability. More than 70 % of the recorded landslides are located in forest areas, which results in a positive information value. While the effects of urban land use are estimated to be widely negligible, grassland and arable land show clear stabilizing influence and are negatively correlated with landslide occurrence.

The value of the susceptibility index ranges from -7.09 to 12.10 and is displayed in the final map in four categories, namely no, low, moderate, and high predisposition. In this study, an expert-based classification is complemented with the technique of equal intervals. The scaling of the susceptibility levels by comparative data analysis recommends setting the lower boundary of landslide susceptibility to a value of 3.00. Index values above this threshold suggest a significant landslide predisposition, whose levels are specified by using three different classes with equal intervals. This guarantees

Table 1 Information values calculated for the attribute classes of the considered geofactors

| Geofactors and attribute classes $A(i)$ | Information value $I_{A(i)}$ |
|---|------------------------------|
| Geomorphometry | |
| Slope gradient | |
| 0°–7° | -1.71 |
| 7°–14° | 0.01 |
| 14°–21° | 2.43 |
| 21°–28° | 4.07 |
| 28°–35° | 4.69 |
| 35°–42° | 4.85 |
| 42°–49° | 4.72 |
| 49°–90° | 0.00 |
| Slope curvature | |
| <i>Strong convex</i> | 3.22 |
| <i>Convex</i> | 0.05 |
| <i>No curvature</i> | -1.00 |
| <i>Concave</i> | 0.13 |
| <i>Strong concave</i> | 2.65 |
| Slope aspect | |
| <i>N</i> | 0.17 |
| <i>NO</i> | 0.27 |
| <i>O</i> | 0.29 |
| <i>SO</i> | -0.10 |
| <i>S</i> | -0.10 |
| <i>SW</i> | -0.04 |
| <i>W</i> | -0.02 |
| <i>NW</i> | -0.11 |
| <i>No aspect</i> | 0.00 |
| Lithology | |
| Quaternary lowland deposits | -2.56 |
| Marlstone | 0.52 |
| Clay-/limestone | 2.69 |
| Sand-/limestone | 1.31 |
| Greywacke/clay shale | -1.01 |
| Granite | 0.00 |
| Land use | |
| Forest | 1.05 |
| Grassland | -0.95 |
| Arable land | -1.82 |
| Urban area | 0.40 |
| Other land use type | 0.00 |

coherent class occupancy and finally results in a less conservative delineation of landslide susceptibility zones.

Spatial Patterns and Key Areas of Landslide Susceptibility

The landslide susceptibility model estimates that about 2 % of the territory of Lower Saxony is potentially affected by mass movements (Fig. 2). A majority of this area belongs to the lowest landslide susceptibility class, which constitutes

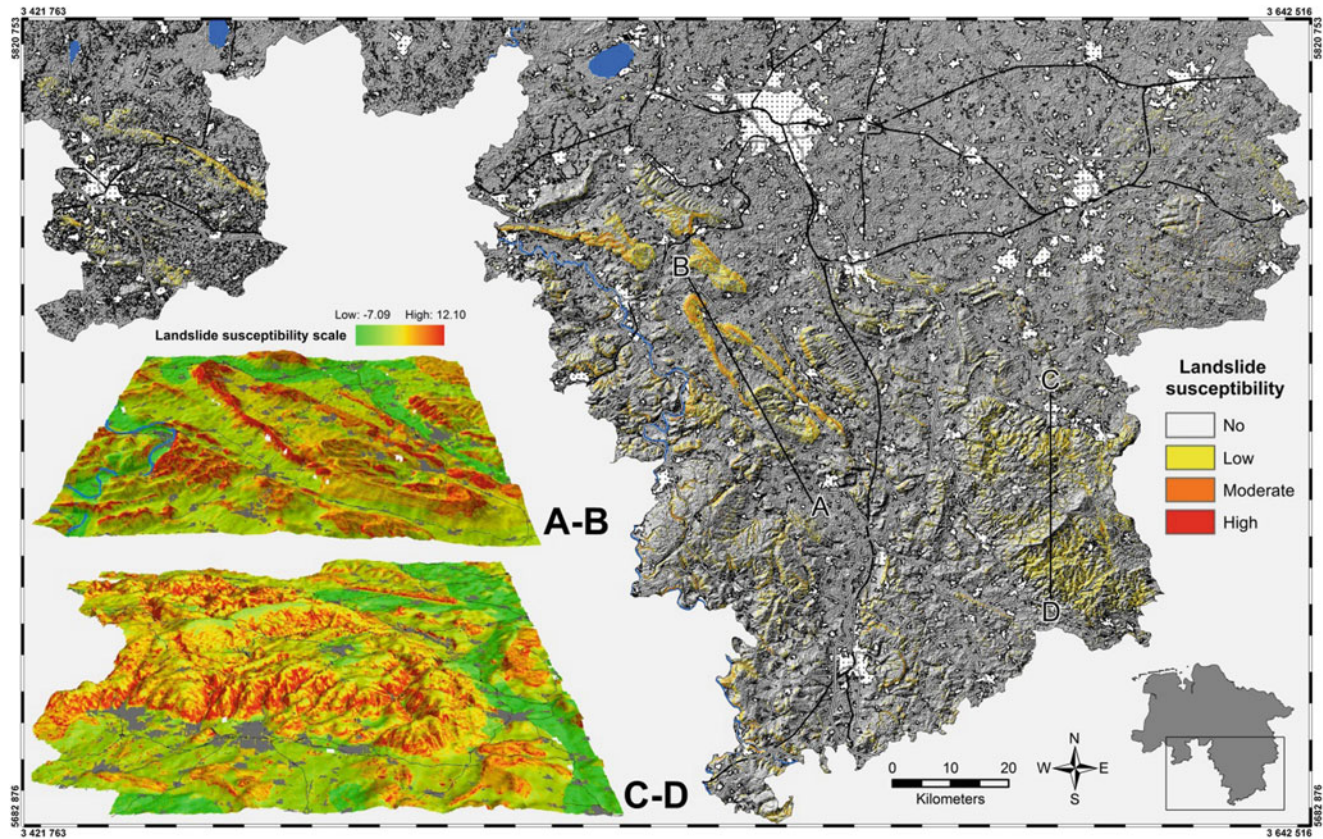


Fig. 2 Landslide susceptibility map for the Federal State of Lower Saxony. Slope instability is widely restricted to the Lower Saxon Uplands illustrated in detail. Two transects display the spatial patterns of landslide susceptibility in the Weser-Leine Uplands and the Harz

Mountains (base map derived from: ASTER GDEM, a product of METI and NASA; geodata provided by the Department of Geo-Information and Land Development of Lower Saxony LGLN)

77 % of the landslide-prone terrain. Moderate landslide predisposition refers to 22 % of the unstable ground. This corresponds to an area of about 200 km². In total, an area of more than 14 km² is identified to be of high landslide susceptibility.

In Lower Saxony, slope instability is widely determined by the spatial patterns of the regional relief configuration. Three key areas of significant landslide susceptibility can be differentiated: first, a zone of moderate to high landslide predisposition is present along the crests of the main scarps and ridges of the Weser-Leine Uplands; second, clusters of high spatial probability of landslide occurrence are located in the Weser river valley; and third, the Harz Mountains are a main landslide distribution area, where substantial landslide susceptibility can be found on many valley sides. In addition, there are isolated zones of high predisposition to landslides, whose locations yet do not follow clear spatial patterns.

Model Validation

The model validation is based on the concept of the success and prediction rate (Chung and Fabbri 2003). To perform the validation, the spatial landslide inventory was split into a modeling and validation set, whereby 15 % of the recorded landslides are classified to the validation set by random selection. The success rate measures how precisely the model reproduces the landslides of the modeling set. In total, 88 % of the landslides included in the model refer to the most susceptible 10 % of the study area. Alternatively, the prediction rate specifies how well the landslides of the validation set are predicted by the model. This rate identifies that 92 % of the independent landslides are located in the most unstable 10 % of the Lower Saxon territory. Both rates prove the accuracy of the model, but are no indicator of its general plausibility.

To test the conditional independence of the input data, contingency statistics and the χ^2 -test are used. A corrected

contingency coefficient of 0.59 proves a clear spatial association between slope gradient and land use. This is verified by the χ^2 -test, which rejects the null hypothesis, indicating that conditional independence is violated. The problem of data dependency is exclusively related to the correlation of these two geofactors.

Discussion

The proposed landslide susceptibility model is specially designed for investigations on large spatial scales, but even though its regional application leads to positive results, there are still enormous conceptual drawbacks. One key assumption of every statistical landslide susceptibility model is the conditional independence of its input data. Significant data dependency is tested to be existent between slope gradient and land use. This dependency is rarely addressed in literature, although land use patterns suggest its omnipresence, especially in Central Europe. However, this correlation is verified to have no vital impact on hazard zonation, as it only overestimates the total value of landslide susceptibility, but does not disturb the statistical relations in the susceptibility scale.

A regional perspective implies not only critical data limitation, but also requires special data properties. For example, medium- and large-scale geologic maps are often too precise in their lithological representation, as a high level of detail implicates many rock type classes showing low landslide frequency, wherefore useful correlations are hardly able to emerge. In this study, a generalized geologic overview map is most suitable, although it has the drawback that some lithological classes are not mutually exclusive. This conflicts with conditional independence, but has to be accepted, since no alternative data sources are available.

Usually, ASTER imagery shows general applicability in regional studies, but deficits in its spatial accuracy reduce model quality. As result of view and image geometry, slope gradient derived from such a DEM is negatively correlated to the size of its grid cells, which implicates a lack of topographic exactness, if applying a DEM with low to medium resolution (Zhang et al. 1999). This type of error is of high relevance, as cross-checking with ground truth data clarifies. In general, there is a systematic bias towards underestimating slope gradient, which primarily affects steep slopes in areas of high terrain variation. The analysis proves a negative deviation of up to 5° to 10° at some landslide sites, a serious error that needs to be addressed in future.

On regional levels, it finally raises the question of whether it is possible to achieve plausible modeling results when using slope gradient as the only input variable. Such an approach reduces the data requirements and simplifies the

investigation process. The validation of a respective model proves its capability for reliable landslide prediction for Lower Saxony. Thus, the slope-based susceptibility model reproduces the susceptibility model based on geomorphometry, lithology, and land use (Fig. 2) with almost 80 % accuracy, as the comparison of both success rates shows.

Conclusions

This study presents a modified Information Value approach, which is proven to have good predictive power and the capability to identify areas of potential slope instability with high spatial accuracy. The developed landslide susceptibility model is well-qualified for regional applications, as it provides an effective method to overcome some major data-related drawbacks on large spatial scales. Although the model is tested to yield results of positive reliability, the analysis reveals further conceptual limitations, which are of fundamental character.

References

- Aleotti P, Chowdhury R (1999) Landslide hazard assessment: summary review and new perspectives. *Bull Eng Geol Environ* 58:21–44
- Chung CJF, Fabbri AG (2003) Validation of spatial prediction models for landslide hazard mapping. *Nat Hazards* 30:451–472
- Damm B (2013) Landslide database for the Federal Republic of Germany, previous version: Database Mass Movements in German Subdued Mountains 1137–2013. August 2013, Univ. Vechta, Germany
- Damm B, Becht M, Varga K, Heckmann T (2010) Relevance of tectonic and structural parameters in Triassic bedrock formations to landslide susceptibility in Quaternary hillslope sediments. *Quaternary Int* 222:143–153
- Guzzetti F, Carrara A, Cardinali M, Reichenbach P (1999) Landslide hazard evaluation: a review of current techniques and their application in a multi-scale study, Central Italy. *Geomorphology* 31:181–216
- Klose M, Damm B, Gerold G (2012) Analysis of Landslide Activity and Soil Moisture in Hillslope Sediments using a Landslide Database and a Soil Water Balance Model. *GEO-ÖKO* 33(3–4):204–231
- Klose M, Gruber D, Damm B, Gerold G (2014) Spatial databases and GIS as tools for regional landslide susceptibility modeling. *Zeitschrift für Geomorphologie* 58:1–36
- Süzen ML, Doyuran V (2004) A comparison of the GIS based landslide susceptibility assessment methods: multivariate versus bivariate. *Environ Geol* 45:665–679
- Van Westen CJ, Van Asch TWJ, Soeters R (2006) Landslide hazard and risk zonation – why is it still so difficult? *Bull Eng Geol Environ* 65:167–184
- Wang HB, Sassa K (2005) Comparative evaluation of landslide susceptibility in Minamata area, Japan. *Environ Geol* 47:956–966
- Yin KL, Yan TZ (1988) Statistical prediction models for slope instability of metamorphosed rocks. In: Bonnard C (ed) *Proceedings of the 5th International Symposium on Landslides*, vol 2. Balkema, Rotterdam, pp 1269–1272
- Zhang X, Drake NA, Wainwright J, Mulligan M (1999) Comparison of slope estimates from low resolution DEMs: Scaling issues and a fractal method for their solution. *Earth Surface Process Landforms* 24:763–779



Regional Scale Landslide Susceptibility Mapping in Emilia Romagna (Italy) as a Tool for Early Warning

Daniela Lagomarsino, Samuele Segoni, Riccardo Fanti, Filippo Catani, and Nicola Casagli

Abstract

The Emilia Romagna region (22,446 km², Northern Italy) is widely affected by landslides. The Civil protection Agency of the Emilia Romagna Region uses a regional scale warning system (WS) for the management of the risk related to rainfall induced landslides. The WS is used to perform a temporal forecasting of landslides, as it provides an alert level for each of the eight subdivisions (called alert zones—AZ) of the regional territory.

To improve the spatial information of the WS, we developed a susceptibility map and we tested the feasibility of coupling the temporal forecasting of the WS with the spatial forecasting of the susceptibility map.

To map the landslide susceptibility at regional scale, we adopted a simple implementation of the Random Forest (RF) classification family. Random forest is a combination of tree (usually binary) Bayesian predictors that allows relating a set of contributing factors with the actual landslides occurrence. As a non-parametric model, it is possible to incorporate a wide range of numeric or categorical data layers and there is no need to select unimodal training data.

Many classical and widely acknowledged landslide predisposing factors have been taken into account as mainly related to lithology, land use and morphometry (primary and secondary attributes derived from the DTM). The use of random forest enabled us to estimate the relative importance of the single input parameters and to select the optimal configuration of the regression model: an automated procedure selected the optimal configuration of parameters discarding the uninfluential and the pejorative ones. To develop the susceptibility map we considered the parameter set characterized by the lowest misclassification probability. To calibrate the model we used a training set and a test set considering the 10 % of the study area with random sampling. Following this approach we obtained a regional scale susceptibility map with 100 m resolution.

We verified that the majority of the landslides forecasted by the WS in the past 7 years (this dataset is completely independent from the one used for the susceptibility assessment) occurred in areas mapped as highly (53 %), very highly (26 %) or moderately (19 %) susceptible to landsliding. Therefore, we concluded that the regional scale susceptibility map can be fruitfully exploited by Civil Protection Authorities to better focus their efforts in case of warnings issued by the regional warning systems.

Keywords

Landslide susceptibility • Rainfall thresholds • Early warning

D. Lagomarsino (✉) • S. Segoni • R. Fanti • F. Catani • N. Casagli
Earth Science Department, University of Firenze, Via La Pira 4,
Florence 50126, Italy
e-mail: daniela.lagomarsino@unifi.it

Introduction

Given the large amount of casualties and damages caused in the world by landslides (Petley 2012), the forecasting of their occurrence by means of warning systems is a largely discussed research topic. However, when the area to be monitored is large (e.g. thousands of square kilometres), it is not straightforward to perform at the same time both spatial and temporal forecasting. Regional scale warning systems are often based on statistical rainfall thresholds, which can be easily implemented to forecast the temporal occurrence of landslides (Caine 1980; Aleotti 2004; Guzzetti et al. 2008; Rosi et al. 2012). The main drawback of this methodology is a poor resolution of the spatial forecasting: thresholds are applied to the whole areal extent encompassing the events used for calibration, without giving hints about the specific location of future landslides initiation. To refine the spatial resolution of such models, in recent years some authors (e.g. Martelloni et al. 2012) proposed a mosaic of several local thresholds instead of a single regional threshold: this approach leads to relate the warnings to a more restricted areal extent, but cannot guarantee to an accurate localization of the landslides. Conversely, landslide susceptibility maps are static instruments that define for a given area the predisposition of the territory to be affected by a landslide (Brabb 1984). In other words, susceptibility maps are used to assess where a landslide should be expected, but they do not contain any temporal information about when a landslide will occur. Several methods were implemented to assess susceptibility maps: most of them are based on classification and regression techniques, such as discriminant analysis (Carrara 1983; Baeza and Corominas 1996), logistic regression (Hosmer and Lemeshow 2000; Lee 2005; Manzo et al. 2012), linear regression (Atkinson and Massari 1998) or Bayesian methods (Yilmaz 2010). In this work we used a simple implementation of Random Forest (Breiman 2001), a methodology that only recently has been applied to landslide susceptibility assessments (Vorpahl et al. 2012; Catani et al. 2013). The integration between the susceptibility map and the warning system of the Emilia Romagna region (Martelloni et al. 2012; Lagomarsino et al. 2013) is used in this work to test the possibility to improve the spatio-temporal forecasting of landslides within regional scale early warnings.

Material and Methods

Study Area

The study area is the Emilia Romagna region (Northern Italy), excluding the alluvial Po plain, a flat territory located to the North-East (Fig. 1).

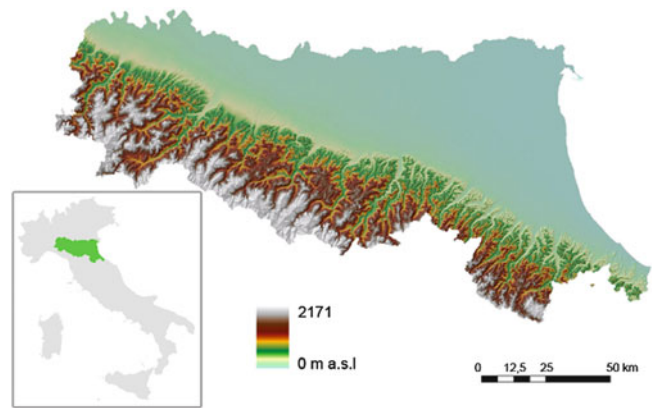


Fig. 1 Study area

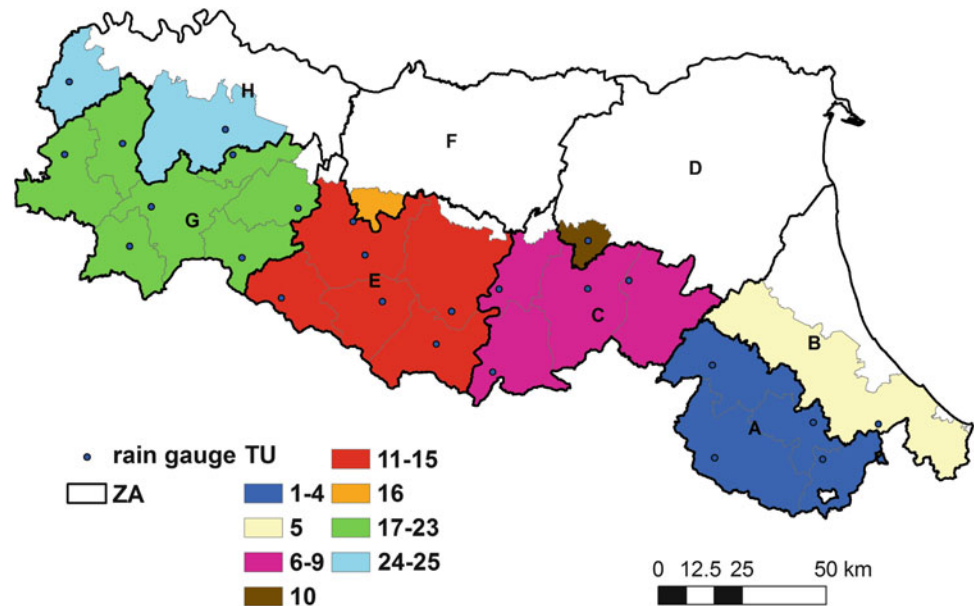
The area is dominated by the Apennines, a folds and trusts belt with a maximum elevation of 2,165 m, which from a geological point of view is mainly constituted by turbidite deposits where layers of massive rock (mainly sandstones and calcarenites) alternate with layers of pelites and where both kinds of layers have a very variable thickness (ranging from centimetres to hundreds of metres). Other very frequent lithologies are clayey lithologies and evaporites. The study area is widely affected by both shallow (soil slips and rapid flows) and deep-seated landslides (mainly rotational–translational slides, slow earth flows, and complex movements).

Temporal Forecast Model

The Civil Protection Agency of the Emilia Romagna Region uses a regional scale warning system for the management of the risk related to rainfall-induced landslides, called SIGMA (Sistema Integrato Gestione Monitoraggio Allerte). The model is based on the concept that exceptionally intense or exceptionally long rainfalls are responsible for triggering landslides (Martelloni et al. 2012; Lagomarsino et al. 2013) and also accounts for snow-melt phenomena (Martelloni et al. 2013).

The operative system divided the regional territory into eight districts, called Alert Zones (AZ), each of these is subdivided into several Territorial Units (TU), defined on the basis of different physiographic and environmental features. For each TU a reference rain gauge is selected: its historical daily recordings were collected and used to build the time series of rainfall cumulates from 1 to 243 days (Fig. 2). A statistical analysis is then carried out in order to define rainfall thresholds based on outlier rainfall values, quantitatively identified by multiples of the standard deviation. The decisional algorithm at the core of the model is based on the comparison between rainfall recordings and the abovementioned thresholds: the model provides a daily

Fig. 2 SIGMA warning system configuration



criticality level for each TU using the four alert levels adopted in the civil protection procedure: “absent”, “ordinary”, “moderate” and “high” (Martelloni et al. 2012; Lagomarsino et al. 2013). The outputs of the TU belonging to the same Alert Zone are aggregated according to a procedure described in Lagomarsino et al. (2013): for each TU a weight is calculated dividing the area affected by landslides with respect to the landslide area of the whole alert zone. The alert zone level is determined by adding the level of each TU multiplied by its weight: a value from 0 to 3 is obtained and it is then related to the alert level used by the Civil Protection Agency.

An alert level for an entire alert zone is obtained, as required by civil protection procedures. The SIGMA warning system can be conveniently used to forecast the temporal occurrence of landslides, but as similar threshold-based models, has a very coarse spatial resolution, as warning levels are issued for each TUs, which have a typical areal extent of about 500 km². To get more detailed information about where an event will occur, a more accurate spatial prediction analysis is required.

Susceptibility Map

To develop the regional susceptibility map, we used a simple implementation of the random forest (RF) classification family, based on the *treebagger* object in Matlab. Random forests are an ensemble learning method for classification that work by constructing a multitude of Bayesian decision trees considering a random selection of training dataset, applying bootstrapping technique (Breiman 2001). The data excluded from the construction of the model are called out-of-bag. Compared to traditional methods it has the

advantage of being able to consider as landslide conditioning variables (LCVs) both numerical and categorical variables, regardless of the statistical distribution of the values of the various parameters. Furthermore, the application of this methodology allows evaluation of the contribution of each parameter to the classification: for any variable, the measure is the increase in classification if the values of that variable are permuted across the out-of-bag observations (Liaw and Wiener 2002; Bachmair and Weiler 2012). The choice of the type and the number of the input parameters is a fundamental step in the susceptibility assessment process (Carrara and Guzzetti 1995; Guzzetti et al. 1999; Pradhan and Lee 2010; Manzo et al. 2012; Catani et al. 2013). In this work we used the LCVs described in Table 1.

The source data are represented by a cell of 20 × 20 m: to perform the calculation of the susceptibility, the average value inside a cell 100 × 100 m is calculated. For each of these parameters were also calculated the standard deviation for numeric variables and the variety for the categorical ones, always inside a window of 100 × 100 m, considering the variability of 25 cells.

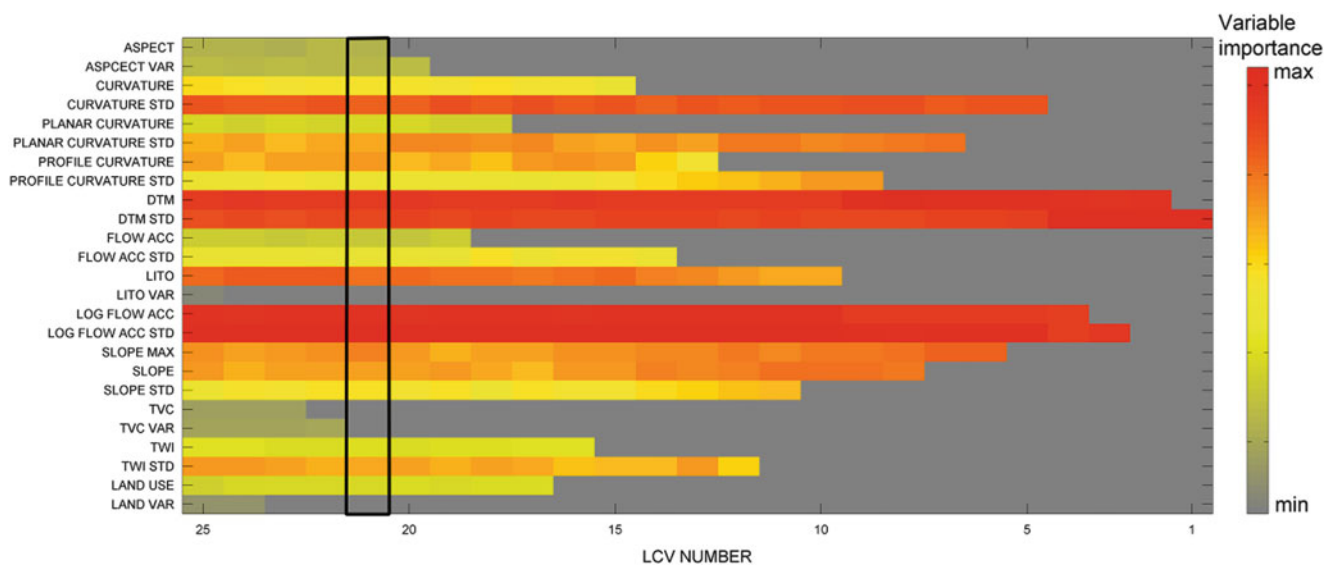
Furthermore, we used the Italian Landslide Inventory—Progetto IFFI (Inventario dei Fenomeni Franosi in Italia), that collects on a national scale about 486,000 landslides: regarding the Emilia Romagna region the mapping was carried out at the 1:10,000 scale, for a total of 70,037 landslides.

Relying on Catani et al. (2013), it was decided to use 10 % of the points of the area for the training set and 10 % for the test: both sets of points were randomly sampled.

To find the optimal configuration of the parameter set, the training set is used to build the model with the complete LCV set, then, iteratively, the least important feature is removed from the parameter set. Each feature subset is applied to the test set: we chose the configuration which

Table 1 Landslide conditioning variables

| Input parameter | Description |
|---------------------------------|--|
| Elevation | DEM value |
| Elevation STD | DEM standard deviation |
| Slope mean | Mean value of slope within a 100 m cell |
| Slope max | Maximum value of slope within a 100 m cell |
| Slope STD | Slope standard deviation |
| Curvature | The second derivative of elevation computed in every direction |
| Curvature STD | Curvature standard deviation |
| Profile curvature | The second derivative of elevation computed in the direction of maximum slope |
| Profile curvature STD | Profile curvature standard deviation |
| Planar curvature | The second derivative of elevation computed orthogonally to the direction of the maximum slope |
| Planar curvature STD | Planar curvature standard deviation |
| Combo curvature | Categorical variable obtained by the combination of planar and profile curvature: 9 different classes are possible |
| Combo curvature variety | Combo curvature variety |
| Aspect | Categorical variable that represents the orientation in the space. It is divided into 9 classes that represent the main 8 cardinal directions and one class for flat areas |
| Aspect variety | Aspect variety |
| Flow Accumulation | The upslope contributing area |
| Flow accumulation STD | Flow accumulation Standard deviation |
| Log Flow Accumulation | Logarithm of the flow accumulation |
| Log Flow Accumulation STD | Log Flow Accumulation Standard deviation |
| Topographic Wetness Index (TWI) | $\ln(\text{Flow accumulation}/\tan \text{ slope})$ |
| TWI STD | TWI standard deviation |
| Lithology | The geological formations are divided into 8 classes |
| Lithology Variety | Lithology variety |
| Land Cover | The land cover is represented by 9 different classes |

**Fig. 3** Importance of LCVs: for each iteration of feature selection. The *black box* highlights the best configuration

involves the lowest value of misclassification probability (MP) (Catani et al. 2013). The result of this operation is shown in Fig. 3, which represents the importance of the different variables to varying LCV number. At each iteration, the least important parameter is excluded from the model and it is shown in gray in figure. The

black box highlights the best configuration, which takes into account 21 LCVs and excludes the following LCVs: variety of lithology, combo curvature, combo curvature variety and land use variety. This configuration is characterized by the lowest MP value (0.21), computed on the test set.

Fig. 4 Susceptibility map of Emilia Romagna region. The TU of the SIGMA warning system are also reported

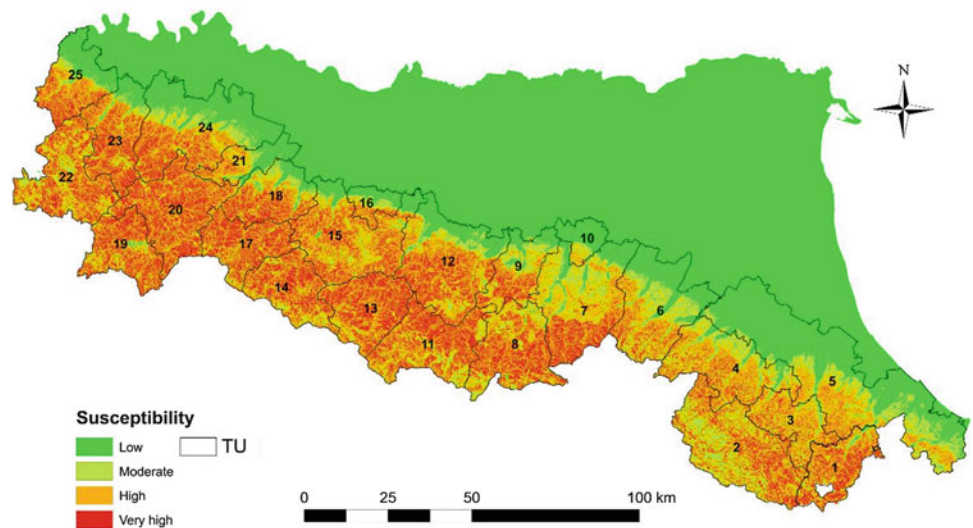
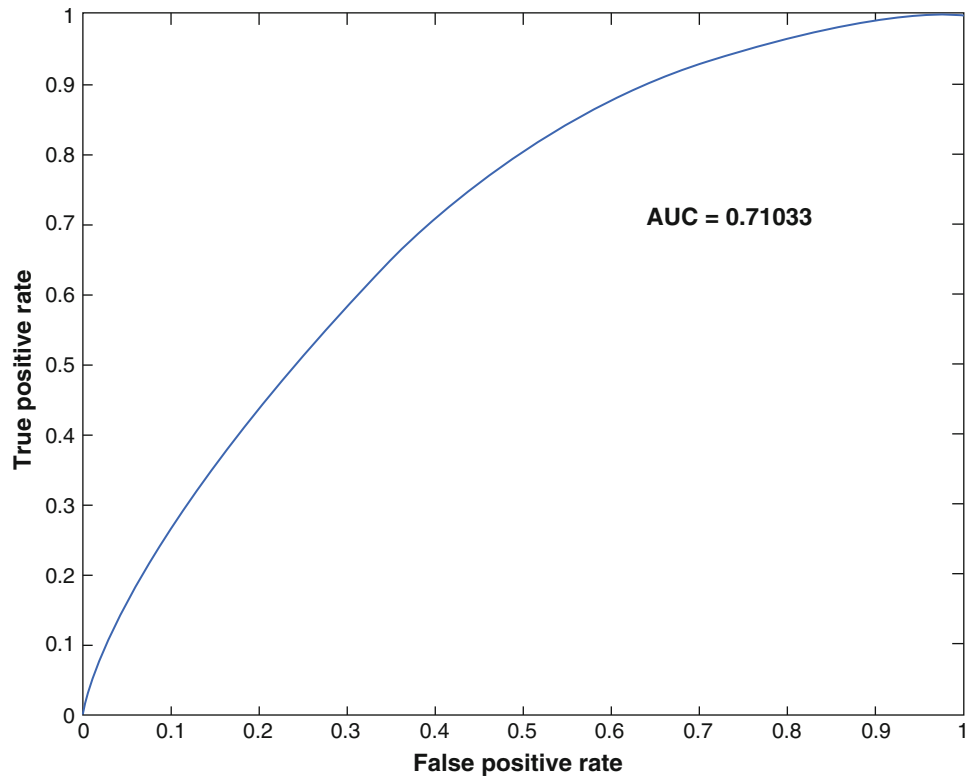


Fig. 5 ROC curve and AUC value



Results

The model returned for the whole Emilia Romagna Region a raster map in which the probability that a pixel belongs to the class “landslide” is represented by a continuous value between 0 and 1.

The values are then reclassified into four classes, obtaining the 100 m resolution susceptibility map showed

in Fig. 4. According to Frattini et al. (2010), we built a ROC (receiver operating characteristic) curve for the quantitative assessment of the susceptibility map. The ROC curve shown in Fig. 5 is obtained by comparing the landslides in the IFFI database and the susceptibility value in the whole area, and the AUC (Area Under Curve) value (0.71) indicates a good model performance.

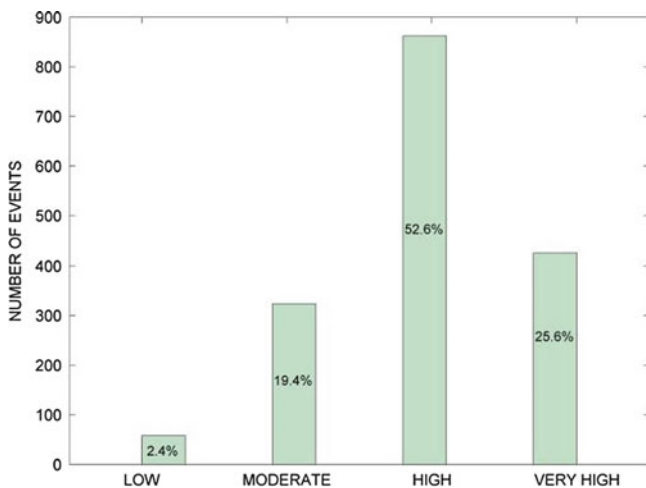


Fig. 6 Percentage of events falling in each susceptibility class

Discussion and Conclusion

The main goal of a susceptibility map is to represent where the territory is affected by landslides and where landslides could happen in the future. This information could be conveniently used in a warning system, as the susceptibility map could be used to identify the locations where, after a rainfall, dormant landslides may reactivate or where new mass movements may be triggered.

To verify the possibility and the usefulness of coupling the susceptibility map to the Emilia Romagna warning system, the database of the landslides recorded in the period 2004–2010 by the Civil Protection Agency has been used. This database contains the date of occurrence and the map reference points of 1,670 landslides; it is the same used to calibrate and validate the SIGMA model and with respect to the database used for the susceptibility assessment (the IFFI inventory) is completely independent and it was compiled using a different methodology. As a preliminary test of compatibility between the two methods, we analyzed the susceptibility class in which the landslides fall: the majority of landslides were located in a high susceptibility class (52.6 %), about 25 % of the events belong to the very high class, 19.4 % to the moderate class and only 2.4 % of the events were erroneously placed within the lower class (Fig. 6).

This preliminary analysis proves that the regional scale susceptibility map can be fruitfully exploited by Civil Protection Authorities to better focus their efforts in case of warnings issued by the regional warning system: instead of issuing an alert in a whole alert zone (typical extent of about 500,000 km²), the susceptibility map could be used to identify the locations characterized by the highest probability of being affected by the

triggering of a new landslide or by the reactivation of a dormant one.

References

- Aleotti P (2004) A warning system for rainfall-induced shallow failures. *Eng Geol* 73:247–265
- Atkinson PM, Massari R (1998) Generalized linear modeling of susceptibility to landsliding in the central Apennines, Italy. *Comput Geosci* 24:373–385
- Bachmair S, Weiler M (2012) Hillslope characteristics as controls of subsurface flow variability. *Hydrol Earth Syst Sci Discuss* 9:6889–6934
- Baeza C, Corominas J (1996) Assessment of shallow landslide susceptibility by means of statistical techniques. In: Balkema AA (ed) *Proceedings of the seventh international symposium on landslides*, Trondheim, Norway, June 17–21.1: 147–152
- Brabb EE (1984) Innovative approaches to landslide hazard mapping. In: *Proceedings 4th international symposium on landslides*, Toronto, 1, 307–324, 16–21 September 1984.
- Breiman L (2001) Random forests. *Machine Learn* 45:5–32
- Caine N (1980) The rainfall intensity–duration control of shallow landslides and debris flows. *Geogr Ann A* 62:23–27
- Carrara A (1983) Multivariate methods for landslide hazard evaluation. *Math Geol* 15(3):403–426
- Carrara A, Guzzetti F (1995) *Geographical information systems in assessing natural hazards*. Kluwer, Dordrecht, The Netherlands, 342 p
- Catani F, Lagomarsino D, Segoni S, Tofani V (2013) Exploring model sensitivity issues across different scales in landslide susceptibility. *Nat Hazards Earth Syst Sci Discuss* 1:583–623. doi:10.5194/nhessd-1-583-2013
- Frattini P, Crosta G, Carrara A (2010) Techniques for evaluating the performance of landslide susceptibility models. *Eng Geol* 111:62–72
- Guzzetti F, Carrara A, Cardinali M, Reichenbach P (1999) Landslide hazard evaluation: a review of current techniques and their application in a multiscale study, Central Italy. *Geomorphology* 31:181–216
- Guzzetti F, Peruccacci S, Rossi M, Stark CP (2008) The rainfall intensity–duration control of shallow landslides and debris flows: an update. *Landslides* 5(1):3–17. doi:10.1007/s10346-007-0112-1
- Hosmer DW, Lemeshow S (2000) *Applied logistic regression*. Wiley, New York
- Lagomarsino D, Segoni S, Fanti R, Catani F (2013) Updating and tuning a regional-scale landslide early warning system. *Landslides* 10(1):91–97
- Lee S (2005) Application of logistic regression model and its validation for landslide susceptibility mapping using GIS and remote sensing data. *Int J Remote Sens* 26(7):1477–1491
- Liaw A, Wiener M (2002) Classification and regression by random Forest. *R News* 2; 18–22
- Manzo G, Tofani V, Segoni S, Battistini A, Catani F (2012) GIS techniques for regional-scale landslide susceptibility assessment: the Sicily (Italy) case study. *Int J Geogr Inform Sci.* 1–20, ISSN:1365–8816
- Martelloni G, Segoni S, Fanti R, Catani F (2012) Rainfall thresholds for the forecasting of landslide occurrence at regional scale. *Landslides* 9(4):485–495
- Martelloni G, Segoni S, Lagomarsino D, Fanti R, Catani F (2013) Snow accumulation/melting model (SAMM) for integrated use in regional scale landslide early warning systems. *Hydrol Earth Syst Sci* 17:1229–1240
- Petley D (2012) Global patterns of loss of life from landslides. *Geology* 40(10):927–930

- Pradhan B, Lee S (2010) Landslide susceptibility assessment and factor effect analysis: backpropagation artificial neural networks and their comparison with frequency ratio and bivariate logistic regression modelling. *Environ Model Software* 25(6):747–759
- Rosi A, Segoni S, Catani F, Casagli N (2012) Statistical and environmental analyses for the definition of a regional rainfall thresholds system for landslide triggering in Tuscany (Italy). *J Geogr Sci* 22(4):617–629
- Vorpahl P, Elsenbeer H, Märker M, Schröder B (2012) How can statistical models help to determine driving factors of landslides? *Ecol Model* 239:27–39
- Yilmaz I (2010) Comparison of landslide susceptibility mapping methodologies for Koyulhisar, Turkey: Conditional probability, logistic regression, artificial neural networks, and support vector machine. *Environ Earth Sci* 61(4):821–836. doi:[10.1007/s12665-009-0394-9](https://doi.org/10.1007/s12665-009-0394-9)



GIS-Based Probabilistic Analysis of Shallow Landslide Susceptibility Using a Transient Hydrogeological Model and Monte Carlo Simulation

Jung-Hyun Lee and Hyuck-Jin Park

Abstract

This study proposes a GIS-based probabilistic analysis method for rainfall-induced shallow landslide susceptibility over an extensive area by integrating a transient hydrogeological model with a Monte Carlo simulation. The geomechanical parameters (such as cohesion and friction angle) used in the slope model have been considered as random variables due to the uncertainty and variability caused by complex geological conditions and spatial variability. Therefore, to properly account for the uncertainty in geomechanical parameters, a probabilistic analysis method should be used and Monte Carlo simulation was used in this study. In addition, the transient hydrogeological model was coupled with an infinite slope model to assess the pore-pressure response caused by transient rainfall infiltration. This process was performed in GIS-based environments, since GIS has strong spatial data processing capacity. The proposed approach was applied to the Inje area, Korea, which experienced a large number of landslides in July 2006, in order to evaluate its feasibility. The spatial database for input parameters and the landslide inventory map were constructed in a grid-based GIS environment. To evaluate the performance of the model, the results of the landslide susceptibility assessment were compared with the landslide inventory using receiver operating characteristics (ROC) graphs. The proposed approach demonstrated good predictive performance when compared with landslide occurrence locations. In addition, the probabilistic analysis showed better performance than the deterministic analysis.

Keywords

GIS • Infinite slope model • Transient hydrogeological • Monte Carlo simulation

Introduction

Landslides are a common geological hazard experienced during the rainy season in Korea. They cause the loss of on average 23 lives each year, which accounts for nearly 25 % of annual casualties due to natural disasters. Therefore, prediction of the location and time for rainfall-induced shallow landslide occurrence is an important but difficult task. This is because the occurrence of landslides is controlled

by various spatial and climatic factors. Therefore, GIS (Geographic Information System) has been widely used to analyze susceptibility to landslides or their hazards because GIS has a strong capability for processing spatially distributed data.

GIS-based landslide hazard assessment methods can be divided into two categories: statistical methods and process-based (or geotechnical) approaches. The statistical methods analyze the statistical relationship between landslide occurrences and related factors, such as soil type, land use, slope geometry, vegetation and parent material. However, statistical methods only consider relationships between landslide occurrences and related factors, but not the failure mechanisms. In contrast, the process-based approach

J.-H. Lee • H.-J. Park (✉)
Department of Geoinformation Engineering, Sejong University, 98
Gunja-dong, Gwangjin-gu, Seoul, Republic of Korea
e-mail: fraivent@gmail.com; hjpark@sejong.ac.kr

analyzes the mechanical condition of slopes and evaluates their stability using mathematical calculations. In this approach, the physical properties of a particular slope are obtained from investigations and tests, and a physically based model is used to evaluate landslide susceptibility. Most recent physically based models are combined with a hydrogeological model to evaluate the effect of pore water pressure, which increases as a consequence of rainfall and finally triggers shallow landslides.

In the physically based model, sufficient and accurate information has to be obtained to construct an accurate landslide susceptibility map. However, the input parameters used in this approach should be obtained from a very wide study area, often with limited sampling; thus, uncertainties are inevitably involved in the physically based model analysis. In particular, the strength parameters of slope materials, such as cohesion and friction angle, are inherently spatially heterogeneous, as the slope material is produced by natural processes (Baecher and Christian 2003; Carrara et al. 2008; Chowdhury et al. 2010). Therefore, to deal properly with the uncertainty and variability in input parameters for the physically based model analysis, the probabilistic analysis method was used, considering the strength parameters as random variables in this study. Therefore, Monte Carlo simulation was used for the probabilistic analysis, with GIS integration. The proposed approach was applied to assess the feasibility of the approach and to build a landslide susceptibility map for the study site.

Infinite Slope Model and Hydrogeological Model

The infinite slope model has been used as a physically based model for rainfall-induced shallow landslides in many previous works because of its effectiveness in landslide hazard analysis (Pack et al. 1998, 2001; Frattini et al. 2004; Huang et al. 2006; Rosso et al. 2006; Godt et al. 2008; Picarelli et al. 2008; D'Amato Avanzi et al. 2009; Harp et al. 2009; Apip et al. 2010; Griffiths et al. 2011; Santoso et al. 2011; Ho et al. 2012; Park et al. 2013). According to the National Institute for Disaster Prevention (NIDP 2000), this model is also appropriate for Korean landslides, where sliding surfaces are commonly located at shallow depths. The infinite slope model has been used previously in site-specific studies, but the adoption of GIS allows the analysis, modeling and spatializing of slope stability conditions using this simple geotechnical model for a broad area (Park et al. 2013).

The factor of safety for an infinite slope can be calculated as:

$$FS = \frac{c' + (\gamma \cdot z - \gamma_w \cdot h_w) \cos^2 \alpha \tan \phi'}{\gamma \cdot z \cdot \sin \alpha \cdot \cos \alpha} \quad (1)$$

where α is the slope angle, γ is the unit weight of soil, γ_w is the unit weight of water, z is the soil depth from the ground surface, h_w is the saturated soil thickness above the slip surface, c' is the effective cohesion and ϕ' is the effective friction angle (Coduto et al. 2010). For simplicity, (1) assumes that the groundwater level in an infinite slope is parallel to the surface and located at h_w .

However, an increase of groundwater level ultimately causes slope failure; thus, knowledge of the groundwater level is important for predicting and preventing slope instability. It is practically impossible, however, to measure the groundwater levels over an extensive area. Therefore, for analysis of the pore water pressure regime, the present study used a hydrological model that can evaluate rainfall-driven pore water pressure and can be coupled to the infinite slope model. The hydrogeological model uses analytical solutions for the pore water pressure response to rainfall and can be used for shallow landslide hazard analysis. The hydrogeological model can be classified into two categories on the basis of the simplifying assumption: steady and transient models. The steady model assumes that rainfall infiltration is at its steady state, and saturated water flows parallel to the slope surface. In contrast, the transient model performs transient seepage analysis using the linearized solution of Richards' equation (Iverson 2000; Baum et al. 2002). In this study, the transient model was used because it provides more realistic analysis results. In particular, this study used the TRIGRS (Transient Rainfall Infiltration and Grid Based Regional Slope stability analysis) model, which was developed to account for the transient effects of rainfall on shallow landslide initiation and combines an analytical solution for groundwater flow in one vertical dimension with an infinite slope stability calculation (Baum et al. 2002, 2008; Savage et al. 2004).

Monte Carlo Simulation

As mentioned previously, uncertainties are inevitably involved in the determination of the strength parameters because of the very large size of the study area and the limited number of samples. Therefore, applying the deterministic approach to an extensive study area can be particularly difficult or impossible because of the uncertainties and difficulties in obtaining, checking and processing large spatial data sets (Zhou et al. 2003). For these reasons, the parameters should be considered as random variables rather than having single, deterministic values. Consequently, cohesion and friction angle were considered as random variables, and probabilistic analysis was employed to properly account for uncertainty and variability in input parameters.

The Monte Carlo simulation approach was used as the probabilistic approach in this study to analyze the

probabilistic properties of random variables and evaluate the probability of slope failure. The Monte Carlo simulation is known as the most complete probabilistic analysis, since all the random variables are represented by their probability density function and the probability of failure as the result of reliability analysis is represented by the probability density function. The advantages of Monte Carlo simulation are that it is relatively easy to implement on a computer and it can deal with a wide range of functions, including those that cannot be expressed conveniently in an explicit form (Baecher and Christian 2003). Therefore, in this study, Monte Carlo simulation was used in the evaluation of the probability of slope failure. In the simulation procedure, random numbers between zero and one were generated from a uniform distribution. Then, using the cumulative distribution of the probability density function for each variable, a unique value for each variable was selected randomly. The group of randomly selected parameters was combined with the fixed input data to generate a single random value for the factor of safety. This process was repeated 5,000 times to generate a sufficient number of different factors of safety.

Study Area and Spatial Database Construction

The Inje area of Korea was selected as a suitable test site for the proposed approach. The study site lies between latitudes $38^{\circ}3'3.93''\text{N}$ and $38^{\circ}15'58.55''\text{N}$ and longitudes $128^{\circ}11'48.81''\text{E}$ and $128^{\circ}18'8.99''\text{E}$. The prevalent geological unit exposed in the study area is Mesozoic Inje granite. On 15–16 July 2006, this area experienced heavy rainfall of 322.5 mm, and over 800 landslides were reported.

The accurate detection of landslide locations is important for landslide susceptibility analysis. For this work, aerial photographs taken before and after the landslides were used to detect event locations. For the analysis, digital aerial photographs with a ground resolution of 50 cm were obtained from Samah Aerial Survey Co. Ltd and the National Geographic Information Institute (NGII) of Korea.

Digitized terrain information is used to acquire the slope angle as a geometric attribute. To achieve this, using 1:5,000 scale topographic maps, a digital elevation model (DEM) with a 10 m resolution was constructed. Using the DEM, the slope angle and specific contributing areas for groundwater flow were calculated. Further, the soil thickness in the study area was acquired from 1:25,000 scale digital soil maps produced by the National Institute of Agricultural Science. In addition, a geological map was used to obtain the contributing lithology.

In this study, the requisite geotechnical and hydrogeological soil parameters were obtained from laboratory tests for the study area. Soil samples were collected from

the landslide occurrence locations in each geological unit. For each sampling location, six to nine soil samples were obtained for the laboratory tests and direct shear tests were performed to obtain shear strength parameters for each soil type. Laboratory permeability tests were also performed for hydraulic conductivity of the ground materials. The unit weights of each soil type were also obtained from laboratory tests. However, as mentioned in previous works (Chowdhury and Flentje 2003; Zhou et al. 2003; Xie et al. 2004; Shou and Chen 2005; Huang et al. 2006; Zolfaghari and Heath 2008; Griffiths et al. 2011), cohesion and friction angle of slope materials were considered to be the major sources of uncertainty because of spatial variability and limited sampling. Thus, in the probabilistic analysis, cohesion and friction angle were considered as random variables. To quantify their random properties, the means and standard deviations for cohesion and friction angle were evaluated from the results of laboratory testing. In addition, the probability density functions were estimated based on results published by others (Hoek 2007). Previous studies have noted that cohesion and friction angle were usually normally distributed (Mostyn and Li 1993; Lacasse and Nadim 1996; Nilsen 2000; Zhou et al. 2003; Pathak and Nilsen 2004; Park et al. 2005; Liu and Wu 2008; Zolfaghari and Heath 2008; Wang et al. 2010, Melchiorre and Frattini 2011; Park et al. 2012, 2013). Thus, a normal distribution was used as the probability density function for cohesion and friction angle in this study.

The precipitation input for the hydrogeological model, such as rainfall intensity, is one of the most important parameters to be obtained. Rainfall intensity values for the hydrogeological model were obtained from the Inje automatic weather system, which is located at latitude $38^{\circ}3'\text{N}$ and longitude $128^{\circ}10'\text{E}$, the closest and most representative rain gauge in the study area. The rainfall intensity for the study area was obtained from the hourly rainfall records during the rainstorm on 15–16 July 2006 (Fig. 1).

Evaluation of Model Performance

In landslide susceptibility analysis, model validation is a fundamental step in determining model performance. Validation refers to comparing the model predictions with the real-world data set to assess the accuracy or predictive power (Begueria 2006). In this study a receiver operating characteristics (ROC) graph was used to assess the performance of models, because the ROC graph is a very useful tool for visualizing and evaluating model performance and provides a diagnostic that may be used to distinguish between two classes (true class and modeled class) of events (Swets 1988; Fawcett 2006). In ROC analysis, true class instances (observation or landslide occurrence) are compared with modeled class instances (landslide prediction)

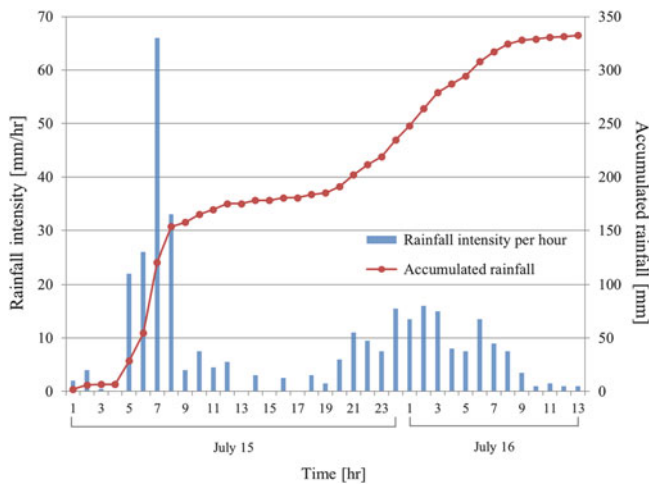


Fig. 1 Rainfall records of the rainstorm on 15-16 July 2006 in the Inje area

using a classification model. The observations are classified as positive or negative depending on whether they indicate occurrence or non-occurrence of a landslide. Predictions are classified as yes or no depending on whether they predicted ‘unstable’ or ‘stable’ conditions (Cepeda et al. 2010). Two important measures of model performance (true-positive rate and false-positive rate) are commonly used for model validation. The true-positive rate is the ratio of the number of true positives to the total number of positives, and the false-positive rate is the ratio of the number of false positives to the total number of negatives (Fawcett 2006). These two metrics are used to plot the ROC graph, which is a two-dimensional graph in which the true-positive rate is plotted on the y-axis and the false-positive rate on the x-axis. Model results that plot toward the upper left of the graph are generally considered superior on the ROC graph (Godt et al. 2008). Since an ROC curve is a two-dimensional depiction of model performance, a single scalar value representing the expected performance is needed to compare model performance. A common method is to calculate the area under the curve (AUC). Since the AUC is a portion of the area of the unit square, its value will always be between 0 and 1, and the larger the area, the better the model’s performance.

Results

The probabilistic analysis was conducted following the procedure using Monte Carlo simulation with the input parameters listed in Table 1. First, the groundwater levels for each pixel were calculated using the hydrogeological model and hydraulic input parameters. TRIGRS model

Table 1 Input parameters used in this study

| Geomechanical parameters | Mean | Standard deviation |
|---------------------------------|-------|--------------------|
| Unit weight [kN/m^3] | 15.4 | – |
| Cohesion [kN/m^2] | 7.6 | 5.2 |
| Friction [degree] | 31.5 | 5.5 |
| Hydraulic conductivity [m/h] | 0.046 | – |

calculates the groundwater level over time during the rainfall and the groundwater levels at 8 h were evaluated for each pixel with the consideration of landslide occurrence time. Then, the factor of safety was evaluated for each pixel using the slope geometry, groundwater levels, and the randomly generated cohesion and friction angle for each cell. Based on the repeated factor of safety calculations, the probability of failure for each pixel was obtained from the factor of safety distribution. Figure 2 shows the spatial distribution map for the probability of failure calculated using the coupled infinite slope model with TRIGRS model and Monte Carlo simulation. As can be seen in Fig. 3, 78.3 % of actual landslides (or the mapped landslides in the inventory map) were evaluated as unstable, meaning that the true-positive rate, which is the ratio of the number of correctly predicted landslide grid cells (true positives) to the total number of landslide occurrence grid cells (positives), was calculated as 0.784. In addition, 28.7 % of non-landslide grid cells were predicted as unstable, which means that the false-positive rate was 0.287. Thus, the evaluated AUC from the ROC graph in Fig. 3 was 0.748.

To compare the results of the probabilistic and deterministic analyses, a deterministic analysis was also conducted on the basis of the factor of safety concept. In the deterministic analysis, the infinite slope model with TRIGRS model was used, and the same deterministic input parameters (e.g., slope angle and soil thickness) were used to evaluate the factor of safety. In addition, mean values of the random variable (e.g. cohesion and friction angle) were used as the representative single values for the deterministic analysis. Figure 4 shows the spatial distribution map for the factor of safety calculated using the coupled infinite slope model with TRIGRS model. As can be seen in Fig. 3, true-positive rate and false-positive rate values were evaluated as 0.498 and 0.163, respectively. Then AUC was evaluated as 0.667. As can be seen in Fig. 3, the point of the probabilistic analysis in the ROC graph would be located closer to the (0,1) position than that of the deterministic analysis. In addition, the AUC value of the probabilistic analysis was higher. Consequently, when the results of the probabilistic analysis coupled with the hydrogeological model were compared with those of the deterministic analysis coupled with the hydrogeological model, the performance of the probabilistic analysis was superior.



Fig. 2 Probability of failure evaluated using rainfall intensity of rainstorm after 8 h

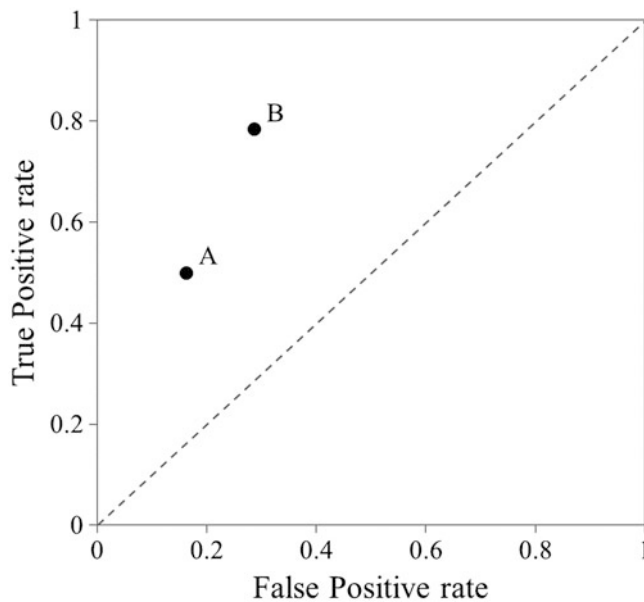


Fig. 3 ROC graph comparing with (a) the deterministic analysis and (b) probabilistic analysis



Fig. 4 Factor of safety evaluated using rainfall intensity of rainstorm after 8 h

Acknowledgments This research was supported by the Public Welfare & Safety Research Program through the National Research Foundation of Korea (NRF) funded by the Ministry of Science, ICT & Future Planning (2012M3A2A1050984).

References

- Apip TK, Yamashiki Y, Sassa K, Ibrahim AB, Fukuoka H (2010) A distributed hydrological-geotechnical model using satellite-derived rainfall estimates for shallow landslide prediction system at a catchment scale. *Landslides* 7(3):237–258
- Baecher GB, Christian JT (2003) *Reliability and statistics in geotechnical engineering*. Wiley, 605p
- Baum RL, Savage WZ, Godt JW (2002) TRIGRS: a fortran program for transient rainfall infiltration and grid based regional slope stability analysis. U.S. Geological Survey, Colorado. Open-File Report 02-0424, 35p
- Baum RL, Savage WZ, Godt JW (2008) TRIGRS- A Fortran program for transient rainfall infiltration and grid based regional slope-stability analysis, Version 2.0. U.S. Geological Survey
- Begueria S (2006) Validation and evaluation of predictive models in hazard assessment and risk management. *Nat Hazards* 37:315–329
- Carrara A, Crosta GB, Frattini P (2008) Comparing models of debris-flow susceptibility in the alpine environment. *Geomorphology* 94 (3–4):353–378
- Cepeda J, Chavez JA, Martinez CC (2010) Procedure for the selection of runout model parameters from landslide back analyses: application to the Metropolitan area of San Salvador, El Salvador. *Landslides* 7:105–116
- Chowdhury R, Flentje P (2003) Role of slope reliability analysis in landslide risk management. *Bull Eng Geol Environ* 62(1):41–46
- Chowdhury R, Flentje P, Bhattacharya G (2010) *Geotechnical slope analysis*. CRC Press, 737p
- Coduto DP, Yeung MR, Kitch WA (2010) *Geotechnical engineering: principles and practices*, 2nd edn. Pearson, 814p
- D'Amato Avanzi G, Falaschi F, Giannecchini R, Puccinelli A (2009) Soil slip susceptibility assessment using mechanical-hydrological approach and GIS techniques: an application in the Apuan Alps. *Nat Hazards* 50(3):591–603
- Fawcett T (2006) An introduction to ROC analysis. *Pattern Recognition Lett* 27:861–874
- Frattini P, Crosta GB, Fusi N, Dal Negro P (2004) Shallow landslides in pyroclastic soils: a distributed modeling approach for hazard assessment. *Eng Geol* 73(3):277–295
- Godt JW, Baum RL, Savage WZ, Salciarini D, Schulz WH, Harp EL (2008) Transient deterministic shallow landslide modeling: requirements for susceptibility and hazard assessments in a GIS framework. *Eng Geol* 102(3):214–226
- Griffiths DV, Huang J, Fenton GA (2011) Probabilistic infinite slope analysis. *Comput Geotech* 38(4):577–584
- Harp EL, Reid ME, McKenna JP, Michael JA (2009) Mapping of hazard from rainfall-triggered landslides in developing countries: examples from Honduras and Micronesia. *Eng Geol* 104(3):295–311
- Ho JY, Lee KT, Chang TC, Wang ZY, Liao YH (2012) Influence of spatial distribution of soil thickness on shallow landslide prediction. *Eng Geol* 124:38–46
- Hoek E (2007) *Rock engineering: course note by Evert Hoek*. URL: <http://www.rockeng.utoronto.ca/Hoekcorner.htm>.
- Huang JC, Kao SJ, Hsu ML, Lin JC (2006) Stochastic procedure to extract and to integrate landslide susceptibility maps: an example of mountainous watershed in Taiwan. *Nat Hazard Earth Syst Sci* 6 (5):803–815
- Iverson RM (2000) Landslide triggering by rain infiltration. *Water Resour Res* 36(7):1897–1910
- Lacasse S, Nadim F (1996) Uncertainties in characterizing soil properties. *Geotech* 58(Special Publ):49–75
- Liu C, Wu C (2008) Mapping susceptibility of rainfall-triggered shallow landslides using a probabilistic approach. *Environ Geol* 55:907–915

- Melchiorre C, Frattini P (2011) Modeling probability of rainfall-induced shallow landslides in a changing climate, Otta, Central Norway. *Climate Change*. doi:10.1007/s10584-011-0325-0
- Mostyn GR, Li KS (1993) Probabilistic slope analysis - state of play. In: *Proceeding of conference on probabilistic method in geotechnical engineering*. pp 89–109
- NIDP (National Institute for Disaster Prevention) (2000) *Fundamental issues for landslide hazard avoidance or mitigation plans*. Research Report. 276p. in Korean
- Nilsen B (2000) New trend in rock slope stability analysis. *Bull Eng Geol Environ* 58:173–178
- Pack TT, Tarboton DG, Goodwin CN (1998) The SINMAP approach to terrain stability mapping. In: *Proceedings of 8th congress of the international association of engineering geology*, Vancouver, B.C., Canada. pp 1157–1165
- Pack TT, Tarboton DG, Goodwin CN (2001) Assessing terrain stability in a GIS using SINMAP. 15th Annual GIS Conference, GIS, 2001
- Park HJ, West TR, Woo I (2005) Probabilistic analysis of rock slope stability and random properties of discontinuity parameters, Interstate Highway 40. *Eng Geol* 79:230–250
- Park HJ, Um JG, Woo I, Kim JW (2012) Application of fuzzy set theory to evaluate the probability of failure in rock slopes. *Eng Geol* 125:92–101
- Park HJ, Lee JH, Woo I (2013) Assessment of rainfall-induced shallow landslide susceptibility using a GIS-based probabilistic approach. *Eng Geol* 161:1–15
- Pathak S, Nilsen B (2004) Probabilistic rock slope stability analysis for Himalayan condition. *Bull Eng Geol Environ* 63:25–32
- Picarelli L, Olivares L, Avolio B (2008) Zoning for flowslide and debris flow in pyroclastic soils of Campania Region based on infinite slope analysis. *Eng Geol* 102(3):132–141
- Rosso R, Rulli MC, Vannucchi G (2006) A physically based model for the hydrologic control on shallow landsliding. *Water Resour Res* 42(6), W06410. doi:10.1029/2005WR004369
- Santoso AM, Phoon KK, Quek ST (2011) Effects of soil spatial variability on rainfall-induced landslides. *Comput Struct* 89(11):893–900
- Savage WZ, Godt JW, Baum RL (2004) Modeling time dependent areal slope stability. In: Lacera WA, Erlich M, Fontoura SAB, Sayao ASF (eds) *Landslide evaluation and stabilization*. Proceedings of 9th international symposium on landslides. Balkema, Rotterdam. pp 23–36
- Shou K, Chen Y (2005) Spatial risk analysis of Li-shan landslide in Taiwan. *Eng Geol* 80(3):199–213
- Swets J (1988) Measuring the accuracy of diagnostic systems. *Science* 240:1285–1293
- Wang Y, Cao Z, Au S (2010) Efficient Monte Carlo simulation of parameter sensitivity in probabilistic slope stability analysis. *Comput Geotech* 37(7):1015–1022
- Xie M, Esaki T, Zhou G (2004) GIS based probabilistic mapping of landslide hazard using a three dimensional deterministic model. *Nat Hazards* 33(2):265–282
- Zhou G, Esaki T, Mitani Y, Xie M, Mori J (2003) Spatial probabilistic modeling of slope failure using an integrated GIS Monte Carlo simulation approach. *Eng Geol* 68(3):373–386
- Zolfaghari A, Heath AC (2008) A GIS application for assessing landslide hazard over a large area. *Comput Geotech* 35(2):278–285



Collapse Landslide and Mudslides Hazard Zonation

Mingxue Liu, Xiang Chen, and Shanni Yang

Abstract

This paper aims at finding out the functional relationship between collapse landslide mudslides and its impact factors through statistical analysis under logistic regression model and certainty factor. This study tries to map hazard zonation according the level of risk of collapse landslide and mudslides occurring in Guizhou Province using GIS technology. The result shows that the hazard zonation method based on logistic regression model and certainty factor for collapse landslide and mudslides is effective.

Keywords

Collapse • Landslide • Mudslides • Logistic regression model • Certainty factor • Hazard zonation

Introduction

Hazard zonation is the basis of collapse landslide and mudslides forecasting and warning, it is to classify the possibility of collapse landslide and mudslides occurring within the research area (Wang and Zhong 2009). The collapse landslide and mudslides refers to geological disasters caused by natural causes, such rainfall, earthquake, rather than geological disasters caused by human, for example excavation.

The method of hazard zonation can be selected according to the size of research area and how detailed the information for the area. For smaller areas, if the details of the rock and soil are available, evaluation with appropriate physical model can be used; for larger areas, if the details of past collapse landslide and mudslides are abundant, a statistical model to evaluate it can be adopted (Wang et al. 2004).

Statistical analysis model is a kind of method for evaluating the risk of collapse landslide and mudslides occurring in larger areas by use of GIS technology (Zhang

and Zhang 1998). First, different thematic maps should be drawn to represent different impact factors by taking advantage of GIS spatial analysis; then mathematical operations can be done with different thematic maps, the new thematic map we get from the operation will be the result of collapse landslide and mudslides hazard zonation.

However, there are two problems in practical operation. One is that the weights of impact factors are influenced by humans, because they mainly rely on expertise: first is to decide the impact factor of hazard, and then determine impact factor weights by use of expert scoring method, finally complete hazard zoning with all impact factors with calculation and analysis (Miles and Ho 1999). Another problem is that heterogeneous data cannot enter mathematical calculations directly, this means that the impact factors of occurring collapse landslide and mudslides exist in various ways. Those can be either in continuous form, such as ground elevation; or in discrete form, such as rock type (Dai and Li 2000).

M. Liu (✉) • X. Chen • S. Yang
School of Civil Engineering, Beijing Jiaotong University, Beijing
100044, China
e-mail: 947531522@qq.com; chx1120@126.com; 825212414@qq.com

Theory and Method

To solve these two problems, the statistical analysis method based on the logistic regression model and certainty factor of collapse landslide and mudslides occurring is established in the paper.

Since the probability of the occurring disaster and its impact factors is not a continuous variable, linear regression model cannot be applied to this analysis. But log-linear model can be adopted according to the characteristics of this study, and logistic regression model is a special form of log-linear model (Wang and Guo 2001).

Logistic regression model can be expressed as following (Pan et al. 2009): Defining p as the probability of occurrence of an event, so the range of p is $[0, 1]$. Then $(1-p)$ is the probability of non-occurrence of an event. After calculating natural logarithm with the ratio of the two, so we can get $\ln [p/(1-p)]$. Using $\ln[p/(1-p)]$ as dependent variable, and impact factors x_i ($i = 1, 2, 3, \dots, n$) as independent variables, then we can get (1) referred to linear regression model as follow:

$$\ln \left(\frac{p}{1-p} \right) = B_0 + B_1x_1 + B_2x_2 + \dots + B_nx_n \quad (1)$$

where, B_0 is regression constant, B_i ($i = 1, 2, 3, \dots, n$) are regression coefficients. Then the (2) of p is as following:

$$p = \frac{\exp(z)}{1 + \exp(z)} = \frac{\exp(B_0 + B_1x_1 + B_2x_2 + \dots + B_nx_n)}{1 + \exp(B_0 + B_1x_1 + B_2x_2 + \dots + B_nx_n)} \quad (2)$$

The relationship between p and z is shown in Fig. 1. If the range of logistic regression independent variables is smaller, the range of z will be within $[-8, 8]$, the result of p is between 0.000 and 1.000; if the range of logistic regression independent variables is wider, resulting in $z < -8$ or $z > 8$, the p will be out of $[0.000, 1.000]$. To obtain the probability of collapse landslide and mudslides occurring, the impact factors must be transformed into data that are quantized to 0 and within $[-8, 8]$. Then it is the certainty factor that works with these characteristics.

As a probability function, certainty factor (CF) had been proposed by Shortliffe and Buchanan in the beginning, then improved by Heckeman (1986), and the expression is as (3).

$$CF = \begin{cases} \frac{PP_a - PP_s}{PP_a(1 - PP_s)}, & PP_a \geq PP_s \\ \frac{PP_a - PP_s}{PP_s(1 - PP_a)}, & PP_a < PP_s \end{cases} \quad (3)$$

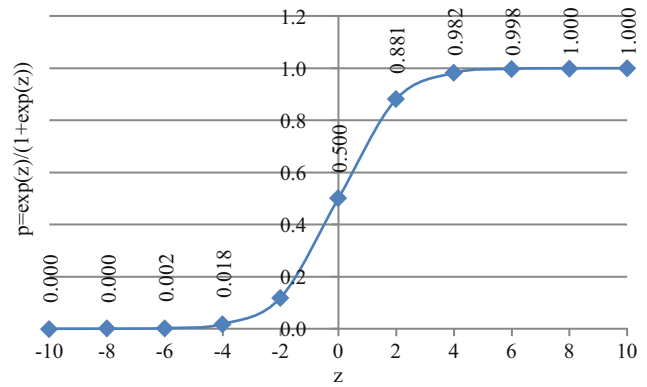


Fig. 1 Relationship between p and z

where, pp_a works as the conditional probability that event does occur in data class a , and can be defined as the ratio of occurred hazard area and the total area of data class a under this circumstances; pp_s is the priori probability that event does occur in all data class, and can be defined as the ratio of occurred hazard area and the area of all data class. The range of CF from (3) is $[-1, 1]$. If CF is closer to 1, it indicates that the probability of event occurring is greater, this means that the probability of occurring hazards is close to 1; If CF is closer to -1 , it indicates that the probability of event occurring is smaller, and this means the probability of occurring hazards is close to 0; If CF is equal to 0, it represents the priori probability is equal to the conditional probability and the event occurs or not cannot be determined, this means the probability of occurring hazards is 0.5.

So, the method is: First, a calculation of the certainty factor of collapse landslide and mudslides occurring is done according to the area of past landslides in impact factor subset and the area of impact factor subset; Second, defining the possibility of collapse landslide or mudslides occurring as dependent variable, defining the certainty factor of disaster occurring in subset as independent variable, and an analysis is done to find out the functional relationship between them using logistic regression model; Third, a calculation of the probability, p , of collapse landslide or mudslides occurring is initiated, trying to divide the research area into 10 risk level sub-area according to the p result with the aim to map the hazard zonation of collapse landslide and mudslides. Finally, an evaluation on the hazard zonation of collapse landslide and mudslides is carried out.

Impact Factor and CF Calculation

It is an important step in collapse landslide and mudslides hazard zonation to find out its impact factors. There is a wide range of impact factors that impact collapse landslide and mudslides in different ways. Those factors can be divided

Table 1 Subset of impact factors and CF value

| Impact factor | Subset | Area of subset (km^2) | Disaster area of subset (km^2) | CF |
|----------------------------|-----------|---------------------------|------------------------------------|--------|
| Class of rock and soil | I | 185.035 | 0.000 | -1.000 |
| | II | 285.539 | 0.000 | -1.000 |
| | III | 37,313.344 | 1.535 | -0.472 |
| | IV | 93,299.291 | 10.784 | 0.326 |
| | V | 44,958.020 | 1.391 | -0.603 |
| Slope ($^{\circ}$) | <7 | 35,432.641 | 2.457 | -0.110 |
| | 7 ~ 14 | 53,548.921 | 4.702 | 0.113 |
| | 14 ~ 21 | 43,940.520 | 3.690 | 0.072 |
| | 21 ~ 28 | 25,876.081 | 1.835 | -0.089 |
| | 28 ~ 35 | 11,624.400 | 1.021 | 0.114 |
| | >35 | 5,605.200 | 0.005 | -0.988 |
| Aspect ($^{\circ}$) | Flat | 394.560 | 0.000 | -0.987 |
| | North | 21,162.600 | 1.811 | 0.090 |
| | Northeast | 20,756.521 | 0.583 | -0.640 |
| | East | 22,793.400 | 1.719 | -0.032 |
| | Southeast | 24,316.201 | 0.109 | -0.942 |
| | South | 21,658.679 | 3.804 | 0.557 |
| | Southwest | 20,215.439 | 2.630 | 0.401 |
| | West | 21,233.879 | 1.965 | 0.159 |
| Elevation (km) | <0.6 | 18,348.841 | 3.173 | 0.550 |
| | 0.6 ~ 0.9 | 45,759.238 | 2.511 | -0.295 |
| | 0.9 ~ 1.3 | 62,924.399 | 2.191 | -0.553 |
| | 1.3 ~ 1.7 | 30,908.881 | 4.035 | 0.403 |
| | 1.7 ~ 2.3 | 16,609.680 | 1.800 | 0.281 |
| | >2.3 | 2,270.160 | 0.000 | -1.000 |
| Distance to river (km) | <1 | 51,445.582 | 10.132 | 0.605 |
| | 1 ~ 2 | 46,133.207 | 1.135 | -0.684 |
| | 2 ~ 4 | 54,372.264 | 1.974 | -0.534 |
| | 4 ~ 8 | 22,478.113 | 0.470 | -0.732 |
| | >8 | 1,612.064 | 0.000 | -1.000 |
| Distance to fault (km) | <2 | 59,921.348 | 2.929 | -0.372 |
| | 2 ~ 4 | 42,133.719 | 2.346 | -0.285 |
| | 4 ~ 10 | 54,294.201 | 5.862 | 0.279 |
| | 10 ~ 18 | 15,082.065 | 0.296 | -0.748 |
| | >18 | 4,609.896 | 2.278 | 0.842 |
| Vegetation | Arbor | 47,062.155 | 1.765 | -0.519 |
| | Bush | 24,837.175 | 0.549 | -0.716 |
| | Others | 104,141.899 | 11.396 | 0.288 |
| Intensity (degrees) | 5 | 85,431.543 | 3.938 | -0.408 |
| | 6 | 89,348.888 | 9.771 | 0.288 |
| | 7 | 1,260.797 | 0.001 | -0.992 |

into factors that reduce strength and factors that increase downward force according to the mechanical state. And those also can be divided into internal and external factors according to impacted ways (Yin and Zhu 2001).

In the paper, the Guizhou Province is defined as study area, and 8 main factors that can lead to the occurrence of collapse landslide and mudslides in the area are selected:

class of rock and soil, ground slope, ground aspect, ground elevation, distance to river, distance to fault, vegetation and seismic intensity. The total study area is 176,041.229 km^2 , with 356 recorded disasters for hazard zonation: total area of disasters is 13.710 km^2 . The classification of each subset impact factors and CF values are shown in Table 1.

Table 2 Results of logistic regression analysis

| Regression items | B | S.E. | Wald | df | Sig. |
|------------------------|--------|-------|--------|----|-------|
| Intensity | -0.317 | 0.260 | 1.482 | 1 | 0.223 |
| Slope | 0.175 | 0.543 | 0.104 | 1 | 0.747 |
| Elevation | 0.587 | 0.196 | 8.995 | 1 | 0.003 |
| Vegetation | 0.079 | 0.208 | 0.144 | 1 | 0.705 |
| Distance to river | 0.746 | 0.146 | 26.146 | 1 | 0.000 |
| Aspect | 0.398 | 0.190 | 4.383 | 1 | 0.036 |
| Class of rock and Soil | 0.158 | 0.202 | 0.610 | 1 | 0.435 |
| Distance to fault | 0.621 | 0.244 | 6.480 | 1 | 0.011 |
| Constant | 0.309 | 0.103 | 9.015 | 1 | 0.003 |

Table 3 Arrangement of |B|

| Impact factors | B | B /Σ B | Arrangement |
|------------------------|-------|--------|-------------|
| Distance to river | 0.746 | 24.2 % | 1 |
| Distance to fault | 0.621 | 20.2 % | 2 |
| Elevation | 0.587 | 19.1 % | 3 |
| Aspect | 0.398 | 12.9 % | 4 |
| Intensity | 0.317 | 10.3 % | 5 |
| Slope | 0.175 | 5.7 % | 6 |
| Class of rock and soil | 0.158 | 5.1 % | 7 |
| Vegetation | 0.079 | 2.6 % | 8 |

Sensitivity Analysis of Impact Factor

For a specific hazard zonation method, it is necessary to analyze the sensitivity of impact factor to lead to the disaster, that means know which factor has more influence on the disaster and which factors has less.

When we define 360 m × 360 m as basic cell size, and spatial analysis can be applied on impact factor thematic maps, so we will have 992 × 853 independent property units within the study area. If we select partial independent property units randomly, put CF value of impact factor as independent variable, the probability of collapse landslide and mudslides occurring as dependent variable (1 represents that hazard has occurred, and 0 represents that hazard has not occurred), then under regression analysis with logistic regression model, we will get the results of logistic regression analysis in Table 2. From left to right in Table 2, there are regression coefficients of the variables or constant (B), standard error (SE), Wald chi-square value (Wald), degrees of freedom (df) and significant (Sig.) respectively. In addition, the classification accuracy of observation is 62.8 %, and it means that the reliability of logistic regression equation is 0.628.

Since the value of each impact factor CF value is in the range of [-1, 1], so the absolute value of regression coefficient can be considered as impact factor weight, and then it can be used to analyze the sensitivity of impact factor. The greater absolute value of impact factor regression coefficient, the greater sensitivity is. The descending order of impact factor regression coefficient absolute value (|B|) is shown in Table 3.

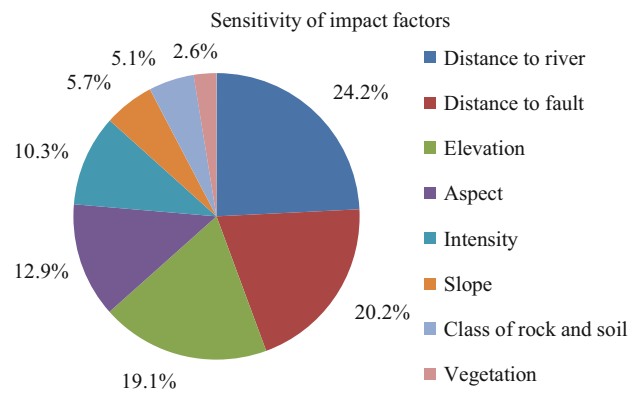


Fig. 2 Sensitivity of impact factors

According to the degree of influence, we can conclude that the descending order of 8 selected impact factors is: distance to river > distance to fault > elevation > aspect > intensity > slope > class of rock and soil > vegetation.

The percentage of each impact factor regression coefficient absolute value and sum of all impact factors regression coefficients absolute values is shown in Fig. 2. It shows that distance to river has the greatest influence on collapse landslide and mudslides hazard in the eight selected impact factors.

Hazard Zone Division

When taking the eight impact factors into the calculation model, we will get the logistic regression formula of the risk evaluation in the study area as following (4):

$$\begin{cases}
 p = \frac{\exp(z)}{1 + \exp(z)} \\
 z = 0.309 + 0.175x_1 - 0.317x_2 + 0.587x_3 \\
 + 0.394 + 0.158x_5 + 0.621x_6 + 0.079x_7 \\
 + 0.746x_8
 \end{cases} \quad (4)$$

where, p is the probability of occurring hazard, x_1 is CF values of slope, x_2 is CF values of intensity, x_3 is CF values of elevation, x_4 is CF values of aspect, x_5 is CF values of rock and soil class, x_6 is CF values of distance to fault, x_7 is CF values of vegetation, x_8 is CF values of distance to river.

According to (4), we can calculate the probability p of collapse landslide or mudslides occurring in Guizhou Province, further divide the total area into 10 equal parts according to p , and define as I, II ~ X hazard level from lower to higher. Hazard zonation is shown in Fig. 3, and the percentage of each risk level area in total area is shown in Fig. 4.

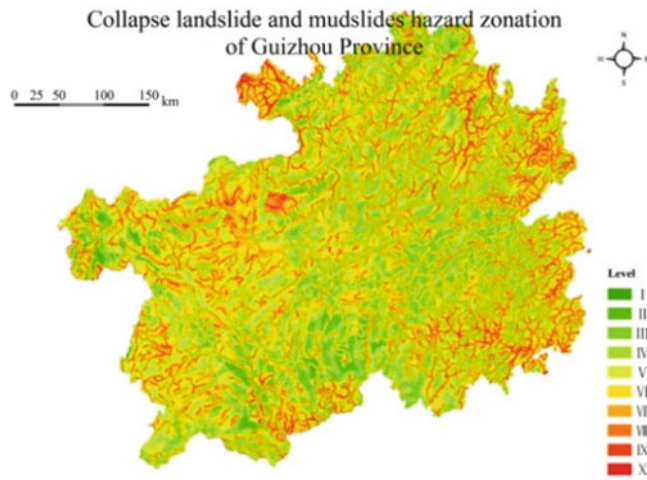


Fig. 3 Collapse landslide and mudslides hazard zonation of Guizhou Province

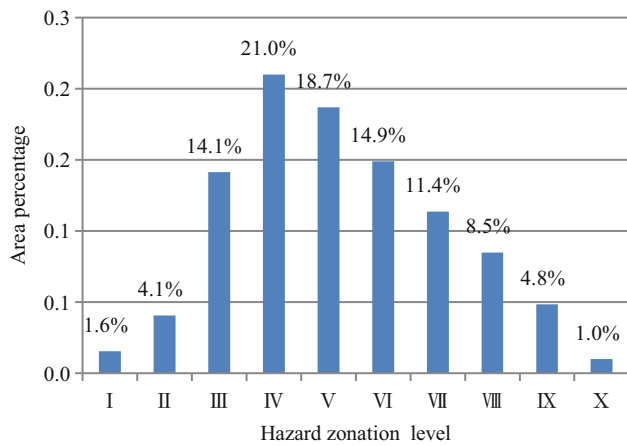


Fig. 4 Area percentage of each hazard zonation level

Effect Evaluation

The effect of hazard zonation can be illustrated from the percentage of hazard area in total area in each risk level zone. As shown in Fig. 5, the effect of the hazard zone division is sufficient in general.

In addition, the calculation of CF value of each risk level is able to indicate the difficulties of hazard occurrence in the zone. As shown in Fig. 6, from level I to level X, CF value transits from negative to positive overall this means that the probability of collapse landslide and mudslides occurring is

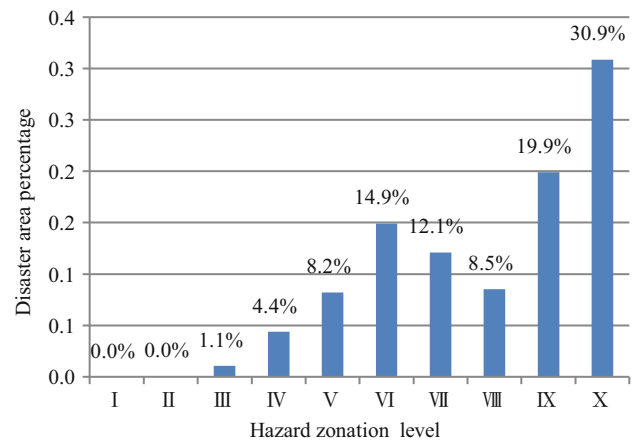


Fig. 5 Percentage of disaster area on each hazard zonation level

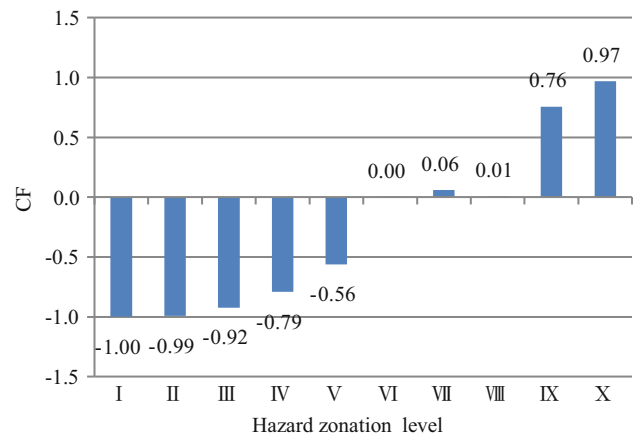


Fig. 6 CF value of each hazard zonation level

increasing, and the level of the risk zone is from lower to higher consecutively. This also means that the evaluation results align with the actual situation.

Conclusions

Even though the collapse landslide and mudslides hazard zonation of Guizhou Province is feasible, there are some problems in the method for collapse landslide and mudslides hazard zonation based on logistic regression model and certainty factor. These include the need for a large number of collapse landslide or mudslides records; need to determine the appropriate size of independent properties unit; need to divide numeric impact factors into subset artificially.

However it is an effective way to solve the problem of the weights of impact factors, which are influenced by human activity and because heterogeneous data cannot be used to perform mathematical calculations directly.

Acknowledgments The work was supported by National Natural Science Foundation of China (Project Grant No. 41002092) and the Fundamental Research Funds for Central Universities (2011JBM265).

References

- Dai F, LI J (2000) Applications of geographical information systems in landslide studies. *J Geol Sci Technol Inform* 19(1):91–96
- Heckeman (1986) Probabilistic interpretation of MYCIN's certainty factors. In: Kanal LN, Lemmer JF (eds) *Uncertainty in artificial intelligence*. Elsevier, New York, pp 298–311
- Miles SB, Ho CL (1999) Rigorous landslide hazard zonation using Newmark's method and stochastic ground motion simulation. *Soil Dynam Earthquake Eng* 18(4):305–323
- Pan Y, Cong W, Pan M (2009) Research on hazard zonation of debris flows in Xiuyan County, Liaoning Province based on GIS. *Scientiarum Naturalium Universitatis Pekinensis* 4:33–38
- Wang YQ, Wang L, Zhang X (2004) GIS based seismic landslide zonation of the Loess Plateau. *Scientia Geographica Sinica* 24(2): 170–176
- Wang J, Guo Z (2001) Methods and application of logistic regression model. Higher Education Press, Beijing, pp 1–12
- Wang W, Zhong S (2009) The application of GIS-based logistic regression for geological hazards zonation. *Geotech Investig Survey* 11: 5–10
- Yin K, Zhu L (2001) Landslide hazard zonation and application of GIS. *Earth Sci Front* 18(2):279–284
- Zhang L, Zhang Y (eds) (1998) *Assessment theory and practice of geological hazard*. Geological Publishing House, Beijing. ISBN 9571136468



Mapping and Management of Landslide Risk in the City of Azazga (Algeria)

Lynda Djerbal, Nassima Alimrina, Bachir Melbouci, and Ramdane Bahar

Abstract

The management of major landslides faces several difficulties especially when important stakes are exposed to risk. The landslide of the city Azazga is one of the most extensive cases observed in Algeria. This is an instability reactivated by specific climate events such as floods of 1974 and snow of 2012. Landslides affect the center town of the region of Azazga situated 20 Km East of Tizi-Ouzou (northern Algeria). They affect a highly urbanized area and endanger vital structures such as the regional hospital. Managing this risk requires the development of an effective management methodology as well as a good knowledge of site conditions, the causes and the extent of the landslide. To better characterize this extensive instability, a geographic information system was created for the study site. This GIS greatly facilitates the interpretation of spatial data.

The aim of this work is to investigate the potential risk posed by landslides in the city of Azazga. This potential is estimated from observations and exploration of the site using the method of Djerbal and Melbouci (2013). A risk management methodology is then developed for this site. The results obtained show that the very strong hazard affects a large area of the city Azazga.

Keywords

Landslides • Characterization • GIS • Mapping • Risk Management

L. Djerbal (✉)

Laboratory Geomaterials, Environment and Installations of Tizi-Ouzou (LGEA), BP. 15000 RP, Tizi-Ouzou, Algeria
e-mail: ldjrbal@yahoo.fr

N. Alimrina • R. Bahar

University of Sciences and Technology Houari Boumediene, BP 32 El Alia, 16111, Algiers, (LGEA), Tizi-Ouzou, Algeria
e-mail: alimnassima_2010@yahoo.fr; rbahar@usthb.dz

B. Melbouci

University Mouloud Mammeri of Tizi-Ouzou, (LGEA), BP. 15000 RP, Tizi-Ouzou, Algeria
e-mail: melbouciba@hotmail.fr

Introduction

The region Azazga is located about 20 km east of Tizi-Ouzou (Fig. 1). The city has experienced several instabilities of land since 1952 (L.C.T.P. 2006 and L.T.P.C. 1986). However, a period of calm was observed during the 1990s and up to 2002. The long period of snow of February 2012 caused the intense reactivation of some landslides in this site as well as the emergence of large buildings damages. Landslides affect moderate natural slopes (with an inclination of about 10° to 15°); this slope was highly urbanized in recent years. The stakes of this landslide are very heavy because it endangers several buildings and major infrastructure (such as the regional hospital, the Polyclinic, the national road number 12, etc). The potential hazard is evaluated for an area greater than 1,600 ha of the Azazga region (urban area) in this article. Several factors have acted in the initiation of the instabilities

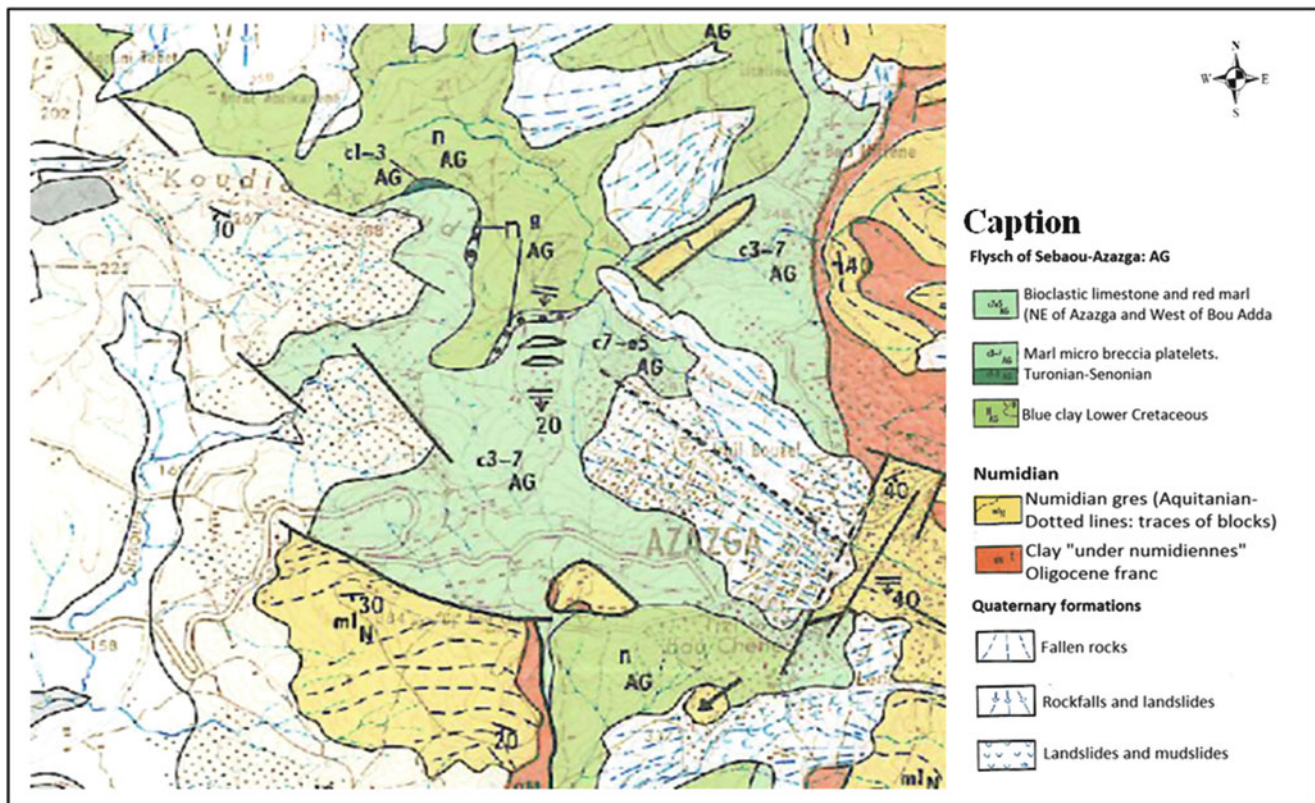


Fig. 1 Geological map of Azazga region (Touahri and Bitam 1997)

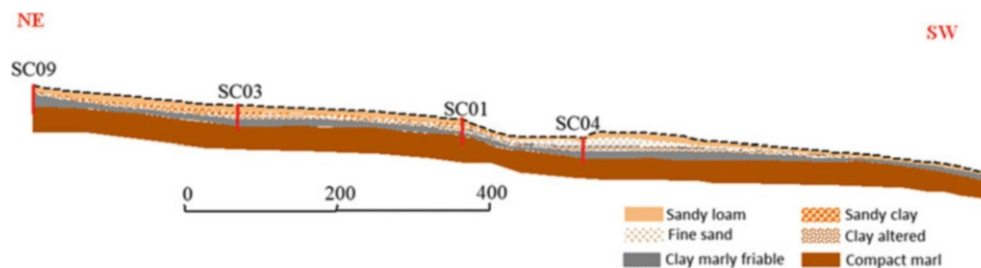


Fig. 2 Geological section of the slope from the centre city of Azazga

of Azazga. These are classic factors already characterized by several authors (Slosson et al. 1992; Azimi and Devarreaux 1996; Durville et al. 2003); which are water, man and geology (Guirous et al. 2013).

Geomorphological and Hydrological Context of the Region

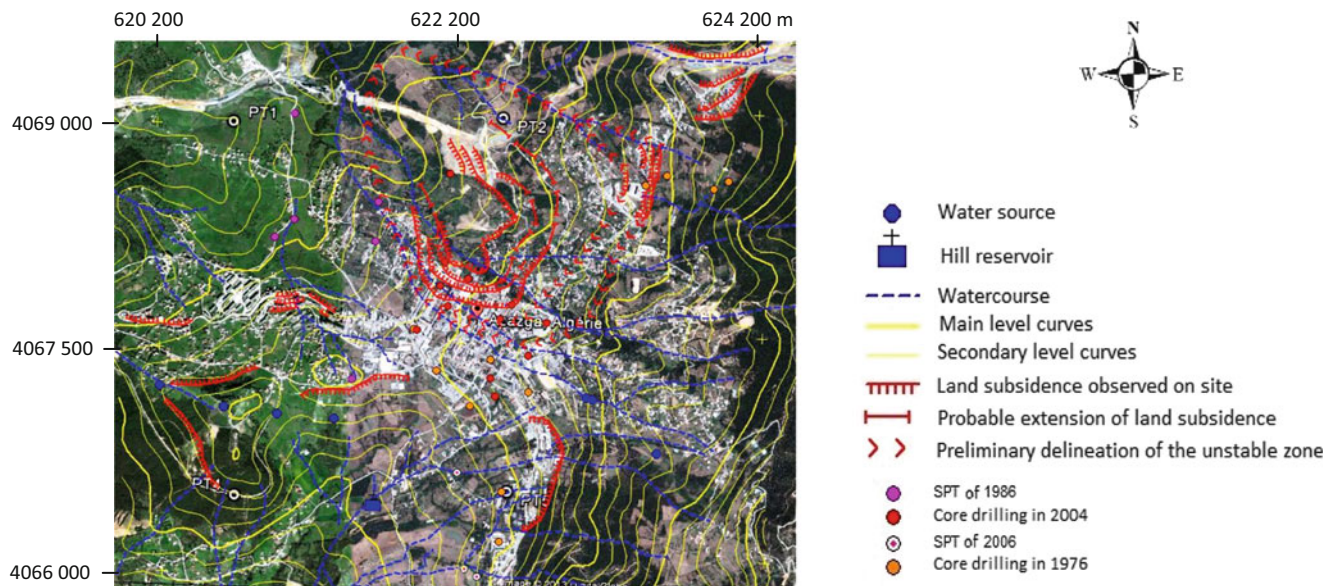
The municipality of Azazga is located, according to the geological map published by the National Office of Geological and Mining Research (ORGM) in 1997, in clayey and marly lands (flysch of Kabylia (Fig. 1)). Flysch are often

overcome by recent deposits consisting of scree and sandy clay. The recognition, conducted in this area during the construction of the various urban sites or the studies of instabilities, shows that the site is underlain by a multi-layer deposit, which has a dip oriented in the direction of the slope for each hillside that makes up this site (Fig. 2). The studied site consists of several juxtaposed hills characterized by low slopes (ranging from 10° to 15°), which are affected by several instabilities. The hydrology of the region, characterized by the presence of sources of water and a level of water close to the natural ground surface, has increased markedly these instabilities. The drainage of surface water being insufficient (the presence

Table 1 Summary results of the soil properties tests in the study region (according to the results of L.C.T.P. 2004)

| Parameters | Number of tests | Mean | Minimum | Maximum | Standard deviation | Variance | Coefficient of asymmetry | Flattening coefficient |
|-------------------------------------|-----------------|---------|---------|---------|--------------------|------------|--------------------------|------------------------|
| W (%) | 38 | 23.6115 | 13.17 | 43.00 | 6.26174 | 0.26519788 | 0.770002 | 1.278695 |
| γ_d (kN/m ³) | 38 | 16.2395 | 13.50 | 19.00 | 0.14122 | 0.08696175 | 0.158364 | -0.819910 |
| γ_{sat} (kN/m ³) | 38 | 19.9605 | 18.00 | 21.90 | 0.09630 | 0.04824391 | -0.032572 | -0.727150 |
| S_r (%) | 37 | 92.2678 | 80.14 | 100.00 | 6.44733 | 0.06987629 | -0.411857 | -0.930892 |
| C' (kPa) | 20 | 55.000 | 15.00 | 145.00 | 0.31197 | 0.5672212 | 1.560877 | 2.554404 |
| ϕ' (°) | 20 | 6.70000 | 3.00 | 14.00 | 2.97534 | 0.44408018 | 0.617043 | 0.336441 |
| W _L (%) | 38 | 54.7868 | 28.60 | 77.00 | 12.69816 | 0.23177395 | -0.199587 | 1.278695 |
| I _p (%) | 37 | 25.4708 | 14.28 | 37.76 | 6.37881 | 0.25043617 | 0.770002 | -0.819910 |

w: water content, γ_d : dry specific weight, γ_{sat} : saturated specific weight, S_r : saturation degree, C': cohesion, ϕ' : friction angle, w_L : liquidity limit, and I_p : plasticity index

**Fig. 3** Overview of the mapping of Azazga region




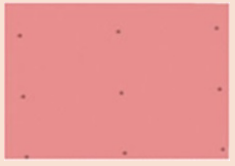

of only a few natural waterways), water easily penetrates in the surface layers of the ground (Quaternary deposits) which are very sensitive to water. The results of the recognition realized in this site show that the strength parameters of the shear surface are very low (L.C.T.P. 2004 and L.T.P.C. 1986). This explains the significant activity of landslides in this area. Moreover, statistical analysis of the results of different tests realized at Azazga shows that the physical properties of materials are characterized by spatial variability and very low. However, the mechanical properties, cohesion and friction angle, have a spatial variability of approximately 50 % (Table 1).

The climate of Azazga region is Mediterranean type characterized by a humid and rainy winters and hot, dry summer. It is also characterized by a significant snow cover, which sometimes reaches more than 1.50 m. These climatic conditions have significantly influenced the activity of landslides in the region. Indeed, reactivation of landslides coincides with exceptional climatic conditions.

Mapping of the Study Site

Geographic Information Systems are effective tools for the study of problems of geotechnical engineering, as they allow the management and geo-referencing of geographic information. To exploit the geographical data, which are incomplete and poorly located in the slope, a Geographic Information System was developed for the Azazga city and its surroundings (Fig. 3). This GIS includes data of different types (geological, morphological, geotechnical, hydrological...). The GIS allowed a good appreciation of site conditions and the mapping of instabilities observed since 2009 at this site. Analysis of the map in Fig. 3 has allowed identify a number of possible causes of sliding, as the complex hydrology of the area characterized by multiple sources of water (clogging of many of these sources). The mapping of the different land subsidence areas shows that landslides affect several slopes of this region. Six active

Table 2 Parameters of the risk model

| Index | Propriety | Map |
|---|---|---|
| Extent of signs of instability observed surface I_i | Three classes are distinguished for this parameter: high disorders $I_i = 3$, means disorders $I_i = 2$ and low disorders to no one $I_i = 1$ |  |
| Rate of change of movement I_v | Four classes defining the rate of evolution of the landslide are observed: very high speed $I_v = 4$ (metric displacement), high speed $I_v = 3$ (decimetre displacement), average speed $I_v = 2$ (millimetre to centimetre displacement) and low speed $I_v = 1$ (minimal or no movement) |  |
| Distribution of rupture I_r | Four classes are observed: very important movement $I_r = 4$ (four failure surfaces), significant movement $I_r = 3$ (tree or two failure surfaces), mean motion $I_r = 2$ (one failure surface), low motion $I_r = 1$ (no failure plane observed) |  |
| Direction of the dip layers I_p | Two types of dip: dip favouring instability $I_p = 2$ (oriented in the direction of the slope of the hillside) and dip that promotes stability $I_p = 1$ (perpendicular to the slope). However, in Azazga just one class of dip is observed ($I_p = 2$) |  |
| Hydrology of the site I_h | Two classes are distinguished to define the hydrology of Azazga region: a hydrology unfavourable to stability $I_h = 2$ (lack of water systems) and a hydrology conducive to stability $I_h = 1$ (presence of water systems); water systems facilitate the flow of rainwater, thus reducing infiltration into the slope |  |

landslides are observed at this site. In addition, the more active is the one that affects the city center, as it spawned during the reactivation of the winter of 2012, where ground displacements have affected an area of about 90 ha.

Assessment and Hazard Mapping Caused by Instabilities in the Azazga Region

The hazard created by landslides Azazga is estimated with the method of Djerbal and Melbouci (2013). It is a method based on the mapping of indices of landslide observed in situ and the monitoring of the movement evolution. The determination of levels of hazard by this method is carried out by performing a cross between slip risk and vulnerability of ground to this risk. In this case, it is the density of urbanization.

| classes | Level of risk | Risk |
|---------|---------------|-----------|
| Class 2 | (6 and 7) | Low |
| Class 3 | (8 to 10) | Medium |
| Class 4 | (11 to 13) | High |
| Class 5 | (14 and 15) | Very high |

Fig. 4 The classes of risk of the landslide in Azazga

Assessment and Mapping of the Risk Level

The evaluation of the hazard created by landslides requires knowledge of the risk of initiation or reactivation of these movements. The risk of slip is determined from field observations. This model has five parameters (Table 2):

Risk assessment requires mapping of the five parameters of the movement (with the designation of the different

Fig. 5 Mapping of the risk level in the Azazga region

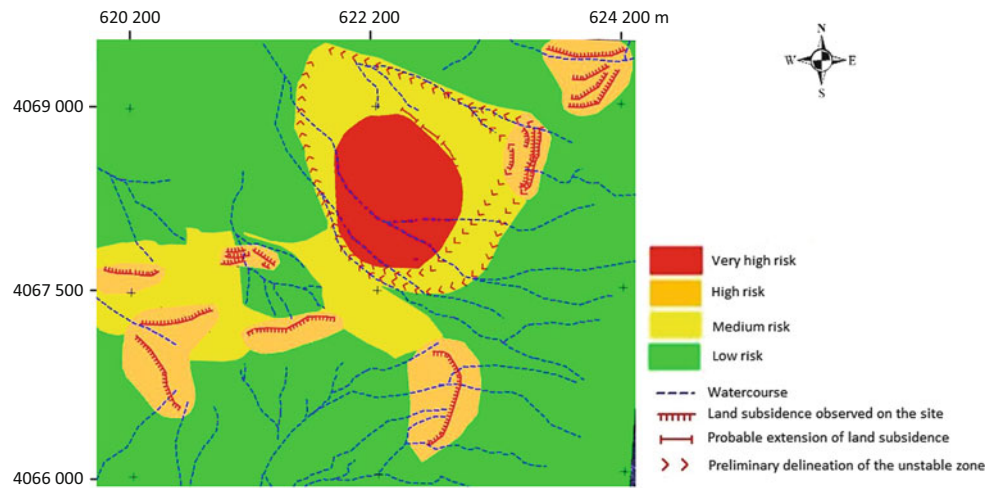
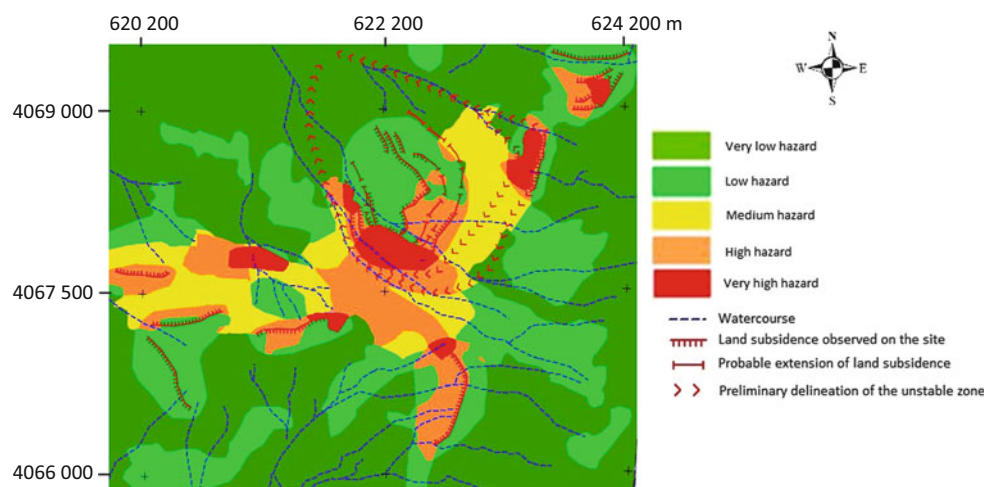


Fig. 6 Combinations of parameters to assess the hazard observed for Azazga region

| Risk \ Stakes | Class 1 | Class 2 | Class 3 |
|---------------|-----------------|---------------|------------------|
| Level 2 | Very low hazard | Low hazard | Medium hazard |
| Level 3 | Very low hazard | Medium hazard | High hazard |
| Level 4 | Low hazard | High hazard | Very high hazard |
| Level 5 | Low hazard | High hazard | Very high hazard |

Fig. 7 Mapping of the hazard level in the Azazga region



weights assigned to the parameters (Djeral and Melbouci 2013)). Risk levels are determined after performing overlay maps of indices that define the parameters of the model using (1). The risk of sliding is distributed into five levels (see Fig. 4). However, in the case of Azazga only four levels were observed, the level of risk very low has not been observed, because the dip of the layers is favourable to the initiation of instability throughout the study site.

$$I_{risk} = I_i + I_v + I_r + I_p + I_h \quad (1)$$

The established map (Fig. 5) shows that several areas of the

site are susceptible to landslide risks. It is mainly the city centre, the Northeast Zone and Southwest area of the site studied.

Assessment and Mapping of the Hazard Level

Hazard classes generated by landslides in the city of Azazga are evaluated using (2) and Fig. 6. We identified for the region Azazga a hazard zone very strong, which cover an area of 42.60 ha and a high hazard area of an area greater than 160 ha (Fig. 7). The highest hazard is determined at the city centre. It also affects the hospital, the technical and the

new post office of this studied region.

$$I_{\text{hazard}} = I_{\text{risk}} \times I_u \quad (2)$$

Conclusion

The municipality of Azazga is one of the regions of Kabylia experiencing significant landslide activity, in recent years. The geological and hydrological context of the site combined with the mismanagement of urbanization works are the factors behind this activity. Indeed, this region is located in a multi layered deposit composed of clay and marl land susceptible to water (quaternary formations).

The application of the method of Djerbal and Melbouci (2013) for this region shows that, despite the low inclination of the slopes, the site presents a potential risk to landslides. Otherwise, areas affected by a high level of risk coincide with those that have suffered major instabilities during the reactivation of the movement of March 2012. In the case of the Azazga region, the risk is major and the stakes are very high. The hazard is then high on most of the urban area.

References

- Azimi C, Devarreaux P (1996) Quelques aspects de la prévision des mouvements de terrain. *Revue française de Géotechnique* 76:63–75
- Djerbal L, Melbouci B (2013) Contribution to the mapping of the landslide of Ain El Hammam (Algeria)'. *Adv Mater Res* 601:332–336
- Durville JL, Berthelon JP, Trinh QV (2003) Calcul de la stabilité des pentes: comparaison entre équilibre limite et éléments finis dans le cas de ruptures non circulaires. *Revue Française de Géotechnique* 104:37–46
- Guirous L, Djerbal L, Alimrina N, Melbouci B, Bahar R (2013) Caractérisation des glissements de terrain de la région de Tizi-Ouzou (Algérie). In : 1st International conference on landslides risk, Ain Drahem – Tabarka, Tunisia, 14, 15 et 16 Mars 2013. pp 117–128
- L.C.T.P. (2004) Étude géotechnique d'urbanisation POS A1 et A5 Azazga. File No. 31.04.0049
- L.C.T.P. (2006) Étude géotechnique des POS D1 et D2 de la ville d'Azazga. File No. 31.03.0042
- L.T.P.C. (1986) étude géotechnique de la ville d'Azazga. File No.27. 85.1012
- Slosson JE, Keene AC, Johnson JA (1992) Landslides mitigation. *Rev Eng Geol* 9: 120
- Touahri B, Bitam L (1997) Carte géologique de l'Algérie: Azzefoun-Azazga. ORGM. Map No.9



Landslide Susceptibility Analysis of Belgrade City Area

Miloš Marjanović, Uroš Đurić, Biljana Abolmasov, and Snežana Bogdanović

Abstract

This article presents preliminary results of a recent analysis of landslide susceptibility over the wider Belgrade City area. Suburban areas of Belgrade have been of particular interest because they are sprawling rapidly and without regulations, so the city needs a regulation plan in these areas. Landslide susceptibility mapping, which has been demonstrated in this work, provides one of the criteria (relative stability of the terrain) for developing such a plan. The analyses of susceptibility involved a state-of-the-art technique based on a machine learning algorithm. The procedure required input data in the form of thematic raster datasets, represented by various geological, geomorphological, and environmental features of the area, as well as a valid landslide inventory for training the algorithm. The resulting map depicts zones of relative (high–low) susceptibility and correlates well with the existing inventory.

Keywords

City of Belgrade • Landslide susceptibility • Machine Learning

Introduction

The City of Belgrade has been spreading rapidly in the past decades, and the new suburban areas have not always matched the development framework regulated by the City's Master Plan. Since the slopes of those hilly suburbs are susceptible to instabilities, acute landslide problems have occurred, affecting dwellings and infrastructure. The City's authorities have conducted a project for compiling a plenary Landslide Inventory and made it publicly available at BeoInfo portal in the past few years (<http://www.mapa.urbel.com/beoinfo>). This policy has given citizens, investors, insurance companies and other potential users a better insight into the distribution of landslide-affected areas, helping them in their personal interests related to

specific locations/parcels. On the other hand, it has inspired research in urban planning, engineering geology and natural hazard assessment, since the data were finally gathered at one place and approved for public use (Samardžić-Petrović et al. 2013; Djurić et al. 2013).

This paper presents preliminary results of a recent analysis of landslide susceptibility over the wider city area. The analysis first involved acquisition of various thematic data (geological, geomorphological, environmental) and a reliable Landslide Inventory, which have then been processed using state-of-the-art algorithms based on machine learning for the further analysis and mapping of susceptibility zones.

Landslide hazard analysis is planned for future research, once the new Landslide Inventory is updated, so that two different Landslide Inventory epochs can be separated. It is also planned to perform a risk analysis that will be carried out once the necessary dwelling data are gathered and processed. In the future course of the research, the landslide susceptibility analysis will be more detailed than in this preliminary work. Hopefully, the results could be used by the target groups (citizens, investors, etc.), but most

M. Marjanović (✉) • U. Đurić • B. Abolmasov • S. Bogdanović
Department for Geotechnics, University of Belgrade, Đušina 7,
Belgrade 11000, Serbia
e-mail: milos.marjanovic@rgf.bg.ac.rs; djuric@rgf.bg.ac.rs;
biljana@rgf.bg.ac.rs; snezana.zecevic@rgf.rs

importantly by decision makers from the City's authorities and related public services for urban planning and development in the near future.

Characteristics of the Study Area

The study area includes the parts of the territory of the City of Belgrade (the capital of the Republic of Serbia), i.e. the territories south of the Sava and Danube rivers. Geographic extents of the study area are as follows: N4994905-4902405 and E7419130-7488830 (MGI Transverse Mercator/Zone 7—ArcGIS predefined spatial reference system). For modeling purposes, the study area has been divided into training and testing parts (Fig. 1).

The training included the territory of the Belgrade Master Plan, while the remaining part was adopted as the testing area (Fig. 1).

The study area has a relatively simple geological setting. Bedrock comprising the oldest Cretaceous flysch formations emerges at the SW outskirts, while the superimposed Miocene formations dominate most of the remaining area. The Miocene formations are very diverse and range from poorly cemented sandstone and limestone (organogenic) to marl, clay and their transitions. These units are locally intercepted by Cretaceous flysch and exceptionally, by a few magmatites and their associations. Quaternary sediments are also widespread, and arch along the Sava and Danube river banks (Marković et al. 1985).

Most of the landslides are deep-seated and occur in the Miocene formations, but they often involve the overlying Quaternary units such as loess and diluvium in the sliding process. Shallow landslides in thick Quaternary formations are uncommon. The landslide triggering mechanism is believed to be the linear erosion that undercuts the Sava and Danube river banks or the banks of their few tributaries inland. This is coupled with the excessive rainfall and associated groundwater oscillations. The human factor is also very influential, particularly in the rapidly sprawling suburbs, where construction activity is not sufficiently controlled.

Related Work

Previous research studies on landslide assessment in the study area are numerous, particularly those using the conventional approach of landslide investigation (a combination of geotechnical and engineering-geological approaches). There have been countless geological and geotechnical investigations from various periods. These range from individual investigations of the smaller construction projects, to capital objects and systematic surveys (Marković et al.

1985). The problem is that the data have not been collected systematically and saved to a central database, but there are some initiatives striving towards that end. Another issue is the inconsistency of the criteria used in the various investigations. All these issues affect the data quality and consistency, so that the proposed landslide susceptibility and hazard analysis turned out to be less routine than expected.

In this research study, landslide susceptibility is conducted as proposed by the prominent international guidelines (Fell et al. 2008). The work of several researchers that have been applying machine learning to landslide susceptibility mapping has been particularly inspiring.

Methods and Materials

The methods for landslide susceptibility zoning that has been applied in this research are based on the landslide assessment postulates: landslides are likely to spatially/temporally reoccur under similar conditions (Fell et al. 2008). To analyze these conditions, i.e. to match different terrain attributes (geological, geomorphological, environmental etc.) with a landslide inventory (that reveals a spatial distribution of existing landslides), a machine learning approach was followed. In particular, the Support Vector Machines (SVM) technique was used. SVM was used as a binary classifier in a supervised learning scheme. First, the training stage required a portion of the entire area, called the training area, which was represented by terrain attributes and the Landslide Inventory. Subsequently, a classification rule was made relating the inventory to the terrain attributes. Finally, in the testing stage, the obtained classification rule was applied over the rest of the area, called the testing area. Details of the particular machine learning technique will not be addressed in detail, since they can be found elsewhere in the authors' earlier work (Marjanović et al. 2011). Machine learning experiments have been placed and processed in the Weka 3.6 open-source software package and data preprocessing and visualizing in an ArcGIS 10 environment.

Figure 2, below, depicts a workflow that contains all important stages of this research and generalizes our methodological approach.

Datasets

The datasets were collected from different sources and included various thematic data such as geological, geomorphological and environmental data, which should represent the main terrain attributes that can be related to landslide occurrence (Landslide Inventory). These were arranged as 2D raster layers in a GIS environment. The training area (Master Plan territory) and the testing area had exactly the

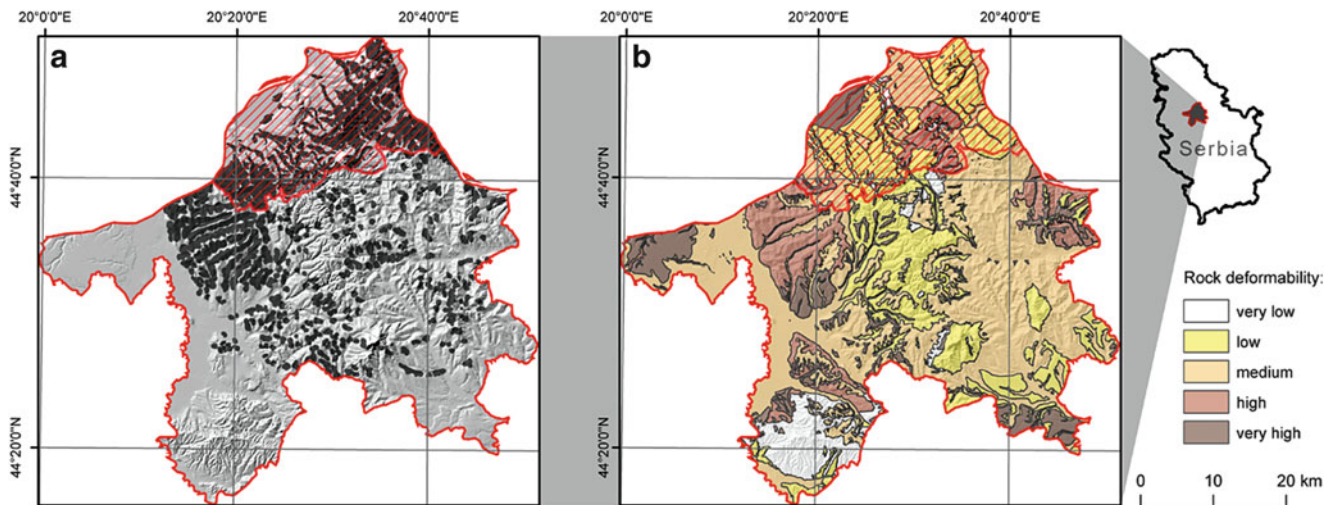


Fig. 1 Geographical setting of the study area (outlined in red, training area is shaded red); (a) simplified Landslide Inventory (all landslides of all types are shown as dark polygons); (b) simplified geological setting

indicating deformability of the rock formations from very low (e.g. solid rocks) to very high (e.g. clay)



Fig. 2 Research workflow

same inputs, with some inconsistency in the case of the Landslide Inventory. For all inputs (training and testing) a 50 m resolution was considered as the most appropriate with respect to the source map scales (1:10,000–1:100,000) and also with respect to the processing demands (finer resolution would cause difficulties in the modeling stage due to the large number of instances). In addition, a sub-variant of the training area dataset with a coarser 100 m resolution was produced for further modeling and experimentation.

Finally, all these GIS layers represented by 2D rasters have been converted to point shape files and then communicated to the ML software by CSV conversion. Then, the numeric data were normalized and nominal data (such as land cover or rock deformability) binarized as dummy variables (e.g. rock deformability had five classes and has therefore been disaggregated into five separate binary layers). For visualization the results have been converted back from CSV format.

Elevation (DEM)

This numeric (morphometric) parameter has been computed from the digitized topographic maps 1:25,000 by means of

TOPOTOASTER conversion in the ArcGIS 10 toolbox. The altitude is related to the potential energy of the slopes, so that the higher slopes are considered more susceptible to landslides.

Slope Aspect

This morphometric parameter was computed from elevation as a standard first-order derivative. It represents the slope exposure to the Sun and suggests that moister NW, N and NE slopes are more prone to landsliding than the dryer southern ones.

Slope Angle

Slope angle is another numeric (morphometric) parameter, computed as a first-order derivative from elevation. It is directly related to landslides since inclination of the slope determines the slope stability, but there are scenarios in which this principle does not apply (solid rocks or loess can be stable in steep slopes).

Slope Curvature

This is also a numeric (morphometric) parameter, but it is computed as a second-order derivative of elevation. It detects convex and concave parts of the slope, which can be an indicator of landslide morphology (concavity can indicate the landslide crests while the convexity can be related to the landslide middle or foot).

Relative Relief

This is a numeric (morphometric) parameter that is computed from elevation by determining the range of the relative altitude difference within a 1000-m radius. It points to the areas of so called high relief energy, i.e. high

variability of relative altitude within the specified radius. Such variability can be considered as a consequence or a predecessor of landslide activity.

Stream Distance

This is a numeric hydrological parameter which simply indicates the proximity to the stream network that has been mapped from the topographic maps at 1:25,000. It is suspected that one of the main triggering mechanisms is due to linear stream erosion, which is why the slopes closer to the streams are more prone to landslides.

Land Cover

This is a nominal layer which has been derived from the CORINE Land Cover map at 1:100,000. It has been simplified from CORINE Level 3 to the following four classes: artificial surfaces, agricultural areas, forests and semi-natural areas and wetlands.

Rock Deformability

Rock deformability (Fig. 1b) is another nominal terrain attribute which is derived by simplifying the geological map at 1:25,000 and 1:100,000. Simplification was necessary because the original maps contained too many similar units. The criterion for simplification was the rock compressibility/deformability according to the literature recommendations (Jovanović et al. 1977). Five classes of geological units represented deformability: Very Low (Mesozoic limestone and other older solid rocks), Low (Miocene limestone, sandstone), Medium (marl), High (sand, loess) and Very High (clay).

Landslide Inventory

The Landslide Inventory (Fig. 1a) was obtained from a synthetic engineering geological map of the Belgrade area at 1:10,000, which has been digitized and published at <http://www.mapa.urbel.com/beoinfo>. The acquisition technique was based on a combination of remote sensing and engineering-geological mapping at a larger scale, but the older landslides have been included too. Moreover, different parts of the inventory have been mapped by different parties and during compilation the criteria homogeneity was not entirely inspected. For these reasons the inventory cannot be dated (it contains older and more recent records) and classified (there are apparent disagreements on landslide typology). This particularly affects the wider study area (testing area), while the Master Plan area had somewhat better data. In turn, the given Landslide Inventory was simplified (some categories were removed, and others aggregated) into three classes: non-landslide, dormant landslide and active landslide.

Table 1 Pair-wise combinations of SVM parameters

| # Combination | C | γ |
|---------------|-------|----------|
| 1 | 1.0 | 0.1 |
| 2 | 10.0 | 0.1 |
| 3 | 100.0 | 0.1 |
| 4 | 1.0 | 1.0 |
| 5 | 10.0 | 1.0 |
| 6 | 100.0 | 1.0 |
| 7 | 1.0 | 10.0 |
| 8 | 10.0 | 10.0 |
| 9 | 100.0 | 10.0 |
| 10 | 1.0 | 100.0 |
| 11 | 10.0 | 100.0 |
| 12 | 100.0 | 100.0 |

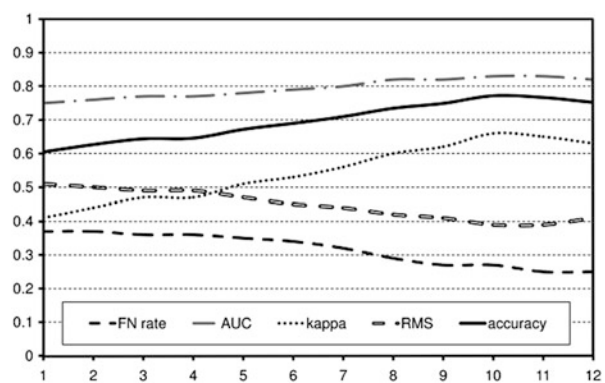


Fig. 3 Optimization of the SVM algorithm; horizontal axis represents C, γ pairs given in Table 1, respectively (note that the lowest error and the highest performance parameters are for combinations 8–11)

Results and Discussion

Two different experiments have been carried out, one with a regular training-testing protocol and one with cross-scaled training-testing.

Regardless of the experiment (i.e. the scale), the optimization of the SVM parameters was the first task, which has been completed using a 10-fold Cross-Validation (CV) technique over the training area, with successive changing of the C (the misclassification penalty) and γ (kernel width) parameters. Theoretically, C should be lower and γ higher for more powerful generalization, but their trade-off differs from one case to another. Herein, the good C, γ combinations were from 8 to 11 (Table 1, Fig. 3), and after the fine tuning $C = 5$ and $\gamma = 70$ were adopted as optimal. Further experimenting could have also been done by CV sampling (Marjanović et al. 2011), but we have proposed a different strategy to increase the generalization capacity and avoid overfit of the algorithm.

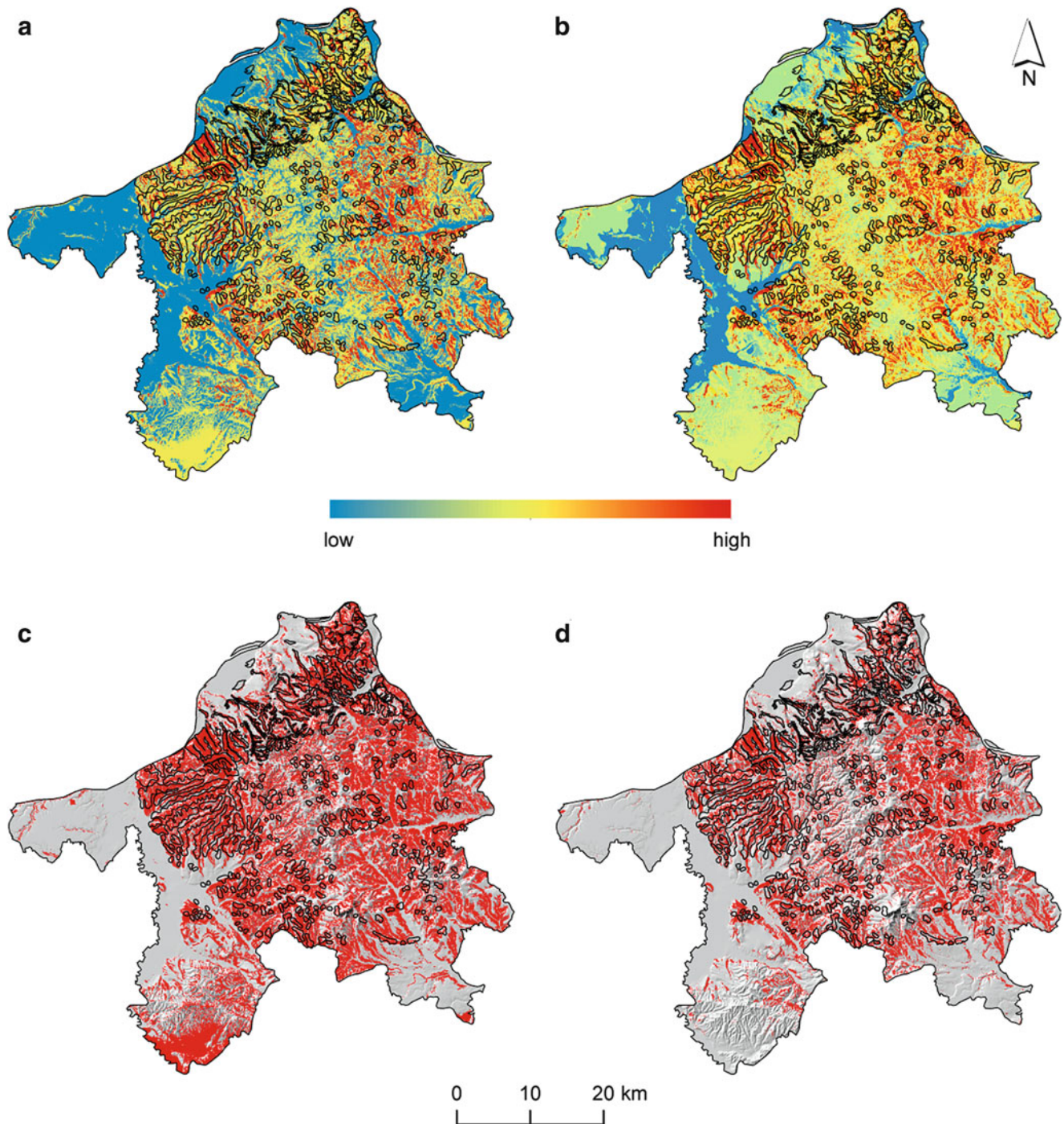


Fig. 4 Landslide susceptibility model with: (a) a regular learning protocol; (b) a cross-scaled learning protocol; (c) and (d) binarized classes for evaluation (black contours represent landslides from the inventory,

color scale in the upper images depicts 0–1 spatial probabilities, i.e. susceptibility, *red polygons* represent predicted landslides)

The size of the training area, defined as administrative unit (Master Plan area) of the city, covers approximately one fifth of the total study area (160,000 of 850,000 instances), and landslide instances counted more than one third of the total training instances (57,000 of 160,000 instances), which is generally sufficient to make plausible predictions. This

convenience was used to generate a balanced training sample which contained equal amount of all Landslide Inventory classes (non-landslide, dormant landslide and active landslide). Since the classes were not equal in size, the smallest class (active landslide), with 14,000 instances, was chosen as reference for the class size of the balanced training set.

Sufficient instances that had occurred in non-landslide and dormant landslide classes were randomly removed. The balanced training set thus, contained three equally-sized classes (14,000 instances each).

The first experiment had a regular training-testing protocol and has been iterated 10 times, each time with a different (balanced) sampling based on a random seed. Each iteration had the same $C = 5$ and $\gamma = 70$. Final result of the first experiment was achieved by averaging ten sub-models. The resulting model maps the high–low susceptibility zones (Fig. 4a).

The second experiment included cross-scaling of training versus testing area. A training set version with coarser resolution was used, while the testing set remained in the original resolution. This intervention was undertaken to inspect the effects of scale and to help the algorithm generalize better. Model processing was quicker because the number of training instances decreased from 160,000 to 40,000 (and in balanced variants from $3 \times 14,000$ to $3 \times 3,500$) due to the downscaling. The final result (Fig. 4b) was given in the form of an averaged high–low susceptibility map. As discussed previously, the Landslide Inventory has had some inconsistency, since the mapping criteria were different for the training and testing area. The evaluation was therefore performed on the basis of a modified inventory that contained only landslide and non-landslide classes (dormant and active landslide classes were aggregated) versus modified susceptibility models that also contained only two classes (Fig. 4c, d). The spatial probability (susceptibility) trade-off for these two classes was at 0.75 (the original susceptibility range was 0–1), so that all instances with spatial probability higher than this were categorized as landslides and lower as non-landslides. Choosing the most appropriate evaluation measurement was also important. There are numerous statistical parameters based on cross-tabulation (confusion matrix) that can be taken into consideration. We choose False Negative rate (*FN rate*), which best suits the given problem, because false negatives are the least desirable in the landslide assessment. For instance, it is much bigger error to classify an existing landslide as a low susceptibility zone than to classify some currently stable area as a high susceptibility zone.

The cross-tabulation of modified models (Fig. 4c, d) gave somewhat better results (lower *FN rate*) for the first model, so the cross-scaling had a negative effect. Both models perform similar in terms of *AUC* and *accuracy*, but it is

Table 2 Model evaluation parameters

| Model | FN rate | FP rate | AUC | Accuracy |
|--------------|---------|---------|------|----------|
| Regular | 0.42 | 0.34 | 0.61 | 0.65 |
| Cross-scaled | 0.63 | 0.21 | 0.58 | 0.72 |

apparent that false positives are more abundant in the first model (Fig. 4c) than in the cross-scaled one (Fig. 4d). It is not only a visual impression but also shown by false positives rate values (Table 2).

Conclusion

Plausible predictions and zoning of landslide susceptibility are possible with the given thematic data inputs and appropriate modeling techniques. Cross-scaling did not improve the generalization capacity of the SVM algorithm and had a negative effect on the model. For further research, hazard and risk analysis are planned, but the issue of an inconsistent and temporally undefined Landslide Inventory and other input data issues (consistency of some inputs, introducing additional morphometric, hydrological, geological or synthetic inputs) should be solved first.

Acknowledgements Supported by the Ministry of Education Science and Technology (Republic of Serbia), project TR 36009.

References

- Djurić U, Marjanović M, Šušić V, Petrović R, Abolmasov B, Zečević S, Basarić I (2013) Land-Use suitability analysis of Belgrade city suburbs using machine learning algorithm. Proceedings of GIS Ostrava 2013, 21–23 January 2013. Ostrava, Czech Republic, pp 49–61
- Fell R, Corominas J, Bonnard C, Cascini L, Leroi E, Savage W (2008) Guidelines for landslide susceptibility, hazard and risk zoning for land use planning. Eng Geol 102:83–84
- Jovanović V, Vlahović M, Vujanić V, Prah L (1977) Izrada sintetskih inženjersko-geoloških karata za izbor najpovoljnije varijante autoputa. Institut za puteve 8:5–13
- Marjanović M, Kovačević M, Bajat B, Voženílek V (2011) Landslide susceptibility assessment using SVM machine learning algorithm. Eng Geol 123:225–234
- Marković B, Veselinović M, Anđelković J, Stevanović P, Roglić Č, Obradović Z (1985) Osnovna geološka karta 1:100000, Tumač za list Beograd K34-113. Federal Geological Survey, Belgrade, 51p
- Samardžić-Petrović M, Bajat B, Kovačević M (2013) Assessing similarities between planned and observed Land Use maps: the Belgrade's municipalities case study. Proceedings of GIS Ostrava 2013, 21–23 January 2013. Ostrava, Czech Republic, pp 13–23



Study on Earthquake-Triggered Landslide Hazard Assessment Under Rainfall Condition

Meng Wang, Jianping Qiao, and Lili Shi

Abstract

Landslides' occurrence results from not only the environmental background conditions of slopes, but also triggering factors, such as rainfall and earthquake etc. This study selected Pengzhou, Dujiangyan, Chongzhou and Dayi cities as the research area, which were affected severely by Wenchuan Ms 8.0 Earthquake. At the aim of assessing regional landslide hazard under the conditions of heavy rainfall and Ms 8.0 earthquake, Newmark model and hydrological distribution model were adopted based on GIS technology. First, the whole study area was divided into cells with grid size $30\text{ m} \times 30\text{ m}$ and the Newmark displacement of each grid in the region was calculated under the roles of heavy rainfall and earthquake. And then, make a coupling analysis between the Newmark displacements and landslides inventory map to establish a curve equation, which will give the hazard degree to each grid. Finally, the earthquake-triggered landslide hazard assessment map was completed. The result shows that the moderate and high hazardous regions cover 37.1 % area and are containing about 82 % landslides. The landslide density has a great relationship with hazard degree and it is increasing with the hazard level increase, which implies the result is accord with the reality and can be used to provide the research foundation for the landslide risk management and the reference for the regional reconstruction planning.

Keywords

Rainfall • Earthquake • Newmark model • Hydrological distribution model • Landslide hazard assessment

Preface

Landslide is a kind of serious phenomenon of slope deformation. The occurrence of it not only results from the slope's environmental conditions, but also the exogenic forces.

Among them, rainfall infiltration and earthquake are most important factors. In the previous studies, researchers are more focusing on the single factor to trigger landslides (Jibson et al. 2000; Koppula 1984; Tang et al. 2001; Miles and Ho 1999; Chen and Lee 2003; Chang and Chiang 2009). But, it is well known that landslide occurrence is the result of many factors. Therefore, this paper mainly studied the earthquake-triggered landslide hazard distribution under rainfall condition.

M. Wang (✉) • J. Qiao
Key Laboratory of Geo-Surface Process and Mountain Hazards,
Institute of Mountain Hazards and Environment, Chinese Academy of
Science, Chengdu 610041, China
e-mail: wm@imde.ac.cn; jqiao@imde.ac.cn

L. Shi
Chengdu Geological Environment Monitoring Station, Chengdu
610072, China
e-mail: shll1127@126.com

Earthquake-Triggered Landslide Hazard Assessment Model

Newmark proposed a new thought to use cumulative permanent displacements of the slope instead of the safety factor and meantime put forward a method to calculate the sliding displacement in 1965 (Newmark 1965). Newmark's method models a landslide as a rigid friction block that slides on an inclined plane. The block has a known critical acceleration, which is simply the threshold base acceleration required to overcome shear resistance and initiate sliding. In the calculation, it is assumed that the water table is paralleled to the sliding surface and the slope surface.

In this paper, hydrological distribution model was coupled with slope stability model based on limit equilibrium theory. Firstly, the earthquake-triggered landslide's critical acceleration was calculated under rainfall condition. And then, Newmark's model was adopted to get slope's permanent displacement. Finally, make a coupling analysis between displacements and landslide inventory map to establish a curve equation, which would give the hazard degree to each grid. Consequently, earthquake-triggered landslide hazard assessment map under rainfall condition was completed.

Slope Stability Model Based on Limit Equilibrium Theory

Before calculating the permanent displacement of slope, the infinite slope model was used to get the safety factor. The function is as following:

$$F_s = \frac{c'}{\gamma Z \sin \alpha} + \left(1 - m \frac{\gamma_w}{\gamma}\right) \frac{\tan \Phi'}{\tan \alpha} \quad (1)$$

Where c' is the effective cohesion (kPa), Φ' is the effective friction angle ($^\circ$), α is slope angle ($^\circ$), m represents the fractional depth of the water table with respect to the total slide depth and is called the saturated factor, t stands for the depth of sliding surface (m), γ is the material unit weight (kN/m^3) and γ_w is the water unit weight (kN/m^3).

Hydrological Distribution Model Based on DEM

The shallow groundwater distribution model under steady flow was used to simulate the saturated factor distribution under non-static rainfall condition.

In Fig. 1, thick lines represent surface line and thin lines shaded areas represent shallow underground runoff with discharge Q . The effective rainfall is q (mm/d). Z_w is the

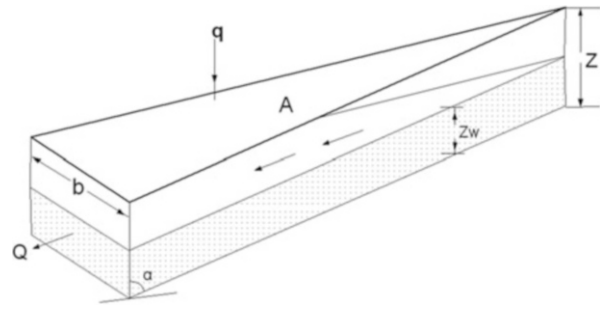


Fig. 1 Hydrological geology model (modified by Lan et al. 2003)

saturated underground runoff depth (m). Z is the vertical thickness of the potential sliding body (m). α is the slope gradient ($^\circ$). A is the total area of the catchment that can supply the groundwater runoff. b is the width of the basic unit. It is assumed that the hydraulic gradient equal to the slope gradient and the hydraulic conductivity distributes evenly in the vertical direction of the landslide, which does not change significantly with depth (Lan et al. 2003). According to the SHALSTAB model established by Dietrich and Montgomery (Rafaelli et al. 2001), the saturation factor m can be calculated by the following formula:

$$m = \frac{Z_w}{Z} = \frac{qA}{Tb \sin \alpha} \quad (2)$$

T is the hydraulic transmissivity (m^2/d).

Newmark Permanent Displacement Model

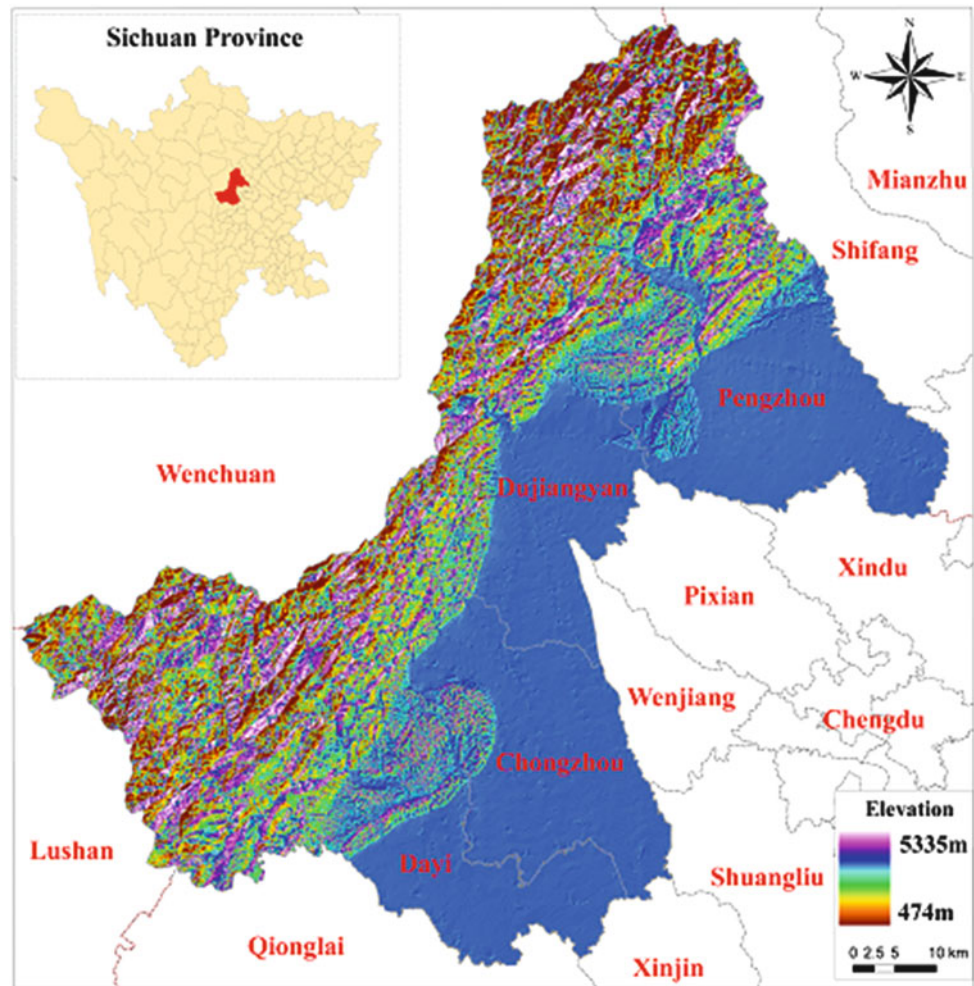
According to formulas (1) and (2), the safety factor of slope can be calculated. And then, use safety factor to calculate the critical acceleration:

$$a_c = (F_s - 1)g \sin \alpha' \quad (3)$$

Where g is the gravity acceleration (m/s^2) and α' represents the slide thrust angle ($^\circ$). For the shallow landslide, α' can be replaced by the slope angle α .

Many researches adopted different factors to get different formulations through statistics at the time of calculating Newmark displacement. While, according the current studies, Arias seismic intensity is widely used (Roberto 2000). Therefore, we also use this factor here. Arias seismic intensity contains all the ground vibration information during the entire shaking time. It is the sum of the square of the seismic acceleration with a certain time and can be approximated by the following:

$$I_a = \frac{\pi}{2g} t_d (0.14 a_{\max})^2 \quad (4)$$

Fig. 2 Location of study area

Where I_a is Arias seismic intensity (m/s), t_d is the shaking time during the earthquake(s), and a_{\max} is the ground peak acceleration.

Finally, use the predictive model with the variables as the Arias seismic intensity and the critical acceleration to calculate the seismic landslide displacement (Jibson 2007):

$$\log D_N = 2.401 \log I_a - 3.481 \log a_c - 3.230 \pm 0.656 \quad (5)$$

Here, the unit of D_N is centimeter and I_a 's is m/s. The last value represents the standard error of the equation. This model has been used to predict the regional landslide hazard under different background conditions.

Case Study

Introduction of Study Area

Pengzhou, Dujiangyan, Chongzhou, and Dayi four cities were affected severely by Wenchuan Ms 8.0 Earthquake. They are located in the central part of Sichuan Province. The

total area of them is 5,265 km². The range of elevation of the study area is from 474 to 5,335 m (Fig. 2). The east border is adjacent to Longquan Mountain and the west border is adjacent to Longmen Mountain. The rivers of the study area are belonging to Minjiang and Tuojiang water systems. The northwest part of the study area is high and the southeast part is low. The terrain is like a ladder and the height difference is 4,861 m. The landform can be classified into High Mountain, Middle Mountain, Low Mountain, Hill, and Plain. The outcrop in the area is almost complete, containing Huangshuihe Group and Sinian System of Proterozoic, Silurian System, Devonian System, Carboniferous System, Permian System, Triassic System, Jurassic System, Cretaceous System, Tertiary System, Quaternary System, and Magmatic rocks. The study area is belonging to Longmenshan Cathaysian Structure and West Sichuan New Cathaysian Structure. The geological structure is complicated and folds and faults are more developed. The main faults are Yinxiu Fault and Guanxian Fault. The study area is subtropical humid monsoon climate and the annual average rainfall is 945.6 mm, concentrating in the July and August.

Table 1 Physical and mechanical property of geotechnical category

| Rocks | ND (kN/m ³) | HT (m ² /d) | C (Kpa) | F (°) |
|--------------------------------------|-------------------------|------------------------|---------|-------|
| Sandstone, shale, mudstone, phyllite | 17.6 | 75 | 26 | 33 |
| Limestone | 19.6 | 95 | 30 | 38 |
| Granite | 21.6 | 60 | 31 | 42 |
| Gabbro | 22.5 | 55 | 52 | 45 |
| Tuff | 15.7 | 80 | 20 | 31 |
| Basalt | 21.6 | 65 | 45 | 38 |
| Gravel | 16.6 | 145 | 0 | 34 |

Note ND natural density, HT hydrological transmissivity, C cohesion, F friction

Spatial Data Pre-processing

The regional seismic landslide hazard assessment under rainfall condition needs many related data, including landslide inventory map, geological map, terrain map, the peak acceleration distribution map, and rainfall contour map etc. This paper used the terrain map at the scale of 1:50,000 to create DEM with the cell size of 25 m × 25 m through GIS technology. And then, the slope gradient map was derived from DEM. The geological map at the scale of 1:200,000 was digitized and the rocks were merged and reclassified into seven types (Table 1).

After the investigation to landslides of the study area, the most of them are shallow landslides and the average depth of them is 2 m. The peak ground acceleration distribution map was drawn by China Earthquake Administration at the scale of 1:1,000,000.

Slope Stability Calculation Under Rainfall Condition

It is assumed that the rainfalls of 24 h is the effective rainfalls and study the regional landslide hazard distribution under the conditions of rainfall and Ms 8.0 earthquake.

Firstly, based on the annual maximum 24-h rainfall contour map and formula (2), the regional saturated factor distribution map could be got (Fig. 3). If the saturation factor is bigger than 1, that means this is the surface runoff region. The cells without data represent the slope gradients of them are zero. These two situations both are unconditionally stable area and do not participate in the subsequent stability calculation.

Based on formula (1), the regional landslide safety factor distribution map was obtained (Fig. 4). If the safety factor is less than 1, that means the low stability of the slope itself. Without any external forces, the instability of the slope still may occur. Therefore, this situation was classified as the unconditionally unstable region and does not participate in the subsequent calculations.

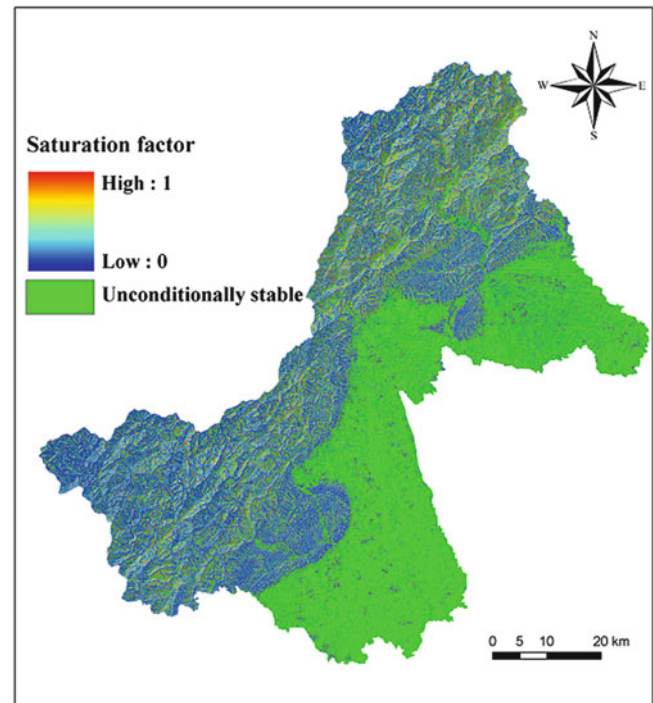


Fig. 3 Saturation factor of study area distribution map

Newmark Permanent Displacement Calculation

According to formulas (3, 4, and 5), the regional critical acceleration map (Fig. 5), Arias seismic intensity map (Fig. 6), and the Newmark permanent displacement map (Fig. 7) were obtained.

Regional Earthquake-Triggered Landslide Hazard Assessment Under Rainfall Condition

That is not correct to just use the Newmark displacement to assess the regional hazard simply. Due to the lithology strength difference, some of the weak strata may generate the landslide only with small displacements. Therefore, in order to properly evaluate the degree of regional landslide

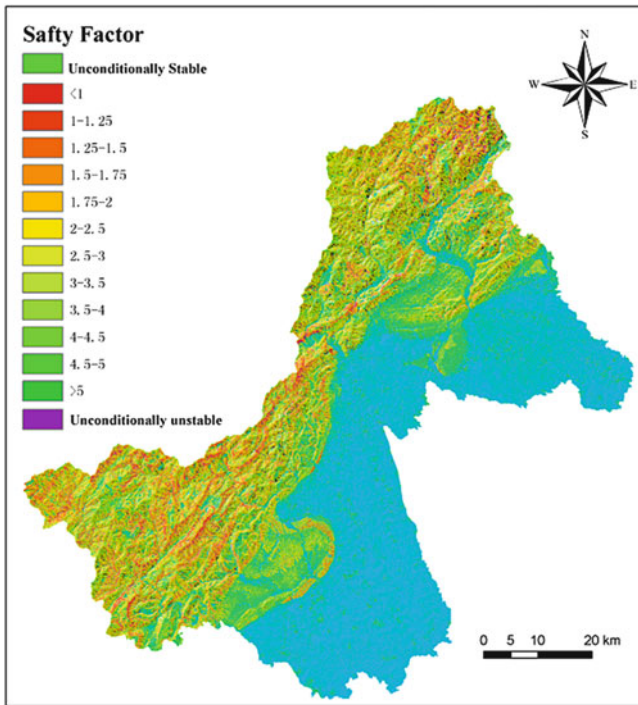


Fig. 4 Safety factor of study area distribution map

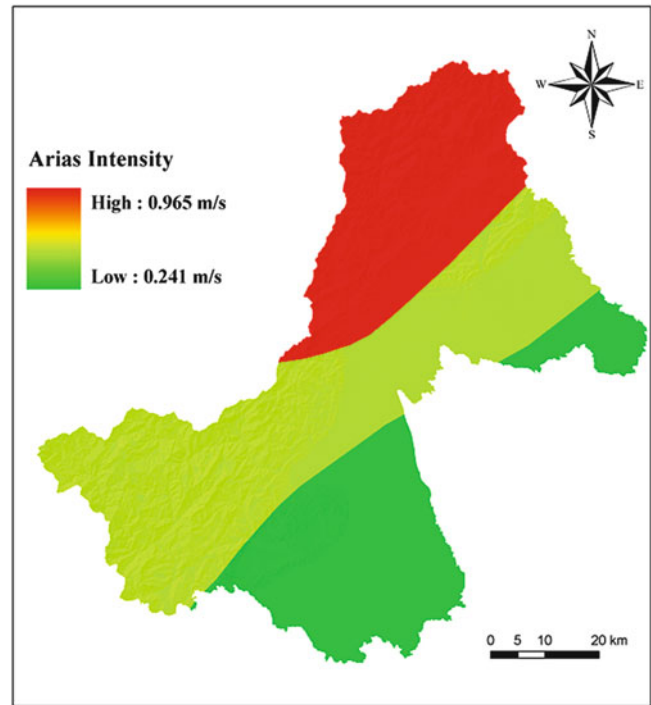


Fig. 6 Arias intensity of study area distribution map

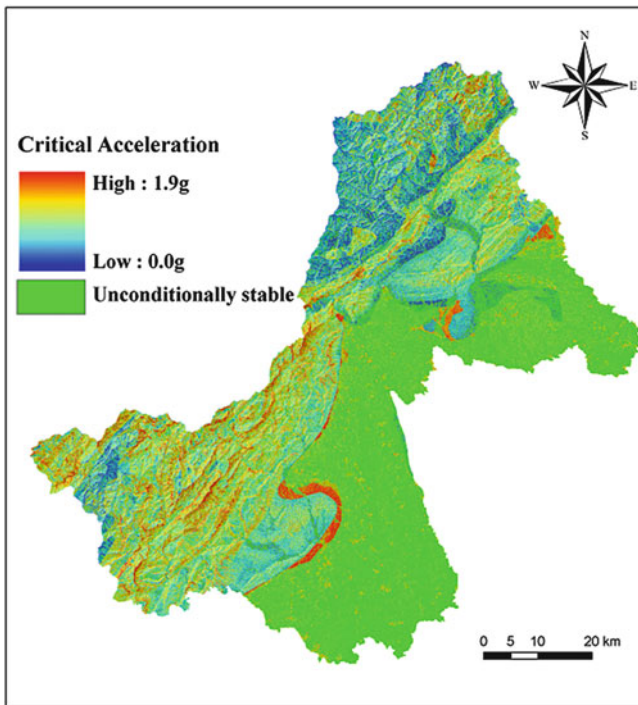


Fig. 5 Critical acceleration of study area distribution map

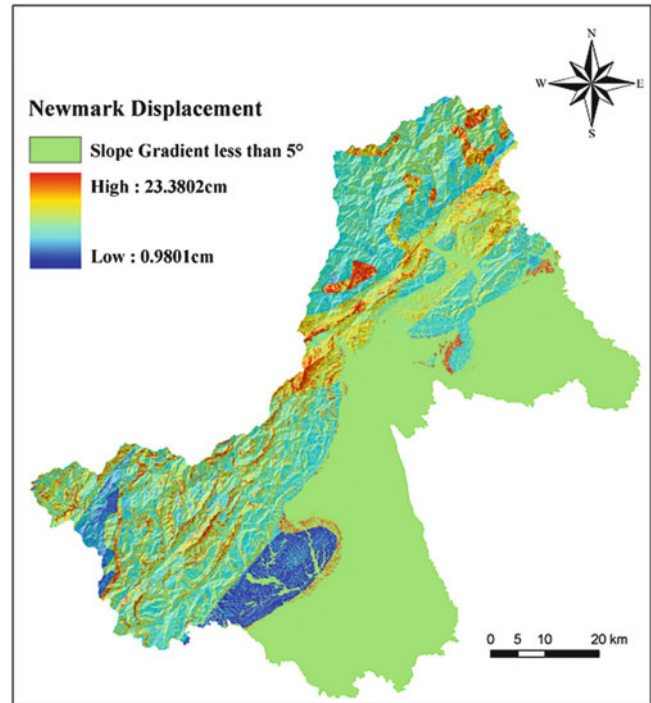


Fig. 7 Newmark displacements of study area distribution map

hazard, it should make a related analysis with actual landslides. After the earthquake, 3,899 landslides were determined by means of remote sensing interpretation and

field investigation. And we used 2,452 landslides obtained by interpretation to make the related analysis with the Newmark displacement and the rest to test the results' reliability.

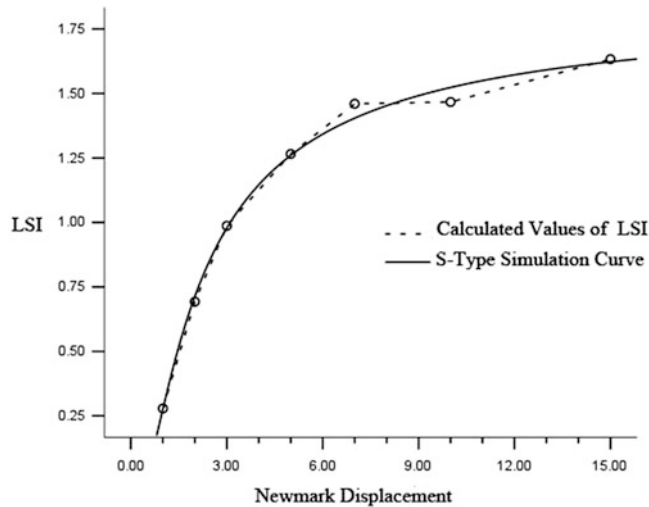


Fig. 8 Seismic landslide hazard degree as a function of Newmark displacement

Here, we adopted the statistics to calculate the landslide susceptibility index I_L (LSI) proposed by Masamn Aniya and the method is as following (Tang and Jorg 1998):

$$\begin{aligned} I_L &= b/a \\ a &= P_{mn}(G)/P_m(G) \\ b &= P_{mn}(L)/P_m(L) \end{aligned} \quad (6)$$

Where $P_{mn}(G)$ represents the cells' number of n type in m factor, $P_m(G)$ represents the total cells' number of factor m , $P_{mn}(L)$ represents the landslides cells' number of n type in m factor, and $P_m(L)$ represents the total landslides cells' number of factor m . The susceptibility index indicates the importance of the factors related to landslides occurrence. The larger the value is, the higher the degree of sensitivity to landslide development is.

The Newmark displacements were divided into seven intervals: <1, 1–2, 2–3, 3–5, 5–7, 7–10, >10 cm. According to formula (6), the landslide susceptibility index of every interval was got and established the relation function between the displacement and the landslide susceptibility index (Fig. 8).

According to the curve fitting of Fig. 8, the equation was established and the R^2 of it is 0.998, meeting the requirements of the simulation.

$$y = e^{(0.611 - 1.898/x)} \quad (R^2 = 0.998) \quad (7)$$

According to the formula (7), we can get the whole regional landslide susceptibility index. In order to reflect the regional landslide hazard degree more intuitively, natural breaks points method was used to classified the results into four grades: safety region (i.e. the unconditional stability region), low hazard region (<0.70), middle hazard region

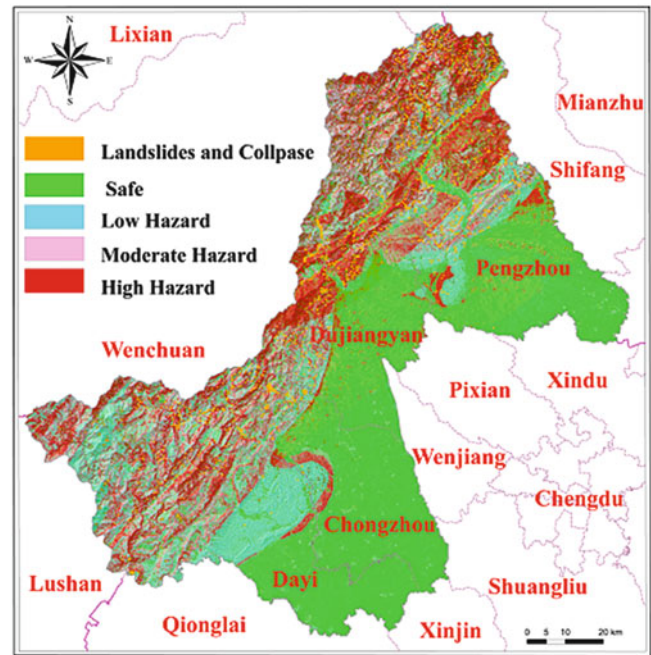


Fig. 9 Seismic landslide hazard zonation map under rainfall

(0.70–1.25), and high hazard region (>1.25 and the unconditional instability region) (Fig. 9).

The relative safety region doesn't have the necessary environmental conditions of landform, lithology, and geological structure to produce landslides. But, under the certain external triggering conditions, such as the road excavation, it may develop small-size landslides occasionally. The low hazard region has the necessary internal environmental conditions and a single external triggering condition to produce medium and small size landslides and the probability of landslide occurrence is low. The middle hazard region has the necessary internal environmental conditions and several external triggering conditions to produce medium and large size landslides and the probability of landslide occurrence is high. The high hazard region has the necessary internal environmental conditions and many external triggering conditions to produce large and especially large size landslides and the probability of landslide occurrence is very high.

Reliability Validation of Regional Seismic Landslide Hazard Zonation

In order to verify the result reliability, 1,447 landslides which did not participate in the statistic analysis were used to make the density distribution analysis. From Table 2, it can be seen that the landslides distribution density has a great relationship with the hazard grade. With the increase of hazard grade, the seismic landslide distribution density is increasing remarkable, too.

Table 2 The relationship between distributing area and landslides number in each level

| Hazard Grade | Area (km ²) | Percentage (%) | Landslides number | Percentage (%) | Density (/km ²) |
|--------------|-------------------------|----------------|-------------------|----------------|-----------------------------|
| Safety | 2,453.3 | 46.6 | 12 | 0.83 | 0.005 |
| Low | 858.2 | 16.3 | 242 | 16.72 | 0.282 |
| Moderate | 968.7 | 18.4 | 468 | 32.34 | 0.483 |
| High | 984.5 | 18.7 | 725 | 50.11 | 0.736 |
| Total | 5,264.7 | 100 | 1,447 | 100 | – |

According to Table 2, the 37.1 % of the study area is belonging to middle and high hazard regions and this area contains 82 % of landslides with a dense distribution density.

Conclusions

This paper selected Pengzhou, Dujingyan, Chongzhou, and Dayi four cities as the study area, which was affected severely by Wenchuan Ms 8.0 Earthquake. At the aim of assessing regional landslide hazard under the conditions of heavy rainfall and Ms 8.0 earthquake, Newmark model and hydrological distribution model were adopted based on GIS technology. The result showed that the moderate and high hazardous regions cover 37.1 % area and are containing about 82 % landslides. The north and central parts of Chongzhou, the north, central, and southwest parts of Dujingyan, the north and west parts of Chongzhou, and the west and southwest parts of Dayi are belonging to the seismic landslide susceptibility region under rainfall condition. In the reliability validation of results, it can be seen that the landslides distribution density has a great relationship with the hazard grade. With the increase of hazard grade, the seismic landslide distribution density is increasing, too. That implies the result is accord with the reality.

However, in the process of research, the author found that there are several issues that need to be further strengthened.

1. The values of c' and ϕ' were got from the limited borehole data and some published literatures. So, the quantification and the accuracy are relative low, which are bound to affect the result precision. Therefore, it is a future direction to improve the parameters' quantitative degree.

2. The vertical ground motion was not considered in the Newmark displacement model, which made the critical acceleration and the permanent displacement be smaller than the real one. So, this can be modified and improved in the future study.

References

- Chang KT, Chiang SH (2009) An integrated model for predicting rainfall-induced landslides. *Geomorphology* 105:366–373
- Chen H, Lee CF (2003) A dynamic model for rainfall-induced landslides on natural slopes. *Geomorphology* 51:269–288
- Jibson RW (2007) Regression models for estimating coseismic landslide displacement. *Eng Geol* 91:209–218
- Jibson RW, Harp EL, Michael JA (2000) A method for producing digital probabilistic seismic landslide hazard maps. *Eng Geol* 58:271–289
- Koppula SD (1984) Pseudo-static analysis of clay slopes subjected to earth-quakes. *Geotechnique* 34(1):71–79
- Lan HX, Zhou CH, Wang LJ et al (2003) GIS based landslide stability and hydrological distribution coupled model. *Chin J Rock Mech Eng* 22(8):1309–1314 (in Chinese)
- Miles SB, Ho CL (1999) Rigorous landslide hazard zonation using Newmark's method and stochastic ground motion simulation. *Soil Dyn Earthq Eng* 18:305–323
- Newmark NM (1965) Effects of earthquakes on dams and embankments. *Geotechnique* 15(2):139–160
- Rafaelli SG, Montgomery DR, Greenberg HM (2001) A comparison of thematic mapping of erosion intensity to GIS-driven process models in an Andean drainage basin. *J Hydrol* 244:33–42
- Romeo R (2000) Seismically induced landslide displacements: a predictive model. *Eng Geol* 58:337–351
- Tang C, Jorg G (1998) The principles and methodology of landslide hazard assessment. *Acta Geograph Sin* 53:149–157 (in Chinese)
- Tang C, Zhu J, Zhang X (2001) GIS based earthquake triggered landslide hazard prediction. *J Seismol Res* 24(1):73–81 (in Chinese)



A GIS Approach to Analysis of Deep-Seated Slope Stability in Complex Geology

Ivan Marchesini, Martin Mergili, Mauro Rossi, Michele Santangelo, Mauro Cardinali, Francesca Ardizzone, Federica Fiorucci, Barbara Schneider-Muntau, Wolfgang Fellin, and Fausto Guzzetti

Abstract

We demonstrate the computer model *r.rotstab.layers* to explore the possibilities of GIS for catchment-scale deep-seated slope stability modelling in complex geology. This model makes use of a modification of the three-dimensional sliding surface model proposed by Hovland and revised and extended by Xie and co-workers. It evaluates the slope stability for a large number of ellipsoidal random slip surfaces which may be truncated at the interfaces between geological layers. This results in a spatial overview of potentially unstable regions. After demonstrating the functionality of the model with an artificial cone-shaped terrain, we test *r.rotstab.layers* for the 10 km² Ripoli area in Umbria, central Italy. According to field observations in the Ripoli area, morpho-structural settings play a crucial role for deep-seated landslide distribution. We have prepared a model of the geological layers based on surface information on the strike and dip of each layer, and we use this model as input for *r.rotstab.layers*. We show that (1) considering the geological layers is essential for the outcome of deep-seated slope stability modelling, and (2) the seepage direction of the groundwater is a major source of uncertainty.

Keywords

Geological layers • Slip ellipsoid • Slope stability • Open source GIS

I. Marchesini • M. Santangelo • M. Cardinali • F. Ardizzone • F. Fiorucci • F. Guzzetti
CNR IRPI, Via Madonna Alta 126, 06128 Perugia, Italy
e-mail: ivan.marchesini@irpi.cnr.it; Michele.santangelo@irpi.cnr.it; mauro.cardinali@irpi.cnr.it; francesca.ardizzone@irpi.cnr.it; federica.fiorucci@irpi.cnr.it; fausto.guzzetti@irpi.cnr.it

M. Mergili (✉)
Institute of Applied Geology, BOKU University, Peter-Jordan-Straße 70, 1190 Vienna, Austria
e-mail: martin.mergili@boku.ac.at

M. Rossi
CNR IRPI, Via Madonna Alta 126, 06128 Perugia, Italy
Department of Earth Sciences, University of Perugia, Piazza dell'Università 1, 06100 Perugia, Italy
e-mail: mauro.rossi@irpi.cnr.it

B. Schneider-Muntau • W. Fellin
Unit of Geotechnical and Tunnel Engineering, University of Innsbruck, Technikerstrasse 13, 6020 Innsbruck, Austria
e-mail: barbara.schneider-muntau@uibk.ac.at; wolfgang.fellin@uibk.ac.at

Introduction

Simple deterministic slope stability models based on the assumption of an infinite slope with a planar failure plane parallel to the slope are commonly implemented in GIS environments (Van Westen et al. 2006). They are well suited for analyzing shallow slope stability. More complex models consider the three-dimensional geometry of possible slope failures and are therefore also suitable for the analysis of deep-seated slope stability (e.g., Bishop 1954; Janbu et al. 1956). Such models rely on complex neighbourhood relationships and their implementation in GIS environments is not trivial (attempts were made, e.g., by Xie et al. 2003, 2004a, b, 2006; Marchesini et al. 2009; and Jia et al. 2012). Mergili et al. (2014) have recently introduced the model *r.rotstab* in order to bridge the gap between the two approaches. They have found out that the model performance for deep-seated landslides may suffer from a

disregard of morpho-structural settings—in particular, the strike and dip of the geological layers—even though a clear statistical relationship with landslide occurrence was shown by Santangelo et al. (2014). In this article, we attempt to overcome this limitation of *r.rotstab* by extending the model with a tool—*r.rotstab.layers*—to include the strike and dip of the geological layers into the slope stability calculations. The objective of the work is to identify the capability of such an approach, as well as its limitations, and the most urgent needs for further research.

Methods

The Model *r.rotstab*

r.rotstab (Mergili et al. 2014) represents a GIS-based, three-dimensional slope stability model capable of dealing with both shallow and deep-seated slope failures. The model is developed as a C-based raster module within the GRASS GIS software (GRASS Development Team 2013). It makes use of a modification of the three-dimensional sliding surface model proposed by Hovland (1977) and revised and extended by Xie et al. (2003, 2004a, b, 2006). Compared to this model, a more advanced approach to compute the seepage forces is introduced, which is described in detail in Mergili et al. (2014). Given a Digital Elevation Model (DEM) and a set of thematic layers, the model evaluates the slope stability for a large number of randomly selected potential slip surfaces, ellipsoidal in shape. Randomization of the ellipsoid parameters is constrained by user-defined minima and maxima of the ellipsoid dimensions and position. Truncated ellipsoids can be used to model the presence of weak layers at defined depths—or defined regular or irregular surfaces—within the soil or the bedrock. Any single GIS raster cell may be intersected by multiple sliding surfaces, each associated with a computed safety factor. For each cell, the lowest value of the safety factor and the depth of the associated slip surface are stored. These pieces of information can be used to obtain a spatial overview of potentially unstable regions over an area of up to several square kilometres.

The Extended Model *r.rotstab.layers*

In *r.rotstab*, the geotechnical parameters required as input are defined on the basis of soil classes, discrete data units containing information on (i) cohesion c , (ii) angle of internal friction ϕ , (iii) dry specific weight γ_d and (iv) saturated water content θ_s . *r.rotstab* further allows the definition of a limited number of layers for each soil class. Each ellipsoid is truncated at each layer bottom it intersects, and the safety

factor is computed for the entire ellipsoid as well as for the truncated shapes. However, this design is not suitable for large amounts of layers in complex geological settings.

r.rotstab.layers is designed in order to overcome this limitation. Relying on input raster datasets representing the bottom of each geological layer, it can handle sets of up to 100 of such layers. The layer data is condensed into a text file which stores the depth of each relevant layer for each raster cell. The geotechnical parameters associated with each layer are required as tabular input. In contrast to *r.rotstab*, the information on the soil classes is provided by the layer data so that no additional horizontal soil classes have to be defined. Here, we present a preliminary version of the model.

Test with an Artificial Cone

Data

A regular cone with a slope of 30° is used to demonstrate the model performance in a controlled way. A set of regular and parallel geological layers with bedding planes at a constant dip of 30° is introduced, resulting in a varying orientation of the layers with respect to the cone surface (Fig. 1). A sequence of alternating 20 m thick strong ($c = 10 \text{ kN/m}^2$, $\phi = 40^\circ$) layers and 2 m thick weak ($c = 5 \text{ kN/m}^2$, $\phi = 20^\circ$) layers is defined, with the uppermost weak layer assumed at a depth of 10 m. In total, 54 layers are considered.

Taking an area of $1,000 \times 1,000 \text{ m}$ and a cell size of 5 m, *r.rotstab.layers* is run for 200,000 randomly centred ellipsoids with a length of 200 m, a width of 125 m and a depth of 20 m. In addition, two pre-defined ellipsoids (E1 and E2 in Fig. 2) are analysed in more detail.

Results and Discussion

Figure 1 shows the spatial variation of the safety factor yielded by *r.rotstab.layers*, assuming dry (a) and fully saturated (b) conditions. The side of the cone with bedding dipping in the direction of the slope clearly shows lower safety factors than the side with bedding dipping into the slope. This effect is enhanced for saturated material when considering layer-parallel seepage forces.

The results for two pre-defined ellipsoids—E1 with cataclinal (see Fig. 2a), E2 with anaclinal layering (see Fig. 2b)—are illustrated in terms of the forces acting along a longitudinal section through the centres of the ellipsoids. The shear resistance is positive in an upslope direction, shear forces and seepage forces are positive in a downslope direction. The shear resistance and the shear force are parallel to the local inclination of the slip surface. The seepage force

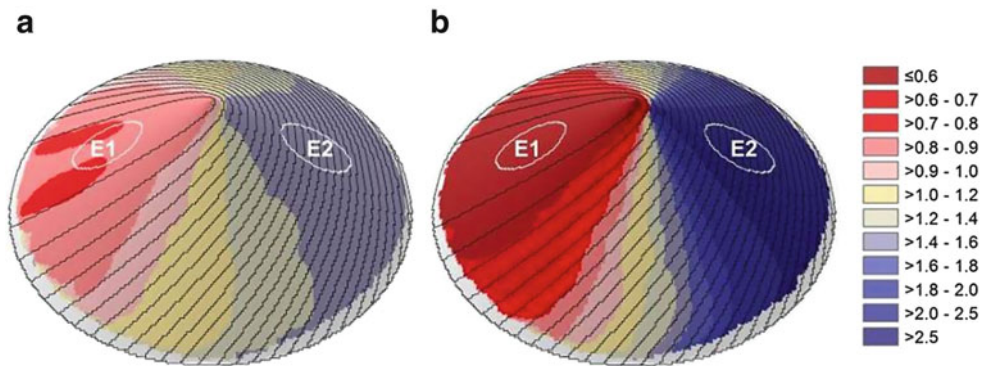


Fig. 1 Safety factors computed with r.rotstab.layers for a regular cone assuming (a) dry material, (b) saturated material with layer-parallel seepage. The black lines represent the traces of the weak layers, the ellipsoids E1 and E2 are analyzed in Fig. 2

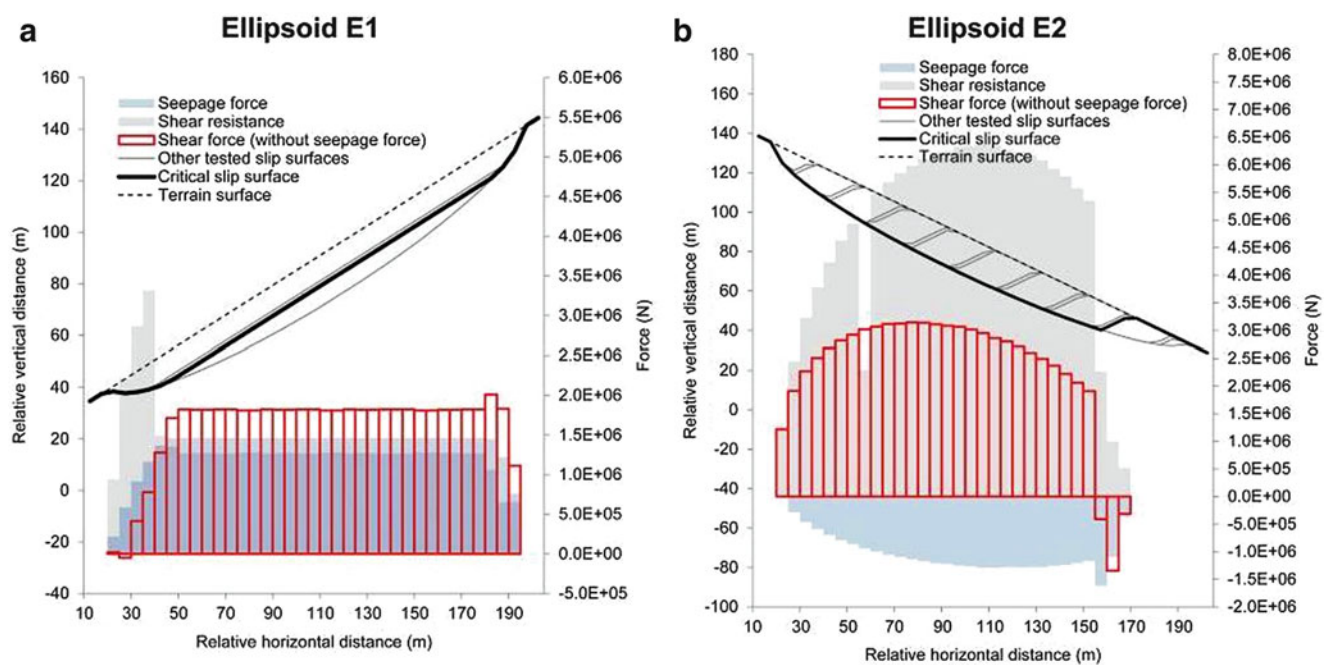


Fig. 2 Forces acting along the main axes of the ellipsoids E1 and E2 (see Fig. 1) for saturated conditions

acts in the direction of the seepage flow and the component parallel to the shear force is evaluated.

For the ellipsoid E1, the most critical slip surface (safety factor = 0.84 for dry conditions, 0.52 for fully saturated conditions) corresponds to the bottom of the only weak layer intersected by the ellipsoid bottom. The shear resistance is higher in the lower part of the ellipsoid, presenting a low inclination and high values of c and ϕ (slip surface within the strong layer). The shear resistance in the upper part of the ellipsoid is lower although high values of c and ϕ are applied, due to the steeper inclination and the lower weight. The patterns observed for the shear force and the seepage force reflect the balance between the inclination and the weight of the overlying saturated material and water, respectively.

The ellipsoid E2 intersects several weak layers of anclinal setting (see Fig. 2b). Much higher safety factors (1.49 for dry conditions, 3.32 for saturated conditions) are observed for saturated than for dry conditions. This is a consequence of (i) the high shear resistance over most of the tested slip surfaces, (ii) the negative shear force of the anclinal-truncated surface and (iii) the negative seepage force (seepage into the slope as prescribed by the anclinal orientation). Even though the effect of the weak layers on the shear resistance is obvious, in some places the spatial resolution does not allow identifying each single weak layer intersecting the ellipsoid bottom (see the single drop of the shear resistance in Fig. 2b).

Application to the Ripoli Area

Data

The Ripoli area is part of the Collazzone area (Umbria, central Italy) which has been intensively studied with regard to landslides in the past 15 years (Guzzetti et al. 2006; Ardizzone et al. 2007; Galli et al. 2008; Rossi et al. 2010; Fiorucci et al. 2011; Mergili et al. 2014). With an area of 9.7 km² (9.9 % of it affected by observed deep-seated landslides) the Ripoli area mainly consists of semi-consolidated clastic sediments. Particularly those with significant clay content are prone to landsliding (Fig. 3). The geotechnical parameters for each class exposed at the surface (Table 1) were determined by a combination of laboratory tests, a geotechnical data base for central Italy and back-calculations (Mergili et al. 2014). The bedding traces of the geological layers were mapped. Strike and dip of the traces were obtained at several places (Marchesini et al. 2013). From these pieces of information we generated the interpolated raster layers of bedding inclination and dip direction Santangelo et al. (2014), that were used to produce the TOBIA index map (Meentemeyer and Moody 2000) and the map of the dip direction relative to the slope (Fig. 3). By means of a GRASS GIS Python script and in particular of the Pygrass library (Zambelli et al. 2013), the elevation of the cells of the bedding surface corresponding to each stratigraphic limit is determined iteratively, starting from the stratigraphic limit outcrop and exploiting dip direction and inclination of the neighbouring cells. Altogether, the bedding planes of 67 layers—all of them >2 m thick—are used as input for *r.rotstab.layers*, each of them assigned to one of the six classes shown in Table 1. In addition we use a 10 m resolution DEM derived from a set of contour lines shown in the 1:10,000 topographic map. The model is run for three sets of assumptions: (i) no layering, with distribution of soil classes according to Fig. 3 and no truncation of the ellipsoid (original *r.rotstab*), (ii) layering, but seepage assumed in slope-parallel direction, (iii) layering with seepage in the dip direction of the layers. All of the assumptions are based on fully saturated material.

The random ellipsoids are constrained according to the dimensions of deep-seated landslides observed in the Collazzone area (length = 65–266 m, width = 55–291 m, depth = 5–20 m, Mergili et al. 2014). One million ellipsoids are tested during each model run.

Results and Discussion

The spatial distribution of the safety factor computed with the assumptions (a), (b) and (c) is illustrated in Fig. 4. The

results are validated with the distribution of observed deep-seated landslides in the Ripoli area. As the ellipsoids have to be centred within the study area, the edges of the area are not fully covered by the computation process and are therefore not considered for the validation procedure. Table 2 summarizes the main indicators of the validation for each of the three model runs. Looking at Fig. 4 and Table 2, it is obvious that assumption (b) yields the most conservative results, compared to the other assumptions. The safety factor is <1 for 70.8 % of the Ripoli area, in contrast to 30.5 % (a) and 23.5 % (c). Whilst 83.5 % of all observed landslide raster cells are identified correctly with assumption (b), this is only the case for 30.4 % of all raster cells without observed landslides. The assumptions (a) and (c) yield reverse patterns. The total rate of true predictions is significantly lower for the outcome of assumption (b) than for the other assumptions (35.1 %, compared to 67.7 % and 73.0 %, respectively; see Table 2). Two aspects of the results deserve a closer discussion: (1) why does assumption (b) lead to more conservative results than the other assumptions? and (2) which of the assumptions is closest to reality, i.e., how to interpret the results with regard to landslide susceptibility mapping?

(1) With assumption (a), only the top layer is considered and assumed to be infinitely thick. For each raster cell, the probability that the ellipsoid surface intersects a susceptible material such as clay is much lower than if a layering approach with a possible truncation of the ellipsoid is adopted (assumptions b and c). With assumption (b), the seepage force always acts in the most unfavourable direction with respect to slope stability. Therefore the safety factors have a tendency to be lower than for assumption (c), where they can also act into the slope and therefore lead to an increased safety factor (see Figs. 1 and 2).

(2) First of all it seems clear that the assumptions (b) and (c) are superior to assumption (a) in capturing the complexity of the topic. Assumption (c) fails to reproduce two prominent landslides in the centre of the study area (see Fig. 4) which are well reproduced by assumption (b). Looking at Fig. 3, these two landslides are associated with orthoclinal layering, leading to seepage forces directed into the slope and therefore high safety factors with regard to assumption (c). However, the question of seepage direction is a complex one and requires more detailed work to be better understood and better implemented in this type of model.

Finally, the high false positive rate related to assumption (b) (see Table 2) is not necessarily purely a consequence of a poor understanding of the phenomenon and/or an insufficient parameterization. False positive raster cells may have been affected by earlier unmapped landslides or be susceptible to future landslides. In contrast, false negative predictions are certainly incorrect.

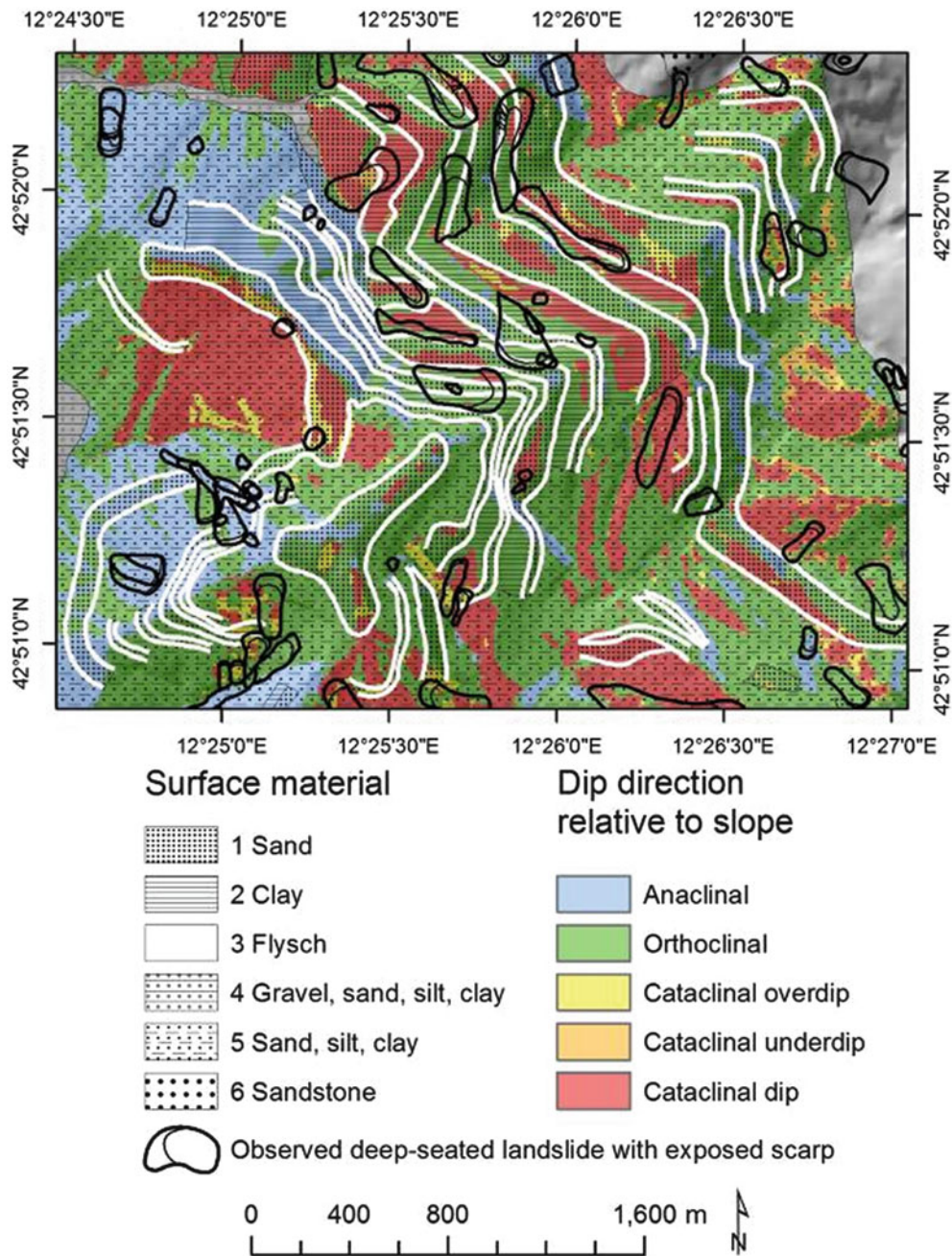


Fig. 3 Ripoli area. The white lines represent the bedding traces of the 67 geological layers considered. Each layer is assigned to one of the classes characterized in Table 1

Table 1 Material properties of the geological classes exposed in the Ripoli area: cohesion c (kN/m²), angle of internal friction ϕ (degrees), dry specific weight γ_d (kN/m³) and saturated water content θ_s (vol. %)

| ID type | γ_d | c | ϕ | θ_s |
|----------------------------|------------|------|--------|------------|
| 1 Sand | 19.0 | 4.0 | 38.0 | 40 |
| 2 Clay | 15.5 | 8.3 | 18.1 | 25 |
| 3 Flysch | 18.0 | 22.0 | 15.0 | 45 |
| 4 Gravel, sand, silt, clay | 19.0 | 13.0 | 30.0 | 45 |
| 5 Sand, silt, clay | 18.0 | 15.0 | 15.0 | 45 |
| 6 Sandstone | 22.0 | 8.5 | 35.0 | 45 |

Conclusions

Employing a preliminary version of the new GIS-based three-dimensional slope stability model r.rotstab.layers, we have shown that the consideration of morpho-structural settings exerts a significant impact on the results of deep-seated slope stability computations. We conclude that the thickness, strike and dip of the geological layers have to be regarded for deep-seated landslide susceptibility mapping

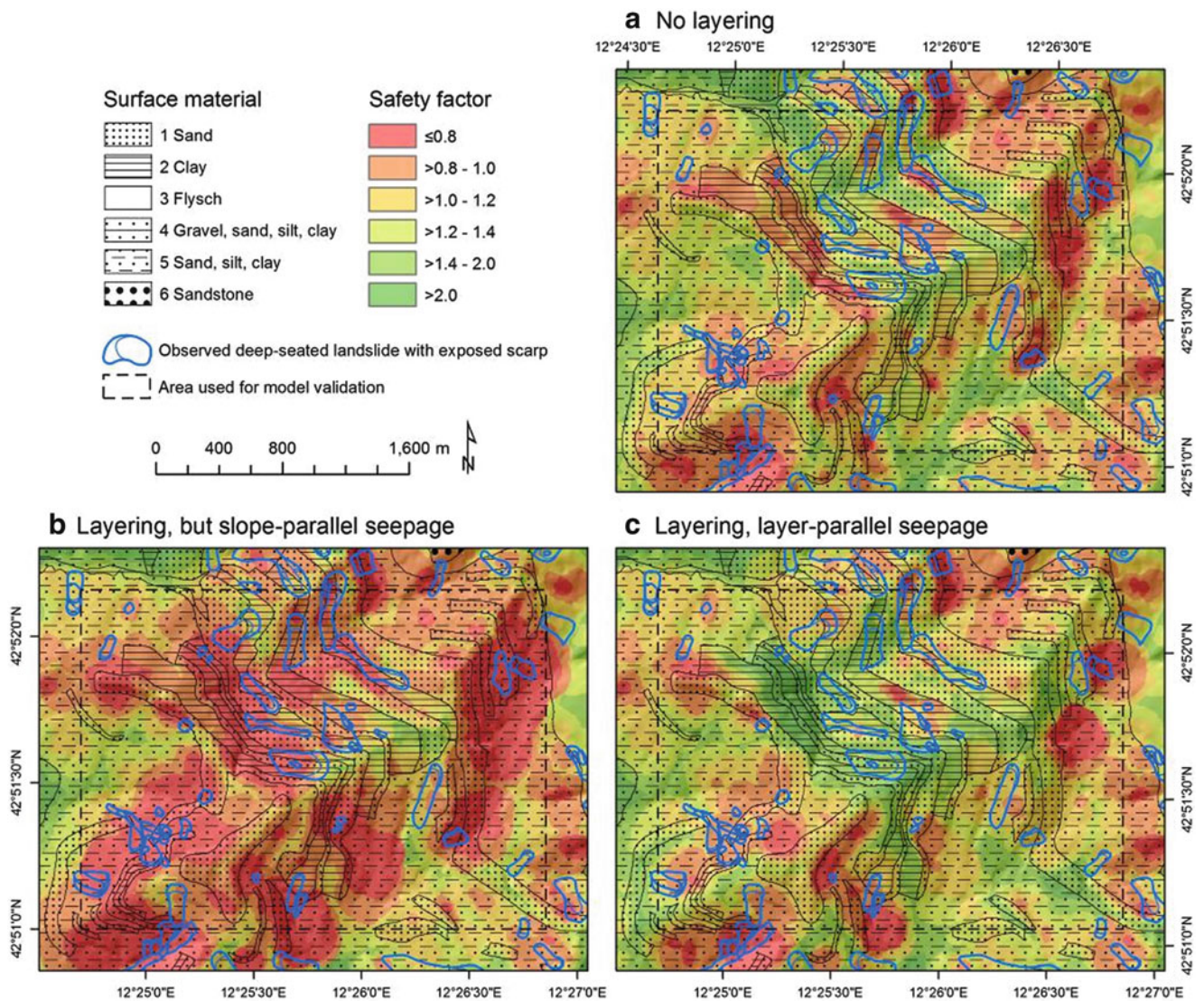


Fig. 4 Safety factors computed with three different assumptions of layering and seepage direction

Table 2 Model results for the Ripoli area

| Predictions indicator | (a) | (b) | (c) |
|---|--------|--------|--------|
| True negative—TN | 64.2 % | 27.7 % | 70.3 % |
| False positive—FP | 27.0 % | 63.4 % | 20.8 % |
| False negative—FN | 5.3 % | 1.5 % | 6.2 % |
| True positive—TP | 3.5 % | 7.4 % | 2.7 % |
| Rate of true non-landslide TN/(TN + FP) | 70.4 % | 30.4 % | 77.1 % |
| Rate of true landslide TP/(FN + TP) | 39.6 % | 83.5 % | 30.2 % |
| Total rate of landslide FP + TP | 30.5 % | 70.8 % | 23.5 % |
| Total rate of true—TN + TP | 67.7 % | 35.1 % | 73.0 % |

(a) No layering, (b) layering, but slope-parallel seepage, (c) layering with seepage in dip direction of layers

efforts. Further, we have demonstrated that the seepage direction strongly influences the safety factor of saturated materials. We therefore recommend more research towards a detailed understanding of the—sometimes complex—seepage patterns in different types and assemblages of regolith.

Acknowledgments Special thanks go to Matthias Benedikt, Stefan Fugger, Sebastian Matz and Stefan Tilg. The work was partially supported by the Italian National Department for Civil Protection, and the Regione dell'Umbria under the contract POR-FESR Umbria 2007–2013.

References

- Ardizzone F, Cardinali M, Galli M, Guzzetti F, Reichenbach P (2007) Identification and mapping of recent rainfall-induced landslides using elevation data collected by airborne Lidar. *Nat Hazards Earth Syst Sci* 7:637–650
- Bishop AW (1954) The use of the slip circle in the stability analysis of slopes. *Geotechnique* 5(1):7–17
- Fiorucci F, Cardinali M, Carlà R, Rossi M, Mondini AC, Santurri L, Ardizzone F, Guzzetti F (2011) Seasonal landslides mapping and estimation of landslide mobilization rates using aerial and satellite images. *Geomorphology* 129(1–2):59–70
- Galli M, Ardizzone F, Cardinali M, Guzzetti F, Reichenbach P (2008) Comparing landslide inventory maps. *Geomorphology* 94:268–289
- Guzzetti F, Galli M, Reichenbach P, Ardizzone F, Cardinali M (2006) Landslide hazard assessment in the Collazzone area, Umbria, Central Italy. *Nat Hazards Earth Syst Sci* 6:115–131
- GRASS Development Team (2013) GRASS GIS. The world's leading Free GIS software. Open source geospatial foundation project. URL: <http://grass.osgeo.org>. Last accessed August 1, 2013
- Hovland HJ (1977) Three-dimensional slope stability analysis method. *J Geotech Eng Div ASCE* 103(GT9):971–986
- Janbu N, Bjerrum L, Kjaernsli B (1956) Soil mechanics applied to some engineering problems. Publication 16, Norwegian Geotechnical Institute, Oslo
- Jia N, Mitani Y, Xie M, Djamaluddin I (2012) Shallow landslide hazard assessment using a three-dimensional deterministic model in a mountainous area. *Comput Geotech* 45:1–10
- Marchesini I, Cencetti C, De Rosa P (2009) A preliminary method for the evaluation of the landslides volume at a regional scale. *Geoinformatica* 13:277–289
- Marchesini I, Santangelo M, Fiorucci F, Cardinali M, Rossi M, Guzzetti F (2013) A GIS method for obtaining geologic bedding attitude. In: Margottini C, Canuti P, Sassa K (eds) *Landslide science and practice*. Springer, Berlin, pp 243–247
- Meentemeyer RK, Moody A (2000) Automated mapping of conformity between topographic and geological surfaces. *Comput Geosci* 26:815–829
- Mergili M, Marchesini I, Rossi M, Guzzetti F, Fellin W (2014) Spatially distributed three-dimensional slope stability modelling in a raster GIS. *Geomorphology* 206:178–195
- Rossi M, Guzzetti F, Reichenbach P, Mondini AC, Peruccacci S (2010) Optimal landslide susceptibility zonation based on multiple forecasts. *Geomorphology* 114:129–142
- Santangelo M, Marchesini I, Cardinali M, Fiorucci F, Rossi M, Bucci F, Guzzetti F (2014) A method for the assessment of the influence of bedding on landslide abundance and types. *Landslides* (Accepted)
- Van Westen CJ, Van Asch TWJ, Soeters R (2006) Landslide hazard and risk zonation – why is it still so difficult? *Bull Eng Geol Environ* 65:167–184
- Xie M, Esaki T, Zhou G, Mitani Y (2003) Three-dimensional stability evaluation of landslides and a sliding process simulation using a new geographic information systems component. *Environ Geol* 43:503–512
- Xie M, Esaki T, Cai M (2004a) A GIS-based method for locating the critical 3D slip surface in a slope. *Comput Geotech* 31:267–277
- Xie M, Esaki T, Zhou G (2004b) GIS-based probabilistic mapping of landslide hazard using a three-dimensional deterministic model. *Nat Hazards* 33:265–282
- Xie M, Esaki T, Qiu C, Wang C (2006) Geographical information system-based computational implementation and application of spatial three-dimensional slope stability analysis. *Comput Geotech* 33:260–274
- Zambelli P, Gebbert S, Ciolli M (2013) Pygrass: an object oriented python Application Programming Interface (API) for Geographic Resources Analysis Support System (GRASS) Geographic Information System (GIS). *ISPRS Int J Geo-Inform* 2(1):201–219



Risk Evaluation of Landslide Topographic Area by Aerial Photointerpretation

Toyohiko Miyagi and Eisaku Hamasaki

Abstract

Landslide topographies are widely distributed in Japan and amount to more than 300,000 sites. The area has potential for various kinds of slope disaster such as reactivation, and high potential of slope failure because of the weak geology. Some landslide deposits are stable already.

Consequently, some method of the risk evaluation is needed. The authors review the history of landslide risk evaluation. The approach started by aerial photointerpretation. The comparative study between the surface features and inner characteristics has a long history. And the AHP approach for risk evaluation is also established.

Keywords

Landslide topography • Aerial photointerpretation • AHP • Risk evaluation

Introduction

Landslides, being natural disasters, are considered threats to life and financial capital. Research on landslides has been employed in the fields of science and technology development that relate to natural disaster prevention. That is to say, it has become applied science that is: 'utilized when landslides unfold and natural disaster occur'. Recent projects on 'understanding the host of risks linked to landslides' or 'risk evaluations of landslide topographies' in Japan's academic community focusing on landslides have made great advances; moving from past counter measures towards forecasting inference of landslide risks. We have promoted and contributed to these developments. Thus, this paper builds on these advances and reflects chronologically on

how 'technology aiming to understand existing risks of landslides' has been constructed and linked to the risk evaluation, and discusses the significance of mapping landslide phenomena.

The Introduction of Aerial Photo Interpretation and Recognition of Landslide Terrain

Engineers and academics have broadly applied utilization of aerial photography since the 1960s. Tohoku University's research laboratory for geography obtained a 1/40,000 monochrome aerial photography set taken by the US military. This was done for the purpose of analysing aerial photography and land classification in national land surveys. In and around 1965, various scholars pointed out that 'landslide topography' formed through landslides can be recognized by aerial photography analysis (ex. Ichise 1964). Furthermore, applying aerial photointerpretation in terrain surveys for dam constructions, cases of unexpected unstable ground 'resampling landslides' were pointed out.

Figure 1 depicts an example of a road showing a range of slope destructions and landslides occurring (B, C, D), while in the background of the landslide D we have large-scale

T. Miyagi (✉)
Faculty of Arts, Department of Regional Management, Tohoku-Gakuin University, Sendai, Miyagi 981-3193, Japan
e-mail: miyagi@izcc.tohoku-gakuin.ac.jp

E. Hamasaki
Department of Technology, Advantech Co., Ltd., Sendai 980-0013, Japan
e-mail: hamasaki@advantech.co.jp

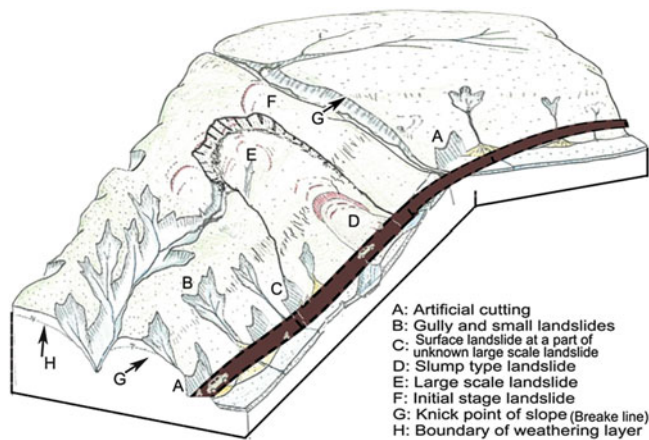


Fig. 1 Relation between landslide topography and slope disasters

landslide topography E which cannot be seen from the road. In this case, landslides C and D are the foremost parts of landslide E and occurred as a result of previous collapse.

Geomorphologists and engineers who have applied the reading of aerial photographs to the foot of volcanoes in the Ōhū Mountains have discovered an expanding topography caused by massive landslides marked by rough undulations and unusual horse-shoe shape cliffs. In an abstract of a conference presentation entitled ‘A Landslide Topography of Funagata Rempō Hokuroku,’ Chida et al. (1971) concluded that the results of a land survey show that this is a landform formed by landslides. At the same time, Hatano analyzed the ‘Sendai’ area using a 1/200,000 topographical map and provided a map highlighting various slope terrains possibly created through landslides (Hatano 1974). Hatano was probably the first in Japan who illustrated the distribution conditions of large-terrain landslides. Since Hatano’s revelations Terado (1978), Miyagi (1979), Shimizu et al. (1982–1988), Japan Landslide Society Tohoku Branch (1992) have put forward distribution maps of landslide terrains for various areas in Japan.

In order to locate ‘landslides’ as significant factors forming slope terrain, time was required for the National Research Center for Disaster Prevention (today the National Research Institute for Earth Science and Disaster Prevention) to conduct research and publish 1/50,000 Landslide topographic area distribution maps. Moreover, the analysis following the discovery of landslide topography was conducted with great scientific interest in important geomorphological questions of ‘how slopes develop’. The introduction of aerial photointerpretation has advanced research on quaternary tectonic movements and the development of topography which has focused on the recognition of terraces and active faults. The recognition of landslides was advanced addressing the question of how to locate mass movement as a factor in explaining the topographical development of slopes.

The analysis of landslides through aerial photointerpretation allows us to distinguish topographical areas created through landslides from those which did not result from landslides. Landslide terrain is clearly demarcated from general slopes through the landslide scarps (Varnes 1978). The main part of a landslide is surrounded by slips and recognized as consisting of moving objects such as the landslide body. Landslide topography is constituted by slip surface so called surface of rupture and moving material called the landslide body. Various types of shape and inclination of slip precipices exist. Moreover, the moving parts themselves undergo various changes in form and substance in the process of movement which appears in the form of micro-topographical features at the surface of the moving part.

From Recognizing and Mapping Landslides to Risk Evaluation of Landslides

As a vast range of landslide topographies has been mapped, the meaning of these distributions became the object of inference. Looking at the distribution of a large quantity of landslide topographies in the southern Ohu mountains in the Tohoku region, criticism was expressed arguing that ‘given the large quantity of landslides disaster prevention would be impossible’, while others questioned the wisdom of referring to ‘everything as a landslide’. It was here that the Japan Landslide Society’s Tohoku and Hokkaido regional branches have published their own reviews on knowledge and technology with regard to landslides and landslide prevention. The publication entitled ‘Landslides and Landslide Topography in the Tohoku Region’ published by the society’s Tohoku branch (Japan Landslide Society Tohoku Branch 1992) has used both terms: ‘landslide’ and ‘landslide topography’, and thus clearly emphasized the differentiation between landslides as a phenomenon of material movement of slopes and landslide topography which is formed as a result of such a phenomenon.

Naturally, the topography caused by the effects of landslides creates particular landslide topographies. Furthermore, it has been pointed out that the micro-topography constituted through landslide topography corresponds to the material character and movement of landslides (Miyagi 1979; Yagi 2003). Landslide topography consists of a host of basic units of topography. Each of the topographic units is formed by peculiar processes; thus, it has been suggested that by understanding the formation of micro-topographies it is possible to investigate the form of movement and the location of the slide structure, as well as the formation processes of landslide topographies, and the mechanisms of landslides (Kimata and Miyagi 1985). Later, this idea was linked to the “Autonomic Destruction Process” of

| Initial situation (Stress field, solid-state of rock, Geology) | | Geomorphic setting (Stages of geomorphic development) | | | Slope gradient | | | | | |
|--|--|---|-----------------------|-------|----------------|-------------------|---------------------------------------|----------------------------------|--------------------------------|---------------------------------------|
| Autonomous destruction process | | Solid-state of rock | Destruction | | | Landform features | | | Trigger of action | |
| | | | Type | Scale | Frequency | Plan | Scarp | Micro landform | Outer | Inner |
| Stage I | Release from residual stress | Elastic | Destruction dominant | Large | Seldom | Round | Crack Sagging Linear graben | Original shape Warp | Deepening Shape of mountain | |
| Stage II | Glide at bedding plane Slump as describe an arc | ↑ | ↑ | ↑ | ↑ | ↑ | Large separation scarp Slide scarp | Block | Type and magnitude of rainfall | inner stress field distribution |
| Stage III | Fractural slip Folding slide Debris slide | | | | | | | | | relocation of water by micro landform |
| Stage IV | Flow type slide | Fluidic | Viscous flow dominant | Small | Frequent | Long oval | Small scarp | Slightly hummocky wavy smooth | | Trap |

Fig. 2 Hypothesis of autonomic destruction processes caused by the occurrence of initial landslides The 1992 published ‘Landslides and Landslide Topographies in the Tohoku Region (Japan Landslide Society Tohoku Branch)’ contains geological maps and allocation maps of landslide topographies, counter-measure examples for local authorities

landslide topographies. Here it was argued that ‘through the occurrence of a destruction of an initial landslide action at the slope the conditions of the material and water system change in the damaged area. This can serve as a cause for the occurrence of secondary landslides. Here, deformed and transformed conditions of the material and water cause peculiar forms of landslide (surface change and formation of micro-topographies as reflections of scale, frequency, and movement form)’ (Miyagi 1990) (see Fig. 2, below). As a result, we can examine the characteristics of the instability and the movement of each specific landslide unit by setting an indicator axis and by investigating the conditions of change.

Time from Occurrence of Initial Landslides Until Reduction and the Intermittent of Landslide Activity

An overwhelmingly large number of landslide topographies take a very long time before reduction. Some argue that in case of large-scale landslides of more than 1 km², a time frame of more than 100,000 years is required (Yanagida and Hasegawa 1993). If this is the case, landslide disasters exist in extremely long time horizons which transcend human time perceptions but are fatal phenomena which can occasionally occur. Many of the existing landslide topographies are not dangerous, but a few have reached stages at which

for landslide prevention, as well as information on how to analyze a landslide topography, geology, allocation, mechanisms and risk. As such, this has been a comprehensive and ambitious work relating to our current tasks

they frequently cause damage. Here, we can assume that depending on the location of the landslide (topographic location conditions: e.g. foremost parts of a movement object which confront frontal slopes of rivers are in unstable conditions), landslides have become more unstable, and a small number of these landslides constitute under a number of specific conditions an unstable area of high risk. Through understanding and evaluating these conditions, we may evaluate which landslide topographies will cause natural disasters in the near future. Experiencing trial and error, risk evaluation of landslide topographies has advanced to its current form.

Substantial analysis of the risk evaluation methods of the landslide topography in the Tohoku region have been conducted for Iwate Prefecture’s Sediment Control Division and Miyagi Prefecture’s Natural Disaster Prevention and Sediment Control Division, and have served as the basis for the drafting of manuals.

Risk Assessment and Efforts of Technological Advancement

It goes without saying that risk assessment, (that is, assessment of the stability and instability of landslide areas which is predicated in the principle of disaster prevention and an understanding of the use of land) is conducted through evaluating the characteristics of the material and water, as

well as the surface of slide. However, given the vast number of existing landslide topographies it is, from an economical and personnel standpoint, impossible to conduct sufficient on-site surveys or boring surveys. It would be a rational solution if the degree of risk could be assessed through some indirect method. The idea of assessing the degree of risk of individual landslide topographies through aerial photograph interpretations, while being only a first step in the process of evaluation, represents a procedure in which critical areas (that is, areas which require careful on-site surveys) are selected and in which surveys are focused.

We were confronted with significant problems in conducting concrete risk assessments. Before we had to assess the risks of a given landslide topography, we did not discuss the basic problem of ‘how unstable were landslide topographies, disregarding the way in which these micro-topographies have been recognized’. That is to say, firstly, we have to consider whether we can find a corresponding relationship between the appearance of a landslide topography (that is, the micro-topography), and internal structure, (that is, the movement form), the material characteristics, and the structure of the slide. Secondly, we have to consider to what extent indicators shown by the landslide topography directly relate to its risk assessment.

Here, we introduce an example which analyses the correspondence between the micro-topography of the moving part of the landslide, the internal part of the moving part which constitutes the topography and the characteristics of the slide surface.

The Ōhokamizawa Landslide area is an active large-scale landslide which reaches a length of 1.3 km, and is one of the prominent landslides in Japan which has been subjected to detailed surveys (see Fig. 3).

Figure 3 above follows this survey data. We explain the data very briefly below. The vertical sections of the slide surface (Surface of rupture) are developing in several active steps, and the landslide topography’s (vertical sections at the ground surface) slope surface and upper parts show a variety of staircase patterns. The material of the moving part consists of background and upper parts of the landslide area of new trenches created through new rocks while the middle part consists of rock debris and colluvium like deposit; the lower region of the moving part consists of cohesive soil (see the bar graph in Fig. 4, below). Using data gathered by a large number of extensometers at the ground surface, we see that the upper-region of the moving part tends to be pulled, while the lower region tends to be placed under pressure. If we look at the micro-topography (minor cliffs, cracks and slope precipices) we see that a host of large-scale scarps is located in the rear of major slope precipices. Around the upper parts surrounding major slopes

a vast number of convex cracks develop. The form of the cracks and minor scarps change to become convex in the lower part, demarcating a large-scale precipice. Furthermore, the 1/3 lower part of the landslide body, the crack and scarp disappears and changes into hummocky ground surface. The evidence alluded to above illustrates that in the process of a large-scale landslide topography, a forefront landslide lower-part of approx. 300 m occurs, while landslides of similar scale repeatedly occur-in this case about four times thus far. In the meantime, each landslide is active through entailing particular slide surfaces, due to the monoclinic structure of slopes in the layers of the given region. Moreover, in the background of the main landslide slope, we see expanding parallel cracks which indicate the occurrence of new landslides.

The evidence introduced here illustrates the moving mechanisms and material characteristics of landslides as expressed in a micro-topography. That is to say, ‘if can predict the particular movement and material characteristics of a landslide, we may be able to analogize the risk of a reoccurrence of a landslide’.

Establishment of an AHP-Based Risk Assessment Method for Landslides

The discussion on risk assessment of Iwate Prefecture began with the recognition of mini-topographies. The method applied at this time is the AHP (Saaty 1980) approach introduced by Hamasaki (Miyagi et al. 2004). Japan experiences landslide disasters almost every year. It is for this reason that many surveys are conducted and countermeasures put in place. Engineers who have rich on-site experience and are familiar with the technology of aerial photointerpretation have supported the basic academic knowledge and contributed to judgments on the risk of landslides in the area. However, in many cases this experience cannot be expressed plainly in words. While senior engineers evaluate someone’s ‘views as appropriate or as the masterly performance’, it is difficult to communicate this understanding to junior scientists and engineers. Risk assessment employing AHP has emerged from the discussions of these engineers who possess these views. Concretely, using practical sample pictures, seven engineers are summoned for the purpose of debating problems of defining a micro-topography constituting a landslide, its recognition, as well as which indicators are important in showing risks of a micro-landform. Through reiterating such debates unclear concepts are restructured into clear definitions. As such, ideas are created as to ‘which micro-landforms are to extent indicators of instability’. **This process transforms tacit**

Aerial photograph of the Ohokamizawa landslide

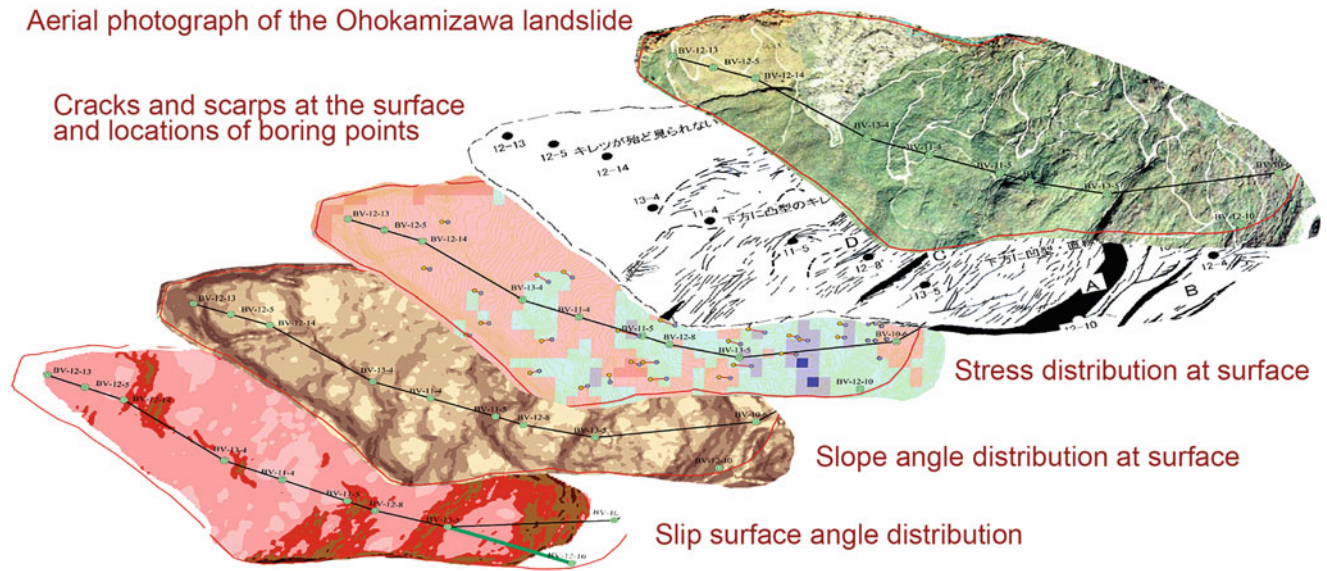


Fig. 3 A series of data in case of Ohokamizawa landslide

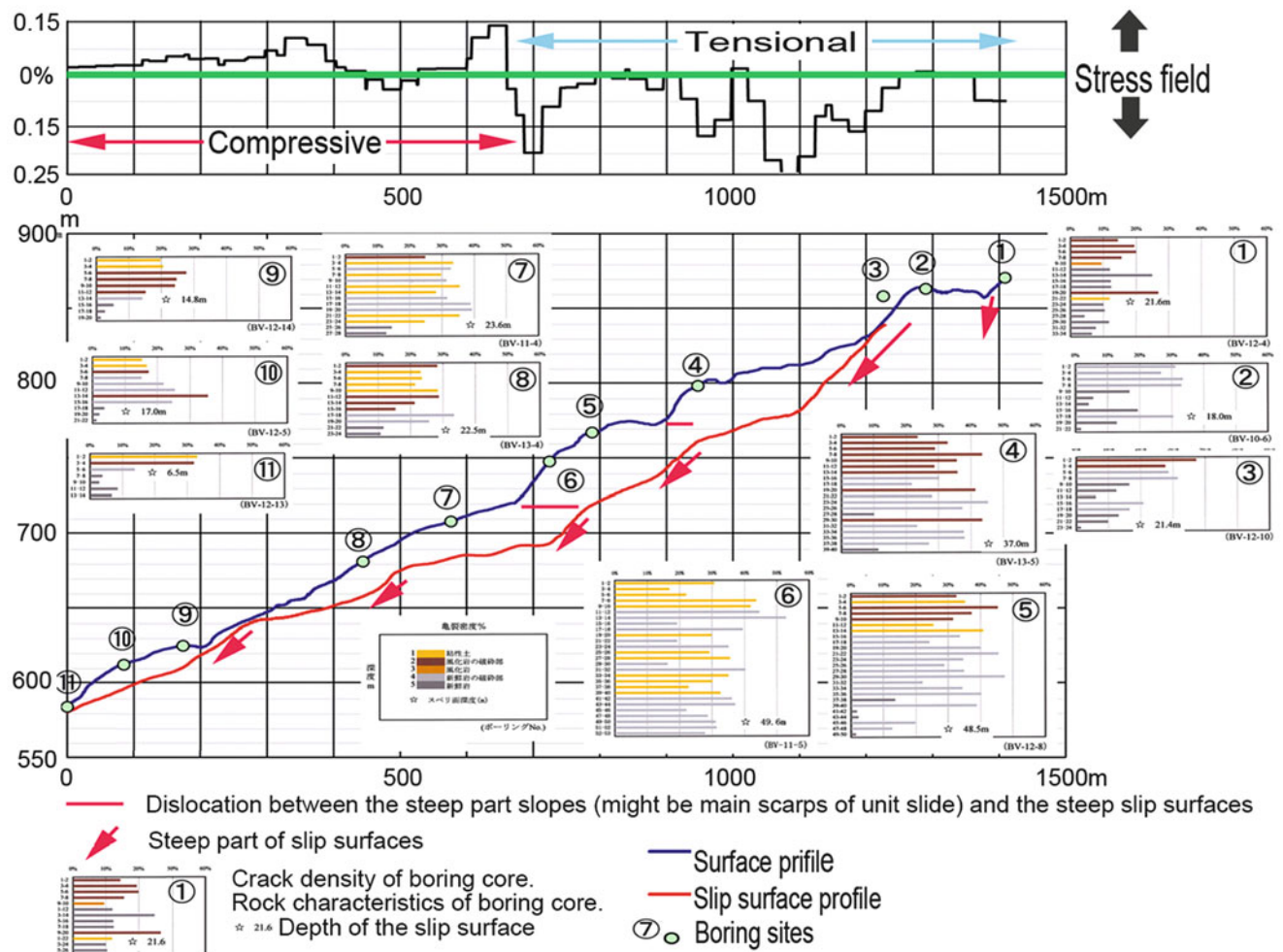


Fig. 4 Landslide cross section of the Ohokamizawa landslide

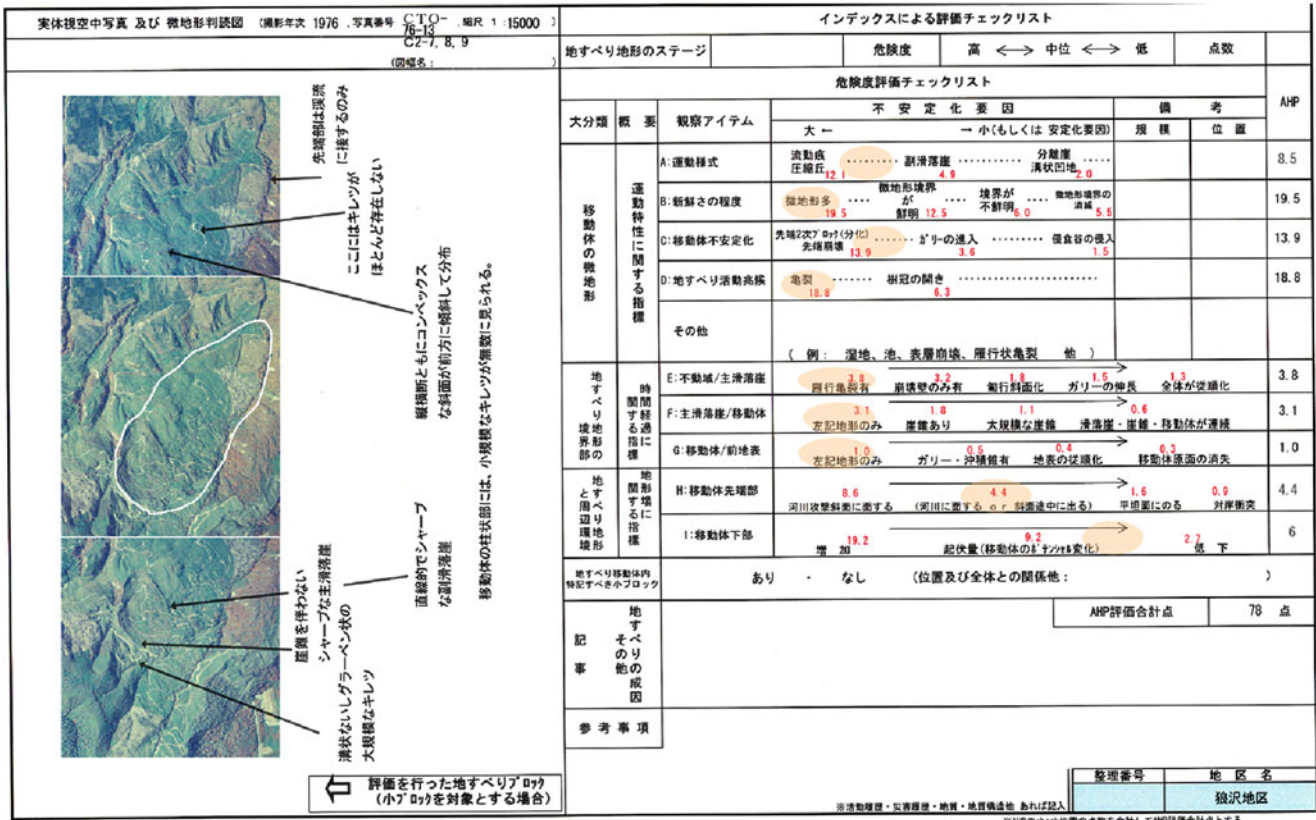


Fig. 5 Example of an AHP evaluation sheet

knowledge into explicit knowledge. It is here that data sheets on landslide risk assessments are produced.

Assessed indicators of micro-landforms are easier to comprehend, if few in number. Definitions of these indicators should be clear. Furthermore, one should not ignore the configuration of the micro-landforms subjected to recognition. Based on these considerations, items shown in Fig. 5 above have been determined and allocated. AHP assessments of each check-item are the outcome of reiterated paired comparisons conducted in discussions among the group of engineers mentioned above. The allocation of the check-items distinguishes between main slip precipices of landslides and their moving parts, while categorizing them into three assessment axes based on their topographic location as a micro-landform's border part, internal region of a moving part, or front-region of a moving part; here, a series of recognition axes are established for each micro-landform. It is not easy to recognize a micro-landform through aerial photointerpretation. Analysts with little experience may come to false assessments which may directly link to ambivalent risk assessment scores. Thus, at present it is necessary to establish training programs for those analysts.

Acknowledgments First of all I would like to express thanks to Vietnam Japan Joint Project Leader Prof. Kyoji Sassa. I also would like to express thanks to Prof. Higaki, Prof. Yagi, Dr. Yoshimatsu, Dr. Abe and all relations of the AHP project.

References

Chida N, Sugawara K, Miura O (1971) Landslide phenomenon in the Northern slope of Mt Funagata. Q J Geogr 23(3):175, in Japanese
 Hatano S (1974) Landforms of rapid massmovement origin (Recent progress in geomorphology 8) Part-2. Soil Mech Found Eng (Tsuchi to Kiso) 22(11):85-93, in Japanese
 Ichise Y (1964) Landslide identification by the aerial photo interpretation. Bull Nat Resour Res 62:13-22, in Japanese
 Japan Landslide Society Tohoku Branch (1992) The landslide and landslide topography in Tohoku, Japan. Landslide society Japan, Tohoku Branch. 141p and 80 maps (in Japanese)
 Kimata R, Miyagi T (1985) Basic components of landslide topography. J Landslide Soc 21(4):1-9, in Japanese
 Miyagi T (1979) Landslide in Miyagi Prefecture. Sci Rep Res Tohoku Univ, Ser 7 (geography) 29:91-101
 Miyagi T (1990) The risk evaluation by the landform classification in landslides. Proc symposium by Japan landslide society. pp 1-5 (in Japanese)
 Miyagi T, Prasada GB, Tanavud C, Potichan A, Hamasaki E (2004) Landslide risk evaluation and mapping: manual of aerial photo

- interpretation for landslide topography and risk management. Rep Nat Res Inst Earth Sci Disaster Prev 66:75–136
- Saaty TL (1980) The analytic hierarchy process. McGraw-Hill Book Company, New York, p 265
- Shimizu F, Oyagi N, Inoguchi T (1982–1988) The maps of landslide topography. National Res Inst Disaster Sci Japan, vol 1–6 (in Japanese)
- Terado T (1978) Large scale mass movements in central part of the Ohou Back borne range. Q J Geogr 30:189–198, in Japanese
- Varnes DJ (1978) Slope movement types and processes. Landslides: analysis and control. T.R.B. Special report No 176, pp 11–33
- Yagi R (2003) Micro topography in the landslide body and the developing processes. Geomorphol J 24(3):261–294, in Japanese
- Yanagida M, Hasegawa S (1993) Morphological dating and dissection process of landslide topography. In Novosad S, Wagner P (eds) Landslide. Proceedings of the 7th international conference and field workshop on landslides, pp 117–121



Accounting for Variability in Rain-Event Intensity and Initial Conditions in Landslide Triggering Return Period Mapping via a Monte Carlo Approach

David J. Peres and Antonino Cancelliere

Abstract

In this study, a Monte Carlo simulation approach is proposed for mapping landslide hazard in terms of return period, in order to account for both rainfall high frequency variability and antecedent precipitation that determine initial conditions. The Monte Carlo approach combines a stochastic rainfall generator with a physically-based landslide triggering model. More in detail, the Monte Carlo simulation methodology comprises the following elements: (a) a seasonal Neyman-Scott Rectangular Pulses (NSRP) model to generate 1,000-years of synthetic hourly point rainfall data; (b) a module for rainfall event identification and separation from dry intervals; (c) the Transient Rainfall Infiltration and Grid-Based Regional Slope-Stability (TRIGRS) model, version 2 (Baum et al. 2008, 2010) to simulate landslide triggering by rainfall infiltration, integrated with (d) a water table recession (WTR) model aimed at computing the initial water table height to be used in simulating rainfall events with event-based model TRIGRS.

An application of the method is carried out to map landslide triggering hazard in the Loco catchment, located in the Peloritani Mountains, Sicily, Italy, an area highly prone to landslide risk.

Results show that return period estimation may be significantly affected by both rainfall high-frequency variability and antecedent precipitation. Comparison with results obtained from the IDF-based procedure, shows that the latter widely-used approach generally leads to an overestimation of the return period of landslide triggering, i.e. a non conservative estimation of landslide hazard. Hence the IDF-based approach should be properly modified to account for at least the effect of antecedent precipitation.

Keywords

Hazard • Stochastic models • Giampilieri • Neyman Scott • TRIGRS

Introduction

Estimation of the return period of landslide triggering has been carried out by several researchers (D'Odorico et al. 2005; Rosso et al. 2006; Salciarini et al. 2008; Tarolli et al. 2011) coupling a hydrological and slope-stability

physically-based deterministic model (cf., e.g., Montgomery and Dietrich 1994; Iverson 2000; Baum et al. 2002, 2008, 2010; D'Odorico et al. 2005; Rosso et al. 2006) with Rainfall Intensity Duration-Frequency (IDF) relationships, typically assuming hyetographs of constant rainfall rate (cf., e.g., Rosso et al. 2006; Salciarini et al. 2008; Tarolli et al. 2011).

On the other hand, D'Odorico et al. (2005) showed that temporal variability of rainfall intensity within events affects potential for landslide triggering. More specifically, they investigated the role of hyetograph shape on landslide triggering using beta-shaped hyetographs with an hillslope

D.J. Peres (✉) • A. Cancelliere
Department of Civil and Environmental Engineering, University of Catania, Viale A. Doria, 6, Catania 95125, Italy
e-mail: djperes@dica.unict.it; acance@dica.unict.it

model given by the combination of the Iverson (2000) and Montgomery and Dietrich (1994) models, showing that variable-intensity hyetographs have a stronger destabilizing effect than constant-intensity ones of the same volume, and thus that return period is underestimated under the commonly-adopted assumption of rainfall of constant intensity.

Furthermore, often the initial condition (initial water table height), is assumed as fixed whereas it exhibits variability stemming from antecedent precipitation, which therefore should be taken into account for the estimation of return period. For instance, the asymptotic solution of Montgomery and Dietrich (1994), used in D'Odorico et al. (2005), does not take into account the aleatory nature of initial conditions, because the steady-state precipitation rate, that determines the initial condition, is a fixed value. Indeed, initial conditions are determined by past rainfall and hence the initial water table depth may be viewed as a random variable, i.e. to each initial condition a different probability to occur should be associated and taken into account in estimating return period, which otherwise would have the meaning of return period conditioned to the prefixed initial condition.

The aim of this work is to propose a Monte Carlo approach for landslide return period estimation which considers stochastic time-variability of rain intensity within rain events and initial water table height to events derived from past rainfall.

In particular, the TRIGRS model by Baum et al. (2008), based on analytical solutions to the 1D vertical infiltration Richards' equation, is combined with a sub-horizontal drainage model based on similar assumptions adopted in Rosso et al. (2006). Long rainfall input to such combined model is stochastically generated via a Neyman-Scott Rectangular Pulses (NSRP) model at the hourly time scale, thus enabling to estimate return periods with good reliability.

An example of application of the approach is presented with reference to the Loco catchment, located in the highly landslide-prone area of the Peloritani Mountains, Sicily, Italy.

Methodology

Monte Carlo Simulation Framework

The Monte Carlo simulation procedure consists of the following steps:

1. A stochastic rainfall model, calibrated on observations at a site nearby the case-study catchment, is used to generate a 1,000-year long hourly rainfall time series
2. The synthetic rainfall time series is pre-processed in order to identify rainfall events and their interarrival durations.

In particular, when two wet spells are separated by a dry time interval less than Δt_{min} , these are considered to belong to the same rainfall event; otherwise two separate rain events are considered. A number N_{re} of rainfall events results from this step

3. An initial value of the water table height is fixed to start simulations of the hydrological response for the whole rainfall time series. For the analyzed case-study area and many similar cases, it may be assumed that at the beginning of each hydrological year the water table is at the basal boundary, because an almost totally-dry season comes before. As this is valid also for the first year, simulation for first event is conducted considering water table at the basal boundary
4. The following procedure is then applied to each rainfall event $i = 1, 2, \dots, N_{re}$:
 - (a) Response in terms of pressure head ψ within rainfall events is computed using the TRIGRS model. As pressure head rise may continue after the end of rainfall, the TRIGRS transient-response simulation-interval is prolonged $\Delta t_a = 23$ h after the ending time $t_{end,i}$ of rainfall events
 - (b) The instant $t_{f,i} = \max(t_{end,i}, t_{max,i})$ is searched, being t_{max} the time instant at which maximum transient pressure head occurs. It follows that the final response to rain event i , in terms of water table height, is $\psi(d_{LZ}, t_{f,i})/\beta$, where $\beta = \cos^2\delta$ (slope parallel flow is assumed). Moreover, the time interval $\Delta t_{i+1} = t_{i+1} - t_{f,i}$ is computed, with t_{i+1} the instant at which rainfall event $i + 1$ begins
 - (c) The water table height at the beginning of rainfall event $i + 1$ is computed by a sub-horizontal drainage model which uses $\psi(d_{LZ}, t_{f,i})/\beta$ and Δt_{i+1}
5. The result is a series of pressure head responses to rainfall events of N_{sim} years, which is analyzed for return period computations.

In the following subsections the rainfall stochastic model, the TRIGRS model and the sub-horizontal drainage model are briefly described.

Rainfall Stochastic Model

At-site rainfall is modelled in this work as a Neyman-Scott Rectangular Pulses process (Rodriguez-Iturbe et al. 1987).

Within the NSRP process framework, the synthetic rainfall time series is originated as follows: first storm origins are generated via a Poisson process of parameter λt ; then a number of rectangular pulses for each storm origin is generated by a Poisson distribution of parameter ν ; each pulse has time origin from its storm origin that is taken from an exponential distribution of parameter β ; the pulse duration is extracted from an exponential distribution with

parameter η and its intensity comes from a Weibull distribution of parameters ξ and b .

We carry out calibration of the NSRP by the method of moments, using numerical optimization of a performance function (e.g., Cowpertwait et al. 1996). Moreover, we assume seasonality of rainfall as piece-wise stationary, i.e. calibrate different models for each stationary period (a month or group of months) within the hydrological year.

TRIGRS Model

The TRIGRS model by Baum et al. (2008) is based on the analytical solution of the 1D Richards' infiltration equation with an exponential soil-water characteristic curve $K(\psi) = K_s e^{\alpha(\psi-\psi_0)}$, where ψ is the pressure head, K_s is the saturated hydraulic conductivity, α is the Soil Water Characteristic Curve parameter and $\psi_0 = -1/\alpha$ is the pressure head at the top of the capillary fringe. Moreover, soil pressure head model requires the following parameters: the residual water content θ_r , the water content at saturation θ_s and the diffusivity at saturation D_0 . Once pressure head is computed, the factor of safety for slope stability is estimated by the following formula:

$$FS(Z, t) = \frac{\tan \phi'}{\tan \delta} + \frac{c' - \psi(Z, t)\gamma_w \tan \phi'}{\gamma_s Z \sin \delta \cos \delta} \quad (1)$$

where c' is soil cohesion for effective stress, ϕ' is the soil friction angle for effective stress, γ_w is the unit weight of groundwater and γ_s is the soil unit weight and δ is the slope angle. As we assume a finite basal boundary depth d_{LZ} , the factor of safety along vertical direction Z is always minimum at the basal boundary $Z = d_{LZ}$.

Water Table Recession Model

Water table height recession between storms is modelled by means of the following mass-conservation equation (cf. Rosso et al. 2006):

$$BhK_S \sin \delta = -A(\vartheta_s - \vartheta_r) \frac{dh}{dt} \quad (2)$$

where A is the contributing area draining across the contour length B of the lower boundary to each element of the catchment cell-discretization; the ratio A/B is the well-known specific upslope contributing area $A/B = BN_d$, where N_d is the number of cells draining into the local one as we determine flow paths via the single direction (D8) method (O'Callaghan and Mark 1984).

Solution to (2) is used to compute the water table height at the beginning of rain event $i + 1$:

$$h_{i+1} = \frac{\psi(d_{LZ}, t_{f,i})}{\cos^2 \delta} \exp \left\{ -\frac{K_S \sin \delta}{BN_d(\vartheta_s - \vartheta_r)} \Delta t_{i+1} \right\} \quad (3)$$

Return Period Estimation

Return period of landslide triggering is defined as the mean interarrival time of a pressure head $\psi \geq \psi_{cr}$ where ψ_{cr} is the critical pressure head, corresponding to $FS = 1$.

It may be worthwhile to mention that the objective is to analyze the probability of landslides for *given* catchment (and climate) conditions. This implies that no modelling of soil parameters' change, and in particular of soil depth (which generally changes at every landslide event), is to be made, as return periods are computed to have the meaning of hazard for that *given* catchment condition.

For the estimation of T_R we consider that in many cases, there is a season that is almost totally dry and long enough to bring to zero the water table height at the beginning of the rainy season. Hence memory is in this case limited to such an hydrological year. This allows to consider hydrological-annual maxima of pore-pressure statistically independent, and to compute the return period of ψ_{cr} with the formula:

$$T_R = \frac{1}{1 - F(\psi_{cr})} \quad (4)$$

where $F(\psi_{cr})$ is the non-exceedance probability of ψ_{cr} . In the case of the Mediterranean area, we consider the hydrological year starting from September. Because simulations are carried out for a large number of years, the empirical cumulative frequency distribution derived from Monte Carlo simulations is directly used as $F(\psi_{cr})$. In particular, for estimating cumulative frequency, we use the formula $F = (m - 0.35)/N_{sim}$ (cf. Stedinger et al. 1993), where m is the rank of the hydrological-year maxima value.

On the other side, the commonly-used approach for the estimation of return period of landslide triggering, involves the estimation of the rainfall Intensity-Duration-Frequency (IDF) curves. Each IDF curve describes the relationship between rainfall Intensity and rainfall Duration for a fixed return period T_R .

The general form of the IDF curves can be determined within the assumption of simple scaling as (Burlando and Rosso 1996):

$$I_F = m_1 x_F t^{n-1} \quad (5)$$

where I_F is the rainfall rate that can be exceeded with a probability of $(1 - F)$ in a year, m_1 the expected value of annual maximum rainfall depth for the unit duration, n the scaling exponent, and x_F the F -quantile of the renormalized variate, i.e. of the ratio between rainfall depth and its mean.

A probability distribution model has to be fitted to annual maxima of the renormalized observed rainfall rates. We choose the general extreme value (GEV) distribution, which has the following cumulative distribution function:

$$F_X(x) = \exp\left\{-\left(1 + \frac{x - \mu_0}{\sigma_0} \xi_0\right)^{-\frac{1}{\xi_0}}\right\} \quad (6)$$

where μ_0 , σ_0 and $\xi_0 \neq 0$ are parameters to be estimated from the sample. For consistency with the Monte Carlo procedure, we estimate the IDF curve parameters from the annual maxima series, of various durations, extracted from the NSRP synthetic hourly series.

Coupling the uniform-hyetograph critical Intensities and Durations, i.e. the $I_{CR} = f(D_{CR})$ relationship, derived by the model simulating the response to uniform hyetographs and a prefixed initial condition (we consider the initial water table at the basal boundary) with the IDF relationship enables to estimate return period of landslide triggering. In fact, for each triggering threshold $I_{CR} = f(D_{CR})$ valid for a given set of hillslope parameters, return period is a function of D_{CR} (see, e.g., Salciarini et al. 2006). Nonetheless, following the approach by Rosso et al. (2006) we search for the minimum return period corresponding to the model-derived triggering condition $I_{CR} = f(D_{CR})$. Hence to each relationship $I_{CR} = f(D_{CR})$ corresponds a single value of T_R .

Application

Case Study

An application of the proposed approach has been carried out with reference to the Loco catchment in the Peloritani Mountains, located near the coastline of northeastern Sicily, Italy (Fig. 1), which has an extent of 0.14 km². A catastrophic debris-flow event occurred on 1 October 2009 in the area, which caused 37 casualties, hundreds of injured and thousands of evacuated people in the Peloritani area.

Soil core samples collected in some points in the catchment indicate depth d_{LZ} of the erodible strata (mainly loamy sands with a significant proportion of gravel) ranging from 4 to 2 m, on slopes from 30° to 40°. Following other researchers (DeRose 1996; Salciarini et al. 2006, 2008; Baum et al. 2010), we assumed a negative exponential $d_{LZ} = \min\{32 \exp(-0.07\delta), 5\}$ relationship between d_{LZ} [m] and slope δ [°], to distribute spatially this information. Bedrock outcropping has been considered in areas with slope $\delta > 50^\circ$. Values of the hydrological and geotechnical parameters are given in Table 1. We assume cohesion as a function of slope, $c'[\text{kPa}] = 5.7 / \{1 + \exp[1 - 0.67(\delta[^\circ] - 35)]\}$. Such a relation reproduces somehow the few

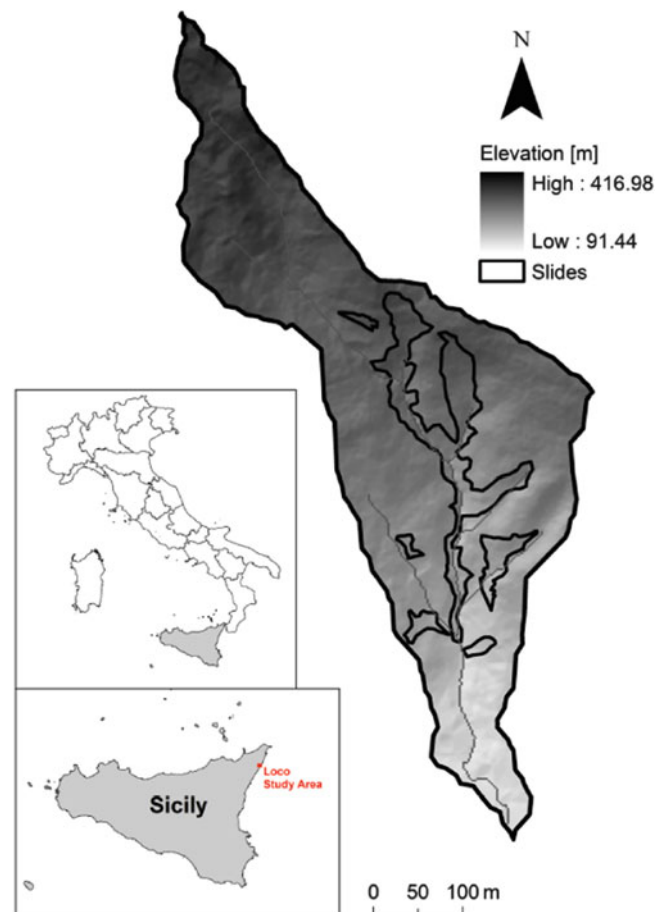


Fig. 1 Location of the Loco Catchment in Sicily, Italy. Slides occurred on 1st October 2009 are superimposed on the 2 m-resolution pre-event DEM

measurements available for c' , which show cohesion to increase with slope roughly from $c' = 0$ at $\delta = 30^\circ$ to $c' = 5.7$ kPa at $\delta = 40^\circ$.

Other data required by the model are given in Table 1. From these data it results $\psi_{cr} = 1.359, 0.640, 0.494, 0.336$ and 0.322 m for slopes of $\delta = 30^\circ, 35^\circ, 40^\circ, 45^\circ$ and 50° , respectively.

It may be worthwhile to mention that this application leads to results which are valid for the catchment conditions on 1 October 2009 event, as the data used in this work have been measured closely in time before that event. So application is aimed at showing how the procedure can be successfully applied to map landslide triggering hazard.

Rainfall series measured from 21 February 2002 to 9 February 2011 (almost 9 years) at Fiumedinisi rain gauge installed near the catchment has been used for calibration of the NSRP model, to generate 1,000 years of hourly synthetic rainfall data.

Based on a preliminary analysis of monthly statistics, six homogeneous rainfall seasons have been identified: (1) September and October, (2) November, (3) December,

Table 1 Hydrological and geotechnical parameters for the Loco catchment

| ϕ' [°] | c' [kPa] | γ_s [N/m ³] | θ_s [-] | θ_r [-] | K_S [m/s] | α [m ⁻¹] | D_o [m ² /s] |
|-------------|------------|--------------------------------|----------------|----------------|--------------------|-----------------------------|---------------------------|
| 37 | 0 ÷ 5.7 | 19,000 | 0.35 | 0.045 | 2×10^{-5} | 3.5 | 5×10^{-5} |

Table 2 Results of the NSRP rainfall model calibration

| Parameter | Jan, Feb, Mar | Sept, Oct | Nov | Dec |
|--|------------------------|-------------------------|------------------------|------------------------|
| λ [h ⁻¹] | 2.295×10^{-3} | 21.195×10^{-3} | 1.485×10^{-3} | 3.185×10^{-3} |
| ν | 44.28 | 1.57 | 42.41 | 42.61 |
| β [h ⁻¹] | 10.16×10^{-3} | 2.118 | 5.955×10^{-3} | 9.876×10^{-3} |
| η [h ⁻¹] | 0.721 | 0.840 | 0.941 | 0.677 |
| ξ [h ^b /mm ^b] | 1.134 | 0.463 | 0.693 | 1.035 |

(4) January–March, (5) April and (6) May–August. Separate sets of parameters of the NSRP model have been determined for each one of the four rainy seasons (in total $5 \times 4 = 20$ parameter values), while the last two seasons have been considered of negligible rainfall. The Weibull shape parameter b has been fixed to 0.6, based on different trials.

Parameters obtained from calibration are shown in Table 2.

We extracted annual maxima of various durations from the generated series. Based on these series the IDF curves were derived. In particular, scale invariance has been assumed for rain durations $3 < D < 96$ h, and the durations of 3, 6, 12, 24, 48 and 96 h were considered for calibration of IDF curves with a GEV distribution assumed for the renormalized variate, leading to $m_1 = 66.74$ mm and $n = 0.1767$, and $\mu_0 = 0.1787$, $\sigma_0 = 0.2845$ and $\xi_0 = 0.7742$ for the parameters of the distribution, estimated via the maximum likelihood method.

These IDF curves were coupled with the hillslope response computed by the model, assuming an initial water table height of zero ($d = d_{LZ}$), to compute return period of landslide triggering following the so-called traditional approach.

Return Period Mapping

Results obtained by the IDF-based approach are compared with those of the Monte Carlo approach in Fig. 2. In particular, the plots show, for different combinations of slope δ and depth to basal boundary d_{LZ} , the exceedance probability of the ratio $\psi(d_{LZ})/\psi_{\text{sat}}$ considering different values of the A/B ratio. The relationship between this variate and factor of safety is given by (2), and is unequivocal once internal friction angle ϕ' , cohesion c' and unit weight of soil γ_s are fixed.

The comparison between the IDF-based curve and the $A/B = 0$ ($N_d = 0$) one, gives information on the role of rainfall intensity variability within a rainfall event, these two curves being derived under the equivalent initial conditions.

This comparison indicates a general tendency of the IDF-based approach to underestimate exceedance probabilities of critical pressure head (i.e. overestimate return period of landslide triggering) thus resulting non-conservative. These results are in agreement with the findings by D'Odorico et al. (2005), which showed that a variable-intensity beta-shaped hyetograph has a stronger destabilising effect than a constant-intensity hyetograph of the same volume.

The plots also confirm that, as expected, the effect of convergent flow, i.e. the specific upslope contributing area, is to increase exceedance probabilities of triggering, since as the ratio A/B increases, so does the probability of an higher initial water table height.

Results obtained through the Monte Carlo approach have been used to obtain the map of Fig. 3, which gives cell by cell the return period of landslide triggering. From this map it can be seen that most of the areas affected by slides on the 1st October 2009 event correspond to those with return periods less than 25 years.

Conclusions

In this study we investigated the use of a Monte Carlo framework for the quantitative assessment of landslide hazard, in terms of return period of landslide triggering. The proposed Monte Carlo approach couples a stochastic rainfall generator based on the Neyman-Scott Rectangular Pulses and a physically-based model for infiltration and slope stability analysis, based on the unsaturated version of the TRIGRS program. Such an approach as opposed to the widely used approach based on rainfall Intensity-Duration-Frequency (IDF) curves for return period estimation, enables to account for both rainfall intensity variability within rainfall events and past rainfall time history that determine the initial conditions of rainfall events. Indeed, the IDF-based approach usually makes use of constant intensity rainfall inputs and prefixed initial conditions (water table height at the beginning of the rainfall event). On the other hand the proposed approach implicitly takes into account the

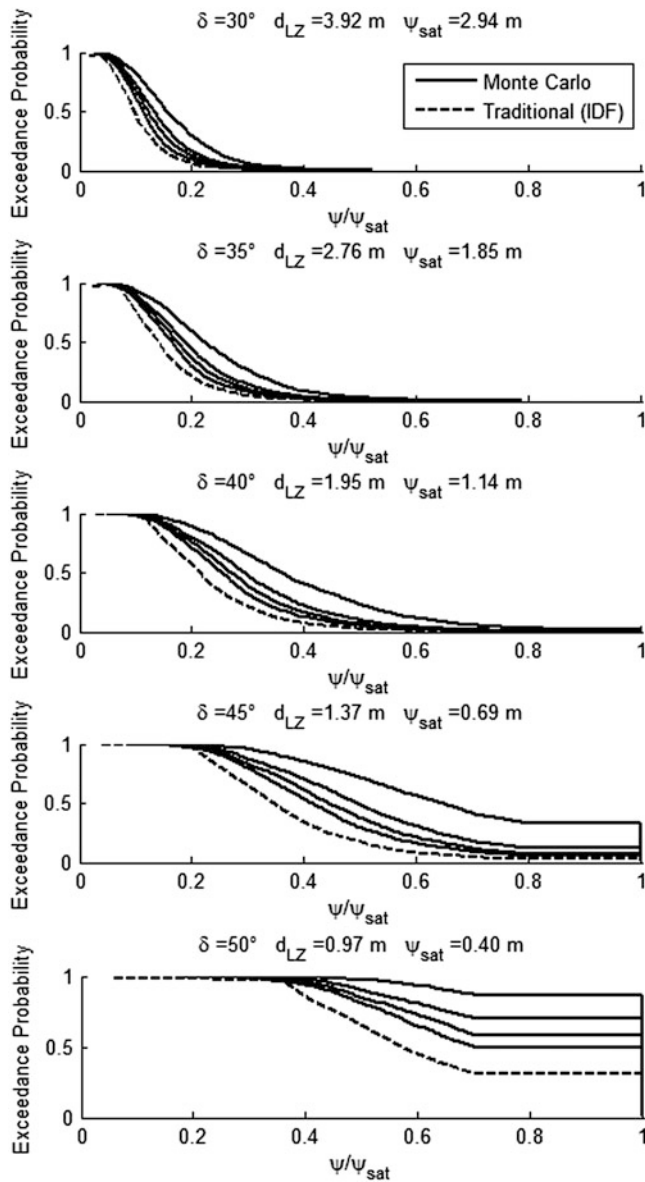


Fig. 2 Comparison of results in exceedance probability of normalized pressure head at the basal boundary, obtained by the IDF-based “traditional” approach (*dotted lines*) and the Monte Carlo approach (*continuous lines*). Different curves for Monte Carlo approach are shown for specific contributing areas of $A/B = 0, 10, 20$ and 50 m, from *left to right* respectively. Each plot corresponds to a combination of slope δ and depth d_{LZ} to basal boundary

probability of the prefixed initial condition for the estimation of return period.

Application to a landslide-prone catchment in Sicily, that has recently experienced catastrophic shallow landslide events, has shown that neglecting these two factors may lead to a significant underestimation of landslide hazard. Thus, both high-frequency rainfall variability and antecedent rainfall history should be accounted for in landslide return period estimation.

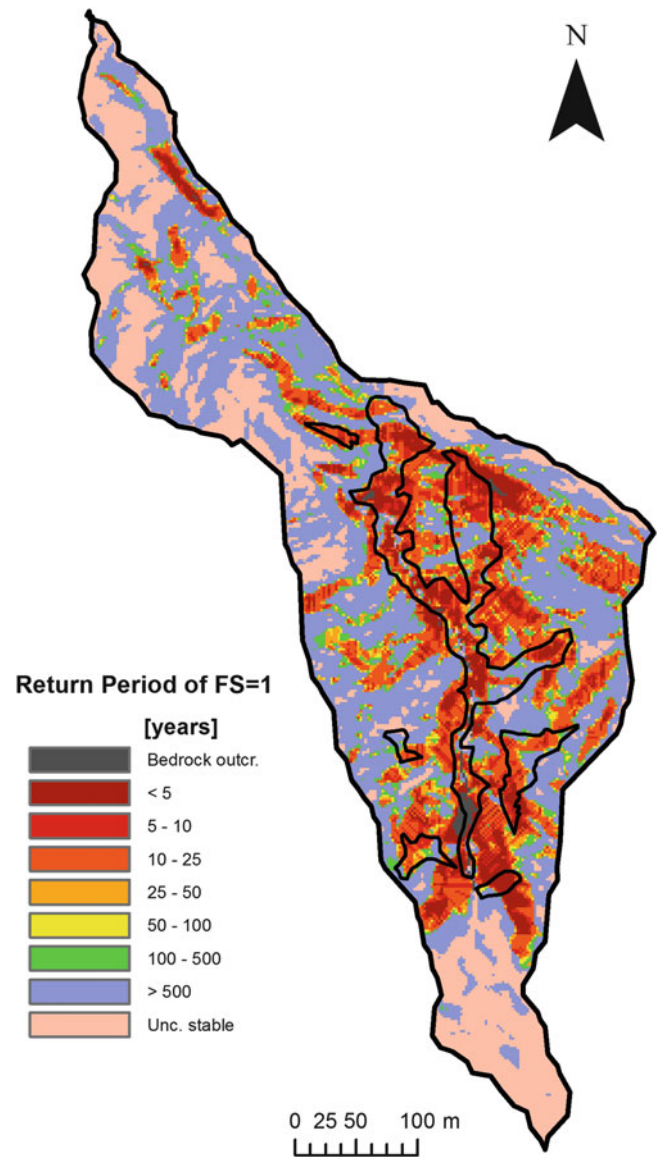


Fig. 3 Return period map derived with the Monte Carlo methodology. Areas affected by slides on the 1 October event are superimposed on this map

A further development of the application exercise conducted in this work, may be to account for the fact that landslide source areas may move rapidly downslope as a debris flow (as occurred on 1 October 2009), in order to incorporate in hazard estimation the specification of areas that are hit by debris movement and deposition.

Acknowledgments This research was partially funded by the Italian Education, University and Research Ministry (MIUR), PON Project No. 01_01503 “Integrated Systems for Hydrogeological Risk Monitoring. Early Warning and Mitigation Along the Main Lifelines”, CUP B31H11000370005. The authors would like to thank Rex L. Baum of United States Geological Survey and Jorge A. Ramirez of Colorado State University for the helpful insights and useful discussions.

References

- Baum RL, Savage WZ, Godt JW (2002) TRIGRS—a FORTRAN program for transient rainfall infiltration and grid-based regional slope-stability analysis. U.S. Geological Survey Open-File Report 02-0424, Reston, Virginia
- Baum RL, Savage WZ, Godt JW (2008) TRIGRS—a FORTRAN program for transient rainfall infiltration and grid-based regional slope-stability analysis, version 2.0. U.S. Geological Survey Open-File Report 2008-1159, Reston, Virginia
- Baum RL, Godt JW, Savage WZ (2010) Estimating the timing and location of shallow rainfall-induced landslides using a model for transient, unsaturated infiltration. *J Geophys Res* 115:F03013. doi:[10.1029/2009JF001321](https://doi.org/10.1029/2009JF001321)
- Burlando P, Rosso R (1996) Scaling and multiscaling models of depth-duration-frequency curves for storm precipitation. *J Hydrol* 187 (1–2):45–64
- Cowperrwait PSP, O’Connell PE, Metcalfe AV, Mawdsley J (1996) Stochastic point process modelling of rainfall. I. Single-site fitting and validation. *J Hydrol* 175(1–4):17–46
- D’Odorico P, Fagherazzi S, Rigon R (2005) Potential for landsliding: dependence on hyetograph characteristics. *J Geophys Res* 110: F01007. doi:[10.1029/2004JF000127](https://doi.org/10.1029/2004JF000127)
- DeRose RC (1996) Relationships between slope morphology, regolith depth, and the incidence of shallow landslides in eastern Taranaki hill country. *Z Geomorphol* 105:49–60
- Iverson RM (2000) Landslide triggering by rain infiltration. *Water Resour Res* 36:1897–1910
- Montgomery DR, Dietrich WE (1994) A physically based model for the topographic control on shallow landsliding. *Water Resour Res* 30:1153–1171
- O’Callaghan JF, Mark DM (1984) The extraction of drainage networks from digital elevation data. *Comput Gr Image Process* 28 (3):323–344
- Rodriguez-Iturbe I, Cox DR, Isham V (1987) Some models for rainfall based on stochastic point processes. *Proc R Soc Lond A Math Phys Sci* 410(1839):269–288
- Rosso R, Rulli MC, Vannucchi G (2006) A physically based model for the hydrologic control on shallow landsliding. *Water Resour Res* 42 (6):1–16
- Salciarini D, Godt JW, Savage WZ, Conversini P, Baum RL, Michael JA (2006) Modeling regional initiation of rainfall-induced shallow landslides in the eastern Umbria Region of central Italy. *Landslides* 3:181–194
- Salciarini D, Godt JW, Savage WZ, Baum RL, Conversini P (2008) Modeling landslide recurrence in Seattle, Washington, USA. *Eng Geol* 102(3–4):227–237
- Stedinger JR, Vogel RM, Foufoula-Georgiou E (1993) Chapter 18: Frequency analysis of extreme events. In: Maidment DR (ed) *Handbook of hydrology*. McGraw Hill, London. ISBN 9780070397323
- Tarolli P, Borga M, Chang K-T, Chiang S-H (2011) Modeling shallow landsliding susceptibility by incorporating heavy rainfall statistical properties. *Geomorphology* 133(3–4):199–211



Predictive Capability of Deterministic and Statistical Models in Weathered Granite Soil Watershed

Ananta Man Singh Pradhan, Jeong-Rim Oh, Min-Su Jung, and Yun-Tae Kim

Abstract

Every year, the Republic of Korea experiences numerous landslides, resulting in property damage and casualties, especially in weathered granite soil slopes.

This paper compares the predictive capability of two different models, namely shallow landslide stability (SHALSTAB), deterministic model and relative effect (RE) model, a statistical bivariate model for producing shallow landslide susceptibility maps.

Deokjeok-ri Creek was selected for the study. The watershed is mainly covered by granitic soil. For SHALSTAB analysis a digital elevation model was used. The soil strength parameters and physical properties of soil were determined in the laboratory. For the statistical model, the input layers of the landslide conditioning factors were prepared in the first stage. The effects of causative factors on slope stability were mapped on topographical maps of 1:5,000 scale. Mainly geomorphic (slope, aspect, elevation, internal relief, and slope shape), hydrology based (drainage distance, stream power index, topographic wetness index, sediment transport index, drainage density and soil drainage characters), soil type and soil depth distribution and forest type and timber age causative factors and field inventory were used for statistical susceptibility mapping. Model performance was assessed using accuracy curve approach. Results show that accuracy is as high as 88.21 % for SHALSTAB, while it is 86.3 % for RE model. Although SHALSTAB has certain drawbacks, as described by previous researchers, this study concluded that in a small watershed and using accurate geotechnical data SHALSTAB can predict the probability of slope failure in Korean mountainous regions.

Keywords

Weathered granite soil • SHALSTAB • Relative effect • Statistical model • Success rate • GIS

Introduction

Landslides constitute a major natural hazard in the Republic of Korea due to high rates of weathering, abundant rainfall and infrastructure development. Korea is experiencing changes in climate parameters, including annual temperature and precipitation (Chung et al. 2004).

During the past 30 years in Korea, average rainfall in summer season increased from 661 mm for the period 1976–1985, to 710 mm for the period 1996–2005, and to 814 mm for the period 1996–2005. Due to these

A.M.S. Pradhan (✉) • Y.-T. Kim
Geosystems Engineering Lab, Pukyong National University, Busan
608-737, South Korea
e-mail: anantageo@hotmail.com; yuntkim@pknu.ac.kr

J.-R. Oh • M.-S. Jung
National Disaster Management Institute (NDMI), Seoul, Republic of
Korea
e-mail: jeongrim@nema.go.kr; msjung@korea.kr

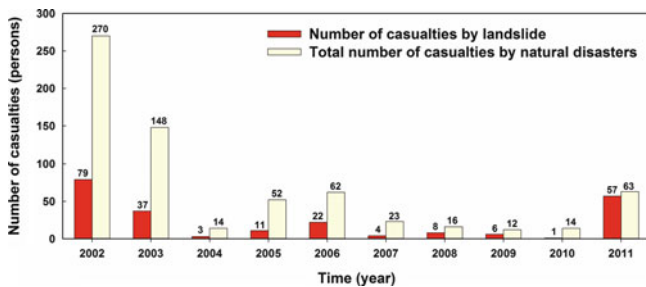


Fig. 1 Total number of casualties by landslide and other natural disaster

concentrated higher rainfalls, rainfall-induced slope failure became more serious in Korea. Usually a concentrated heavy rainfall from July to August has caused slope instability in Korea. Rainfall induced landslides are usually shallow failures on weathered granite slopes in Korea, especially in unsaturated slopes with antecedent rainfall. These slope failures are mainly triggered by rainfall infiltration, which induces a decrease in matric suction as well as in shear strength (Kim et al. 2004; Rahardjo et al. 2001, 2005).

In Korea, about 228 people have been killed by landslides from 2002 to 2011. Statistics from the National Disaster Management Institute (NDMI) shows that landslides are responsible for at least 34 % of all fatalities from natural disaster in Korea (Fig. 1).

Intrinsic factors include geological and geotechnical and geomorphological causes. Intrinsic causes include weak materials, weathered materials and adversely oriented discontinuities such as faults.

The soils at the site are weathered granite, exhibiting a wide range of conditions depending on the degree of weathering, ranging from those close to rock to those that contain fine grains, such as silt or clay. Most subsurface soils are typically in an unsaturated state, especially in mountainous areas. When rainfall infiltrates the ground, the granite soils become partially or fully saturated. This increases the fragility of the soil, resulting in significant loss of the shear strength. As rainfall infiltrates into soils, it decreases matric suction and consequently the loss of shear strength of soil, occurring slope failure. Extrinsic causes include triggering factors such as rainfall, earthquake and human activities. Human activities include excavation of the slope or its toe, loading of the slope or its crest, and mining. Landslides in Korea usually are induced by intensive rainfall in summer season (Kim et al. 2000). Typhoons Yanni (in 1998), Rusa (2002), Maemi (2003), and Ewinia (2006) brought particularly heavy rains that caused many landslides in Korea.

This research aimed to develop and compare landslide prone areas in weathered granite soil using a shallow landslide stability model (SHALSTAB) as a deterministic model

and relative effect (RE) method as a probability technique in the same site in a GIS environment. The predictive capabilities of these models were finally evaluated using an accuracy curve plot.

Study Area

Deokjeok-ri Creek was selected for the study. The watershed is mainly covered by granitic soil. The study area is situated in the north-eastern hills of Korea. This site lies between the latitudes $38^{\circ}04'07''N$ and $38^{\circ}05'42''N$ and the longitudes $128^{\circ}11'11''E$ and $128^{\circ}18'E$. Gangwon-do is the second largest province after Gyeongsangbuk-do. This site is surrounded by high and steep mountains, combined with Korea's rainfall pattern, in which 50–60 % of total annual precipitation occurs in summer, makes the area susceptible to landslides. The area of Deokjeok-ri creek is 33.4 km^2 . Typhoon Ewinia brought record-breaking rainfall to the region. Residents in this area usually live near the main channel of Deokjeok-ri Creek. By the extreme event in July 2006, seventeen people were dead and 12 people were missing in Inje County (Lee and Yoo 2009).

The geologic features of this area include gneisses of the Precambrian Era and granites of the Mesozoic Era. Various fault activities, intensively distributed in this area, have created surface discontinuities, with broken bedrock sloping in various directions. Weathered granite soil is a generic term of soils generated through the weathering of granite, that is, residual soils remaining on the spot. The soils are in a wide range of conditions depending on the degrees of weathering from those close to rock to those that contain fine grains, such as silt or clay. The mechanical properties of decomposed granite soil after being weathered are affected by the contents of primary minerals, such as quartz, mica and feldspar and bed rock structures as well as natural conditions, such as climates and drain conditions (Kwon and Oh 2011). Most subsurface soils are typically in an unsaturated state. In unsaturated soils, suction pressure in the pore water contributes to an increase in the shear strength of the soils. Since decomposed granite soil shows various characteristics of shear behavior dependent on initial conditions such as weathering degree and grain breakage. Rainfall-induced landslides are usually shallow failures in weathered granite slopes in Korea, especially in unsaturated slopes with antecedent rainfall. These slope failures are mainly triggered by rainfall infiltration, which induces a decrease in matric suction as well as in shear strength (Kim et al. 2004; Rahardjo et al. 2005). The climatic regime in the area is temperate with a primary peak of rainfall in summer.

Table 1 Definition of log (QT⁻¹) intervals and instability categories (Montgomery and Dietrich 1994)

| Classes SHALSTAB | Interpretation of class |
|-------------------------|--|
| Chronic instability | Unconditionally unstable and unsaturated |
| Log Q.T-1 < -3.1 | Conditionally unstable and saturated |
| -3.1 < Log Q.T-1 < -2.8 | Unstable and saturated |
| -2.8 < Log Q.T-1 < -2.5 | Unstable and unsaturated |
| -2.5 < Log Q.T-1 < -2.2 | Stable and unsaturated |
| Log Q.T-1 > -2.2 | Unconditionally stable and unsaturated |
| Stable | Unconditionally stable and saturated |

Deterministic Method

The deterministic or physically based model is based on the physical laws of conservation of mass, energy and momentum. This model is mainly used to analyze the probability of landslide when a terrain consists of homogeneous geology and geomorphology (van Westen and Terlien 1996). Montgomery and Dietrich (1994) developed a physically-based model based upon a combination of the infinite slope equation and a hydrological component based on steady-state shallow subsurface flow. This model, called SHALSTAB, has been applied successfully by several researchers in different parts around the world. This methodology is a couple with a hydrological model and an infinite slope stability model using ArcGIS software. The SHALSTAB model predicts the critical rainfall necessary for slope failure throughout a study area (Montgomery and Dietrich 1994).

The formulation adopted by the model is a combination of hydrological and geomechanical components and is described by the (1), shows the main equation to the model to compute for each grid cell as unite mapping.

$$\log \frac{Q}{T} = \frac{\sin \theta}{a/b} \cdot \left[\frac{c'}{\rho_w \cdot g \cdot z \cdot \cos^2 \cdot \tan \varphi} + \frac{\rho_s}{\rho_w} \cdot \left(1 - \frac{\tan \theta}{\tan \phi} \right) \right] \tag{1}$$

where *Q* is the critical rainfall necessary to trigger landslides; *T* is the soil transmissivity (as product of soil thickness and saturated hydraulic conductivity); *a/b* is the contributing area per contour width; *θ* is the local slope, *ρ_w* is the density of water; *g* is the acceleration of gravity, *z* is soil thickness; *ρ_s* is soil bulk density, *φ* is the soil friction angle and *c* is cohesion.

The predictive index of this model (stability index) is expressed in mm day⁻¹ of critical rain and is variable on a scale of values, where lower values indicate a greater propensity for instability and higher values indicate a greater propensity for stability. The levels of instability based on Log Q.T⁻¹ classes have been shown in Table 1.

In the framework of landslide susceptibility analysis, SHALSTAB is not used to compute factor of safety but to provide a relative susceptibility index.

Statistical Method

There are various methods in statistical approach of landslide susceptibility mapping. In this research relative effect method (RE) a bivariate method was used to evaluate landslide susceptibility (van Westen 1997; Neelkantan and Yuvaraj 2013). In this method, a weight value for a causative factor class is defined as a natural logarithm of the landslide density in the class divided by landslide density in the entire map. But in the case of no landslide occurrence in the certain class of the causative factor, the value becomes undefined. The natural logarithmic function log (x) is defined only for x > 0. To overcome this situation relative effect of a parameter as determining factor of slope instability is quantitatively determined by introducing a “relative effect” function. For every unit, the ratio of the unit area to the total area of the study and the ratio of the landslide area in the unit to the area of total landslide are calculated. The following is the formula for calculating the density of each parameter class such as a certain lithological unit or a certain slope class.

$$W_{ij} = \log \left[\left(\frac{f_{ij}}{f} \right) + \varepsilon \right] = \log \left[\left(\frac{A_{ij}^*}{A_{ij}} \times \frac{A}{A^*} \right) + \varepsilon \right] \tag{2}$$

where *W_{ij}* is the weight given to a certain class *i* of parameter *j*, *f_{ij}* is the landslide density within the class *i* of parameter *j*, *f* is the landslide density within the entire map, *A^{*}_{ij}* is the area of landslides in certain class *i* of parameter *j*, *A_{ij}* is area of certain class *i* of parameter *j*, *A^{*}* is the total area of landslide in the entire map, *A* is total area of entire map and *ε* is a value near to zero to avoid undefined value of natural logarithmic function.

The resulting total weights directly indicate the importance of each factor. If the total weight is positive, the factor is favorable for landslide, whereas if it is negative, it is unfavorable.

Table 2 Properties of soil used in this research

| Soil properties | Average value |
|--------------------------------------|---------------------------|
| In-situ permeability | 1.87E-05 (m/s) |
| Internal frictional angle (ϕ) | 35.61 |
| Cohesion | 2.14 (kPa) |
| Density | 1.68 (kg/m ³) |

Materials

In this study, a landslide inventory map was prepared using earlier reports, aerial photographs interpretation and extensive field works. In total 748 landslide scars were mapped and digitized for further analysis. For SHALSTAB a digital elevation model (DEM) with a resolution 10×10 m grid size was prepared by interpolation of contour lines. The in-situ permeability tests were performed in various soil depths. And shear strength parameters and physical properties of soil were determined in the laboratory shown in Table 2.

Average soil depth of the creek was estimated about 1 m. Furthermore, slope percentage map and contributing area were generated automatically by using DEM in GIS environment.

For the RE method, among 748 landslide scars, 673 randomly selected landslides (training data) were taken for making landslide susceptibility model and 75 were used for validation of the model. In the present study the altitude ranges from 195 m to 1,224 m and is reclassified into five classes.

The slope in the study area varies from 0° to 71° and divided into five categories. The slope aspect map was also produced from the DEM. In the present study, the aspect direction is divided into ten classes. Curvature analysis allows dividing the area into concave, convex, and flat surfaces. In the study area relative relief ranges from 0 to 80 m and divided in to four categories for analysis. The river map was used in the ArcGIS 10.1 software to get the proximity to rivers. And drainage density was also generated in GIS environment.

The topographic wetness index (TWI), which combines local upslope contributing area and the entire slope, is commonly used to quantify topographic control on hydrological processes. Stream power index (SPI) measures the erosion power of the stream and is also considered as a factor contributing toward stability within the study area. A dimensionless sediment transport capacity index (STI) that is a nonlinear function of specific discharge and slope was derived by considering the transport capacity limiting sediment flux and catchment evolution erosion theories (Moore and Wilson 1992). In the present study SPI is divided into four classes. Drainage classification of soils refers to the frequency and duration of periods when the soil is saturated with water (Soil Survey Staff 1993). In the present study

**Fig. 2** stability index map obtained by SHALSTAB

drainage characteristics of soil is classified as poorly drained, somewhat poorly drained, moderately drained and well drained. Based on soil classification given by U.S. Department of Agriculture (USDA 1993), there are five soil types within Deokjeok-ri Creek. In this study, relative soil depth is used. There are four main forest types with in Deokjeok-ri Creek. Forest types in Deokjeok-ri Creek are broadleaved forest (mostly Mongolian Oak), mixed forest, larch, red pine, Korean pine, pine plantation forest, broadleaved plantation forest, and poplar forest. The non-forest area is mainly occupied by cultivation and soil deposits. When vegetation was present everywhere, a dramatic change in the size or age of the vegetation helped to distinguish shear zones. The study area shows the different age categories of the timber.

The geologic features of this area include gneisses of the Precambrian Era and granites of the Mesozoic Era.

Result and Discussion

The SHALSTAB map shows seven classes that vary from stable to chronic instability (Fig. 2). The stable class is not susceptible to shallow landslides even with strong rainfall. In contrast, the unstable class is susceptible to landslides even without rainfall. The five intermediate classes shows degrees of instability. To better understand how those class interval were defined, it is considered that transmissivity to be around $65 \text{ m}^2/\text{day}$, $\log Q/T = -3.1$ represents a rainfall amount of $52 \text{ mm}/\text{day}$, and $\log Q/T = -2.2$ represents a rainfall amount of $404 \text{ mm}/\text{day}$.

Figure 3 shows the stability index map obtained by SHALSTAB reveals the area under chronic instability is 2.4 % of the total watershed area. This study found SHALSTAB $\log(Q/T)$ value of < -2.2 flagged 65.14 % of Deokjeok-ri creek accounting for 97.19 % of the landslide of the inventory data (Fig. 4).

For the relative effect (RE) based model, the weighing value of each factor type were calculated from their

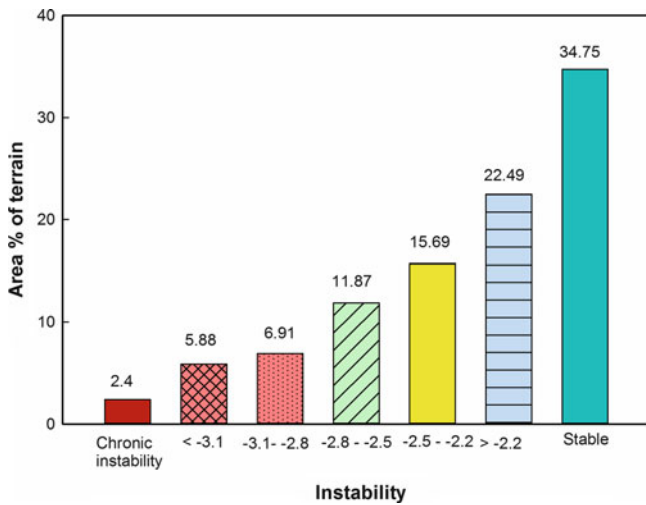


Fig. 3 Area occupied by different instability classes

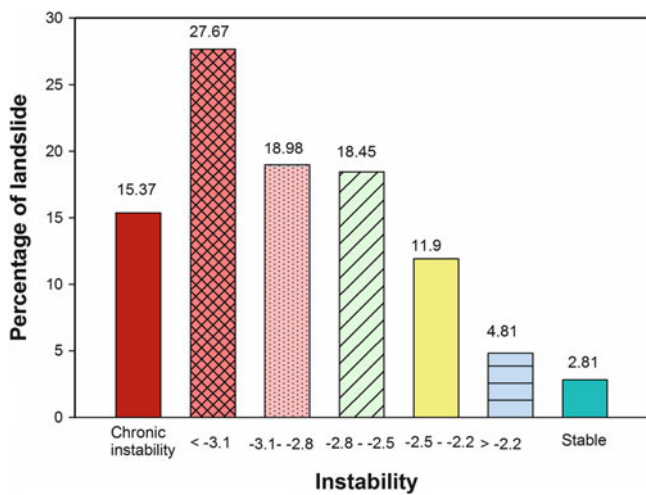


Fig. 4 Area of shallow landslide in different instability classes

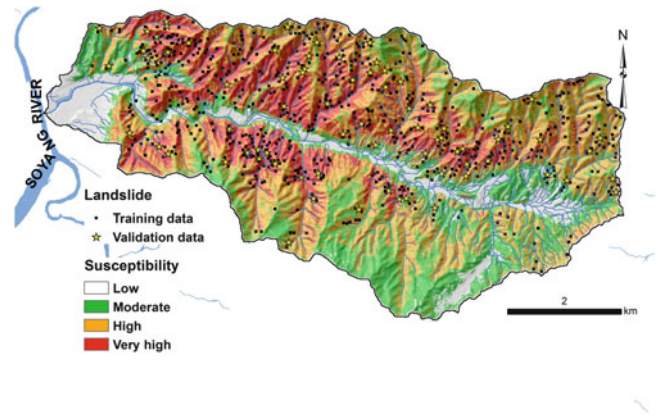


Fig. 5 stability index map obtained by RE

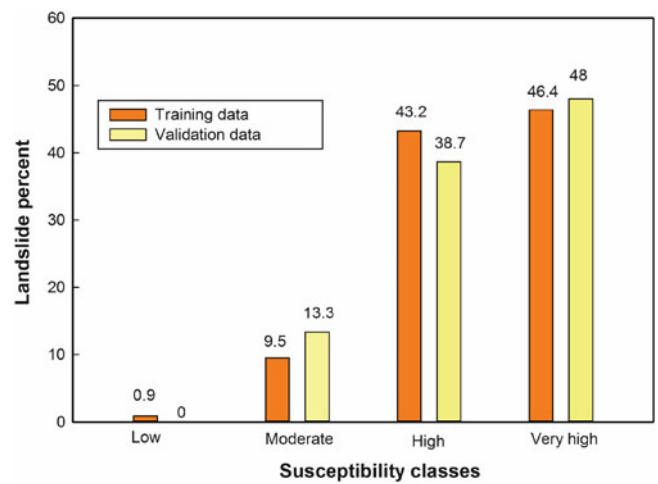


Fig. 6 Area of landslide in different susceptibility classes

relationship to landslide events. Figure 5 shows the landslide susceptibility map obtained by RE model.

The landslide susceptibility map prepared by RE method reveals 47.46 % of the area was categorized as having a low susceptibility, 28.37 % as moderately susceptible, and the remaining 24.17 % was considered to have high (14.85 %) and very high susceptibility (9.32 %).

Figure 6 depicts the percentage of training landslides and validation of landslide data occurrence under different susceptibility classes/conditions. About 89.6 % of the training landslide data were located in the high- or very high-susceptibility class, and 86.7 % of the validation landslide data were identified as having the same class as that projected by the model, demonstrating the reliability of the map. About 9.5 % of the training landslides were in areas having moderate susceptibility, and ~13.3 % of the validation landslides were in the same susceptibility class. Of the

training landslides, ~0.9 % were in low-susceptibility areas, and 0 % of the validation landslides fell within this class.

Model Comparison

The accuracy and predictive capability of the two models was compared using the success rate curves (Vázquez-Selem and Zinck 1994; Zinck et al. 2001; Chung and Fabbri 2003), represents the percentage of correctly classified object (i.e., terrain units) on the y-axis, and the percentage of area classified as positive (i.e., unstable) on the x-axis. A success-rate curve is based on the comparison between the susceptibility map and the landslides used in the modeling (i.e. the training base). This is considered by Chung and Fabbri (2003) as a degree-of-fit measure.

Figure 7 shows the success rate curve which is obtained by plotting the cumulative percentage of observed landslide occurrence against the areal cumulative percentage in decreasing landslide susceptible index values. For

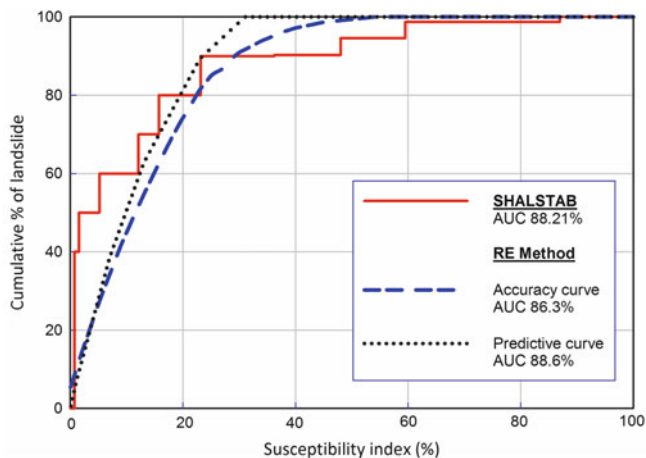


Fig. 7 Accuracy curves of different models

SHALSTAB model all the landslide data were considered for the model. The calculated success rate for SHALSTAB model is 88.21 %. For RE method, the area under a curve is 0.863, which means that the overall success rate of the landslide susceptibility zonation map is 86.3 %. Apart of the success rate, the prediction rate really gives a good estimation of the predictive power of the map. The prediction rate is carried out with validation landslide inventory. The predictive rate of 88.6 % was found for the landslide susceptibility map. The prediction capability of these two models is good. As it can be seen, both models show better performance.

To check the effective spatial distribution of susceptibility zones, both maps produced by SHALSTAB and RE methods were overlaid in GIS and respective percentage coverage in each susceptible class was evaluated. Higher probability class of deterministic susceptibility map could not tally with high susceptibility classes of statistical susceptible map. It means final susceptibility maps prepared using statistical and deterministic methods produced similar results for the low susceptibility zone, whereas high susceptibility areas are not exactly similar. This is because the statistical method is based on density of landslide and the deterministic method is based on hydro-geomechanical properties of soil.

Conclusion

In order to predict future shallow landslides in Deokjeokri creek, landslide susceptibility mapping has been prepared using SHALSTAB and RE methods. Seven different instability classes based on $\log(Q/T)$ parameter were calculated in SHALSTAB. Approximately, 34.75 % of the entire study area was calculated as unconditionally stable. Furthermore, 2.81 % of observed landslides located in the stable zone that indicated error of the model. The RE method, a bivariate method was applied and landslide susceptibility map was prepared using the

result of a combination of sixteen various causative factors responsible for landslide susceptibility. In the RE method, the results show the area under very high and high susceptible zones accounts for 24.14 % of the total hill slope area. In high, very high and moderate hazard zones, about 89.6 % of the total landslides are located. When the map of SHALSTAB model is crossed with the map from RE method, lower susceptibility classes are more or less congruent with each other, however, the higher susceptibility classes could not define this similarity.

Acknowledgments This research was supported by the Public Welfare & Safety Research Program through the National Research Foundation of Korea (NRF) funded by the Ministry of Science, ICT & Future Planning (grant No. 2012M3A2A1050977).

References

- Chung CJ, Fabbri AG (2003) Validation of spatial prediction models for landslide hazard mapping. *Nat Hazards* 30:451–472
- Chung YS, Yoon MB, Kim HS (2004) On climate variations and changes observed in South Korea. *Clim Chang* 66(1–2):151–161
- Kim W, Kim K, Chae B, Cho Y (2000) Case study of landslide types in Korea. *J Eng Geol* 10(2):18–35
- Kim J, Jeong S, Park S, Sharma J (2004) Influence of rainfall induced wetting on the stability of slopes in weathered soils. *Eng Geol* 75 (3–4):251–262
- Kwon Y, Oh S (2011) Physical and mechanical properties of decomposed granite soils sampled in Cheongju, Korea. *Int J Phys Sci* 6(24):5777–5794
- Lee C, Yoo N (2009) A study on debris flow landslide disasters and restoration at Inje of Kangwon Province, Korea. *Korean Soc Hazard Mitig* 9(1):99–105
- Montgomery DR, Dietrich WE (1994) A physically based model for the topographic control of shallow landsliding. *Water Resour Res* 30:1153–1171
- Moore ID, Wilson JP (1992) Length-slope factors for the revised universal soil loss equation: simplified method of estimation. *J Soil Water Conserv* 47:423–428
- Neelkantan R, Yuvaraj S (2013) Relative effect-based landslide hazard zonation mapping in parts of Nilgiris, Tamil Nadu, South India. *Arab J Geosci* 6:4207–4213. doi:10.1007/s12517-012-0693-4
- Rahardjo H, Li XW, Toll DG, Leong EC (2001) The effect of antecedent rainfall on slope stability. *Geotech Geol Eng* 19(3–4):371–399
- Rahardjo H, Lee T, Leong EC, Rezaur RB (2005) Response of a residual soil slope to rainfall. *Can Geotech J* 42(2):340–351
- Soil Survey Staff (1993) “Soil Survey Manual”. Soil Conservation Service. U.S. Department of Agriculture Handbook 18. Archived from the original on 2006-02-14. Retrieved 2006-07-02
- van Westen CJ (1997) Statistical landslide hazard analysis ILWIS 2.1 for Windows application guide. ITC, Enschede, pp 73–84
- van Westen CJ, Terlien TJ (1996) An approach towards deterministic landslide hazard analysis in GIS. A case study from Manizales (Colombia). *Earth Surf Process Landf* 21:853–868
- Vázquez-Selem L, Zinck AJ (1994) Modeling gully distribution on volcanic terrains in the Huasca area, central Mexico. *ITC J* 3:238–251
- Zinck JA, López J, Metternicht GI, Shrestha DP, Vázquez-Selem L (2001) Mapping and modelling mass movements and gullies in mountainous areas using remote sensing and GIS techniques. *Int J Appl Earth Obs Geoinf* 3(1):43–53



Area Based Landslide Hazard and Risk Assessment for Penang Island Malaysia

Shabri Shaharom, Low Tian Huat, and Mohd Asbi Othman

Abstract

The demand for infrastructure development and building construction has encouraged development over new areas of challenging terrain and encroachment into existing, otherwise stable, highland areas. In 2008, The Slope Engineering Branch (CKC) of The Public Works Department had initiated a Slope Hazard and Risk Assessment in Hulu Kelang Ampang Area. In 2010, CKC again has extended the slope hazard and risk assessment to other critical areas i.e., Penang Island which is in line with the long term plan in the National Slope Master Plan. Penang Island has a history of landslide damages following heavy rains. As many development and housing projects are taking place at the hilly terrain, the hill slopes are not exempted for building platforms and excavation in the hilly areas around Penang island is rapidly increasing, amidst regulatory concerns. This has resulted in incidences of geotechnical instability causing numerous landslips, some of which are fatal.

In view of formulating medium term and long term measures towards an effective policy of inspection and monitoring of development in Penang island, An area based landslide hazard assessment was proposed to initiate a slope hazard assessment and mapping for the proposed area. Geographical Information System (GIS) was adopted as the base machine for the production of the landslide hazard and risk map. This paper highlights the area based landslide hazard and risk assessment using GIS application. The landslide hazard and risk assessment methodology and map preparation using GIS application for the study are also highlighted.

Keywords

Landslide • Area based • Slope hazard and risk assessment • GIS • Hazard and risk map

Introduction

The demand for infrastructure development and building construction on Penang Island has forced the development to encroach into hilly areas. Penang Island has history of landslide damages following heavy rains. Due to this frequent landslides occurrence in areas associated with developed hilly areas, Penang Island has been selected by Slope Engineering Branch of Public Works Department Malaysia as a study area after Hulu Kelang Study for the evaluation and mapping of slopes hazard and risk. The study of these areas, known for numerous landslide occurrences

S. Shaharom
Public Works Department Malaysia, Jalan Sultan Salahuddin,
50582 Kuala Lumpur, Malaysia
e-mail: shabri@jkr.gov.my

L.T. Huat (✉) • M.A. Othman
Mohd Asbi & Associates, Jalan PJU 1A/46, Lembah Subang,
47301 Petaling Jaya, Selangor, Malaysia
e-mail: low@asbi_associates.com.my; loretta@jkr.gov.my;
asbi@asbi_associates.com.my

over the last two decades, would provide the Government with a systematic tool for slope management to facilitate immediate remedial measures and long term preventive works.

Landslide Hazard and Risk Assessment Methodology

Slope assessment is used to assess the stability condition of slopes either individually or on a large scale. Slope assessment is also carried out to understand the likely mechanism which triggers potential occurrence of a landslide. Slope management, on the other hand, is an efficient use of available funds for slope rehabilitation works based on priority rankings of slopes using hazard and risk techniques.

Hazard maps have been used throughout the world to identify areas of either existing or potential slope instability. Such maps have been applied to land development projects, new and existing highways, and mining works. In general, hazard maps can be developed in a number of ways, ranging from simple qualitative or historical assessment, to varying degrees of site mapping and scientific analyses involving statistical and other numerical software packages.

The methods of preparing Hazard Maps have been categorized by Hutchinson (1995) into three groups, namely:

1. **The Geotechnical Approach.** This approach involves sampling, logging and testing, and generally is too expensive for large area study. The Geotechnical Approach and Direct Methods (described below) are generally adopted for site specific projects rather than large area study.
2. **Direct Methods.** These methods are based principally on geomorphological mapping, geological mapping and remote sensing (primarily aerial photography). These methods produce a landslide map that can be converted to Hazard Map, through appropriate subdivision and zoning of activity.
3. **Indirect Methods.** The simplest indirect methods involve univariate and bivariate analyses to identify single parameter or pairs of parameters that cause or contribute to slope instability. An example of univariate analysis is a plot of slope failure versus slope height and bivariate analysis, for example slope angle versus slope height. The level of complexity involves multivariate analysis. Multivariate analyses include factor mapping (herein described as factor overlay) combined with numerical methods to identify hazardous areas.

The Indirect Methods assume that there are a number of significant factors that relate to slope instability, and that these factors combined contribute to slope failure.

The common landslide hazard analysis or classification can be divided into four main categories namely;

- (a) **Heuristic Method** (Expert Judgement approach)
- (b) **Statistical Method** (Discriminant or Multivariate Analysis)
- (c) **Deterministic Method** (common Slope Stability Analysis approach)
- (d) **Spatial Method** (Aerial photograph and Satellite Interpretation)

The application of these methods is subjected to the following conditions:

- (a) **The scale of landslide assessment**—In general, if the scale of hazard study is small, simple methods such as heuristic methods and deterministic methods can be adopted. Statistical methods will only be applied when there are sufficient slope failure records and slope numbers.
- (b) **Availability of information**—Some assessment methods such as discriminant analysis require sufficient failure history records in order to obtain an accurate hazard classification. The failure records are required to segregate/discriminate failed and stable slopes based on landslide contributing factors. (see Othman 1989)
- (c) **Type of landslide assessment**—In general, landslide assessment can be divided into two main categories; linear based assessment and area based assessment. Linear based hazard assessment is for slope hazard assessment along linear infrastructures such as roads, expressways, railways and electric transmission lines. As for area based assessment is mainly on development area such as housing development. Spatial method using Geographical Information System (GIS) approach is recommended for the area based hazard assessment.

Both methods of Direct and Indirect approach adopted in Hulu Klang project were adopted in the study. A direct method based on geomorphology is important in this study. Most landslide preparatory causal factors in study area (developed area) were due to human activities, lack of maintenance, design inadequacy and construction problems; the slopes do not behave as predicted in slope stability theory. These unpredicted factors require detailed field inspection and mapping. The geomorphological map prepared from field inspection was used as calibration tools in the hazard assessment.

As for the indirect methods, a heuristic method was adopted in the study. Weightings adopted in the factor overlay approach were derived from the expert's survey and were used to classify the landslide hazards. The layers for this indirect approach are:

- (a) Slope angle
- (b) Flow accumulation
- (c) Land cover

- (d) Geological formation (bedrock type)
- (e) Geological lineament
- (f) Rainfall density
- (g) Failure history

Landslide risk assessment is a process of making recommendations on the decision of whether existing risk is tolerable and the present risk control measures are adequate, and if not, whether alternative risk control measures are justified or should be implemented. The risk assessment incorporates the risk analysis and risk evaluation phases.

Landslide risk is defined as expected number of lives lost, persons injured, damage to property and disruption of economic activity due to particular landslide hazard for a given area and reference period.

In general, risk is a result of the product of probability or hazard (of occurrence of a landslide with a given magnitude) and the consequence of the landslide incident. The equation for Risk (R) is as follows (PWD 2004):

$$\text{Risk} = \text{Hazard}(H) \times \text{Consequences}(C) \quad (1)$$

A complete risk assessment requires quantitative risk assessment which involves the quantification of a number of different types of losses, such as:

- (a) Losses associated with general building stock: structural and non-structural cost of repair or replacement, loss of contents;
- (b) Socioeconomic losses: number of displaced households: number of people requiring temporary shelter, casualties in categories of severity (based on different times of day)
- (c) Transportation and utility lifelines: for components of the lifeline systems—damage probabilities, cost of repair or replacement and expected functionality for various times following a disaster
- (d) Essential facilities: damage probabilities, probability of functionality i.e., loss of hospital beds or operation theaters etc.
- (e) Indirect economic impact: business inventory loss, relocation costs, business income loss, employee wage loss, loss of rental income, long term economic effects on the region.

A major component of risk assessment is the risk analysis. Risk analysis is an estimation of the risk to individuals or populations, property or environment from landslide hazard based on available information. Risk analyses generally follow the following steps:

- (a) Landslide identification
- (b) Estimation of probability of occurrence to estimate landslide hazard

- (c) Evaluation of the vulnerability of the element(s) at risk
- (d) Consequence identification
- (e) Risk estimation

Risk analysis can be either qualitative or quantitative.

Qualitative risk analysis, which uses word form, descriptive or numeric rating scales to describe the magnitude of potential consequences and likelihood that the identified consequences will occur, while quantitative risk analysis is based on numerical values of the probability, vulnerability and consequences, and resulting in a numerical value of the risk.

Geographical Information System (GIS) has been adopted to facilitate the slope hazard and risk assessment and analysis. GIS software is a powerful set of tools for collecting, storing, retrieving at will, transforming and displaying spatial data from the real world for particular set of purposes. Therefore GIS has been selected as the base operation software to analyse slope hazard and produce area based hazard maps. Survey data from the airborne survey using LiDAR (Light Detection and Ranging) was used to produce the base map and spatial layers i.e., slope angle layer and flow accumulation layers etc., for slope hazard analysis. As for risk analysis, database from the field mapping works was adopted in the GIS environment.

Light Detection and Ranging Survey

LiDAR is one of the best techniques to produce geomatic data for any geographical purposes. Figure 1 shows the schematic diagram for data capturing using LiDAR. This option has its own unique solutions to deliver close to ground data accuracy at an airborne speed with little effect from bad weather. It totally eliminates the ground control point need for imagery processing. At very high speed, the current LiDAR mapping technology can provide a very accurate terrain model to produce a contour map of terrain floor of any forest or cleared land to within 0.15 m resolution. Three-dimensional spot heights are produced at 0.2–3 m grids depending on flying height and skewing angle.

One disadvantage of this technology is the limitation to survey the information/features that are hidden from airborne capture such as culverts, pier below bridges, etc. But the big advantage is quick mapping of hostile grounds, densely forested jungle, non-accessible areas or large area which requires high accuracy and intensity of data. Therefore, for the Penang Island study, field mapping by geotechnical engineers and geologists were proposed to overcome this limitation.

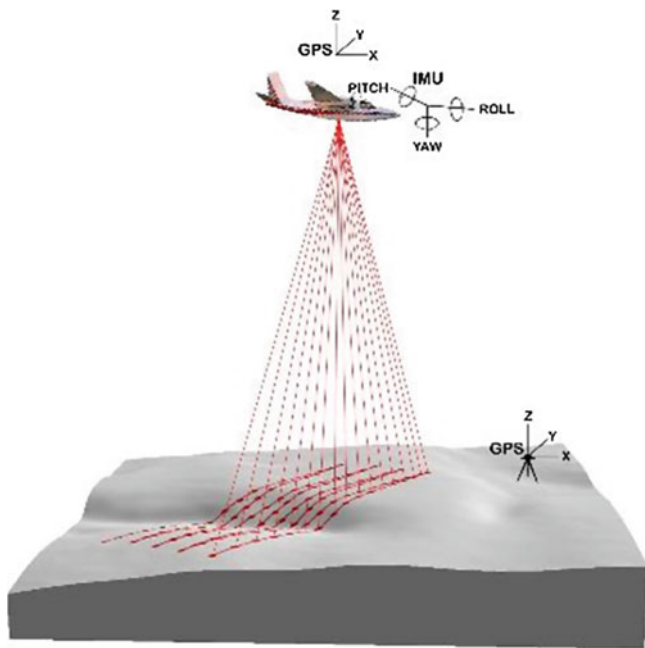


Fig. 1 Illustration of how LiDAR sensing instrument captures elevation points

Hazard Assessment and Analysis

In view of limited landslide records made available, the calculation of landslide hazard rating using statistical approach is not suitable. The common method of hazard classification using multi-variables, discriminant analysis will not provide accurate hazard rating.

Before formulating the hazard rating model, the dependent model parameters shall be identified. A landslide cause tree diagram was prepared to identify all the potential preparatory and triggering causal factors of a landslide. These geographically distributed causal factors or parameters that potentially contribute to landslides are referred to in this study as landslide dependent model parameters. The proposed dependent model parameters used are as follows:

- (a) Slope gradient
- (b) Geology
- (c) Flow accumulation
- (d) Land cover
- (e) Lineament
- (f) Failure history
- (g) Sign of distress
- (h) Rainfall intensity

Sign of distress (obtained from geomorphological mapping) i.e., tension crack, gully, rill and etc., were later taken out as the dependent parameter to avoid hazard

equation being biased towards slopes within developed area (because no field mapping was carried out for forest areas). The sign of distress from the geomorphological map were used for calibration of the hazard equation. Only water seepage was used in the analysis to replace dependent parameter of “Sign of Distress”.

Within each model parameter, different weightings were proposed for different groupings depending on their correlations with landslides as perceived by experts. Groupings within a parameter class were referred to in this study as inter-parameter variables. Figure 2 shows the proposed dependent parameter model and the respective inter-parameter variables.

Pair Wise Comparison Method

The weightings of the possible model parameter in factor overlay method can be formulated using pair wise method. Pair wise comparison is used as a decision making tool in many applications to rank the relative importance of multiple variables. The Pair wise comparison process is proposed to derive the weightings for each of the landslide dependent parameter (Golder and Associates 2006).

The process is based on engineering judgment and compares individually:

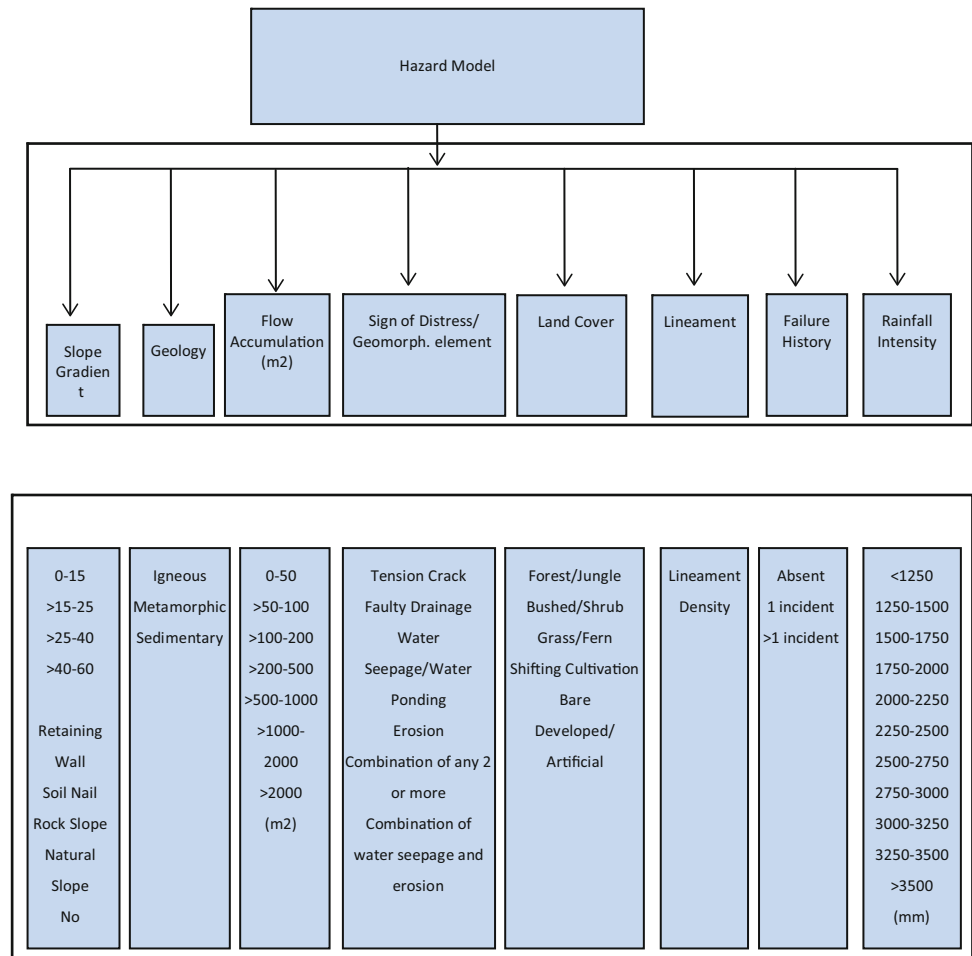
- The relative importance of the parameter in influencing the potential for landslides compared one against another, and
- The degree to which each parameter is more important than each counterpart (Score of 1 if parameter is slightly more important than the compared parameter, 2 for significantly more important and 0 for equally important).

The outcome of the pair wise comparison was tabled and analysed and the results was used to assign weightings to each model parameter. The total value of all the attribute weightings was taken as 1.0. The applied weightings indicate the degree to which the potential for landslide is influenced by each model parameter, relative to the other parameters. The same approach is applied when assigning the weightage for interparameter variables.

The formula for the hazard score is the sum of the products of the dependent parameter and inter-parameter weightings. The formula below illustrates the proposed landslide hazard formula adopted in the study:

There were two hazard formulas deduced for both the study areas of Penang Island and Bukit Kanada, Miri. The hazard formulas are as follows:

Fig. 2 Proposed dependent parameters and inter parameter variables



a) Without signs of distress

$$\begin{aligned}
 \text{Hazard} = & 0.23(\text{slope angle}) + 0.08(\text{geology}) \\
 & + 0.17(\text{flow accumulation}) \\
 & + 0.05(\text{land cover}) + 0.1(\text{lineament}) \\
 & + 0.09(\text{rainfall}) + 0.28(\text{failure history}) \quad (2)
 \end{aligned}$$

b) With signs of distress

$$\begin{aligned}
 \text{Hazard} = & 0.18(\text{slope angle}) + 0.06(\text{geology}) \\
 & + 0.12(\text{flow accumulation}) \\
 & + 0.04(\text{land cover}) + 0.07(\text{lineament}) \\
 & + 0.06(\text{rainfall}) \\
 & + 0.22(\text{failure history}) \\
 & + 0.25(\text{sign of distress}) \quad (3)
 \end{aligned}$$

Five hazard ratings, very low through very high were adopted. The hazard classes adopted in the study are:

- (a) Very high hazard
- (b) High hazard

(c) Medium hazard

(d) Low hazard

(e) Very low hazard

The selection of hazard ratings is somewhat subjective. The ratings indicate the likelihood of a landslide occurring. The hazard classes were first classified by equally dividing the maximum score into five equal classes. Later, during the calibration and verification works the ranges for the classes were further refined based on the geomorphological map. Figure 3 shows a typical tile of ortho-rectified photograph and slope hazard map produce in GIS environment.

Risk Analysis

In general, risk is a result of the product of probability or hazard (of occurrence of a landslide with a given magnitude) and the consequence of the landslide incident. The equation for risk (R) is as follows (PWD 2004):

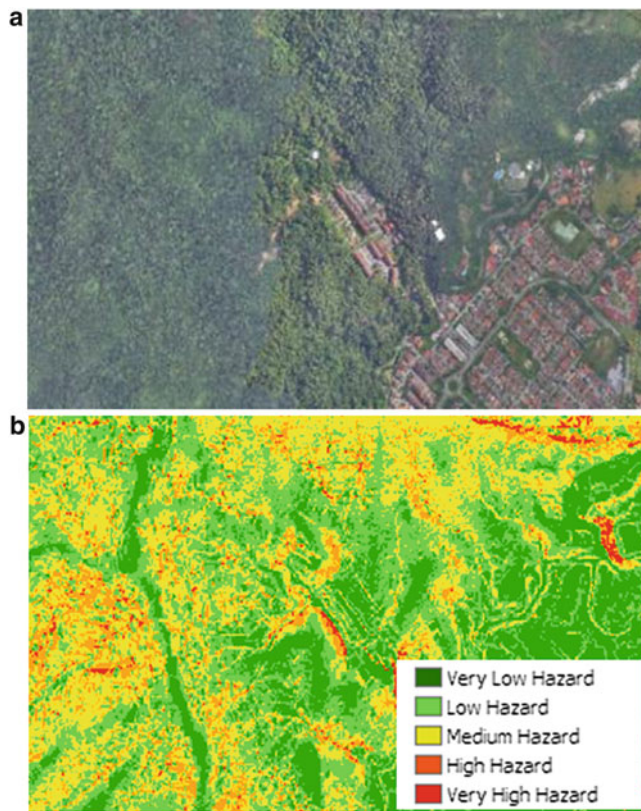


Fig. 3 (a) Ortho-rectified photograph of a typical tile in Penang Island area. (b) Hazard map for Penang Island area

| Risk Classes | Ranges | Meaning |
|--------------|----------|--|
| Very High | > 15 | Total damage of structures and loss of life |
| High | > 9 - 15 | Partial damage of structure and total road closure, with no loss of life |
| Medium | > 6 - 9 | May damage structure or facilities but no loss of life |
| Low | > 3 - 6 | May encroach into structure compound |
| Very Low | ≤ 3 | No risk |

Fig. 4 Risk rating classes

$$RISK(R) = HAZARD(H) \times CONSEQUENCES(C) \quad (4)$$

The risk rating classes is as follows (Fig. 4):

Table 1 Score for distance ratio and slope angle

| Item | Score |
|---|-------|
| DISTANCE RATIO (Distance of element at risk from slope ÷ expected run out distance) (S1) | |
| 0.9–1.0 | 1 |
| 0.75–0.9 | 2 |
| 0.5–0.75 | 3 |
| <0.5 | 4 |
| Element at risk located on the slope | 4 |
| SLOPE ANGLE (S2) | |
| <30° | 1 |
| 30°–45° | 2 |
| 46°–60° | 3 |
| >60° | 4 |

Consequence Modeling

The consequence modeling is divided into two main layers, namely, property layer and infrastructure layer. The equation is as follows:

$$CONSEQUENCES\ SCORE = FATALITY\ SCORE \times IMPACT\ SCORE \quad (5)$$

The impact score is the score of landslide impact due to the debris of landslide. The impact score can be divided into two main components, namely, the ratio of distance from slope and run out distance (S1) and slope angle (S2). The scores for both the distance ratio and slope angle are as in Table 1:

The impact score is the product of distance ratio (S1) and slope angle score (S2). The equation is as follows:

$$IMPACT\ SCORE = S1 \times S2 \quad (6)$$

The fatality score is as in Table 2.

Findings

A total of 1,751 slopes in Penang Island and 86 slopes in Bukit Kanada, Miri area were mapped. The risk condition for these slopes are shown in Fig. 5.

Expert Judgement

The risk scores generated by the system were verified using the outcome from the expert judgment. A total of 20 slopes were assessed by the experts within the study team to ensure the hazard and risk scores generated by the system are in order.

Table 2 Fatality score

| Property's Impact | | Score (based on ranking) |
|----------------------------|-------------------------------|--------------------------|
| | Types of property | |
| High rise structures | Condominiums, apartments | 5 |
| Terrace houses | Bungalows, terraces | 4 |
| Essential structures | Schools, mosque | 5 |
| Non residential structures | TNB | 1 |
| | Park | 2 |
| | Parking | 2 |
| Utilities | Waterline, communication line | 1 |
| Major roads | | 3 |
| Minor roads | | 2 |

| Risk Classification | Number of slopes | |
|----------------------|-----------------------|--------------------------|
| | With Sign of Distress | Without Sign of Distress |
| Very High Risk Slope | 287 | 89 |
| High Risk Slope | 440 | 434 |
| Medium Risk Slope | 284 | 333 |
| Low Risk Slope | 509 | 602 |
| Very Low Risk Slope | 231 | 293 |

Fig. 5 Risk condition for slopes in Penang Island

Conclusion

Slope hazard map can be used to identify areas of either existing or potential slope instability. Calibration by means of ground mapping is essential to ensure the accuracy of the

hazard map. For Penang Island landslide assessment study, Geographical Information System (GIS) was found to be the most suitable system for area based slope hazard and risk assessment.

References

- Golder and Associates (2006) "Stage 2A study; landslide hazard and risk assessment for currumbin hill gold coast" for Gold Coast City Council
- Hutchinson JN (1995) General report: morphological and geotechnical parameters of landslides in relation to geology and hydrogeology. In: 5th international symposium on landslides, Lausanne, Switzerland, vol 2. pp 3–36
- Othman MA (1989) Highway cut slope instability problems in West Malaysia. Ph.D. thesis, 1989, unpublished
- PWD (2004) Slope protection study for Federal Route 22, Tamparuli—Sandakan, Sabah. Final Report. Public Works Department, Malaysia, Unpublished



Landslide Hazard Mapping Using a Poisson Distribution: A Case Study in Penang Island, Malaysia

Lea Tien Tay, Habibah Lateh, Md Kamrul Hossain,
and Anton Abdulbasah Kamil

Abstract

Landsliding is one of the most destructive natural geohazards in Malaysia. Landslide hazard maps are very useful for urban development planning. This paper presents landslide hazard mapping using a new approach, i.e. a Poisson distribution, and compares the result with previous probabilistic approaches, i.e. frequency ratio (FR), statistical index (SI) and landslide nominal susceptibility factor (LNSF). These approaches were implemented in Penang Island to produce landslide hazard maps. The landslide causative factors considered are elevation, slope gradient, slope aspect, curvature, land cover, vegetation cover, distance from nearest road, distance from nearest stream, distance from nearest fault line, geology, soil texture and precipitation. Landslide hazard maps were assessed using the Receiver Operating Characteristics (ROC) method. Accuracy obtained for FR, SI and LNSF are 78.52 %, 78.12 % and 72.93 % respectively. Poisson distribution approach gives high accuracy of 78.51 % as FR.

Keywords

Landslide • Frequency ratio • Susceptibility • Hazard map • Poisson distribution

Introduction

Landslides are a geological phenomenon that involves downward and outward movement of rock, earth or debris. Landslides are hazardous, as they destroy properties and even claim human lives. In Malaysia, landslides happen rather frequently due to heavy rainfall during the annual monsoons: the Southwest Monsoon from late May to September and the Northeast Monsoon from November to March. In recent years from 2000 to 2009, damage due

to landslides has been particularly high (Pradhan and Lee 2010). Although it is difficult to predict landslide events, areas may be divided into different ranks according to their degree of potential hazard due to mass movement (Varnes 1984). The identification of high risk areas is important in landslide prediction and warning systems. In this paper, Penang Island is the selected area of interest for landslide hazard analysis, as it has suffered substantial damage due to landslides in recent years. In recent years, there have been many studies of landslide hazard evaluation using GIS and various evaluation techniques. Probabilistic methods such as frequency ratio have been applied many times to achieve favorable results in landslide hazard evaluation (Pradhan and Lee 2010; Lee and Talib 2005). The landslide nominal susceptibility factor has also been used to generate landslide susceptibility and hazard maps (Saha et al. 2005). To the best of our knowledge, this study is the first time the Poisson distribution has been used for landslide hazard mapping.

L.T. Tay (✉)
Universiti Sains Malaysia, Engineering Campus, 14300 Penang,
Malaysia
e-mail: tay@usm.my

H. Lateh • M.K. Hossain • A.A. Kamil
School of Distance Education, Universiti Sains Malaysia, 11800 USM
Penang, Malaysia
e-mail: habibah@usm.my

Study Area

The area selected for this study is Penang Island (Fig. 1), due to its heavy frequency of landslides over the years. Penang is one of the 13 states of Malaysia located on the North West of Peninsular Malaysia. It is bounded to the north and east by the state of Kedah, to the south by the state of Perak and to the west by the Strait of Malacca. Penang consists of both the island of Penang and a coastal strip on the mainland known as Province Wellesley. In this paper, the island of Penang is considered for landslide evaluation mapping. The island, which is separated from the mainland by a channel, covers an area of 285 km². It is located about 5° 15'N to 5° 30'N latitude and 100° 10'E to 100° 20'E longitude. Elevation of the terrain ranges from 0 to 820 m above sea level and slope gradient ranges from 0° to 87°. Penang Island is affected by fault lines that run from north to south mainly in the centre of the island. The land cover of Penang Island consists of mainly swamp, plantation, forest, grassland and urban area. Vegetation cover consists mainly of forest and fruit plantations. The temperature of Penang Island ranges from between 29 to 32 °C and the average amount of rainfall varies from 2,254 to 2,903 mm annually.

Data Sets

Data collection on a geographical database of Penang Island is done through application of remote sensing methods and GIS. Topographical, geological and various images of Penang Island were obtained from various departments in Malaysia including Meteorological department, Jabatan Pengairandan Saliran (JPS), Department of Agriculture (DOA), Minerals and Geoscience Department (JMG), Jabatan Ukur dan Pemetaan Malaysia (JUPEM) and Pusat PeGIS. Landslide occurrence points in Penang Island are also collected and transformed into a spatial database for probabilistic landslide susceptibility analysis. Most landslides happened in the mountainous terrain of the island, which is situated in the middle of the island. These landslides consist of mainly shallow rotational debris slides, debris flows and rock falls. Identification and mapping of a suitable set of instability and causative factors having a relationship with slope failures requires prior knowledge of the main causes of landslides (Guzzetti et al. 1999). To apply the probabilistic methods, data sets of landslide-causative factors were collected and constructed as a spatial database. Twelve landslide-causative factors were considered in calculating the probability of landslides.

From the topographic database, digital elevation models (DEM) were constructed with a resolution of 5-m. From the DEM, elevation was extracted. Elevation was then used to compute slope angle, slope aspect and slope curvature.



Fig. 1 Penang Island (Source. Google map)

Distance from drainage and distance from road were calculated from the drainage map and the road map, each available as digital maps respectively. Van Westen et al. (2003) suggested that buffer zones for line features, such as, rivers and roads should be set to 50 m. Similarly, distances from fault lines of Penang Island were calculated and segregated into 100 m intervals. A soil texture database of the island, which included sand, clay and urban land, was obtained as well. The land-use map consists of 17 classes of land usage. The vegetation cover map consists of 14 classes. The geologic map, showing the types of rocks and granites of Penang Island is used as one of the landslide-causative factors. Rainfall or precipitation is one of the most efficient triggering factors of landslides, as it dampens soils and washes away debris and rocks, creating landslides. There are only a few rain gauge stations in Penang Island, therefore, interpolation had to be used to prepare the precipitation map. Using 29 years of historical rainfall data (1980–2008), statistical distribution of the accumulated average precipitation was prepared using ArcGIS software's inverse weight distance interpolation method.

Methods

The probabilistic approach to landslide hazard analysis has been proven to be very useful in landslide prediction. The advantages of this approach lie in its high efficiency, low

cost, easy implementation and a better understanding of the relationships between landslides and landslide-causative factors. In probabilistic methods, each factor's data weights are calculated based on class distribution and its landslide density (Suzen and Doyuran 2004). These weights represent the importance of each factor to landslide occurrence and are used to produce a landslide hazard index.

Frequency Ratio

The frequency ratio (FR) approach is a variant of the probabilistic method that is based on the observed relationships between the distribution of landslides and landslide-causative factors. Spatial relationships and correlations between landslide occurrence and its factors are computed and these correlations show how closely related the factors are to landslide occurrence. Frequency ratio or weight of each class is computed by dividing the landslide density of a class with the total landslide density as follows

$$FR_{ab} = \frac{Aab^*}{Aab} \times \frac{A}{A^*}$$

FR = Frequency ratio of each factor.

Aab* = Area of observed landslides of class a of factor b.

Aab = Area of class a of factor b.

A = Total area of the map.

A* = Total area of observed landslides of the map.

A value of 1 is the neutral value and values higher than 1 show a higher positive correlation between the class of a factor with the landslide. To calculate the landslide hazard index (LHI), each pixel's frequency ratio on the map is summed as in the equation below. It is then inferred that areas with higher values of frequency ratio are areas that are more prone to landslides.

$$LHI(\text{Landslide hazard index}) = FR_1 + FR_2 + \dots + FR_N$$

where FR = Frequency ratio of each factor.

Statistical Index

Statistical index (SI) is another probabilistic approach that is very similar to frequency ratio. It was introduced by Van Westen and Terlien (1996). In recent years, researchers have applied this method for landslide susceptibility analysis (Long 2008) and termed the method statistical index. In this method, the weight for every class of each factor is defined as the natural logarithm of the landslide density in the class divided by the total landslide density.

Mathematically, it is almost the same as frequency ratio, as the method simply takes the natural logarithm of the frequency ratios, as shown in equation below

$$SI_{ab} = \ln\left(\frac{Aab^*}{Aab} \times \frac{A}{A^*}\right)$$

Summation of the statistical index of each factor in every pixel produces the landslide hazard index (LHI) as in equation below.

$$LHI = SI_1 + SI_2 + \dots + SI_N$$

SI = statistical index weight of each factor.

For ratios less than 1, the weight will be negative and vice versa. Negative values show decreasing correlation between the class with landslide and vice versa. In the case of no landslide occurrence, the weight of that particular class is assigned as 0. Thus, a class that has a weight of 0 shows no correlation with landslide occurrence and does not contribute to the landslide hazard index.

Landslide Nominal Susceptibility Factor

The landslide nominal susceptibility factor (LNSF) approach (Saha et al. 2005) is a modification of a method originally proposed by Gupta and Joshi (1990). The nominal risk factor is defined as follows

$$LNSF_i = Npix(S_i) * n / \left(\sum Npix(S_i) \right)$$

where Npix (Si) = number of pixels of landslide in the thematic class of i

n = number of thematic classes of respective factor

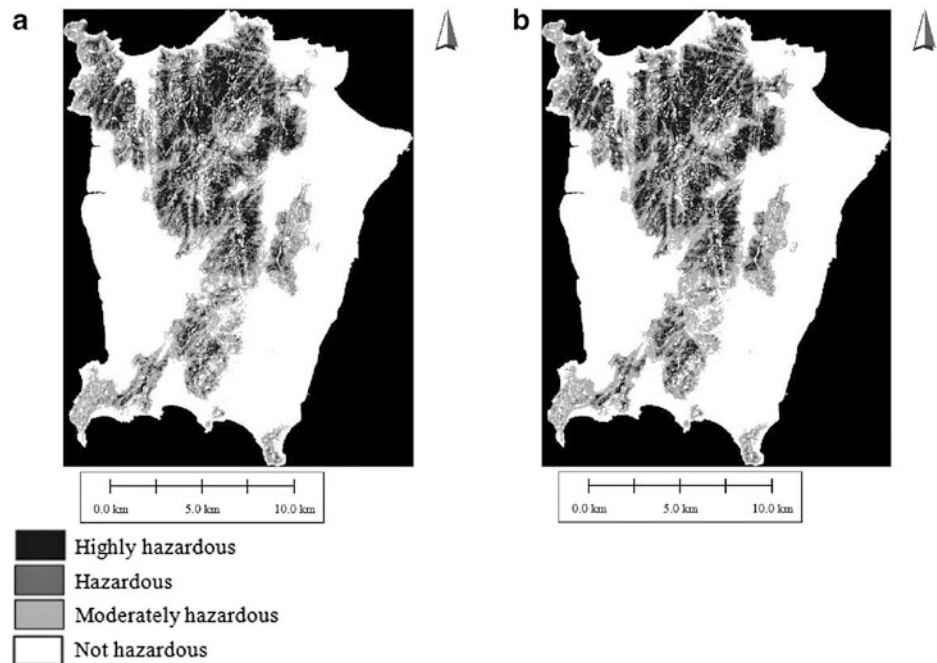
A value greater than one for LNSF means more susceptible to landsliding, whereas a LNSF value less than one means less susceptible. The nominal risk factors of each factor are summed to produce the Landslide Hazard Index (LHI) for the LNSF method.

Poisson Distribution

The Poisson distribution is a discrete distribution (Haight 1967), and it is useful in ecological studies. In this study, the Poisson distribution is used for "landslides" which is a geological event. The distribution function for the Poisson distribution is defined as

$$P[X] = \frac{\exp(-\theta) * \theta^X}{X!}$$

Fig. 2 Landslide hazard maps for Penang Island generated using (a) Frequency ratio and (b) statistical index



To estimate the probability of one landslide under a characteristic, the Poisson distribution is simplified as follows:

$$P[x = 1] = \exp(-\theta) * \theta$$

where

$$\theta = \frac{\text{Number of Landslide}}{\text{Total Number of Observations}}$$

Higher values of the probability for a characteristic shows a high risk of landslide occurrence.

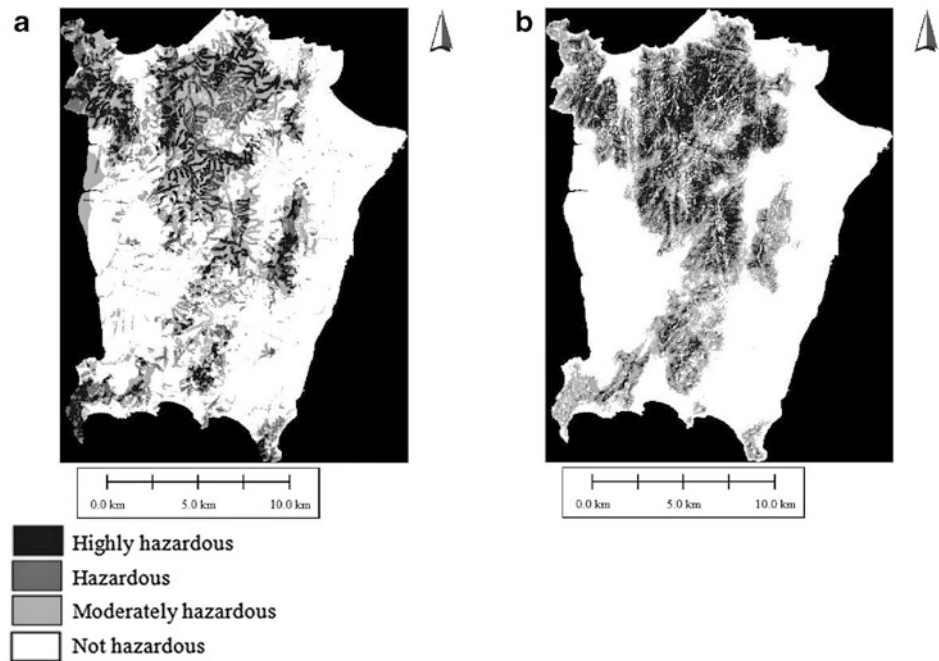
Verification and Discussion

To verify the efficiency and accuracy of each method, the ROC (receiver operating characteristics) method was employed. Two assumptions are needed in order to verify the maps. One is that landslides are related to spatial information such as slope and aspect, and the other is that future landslides will be affected by triggering factors such as rainfall (Chung and Fabbri 1999). Both assumptions are satisfied in this study. ROC curves explain how well the prediction models fit the data of landslide-causative factors with landslide occurrences to predict future landslides. Verification by ROC is done by first sorting the landslide hazard indexes (LHI) in a descending order. The ordered indexes are then divided into 100 classes and set on the y-axis, with

accumulated 1 % intervals on the x-axis (Pradhan and Lee 2010). The resulting graph shows a curve that explains how well the model and factors predict future landslides (Chung and Fabbri 1999). The area under the curves reflects the accuracies of the prediction models and is one of the commonly used accuracy statistics in natural hazard assessments (Beguria 2006). Landslide hazard maps produced using frequency ratio, statistical index, LNSF and Poisson distribution achieve accuracies of 78.52 %, 78.12 %, 72.93 % and 78.51 %, respectively. Frequency ratios and Poisson distributions are capable of producing a landslide hazard map with the highest accuracy among these four approaches in this study area. Both approaches work equally well, with most of the landslide locations found to be within the highest 20 % of the landslide hazard index. The LNSF approach is found to be less effective in producing landslide hazard maps as compared to the other three approaches.

Landslide hazard mapping is done by segregating the LHI (landslide hazard index) into several categories of risks. In this study, the indexes are categorized into four groups: Highly hazardous for the highest 10 % of the indexes (90–100 %), Hazardous for the next 10 % (80–90 %), Moderately hazardous for the next 20 % (60–80 %) and Not hazardous for the remaining 60 % (0–60 %). Figure 2 shows the landslide hazard maps produced using the frequency ratio method and statistical index. Landslide hazard maps produced using the landslide nominal susceptibility factor and Poisson distribution are shown in Fig. 3.

Fig. 3 Landslide hazard maps for Penang Island generated using (a) landslide nominal susceptibility factor and (b) poisson distribution



Conclusion

Due to the limitation of flat land in Penang Island, more hill areas are being exploited for housing and development. This creates a scenario in which a landslide assessment is needed to warn people of potential landslides in risky areas. Prediction models such as statistical or probabilistic methods are simple methods which have been proven to yield good results in landslide prediction. Landslide causative factors depend on the availability of GIS images of the research area. In this paper, landslide hazard maps of Penang Island were produced with frequency ratios, statistical indexes, nominal susceptibility factors and Poisson distributions using twelve landslide-causative factors. The frequency ratio and Poisson distribution methods are proven to produce landslide hazard maps with the highest accuracy, followed by statistical index and nominal susceptibility factor. The accuracies show that the Poisson distribution also can be used as a tool for hazard mapping and these maps can be useful in the planning of future urban infrastructure development.

Acknowledgments The authors would like to thank Jabatan Pengairan dan Saliran (JPS) and Minerals and Geoscience Department (JMG) for the data provided. The authors would also thank Universiti Sains Malaysia for the facilities provided.

References

Beguria S (2006) Validation and evaluation of predictive models in hazard assessment and risk management. *Nat Hazards* 37:315–329

- Chung CF, Fabbri AG (1999) Probabilistic prediction models for landslide hazard mapping. *Photogramm Eng Remote Sensing* 65 (12):1389–1399
- Gupta RP, Joshi BC (1990) Landslide hazard zonation using the GIS approach—a case study from the Ramganga catchment, Himalayas. *Eng Geol* 28:119–131
- Guzzetti F, Carrara A, Cardinali M, Reichenbach P (1999) Landslide hazard evaluation: a review of current techniques and their application in a multi-scale study, Central Italy. *Geomorphology* 31:181–216
- Haight FA (1967) *Handbook of the poisson distribution*. Wiley, New York, 168 p
- Lee S, Talib JA (2005) Probabilistic landslide susceptibility and factor effect analysis. *Environ Geol* 47:982–990
- Long NT (2008) Landslide susceptibility mapping of the mountainous area in a Luoi district, ThuaThien Hue province. *Vrije Universiteit Brussel, Vietnam*
- Pradhan B, Lee S (2010) Delineation of landslide hazard areas on Penang Island, Malaysia, by using frequency ratio, logistic regression, and artificial neural network models. *Environ Earth Sci* 60 (5):1037–1054
- Saha AK, Gupta PR, Sarkar I, Arora MK, Csaplovics E (2005) An approach for GIS-based statistical landslide susceptibility zoning—with a case study in the Himalayas. *Landslides* 2(1):61–69
- Suzen ML, Doyuran V (2004) A comparison of the GIS based landslide susceptibility assessment methods: multivariate versus bivariate. *Environ Geol* 45:665–679
- Van Westen CJ, Terlien MJT (1996) An approach towards deterministic landslide hazard analysis in GIS: a case study from Manizales, Colombia. *Earth Surf Process Landf* 21(9):853–868
- Van Westen CJ, Rengers N, Soeters R (2003) Use of geomorphological information in indirect landslide susceptibility assessment. *Nat Hazards* 30:399–419
- Varnes DJ (1984) *Landslide hazard zonation: a review of principles and practice*. UNESCO, Paris, 60 pp



Shallow Landslide Susceptibility Mapping for Zagreb Hilly Area, Croatia

Chunxiang Wang, Snjezana Mihalić Arbanas, Hideaki Marui, Naoki Watanabe, and Gen Furuya

Abstract

The aim of this study is to map the landslide susceptibility of the hilly area of Mt. Medvednica located in the northwestern part of the City of Zagreb, Croatia. Landslides in this region are mostly shallow movements of superficial deposits along contacts with fresh deposits of soil and cause significant economic losses by damaging houses and the urban infrastructure. The method used here is the deterministic slope stability analysis model SINMAP which is developed by Pack et al. (A stability index approach to terrain stability hazard mapping. SINMAP user's manual, 1998; A stability index approach to terrain stability hazard mapping. SINMAP user's manual, 2005). SINMAP is a raster based slope stability predictive tool based on coupled hydrological-infinite slope stability model. This approach applies to shallow translational landsliding phenomena controlled by shallow ground water convergence. The input data required for this model are (1) inventory of past landslides in a point vector format, (2) Digital Elevation Model (DEM) of the study area, (3) geotechnical data such as soils strength properties, thickness of soil above the failure plane, and (4) hydrological data such as soil hydraulic conductivity and the rainfall. Because the geotechnical data and hydrological data are highly variable in both space and time, the method does not require numerically precise input and accepts ranges of values that represent this uncertainly. The major output of this model is the stability index grid theme, which can be used as a landslide susceptibility map. The results also provided slope area plots and statistical summary for each calibration region in the study area facilitating the data interpretation. The landslide susceptibility map which is developed in this study is also compared with the results from the Analytic Hierarchy Process (AHP) method and aerial photo interpretation.

Keywords

Shallow landslide • Susceptibility mapping • GIS • SINMAP

C. Wang (✉) • H. Marui • N. Watanabe
Research Institute for Natural Hazards and Disaster Recovery, Niigata University, 8050 Ikarashi-Nincho, Nishi-ku, Niigata 950-2181, Japan
e-mail: wangcx@gs.niigata-u.ac.jp; maruihi@cc.niigata-u.ac.jp; jibanken@cc.niigata-u.ac.jp

S.M. Arbanas
Faculty of Mining, Geology and Petroleum Engineering, University of Zagreb, Pierottijeva 6, Zagreb, Croatia
e-mail: smihalic@rgn.hr

G. Furuya
Toyama Prefectural University, 5180 Kurokawa, Imizu-shi, Toyama 939-0398, Japan
e-mail: gfuruya@pu-toyama.ac.jp

Introduction

The City of Zagreb is located in northwest Croatia in the western part of the Pannonian Basin. The urbanized area is located below the forest region of Mt. Medvednica to the north and extends to the flood plain of the Sava River in the south. Approximately 40 % of the urban area is located in hilly areas in which landslides are the main geological hazard. Landslides in the hilly area of Zagreb are mostly small and shallow movements of superficial deposits along contacts

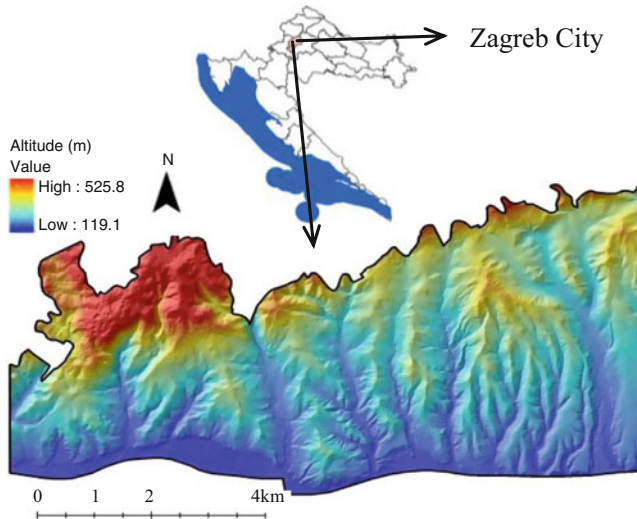


Fig. 1 Location and DEM of the study area

with fresh deposits of soil (Mihalić and Arbanas 2013). Despite this, landslides cause significant economic losses by damaging houses and the urban infrastructure.

The hilly area of Mt. Medvednica, which covers about 180 km², is the pilot area of Japanese-Croatian scientific joint-research project ‘Risk Identification and Land-Use Planning for Disaster Mitigation of Landslides and Floods in Croatia’. The study area which is approximately 45 km² is part of the hilly area of Mt. Medvednica. Figure 1 shows the digital elevation model of the study area.

The most frequent triggering factors of landslides are rainfall. The objectives of the study are to map the shallow landslide susceptibility using the SINMAP model considering three different precipitation scenarios and to compare landslide susceptibility maps generated by this study with the results by Analytical Hierarchy Process (AHP) method and aerial photo interpretation.

The Infinite Slope Stability Model SINMAP

The SINMAP (Stability INDEX MAPping) methodology is based upon the infinite slope stability model that balances the destabilizing components of gravity and the restoring components of friction and cohesion on a failure plane parallel to the ground surface with edge effects neglected. The details of the SINMAP model are available in Pack et al. (1998, 2005). The summary of the SINMAP modeling approach is provided in the following section.

The SINMAP developed by Pack et al. (1998) is based on a combination of an infinite slope stability model and a hydrological model used to define a stability index (SI) (1), which is defined as the probability of a stable slope, assuming a

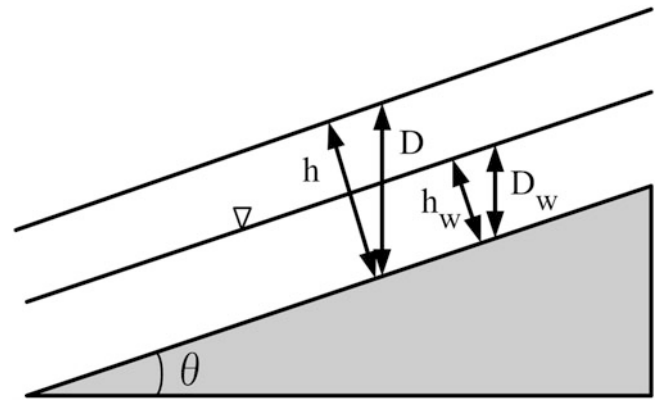


Fig. 2 Infinite slope stability model schematic

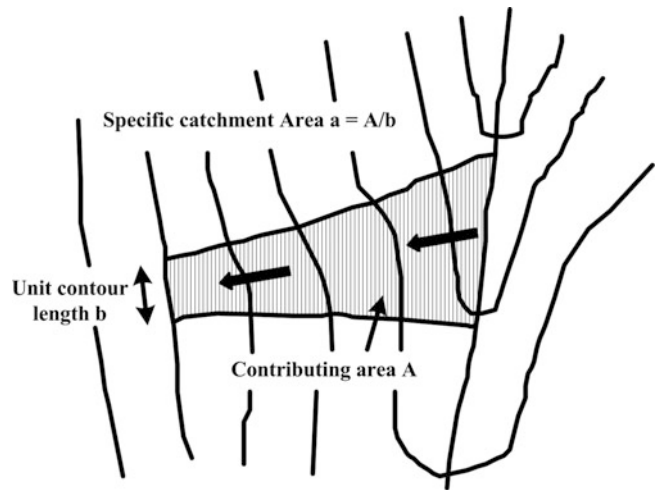


Fig. 3 Definition of specific catchment area

uniform distribution of the parameters on the uncertainty margins; this index ranges from 0 (unstable) to 1 (stable).

$$FS = \frac{C + \cos \theta [1 - \min(\frac{R a}{T \sin \theta}, 1)] r \tan \phi}{\sin \theta} \quad (1)$$

where, $C = (C_r + C_s)/(h\rho_s g)$ is the combined cohesion of roots and soil made dimensionless relative to the perpendicular soil thickness. $h = D \cos \theta$ is soil thickness, perpendicular to the slope. Figure 2 illustrates the geometry. $r = \rho_w/\rho_s$ is the water to soil density ratio. θ is the angle of the slope ($^\circ$), and ϕ is the angle of internal friction ($^\circ$). The relative wetness which is expressed as (2) is incorporated into SINMAP.

$$w = \min\left(\frac{R a}{T \sin \theta}, 1\right) \quad (2)$$

The ratio R/T is the ratio of the steady-state recharge (m/h) and the soil transmissivity (m²/h). The specific area of the basin, ‘a’, is defined by the surface area in relation to the contour length of the unit (m²/m) (Fig. 3). A value of 1

Table 1 SINMAP stability index (SI) classification

| Stability index values (SI) | Classification |
|-----------------------------|-------------------|
| $SI > 1.5$ | Stable |
| $1.5 > SI > 1.25$ | Moderately stable |
| $1.25 > SI > 1.0$ | Quasi-stable |
| $1.0 > SI > 0.5$ | Lower threshold |
| $0.5 > SI > 0.0$ | Upper threshold |
| $0.0 > SI$ | Defended |

indicates that any excess above this limit will be assigned to one surface flow that flows over the soil surface.

SINMAP is utilized in the study for modelling the rainfall-triggered shallow landslides at a regional scale and allows uncertainty in the three variables (C , $\tan\phi$, and R/T) through the specification of upper and lower boundaries. These boundaries define uniform probability distributions over which these parameters are assumed to vary at random. Denoting $R/T = x$, $\tan\phi = t$, and the uniform distributions with upper and lower boundaries as $C \sim U(C1, C2)$, $x \sim U(x1, x2)$, and $t \sim U(t1, t2)$, the probability is evaluated over the distributions of C , x , and t . The smallest C and t ($C1$ and $t1$) together with the largest x ($x2$) defines the worst-case (most conservative) scenario under the assumed uncertainty (variability) in the parameters. Areas under this worst-case scenario where FS is greater than 1 are, according to this model, unconditionally stable. For areas where the minimum factor of safety is less than 1, there is a probability of failure. This is a spatial probability due to the uncertainty (spatial variability) in C , $\tan\phi$ and T . In these regions with $FS_{min} < 1$, SI is defined as $SI = \text{Prob}(FS > 1)$. The best-case scenario is when $C = C2$, $x = x1$, and $t = t2$. In the case that $FS_{max} < 1$, then $SI = \text{Prob}(FS > 1) = 0$.

For assessing the probability of shallow landslides, Table 1 shows how broad stability classes are defined in terms of the stability index (SI).

Data Processing

In order to use the SINMAP methodology to establish a shallow landslide susceptibility map for the study area, several steps are accomplished starting from input data, which depends on the digital elevation model (DEM), landslide inventory and ending with the final result, which is a grid theme that divides the study area into several zones depending on the stability index. A topographical map of the study area is a 5-m DEM shown in Fig. 1. For calibration purposes, the landslide inventory map is needed. In this study, two landslide inventories are used. One is a geomorphological landslide inventory map compiled from field investigation by the

Table 2 Parameters values used for the study area

| Case | DC | | FA (°) | | R (mm/day) | T/R (m) | |
|------|-----|-----|--------|----|------------|---------|-------|
| | Lb | Ub | Lb | Ub | | Lb | Ub |
| 1 | 0.1 | 0.7 | 10 | 30 | 50 | 345 | 1,382 |
| 2 | 0.1 | 0.7 | 10 | 30 | 100 | 172 | 691 |
| 3 | 0.1 | 0.7 | 10 | 30 | 150 | 115 | 460 |

DC dimensionless cohesion, FA friction angle, Lb lower bound value, Ub upper bound value

Croatian Geological Survey, and another is obtained by interpreting aerial photographs from a report of the Japan-Croatia project. Nearly 52-year-long daily rainfall record from 1961 to 2012 was used to determine rainfall magnitude for the study area. The maximum precipitation is 95.8 mm/day in August 4, 1989, and the cumulative total in any 7-day period is 134 mm in November, 1962. Hydrological data are input into the model in the form of a wetness index (T/R) parameter. According to the SINMAP Manual (2005), the parameter (T/R) is considered as the length of hill slope required to develop saturation in the critical wet period. T is the transmissivity or the vertical integral of the hydraulic conductivity of soil zone and is determined by $T = (ks)h$, where ks is the hydraulic conductivity or the permeability of the soils and h is the thickness of the soil above the failure surface. Hydraulic conductivity of the weathered surface zone is $10^{-5} \sim 10^{-3}$ m/s. Cohesion index and the soils internal friction angle are the geotechnical data input into the model. Cohesion index is the relative contribution of soil and root cohesive forces, combined, to slope stability. In this study, the failure surface is assumed to be below the root zone. Therefore, cohesive strength of soil (C_s) only is considered. As the most frequent triggering factors of landslides are rainfall, three different rainfall recharge scenarios: 50, 100 and 150 mm/day are considered. Table 2 shows the parameters values used for the study area.

Results

Using the DEM and the input parameters, the SINMAP model was used to derive a stability index map. The SI distribution maps of the three different rainfall recharge scenarios are shown in Fig. 4a–c, respectively.

The percentage of area classified as unstable was about 48, 64, and 67 % for the three different rainfall rates, 50, 100 and 150 mm/day, respectively. Upper threshold covers 0.27, 0.35, and 0.45 %, respectively. Rainfall recharge decreases the safety factor over time. These maps are very useful for identifying where and when the critical slope with high landslide susceptibility will occur. Figure 5 shows the

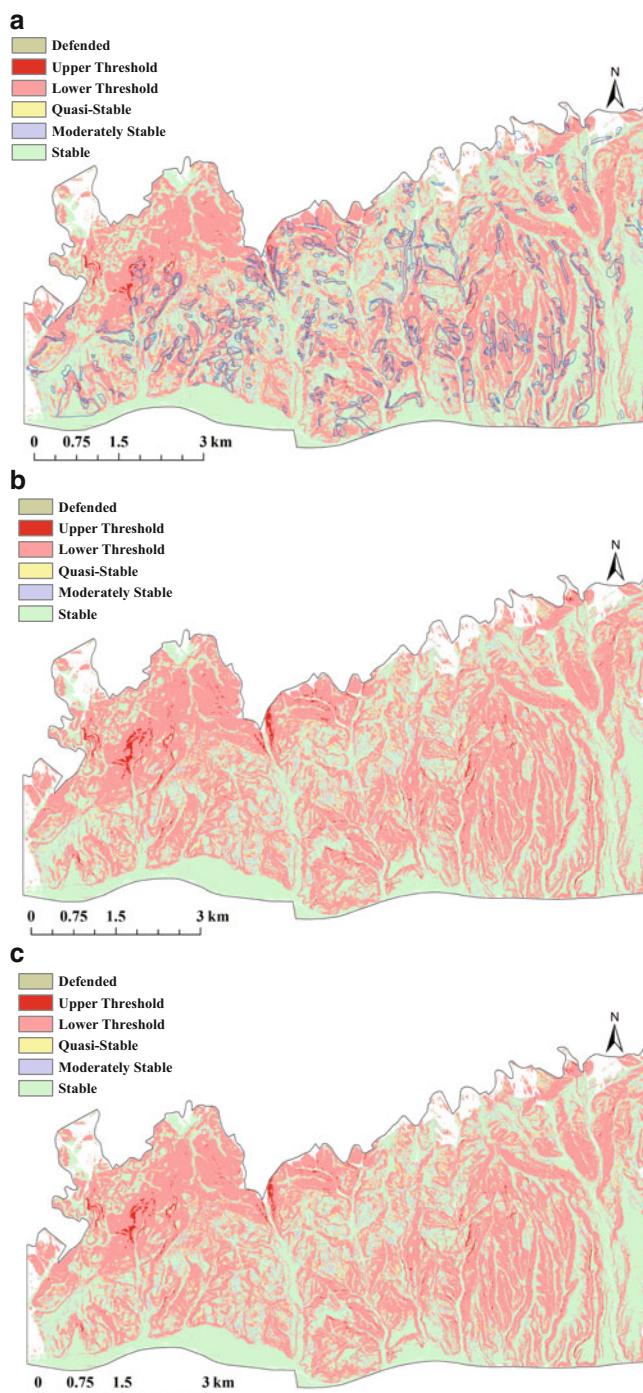


Fig. 4 Slope stability index with three different precipitation cases. (a) 50 mm/day, (b) 100 mm/day, (c) 150 mm/day

distribution of the 142 inventoried landslides made by Analytical Hierarchy Process (AHP) method and aerial photo interpretation (Hamasaki and Miyagi 2012). The result indicates that 101 landslides have been identified as the

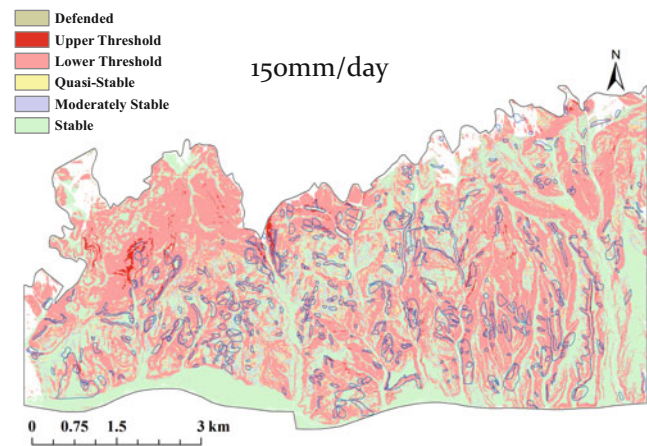


Fig. 5 The shallow landslide susceptibility map with the inventoried landslides made by AHP method and aerial photo interpretation

lower stability classes and only 17 landslides have been identified as the “stable” class.

Conclusions

The deterministic slope stability model SINMAP was used to assess the susceptibility of slopes to shallow landslides in the study area of the hilly area of Mt. Medvednica, under daily rainfall with three different scenarios. The percentage of area classified as unstable were about 48, 64, and 67 % for three different rainfall rates, 50, 100 and 150 mm/day respectively. From the results shown in Fig. 4, we can see that there is no big difference for the unstable areas between 100 and 150 mm/day.

The natural causative factors such as geology, thickness of soil layer, slope angle range, hydrology, and landforms are reasonably represented in the SINMAP model. Therefore, it is reasonable to assume that this model can be utilized as a tool for identification of landslide hazard zones in the study area. The preliminary results could be regarded as a good reference to make the hazard map and land use guideline of Japan-Croatia joint project.

However, in SINMAP model, the input data for the landslide inventory are point-shapefiles. Because a point cannot interpret the dangerous degree of landslide unit, in order to get more reasonable result, the landslide inventory should be polygon-shapefiles.

Acknowledgments This research was performed as a part of Japanese-Croatian joint research project on “Risk Identification and Land-Use Planning for Disaster Mitigation of Landslides and Floods in Croatia”, which was funded by JST-JICA Science and Technology Research Partnership for Sustainable Development Project (SATREPS).

References

- Hamasaki E, Miyagi T (2012) Report of Japanese-Croatian joint project “Risk identification and land-use planning for disaster mitigation of landslides and floods in Croatia” (In Japanese)
- Mihalić S, Arbanas Ž (2013) The Croatian–Japanese joint research project on landslides: activities and public benefits. In: Sassa K et al (eds): Landslides: global risk preparedness. Springer, Heidelberg, pp 335–351. doi: [10.1007/978-3-642-22087-6_24](https://doi.org/10.1007/978-3-642-22087-6_24)
- Pack RT, Tarboton DG, Goodwin CN (1998) A stability index approach to terrain stability hazard mapping. SINMAP user’s manual, p 68
- Pack RT, Tarboton DG, Goodwin CN, Prasad A (2005) A stability index approach to terrain stability hazard mapping. SINMAP 2 user’s manual, p 65



Hazardous Activation of Landslides Within Western Carpathian Region (Ukraine)

Olexandr Trofymchuk, Olexandr Kolodyazhnyy, and Evgeniy Yakovlev

Abstract

The Western Carpathian Region (Zakarpatska territory of Ukraine) occupies 2 % of Ukrainian territory but about 5 % of total quantity of landslides (22,000) are situated there. Specific spatial density of landslides is four times greater than the rest of the territory. Anomalous levels of the landslide activity within the Western Carpathian Region is the result of active interaction tectonic (high density of faults), hydrological (dense river net) and hydrometeorological (regional precipitations two times more) factors. During the last two to three decades regional landslide activation is connected with the influence of global climate changes (GCC). Main factors of the GCC influence on the additional landslide activation are the following:

- Increasing of the storm rainfall;
- Rising of the river water level during flooding.

Keywords

Geographical inform system • Landslide field • Longitudinal acceleration

Introduction

The Western Carpathian Region is affected by 1,100 landslides in its 8,000-km² territory. This averages about 0.15 landslides/1 km², which is the highest density of landslides within the Ukraine. The main type of landslide within the Western Carpathian Region is earth flow; these are mostly generated in the clay and semi-clay layers of Quaternary age. Total thickness of the deformed layers is 4–6 m. This type of landslide is more widespread. Landslides with glide mechanism of movement are mostly generated within steep upper zones of slopes. Complex

landslides are developed in the zones of crossing the river valleys and tectonic structures.

During three cycles (1998, 2001, 2010 years) of high precipitation, total number of active landslide was about 30 % of known landslides. This anomalously high percentage was connected with the complex influence of natural and technogenic factors:

- Crossing the slopes of dense river net;
- Seismological activity connected with six local zones of earthquakes;
- Active deforestation of slopes during last decades of twentieth century (from 60 % till 25 % and lesser);
- Increasing influence of global climate changes factors (heating, increasing of precipitations, flooding etc.).

Investigations of the Institute of Telecommunication and Global Information Space, National Academy of Sciences of Ukraine, and Ukrainian Land and Resources Management Centre have established the regional regularity in the new stage of natural and technogenic development of landslides (by means of remote data, geophysical engineering, geological and mathematical models).

O. Trofymchuk • E. Yakovlev (✉)

Institute of Telecommunication and Global Information Space of National Academy of Sciences of Ukraine, Chokolivskiy Blvd., 13, 03186 Kyiv, Ukraine
e-mail: yakovlev@niss.gov.ua

O. Kolodyazhnyy

Ukrainian Land and Resources Management Centre, Chokolivskiy Blvd., 13, 03186 Kyiv, Ukraine

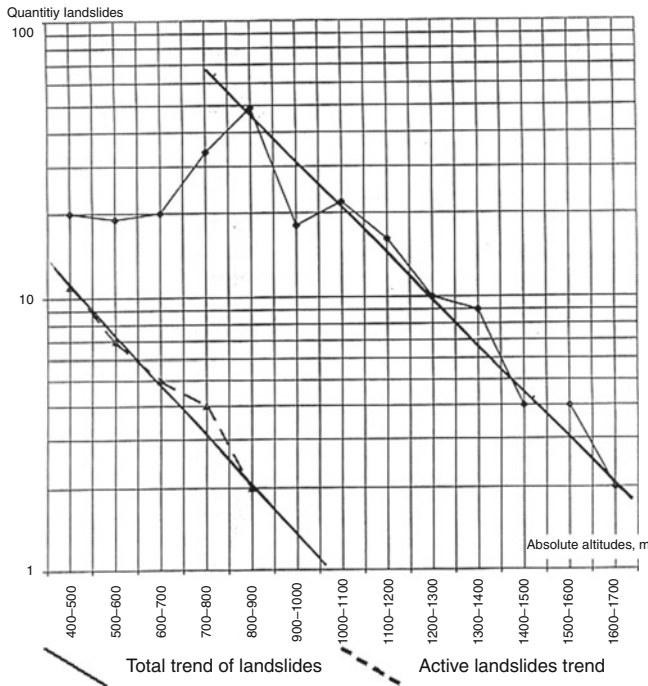


Fig. 1 Semilogarithmic function of the landslide distribution from the absolute altitudes within Western Carpathian Region

Landslide Distribution

Local clusters of landslides create the specific fields with the linear semi-logarithmic distribution in the elevation of the slopes within individual river basins (Fig. 1). In a semilogarithmic plot, Fig. 1 shows the distribution of landslides by elevation in the western Carpathians. The distribution of active landslides shows an inverse linear trend with decreasing numbers of active landslides from elevation 400 to 900 m above sea level. Similarly, the distribution of all landslides shows an inverse linear relationship between elevations 800 and 1,600 m. Total number of landslides drops off from the maximum, 50 at about 800 m to 20 at 600 m elevation with similar amounts at about 400 and 500 m elevation.

Analysis of semilogarithmic trend of landslide distribution shows the active connection between natural and technogenic factors of slope's surface transformations. Most active landslides are occurring within sites with low altitudes, where the road net density, index of deforestation and density of settlements have the highest values.

Due to the stable increase of the technogenic factors their influence on the number of active landslides is very big—about 15–20 % and more (Fig. 1).

Principle new and additional factors of landslide activation within Zakarpatsky region are increase of seismic movements after anomalously heavy rainfall and flooding.

Table 1 Time distribution of the earthquakes ($I \geq 5$ balls) and anomalous flooding within Zakarpatsky region

| Major floods (1882–2004 years) | Time interval between floods tfl, years | Earthquakes, years ($I \geq 5$) | Time interval between earthquakes tq, years |
|--------------------------------|---|-----------------------------------|---|
| 1882 | 0 | 1738 | 0 |
| 1887 | 5 | 1802 | 64 |
| 1902 | 15 | 1829 | 27 |
| 1912 | 10 | 1838 | 9 |
| 1925 | 13 | 1908 | 70 |
| 1941 | 16 | 1912 | 4 |
| 1947 | 6 | 1934 | 22 |
| 1970 | 23 | 1940 | 6 |
| 1978 | 8 | 1977 | 37 |
| 1980 | 2 | 1986 | 9 |
| 1998 | 18 | 1990 | 4 |
| 2001 | 3 | | |

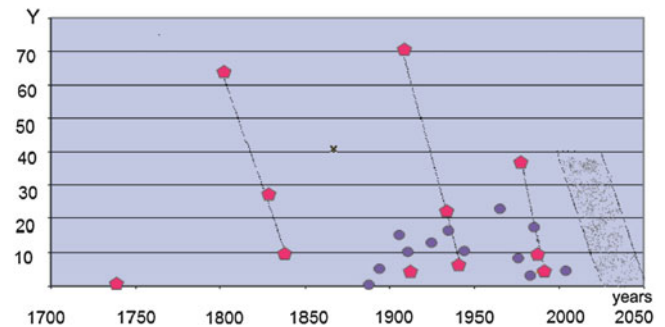


Fig. 2 Correlation between flooding and local earthquakes within Zakarpatsky region. Y—time interval between earthquakes and floods; \blacklozenge —events of earthquakes; \bullet —events of regional floodings; \square —predicted zone of activation of floods and earthquakes before landslides

We have established connection between anomalous rainfall, flooding and earthquakes during the last decades (Table 1, Fig. 2).

The intensity of earthquakes is about 5–6 but their frequency is growing and time interval between cycles of activations being shortened (Fig. 2).

Seismic shaking is effective in the case where the slope is oriented perpendicular to the seismic wave front (directions of steepest slope and wave propagation are parallel). Additional angle of steepness in such situation is about $\alpha_0 = \arctg (as/g)$, whereas—acceleration of longitudinal wave, m/s; g—acceleration of natural gravity.

Taking above mentioned into consideration the complex hazard mapping of landslides within the affected territories is the most effective method for reliable forecasting, preliminary elaboration of protective measurements and reducing of landslides danger on the regional and state levels.

Table 2 Engineering-seismogeophysical parameters of Carpathian region

| Administrative unit name | Zakarpattia | Ivano-Frankivsk | Lviv | Chernivtsi | All four units |
|--|-------------|-----------------|-------|------------|----------------|
| Unit area, 1,000 km ² | 12.8 | 13.9 | 21.8 | 8.1 | 56.6 |
| Flooded area, km ² | 0.001 | 0.014 | 0.25 | 0.15 | 0.415 |
| Flooded area % | 0.01 | 0.10 | 1.15 | 1.85 | |
| Landslide number | 1251 | 790 | 1347 | 1467 | 4855 |
| Landslide density, n/10 ³ km ² | 253.98 | 56.83 | 61.79 | 181.11 | 86 |
| Seismicity, magnitude | 8 | 8 | 8 | 7 | |
| Horizontal acceleration, g | 0.25 | 0.25 | 0.25 | 0.1 | 0.1–0.25 |
| Additional steepness α , degrees | 14 | 14 | 14 | 5 | 5–14 |

Data studies undertaken indicate that on the modern stage the displays of processes of change are localized on the slope's forms of the certain geological structure, the geohydrology and engineering-seismogeophysical regime (Table 2).

Analysis of Spatial Data

This paper explains the results of the development and testing of joint use of remote sensing (RS) technologies, modern and archive topographical maps, geographical information system (GIS) and simulation tools for investigation of land cover/use changes and contributing factors affecting the original slope stability, and prediction of landslide development for the Carpathian region (Ukraine). Within the Carpathian region great landslide activity occurred after big floods in 1998 and 2001. Advantages of joint use of remote sensing (RS) technologies, geographical information system (GIS) and simulation tools for investigation of complicated processes in environment, natural hazard management, etc. are presented for Carpathian region (Ukraine). The whole cycle from RS data processing, geospatial and multi-criteria analysis up to thematic spatial information publication are implemented. Space images and archived topographical maps are used for detection of changes in land cover/use and analysis of possible impact on landslide process development. The model was designed and implemented using spatial multi-criteria evaluation techniques in a GIS system.

In order to assess the landslide hazard the following contributing factors were used:

- Forest coverage presence or absence;
- Area height;
- Slope angle;
- Soil types;
- Rainfall distribution;
- Distance to settlements;
- Distance to roads, power lines, etc.;
- Distance to water objects (rivers, lakes, etc.).

The soil moisture is a factor also, but it is very spatially and temporally changeable. Aerial and space sensing can be useful, but integral indices based on permanent observations

are needed for taking into account as contributing factor. At the same time the changes of soil moisture can be considered within other factors under expert assessments use.

Archive map analysis identified the availability of Carpathian region paper maps for the time periods of 1930–1940, 1950–1960 and 1970. The maps of a test area with a large number of landslides were scanned and georeferenced using modern digital topographical map with the scale 1:200,000. Thematic layers of the forest-covered areas for 1944, 1961 and 1976 years were created. Modern forest maps showing conditions in years 1988 and 2000 based on Landsat imagery were obtained. Land cover change analysis maps were created and used in further research.

The next stages of multi-criteria analysis using GIS capacities were executed:

- Receiving and/or updating land cover, topography, etc. data layers—Digital Elevation Model (DEM), rivers, roads, settlements, soils, forest cover, etc.;
- Identification of heights and slope gradients, and creation of data layers of distances from existing landslides to rivers, settlements, roads;
- Laying out distances on intervals and ranking;
- Weight coefficient calculations and data layers matching.

The method of expert assessments (Saaty pairwise comparison) for identification of weight coefficients for landslide contributing factors was used. The elements of the comparison matrix were received by the alternative comparison with all other factors from the set. The matrix element is a number which presents a result of comparison relative to criteria. Relative weights were calculated as a result of comparison matrix processing.

Hazard Map

The landslide hazard map for Carpathian region was obtained (Fig. 3). Good enough correlation between predicted areas and distribution of existing landslides has to be noted. Landslide hazard areas without existing landslides need special attention for further investigation so possible protection actions can be planned.

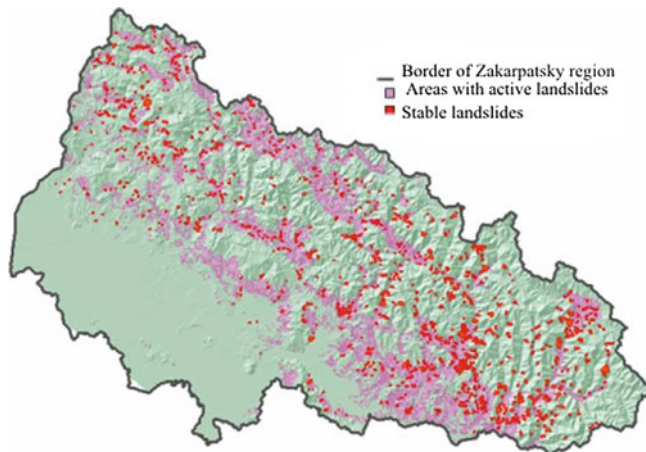


Fig. 3 Remote data about distribution of the landslides sites within Zakarpatsky region

Output data and work results were joined using Dynamic Atlas software (SKE Inc., Canada) that provide capacities for wide use and distribution.

In recent years on results researches of Institute of Telecommunication and Global Information Space of National Academy of Science, Institute of Geological Sciences of National Academy of Science, State Enterprise the “Research Institute of Building Constructions” and other establishments have shown that largely the following natural and technogenic processes are influencing the dynamics of landslide generation:

- Regional flooding of landscapes as a result of practically complete damming of the river network (a cascade of storage pools, many levees), decline of natural drainage on 70–80 % of hillsides and rising of groundwater table;
- Global changes of climate with the increase of precipitation, temperatures, that assists the increase of water saturation of overhead zone of slopes, decline of their strength;
- Global and regional activation of seismicity;
- Increasing technogenic transformations of slope forms within the territories of industrial-municipal agglomeration, mine destroyed territories, spreading of road network.

Monitoring, Prediction and Warning of Landslides



Introduction: Monitoring, Prediction and Warning of Landslides

Željko Arbanas, Teuku Faisal Fathani, Ziaoddin Shoaie, Byung-Gon Chae, and Paolo Tommasi

Abstract

The WLF3 B5.Session Monitoring, prediction and warning of landslides, as a part of WLF3 session Group B. Sessions for Methods of Landslide Studies, gathers the main elements in the landslides risk reduction and landslides sustainable disaster management: monitoring, prediction and warning of landslides. Sixteen contributions from eleven countries around the world have been submitted and, after review process, accepted for publishing. The best practice techniques and experiences on monitoring, prediction and warning of landslides caused by different triggering factors are presented in this Session. In this introduction to the WLF3 B5 Session Monitoring, prediction and warning of landslides, a short summary of each of the accepted papers is presented divided regarding to their general topics.

Keywords

Landslides • Monitoring • Equipment • Measurement • Prediction • Early warning system

Introduction

The WLF3 B5 Session Monitoring, prediction and warning of landslides, as a part of Group B Sessions for Methods of Landslide Studies, gathers the main elements in the landslides risk reduction and landslides sustainable

disaster management: monitoring, prediction and warning of landslides.

In landslides risk reduction and sustainable disaster management, the main roles have three closely connected elements: monitoring, prediction and warning of landslides. The monitoring of existing landslides, as well as locations susceptible to possible landsliding, using different techniques to produce the basic data for landslide prediction. Predictions of landslide occurrences should be based on a deep understanding of all processes which lead to slope failures in soil and rock mass slopes and their relationships with available measured monitoring data. Early warning systems, based on landslide monitoring results and landslide prediction, are the most economical landslide risk reduction measure. In this Session, the states of the art, best practice techniques and overall experiences in monitoring, prediction and warning of landslides caused by different triggering factors in different parts of the world are presented.

Sixteen contributions from eleven countries (Brazil, China, Croatia, Hong Kong, India, Indonesia, Italy, Korea, Malaysia, Slovenia and United Kingdom) have been submitted and, after review process, accepted for publishing in this

Ž. Arbanas (✉)

Faculty of Civil Engineering, University of Rijeka, Rijeka 51000, Croatia

e-mail: zeljko.arbanas@gradri.uniri.hr

T.F. Fathani

Department of Civil and Environmental Engineering, Universitas Gadjah Mada, Yogyakarta 55281, Indonesia

Z. Shoaie

Department of International Scientific and Research Affairs, Agricultural Research and Education Organization (AREO), Tehran, Iran

B.-G. Chae

Geologic Hazards Department, Korea Institute of Geoscience and Mineral Resources, Daejeon 305-350, South Korea

P. Tommasi

Institute for Geoengineering and environmental geology, National Research Council, Rome 00184, Italy

session. These contributions can be divided in the following general topics:

- Technological developments;
- Monitoring of landslides;
- Early warning systems based on measurements of landslide displacements and soil properties;
- Early warning systems based on rainfall monitoring and hydrological models;
- Warning and emergency management.

In this introduction to the WLF3 B5 Session Monitoring, prediction and warning of landslides, a short summary of each of the accepted papers is presented within previously defined general topics.

Technological Developments

Eyo et al. (2014) in their paper entitled “Application of low-cost tools and techniques for landslide monitoring” propose a low-cost landslide monitoring system using the Reverse Real-Time Kinematic (RRTK) technique. This is a server-based processing technique, which utilizes two-way communication channels for computation and the transmission of the user’s accurate position. The basic infrastructure requirements for RRTK for a low-cost landslide monitoring application are described. In order to implement the proposed RRTK algorithm, real-time data of raw Global Positioning System (GPS) data of both the reference and rover stations are streamed to the control center. A high pass filtering technique was employed to detect outliers in the observations and the autocorrelation of GPS time series was investigated to validate the presence of white and colored noises in the GPS observations. The proposed new monitoring technique using RRTK principles and server-based processing methods was successfully tested using data from test sites located at the Universiti Teknologi Malaysia.

Segalini et al. (2014) report on the efficiency of a novel inclinometer type in the paper “Automated inclinometer monitoring based on micro electro-mechanical system technology: applications and verification”. The new device, called Modular Underground Monitoring System (MUMS) is intended to be applied for natural and artificial slope deformation monitoring, and landslide dynamics control, assessment and forecasting. The paper compares the classic inclinometer devices and the new MUMS device, which can also be equipped with other electronic sensors. The paper also describes successful application of MUMS at three landslides in Italy: the Tiedoli Landslide, the Roccamurata Landslide and the Boschetto Landslide.

Wang et al. (2014) in their paper “Energy demodulation-based all-fiber warning system for landslides” present a new landslide warning technology. The system can measure the signal of energy change in the fiber caused by micro bending

or breakage associated with the displacement of landslides, and sends alarms at once when the signal intensity in the fiber weakens to the threshold. In the paper, this energy demodulation-based all-fiber warning system is described in detail. Compared with conventional monitoring technologies, this technology has many unique advantages, such as a graded alarm system, real-time response, remote monitoring and low cost. At the present time this system is used in landslide warning in China and a successful application of the system at the Gaoqin Landslide is described in the paper.

Zhu et al. (2014) describe a landslide monitoring technique using distributed fiber-optic sensing technologies. The advances in distributed fiber optic sensing (DFOS) technologies enable automatic, remote and long-distance slope monitoring and early-warning of potential geological disasters. Compared with conventional geotechnical sensors and instrumentation, the fiber optic sensors have a number of advantages such as high accuracy and repeatability, better durability and enhanced integration capability. In their paper “Laboratory studies on slope stability monitoring using distributed fiber-optic sensing technologies” Zhu et al. (2014) present the quasi-distributed Fiber Bragg Grating (FBG) and fully-distributed Brillouin Optical Time-Domain Analysis (BOTDA) sensing technologies for monitoring of slope stability problems in laboratory model tests. The reliability of the DFOS-based slope monitoring systems has been verified through analyses of the strain monitoring results.

Monitoring of Landslides

Arbanas et al. (2014) in the paper entitled “A landslide monitoring and early warning system using integration of GPS, TPS and conventional geotechnical monitoring methods” present an advanced comprehensive monitoring system designed and used on the Grohovo Landslide in Croatia. The landslide monitoring results should provide a basis for development and validation of landslide numerical modelling and adequate hazard management. Equipment selection was based on scientific requirements and consideration of possible ranges of monitored values and sensor precision. Use of different geodetic and geotechnical sensors, in combination with hydrological monitoring equipment which should measure data on precipitation and pore pressures in the landslide profile, allows reconstruction of relationships between rainfall, groundwater level and consequent landslide behavior as a base for establishing an early warning system. The most important step in establishing an early warning system was linking sensor measurements and possible failure mechanisms with consequences that should follow the occurrence of sliding (landslide risk). This paper presents the main ideas and advances of the monitoring

equipment fusion as well as weaknesses of the applied monitoring system at the Grohovo Landslide.

Krkač et al. (2014) in their paper entitled “Review of monitoring parameters of the Kostanjek Landslide (Zagreb, Croatia)” present initial results obtained from sensors and instruments of an advanced comprehensive monitoring system installed on the Kostanjek Landslide in Croatia. External triggers at the Kostanjek Landslide are measured with rain gauges and accelerometers. Displacements at the surface are measured by 15 GNSS sensors and 9 extensometers, while subsurface displacement is measured by vertical extensometers and an inclinometer. Hydrological measurements consist of groundwater level measurements, discharge measurements, and chemical and isotope analysis. The paper describes landslide reactivation due to external triggers in the winter period of 2012/2013, when during the period from September 2012 to March 2013 the total cumulative precipitation was 793.7 mm and horizontal displacements were in the range of 9–20 cm. The installed monitoring sensor network will provide reliable data for the establishment of relations between landslide causal factors and landslide displacement rates aimed at establishing threshold values for early warning system at the Kostanjek Landslide.

Kumar et al. (2014) describe monitoring systems installed on two of the most critical landslides on one of the important highways in India, which connects the north western Himalayan state of Uttarakhand to the rest of the country. The entire Himalayan road network suffers extensive damage from a large number of landslides of different shapes and sizes. A large number of the landslides on each highway have occurred repeatedly during every year for many decades, causing extensive risk to life of commuters, loss of revenue from direct and indirect losses and hardship for the people, thus influencing the socio-economic conditions of the region. In the paper entitled “Monitoring of critical Himalayan landslides and design of preventive measures” the very simple monitoring systems installed at the Kaliasaur Landslide and the Patalganga Landslide consisting of specially designed grooved steel pedestals, a total station and a Differential Global Positioning System (DGPS) are presented. The results of monitoring will encourage utilizing the same system for other Himalayan landslides of a recurring nature instead of investing in heavy-duty, costly and sophisticated monitoring instrumentation.

Early Warning Systems Based on Measurements of Landslides Displacements and Soil Properties

Chae et al. (2014) in their paper “Suggestion of a landslide early warning method using a gradient of volumetric water content” presents the study of a real-time landslide

monitoring system to observe physical property changes in soils in a slope during rainfall events. This monitoring system proposes the measurement of volumetric water content, which was compared with the results of laboratory flume tests to identify landslide indicators in the soils. The response of volumetric water content to rainfall events is more immediate than that of pore-water pressure, and volumetric water content attains its maximum value for some time before a slope failure. Based on laboratory results, it is possible to suggest a threshold value of the volumetric water content gradient demarcating the conditions for slope stability and slope failure. This threshold can thus serve as the basis for an early warning system for landslides considering both rainfall and soil properties. The proposal is successfully confirmed by landslide monitoring on the Deoksan test site in Korea.

Fathani et al. (2014) in their paper entitled “An adaptive and sustained landslide monitoring and early warning system” describe the technical system to support landslide disaster risk reduction consisting of several technical components such as instruments for a landslide early warning system (extensometers, tiltmeters, inclinometers, rain gauges, ultrasonic water level sensors, IP cameras) and supported by a smart-grid for landslide hazard communication, monitoring and early warning. Faculty of Engineering, Universitas Gadjah Mada Indonesia have developed simple and low-cost equipment for landslide monitoring and early warning since 2007. This real-time monitoring and early warning of landslides and debris floods has been implemented at eight geothermal areas in Sumatra, Java and Sulawesi Islands. The system is designed by using real-time landslide monitoring and early warning instruments, and also may involve human sensors—selected trained people in the local community, who have been dedicated in their commitment for doing ground checking and sending reports related to any observed warning signs of potential landslides.

The paper “Early warning and real-time slope monitoring systems in West and East Malaysia” prepared by Fung et al. (2014) presents the application of slope safety warning systems on two slopes along strategic roads in Malaysia: the first is located in Perak at the 46th km of the Simpang Pulai—Kuala Berang Highway and the second is an old fill embankment slope located at the 50.4th km of the Federal Road 500 between Penampang and Tambunan of Sabah. At the first location, monitoring and early warning were established by installation of a robotic total station, while at second location the automatic instruments include a rain gauge station, two sets of piezometers, tiltmeters, and two manual inclinometers to determine subsurface soil movements. Based on measured results (rainfall and movements), warning criteria were proposed. The data collected on site are managed by the same web-based data

management system. The system is accessible to authorized users as a web service through the client software.

Early Warning Systems Based on Rainfall Monitoring and Hydrological Models

Komac et al. (2014) in their paper “A national warning system for rainfall-induced landslides in Slovenia” present a result of the project for forecasting the possible occurrence of rainfall-induced landslides in Slovenia (Masprem Project). The landslide hazard forecasting and warning system is based on three pillars—the landslide susceptibility model, the precipitation forecast and the triggering values related to specific rocks/soils. Triggering values were derived using two separate approaches. In the first an overlay of 29 different engineering geological units (rock/soil types) and the data on maximum 24-h precipitation with the return period of 100 years (ten classes of intensities; class span was 30 mm) was performed and the number of landslides statistically compared against the size of these unique areas. The second approach is rainfall event oriented, in which analyses of the landslide triggering values were compared with the landslide occurrence and its duration. After calculation of the most plausible landslide hazard probability model, it has to be relayed to the end-users: decision makers or the general public via the internet. The quality of the forecasted landslide hazard probability prediction was tested only for the 8 days period prior to a major landslide event that occurred on 5th November 2012 and resulted in a landslide hazard probability model for the area of Slovenia.

In the paper “Latest developments of Hong Kong’s Landslip Warning System” Wong et al. (2014) present an overview of the major components of the Hong Kong Landslip Warning System and describe the technical basis of the System. The Geotechnical Engineering Office (GEO) has been operating a territory-wide Landslip Warning System, in conjunction with the Hong Kong Observatory (HKO), since 1977. The purpose is to alert the general public of possible landslide risks during periods of heavy rainfall. The GEO has been operating an extensive automatic raingauge network to provide real-time rainfall information for use in the Landslip Warning System. Computer programs are developed and implemented, together with other proprietary software packages, to acquire and analyze real-time rainfall data from the raingauges, display aspects of rainfall development and predict the number of landslides (based on 24-h recorded rainfall, 21-h recorded rainfall + 3-h forecasted rainfall, and 23-h recorded rainfall + 1-h forecasted rainfall respectively) using a rainfall-landslide correlation model. A revamped project of the GEO Raingauge System is in progress to further improve the system performance and reliability in order to better support decision-making on the

issuing of Landslip Warnings. The probabilistic-based rainfall-landslide correlation model for man-made slopes, established on the basis of the most recent landslide and rainfall data, is being used in the current Landslip Warning algorithm.

Yang et al. (2014) in their paper “A multi-scaled early warning method for rainfall-induced mountain hazards” propose a multi-scale, real-time early warning method, which combines large-scale regional hazard maps as well as site-specific hazard site monitoring. The real-time early warning map for regional scale rainfall-induced mountain hazards was developed by considering the triggering factors of rainfall distribution in addition to pertinent environment factors. The probability-based prediction method of regional scale rainfall-induced mountain hazards was developed by combining the hazard zonation map with the probability of regional precipitation. The prediction model was established through the analysis of geological and hydrological factors of the specified area, combined with the analysis of mountain hazard occurrences and the corresponding regional precipitation data. A site-specific, real-time monitoring and early warning system was constructed for five mountain hazard sites, including three debris flow and two landslide zones along the Longmenshan fault in Dujiangyan and Pengzhou County, Chengdu City in China. A monitored artificial rainfall test was conducted on a natural slope and was used to identify the threshold value to elicit an early warning that provides guidance and an approximate time for evacuation and preparation for potential landslides by comparing monitored rainfall intensity and its duration.

Warning and Emergency Management

Dourado et al. (2014) present the use of RADAR imagery in supporting rescue and recovery actions for landslide and flood disasters in Rio de Janeiro State, Brazil. In the paper “RADAR images supporting rescue and recovery actions for landslide and flood disasters—a Rio de Janeiro State case study” the images from optical sensors are described as very useful tools for identifying areas that suffered some impact during catastrophic events. The main advantage of using RADAR images is the possibility of monitoring areas of interest, even when there is cloud cover or at night. From RADAR images, in the post-disaster period, it could be easy to identify areas that suffered some kind of landscape change (mass movements, floods, etc.). The flood monitoring is based on the Normalized Difference Sigma Naught Index (NDSI), which compares the surface roughness of the image before the flood (Master Image) with the roughness in the same surface in the new image acquired during the flood (Slave Image). To monitor landslides, the methods for analysis of the data are Coherent Change Detection (CCD) and

Polarimetric Interferometry (Pol-InSAR) to map areas where there are landslide-generated changes in the roughness of the surface terrain (scars of landslides). Differential Interferometry (DInSAR) is used to map areas where the movement was not enough to significantly alter the landscape. If the system runs as planned, in an integrated way with the Civil Defense, it will become a very useful tool in rescue actions immediately after the disaster and as a tool in post-disaster planning.

Marino et al. (2014) in their paper “Geotechnologies for supporting regular surveys and catastrophic events of Rio de Janeiro Geological Survey—A case study” present a data management system related to the geological risk in the Rio de Janeiro State, Brazil, developed to support field teams and bring more practicality and organization during field assessment activities. The proposed methods combine a Geographic Information System (GIS), telecommunications networks and mobile devices to enhance the process from data acquisition by field teams, to organization and presentation for remote coordinators. The system consists of the assemblage of a georeferenced database to organize field-collected data related to mass movement assessments. The GIS VICON/SAGA—Vigilance and Control was designated to support the database. It provides interfaces for data collection, querying, filtering, report and map generation. The database was structured to store the event location, measure susceptible or affected areas, retrieve information such as the number of people affected or killed, and buildings affected or destroyed by mass movements. The GIS brings two specific interfaces for data input: from PC, using web browsers or from the field, using mobile devices, on an Android OS application. For information retrieval, some interfaces were developed, such as a query system for alphanumeric-tabular reports and others for spatial query procedures for map generation. Databases organize all information coming from multiple sources in real time and can be spatially visualized and analyzed using GIS. Each piece of information is grouped by type (evaluation of sliding, search and rescue) and standardized through predefined forms, providing filtered queries performed from search criteria. Reports and maps are generated for spatial analysis by any other analysis tool. As a final result, citizens and “Emergency Teams” consume information, logically organized and certified, from the manager. After compilation of all data, the manager in command can evaluate the situation and prioritize immediate response to the most dangerous cases in each situation and facilitate developing emergency actions.

Winter et al. (2014) present technical and perceptual evaluations of a novel form of landslide warning road signs known as ‘wig-wags’. The ‘wig-wag’ signs incorporate a standard rockfall/landslide red warning triangle, flashing

lights and a sub-plate that warns of ‘higher risk when lights flash’ (i.e. during periods of high rainfall) and they have been trialed at an important debris-flow site in Scotland. The paper “Evaluation of ‘wig-wag’ landslide warning signs” presents results of evaluation after a 2-year trial of such signs at the highly active A83 Rest and be Thankful site in Scotland. The following objectives are considered: technical evaluation to determine the efficacy of the wig-wag switch-off/switch-on protocol in terms of its alignment with actual events and also to assess the rainfall threshold used for the switch-on; and evaluation of drivers’ attitudes and behavioral responses (perceptual evaluation) to explore the attitudes held by local and non-local drivers towards landslide wig-wag signs on the A83 in terms of their perceived meaning and their impact on road safety. The evidence from both the technical and perceptual evaluations indicated that the wig-wag signs trial has a satisfactory outcome and that the flashing lights prompt generally desirable behaviors in the majority of cases.

Acknowledgments The conveners of the B5 Session for Methods of Landslide Studies: Monitoring, prediction and warning of landslides would like to thank all the reviewers who have reviewed the papers submitted to this Session. The papers in the Session are significantly improved through mindful editing conducted by Eileen McSaveney and Mauri McSaveney. Their editorial work is highly appreciated.

References

- Arbanas Ž, Sassa K, Nagai O, Jagodnik V, Vivoda M, Dugonjić Jovančević S, Peranić J, Ljutić K (2014) A landslide monitoring and early warning system using integration of GPS, TPS and conventional geotechnical monitoring methods. In: K. Sassa et al. (eds.), *Landslide Science for a Safer Geoenvironment*, Vol. 2, Springer International Publishing Switzerland
- Chae B-G, Choi J, Seo Y-S (2014) Suggestion of a landslide early warning method using a gradient of volumetric water content. In: K. Sassa et al. (eds.), *Landslide Science for a Safer Geoenvironment*, Vol. 2, Springer International Publishing Switzerland
- Dourado F, Freitas A, Fernandes N (2014) RADAR images supporting rescue and recovery actions for landslide and flood disasters: a Rio de Janeiro State case study. In: K. Sassa et al. (eds.), *Landslide Science for a Safer Geoenvironment*, Vol. 2, Springer International Publishing Switzerland
- Eyo E, Musa T, Omar K, Idris KM, Bayrak T, Onuigbo I (2014) Application of low-cost tools and techniques for landslide monitoring. In: K. Sassa et al. (eds.), *Landslide Science for a Safer Geoenvironment*, Vol. 2, Springer International Publishing Switzerland
- Fathani TF, Karnawati D, Wilopo W (2014) An adaptive and sustained landslide monitoring and early warning system. In: K. Sassa et al. (eds.), *Landslide Science for a Safer Geoenvironment*, Vol. 2, Springer International Publishing Switzerland
- Fung WHT, Kinsil RJ, Jamaludin S, Krishnan S (2014) Early warning and real-time slope monitoring systems in West and East Malaysia. In: K. Sassa et al. (eds.), *Landslide Science for a Safer Geoenvironment*, Vol. 2, Springer International Publishing Switzerland

- Komac M, Šinigoj J, Jemec Auflič M (2014) A national warning system for rainfall-induced landslides in Slovenia. In: K. Sassa et al. (eds.), *Landslide Science for a Safer Geoenvironment*, Vol. 2, Springer International Publishing Switzerland
- Krkač M, Mihalić Arbanas S, Arbanas Ž, Bernat S, Špehar K, Watanabe N, Nagai O, Sassa K, Marui H, Furuya G, Wang C, Rubinić J, Matsunami K (2014) Review of monitoring parameters of the Kostanjek Landslide (Zagreb, Croatia). In: K. Sassa et al. (eds.), *Landslide Science for a Safer Geoenvironment*, Vol. 2, Springer International Publishing Switzerland
- Kumar K, Prasad PS, Kathait A, Negi I (2014) Monitoring of critical Himalayan landslides and design of preventive measures. In: K. Sassa et al. (eds.), *Landslide Science for a Safer Geoenvironment*, Vol. 2, Springer International Publishing Switzerland
- Marino T, Dourado F, Amaral C, Xavier-da-Silva J (2014) Geotechnologies for surveys and catastrophic events of Rio de Janeiro Geological Survey: a case study. In: K. Sassa et al. (eds.), *Landslide Science for a Safer Geoenvironment*, Vol. 2, Springer International Publishing Switzerland
- Segalini A, Chiapponi L, Pastarini B, Carini C (2014) Automated inclinometer monitoring based on micro electro-mechanical system technology: applications and verification. In: K. Sassa et al. (eds.), *Landslide Science for a Safer Geoenvironment*, Vol. 2, Springer International Publishing Switzerland
- Wang X, Wei G, Shi B, Xu F, Tong H (2014) Energy demodulation-based all-fiber warning system for landslides. In: K. Sassa et al. (eds.), *Landslide Science for a Safer Geoenvironment*, Vol. 2, Springer International Publishing Switzerland
- Winter MG, Kinnear N, Shearer B, Lloyd L, Helman S (2014) Evaluation of 'wig-wag' landslide warning signs. In: K. Sassa et al. (eds.), *Landslide Science for a Safer Geoenvironment*, Vol. 2, Springer International Publishing Switzerland
- Wong ACW, Ting SM, Shiu YK, Ho KKS (2014) Latest developments of Hong Kong's Landslip Warning System. In: K. Sassa et al. (eds.), *Landslide Science for a Safer Geoenvironment*, Vol. 2, Springer International Publishing Switzerland
- Yang Z, Qiao J, Huang D, Tian H, Jiang Y, Shi L (2014) A multi-scaled early warning method for rainfall-induced mountain hazards. In: K. Sassa et al. (eds.), *Landslide Science for a Safer Geoenvironment*, Vol. 2, Springer International Publishing Switzerland
- Zhu H, Shi B, Yan J, Zhang C, Zhang J, Song Z (2014) Laboratory studies on slope stability monitoring using distributed fiber-optic sensing technologies. In: K. Sassa et al. (eds.), *Landslide Science for a Safer Geoenvironment*, Vol. 2, Springer International Publishing Switzerland



Suggestion of a Landslide Early Warning Method Using a Gradient of Volumetric Water Content

Byung-Gon Chae, Junghae Choi, and Yong-Seok Seo

Abstract

This study involved the installation of a real-time monitoring system to observe physical property changes in soils in a slope during rainfall events. This monitoring included the measurement of volumetric water content, which was compared with the results of laboratory flume tests to identify landslide indicators in the soils. The response of volumetric water content to rainfall events is more immediate than that of pore-water pressure, and volumetric water content retains its maximum value for some time before a slope failure. Therefore, an alternative method for landslide monitoring can be based on the observation of volumetric water content and its changes over a time at shallow soil depths. Although no landslide occurred, the field monitoring results showed a directly proportional relationship between the effective cumulative rainfall and the gradient of volumetric water content per unit time (t/t_{max}). This preliminary study thus related slope failure to the volumetric water content gradient as a function of rainfall. Laboratory results showed that a high amount of rainfall and a high gradient of volumetric water content can induce slope failure. Based on these results, it is possible to suggest a threshold value of the volumetric water content gradient demarcating the conditions for slope stability and slope failure. This threshold can thus serve as the basis of an early warning system for landslides considering both rainfall and soil properties.

Keywords

Landslides • Early warning • Monitoring • Volumetric water content

Introduction

An early warning system is necessary to enable the early detection of landslide indicators and timely evacuation of residents from landslide-prone areas. Early detection of

landslide indicators over large areas of natural terrain can be accomplished by monitoring rainfall and changes in the physical properties of soils and rocks in real time or near-real time (Montgomery et al. 2009). Most landslide warning methods use warning thresholds that consider rainfall and changes in soil physical properties; if rainfall or a relevant physical property of the soil exceeds a determined threshold, the potentially affected public is warned about the likelihood of landslides. However, these methods have been proposed as site-specific thresholds for regional or local areas due to unavailability of sufficient data on landslides and the factors influencing them on a global scale. There are two basic methods for determining landslide-triggering rainfall thresholds: empirical methods and physical methods. Empirical methods are based on statistical relationships between

B.-G. Chae (✉) • J. Choi
Geologic Hazards Department, Korea Institute of Geoscience and Mineral Resources, 124 Gwahang-no, Yuseong-gu, Daejeon 305-350, South Korea
e-mail: bgchae@kigam.re.kr; jhchoi@kigam.re.kr

Y.-S. Seo
Department of Earth and Environments, Chungbuk National University, Cheongju, Chungbuk Province 361-763, South Korea
e-mail: ysseo@cbu.ac.kr

historic rainfall parameters and landslide occurrence (Caine 1980; Brand et al. 1984; Larsen and Simon 1993, Marchi et al. 2002; Aleotti 2004; Guzzetti et al. 2007). Physical methods are based on numerical models considering physical relationships among rainfall, soil properties, rainfall seepage, volumetric water content, and pore pressure and their contributions to slope stability (Montgomery and Dietrich 1994; Iverson 2000; Crosta 1998; Crosta and Frattini 2003).

Considering the relationship between rainfall and landslides, the goal of the present study was to propose a basis for a landslide early warning method using real-time monitoring of rainfall and the gradient of volumetric water content in soils on natural terrain in Korea. For this study, a real-time monitoring system was installed to observe the changes in soil physical properties along the slopes in a valley during rainfall events. Among the parameters measured by the monitoring system, soil volumetric water content was selected for analysis to identify indicators of landslide events. The data collected in the field were compared with volumetric water content values acquired from laboratory flume tests to better understand the relationship between landslide triggering and changes in volumetric water content. Based on the preliminary results of this analysis, we propose a method for landslide early warning using a threshold of the volumetric water content gradient, a value which is dependent on both rainfall conditions and soil properties.

Landslide Monitoring System in the Study Area

The study area was located in Deoksan, Inje County, Gangwon Province, Korea (Fig. 1). The area is primarily of mountainous topography, occupying 80 % of the total area. The study area has relatively steep slope angles, of which 39.6 % are between 31° and 40° , representing the highest percentage of all measured slopes (Fig. 1). The lithology of the study area is composed of Pre-Cambrian granitic gneiss with a high density of foliations and shear fractures resulting from complex metamorphism. The area contains thick colluvium, averaging 4 m thick near the bottom of the slope and 0.5–2 m thick at the top and middle. The profile of the weathered soil layer on the mountain slope shows typical colluvial features composed of loosely compacted angular rock fragments with poor sorting and sandy silt particles. The soil is uniformly moist from top to bottom, implying a high permeability coefficient in the soil layer. The dominant size of boulders along the bed of the valley is 60×50 cm, resulting from the high density of shear fractures. This feature clearly indicates that the soil layer is composed of material from previous landslides, and

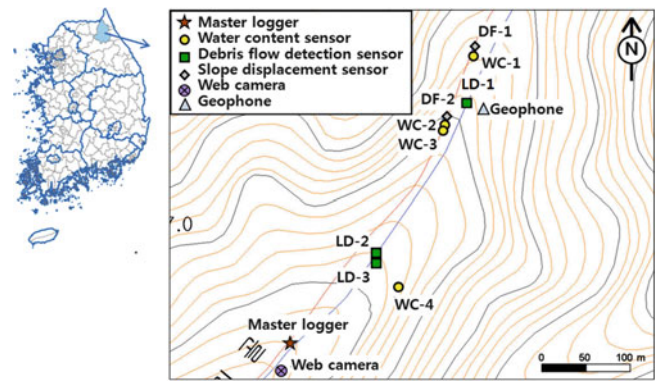


Fig. 1 Location of the rainfall monitoring system in the study area and the distribution of monitoring sensors in the monitoring valley

there have been many landslides and debris flows in the study area.

A landslide monitoring system was installed at the Deoksan test site. There were large debris flows caused by heavy rainfalls in 2006 and 2007, and because the site has high potential for future debris flows, this area was selected as a pilot monitoring site for this study. The monitoring system was composed of one master data logger, three sets of debris flow detection sensors, two sets of slope displacement sensors, four sets of water content sensors, one geophone, and one web camera (Fig. 1). The monitoring system was installed in mountainous areas and was therefore designed with an independent power supply system and a wireless communication network. Each sensor was connected to a radio frequency (RF) logger that was developed for wireless communication with the master data logger used in this study. The master data logger saved the transmitted data from each sensor through the RF logger and sent the data to a monitoring server in a remote area by TCP/IP communication using a code division multiple access (CDMA) modem.

Rainfall Infiltration Characteristics in the Study Area

In this study, four water content sensors (WC) were installed at the upper, middle, and lower parts of the valley at depths of 50 cm and 80 cm (Fig. 2). The sensors were installed in boreholes 10 cm in diameter. The initial volumetric water content was 14–15 % in January 2008, when the sensors were installed. A subset of the volumetric water content data measured since January 2008 is shown in Fig. 3, spanning from June to August in both 2008 and 2009. Changes in volumetric water content were closely matched by rainfall events. Volumetric water content increased rapidly immediately after the start of rainfall and decreased gradually after the rainfall event ceased.

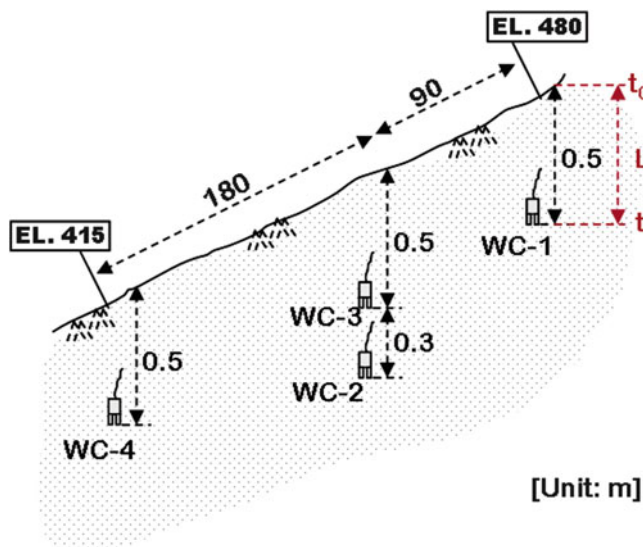


Fig. 2 Cross-section of the installation depths of volumetric water content sensors (WC) along the valley

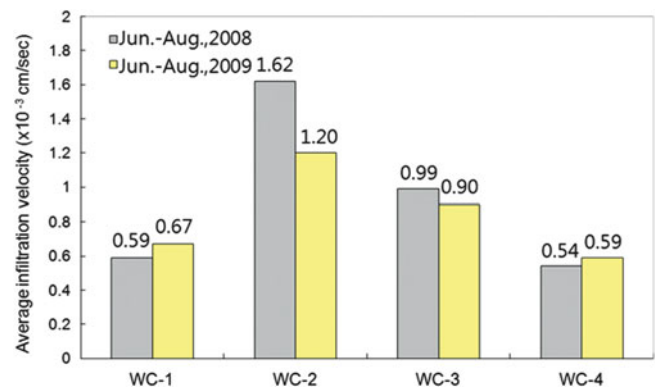


Fig. 4 Average infiltration velocity of rainfall detected by each measurement sensor

To understand the infiltration characteristics at the Deoksan test site, the average velocity of infiltration into the soil was calculated based on the volumetric water content. Infiltration velocity was calculated at each measurement position from (1):

$$V = \frac{L}{(t - t_0)} \quad (1)$$

where V is the infiltration velocity into subsurface, L is the vertical distance between the surface and the measurement position, t_0 is arrival time of rainfall at the surface, and t is the time of the maximum volumetric water content at the measurement position (Kim et al. 2009). Infiltration velocity is the rate of movement of water into the soil. Gardner (1958) explained infiltration velocity under full saturation of the ground surface in terms of the saturated hydraulic conductivity and porosity. Because rainfall does not change the ground condition from an unsaturated condition to a fully saturated condition at the beginning of rainfall, it is inappropriate to apply the saturated hydraulic condition in the field. Therefore, we calculated the infiltration velocity by measuring the wetting front behavior and the time difference of this behavior along the vertical direction in the soil. Infiltration velocity is reduced with increasing depth from the surface by the matric suction reduction effect (Rab et al. 1987).

Although the water content sensors were closely distributed, spaced 200–300 m apart, and the stratigraphy of the soil layer was nearly uniform, the average infiltration velocities were different at each sensor. The infiltration velocities of WC-1 and WC-4 were similar at the 50-cm depth, but WC-2 and WC-3 showed greater velocities than WC-1 and WC-4 (Fig. 4). This difference in infiltration velocities was likely related to topographic characteristics. WC-1 and WC-4 were installed on steep slopes, whereas WC-2 and WC-3 were located on relatively gentle slopes. Surface runoff of rainfall is more active on steep slopes than on gentle slopes; therefore, rainfall may infiltrate further into the soil on gentle slopes under

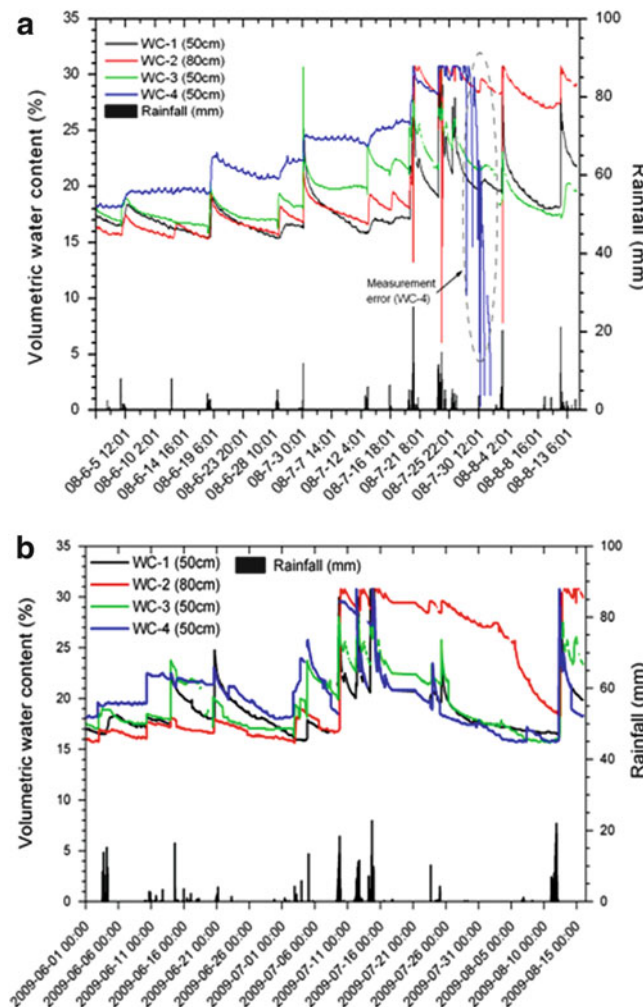


Fig. 3 Distribution of volumetric water content in the soil measured by the water content sensors in 2008 (a) and 2009 (b)

the same rainfall conditions. The higher infiltration velocity of rainfall at WC-2 and WC-3 was due to the more gentle slope angles there than at the locations of WC-1 and WC-4.

Suggestion of a Landslide Early Warning Method Based on Volumetric Water Content

Volumetric water content, which is closely related to the wetting front behavior of rainfall, is influenced by the porosity, effective porosity, and density of soil. The soil condition is gradually changed from an unsaturated condition to a saturated condition by the infiltration of rainfall. When the volumetric water content reaches the maximum value in the saturated condition, it maintains the maximum value uniformly with further rainfall within a similar range of porosity (Stephens 1995). It is possible to measure the volumetric water content at each soil depth and so facilitate more accurate recognition of changes in the degree of saturation with rainfall in the soil.

In this study, we analyzed the changing relationship between volumetric water content and rainfall based on field measurements at the Deoksan test site in an attempt to develop an alternative method for landslide early warning. We also performed laboratory flume tests with artificial rainfall to understand the changes in volumetric water content at the moment of landslide triggering by rainfall. The relationship between rainfall and volumetric water content was analyzed for sliding and stable conditions based on the results from both flume tests and field monitoring.

Relationship Between Water Content and Landslide Triggering in Soils in Laboratory Flume Tests

The soil samples for the laboratory flume tests were completely weathered granitic gneiss soils that were collected at the Deoksan test site. The flume was 2.2 m long and 30 cm wide and the slope angle was 30°. An artificial rainfall simulator was installed above the flume with a rainfall intensity controller (Fig. 5). In this study, three model slopes were designed using unsaturated granitic gneiss weathered soils with dry unit weights of 1.50 t/m³ and 1.33 t/m³, both with a thickness of 30 cm. Four volumetric water content sensors (ThetaProbe ML2x, Delta-T Devices Ltd.) and three pore-water pressure sensors (Model PL1M, Sensors, Inc.) were installed at the bottom of the flume to measure the water content in the slope.

As shown in Fig. 6, pore-water pressures gradually increased until slope failure and abruptly decreased immediately after slope failure. Therefore, it is difficult to identify slope failure in advance or to determine a baseline slope failure time using only pore-water pressure. However, it is possible to predict a slope failure time using the gradient of volumetric water content for two reasons: (1) the response of

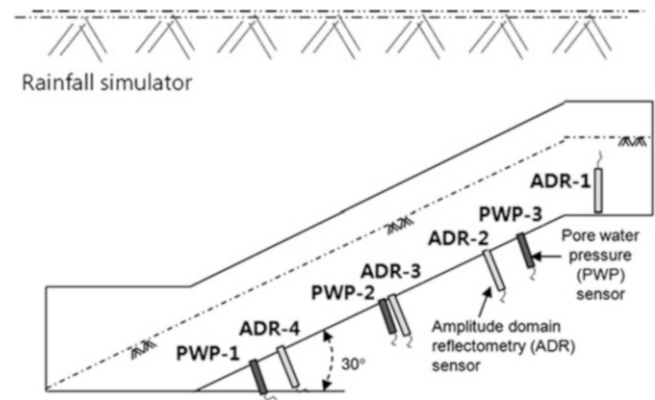


Fig. 5 Schematic diagram of the flume test equipment of the installed ADR sensors and pore-water pressure sensors

the volumetric water content is faster than that of pore-water pressure because it can be measured immediately after rainfall infiltration, even before the increase of pore-water pressure, and (2) volumetric water content maintains its maximum value for some time before slope failure (Sun et al. 1998). Volumetric water content reaches its maximum value when the soil becomes fully saturated by rainfall, resulting in slope failure due to decreases in both the shear strength and cohesion of the soil (Huang et al. 2009). Therefore, analyzing volumetric water content along with rainfall is an applicable method for predicting landslides in advance.

Suggestions for a Landslide Early Warning Method Based on a Change Ratio of Volumetric Water Content

Volumetric water content is the fraction of the total volume of soil that is occupied by water. Because it has a close relationship with soil porosity, volumetric water content is equivalent to the saturation degree in cases when the pores are fully filled with water (Fredlund and Rahardjo 1993). Volumetric water content is a relative value that differs from gravimetric water content, which measures the weights of soil and water. Therefore, it is reasonable to measure the volumetric water content and rainfall duration, rather than the gravimetric water content, for landslide prediction over a broad area experiencing different rainfall amounts.

The results of the laboratory flume tests were compared with field monitoring results in this study to analyze the relationship between slope failure and changes in volumetric water content caused by rainfall. We analyzed the gradient of volumetric water content from the starting time of increasing volumetric water content (t) to the time of maximum volumetric water content (t_{max}) for one rainfall event. Because t/t_{max} is a time ratio of volumetric water content change, it ranges from 0 to 1. Therefore, t/t_{max} is simply a dimensionless unit of time.

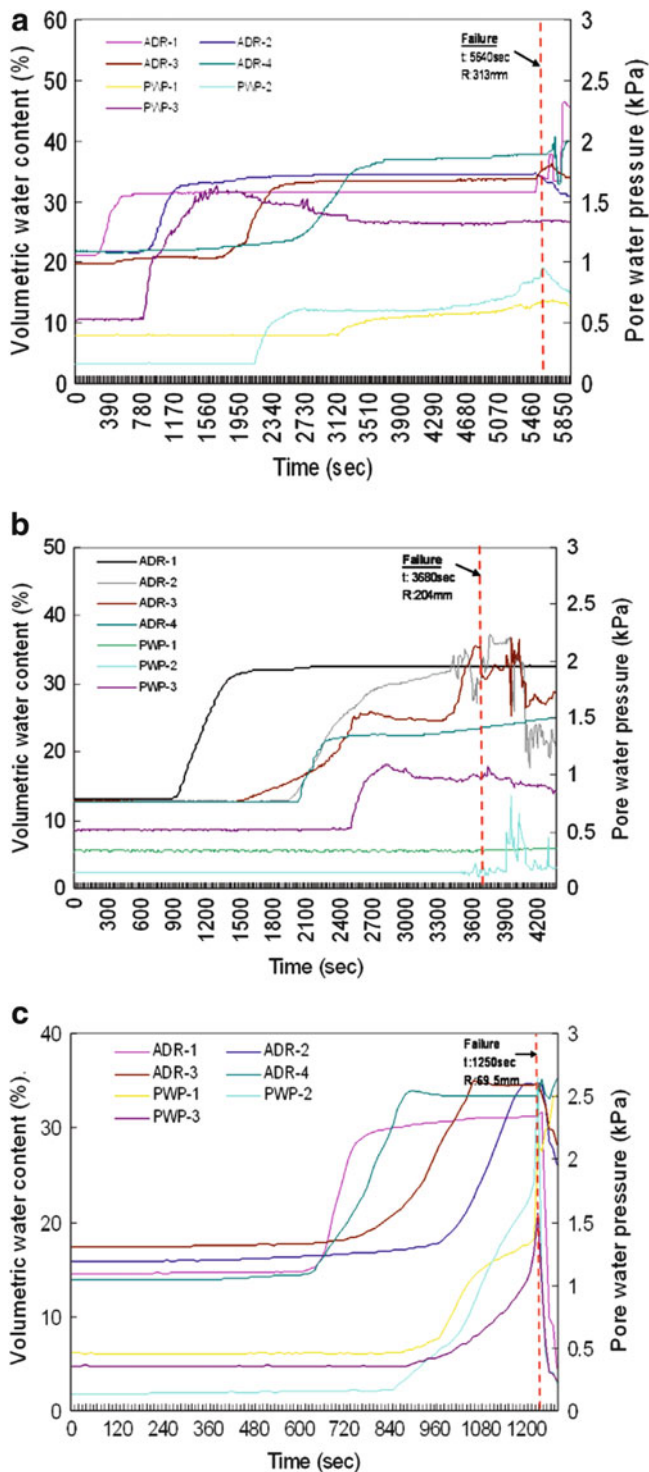


Fig. 6 Variations of volumetric water content and pore-water pressure under a rainfall intensity of 200 mm/h in the flume tests. *ADR* amplitude domain reflectometry sensor, *PWP* pore water pressure sensor. (a) Test 1, (b) Test 2, (c) Test 3

Figure 7 shows a comparison of the changes in volumetric water content gradient with rainfall amount based on the data from the field monitoring and the laboratory flume tests. The volumetric water content gradient was steep for low

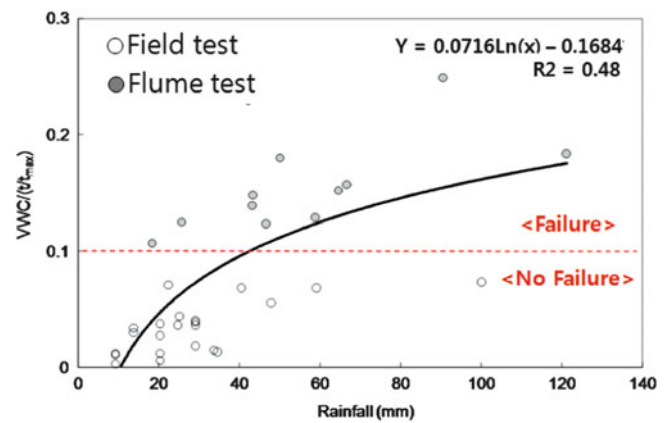


Fig. 7 Relationship between volumetric water content gradient and rainfall based on the data from field monitoring and laboratory flume tests

rainfall amounts and became gentle with an increase in rainfall amount. This phenomenon is related to the low initial volumetric water content of unsaturated soil, indicating a slow infiltration of rainfall under high volumetric water content conditions induced by the antecedent rainfall. In the case of the laboratory flume tests with slope failures, the gradient of volumetric water content is plotted in a range between 0.107 and 0.249. Conversely, field monitoring results without slope failure from June to August in both 2008 and 2009 show a range of volumetric water content gradients between 0.003 and 0.073. The results show that a large rainfall amount and a high gradient of volumetric water content contribute to slope failures.

Based on the above results of the preliminary study, we suggest a threshold for the volumetric water content gradient marking the point between slope failure and stability. This threshold could provide a baseline for the early warning of landslides that are triggered by rainfall. Comparison of the results for the volumetric water content gradient showed that a landslide tends to be triggered at a volumetric water content gradient of over 0.1 in the case of the granitic gneiss weathered soil of the Deoksan test site (Fig. 7). Therefore, the analysis of volumetric water content gradient could be chosen as a possible method for a landslide early warning by considering both rainfall and soil properties. However, it is necessary to determine a threshold volumetric water content gradient based on long-term field monitoring and various scenarios in laboratory tests because the gradient will differ depending on topography, geology, and soil properties experiencing the same rainfall conditions.

Conclusions

This study was performed to determine a method for landslide early warning by real-time monitoring of rainfall and the volumetric water content gradient in soil on natural terrain in Korea. According to the flume test

results, pore-water pressures gradually increased until slope failure and abruptly decreased immediately after slope failure. However, the volumetric water content maintained a uniform maximum value before slope failure, exhibiting a more rapid increase than that of the pore-water pressure. Therefore, it is easier to identify a slope failure in advance and to determine a baseline slope failure time using volumetric water content than pore-water pressure. This indicates that observation of volumetric water content may be a viable method for predicting landslides.

As a preliminary study, this work related slope failure to the volumetric water content gradient dependent on rainfall conditions. In case of the laboratory flume tests with slope failures, the volumetric water content gradient was distributed in the range of 0.107–0.249. The field monitoring results without slope failure showed a gradient range of volumetric water content between 0.003 and 0.073 at the study area. The results demonstrate that a large amount of rainfall and a high gradient of volumetric water content contribute to slope failures. Based on the above results, we suggest a threshold for volumetric water content gradient for the early warning of landslides that are triggered by rainfall. Our results showed that a landslide tends to be triggered at volumetric water content gradient over 0.1 in the case of the Deoksan test site. In future studies, other site-specific threshold volumetric water content gradients, which are dependent on topography, geology, and soil properties, can be determined by long-term field monitoring and laboratory tests.

Acknowledgments This research was supported by the Public Welfare & Safety Research Program through the National Research Foundation of Korea (NRF) funded by the Ministry of Science, ICT & Future Planning (Grant No. 2012M3A2A1050983).

References

- Aleotti P (2004) A warning system for rainfall-induced shallow failures. *Eng Geol* 73:247–268
- Brand EW, Premchitt J, Phillipson HB (1984) Relationship between rainfall and landslides in Hong Kong. In: *Proceedings of the IV international symposium on landslides*, Toronto, Canada, 19–21 September 1984, vol 1, pp 377–384
- Caine N (1980) The rainfall intensity duration control of shallow landslides and debris flows. *Geogr Ann* 62:23–27
- Crosta G (1998) Regionalization of rainfall thresholds: an aid to landslide hazard evaluation. *Environ Geol* 35:131–145
- Crosta GB, Frattini P (2003) Distributed modeling of shallow landslides triggered by intense rainfall. *Nat Hazards Earth Syst Sci* 3:81–93
- Fredlund DG, Rahardjo H (1993) *Soil mechanics for unsaturated soils*. Wiley, New York, 517 p
- Gardner WR (1958) Some steady state solutions of the unsaturated moisture flow equation with application to evaporation from a water table. *Soil Sci* 85:228–232
- Guzzetti F, Perucacci S, Rossi M, Stark CP (2007) The rainfall thresholds for the initiation of landslides in central and southern Europe. *Meteorol Atmos Phys* 98:239–267. doi:10.1007/s00703-007-0262-7
- Huang C-C, Ju Y-J, Hwu L-K, Lee J-L (2009) Internal soil moisture and piezometric responses to rainfall-induced shallow slope failures. *J Hydrol* 370:39–51
- Iverson RM (2000) Landslide triggering by rain infiltration. *Water Resour Res* 30:1897–1910
- Kim M-I, Chae B-G, Jeong G-C (2009) Correlation of unsaturated soil and dielectric property for monitoring of subsurface characteristics: development of unsaturated dielectric mixing models and its application. *Environ Geol* 57:49–58
- Larsen MC, Simon A (1993) A rainfall intensity-duration threshold relation for landslides in a humid-tropical environment, Puerto Rico. *Geogr Ann* 75:13–23
- Marchi L, Arattano M, Deganutti AM (2002) Ten years of debris-flow monitoring in Moscardo Torrent (Italian Alps). *Geomorphology* 46:1–17
- Montgomery DR, Dietrich WE (1994) A physically-based model for the topographic control on shallow landsliding. *Water Resour Res* 30:1153–1171
- Montgomery DR, Schmidt KM, Dietrich WE, McKean J (2009) Instrumental record of debris flow initiation during natural rainfall: implications for modeling slope stability. *J Geophys Res*. doi:10.1029/2008JF001078
- Rab MA, Willatt ST, Olsson KA (1987) Hydraulic properties of a duplex soil determined from in situ measurements. *Aust J Soil Res* 25(1):1–7
- Stephens DB (1995) *Vadose zone hydrology*. CRC, Boca Raton, FL, 347 p
- Sun HW, Wong HN, Ho KKS (1998) Analysis of infiltration in unsaturated ground. In: *Proceedings of the annual seminar on slope engineering in Hong Kong*, pp 101–109



RADAR Images Supporting Rescue and Recovery Actions for Landslide and Flood Disasters: A Rio de Janeiro State Case Study

Francisco Dourado, Aline Freitas, and Nelson Fernandes

Abstract

The use of RADAR images for monitoring natural disasters has two advantages compared to optical satellite images: RADAR images can be collected day or night, and regardless of weather. In major disasters related to landslides or floods, weather conditions are adverse and generally includes dense cloud cover that prevents use of optical satellite images. In a project approved between the Japan Aerospace Exploration Agency and the University of Rio de Janeiro State, there was an agreement to transfer up to twenty PALSAR2 images (with up to one meter spatial resolution) for monitoring natural disasters related to landslides or floods in Rio de Janeiro State. The procedure for monitoring is to collect ten images before the Brazilian rainy season (which in Rio de Janeiro starts in November-December and finishes around March-April. This is the opposite of Asia, which is in the dry season, so the satellite can be provided quickly in this period) to be used to obtain reference images for the follow methods: Coherent Change Detection (CCD) and Differential/Polarimetric Interferometry (DInSAR/Pol-InSAR). When a disaster with landslides or floods happens, it will be possible, to quickly and without any weather problems, detect if some land has slipped (mapping potential areas to slip), and if some areas are flooded. The main objective of this project is to subsidize the creation of maps for government agencies to use in planning strategies to minimize the hazard impacts and to assist governmental agencies at two stages: (1) during the disaster: helping rescuers and rescue efforts, indicating priority areas to be worked on and the numbers of people affected; and (2) after the disaster: mapping the extent of the affected areas, to assist in planning the recovery of these areas.

Keywords

RADAR • Remote sensing • NDSI • DInSAR • Pol-InSAR

F. Dourado (✉)

Applied Geology Department, University of Rio de Janeiro State, Rua São Francisco Xavier, 524 - Room 2019A, Rio de Janeiro, Brazil
e-mail: fdourado@uerj.br

A. Freitas

Geological Survey of Rio de Janeiro State, Rua Marechal Deodoro, 351, Niterói, Brazil
e-mail: afsilva@drm.rj.gov.br

N. Fernandes

Geography Department, CCMN, IGEO, Federal University of Rio de Janeiro, Bloco H, Room 8, Cidade Universitária, Rio de Janeiro, Brazil
e-mail: nelsonff@acd.ufrj.br

Introduction

Global climate change, on the local scale, affects areas in different ways. Sometimes climate shifts can be observed by the changes in land use, and other times, in variations in the regularity and magnitude of natural disasters caused by extreme weather events.

Climate changes can modify land use. Assuming an increase in the mean of Earth temperature, cooler regions could become fertile, but on the other hand, regions with high productivity could be affected by higher temperatures

Table 1 Latest large mass movement events and flooding in Brazil

| Site | State | Kind of event | Date | Victims | Affected |
|--------------------------------|-------|---------------|------------|---------|------------|
| Morro do Bumba, Niterói | RJ | MM | April/2010 | 166 | >1,000,000 |
| Região Serrana | RJ | MM and FL | Jan/2011 | 947 | >2,000,000 |
| Vale do Itajaí | SC | FL | Set/2011 | 1 | >50,000 |
| Rio Una | AL/PE | FL | June/2010 | 47 | >80,000 |
| Ilha Grande and Angra dos Reis | RJ | MM | Jan/2010 | 53 | >100,000 |
| Morretes/Antonina | PR | MM | Mar/2011 | 5 | >20,000 |
| Morro do Baú, Vale do Itajaí | SC | MM and FL | Nov/2008 | 135 | >10,000 |
| São Luiz do Paraitinga | SP | FL | Jan/2010 | 53 | >10,000 |

MM mass movement, *FL* flood

and have as a consequence changes in rain precipitation and evaporation rate, for example. The opposite, a decrease in the mean of Earth temperature, doesn't make cold areas any more productive, and in addition could decrease the productivity in highly productive areas, resulting in a much greater impact on global food supplies.

Climate changes are not limited to modifying the mean of Earth temperature; there can also be changes in the patterns of rainfall, which affects agricultural productivity, and can alter the distribution pattern, frequency and intensity of floods and landslides, among other effects.

Landslides and floods are hazards that cause death and destruction. In addition to destroying buildings and houses, they can interrupt communication and transport systems, and water supplies and sewage, drastically affecting the entire infrastructure of a region.

In Brazil there has been an increase in the number of deaths caused by natural disasters linked to extreme weather events. In recent years, thousands of people died and tens of thousands were left homeless, and millions were affected by natural disasters (Table 1). Among the natural disasters that occur in Brazil, landslides and floods are the biggest killers and generate more damage to the economy. Comparatively, the number of events in the 2000s was 2,400 % higher for mass movements and 400 % for flooding and waterlogging. The number of affected municipalities in 1991 and 2010 were 276 and 3,027 respectively. The identification of risk areas is the first step in managing these risks. The best and the most reliable methods for identifying areas of risk mapping is "in loco", with field work, on a scale where it is possible to identify points of susceptibility and their associated risks. Unfortunately this technique demands highly skilled professionals and consumes a large number of working hours, which dramatically increases the cost of mapping. Such resources and skilled professionals are not always available to local governments.

The use of indirect or remote methods generally reduces both the cost of identification and the time it takes to perform the mapping. However, the scale of work is still limited to the spatial resolution of the remote data obtained.

The images from optical sensors are very useful tools for identifying areas that suffered some impact during

catastrophic events. The high spatial resolution of the images currently available and supervised classification algorithms enable these regions to be identified quickly.

The main advantage of using images of RADAR is the possibility of monitoring areas of interest, even when there is cloud cover or at night. From RADAR images, in the post-disaster period, we can easily identify areas that suffered some kind of landscape change (mass movements, floods, etc.). In areas where the images identify small movements, but without a marked change in the landscape, we can also assume that these areas will be prone to later rapid movements that may cause damage and fatalities.

Study Area

The study area for this work is Rio de Janeiro State, located in south-eastern part of Brazil. Historically the main dangers that occur in the state are landslides and floods. The state is administratively divided into eight regions, illustrated in Fig. 1.

The main morphological units found in Rio de Janeiro State are (1) the lowlands, occurring mainly in the Metropolitan Region, Lagoons Region and North Region; and (2) the highly rugged terrain and great slopes found in the Mountain Region, Metropolitan Region and Ilha Grande Bay Region.

Rio de Janeiro State has a population nearly of 16 million people in an area of approximately 44,000 km², with an average population density about 366 inhabitants per km². The distribution of this population is uneven, and largely urban. The most densely populated administrative region is the Metropolitan Region with 2,208 inhabitants per km². The regions where more mass movements occur are the Metropolitan Region and Mountain Region (116 inhabitants per km²), while the administrative regions that have more floods are the Metropolitan Region and the Northern Region (87 inhabitants per km²) (IBGE 2013).

Comparatively, mass movements cause more deaths than flooding. Between 2010 and 2011, during the last three major events that occurred in the state of Rio de Janeiro,

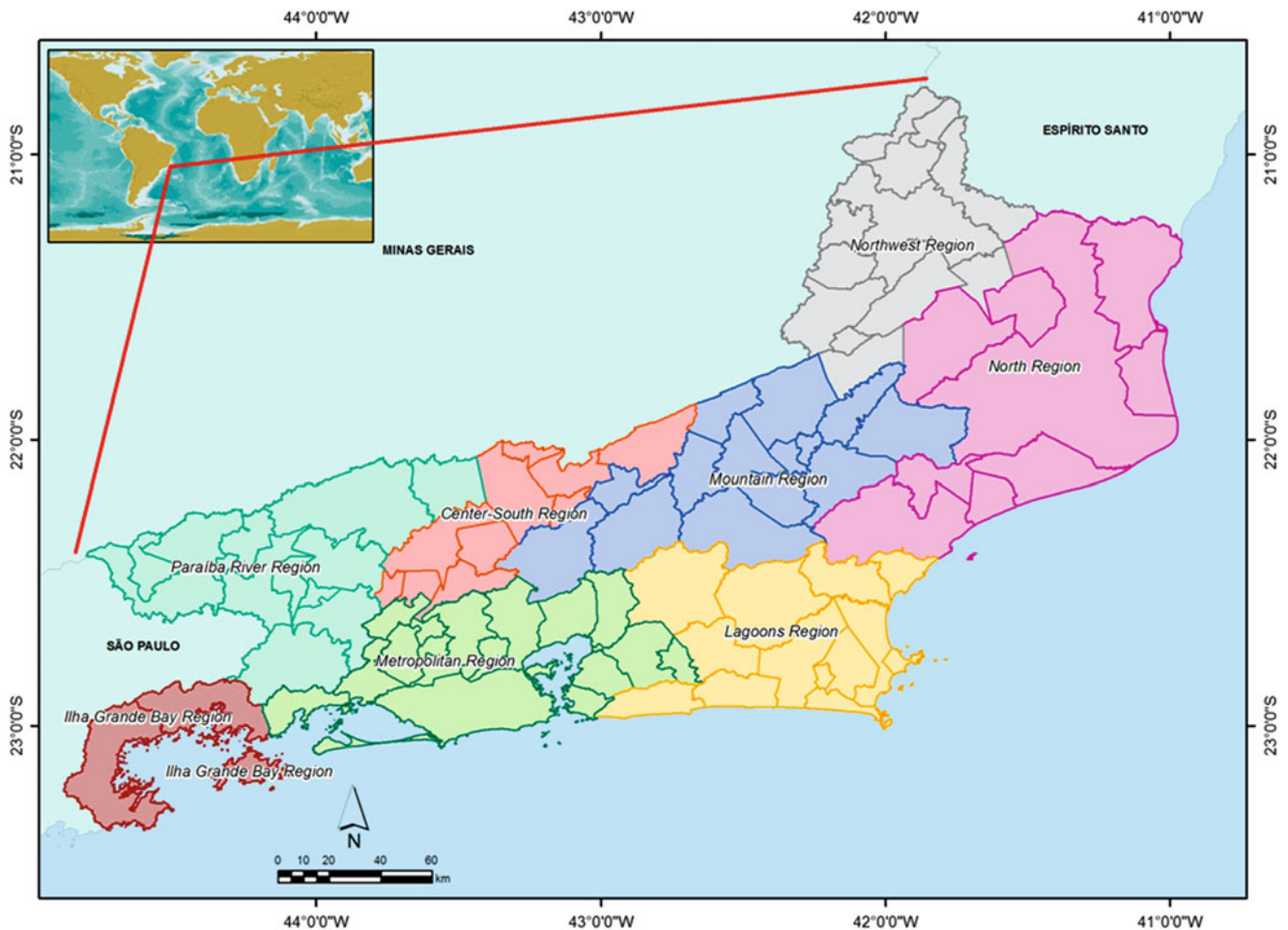


Fig. 1 Rio de Janeiro State: Ilha Grande Bay Region (red); Paraíba River Region (light green); Center-South Region (salmon); Metropolitan Region (green); Mountain Region (blue); Lagoons Region (orange); North Region (pink); Northwest Region (grey)

1,166 people were killed due to mass movements, and there were 7 deaths directly related to flooding.

Thus, even though hazards affect the entire state of Rio de Janeiro, the Metropolitan Region will be our main area of monitoring because of three key points: (1) the region has morphological features with large slopes, together with low-land areas almost at sea level; (2) the region has the highest population density of the state and; (3) it has records of the most recent recurring events. In addition, due to the morphological characteristics of the land, the Mountain Region will be monitored for landslides and the Northern Region for floods.

Objectives

The main objective of this work is to evaluate the efficiency of the use of images from Synthetic Aperture Radar to monitor areas susceptible to mass movements and floods in Rio de Janeiro State.

From these RADAR images, we will generate two types of maps that can be used by Civil Defense for two different purposes:

- Mapping areas where landslides have happened or that have been flooded—based on these maps it is possible to devise strategies and priorities for emergency actions. Integrating these data with population information, it will be possible to prioritize the areas to be served. And further, to quantify the number of occurrences in terms of the total area affected (in km^2 or m^2 , for example).
- Mapping areas that suffered some slight mass movement, but have not completed the process of slipping. These maps will indicate the extent of the affected areas, to assist in planning of recovery and indicating areas more likely to have continued slippage if the factors triggering the movement continue to act. In these cases, the triggering value that will start the next movement should be smaller than the trigger that caused the previous event, because the initial movement may have created new planes of discontinuity or increased the existing planes, raising landslide susceptibility in the area.

Methods

The area will be monitored for catastrophic flooding associated with extreme weather events that occur during the rainy season in Brazil (concentrated between the months of November to April). To determine the best acquisition period for reference images, we must remember that the dynamic changes in soil use in Brazil are very large. Thus, for comparison of conditions before and during the disaster, the ideal is that the images be acquired as late as possible before the rainy season. If we use an image from a period that is a long time before the catastrophic event, it can be misleading to compare anthropogenic changes in land use from features caused by the real floods. The best period for acquisition of reference images for extreme weather events of catastrophic landslides and flooding in Brazil is between the months of June and August, when rainfalls are lower. As mentioned, the period with the greatest potential for flooding occurs between November to April, but, of course, the exact date of the extreme catastrophic events could not be provided at the time of preparation of this proposal. The request for images of the events in emergencies will be made to the Japan Aerospace Exploration Agency (JAXA), according to when they occur and the technical availability of the satellite.

The monitoring of landslides and floods is done by using Synthetic Aperture Radar images (SAR) (Rott 2009). Mathematical processing is used to identify and map areas that suffered some kind of modification on its surface.

In this project we used PALSAR2 images in the L-Band (1–2 GHz/15–30 cm) onboard an ALOS2 platform. The sensor has six modes of acquiring data, with full polarization capability in some modes. The spatial resolution is between 1 and 100 m and the temporal resolution of up to 14 days. For disaster monitoring, the mode used is Ultra-Fine Mode with 3 m of spatial resolution and dual polarization (HH + HV or VV + VH) (Kankaku et al. 2009).

To monitor a flood disaster, the processing adopted is Normalized Difference Sigma Naught Index (NDSI) (Furuta et al. 2013). To monitor landslides, the methods for the analysis of the data will be Coherent Change Detection (CCD) and Polarimetric Interferometry (Pol-InSAR) to map scars of landslides (Furuta et al. 2013; Cigna et al. 2011). Differential Interferometry (DInSAR) will be used to map areas where the movement was not enough too significantly to change the landscape, but that generated a shift (Herrera et al. 2013; Cascini et al. 2010).

Discussion

Landslides and floods are the most important natural hazards occurring in Brazil. Hazards are a dangerous phenomena, substances, human activities or conditions that may cause

loss of life, injury or other health impacts, property damage, loss of livelihoods and services, social and economic disruption, or environmental damage (UNISDR 2009). Disasters need triggers to start the dangerous processes happening.

The trigger associated with floods is a large volume of rain that falls in a time less than the flow capacity of the river basin, thus the water level in the basin rises, flooding areas that are usually dry. Except in cases where they are started by earthquakes, the vast majority of landslides occur when soil moisture increases due to water infiltration, increasing the pore pressure and consequently decreasing cohesion, thus leading to rupture. This phenomenon occurs when there is excess water and is generally associated, as in the case of floods, with a large amount of rain in a concentrated period of time.

In both cases, the trigger of these hazards is heavy rainfall that is always associated with a cloud cover that prevents the use of optical satellite images or surveys using aerial photographs. Having a great advantage in the case of the monitoring of landslides and floods, the use of RADAR images does not depend on weather conditions. On the other hand, compared to optical images, currently RADAR images are at a disadvantage in terms of spatial resolution (size of the area that is represented in a pixel in the image) and time resolution (the time it takes for an area to be imaged from the same position configurations of the satellite).

The flood monitoring will be based on the Normalized Difference Sigma Naught Index (NDSI), which compares the surface roughness of the image before the flood (Master Image) with the roughness in the same surface in the new image acquired during the flood (Slave Image). The Master Image presents roughness compatible with the land use and surface coverage by varying the texture according to its classification. In the Slave Image, areas that are flooded show low backscattering due to the specular surface formed by the reflecting pool. The NDSI identifies areas where changes occurred in the backscattering. The greater the difference, the greater will be the value of NDSI.

This method has a weakness, that is the time taken to acquire the Slave Image. The sooner after the event the image is acquired, the better the accuracy of the results. The Slave Image should be collected while there are still bodies of water (for example pools, temporary lakes or lagoons, etc.) created by the flood, that cause the low backscattering. When the body of water disappears (after the finish of the flood), wet soil will still cause a decrease in the backscattering, but the values will not be as low as those recorded when there is a body of water. Thus, the accuracy of the method also decreases.

To monitor landslides, the methods for analysis of the data will be Coherent Change Detection (CCD) and Polarimetric Interferometry (Pol-InSAR) to map areas where there are landslide-generated changes in the roughness of the surface terrain (scars of landslides). Differential

Interferometry (DInSAR) is used to map areas where the movement was not enough to significantly alter the landscape, but that generated a shift sufficient to be measured by the method and that may indicate a potential area for new catastrophic movements.

As NDSI procedures, the CCD and the Pol-InSAR procedures require that two images be compared (Master Image and Slave Image) and from this comparison areas are identified that had suffered changes in their surfaces. Pol-InSAR identifies areas which had a change of position (horizontal or vertical shifts), through DInSAR it is possible to measure the position's variation.

Once calculated, variations in roughness enabled us to identify areas that have suffered landslides and divide them into two sets or classes: one group which show a high volume of material and large displacement and a second group that show a small movement, some centimeters, independent of volume. In the areas where the shift was large, landslides occurred. Areas where the shift was small (the movement wasn't completed) are those with a bigger predisposition for movement to occur next. In addition, in these areas, the trigger's value will be lower due to weakness planes created during these small movements.

Among the methods presented, the Pol-InSAR and DInSAR require more complex processing. There are no free programs for these procedures and the available software is very expensive.

Conclusions

Rio de Janeiro State has no system of emergency identification and mapping of large areas affected by landslides and floods. Currently, the mapping was done by emergency teams in relatively small areas and depends directly on aerial photographs, which in turn depend on favorable weather conditions to fly and on seat availability on the aircraft where priority is given to search and rescue of victims.

On the other hand, the mapping of large areas is possible using RADAR images that do not depend on weather conditions. Depending on the RADAR system, the time resolution can be some days. The use of an airborne platform (aircraft or Unmanned Aerial Vehicle/UVA) can reduce the time resolution to hours.

From the analysis of RADAR images it is possible to create maps of areas flooded or of landslide distribution, quantifying the number of occurrences and the total area affected. It is also possible to devise strategies and priorities for emergency response and build maps of the

areas most susceptible to landslides, assisting in the planning of recovery of these areas.

A disadvantage of the use of images from RADAR are (1) it is expensive; (2) the high cost of image processing software and; (3) the small community of experts in Brazil that know how to use this tool—which generates high costs for personnel. These three points make it difficult to popularize the use of this tool.

If the proposed system runs as planned, in an integrated way with the Civil Defense, it will become a very useful tool in rescue actions immediately after the disaster and as a tool in post-disaster planning.

Acknowledgments The authors thank Japan Aerospace Exploration Agency (JAXA) for having accepted the proposed work presented in 4th ALOS Research Announcement, their availability to collect images PALSAR2 and the resulting transfer. Also we thank Fundação Carlos Chagas Filho de Amparo à Pesquisa do Estado do Rio de Janeiro (FAPERJ), Coordenação de Aperfeiçoamento de Pessoal de Nível Superior (CAPES), Conselho Nacional de Desenvolvimento Científico e Tecnológico (CNPq) and Universidade do Estado do Rio de Janeiro (UERJ) for the resources received for the air tickets and stay at this forum.

References

- Cascini L, Fornaro G, Peduto D (2010) Advanced low- and full-resolution DInSAR map generation for slow-moving landslide analysis at different scales. *Eng Geol* 112:29–42
- Cigna F, Del Ventisette C, Liguori V, Casagli N (2011) Advanced radar-interpretation of InSAR time series for mapping and characterization of geological processes. *Nat Hazards Earth Syst Sci* 11:865–881
- Furuta R, Koizumi E, Chikahisa H, Kitayama N (2013) Combination use of ALOS PALSAR analytical data to landslides detection. <http://www.csr.ncu.edu.tw/08CSRWeb/ChinVer/C7Info/2010RSDMM/PPTpdf/5.pdf>. 10 July 2013
- Herrera G, Gutiérrez F, García-Davalillo JC, Guerrero J, Notti D, Galve JP, Fernandez-Merodo JA, Cooksley G (2013) Multi-sensor advanced DInSAR monitoring of very slow landslides: the Tena Valley case study (Central Spanish Pyrenees). *Remote Sens Environ* 128:31–43
- Instituto Brasileiro de Geografia e Estatística (IBGE) (2013) Banco de Dados Agregados. Sistema IBGE de Recuperação Automática—SIDRA. <http://www.sidra.ibge.gov.br>. 10 July 2013
- Kankaku Y, Osawa Y, Suzuki S, Watanabe T (2009) The overview of the L-band SAR Onboard ALOS-2. In: *Progress in electromagnetics research symposium proceedings*, 18–21 August, Moscow, Russia, pp 735–738
- Rott H (2009) Advances in interferometric synthetic aperture radar (InSAR) in earth system science. *Phys Geogr* 33(6):769–791
- UNISDR (2009) Terminology on disaster risk reduction. http://www.unisdr.org/files/7817_UNISDRTerminologyEnglish.pdf. 10 July 2013



Application of Low-Cost Tools and Techniques for Landslide Monitoring

Etim Eyo, Tajul Musa, Kamaludin Omar, Khairulnizam M. Idris, Temel Bayrak, and Ifeanyi Onuigbo

Abstract

This paper proposes a low-cost landslide monitoring system using the Reverse Real-Time Kinematic (RRTK) technique. The server-based processing technique, which utilizes the two-way communication channel for the computation and transmission of the user's accurate position, is discussed. The basic infrastructure requirements for RRTK in low-cost landslide monitoring application are described. In order to implement the proposed RRTK algorithm, real-time data streaming of raw Global Positioning System (GPS) data of both the reference and rover station(s) to the control centre, are performed. A high pass filtering technique was employed to detect outliers in the observations. Finally, the auto-correlation of GPS time series was investigated to validate the presence of white and coloured noises in the GPS observations.

Keywords

Landslide monitoring • Low-cost • GPS • Reverse • Real-time kinematic • Data streaming

E. Eyo (✉) • T. Musa • K. Omar
GNSS and Geodynamics Research Group, Department of Geomatic Engineering, Faculty of Geoinformation and Real Estate, Universiti Teknologi Malaysia, 81310 UTM Skudai, Johor Darul Ta'zim, Malaysia
e-mail: eeetim2@live.utm.my; tajulariffin@utm.my; kamaludinomar@utm.my

K.M. Idris
Photogrammetry and Laser Scanning Research Group, Department of Geomatic Engineering, Faculty of Geoinformation and Real Estate, Universiti Teknologi Malaysia, 81310 UTM Skudai, Johor Darul Ta'zim, Malaysia
e-mail: khairulnizami@utm.my

T. Bayrak
Department of Geomatics Engineering, Faculty of Engineering, Gümüşhane University, Gümüşhane, Turkey
e-mail: tbayrak@gumushane.edu.tr

I. Onuigbo
Department of Surveying and Geoinformatics, School of Environmental Technology, Federal University of Technology, Minna, Niger State, Nigeria
e-mail: anyionuigbo2006@yahoo.com

Introduction

The main goal of our ongoing research is to design a low-cost monitoring system for landslide investigation using the Reverse Real-Time Kinematic (RRTK) technique. For a standard RTK-GPS operation, dual-frequency geodetic-grade receivers with the supporting firmware are usually required. However, the high cost of these receivers and the supporting software is one of the reasons limiting the use of RTK GPS for several monitoring applications (Takasu and Yasuda 2009). The big challenge, therefore, in GNSS monitoring is how to reduce the cost of the monitoring scheme. The cost of monitoring includes the costs of RTK GPS receivers, power supply, communication, logistics, and personnel.

In this paper, a new landslide deformation monitoring concept that uses the RRTK principle is proposed. In order to support this proposed technique, real-time data streaming of raw GPS data of reference and rover stations was carried out using the ISKANDARnet infrastructure and Ntrip protocol.

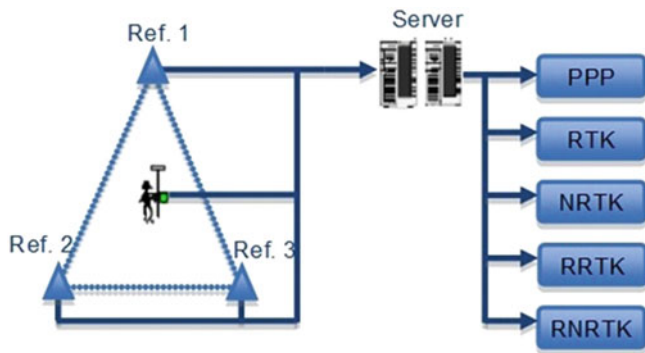


Fig. 1 Server-based RTK concept (Feng et al. 2009)

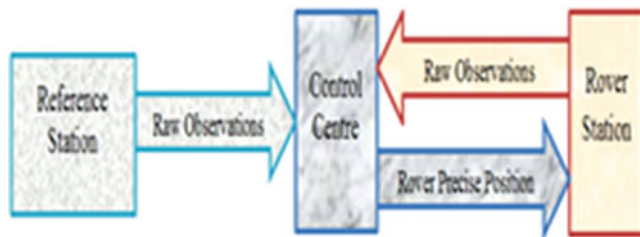


Fig. 2 Two-way communication channel

The Server-Based Processing Technique

The conceptual framework of this study is based on the server-based RTK processing concept. According to Feng et al. (2009), the server-based RTK processing concept can be used in various RTK techniques (see Fig. 1): precise point positioning (PPP), standard single-baseline RTK, network-RTK (NRTK), reverse single-baseline RTK (RRTK), and reverse network RTK (RNRTK).

The last two techniques (RRTK and RNRTK) combine the server-based processing concept and two-way communication for the computation and transmission of the user's accurate position. The reverse technique, which technically alters the one-way communication flow in the conventional RTK technique, involves a two-way communication (see Fig. 2) which requires the field users to transmit their raw observations to a control centre for the computation of the position solution, after which the computed solution along with the quality control indicators are transmitted back to the field users.

The main advantages that the server-based processing technique can provide for landslide monitoring applications are that the costs and tasks of the monitoring scheme will be drastically reduced, as low-cost receiver hardware will be utilized for real-time streaming of raw GPS measurements and complex algorithms and computations at the user end will be eliminated (Rizos 2007; Zinas et al. 2012).

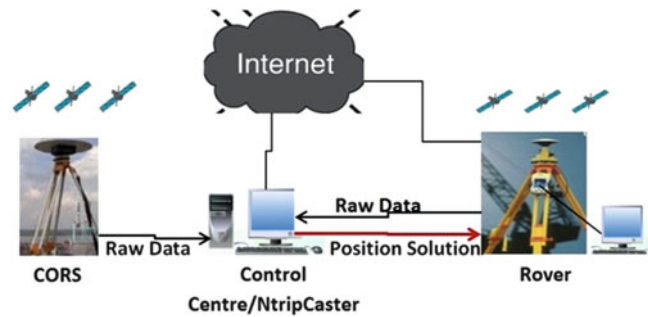


Fig. 3 The architecture of the RRTK technique

Infrastructure for Reverse RTK

The infrastructure requirements for the RRTK technique (see Fig. 3) include the following: receivers, software, power management, communication, continuously operating reference stations (CORS), and data handling and processing.

In this study, a low-cost positioning system using a Magellan Professional AC12 GPS OEM receiver, which cost a few hundred US dollars, is being designed. This receiver provides precise carrier phase outputs and can be used in high accuracy applications such as land and marine navigation, deformation monitoring, asset and personnel tracking and relative navigation (Alkan and Saka 2009).

The software requirements to operate the reverse RTK algorithms could be quite expensive. To avoid the inherent costs in software development, this study employs the RTKLIB software. The unique advantages of RTKLIB are that it supports low-cost receivers to stream raw measurement data of GPS signals, and enables users to design and operate original low-cost RTK GPS systems (Takasu and Yasuda 2009).

Secure energy supply is of paramount importance in landslide monitoring, which is often carried out in remote locations with little or no access to an electricity network. The main facilities that have an energy demand include sensor equipment, and communication and data processing (control centre) infrastructure. The main concern here is to choose facilities with the capacity to minimise power usage in order to extend battery life.

There are many options available for supporting the data transmission component of the RRTK system. These include radio-based communications, Internet communications, and wireless communications. A technique using the Internet for streaming GNSS data between different user equipment for precise positioning and navigation known as "Networked Transport of RTCM via Internet Protocol (NTRIP)" is used for the real-time GPS data streaming in this study.



Fig. 4 Distribution of ISKANDARnet reference stations (as modified in Google Maps)

The server-based processing technique usually uses existing GPS/GNSS CORS infrastructure. The CORS facilities utilized for this study is the ISKANDARnet. The control centre of ISKANDARnet is located in the Faculty of Geoinformation and Real Estate, Universiti Teknologi Malaysia (Shariff et al. 2009). At the time of writing of this paper, ISKANDARnet consists of four reference stations (*ISK1*, *ISK2*, *ISK3*, and *ISK4*), while more reference stations are being planned for the future. The distribution of the current ISKANDARnet reference stations is shown in Fig. 4.

Data handling consists of storing, processing, and presenting data in a format useful for the required application. In the RRTK technique, a greater proportion of positioning computation is shifted from the user end to the control centre. RRTK positioning requires transmission (typically every second) of reference and rover stations to the control centre. The volume of data involved can be very huge and efficient processing can be challenging.

Experimental Data Collection and Processing

The proposed new monitoring technique using RRTK principle and server-based processing methods was tested using data from test sites located at the Universiti Teknologi Malaysia. A 388-second dataset acquired at 1 s intervals on March 18, 2013, was processed to test the performance of the developed methods. The reference station and rover configuration are shown in Fig. 5.

The processing of the real-time GPS data was performed using the modified RTKLIB software package, based on server-based processing methods. In this approach, the rover station was processed using the single-base RTK technique from the closest reference station. The reference

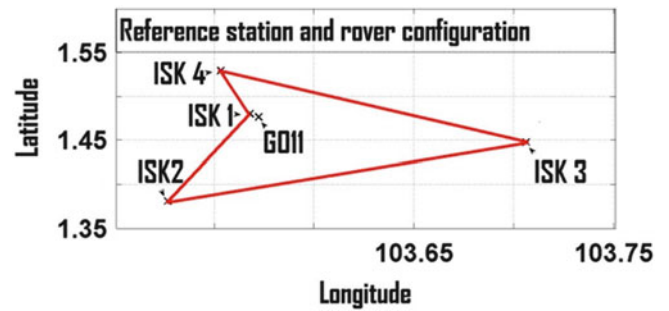


Fig. 5 Test network consisting of four reference stations (*ISK1*, *ISK2*, *ISK3* and *ISK4*) and one rover (*G011*)

station used for the data streaming at *G011* was *ISK 3*, a distance of about 23 km apart. In the next test campaign, all the reference stations will be utilized in processing the rover position. The results of the baselines solutions are presented in the local Cartesian coordinates.

The baseline of about 23 km may have introduced distance-related errors into the observations. Also, the high latency rate caused by fluctuations in Internet service in the streaming of data to the control centre, may have contributed to delay in resolving ambiguity for the determination of the position solution. In order to detect outliers in the observations, a high-pass filter was implemented. In this study, a weighted mean value is calculated from the coordinates and sigma according to (1) (Sundström 2009):

$$X_f = X - \hat{X}, \quad (1)$$

where X_f is the filtered position, X is the observed value and \hat{X} is the weighted mean value obtained from:

$$\hat{X} = \sum_{i=1}^N X_i \cdot w_i, \quad (2)$$

where N is the total number of observations for the filter and w is the weight obtained from (3):

$$w_i = \frac{\frac{1}{\sigma^2}}{\sum_{j=1}^N \frac{1}{\sigma^2}}, \quad (3)$$

where σ is the standard deviation value of Easting, Northing and Height.

The autocorrelation of GPS time series was also investigated. The observation time series is described as $(Y_1, Y_2, Y_3, \dots, Y_k, \dots, Y_n)$, which are made at equidistant time intervals Δt . N is the total number of the observations. The mean value of all observations is computed as \bar{Y} ; then the autocorrelation coefficient (R_h) of the observation series is computed as follows:

$$R_h = C_h / C_o, \quad (4)$$

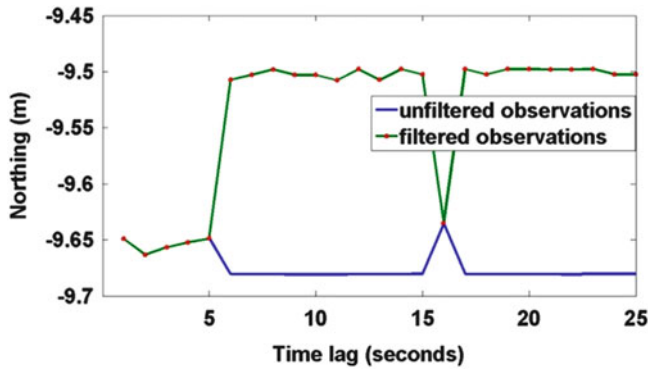


Fig. 6 Filtered and unfiltered observations for Northing components

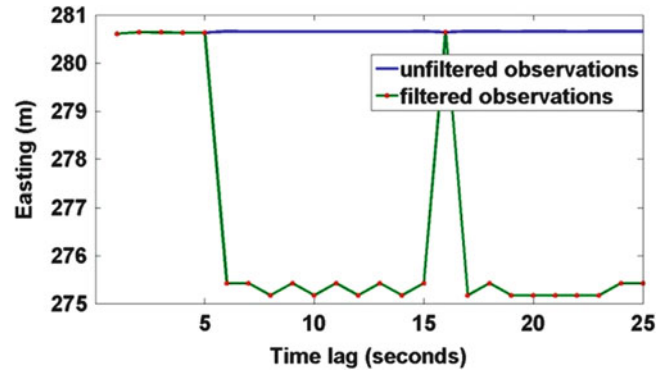


Fig. 7 Filtered and unfiltered observations for Easting components

where C_h is the autocovariance function:

$$C_h = \sum_{t=1}^{N-h} (Y_t - \bar{Y})(Y_{t+h} - \bar{Y})/N, \quad (5)$$

and C_o is the variance function:

$$C_o = \sum_{t=1}^N (Y_t - \bar{Y})^2/N, \quad (6)$$

h is time lag ($h = 1, 2, 3, \dots$).

The plot of R_h for varying h is called the correlogram for the random process Y_k . The correlogram is used to check for serial dependency in an observed time series.

Results and Analysis

The plots of both filtered and unfiltered observations for the first 25 s are given in Figs. 6, 7 and 8. It is shown that the implementation of the high-pass filter has been able to detect outliers in the observations. The observations of first 5 s and 16 s are outliers. The noises were due to the fact that the position solutions of first 5 s were in a float solution as the system was still in the initialization stage. The fixed solution commenced from the sixth second observation.

The plot of the standard deviation values for the first 25 s is given in Fig. 9. The standard deviation values for the three components were generally high in observations of first 5 s and 16 s; Northing and Easting having the highest values of about 1 m, and height of more than 3 m. The standard deviation values for the subsequent observations were about 1 mm for Northing and Easting and about 3 mm for Height.

The plot of the displacement vectors for Northing, Easting and Height components, for the first 25 s is given in Fig. 10. It is shown that the displacements are affected by

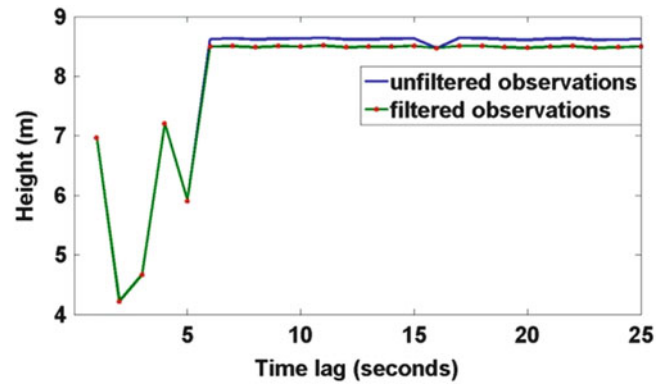


Fig. 8 Filtered and unfiltered observations for Height components

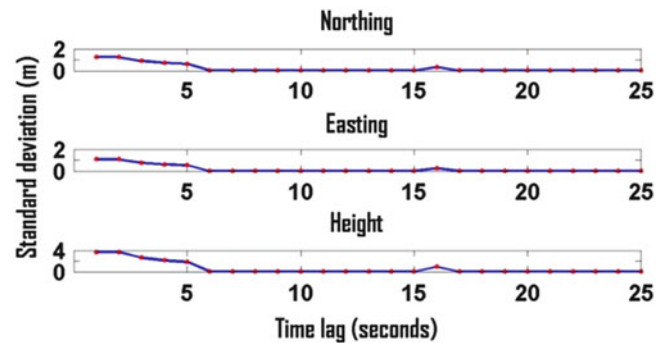


Fig. 9 Standard deviation values for Northing, Easting, and Height components

high standard deviation values—that is, large displacements have high standard deviation values.

The autocorrelation functions of the GPS time series for Northing, Easting, and Height, respectively are shown in Figs. 11, 12 and 13.

In the correlogram of Northing (Fig. 11), the autocorrelation functions take the value $R_o = 0.003$ and decrease exponentially until time lag 300 s when the autocorrelation of the observations is not so obvious. In the correlogram of Easting

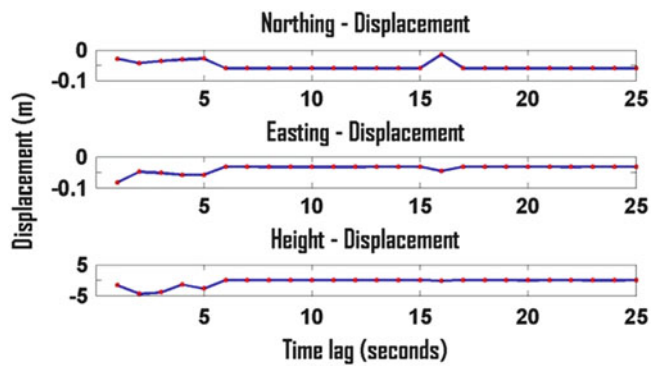


Fig. 10 Displacement vectors for Northing, Easting, and Height components

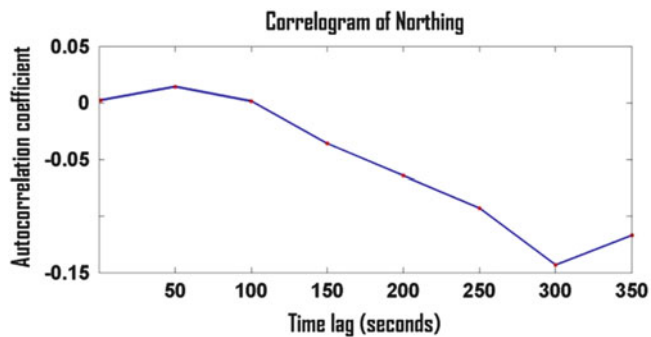


Fig. 11 Correlogram of Northing components for time lag 0–350 s

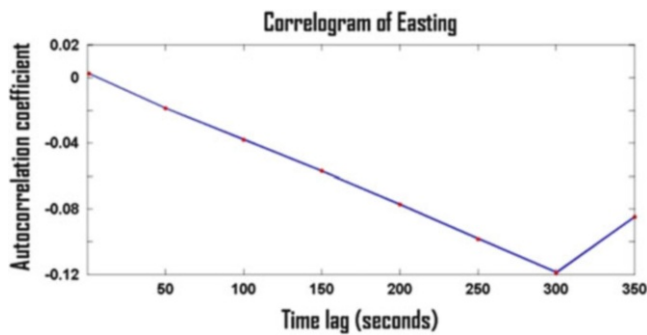


Fig. 12 Correlogram of Easting components for time lag 0–350 s

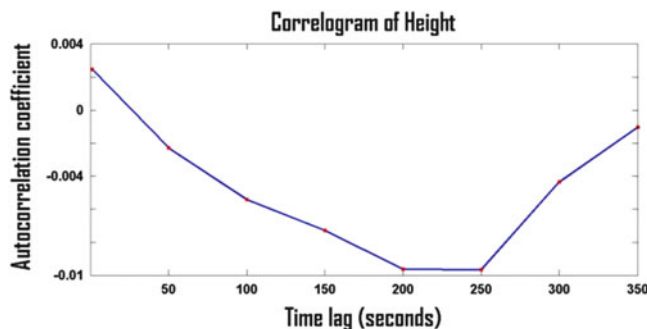


Fig. 13 Correlogram of Height components for time lag 0–350 s

(Fig. 12), the autocorrelation functions take the value $R_o = 0.003$ and decrease exponentially until the time lag 300 s when the autocorrelation of the observations is not so obvious. In the correlogram of Height (Fig. 13), the autocorrelation functions take the value $R_o = 0.003$ and decrease exponentially until the time lag 200 s when the autocorrelation of the observations is not so obvious. These deviations show that the GPS measurements contain white and coloured noise. The coloured noises in the GPS measurements follow an exponential distribution. When the time lag is larger, for example 200 s, the autocorrelation of the observations is not so obvious. But when the time lag is smaller, for example 1 s, the autocorrelation coefficient between two observations becomes larger.

Summary and Outlook

We have discussed the concept, principles, and infrastructure requirements of a proposed low-cost landslide monitoring system using RRTK technique. In order to implement the RRTK algorithm, a real-time data streaming of raw GPS data of the reference and rover stations was performed by utilizing the ISKANDARnet infrastructure and Ntrip protocol. The main purpose of the data streaming was to investigate the quality of the measurements. A high-pass filter was implemented to detect outliers in the measurements. Auto-correlation analysis of GPS time series was also carried out to validate the presence of white and coloured noise in the GPS measurements.

The main problems encountered during field work include power supply problems and fluctuations in Internet services. There is a great concern for power supply because a typical landslide site may be located in remote areas where access to the electric network is not readily available. The fluctuation in Internet services was a big concern as this may have contributed to a high latency rate in the streaming of the data.

The next phase of the study will involve the implementation of RRTK GPS technique on real-world landslide sites.

Acknowledgements The authors would like to express their sincere appreciation to Universiti Teknologi Malaysia and the Ministry of Science, Technology and Innovation (MOSTI) of Malaysia for the eScienceFund (4S074) given to this research project.

References

- Alkan RM, Saka MH (2009) A performance analysis of low-cost GPS receivers in kinematic applications. *J Navig* 62(4):687–697
- Feng Y, Rizos C, Higgins M, Lim S, Tang M (2009) Developing regional precise positioning services using the legacy and future GNSS receivers. *J Glob Positioning Syst* 8(1):17–25

- Rizos C (2007) Alternatives to current GPS-RTK services and some implications for CORS infrastructure and operations. *GPS Solutions* 11(3):151–158
- Shariff NS, Musa, TA, Ses S, Omar K, Rizos C, Lim S (2009) ISKANDARnet: a network-based real-time kinematic positioning system in ISKANDAR Malaysia for Research Platform. South East Asian Survey Congress, Bali International Convention Center, Nusa Dua, Bali, Indonesia, 4–7 August
- Sundström J (2009) Evaluation of high rate real time GPS based tsunami warning system. M.Sc. thesis, Space Geodesy and Geodynamics Research Group, Chalmers University of Technology, Göteborg, Sweden
- Takasu T, Yasuda A (2009) Development of the low-cost RTK GPS receiver with the open source program package RTKLIB. In: International symposium on GPS/GNSS, International Convention Centre Jeju, Korea
- Zinas N, Parkins A, Ziebart M (2012) Improved network-based single-epoch ambiguity resolution using centralized GNSS network processing. *GPS Solutions*, 23 February 2012, pp 1–11



An Adaptive and Sustained Landslide Monitoring and Early Warning System

Teuku Faisal Fathani, Dwikorita Karnawati, and Wahyu Wilopo

Abstract

Areas prone to mass movement are widespread in Indonesia. The potential for landslide disasters in several regions is controlled by the geotechnical and geological conditions and triggered by high intensity rainfall and/or earthquake activity. The vulnerability to landslides is made worse by intensive land-use development. The urgent issues to be addressed are the dense populations residing in areas prone to mass movement and the failure to relocate the local people to safer areas for socio-economic reasons. Therefore, landslide monitoring, prediction, and early warning systems are urgently required to guarantee the safety of communities living in such areas. A long running and sustainable community-based landslide monitoring and early warning system (EWS) has been developed in Indonesia, with establishment of collaboration among the local government, universities, private sectors, NGOs, and the disaster management community. The main purpose of the program is to establish a strategic approach for disaster risk reduction through the implementation of information flow (for warning levels) and order/command systems (for evacuation). These activities have already met the community needs, helped save lives, and continued to obtain solid community support. In order to extend the effort, further challenges are to expand the project coverage, and propose more effective landslide monitoring, early warning, analysis, and visualization. In addition, the capabilities in socio-economic risk assessment need to be expedited to help identify those most at risk within the community. This paper describes the achievements and the current activities of the IPL Project (IPL-158) "Development of Community-based Landslide Early Warning System".

Keywords

Landslide monitoring sensors • Information flow • Command system • Community empowerment

Introduction

As a basis for landslide mitigation, the implementation of preventive measures usually focuses on avoiding slope failure, diverting the moving mass away from vulnerable elements, or building reinforcement to protect the threatened elements. However, the importance of early warning systems may rise if landslide mass stabilizing action is considered expensive in financial and/or environmental terms. The implementation of early warning systems may, at least, avoid damage and the loss of human lives (Corominas et al. 2005).

T.F. Fathani (✉)
Department of Civil and Environmental Engineering, Universitas
Gadjah Mada, Jalan Grafika No. 2, Yogyakarta 55281, Indonesia
e-mail: tfathani@ugm.ac.id

D. Karnawati • W. Wilopo
Department of Geological Engineering, Universitas Gadjah Mada,
Jalan Grafika No. 2, Yogyakarta 55281, Indonesia
e-mail: dwikoritakarnawati@yahoo.com; wwilopo@gadjahmada.edu

Ideally, zones with a high susceptibility and landslide risk should be prevented from being developed. Unfortunately, quite often the susceptible particular zone has been developed as a dense settlement of housing and infrastructure areas and the relocation of people living in this area to a safer zone cannot be conducted due to some socio-economic constraints. Thus, the development of a landslide warning system becomes very critical to protect the people living in the landslide-prone areas (Anderson et al. 2011; Halcombe et al. 2012).

In order to guarantee the effectiveness of the landslide early warning system, the developed system should be simple to operate and appropriately installed in the most suitable sites. Consequently, this system should incorporate both technical and social approaches. The determination of early warning criteria is considered as one of several involvements in a technical approach (Fathani et al. 2011; Fathani and Karnawati 2010).

The application of the most appropriate and adaptive technology for an early warning system is considered crucial to reduce the risk of landslide disasters. Unfortunately, the effectiveness in implementing an early warning system cannot be guaranteed due to inadequate consideration of the social, cultural, and economic conditions. Accordingly, the need to integrate social considerations into the technical system should be addressed in order to assure the effectiveness in the implementation of such an approach.

Development of the Technical System

The technical system to support landslide disaster risk reduction was developed by Fathani and Karnawati (2012), and consists of several technical components such as instruments for a landslide early warning system recommended by Fathani et al. (2008) and also Fathani and Karnawati (2010), supported by the smart-grid for landslide hazard communication, monitoring and early warning developed by Karnawati et al. (2011b, 2012).

Faculty of Engineering, Universitas Gadjah Mada Indonesia has developed simple and low-cost equipment for landslide monitoring and early warning since 2007. Initially, two types of simple extensometers and rain gauge were installed at several pilot areas in Central Java and East Java Provinces. The first type of extensometer is a handmade manual reading extensometer and the other type is an automatic extensometer for monitoring ground surface movement. Both types of extensometers, coupled with an Automatic Rainfall Recorder (ARR), are connected to the alarm system to directly warn the local community to take necessary actions in dealing with potential landslide disasters (Fathani et al. 2008).

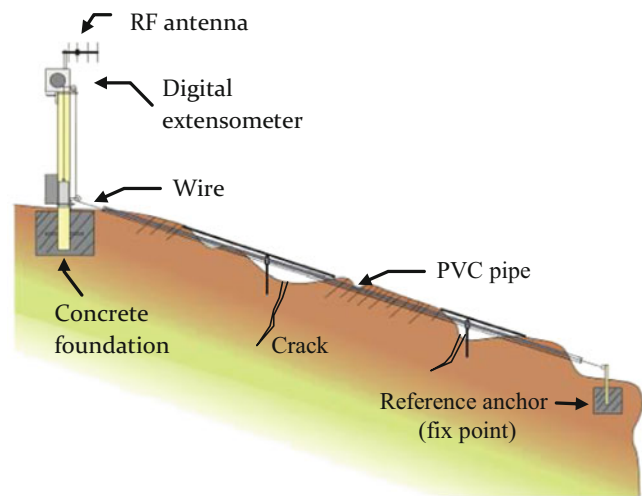


Fig. 1 The installation scheme for an extensometer

In line with the installation of simple monitoring equipment, the Asian Joint Research Project for Early Warning of Landslides has conducted a field survey to support the installation of real-time landslide monitoring equipment. A pilot area has been established in the Banjarnegara Regency, Central Java Province. This monitoring system presents the results of real-time measurement by using long-span extensometers, a raingauge, and pore pressure sensors, with monitoring of the scene by IP camera. The real-time monitoring equipment consists of outdoor and indoor units. The outdoor unit is fixed on a center pole and consists of a fieldserver, two extensometers, a raingauge, an IP camera and water pressure sensor. The fieldserver is a sensing device with a real-time online data display system which gathers the data from multiple sensors and shows it in a webserver.

Since 2012, a real-time landslide monitoring and early warning has been developed by Universitas Gadjah Mada. The system comprises several sensors: namely a digital extensometer, wireless tiltmeter, inclinometer, Automatic Rainfall Recorder (ARR), ultrasonic water level sensor and an IP Camera, and other sensors can be added, such as pore water pressure and inclinometer sensors.

Extensometers are used to measure any change in the distance between two fixed points across the crack and are attached to the soil slope to be monitored. The system adopts the auto-monitoring and event trigger method. When the variations occur, the signal of 1 mm displacement triggers the transmitter and at the same time, the digital data with a highly precise position is transmitted to the server. Figure 1 shows the installation of a wireless-digital extensometer.

A wireless tiltmeter is a compact, waterproof tilt meter with a range of 0° – 80° in X and Y axis from horizontal (Fig. 2). It is used to monitor changes in the inclination of an unstable slope. Tiltmeter data can provide an accurate

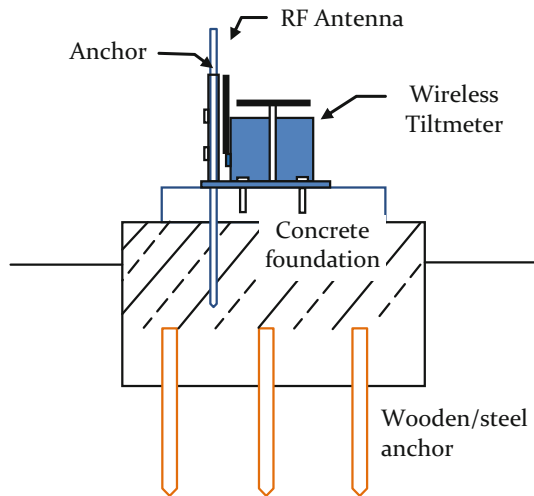


Fig. 2 The installation of a wireless tiltmeter

history of slope inclination and provide early warning of a potential landslide hazard. The system adopts the auto-monitoring and event trigger method. When the variations occur, the signal of 0.1° inclination triggers the transmitter and at the same time, the digital data is transmitted to the server.

The collected data from the extensometer, tiltmeter, ARR and AWLR processed by microcontroller are sent point to point in a wireless network. The data is received by a field server; its functions are to receive, store, analyze and resend data to the central server, and decide when to announce early warnings to the local residents. The received data is then stored in a digital storing media (memory card). The central server consists of receiver equipment and a specific Personal Computer (PC) to monitor data visually. The PC, which is connected to the internet, will upload all the data to a web server; therefore, the data can be monitored from any place with internet access. Figure 3 shows a network diagram of a telemetric system for real-time landslide monitoring and early warning.

This real-time monitoring and early warning of landslides and debris floods has been implemented at eight geothermal areas in Sumatera, Java and Sulawesi Islands. This system was developed based on cooperation between the Faculty of Engineering Universitas Gadjah Mada and the Indonesian State-owned Oil and Natural Gas Corporation. In order to support this system installation, geological and geotechnical investigations have been conducted to examine the level of risk at the geothermal areas. Accordingly, several methods of landslide preventive measures in term of control works and restraint works were designed and applied to the high risk slopes.

Information Flow and Command System to Support a Landslide Monitoring and Early Warning System

Based on long experience, landslide monitoring and early warning systems should be based on the most appropriate and adaptive technology, with the involvement of the local authority and community participation. Therefore, both technical and communication skills are the main requirements to achieve success in an early warning system program. The system should include some technical aspects such as geological surveys and site selection, design of monitoring equipment which is simple (low-cost) but effective, determination of early warning levels (warning criteria), installation, operation and maintenance at the field site. Social aspects should include social mapping and evaluation, public consultation and dissemination of a program, and community empowerment, including the technical training and evacuation drills for landslide hazard preparedness (Karnawati et al. 2011a).

One of the most critical considerations in disaster risk reduction in Indonesia is the assurance of an effective and sustainable information flow (during warning level) and order/command flow (for evacuation). The local disaster management agency at district or provincial level acts as the center of this monitoring and early warning system. The role of universities and NGOs is to facilitate the stakeholders involved in this information and command system. Figure 4 shows the information flow and command system to support landslide monitoring and early warning.

The proposed model of landslide early warning has been quite effective and strategic in improving community resilience at landslide-vulnerable villages. It is also crucial that the system should be developed through community participation and the provision of simple and low-cost technology up to real-time technology for early warning.

Discussion

The most adaptive and sustained landslide disaster risk reduction in Indonesia requires a consistent strategy and support from the government, universities, NGOs and private sectors for the implementation of community-based projects. However, there is still a gap and disconnection between the institutional and strategic approaches to disaster risk reduction which will affect the effectiveness of community-based projects in landslide-prone areas.

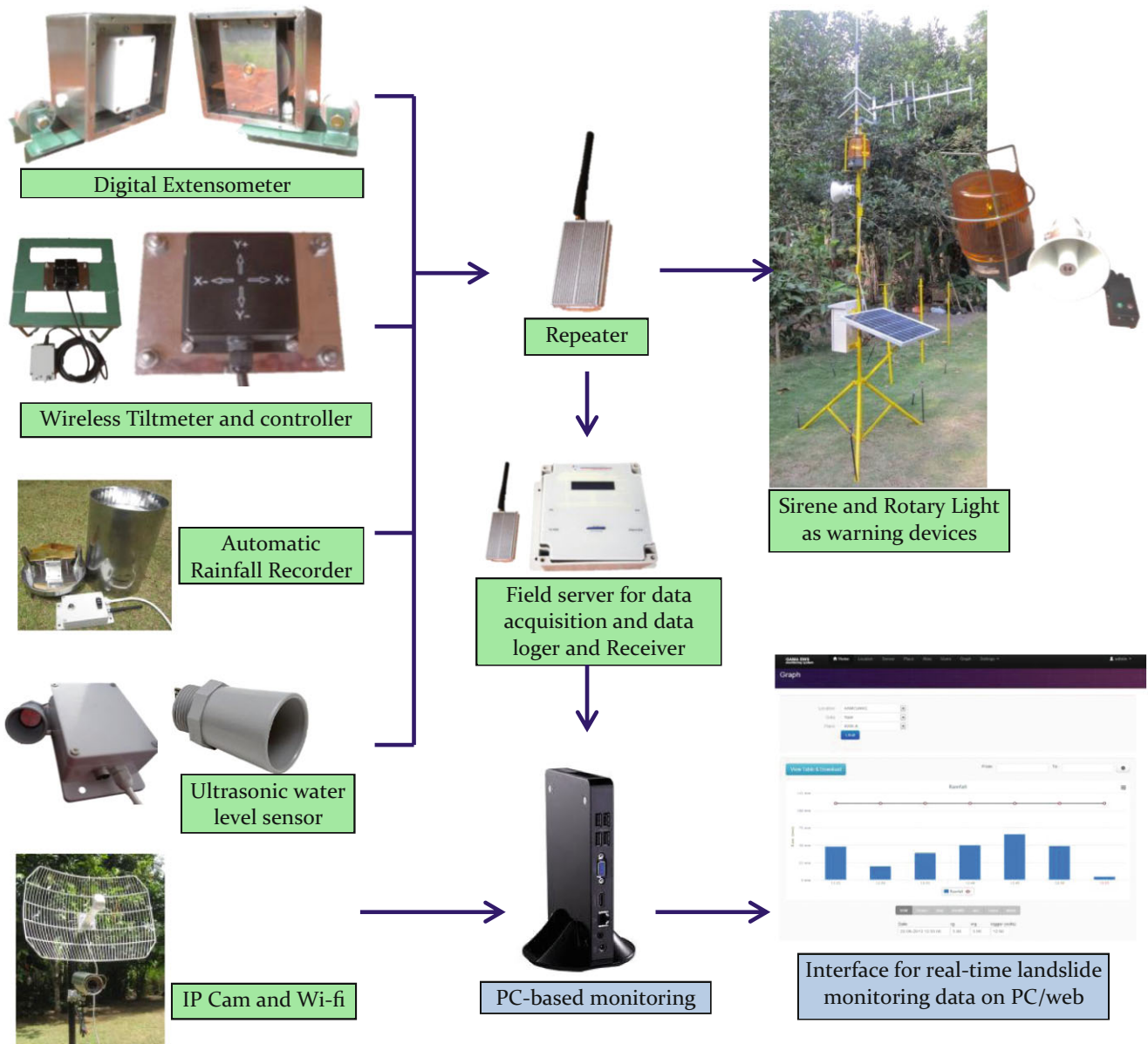


Fig. 3 Network diagram of a telemetric system for real-time landslide monitoring and early warning

Accordingly, the outcomes from community-based activities remain isolated in time and locale, and are deprived of higher-level resources and visibilities required to sustain long-term risk reduction activities and spread capacities to other communities.

The newly developed system facilitates a network of sensors for monitoring and transmitting the hazard level to the local authorities and local community by using the sustained information flow and command system. The sensor is designed by using real-time landslide monitoring

and early warning instruments, and also may involve human sensors which comprise selected trained-people in the local community, who have been dedicated in their commitment for doing ground checking and sending reports related to any observed warning signs of potential landslides. Their understanding of the causes and landslide triggering mechanisms is crucial to establishing appropriate concepts and methods for landslide monitoring, determining warning criteria for hazard prediction and risk assessment in the region.

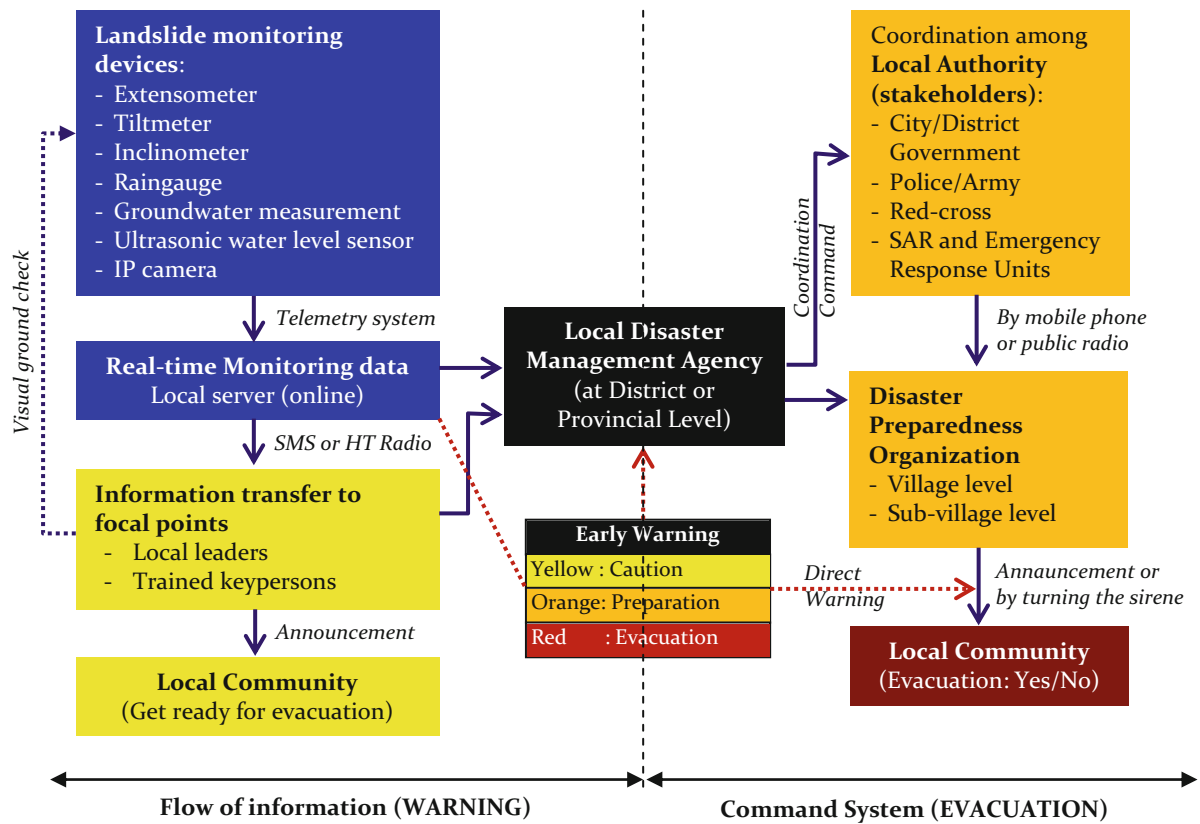


Fig. 4 Flow of information and command system for landslide monitoring and early warning

Acknowledgments The authors would like to thank the International Consortium on Landslides (ICL), Indonesian Ministry of National Education, Indonesian National Agency for Disaster Management (BNPB), and PT. Pertamina Geothermal Energy for their support to this research project.

References

Anderson MG, Halcombe E, Blake JR, Ghesquire F, Holm-Nielsen N, Fisseha T (2011) Reducing landslide risk in communities; evidence for the Eastern Caribbean. *Appl Geogr* 31:590–599

Corominas J, Moya J, Ledesma A, Lloret A, Gili JA (2005) Prediction of ground displacements and velocities from groundwater level changes at the Vallcebre landslide (Eastern Pyrenees, Spain). *Landslides* 2:83–96. doi:10.1007/s10346-005-0049-1

Fathani TF, Karnawati D (2010) Early warning of landslide for disaster risk reduction in Central Java Indonesia. In: Sassa K, Yueping Y (eds) *Early warning of landslides*. Geological Publishing House, Beijing, pp 159–166

Fathani TF, Karnawati D (2012) Lessons learned in the development of landslide early warning system in Indonesia. In: *Proceeding of IPL symposium 2012*, UNESCO HQ, Paris, pp 30–34

Fathani TF, Karnawati D, Sassa K, Fukuoka H, Honda K (2008) Development of landslide monitoring and early warning system in Indonesia. In: *Proceedings of the 1st world landslide forum, IPL-ISDR*, Tokyo, pp 195–198

Fathani TF, Karnawati D, Legono D, Faris F (2011) Development of early warning system for rainfall-induced landslide in Indonesia. In: *Proceeding of the 2nd international workshop on multimodal sediment disaster*, Asian Cloud Network on Disaster Research, Tainan, Taiwan, pp 103–113

Halcombe E, Smith S, Wright E, Anderson MG (2012) Integrated approach for evaluating the effectiveness of landslide risk reduction in unplanned communities in the Caribbean. *Nat Hazards* 61:351–385

Karnawati D, Fathani TF, Andayani B, Legono D, Burton PW (2011a) Landslide hazard and community-based risk reduction effort in Karanganyar and the surrounding area Central Java, Indonesia. *J Mt Sci* 8(2):149–153

Karnawati D, Fathani TF, Wilopo W, Setianto A, Andayani B (2011b) Promoting the hybrid socio-technical approach for effective disaster risk reduction in developing countries. In: Brebbia CA, Kassab AJ, Divo EA (eds) *Disaster management and human health risk II*. WIT Press, Southampton, pp 175–182

Karnawati D, Frost EG, Fathani TF, Subroto (2012) Smart grid for landslide monitoring and early warning system in Indonesia. In: *Proceedings of the 10th anniversary of ICL*, January 2012, Kyoto, pp 72–77



Early Warning and Real-Time Slope Monitoring Systems in West and East Malaysia

William H.T. Fung, Richard J. Kinsil, Suhaimi Jamaludin, and Sashi Krishnan

Abstract

This paper presents the application of slope safety warning systems on two slopes along strategic roads in Malaysia. The systems are used as an alternative to further structural reinforcement or remedial work. Their purpose is to provide long-term monitoring and early warning to facilitate the understanding of slope behaviour, and to manage landslide risk faced by road users. The first application is in West Malaysia. It is a slope cut that is located at the 46th km of the Simpang Pulai—Kuala Berang Highway. The second case is an embankment fill located at the 50.4th km of the Federal Road 500 between Penampang and Tambunan of Sabah. The first slope has had a long history of continual slow deformation, while the behaviour of the latter is closely linked with rainfall conditions. In view of the distinct slope movement patterns, on-site instrumentation techniques are different, and geodetic, geotechnical and hydrogeological monitoring techniques are utilised. As the slopes are situated in mountainous terrain, unfavourable weather conditions and remoteness of the sites pose serious challenges to the specification of lightning protection, power supply and data communication systems. Although the on-site system components are site specific, they are controlled by the same web-based instrumentation data management system. To allow representative indices of slope instability to be used in the warning module of the systems, diverse criteria are adopted. Apart from the conventional ones that make use of rainfall, groundwater level and soil deformation/movement, for the slope in Perak, creeping as described by landslide velocity is incorporated as a warning indicator. To reduce the likelihood and consequences of catastrophic collapse, understanding of slope behaviour is a pre-requisite. Such understanding is possible with systems that provide timely measurement of actual slope performance, and an early warning for impending danger.

Keywords

Early warning • Real-time slope monitoring system • Web-based instrumentation data management system • Warning criteria

W.H.T. Fung (✉)

Fugro Geotechnical Services Ltd. Unit 8, 10/F Worldwide Industrial Centre, 43-47 Shan Mei Street, Fotan, Shatin, N.T., Hong Kong
e-mail: wfung@fugro.com.hk

R.J. Kinsil

Slope Engineering Branch, Public Works Department Headquarters of Malaysia, Jalan Sembulan, 88582 Kota Kinabalu, Sabah, Malaysia
e-mail: Richard.Kinsil@sabah.gov.my

S. Jamaludin

Slope Engineering Branch, Public Works Department Headquarters of Malaysia, Jalan Sultan Salahuddin, 50582 Kuala Lumpur, Malaysia
e-mail: suhaimij@jkr.gov.my

S. Krishnan

Konsortium MyStar Communications Sdn. Bhd., 23-3, Jalan 4/109 F, Plaza Danau Desa 2, Taman Danau Desa, 58100 Kuala Lumpur, Malaysia
e-mail: sashi.krishnan@mystar-msc.com

Introduction

Conventionally, monitoring data from slope instrumentation are taken manually on site using portable equipment. In some projects where continuous data are required, automatic devices are installed to capture the data. However, it is still common to manually retrieve the data from the instruments. In recent years, the instruments, and communication technology, have advanced considerably. Real-time continuous slope monitoring systems have become feasible. Such technologies have found growing importance in slope monitoring. In particular, they are extremely useful for slopes where there is active movement and landslides are a hazard, while the processes controlling the movement are not clear. Real-time slope monitoring is a means for better understanding of slope behaviour, and, just as importantly, used to give early warning of impending danger.

This paper deals with the application of early warning and real-time slope monitoring systems, or termed herein as slope safety warning systems, in West and East Malaysia. This has been applied on two slopes that have been of concern. The first application is implemented on a slope cut along the second East-West Coast Highway in West Malaysia. It is located in Perak at the 46th km of the Simpang Pulai—Kuala Berang Highway. The second case is an old fill embankment slope located at the 50.4th km of the Federal Road 500 between Penampang and Tambunan of Sabah. The former slope cut has been moving since its completion in 2004, while the behaviour of the latter is closely linked with the rainfall conditions. The distinct movement patterns prescribe specific instrumentation techniques for their monitoring.

Slope Monitoring in West Malaysia

The slope cut on the second East-West Coast Highway, has shown signs of stress since the completion of the highway in 2004. A series of remedial works were carried out, but this could not inhibit the instability. The development of the instability was detailed by Jamaludin et al. (2012) in conjunction with the geological setting and landslide processes operating at the site. A general view of the slope is presented in Fig. 1. A large mass of ground has been activated, and further remedial work is not economically justifiable without a better understanding of the slope behaviour. The extent of the unstable portion of the cut is approximately 150 m long and 24–60 m high.

In the present situation where complete safety is exceptionally expensive, if not impossible, and the use of the highway by the public is to be maintained, a risk management approach would definitely help decision making. A key



Fig. 1 Overview of slope at 46th km, Simpang Pulai—Kuala Berang Highway

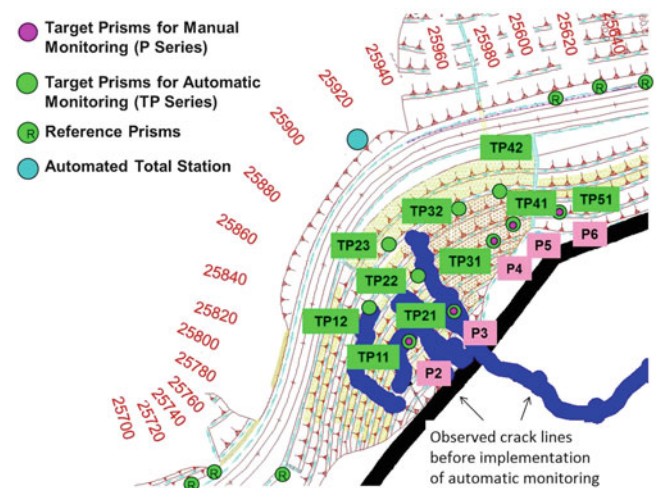


Fig. 2 Layout of monitoring prisms

element of the approach is the implementation of an early warning and real-time slope monitoring system to provide the authorities with timely actual measurements of slope movement and advanced warning of impending danger.

Instrumentation Installed on a Continuously Moving Slope

The continuous movement observed in the slope is too extensive to be taken care by any conventional geotechnical instrumentation. Instead, geodetic monitoring using a robotic total station has been put in place. It was based on the large deformation observed with manual equipment during the construction stage. An additional advantage over other common geotechnical sensors is that the instruments installed on the slope are not of an electrical type that are vulnerable to lightning damage. The measurements are taken by a robotic total station with laser beams. The monitoring is run by an automated robotic total station, controlled by in-house software suites for programming, and data acquisition and processing.

With respect to data communications, the remoteness and adverse weather conditions preclude the use of conventional mobile and wireless techniques. To provide reliable



Fig. 3 Setup of robotic total station (*left*), and antenna for satellite communications (*right*)

communication and power systems, specially designed satellite communications and power systems were deployed. Figure 2 presents the layout of the monitoring targets, while the physical setup of the monitoring station at the site can be seen in Fig. 3.

To permit the monitoring system to assume its role as a slope safety warning system, the on-site components must be integrated with a web-based instrumentation data management system. An in-house product is used for this purpose. Its core is a relational database system that runs on a geographic information system platform. This provides rapid data retrieval/storage, processing, presentation, and diverse automatic alert triggers. Fung et al. (2010) discussed details of the operating software suites, and the instrumentation installation.

Since the installation of the complete system at the end of 2009, the system has been running up to the present, which provides valuable data to enable better comprehension of slope performance. In addition to deformation monitoring, further use of the data has been made to reduce the landslide risk.

Monitoring of Slope Movements and Their Velocity

Prior to implementation of the current monitoring system, a manual optical survey of the slope already indicated a total slope movement >5 m at several locations, with a maximum of 7 m from December 2007 to December 2009. This was associated with the failure of a series of slope remedial works. Since the current system was in place at the end of 2009, the slope has moved further by a maximum of 10 m, as illustrated in Fig. 4. Emphasis is placed on the uppermost target prisms located within the unstable slope cut, named TP11 to TP51.

Jamaludin et al. (2008, 2012) have discussed the development of the observed movement patterns of slopes in the

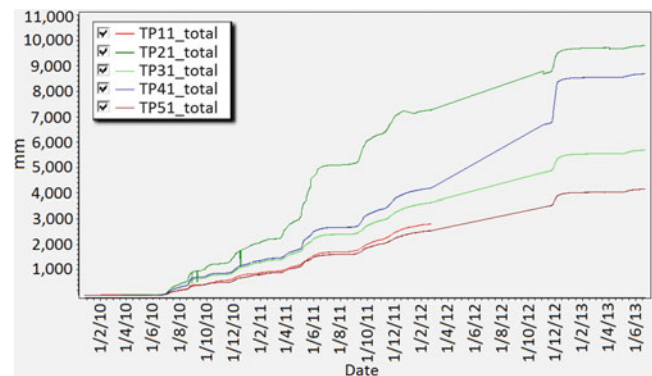


Fig. 4 Total slope displacement of uppermost prisms

area, and suggested that the patterns follow the creep model proposed by Varnes (1978). In essence, the model consists of three stages: primary, secondary and tertiary creep. Primary creep is associated with a high displacement rate, while a quasi-static rate of movement occurs in the secondary creep stage. The tertiary creep is associated with an increasing rate of movement. Jamaludin et al. (2012) suggested that the slope is currently in the secondary creep phase. As such, monitoring should be continued until signs of tertiary creep occur, when the rate of slope movement increases dramatically. Indeed, the movement rate has formed a key part of the warning system.

The rate of surface movement observed in concerned target prisms is shown in Fig. 5. Except for TP21, the slope movement stays in the Slow velocity class (Cruden and Varnes 1996).

Figure 6 presents the results only within the Slow velocity class. The slope movement rate patterns resemble those as depicted by Leroueil et al. (1996) for active landslides in the reactivated stage. It is considered that the recorded patterns are related to minor local failures that have been seen on the site.

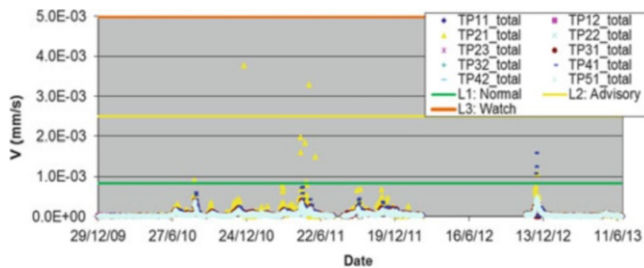


Fig. 5 Velocity versus time plot

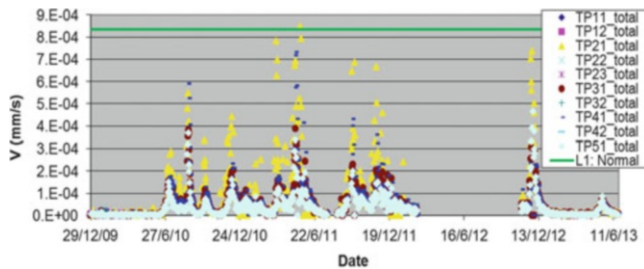


Fig. 6 Velocity versus time plot for activation of local failures

Warning Criteria Based on Movement Rate

Since completion of the slope cut on the highway in 2004, continuous deformations have been observed. Moreover, the slope deformations obtained from both manual and automatic optical survey have been large. Conventional warning criteria based on magnitude of movement alone are not meaningful from the perspective of risk mitigation. As previously discussed, the creep model would be applicable for describing the development of slope failure.

Catastrophic failure cannot be arrested. However, landslide risk for road users can be largely mitigated by incorporating a pre-failure warning framework based on slope movement rate into the monitoring system, as suggested by Fung et al. (2010). Such a framework was proposed by Jamaludin et al. (2012), and included in the monitoring system. Towards accelerating creep, the movement rate will be increasing, and high. Jamaludin et al. (2012) suggested warning criteria for the failure phase of the slope, based on different velocity threshold values, adapted from those proposed by Cruden and Varnes (1996) with due consideration of the measuring technique accuracy. The criteria are summarised in Table 1.

The threshold levels have also been presented in Figs. 5 and 6. As shown, the slope has been very active, with continuous movement, whereas the movement rate generally stays below the first threshold.

Table 1 Proposed warning criteria for movement rate

| Alarm level | Velocity limit | Proposed response |
|-------------------|---------------------------|--|
| Level 1: Normal | <3 mm/h (72 mm/day) | Daily data monitoring by JKR staff |
| Level 2: Advisory | 3–9 mm/h (216 mm/day) | Continuous monitoring, data analysis and review, field observation |
| Level 3: Watch | 9–18 mm/h (432 mm/day) | Increase preparedness, continuous data analysis, inform police/preparedness team |
| Level 4: Danger | >18 mm/h (432 mm/day) | Continuous monitoring, decision to be made (to evacuate/close the road) |

Slope Monitoring in East Malaysia

The second slope is an embankment fill located along the Federal Road 500, between Penampang and Tambunan of Sabah. A general view of the slope is presented in Fig. 7. The road is a strategic one and connects the lowland areas of the west coast to the interior regions of Sabah. The stretch of the road where the slope fill lies is constructed across the steep slopes of the Crocker Range, which is dominated by sedimentary rocks. As identified in the National Slope Master Plan 2009–2023 (CKC 2009), the area is characterised as a landslide-prone area. The occurrence of landslides along the stretch is quite common during monsoons every year, in the southwest and northeast directions.

Many of the slope fills along the mountainous stretch of the road are old embankments. They usually block the natural drainage, and rely on post-construction man-made drainage to help discharge rainwater away from inside the fills. In addition, surface runoff is another main cause of slope failure, as it allows rainwater to penetrate and percolate into the slope face and weaken the soil due to high moisture. Surface drainage and protection is necessary to maintain the slope safety.

Although routine maintenance is in place, sign of stress, such as surface cracks and displaced channels, have been observed on the embankment fill, as shown in Fig. 8. To facilitate the understanding of the fill embankment behaviour, and provide an alert mechanism for road users and the authorities about its stability, a safety monitoring system is now operational.

This is an autonomous system that allows real-time automatic recording of rainfall, groundwater level and slope movement. It provides data availability in all weather conditions, through the same web-based system. Most importantly, alerts will be triggered automatically by the system to provide early warnings to the authorities so that preventive action can be taken accordingly.



Fig. 7 Panoramic view of embankment fill at Federal Road between Penampang and Tambunan



Fig. 8 Surface cracks (inset showing a displaced channel)

Instrumentation for an Intermittently Triggered Slope Fill

Instrumentation based on geotechnical and hydrogeological monitoring techniques is utilised to investigate the slope behaviour and to provide early warning alert. The automatic instruments include a rain gauge station, two sets of piezometers, tiltmeters, and two manual inclinometers to establish subsurface soil movements.

The system was operational in early March 2013 before the approaching southwest monsoon (May to September). As shown in Fig. 9, there have been five peaks up to mid-June of the same year. The rolling 24-h rainfall exceeds the first threshold level of 50 mm in 24 h for landslide warning in April. As it will be highlighted, the rolling 24-h rainfall has been found to be a useful indicator for landslide occurrence. For completeness, the recorded hourly rainfall is also presented on Fig. 9.

A graph showing rainfall against water level is presented in Fig. 10 for easy comparison. The change in water level was not abrupt, except for the first rainstorm. It is also interesting to note the corresponding slope movement during the same period. As illustrated in Fig. 11, the slope was activated whenever the rolling 24-h rainfall exceeded the trigger levels.

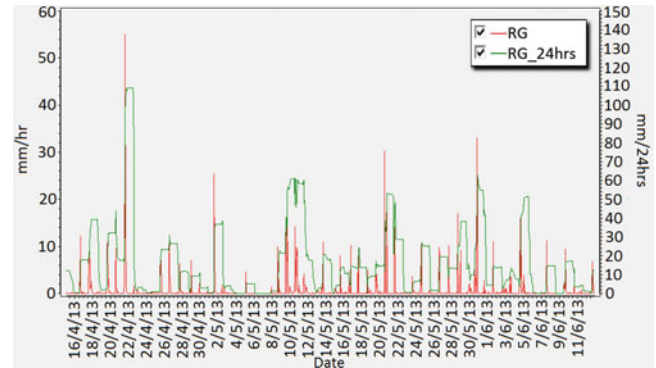


Fig. 9 Graphs of hourly and rolling 24-h rainfall

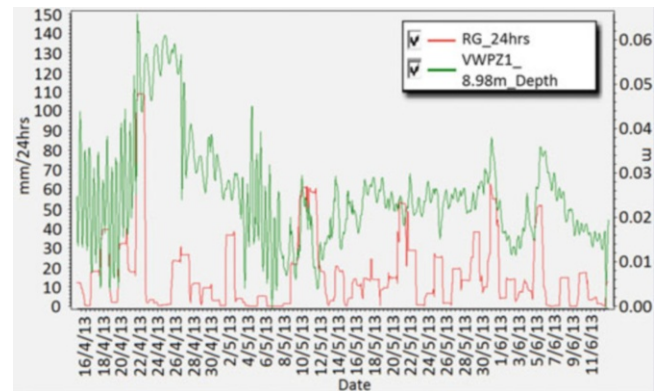


Fig. 10 Rolling 24-h rainfall and groundwater level

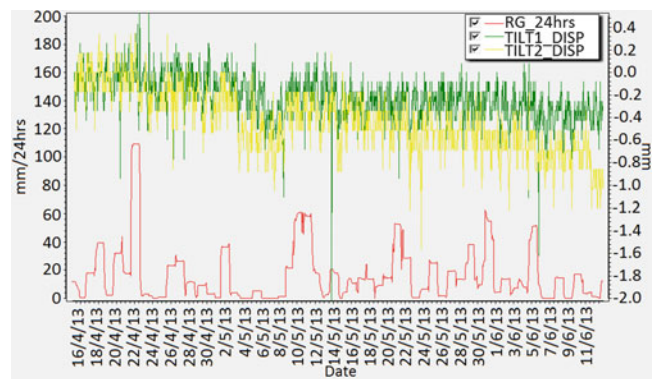


Fig. 11 Rolling 24-h rainfall and slope movement

Warning Criteria Based on Rainfall and Movement

Brand et al. (1984) reported on the work for understanding of the relationship between rainfall and man-made slope failures in Hong Kong. The number of casualties was very small unless the maximum hourly rainfall approached

Table 2 Proposed warning criteria for rainfall, water level and movement

| Parameters | Advisory | Watch | Warning |
|-------------------------|----------|-------|---------|
| Hourly RF (mm) | 30 | 45 | 60 |
| Rolling 24-h RF (mm) | 50 | 100 | 150 |
| Rise in water level (m) | 1 | 2 | 3 |
| Soil movement (mm) | 50 | 100 | 150 |

70 mm/h. In addition, Brand et al. (1984) found that a threshold rainfall of 175 mm in the preceding 24 h would warrant the issue of a landslide warning. The current landslip warning system in Hong Kong has gone further, as summarised by Chan and Pun (2004). It is based on the correlation between slope failure rate and maximum rolling 24-h rainfall. Its applicability to the present case may need further justification. However, it is still worthwhile to follow the approach, as rainfall-induced landslides are common in both places. When, for example, the rain gauge records rolling rainfall of more than 100 mm in 24 h, consultation between concerned authorities should begin.

The original intent of tiltmeter installation was to provide a triggering device for slope instability. However, as an indicator for road maintenance, such as surface cracks and damaged drainage channels, further use of the measured parameters is made. Warning criteria for slope movement as inferred from the tiltmeter measurements has been adopted. In addition, similar criteria have been set for the rise of water level to attract the attention of the authorities to the change in the groundwater regime. Table 2 summarises the proposed warning criteria for the site.

Web-Based Data Management System

The data collected on site are managed by the same web-based data management system. An individual system was prepared for each site and installed in the Public Works Departments of the federal and Sabah governments in Kuala Lumpur and Kota Kinabalu, respectively. The system is accessible to authorised users as a web service through the client software. It is important to note that the data of different nature are coming from geodetic, geotechnical and hydrogeological instrumentation, but they are directly handled by the same system. The system is a complete information hub that can manage projects gathering data of different types and analyse them together. This is particularly important for handling large-scale projects or managing several project sites with the same hub.

Summary and Conclusions

To reduce the likelihood and consequences of catastrophic collapse, understanding of slope behaviour is a pre-requisite. Such understanding is important to the two reported cases where the slope movement may not be stopped or it is not justifiable economically to construct civil engineering works to arrest it. As the slopes are part of the strategic roads, a risk management approach must be adopted to mitigate the risk faced by road users, and help the authorities make decisions.

Nowadays, instrumentation and computer information technologies have advanced considerably. Such technologies have found their growing importance in real-time slope monitoring. By incorporating appropriate slope activity models into the monitoring system, the measurement of slope performance and hydrogeological conditions will provide more insight into the underlying slope behaviour.

Just as importantly, the system permits threshold levels for different slope performance indices to be predefined and refined in the system as advanced warning criteria. Apart from conventional criteria making use of rainfall, groundwater levels and soil deformation/movement, landslide velocity is used as a warning indicator. In the end, the system becomes a slope safety monitoring system as well as a risk management tool, which provides real-time slope monitoring and early warning services.

Acknowledgments This paper is published with the permission of the Heads of the Public Works Department of the federal and Sabah state governments for use of the information on the slope monitoring projects.

References

- Brand EW, Premchitt J, Phillipson HB (1984) Relationship between rainfall and landslides in Hong Kong. In: Proceedings of 4th international symposium on landslides, Toronto, vol 1. pp 377–384
- Chan RKS, Pun WK (2004) Landslip warning system in Hong Kong. *Geotech Instrum News* 41:33–35
- CKC (Cawangan Kejuruteraan Cerun) (2009) National slope master plan 2009–2023. Cawangan Kejuruteraan Cerun, Malaysia
- Cruden DM, Varnes DJ (1996) Landslide types and processes. Landslides: investigation and mitigation. Transportation Research Board National Research Council, Special Report 247, Washington, DC, pp 36–75
- Fung WHT, Le Goff D, Krishnan S (2010) Instrumentation data monitoring system for slope safety monitoring in Malaysia. In: Proceedings of international conference on slope 2010 geotechnique and geosynthetics for slopes, 27–30 July 2010, Chiang Mai, Thailand, pp 309–315

- Jamaludin S, Jaafar KB, Abdullah CH, Mohamad A (2008) Landslide warning system for Mount Pass, Malaysia based on surface monitoring technique. In: Proceedings of international conference on management of landslide hazard in the Asia-Pacific region, 11–15 November 2008, Sendai, Japan, pp 354–364
- Jamaludin S, Abdullah CH, Jaafar KB (2012) Monitoring of slow moving landslide at 46th km of Simpang Pulai—Gua Musang Highway, Malaysia. In: Proceedings of 11th international symposium on landslides and 2nd North American symposium on landslides, 2–8 June 2012, Banff, Canada, vol 2. pp 1387–1392
- Leroueil S, Locat J, Vaunat J, Picarelli L, Faure R (1996) Geotechnical characterisation of slope movements. In: Proceedings of 7th international symposium on landslides. Trondheim, Norway, vol 1. pp 53–74
- Varnes DJ (1978) Slope movement types and processes. Landslides—analysis and control, National Academy of Sciences Transportation Research Board Special Report 176, Washington, DC, pp 11–33



A National Warning System for Rainfall-Induced Landslides in Slovenia

Marko Komac, Jasna Šinigoj, and Mateja Jemec Auflič

Abstract

In Slovenia intense short and less intense long-duration rainfall is a primary cause of shallow landslides that some estimates put at 10,000, or approximately one landslide per two square kilometres. These events impose a huge burden on local and state budgets, occasionally even taking lives. At least part of the damage (and the loss of lives) could be prevented with a reliable near real-time landslide hazard forecast system that would continuously draw from three data/model pillars: the precipitation forecast model, the landslide susceptibility model and the rainfall triggering values for landslide occurrence. Each of the three pillars brings some uncertainty to the landslide hazard forecast. A project was set up to forecast the possible occurrence of rainfall-induced landslides in Slovenia (acronym “Masprem”), tackling all three pillars, but focusing primarily on the rainfall triggering values. With the goal of an automated near real-time landslide hazard forecast that will eventually be promptly available online to the general public, the challenges of precipitation forecast data conversion and transfer between two servers, continuous forecast model development and serving the intermediate forecast results on the web were dealt with. The project set up a challenging task, to model the landslide hazard through time for the whole of Slovenia at a coarser scale and to model the same hazard for selected municipalities at a more detailed scale. The results and lessons learned will be presented in this paper.

Keywords

Landslide hazard • Early warning system • Rainfall • Slovenia

Introduction

Rainfall-induced landslides are the most frequent landslides in Slovenia. To tackle the problem from a prevention aspect, the project “Masprem” was financed by the Slovenian disaster relief office at the Ministry for defence.

The concept of the landslide hazard forecasting and warning system is based on three pillars—the landslide

susceptibility model, the precipitation forecast and the triggering values related to specific rocks/soils. While the first and the last are in the domain of geologists (and hence governed by the quality of geological data) the middle one is derived from the meteorological forecast models and is subject to weather modelling. As such it falls in the domain of atmospheric and hydraulic sciences. As to the landslide susceptibility and landslide rainfall triggering threshold modelling, there has been extensive research in the past in the area of Slovenia (Komac 2005, 2006, 2012; Komac and Ribičič 2006; Jemec Auflič and Komac 2011b; Žibret et al. 2012). Each of the three pillars has embedded uncertainties that individually and jointly pose big challenges for forecasting prediction accuracy. One of the goals of the

M. Komac (✉) • J. Šinigoj • M.J. Auflič
Geological Survey of Slovenia, Dimičeva ulica 14, 1000 Ljubljana, Slovenia
e-mail: marko.komac@geo-zs.si; jasna.sinigoj@geo-zs.si; mateja.jemec@geo-zs.si

project was also to assess the sources of these uncertainties and to propose future steps to minimise them.

Study Area and the Data Used

The warning system was developed for the whole of Slovenia, which spreads over 20,000 km². The elevation of Slovenian territory ranges from 0 to 2,864 m a.s.l., where the mountainous areas dominate in the western part of the country (Alps). Elevations gradually drop towards the eastern part of the country (Pannonian Basin) and with it also the terrain roughness gradually diminishes. The average annual precipitation ranges from below 900 mm in the eastern parts of the country to over 3,200 mm in the north-western parts (ARSO 2013). The precipitation peaks coincide with the Alpine area and the minimums with the eastern-laying plains and the southern coast. Wetter parts of Slovenia may occasionally have more than 1,400 mm of precipitation in 1 month (ARSO 2006) or even 510 mm in 1 day (ARSO 2013). In one of such event on 17th Nov 2000, a landslide occurred that in its second stage transformed into a devastating debris-flow, which killed seven people in the village of Log pod Mangartom (Mikoš et al. 2007).

Slovenian geology is very variable and consequentially landslides occur in almost all parts of the country. As rainfall-induced landslides prevail in Slovenia, the relation between the triggering threshold values of rainfall and the occurrence of landslides in a specific rock/soil needed to be assessed in order to relate the landslide susceptibility and precipitation models.

The original landslide susceptibility model was developed in GIS with a pixel resolution of 25 m (Komac and Ribičič 2006), while the updated version had a pixel resolution of 12.5 m. According to the later model (Komac et al. 2011) almost 30 % of the Slovenian terrain is susceptible to landsliding. Triggering values were calculated for the whole of Slovenia (Komac 2005) and for three separate storms, in 2007, 2010 and 2012 that had local effects (Jemec Auflič and Komac 2011a, b; Jemec Auflič et al. 2013; Komac and Jemec Auflič 2013). The precipitation data is acquired on a daily basis from the Environmental Agency of the Republic of Slovenia (EARS) via the FTP protocol (Komac et al. 2013). To validate the final landslide hazard prediction models, the precipitation data for the period 28th October to 5th November 2012 were acquired from the archive of the EARS. Unfortunately, no earlier data exists, so the validation for a longer period of antecedent rainfall was not possible.

What also needs to be emphasised at this point is that the uncertainties related to the three types of input data are to some extent different. For the input data involved in the final landslide hazard forecasting system, an approach was adopted in which landslide susceptibility model and

triggering values data were treated as static components and the precipitation forecast data as a dynamic component of the system.

Methods

The conceptual diagram of the landslide hazard forecasting system is shown in Fig. 1. The three components that represent the three pillars of the landslide hazard forecasting system are denoted with an asterisk. As it is shown in Fig. 1, each final landslide forecast model is derived in two steps. First the landslide triggering probability due to precipitation (P_{LTR}) is calculated by combining the forecasted (and ideally nowcasted) precipitation (R_F) and the spatially related triggering values. In the second step the landslide susceptibility (LSS) is combined with the landslide triggering probability due to rainfall (P_{LTR}). The result is the landslide hazard forecast probability (P_{LSH}) model.

The three input models were combined using the following statements:

IF (([forecasted precipitation value] + [antecedent rainfall value D0 (nowcasted value)]) > [rainfall triggering value D0]) OR (([forecasted precipitation value] + [antecedent rainfall value D2 (nowcasted value)]) > [rainfall triggering value D2]) OR (([forecasted precipitation value] + [antecedent rainfall value D5 (nowcasted value)]) > [rainfall triggering value D5]) . . .

$$\begin{aligned} &\text{AND [landslide susceptibility value] = 1 - 5} \\ &\text{THEN} \\ &[\text{forecasted landslide hazard value}] = 1 - 5. \end{aligned} \quad (1)$$

The focus will be on presenting the final steps of the derivation of the landslide hazard forecast model, while methods of deriving the three pillars, being an important part of the system, will be briefly described below, followed by a more detailed description of the two steps for deriving the landslide hazard forecast model.

The landslide susceptibility model was adopted from Komac et al. (2011), where the model values were classified into six classes—none/negligible (0), very low (1), low (2), moderate (3), high (4), and very high (5), where for each cell (x, y) the susceptibility could be described as $LSS(x, y)$.

Triggering values were derived from two separate approaches. In the first an overlay of 29 different engineering geological units (rock/soil types) and the data on maximum 24-h precipitation with the return period of 100 years (ten classes of intensities; class span was 30 mm) was performed and the number of landslides statistically compared against the size of these unique areas. The second approach was adopted from Komac and Jemec Auflič (2013) and was rainfall-event oriented. Here analyses of

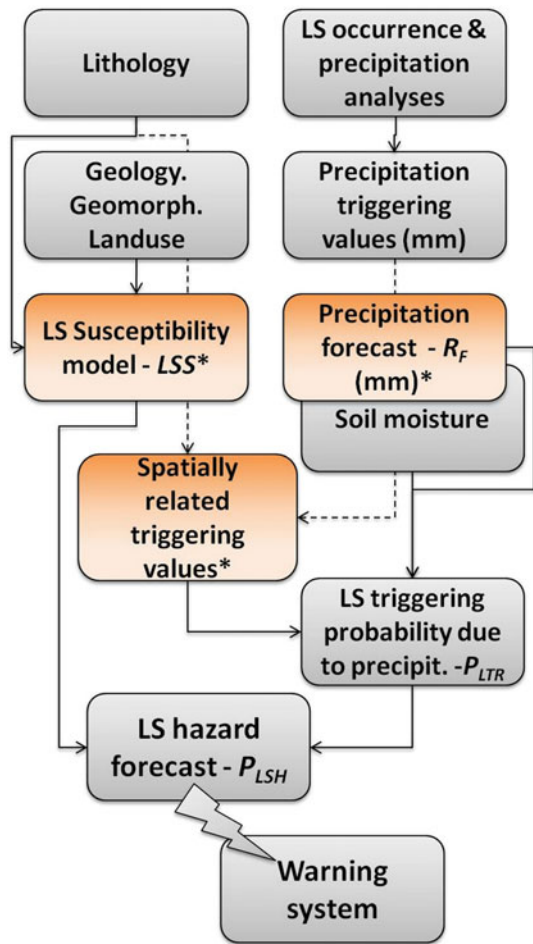


Fig. 1 Conceptual model for modelling the landslide (LS) hazard forecasting system

the landslide triggering values were compared against the landslide occurrence and its duration. The main question was what amount of rainfall in relation to duration saturates rock/soil to the point of triggering the landslide?

Different authors used different periods of antecedent rainfall; Kim et al. (1992) used a 3-day period, Crozier (1999) and Glade et al. (2000) used a 10-day period, and Aleotti (2004) chose 7, 10, and 15 days, Chleborad (2003) divided an 18-day period into a 3-day rainfall event with 15 days of antecedent rainfall. For this research, the average daily rainfall amounts on the day of the landslide event and for 2, 5, 10, 15, 20, 25 and 30 days prior to the landslide occurrence were analysed for every rock/soil type to assess the amount of rainfall that represents the threshold for the landsliding process to start. The landslide hazard forecasting system will check whether the cumulative amount of forecasted precipitation and already fallen rain exceeds the threshold values each time it calculates the forecast and based on this information the system will predict the landslide hazard.

Table 1 shows examples of the analyses results of the triggering values for 24-h (minimum and maximum triggering values) and for 48-h rainfall, and the average daily precipitation according to the duration of the considered antecedent period (D0—day of the event; D2—average of the last 2 days prior to the landslide event, etc.) for some of the rock/soil types (out of 29 altogether). All values of rainfall are given in mm.

The rainfall forecast models for the 24-h period (Aladin-SI) were (and still are) calculated at the EARS and the methods for deriving these models are beyond of the scope of this paper and hence won't be presented here.

To account for the potential error in the triggering thresholds gradual transition between the rainfall values below which the landslide triggering probability due to rainfall (P_{LTR}) is negligible and the landslide triggering threshold (above which landslides occur with much higher probability) the fuzzy logic (Zadeh 1965) approach was used. A similar approach has been proposed by White et al. (1996). Below a certain value (R_{Tmin}) the probability (membership value) of the event triggering is (almost) none (0 % or 0), while above a certain value (R_{Tmax}) the probability of the event triggering is (almost) certain (100 % or 1). In between the two values, the probability of triggering rises from 0 to 1, depending upon the membership function that defines the transition. The difference between the R_{Tmin} and R_{Tmax} was set to 30 mm to account for the classification error. For each location (cell) x, y it can be stated that:

$$\begin{aligned}
 & \text{IF } R_{sum}(x, y) > R_{Tmax}(x, y) \text{ THEN } P_{LTR} = 1 \text{ OR} \\
 & \text{IF } R_{sum}(x, y) < R_{Tmin}(x, y) \text{ THEN } P_{LTR} = 0 \text{ OR} \\
 & \text{IF } R_{Tmin}(x, y) \leq R_{sum}(x, y) \leq R_{Tmax}(x, y) \text{ THEN } P_{LTR} = (0, 1),
 \end{aligned}
 \tag{2}$$

$$\text{and } R_{sum}(x, y) = R_F(x, y) + R_A(x, y).
 \tag{3}$$

The $R_A(x, y)$ is the cumulative amount of the antecedent rainfall in D days ($D = 0-t$) prior the potential landslide occurrence for the cell x, y , where the amount for a specific day represents the rainfall for the 24-h period starting at midnight UTC for the previous day. The $R_F(x, y)$ represents the forecasted rainfall amount for the cell x, y and it was acquired from the Aladin-SI models, and P_{LTR} represents the landslide triggering probability due to rainfall. The gradual transition (membership function) between membership values was linear and was defined as:

$$P_{LTR}(x, y) | R_{Tmin}(x, y) \leq R_{sum}(x, y) \leq R_{Tmax}(x, y) | = \frac{(R_{sum}(x, y) - R_{Tmin}(x, y))}{(R_{Tmax}(x, y) - R_{Tmin}(x, y)) + 30}
 \tag{4}$$

Eight models were produced, one for every day that preceded the major triggering event on 5th Nov 2012. Each of the models cumulatively comprised the rainfall amounts

Table 1 Analyses results of the triggering values for some of the analysed rock/soil types (Rock/soil) for the 24-h (24-h min—minimum; 24-h max—maximum triggering values) and 48-h rainfall (48-h), and the average daily precipitation according to the duration of the considered antecedent period (D0—day of the event; D2—average of the last 2 days prior to the landslide event. . . D30—average of the last 30 days prior to the landslide event)

| # | Rock/soil | 24-h min | 24-h max | 48-h | D30 | D25 | D20 | D15 | D10 | D5 | D2 | D0 |
|----|---------------------------------------|----------|----------|---------|-----|-----|------|------|------|------|------|------|
| 1 | Mainly clayey soils | 90 | 120 | – | 4.3 | 4.9 | 5.7 | 7.5 | 11.3 | 10.2 | 25.6 | 47 |
| 5 | Gravelly soils with clay component | 150 | 180 | 150–180 | 7.2 | 8.2 | 8.5 | 9.6 | 11.7 | 7.4 | 16.3 | 65.6 |
| 6 | Scree deposits, glacialigenic diamics | 210 | 240 | 270–300 | 7.2 | 7.4 | 8.0 | 9.3 | 10.8 | 13.1 | 25.5 | 56.0 |
| 13 | Alternation of different soft rocks | 60 | 90 | <150 | 6.7 | 7.7 | 8.3 | 9.7 | 12.5 | 14.5 | 27.5 | 44.4 |
| 15 | Shales with other rocks | 90 | 150 | <150 | 8.2 | 9.6 | 10.4 | 12.0 | 15.3 | 18.6 | 33.3 | 55.5 |
| 22 | Limestones with marls | 60 | 150 | <150 | 6.2 | 6.6 | 7.3 | 8.7 | 11.0 | 12.3 | 29.4 | 41.5 |
| 27 | Keratophyre, diabases. . . | 60 | 150 | <150 | 7.6 | 8.5 | 9.4 | 10.0 | 11.2 | 13.8 | 21.9 | 77.6 |

for the whole period, from including 1 day prior to the event to the day prior to the event that it was calculated for (i.e. model for the fifth day prior to the event included cumulative amounts of precipitation for all 5 days prior to the event, except for the precipitation on the day of the event). At the time of the testing these amounts represented a simulated in-situ situation and will be in the future derived from the systematically calculated daily models prepared at EARS. In addition to this cumulative amount of the actual rainfall, a forecasted value (rainfall amount; R_F) was added from the Aladin-SI model, as it would be when the landslide hazard forecasting system will be fully operational. According to (2) and (4), calculated values of the triggering probability between R_{Tmin} and R_{Tmax} ranged continuously from 0 to 1 and were for further steps rounded to the first decimal and hence classified into 11 different values (0, 0.1, 0.2 . . . 1).

Next the landslide triggering probability due to rainfall (P_{LTR}) was calculated, the forecasted landslide hazard probability at a given cell $P_{LSH}(x, y)$ in a given period (0, t; t = 1–8 days) was calculated using the following equation:

$$P_{LSH}(x, y)(o, t) = P_{LTR}(x, y)(o, t) \times LSS(x, y). \quad (5)$$

The matrix of all $P_{LSH}(x, y)$ combinations is shown in Table 2. After the classification of the $P_{LSH}(x, y)$ values, the discrete values ranged from 1 to 5 and the pertinent descriptions were assigned to them; very low for 1 (values 0–1), low for 2 (values 1–2), moderate for 3 (values 2–3), high for 4 (values 3–4), and very high for 5 (values 4–5).

The quality of the forecasted landslide hazard probability prediction (P_{LSH}) was tested only for the 8 days period prior to the major landslide event (t = 0, 8 days) that occurred on 5th November 2012, as no earlier precipitation data was available. Figure 2 shows the landslide hazard probability prediction model for 5th Nov 2012, based on the input model for the 8-days precipitation period (P_{LTR} for 8 days).

All eight developed landslide hazard probability models were overlaid with the 352 landslides that occurred on the

Table 2 The condition matrix of all possible combinations of the landslide triggering probability due to rainfall (P_{LTR}) and the landslide susceptibility (LSS), the first being presented in the first columns and the second being presented in the first row

| $P_{LTR} \backslash LSS$ | 1 | 2 | 3 | 4 | 5 |
|--------------------------|-----|-----|-----|-----|-----|
| 0 (0) | 0 | 0 | 0 | 0 | 0 |
| 1 (0–0.1) | 0.1 | 0.2 | 0.3 | 0.4 | 0.5 |
| 2 (0.1–0.2) | 0.2 | 0.4 | 0.6 | 0.8 | 1 |
| 3 (0.2–0.3) | 0.3 | 0.6 | 0.9 | 1.2 | 1.5 |
| 4 (0.3–0.4) | 0.4 | 0.8 | 1.2 | 1.6 | 2 |
| 5 (0.4–0.5) | 0.5 | 1 | 1.5 | 2 | 2.5 |
| 6 (0.5–0.6) | 0.6 | 1.2 | 1.8 | 2.4 | 3 |
| 7 (0.6–0.7) | 0.7 | 1.4 | 2.1 | 2.8 | 3.5 |
| 8 (0.7–0.8) | 0.8 | 1.6 | 2.4 | 3.2 | 4 |
| 9 (0.8–0.9) | 0.9 | 1.8 | 2.7 | 3.6 | 4.5 |
| 10 (0.9–1) | 1 | 2 | 3 | 4 | 5 |

same day (5th November 2013) and the membership to all five hazard probability classes (plus additional hazard probability class) of the P_{LSH} models was assessed.

Results and Discussion

As expected, the landslide triggering analysis results in Table 1 show the increase of threshold as the duration of the considered antecedent period shortens. The values of the rainfall on the day of the landslide event (column D0 in Table 1) are lower than the statistically derived triggering values for a 24-h period (column 24-h min in Table 1), on average three times.

The cross analysis of the distribution of landslides that occurred on 5th November 2012 with the six hazard probability classes of the eight P_{LSH} models showed that the best prediction results were achieved with models that included the longer period of antecedent rainfall, namely the models for 7 and 8 days prior to the event. Still, in all models 35

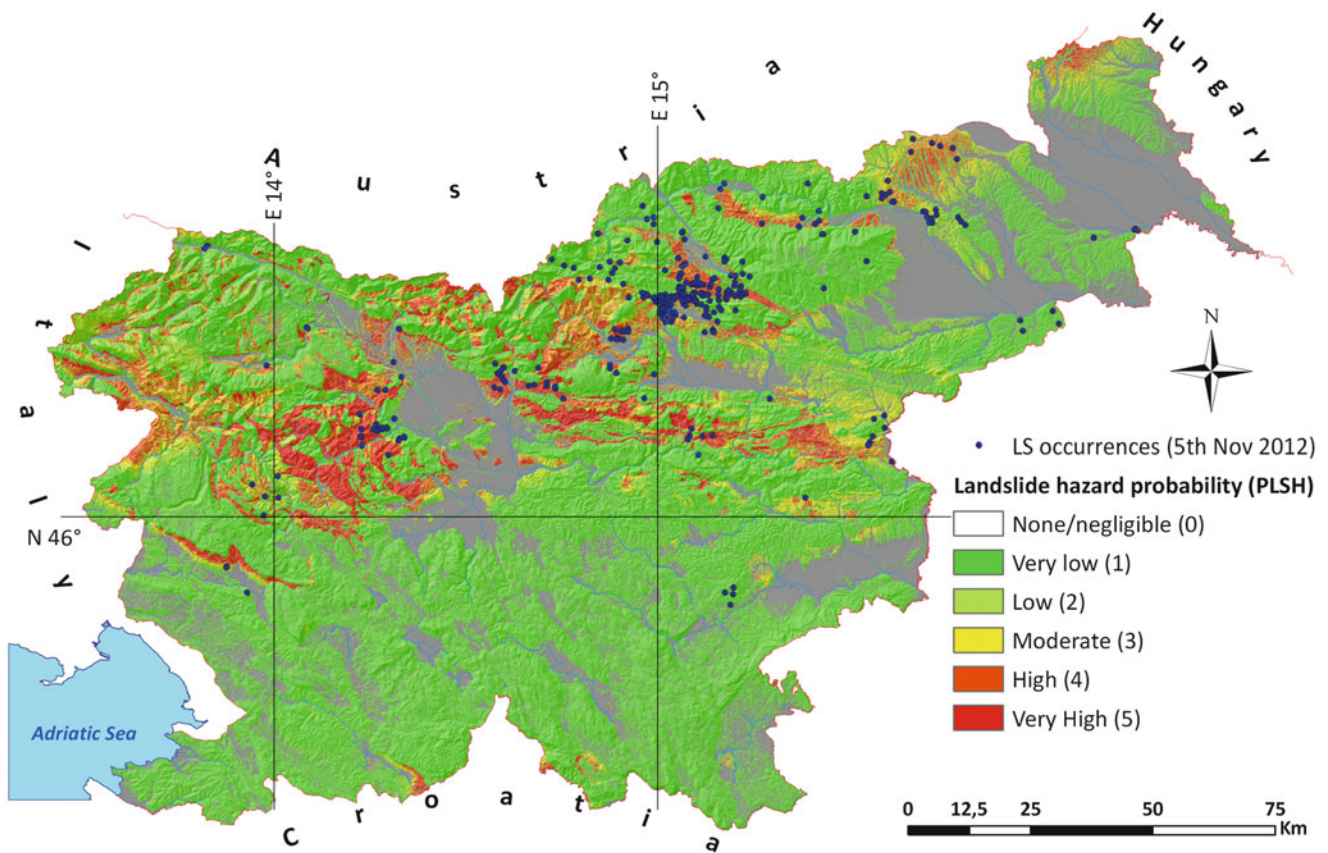


Fig. 2 Landslide hazard probability model (PLSH_8) for the area of Slovenia on 5 November 2012

(9.9 %) landslides occurred in areas where they shouldn't occur. This error is most likely a result of the generalisation of the digital elevation model and/or the geological map.

Landslide Warning System

After the calculation of the most plausible landslide hazard probability model, this has to be relayed to the end-user, whether the decision makers or general public. The most suitable tool for communication is the internet and for this purpose an interface/module was developed using open source software. Programming was performed in Java and the results were transformed into the Web Map Service standard, used for displaying GIS related raster images/data, and put on the internet via web application.

Conclusions

The development of a landslide hazard probability model based on the combination of landslide susceptibility properties and the landslide triggering probability due to rainfall was presented. Such an effort represents a huge

challenge from both the research and technical aspects. Significant progress has been made in the area of minimising input data uncertainties, yet much of this goal still remains to be tackled in future endeavours.

The landslide susceptibility model has the lowest uncertainty; the rainfall triggering values have limited (a band) uncertainty that is related to the fuzzy transition between the stable and the unstable state of the slope/material. The highest embedded uncertainty is in the precipitation forecast data and this is reflected also in the probability models derived from these data.

Inclusion of nowcasting in the forecasting models could considerably improve the landslide hazard warning system, hence much work for the system optimisation is still needed. This aspect will be dealt with in future system calibrations.

Acknowledgments The authors would like to thank the Administration of the Republic of Slovenia for civil protection and disaster relief and Ministry of Defence of the Republic of Slovenia for financing the project MasPrem, and DG Information Society at the European Commission for financing the project InGeoClouds (Ref. 297300), within which all presented work was performed. Authors would like to thank colleagues with which they conducted the research and worked on the project.

References

- Aleotti P (2004) A warning system for rainfall-induced shallow failures. *Eng Geol* 73:247–265
- ARSO (2006) Podnebne razmere v Sloveniji (obdobje 1971–2000) (in Slovene). Environmental Agency, Of the Republic of Slovenia, Ljubljana, 28 p. ISBN unknown
- ARSO (2013) Map of maximum 24-h rainfall with a 100 years return period (in mm/24 h) for the period of 1961–2000. Ministry for Environment and Spatial Planning, Environmental Agency of the Republic of Slovenia. <http://meteo.arso.gov.si/met/en/app/webmet/>. Last accessed 5 Aug 2013
- Chleborad AF (2003) Preliminary evaluation of a precipitation threshold for anticipating the occurrence of landslides in the Seattle, Washington, Area. US Geological Survey. Open-File Report 03–463. <http://pubs.usgs.gov/of/2003/ofr-03-463/ofr-03-0463.html>. Last accessed 17 Mar 2013
- Crozier MJ (1999) Prediction of rainfall-triggered landslides: a test of the antecedent water status model. *Earth Surf Process Landf* 24:825–833
- Glade T, Crozier MJ, Smith P (2000) Applying probability determination to refine landslide-triggering rainfall thresholds using an empirical antecedent daily rainfall model. *Pure Appl Geophys* 157 (6–8):1059–1079
- Jemec Auflič M, Komac M (2011a) Rainfall patterns for shallow landsliding in perialpine Slovenia. *Nat Hazards* 67(3):1011–1023
- Jemec Auflič M, Komac M (2011b) Vpliv predhodnih padavin na pojavljanje plazov. 20th meeting of Slovenian geologists, November 2011, Ljubljana, Slovenia, pp 39–42
- Jemec Auflič M, Peternel T, Komac M (2013) Sprožilne padavine in nastanek zemeljskih plazov: primer padavinski dogodek 4. in 5. novembra 2012. 21st meeting of Slovenian geologists, November 2012, Ljubljana, Slovenia, pp 47–51
- Kim SK, Hong WP, Kim YM (1992) Prediction of rainfall-triggered landslides in Korea. *Landslides*. In: Proceedings of the sixth international symposium on landslides, 10–14 February 1992, Christchurch, New Zealand, vol 2. pp 989–994
- Komac M (2005) Rainstorms as a landslide-triggering factor in Slovenia. *Geologija* 48(2):263–279
- Komac M (2006) A landslide susceptibility model using the analytical hierarchy process method and multivariate statistics in perialpine Slovenia. *Geomorphology* 74:17–28
- Komac M (2012) Regional landslide susceptibility model using the Monte Carlo approach—the case of Slovenia. *Geol Q* 56(1):41–54
- Komac M, Jemec Auflič M (2013) Sistem zgodnjega opozarjanja za primer nevarnosti proženja zemeljskih plazov—MASPREM. Razvoj dinamičnega modela za zgodnje opozarjanje za primer nevarnosti proženja zemeljskih plazov v odvisnosti od napovedane količine padavin (in Slovene). Geological Survey of Slovenia, Ljubljana, 27 p, ISBN unknown
- Komac M, Ribičič M (2006) Landslide susceptibility map of Slovenia at scale 1:250.000. *Geologija* 49(2):295–309. doi:10.5474/geologija.2006.022
- Komac M, Šinigoj J, Kumelj Š, Jemec Auflič M, Bavec M, Čarman M, Hribernik K, Krivic M, Požar M, Podboj M (2011) Sistem zgodnjega opozarjanja za primer nevarnosti proženja zemeljskih plazov—MASPREM. Poročilo ob prvem mejniku (in Slovene). Geological Survey of Slovenia, Ljubljana, 39 p
- Komac M, Šinigoj J, Jemec Auflič M, Čarman M, Jež J, Peternel T, Krivic M, Požar M, Podboj M, Hribernik K, Krajnik M (2013) Sistem zgodnjega opozarjanja za primer nevarnosti proženja zemeljskih plazov—MASPREM. Poročilo ob petem mejniku (in Slovene). Geological Survey of Slovenia, Ljubljana, 34 p
- Mikoš M, Fazarinc R, Majes B (2007) Delineation of risk area in Log pod Mangrtom due to debris flows from the Stože landslide. *Acta Geogr Slov* 47(2):171–198
- White ID, Mottershead DN, Harrison J (1996) Environmental systems. Chapman and Hall, London, 616 p
- Zadeh LA (1965) Fuzzy sets. *Inf Control* 8(3):338–353
- Žibret G, Komac M, Jemec Auflič M (2012) PSInSAR displacements related to soil creep and rainfall intensities in the Alpine foreland of western Slovenia. *Geomorphology* 175–176:107–114



Monitoring of Critical Himalayan Landslides and Design of Preventive Measures

Kishor Kumar, Pulikanti Subramanya Prasad, Anil Kathait, and Indervir Negi

Abstract

The entire Himalayan road network suffers extensive damage from a large number of landslides of different shapes and sizes. A large number of landslides on each highway have occurred repeatedly during every year for many decades, causing extensive risk to life of commuters, loss of revenue from direct and indirect losses and hardship for the people, thus influencing the socio-economic conditions of the region. One of the important highways of the country, which connects the north western Himalayan state of Uttarakhand to rest of the country, suffers from large numbers of such landslides. Two of the most critical landslides have been selected as pacesetter examples for investigation, monitoring and prevention. These two landslides have been monitored using a very simple system consisting of specially designed grooved steel pedestals, total station and DGPS (Differential Global Positioning System). The results of monitoring have encouraged utilising the same system for other Himalayan landslides of a recurring nature instead of investing in heavy-duty, costly and sophisticated instrumentation. This paper gives a detailed account of two landslides and the monitoring processes followed in a scheme of remedial measures for their long-term prevention.

Keywords

Landslides • Instrumentation • Monitoring • Remediation

Introduction

The Himalaya, the most impressive and fascinating mountain chain in the world belongs to all human beings because of its divine connection with the whole of the world. Its peculiar geo-environmental characteristics, its varied flora and fauna with high medicinal values, its dynamic geological history, high mountains, glaciers, holy rivers, and active denudation processes make it a fragile land mass. The Himalaya region is often in news because of repeated disastrous events. We often blame its fragile geo-environmental setup for these repeated disasters and not the humans who invade onto its sensitive

natural setting through their unmindful development. The construction of roads and highways is one such activity which can be held responsible for repeated devastation due to landslides on and off the roads.

All the hilly states in Himalayan region are severely affected by road construction. On an average every kilometre of road has at least two landslides and Himalayan roads extend over 60,000 km. Every rainy season brings a series of new landslides and also recurrence of old ones, leaving trails of devastation each time they occur. There is no warning required in the areas that experience landslides because they are a regular phenomenon during every rainy season. However, it is a common practice to react after the disaster rather than taking a proactive approach to pre-disaster planning. By following the normally accepted practice, the country loses many lives and a huge sum of revenue while only partly restoring the works. As a result,

K. Kumar (✉) • P.S. Prasad • A. Kathait • I. Negi
CSIR-Central Road Research Institute, New Delhi 110025, India
e-mail: kishornhrm@gmail.com; pulikanti@gmail.com;
kathaitanil@gmail.com; inder.ivgeo@gmail.com

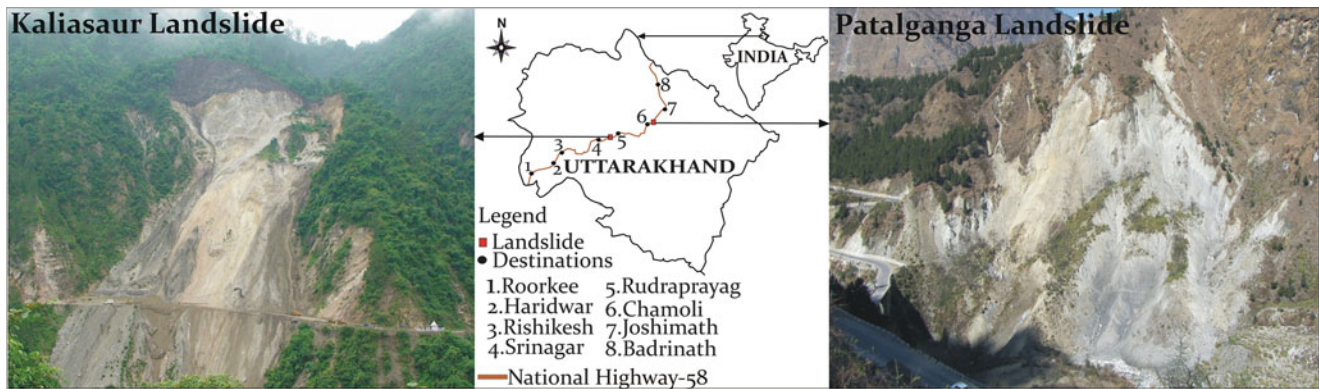


Fig. 1 The Kaliasaur and Patalganga landslides and their location on NH-58

the communications routes, which are the essential life lines during any disaster, may be blocked during much required rescue and rehabilitation efforts.

The high intensity cloudbursts that led to the flash floods on June 15 to June 18, 2013, in many part of the north western Himalayan region were unprecedented. According to the official estimates around 5,000 plus people have been killed and property worth 488 million dollars has been destroyed. It was observed that older critical landslides which had been left unattended together with newly generated landslides, caused great hindrance in the rescue and rehabilitation process. There are a number of such landslides on various highways of the country, which need to be remediated and their behaviour continuously monitored. In this paper, two of such landslides, the Kaliasaur and Patalganga landslides (Fig. 1) which are over five decades old, are discussed to showcase examples of cost-effective and accurate monitoring for an early warning of landslides which could be affordable for all the landslides.

Kaliasaur Landslide

The Kaliasaur slide extends for 100 m along the highway, 353 m up to the active crown and 152 m up to the toe, covering an area of 50,500 m². The historical records of this landslide since 1920 have widely been published (Bhandari 1987; Kumar et al. 2008; Kimothi et al. 2010; CRRRI 2010; Kumar et al. 2011a, b, 2012, 2013; Negi et al. 2012). Though, landsliding has recurred during every rainy season, larger magnitude sliding occurred in the years 1969, 1984, 2010 and 2013. In 2010, the slide blocked the highway intermittently for about 5 months. The loss of at least two human lives was reported. The extra cost of the use of

alternate routes by the small and heavy vehicles is estimated as 16.4 million (approx.) Indian rupees, only for detouring during the 45 days of blockage, not to mention other financial losses. There is a lack of records on losses incurred, however, the records of sliding and road blockage over last five decades indicate a huge sum of revenue lost, to the tune of several hundred billion Indian rupees spent on repeated partial restoration.

The morphological changes on the slope of the slide, particularly since 1984, indicate that it was retrogressive until 2008, and thereafter transformed into a progressive mode. The slope material consists of quartzite, metavolcanic and slate rocks of moderate to highly fragile nature. The quartzite rocks are highly crushed in the cliff area and form gouge material. The extent of fracturing is probably due to an active tectonic past (CRRRI 2010). Topographic expressions of faults are observed all through the landslide. North Almora thrust separates the Chandpur phyllites from the Quartzites (Singh and Goel 1999) located adjacent to this area, while Kaliasaur fault and many other minor faults are located within or across the landslide boundary (CRRRI 2010). The alternation of slate and intrusions of metavolcanic rocks with the jointed quartzite have also played a major role in continuous sliding. The softer slate and metavolcanic rocks quickly weather and erode, while jointed quartzite blocks lose support and subsequently fail. During the dry season, the slide has a quiet and stable slope because the debris material on the slope becomes very hard, while during rains it becomes saturated and flows down, leaving numerous deep rills and gullies on the slope. These gullies subsequently become deeper and scoured due to increasing water flow during heavy rain and on failing form numerous small scars on the slope. This process was earlier confined within the slide boundary and crown area, but now all through boundary such gullies and scars are visible.

Monitoring Outcomes

The landslide is still active and causes considerable damage to the highway and risk to commuters. To measure the movement of the landslide, 75 specially designed steel pedestals have been installed in preselected locations within the slide body and adjacent area. Their original position was recorded using DGPS (Differential Global Positioning System) and TS (Total Station). Subsequent monitoring with DGPS and TS was carried out. It was noticed that the pedestals installed within the slide boundary did not move much except at a few locations. These locations were on the loose debris mass, and rest of the pedestals that have shown movement were located near and around the crown, indicating movement only above the crown (CRRRI 2010). Out of 75 pedestals, only a few have shown a significant amount of movement (Fig. 2 and Table 1). The maximum movement in the landslide recorded was 3.78 m and minimum is 0.73 m (after three sessions of monitoring).

Monitoring results, when matched with field conditions, indicated surficial movement from the crown part. These results coincide with the activity of the slide observed mostly from above the crown area. At that stage sufficient warning was passed on to take immediate measures before the coming monsoon season.

Unfortunately, the measures could not be taken and the slide was reactivated in the month of July-September 2010, resulting in damage to the road and intermittently sliding for 5 months, including the loss of several lives.

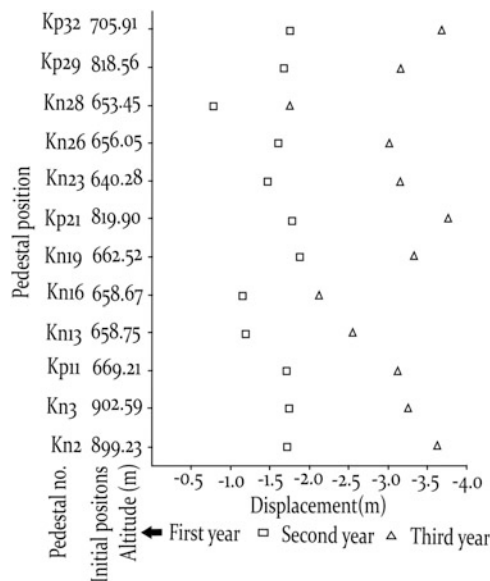


Fig. 2 Pedestals showing significant displacement after monitoring result

Table 1 Pedestals showing significant displacement on the slope

| Pedestal No. | Initial position | Second position/ Displacement (m) | Third position/ Displacement (m) |
|--------------|------------------|-----------------------------------|----------------------------------|
| Kn 2 | 899.23 | 897.51/1.72 | 895.58/1.93 |
| Kn 3 | 902.59 | 900.86/1.73 | 899.34/1.52 |
| Kp 11 | 669.21 | 667.52/1.69 | 666.09/1.43 |
| Kn 13 | 658.75 | 657.57/1.18 | 656.19/1.38 |
| Kn 16 | 658.67 | 657.53/1.14 | 656.58/0.95 |
| Kn 19 | 662.52 | 660.65/1.87 | 659.17/1.48 |
| Kp 21 | 819.90 | 818.12/1.78 | 816.12/2.00 |
| Kn 23 | 640.28 | 638.80/1.48 | 637.11/1.69 |
| Kn 26 | 656.05 | 654.44/1.61 | 653.03/1.41 |
| Kn 28 | 653.45 | 652.68/0.77 | 651.71/0.97 |
| Kp 29 | 818.56 | 816.89/1.67 | 815.41/1.48 |
| Kp 32 | 705.91 | 704.17/1.74 | 702.22/1.95 |

Remedial Measure Suggested Before Reactivation

The historical background of the landslide indicated the initial triggering factor was intense toe erosion during the rainy season by the river Alaknanda. As a usual practice, after every landslide incident and damage to the highway, the same restoration work was carried out; instead of strengthening the downhill side slope the uphill slope was cut. This practice was repeated almost every time the road was damaged. At present, the cutting of the toe by the river has become irrelevant because the height of the road has increased many times more than during its initial construction. The crown part is now the main component which slides every time the heavy rain falls. And, every time huge debris slides are generated and damage the road. Therefore, the first priority to prevent the slide is by stabilizing the unstable slope. But due to the exorbitant cost, as well as difficulty in implementing the measures, measures have been proposed that, instead of preventing slides, protect the road from damage to avoid repeated cutting of the uphill slope. This could have resulted in stabilizing the entire slope in subsequent times. In view of that, the following measures have been suggested, shown in Fig. 3 (CRRRI 2010):

1. To cover the slope at the crest part with a steel rope net of aperture size 300 mm × 300 mm to prevent material from sliding, rolling or falling on the slope downhill.
2. Rockfall barriers/gabion walls have been proposed to collect the boulders coming through the steel rope net.
3. In addition, it was proposed to compact the slide debris on the slope in-situ along with steeped gabion walls of 2 m/1.5 m/1 m with an option of drainage.
4. A similar gabion structure was to be applied for the toe to the road level.

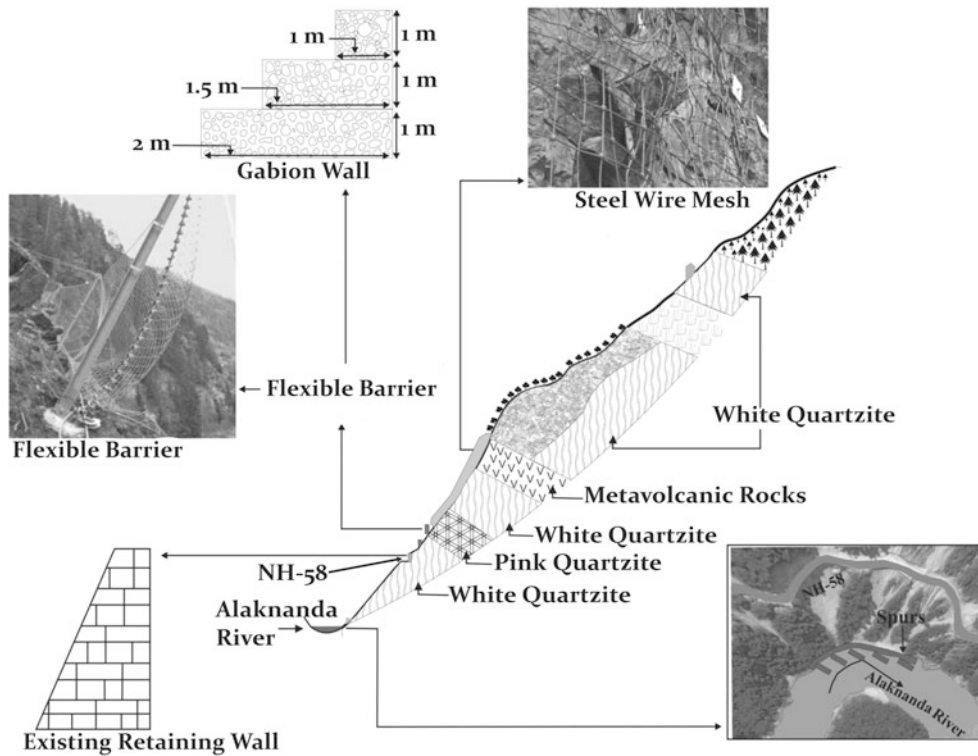


Fig. 3 A scheme of remedial measures for stabilisation of slope

Patalganga Landslide

Patalganga is a moderate landslide, located at 460.2 km on NH-58, on the right bank of Patalganga River. It extended for about 390 m in length and 320 m in width covering an area of 79,370 m². In the year 2005 it advanced to 457 m in length, 338 m in width and in area 109,121 m² (CRRRI 2012). The slope material of the landslide area is composed of recent sediments, largely assorted moraine with a steep slope angle (80°–90°). The flash flood of July 1970 in Patalganga and subsequently in the Alaknanda River, which caused loss of life and property of an unprecedented magnitude, was a rare catastrophe for the Himalayan region (Bhandari 2003). It was during this catastrophic event this slide was developed at a location of a small hamlet, which was completely washed away. Since then the landslide has occurred repeatedly during every monsoon. At the toe of the slide there is a narrow gorge over which a bridge connects the NH-58. The slide has the potential to block the narrow gorge and form an artificial dam which on breaching may wash away the bridge and recreate the historical flash flood conditions of 1970. The landslide blocked the River Alaknanda, forming a 45 m high dam within a very short span of time. On breaching, the dam created havoc, destroying everything in its path for 100 km downstream of Alaknanda. In view of this, the slide was assigned for

monitoring. The recurrence, although of low magnitude, reminded the public about the 1970 tragedy when Patalganga was blocked at a narrow constriction and became the cause of the fateful event of 1970.

Monitoring Outcomes

In the year 2008, 65 specially designed steel pedestals were installed in the landslide body and their original position was fixed using DGPS (Differential Global Positioning System). The pedestals were monitored before and after the monsoon seasons to find out the degree of displacement. The slide was monitored three times. The movement of the pedestals is attributed to the movement of the blocks (formed by dilatational and shear fractures in the main body) resting on the slip surfaces on which pedestals were installed. Monitoring of Patalganga landslide shows that it has a shallow kind of movement. Current monitoring of the slide reveals that the movement ranges from 0.31 to 8.68 m (Fig. 4 and Table 2). Movement of lower magnitude has been observed in the upper parts of the landslide area, whereas higher magnitude movement has been recorded in the lower parts of landslide area.

It shows that erosion occurs in the landslide toe parts during rainy season. Most of the movement of the pedestals trends towards SW and WNW directions.

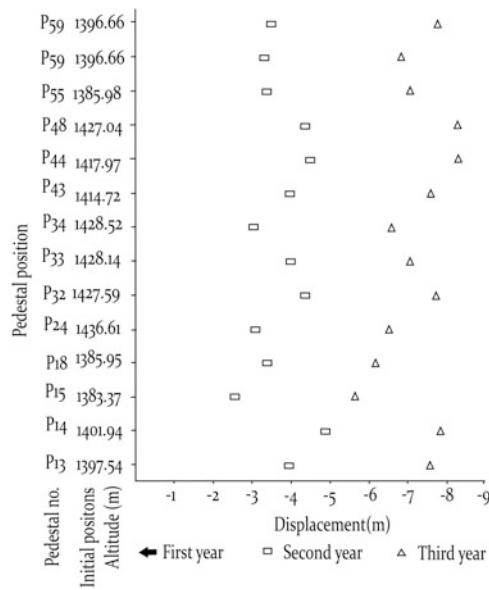


Fig. 4 Pedestals showing significant displacement after monitoring result

Table 2 Pedestals showing significant movement on the slope

| Pedestal No. | Initial position | Second position/ Displacement (m) | Third position/ Displacement (m) |
|--------------|------------------|--------------------------------------|-------------------------------------|
| P13 | 1,397.54 | 1,393.56/3.98 | 1,389.99/3.58 |
| P14 | 1,401.94 | 1,397.01/4.94 | 1,394.07/2.94 |
| P15 | 1,383.37 | 1,380.86/2.51 | 1,377.77/3.09 |
| P18 | 1,385.95 | 1,382.55/3.40 | 1,379.80/2.75 |
| P24 | 1,436.61 | 1,433.52/3.09 | 1,430.11/3.41 |
| P32 | 1,427.59 | 1,423.26/4.34 | 1,419.90/3.36 |
| P33 | 1,428.14 | 1,424.23/3.91 | 1,421.09/3.13 |
| P34 | 1,428.52 | 1,425.55/2.98 | 1,422/3.55 |
| P43 | 1,414.72 | 1,410.77/3.95 | 1,407.22/3.55 |
| P44 | 1,417.97 | 1,413.54/4.43 | 1,409.70/3.83 |
| P48 | 1,427.04 | 1,422.73/4.31 | 1,418.83/3.91 |
| P55 | 1,385.98 | 1,382.68/3.30 | 1,378.98/3.70 |
| P59 | 1,396.66 | 1,393.39/3.28 | 1,389.91/3.48 |
| P60 | 1,389.07 | 1,385.64/3.43 | 1,381.41/4.23 |

Remedial Measures

As indicated in Fig. 5, a scheme of remedial measures for Patalganga landslide has been suggested. Soil nailing for a height of 5 m at the crown portion of the slide and a 4-m high gabion at the toe of the slide to prevent erosion and meandering of the Patalganga River were designed and suggested (Fig. 5). Provision for benches in the middle portion of the slide was also made.

To prevent rills and gullies, longitudinal and transverse drains were suggested to collect surface runoff. The stability analysis of landslide after incorporating remedial measures was carried out under limit equilibrium conditions by using GEO5 software. The Factor of Safety was rechecked as 1.23.

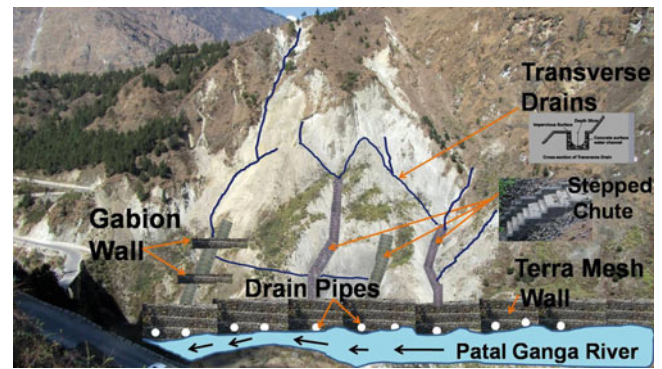


Fig. 5 Remedial measures for Patalganga landslide

Conclusion

Monitoring of landslides for early warning is a challenging area, and costly in terms of involving high precision technology and skill. However, this paper highlights cost-effective ways of monitoring the critical landslides which generally become reactivated during rains. Though, early warning may not be given in hours, the continuous monitoring results are useful in predicting the magnitude of sliding during the rains, as it has been for the described landslides.

References

Bhandari RK (1987) Slope stability in the fragile Himalaya and strategy for development. Ninth IGS Lecture. *J IGE* 17(1):1-7

Bhandari RK (2003) Two great landslide tragedies of India. In: Gupta HK (ed) Disaster management. Orient Longman, New Delhi, pp 110-127

CRRRI (Central Road Research Institute) (2010) Investigation of Kaliasaur landslide on national highway-58 and design of control measures for its long-terms stability. Unpublished project report submitted to Department of science and technology (DST), Govt. of India, New Delhi

CRRRI (Central Road Research Institute) (2012) Vulnerability of road related infrastructures/facilities against natural hazards in hilly regions. Unpublished report of 11th five plan network project submitted to CSIR-Structural Engineering Research Centre (CSIR-SERC), Chennai

Kimothi S, Kumar K, Mathur S (2010) Rock mass and slope mass characterization of Kaliasaur landslide area (Uttarakhand) on National Highway-58 and correlation of results with deformation conditions. *J Himalayan Geol* 33(2):133-143

Kumar K, Kimothi S, Goyal N, Prasad PS, Rawat S, Mathur S (2008) Dynamic nature of Kaliasaur landslide: a geomorphological appraisal. In: Diamond jubilee conference on "Landslide Management: Present Scenario and Future Directions" conducted by Central Building Research Institute, Roorkee, 10-12 February

Kumar K, Prasad PS, Kimothi S, Negi IS, Kathait A, Dash A, Mathur S (2011a) Kinematic slope stability analysis of Kaliasaur landslide on NH-58, Garhwal Himalaya. In: Third Indian rock conference: INDOROCK-2011, 13-15 October, Indian Society for Rock Mechanics and Tunneling Technology, Roorkee Chapter, Roorkee, pp 341-350

- Kumar K, Prasad PS, Negi IS, Kathiat A, Kimothi S, Singh K, Mathur S (2011b) Recent reactivation of Kaliasaur landslide and impact thereafter. In: Proceedings of the landslide hazard—consequences and challenges, CSIR-CBRI, Roorkee, 10–12 February, pp 48–58
- Kumar K, Devrani R, Kathait A, Aggarwal N (2012) Micro-hazard evaluation and validation of landslide in a part of north western Garhwal lesser Himalaya, India. *Int J Geo Geosci* 2(3):88–90
- Kumar K, Prasad PS, Kathait A, Singh I (2013) Over eight decades old “Young” landslide—a case study. In: Seventh international conference on case histories in geotechnical engineering, 29 April–4 May 2013, Chicago
- Negi IS, Kumar K, Kathait A, Prasad PS (2012) Cost assessment of losses due to recent reactivation of Kaliasaur Landslide on National Highway 58 in Garhwal Himalaya. *Nat Hazards* 68 (2):901–914
- Singh B, Goel RK (1999) *Rock mass classification: a practical approach in civil engineering*. Elsevier Science and Technology, UK, p 192



Geotechnologies for Surveys and Catastrophic Events of Rio de Janeiro Geological Survey: A Case Study

Tiago Marino, Francisco Dourado, Claudio Amaral, and Jorge Xavier-da-Silva

Abstract

Automatic collection of field data enhances task speed and reduces the number of database input errors. The Geological Survey of Rio de Janeiro (DRM-RJ) has accumulated a large volume of information regarding mass movements in the state during recent years. A huge volume of surveys are requested by the Municipal and State Civil Defenses, generating an even larger amount of reports, photographs, sketches and other documents associated with these field activities every year. In recent years, the volume has significantly increased as a result of major disasters that occurred in the state (in Angra dos Reis, the Morro do Bumba in Niterói and a “Megadisaster” in Mountain Region) which demanded thousands of surveys. Resulting from technical cooperation between the DRM-RJ, State University of Rio de Janeiro, Federal University of Rio de Janeiro and the Federal Rural University of Rio de Janeiro, a data management system related to the geological risk of the Rio de Janeiro State was developed to support field teams and bring more practicality and organization during field assessment activities. The system consists of the assemblage of a georeferenced database to organize field-collected data related to mass movement assessments. The GIS VICON/SAGA—Vigilance and Control (<http://www.viconsaga.com.br>) was designated to support this database. It provides interfaces for data collection, querying, filtering, and report and map generation. The database was structured to store the event location, measure susceptible or affected areas, retrieve information such as number of people affected or killed, and buildings affected or destroyed by mass movements. GIS brings two specific interfaces for data input: from a PC, using web browsers or from the field, using mobile devices, on an Android OS application. For information retrieving, some interfaces were developed, such as a query system for alphanumeric-tabular reports and for other spatial query procedures for map generation.

T. Marino (✉)

Departamento de Geociências, Center for Scientific Support in Disasters (CENACID), Instituto de Agronomia, Federal Rural University of Rio de Janeiro, BR-465, Km 7, Seropédica, Rio de Janeiro, Brazil
e-mail: tiagomarino@ufrj.br

F. Dourado

Applied Geology Department, Center for Scientific Support in Disasters (CENACID), University of Rio de Janeiro State, Rua São Francisco Xavier, 524 - Room 2019A, Rio de Janeiro, Brazil
e-mail: fdourado@uerj.br

C. Amaral

Applied Geology Department, University of Rio de Janeiro State, Rua São Francisco Xavier, 524 - Room 2019F, Rio de Janeiro, Brazil
e-mail: camaral@pcrj.rj.gov.br

J. Xavier-da-Silva

Federal University of Rio de Janeiro, Av. Athos da Silveira Ramos, 274 - Bloco I - Sala 01, Cidade Universitária, Rio de Janeiro, Brazil
e-mail: xavier.lageop@gmail.com

Keywords

Geographical Information System • GIS • Mobile applications • Risk • Mobile devices • Field assessments • Mass movements

Introduction

Information is the most valuable resource during emergencies and disasters. It is the basis for coordination and decision making during the emergency response. It is an essential aspect of an organization's ability to gain (or lose) visibility and credibility and has a powerful impact on how national and international resources are mobilized. Above all, information is necessary for providing rapid and effective assistance to those affected by a disaster. It is also essential for after-actions analysis, evaluation, and lessons learned.

An emergency response activity usually involves several teams from different organizations working cooperatively to save lives or properties. These teams have to make many decisions under time pressure to accomplish their goals. Most decisions require contextual knowledge coming from the emergency settings, including those which report emergency teams' field surveys.

This work proposes a mobile device platform which allows different field agents filling out structured forms, enriched by multimedia content, during their surveys. All data gathered can be uploaded direct from the site, in real-time, through telecommunication network (or Wi-Fi) technologies (Cordeiro et al. 2011). The platform also provides a backup data storage mechanism whenever connection is not available, for later uploads.

This platform development was based in a technical cooperation between field surveys experts from Geological Survey of Rio de Janeiro (DRM/RJ) and State University of Rio de Janeiro (UERJ) and Geographical Information Systems (GIS) researchers from the Federal University of Rio de Janeiro Geoprocessing Laboratory.

Although other initiatives exist to address this problem (such as ESRI ArcGISTM for Mobile), unlike commercial applications, VICON/SAGA consists of a freeware and flexible tool, fully customized for disaster relief needs, built and improved by people with specific demands who face different disasters situations and have years of experience. The platform is currently running and available at VICON/SAGA website (<http://www.viconsaga.com.br>).

Motivation from a Case Study

This case study presents a real situation experienced during routine activities in assessments of areas with slips where the collected data, as well as multimedia information, must be recorded and later organized into a Geographical Information System (GIS). From the difficulties found during this process, the group has identified an opportunity to enhance and improve the process through adoption of information technology during data-gathering activities.

Specialists from the Geological Survey of Rio de Janeiro (DRM/RJ) and University of Rio de Janeiro State (UERJ), have been supporting the response in almost all the most significant disasters related to landslides in Rio de Janeiro state (Fig. 1), where there have been an increasing number of deaths caused by natural disasters linked to extreme weather events. In recent years, thousands of people died, tens of thousands were left homeless and millions were affected by natural disasters.

Among the natural disasters that occur in Rio de Janeiro State, landslides and floods are the biggest killers and generate more damage to the economy. Comparatively, the number of events in the 2000s was 2,400 % higher for mass movements and 400 % for flooding and waterlogging.

To describe these hazard processes, in particular the landslides, a database structure (Fig. 2) was created to describe the events in both their geological characteristics as well as potential sources of loss. The data are used to calculate the risk in regions or areas related to each event or set of events.

The database consists of a main table where general information is recorded shortly after the event and the triggers are identified. Associated with the main table are auxiliary tables which also describe the moments immediately after the event, and can register the temporal evolution of the hazards process, if observed. For this reason, the record of date of the subsequent comments is very important to evaluate the evolution of the process.

This relative evaluation allows authorities to prioritize immediate response to the most dangerous landslides systems in each situation and facilitates development of



Fig. 1 Landslide assessment by DRM specialist members in Teresópolis, Brazil in 2011

emergency actions, including actions to prevent the continuation of the movements, to monitor the evolution of the landslides, to select systems to perform detailed studies or even to evacuate the people.

However, all gathered data that originated from assessments during a field journey are still registered in handwritten forms as well as in site images and videos, stored in digital cameras. When agents arrive at the base station, they must still join, validate, and upload all collected data (forms, images, videos) after a tiring workday. Several times, during one journey, dozens of locations are visited and evaluated, generating a large amount of data, which often makes the data upload process more difficult at the end of the day. When agents work in the field, many pictures and videos are generated and many papers are used as drafts. Much of the produced material can be discarded due to duplicates or bad quality photos, or even by lack of relevance. All this bulk data contributes to increasing complexity in the upload task. Often, after a gruelling workday, the agent looks at the pictures taken by himself that same day and cannot identify from which location the photo was taken. The site incursions make agents so busy that is almost impossible to take notes about each photo in order to avoid confusion later.

Through many missions experienced and repeatedly facing this kind of problem, specialist realized the opportunity of speeding up this process through the use of mobile devices. The following section will present each step related to a platform's operation, showing the sequence of procedures, starting at analyst's field surveys, screening data and transmission, until it is available to the coordinator (located in the headquarters), so that, even remotely, it will be possible to analyse and make decisions, practically in real time.

Platform Operation

The proposed methods combine Geographic Information Systems (GIS), telecommunications networks and mobile devices, aiming to enhance the process of data acquisition by field teams, and data organization and presentation for remote coordinators (Diniz et al. 2005). Figure 3 shows an illustration presenting the architecture components and processes involved. Each step of the process (A, B, C, D) is detailed in the following sections.

(A) Field data collecting platform

During the disaster response several field teams work on different clusters (technical, medical, rescue, basic infrastructure reconstruction) (UNDAC 2013), applying their previous personal knowledge (geologists, engineers, etc.) combined with the "Current Contextual Knowledge" (acquired from site surveys), producing technical reports resulting from the combination of knowledge which results in the "Combined knowledge". The data acquisition phase is usually composed of a written report, as well as multimedia content such as photos and videos portraying the local scene.

A major problem facing a large number of surveys in a short period of time is related to the organization of all generated data. The mobile device solution rises at this stage as an organizer for all that generated information. The platform has a data input module designed for smartphones and tablets, checking the location coordinates from its GPS sensor, and it also uses an integrated digital camera to acquire images and videos (as shown in Fig. 4). It should be remembered that all surveys are completed based on standard forms, predefined by each working group, fully customizable, in order to standardize each kind of inspection and increase data analysis capacity by remote coordinators. All data is stored in the device database. If a telecommunications network is available at the time, agents can upload data to the server database, hosted on the Internet and then available online to remote coordinators, wherever they are.

(B) Mobile platform data transmission and backup plan

Logically, a solution based in the massive use of telecommunications needs the full operation of these services so that the data traffic is possible. Facing emergency scenarios of great magnitude, access roads, water supply networks and light, and communication media are commonly interrupted due to harmful events, such as falling trees, explosions, and floods.

Just at the time the availability of this infrastructure is badly needed for the effectiveness of the response to

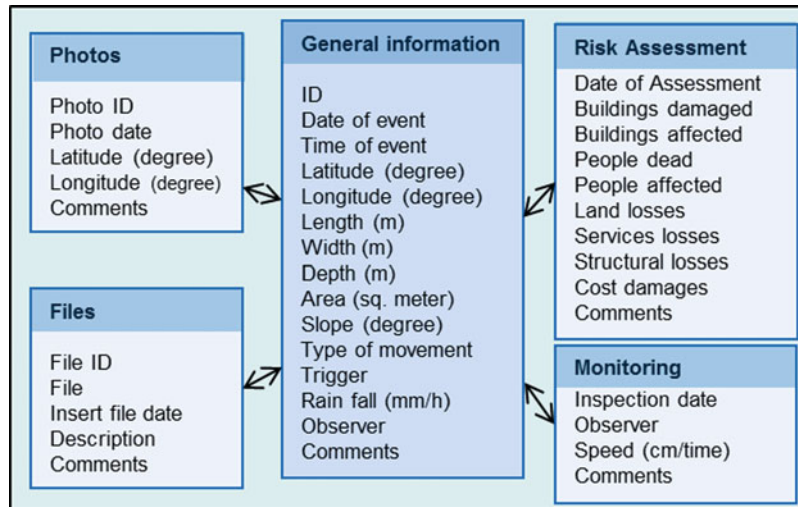


Fig. 2 Database schema for geological-risk assessment

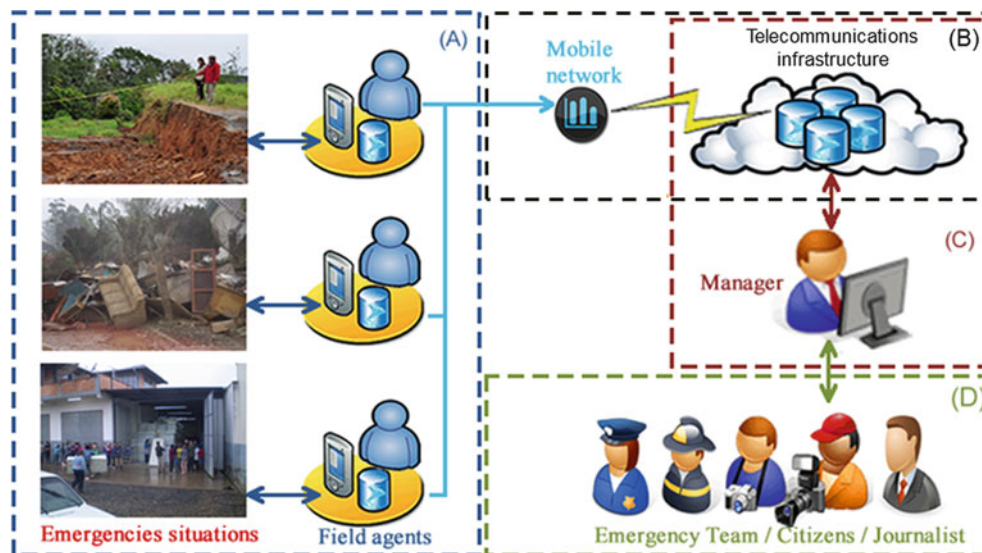


Fig. 3 Components and processes from methodology architecture

the emergency, they are often limited, requiring time for their reinstatement.

However, due to the great importance of communications for the society and response teams, efforts to rapidly re-establish primary services to society are prioritized, so that the community does not suffer further with its interruption and response is not impaired.

For the major natural disasters in which the team UNDAC (United Nations Disaster Assessment & Coordination) collaborates, the UN Office divides its teams into subgroups, called clusters, responsible for restructuring and maintenance of primary services such as nutrition, health, water and sanitation, temporary shelter, camp management and coordination,

security, recovery, logistics and telecommunications (UNDAC 2013).

Specifically, in the telecommunications cluster, the UNDAC has partners like the French NGO, Telecoms Sans Frontieres (TSF), which mobilizes human and material resources to guarantee the establishment of communications at the scene until normalcy is re-established.

Thus, even though it is a platform-dependent telecommunications service, this is no longer seen as a critical factor for the mobile data collecting platform operation. Moreover, even if communication is lost, the device is completely capable of storing all data in an internal database, ready for upload as soon as connections are available again. Even in the worst

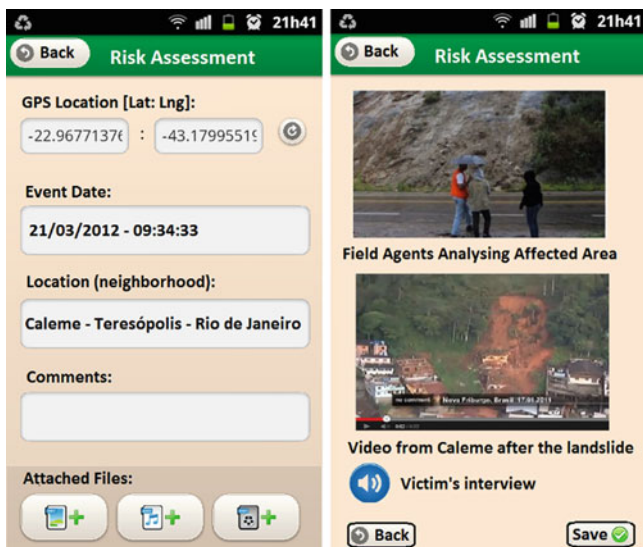


Fig. 4 VICON/SAGA: Mobile data gathering platform screen

case, when telecommunication is not available, data can be transferred through cable from the mobile device to a desktop.

(C) Manager data visualization

Emergency management processes are highly time-critical and response activities must be defined and performed quickly and efficiently. The figure “Manager” in this case is a composite from highly experienced professionals, commanders and public administrators, working in emergency management offices.

Coordinators usually operate and make decisions, remotely managing all kinds of available information. Databases organize all this information coming from multiple sources in real time and it can be spatially visualized and analysed using Geographic Information Systems (GIS). As the agents submit new information in real time, new points (or areas) of information emerge in the Management System in real-time. Each piece of information is grouped by type (e.g. evaluation of landsliding, search and rescue) and standardized through predefined forms, providing filtered queries performed from search criteria.

Figure 5 depicts the Geographic Information System with field information available on the coordination segment. Reports and maps can be generated for spatial analysis proceedings by any other analysis tools.

(D) Manager decisions

Citizens and “Emergency Teams” consume information, logically organized and certified, from the manager. After compilation of all data, the managers in command can evaluate the situation and prioritize immediately response to the most dangerous cases in

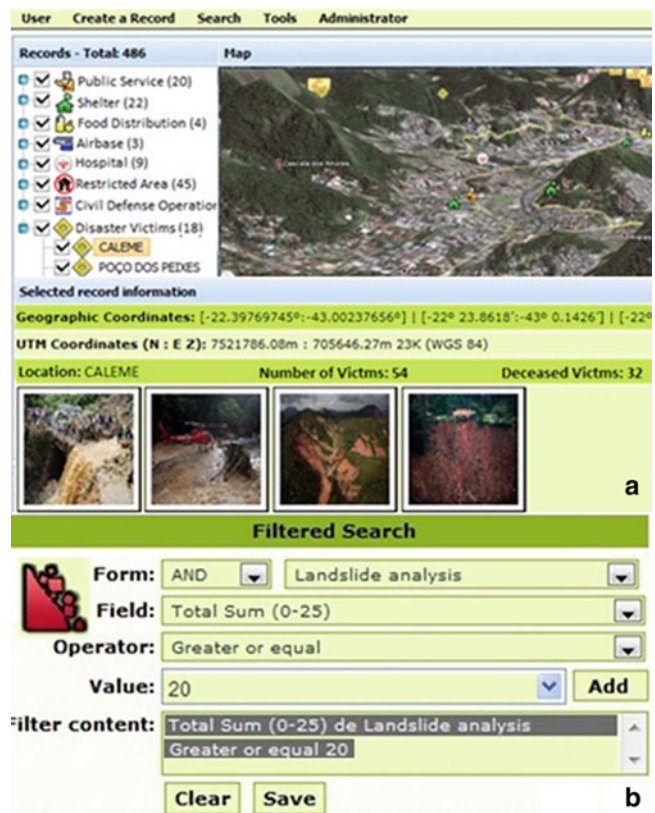


Fig. 5 (a) Information related to disaster: georeferenced, classified and available in real time on a Geographic Information System for coordination segment; (b) Information filtering interface to refine result set

each situation and facilitate developing emergency actions. They direct the emergency teams, citizens and journalists to support them with useful information in order to reduce the response emergence time, leading to more effective work.

Conclusions and Further Work

This work presented a mobile platform which allows online registration from different field agents during their evaluations. Field agents can also customize forms for different information classes (i.e. landslide assessment, rescued persons, blocked roads) and still retain the ability to attach images, videos, and other files related to each inspection. Incoming data are stored into a web database available for evaluation by real-time coordinators wherever they are (sometimes over a thousand of miles away from the disaster area).

According to Marrella et al. (2011), the use of mobile devices and applications in these scenarios is very valuable as they can improve collaboration, coordination, and communication among team members. Most of the tasks are highly critical and time demanding, e.g. saving minutes could result in saving people’s lives.

Although the platform depends on telecommunications network availability, considering the increasing importance of such infrastructure for a community, this is not a critical point for the proper functioning of the methodology, even under catastrophic situations. Nevertheless, even in the absence of network infrastructure, the platform implements a mitigation plan for these extreme cases, storing the collected data in a database within the device itself.

Finally, efforts can be made in order to allow distributed sensors data upload, remotely transmitted in real time, for any phenomenon of interest monitoring, for example, the evolution of an erosive process through distance sensors, level of rivers, rainfall; all these can be collected through sensors, today, increasingly cheap and easy to implement, generating time series and enriching the knowledge base for decision making.

References

- Cordeiro KF, Campos MLM, Borges MRS, Marino TB (2011) Use of linked data in the design of information infrastructure for collaborative emergency management system. In: CSCWD—the 15th international conference on computer supported cooperative work in design, Lausanne, Switzerland
- Diniz VB, Borges MRS, Gomes JO, Canós JH (2005) Knowledge management support for collaborative emergency response. In: Proceedings of the 9th international Conference on computer supported cooperative work in design, IEEE, vol 2. pp 1188–1193
- Marrella A, Mecella M, Russo A (2011) Collaboration on-the-field: suggestions and Beyond. In: 8th international conference on information systems for crisis response and management (ISCRAM 2011)
- UNDAC (United Nations Disaster Assessment and Coordination) (2013) How are disaster relief efforts organised?—Cluster approach and key actors. Available at <http://business.un.org/en/documents/6852>



Automated Inclinometer Monitoring Based on Micro Electro-Mechanical System Technology: Applications and Verification

Andrea Segalini, Luca Chiapponi, Benedetta Pastarini, and Corrado Carini

Abstract

The paper illustrates the efficiency of a novel inclinometer device by comparing results obtained from some prototypes installed in three landslides and those derived from classic inclinometers. The new device, called Modular Underground Monitoring System (MUMS) is intended to be applied for natural and artificial slope deformation monitoring and landslides dynamics control, assessment and forecasting. The MUMS instrumentation was developed from the idea of replacing the standard measurement procedure by locating nodes at known distances along a connecting cable placed within a vertical borehole. Each node measures its local orientation (related to the National Elevation Dataset (NED)) by means of a micro electro-mechanical system (MEMS) formed by a 3D digital linear acceleration sensor and a 3D magnetic sensor. This allows us to determine the direction cosines of the borehole axis in each node and calculate its 3D shape and deformation along the whole borehole. This paper compares the classic instruments and the new MUMS device, with evidence of the advantages of measurement automation and economy in the use of the proposed device, which could also be equipped with other electronic instruments that would allow the measurement of other interesting physical quantities (i.e. pore pressure, temperature, stresses etc.) together with displacement components. The comparison is carried out through the examination of few installation in various types of landslides, with particular attention to the accuracy and repeatability of the measurements that are automatically made.

Keywords

Landslide monitoring • In place inclinometer • Real time monitoring • Landslide dynamics

Introduction

The automatic measurement of displacements in the underground is of considerable interest in the field of slope stability and, in general, of geotechnics. In particular, the possibility of measuring continuously the movements along the entire length of a vertical inclinometer provides new hints for the study of landslides and their mechanisms of activation and propagation. Furthermore, the possibility of adding to the orientation data the continuous recording of pore water pressure and temperature promises a far more complete knowledge of the phenomena. In recent years, with the introduction of micro electro-mechanical

A. Segalini (✉) • L. Chiapponi • B. Pastarini
Università degli Studi di Parma, DICATeA, Parco Area delle Scienze,
181/a, Parma 43124, Italy
e-mail: andrea.segalini@unipr.it; luca.chiapponi@unipr.it; benedetta.pastarini@unipr.it

C. Carini
GEI s.r.l., Via R. Koch, 55/a, Pilastrello, Parma 43123, Italy
e-mail: corrado@geielettronica.it

system (MEMS) accelerometer sensors, there has been a substantial development of slope monitoring techniques, associated with a significant reduction in the cost of the equipment that is starting to change the methods of inclinometer instrumentation.

In particular, a new system has been recently presented (Segalini and Carini 2013), called MUMS (Modular Underground Monitoring System), finalized to measure and record the data described above. The features of the system and its peculiarities can be found in previous publications, as well as preliminary considerations of the accuracy that can be expected from the use of such systems (Segalini et al. 2013).

This article discusses some applications of the MUMS system for landslide monitoring, analysing the results and providing insights about the reliability of the measurements and the applicability of such systems to specific cases.

Instrumented Landslides

This chapter introduces the characteristics of three landslides that have been monitored by means of a traditional inclinometer linked to an automatic MUMS. The duration of observations is variable, from a few months to several years.

Tiedoli Landslide

The Tiedoli landslide (Segalini et al. 2009) involves the entire debris-covered portion of the slope. The debris ranges in grain size from clay to boulders. The crown of the landslide is located just below a very steep cliff where the rock formation outcrops and its foot is located at the bottom of the Taro River valley. The total volume involved in the movement is approximately 10 million cubic meters. The depth of the sliding surface varies from head to toe, having an average value between 15 and 20 m. The upper portion of the slide is constituted by a flow that reaches a depth of 22 m from the ground surface and is characterized by an average velocity of 6–7 cm/year. In the area subjected to the landslide movement, the turbiditic sequence of the Ranzano Sandstones Unit is in tectonic contact with the San Siro Claystones, part of the Ligurian Units of Cretaceous age (Vescovi 2002).

The landslide has been instrumented with inclinometers, piezometers and topographic markers in the past. The reason for the placement of these instruments is tied to the presence on the landslide body of an urban waste disposal site that has operated since 1980 (Segalini et al. 2009). Most of these instruments are connected to an automated monitoring system that can be governed remotely and is able to send an

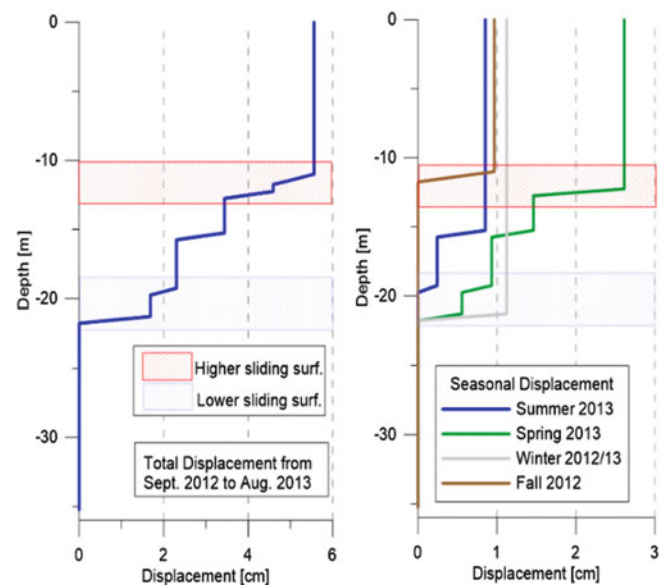


Fig. 1 Total displacement measured with the MUMS system in 1 year (*left*) and total displacement during each season (*right*) at the Tiedoli landslide

alarm signal if some threshold values of superficial velocity or piezometric water level are exceeded. The main movement is related to the waste disposal activities that ceased by the end of 2007. The landslide features have been evaluated and confirmed through the interpretation of the inclinometer readings (Segalini et al. 2009) from various boreholes drilled in the medium-lower portion of the landslide, on top and below the lower embankment of the waste disposal site. Figure 1 shows the total displacement along the inclinometer, and the locations of the two main sliding surfaces: the first between 10 and 13 m depth, and the second between 19 and 22 m.

Roccamurata Landslide

The town of Roccamurata is located on the right bank of the Taro river valley, Parma Province, Italy. The small town has grown around the railway crossing along the municipal road that borders the railway and the Taro river right bank for about 1 km (Fig. 3). The small town is divided in two portion by the Prato Ticino creek, a right tributary of the Taro River. Two distinct landslides are affecting the township area (Masetti et al. 2009).

- The eastern landslide has been identified as an earth flow with a NNW direction, starting from an elevation of around 425 m a.s.l. and reaching the Roccamurata town at the elevation of 325 m a.s.l. This landslide is currently not active.

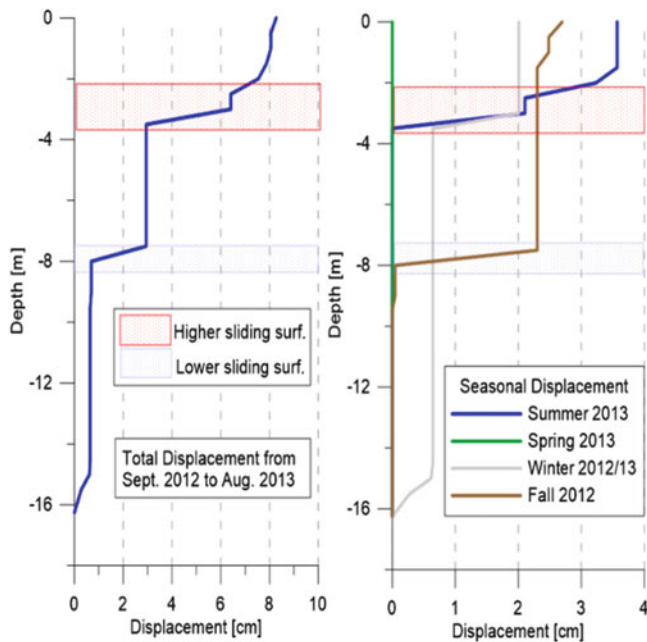


Fig. 2 Total displacement measured with the MUMS system in 1 year (*left*) and total displacement during each season (*right*) at the Roccamurata landslide

- The western landslide has been identified as a rotational slide on the basis of the inclinometer readings; the rupture surface toe is surfacing on the paved road in the town of Roccamurata. The landslide is active and involves the monogenic serpentinitic breccias of the Casanova complex that make up the surface portion of the slope in the landslide area.

This landslide involves several buildings that have been severely damaged, as well as the road that runs through the town (Fig. 3). Inclinometer readings carried out for 11 months, from February 2007 until January 2008, had shown a total movement of about 8 cm/year; the landslide is thus classified as very slow, according to IUGS/WGL (1995). The last geological survey, carried out in January 2012, was aimed at further understanding the lithological settings around the Roccamurata landslide in order to plan possible remediation. The landslide activity caused damage to several buildings of the small village, forcing some families to leave their homes.

The new borehole ROCC51 was equipped with the MUMS device. This device integrates a multiple sensors inclinometer and a single piezometer.

The old deformation measurements were confirmed by the new inclinometers installed during the last geological campaign (Fig. 2). In particular, both the traditional inclinometer installed in the toe of the landslide and the MUMS device (installed within 2 m distance) have shown a sliding surface located at a depth of 4 m below the surface, in

agreement with what was observed in the past. The manual inclinometer was read twice after a zero reading during the 2012 spring and summer seasons and then left unattended until the next spring. The total displacement recorded in the 65 days interval was around 8 mm at 4 m depth; this would add up to a total displacement of 5 cm per year, considering a constant velocity of the landslide equal to the average value calculated in the 65 days interval. By the following spring (2013) it became unusable, since the inclinometer probe wasn't able to pass below the 4 m depth, due to the landslide movement. On the other hand, the MUMS installed towards the end of summer 2012 is still operational. Figure 2 (*left*) shows the total cumulative displacement recorded by the MUMS inclinometer in the whole year. The total displacement is around 8 cm, 2.5 cm of which is occurring at the lower sliding surface (8 m depth) and the remaining 5.5 cm is occurring at 4 m depth, as shown in Fig. 2 (*right*).

Boschetto Landslide

The area affected by the landslide (see Fig. 3) is characterized by the widespread presence of debris accumulations defined as quiescent landslide deposits of a complex landslide (Regione Emilia Romagna 2010), with a prevailing lithology of the Tizzano pink marl formation—Castelmozzano member (Fig. 4). In particular, the borehole instrumented with the MUMS is located in the top portion of a colluvium deposit that is probably the upper portion of a deposit of an old quiescent landslide. The positioning of the borehole drilling was aimed at identifying the thickness of debris that lies above the bedrock, and to collect some undisturbed samples for geotechnical laboratory analysis.

Afterwards, the borehole was instrumented with the MUMS chain to verify the stability conditions of the area crossed by the new provisional road link. As can be derived from Vescovi (2002) and from the Landslide Map of the Emilia Romagna region (Cartografia del Dissesto Idrogeologico 2010), the recent activation of the landslide has involved a previously stable portion of the colluvium debris, causing a southbound expansion of the perimeter of the instability area already mapped in the Regional Cartography of the Emilia Romagna (1991).

The entire slope is characterized by the presence of the Tizzano pink marl formation: a limestone-marl sequence that evolves upward to arenaceous-pelitic and arenaceous-pelitic-calcareous.

The formation, deposited by turbidite flows originating from terrestrial and intrabasin sources, is subdivided into three members. The lower contact is of uncertain nature, but the lowest member is the Monte Caio flysch. This



Fig. 3 View of the the Roccamurata landslide taken from the left bank of the Taro River (*above*); the Boschetto landslide crown area, taken a few days after its reactivation (*below*)

formation can be temporally ascribed to the Daniano—Lower Luteziano.

The Castelmozzano member, in particular, is generally formed of grey marl and marly pelitic structures interspersed with whitish limestones and nummulite-rich calcarenities (Iaccarino and Follini 1970) in medium to thick layers and, locally, by lithified sandstone layers of medium thickness from the lower to middle Eocene (Cerrina Feroni et al. 1994). The tectonic development of the formation and its weathering favor the formation of a debris mantle on the slopes that locally has become several meters thick. The landslide is part of this; the most significant section is shown in Fig. 4.

In this particular landslide, the MUMS inclinometer was installed on June 26, 2013, therefore the displacement

reported in Fig. 5 does not cover a complete seasonal year. However some interesting observations can be pointed out: the deeper small displacement occurred at a depth of 16 m, at the contact between the slope debris cover and the Tizzano pink marl rock formation. The upper portion of the debris is intersected by a movement that occurred around 2.5 m of depth and is related to the excavation of a nearby drainage trench, carried out during the construction of the new provisional road link.

The larger amount of displacement (around 7–8 mm) directly induced by the landslide occurred at around 10 m depth, approximately corresponding to the lower excursion level of the water table. A similar displacement (7 mm) was measured in a nearby traditional inclinometer in a time interval of 36 days.

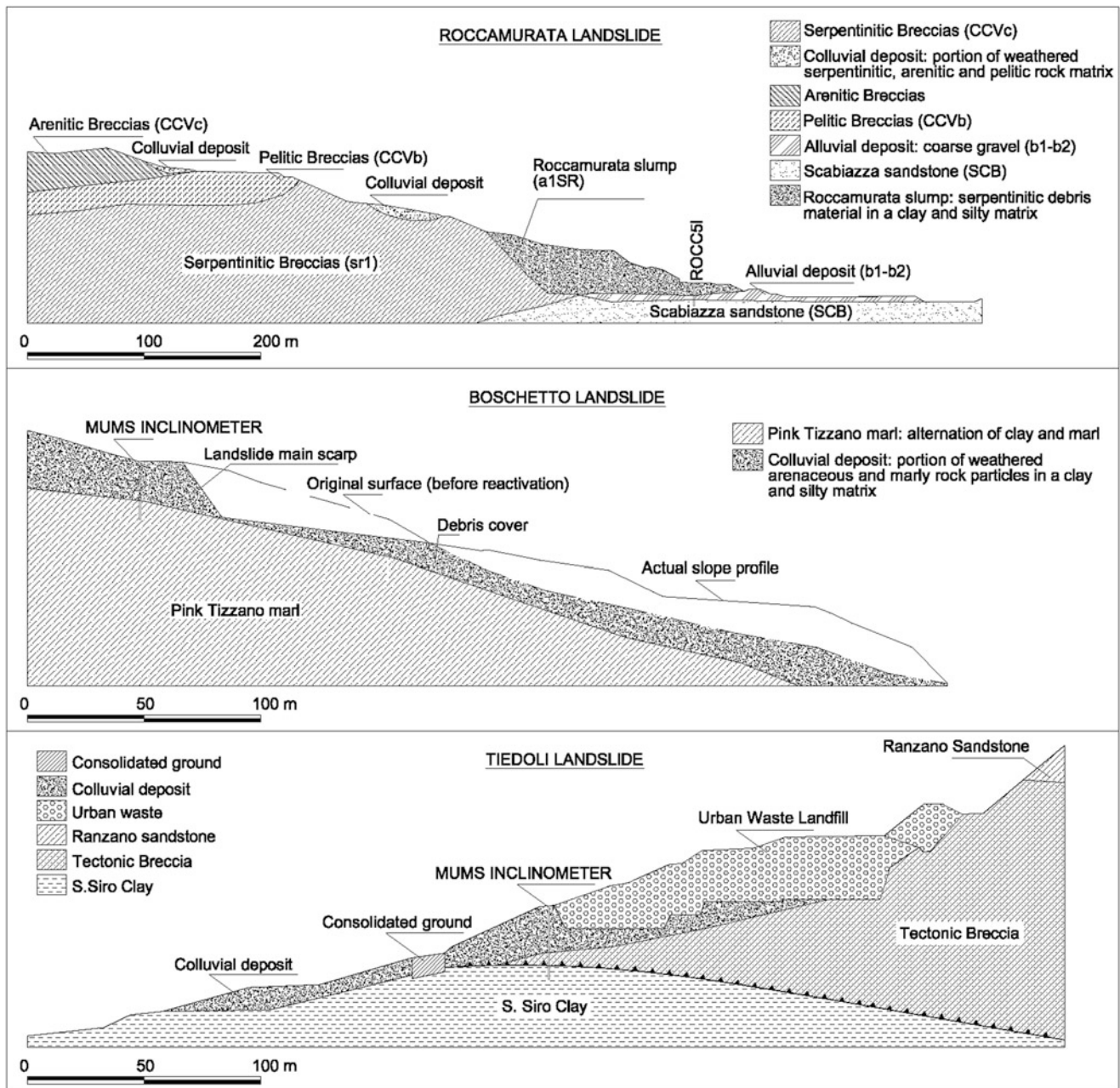


Fig. 4 Geological sections of the three landslides with indication of the positions of the MUMS inclinometers

Comparison Between Manual and Automatic Measurements

In this section the problem of comparing the results of the measurements obtained by manual inclinometers and those derived from the MUMS chain is discussed.

As already stated, for each monitored landslide, the comparison between the total displacement measured with a traditional inclinometer and MUMS were in very good agreement. Some of the traditional measurements were carried out contemporarily with the MUMS (Boschetto and

Roccamurata landslides) while other were compared with published literature (Tiedoli landslide).

The three landslides have shown different dynamic behavior, having more than one sliding surface and each one being of different thickness. The lower surface of the Roccamurata landslide (Fig. 2) is very thin, influencing the readings of a single MUMS node, while the upper surfaces of both Tiedoli (Fig. 1) and Roccamurata (Fig. 2) are more than 2 m thick, influencing three or four MUMS nodes. This should be taken in to account when planning the installation of traditional in-place inclinometers, since generally only two or three

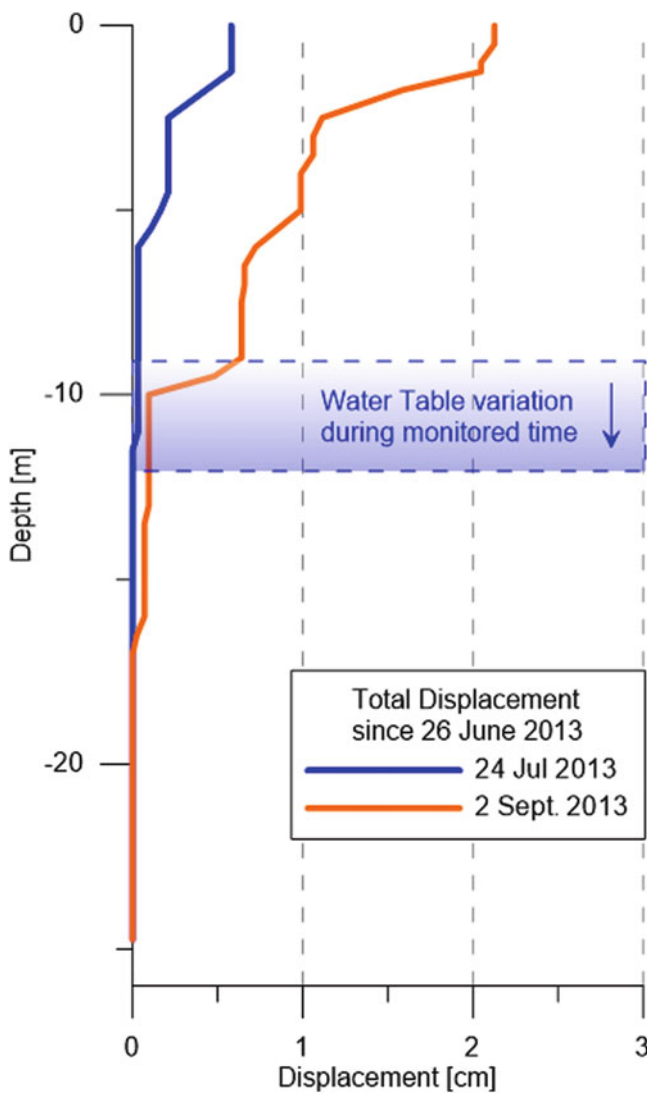


Fig. 5 Total displacement measured with the MUMS system in 28 and 68 days at the Boschetto landslide. The piezometer node installed in the MUMS at a depth of 15 m showed a variation of the water table between 9 and 12 m below ground surface during that time span

probes are installed at each location, potentially losing information on the real displacement that has occurred.

Furthermore, considering the time at which the landslide became active, both Tiedoli and Roccamurata landslides have shown differences in the time and location of their movements. Observing the Tiedoli displacement (Fig. 1—right) it appears evident that the total displacement is composed of two portions: the first occurring at the upper sliding surface - shear band - during the spring and autumn seasons, when the water table is highest, and the second occurring at the lower sliding surface during the summer and winter seasons. Other correlations between displacement and water table level, underground temperatures and smaller time interval could be made, considering that the database of these particular MUMS devices has a frequency of one reading per hour.

Even in shorter monitoring periods, as in the case of the Boschetto landslide, the use of the MUMS chain appears to be very useful for the interpretation of separate events. In this particular case it was possible to point out the effects of the nearby construction of a drainage trench, as well as the correlation between the depth of the sliding surface and the temporary variation of the water table level. Further progress in the monitoring will allow for a better understanding of the landslide dynamics and provide real time evaluation of the landslide hazard.

Concluding Remarks

The paper describes some application of the MUMS system, showing how it allows for a better understanding of the type, location and origin of unstable slope movements. That, in turn, should help in understanding the triggering causes and the evolution mechanisms of landslides and provide an innovative and substantial contribution to their stability analysis and control.

References

- Cerrina Feroni A, Fontanesi G, Martinelli P, Ottria G (1994) Elementi di correlazione stratigrafica fra il Membro di Bersatico (Formazione delle Marne rosate di Tizzano) e il Membro di Poviago (Formazione di Val Luretta) nell'Appennino settentrionale. *Atti Tic. Sc. della Terra*, vol. Sp., 1. pp 117–122, Pavia
- Cartografia del Dissesto Idrogeologico (2010) Regione Emilia Romagna. <http://ambiente.regione.emilia-romagna.it/geologia/cartografia/webgis-banchedati/cartografia-dissesto-idrogeologico>
- Iaccarino S, Follini MP (1970) Nanoplankton calcareo del Flysch cretaceo di M. Caio e delle "marne rosate" paleoceniche di Tizzano Val Parma (Appennino settentrionale). *Riv It Paleont Strat* 76(4): 579–618, 1 figg., 5 tavv., Milano
- IUGS/WGL—International Union of Geological Science Working Group on Landslides (1995) A suggested method for describing the rate of movement of a landslide. *IAEG Bull* 52:75–78
- Masetti G, Ottria G, Diena M, Ghiselli F (2009) Geometry and kinematics of the Roccamurata landslide (Northern Apennines, Italy). In: *Proceedings of 6th EUREGEO, European congress on REGIONAL GEOScientific Cartography and Information Systems*, Munich, Germany, 9–12 June 2009, vol 1. pp 452–455, Abstract
- Regione Emilia Romagna (1991) *Carta Geologica dell'Appennino Emiliano-Romagnolo*, Foglio 217 Neviano degli Arduini. Regione Emilia-Romagna, S.EL.CA, Firenze [14]
- Segalini A, Carini C (2013) Underground landslide displacement monitoring: a new MMES based device. In: Margottini C, Canuti P, Sassa K (eds) *Landslide science and practice*, vol 2: Early warning, instrumentation and monitoring. Springer, London, pp 87–93. doi:10.1007/978-3-642-31445-2
- Segalini A, Giani GP, Ferrero AM (2009) Geomechanical studies on slow slope movements in Parma Apennine. *Eng Geol* 109:31–44. doi:10.1016/j.enggeo.2008.11.003
- Segalini A, Chiapponi L, Carini C (2013) Evaluation of a novel inclinometer device based on MMES technology through comparison with traditional inclinometers in landslide applications. *Geophysical research abstracts*, vol 15. EGU2013-1993, 2013, EGU General Assembly 2013
- Vescovi P (2002) *Note illustrative della Carta Geologica d'Italia*. Scala 1:50.000. Borgo Val di Taro, Foglio 216. Regione Emilia Romagna. F.EL.CA Firenze



Energy Demodulation-Based All-Fiber Warning System for Landslides

Xing Wang, Guangqing Wei, Bin Shi, Fenggao Xu, and Hengjin Tong

Abstract

In this paper, a new landslide warning technology, called the energy demodulation-based all-fiber warning system, is introduced. The system can measure the signal of energy change in fiber caused by micro-bending or breakage associated with the displacement of a landslide, and sends alarms at once when the signal intensity in the fiber weakens to a defined threshold. Compared with conventional monitoring technologies, this technology has many unique advantages, such as graded alarming, real-time response, remote monitoring, low cost, and a passive optical network. It is a very convenient and applicable landslide warning system. At present time this system has been developed and used in landslide warning in China.

Keywords

Landslide • Warning system • Energy demodulation • Fiber

Introduction

China is a country with many landslide disasters. The economic losses caused by landslides are over \$1.5 billion per year. It is very difficult to forecast the place, time and intensity of the landslides accurately; resulting in serious losses. Therefore, how to conduct warnings effectively is a critical task for mitigating and preventing landslide disasters.

The conventional monitoring and early-warning technologies for landslides mainly include inclinometers, displacement meters, strain gauges, water level gauges and others (Gong et al. 2005), which all are types of point-monitoring, and cannot indicate the danger signals visually. As a new monitoring technique, Distributed Fiber Optic Sensing (DFOS) technology has developed rapidly since the 1980s. It uses fiber as a

medium, and light as the carrier. The energy demodulation based all-fiber warning system for landslides, developed by Advanced Computational Engineering Institute for Earth Environment (ACEI) in 2012, is derived from Distributed Fiber Optic Sensing (DFOS) technology. In addition to its utility for distributed and remote monitoring, this system has other advantages over traditional monitoring, such as high sensitivity, real-time response, long monitoring distances, ease of forming a network in a certain range, and low cost (Shi et al. 2004; Sun et al. 2012; Gao et al. 2011). It can not only trace the deformation during the movement of a landslide body, but also carry out early-warning in a timely and effective manner. This system has been successfully developed and patented by Suzhou NanZee Sensing Technology Co. Ltd. in China and has been popularized in the landslide monitoring market. In this paper the principles, composition, functions and other issues related to the system are discussed.

X. Wang (✉) • B. Shi • H. Tong
School of Earth Sciences and Engineering, Nanjing University,
163 Xianlin Avenue, Nanjing 210023, China
e-mail: 465802859@163.com; shibin@nju.edu.cn; thj_king@126.com

G. Wei • F. Xu
Nanzee Sensing Technology Co. Ltd, 150 Renai road,
Suzhou 215123, China
e-mail: wgq@nzsensing.com

Principles

Artificial, geo-structural and environmental factors are three basic elements affecting slope stability. Artificial factors include blasting vibration, excavation, and transportation.

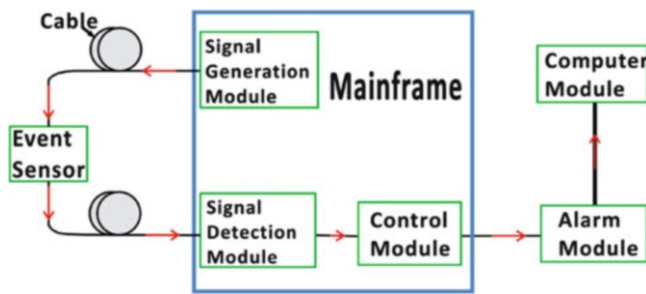


Fig. 1 A schematic diagram of an all-fiber warning system for landslides (The red arrow indicates the signal transmission)

Geo-structural factors include the angle of slope, attitude of rocks, rock weathering degree and completeness, and physical and mechanical parameters of the soil. Environmental factors include precipitation, and movement of groundwater. Horizontal and vertical displacement and cracks in the slope are impacts that all these factors have.

An all-fiber warning system for landslides can sense the displacement of soil and rock masses through the change of energy intensity of light in the cable. When the stress or displacement caused by the abnormal stress in the slope affects the system, it can convert the soil and rock movement into a change of signal energy intensity, due to micro-bending or breakage in the cable. Combined with the specific geological conditions and influencing factors of the slope, a reasonable threshold range can be assigned. When the displacement of the slope increases, the energy transfer rate can be affected by micro-bending in the cable. When the optical signal energy breaks through a predetermined threshold, the alarm module connected to the alarm device will send out an alert message immediately. The schematic diagram of an all-fiber monitoring and early warning system for landslides is shown in Fig. 1.

Components

The all-fiber warning system for landslides includes event sensors, a Host, an alarm module and a power supply module.

Event Sensors

Event sensors are used for detecting the deformation and displacement of landslides. Different physical and mechanical types of events require different sensors. Figure 2 is an event sensor that can sense the stress changes in the landslides. The stress determines the tightness of two serrated blocks. The tighter the saw tooth blocks are, the weaker the intensity of the optical signal transmission rate will be.

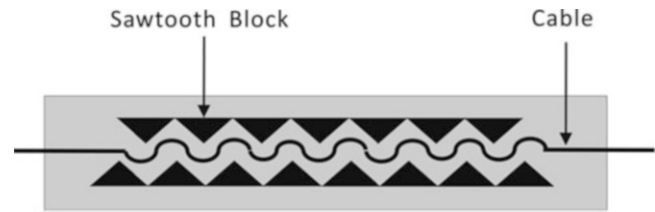


Fig. 2 Pressure probe meter (as stress affects the sawtooth block, the light intensity in the cable will change)

The Host

The Host for the all-fiber warning system for landslides includes a signal generating module, a signal detection module and a control module. The signal generation module can generate an optical signal, which can be a continuous optical signal, a pulse signal or a pulse frequency modulation optical signal. These signals are connected with the event sensors through the cable. The signal detection module is used for detecting the intensity of the light through the event sensors. The main function of the control module is setting the threshold value, judging the signal from the signal detected and sending commands to the alarm module. The relationships between modules in the Host are shown in Fig. 3.

The main power unit provides energy for the normal work of the whole system. The photoelectric conversion circuit module can convert the light signal into an electronic signal and the threshold grading judgment module will then receive the message. According to the received message, the judgment module performs a judgment and reports to the controller and interactive processing circuit module. The controller makes the decision whether the alarm circuits should send an alarm. The close relationship between the modules is well established. The integrated Host and some physical modules are showed in Fig. 4.

The Alarm Module

The alarm module can send the message in various ways. The alarm signal can be transmitted through sound and light in the area close to the danger. For further away, mobile phone text messages can be a good option. Remote scheduling and guiding work can be communicated via wireless transmitting networks.

The Power Supply Module

The power consumption of the whole framework and alarm is very small. Considering uncertainties in the environment of the landslide, solar cells will be a good choice.

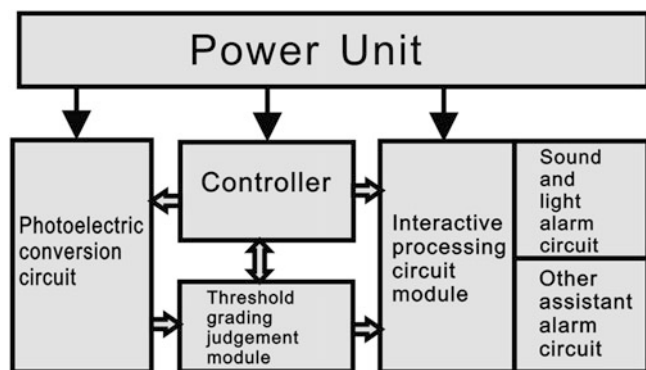


Fig. 3 Relationships between modules in the host

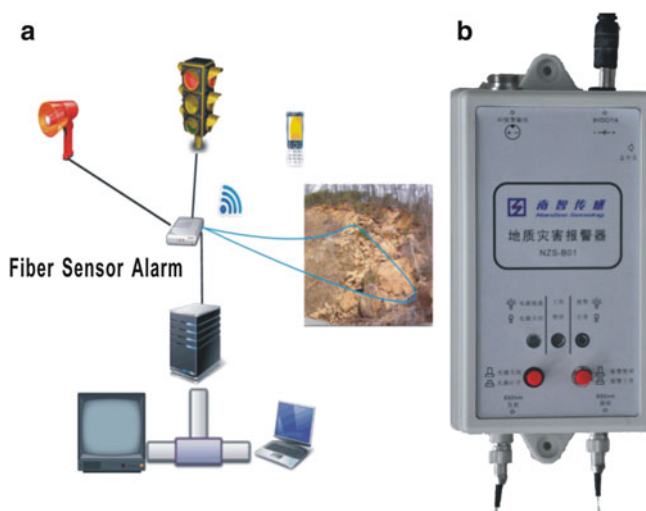


Fig. 4 (a) The entire physical system. (b) The integrated host

Features

An all-fiber warning system for landslides has real-time, synchronization of the event and the warning. In addition, the fiber consists of silica, which is anti-electromagnetic, resistant to corrosion and oxidation and is electrically insulated (Jiang et al. 2005). It is suitable for the harsh environment in the field. The system belongs to a wide range of accurate monitoring and early-warning devices, which can cover a radius of 5–10 km. It also has other incomparable advantages.

Grading Demodulation Alarm

Different geological conditions and external environments affect the landslide differently. The important reason for a high rate of false alarms is the lack of pertinence to conditions. One problem is that some slopes have not satisfied the sliding conditions or exceeded a chosen threshold. Therefore, different geological conditions for landslide

early warning system should be set according to the local conditions. The alarm threshold can be graded in multiple levels, and different alarms can vary with these multiple grades. In this way, it can greatly improve the science and accuracy of the early-warning system. Meanwhile, the system does not need to measure a specific deformation value. When the light intensity is lower than the threshold, the system sends an alarm at once.

Local Monitoring and Early-Warning Networks

Landslides always appear in specific areas. Some single landslides are very large; some landslides occur in the form of a landslide group. In a certain area, the all-fiber warning system can be integrated into a monitoring net through a cable, forming a regional network. In this way, the efficiency and management of the monitoring and early-warning system can be greatly improved.

Low Cost of the Entire System

The system does not need expensive modulation and demodulation devices, and optical fiber is also very cheap. All in all, the cost of the entire system is just one tenth to one percent of the cost of conventional means. Easy installation and precise warning make the system more efficient and more reliable.

The Threshold Setting

The alarm thresholds in an all-fiber warning system for landslides depend on the geotechnical structure and environmental factors for the stability of the slope. Based on our experiences and extensive data analysis, the following three factors can be used to determine the alarm thresholds, i.e. horizontal displacement, vertical displacement and widening cracks (Qiao et al. 2009). When one of the following situations occurs, the warning should be carried out:

1. The average horizontal displacement of all measuring points in the slope body is more than 5 mm/day in the same direction (or nearly the same direction);
2. The horizontal displacement of any single measuring point in the slope body is more than 10 mm/day in the same direction (or nearly the same direction);
3. The average settling rate of all measuring points in the slope body is larger than 3 mm/day;
4. The settling of any single measuring point in the slope body is more than 10 mm/day;
5. The average broadening rate of all measuring cracks is larger than 3 mm/day;

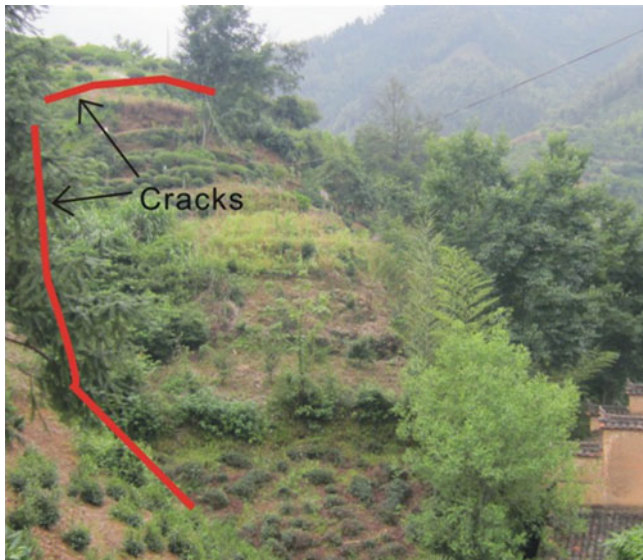


Fig. 5 The profile of the Gaoqin landslide (the red lines indicate the cracks around the landslide)

6. The rate of widening of a single measuring crack is more than 7 mm/day;
7. The width of a single measuring crack is more than 50 mm.

These circumstances cover all the unexpected situations during the creep of soil and rock formations in the landslides. Some changes are invisible, so it is hard to measure displacement or deformation, while others may be recognized easily. For any landslides that need to be monitored, just install the event sensors at the site where the unexpected situations can be recognized easily (Li et al. 2011).

For the alarm system, further analyses need to be carried out for assessing the slope stability, based on the engineering geology, hydrogeology, and deformation mechanisms of the slope (Xu 2012).

Gaoqin Landslide Case Study

The GaoQin Landslide, located in Huangshan Mountains, south China, is a threat to over 55 people. According to the results of advanced investigation, this landslide is caused by heavy rains. The bedrock beneath the unconsolidated superficial formation is heavily jointed and fissured. The resulting infiltration of rain and surface water increases the gravity forces and at the same time decreases the soil and rock resistance, and causes the landsliding.

Around the body of the landslide, many cracks caused by creep of the landslide were found. Along the trailing edge, there is a 3.0 m long and 2.0 mm wide crack. Along the side edge, there is a 10 m long, 10–20 mm wide crack covered by a soil layer. Since the cracks are visible, we can install the event sensors near these features (see Fig. 5).

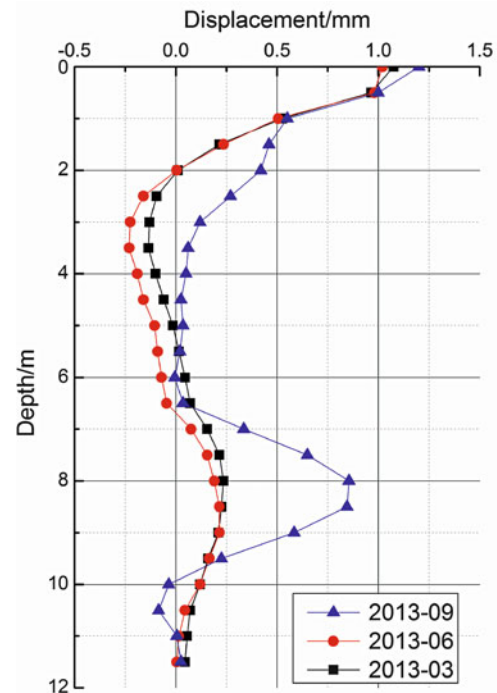


Fig. 6 The horizontal displacement of the Gaoqin landslide

For comparison, the inclinometer was installed in a borehole that extended to the bed rock beneath the slip surface in the central part of the landslide body. The monitoring started from December 2012, once every 3 months. The data from the inclinometer indicate the deformation of the landslide is very small (Fig. 6). The maximum displacement is a little over 1 mm during nearly 6 months. Obviously, the deformation does not surpass the threshold, and according to the site survey, the entire warning system goes well.

Conclusion

This paper introduces a new landslide warning technology—the energy demodulation-based all-fiber warning system for landslides, which consists of event sensors, the Host, an alarm module, and power modules. Compared with conventional monitoring techniques, the system has many unique advantages, such as graded alarms, real-time response, remote monitoring, low cost, and a passive optical network. It is a very convenient and ideal landslide warning system.

The system has been developed and patented by Suzhou NanZee Sensing Technology Co. Ltd. and applied in landslide monitoring in China.

Acknowledgments The authors gratefully acknowledge the financial support provided by the National Basic Research Program of China (973 Program) (No. 2011CB710605), National Key Project of Scientific and Technical Supporting Programs Funded (No. 2012BAK10B05),

the State Key Program of National Natural Science of China (No. 41230636).

References

- Gao DW, Liu JX, Song J (2011) The application of transient electromagnetic method in the study of landslide warning. In: Chinese geophysical society twenty-seventh annual meeting proceedings
- Gong DW, Zhang PZ, Wu CQ (2005) Research and new development of landslide activity monitoring. *Sens World* 11(6):10–14
- Jiang CG, Liu FJ, Dong XM, Peng JG (2005) Research and manufacture on integrated monitoring system of landslide. *J Saf Sci Technol* 1(6):19–24
- Li C, Jiang QH, Zhou CB (2011) Research on early warning criterion of landslides using case-based reasoning. *Rock Soil Mech* 32(4):1069–1076
- Qiao JP, Yang ZJ, Tian HL (2009) Probability analysis based method for rainfall-induced landslide warning. *J Eng Geol* 17(3):343–348
- Shi B, Ding Y, Xu HZ (2004) An application of distributed optic fiber strain measurement to early-warning of landslide. *J Eng Geol* 12(1):515–518
- Sun YJ, Tong HJ, Shi B, Gao L (2012) Status analysis for the application of DFOS technology in the monitoring of slope stability. *J Eng Geol* 12:8601–8639
- Xu Q (2012) The theoretical studies on prediction of landslides using slope deformation process data. *J Eng Geol* 20(2):145–151



Evaluation of ‘Wig-Wag’ Landslide Warning Signs

Mike G. Winter, Neale Kinnear, Barbara Shearer, Louise Lloyd,
and Shaun Helman

Abstract

This paper presents technical and perceptual evaluations of a novel form of landslide warning road sign. The signs, known as ‘wig-wags,’ incorporate a standard rockfall/landslide red warning triangle, flashing lights and a sub-plate that warns of ‘higher risk when lights flash’ (i.e., during periods of high rainfall) and have been trialled at an important debris-flow site in Scotland. It is broadly concluded that the trial has had a satisfactory technical outcome, albeit that the rainfall triggers used to activate the signs need further development. The results of the perceptual evaluation indicate that, in general, desired driver behaviours are promoted by the use of the signs.

Keywords

Landslides • Debris flow • Rainfall • Temporal • Warning • Sign

Introduction

Landslides in the form of rainfall-induced debris flows are a common occurrence in Scotland. The events of August 2004, which adversely affected the trunk road network, led to the Scottish Road Network Landslides Study (Winter et al. 2005, 2009). The overall purpose of that study was to systematically assess and rank the hazards posed by debris flows and to put in place a management and mitigation strategy for the Scottish trunk road network.

The approaches to management and mitigation were based upon exposure reduction and hazard reduction respectively (Winter et al. 2009). There are many forms of landslide management and mitigation (e.g., VanDine 1996) and a classification scheme has been developed (Winter 2013a, b).

This particular scheme is intended to provide a common lexicon and to allow a clear focus on outcomes from such activities, whilst avoiding an overemphasis on individual processes and techniques. This approach ought to be of particular value to those who fund such works, including infrastructure owners and local governments. Management involves the reduction of the exposure of road users to the hazard by means of either:

1. Education;
2. Geographical (non-temporal) warnings; or
3. Response (including temporal, or early, warnings).

Mitigation primarily, but not exclusively, involves reduction of the actual hazard by means of:

- (a) Works to engineer or protect the elements at risk;
- (b) Remediation of the hazard to reduce the probability of failure; or
- (c) Removal, or evacuation, of the elements at risk

One of the recommendations put forward by Winter et al. (2009) was that a form of temporal road sign incorporating a standard rockfall/landslide red warning triangle, flashing lights and a sub-plate that warns of ‘higher risk when lights flash’ (i.e., during periods of high rainfall) might be suitable for sites where debris flow events occur on a regular basis. The signs provide both a geographical and temporal warning

M.G. Winter (✉) • B. Shearer
Transport Research Laboratory (TRL), 13/109 Swanston Road,
Edinburgh EH10 7DS, UK
e-mail: mwinter@trl.co.uk; bshearer@trl.co.uk

N. Kinnear • L. Lloyd • S. Helman
Transport Research Laboratory (TRL), Crowthorne House, Nine Mile
Ride, Wokingham RG40 3GA, UK
e-mail: nkinnear@trl.co.uk; lloyd@trl.co.uk; shelman@trl.co.uk

of potential landslides as part of a management strategy and are colloquially known as ‘wig-wags’.

A 2-year trial (since extended) of such signs began in January 2011 at the highly active A83 Rest and be Thankful site (Winter and Corby 2012), with the following objectives:

- Technical evaluation: Determine the efficacy of the wig-wag switch-off/switch-on protocol in terms of its alignment with actual events and also to assess the rainfall threshold used for the switch-on.
- Evaluation of drivers’ attitudes and behavioural responses (perceptual evaluation): Explore the attitudes held by local and non-local drivers towards landslide wig-wag signs on the A83 in terms of their perceived meaning and their impact on road safety.

The full evaluation, which is summarised in this paper, is presented by Winter et al. (2013).

‘Wig-Wag’ Signs

The design of the wig-wag signs incorporates both a static landslide warning sign and lights that flash during periods of heavy rainfall, to indicate an elevated risk of landslide (Figs. 1 and 2). Similar signs are commonly used to indicate the presence of school crossings or ice, both of which have a clear temporal aspect and are eminently suited to the use of flashing lights when such risks are at a higher level than at other times (i.e., at school start and end times, and during periods of cold weather, respectively).

Six signs were installed, three each for eastbound and westbound traffic. The sign plates are permanently visible to drivers and the flashing lights are switched on remotely, using mobile telecommunications technology, in response to warnings (or forecasts) of heavy rain. When the lights are switched on, to indicate a period of higher risk (of landslides), a notification is placed on the Traffic Scotland website (<http://www.trafficscotland.org>); such notifications are frequently broadcast both locally and nationally.

The wig-wag signs are switched on by the Traffic Scotland Control Centre in response to heavy-rain warnings. These are predicated upon meteorological forecasts that suggest that one or other of two threshold values is likely to be exceeded. The thresholds are defined by the Met Office as follows:

- 25 mm in a 24 h period, or
- 4 mm in a 3 h period.

The lights then flash from the time that the forecast period commences until 6 h after the forecast period finishes. The 6-h period was agreed, at the outset of the trial, as the best estimate of the period over which a residual risk would persist. The warning is also emailed to the Operating Company (Scotland TransServ) who consult with Transport



Fig. 1 Format of landslide wig-wag warning sign

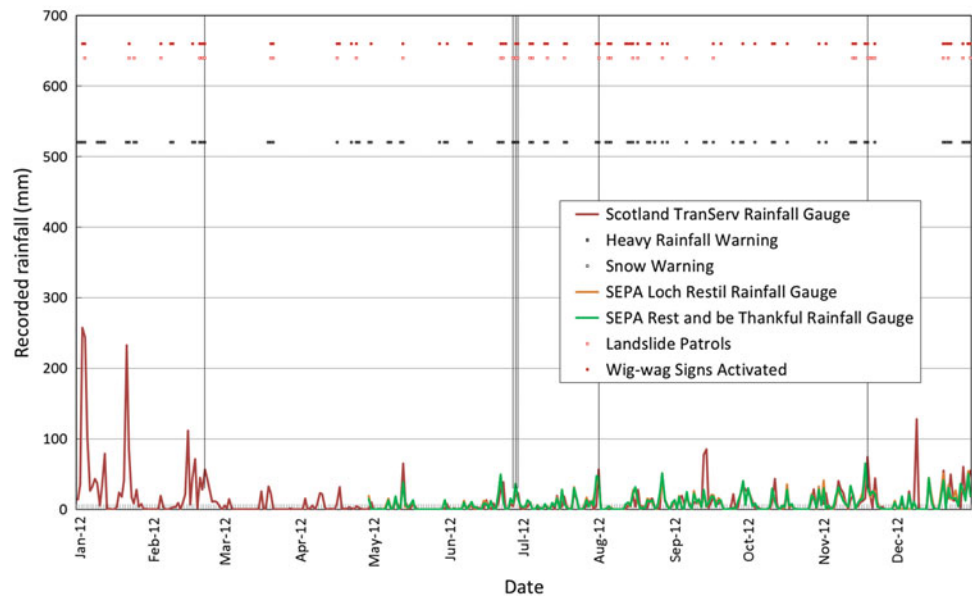


Fig. 2 Wig-wag warning sign in operation

Scotland and make a decision on whether landslide patrols should be activated; these operate only in daylight hours.

The wig-wags have prompted diverse views from road users and local residents. The promulgation of messages in the media, when the lights are switched on, along the lines of “There is a higher risk of landslides at the Rest and be Thankful . . . nothing has happened but drivers should be advised to take care . . .”, may erroneously send out the message that mid-Argyll is effectively closed for business at such times. Such a message was not stated in the recommendations made by Winter et al. (2009); what was contained in those recommendations was that such signs should be used to alert drivers to the need to take extra care and appropriate actions for drivers were detailed

Fig. 3 Rainfall data, weather warnings and wig-wag switch-on periods for the Rest and be Thankful rainfall for 2012



therein. These messages were repeated and reinforced in leaflets issued jointly by Transport Scotland and Scotland TranServ. These leaflets included the following messages:

These new [wig-wag] signs will flash when there is a higher risk of a landslide, alerting drivers to take extra care while continuing their travel on the road.

Our aim is to keep roads open as safely as possible and you can help make your trip even safer by:

- *planning your journey in advance at <http://www.trafficscotland.org>*
- *checking the weather forecast before you set off*
- *allowing extra travel time*
- *being alert for water or debris on the road*
- *listening for travel bulletins and looking for roadside messages displayed on Variable Message signs*
- *avoid stopping on bridges or next to water courses in mountainous areas*
- *planning your stops in towns and villages rather than the open roadside*

For more information about the Landslide Action Plan and Wig-Wag trial visit <http://www.transportscotland.gov.uk/>.

Technical Evaluation

The technical evaluation assesses, both qualitatively and quantitatively, the success or otherwise of the procedures and methods used to switch the wig-wag signs on and off. In order to evaluate the success of the initiative, what should be assessed is whether the wig-wags were switched on too frequently when debris flow events did not occur—‘false positive’—and switched off when debris flow events did occur—‘false negative’.

Table 1 ‘False positives’ indicated by the wig-wag signs

| | 2011 | 2012 | Total |
|-----------------|------|------|-------|
| Number of times | 20 | 35 | 55 |
| Number of days | 41 | 54 | 95 |

A number of data sources for the years 2011 and 2012 were used (e.g., Fig. 3), including:

- Rainfall data from a variety of sources, including gauges installed in April 2012 as part of ongoing work on rainfall trigger thresholds in the area.
- Heavy rainfall warning days.
- Snow warning days.
- The days on which the flashing lights on the wig-wag signs were activated.
- The times and dates of debris flows in the area.

The number of times that the wig-wags indicated ‘false positives’, and the number of days on which that occurred, is detailed in Table 1.

It is clear from Table 1 that there was a significant number of ‘false positives’ and that these were of significant duration. With a system of this nature ‘false positives’ are to be expected, particularly one that is under trial and subject to ongoing development. There seems little doubt that, given time, the forecast values used to initiate switch-on of the wig-wag signs can be improved, as described by Winter et al. (2013). During 2011 and 2012 the wig-wags were switched on for 11 % and 15 % of the year when the switch-on period did not contain a debris-flow occurrence.

There was a small number of occasions when wig-wags were not switched on despite a heavy rainfall warning being in force. The majority of these can be explained by the 6 h

that the wig-wags are intended to switch on after a heavy rainfall warning ceases to be in force, their activation by snow warnings, and possible breakdowns. It does seem likely that there was a small number of occasions when a heavy rainfall warning was in force and the wig-wags were not switched on. A review of the procedures for switch-on and switch-off is needed to ensure that this happens as infrequently as possible.

Eight debris flow events were identified in the area during 2011 and 2012. Of these, six occurred when a heavy rainfall warning was in force and the wig-wags were switched on. A seventh seems most likely to have also occurred during the warning period when the wig-wags were switched on, although this cannot be confirmed with any degree of certainty as the debris flow did not reach the road and was, most likely, not observed until some time after its occurrence.

The eighth event (1 December 2011), occurred when there was no weather warning current and the wig-wags were switched off at the time (switch-off was at around midday on 30 November). The event occurred on the first day following a change of weather warning supplier. This change over in the source of the weather warnings is not thought to have adversely affected operation of the system. The fact that the landslide event occurred when there was not a heavy rainfall warning active and the wig-wag signs were switched off means that it must be classed as a ‘false negative’.

However, the nature of this debris flow event was somewhat different to those that more typically affect the area. Typically the events start high on the hillside as a small translational slide that enters an existing stream channel and then, if there is sufficient water, it erodes material from the stream walls and becomes a debris flow within that channel (e.g., Winter et al. 2006). The December 2011 event, being very close to the road, effectively comprised only the translational slide phase and the translational slide itself appears to have been somewhat larger than is typical (Fig. 4).

It may also be that the 6-h period between the end of the heavy rainfall warning and the switch-off of the wig-wags needs to be extended, or to incorporate some flexibility depending upon the antecedent conditions. This will be considered as part of ongoing work to further develop the tentative rainfall intensity-duration threshold described by Winter et al. (2010, 2013). At present the heavy rainfall warnings are used to activate the wig-wag signs and the number of ‘false positives’ confirms the view that the amount of rainfall required to trigger debris flows is underestimated. This seems to be a function of the rather sparse rainfall gauge network, which is primarily intended for the collection of synoptic data.

Debris flow events are shown as vertical lines. Landslide patrol periods are also shown.



Fig. 4 A83 Rest and be Thankful debris flow event of 1 December 2011 (Courtesy of Scotland TranServ.)

Perceptual Evaluation

For the perceptual evaluation, a face-to-face questionnaire survey was conducted to determine attitudes, perceptions and self-reported behavioural reactions to the signs by local and non-local drivers, when the signs are switched on and when they are off.

The aim of the work was to establish the impact of the installation of landslide wig-wag signs on the A83 Rest and be Thankful on driver behaviour and attitudes. A survey design was utilised to measure drivers’ speed choice for a range of driving scenes, including landslide and other wig-wag signs, whereby speed choice was considered a proxy for behavioural response. Road scenes were matched and digitally altered to allow direct comparison of participant responses where the sign was active (i.e., flashing), not active, and removed from the scene. The face-to-face survey sought to answer the following questions:

1. What is the effect of installing a landslide wig-wag sign on drivers’ self-reported behaviours?
2. What effect does the type of sign (e.g., landslide wig-wag sign versus other wig-wag warning signs) have on drivers’ behaviours?

3. What do drivers report they would do if they passed a wig-wag sign when the lights are flashing?
4. What do drivers think they should do if they pass a wig-wag sign when the lights are flashing?
5. Do drivers think the signs make the road safer and do drivers take the precautions that Transport Scotland publicised?
6. Are there differences between local and non-local drivers?

Overall results indicate that there is no effect on drivers' speed choice resulting from the presence of an inactive landslide wig-wag sign, and that the effect of activating the flashing lights on a landslide wig-wag sign is a reduction in chosen speed. This is a desirable outcome, as it suggests that the installation of the signs has not resulted in any unexpected behavioural response from drivers and that drivers are responding as anticipated when the signs are activated (i.e., they are taking more care). This result was apparent for both local and non-local drivers, although non-local drivers' speed reductions to flashing landslide wig-wag signs are more pronounced.

While the overall findings suggest that drivers' behavioural response to landslide wig-wag signs is in the desired direction (i.e., drivers reduce speed in response to a flashing landslide wig-wag sign), results indicate that drivers' reduction in stated speed to both flashing ice warning and school wig-wag signs was found to be greater than that of landslide wig-wag signs. In addition, the pattern of data was less consistent by sign location and by questionnaire order for the landslide signs. These differences by sign type could be for a number of reasons. For example, it might suggest that drivers are uncertain of the correct response to a flashing landslide wig-wag sign and do not consider the risk of a landslide to be as immediate as that of either ice on the road or school children being present.

This interpretation is supported by what drivers report they would do if they passed a wig-wag sign when it was flashing. Almost every respondent reported that they would reduce their speed upon seeing a flashing school wig-wag sign, and 85 % of respondents would slow down in response to a flashing ice warning wig-wag sign. In comparison, only 68 % of respondents reported that they would slow down for a flashing landslide wig-wag warning sign. Interestingly, 13 % of respondents reported that they would turn around or stop upon seeing a flashing landslide wig-wag sign and 2 % of respondents reported that they would speed up. The lesser consistency in stated responses for flashing landslide wig-wag signs suggests that the link between the risk factor being signalled (landslides) and the desired behavioural response (slow down) is not as obvious as it is for the 'ice' and 'school' risk factors. Presumably this is due to the immediacy of the threat in the landslide setting being less obvious than in the 'ice' and 'school' settings.

A similar pattern is present in the beliefs drivers stated about what they thought they *should* do when seeing a flashing landslide wig-wag sign. One-hundred per cent of drivers reported that they *should* slow down when passing a flashing school wig-wag sign. This drops to 92 % of drivers for a flashing ice warning wig-wag sign and drops further to 83 % for a flashing landslide wig-wag sign. A proportion of drivers believe that the correct response to passing a flashing landslide wig-wag sign is to continue at the same speed (5 %), turn around (5 %), stop (5 %) or speed up (1 %). This is consistent with the proportions who report that this is what they *would* do and suggests that some drivers are unaware of the desired response, specifically for the landslide wig-wag signs. Further analysis revealed that this group of drivers are largely non-locals and may have therefore missed out on any marketing material disseminated when the signs were installed. It is possible that their behavioural response is a result of a lack of knowledge of the desired response rather than a deliberate act of non-compliance.

Of participants who drove the road regularly, the majority (71 %) reported that they agreed that the signs had made the road safer (34 % strongly agreed) although 18 % disagreed with this statement (7 % strongly disagreed). Over half of these drivers also reported following Transport Scotland's guidelines when using the A83 to check the weather forecast, allow extra time for their journey and listen to travel updates on the radio.

Discussion and Conclusions

The A83 at the Rest and be Thankful is a locality that is known for the frequency with which debris flow events occur, much more than any other part of the trunk road network in Scotland. It is thus well-suited to the use of this type of temporal warning. The potential application of this approach to other parts of the network is limited and any proposals should be the subject of detailed location-specific assessment.

Eight debris flow events occurred in the Rest and be Thankful area during the 2011 and 2012 trial period. Six of those occurred during periods when a heavy Rainfall Warning was in force and the wig-wags were switched on and a seventh was most likely contained within that group, albeit that there is some doubt about the precise timing of the event. The eighth event occurred during a period when there was no heavy Rainfall Warning in force and the wig-wag signs were switched off ('false negative'). There may be good reasons for this and some modification to the period during which the wig-wags remain switched on after the heavy Rainfall Warning ceases to be in force may be needed.

Nevertheless, there was a significant number of 'false positives'. These are to be expected with a system of this

nature, particularly one that is under trial and subject to ongoing development.

Work to further develop the currently tentative rainfall intensity-duration debris flow threshold is ongoing (Winter et al. 2010). Certainly the thresholds currently used are low compared to others used internationally.

The results of the survey undertaken to evaluate driver perception of the wig-wags signs have established that overall, the installation of landslide wig-wag signs on the A83 does not appear to have had any negative effect on drivers' behaviour (as measured by speed choice) overall.

Both local and non-local drivers who have experience of driving the A83 reported slower speed choice on average when landslide wig-wag signs are flashing, with non-local drivers reducing their speeds more than local drivers on average. For all drivers, the reduction in speeds to flashing landslide wig-wag signs was not as pronounced as that for flashing ice warning or school wig-wag signs.

The available evidence supports the assertion that this is the result of the link between the risk factor and required behaviour being weaker in the 'landslide' setting than in the 'ice' and 'school' settings, where the immediacy of the threat may be more obvious.

The evidence from both the technical and perceptual evaluations indicated that the wig-wag signs trial has a satisfactory outcome and that the flashing lights prompt generally desirable behaviours in the majority of cases. Notwithstanding this, there are areas for improvement and specific recommendations are made by Winter et al. (2013).

That the wig-wag signs have prompted diverse views from road users and local residents is beyond doubt. However, the message that 'mid-Argyll is effectively closed for business' when the signs are flashing does not seem to be borne out by the perceptual evaluation in which a relatively small proportion of respondents suggested that they would turn around on encountering a flashing landslide wig-wag sign. Indeed, over 70 % of participants in

the survey stated that they agreed with the statement that the signs made the road safer, albeit that 18 % disagreed with the statement. It does thus seem that this message, erroneous as it is, is most likely a result of media reports that originate from the notifications that are placed on the Traffic Scotland website when the signs are activated.

It seems appropriate to continue efforts to promulgate messages about desired behaviours and these might be increased for non-local drivers.

Acknowledgments Transport Scotland's funding of this work is gratefully acknowledged.

References

- VanDine DF (1996) Debris flow control structures for forest engineering. Ministry of Forests Research Program, Working Paper 22/1996. Ministry of Forests, Victoria, BC
- Winter MG (2013a) Discussion session 4.3: landslides. Geotechnics of hard soils—weak rocks. In: Anagnostopoulos A, Pachakis M, Tsatsanifos C (eds) Proceedings, XV European conference on soil mechanics and geotechnical engineering, vol 4. IOS Press, Amsterdam, pp 427–434
- Winter MG (2013b) A classification scheme for landslide management and mitigation. *Int J Landslide Environ* 1(1):123–124
- Winter MG, Corby A (2012) A83 Rest and be Thankful: ecological and related landslide mitigation options. Published Project Report PPR 636. Transport Research Laboratory, Wokingham
- Winter MG, Macgregor F, Shackman L (eds) (2005) Scottish road network landslides study. Transport Scotland, Edinburgh, 119 p
- Winter MG, Heald A, Parsons J, Shackman L, Macgregor F (2006) Scottish debris flow events of August 2004. *Q J Eng Geol Hydrogeol* 39(1):73–78
- Winter MG, Macgregor F, Shackman L (eds) (2009) Scottish road network landslides study: implementation. Transport Scotland, Edinburgh, 278 p
- Winter MG, Dent J, Macgregor F, Dempsey P, Motion A, Shackman L (2010) Debris flow, rainfall and climate change in Scotland. *Q J Eng Geol Hydrogeol* 43(4):429–446
- Winter MG, Kinnear N, Shearer B, Lloyd L, Helman S (2013) A technical and perceptual evaluation of wig-wag signs at the A83 Rest and be Thankful. Published Project Report PPR 664. Transport Research Laboratory, Wokingham



Latest Developments of Hong Kong's Landslip Warning System

A.C.W. Wong, S.M. Ting, Y.K. Shiu, and K.K.S. Ho

Abstract

The Geotechnical Engineering Office (GEO) has been operating, in conjunction with the Hong Kong Observatory (HKO), a territory-wide Landslip Warning System for over 35 years. The objective of the System is to alert the general public of possible landslide risks during periods of heavy rainfall. The GEO operates an extensive network of automatic raingauges which provides real-time rainfall information for use in the Landslip Warning System. Over the years, various measures have been implemented to enhance the efficiency and reliability of the rain gauge system. Rainfall-landslide correlation models, which support the algorithm of the Landslip Warning System, have recently been updated to incorporate the most recent landslide and rainfall data using advanced geospatial and statistical techniques. This paper gives an overview of the major components of the Hong Kong Landslip Warning System and describes the technical basis of the System.

Keywords

Landslip warning • Rain gauge system • Rainfall-landslide correlation • Natural terrain landslides • Emergency preparedness planning

Introduction

The Geotechnical Engineering Office (GEO) has been operating a territory-wide Landslip Warning System, in conjunction with the Hong Kong Observatory (HKO), since 1977. The purpose is to alert the general public of possible landslide risks during periods of heavy rainfall.

The operation of the Landslip Warning System requires information on real-time rainfall and sufficiently reliable short-term forecasts of rainfall, together with a good understanding of the relationship between rainfall and landslides.

An extensive network of automatic raingauges has been installed to provide real-time information on the actual

rainfall. Over the years, various measures and initiatives have been taken to enhance the efficiency and reliability of the Rain gauge System. This system provides real-time information on actual and forecasted rainfall for more effective decision-making on whether and when to issue a landslip warning.

Various improvements in the rainfall-landslide correlation models have been made over the years. These have led to more reliable prediction of landslides and hence to better performance of the Landslip Warning System.

The recent development of storm-based rainfall-natural terrain landslide correlations has resulted in the formulation of a new Natural Terrain Landslip Alert framework for enhanced landslide emergency preparedness.

This paper gives an overview of the major components of the Landslip Warning System and consolidates the extensive experience in using the system as a risk management tool. The key elements of the Rain gauge System, together with recent improvement measures, are described. The development work undertaken to establish the prevailing rainfall-

A.C.W. Wong (✉) • S.M. Ting • Y.K. Shiu • K.K.S. Ho
Civil Engineering and Development Department, Geotechnical Engineering Office, Civil Engineering and Development Building, 101, Princess Margaret Road, Ho Man Tin, Kowloon, Hong Kong
e-mail: alancwong@cedd.gov.hk; smting@cedd.gov.hk; ykshiu@cedd.gov.hk; kenho@cedd.gov.hk

landslide correlations for man-made slope failures and the Natural Terrain Landslip Alert framework respectively are summarized.

GEO Raingauge System

The GEO has been operating an extensive automatic raingauge network to provide real-time rainfall information for use in the Landslip Warning System since 1984. The efficiency and reliability of the raingauge network has been enhanced by various measures, including the improvement of network coverage, system robustness, information dissemination and system architecture.

The existing network (Fig. 1) comprises 88 GEO and 22 HKO automatic raingauge field stations with an average raingauge density of 10 km²/gauge. Real-time rainfall data from the GEO raingauges are transmitted via a General Packet Radio Service (GPRS) network and Metro Ethernet network services at 5-min intervals to the GEO Control Centre, which is equipped with a number of server computers (i.e. the GEO computer system) for receiving and processing the data. Data transmission and data sharing between HKO and GEO is carried out by means of dedicated leased lines.

Each field raingauge station consists of a tipping bucket rainfall measuring unit and a data-logger (with an internal modem) powered by solar energy (Fig. 2). To ensure reliable rainfall data acquisition by the field raingauge stations, each raingauge is calibrated and tested before the onset of the wet season each year.

Computer programs are developed for the operation of the GEO computer system. They are implemented together with other proprietary software packages to acquire and analyse real-time rainfall data from the raingauges, display situation of rainfall development (such as rainfall contour maps, cumulative rainfall curves, etc.) and predict the number of landslides (based on 24-h recorded rainfall, 21-h recorded rainfall + 3-h forecasted rainfall, and 23-h recorded rainfall + 1-h forecasted rainfall respectively) using a rainfall-landslide correlation model. The predicted landslide numbers are checked automatically against the pre-defined criteria for issuing a Landslip Warning. Rainfall and landslide warning-related information is disseminated through both Intranet and Internet. Authorized users can access the information using desktop computers, notebook computers, tablets or smart phones. Figure 3 shows the diagrammatic structure of the GEO Raingauge System.

In addition to real-time rainfall data, short-term rainfall forecasting data (1-h to 3-h) provided by HKO are incorporated in the Raingauge System to support decision-making on the issuing of Landslip Warnings. The rainfall forecast is provided by HKO's Short-Range Warning of

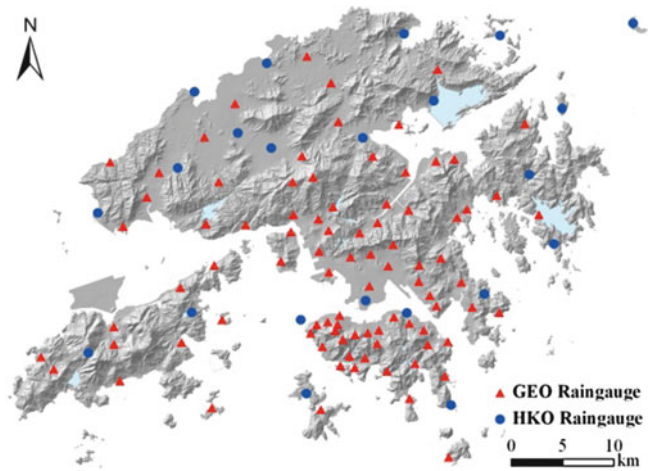


Fig. 1 Locations of GEO and HKO field raingauge stations



Fig. 2 Field raingauge station

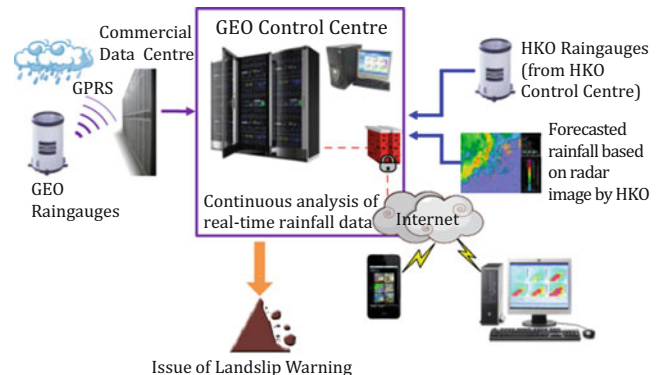


Fig. 3 GEO raingauge system

Intense Rainstorms in Localized Systems (SWIRLS) (Li et al. 2000). SWIRLS operates based on real-time correlation between radar echo intensity and rainfall amount recorded on the ground by raingauges, and consideration of predicted rain cloud movements.

Currently, the GEO Raingauge System is in the process of being revamped. The system hardware is being upgraded and the system architecture will be streamlined with a view to improving the system reliability and performance. The frequency of real-time data transmission will also be increased from 5 to 1 min.

The GEO is exploring the possible use of HKO's real-time rainfall data generated by the radar-raingauge co-Kriging technique (Yeung et al. 2010) in operating the Landslip Warning System. This advanced quantitative precipitation estimate technique could help to produce a more realistic rainfall distribution pattern, in particular in areas where the raingauge density is low (such as the boundary areas of the territory). In addition, HKO is exploring the feasibility of providing medium-term (2–3 days) probabilistic rainfall forecasts based on numerical weather prediction model outputs to improve landslide emergency preparedness.

Evolution of Rainfall-Landslide Correlation Models

From 1977 to 1984, the Landslip Warning System was operated based on the rainfall threshold model of Lumb (1975). Brand et al. (1984) reported on the work carried out for the development of Landslip Warning Criteria in the early 1980s, which were used for much of the 1980s and 1990s. These two models were largely based on the rainfall threshold concept, i.e. the rainfall intensity above which a large number of landslides would occur, as observed in past rainstorms. The system at that time was operated based on the rainfall recorded by a single raingauge.

The rainfall-landslide correlations were completely revamped in the late 1990s. At that time, the focus of the development work on rainfall-landslide correlations turned to statistical analyses of the relationship between rainfall intensity and landslide density/probability. Such analyses became possible because of the availability of a more complete catalogue of slopes, and more comprehensive data on the time of occurrence, spatial and temporal distribution of landslides and rainfall intensity since the 1980s.

The third generation rainfall-landslide correlation model was established based on the work of Pun et al. (1999). The model was used to operate the Landslip Warning in the late 1990s until 2003. It was subsequently replaced by the fourth generation correlation model based on the framework proposed by Yu et al. (2003).

Prevailing Rainfall-Landslide Correlations for Man-Made Slopes

The prevailing Landslip Warning Algorithm is based on the fourth generation rainfall-landslide correlation model. It adopts a probability-based framework, which can be integrated with the spatial distribution of the registered man-made slopes and the spatial and temporal variation of rainfall to predict the number and distribution of landslides. Rainfall and landslide data obtained from 1996 to 2010 are used. The model allows a realistic projection of the landslide pattern in real time as the rainfall pattern develops, which is essential for effective operation of the Landslip Warning System.

From experience, different types of man-made slopes have different responses to the same rainfall intensities. A rainfall-landslide frequency correlation has been developed for each of the four main types of man-made slopes in Hong Kong, namely soil cut slopes, rock cut slopes, fill slopes and retaining walls (Fig. 4). For all of the four correlation models, the correlation lines correspond to a bi-linear relationship between landslide frequency and rainfall intensity. The gradients of the lines (in semi-log scale) are significantly greater for rainfall with lower intensity than those for rainfall with higher intensity.

Issue of Landslip Warnings

The prevailing Landslip Warning Trigger Level is at a point when the predicted landslide number over the territory equals or exceeds 15, with a consideration of both recorded rainfall and short-term rainfall forecasts. This generally corresponds to a situation where a large part of the territory is subject to a rolling 24-h rainfall in the range between 150 mm and 250 mm. Based on the experience gained over the past 10 years, setting the Landslip Warning Trigger Level at 15 predicted landslides could achieve satisfying results in terms of landslide emergency preparedness (e.g. mobilization of an emergency control centre and emergency teams on stand-by for inspection of landslides and provision of advice on emergency actions or measures to reduce landslide risk) and warning provision to the public.

Decision-making on the issue of a Landslip Warning is not a straightward process. It usually involves a lot of expert judgement. When deciding on whether a Landslip Warning is to be issued and its timing of issue, factors such as the real-time predicted landslide number, the actual reported landslide number at the time, and the uncertainty of rainfall forecast, etc., need to be considered. Close communication

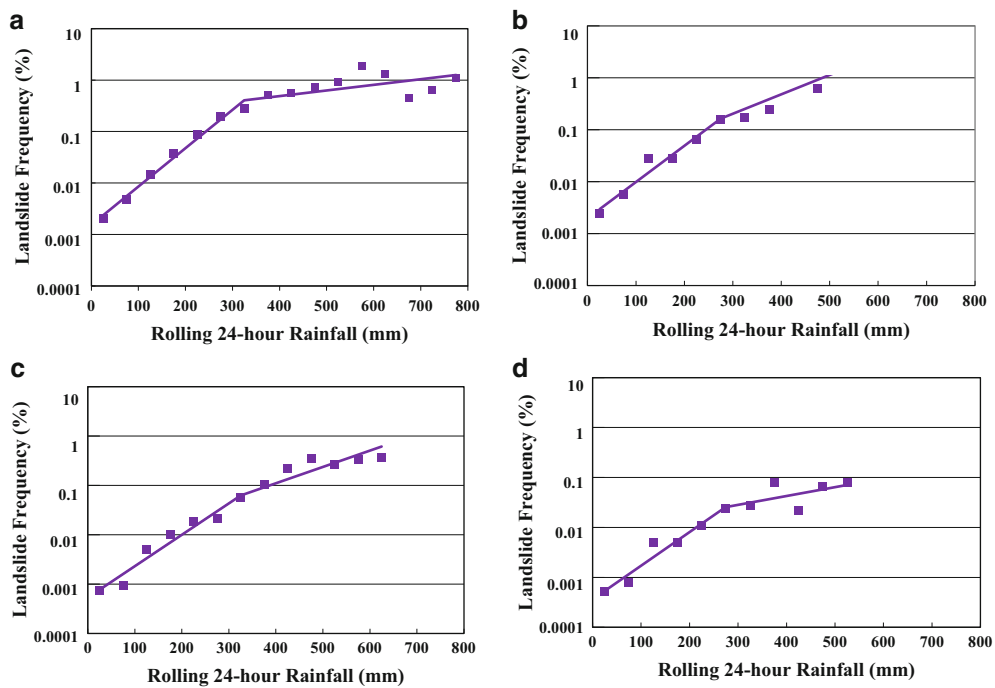


Fig. 4 Correlations between landslide frequency and rolling 24-h rainfall. (a) Soil cut slopes, (b) Rock slopes, (c) Fill slopes, (d) Retaining walls

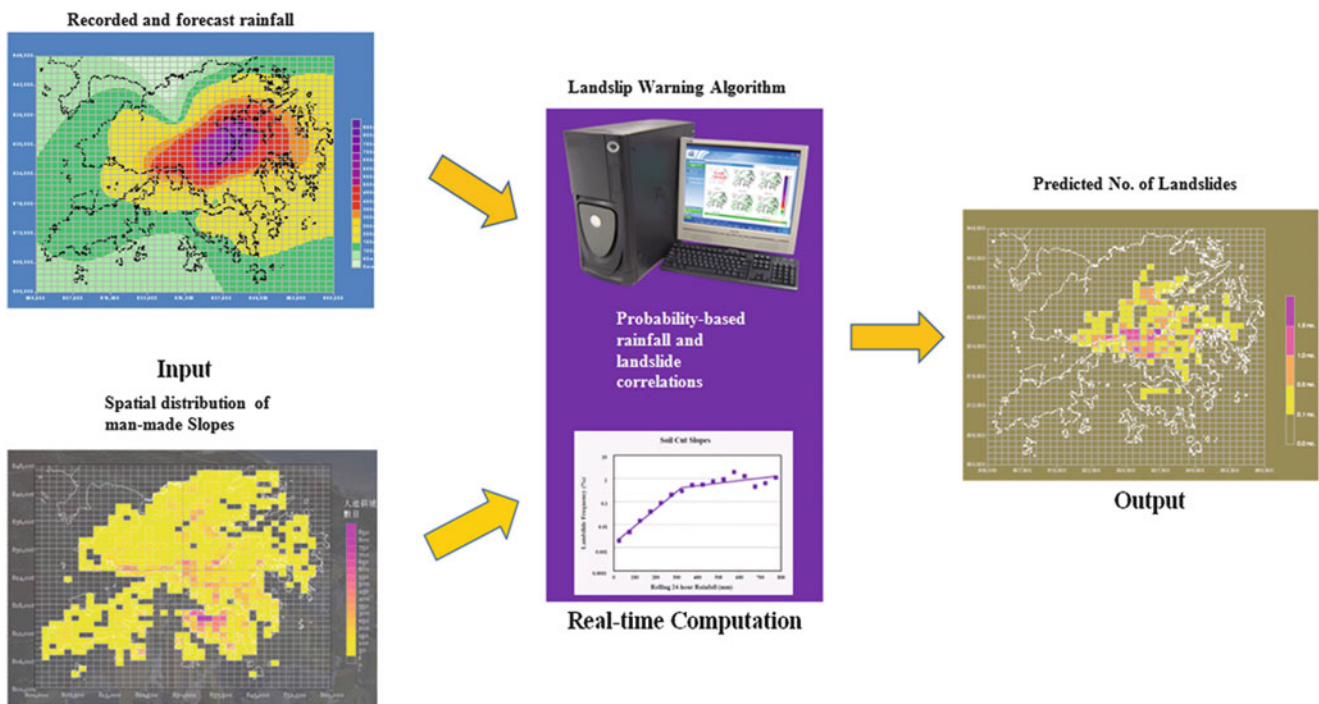


Fig. 5 Workflow of the prevailing landslide warning system

has to be maintained between GEO and HKO. The workflow of the prevailing Landslip Warning algorithm is shown in Fig. 5.

When a Landslip Warning is issued, local radio and television stations are notified and requested to broadcast the warning to the public at regular intervals, together with

advice on the precautionary measures that should be taken by the general public.

Landslip Potential Index

The GEO has developed an index, called the Landslide Potential Index (LPI), to describe the rainstorm severity with respect to its potential to cause landslides (GEO 2009). The LPI of a rainstorm is determined based on the probable number of landslides that could be caused by a given storm relative to the Kwun Lung Lau landslide event of July 1994. The rainstorm in July 1994 caused the Kwun Lung Lau landslide, with five fatalities and three serious injuries, and it is set with an LPI of 10. A rainstorm with an LPI of 5 could be considered to be half as severe as the Kwun Lung Lau rainstorm in causing landslides. To enable the public to better understand the severity of a rainstorm with the issue of the Landslip Warning, the LPI of the rainstorm will be uploaded onto the Hong Kong Slope Safety Website (<http://hkss.cedd.gov.hk/hkss/eng/index.aspx>) within a week after the cancellation of a Landslip Warning.

Natural Terrain Landslip Alert Criteria

General

Past experience shows that in extreme rainstorm events (like the June 2008 rainstorm which resulted in about 2,400 natural terrain landslides), very different hazard scenarios and landslide patterns would result when compared to a moderately heavy rainstorm event (e.g. 24-h rainfall of about 200–300 mm). This would likely result in significant implications for emergency preparedness and response planning.

Establishment of Storm-Based Rainfall-Natural Terrain Landslide Correlations

The prediction of the spatial distribution and number of natural terrain landslides during a storm forms the operation basis of the Natural Terrain Landslip Alert Criteria. Practical and reliable storm-based rainfall-landslide correlations are required.

With the use of the 1985–2008 natural terrain landslide data from the Enhanced Natural Terrain Landslide Inventory (MFJV 2007) and inspections for natural terrain landslides of the June 2008 rainstorm, two sets of storm-based rainfall-landslide correlations have been developed using statistical methods. One is based on normalized maximum rolling 24-h

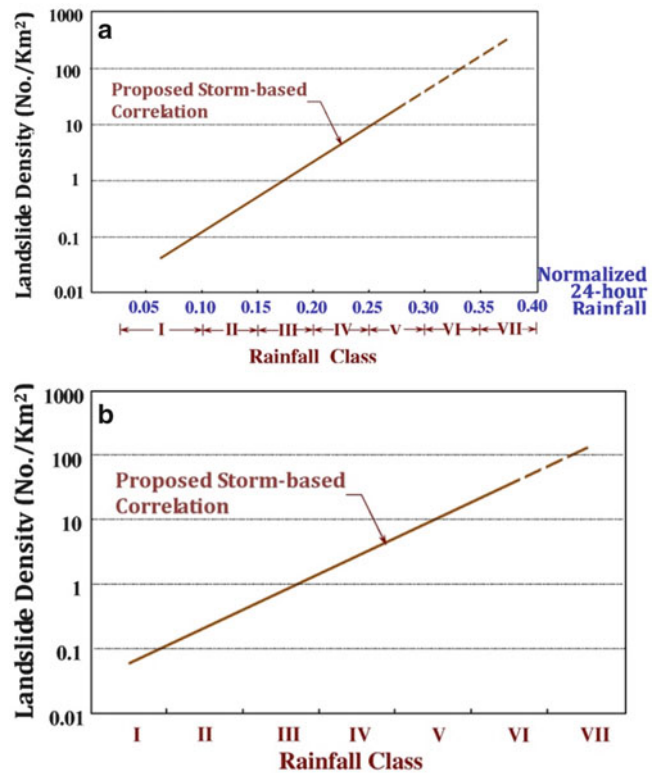


Fig. 6 Storm-based rainfall-natural terrain landslide correlations. (a) Correlation based on normalized maximum rolling 24-h rainfall. (b) Correlation based on normalized maximum rolling 4-h and 24-h rainfalls

rainfall and the other on combined consideration of normalized maximum rolling 4-h and 24-h rainfalls (Fig. 6a, b) (Chan et al. 2012).

Consideration of Spatial Effects of Landslide Risk

Natural terrain landslides occurring in different regions of Hong Kong pose different risk levels due to variation in the development settings. The relative risk levels for different regions may be better reflected by suitable scaling up the predicted number of natural terrain landslides in more developed areas to account for the likely corresponding consequence and hence landslide risk.

Based on the broad development settings, the whole territory is divided into five regions and a scaling factor is assigned to each region. The scaling factors are used to scale the predicted number of landslides in order to derive an equivalent number of natural terrain landslides that are notionally 'felt' by the community and hence relevant to landslide alert consideration.

Table 1 Natural terrain landslip alert criteria framework

| Equivalent number of predicted natural terrain landslides | Alert level | Scenarios |
|---|-------------|---|
| ≥500 to <1,000 | 1 | Alert of possible widespread natural terrain landslides |
| ≥1,000 to <2,000 | 2 | Warning of widespread natural terrain landslides |
| ≥2,000 | 3 | Warning of very widespread natural terrain landslides |

Three-Tier Natural Terrain Landslip Alert Criteria

The Natural Terrain Landslip Alert Criteria are a three-tier alert system (Table 1). The alert levels are determined on the basis of the actual recorded rainfall and an equivalent number of predicted natural terrain landslides, which accounts for the relative landslide risks of different regions.

The number of natural terrain landslides may be predicted using the mean correlation shown in Fig. 6a (i.e. the correlation based on normalized maximum rolling 24-h rainfall) or b (i.e. the correlation based on combined normalized maximum rolling 4-h and 24-h rainfalls), or a combination of the respective correlations.

A calibration exercise using ten previous severe rainstorms which caused several hundreds to over 2,000 natural terrain landslides since 1985 showed that a better fit could be obtained using the mean of the predicted number of landslides of both correlations.

With this Natural Terrain Landslip Alert framework, it is expected that on average five alerts would be issued in about 25 years, with a Level 2/Level 3 alert being issued about once every 10 years.

Implementation

The new alert criteria for natural terrain landslides are being operated as internal alerts for reference by Government emergency managers. For example, when widespread natural terrain landslides are predicted, the arrangement within the GEO is to mobilize special standby emergency teams comprising professionals with requisite engineering geological expertise to inspect the natural terrain landslides and assess the residual risks.

Conclusions

Significant efforts have been made to continuously improve the Landslip Warning System in Hong Kong over the years. A revamp project of the GEO Rain gauge System is in progress to further improve the system performance and reliability in order to better support decision-making on the issuing of Landslip Warnings. The probabilistic-based rainfall-landslide correlation model for man-made slopes, established based on the most recent landslide and rainfall data, is being used in the current Landslip Warning algorithm. A new set of Natural Terrain Landslip Alert Criteria has been additionally formulated for internal use for enhanced landslide emergency preparedness in respect of widespread natural terrain landslide events.

Acknowledgments This paper is published with the permission of the Head of the Geotechnical Engineering Office and the Director of Civil Engineering and Development, Government of the Hong Kong Special Administrative Region.

References

- Brand EW, Premchitt J, Phillipson HB (1984) Relationship between rainfall and landslides in Hong Kong. In: Proceedings of the 4th international symposium on landslides, Toronto, vol. 1. pp 377–384
- Chan CHW, Ting SM, Wong ACW (2012) Development of natural terrain landslip alert criteria (Special Project Report SPR 1/2012). Geotechnical Engineering Office, Hong Kong, 68 p
- GEO (2009) GEO information note—landslide potential index. Geotechnical Engineering Office, Hong Kong, 4 p
- Li PW, Wong WK, Chan KY, Lai EST (2000) SWIRLS—an evolving nowcasting system (Hong Kong Observatory Technical Note No. 100). Hong Kong Observatory, Hong Kong
- Lumb P (1975) Slope failures in Hong Kong. *Q J Eng Geol* 8:31–65
- MFJV (2007) Agreement No. CE 15/2005 (GE), natural terrain landslide identification—feasibility, final report on compilation of the Enhanced Natural Terrain Landslide Inventory (ENTLI). Geotechnical Engineering Office, Hong Kong, 113 p
- Pun WK, Wong ACW, Pang PLR (1999) Review of landslip warning criteria 1998/1999 (Special Project Report SPR 4/99). Geotechnical Engineering Office, Hong Kong, 77 p
- Yeung HY, Man C, Seed A, Chan ST (2010) Development of a localized radar-rain gauge co-kriging QPE scheme for potential use in quality control of real-time rainfall data. In: The third WMO international conference on quantitative precipitation estimation and quantitative precipitation forecasting and hydrology, 12–18 October 2010, Nanjing, China
- Yu YF, Lam JS, Siu CK (2003) Interim report on review of landslip warning criteria 2003 (Special Project Report SPR 4/2003). Geotechnical Engineering Office, Hong Kong, 19 p



A Multi-Scaled Early Warning Method for Rainfall-Induced Mountain Hazards

Zong-ji Yang, Jian-ping Qiao, Dong Huang, Hong-ling Tian, Yuan-jun Jiang, and Lili Shi

Abstract

The magnitude 8 (8M) earthquake (“Wenchuan earthquake”) that hit Sichuan province on May 12, 2008 highlighted the need for the development of large-scale early warning systems in the region surrounding the Longmenshan fault. Many of the deaths from this disaster were not from the earthquake itself, but from the landslides and other hazards that it caused. To this end, real-time monitoring and early warning of mountainous hazards (e.g. landslides, debris flows) are efficient non-engineering measures for disaster prevention and mitigation. Thus, to ensure effective disaster prediction and reduction within this region, a system of real-time regional and site-specific monitoring of mountainous hazards, coupled with early warning, is necessary. We propose here a multi-scaled, real-time early warning method. It combines large-scale regional hazard calculations and site-specific hazard monitoring with subsequent early warning. Real-time monitoring and early warning systems were constructed in five mountain hazard sites along the Longmenshan fault line, including three debris flow and two landslide zones. For early disaster warning, the threshold value of precipitation needed to trigger the post-earthquake mountainous hazard should be measured. However, identification of such threshold values is one of the most difficult issues for regional and site-specific mountainous hazard monitoring and early warning systems. To account for this difficulty, this study utilized a natural coseismic landslide from the Taziping Village of Hongkou County in Dujianyan City to identify the critical values and threshold parameters that resulted. After this experimental field test, the correlation of rainfall intensity with rainfall duration was calculated. The results indicated that the experimental field test was capable of identifying the threshold factors for the rainfall-induced mountain hazards.

Keywords

Mountain hazards • Early warning • Multi-scaled • Threshold identification • Rainfall induced

Z.-j. Yang (✉)

Key Laboratory of Mountain hazards and Surface process, Institute of Mountain hazards and Environment, Chinese Academy of Science, Chengdu 610041, China
e-mail: yzj@imde.ac.cn

J.-p. Qiao • D. Huang • H.-l. Tian • Y.-j. Jiang
Institute of Mountain hazards and Environment, Chinese Academy of Science, Chengdu 610041, China
e-mail: jpqiao@imde.ac.cn; hd1017@sohu.com; thl@imde.ac.cn; yuanjun.jiang.civil@gmail.com

L. Shi
Chengdu Institute of Geo-Environment Monitoring, Chengdu 610042, China
e-mail: shll1127@126.com

Introduction

After the 8M Wenchuan earthquake in 2008, the number and scale of mountain hazards it triggered were of a magnitude never before seen in China. One of the most damaging post-earthquake effects was rainfall-induced debris flows. These flows, while inherently dangerous, were made even more ruinous through being enhanced by the dramatically altered terrain (e.g. slope failures) brought on by the earthquake. These post-earthquake, rainfall-induced hazards became the most dangerous threat to the

area and caused catastrophic destruction to the Wenchuan earthquake-hit region of Sichuan province. In the past, the most important tools to counteract the effects of such hazards have been mechanical in nature. For example, retaining walls and ground anchors have been widely used to prevent slope failures. However, they are expensive and it is not realistic to apply mechanical measures at every potential site of slope failure. Moreover, mountain hazard sites are extremely common in the Wenchuan earthquake region, with most occurring at extremely large scales. Therefore, careful real-time monitoring and early warning of such hazards at both regional and site-specific scales is a reasonable alternative in the Wenchuan earthquake region. Past multi-disciplinary work using this approach achieved significant improvements in both mountain hazard monitoring and early warning. We propose here a multi-scale, real-time early warning method, which combines large-scale regional hazard maps as well as site-specific scale hazard site monitoring.

Multi-Scale, Real-Time Early Warning

Monitoring and early warning are two of the most efficient ways to mitigate mountain hazards such as landslides and debris flows. The combination of regional scale early warning and site-specific monitoring proposed in this study are aimed at making the early warning more accurate and precise. First, the riskiest areas were determined based on the rainfall distribution map and hazards zonation map during a specified rainfall period. These risk-areas then had site-specific hazards sites identified so that the local communities could be monitored. Residents within these hazardous areas could then decide to evacuate by using the calculated threshold value for site-specific disasters within their area (Fig. 1).

The real-time early warning map for regional scale rainfall-induced mountain hazards was developed by considering the triggering factor of rainfall distribution, in addition to pertinent environment factors. The probability-based prediction method of regional scale rainfall-induced mountain hazards was developed by combining the hazard zonation map with the probability of regional precipitation. The prediction model was established through the analysis of geological and hydrological factors of the specified area, combined with the analysis of mountain hazard occurrences and the corresponding regional precipitation data. A site-specific, real-time monitoring and early warning system was constructed for five mountain hazard sites, including three debris flow and two landslide zones along the Longmenshan fault in Dujiangyan and Pengzhou County, Chengdu City (Fig. 2). In order to provide early warning prior to a potential rainfall-induced hazard, historical and experimental data were used to calculate the threshold value of precipitation from each of the individual monitoring sites.

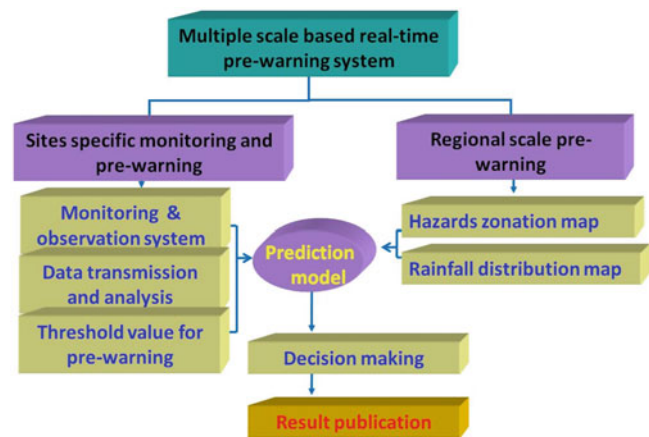


Fig. 1 Framework of multi-scale, real-time early warning system

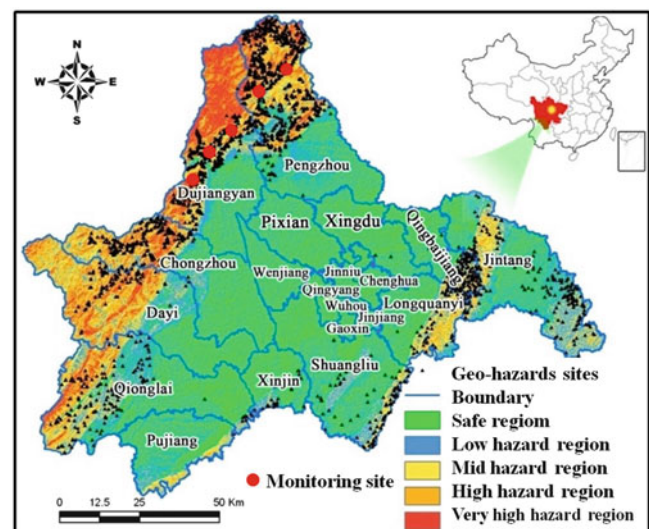


Fig. 2 Location and spatial probability map of study area

Study Area

The study area is the region of the city of Chengdu, which is located in the middle of Sichuan province. This area was hard-hit by the 8M Wenchuan earthquake and was heavily damaged. The region of Chengdu city covers about 12,390 km², with a latitude range of 30°05' to 31°26'N, and longitude range of 102°54' to 104°53'E. The study area is situated in a subtropical humid monsoon climate zone, with an annual average temperature of 16.7°. The annual average precipitation is about 1,234.8 mm, with a maximum of 1,605.4 mm in 1978. Rainfall is most concentrated in the period between June and September. Precipitation decreases from southeast to northwest, where the average precipitation is about 1,800 mm. The landforms of the area change from high mountains to middle mountains and small hills, ultimately ending in a flat plain. The elevation in the study area ranges from a minimum of 387 m

above sea level (a.s.l.) to a maximum of 5,364 m a.s.l., with about a 5,000 m height difference. About two-thirds of the Chengdu city region lies within mountainous areas while the remaining one-third is a flat plain. The Minjiang River and its branches drain this area. Geologically, this area is located along a tectonic-transition belt between the Chengdu plain and Longquanshan Mountains. In turn, they are a part of the Cathaysian structural system, which also belongs to the Yangtze para-platform and the Qinghai-Tibet quasi-geosynclinal area. There are three major pressure-shear faults crossing the area, all with a northeast orientation. These faults include the Beichuan-Yinxu faults, the Longquanshan faults and the Guanxian faults. The study area is underlain by bedrock varying in age from the Quaternary period to the Proterozoic eon. The average thickness of the crust is approximately 20,000 m. The strata include sandstones, mudstones carbonates, carbonates intercalated with clastics, igneous rocks, metamorphic rocks and shale, as well as unconsolidated Quaternary deposit layers.

Early Warning Method

Providing regional scale, early warning for mountain hazards is often very difficult because their mechanisms of action vary greatly from place to place. Moreover, the factors affecting slope stability are closely interconnected and can vary greatly. Factors that can affect the slope stability can be divided into two categories: preparatory factors and external triggering factors (Qiao et al. 2009; Yang et al. 2010a, b; Tian et al. 2010; Huang and Yuin 2010). Preparatory factors mainly include geological circumstance and geomorphology settings. External triggering factors, however, provide external dynamic conditions for mountain hazards to develop. Both preparatory and triggering factors affect the occurrence of mountain hazards. The former have a spatial distribution, which can be delineated by the regional mountain hazards assessment zonation (Qiao et al. 2004; Wang et al. 2010), while the latter possesses a temporal distribution which can change over time, thus making it more difficult to account for in early warning scenarios. As a consequence, “hazards zonation mapping” is often conducted in a manner in which the triggering factors of mountain hazards are *not* considered in determining the probability of mountain hazard occurrences. Alternatively, direct overlaying of the annual precipitation contour map can also be problematic in conducting hazard zonation mapping, even within the same region, because there are differences in rainfall across space and time. In this study, the real-time prediction map for rainfall-induced mountain hazards was developed by considering the triggering factors related to rainfall distribution in addition to relevant environmental factors. The probability-based prediction method of rainfall-induced regional mountain hazards was proposed

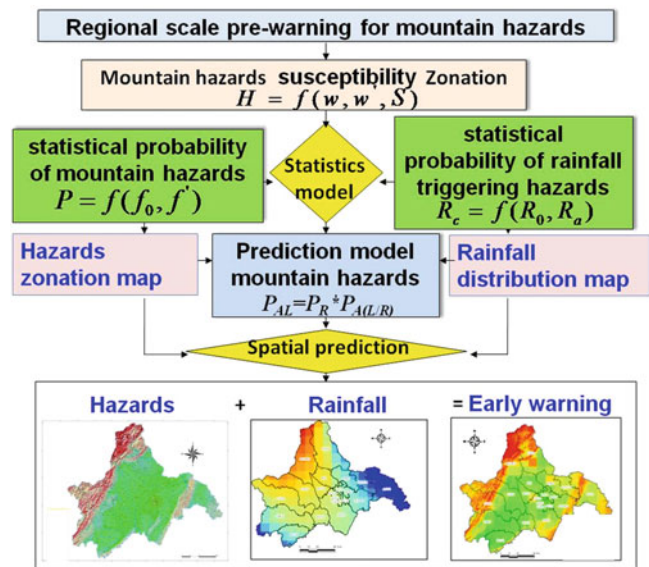


Fig. 3 Framework of regional scale early warning method

through a combination of mountain hazard zonation and the probability of regional precipitation (Fig. 3). The prediction model was established through the analysis of geological and hydrological factors of the specified study area, which was combined with the analysis of mountain hazards occurrence data and corresponding precipitation data (Yang et al. 2012).

A site-specific, real-time monitoring and early warning system for five typical mountain hazards sites was constructed in Dujiangyan and Pengzhou County, Chengdu City. These five sites were along the Longmenshan fault and included the two major mountain hazards: debris flows (three sites) and landslides (two sites). The system monitored the behaviour of rainfall-triggered mountain hazards with both inexpensive and sophisticated sensors. Inclinometers are a low-cost and simple monitoring method for rainfall-induced landslides. They use tilt sensors on the surface of a given slope to detect abnormal deformation; these sensors are coupled to a wireless sensor unit with a MEMS tilt sensor and a volumetric water content sensor (Towhata et al. 2011; Uchimura et al. 2010, 2011). Other tools included rainfall gauges, pore pressure meters, water content meters, a video monitoring system for both landslides and debris flows, ultrasonic mud level meters, and infrasound monitoring meters for debris flows (Fig. 4). All data gathered from these devices were subsequently gathered and transferred through a wireless network.

Identification of Threshold Values

In order to effectively carry out disaster reduction and early warning, the threshold value of the precipitation that most probably triggers post-earthquake mountain hazards should be determined.

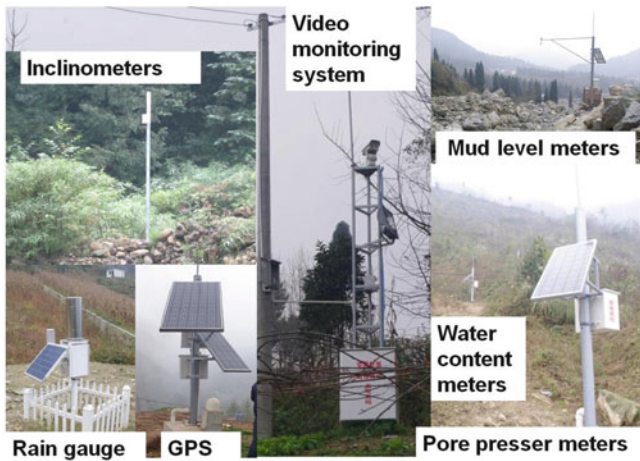


Fig. 4 Photos of site-specific, real-time monitoring and early warning system

Statistical Rainfall Threshold

In every year following the Wenchuan earthquake, heavy rainstorms have triggered significant debris flows within the region. For example, on August 13th 2010, heavy rainstorms triggered debris flows in Qingping County, Longchi County and Yingxiu County. These debris flows had a high correlation with the both the active fault and high earthquake intensities. These correlations reflect the damaging, compound effect of earthquakes and heavy rainfall. Past research has focused on other earthquake-hit regions to determine the threshold value of precipitation. The amount of accumulated precipitation as well as the rainfall intensity needed to trigger mountain hazards have been greatly reduced following the earthquake, based on comparisons with data from before the earthquake. Generally speaking, empirical and statistical methods can be used to define the threshold value of rainfall-triggered mountain hazards on a regional scale, by comparing the statistics of mountain hazards with the rainfall data from the latest rainfall-induced mountain hazards recorded within the Wenchuan earthquake region. From these data the rainfall needed to cause regional mountain hazards can be calculated (Fig. 5). Although the sample size is limited, by comparing the rainfall required to trigger debris flows we can also use the assumptions of the triggering values from the past events, as shown in Fig. 5, because geological settings show some common influence on regional scale mountain hazards; e.g. in the south section the geology consists of mainly magmatic rocks, while in north section, it is metamorphic rocks. As shown in Fig. 5, an approximate threshold value was proposed. As can be seen from Fig. 5, the average 24-h cumulative rainfall is 149 mm and the average 1-h rainfall intensity is 36.3 mm/h in the south section of the earthquake region. The north section shows an average 24-h cumulative rainfall of 248 mm and an average 1-h rainfall intensity of 55 mm/h.

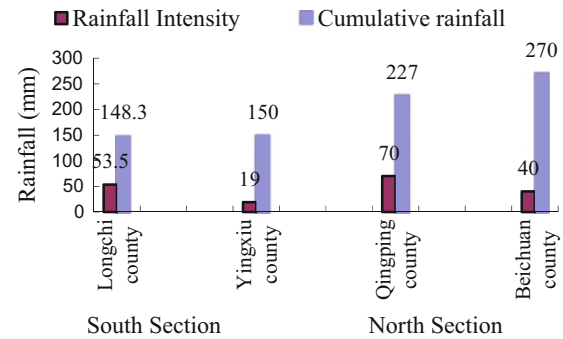


Fig. 5 Statistics of mountain hazards and rainfall data in the Wenchuan earthquake region. Cumulative rainfall and rainfall intensities given above can be a guide for the early warning of hazards in these counties

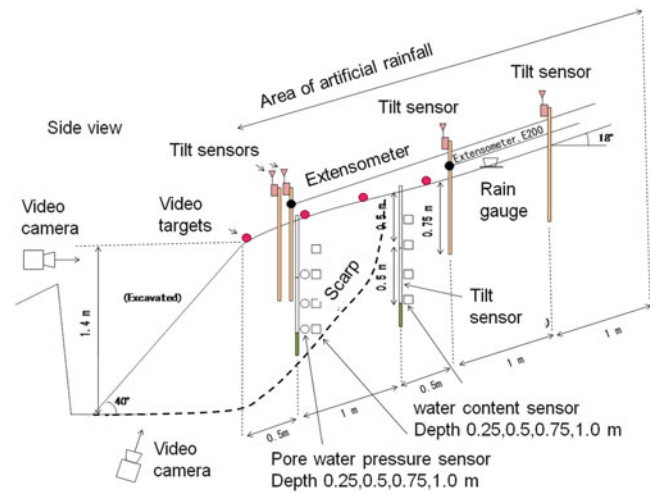


Fig. 6 Cross-section of artificial rainfall test

Experimental Identification of Threshold Value

An artificial rainfall test was conducted on a monitored slope of a weathered, andesitic deposit in order to observe both the critical threshold value and the correlation with pre-failure behaviours for that slope. The monitoring site was located on Taziping landslide slope in Dujiangyan County, Sichuan Province. Figure 6 illustrates a cross-section of experimental test on this slope, while a photo of the site with the monitoring instruments is shown in Fig. 7.

The slope consisted of loose gravel and sand. The blow counts were determined by portable dynamic cone penetration test and were found to be less than 10 for 10 cm of penetration. The slope angle was around 18° , and its lower end was excavated for a depth of 1.4 m with an angle of 40° . Then, artificial heavy rainfall was mimicked, as shown in Fig. 8. Major deformation was observed and the slope failed progressively from the bottom up, with a scarp angle of $40\text{--}50^\circ$. The final shape of the scarp is shown with a thick, broken line in Fig. 9. The progression of artificial rainfall tests and the rainfall parameters are shown in Table 1 and the



Fig. 7 Photo of the site together with the instruments



Fig. 9 The final shape of scarp and slope after failures, demonstrating progressive failure during the test

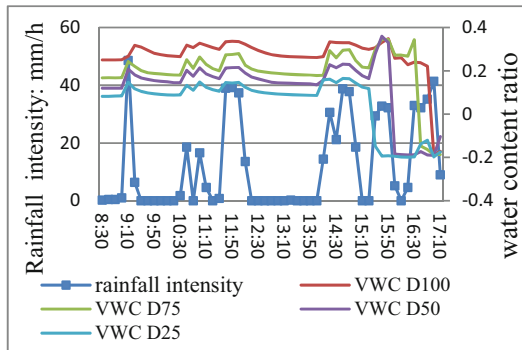


Fig. 8 Rainfall of the site for the artificial rainfall test

record of rainfall intensity of all six slope failure and major deformations was found to be between 29.4 and 54.2 mm/h. Finally, the average rainfall intensity was 48.1 mm/h, which can be defined as the threshold value for the failure of the slope.

Figure 10 shows Intensity-Duration (I-D) plots for rainfall-induced mountain hazard threshold values that have been widely adopted in early warning slope failures (Huang et al. 2010). Figure 10 indicates that these threshold I-D relationships vary widely, suggesting that a high degree of uncertainty is always associated in using these empirical relationships.

The comparison also suggests that these greatly varied thresholds may be a result of various geological and environmental conditions in the source area. Such variation has often been ignored in many studies of rainfall threshold identification. As a result, by experimental tests on the natural slope of Taziping landslide, the meteorology-based I-D thresholds of slope failure can be more accurate for

Table 1 Artificial rain test parameters and results

| Failure | Time (m:s) | Rain intensity (mm/h) | Volume of failure (m ³) |
|---------|------------|-----------------------|-------------------------------------|
| 1 | 9:08 | 54.2 | 0.23 |
| 2 | 10:59 | 43.4 | 0.85 |
| 3 | 11:48 | 79.2 | 0.24 |
| 4 | 14:15 | 45.0 | 0.50 |
| 5 | 15:29 | 29.4 | 0.40 |
| 6 | 16:36 | 37.6 | 0.12 |
| Average | – | 48.1 | 0.39 |

rainfall induced early warning of Taziping landslide failure. The correlation of rainfall intensity and rainfall duration (I-D plots) was given as shown in Fig. 10.

This can be applied to early warning by comparing the I-D envelope with real-time monitoring rainfall data. If the monitoring rainfall intensity in Taziping landslide is about 45 mm/h, local residents must be cautious because slope failure may occur in hours, while the situation should be quite urgent if the monitoring rainfall intensity is up to 120 mm/h according to the I-D envelope in the Taziping landslide. The I-D envelope can be summarized in the following formula by analysing experimental data:

$$I = 155.2T^{0.17}, \tag{1}$$

where I-rainfall intensity and T-rainfall duration. By the formula above, an envelope threshold for the early warning of Taziping landslide may give guidance and an approximate time for evacuation and preparation for potential landslides by comparing monitoring rainfall intensities and its duration.

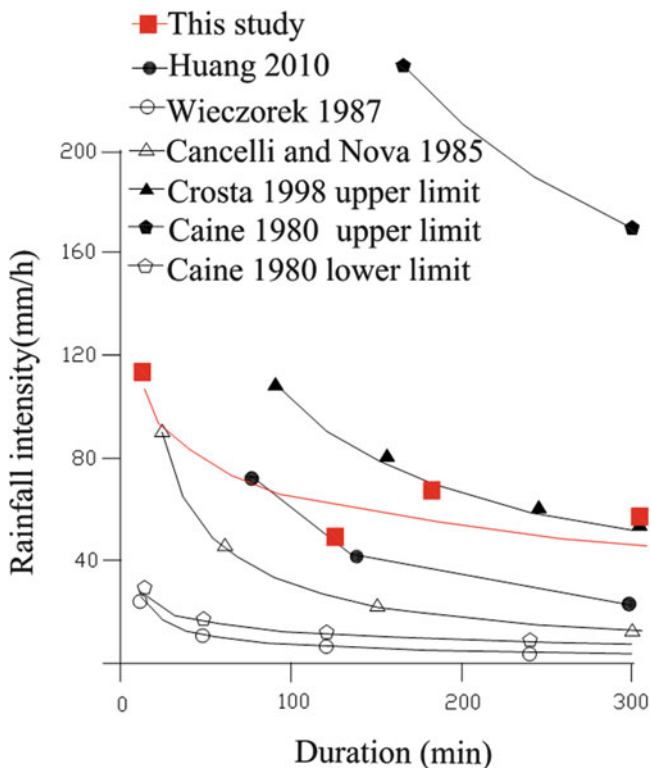


Fig. 10 Comparisons of various Intensity–Duration (I–D) thresholds in the present study

Conclusion

The compound effect of an earthquake with subsequent rainfall can trigger massive debris flows in earthquake-hit areas. The early warning of rainfall-induced mountain hazards such as landslides and debris flows have an intrinsically high uncertainty and are thus, difficult to predict. To improve the accuracy of mountain hazard early warnings will require a better understanding of the mechanisms responsible for internal-response-based slope failure. This study proposed a multi-scale, early warning method for rainfall-induced mountain hazards. The model combined regional and site-specific hazards that were then applied to Chengdu City. A monitored artificial rainfall test was then conducted on a natural slope and was used to identify the threshold value to elicit an early warning. In the future, the I–D criterion, along with the statistics results proposed here, will be useful for more accurate slope failure predictions in Taziping landslide. Admittedly, a limited test with an artificial slope may in practice not give good results, while the method, which is based on multi-scaled early warning and detailed

works of experimental tests and statistics on individual monitoring sites, may enhance the accuracy of early warning for mountain hazards based on continuous verifications with monitoring data. In this manner, it is hoped that the destruction and loss of life resulting from such disasters can be mitigated.

Acknowledgments This study is financially supported by National Natural Science Foundation of China (Grant No. 41001007), Scientific and technological support projects (Grant No.2011BAK12B022, 2011BAK12B01) of the Ministry of Science, International cooperation program of China (2013DFA21720), and National Basic Research Program of China 973 (Grant No. 2010CB731504).

References

- Huang C, Yuin S (2010) Experimental investigation of rainfall criteria for shallow slope failures. *Geomorphology* 120:326–338
- Huang D, Qiao J, Uchimura T, Wang L (2010) Research and application of landslide real-time monitoring system based on unsaturated soil mechanics. *Disaster Adv* 3(4):99–104
- Qiao J, Wu C, Tian H (2004) Contribution rate research of stratum to landslide growth of Yanyang-Wushan segment in three gorges reservoir region (in Chinese). *Chin J Rock Mech Eng* 23 (17):2920–2924
- Qiao J, Yang Z, Tian H (2009) Probability analysis based method for rainfall-induced landslide warning (in Chinese). *J Eng Geol* 17 (3):343–349
- Tian H, Nan H, Yang Z (2010) Benefit-cost analysis of geological disaster mitigation and example. *China. Disaster Adv* 3(4):163–165
- Towhata I, Uchimura T, Wang L, Qiao J (2011) Validation and strategy of early warning instrument for mitigation of precipitation-induced slope failure. In: *Proceedings of Indian geotechnical conference*, 15–17 December, Kochi, pp 3–6
- Uchimura T, Towhata I, Anh T, Fukuda J, Bautista C, Wang L, Seko I, Uchida T, Matsuoka A, Ito Y, Onda Y, Iwagami S, Kim M, Sakai N (2010) Simple monitoring method for precaution of landslides watching tilting and water contents on slopes surface. *Landslides* 7(3):351–357
- Uchimura T, Towhata I, Wang L, Qiao J (2011) Validation and interpretation of monitored behavior of slopes vulnerable to failure. In: *Proceedings of the second world landslide forum*, 3–7 October, Rome, pp 589–595
- Wang M, Qiao J, He S (2010) GIS-based earthquake-triggered landslide hazard zoning using contributing weight model. *J Mt Sci* 7:339–352
- Yang Z, Qiao J, Tian H, Huang D, Wang M (2010a) Study on rainfall-induced regional geohazard prediction following Wenchuan earthquake (in Chinese). *J Sichuan Univ (Eng Sci Edn)* 42(S1):38–42
- Yang Z, Qiao J, Tian H, Hang D, Wang M (2010b) Epicentral distance and impacts of rainfall on geohazards after the 5.12 Wenchuan earthquake, China. *Disaster Adv* 3(4):151–156
- Yang Z, Qiao J, Tian H, Hang D, Wang M (2012) Real-time regional rainfall induced geohazards prediction method in the Wenchuan earthquake region, China. *Disaster Adv* 5(4):408–454



Laboratory Studies on Slope Stability Monitoring Using Distributed Fiber-Optic Sensing Technologies

Hong-Hu Zhu, Bin Shi, Jun-Fan Yan, Cheng-Cheng Zhang, Jie Zhang, and Zhan-Pu Song

Abstract

The advances in distributed fiber optic sensing (DFOS) technologies enable automatic, remote and long-distance slope monitoring and early-warning of potential geological disasters. Compared with conventional geotechnical instruments, the fiber optic sensors have a number of advantages such as higher accuracy and repeatability, better durability, and enhanced integration capability. In this paper, the quasi-distributed Fiber Bragg Grating (FBG) and fully-distributed Brillouin Optical Time-Domain Analysis (BOTDA) sensing technologies are applied for monitoring of slope stability problems in laboratory model tests. The sensing principles and the implementation methods are introduced, followed by two case studies. The fiber optic sensors were embedded in the model slopes for strain monitoring of a soil mass during seepage and surcharge loading, respectively. The reliability of the DFOS based slope monitoring systems has been verified through the analyses of the strain monitoring results.

Keywords

Fiber optic sensing • Slope monitoring • Geotechnical instrumentation

Introduction

Geotechnical instrumentation plays an important role in evaluating slope stability and identifying potential landslide hazards. Currently, typical shortcomings associated with

many conventional monitoring technologies of slope stability include low long-term accuracy, poor durability, and limited integration capability. Additionally, the collected measurement data from discrete locations can hardly reflect the overall stability of a slope.

The advances in distributed fiber optic sensing (DFOS) technologies enable automatic, remote and long-distance slope monitoring and early-warning of geological disasters (Dunnicliff 1993; Shi et al. 2003). These technologies have been successfully applied for the health monitoring of a variety of civil infrastructures, such as bridges, high-rise buildings, and tunnels (Shi et al. 2003; Zhang et al. 2006; Wang et al. 2013). The fiber optic sensors not only have the advantages of immunity to electromagnetic interference, tiny size, high accuracy and repeatability, and excellent durability, but also can be integrated to form a quasi-distributed or fully-distributed fiber optic sensing network (see Fig. 1). In recent years, the potential of the DFOS-based slope monitoring system has been recognized all over the world (Yoshida et al. 2007; Ho et al. 2006; Iten et al. 2008;

H.-H. Zhu (✉)

School of Earth Sciences and Engineering, Nanjing University,
163 Xianlin Avenue, Nanjing 210046, China

Nanjing University High-tech Institute at Suzhou, 150 Ren'ai Road,
Suzhou 215123, China
e-mail: zhh@nju.edu.cn

B. Shi • J.-F. Yan • C.-C. Zhang • Z.-P. Song

School of Earth Sciences and Engineering, Nanjing University,
163 Xianlin Avenue, Nanjing 210046, China
e-mail: shibin@nju.edu.cn; yjf880326@126.com;
zhangchengcheng@gmail.com; 157077450@qq.com

J. Zhang

Department of Geotechnical Engineering, Tongji University,
1239 Siping Road, Shanghai 200092, China
e-mail: cezhangjie@tongji.edu.cn

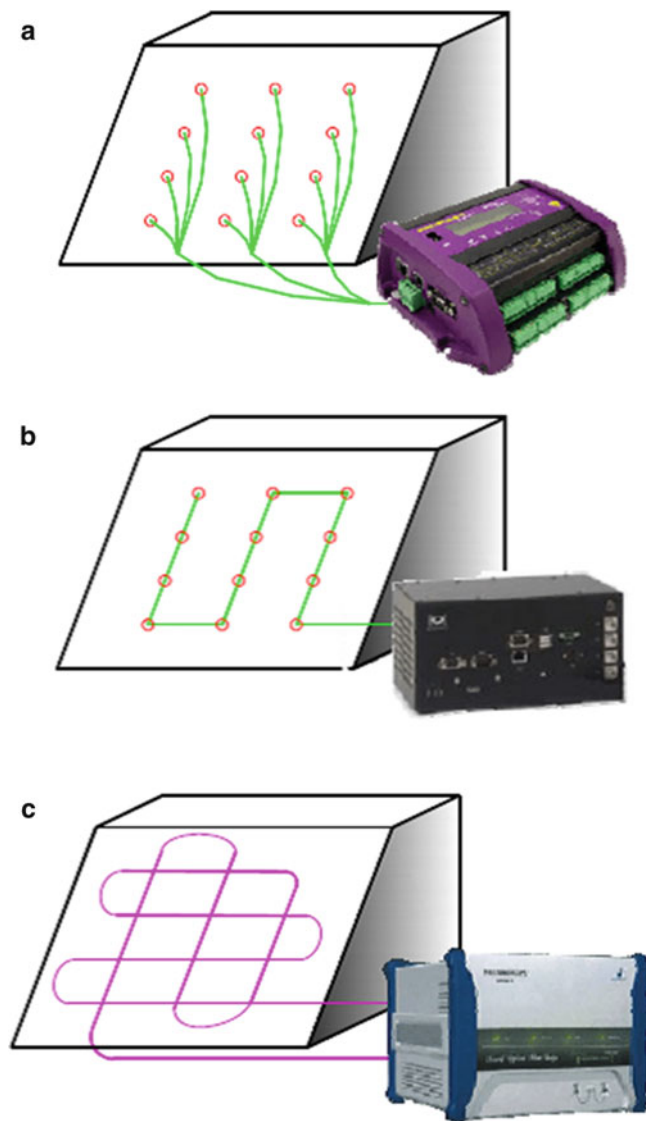


Fig. 1 Comparison of different types of slope monitoring technologies. (a) In point-measurement, (b) quasi-distributed measurement, (c) fully-distributed measurement

Shi et al. 2008; Wang et al. 2009; Pei et al. 2011; Zhu et al. 2011, 2012). However, the performance evaluation of slopes based on the DFOS monitoring results is quite different from conventional methods and requires further investigation.

In this paper, the DFOS technologies have been applied to strain monitoring within small-scale model slopes in two commonly encountered conditions. The strain variations measured by the fiber optic sensors indicate the evolution of stability condition of the model slopes under increased surcharge loading and water seepage process, respectively. The effectiveness of the DFOS system in monitoring slope stability is verified.

Distributed Fiber Optic Sensing Technologies

Quasi-Distributed Fiber Bragg Grating Technology

The photosensitivity in optical fiber was first discovered by Hill et al. (1978). It was found that the Bragg wavelength of the light that a Fiber Bragg Grating (FBG) sensor reflects is strain and temperature dependent. A change in strain or temperature will alter the Bragg wavelength and can be formulated as follows (Othonos and Kalli 1999)

$$\frac{\Delta\lambda_B}{\lambda_B} = (1 - p^{eff})\Delta\varepsilon + (\alpha + \xi)\Delta T \quad (1)$$

where $\Delta\lambda_B$ is the change in the Bragg wavelength due to strain and temperature changes; λ_B is the original Bragg wavelength under strain free and 0 °C condition; p^{eff} is the photo-elastic parameter; and α and ξ are the thermal expansion and thermo-optic coefficients, respectively. With the above features, the FBG sensors with different Bragg wavelengths can be connected in series to form a quasi-distributed sensing array with high accuracy. The FBG sensor is by far the most commonly used fiber optic sensor in civil engineering, as well as in fiber-optic communication as the optical filter.

Fully-Distributed Brillouin Optical Time-Domain Analysis Technologies

In the sensing technology of Brillouin optical time-domain analysis (BOTDA), the Brillouin frequency shift of the scattering light of a single-mode optical fiber has a linear relationship with the applied strain and temperature (Horiguchi and Tateda 1989). This relationship can be expressed by (Bernini et al. 2002)

$$v_B(\varepsilon, T) = v_B(\varepsilon_0, T_0) + \frac{\partial v_B(\varepsilon, T)}{\partial \varepsilon} \times (\varepsilon - \varepsilon_0) + \frac{\partial v_B(\varepsilon, T)}{\partial T} \times (T - T_0) \quad (2)$$

where $v_B(\varepsilon, T)$ and $v_B(\varepsilon_0, T_0)$ are the frequency shift of the Brillouin scattering light before and after the measurement, respectively; ε and ε_0 are the axial strain before and after the measurement, respectively; T and T_0 are the temperature before and after the measurement, respectively; and the coefficients $\partial v_B(\varepsilon, T)/\partial \varepsilon$ and $\partial v_B(\varepsilon, T)/\partial T$ are 0.05 MHz/ $\mu\varepsilon$ and 1.2 MHz/°C, respectively. The measured strain and temperature is expressed as the averaged value

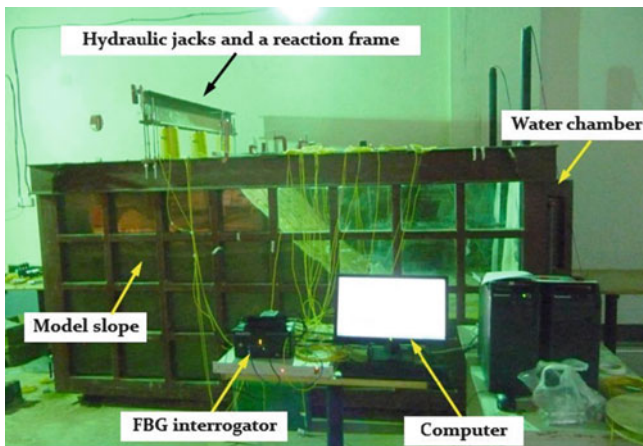


Fig. 2 Photo of the model test for Case 1

over its spatial resolution. Using BOTDA technology, the strain and temperature generated in optical fibers of the length up to 25 km can be measured as distributed in the longitudinal direction (Neubrex Co. Ltd 2011).

Applications to Laboratory Model Tests

Case 1: Strain Monitoring of a Soil Slope Under Seepage

In order to investigate the influence of reservoir operation on the deformation pattern of adjacent slopes and verify the effectiveness of FBG technology in slope stability monitoring, a small-scale model test of soil slope was conducted in Key Laboratory of Distributed Sensing & Monitoring Technology in Infrastructure Engineering of Suzhou, China. This model test was performed under 1 g condition in a steel chamber with a length of 3 m and a width of 1.5 m. Figure 2 shows the setup of the model test.

The model slope has a slope angle of 45°. During model construction, a single-mode optical fiber containing nine FBG strain sensors connected in series was embedded in the slope mass. The FBG sensors were coated using a tight-buffer PVC coating so as to protect them from damage during installation. An sm125 FBG optical sensing interrogator was employed to record real-time data. During testing, the groundwater level inside the slope was varied by changing the water levels in the water chambers at the two sides of the model slope, so that water seepage inside the slope mass was induced.

Figure 3 presents the horizontal strain results measured by three embedded FBG sensors during the model test. The monitoring results show that:

1. When the water level inside the slope mass was manually increased, the measured horizontal strains

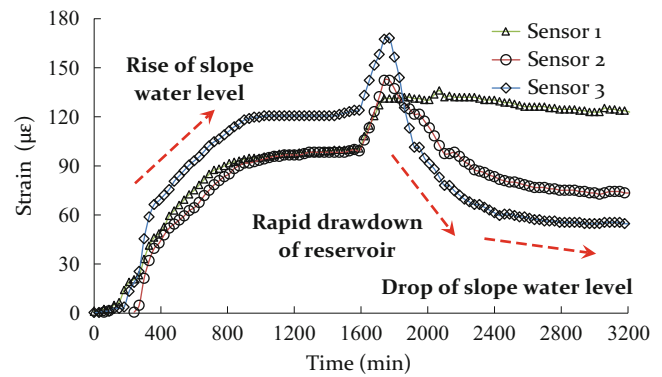


Fig. 3 Horizontal strain monitoring results of the slope mass subjected to seepage

increased at a considerable high rate. This strain variation corresponds to increased horizontal mass movement, which is normally considered as a sign for slope stability deterioration.

2. When the water level of the reservoir fell suddenly, the horizontal strains accumulated rapidly and reached their peaks. This indicates that the slope movement, especially the horizontal component, is quite evidently affected by the drawdown of the reservoir level. For a slope with marginal stability, seepage-triggered slope instability is likely to occur.
3. After the rapid drawdown of reservoir, water level inside the model slope dropped gradually. There were considerable plastic strains in the slope mass after the seepage circle/water level fluctuation circle.

This experimental study verifies that the distributed fiber optic sensors can capture the strain variations within the model slope subjected to seepage, which is important for slope stability monitoring.

Case 2: Strain Monitoring of a Loaded Soil Nailed Slope

To verify the effectiveness of the fully-distributed BOTDA technology for slope stability monitoring with surface surcharge, a laboratory slope model test was conducted. The model slope has a slope height of 0.8 m and a base height of 0.5 m. The surcharge loading was applied on the slope crest, as shown in Fig. 4.

The BOTDA sensing network was established to monitor strain distributions within the model slope. During model construction, three layers of 0.9 mm-diameter sensing fibers were horizontally embedded in the slope mass. Eight characteristic points were prepared along the fiber in order to facilitate the identification of the boundary of each segment. For every point, a 1-m-long sensing fiber was looped and packaged in a plastic box for temperature compensation.

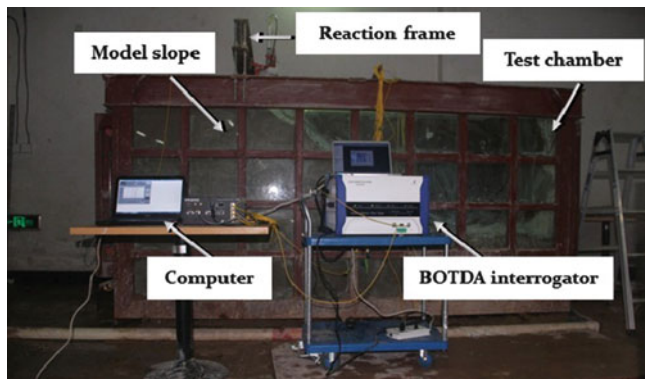


Fig. 4 Photo of the model test for Case 2

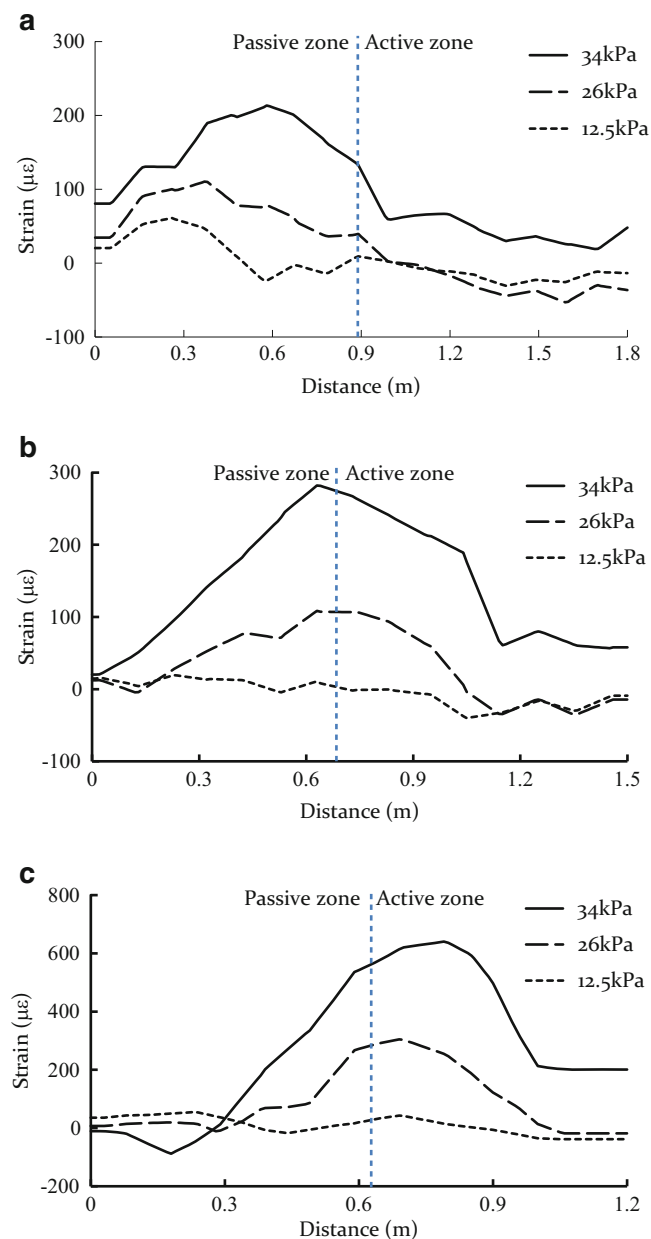


Fig. 5 Strain monitoring results of the slope mass subjected to increased surcharge loading. (a) Monitoring layer at 0.6 m elevation, (b) monitoring layer at 0.85 m elevation, (c) monitoring layer at 1.1 m elevation

Figure 5 presents the fiber optic monitoring results. In this figure, the line separating the active and passive zones is the location of the critical slip surface computed by limit equilibrium analysis performed using SLOPE/W. The monitoring results show that the measured strain can reasonably reflect the deformation behavior of the model slope. With the increase of loading, the strains increased as expected. When the critical condition of slope stability was imminent, strain inhomogeneity within the model slope became obvious. This phenomenon indicates that shear strains accumulated within the soil mass and the slope slip surface gradually formed.

According to the monitoring results, the strains of the passive zone at a lower slope elevation were large while the strains of the active zone were relatively small. For the slope mass at a higher elevation, the active zone of the slope had larger strains than the passive zone. The strain distribution pattern seems to be dependent on the location of the slope slip surface, which is reasonable.

Conclusions

In this paper, the working principles of two DFOS technologies and their applications in laboratory-scale model tests have been presented. The following conclusions are drawn:

1. The model test of slope subjected to seepage shows that the embedded FBG sensors can capture the strains induced by seepage within a slope mass effectively. The proposed installation and protection methods are proved to be sufficient and effective.
2. The distributions of horizontal strain measured by the BOTDA strain sensing fibers in the surface loaded model slope indicate the development of potential slip surface in the slope.
3. The capability of the DFOS technology to provide valuable data for performance evaluation of slopes with high accuracy is verified. Slope stability assessment can be implemented based on the distributed strain monitoring results.

Acknowledgments The authors gratefully acknowledge the financial support provided by National Basic Research Program of China (973 Program) (No. 2011CB710605), National Natural Science Foundation of China (Nos. 41102174, 41302217), Open Fund of the State Key Laboratory of Geohazard Prevention and Geoenvironment Protection (No. SKLGP2012K011), and Suzhou Science and Technology Development Program (No. SYG201213).

References

- Bernini R, Minardo A, Zeni L (2002) Reconstruction technique for stimulated Brillouin scattering distributed fiber-optic sensors. *Opt Eng* 41(9):186–194
- Dunnicliff J (1993) *Geotechnical instrumentation for monitoring field performance*. Wiley, New York, 608 p. ISBN 9780471005469

- Hill KO, Fujii Y, Johnson DC, Kawasaki BS (1978) Photosensitivity in optical fiber waveguides: application to reflection filter fabrication. *Appl Phys Lett* 32(10):647–649
- Ho YT, Huang AB, Lee JT (2006) Development of a fibre Bragg grating sensed ground movement monitoring system. *Meas Sci Technol* 17(7):1733–1740
- Horiguchi T, Tateda M (1989) BOTDA-nondestructive measurement of single-mode optical fiber attenuation characteristics using Brillouin interaction: theory. *J Lightwave Technol* 7(8):1170–1176
- Iten M, Puzrin AM, Schmid A (2008) Landslide monitoring using a road-embedded optical fiber sensor. In: *Proceedings of SPIE 6933*, 2008. San Diego, CA. No. 693302
- Neubrex Co. Ltd (2011) NEUBRESCOPE NBX-6050A Catalogue. Kobe, Japan
- Othonos A, Kalli K (1999) *Fiber Bragg gratings: fundamentals and applications in telecommunications and sensing*. Artech House, London, 422 p. ISBN 9780890063446
- Pei HF, Cui P, Yin JH, Zhu HH, Chen XQ, Pei LZ, Xu DS (2011) Monitoring and warning of landslides and debris flows using an optical fiber sensor technology. *J Mt Sci* 8(5):728–738
- Shi B, Xu HZ, Chen B, Zhang D, Ding Y, Cui HL, Gao JQ (2003) A feasibility study on the application of fiber-optic distributed sensors for strain measurement in the Taiwan strait tunnel project. *Mar Georesour Geotechnol* 21(3–4):333–343
- Shi B, Sui H, Zhang D, Wang J, Wei G Q, Piao CD (2008) Distributive monitoring of the slope engineering. In: *Proceedings of the 10th international symposium on landslides and engineered slopes*, 30 June–4 July 2008. Xi'an, China. pp 1283–1288
- Wang BJ, Li K, Shi B, Wei Q (2009) Test on application of distributed fiber optic sensing technique into soil slope monitoring. *Landslides* 6(1):61–68
- Wang F, Zhang DM, Zhu HH, Huang HW, Yin JH (2013) Impact of overhead excavation on an existing shield tunnel: field monitoring and a full 3D finite element analysis. *Comput Mater Continua* 34(1):63–81
- Yoshida Y, Kashiwai Y, Murakami E, Ishida S, Hashiguchi N (2007) Development of the monitoring system for slope deformations with fiber Bragg grating arrays. In: *Proceedings of SPIE 4694*, 2002, San Diego, CA, pp 296–303
- Zhang W, Gao JQ, Shi B, Cui HL, Zhu H (2006) Health monitoring of rehabilitated concrete bridges using distributed optical fiber sensing. *Comput Aided Civil Infrastruct Eng* 21(6):411–424
- Zhu ZW, Liu DY, Yuan QY, Liu B, Liu JC (2011) A novel distributed optic fiber transducer for landslides monitoring. *Opt Lasers Eng* 49(7):1019–1024
- Zhu HH, Ho ANL, Yin JH, Sun HW, Pei HF, Hong CY (2012) An optical fibre monitoring system for evaluating the performance of a soil nailed slope. *Smart Struct Syst* 9(5):393–410



A Landslide Monitoring and Early Warning System Using Integration of GPS, TPS and Conventional Geotechnical Monitoring Methods

Željko Arbanas, Kyoji Sassa, Osamu Nagai, Vedran Jagodnik, Martina Vivoda, Sanja Dugonjić Jovančević, Josip Peranić, and Kristijan Ljutić

Abstract

An advanced comprehensive monitoring system was designed and used on the Grohovo Landslide in Croatia. Equipment selection was based on scientific requirements and consideration of possible ranges of monitored values and sensors precision. Establishment of an early warning system and defining of alarm thresholds is based on existing knowledge of the landslide behavior as well as collected comprehensive monitoring data. The focus of the early warning system establishment at Grohovo Landslide was on an effective combination of sensors (equipment fusion) with respect to detecting device malfunctions and reducing false alarms in the future. The weakest component in the Grohovo Landslide monitoring system is power supply based on solar devices, field data collecting and the data transmitting from the field PC to the control room at the University of Rijeka. This paper presents the main ideas and advances of the monitoring equipment fusion as well as weaknesses of the applied monitoring system at the Grohovo Landslide.

Keywords

Landslide • Monitoring system • Multiple sensors • Equipment fusion • Early warning

Introduction

Examples and case studies of comprehensive landslide monitoring and early warning systems presented in scientific papers are numerous but, because of the variability of landslide types and processes, targets of landslide investigation,

field conditions and ongoing technological development of monitoring sensors, no standardization can be adopted as a universal solution for system setups for landslide monitoring (Arbanas et al. 2013). The landslide monitoring results should provide a basis for development and validation of landslide numerical modelling and adequate hazard management. In practice many different techniques and different type of sensors are used to monitor landslide activity. The use of multiple sensors for the same purpose (equipment fusion) and at the same position should be very useful to guarantee redundancy of measurements that can prevent loss of data if one instrument fails. Using the same position for different types of monitoring sensors can also allow spatial correlation of measurement data on the landslide surface and inside the landslide profile. Use of different geodetic and geotechnical sensors in combination with hydrological monitoring equipment, which should measure data on precipitation and pore pressures in the landslide profile allows reconstruction of relationships between rainfall, groundwater level and consequent landslide behavior as a base for

Ž. Arbanas (✉) • V. Jagodnik • M. Vivoda • S. Dugonjić Jovančević • J. Peranić

Geotechnical Department, Faculty of Civil Engineering, University of Rijeka, Radmile Matejčić 3, Rijeka 51000, Croatia

e-mail: zeljko.arbanas@gradri.uniri.hr; vedran.jagodnik@gradri.uniri.hr; martina.vivoda@gradri.uniri.hr; sanja.dugonjic@gradri.uniri.hr; josip.peranic@gradri.uniri.hr

K. Sassa • O. Nagai

International Consortium on Landslides (ICL), Kyoto University, Uji-Campus, Kyoto 611-0011, Japan

e-mail: sassa@iclhq.org; nagai@coral.ocn.ne.jp

K. Ljutić

4D Monitoring Ltd, Milčetići 20, Milčetići 51511, Croatia

e-mail: kristijan.ljusic@4d-monitoring.com

establishing an early warning system. The most important step in early warning system establishment is linking sensor measurements and possible failure mechanisms with consequences that should follow the occurrence of sliding (landslide risk) (Arbanas et al. 2013).

Based on these presumptions, an advanced comprehensive monitoring system was designed and used on the Grohovo Landslide in Croatia. The Grohovo Landslide is the largest active landslide along the Croatian part of the Adriatic coast, located on the northeastern slope of the Rječina Valley near the City of Rijeka. In 2009 the Croatian-Japanese joint research project “Risk Identification and Land-Use Planning for Disaster Mitigation of Landslides and Floods in Croatia” was initiated, and Grohovo Landslide was chosen as a pilot area for comprehensive monitoring, which includes geodetic and geotechnical monitoring equipment installed from March 2011 to the end of 2011. It is planned to integrate all measurement data in a unique system for landslide risk management and an early warning system.

Characteristics, Historical Data and Hazard Scenarios for the Grohovo Landslide

The Grohovo Landslide is near the City of Rijeka, the largest Croatian port on the northeastern Adriatic coast. The landslide area, situated on the Rječina River Valley slopes, is part of a dominant morphostructural unit that strikes in the northwest-southeast direction along the Rječina Valley, and continues to the southeast through the Sušačka Draga Valley, Bakar Bay and the Vinodol Valley (Velić and Vlahović 2009). The Grohovo Landslide is on the north-eastern slope of a typical karstic river originating from a strong karstic spring at the foot of the Gorski Kotar Mountains. Cretaceous and Paleogene limestone lie at the top of the slopes, while Paleogene siliciclastic rocks (flysch deposits) are situated on the lower parts of slopes and in the bottom of the Rječina River Valley. The flysch complex is a block that has been squeezed between the limestone rock blocks on the northeastern and southwestern sides. The siliciclastic (flysch) bedrock is lithologically heterogeneous, with common vertical and lateral alternations of different lithological sequences. Petrological analysis of the bedrock has shown the presence of silty marl, laminated silt to silty shale and fine-grained sandstones (Benac et al. 2005, 2011). Unlike the limestone, flysch is prone to weathering, with a clayey weathering zone forming over the flysch bedrock. Over time, the coarse-grained fragments originating from rockfalls were mixed with clay from the weathered flysch zone, forming a slope with superficial deposits a few metres thick.

According to historical documents in the Croatian State Archive [State archive in Rijeka, Technical department (1840–1918). (unpublished documents)] in Rijeka, the first

sliding in the Rječina Valley near the Grohovo Village occurred in 1767, when numerous landslides and rockfalls were caused by the 1750 earthquake, which had an epicenter in the City of Rijeka. Large landslides triggered by rainfall and floods were noticed on both river banks near the Grohovo Village at the end of the nineteenth century (Arbanas et al. 2012, Vivoda et al. 2012). Numerous landslides occurred during the first half of the twentieth century without significant damage to facilities on the river banks. A new landslide on the nearby northeastern slope occurred and was stabilized during construction of the Valići Dam in 1960. Because of the relatively small volume of the Valići Lake, the dam reservoir cannot hold the entire inflow during heavy rain and a relatively large quantity of water must be released in the downstream part of the Rječina River. In these situations, erosion along the Rječina River presents a possible landslide hazard (Mihalić and Arbanas 2013).

The last complex retrogressive landslide (Fig. 1) was reactivated in December 1996, at the location of the landslide from nineteenth century on the northeastern slope, with significantly smaller volume, when about $1 \times 10^6 \text{ m}^3$ moved down the slope and buried the Rječina river channel. Slip surfaces have been formed on the contact of the superficial deposits and flysch bedrock. After this sliding occurrence, a complex composite landslide with 13 sliding bodies developed retrogressively, including movements of the carbonate mega-blocks at the top of the slope (Benac et al. 2005). The landslide bodies represent different types of mass movements, forming a total volume of approximately $3 \times 10^6 \text{ m}^3$. The geometry of the total complex landslide, described according to WP/WLI Suggested Nomenclature for Landslides (IAEG 1990), is as follows: $L = 425 \text{ m}$; $L_d = 420 \text{ m}$; $L_r = 405 \text{ m}$; $W_d = 200 \text{ m}$; $W_r = 200 \text{ m}$; $D_d = 6\text{--}20 \text{ m}$; $D_r = 6\text{--}9 (20) \text{ m}$; $\Delta H = 165 \text{ m}$ (Arbanas et al. 2012).

Based on existing monitoring results (Benac et al. 2005), stability analyses of the wider landslide area, as well as detailed 3D analyses of the reactivated landslide (Wang et al. 2013a, Vivoda et al. 2013), a real hazard of further sliding in the Rječina River Valley was identified. The main risk is possible damming of the Rječina River, forming a lake which could burst out as a possible water wave that represents a serious danger to facilities as well as citizens in the City of Rijeka, at the mouth of the Rječina River. Widening of the existing Grohovo Landslide could also destabilize carbonate mega-blocks on the limestone scarp at the top of the landslide, which would endanger villages at the top of the slope. Another threat is the possibility of landslides on slopes along Valići Lake and filling the lake with the landslide mass. In addition, other sliding phenomena can damage buildings, roads and other facilities in different parts of the valley (Arbanas et al. 2010, 2012).

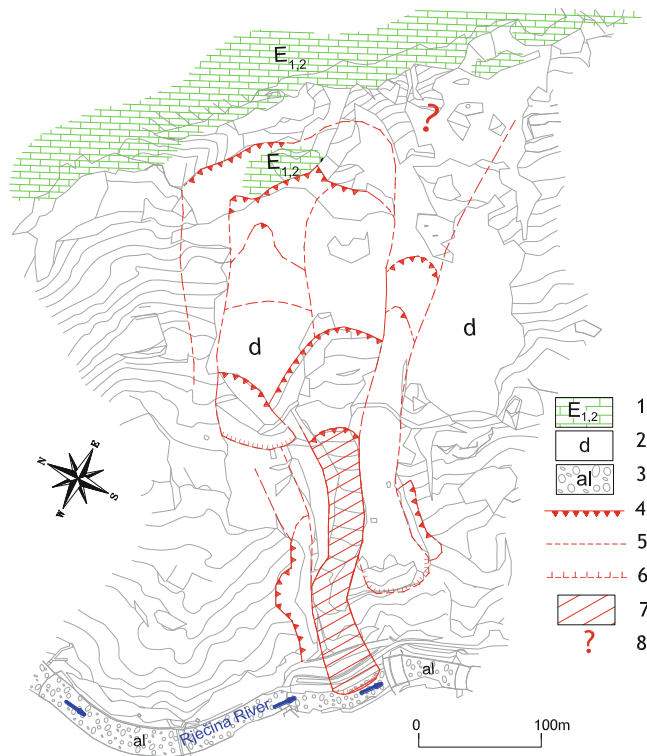


Fig. 1 The Grohovo Landslide engineering geological map: 1- Paleogene limestone; 2-superficial deposits; 3-recent alluvial sediments; 4-open cracks; 5-shearing cracks; 6-landslide toe; 7-initial landslide body; 8-retrogressive landslide in development (Benac et al. 2011)

Comprehensive Monitoring System on the Grohovo Landslide

Geodetic and Geotechnical Monitoring Equipment

Geodetic monitoring consists of a robotic total station (Leica TM30) measuring 25 geodetic benchmarks (prisms) and a Global Positioning System (GPS) master unit (Leica GMX901) with 9 GPS receivers (rovers). The robotic total station and the GPS master unit are located in a relatively stable area, on the top of the slope opposite to the landslide, together with a meteorological sensor, and web cam (Figs. 2 and 3).

The robotic station measures 25 benchmarks (prisms) located on the landslide body, on the top of the main scarp and, as reference points, around the landslide, every 30 min. The GPS network is composed of the GPS master unit, which is a reference station for 4 single frequency GPS rovers located in the landslide body, 3 single frequency GPS rovers located on top of the limestone scarp above the landslide, a single frequency GPS rover located on a dam near the landslide, and 1 reference single frequency GPS rover located on the roof of the Faculty building in

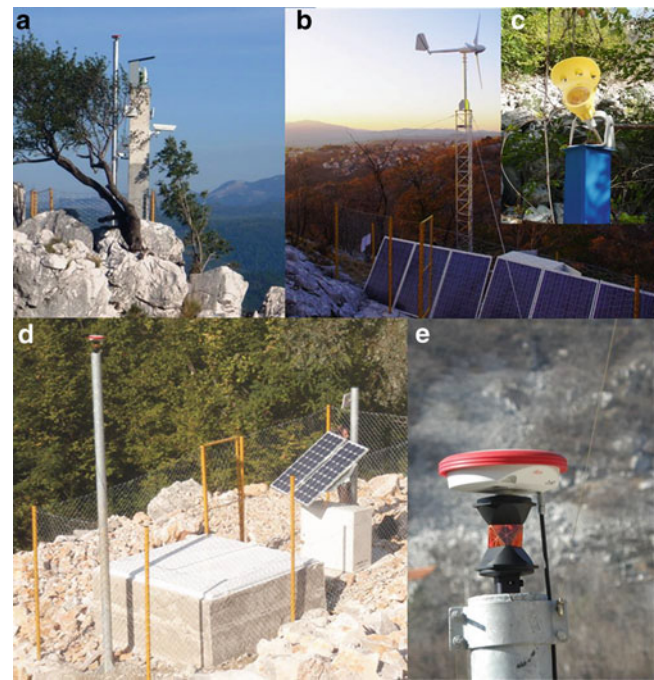


Fig. 2 Installed monitoring equipment (a) poles carrying robotic total station, meteorological sensors, web cam, and GPS master unit, (b) solar panels mini power plant, (c) geodetic prism in the field, (d) single frequency GPS rover; container with the inclinometer, vertical extensometers, pore pressure gauges inside, (e) GPS antenna and geodetic prism in fusion

University Campus, chosen as a stable reference rover. Data are transmitted by a Wi-Fi system from each rover to the GPS master unit connected to the field master unit PC, in which the GNSS Spider software creates measurement data files. The master unit PC can be reached remotely by an UMTS module from the main working station at the Faculty of Civil Engineering. The robotic total station, master GPS rover and field PC are powered from a windmill and solar panel mini power plant (Fig. 2b), while other GPS rovers in the landslide site use their own solar panel installations (Fig. 2d). After installation in summer 2011, geodetic monitoring and data collection were started in September 2011.

The geotechnical monitoring system includes 2 vertical inclinometers, and 4 wire extensometers; 13 long- and 3 short-span extensometers, 4 pore-pressure gauges, a weather station and a rain gauge (Fig. 3). Pore-pressure gauges, inclinometers and vertical extensometers are installed at two locations inside the central part of the landslide body at the same locations as the GPS rovers and prisms (Figs. 2d and 3). Long-span extensometers (NetLG 501E Osasi, 13 pcs) are installed in a continuous line from the Rječina riverbed to the limestone mega-blocks at the top of the slope (Fig. 3), while short-span extensometers (NetLG 501E Osasi, 3 pcs) are installed over the open cracks at the top of the landslide. To obtain the measured data from the

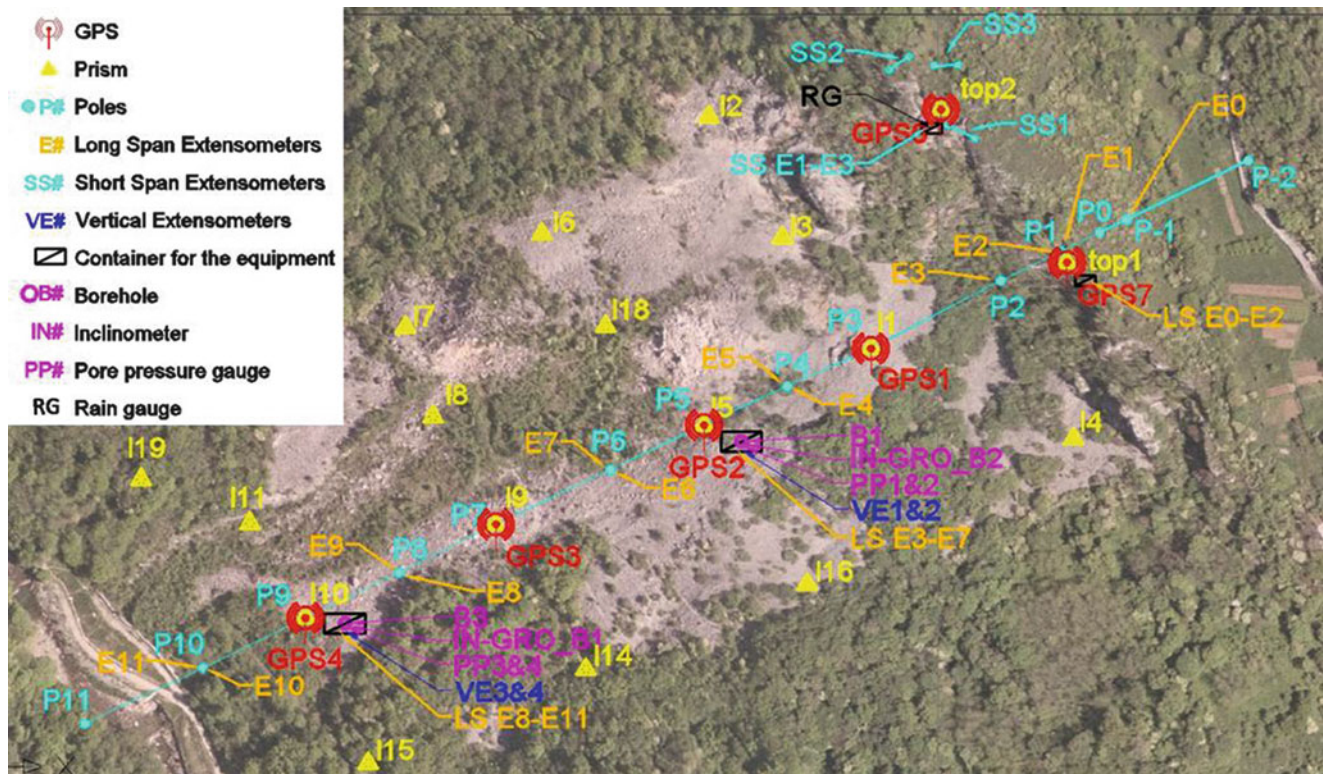


Fig. 3 Layout of the monitoring system installed on the landslide body

geotechnical monitoring equipment, it is necessary to download data directly from the installed sensors.

All installed equipment (except the vertical inclinometers) should be connected in one monitoring system with continuous measured data transmitting to the central computer unit at the Faculty of Civil Engineering in Campus. This is a necessary requirement for establishing a comprehensive monitoring system and early warning system and landslide risk management (Arbanas et al. 2010, 2012).

Need for Monitoring Equipment Fusion

In the past decade, GPS technologies have been frequently applied to landslide studies worldwide, both as a complement and an alternative to conventional landslide surveying methods. Analyzing monitoring results at many active landslides using GPS and GNSS, it has been demonstrated that GPS technologies significantly increase accuracy, productivity, monitoring capability, rapidity, flexibility, and economy as compared to classical geodetic and geotechnical survey techniques, such as TPS, inclinometers and wire extensometers (Wang et al. 2013b). In combination with other geodetic and geotechnical sensors, GPS monitoring should assist in providing a comprehensive set of data that would ensure safe monitoring system operation.

The use of multiple sensors for the same purpose (equipment fusion) and at the same position should be very useful to guarantee redundancy of measurements that can prevent loss of data if one instrument fails. The weakest link in the Grohovo Landslide monitoring system is power supply based on solar devices. After the first data collection period, it was found that the energy consumption was higher than the solar power plant could produce during winter, and it may be necessary to supplement the solar power plant with a windmill. Stable energy production is necessary for effective monitoring and early warning and during the next stage an electricity consumption control system will be developed to prevent shutdown of the overall system and loss of data. This system will monitor battery condition and, if necessary, shut down parts of the monitoring system, starting from the less important sensors and equipment (webcam, GPS, TPS, PC). It will also be important to ensure self-storing of measured data on GPS rovers installed in the landslide. In the case where the main GPS unit is shut down, GPS data cannot be transmitted and all data would be lost.

Selection of the same position for different types of monitoring sensors can also allow spatial correlation of measurement data on the landslide surface and inside the landslide profile. It is very important that measurements of surface movement (GPS, TPS, long-span wire extensometers) can be correlated to the equipment installed

inside the landslide profile (inclinometers, vertical wire extensometers, pore pressure gauges). The measured values of movements and displacements recorded at GPS and prisms (Fig. 2e), connected with wire extensometers installed over the Grohovo landslide, and in combination with inclinometers results (Fig. 4) enable reconstruction of landslide development. An important role in development reconstruction was using the results of in-line installed wire extensometers measurements. Displacements measured on in-line installed wire extensometers from the Rječina riverbed to the limestone mega-blocks at the top of the landslide pointed to compression in the foot of the landslide body and extension in the upper part of the landslide.

Use of different geodetic and geotechnical sensor fusion in combination with hydrological monitoring equipment, which records data about precipitation and pore pressures in the landslide profile, enables reconstruction of relationships between rainfall, groundwater level and consequent landslide behavior as a base for establishing an early warning system. The analyses necessary for an early warning system should link sensor measurements data and possible failure mechanisms with consequences that would follow the sliding occurrence (landslide risk) (Arbanas et al. 2013). In designing the Grohovo Landslide early warning system it was necessary to:

- Identify real hazards of further sliding and possible direct and indirect threats,
- Identify possible movements and landslide widening with high hazard,
- Select appropriate equipment relating to position in the field and measurement accuracy as a competent equipment to initiate an alarm and
- Define critical limit values (criteria values) that indicating the onset of new sliding and trigger an alarm.

Analyses of the past and prediction of future landslide behavior are the most important steps to consider in development of an early warning system, while equipment selection should depend on measurement of appropriate values with required accuracy. In case of the Grohovo Landslide, the accuracy of the wire extensometer measurements (<0.1 mm) and real-time recording have an advantage over GPS and TPS measurements. Both measurements are still unreliable because of unstable power supply. The accuracy of TPS measurements is <1.0 mm but from the measurement results, it is very clear that the collected data are liable to numerous influences such as daily, monthly and yearly temperature and humidity variations and local disturbing effects caused by deformation of poles on which the robotic total station and GPS master unit receiver are installed (Arbanas et al. 2012, 2013). The accuracy of GPS measurement is <2.0 mm but this accuracy is obtained only after 6 h of data post-processing. This fact eliminated GPS data as appropriate equipment to trigger the alarm in an early warning system.

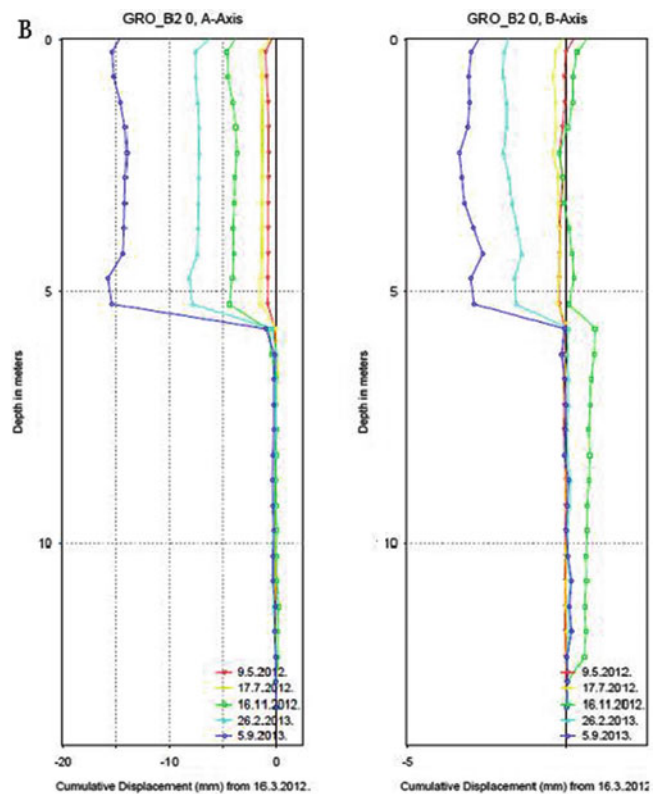


Fig. 4 Inclinometer measuring data at B2 position (see Fig. 3), slip surface at 6 m

The Grohovo Landslide early warning would be established after completion of the monitoring system and enabling of transmission of real-time extensometers data to the central computer unit with defined critical limit values that indicate the onset of new sliding and trigger the alarm.

Conclusions

A comprehensive integrated monitoring system on Grohovo Landslide consists of a GPS survey network composed of a GPS master unit which is a reference station for 9 single frequency GPS rovers and a robotic total station which measures 25 benchmarks (prisms) every 30 min. The monitoring data collected are may be influenced by local disturbing effects caused by deformation of the poles holding the robotic total station and GPS master unit. The geotechnical monitoring system includes 2 vertical inclinometers and 4 wire extensometers; 113 long- and 3 short-span extensometers, 4 pore pressure gauges, a weather station and rain gauge, installed on the same position as certain parts of the geodetic monitoring equipment. Selection of the same position for different types of monitoring equipment enables spatial correlation of measurement data on the landslide. In combination with hydrological measurements it will be possible to construct relationships between rainfall,

groundwater level and appropriate landslide behavior, to establish an early warning system. Definition of alarm thresholds will be based on existing knowledge of the Grohovo landslide behavior and on the collected consequent comprehensive monitoring data as well.

Acknowledgments Presented results have been obtained with the financial support from JST/JICA's SATREPS Program (Science and Technology Research Partnership for Sustainable Development) to the Croatian-Japanese joint research project "Risk Identification and Land-Use Planning for Disaster Mitigation of Landslides and Floods in Croatia". This support is gratefully acknowledged.

References

- Arbanas Ž, Benac Č, Dugonjić S (2010) Dynamics and behavior of the Grohovo Landslide. In: Arbanas Ž, Mihalić S, Ožanić N, Marui H (eds) Proceedings of the 1st workshop of the project risk identification and land-use planning for disaster mitigation of landslides and floods in Croatia, Dubrovnik, 22–24 November 2010, JICA, Zagreb, p 5
- Arbanas Ž, Sassa K, Marui H, Mihalić S (2012) Comprehensive monitoring system on the Grohovo Landslide, Croatia. In: Eberhardt E, Froese C, Turner K, Leroueil S (eds) Proceedings of the 11th international and 2nd North American symposium on landslides: landslides and engineered slopes: protecting society through improved understanding, in Banff, Canada, 2–8 June 2012, CRC, Vancouver, pp 1441–1447
- Arbanas Ž, Jagodnik V, Ljutić K, Vivoda M, Dugonjić Jovančević S (2013) Remote monitoring of a landslide using integration of GPS, TPS and conventional geotechnical monitoring methods. In: Mihalić Arbanas S, Arbanas Ž (eds) Proceedings of the 1st symposium on landslides in Adriatic Balkan Region, 7–9 March 2013, Zagreb, Croatia
- Benac Č, Arbanas Ž, Jurak V, Oštrić M, Ožanić N (2005) Complex landslide in the Rječina River valley (Croatia): origin and sliding mechanism. *Bull Eng Geol Environ* 64(4):361–371
- Benac Č, Dugonjić S, Vivoda M, Oštrić M, Arbanas Ž (2011) Complex landslide in the Rječina Valley: results of monitoring 1998–2010. *Geol Croat* 64(3):239–249
- IAEG (1990) Suggested nomenclature for landslides. *Bull Int Assoc Eng Geol* 41:13–16
- Mihalić S, Arbanas Ž (2013) The Croatian–Japanese joint research project on landslides: activities and public benefits. In: Sassa K, Rouhban B, Briceno S, He B (eds) *Landslides: global risk preparedness*. Springer, Berlin, pp 345–361
- Velić I, Vlahović I (2009) Geological map of the Republic of Croatia 1:300,000. Croatian Geological Survey, Zagreb
- Vivoda M, Benac Č, Žic E, Đomlija P, Dugonjić Jovančević S (2012) Geohazards in the Rječina Valley in the past and present. *Croatian Waters* 20:105–116
- Vivoda M, Dugonjić Jovančević S, Arbanas Ž (2013) Landslide occurrence prediction in the Rječina River Valley as a base for an early warning system. In: Mihalić Arbanas S, Arbanas Ž (eds) Proceedings of the 1st symposium on landslides in Adriatic Balkan Region, 7–9 March 2013, Zagreb, Croatia
- Wang C, Arbanas Ž, Mihalić S, Marui H (2013a) Three dimensional stability analysis of the Grohovo landslide in Croatia. In: Margottini C, Canuti P, Sassa K (eds) Proceedings of the 2nd world landslide forum, Rome, 3–9 October 2011, Springer, Heidelberg, pp 47–52
- Wang G, Kearns TJ, Yu J, Saenz G (2013b) A stable reference frame for landslide monitoring using GPS in the Puerto Rico and Virgin Islands region. *Landslides* (2013):1–11



Review of Monitoring Parameters of the Kostanjek Landslide (Zagreb, Croatia)

Martin Krkač, Snježana Mihalić Arbanas, Željko Arbanas, Sanja Bernat, Kristijan Špehar, Naoki Watanabe, Osamu Nagai, Kyoji Sassa, Hideaki Marui, Gen Furuya, Chunxiang Wang, Josip Rubinić, and Koji Matsunami

Abstract

Since 2011, in the framework of the Croatian-Japanese SATREPS FY2008 Project, scientists have been working on the establishment of the Kostanjek landslide monitoring system in the City of Zagreb (Croatia). External triggers at Kostanjek landslide are measured with rain gauge and accelerometers. Displacements at the surface are measured by GNSS sensors and extensometers, while subsurface displacement is measured by vertical extensometers and inclinometer. Hydrological measurements consist of groundwater level measurements, discharge measurements, chemical and isotope analysis. Monitoring sensors recorded landslide reactivation due to external triggers in the winter period of 2012/2013. During the period from September 2012 to March 2013 the total cumulative precipitation was 793.7 mm and horizontal displacements were in the range of 9–20 cm. The installed monitoring sensor network proved to provide reliable data for the establishment of relations between landslide causal factors and landslide displacement rates aimed at establishing threshold values for early warning system.

Keywords

Kostanjek landslide • Monitoring system • Monitoring parameters • External triggers • Displacement • Hydrologic properties

M. Krkač (✉) • S. Mihalić Arbanas • S. Bernat

Faculty of Mining, Geology and Petroleum Engineering, University of Zagreb, Pierottijeva 6, Zagreb, Croatia

e-mail: mkrkac@rgn.hr; smihalic@rgn.hr; sanja.bernat@rgn.hr

Ž. Arbanas • J. Rubinić

Faculty of Civil Engineering, University of Rijeka, Radmile Matejčić 3, Rijeka, Croatia

e-mail: zeljko.arbanas@gradri.uniri.hr; josip.rubinic@gradri.uniri.hr

K. Špehar

Faculty of Natural Science, University of Zagreb, Horvatovac 102a, Zagreb, Croatia

e-mail: spehar.kristijan@gmail.com

N. Watanabe • H. Marui • C. Wang

Research Institute for Natural Hazards and Disaster Recovery, Niigata University, 8050 Ikarashi-Nincho, Nishi-ku, Niigata, Japan

e-mail: jibanken@cc.niigata-u.ac.jp; maruihi@cc.niigata-u.ac.jp; wangcx@gs.niigata-u.ac.jp

O. Nagai • K. Sassa

International Consortium on Landslides (ICL), Uji-Campus, Kyoto 611-0011, Japan

e-mail: nagai@iclhq.org; sassa@iclhq.org

G. Furuya

Department of Environmental Engineering, Faculty of Engineering, Toyama Prefectural University, 5180 Kurokawa, Imizu-shi,

Toyama 939-0398, Japan

e-mail: gfuruya@pu-toyama.ac.jp

K. Matsunami

Earthquake Disaster Research Division, Disaster Prevention Research Institute, Kyoto University, Gokasho, Uji, Kyoto 611-0011, Japan

e-mail: matsunami@ekanji.jp

Introduction

Kostanjek landslide is a reactivated deep-seated large translational landslide in an urbanized part of the City of Zagreb (Croatia), in Sarmatian and Panonian marls. The landslide initially developed in 1963 as a consequence of mining activities, i.e. undercutting of the slope toe in an open marl pit and uncontrolled massive blasting. In 2009 Kostanjek landslide became a pilot area for research activities in the framework of Japanese-Croatian bilateral SATREPS FY2008 project 'Risk Identification and Land-Use Planning for Disaster Mitigation of Landslides and Floods in Croatia'. One of the objectives of the scientific research was establishment of a landslide monitoring system and assessment of the hazard of further slope movement. Landslide monitoring activities (equipment installation and data collection) were initiated in 2011 (Mihalić Arbanas et al. 2013).

The scope of the paper is to review the monitoring parameters which have been continuously and discontinuously observed at the Kostanjek landslide. According to Baroň et al. (2012) monitoring parameters are defined as any phenomenon or factor related to a slope (area of interest), which could be quantified and monitored over time. Parameters which can influence slope failure conditions and which are monitored at Kostanjek landslide are: (1) external triggers (rainfall and earthquakes); (2) slope movement; and, (3) hydrological properties (groundwater levels, discharge, water chemistry). The idea was to develop a system for the collection of reliable data which would be used in future application as: (1) input data for interpretation of engineering geological or kinematic models of this landslide; and (2) thresholds for decision-making and warning of citizens in the most dangerous zones inside the landslide area.

Monitoring at the Kostanjek landslide should provide high resolution spatial and temporal data, because this landslide is generally characterized by small oscillations of heterogeneous velocities. Except for the high resolution data, the data should be as accurate as possible to enable differentiation between minimal seasonal changes and changes related to periods of acceleration when failure can occur. High resolution and high accuracy of data are also necessary to define critical thresholds of triggering factors, i.e. to setup an early warning system.

External Triggers

Meteorological Conditions

According to historical data from the meteorological station Zagreb-Grič, the mean annual precipitation in the City of Zagreb for the period 1962–2012 is 874.4 mm. The Zagreb-

Grič station is the main meteorological station in the City of Zagreb, located about 9 km east from the Kostanjek landslide. Krkač et al. (2014) showed similar rainfall regimes between the Zagreb-Grič and the Kostanjek landslide locations. The City of Zagreb experienced a period of intense rainfall from September to December 2012 and a period of intense rainfall and snow from January to March 2013 (Fig. 1). During the 13th and 14th of January 54 cm of snow fell, which is the third highest snowfall recorded at the Zagreb-Grič station since its establishment in 1861 (DHMZ 2013). This extremely wet period with cumulative precipitation of 793.7 mm, which corresponds to about 90 % of mean annual precipitation, caused a reactivation of a large number of landslides in NW Croatia (Bernat et al. 2014) and reactivation of the Kostanjek landslide.

At the area of the Kostanjek landslide rainfall has been monitoring with a 0.5 mm tipping-bucket rain gauge, installed in the central part of the landslide, since September 2011. Figure 1 shows a comparison of cumulative precipitation from the Zagreb-Grič weather station and the Kostanjek rain gauge. The difference between precipitation and rainfall quantities (20 %) is greater than the real difference due to the limitations of the rain gauge: (1) it cannot measure rain during the winter period when snow cover blocks penetration of rain into the gauge; (2) it measures only water that originate from snow cover which melts on the funnel of the device—this snow cover, whose melting can be detected by this device, is usually smaller than the representative value, as a consequence of local meteorological conditions (e.g. wind). This implies limited use of a rain gauge, as a sensor for monitoring of meteorological trigger(s) in snowy periods, and the necessity of using data from a local meteorological station.

Seismicity/Earthquakes

The geophysical measurement sensor network at the Kostanjek landslide includes seven accelerometers installed inside the landslide area to: (1) monitor local micro earthquake activity in the landslide area; (2) monitor regional earthquake activity, including strong motion; (3) monitor any ground tremors associated with landslide movement, including possible ground inclination. The monitoring system consists of a 3-component Micro-Electro-Mechanical System (MEMS) accelerometers and 3-channel autonomous broadband digital recorders with GPS to maintain accurate synchronization. Three accelerometers are installed in the center of landslide: one below the sliding surface, at a depth of 90 m; and two inside the landslide mass, at depths of 20 m and 2 m. Four accelerometers are installed near the surface, at depths of approximately 1.5 m. They are spatially arranged to cover all parts of the landslide area.

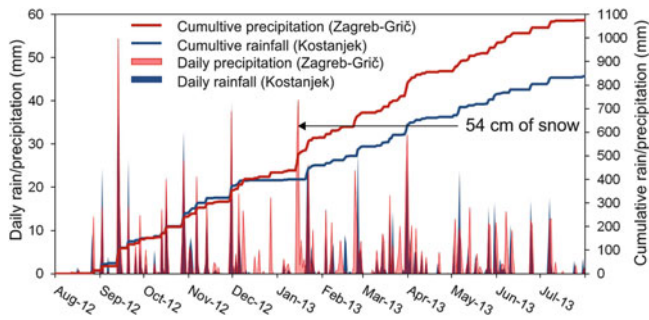


Fig. 1 Cumulative and daily precipitation from the Zagreb-Grič station and cumulative and daily rainfall from the Kostanjek rain gauge (August 2012–July 2013)

Since the start of seismic monitoring in April 2013, 16 earthquakes occurred. During this period none of the periods of displacement can be attributed to earthquake-induced ground motions. Examples of accelerograms for an earthquake $M=2.2$ that occurred approximately 19 km NE from Kostanjek landslide, at a depth of 2 km, are presented in Fig. 2.

Slope Movements

Subsurface movements at Kostanjek landslide are continuously monitored by four borehole wire extensometers and occasionally by one inclinometer. Direct monitoring of movements at the landslide surface, i.e. monitoring of the actual state of slope activity, is continuously performed by extensometers and GNSS sensors.

An inclinometer casing was installed in March 2012, in a 100 m deep borehole. The inclinometric profiles (Fig. 3), based on three measurements, indicate that the failure occurs in a thin basal shear zone in Sarmatian marls at a depth of 62.5 m. The total amount of displacement measured for the period from April 2012 to February 2013 was 60 mm. Deformation above 62.5 m can be considered as negligible with respect to the interpretation of landslide mechanisms. Deformation at the depth of 15–30 m is probably a consequence of inclinometer tube installation, because of the existence of the voids between the inclinometer casing and the in-situ ground (Stark and Choi 2008).

In September 2013 four vertical extensometers were installed in a 75 m deep borehole in the central part of the landslide, near borehole with inclinometer casing. In the period September 2013–November 2013 there were no measured displacements. This is partly because the measurements were undertaken after dry summer period without larger landslide movements. The second reason is that vertical extensometer measurements in the early stage of measurement are smaller and do not correspond to the actual displacements (Corominas et al. 2000).

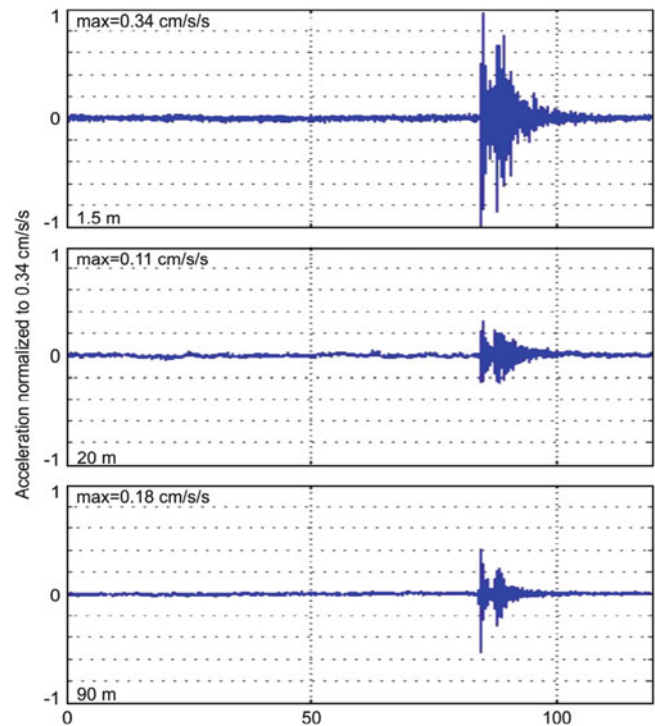


Fig. 2 Earthquake accelerograms recorded by MEMS accelerometers installed in the central part of landslide

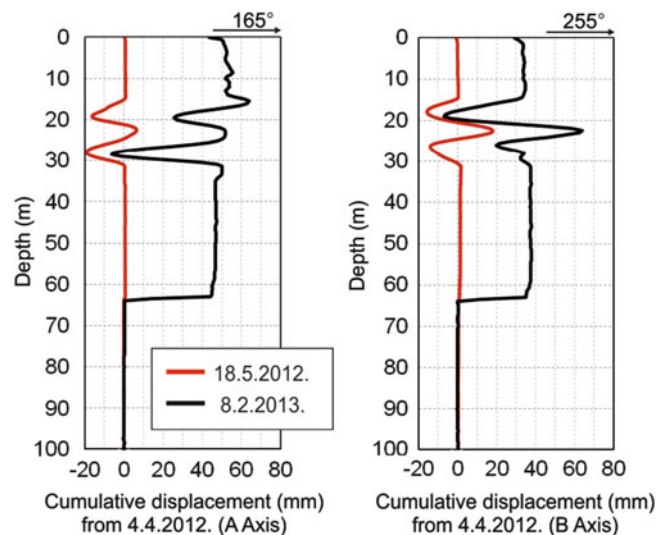


Fig. 3 Cumulative inclinometer displacements

Seven long- and two short-span wire extensometers, which provide continuous data on relative displacement between two points, were installed in the period from March 2011 to September 2013. During the winter period 2012/2013 three of seven extensometers installed at that time, showed significant displacement: a long-span extensometer crossing the main crack; a short-span extensometer

crossing a flank crack in the east side of landslide; and a short-span extensometer in the tunnel crossing the sliding surface (Fig. 4). All three extensometers displayed extension, but the amount of measured displacement varies from 40 mm on the fracture on the flank of the landslide body to 72.5 mm on the main crack and 97 mm in the central part of landslide where sliding surface intersects the tunnel.

GNSS monitoring system consists of 15 double-frequency NetR9 TI-2 GNSS receivers with Zephyr Geodetic 2 GNSS antennas installed at the landslide surface. All 15 GNSS sensors measure absolute displacement compared to 16th GNSS reference station, which is considered as a stable GNSS and is approximately 7 km from the landslide. The first GNSS sensor was installed in September 2012. During the monitoring period almost all sensors measured movement, from 4 to 20 cm. Figure 5 shows the evolution of surface displacement of four GNSS sensors with a major period of displacement from December 2012 to May 2013. The maximum rates of movement, with velocities of 2–4 mm/day, occurred during the first week of April. The amount of movements in the central part of landslide is approximately two to four times higher than movements near the landslide borders, which implies frictional resistance at the right flank (Allison and Brunsten 1990) and, together with 25 mm of subsiding, occurrence of graben in the northern part of landslide.

Hydrologic Properties

Groundwater Level/Pore-Water Pressure

Continuous water level monitoring started with installation of two water level sensors in two domestic wells with no or occasional usage in June 2012. The measuring was to determine the groundwater level of the shallowest aquifer. Wells are located near the main scarp, at the north (in Bizek II St.), and west from cuts at an abandoned marl open pit (in Vodopijjn Breg St.). Changes in groundwater level for both wells show a similar appearance (Fig. 6). However, a much deeper well in Vodopijjn Breg St. shows the much stronger influence of daily rainfall and a greater oscillation of groundwater depth (from 13 to 21 m), while the well in Bizek II shows a maximum change of only 4 m in groundwater level during the same period (Krkač et al. 2014).

An additional water level sensor was installed in the central part of landslide in a borehole with an accelerometer in January 2013. The data obtained from the water level sensor gives an average position of the water table between the top of the borehole and the depth of 35 m, whereas below this depth the borehole is sealed. Measurements are registered every hour. Figure 6 shows the averaged data over each 24 hour period. The three episodes of increased

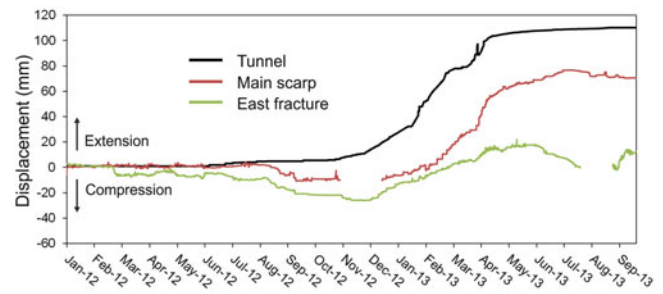


Fig. 4 Extensometer measurements in the underground (in the tunnel) and at the surface, across the main scarp and fracture in the eastern part of the landslide

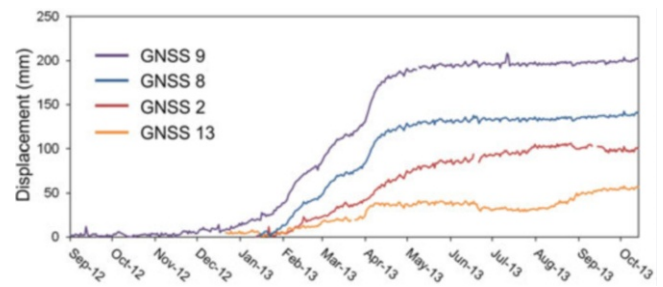


Fig. 5 Cumulative horizontal displacements versus time for GNSS 2 and 13 (near the landslide boundary) and GNSS 8 and 9 (in the central part of the landslide)

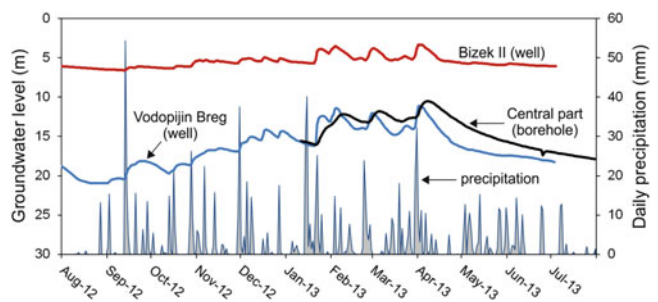


Fig. 6 Daily groundwater levels at Kostanjek landslide

groundwater levels in wells and in borehole, together with their peaks coincide with periods of accelerated movements in the winter of 2013.

Three pore pressure gauges were also installed in the central part of landslide in September 2013. The deepest one measures pore pressure within the area of the sliding surface in Sarmatian silts at a depth from 60 to 65 m. The middle one measures pore pressure within the landslide body, i.e. within the lower Panonian silts at a depth from 50 to 55 m, and the shallowest one measures pore pressure within upper Panonian silts and sandy silts at a depth from 30 to 38 m.

Water Balance: Inflow and Outflow, Surface Flow

The objective of hydrological research is study of groundwater dynamics and its relation to Kostanjek landslide movements. Inflow and discharge regime is continuously measured at two locations: (1) at the entrance of the tunnel which passes through the slip surface; (2) at the spring of the Dolje Stream, approximately one kilometer north from the landslide. At each location an outflow weir was constructed and water level sensor was installed. The relationships between water levels and discharge were established on the basis of several discharge measurements with a standard current meter. Daily discharges at the weirs are presented in Fig. 7.

Discharge at the spring of Dolje Stream varies in a range from 2.5 to 12.5 l/s. Discharge reacts relatively quickly and shows large oscillations related to rainfall. The maximum measured discharges, at the Dolje Spring, were in the following periods: 21–23 January 2012, 2–4 February 2013, and 30 March to 4 April 2013. These peaks of discharge, related to heavy rainfall and snow melting, together with peak from 9–10 March 2013, correspond to the periods of maximum landslide movement rates.

Discharge at the tunnel entrance varies from 4.2 to 7.5 l/s. The highest values of the discharge were in the following periods: 15 January to 1 February 2013, and 21 February to 15 March 2013. At the end of the March, the weir at the tunnel entrance was drowned because of landslide deformation in the downstream area.

Water Chemistry and Isotopic Compositions

The hydrochemical characteristics of groundwater reflect the mineralogical composition of solid phases of the parent rock through which the groundwater flows and also provide signatures as natural tracers to better understand groundwater migration (Watanabe et al. 2012). During the September 2011 and June 2012, one sample of spring water, seven samples of stream water, 11 samples from the tunnel and 74 groundwater samples from private wells were collected for hydrochemical and isotope analyses. The pH, EC and temperature of all samples were determined in the field, while Na, NH₄, K, Mg, Ca, Sr, HCO₃ and CO₃ as alkalinity, Cl, NO₃ and SO₄, also $\delta^{18}\text{O}$ and $\delta^2\text{H}$, were analyzed in the laboratory of the Niigata University.

The hydrochemistry of groundwater from shallow aquifers (wells) are classified into four types: (1) Ca-HCO₃ type; (2) SO₄-rich Ca-HCO₃ type ($0.28 < \text{SO}_4/\text{HCO}_3 < 0.40$); (3) Mg-rich HCO₃ type ($0.19 < \text{Mg}/\text{Ca} < 0.55$); (4) Cl-rich type ($\text{Cl} > 100 \text{ mg/L}$). Ca-HCO₃ type waters are closely related to the bedrock rock type (marls), and are

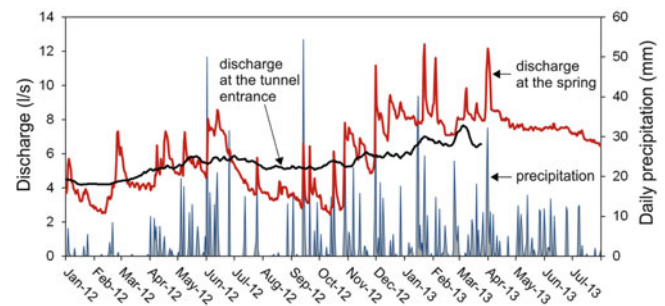


Fig. 7 Daily discharges at the tunnel entrance and spring of the Dolje Stream

predominately distributed over the research area. The SO₄-rich Ca-HCO₃ type waters, probably influenced by gypsum or aragonite in the landslide hinterland, are scattered in the northern and SW part of the research area. The Cl-rich type waters (most probably of anthropogenic origin) are scattered in the northern and western, relatively densely populated part of the research area. The Mg-rich HCO₃ type waters are sporadically distributed in the northernmost part, behind the head of landslide and in the eastern and south-eastern part of the landslide. In addition, spring water from dolomite in the tunnel is also of a Mg-rich HCO₃ type, but more enriched in Mg and depleted in Sr than the Mg-rich HCO₃ type waters in the landslide. It can be concluded that the dolomite is major source of Mg in waters from the research area.

Isotopic compositions of $\delta^{18}\text{O}$ and $\delta^2\text{H}$ of all waters are of meteoric origin, although spring waters in the tunnel are depleted in $\delta^{18}\text{O}$ and $\delta^2\text{H}$ compared with other sources. The isotopic depleted compositions suggest that these waters are recharged in the higher (northern) dolomitic area and migrate through the dolomite aquifer to the depths of the landslide mass. Mg-rich HCO₃ groundwater types show a tendency to be slightly depleted in $\delta^{18}\text{O}$ and $\delta^2\text{H}$ comparing with the other groundwater types. It seems that Mg-rich HCO₃ groundwater type is influenced by isotopic depleted waters from the dolomite aquifer.

According to chemical and isotopic compositions, it is clear that Mg-rich HCO₃ type waters are originally formed by mixing of common Ca-HCO₃ type water with Mg-Ca-HCO₃ type water derived from the dolomite aquifer. Therefore, it is most likely that the Mg-rich artesian waters from the deep dolomite aquifer are continuously injected into shallow aquifers in the landslide mass. Such injection of deep artesian waters has an impact upon groundwater behavior in the landslide mass and is also one of the key factors controlling the stability of the Kostanjek landslide. This interpretation coincides with Ortolan's (1996) hypothesis that an artesian aquifer in Badenian limestone and Triassic dolomite underlays Sarmatian and Panonian rocks and the Kostanjek landslide.

Discussion and Conclusions

External Triggers

Rainfall and earthquakes are monitored by sensors for continuous measurement installed at the Kostanjek landslide. External trigger monitoring is of crucial importance because of their influence on reactivation of the landslide and establishment of an early warning system.

A disadvantage of the installed rain gauge is that it does not provide accurate precipitation data during snowy periods. Moreover, the Kostanjek landslide reactivation in the winter and spring of 2013 was triggered by precipitation (rainfall and melting of thick snow cover). Because of this reason it is necessary to install an additional meteorological station in the area of the Kostanjek landslide which will monitor precipitation and other meteorological factors.

Seven accelerometers with continuous monitoring, installed at five locations at the landslide surface and at different depths, also provide good spatial and temporal data which can record local conditions inside the landslide body (depth of 90 m; total landslide area of 1 km²) and in the rock mass below the sliding surface. These accelerometers can record ground shaking (accelerations) in response to earthquakes (trigger) and response to landslide movements (activity). According to Massey (2010), there is possibility that installed accelerometers can not record low strain rate displacements such as creep.

Slope Movements

Slope movement measurements provide data about the actual state of slope activity, i.e. they define the dynamic status of a mass movement, enable recognition and quantification of the reactivation phase, enable definition of threshold values and eventually enable forecasting of the catastrophic phase (Baroň et al. 2012). Subsurface movement at the Kostanjek landslide, measured by inclinometer, provided reliable data about sliding surface depth, mechanical behavior and displacement rate until February 2013. After this period the inclinometer casing became impassable due to large displacement at the sliding surface. Although the inclinometer data are of good quality, the temporal resolution (just a few measurements in 1 year) and spatial resolution (one borehole in the central part of the landslide) are very poor. Poor spatial resolutions spoiled the possibility of confirming the existing landslide model or reinterpretation for an improved landslide model.

Partial improvement of the subsurface movement monitoring was introduced by installation of four vertical wire extensometers of different depths, installed in the borehole

near the existing inclinometer casing. They will provide continuous displacement monitoring data even in the case of larger displacements. However, additional inclinometers in different part of the landslide are necessary to provide reliable data about landslide geometry.

High resolution temporal and spatial data at Kostanjek are obtained from surface movement monitoring by GNSS sensor network and a large number of wire extensometers. Fifteen densely distributed GNSS sensors can provide high accuracy data depending on post-processing time, while the temporal resolution of the data can be every second (in real time kinematic mode). These near-real and real time movement data satisfy the requirements for failure prediction, using for example the Fukuzono (1985) method. Seven extensometers provide data every 1 h. Unreliability of extensometer data can be caused by significant influence of meteorological conditions to registered displacements, however, which is necessary to take into consideration during interpretation of movement, velocity and acceleration.

Hydrologic Properties

Properties that have the most significant influences on landslide behavior are hydrological properties. Equipment for monitoring of superficial movements measured landslide displacements of 4–20 cm in different parts of landslide, with periods of maximum velocities (2–4 mm/day) which correspond to the peaks of ground-water levels measured in the central part of the landslide.

Pore water pressure/water level data at the Kostanjek landslide provide good temporal data (every 1 h), but the sensors are installed at only few locations and in different parts of the landslide body. Three piezometers with pore pressure gauges are installed in the central part of the landslide body: one is in the zone of the sliding surface and two are in the landslide mass. Other water level gauges are installed in the upper part of the landslide body. Although water level sensors installed in the upper part of the landslide body do not actually measure water level in the sliding surface area, the data shows good correlation with landslide movements. However, additional piezometers are necessary, in different part of the landslide, to provide measurements of pore water pressure for better understanding of landslide behavior and correlation with causal factors.

Geochemical measurements undertaken to better understand groundwater flow patterns were performed on samples taken at 74 locations. They provide high spatial resolution data. Samples taken in two different periods did not show any significant differences, which indicates that the temporal resolution is also of satisfying quality.

Acknowledgments Results presented herein have been obtained with financial support from JST/JICA's SATREPS (Science and Technology Research Partnership for Sustainable Development) Program. This support is gratefully acknowledged. The authors would also like to thank Croatian Meteorological and Hydrological Service for precipitation data.

References

- Allison RJ, Brunsten D (1990) Some mudslide movement patterns. *Earth Surf Process Landf* 15(4):297–311
- Baroň I, Supper R, Ottowitz D (2012) Report on evaluation of mass movement indicators. SafeLand deliverable D4.6. Geological Survey of Austria. Vienna, 382 p
- Bernat S, Mihalić Arbanas S, Krkač M (2014) Landslides triggered in the continental part of Croatia by extreme rainfalls in the winter of 2013. In: Proceedings of XII IAEG congress, 15–19 September 2014, Torino
- Corominas J, Moya J, Lloret J, Gili JA, Angeli MG, Pasuto A, Silvano S (2000) Measurement of landslide displacements using a wire extensometer. *Eng Geol* 55:149–166
- Fukuzono T (1985) A new method for predicting the failure time of a slope. In: Proceedings of IVth ICFL, Japan Landslide Soc, Tokyo
- DHMZ (Meteorological and Hydrological Service) (2013) Meteorological and hydrological bulletin 3 (in Croatian)
- Krkač M, Rubinić J, Kalajžić J (2014) Analysis of water fluctuation dynamics in the wider area of the Kostanjek landslide. In: Proceedings of 1st regional symposium on landslides in the Adriatic-Balkan Region, 6–9 April 2013, Zagreb
- Massey CI (2010) The dynamics of reactivated landslides: Utiku and Taihape, North Island, New Zealand. Ph.D. thesis, Durham University, Durham, UK
- Mihalić Arbanas S, Arbanas Ž, Krkač M (2013) TXT-tool 2.385-1.2 a comprehensive landslide monitoring system: the Kostanjek landslide, Croatia. In: Sassa K et al (eds) ICL landslide teaching tool. ICL, Kyoto, pp 158–168. ISBN 978-4-9903382-2-0
- Ortolan Ž (1996) Development of 3D engineering geological model of deep landslide with multiple sliding surfaces (Example of the Kostanjek Landslide). Ph.D. thesis, Faculty of Mining, Geology and Petroleum Engineering, University of Zagreb, Zagreb, Croatia (in Croatian).
- Stark TD, Choi H (2008) Slope inclinometers for landslides. *Landslides* 5(3):339–350
- Watanabe N, Krkač M, Furuya G, Wang C, Mihalić Arbanas S (2012) Hydrochemical characteristics of groundwater from the Kostanjek Landslide in Croatia. In: Proceedings of the 2nd project workshop of the Croatia - Japan project on risk identification and land-use planning for disaster mitigation of landslides and floods in Croatia, Rijeka, 15–17 Dec 2011

Part VI

Risk Assessment



Introduction: Risk Assessment

Huabin Wang, Rejean Couture, and Cees Van Westen

Landslides can result in enormous casualties and huge economic losses in mountainous regions. In recent years, interest in landslide risk assessment has grown substantially. Landslide risk assessment aims to determine the expected degree of loss due to landslides and the expected number of fatalities, people injured, damage to property and disruption of economic activity. This session addresses the landslide risk assessment, to establish criteria for ranking risk posed by different types of mass movements, to quantify the impact that mass movements have on population, structures and infrastructures, and to enhance strategies for avoiding or mitigating landslide risk.

In this session, Dr. Jiang and his colleagues chose natural and geographical factors, geological structure, lithology, surface water system, hydro-geological conditions, and the distribution of geological disasters as index for landslide hazard assessment using a fuzzy mathematics method in the three sites. In addition, Liu Donghao and Sun Cheng studied an fossil landslide on the urban fringe of metropolitan Region in Beijing, China. After the detailed analysis, topographical features, lithologic condition, formation conditions, as well as the formation conditions of landslide, qualitative analyses and a quantitative method were then adopted for the stability evaluation of the fossil landslide.

In order to consider the influence of the landslide slaking on the magnitude of impact energy, Mr. Wang and his colleagues established an evaluation model of landslide risk using the PFC in order to analyze the landslide impact energy on the possible afflicted body in Jiangping

hydropower station, Hubei, China. In their work, the interaction of grains is allowed to make a completely inelastic collision, and the landslide under different horizontal movement distance and geotechnical strength parameters is discussed to evaluate the landslide risk. Meanwhile, a back-analysis of a debris flow event was carried out by Dr. Hussin and their collaborators using MassMov2D to create a set of parameter ranges for forward-predicting runouts with mitigation measures. In their work, simulations from back-analysis were compared with the forward-predicted models to determine changes in the spread and intensity of debris flows affecting elements at risk, e.g. houses and roads.

Globally, the costs of landslide damage are proven to be of economic significance, but yet efforts for their systematic estimation are still rare. Mr. Klose and his coauthors presents a short summary of the challenges and concepts in previous landslide loss studies and introduces a methodological framework for the estimation of direct landslide costs in industrialized countries. A case study of landslide losses for federal roads in the Lower Saxon Uplands (NW Germany) exemplifies the application of this methodology in a regional setting. Landslide costs were spatially extrapolated from sub-regional levels after their calculation in representative case study areas. In the first step, cost survey is closely linked with methods of cost modeling, which in turn take advantage of landslide database information. The cost extrapolation to large-scale levels was then realized by a landslide susceptibility model combining cost figures with indices of infrastructure exposure.

H. Wang (✉)

School of Civil Engineering and Mechanics, Huazhong University of Science and Technology, Wuhan, Hubei, China
e-mail: huabin@mail.hust.edu.cn

R. Couture

Geological Survey of Canada, Natural Resources Canada, Ottawa, ON, Canada

C. Van Westen

International Institute for Geo-Information Science and Earth Observation, Enschede, The Netherlands



Site Selection Study for Hazardous Waste Based on Fuzzy Comprehensive Evaluation Method

Jiang Bing, Wei Yunjie, Xu Mo, and Han Caiyi

Abstract

This paper takes sites engineering geological environmental conditions as the main line. On the basis of full data collection, this paper chooses natural and geographical factors, geological structure, lithology, surface water system, hydro-geological conditions, and the distribution of geological disasters as index. According to defined index system and index weight defined by experts, fuzzy mathematics method is used to establish the mathematics models of the three sites. By calculation and analysis, the 3# site is the best as solid waste disposal center site in Chengdu, which can provide references for site selection of hazardous solid waste in mountainous cities.

Keywords

Hazardous waste • Site selection • Fuzzy comprehensive evaluation method

Introduction

Hazardous waste, except for radioactive waste, means waste that has chemical reactivity, toxicity, explosion hazard, corrosivity and other properties that can cause harm to human health and environment (Jin and Yao 2001). Because of its complicated chemical properties, high toxicity, explosion hazard, corrosivity and other properties, the hazardous waste can cause great harm to the environment, and is the key pollution source of soil, air, water, especially the groundwater, and has attracted widespread concern all over the world. Reduction, reclamation and decontamination are the three technological measures mainly adopted to deal with such pollution. Moreover, hazardous waste, by various

methods, was detoxified, separated, and concentrated, and the secure landfill is widely used of various disposal methods (Liu et al. 2004). The managements of solid waste remain uncommon in Chinese urban area, and depend on direct stacking and other simple disposal approaches to absorb over a long period of time, and the waste is not detoxified basically. This results in serious management problem of the pollution of urban solid waste (Guo et al. 2005).

State Environmental Protection Administration promulgated the National Hazardous Waste and Medical Waste Disposal Facilities Construction Plan, which was replied by State Council, on January 19th, 2004. The State Council requires the People Governments of various provinces; autonomous regions and municipalities must fully implement the construction of hazardous waste and medical waste disposal facilities and radioactive waste storages, and enforce the project construction managements. Therefore, the site selection of hazardous waste landfill becomes the key problem during the process of construction. Furthermore, the main controlling factor is the problem of interaction and coordination with geological environment and disposal project.

The Proposed hazardous waste disposal center of Chengdu is located in Ludai town of the Longquanyi

J. Bing (✉) • X. Mo • H. Caiyi
State Key Laboratory of Geohazard Prevention and Geoenvironment Protection, Chengdu University of Technology, Chengdu, Sichuan, China
e-mail: 448124138@qq.com; xm@cdut.edu.cn

W. Yunjie
China Institute for Geo-Environment Monitoring, Beijing 100081, China
e-mail: wyj1973@126.com

district. This project is one of the important projects of Chengdu, and its annual handling capacity is 12.2×10^4 t. Among them, 1.2×10^4 t will be comprehensively utilized, 1.0×10^4 t will be burned (excluding medical waste), 10.0×10^4 t will be securely landfilled. The engineering site locates in the middle of Longquan Mountain, which belongs to a valley-type landfill site. The main projects contain dams, landfills, sewage treatment plants and other facilities. The project is currently at the preliminary stage of investigation and designation. It has three optional sites, the 1# optional site, the 2# optional site and the 3# optional site. The scope of area is from $104^{\circ}20'51''$ to $104^{\circ}21'46''$, and $30^{\circ}39'10''$ to $30^{\circ}39'57''$. The dimensions of all sites are 0.473 km^2 . This paper using fuzzy comprehensive evaluation method, and taking the site selection of hazardous solid waste landfill in Chengdu as an example, studies impact factors and selection methods for the site of hazardous solid waste in mountainous area, and to provide references for site selection of hazardous solid waste in those cities.

Environmental Geological Conditions

Terrain and Physiognomy

The ridge which lies on the NE side of the 1# site of the pre-concentration area is called burned bridge. Along the slope, a number of NE-SW direction rushing gullies were developed; especially the depth of the Jiangjia Bay rushing gully locating on the eastern side of the site is the deepest. There also developed several SW-NE direction gullies on the slope of the Daliang Mountain at the west side of the site, but the high and steep artificial slope has been formatted in the slope because of the excavation by the workers of the brickfield, and the original landscape has been destroyed. In the southeast of the peripheral, the geomorphology is relative wide and gentle, shows fan-shaped, and disperse toward southeast. There are several rushing gullies importing Longfeng Ditch along the slope in the area of Yingtao Bay.

The overall shape of the 2# site looks like a circular, the terrain is decreasing from southeast to northeast in these areas, because of cutting by rushing gully, in the western side (the left of Lujia Bay rushing gully), the slope is relatively steep, and shows step-like; however, in the NE side of the site (the SW side slope of the Daliang Mountain), the slope is wide and gentle, the slope gradient is about 10° – 20° , and there are four miniature gullies developed.

In the 3# site, there is a rushing gully whose direction of the flowing is from south to north cross through the site (see Fig. 1). The overall shape also looks like a circular, and the terrain is decreasing from north to south. There is an unnamed hill locating on the west side of the site, and a reservoir is located between this hill and Zhongjia Mountain

which is at the west side of the site. The Yejia Old House on the east side of the site is located on a gentle slope (the SW slope of the Dayouao Mountain), and the slope gradient is about 10° – 25° . Generally speaking, all the assessment area is showing a valley between mountains geomorphology.

Geological Tectonic

In the whole domain, 1# and 2# site are located between the Jinlong Temple anticline and Luojia Mountain syncline. For both of them are affected by the Quartet Mountain fault and the Longquan Mountain west slope fault, the spatial occurrence of layers are up and down. According to the stratigraphic distribution and the occurrence changing, the main tectonic of the project area is composed of a short axis anticline being NW direction. In the east of DaLiang Mountain areas (most areas of the 2# site), these areas are mainly located in the south east wing of anticline, the strata direction of which is NE, and tilts to the SE, the inclined angle is from 10° to 40° , especially local area is up to 60° , while in the west of DaLiang Mountain areas (most areas of the 3# site), these areas are mainly located in the northwest wing of anticline, its main trend direction of strata is NW, the inclined angle is relatively moderate and the biggest are less than 30° , however, to the north of Wen'an town, the trend direction of strata changes to NW, and tilts to the SW, the inclined angle is about 30° . The 1# and 2# site are located on the secondary fold of the west wing of the box-shaped compound anticline of Longquan Mountain. The 3# site is located on the middle segment of the west wing of the box-shaped compound anticline of Longquan Mountain, which is in the NNE~NE trending fault belt of Longquan Mountain composed by the west slope fault of Longquan Mountain and the east slope fault of Longquan Mountain. The overall trend of Longquan Mountain fault belt is about $N20^{\circ}$ – $30^{\circ}E$, from Zhongjiang town in the north, to the south through the Jintang, Longquanyi, Jiulongchang and Renshou town, and till near Xingtang Town of Leshan City, the length is 230 km. The west fault and east fault are relatively tilted to each other, what's more, it extends to the core department of the anticline, and disappears in the triassic strata. The 3# site is located on the end of south segment of the Luojia Mountain syncline, which belongs to the raising the pinch-out side of the syncline, in the Quartet Mountain zone and in the northern of which the main tendency is toward north, and it is a small syncline in the southern zone.

Formation Lithology

The 1# and 2# site are located on the middle segment of Longquan Mountain, the exposure strata is J3p. According

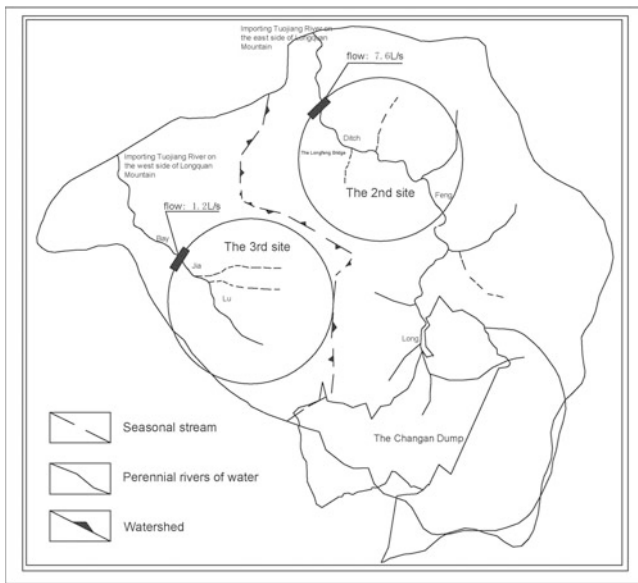


Fig. 1 water system graph of the site area

to the survey that jurassic formation is located in the middle and upper segment of the J3p in the project area, the main material of the overburden layer are the guar ternary loose sediments, the depth of which is from 1 to 8 m. The 3# site is also located on the middle segment of Longquan Mountain, the mainly exposure strata is J3p, the main material of the overburden layer are the guar ternary loose sediments, the depth of which is from 1 to 10 m. According to their formation, structural characteristics and traits, these materials can be divided into three types, artificial filled soil, residual, talus deposit, alluvial, diluvial deposit.

Surface Water System and Hydro-Geological Conditions

The 1# site area locates in the Longfeng River system. The main stream inflows (the source is located in already built Chang'an garbage plant) from the southeast of the site and two tributaries respectively mingle in it in the Cherry Bay and the Jiangjia Bay. The stream ultimately outflows in the northwest of the site. Then it passes through the Longquan Mountain along hills and joins the Tuojiang River at the east of the mountain. The 2# site locates in the Lujia Bay river system. The river rises in the southeast of the site and flows ultimately northward out of the site, and then joins the upper Tuojiang River. The river is flowing water all the year round. The 3# site has two river systems. The main river rises in the central northern of the site and two tributaries respectively mingle in it in Xuetangwo and Linjia Bay. The Xuetangwo tributary is mainly from the Liyu reservoir and ultimately

outflows in the south of the site and finally joins the Tuojiang River along hills (Fig. 1).

The stratum outcrops in the area is Penglaizhen Formation of the Upper Jurassic. The major lithology is interbedded in unequal thick composed by sandstone, mudstone, silt mudstone and pelitic siltstone. Among them, the content of sandstone is higher relatively in the upper middle and the bottom. Sandstone is brittle and develops more fractures. So the sandstone is rich in fissure water and is the major aquifer in the project area. In contrast, the clay layer has poor permeability and is water-resisting layer. After investigation, the 1# and the 2# sites have not yet found springs formed in Quaternary loose sediments, however, in the 3# site a spring found formed in Quaternary loose sediments near the central south (B9) of the site, and with a very small flow rate. In the low-lying area of the spring vent, the water barely flows.

The Distribution of Geohazards

According to investigation, two landslides developed at site 1#, one at site 2#, two at site 3#, all of their size are small. Besides, four unstable slopes developed at site 3#, the size are generally small and in stable condition basically at present. 18 collapse bodies developed both at site 1# and site 2#, while 15 are developed at site 3#.

Fuzzy Comprehensive Evaluation

In practice, comprehensive evaluation is a kind of evaluation to one thing which often involves many factors/indices and requires a general assessment, not only from one particular factor. The steps of such fuzzy comprehensive evaluation model as following Wang and Li (2008):

1. Ensure the evaluation factors and grades. Suppose that $U = \{u_1, u_2, \dots, u_m\}$ is the m kinds of factors to the evaluation target, $V = \{v_1, v_2, \dots, v_n\}$ is the n kinds of judgment to the condition of each factor, where m is the number of assessment factors, n is the number of remarks.
2. Determine the evaluation matrix and the weight. Firstly, do single factor evaluation to $u_i (i = 1, 2, \dots, m)$ from the factor set, determine the membership r_{ij} from factor u_i to grade $v_j (j = 1, 2, \dots, n)$, then get the set of single factor evaluation u_i .

$$r_i = (r_{i1}, r_{i2}, \dots, r_{in})$$

So the assessment sets of m factors can construct a general evaluation matrix R , which means that each object evaluated to determine the fuzzy relationship of matrix R from U to V .

$$R = (rij)m \times n$$

Where, rij stands for frequency distribution from the factor ui to the remark vj, in generally, which will be normalized to meet $\sum_{j=1}^n rij = 1$.

- Fuzzy comprehensive evaluation and decision-making. The different lines in R reflect the degree of membership to the fuzzy sets from different single factor. If synthesize the different lines with fuzzy weight A, it can get the membership degree of evaluated object to various grades in general, which is called as the results vector of fuzzy comprehensive.

Import a fuzzy set of B from V, called fuzzy assessment and decision-making collection.

$$B = \{b1, b2, \dots, bn\}.$$

So that $B = A \times R$, fuzzy transform. If the evaluation result $b_j \neq 1$, then it needs to be normalized.

Matrix B is a degree description of comprehension condition grades from every evaluated object, which can't directly assess the objects without a further processing. The method which always be used is maximum degree-of-membership theory in order to get the final assessment value. Here, only use the maximum of $b_{(jj = 1, 2, \dots, n)}$, not make full use of the information from B. Therefore, it can consider comprehensively the evaluation index and result from each grade to get a more practical assessment value.

Suppose that the parameters of column vector related to each grade vj are:

$$C = (c1, c2, \dots, cn)^T$$

Then, the assessment result of grade parameter is (Table 1):

$$B \times C = p,$$

where p is a real number.

Site Selection of Hazards Waste

According to field investigation and analysis, the final assessment indices are determined as three layers for those three candidate sites. Based on the feature of indices to divide layer modular structure and construct a three layers model.

The first layer is: $U = \{u1, u2, \dots, un\}$;

The second layer is: $u1 = \{u11, u12, u13\}$; $u2 = \{u21, u22\}$; $u3 = \{u31, u32\}$; $u5 = \{u51, u52, u53\}$

Table 1 The distribution of geohazards at the proposed site

| Sites No. | Number of geohazards | | |
|-----------|----------------------|-----------------|----------------|
| | Landslide | Collapse bodies | Unstable slope |
| 1# | 2 | 18 | 0 |
| 2# | 1 | | 0 |
| 3# | 2 | 15 | 4 |

The third layer is: $u13 = \{u131, u132, u133\}$; $u22 = \{u221, u222\}$

According to the impact degree of every factor to the waste disposal center, after assessment, the index weight determined are as followed:

$$A = (0.3, 0.2, 0.2, 0.2, 0.1); A1 = (0.2, 0.4, 0.4); A2 = (0.4, 0.6); A3 = (0.6, 0.4); A5 = (0.5, 0.3, 0.2)$$

According to the index system and factor weight determined above, the mathematics model construction of three layers fuzzy comprehension evaluation to the three sites, showed in Table 2.

The three candidate sites of waste disposal center in Chengdu constitute the decision set $V = \{a1, a2, a3\}$. According to the investigation data and some disposals to get the fuzzy comprehension evaluated value, showed in Table 3.

Make fuzzy comprehension assessment to the data above:

Firstly, make the single-factor evaluations of Natural geographic of Table 3. $u13 = \{u131, u132, u133\}$, the weight $A13 = \{1/6, 1/6, 2/3\}$, the single-factor evaluation matrix composed by fuzzy assessment $u131, u132, u133$ from Table 2 is:

$$R13 = \begin{pmatrix} 0.60 & 0.72 & 0.80 \\ 0.72 & 0.75 & 0.53 \\ 0.82 & 0.85 & 0.73 \end{pmatrix}$$

Calculate $B13 = A13 \times R13 = (0.77, 0.81, 0.71)$;

$$B11 = (0.62, 0.55, 0.62);$$

$$B12 = (0.70, 0.82, 0.78);$$

$$B1 = A1 \times R1 = (0.69, 0.76, 0.72);$$

The same can be calculated:

$$R22 = \begin{pmatrix} 0.62 & 0.85 & 0.63 \\ 0.66 & 0.81 & 0.70 \end{pmatrix}$$

$$B22 = A22 \times R22 = (0.69, 0.76, 0.72);$$

$$B21 = (0.80, 0.80, 0.80);$$

$$B2 = A2 \times R2 = (0.73, 0.78, 0.75);$$

$$B3 = A3 \times R3 = (0.85, 0.83, 0.85);$$

$$B4 = (0.78, 0.80, 0.77);$$

$$B5 = A5 \times R5 = (0.80, 0.79, 0.82)$$

Table 2 Three model of site selection for hazards waste in Chengdu city

| Indices from the first layer | Indices from the second layer | Indices from the third layer |
|--|---|--|
| Natural geographic factor $u_1(0.3)$ | Distance from city $u_{11}(0.2)$ | |
| | Topography $u_{12}(0.4)$ | |
| | Surface water $u_{13}(0.4)$ | Length of main channel $u_{131}(1/6)$ Number of branch channel with perennial water $u_{132}(1/6)$ Catchment area $u_{133}(2/3)$ |
| Geological structure factor $u_2(0.2)$ | Regional tectonic setting $u_{21}(0.4)$ | |
| | Site geological structure $u_{22}(0.6)$ | Anticline $u_{221}(1/3)$ Syncline $u_{222}(2/3)$ |
| Stratum lithology $u_3(0.2)$ | Mudstone thickness $u_{31}(0.6)$ | |
| | Cover thickness $u_{32}(0.4)$ | |
| Hydrogeology condition $u_4(0.2)$ | Ground water level $u_4(1.0)$ | |
| Geohazard $u_5(0.1)$ | Landslide $u_{51}(0.5)$ | |
| | Rock fall $u_{52}(0.3)$ | |
| | Unstable slope $u_{53}(0.2)$ | |

Table 3 Fuzzy comprehension assessment of site selection for solid waste in Chengdu

| Affect factor | Site | | |
|---|------|------|------|
| | 1# | 2# | 3# |
| Distance from city | 0.62 | 0.55 | 0.62 |
| Topography | 0.70 | 0.82 | 0.78 |
| Length of main channel | 0.60 | 0.72 | 0.80 |
| Number of branch channel with perennial water | 0.72 | 0.75 | 0.53 |
| Catchment area | 0.82 | 0.85 | 0.73 |
| Geological structure factor | 0.56 | 0.75 | 0.56 |
| Regional tectonic setting | 0.80 | 0.80 | 0.80 |
| Site anticline | 0.62 | 0.85 | 0.63 |
| Site syncline | 0.66 | 0.81 | 0.70 |
| Mudstone thickness | 0.81 | 0.81 | 0.81 |
| Cover thickness | 0.90 | 0.85 | 0.91 |
| Ground water level | 0.82 | 0.80 | 0.77 |
| Landslide | 0.82 | 0.78 | 0.85 |
| Rock fall | 0.72 | 0.80 | 0.72 |
| Unstable slope | 0.90 | 0.82 | 0.90 |

Then make higher comprehension assessment according to the data above:

$U = \{u_1, u_2, u_3, u_4, u_5\}$, the weight $A = \{0.3, 0.2, 0.2, 0.2, 0.1\}$, so comprehension assessment: $B = A \times R = (0.77, 0.75, 0.79)$

Then, the result sorts of comprehension assessment for the three candidate sites are: a3, a2, a1. Therefore, a3 is the optimal site for solid waste disposal center in Chengdu.

- Through study the relationship of each environmental geology factor from each site comprehensively, and by the method of fuzzy mathematics, the fuzzy comprehension assessment mathematics model with three layers to the three sites respectively are established.
- The fuzzy assessment model uses hierarchy structure, through calculation and comparison, 3# is the optimal site for solid waste disposal center in Chengdu.

Conclusion

Through the analysis above, the conclusion summarized as following:

- The factors of site selection for solid waste disposal in mountain area city mainly are natural geographic factor, geological structure factor, stratum lithology, surface water, hydrogeology condition, distribution of geohazard and so on.

Acknowledgment Project supported by the National Natural Science Foundation of China (Grant No. 41172254)

References

Guo X, Xu Z, Wang W et al (2005) Investigation and research on solid waste management in townships. *J Saf Environ* 5(4):83–85

-
- Jin M, Yao C (2001) Technical concept of disposing dangerous solid waste. *Zhe Jiang Chem* 32(2):28–29
- Liu J, Xia Q, Ming C (2004) Geotechnical characteristics and countermeasures for dangerous solid waste landfill Center of Nanjing City. *Jiangsu Geology* 28(2): 113–115
- Wang L, Li H (2008) Study on logistics center location based on fuzzy comprehension assessment. *Rail Freight* 11:5–11



Research of Stability of an Fossil Landslide on the Urban Fringe of Metropolitan Region in Beijing, China

Dong-hao Liu and Cheng Sun

Abstract

This paper study an fossil landslide on the urban fringe of metropolitan Region in Beijing, China. Topographical features, lithologic condition, formation conditions, as well as the formation conditions of landslide was detailed analysis. We adopt the method of qualitative analysis and quantitative method to research the stability of the fossil landslide. The calculation results show that, under heavy rain conditions, although landslide is still in a stable state, but the safety coefficient decreased more, but the stability became stable. Detailed geotechnical investigations for evaluating the stability of the landslide are carried out in this study with due consideration for future risk. Finally, the corresponding engineering activities in the process of prevention and prevention measures are given according to our research.

Keywords

Fossil landslide • Characteristic • Formation conditions • Stability

Introduction

Beijing is undergoing the process of rapid urbanization. Staggering urban expansion in metropolitan area make communities sprawl to suburbanization area. Large landslides do sometimes exist in this area, where happens a lot of [human activities](#).

It is worth to make efforts to understand the [characteristic](#) of fossil landslide. First, since fossil landslide is potentially unstable, determining what level of instability is important requires subjective judgments. To make these decisions, we must assess the influence of unstable lands on the resources and values that instability is likely to affect. Third, the environmental hazards posed by some types of instability can be avoided through extra effort in engineering and design. If the relative importance to ecosystem values of

different types of instabilities can be assessed, the sites needing modification of operational guidelines can be identified and prioritized (Zhang et al. 1994).

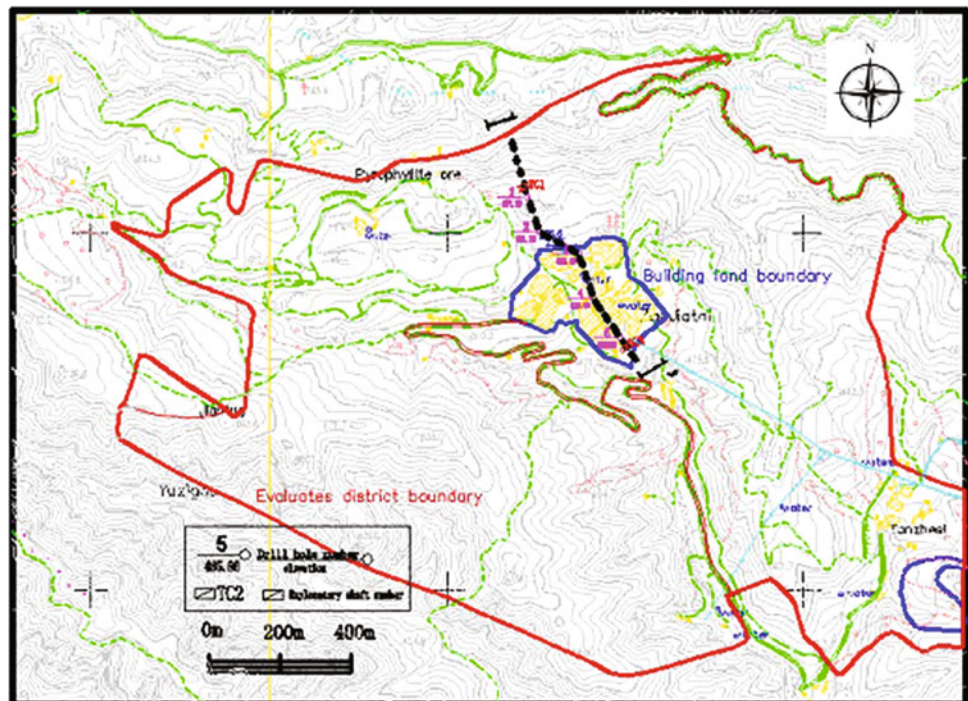
It is shown in engineering practice that the correct understanding and using of geological and mechanical model are the fundamental keys for the prevention of large-scale landslides. This paper presents an attempt to address the nature of an fossil landslide in Beijing, China, in order to help to prevent the landsliding in future.

Geographical Location of the Fossil Landslide

This paper takes an fossil landslide in Beijing, China as the study object (Fig. 1). The Zhaojiatai village is a fossil landslide which located in Tanzhe Temple. Tanzhe Temple, located in Mentougou District of southeastern Beijing, which is the oldest temples in Beijing with 1,700 years of history. The Zhaojiatai village is involved in an project called “Old village renovation planning”. Four hundred house is involved in this project, and the road is proposed widen to about 12 m.

D.-h. Liu (✉) • C. Sun
China ordnance industry survey and geotechnical institute, XiBian Gate
Avenue 79, Beijing 100053, China
e-mail: ldh831013@sina.com; sunz0412@163.com

Fig. 1 The location of the fossil landslide in Beijing



According to previous records, 20 years have been passed since the village moved here. The fossil landslide hasn't cause serious hazards such as tension fracture and so on. Old buildings also preserved well scene then. Only a handful of building wall appeared irregular cracks, which caused by uneven foundation. No landslide phenomenon has been made in recent years, the village or hidden trouble, suggests that the village ground is stabile, with no slip signs.

An fossil landslide was found to the east of Zhaojiatai village. The fossil landslide is covered about 4,900 m². The length of landslide is about 90 m long. It maintains a fairly uniform width of about 85 m, but narrows slightly near the mountain front and at the toe. The volume of this landslide is 19,600 m³. This landslide mainly make up of talus stone, and gravel soil. The soil is loose. The landslide is steep, with the slope angle of 50° ~ 60°. There are roads across the landslide. There is a crack appears at the posterior section of the landslide. The crack extend about 60 m, with the width of 40 m. Difference of elevation appears in backwall of the landslide. The maximum difference of elevation reach to 50 cm. There are cracks appears in abandoned walls. East backwall of landslide is make up of sandstone, crack is occurred in local. The local rock crack. Landslide is located in the west of the village. There is a fracture surface, with the angle of 165°. Front slope located on the eastern side ditch bottom of this village. No obvious deformation was found in this investigation.

The exact time of movement is uncertain, but evidence suggests that the landslide movement has happened many

years ago. The time would before the arrival of humans in the area. There is no evidence of recent movement of the landslides.

On July 21, 2012, Beijing is in a complete heavy rainstorms since there have been complete meteorological records. The fossil landslide does not show signs of landslide. However, local collapses have occurred many times, which obstruct the traffic as well as causing a lot of inconvenience to the villagers production and living.

Topographical Features of Landslide

The mountain is steep, with gully topography. The vegetation condition is good. The mountain has an elevation of 371.20 ~ 371.20 m, and the relative elevation is nearly 500 m. The terrain is uneven, general configuration of which is complex. The headwall profile of the landslide looks like a jumping platform, with 3 ~ 4 sections, which is shown in Fig. 2. Each of the platform is tilt inward, with a slope angle of 3 ~ 5°. This landslide shows the reverse slope characteristic, which is the unique feature of landslide. The posterior headwall of the landslide has a slope angle of 60° ~ 80°, and the elevation difference is 40 ~ 50 m. The posterior headwall of the landslide is made up primarily of shrubs weeds and dry land. The central section of the landslide is echelon in longitudinal direction, mainly made up of dry land. There are some villagers adjacent to the foot of the headwall.

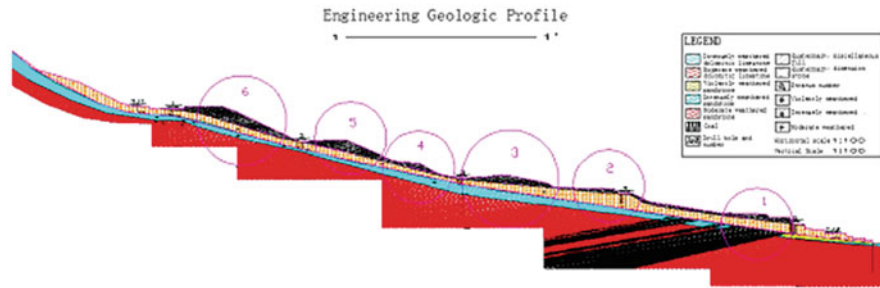


Fig. 2 The profile of the landslide

The Lithology and Structural Characteristics

The source area naturally divides into an upper headwall and a lower pocket. The landslide is covered with quaternary remnants diluvia layer, with the thickness of 0.50 ~ 26.00 m. The upper layer is relatively loose. The strength of the upper layer reduced obviously when encounters water, which forms potential sliding surface between the upper layer and lower layer. The lithology of sandstone is shale, breccia, limestone, and coal measures strata.

This landslide is mainly composed of Quaternary eluvial soil and breakstone. The landslide is sinking in vertical direction, and the front of which is sliding. The Quaternary eluvial soil is relatively thicker. The residual is mainly composite of cohesive soil and stone. The content of stone is about 10 ~ 30 %, with the grain size 10–50 mm.

The Formation Conditions of Landslide

A lot of research shows that the fundamental cause for large-scale landslide in China is due to the topographical and geomorphological conditions. About 80 % of large-scale landslides were found in the first slope-descending zone of the mainland topography around the eastern margin of Tibet plateau. Moreover, this area is the most active area of the plate tectonic activities. The intensive interactions between the endogenic and epigenetic geological process cause serious dynamic change of the high steep slope, which are resulted in the development of large-scale landslides. Strong earthquake, extreme weather conditions and the global climatic change are the main triggering factors of large-scale landslides.

Topography (Liao 2007)

Topography factors provide the space and energy for sliding. Zhaojiatai village belongs to low mountain landscape, with a

steep mountain slope. Topography in this area is fluctuated, the relative dispersion of which is 494 m. The whole slope angle of $30^{\circ} \sim 40^{\circ}$, and the local slope angle is $60^{\circ} \sim 80^{\circ}$. Topography of bottom of the slope is open valley and low-lying land. The open topography provides both sliding energy and well spatial condition for the landslide.

Lithologic Factors (Liu and Tan 2008)

Lithologic factors control range of the sliding body and location of potential sliding surface. This landslide was mainly make up of talus stone, and gravel soil. The loose soil has forms a potential sliding surface for its easy sliding stratum.

The role lithologic factor plays in the formation of landsliding mainly reflects in the following two aspects. First, the talus stone and miscellaneous is loose in this area. The natural state because the built-in function and make the friction force between particles is bigger. When encounters heavy rainfall conditions, miscellaneous reach soft state or plastic flow state which reduce friction effect. Therefore, detritus between the stone and miscellaneous often forms potential sliding surface. The second aspect is inclined structure of the landsliding. Landslide inclined structure exists in the interface within the region from the top to the foot of the mountain the soil rock. The lower layer is rock. The intermediate section is detritus. The loose soil can form a potential sliding surface for its lithologic characteristic.

Geological Condition (Song et al. 1994)

The fossil landslide is located in south of Jiulong mountain. The Kowloon hills extent about 20 km, along the northeast direction. Syncline wings covered by the Jurassic and Upper Paleozoic strata. The southwest mountain ridge is gentle, with a angle of $15^{\circ} \sim 20^{\circ}$. The southwest mountain ridge is steep, has a slope angle of $30^{\circ} \sim 40^{\circ}$.

Table 1 Model parameter

| Parameter | γ (kN/m ³) | | c (kPa) | | φ (degree) | |
|--|-------------------------------|----------------------|-------------------|----------------------|--------------------|----------------------|
| | Present condition | Heavy rain condition | Present condition | Heavy rain condition | Present condition | Heavy rain condition |
| | Layer | | | | | |
| Miscellaneous ① | 19.0 | 20.0 | 2 | 1 | 22.0 | 19.5 |
| Block rock ② | 22.0 | 23.0 | 5 | 3 | 30.0 | 28.0 |
| Silty clay-clayey silt ② ₁ | 19.5 | 20.5 | 20 | 17 | 10.0 | 8.0 |
| Intensely weathered sandstone ④ ₁ | 22.0 | 23.0 | 5 | 3 | 35.0 | 30.0 |

There are three small fault exist in this area. One of the fault is through Zhaojiatai village. Another located to the west of the study area. The third located on the north of the study area. All the three faults are secondary fracture, none of them is Holocene active fault.

Human Activities (Zhang et al. 1994)

Human activity is mostly flat slope cutting slope and road building. The upper slope of local farmers flat slope cutting slope roads, which changed the original stable stress distribution, resulted in the reduction of stability. Farmers cut slope at the front of landslide and slope feet road and building, makes the feet and the front of landslide soil cutting slope of landslide in the front of landslide soil lacks the support or support, however, results in the decrease of the stability of the slope. These human activities make low slope at the steady state, directly threatens the safety of slope with the surrounding residents.

Rainfall (Xu and Shang 2008)

The planning construction area belongs to warm temperate continental monsoon climate. There is a large valley development in the assessment area. It is hot and rainy in summer. Only have water in the rainy season. There is a spring in the northeast of Zhaojiatai village, flow of which is about 5 t/h. There is also a set of pool in the village.

Rainfall is one of the induced factors in the formation of landslide. First, rainfall given rise of underground water in this area, made the dynamic hydrostatic pressure increased. On the other hand, slope caused by the increase of soil bulk density. The landslide surface soil will under pressure in condition of saturation. Third, rain cause the reduction of the cohesion and internal friction angle of rock and soil body, make the stability of rock mass under the lower slopes.

Evaluation the Stability of the Landslide

Qualitative Analysis (Lei 1991)

The landslide belongs to low mountain landscape. The mountain slope is steep at both ends, and the central section is placid. The front of landslide sliding space condition is good, the cutting slope and slope foot excavation of human engineering activities such as strong under the condition of heavy rainfall, soil and rock sliding surface is sensitive to water, and easily to slide when encounter water.

Overall and Local Stability of the Landslide

We use [polygonometry](#) method in globe profile to derive the stability of the landslide, and arc method was performed in derive local stability. Using the principle of geotechnical, slope stability analysis module for section as a whole and partial stability calculation according to two kinds of working condition of natural and storm. The complex soil layer, the standard with general method, seismic fortification intensity of 7°.

Model parameter selection for physical and mechanical parameters of rock mass, the calculation of specific parameters according to the experience of the laboratory test and comprehensive. Model parameter was shown in Table 1, the results stability of profile was shown in Table 2.

The overall and local steps natural state, the landslide sliding surface is in a stable state. Storm conditions, only on the surface of the sliding stability coefficient is 1.08, in the stable state. All the profile and other sliding surface in the stability state. Overall, the landslide from the current situation in general in a stable state, only the steps of the sliding surface in the stable state. As a result, the landslide sliding surface near the location prediction level to assess the risk of landslides as big, other location estimate for the small risk of landslides.

Based on the above analysis of slope and connected by engineering concrete example, a model of landslide is

Table 2 Stability of profile

| Profile | Method | Heavy rain condition | | Present situation | |
|--------------------|--------------------|----------------------|----------------------|-------------------|----------------------|
| | | Safety factor | Stability evaluation | Safety factor | Stability evaluation |
| 1-1' Whole profile | Fold line method | 2.014 | Stability | 2.21 | Stability |
| 1 Sliding surface | Slip circle method | 1.682 | Stability | 1.97 | Stability |
| 2 Sliding surface | Slip circle method | 2.265 | Stability | 4.11 | Stability |
| 3 Sliding surface | Slip circle method | 3.661 | Stability | 4.23 | Stability |
| 4 Sliding surface | Slip circle method | 2.191 | Stability | 2.47 | Stability |
| 5 Sliding surface | Slip circle method | 1.658 | Stability | 1.91 | Stability |
| 6 Sliding surface | Slip circle method | 1.080 | Basically stability | 1.25 | Stability |

established by the analytic means of mathematic statistics. According to this model, the mechanism of instability of shallow landslide under intensive rainfall is revealed. Furthermore, it is revealed also that intensive rainfall is the most decisive triggering factor of the landsliding.

Prevention Measures

The places with low stability safety factor and construction suitability, have a relatively lower construction suitability. We should do a detailed survey before engineering construction.

Second, stage of engineering construction, shall be carried out according to the engineering geological exploration. We should try not to change the original geological environment, and to reduce the steep slope of cut slope of existing scarp area and in the future construction of excavation. Slope stability analysis should be done for the construction of slope supporting system and permanent support. The design scheme of slope stability analysis, slope is in unstable condition, if the design should be taken to secure the retaining wall slope rate or the necessary structure (e.g., retaining wall or anchorage system), to maintain the permanent stability of slope.

Third, in the process of engineering construction, to dismantle the construction waste and excavation, which produced during stacking. choose appropriate position follow both can affect the ecological environment, but not for debris flow provenance principle. The abandoned building garbage wastes should be appropriate handle with.

Control measures should be carried out. The protection of vegetation, in construction process and the bare hillsides to strengthen the greening should be pay attention to. The mountain should not be transformed on a large scale. The slope drainage system should be strength, according to [geological condition](#). build up the intercepting drain, enhance flood debris flow and so on.

Finally, a detailed and systematic monitoring program should be carried out. We should strengthen the geological

disaster monitoring system, and establishment emergency contingency plans.

Discussion and Conclusions

Landslide is significantly hazardous especially on the urban fringe of metropolitan region, because of their possible catastrophic damage on downstream settlements and infrastructures. Some constructional engineering is now on the agenda in these areas. Although there is no geomorphic evidence indicating that this landslide is still active, it has not yet reached the position of minimum potential energy. Hence, it is possible for the landslide to be reactivated under certain conditions. However, the risks of extreme, if rare, hazards from future landsliding events may be seriously underestimated. The ability to identify the occurrence of such events and interpret the consequence is necessary for estimating future risks.

Detailed geotechnical investigations for evaluating the stability of the landslide are carried out in this study with due consideration for future risk.

References

- Lei X-Y (1991) Stability and human activities of landslides in Bailuyuan of Xi'an City. *Geol Rev* 37(3):258-264
- Liao W-D (2007) Analysis of the characteristics of White Hart landslides in Xi'an city and causes. *J Disaster Prev Mitig* 27 (1):80-85
- Liu Y, Tan L (2008) Analysis on forming mechanism and deformation characteristics of shallow bedded rock landslide. *Chin J Undergr Space Eng* 4(6):1052-1055
- Song K-Q, Cui Z-X, Yuan J-G (1994) The creep characteristic analysis and prediction of Guliu slide. *Chin J Geotech Eng* 16(4): 56-64
- Xu J-C, Shang Y-Q (2008) The effect of rainfall shallow debris landslide collapse failure mechanism study. *J Nat Disaster* 17(3): 117-124
- Zhang Z-Y, Huang R-Q, Wang R-S (1994) Study on interaction of human engineering activities and geological environment. South-west transportation university press, Chengdu, pp 150, ISBN: _number_ : 7502812210



Estimation of Direct Landslide Costs in Industrialized Countries: Challenges, Concepts, and Case Study

Martin Klose, Lynn Highland, Bodo Damm, and Birgit Terhorst

Abstract

This paper presents a short summary of the challenges and concepts in previous landslide loss studies and introduces a methodological framework for the estimation of direct landslide costs in industrialized countries. A case study of landslide losses for federal roads in the Lower Saxon Uplands (NW Germany) exemplifies the application of this methodology in a regional setting.

Globally, the costs of landslide damage are proven to be of economic significance, but yet efforts for their systematic estimation are still rare. The evaluation of landslide costs requires the consideration of complex causalities and high spatiotemporal variability. Landslide impacts on economic systems vary as a function of their level of development, and specific methodologies are required for different geographic areas due to the difficulty of comparing widely dissimilar types of economies.

In this approach, landslide costs are spatially extrapolated from sub-regional levels after their calculation in representative case study areas. In the first step, cost survey is closely linked with methods of cost modeling, which in turn take advantage of landslide database information. The cost extrapolation to large-scale levels is realized by a landslide susceptibility model combining cost figures with indices of infrastructure exposure.

Keywords

Direct landslide losses • Cost estimation • Industrialized countries

M. Klose (✉) • B. Damm
ISPA, University of Vechta, Universitätsstr. 5, 49377 Vechta, Germany
e-mail: mklose@ispa.uni-vechta.de; bdamm@ispa.uni-vechta.de

L. Highland
U.S. Geological Survey, Mail Stop 966, Denver Federal Center, Box
25046, Denver, CO 80225, USA
e-mail: highland@usgs.gov

B. Terhorst
Institute of Geography and Geology, University of Würzburg, Am
Hubland, 97074 Würzburg, Germany
e-mail: birgit.terhorst@uni-wuerzburg.de

Introduction

Today's global disaster and landslide hazard databases provide vital information on the large number of landslide catastrophes that probably cause hundreds of millions of dollars in annual losses worldwide (CRED 2013). The total costs of global landslide activity exceed the sum of these single, exceptional landslide disasters, and are rather driven by the thousands of smaller, less dramatic landslide events and insidious landslide losses, which are widespread on the world's rapidly developing hillsides. Despite evidence that landslides burden global society with billions of dollars in damage costs each year (Kjekstad and Highland 2009), there remains a deficit of reliable cost estimates obtained using methods that provide a representative view of the structure and long-term average of landslide costs. This is mainly due

to unique challenges in the study of landslide costs, which relate not only to complexity in landslide occurrence, but also dependency on a variety of cost factors independent of landslide magnitude. Although fundamental understanding of landslide costs is critical to promote disaster resilience and economic well-being of communities worldwide, most current research is about advancing the achievements of early cost studies, especially those in the United States (Schuster 1996).

Many U.S. cost studies focused on the compilation of data sets on landslide costs in specific case study regions during periods of increased landslide activity. Based on cost survey, these studies developed annual reference costs as reference points and extrapolated these cost figures to obtain regional and national cost estimates. Up until now, there has been high priority placed on cost assessment for transportation, especially the U.S. highway system. In recent investigations, cost survey, which typically includes expert interviews and archive studies, is also combined with probabilistic cost modeling and methods of socioeconomic evaluation (Crovelli and Coe 2009). Special emphasis is placed on the development of strategies for retrieving cost data more systematically, because lack of documentation and data transparency is often identified as a major drawback of early U.S. cost studies (Highland 2006).

In Europe, the study of landslide costs has only recently received attention, as is the case in most parts of the world. Thus, globally just a few additional studies are available so far. Recent studies have identified promising concepts, including classification of potential socioeconomic losses and design of cost scenarios (Alimohammadlou et al. 2013; Vranken et al. 2013). The potential of new tools for cost modeling based on landslide databases and disaster response models will improve the applicability of small-scale to large-scale extrapolations (Klose et al. 2012).

The challenges in estimating landslide costs are significant, but improved options in cost survey and cost modeling address these concerns, and have reduced uncertainty. In what follows, a summary of the evolution of landslide loss studies, and a methodological framework for the estimation of landslide costs in industrialized countries is presented.

Challenges and New Options in Landslide Cost Estimation

The Complex Nature of Landslide Costs

A major challenge of systematic cost estimation originates from the nature of landslide occurrence itself. Landslides are often local phenomena with limited areal extension, but show complex distribution in space and time, as do their costs (Fig. 1). In general, there are two extreme patterns of

landslide costs that are identifiable: local clustering that results from a single and large triggering event; and widespread dispersion over periods of time. Typical for the temporal dimension of landslide costs is high cost volatility accompanied by a significant portion of costs that is roughly constant over time. In contrast with most other natural hazards, landslides impact society not only as sudden disasters with large associated costs; they also cause isolated but prolonged damage leading to significant insidious losses. Ironically, such damage receives little attention, making landslides a costly everyday hazard in many areas.

Besides these spatiotemporal factors, cost complexity is influenced by landslide types and processes and methods of disaster response. Most types of landslides result in specific kinds of damage, such as that experienced by transportation-related infrastructure. Usually, their translation into monetary losses is difficult, since they are beyond functional expression through simplified damage-cost-relationships. One important reason is that a major part of damage and avoidance costs depends on the practices of post-disaster mitigation and the state-of-the-art of remediation and prevention. These cost factors are widely controlled by the level of public and individual risk acceptance, and thus the underlying societal conditions. As a result of disparities in technical and adaptive standards, coping with landslides differs throughout the world. This also causes their impacts and costs to vary geographically, specifically as a function of the region's level of economic development.

Supportive Database Systems and GIS Technology

Currently, all approaches of landslide cost estimation benefit from the advancement in database technology and the functionality of tools such as geographical information systems (GIS). The recent progress in digital data organization and archiving extends the pool of usable damage and cost information in online archives or accounting systems and simplifies its storage in scientific databases. Along with improved methods of computerized data inquiry, these tools provide effective data capabilities for cost survey and support data acquisition. Additionally, new geospatial tools and web resources foster landslide news tracking and disaster documentation, which improves the quality of landslide databases used for cost estimation.

Despite advanced information access and data processing, the compilation of accurate cost data is still labor-intensive and time consuming. Consequently, consistent loss records with a high degree of data homogeneity are difficult to compile on regional or national scales. As a result, cost estimations are nearly always fraught with high uncertainty. For example, GIS technology can eliminate the



Fig. 1 Landslides are characterized by a complex distribution in space and time, which makes cost estimation difficult. This photograph shows widespread landslide activity on highly urbanized slopes in southern

California (USA) as result of severe winter storms in December 2004, and January, February, and March 2005 (Photo by J. Godt, USGS)

problems of scale incompatibility that often occur when combining different data sets that occur at different geographical scales, which was a significant drawback before the use of GIS.

Methodological Framework for Estimating Landslide Costs

General Overview

The presented methodology is a two-tier approach with special focus on the estimation of direct landslide costs in industrialized countries. The methodology relies upon a framework to spatially extrapolate landslide costs from sub-regional levels by combining cost figures from representative case study areas with index values of infrastructure exposure at larger, regional levels (Fig. 2).

An effective starting point for cost estimation is a landslide database, such as one of those maintained by our working group (Damm 2013; USGS 2013). The main idea of this approach is to calculate past landslide costs by applying various techniques to broaden and monetize these pre-existing data sets. The key tools to compile cost data on sub-regional levels are cost survey and cost modeling. The goal

is to obtain specific cost figures for exemplary case study areas over a reasonably reliable time period of about 30 years ago to present, which is a time period when landslide inventories and assessments provide the most detailed, comprehensive data.

The focus of the second tier is to approximate landslide costs over broader areas by cost extrapolation. This extrapolation is performed using an infrastructure exposure model derived from landslide susceptibility modeling. The purpose of this model is to identify the area of infrastructure potentially at risk and to enable the development of indices of infrastructure exposure. The assumption behind the concept of cost extrapolation is that identified hazard areas probably experience similar costs per area as comparable areas at risk in various case study regions.

Cost Compilation on Sub-regional Levels

A key aspect of sub-regional cost compilation is cost survey. The ultimate goal is to retrieve first-hand loss data for recent landslides through targeted expert interviews and data mining of accounting and archive systems. Cost survey is of special importance for two reasons: first, it usually provides the best and most reliable cost estimates; and

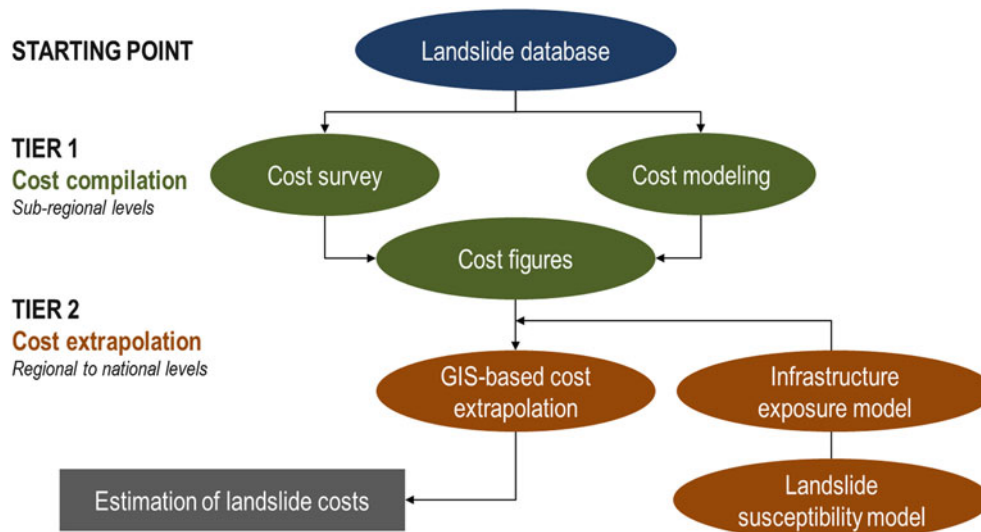


Fig. 2 Methodological framework for landslide cost estimation

second, it is in some cases the only way to obtain data on landslide losses.

The second major tool of cost compilation is cost modeling based on landslide databases (Klose et al. 2012). The objective of cost modeling is to estimate direct landslide costs by using database information on landslide process types and associated damage. The workflow of cost modeling starts with the assignment of a landslide event to a disaster response model. These models are designed to simulate the different steps of cost-relevant mitigation for various land use classes after specific types of landslides. Each disaster response model is a cost chain that provides the costs involved in coping with landslide hazards over the full disaster cycle. The simulated steps of disaster response are first calculated by applying cost modules, which have been previously computed. The function of cost modules is to monetize some of the most common emergency, recovery, and mitigation measures. The cost modules are based on prices listed in construction cost databases or refer to cost proxies from disaster planning and engineering practice. To simplify cost modeling, detailed cost modules are replaced by overall cost categories of the total costs of certain types of landslide damage.

The key economic data for cost extrapolation are cost figures derived from the results of sub-regional cost compilation. The idea of these cost figures is to break down the costs in affected land use classes to their spatial extension. Thus, each cost figure defines the total costs per km or km² of specific types of land use area, which enables cost extrapolation.

Cost Extrapolation to Regional and National Levels

The core focus of cost extrapolation is to continue cost estimation on regional and national levels by applying GIS-based tools to upscale the results of sub-regional cost compilation. Two basic modeling concepts are used in this context: first, a landslide susceptibility model, preferably one with special capability for regional applications (Klose et al. 2014), enables the spatial identification of areas with predisposition to landslides; and second, this model is modified to an infrastructure exposure model that provides the spatial distribution of potentially endangered land use types. The purpose of this infrastructure exposure model is to support the calculation of exposure indices that approximate the spatial extent of the hazard area in each land use class. The data on infrastructure exposure is used to update the cost figures, so that they describe the land use class's costs per area at risk; this is more precise, if differentiated in the levels of landslide susceptibility. Subsequently, cost extrapolation of sectorial or overall landslide costs is performed by simple spatial operations in a GIS application.

Validation of the Cost Estimation on Both Spatial Levels

The validation of the obtained cost estimates is an essential part of this methodology and concerns both cost modeling

and cost extrapolation. A validation system should be used to cross-check the results of cost modeling with reference data from cost survey. Many different techniques are available to evaluate the accuracy and quality of landslide susceptibility models. The concept of the prediction and success rate proves to be most effective for regional applications (Chung and Fabbri 2003; Klose et al. 2014).

Regional Application and Test of the Methodology

Local Costs at Highways: A Case Study in NW Germany

The proposed methodology has been applied to estimate regional landslide costs for federal roads in the Lower Saxon Uplands in NW Germany. The case study area for cost compilation covers about 250 km² and is part of the Upper Weser region, where federal roads either pass through landslide-prone river valleys or traverse large plateaus with widespread areas that are free of any hazard potential. Landslide susceptibility and exposure is derived on the basis of a bivariate statistical modeling concept, known as the Information Value approach for regional applications (Klose et al. 2014). This model predicts that about 15 km of federal roads are located in potential hazard areas. Most of the 33 landslides that had been recorded between 1980 and 2010 caused damage and resulted in costs related to the repair of cut slopes and embankments or hazard mitigation with rock-fall barriers and slope stabilization systems (Fig. 3). In this 31-year period, direct landslide costs were about \$23.5 million (in 2013 values), which corresponds to annual average costs of around \$0.76 million. The annual costs per km of potentially endangered road account for more than \$52,000 on average (Fig. 4).

Regional Costs at Highways: An Estimate for NW Germany

The Lower Saxon Uplands are a mountain area in Central Europe with both key areas and local clusters of landslide hazard exposure to road infrastructures. This test region makes up less than 0.2 % of the EU-28 territory and contains about 3 % of the federal road network in Germany. The regional hazard patterns widely approximate those of the case study area. In total, 77 km of federal roads are built



Fig. 3 Typical landslide damage to federal roads in the Lower Saxon Uplands (NW Germany) that caused repair costs of about \$210,000 (in 2013 values) in the year 2003

on unstable slopes, whereby a major part can be found in deep-cut river valleys of the Harz Mountains. The regional cost extrapolation for federal roads results in an estimate of annual average costs of about \$4.02 million (Fig. 4).

Discussion

The specific problems of estimating landslide costs for trans-regional levels require a special combination of methods and a concept for systematic data fusion. The presented methodological framework is one first step towards an integrated research design for landslide cost estimation in industrialized countries.

A test application of this preliminary toolkit proves its basic capacity to serve as a valuable basis for more elaborate regional or national cost studies in the future. Although it reduces critical dependency to empirical cost data on macro levels, the prerequisite of comprehensive loss records for selected case study regions is seen as major drawback, as their compilation is still a challenging task.

Further research work has to address crucial weak points related to the concept of infrastructure exposure. In its current usage, it simply defines a potential threat for infrastructures located on a probable landslide mass, but ignores hazard exposure in potential pathways of landslide movement. A major economic research question is whether to operate with annual average or median costs, for example, as this decision strongly influences the results of future cost studies.

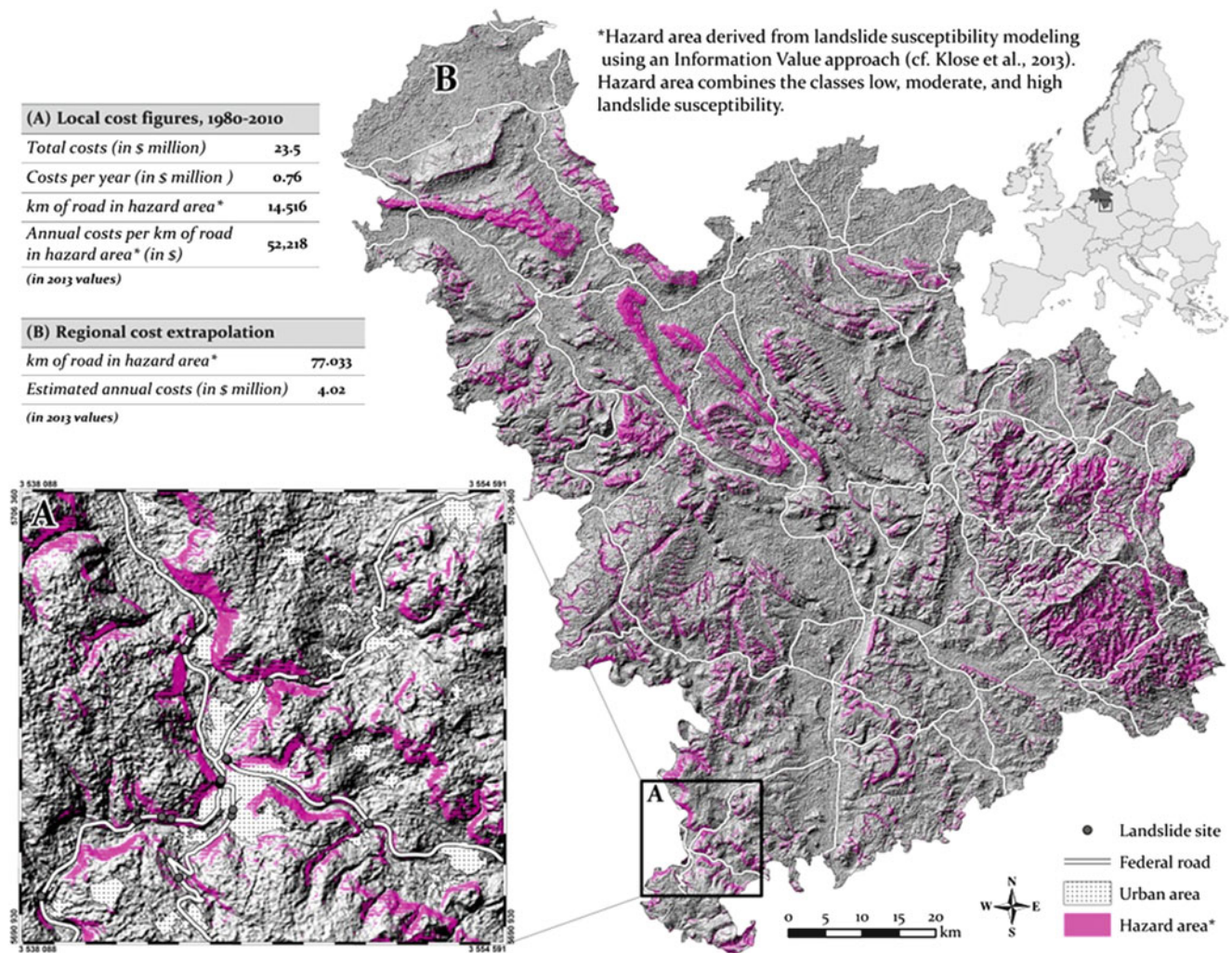


Fig. 4 Cost extrapolation for federal roads in the Lower Saxon Uplands (NW Germany) based on cost compilation for a sub-regional case study area in the Upper Weser region and a regional infrastructure exposure model

Conclusions

The annual costs of global landslide damage probably account for billions of dollars, but yet there is still a lack of concepts and tools for their systematic estimation. This mainly relates to the complex nature of landslide occurrence and cost dependency to highly diverse cost factors. This paper presented a preliminary framework of well-established and newly developed methods that in combination may allow for effective ways to overcome this huge research deficit in future cost evaluations.

References

- Alimohammadlou Y, Najafi A, Yalcin A (2013) Landslide process and impacts: a proposed classification method. *Catena* 104:219–232
- Chung CJF, Fabbri AG (2003) Validation of spatial prediction models for landslide hazard mapping. *Nat Hazards* 30:451–472
- CRED (2013) EM-DAT: the OFDA/CRED International Disaster Database. Université catholique de Louvain, Brussels, Belgium. <http://www.emdat.be>. Last accessed 4 August 2013
- Crovelli RA, Coe JA (2009) Probabilistic estimation of numbers and costs of future landslides in the San Francisco Bay region. *Georisk* 3 (4):206–223
- Damm B (2013) Landslide database for the Federal Republic of Germany, previous version: Database Mass Movements in German Subdued Mountains 1137-2013. August 2013, University of Vechta, Germany
- Highland L (2006) Estimating landslide losses—preliminary results of a seven-state pilot project: U.S. Geological Survey Open-File Report 2006–1032, 11 p
- Kjekstad O, Highland L (2009) Economic and social impacts of landslides. In: Sassa K, Canuti P (eds) *Landslides—disaster risk reduction*. Springer, Berlin, pp 573–587
- Klose M, Damm B, Terhorst B, Schulz N, Gerold G (2012) Economic loss by landslides: development of an empirical calculation model with regional application to German subdued mountains. In: Koboltschnig G, Hübl J, Braun J (eds) *Extended abstracts of the 12th interpraevent congress*, 23–26 April 2012, Grenoble, France, pp 214–215

- Klose M, Gruber D, Damm B, Gerold G (2014) Spatial databases and GIS as tools for regional landslide susceptibility modeling. *Zeitschrift für Geomorphologie* 58:1–36
- Schuster RL (1996) Socioeconomic significance of landslides. In: Turner AK, Schuster RL (eds) *Landslides: investigation and mitigation*. Transportation Research Board Special Report 247. National Academy Press, Washington, DC, pp 12–35
- USGS (2013) Landslide inventory pilot project. <http://landslides.usgs.gov/regional/inventory/>. Last accessed 29 July 2013
- Vranken L, Van Turnhout P, Van Den Eeckhaut M, Vandekerckhove L, Poesen J (2013) Economic valuation of landslide damage in hilly regions: a case study from Flanders, Belgium. *Sci Total Environ* 447:323–336



Estimation of Landslide Impact Disaster by Discrete Element Method: Jiangping Hydropower Station, Hubei, China

S.N. Wang, Chong Shi, Weiya Xu, Yulong Zhang, and Hailong Zhang

Abstract

An evaluation model of landslide risk is established with PFC in order to study the impact effect of landslide on existing buildings in Jiangping hydropower station, Hubei, China. The corresponding numerical parameters of parallel bonding are obtained during the calibration step, in which some biaxial compression tests are carried out. The conversions of energies among body force work, kinetic energy, strain energy, friction work and bond energy during the process of landslide motion are discussed based on the law of conservation of energy. Then the relationships among the impact energy, the geotechnical strength parameters and the outrun distance of landslide are studied. The results show that the calculated impact energy gotten from the proposed landslide model is far less than that gained from the rigid body model. The calculation of the proposed method is on the safe side. The total energy carried by the landslide is originated from the loss of potential energy. The calculated impact force has a less effect on the buildings because the dissipation of the friction energy caused by medium disintegration is neglected in the later. The weaker the degree of the medium cementation is, the greater the proportion of the friction energy dissipation is, and the smaller the corresponding proportion of landslide impact energy is. The landslide impact energy has a linear relation with the bond force between particles, and the maximum landslide impact energy decreases exponentially with the increase of the landslide horizontal movement distance. The simulation also shows that the ratio of the impact energy accounting for the total loss of potential energy in the proposed weak bond model is more than about two times of the sledge model, as well as more than about three times of the strong bond model. The proposed model is closer to the actual landslide motion process, so it has great promise in estimating the hazard of landslide on buildings.

Keywords

Landslide disaster • Impact energy • Dynamics simulation • Discrete element method • Slope engineering • Jiangping hydropower station

Introduction

A landslide is a common geologic disaster. Its essence is a complex dynamic evolution process of geological body. When a landslide occurs, huge mass energy would be released and may cause different degree of impact damage on buildings at the toe of slope. If the impact energy is large enough, the buildings would be destroyed

S.N. Wang • C. Shi (✉) • W. Xu • Y.L. Zhang • H.L. Zhang
Department of Civil Engineering, Hohai University, Nanjing 210098,
China
e-mail: myresort@126.com; scvictory@hhu.edu.cn; wyxu@hhu.edu.cn;
ylz_edu@163.com; sealng@126.com

immediately. Therefore, the quantitative analysis on a landslide is greatly affected by the estimation of the landslide impact energy (Uzielli et al. 2008; Wu et al. 2010).

Generally, the most common method used in calculating the sliding speed of a landslide is the kinetic energy theorem. When a landslide begins to slide, the potential energy will be released to overcome the frictional resistance of the sliding surface and be transformed into kinetic energy of the landslide at the same time. According to the kinetic energy theorem, the work of external force on the landslide is equal to the change of the landslide kinetic energy. So the velocity of the landslide can be calculated easily. Prediction and estimation about the velocity of a landslide (Scheidegger 1973) were firstly proposed according to the law of conservation of energy, in which the velocity of a landslide was deduced according to the transform principles between the kinetic energy and the potential energy. Subsequently, Hunter and Fell (2003) divided the landslide into an impact body and an afflicted body, and a 2D rigid body model of landslide was established to analyze the landslide impact effect. Then the judgment about the accumulation effect of impact force over some impact time, as a main criteria, was also proposed to evaluate whether buildings were destructed or not (Zhang et al. 2006; Huang et al. 2009).

A landslide will slow down gradually at the later stage of sliding, and would stop at a certain distance from the slope toe owing to the larger frictional resistance. It shows that the landslide has an obvious spatial effect. The most famous model used in prediction of sliding distance is the sledge model (Sassa 1985; Zhang 2011). It supposes that all energy losing in the sliding process is caused by the friction of bottom sliding surface. If the landslide body is regarded as rigid body, the height deviation and the horizontal movement distance of the landslide taking place before and after are known, then the potential loss of the landslide should be the energy loss caused by the friction work (Zhang et al. 2009; Chen et al. 2010). However, though the kinetic energy theorem is relatively suitable for analyzing a linearity sliding surface, if the doing work of the surface friction resistance are only considered the method will lead to a large error for a non-linear sliding surface in the calculation of landslide impact energy, especially when the sliding surface is curved, there will be some fracture and slaking phenomena involved along the surface of landslide (Pan 1980). What's more, the calculation result based on the kinetic energy theorem is an average velocity of the entire landslide body, so it cannot reflect the dynamic changes of velocity in the sliding process. Some related landslide tests have shown that the integrity of a landslide body has a great influence on the magnitude of impact energy (Kaynia et al. 2008). If the landslide body is pulverized completely in the sliding process, the landslide impact energy will greatly decrease; on the contrary, if the integrity of the landslide

body is well, the landslide impact energy will be extremely obvious.

Actually, the energy loss of landslide is not only caused by the friction resistance of sliding surface but also related to some internal factors, such as collision, slaking and rolling friction. Therefore, it is too difficult to give an accurate assessment of landslide hazard by the simplified analysis based on the kinetic energy theorem. In this work, in order to consider the influence of the landslide slaking on the magnitude of impact energy, the interaction of grains is allowed to make a completely inelastic collision, and an evaluation model of landslide risk is established with PFC in order to analyze the landslide impact energy on the possible afflicted body. Then the landslides under different horizontal movement distance and geotechnical strength parameters are discussed to evaluate the landslide risk.

Engineering Situation

The workshop of Jiangping hydropower station in Hubei, China, is located on the riverbed's left side of downstream, which belongs to the first terrace between the excavation boundaries of dam site and No. 15 gully. The catchment area controlled by the dam site is 2,140 km², the designed operating impounded level is 470.0 m, the total installed capacity is 450 MW, and the rated head is 153.0 m. It belongs to the lager project (I) according to the classification and design safety standard of hydropower project in China.

The slope gradient above 350 m in elevation is 65–75°, and below 350 m is 20–30°. The medium above 300 m in elevation are residul, travertine cementation sediment and a small mount of landslide deposits about 5–15 m in thickness. The layer below 300 m in elevation is riverbed overburden, which thickness is 20–24 m and can also be divided into two layers. The upper part is modern fluvial deposits. It is composed of sand gravel, crushed stone, rubble and little sand soil, and the thickness of them is 4–5 m. The lower part is sedimentary facie of barrier lake, which is composed of humus brown-gray gravel, siltstone and fine sand, and the thickness of them is about 14–19 m. The cue depth of No. 15 gully is 10–15 m, which is developed and close to the ground workshop. The flow of water is 0–5 L/s in dry season while 50–100 L/s in flood season. The thickness of collapsed accumulation layer in the gully outlet is 3–15 m. In the gully bottom above 315 m in elevation, there are exposed siltstone bedrocks. And on the both sides of the gully, there are residul, travertine cementation sediment about 3–15 m in thickness.

The layer above 360 m in elevation is thick-layer limestone. While below 300 m in elevation is siltstone and slate. In this segement of slope, faults develop well and dissect the scarps of the upper bedrock in large angle. The trend of some

Fig. 1 Potential landslide volume and sliding surface

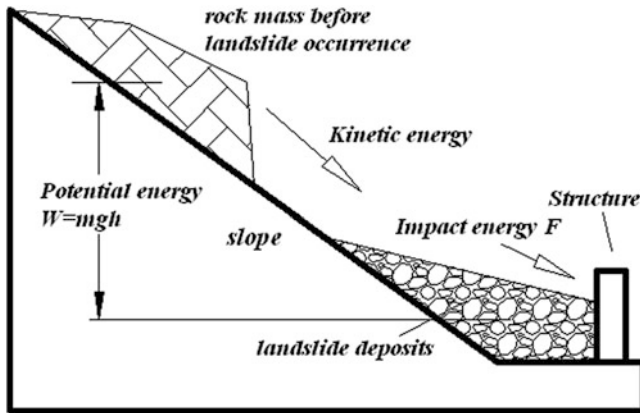
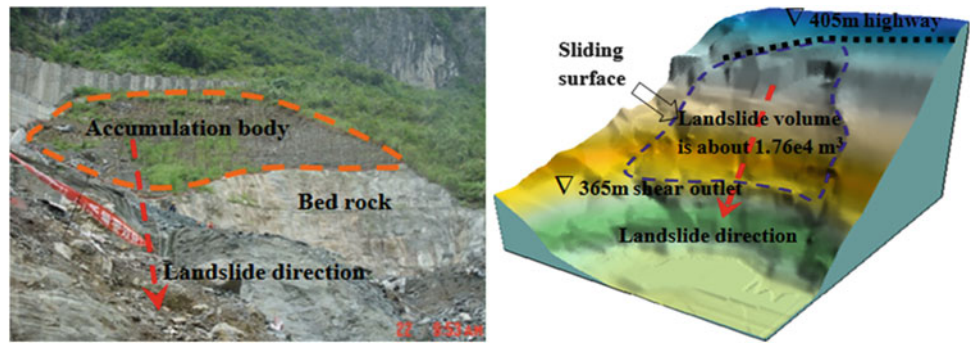


Fig. 2 The conceptual model of landslide

faults are even coincident with that of the slope. The geological analysis indicates that there is only the faults combining with each other or the layer surface but no deep blocks with low stability formed. The in situ survey shows that the blocks with bad stability, the loose bodies and the wing body formed by joint combination develop well in superficial layer. The rock mass is weaker and have been broken seriously about 10–20 m in depth. Once the slope is disturbed by the external factors such as rainfall, excavation and earthquake, it may offer greater potential for a landslide, as shown in Fig. 1. And because the sliding direction of the landslide points at the workshop, when the landslide arrives at the toe of the slope, it may threaten the safety of the workshop. Therefore, determine how to estimate the landslide risk under unfavourable load reasonably is very necessary for the treatment of the slope and the precaution of landslide impact disaster on the workshop.

Damage Assessment of a Landslide

The landslide is the result of combined action of landslide body and buildings as shown in Fig. 2. There are great differences in disaster results for the same landslide due to different locations and types of the buildings. Thus, it is far

from enough to only analyze the stability of the landslide body in a disaster loss assessment, the degree of impact damage for the buildings caused by a landslide should be also taken into account. In general, it is believed that the influence of landslide impact energy on the buildings is mainly controlled by the frictional coefficient of sliding surface, the internal bond strength of landslide oneself and the distribution of buildings.

However, though the loss of gravitational potential energy will overcome the frictional resistance converting into kinetic energy, the impact energy will be gradually transformed into the strain energy of the buildings in the sliding process and the strain energy of the buildings will be dissipated by degrees due to the unrecoverable plastic deformation as shown in Fig. 3. Those dissipations may lead to both the collapse and damage of the buildings. The damage of the buildings with varied anti-impact strength will also be different.

At present, it still little uses the transient impact force in the field of landslide dynamic mechanics as a standard to judge whether a building is destroyed or not but adopts the impact energy to evaluate the security of the buildings.

If the maximum landslide impact energy on a building is regarded as the safety indicator to evaluate the security of the afflicted body, the main landslide disaster cause for the building is supposed as the horizontal impact damage, the horizontal displacement of the building is neglected, then the numerical anti-impact energy of the building in good condition of rigid constraints is just the definite integration of impact force changing from 0 to U_{max} (U_{max} is the maximum deformation of the building).

If the landslide movement is divided into the sliding stage and the impact stage, the kinetic energy will increase with the loss of potential energy in the first stage while the sliding speed will decrease gradually for the properties of landslide oneself and barriers in the later stage. The transforming relationship of the landslide energy can be expressed according to the law of conservation of energy as follows:

$$W_I = W_A - W_{f1} - W_{f2} - W_{f3} \quad (1)$$

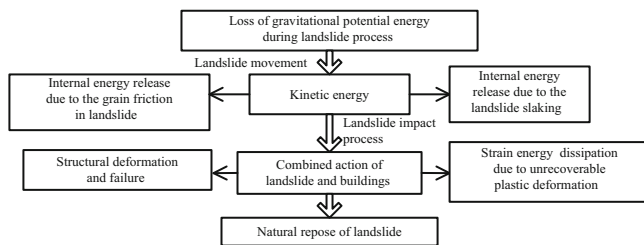


Fig. 3 Energy conversion sketch of landslide

Where W_I is the dissipation of landslide impact energy on the building (J); W_A is the landslide gravitational potential energy at the initial position (J); W_{f1} is the dissipation of friction energy on the sliding surface in the landslide movement process (J); W_{f2} is the dissipation of internal energy in the sliding stage; W_{f3} is the dissipation of internal energy in the impact stage (J).

Generally, the dissipations of the friction energy W_{f1} and the internal energy W_{f2} are neglected in the rigid energy analysis. However, those energies occupy a great proportion in the actual loss of the potential energy. The deviations of calculated energy may be very large compared with the actual situation, and the landslide hazard would also be difficult to be assessed reasonably. Therefore, determining how to take those energy losses into account is the key problem to solve such problems. The discrete element method just has advantages in solving those issues since large deformation can be simulated.

If a landslide is regarded as an union that is composed of thousands of small blocks, then the accumulated effect of impact force is equal to the reduction of landslide momentum under the impact force according to the momentum theorem.

$$\sum m_i v'_i = \int_{t_1}^{t_2} F(t) dt \quad (2)$$

Where m is the mass of the landslide body in unit width (m/s); v' is the impact speed (m/s); t_1 and t_2 are the beginning and ending time of the landslide impact (s); $F(t)$ is the impact force of unit thickness (N s).

If the landslide body is just little broken and regarded as a consistent in deformation, then the reduction of kinetic energy can just be deemed to the impact energy approximately.

$$W'_I = (\sum m_i v_i'^2) / 2 \approx \left(\int_{t_1}^{t_2} F(t) dt \right)^2 / (2 \sum m_i) \quad (3)$$

Actually, the kinematic velocity of each part is inconsistent after the landslide body is slaked, and there may be a certain error in formula (3) when the impact energy is estimated.

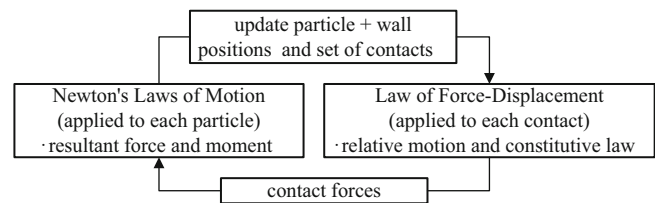


Fig. 4 Calculation principle in PFC2D (Itasca Consulting Group 2004)

Numerical Simulation of the Landslide

Numerical Simulation Concept

PFC2D (Two Dimension Particle Flow code) provides a powerful and useful tool for studying meso-mechanical behaviors of granular materials (Itasca Consulting Group 2004). A discrete element method is used to simulate structural problems and interactions of arbitrary shape blocks, which are made up of connected particles. The local simulation results are expected to study boundary value problem of continuity constitutive calculation. The response of material mechanics can be mapped from the physical domain to the mathematical domain. In PFC, the contact forces and positions of particles are continuously updated by explicit finite difference method, the law of force-displacement and Newton's law of motion are applied alternatively in order to simulate the motion and interaction of particle medium, as shown in Fig. 4.

All physical mechanical behaviors of granular materials can be simulated through their contact constitutive relations in PFC. The contact stiffness model at every contact position is made of three parts, including the contact stiffness model, the sliding model and the bonding model.

1. Contact Stiffness Model

When particles are in a relatively balanced state, the contact force of each particle is a constant. The contact force between particles has a proportional relation with the overlap region and average stiffness of particles.

$$\begin{cases} F_i^n = K^n U^n n_i \\ \Delta F_i^s = k^s \Delta U_i^s \end{cases} \quad (4)$$

Where F_i^n is the normal contact force (N); K_n is the normal secant contact stiffness that describes the relationship between the total normal stress and the total normal displacement (Pa); U_n is the total normal displacement (m); n_i is the unit normal vector; ΔF_i^s is the shear stress increment (N); k_s is the shear stiffness that describes the relationship between the increments of shear stress and shear displacement (Pa); ΔU_i^s is the shear displacement increment (m).

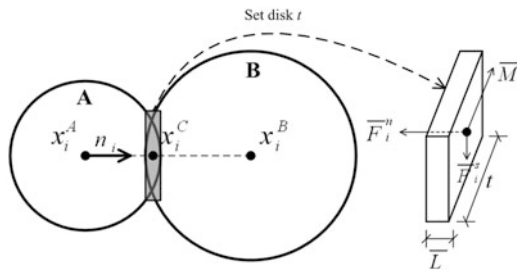


Fig. 5 The parallel bond contact

2. Sliding Model

The sliding model is an inherent feature of inter-contacting entities. If a relative displacement occurs between two particles, the relationship between tangential contact force and normal contact force can be represented by the sliding model. The contacts between particles are inspected through checking the maximum allowable shearing stress. If $F_i^s > \mu F_i^n$ (μ is the sliding friction coefficient), a sliding movement will be allowed.

3. Bond Model

In this study, the contact bond model is used for soil mass to denote its loose feature while the parallel bond model is used for rock mass to limit the total of normal stress and shear stress at contact positions since it can bear both force and torque at the same moment as shown in the Fig. 5. The contact bond only affects a small area around contact point. The parallel bond works within a limited range of circular section among particles.

In Fig. 5, x_i^A denotes the center position of particle A (m); x_i^B denotes the center position of particle B (m); x_i^C denotes the center position of contact (m); F_i^n denotes the i th normal contact force (N); F_i^s denotes the i th tangential contact force (N); \bar{M} denotes the i th torque (N s); \bar{L} denotes the overlapping between particles and t is the thickness of disks (m).

Because the landslide impact force is related to its meso-mechanical parameters in the landslide process, the contact type and the meso-structure parameters of the model should be determined through a numerical calibration prior based on the strength parameters of a landslide’s rock and soil mass stemming from a conventional laboratory test. And once the basic meso-mechanical parameters are determined, the landslide impact disaster can be simulated.

Numerical Modelling of the Landslide

The landslide will be simulated to estimate the landslide impact disaster by the energy statistic program, in which a PFC model will be established by PFC with different particle

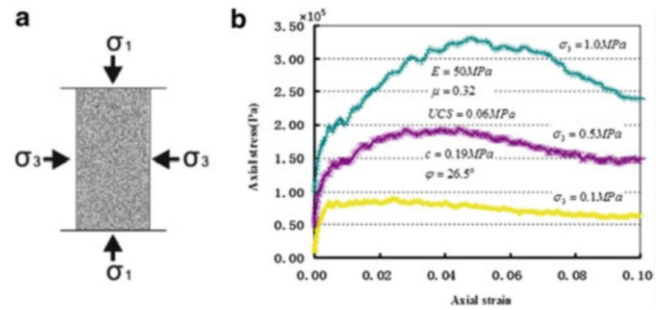


Fig. 6 Calibration of landslide parameters

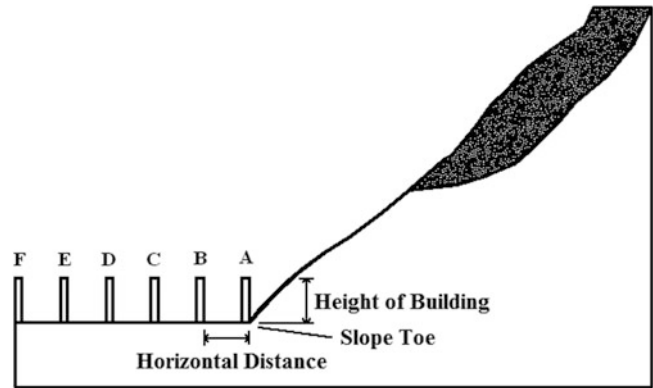


Fig. 7 Impact model of landslide energy

size. However, there is still no theoretical formula for transforming the meso parameters into the corresponding macro parameters directly because the macro mechanical characters of material are determined by the properties of material itself. So a series of biaxial tests should be carried out to calibrate the macro-mechanical characteristics of rock and soil mass. The optimization method should also be adopted to select the closest meso parameters matching with the results of the macro-test as the media parameters of micro-mechanical characters of landslide. In this work, the elastic modulus of material is 0.05 GPa and the corresponding Poisson’s ratio is 0.32. All bond particles with the radius from 0.1 m to 0.3 m are generated randomly in the range of 5 m × 10 m using circular disks as shown in Fig. 6a. The lateral pressures are applied, including 0.0 MPa, 0.1 MPa, 0.5 MPa and 1.0 MPa. For the rock mass, the parallel bond radius multiplier pb_rad is 0.8, and the bonding strength is pb_n = pb_s = 1e5 N. Then the stress–strain curve is obtained by the calibration tests as shown in Fig. 6b.

The energy impact model of the landslide matching with the actual engineering are established with different horizontal outrun distance as shown in Fig. 7. The models uses the same particle composition with the biaxial compression experiment. It is made up of 4,364 particles, the random radius of which lies between 0.1–0.3 m. The porosity of the model is 0.15 and the model area of the landslide body is

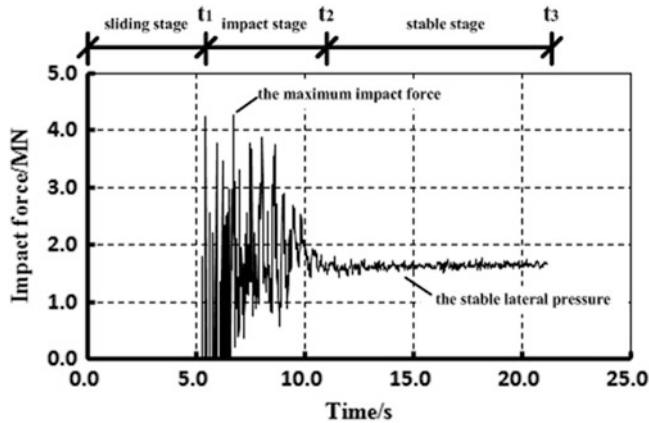


Fig. 8 Typical load curve under impact effect

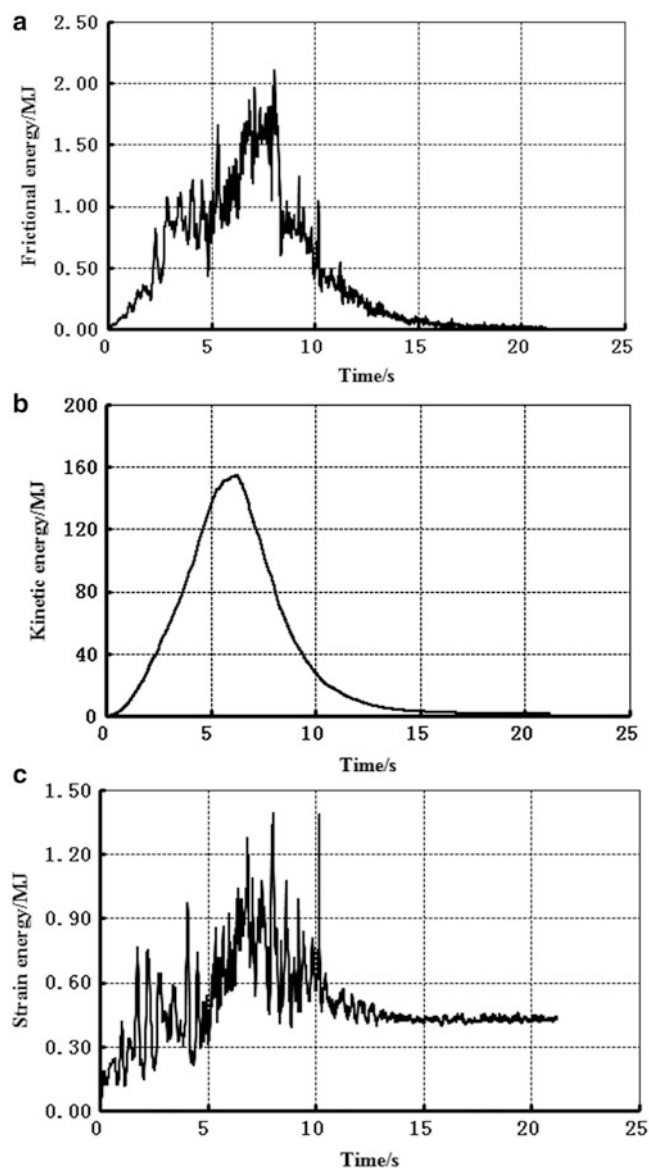


Fig. 9 Energy transform during sliding process. (a) Frictional energy, (b) kinetic energy, (c) strain energy

646 m². The rigid blocks modeled by walls as the buildings are set at the different horizontal disaster from the slope toe in order to analyze the changes of impact energy.

Typical Impact Curve of the Landslide

There are three situations taken into consideration based on the normal and tangential cohesion between particles: a. weak bond strength $pb_n = pb_s = 1e5 N$, b. moderate bond strength $pb_n = pb_s = 1e6 N$, c. strong bond strength $pb_n = pb_s = 1e7 N$. The value of damp is set to zero. The typical impact curve of the landslide is shown in Fig. 8. The whole landslide process can be divide into three stage: free sliding stage (0, t_1), fluctuating impact stage (t_1 , t_2) and stable stage (t_2 , t_3). During the first stage the landslide begins to slide under the action of gravity or external force and is slaked owing to the damage of cementation among particles. When the landslide arrives at the limited position it has an impact on the buildings. The maximum impact force on the buildings occurs in the impact stage. When the landslide is hindered, the former geomaterials will be squeezed by the later, and the impact energy will increase the decrease of the kinetic energy. If the landslide impact cannot cause a building damage, the landslide will accumulate in the front of obstacles. But if the landslide impact can cause the building damage, the obstacles will be damaged in the increasing stage of impact energy and the landslide will even pass over the obstacles at a higher sliding speed. When the landslide is in the last stage, the impact energy will be converted into the lateral pressure gradually. But if the failure occurs in this stage, the static lateral pressure must be the culprits.

However, the total motion energy mainly comes from the loss of potential energy in the sliding process. If the strength of medium is weaker, the frictional energy will account for a large proportion in the loss of potential energy. The larger the proportion is, the smaller the corresponding impact energy is. The transformation of different energies during the sliding process is shown in Fig. 9 comparing with the values before the landslide slides. Both the frictional energy and the kinetic energy present the changes of “firstly increase then decrease”, which is in accordance with the status of the landslide. That the final strain energy is not equal to zero is just for the reason of the accumulation by gravity. Table 1 is the calculated impact energy of unit width under different control parameters.

It is easily to find that the impact energy on the buildings located at slope toe is the biggest. The impact energy reduces exponentially with the increase of sliding distance as shown in Fig. 10. When the landslide reaches the slope toe, it will decrease gradually in the stage when the landslide moves in the horizontal. Therefore, the damage risk of the buildings can be decrease effectively by a reasonable distance. What’s

Table 1 Calculation results of impact energy of unit width under different parameters

| No. | Distance from the slope toe/m | Bonding degree of landslide | Friction coefficient of sliding surface | Potential energy loss/MJ | Strain energy/MJ | Maximum kinetic energy/MJ | Fraction energy/MJ | Impact energy/MJ | Impact energy/potential energy loss |
|-----|-------------------------------|-----------------------------|---|--------------------------|------------------|---------------------------|--------------------|------------------|-------------------------------------|
| 1 | 10 | Weak | 0.5 | 520 | 3.15 | 141 | 493 | 222.16 | 0.427 |
| 2 | 20 | Weak | 0.5 | 553 | 2.01 | 147 | 542 | 94.6 | 0.153 |
| 3 | 30 | Weak | 0.5 | 586 | 1.39 | 154 | 579 | 46.55 | 0.079 |
| 4 | 40 | Weak | 0.5 | 593 | 1.22 | 155 | 584 | 21.3 | 0.036 |
| 5 | 50 | Weak | 0.5 | 626 | 1.17 | 158 | 619 | 14.69 | 0.023 |
| 6 | 30 | Weak | 0.2 | 594 | 1.99 | 199 | 565 | 60.99 | 0.103 |
| 7 | 30 | Moderate | 0.2 | 612 | 1.48 | 217 | 597 | 82.98 | 0.136 |
| 8 | 30 | Moderate | 0.5 | 610 | 1.47 | 158 | 578 | 46.55 | 0.076 |
| 9 | 30 | Moderate | 1.0 | 608 | 1.28 | 133 | 556 | 19.88 | 0.033 |
| 10 | 30 | Moderate | 2.0 | 613 | 1.56 | 141 | 544 | 11.23 | 0.018 |
| 11 | 30 | Moderate | 3.0 | 616 | 1.58 | 145 | 528 | 4.91 | 0.008 |
| 12 | 30 | Strong | 0.2 | 596 | 1.95 | 206.3 | 594 | 89.47 | 0.150 |

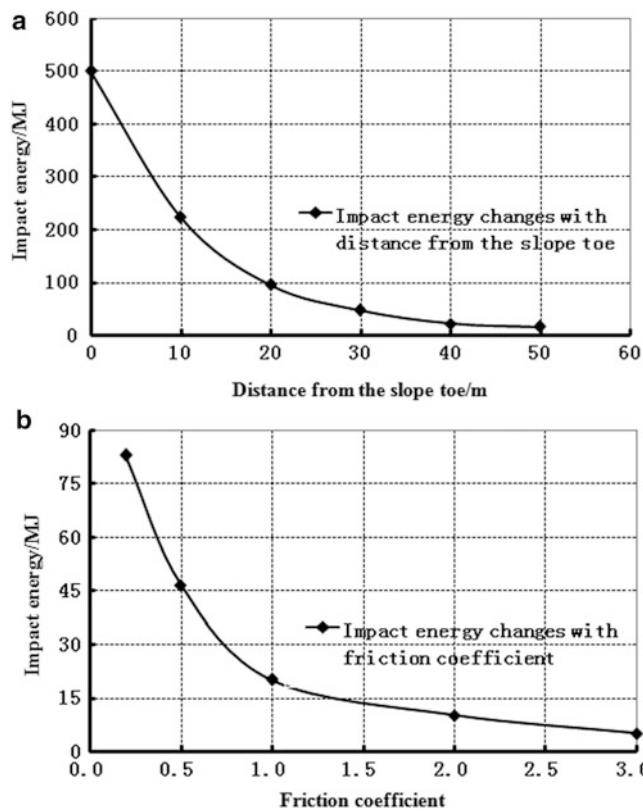


Fig. 10 Attenuation relationships of impact energy to structures caused by landslide

more, for the medium bonds together before sliding, the landslide has a certain strain energy. When the landslide is in initial sliding state, those strain energy will be released, which is just the reason for why the loss of potential energy is less than the sum of other energies. When the bonds are destroyed gradually because of the squeezing between particles the total strain energy will be increased. And because the proportion of strain energy accounts for the

loss of potential energy less than 1 %, this kind of energy can be neglected in energy calculation.

It is obviously that the geometric characteristics of the landslide body are important factors, which will lead to a great differences in the impact energies under different practical projects. If the collisions between the landslide and the buildings are completely inelastic, then the impact energy with different rock parameters and horizontal distance will also be different. If the bond of the landslide is strong, the dissipation of friction energy between particles will be little, the proportion of impact energy transformed from kinetic energy will be high, and thus the impact energy at slope toe will have an extremely high value and strong destruction.

In this work, the time when the actual impact energy is equal to the 5 % of kinetic energy across the slope toe is taken as the ending time of simulation.

Research on the Impact Damage

The Effect of Landslide Medium Strength on Impact Energy

If the deformation parameters of geotechnical parameters are constant, the normal and tangential cohesion changes proportionately, the law of landslide impact energy can be obtained as shown in Fig. 11, in which the degree of bond is moderate and the friction coefficient is 0.2, being taken as the standard of zero. It shows that when the cohesion between particles changes the landslide impact energy has an approximate linear change accordingly, which just indicates that the bond strength of landslide has an important influence on impact force.

The landslide impact energy of No. 12 with strong bond strength is 5 % less than that of No. 6 with weak bond

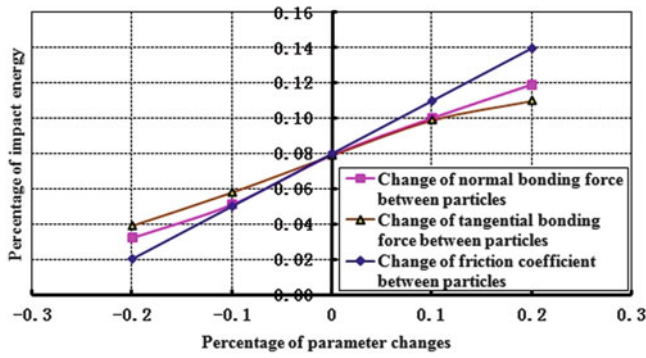


Fig. 11 Impact energy under different increment of meso-parameters (Position B as shown in Fig. 7)

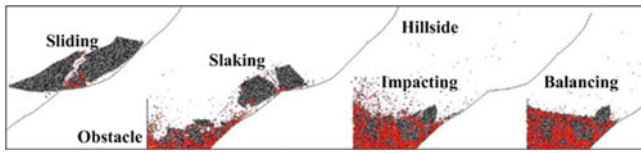


Fig. 12 Impact process for landslide

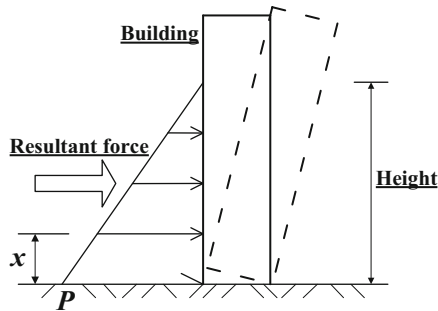


Fig. 13 Simplified impact damage model

strength as shown in Table 1. It shows that even if the landslide has a strong strength, it still will make a lot of internal energy dissipation and be crushed at the slope toe as shown in Fig. 12. The bigger the red region is, the more the damage of cementations is. It will cause a rapidly drop in impact energy over a certain sliding distance. However, because the landslide with weak bond strength is fragmented by nature, the internal energy dissipation caused by collision with the ground is lower in the slope toe so the proportion of the potential energy transformed into the impact energy is higher. If the buildings are just located at the slope toe, the landslide impact is more obvious for the stage of dissipation lack of internal energy. Thus, a certain buffering distance should be reserved to decrease the impact risk of landslide which has a potential sliding hazard.

Research on Judgment Method of Structure Damage

The impact energy resistance of the afflicted body with good conditions can be denoted as Q_{\max} to reflect the anti-disaster ability of the buildings. And because the rigidity of common structure is large, the elastic deformation stage is far short than its plastic deformation stage, so all deformation stages of the afflicted structures can be regarded as the plastic deformation stages. The impact energy resistance of the afflicted body can be defined as $q = Q_{\max} - W_I$ according to the law of conservation of energy.

The coefficient of damage degree can also be defined as follows:

$$\eta = \begin{cases} W_I/Q_{\max} & W_I \leq Q_{\max} \\ 1 & W_I > Q_{\max} \end{cases} \quad (5)$$

The (5) is a vulnerability quantitative evaluation model of an afflicted body in landslide. The landslide impact curve can be obtained by numerical simulation with granular discrete element method, the impact energy resistance can be calculated by the finite element method, and then both of which can identify specific deformation damage state of the afflicted body. The risk assessment for the landslide impact disaster can be realized by making connections between the damage coefficients and the specific deformation of features.

Because the damage due to the landslide on simple affected block begins from one side of the building, the landslide impact on the building can be simplified as a cantilever that bears the horizontal resultant force as shown in Fig. 13.

The bending energy of the structure under horizontal impact force can be expressed as follows (He et al. 2009).

$$Q_{\max} = \frac{P^2 x^3}{6EI} \quad (6)$$

Where P is the maximum horizontal impact force of inverse triangle load, which has an effect on the side of the building (N); EI is the impact-resistance stiffness of the building. The lateral bending stiffness of structures EI is taken as $EI = 11PH^4/(120u_0)$, u_0 is the roof displacement (m), H is the building height (m).

After the impact and bending energy are obtained (5) can be used to distinguish state of the structure under a landslide impact. For the slope of Jiangping hydropower station, the building is brick structure located at about 30 m far from the slope toe where once a landslide occurs it may have an impact on the buildings. According to the in situ investigation, the wall is built of MU10 sintered brick and MU7.5 cements mixing mortar, thickness of 240 mm. As general

Table 2 Calculation of impact energy of unit width under different method

| Method | Distance to slope toe/m | Bonding degree of landslide | Friction coefficient of sliding surface | Potential energy loss/MJ | Strain energy/MJ | Maximum kinetic energy/MJ | Friction energy/MJ | Impact energy/MJ | Impact energy/potential energy loss |
|--------------------|-------------------------|-----------------------------|---|--------------------------|------------------|---------------------------|--------------------|------------------|-------------------------------------|
| The proposed model | 30 | Weak | 0.2 | 594 | 1.99 | 198.6 | 565 | 60.99 | 0.103 |
| | 30 | Strong | 0.2 | 596 | 1.95 | 206.3 | 594 | 89.47 | 0.150 |
| Sledge model | 30 | / | 0.2 | 596 | / | / | / | 268.2 | 0.453 |

masonry structure takes on greater brittle, it can be regarded as failure when the afflicted buildings do not meet the design requirements, Q_{\max} is determined as 8.46 MJ according to corresponding designed parameters. All impact energies of above case exceed the threshold, so it will be very dangerous once the landslide sliding occurs. Some measure must be done to improve the stability to avoid sliding.

Impact Energy Comparison with Different Method

According to the Table 2, for the same landslide, the sledge model with the rigid body hypothesis transforms 45.3 % of the total inertia energy loss into the impact energy, while the proposed model using PFC transforms more than about two times of the impact energy of the sledge model, as well as more than about three times in the state of strong bond. It also shows that more than about 30 % of total energy is dissipated in the internal friction work.

The landslide impact will be largely exaggerated because the internal friction work is classified to the kinetic energy, which makes the building more dangerous. With a granular discrete element method, several energy are easily distinguished and tracked, the results will be more close to reality if the parameters of rock and soil is accurate.

Discussions

A landslide impact is a geological disaster triggered by earthquake or rainfall. The stability of landslide is of concern to the government and engineers. Therefore, the dynamic process analysis for the formation of the landslide impact is very important in planning the mitigation measures. In order to understand the landslide impact disaster, the numerical simulation methods are a helpful way since it can not only simulate the large deformation but also monitor and record the the formation process of the landslide. To date, the numerical simulation for the formation of the landslide can be achieved through two steps: slope failure and energy statistic. Establishing a dynamic analysis model to simulate the whole landslide movement would be very helpful to

estimate the impact on the buildings. But there are two key issues for researchers and engineers taken into account for the numerical simulation of landslide impact disaster: the mechanism of landslide and the mechanical parameters of rock and soil mass. Both of them are the prior conditions of calculation.

In this work, the landslide is regarded as a process of energy releasing, in which the meso mechanical parameters is cablicated with biaxial compression tests to meet the actual macro mechanical behaviour. The langslide impact energy is measured to estimate the damage of the buildings. Through the results of numerical simulation, it is found that the impact energy is connected with both the friction coefficient of sliding surface and the strength of landslide itself, and the landslide impact energy which makes the buildings damaged is approximately equal to the difference between the loss of potential energy and the increase of dissipated internal energy. The impact energy after considering the geotechnical medium can be disintegrated in sliding process is far less than that of rigid body model, since the friction energy dissipation caused by broken medium is neglected in the latter.

There are five mian kinds of energies transformed in the sliding process. The loss of potential energy is the origination of the total energy of landslide. If the bonding degree of the landslide is weaker and the frictional energy is larger, the impact energy will be smaller. On the contrary, if the integrity of the landslide is better, the impact energy will be larger. The impact energy of the landslide has a linear relation with the adhesive force between particles, and decreases rapidly because of the collision with ground at the slope toe. Meanwhile, since the maximum impact energy of the landslide decreases exponentially with the increase of landslide horizontal outrun distance, the damage risk of the landslide on buildings can be reduce effectively through setting a reasonable safety distance. The geometric characteristic of the landslide also plays an important role in the influence factor of impact energy. Therefore, the dissipated internal energy of the landslide in a granular discrete element model can be considered of with less exaggeration, compared with the rigid body model, and the impact energy should be more close to the practical engineering than the conventional method.

Conclusions

A landslide impact energy analysis model of the Jiangping hydropower station's slope in Hubei, China is established by PFC to evaluate the landslide impact disaster on the buildings. The energy changes of landslide is tracked, the reasonable impact curve is obtained, and the transformation of various energies is studied. The results show that the landslide process is influenced by the bond strength and the residual friction coefficient of the landslide on itself. The disintegration of rock and soil mass is influenced by the assumed bond strength seriously while the landslide run-out distance and speed are mainly influenced by the assumed residual friction coefficient. Moreover, the computational results also indicate that the proposed method using a granular discrete element method is more close to reality if the parameters of rock and soil is accurate.

Acknowledgements The work is supported financially by the National Natural Science Foundation of China (51309089), the Project (2011CB013504) support by the National Basic Research Program of China (973 Program), and the National Key Technology R&D Program (2013BAB06B00).

References

- Chen HK, Tang HM, Xian XF et al (2010) Experimental model of debris flow impact features. *J Chong Univ* 33(5):114–119 (in Chinese)
- He SM, Wu Y, Shen J (2009) Simplified calculation of impact force of massive stone in debris flow. *J Nat Disast* 18(5):52–56 (in Chinese)
- Huang RQ, Wang YS, Dong XJ (2009) The 6th August 2009 field urgent investigation on the geo-hazard of the rock fall damming in Houziyan, Shunhe, Hanyuan, Sichuan. *J Eng Geol* 17(4):445–448 (in Chinese)
- Hunter G, Fell R (2003) Travel distance angle for “rapid” landslides in constructed and natural soil slopes. *Can Geotech J* 40(6):1123–1141
- Itasca Consulting Group (2004) PFC2D (particle flow code in 2 dimensions) (Version 3.1). Itasca Consulting Group, Inc., Minneapolis
- Kaynia AM, Parathoma KM, Neuhauser B et al (2008) Probabilistic assessment of vulnerability to landslide: application to the village of Lichtenstein, Baden-Württemberg, Germany. *Eng Geol* 101(1/2):33–48
- Pan JZ (1980) Building stability against sliding and analysis of landslide. China Waterpower Press, Beijing, 238p. ISBN: 15047-4020 (in Chinese)
- Sassa K (1985) Geotechnical classification of landslides. In: Proceeding of 4th international conference and field workshop on landslides. Balkema AA., Rotterdam, pp 31–40
- Scheidegger AE (1973) On the prediction of the reach and velocity of catastrophic landslides. *Rock Mech* 5(4):231–236
- Uzielli M, Nadim F, Lacasse S et al (2008) A conceptual framework for quantitative estimation of physical vulnerability to landslides. *Eng Geol* 102(3/4):251–256
- Wu Y, Liu DS, Lu X, Song QH (2010) A quantitative assessment model for property risk caused by single landslide. *Rock Soil Mech* 31(2):342–348 (in Chinese)
- Zhang KL (2011) Study on the kinematical model and its application for landslide movement. Chang’an University, Xi’an, China (in Chinese)
- Zhang Y, Wei FQ, Jia SW et al (2006) Experimental research of unreinforced masonry wall under dynamic impact of debris flow. *J Mount Sci* 24(3):340–345 (In Chinese)
- Zhang DX, Wang GH, Luo CY et al (2009) A rapid loess flowslide triggered by irrigation in China. *Landslides* 6(1):55–60



Assessing the Effect of Mitigation Measures on Landslide Hazard Using 2D Numerical Runout Modelling

Haydar Y. Hussin, Roxana Ciurean, Simone Frigerio, Gianluca Marcato, Chiara Calligaris, Paola Reichenbach, Cees van Westen, and Thomas Glade

Abstract

Landslide mitigation measures are used to reduce the risk affecting mountain communities. The quantitative estimation of the change or reduction in risk, after implementing mitigation measures, requires modeling of past events and the forward prediction of possible future occurrences. However, the forward-prediction of landslide hazard is subjected to uncertainties due to the lack of knowledge on some key aspects like the possible source volume that can be triggered and model parameters that determine the landslide runout. In this study, a back-analysis of a debris flow event was carried out using MassMov2D to create a set of parameter ranges for forward-predicting runouts with mitigation measures. We approached the issue of uncertainty by systematically sampling parameters from wide ranges and running hundreds of different runout scenarios. Simulations from back-analysis were compared with the forward-predicted models to determine changes in the spread and intensity of debris flows affecting elements at risk (e.g. houses and roads). This study is a first step towards a quantitative risk assessment (QRA) being carried out within the EC FP-7 funded CHANGES network (Grant Agreement No. 263953).

Keywords

Landslide runout • 2D numerical modelling • Landslide mitigation • Landslide hazard and risk

H.Y. Hussin (✉)
CNR-IRPI, Via Madonna Alta 126, 06128 Perugia, Italy

Faculty of Geo-Information Science and Earth Observation (ITC), University of Twente, 7500 AE, P.O. Box 217, Enschede, The Netherlands
e-mail: haydar.hussin@irpi.cnr.it; h.y.hussin@utwente.nl

R. Ciurean • T. Glade
Department of Geography and Regional Research, University of Vienna, Universitätsstrasse 7, 1010 Vienna, Austria
e-mail: roxana.liliana.ciurean@univie.ac.at; thomas.glade@univie.ac.at

S. Frigerio • G. Marcato
CNR-IRPI, Corso Stati Uniti 4, 35127 Padova, Italy
e-mail: simone.frigerio@irpi.cnr.it; gianluca.marcato@irpi.cnr.it

C. Calligaris
Department of Mathematics and Geosciences, University of Trieste, Via Weiss 2, 34128 Trieste, Italy
e-mail: calligar@units.it

P. Reichenbach
CNR-IRPI, Via Madonna Alta 126, 06128 Perugia, Italy
e-mail: paola.reichenbach2@irpi.cnr.it

C. van Westen
Faculty of Geo-Information Science and Earth Observation (ITC), University of Twente, 7500 AE, P.O. Box 217, Enschede, The Netherlands
e-mail: c.j.vanwesten@utwente.nl



Fig. 1 (Left) The Abitato Cucco 2003 debris flow from the initiation to the deposit zone and (right) the breach of the barrier which damaged several houses

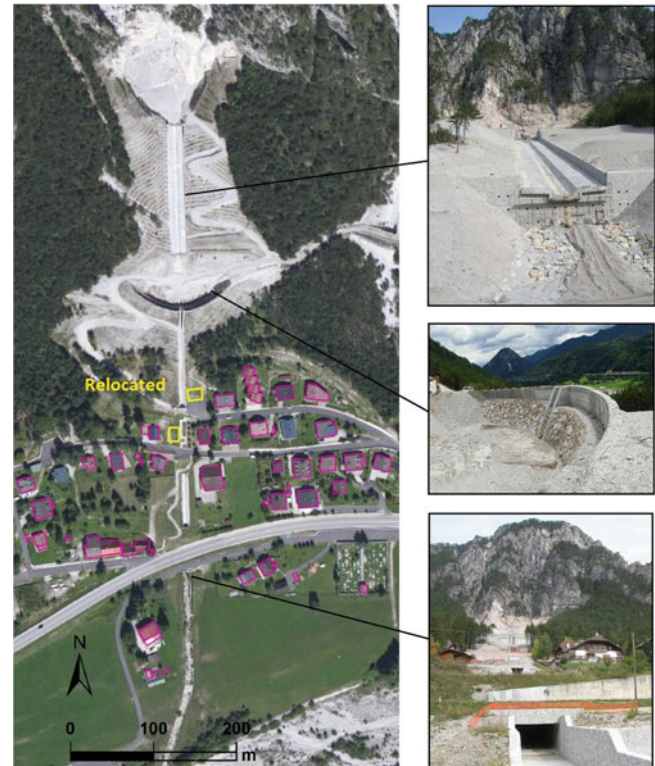


Fig. 2 The mitigation measures constructed at the Abitato Cucco basin following the 2003 event, including the two houses that were relocated

Introduction

Numerical 2D runout models are used to study the flow behaviour of landslide runouts and to produce hazard maps for areas at risk (e.g. alluvial and debris fans). More recently, 2D runout models are being applied to forward predict or forecast the effect of existing mitigation measures on future landslide and debris flow runouts, deposit heights and velocities (Takahashi 2009; Graf and McArdell 2011; Liu et al. 2012). However, using model parameters from back-analyses to forward-predict future runouts can lead to uncertainties in the modelling results (Pirulli 2010), especially if parameters from “past” events are used with “new” DEMs containing mitigation measures. Therefore, it is necessary to produce multiple scenarios in forward predictive modelling of debris flows when analysing the effectiveness of mitigation measures.

We propose in this study to use parametric sampling from ranges based on back-analysis of past events and expert knowledge to forward predict multiple debris flow runout scenarios with recently constructed mitigation measures using a high resolution DEM. The goal is to analyse whether infrastructure in the study area is still at risk of being hit by debris flows. This information can be used as a first step in determining the quantitative change in risk and the residual risk after implementing mitigation measures.

Study Area and Mitigation Measures

The Abitato Cucco settlement in the municipality of Malborghetto-Valbruna forms a section of the Val Canale valley of the Fella River basin (Friuli-Venezia Giulia region, Eastern Italian Alps). On the 29th of August 2003, a debris flow was triggered by a severe rainfall event, mobilizing approximately 10,000 m³ of debris which breached an existing mitigation barrier. Deposit heights exceeding 2 m affected 13 to 14 houses (Fig. 1).

An estimated total of 1 million cubic meters of debris and sediments in the Val Canale valley were mobilized (Tropeano et al. 2004). Some of the recorded rainfall values that triggered the event were: 88.6, 233.4 and 343.0 mm for periods of 1, 3 and 6 h, respectively (Calligaris and Zini 2012). According to the analysis of rainfall data, the Abitato Cucco debris flow had an estimated return period of 500 years.

After the 2003 event, the Civil Protection of the Friuli-Venezia Giulia region started works on new mitigation measures. Figure 2 shows the changes made at the Abitato Cucco area. A small retention basin was constructed at the upper part with a 10 m deep retention dam in the middle-section, followed by a channel with a series of culverts leading to the Fella River. Two houses were relocated due to this adjustment.

Table 1 Model parameter ranges used in the 400 simulations of the 2003 debris flow event and the best performing values obtained from the back-analysis

| Model parameters | Ranges used | Best performing values |
|---|--------------|------------------------|
| Release volume, V (m^3) | 4,000–20,000 | 12,000–16,000 |
| Debris flow bulk density, D (kg/m^3) | 1,700–2,200 | 1,850–2,000 |
| Chézy roughness coefficient, ξ (m/s^2) | 10–3,000 | 100–600 |
| Basal friction angle, μ ($^\circ$) | 5–50 | 5–15 |
| Angle of internal friction, α ($^\circ$) | 5–50 | 15–40 |

Numerical Runout Modelling and Back Analysis

The Abitato Cucco debris flow was back-analysed by Calligaris and Zini (2012) with the commercial Flo-2D software. They used a 5 m DEM acquired from a pre-event laser scanning. Then an attempt was made to forward-predict a debris flow by manually manipulating the 5 m DEM to simulate the new mitigation measures based on field observations from 2007. However, after the 2003 event, thousands of cubic meters of material were removed, which completely changed the morphology of the area. Therefore, a new 1 m DEM was acquired in June 2008 by the Civil Protection of the Friuli-Venezia Giulia region, which includes the completed mitigation works. Before this DEM can be used for forward-prediction, a back-analysis is required according to the numerical runout model that is chosen.

In this study, we applied the two dimensional single-phase MassMov2D runout model (Beguería et al. 2009) running in the PCRaster GIS environmental modelling software (Wesseling et al. 1996; Karssenberget al. 2001). There are several reasons for this choice: (1) the model runs in a free and powerful open-source environment, (2) simulation times are faster than other conventional runout modelling software like Flo-2D or RAMMS, (3) different rheologies (e. g. Voellmy, Bingham and Coulomb friction) can be applied and compared with one another, (4) users can add their own rheology or adjust and implement the model code to their own needs, (5) and finally, batch-file capabilities can easily produce hundreds or thousands of models within several hours for model calibration, sensitivity analyses or stochastic approaches. For detailed information on the description and governing equations of MassMov2D, the reader is referred to Beguería et al. (2009).

After testing different rheologies in MassMov2D, the Voellmy rheology performed the best. The initiation volume was represented as a block release polygon with a specific height (m). This volume was released at the start of the deposit zone (Fig. 1). A total of five parameters were calibrated in the Abitato Cucco back-analysis: the debris flow release volume (V), the debris flow bulk density (D),

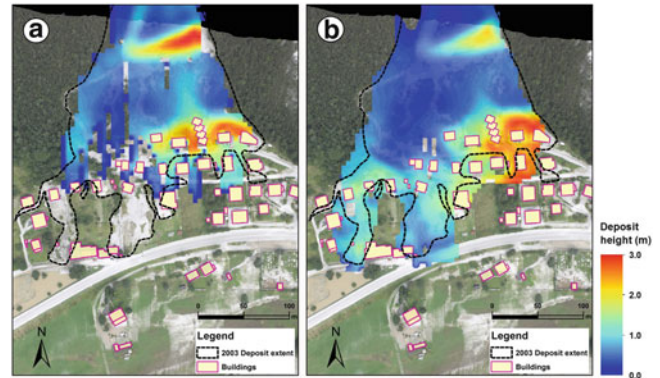


Fig. 3 Back-analysis in 5 m resolution of the 2003 event: (a) model with the best estimation of deposit heights ($V = 13,000 m^3$, $D = 1,850 kg/m^3$, $\xi = 300 m/s^2$, $\mu = 10^\circ$, $\alpha = 20^\circ$) and (b) the best performing model in terms of runout extent ($V = 16,000 m^3$, $D = 2,000 kg/m^3$, $\xi = 600 m/s^2$, $\mu = 12^\circ$, $\alpha = 15^\circ$)

the Chézy roughness coefficient (ξ), the basal friction angle (μ) and the angle of internal friction (α). The parameters were systematically sampled in equal intervals and equal probability from a very wide range to produce 400 simulations using the pre-2003 event 5 m DEM. The best performing model parameter ranges are shown in Table 1.

The required debris flow initiation volume for back analysis ranged at 12,000–14,000 m^3 , which is slightly higher than the original estimation of 10,000 m^3 made by Calligaris and Zini (2012). According to Tropeano et al. (2004) the bulk density ranged from 1,700 to 2,200 kg/m^3 , which is in agreement with our best performing values. The Chézy roughness coefficient was purely determined through back-analysis results. Also, due to lack of field samples and laboratory analysis, friction angles (μ , α) were approximated from model calibrations.

Figure 3 shows the best two performing models in the back-analysis of the 2003 debris flow. The first model does well estimating the deposit height with a slight underestimation of the runout distance (Fig. 3a). The second model gives a more accurate runout extent but with slight overestimations of deposit height at the debris flow toe, and underestimates the height behind the mitigation barrier (Fig. 3b).

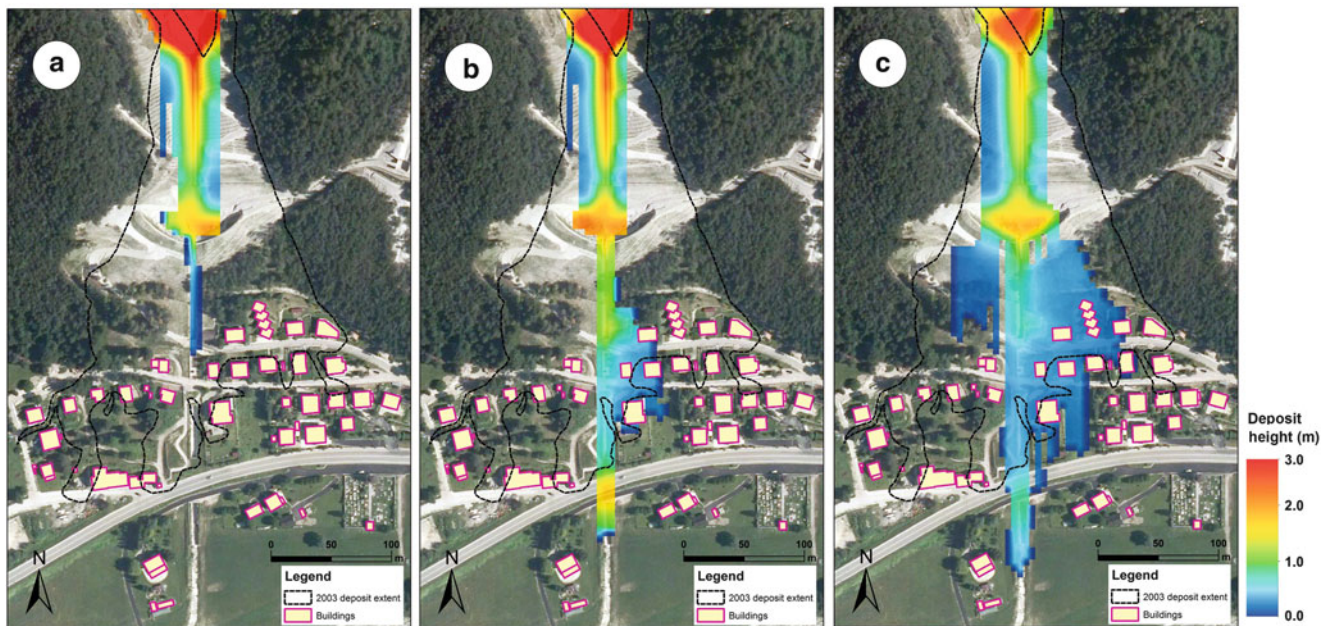


Fig. 4 Examples of the three main type of forward prediction scenarios using the latest upscaled 5 m DEM (June, 2008): (a) no breaching at the retention dam ($V = 12,000 \text{ m}^3$, $D = 2,000 \text{ kg/m}^3$, $\xi = 300 \text{ m/s}^2$, $\mu = 10^\circ$, $\alpha = 10^\circ$), (b) debris breaches only at the

lower channel ($V = 12,000 \text{ m}^3$, $D = 2,000 \text{ kg/m}^3$, $\xi = 100 \text{ m/s}^2$, $\mu = 8^\circ$, $\alpha = 15^\circ$), and (c) breaching of the flow at the dam and lower channel areas ($V = 12,000 \text{ m}^3$, $D = 2,000 \text{ kg/m}^3$, $\xi = 100 \text{ m/s}^2$, $\mu = 5^\circ$, $\alpha = 40^\circ$)

Forward-Prediction Modelling

Forward-prediction modelling with the latest DEM (June, 2008) was carried out first in 5 m resolution by up-scaling the 1 m DEM in order to directly compare the 2008 situation with 2003. This was followed by modelling in the original 1 m resolution in order to forward-predict the most accurate runout extent and heights. We also compared the 5 m model with the 1 m model to analyse the effect of the DEM resolution on the runout modelling.

The best performing range of parameter values in the back-analysis (Table 1) were used to carry out 100 simulations for forward-prediction scenarios using the 5 m DEM. The results of the 100 5 m resolution models can be classified into three main scenarios: (1) no debris flow breaches, (2) breaching of the retention dam and lower channel, or (3) breaching only at the lower channel (Fig. 4).

All 5 m runout models show an accumulation of debris of more than 3 m at the upstream artificial basin. This indicates that the mitigation system significantly decreases the possibility of large debris flow heights to reach downstream. The maximum deposit height in the most extreme scenarios near the houses is no more than 0.85 m. This is a substantial decrease compared to the 2003 deposit heights of 2.0 to 2.5 m. Breaching of the dam and lower channel occurs mainly towards the east side of the settlement. The western part of the settlement is almost unaffected. Scenario 1 models show deposits of maximum 0.15 m on the eastern

channel banks, while scenario 2 and 3 have more significant deposit heights and flow velocities. The most extreme scenarios affect approximately 8–10 houses, with scenario 2 type simulations affecting a maximum of 3–4 houses.

A total of 50 forward-prediction simulations were produced using the 1 m DEM due to time constraints of modelling in a 1 m resolution. A simulation averaged around 30–40 min compared to a 3–5 min simulation time in 5 m resolution. Similar to the 5 m simulations, the 1 m models were also categorized into scenario types. Non-breaching scenarios in 1 m resolution were less common than in the 5 m simulations. Therefore, we defined the 1 m scenarios into the following three types: (1) breaching at the east channel bank (2) breaching at both channel banks and (3) breaching at the dam and lower channel area (Fig. 5).

The 1 m simulations give a very different view on possible scenarios due to the more accurate depiction of the dam and channel geometry. The modelled debris flows are more confined, pushing the higher deposits further downstream. The thicker deposits that stopped at the upper basin in the 5 m models are now located near the retention dam in the 1 m simulations. Breaches at the lower channel are much more subtle and follow better the topography, with higher deposits found near the houses next to the channel. The average outputs of both 5 m and 1 m simulations can be compared with one another in Table 2. The results show that 1 m model scenarios generally affect less houses, but show higher intensity values. This is possibly due to the more

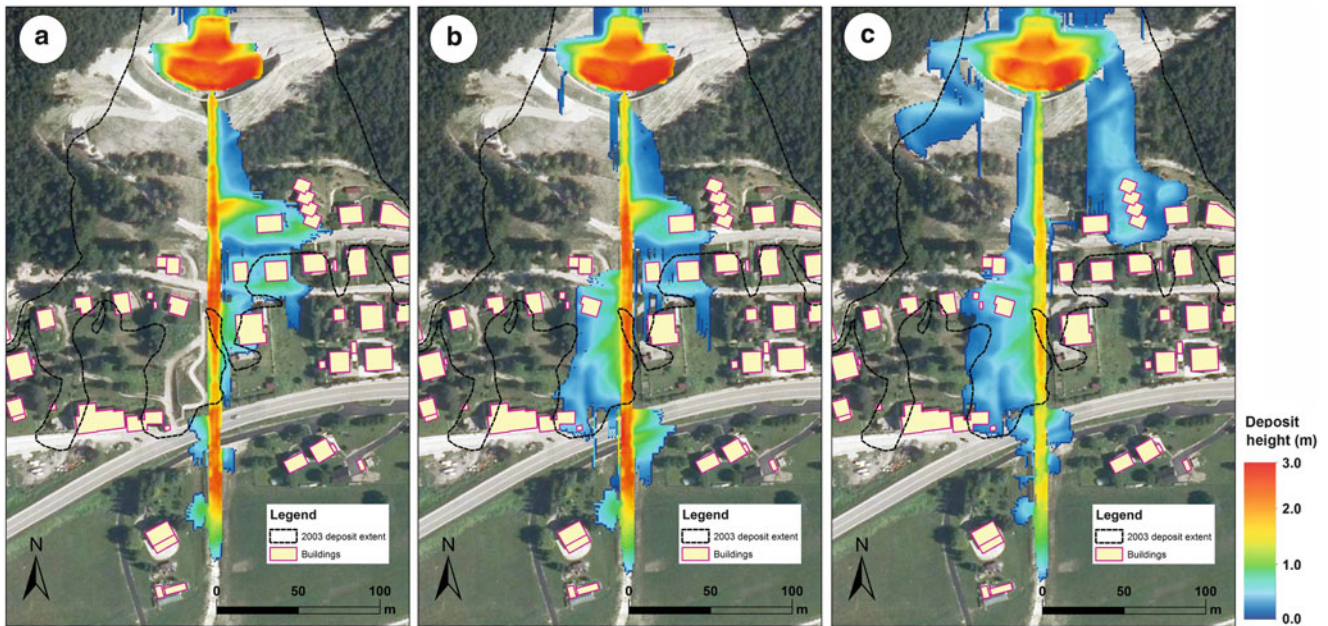


Fig. 5 The three general types of forward-predicted scenarios using the original 1 m DEM (June, 2008): (a) debris flow breaching at the east channel bank ($V = 13,000 \text{ m}^3$, $D = 1,850 \text{ kg/m}^3$, $\xi = 100 \text{ m/s}^2$, $\mu = 10^\circ$, $\alpha = 30^\circ$), (b) breaching at both sides of the channel

($V = 12,000 \text{ m}^3$, $D = 1,850 \text{ kg/m}^3$, $\xi = 100 \text{ m/s}^2$, $\mu = 8^\circ$, $\alpha = 30^\circ$), and (c) breaching at the retention dam and lower channel ($V = 13,000 \text{ m}^3$, $D = 1,850 \text{ kg/m}^3$, $\xi = 100 \text{ m/s}^2$, $\mu = 8^\circ$, $\alpha = 40^\circ$)

Table 2 Average modelled intensities and number of houses affected for all scenario types (3 scenarios in 5 m and 1 m resolution)

| Forward predictions | Maximum flow height near houses | Maximum velocity near houses | Number of houses affected |
|---------------------|---------------------------------|------------------------------|---------------------------|
| Scenario 1 (5 m) | 0.15 m | 0 m/s | 0 |
| Scenario 2 (5 m) | 0.52 m | 2.2 m/s | 4–5 |
| Scenario 3 (5 m) | 0.85 m | 3.6 m/s | 8–10 |
| Scenario 1 (1 m) | 1.05 m | 3.9 m/s | 2–3 |
| Scenario 2 (1 m) | 0.76 m | 2.7 m/s | 3–4 |
| Scenario 3 (1 m) | 0.47 m | 1.8 m/s | 5–6 |

confined flow in the 1 m simulations, forcing the velocity and height to slightly increase in narrower sections of the flow.

Discussion and Conclusions

The limitations of forward-predicting landslide runouts can be related to several assumptions that have been made in this study. Forward-analysis was carried out using a similar initiation volume as the 2003 event. However, it is known that debris flow source areas need time to recharge and accumulate enough sediment in order for a similar past event to reoccur (Glade 2005). This problem can therefore cause changes in the magnitude of a certain return period. A thorough assessment of the source area is required to analyse possible changes in debris recharge, which accordingly can change the input initiation volume for modelling.

Debris flow entrainment was assumed to be part of the initiation volume. Despite the relative short distance between source and deposit zones, entrainment can still

play a substantial role in the formation of the final deposit heights and velocities in deposit zones (McDougall and Hungr 2005; Hussin et al. 2012). Furthermore, the use of a block release polygon instead of a hydrograph can have some disadvantages. Hydrographs are able to more accurately describe boundary conditions, surges and the timing of flows reaching deposit zones (Hürlimann et al. 2003).

The DEM resolution has shown to be very significant in modelling debris flow runouts, especially in artificially channelized areas which are more difficult to model than flows spreading on open slopes or debris fans. The high resolution 1 m runout simulations show more realistic flow scenarios, where the retention dam and channels are more accurately defined. Differences in flow extent and heights between the 5 m and 1 m models change the predicted areas and houses being affected. Thus, it is highly recommended to model debris flows in the highest resolution possible when assessing the effectiveness of mitigation strategies.

The accurate representation of different types of mitigation measures in a DEM can be very difficult, regardless of the detail or resolution of the DEM. In our work, we assumed the culverts to be an open channel system, simulating their inflow points by creating very small obstacles in the channel bed. This assumption was required due to the restriction of our chosen model. Other models like Flo-2D are capable of modelling with culverts, tunnels and other obstacles. Therefore, comparing the two different models is planned in the near future for our continuing research.

This study applied specific ranges from back-analysis to forward-predict possible future runouts. However, some model parameters, like the Chézy roughness coefficient, cannot be measured in laboratory or field studies. These parameters can only be obtained by calibrating runout models using a DEM representing the past event. Therefore, applying back-calibrated parameters for forward-prediction using completely different DEMs causes a source of uncertainty in prediction outputs. We have tried to approach this uncertainty by simulating many runs and classifying the large amount of produced models into several scenario types. Our approach gives some indications of possible types of scenarios and the number of buildings that can be affected in the future. The application of wider parameter ranges to produce many landslide runout simulations, results in multiple possible scenarios. This is an indication of the importance of acknowledging uncertainties in landslide mitigation planning and the need to address the difficulties in predicting residual landslide risk.

Acknowledgments The work in this paper is part of the CHANGES project, a Marie Curie Initial Training Network funded by the European Commission's 7th Framework Programme (Grant Agreement No. 263953). We acknowledge our gratitude to all our colleagues at CNR-IRPI (Padova and Perugia) who continually support us in this ongoing research. We thank the Civil Protection (Palmanova) and Geological Survey (Trieste) of the Friuli-Venezia Giulia region for their data sharing and cooperation. Finally, many thanks go to Dr. Chiara Calligaris (Department of Mathematics and Geosciences, University of Trieste) for sharing her important experience on surveying and modelling of landslides in our study area.

References

- Beguería S, Van Asch TWJ, Malet JP, Gröndahl S (2009) A GIS-based numerical model for simulating the kinematics of mud and debris flows over complex terrain. *Nat Hazards Earth Syst Sci* 9(6): 1897–1909. doi:[10.5194/nhess-9-1897-2009](https://doi.org/10.5194/nhess-9-1897-2009)
- Calligaris C, Zini L (2012) Debris flow phenomena: a short overview? In: Dar IA (ed) *Earth Sciences*. INTECH, Croatia, pp 71–90
- Glade T (2005) Linking debris-flow hazard assessments with geomorphology. *Geomorphology* 66(1–4):189–213, doi: <http://dx.doi.org/10.1016/j.geomorph.2004.09.023>
- Graf C, McArdeell BW (2011) Debris-flow monitoring and debris-flow runout modelling before and after construction of mitigation measures: an example from an instable zone in the Southern Swiss Alps. In: Lambiel C, Reynard E, Scapozza C (eds) *La géomorphologie alpine: entre patrimoine et contrainte*. Actes du colloque de la Société Suisse de Géomorphologie, 3–5 septembre 2009, Olivone. *Géovisions* 36. Université, Institut de géographie, Lausanne, pp 243–258
- Hürlimann M, Rickenmann D, Graf C (2003) Field and monitoring data of debris-flow events in the Swiss Alps. *Can Geotech J* 40:161–175
- Hussin HY, Quan Luna B, van Westen CJ, Christen M, Malet JP, van Asch TWJ (2012) Parameterization of a numerical 2-D debris flow model with entrainment: a case study of the Faucon catchment, Southern French Alps. *Nat Hazards Earth Syst Sci* 12(10): 3075–3090. doi:[10.5194/nhess-12-3075-2012](https://doi.org/10.5194/nhess-12-3075-2012)
- Karssenber D, Burrough PA, Sluiter R, de Jong K (2001) The PCRaster software and course materials for teaching numerical modelling in the environmental sciences. *Trans GIS* 5(2):99–110. doi:[10.1111/1467-9671.00070](https://doi.org/10.1111/1467-9671.00070)
- Liu J, Nakatani K, Mizuyama T (2012) Hazard mitigation planning for debris flow based on numerical simulation using Kanako simulator. *J Mt Sci* 9(4):529–537. doi:[10.1007/s11629-012-2225-9](https://doi.org/10.1007/s11629-012-2225-9)
- McDougall S, Hungr O (2005) Dynamic modelling of entrainment in rapid landslides. *Can Geotech J* 42:1437–1448
- Pirulli M (2010) On the use of the calibration-based approach for debris-flow forward-analyses. *Nat Hazards Earth Syst Sci* 10(5): 1009–1019. doi:[10.5194/nhess-10-1009-2010](https://doi.org/10.5194/nhess-10-1009-2010)
- Takahashi T (2009) Mechanics-Based Approach Toward the Mitigation of Debris Flow Disasters. In: Canuti P, Sassa K (eds) *Landslides – disaster risk reduction*. Springer, Berlin, pp 89–113. doi:[10.1007/978-3-540-69970-5_5](https://doi.org/10.1007/978-3-540-69970-5_5)
- Tropeano D, Turconi L, Sanna S (2004) Debris flows triggered by the 29 August 2003 cloudburst in Val Canale, eastern Italian Alps. In: *Proceedings of the 10th internationales symposium interpraevent 2004*, pp 121–132
- Wesseling CG, Karssenber D-J, Burrough PA, Van Deursen WPA (1996) Integrating dynamic environmental models in GIS: the development of a dynamic modelling language. *Trans GIS* 1(1): 40–48. doi:[10.1111/j.1467-9671.1996.tb00032.x](https://doi.org/10.1111/j.1467-9671.1996.tb00032.x)

Part VII

Remedial Measures and Prevention Works



Introduction: Remedial Measures and Prevention Works

Rolf Katzenbach and Sebastian Fischer

Abstract

The session “Remedial Measures and Prevention Works” deals with contributions which are focussed on the scientific background and also practical experiences. Ways of sustainable disaster management and disaster prevention will be demonstrated.

Keywords

Landslide • Remedial measures • Prevention works • Multidisciplinary

Introduction

Landslides belong to the group of extremely heavy natural hazards which often cause extraordinary damage. The successful handling and prevention of landslides is an important field for civil engineers in a multidisciplinary cooperation together with the colleagues from natural sciences, economics, politics etc.

Due to growing population more and more settlement area is needed, which is often including improper regions (e.g. mountain and coast regions) with raised risk of various kinds of disasters. Another reason for the raising of risks can be the opencast mining for raw material production. An essential element of the opencast mining is the loose deposition of the removed overburden, the so-called “overburden dump”. Due to the end of groundwater conservation these loose bedded slope areas are flooded. In consequence the slopes are in danger of becoming liquefied. The result of a liquefaction in these slopes will unavoidably be a slope slide. Such a slope slide can extend up to several hundred meters and can move several million cubic meters of material. An upsetting example for such a landslide is the slope failure in the German village of Nachterstedt on July 18, 2009, which made necessary remedial measures and also prevention

works for the further utilisation of the region. The phenomena of liquefaction is not limited on slopes in series of opencast mining. Especially in earthquake regions the phenomena of liquefaction is well known.

The session “remedial measures and prevention works” presents ways to stabilize or prevent landslide, it is consisting of the following seven contributions which can be categorised in contributions focussing on the theoretical background and experiments:

- Da Z., Lidan L., Seismic Damage Assessment of Gravity Retaining Wall Based on Grey Correlation and Fuzzy Mathematics;
- Noor M.J. Md., Saidin M.A., Tahir S.M., Effectiveness of Hybrid Anchor Soil Nail in Stabilizing Slope and Stability Assessment According To the Actual Mechanics;
- Segalini A., Brighenti R., Umili G., A simplified analytical model for the design of flexible barriers against debris flows;

and contributions dealing with problems occurred in practice:

- Bellas, M., Voulgaridis G., Study of a landslide;
- Sadagah B., A vigorous debris flow incident at Al-Hada descent and remedial measures;
- Suljić N., Application of reinforced concrete retaining wall at the rehabilitation of landslides on roads;
- Zaporozhchenko E., Butenko A., Engineering solutions for elimination of the risk of destruction of moraine.

The intent is to inform the reader of available options and their application in practice or their actual state of technology.

R. Katzenbach • S. Fischer (✉)
Department of Civil and Environmental Engineering, Technische
Universität Darmstadt, Darmstadt, Germany
e-mail: fischer@geotechnik.tu-darmstadt.de



Study of a Landslide in Dafnoula Village, Epirus Region, Greece

Michael Bellas and Georgios Voulgaridis

Abstract

Landslide phenomena are very common in western Greece due to high rainfalls. The current study refers to a landslide that occurred during the winter of 2010 in the residential area of Dafnoula village. Dafnoula is located in northwestern Greece, Epirus prefecture, on a slope with an average inclination of 25° . The formation affected by the landslide was the flysch soil mantle of the Ionian geotectonic zone, whereas the bedrock remained intact. The landslide caused a wide range of damage, including the collapse of a house, a warehouse, and an artificial embankment-terrace and its concrete retaining wall. At the foot of the landslide there was a backfilling of the road below and the complete destruction of its pavement. For this study a 20 m depth borehole and five research pits were opened. A study of the fluid–solid coupling phenomenon and a slope stability analysis, with the use of the Finite Element Method was initially performed. Furthermore, a landslide analysis was carried out using a conventional Limit Equilibrium Method under the DIN Design Standards. Finally, remedial measures were proposed, including the construction of a retaining piled wall, in combination with the use of reinforced shotcrete, the partial substitution of the in situ unstable soil with crushed stone, and the construction of a drainage trench.

Keywords

Landslide • Greece • Epirus region • Slope stability analysis

Geomorphological and Hydrological Setting

Dafnoula village is located at the NW region of Greece, in the Epirus region, and belongs to Ioannina county as a district of municipality of Ioannina. The village is developed in three consecutively abutments. The landslide we are dealing with activated for the first time in 1960 and reactivated in December of 2010 in the middle abutment after a constant medium rainfall. The geographic coordinates of the landslide's head are given in Table 1.

The landslide occurred in a slope with a inclination of 25° , in the central part of the village. Below it and at a distance of 200 m a ravine with intermittent flow is developed. The absolute height of the landslide's head is approximately 830 m.

The meteorological information obtained by the closest station located in Ioannina are provided below and refer to the period during 1995–2006. Based on the station's information, Table 2 was developed for the rainy months of Greece (October, November, December, January, February and March) with a maximum 24-h precipitation activity specified as 105 mm/day:

The highest rainfall periods are observed during November and December. During the same months, the landslide studied in this paper was reactivated in December 2010, when the precipitation of the whole month fell within 3 days.

M. Bellas (✉) • G. Voulgaridis
Institute of Geology and Mineral Exploration, Athens, Greece
e-mail: Bellas@igme.gr; Ge.voulg@gmail.com

Table 1 Geographic coordinates of the hill of Dafnoula village

| | |
|----------------------|-----------------|
| Geographic latitude | 39° 36' 18.72"N |
| Geographic longitude | 20° 59' 18.26"E |

Table 2 Average monthly precipitation in mm

| Month | Oct | Nov | Dec | Jan | Feb | Mar |
|------------------------------------|------|-------|-------|-------|-------|------|
| Average monthly precipitation (mm) | 99.5 | 167.9 | 174.9 | 124.2 | 116.0 | 95.4 |

Geological and Geotechnical Information

The area of Dafnoula belongs to the Ionian geotectonic zone and the geological bedrock that covers the entire building area is the formation of flysch, which shows a stratigraphic inclination of around 10°, aligned with the topographic slope. Flysch consists of alternating beds of silt, shales and sandstones. Generally it appears impermeable and is covered by a soil mantle consisting of silt and sands. The soil mantle has average permeability. A borehole was drilled in this area, showing that the thickness of the soil mantle in the landsliding area is of the order of 4.5 m. The hydraulic load required for the activation of the landslide came from the transient medium rainfall which accumulated inside the disintegration mantle. Just before, as well as during the landslide, discharge was observed by the residents of the village in the area of the levee, at the bottom of the slope, and right above it.

Table 3 gives a description of the borehole that was drilled a few meters below of the head of the landslide.

Also, in order to investigate soil conditions in the area downstream of the landslide area, five research pits were drilled, which are described in Table 4.

Flysch was encountered in the pits ΔO-2 at 2.80 m in ΔO-3 at 3.00 m and in ΔO-4 throughout the entire pit. In the other two, only a weathering mantle of flysch was met. Also, laboratory tests were conducted in order to specify the physical characteristics. Some of the results are given in Tables 5 and 6.

Finally, after the laboratory sieve analysis given above, the soil mantle formation was specified as clay loam material, with the use of the soil texture triangle given in Fig. 1.

Damage

The landslide caused the creation of through-cracks in a warehouse and overthrow of a house, as well as the destruction of a concrete courtyard and the embankment along the retaining wall of a newly built house. Finally the concrete

Table 3 Description of the borehole drilled at the bottom of the landslide

| Depth (m) | Description |
|------------|--|
| 0.00–4.50 | Weathering mantle of flysch consisting of loose weathering products of sandstone and brown siltstone |
| 4.50–20.00 | Bedrock consisting of unweathered fine bedded fragmented sandstones and siltstones |
| 20.00 | End of borehole |

Table 4 Description of the five research pits

| Pits | Depth of pit (m) | Soil mantle |
|------|------------------|-------------|
| ΔO-1 | 3.30 | 0–3.30 |
| ΔO-2 | 3.30 | 0–2.80 |
| ΔO-3 | 3.30 | 0–3.00 |
| ΔO-4 | 2.20 | 0 |
| ΔO-5 | 3.50 | 0–3.50 |

Table 5 Description of the Atterberg limits specified by the laboratory tests

| | Min | Max | Mid |
|----|------|------|------|
| LL | 28.3 | 36.3 | 32.3 |
| PL | 18.2 | 23.5 | 20.9 |
| PI | 5.4 | 11.8 | 8.6 |

Table 6 Results of the sieve analysis conducted

| Grains | Content (%) |
|--------|-------------|
| Clay | 16 |
| Silt | 37 |
| Sand | 34 |
| Gravel | 13 |

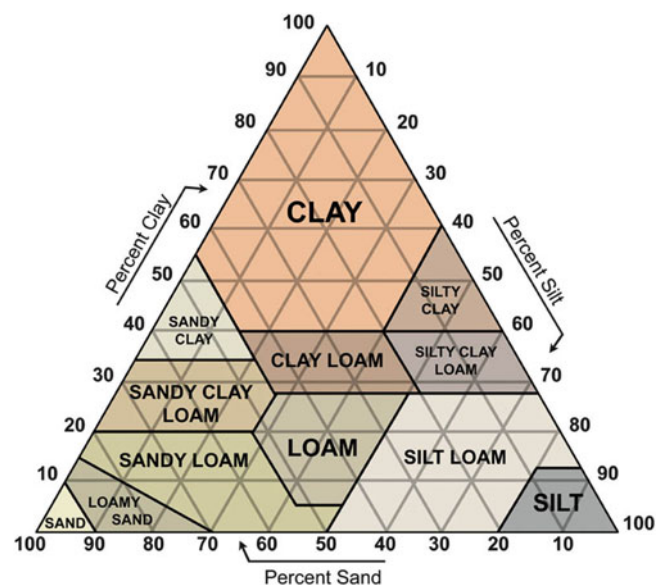


Fig. 1 Soil texture triangle (US Department of Agriculture, Natural Resources Conservation Service)

pavement of the road below was destroyed and the materials of the foot of the landslide covered two-thirds of this road.

$$\begin{cases} d\sigma_{ij} = [D_{ep}]d\varepsilon_{ij} \\ d\varepsilon_{ij} = [B]du_{ij} \end{cases} \quad (4)$$

Numerical Analysis of the Fluid–Solid Coupling and the Rainfall-Induced Landslide Using a Nonlinear Finite Element Method

Introduction

Elastoplastic Model

The Finite Element Method is a very widely used and powerful method for solving partial differential equations and is applied to a wide variety of engineering problems, from diffusion problems to materials behavior. However, since the materials found in nature, and especially geomaterials, do not behave linearly but instead non-linearly, the application of the non-linear Finite Element Analysis is required to obtain exact results when solving for these types of materials.

As it is well known, the stress equations for a two dimensional plane strain problem are given for x and y dimensions respectively (Navier equations):

$$\begin{cases} \mu \nabla^2 u + (\lambda + \mu) \frac{\partial}{\partial x} \left(\frac{\partial u}{\partial x} + \frac{\partial v}{\partial x} \right) + F_x = [\rho] \frac{\partial^2 u}{\partial t^2} \\ \mu \nabla^2 v + (\lambda + \mu) \frac{\partial}{\partial y} \left(\frac{\partial u}{\partial x} + \frac{\partial v}{\partial x} \right) + F_y = [\rho] \frac{\partial^2 v}{\partial t^2} \end{cases} \quad (1)$$

or in the general expression,

$$(\lambda + \mu)u_{k,ki} + \mu u_{i,kk} + F = \rho \frac{\partial^2 u_i}{\partial t^2} \quad (2)$$

where,

- λ, μ : are the Lamé coefficients
- u : are the displacements in x dimension
- v : are the displacements in y dimension
- F_x : are the body forces in x dimension
- F_y : are the body forces in y dimension respectively
- F : is the vector of body forces
- ρ : is the density of the material

We further take into account the elastoplastic behavior of the geomaterial, where the change of strain $d\varepsilon_{ij}$ is consisted of two parts, both an elastic and a plastic part, as expressed below (as referred by Potts DM and Zdravkovic L):

$$[d\varepsilon_{ij}] = [d\varepsilon_{ij}]_e + [d\varepsilon_{ij}]_{ep} \quad (3)$$

as well as the geomaterial characteristics summarized in the elastoplastic constitutive matrix $[D_{ep}]$ and the constitutive equations:

where,

$[D_{ep}]$: is the elastoplastic constitutive matrix given by the (5):

$$[D_{ep}] = [D_e] - \frac{[D_e] \left\{ \frac{\partial P(\sigma, m)}{\partial \sigma} \right\} \left\{ \frac{\partial F(\sigma, k)}{\partial \sigma} \right\}^T [D_e]}{\left\{ \frac{\partial P(\sigma, m)}{\partial \sigma} \right\} \left\{ \frac{\partial F(\sigma, k)}{\partial \sigma} \right\}^T [D_e] + A} \quad (5)$$

where,

$\left\{ \frac{\partial F(\sigma, k)}{\partial \sigma} \right\}$: is the yield function

$\left\{ \frac{\partial P(\sigma, m)}{\partial \sigma} \right\}$: is the plastic potential, and

A: is a parameter given by:

$$A = \frac{1}{\lambda} \left\{ \frac{\partial F(\sigma, k)}{\partial k} \right\}^T \{\Delta k\} \quad (6)$$

where λ is a scalar.

Seepage Model

Under undrained conditions the stress field is a result of both the effective stresses and the stresses produced by the pore pressures. The constitutive equation is given by:

$$\frac{\partial \varepsilon}{\partial t} = n\beta \frac{\partial \sigma}{\partial t} - \bar{v} \quad (7)$$

where,

\bar{v} : is the divergence of the pore water (Darcy's velocity)

σ : is the pore pressure

ε : is the strain, and

β : is the compressibility of the pore water.

The diffusion phenomenon within the geomaterial is expressed by the parabolic partial differential equation:

$$\frac{\partial H}{\partial t} = c \nabla^2 H + s_{(x,t,H,\nabla H)} \quad (8)$$

where,

c: is the diffusion coefficient

s: is the source term representing external sources

The diffusion coefficient is given by the equation:

$$c = K/S \quad (9)$$

where,

S: is the storage coefficient

K: is the permeability coefficient

The relationship between the total hydraulic head and the pore pressures is given by the equation:

$$H = \frac{P_w}{\gamma_w} + (Xi_x + Yi_y + Zi_z) \quad (10)$$

where $i = \{i_x + i_y + i_z\}$ is the unit vector parallel and in opposite direction to gravity.

Taking into account all of the above, we end up to the seepage equation for x and y dimensions:

$$S \frac{\partial H}{\partial t} = \frac{\partial}{\partial x} \left(K_x \frac{\partial H}{\partial x} \right) + \frac{\partial}{\partial y} \left(K_y \frac{\partial H}{\partial y} \right) + S(x, t, H, \nabla H) \quad (11)$$

where,

H: is the Total head

S: is the Storage coefficient,

K: is the Permeability coefficient

s: is the source term

Equation (11) represents the Darcy's law.

Formulation and Solution of the Finite Element Model

The nonlinear finite element analysis is a finite element analysis performed with the use of an iterative procedure for root finding (usually Newton-Raphson scheme) since the material characteristics, i.e. elastoplastic constitutive matrix, depend on the displacements.

The coupled seepage flow-deformation is expressed by the equations (as referred by Li J, Liu X and Jiang Z):

$$\begin{aligned} \sigma_{ij} &= \sigma'_{ij} + \alpha(p_w)\delta_{ij} + F_v^- \\ \frac{\partial \varepsilon}{\partial t} &= n\beta \frac{\partial p_w}{\partial t} - \bar{v} \end{aligned} \quad (12)$$

where,

σ_{ij} : are the total stresses

σ'_{ij} : are the effective stresses

p_w : are the pore pressures

δ_{ij} : is the Kronecker's delta, and

F_v^- : is the force vector

\bar{v} : is the divergence of the pore water (Darcy's velocity)

p_w : is the pore pressure

ε : is the strain, and

β : is the compressibility of the pore water

According to the principle of virtual work, we have:

$$W_{inertia} + W_{external} = W_{internal} \quad (13)$$

where,

$W_{inertia}$: is the work produced by the inertia forces

$W_{external}$: is the work produced by the external forces

$W_{internal}$: is the work produced by the internal forces

the work produced by the inertia forces is expressed as follows:

$$W_{inertia} = \int_{\Omega} \delta^T (f_{inertia}) \partial \Omega \quad (14)$$

where,

$$f_{inertia} = -\rho \frac{\partial^2 u}{\partial t^2}$$

By implementing the finite element algorithm, we end up with the following results:

$$W_{inertia} = \int_{\Omega} \delta^T \left(-\rho \frac{\partial^2 u}{\partial t^2} \right) \partial \Omega \Rightarrow$$

$$W_{inertia} = \int_{\Omega} \delta^{eT} N_e^T \left(-\rho N_e \frac{\partial^2 u_e}{\partial t^2} \right) \partial \Omega \Rightarrow$$

$$W_{inertia} = -\delta^{eT} \left(\int_{\Omega} N_e^T \rho N_e \partial \Omega \right) \ddot{u}_e \quad (15)$$

where,

$[M^e] = \left(\int_{\Omega} N_e^T \rho N_e \partial \Omega \right)$ is called the mass matrix and

\ddot{u}_e : is the second derivative of elemental displacement with respect to time

The work produced by the external forces is expressed as follows:

$$W_{external} = \int_{\Omega} \delta^T (f_{ext}) \partial \Omega \quad (16)$$

By implementing the finite element algorithm again, we obtain:

$$W_{external} = \int_{\Omega} \delta^T (f_{ext}) \partial \Omega \Rightarrow$$

$$W_{external} = \int_{\Omega} \delta^{eT} N_e^T (f_{ext}^e) \partial \Omega \Rightarrow$$

$$W_{external} = \delta^{eT} \int_{\Omega} N_e^T (f_{ext}^e) \partial \Omega \Rightarrow$$

$$W_{external} = \delta^{eT} \left(\int_{\Omega} N_e^T \partial \Omega \right) f_{ext}^e \quad (17)$$

Finally, the work produced by the internal forces is expressed as follows:

$$W_{internal} = \int_{\Omega} \delta^T (f_{int}) \partial \Omega \quad (18)$$

By implementing the finite element algorithm we obtain:

$$\begin{aligned} W_{internal} &= \int_{\Omega} \delta^T (f_{int}) \partial \Omega \Rightarrow \\ W_{internal} &= \int_{\Omega} \delta^T \nabla (D_{ep} \nabla u) \partial \Omega \Rightarrow \\ W_{internal} &= \int_{\Omega} \delta^T N_e^T \nabla (D_{ep} \nabla N_e u^e) \partial \Omega \end{aligned}$$

and by integrating by parts we finally obtain:

$$W_{internal} = \delta^T \left(\int_{\Omega} B^T D_{ep} B \partial \Omega \right) u^e \quad (19)$$

where,

$[K_T^e] = (\int_{\Omega} B^T D_{ep} B \partial \Omega)$ is the tangential stiffness matrix and u^e : are the elemental nodal unknowns (displacements)

Assembling all of the above we end up to the following system for each element:

$$\begin{aligned} -[M^e] \ddot{u}_e + f_E^e &= [K_T^e] u^e \text{ or} \\ [M^e] \ddot{u}_e + [K_T^e] u^e &= f_E^e \end{aligned} \quad (20)$$

and in terms of global coordinate system:

$$[M] \ddot{u} + [K_T] u = F \quad (21)$$

Since we need to model the geomaterial's load path dependent behavior, a combination of Newton-Raphson's scheme with the incremental method is required. Furthermore, by considering solution only in space, we end up to the following expression:

$$[K_T] \{\Delta u\}^i = \{\Delta F\}^i \quad (22)$$

where:

$\{\Delta u\}^i$: is the incremental displacement

$\{\Delta F\}^i$: is the incremental load step

The load produced by the weight is expressed as:

$$\bar{W} = \gamma \int_{\Omega} N_i^{(e)} \partial V_e \quad (23)$$

whereas the additional external load (structural load) is given by:

$$\bar{R} = \int_{\Gamma^e} N_i^{(e)} D_{ep} \nabla u \partial \Gamma^e \quad (24)$$

In order for the plastic deformation and failure to occur, the total stresses have to be calculated at the

nodes and to satisfy both the finite element solution and the Mohr-Coulomb failure criterion which is given by the equation:

$$F_{(I_1, J_2, \theta)} = -\frac{I_1}{3} \sin \Phi + \sqrt{J_2} \left[\cos \theta + \frac{1}{\sqrt{3}} \sin \theta \sin \Phi \right] - c \cos \Phi \quad (25)$$

Regarding the seepage flow analysis, using the weighted residual approach this time, we obtain:

$$S \frac{\partial H}{\partial t} = \nabla (K_{(x,y)} \nabla H_{(x,y)}) + s$$

$$R = \int_{\Omega} W_i \left(\frac{\partial}{\partial x} \left(K_x \frac{\partial H}{\partial x} \right) + \frac{\partial}{\partial y} \left(K_y \frac{\partial H}{\partial y} \right) + s - \left(S \frac{\partial H}{\partial t} \right) \right) \partial \Omega$$

where,

$W_i = N_i x^m$ denotes the weight functions

N_i : denotes the interpolation functions

x^m : is a factor expressing the coordinate system and is equal to 1 for the Cartesian coordinate system (Exadaktylos G, Asimidis V)

By implementing both integration by parts as well as the finite element algorithm, and by rearranging, we obtain for each element:

$$\begin{aligned} \sum_e R &= \sum_e \int_{\Gamma} N_i \left(\left(K_x \frac{\partial H}{\partial x} n_x \right) + \left(K_y \frac{\partial H}{\partial y} n_y \right) \right) \partial \Gamma \\ &\quad - \sum_e \int_{\Omega} \left[K_x \frac{\partial N_i}{\partial x} \frac{\partial H}{\partial x} + K_y \frac{\partial N_i}{\partial y} \frac{\partial H}{\partial y} \right] \partial \Omega \\ &\quad + \sum_e \int_{\Omega} N_i s \partial \Omega - \sum_e \int_{\Omega} N_i \left(S \frac{\partial H}{\partial t} \right) \partial \Omega \Rightarrow \\ R^e &= \int_{\Gamma^e} N_i \left(\left(K_x \frac{\partial H}{\partial x} n_x \right) + \left(K_y \frac{\partial H}{\partial y} n_y \right) \right) \partial \Gamma^e \\ &\quad - \int_{\Omega^e} \left[K_x \frac{\partial N_i}{\partial x} \frac{\partial N_j}{\partial x} + K_y \frac{\partial N_i}{\partial y} \frac{\partial N_j}{\partial y} \right] \partial \Omega^e \{H^e\} \\ &\quad + \int_{\Omega^e} N_i s \partial \Omega^e - \int_{\Omega^e} N_i S N_j \partial \Omega^e \{ \dot{H}^e \} \end{aligned} \quad (26)$$

where,

R : denotes the error term due to the approximations.

By setting $R^e = 0$ and rearranging, we further obtain:

$$\int_{\Omega^e} \left[K_x \frac{\partial N_i}{\partial x} \frac{\partial N_j}{\partial x} + K_y \frac{\partial N_i}{\partial y} \frac{\partial N_j}{\partial y} \right] \partial \Omega^e \{H^e\} + \int_{\Omega^e} N_i S N_j \partial \Omega^e \{\dot{H}^e\} \\ = \int_{\Omega^e} N_i s \partial \Omega^e + \int_{\Gamma^e} N_i \left(\left(K_x \frac{\partial H}{\partial x} \right) + \left(K_y \frac{\partial H}{\partial y} \right) \right) \partial \Gamma^e \quad (27)$$

or

$$[S^e] \dot{H}^e + [K^e] H^e = P^e \quad (28)$$

where,

$[K^e] = \int_{\Omega^e} \left[K_x \frac{\partial N_i}{\partial x} \frac{\partial N_j}{\partial x} + K_y \frac{\partial N_i}{\partial y} \frac{\partial N_j}{\partial y} \right] \partial \Omega^e$ is called the Permeability matrix

$[S^e] = \int_{\Omega^e} N_i S N_j \partial \Omega^e$ is called the Storage matrix

$P^e = \int_{\Omega^e} N_i s \partial \Omega^e + \int_{\Gamma^e} N_i \left(\left(K_x \frac{\partial H}{\partial x} \right) + \left(K_y \frac{\partial H}{\partial y} \right) \right) \partial \Gamma^e$ is called the local element source vector

\dot{H}^e : denotes the first derivative of the elemental nodal unknowns in respect to time and

H^e : denotes the values of the nodal unknowns

Considering that the Permeability matrix depends on the hydraulic head, nonlinearities appear. Again, a combination of Newton-Raphson's method with the incremental method is applied, and considering only space solution, we end up at the expression:

$$[K] \{\Delta H\}^i = \{\Delta P\}^i \quad (29)$$

where,

$\{\Delta H\}^i$: is the incremental head, and

$\{\Delta P\}^i$: is the incremental load step

Slope Stability Analysis

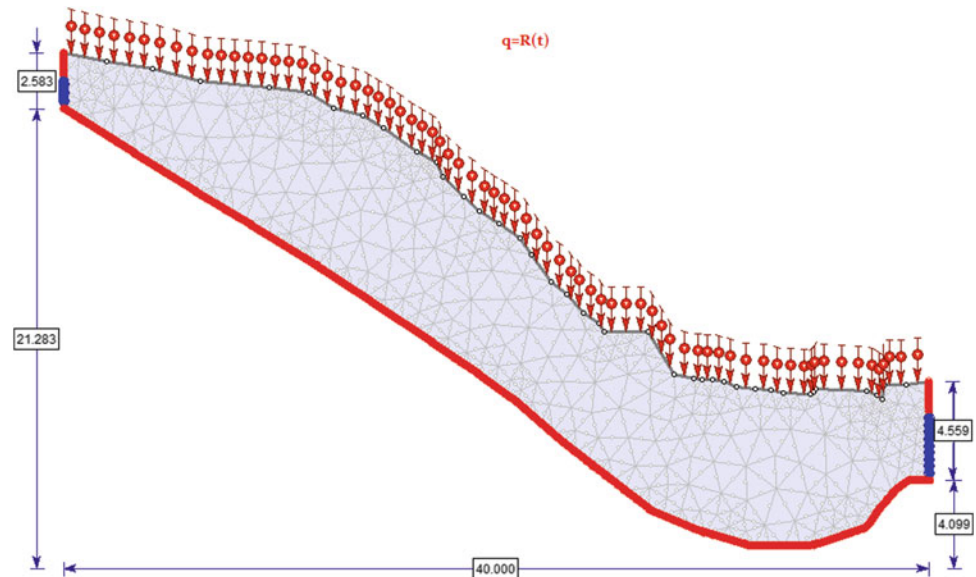
For the slope of Dafnoula village in this paper, both a nonlinear FEM analysis along with the application of the SSR method (Griffiths DV and Lane PA) and a transient nonlinear FEM analysis of the seepage flow is performed in order to define the stability of the slope before the medium rainfall phenomenon and its impact on the slope's stability after occurring. The boundary conditions applied for the seepage analysis are:

1. Rainfall infiltration on the slope's free surface (inflowing flux based on the rainfall data obtained): $q = 1.25 \times 10^{-6}$ m/s for a duration of 60 h.
2. Constant total heads (H_1) and (H_2) are applied on the mantle's left and right boundary respectively with the values of 50.6 m and 33.2 m respectively.
3. Both the bottom boundary of the mantle, which represents the contact between the mantle and the flysch, and the boundaries over the groundwater table are considered impervious.
4. The permeability of the clay loam soil mantle, which is equal to 7.25×10^{-7} m/s

The soil mantle's seepage model developed for the nonlinear FEA is presented in Fig. 2

We apply a transient FEM analysis for the seepage flow within the slope's disintegration mantle using 632 quadratic triangular elements for a constant period of 60 h. From the seepage analysis we obtain the following results both for the pore pressure distribution and for the change of the matric suction (Figs. 3, 4, 5, 6).

Fig. 2 Seepage model for the nonlinear FEM analysis of the soil mantle slope. The finite element mesh consists of 632 quadratic triangular elements and 1,415 nodes



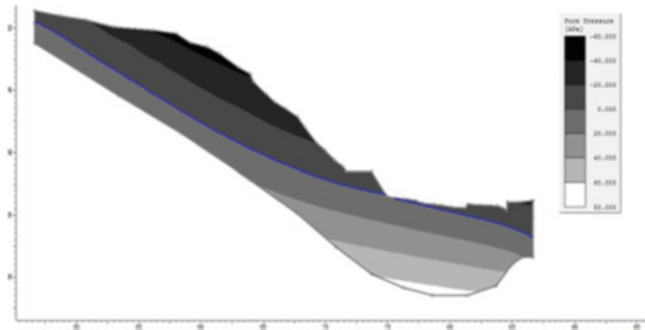


Fig. 3 Pore pressure distribution within the slope during the initial conditions

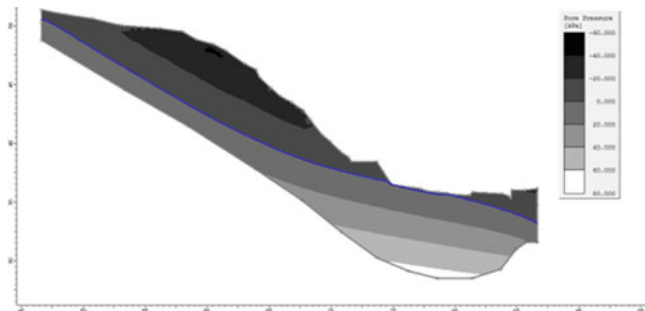


Fig. 4 Pore pressure distribution within the slope in the first 24 h of medium constant rainfall

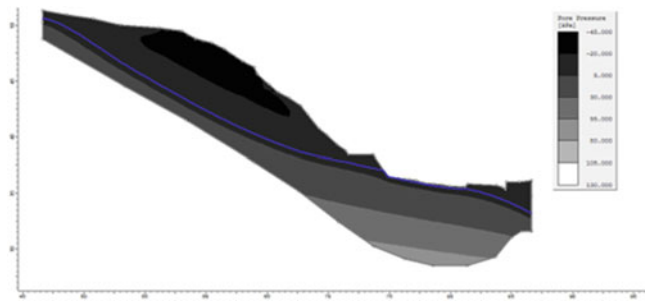


Fig. 5 Pore pressure distribution within the slope in the next 24 h (48 h of medium constant rainfall)

After obtaining the results from the seepage analysis, a FEM analysis for the elastoplastic model is applied for each state respectively. The strength parameters obtained by laboratory tests are described in Table 7.

By also taking into account the forces generated both by the loads due to the structures existing on the head of the slope (house and a warehouse) which is equal to 100 kN/m² and by the weight of the slope, as well as that the flow is taken as a non-associated flow (dilation angle $\psi = 0$), we obtain the following results for each time-step respectively, starting from the study of the slope's behavior under dry conditions (with the accuracy of two decimals) (Figs. 7, 8, 9, 10, 11).

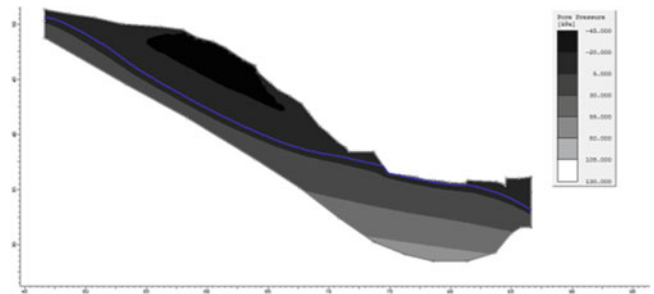


Fig. 6 Pore pressure distribution within the slope in the next 36 h (60 h of medium constant rainfall)

Table 7 Mechanical parameters used for both the numerical analysis (FEM) and the Limit Equilibrium Method

| Parameters | Value |
|-------------------------------|----------|
| C_{resid} (kPa) | 26.0 |
| Φ_{resid} (°) | 15.0 |
| E (kPa) | 17,000.0 |
| ν | 0.3 |
| γ (kN/m ³) | 17.0 |
| Ψ | 0.0 |

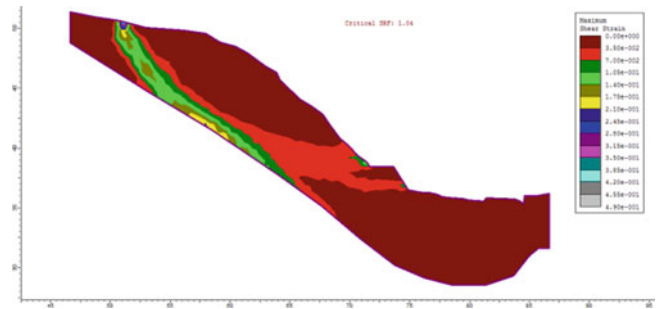


Fig. 7 Failure surface under dry conditions. The critical SRF is 1.04, thus indicating that the slope is already in a dangerous state without any fluid–solid interaction

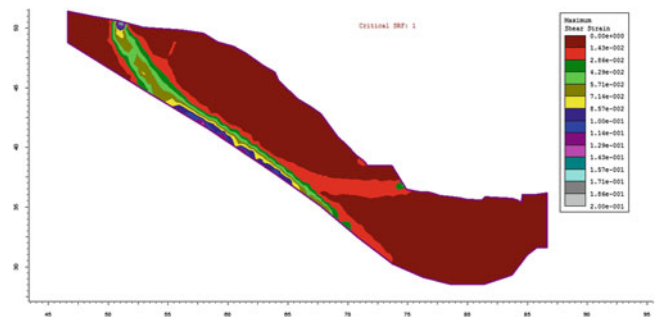


Fig. 8 Failure surface by taking account of both the effective stresses and the pore pressures generated during the initial conditions. The critical SRF is 1.00

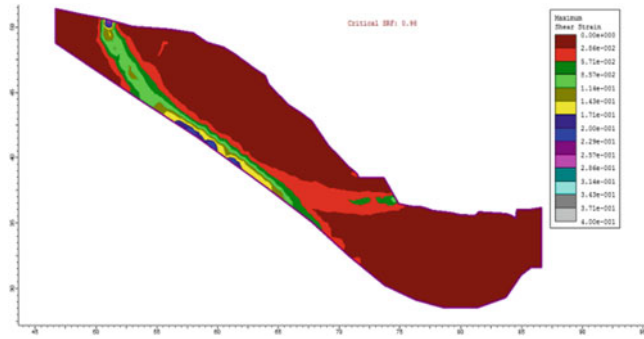


Fig. 9 Failure surface by taking account of both the effective stresses and the pore pressures generated in the first 24 h. The critical SRF is 0.98

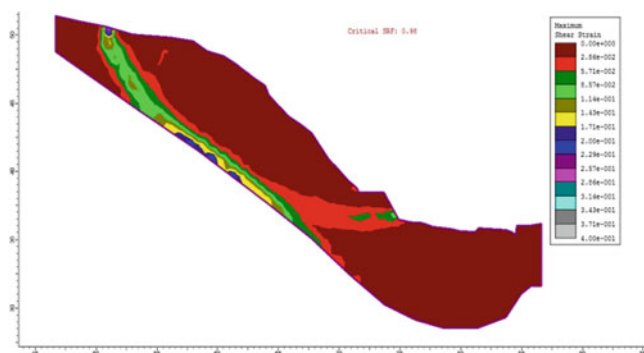


Fig. 10 Failure surface by taking account of both the effective stresses and the pore pressures generated in the next 24 h (totally 48 h). The critical SRF is again 0.98

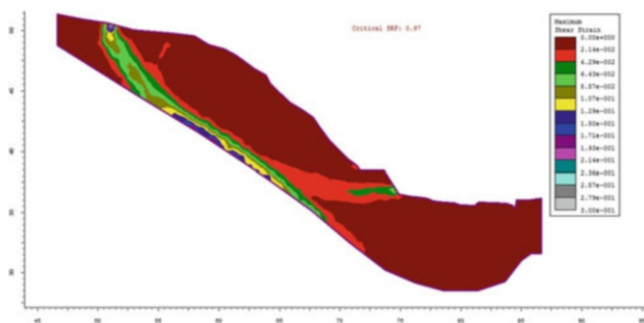


Fig. 11 Failure surface by taking account both the effective stresses and the pore pressures generated in the next 36 h (totally 60 h). The critical SRF is 0.97

Study of the Landslide with the Use of Limit Equilibrium Methods

The study area is registered, according to the Greek Seismic Code (OASP 2003), in a zone II seismic hazard area, wherein the horizontal seismic acceleration factor is

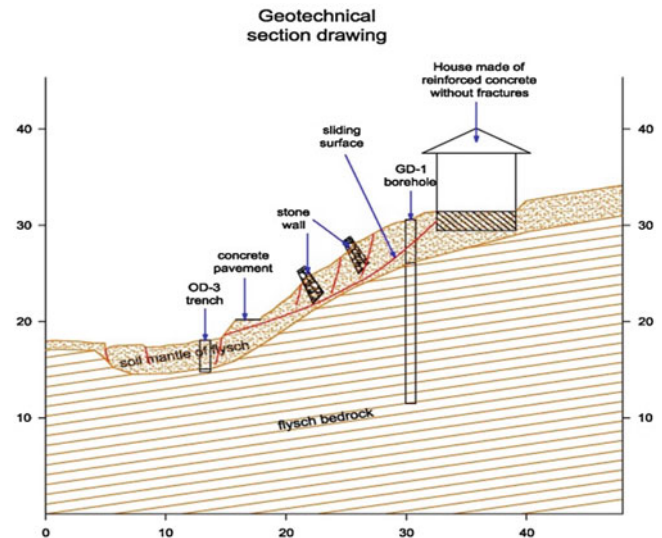


Fig. 12 Geotechnical section drawing, showing the status of sliding slope as it looks after the last landslide

$a = 0.24$ g, and the vertical component equals $0.30 \times a = 0.30 \times 0.24 = 0.07$ g. Besides performing a FEM slope stability analysis, we also conducted a LEM analysis by using the software LARIX-5S under the DIN 1054 Geotechnical Standard. The slope status thus formed after the onset of the landslide is that shown in the following sketch geotechnical section (Fig. 12).

The assumptions we made for solving the stability of the slope are the following:

- Horizontal seismic acceleration coefficient $a_h = 0.24$ g
- Vertical component of seismic acceleration is $a_v = 0.07$ g = 0.24 g
- The geotechnical formations involved in the structure of the slope are two: (a) The overlying disintegration mantle of flysch and (b) the underlying rocky formation of flysch belonging to “the Ionian geotectonic zone”. The distinction was based on visual field observations, and the evaluation of research trenches and a sampling borehole that were executed in the studied area. The separated formations and their geotechnical characteristics, used to solve the slope stability problem and the retaining wall are given in Table 7.

Based on the above assumptions, an analysis with the Key limit equilibrium method (as referred by Chowdhury R, Flentje P, Bhattacharya) was conducted, under the DIN 1054 Geotechnical Standard, which provided us with a minimum safety factor of the slope equal to 0.85 and with a radius of $R = 20$ m. The circle that simulates the situation formed after the onset of the landslide is given in Fig. 13.

The assumptions that we took into consideration for the dimensioning of the retaining wall are:

- The retained slope is considered inclined with a constant inclination (average slope gradient) of 15° .

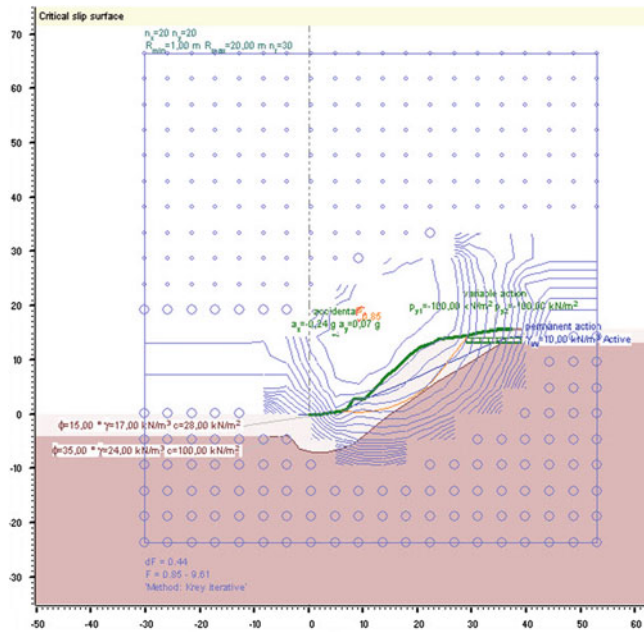


Fig. 13 Sketch of the geotechnical cross section showing the result of slope stability analysis and the slip surface by using the LARIX-5S software. The safety factor is 0.85

- To solve the retaining wall we supposed that it will withstand an open excavation of about 4.5 m. This assumption was made in order to anticipate future movements of soil mass in front of the wall.
- The level of groundwater, estimated in 2.0 m depth towards the upstream section and 4.5 m within the displaced soil materials, downstream of the retaining wall.
- The solution assumed non-intersecting piles of 0.80 m diameter, having axial distances of 2.00 m.
- The analysis for the retaining wall was made with the programs LARIX-5G, WALL and WALL DIMENSIONING.

Study and Suggestions for Remedial Measures for the Landslide of Dafnoula Hill

To protect the slope against future reactivated landslides, the following measures are proposed, based on the Eurocode 2 standard design analysis performed above:

1. Construction of a retaining wall, comprising 35 800-mm diameter vertical with an axial distance between adjacent columns of 2 m and length of 12 m for each pile. The reinforcement of each pile will comprise 20 22-mm diameter steel rods and round stirrups $\Phi 10/10$ cm as illustrated in Fig. 14:

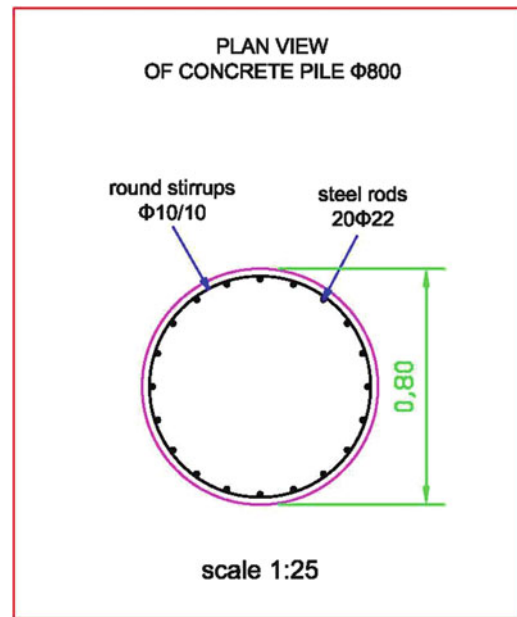


Fig. 14 Plan view of concrete pile $\Phi 800$, with 20 $\Phi 22$ steel rods and round stirrups $\Phi 10/10$

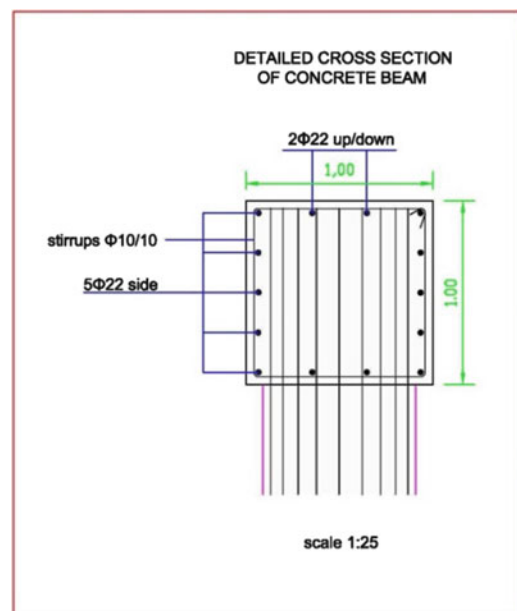


Fig. 15 Detailed cross section of concrete beam and plan view of concrete pile

2. Above the piles a connecting beam will be constructed with dimensions 1.00 m \times 1.00 m and reinforcement as shown in Fig. 15:
The plan view of the two adjacent piles is illustrated in Fig. 16.
3. Above the retaining wall the in situ soil will be replaced with crushed stones and, geogrid and geotextile will be

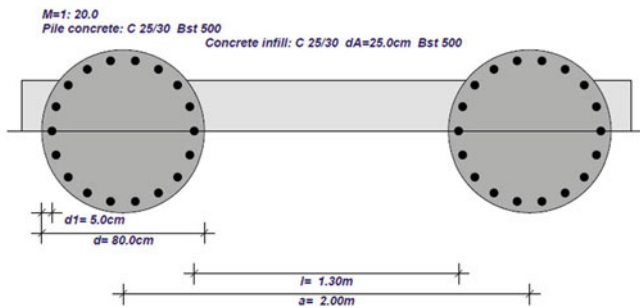


Fig. 16 Plan view of two adjacent piles

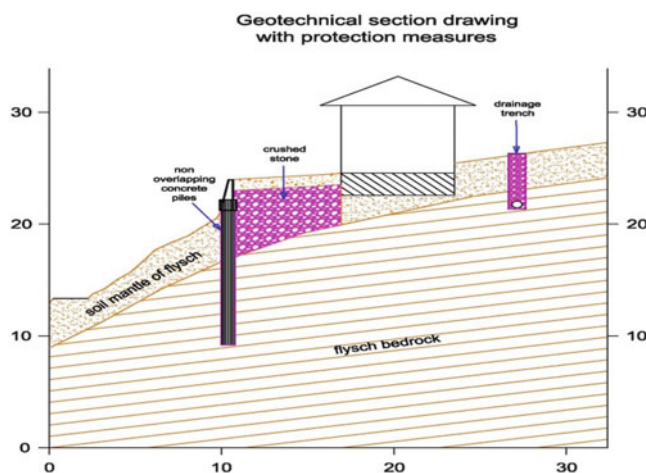


Fig. 17 Geotechnical section drawing, with protection measures



Fig. 18 Satellite image of the studied area, showing the proposed retaining wall and drainage trench, for the protection of the houses above the landslide

placed on the top for the infiltration of water. Above that the top soil will be used for planting grass, small bushes or plants.

- Upstream of the houses a drainage trench will be constructed with a depth of 5 m, in terms of reaching the impermeable flysch bedrock. In the bottom of the trench a perforated pipe will be placed and the entire trench will be covered with rounded gravels to obtain high permeability. The geotechnical section drawing, along with the protective measures, is given in Fig. 17.

A satellite image of the area of Dafnoula village is illustrated in Fig. 18 along with the final design of the remedial measures:

Conclusions

The landslide studied in this paper is situated in the northwestern part of Greece in a small village of Prefecture of Epirus called Dafnoula and occurred after approximately 60 h of constant medium rainfall during the December of 2010. The formation that underwent failure was the disintegration mantle, of the flysch, whereas the flysch bedrock didn't show any sign of displacement. The flysch's disintegration mantle does not have a permanent aquifer, but instead a temporary one was developed within the soil mantle which was already in a dangerous state. The landslide caused a wide range of damage, including the collapse of a house, a warehouse, and an artificial embankment-terrace and its concrete retaining wall. At the foot of the landslide there was a backfilling of the road below and the complete destruction of its pavement. From the slope stability analysis it was found that the safety factor under fluid–solid coupling dropped gradually from 1.04 to 0.97 (critical safety factor of failure state), while from the stability analysis under the DIN 1054 Geotechnical Standard the slip circle has a radius of approximately 20 m and a safety factor of instability equal to 0.85. For the protection of the houses above the head of the landslide several remedial measures were proposed, including the construction of a retaining wall made of concrete piles, the construction of a drainage trench above all the nearby houses and, finally, the replacement of the in-situ soil mantle with crushed stone.

References

- Chowdhury R, Flentje P, Bhattacharya G (2009) Geotechnical slope analysis. CRC Press Publishing. ISBN: 9780415469746
- Exadaktylos G, Asimidis V (AMIREG) (2004) Numerical solution of 1D parabolic PDEs by using an isoparametric finite element method with examples from Rock Engineering, Hania 2004, Greece, pp 23–30

- Griffiths DV, Lane PA (1999) Slope stability analysis by finite elements. *Geotechnique* 49:387–403
- Li J, Liu X, Jiang Z (2009) Coupled numerical simulation of slope stability with unsaturated soil under rainfall condition. 2009 International Forum on Porous Flow and Applications, Wuhan, China, ISBN-10: 0-9806057-0-9
- OASP (2000, 2003 revision) Hellenic Seismic regulation. OASP Publishing, pp 173–183
- Potts DM, Zdravkovic L (1999) Finite element analysis in geotechnical engineering. Theory and application, vol 1. Thomas Telford Publishing. ISBN: 0727727532



Seismic Damage Assessment of Gravity Retaining Walls Based on Grey Correlation and Fuzzy Mathematics

Zheng Da and Liang Lidan

Abstract

Strong earthquake shaking in the Longmen Mountain area in 2008 led to severe damage to many retaining structures. How to assess damaged retaining walls in the earthquake zone was a problem that required an urgent solution. This paper summarizes five types of retaining-wall failure modes through analysis of earthquake damage in the research area, including sliding failure, settlement failure, toppling failure, material failure, and overtopping failure. Then the factors influencing seismic safety evaluations were qualitatively analysed and classified on the basis of comprehensive principles, important principles and scientific principles. Along with the failure modes of retaining walls, we also examined the critical factors and some general factors. We took a value of 60 % damage to be a critical factor, and the general factors divided into two levels, and 10 indexes: the sliding distance, the settlement depth, the inclination angle, the number of cracks, the ratio of crack length and the retaining wall length, the ratio of crack depth and the retaining wall thickness, the crack width, the dislocation distance, the range of retaining wall collapse, and the coverage of rock and soil on the retaining wall. The seismic safety evaluation system for retaining walls was built by grey correlation analysis and fuzzy mathematic theory. Its use can allow prevention to replace repair and can aid post-earthquake recovery and reconstruction.

Keywords

Retaining wall • Seismic damage evaluation • Grey correlation • Fuzzy mathematics

Introduction

The Longmen Mountain region is located in the transition zone between the Sichuan Basin and the Qinghai-Tibet Plateau and has a complex geological structure and fracture development. It is a typical representative of hazardous mountain areas in China with belts with strong seismic activity. In the 2008 Wenchuan “5.12” Earthquake, the strong seismic shaking led to severe damage to a large

number of built slope-retaining structures, significantly reducing their safety and durability. The survey shows that there were 348 retaining walls with varying degrees of damage in the worst-hit disaster area, of which the destruction of gravity retaining walls accounted for 97.1 % of the total amount of destroyed retaining walls. How to quickly and efficiently identify retaining wall damage, and conduct a comprehensive assessment of their security became a technical difficulty to be solved during the recovery and reconstruction process.

Safety assessment of retaining structural engineering began in the 1970s when the Norwegian scholar Kaare Høeg adopted reliability theory to study the safety degree of structures but did not develop a system of assessment methods. In China, Du Yongfeng et al. (2008) introduced a

Z. Da (✉) • L. Lidan
State Key Laboratory of Geohazard Prevention and Geoenvironment Protection, Chengdu University of Technology, Chengdu, Sichuan 610059, China
e-mail: zhengda@cdu.cn; 779851029@qq.com

Table 1 Failure modes of retaining walls in the Longmen Mountain region

| Failure mode | Failure mechanism | Deformation characteristics |
|-----------------------|--|--|
| Sliding failure | Ground motion results in increasing earth pressure on the back of the wall; the lack of lateral resistance of the wall leads to the overall wall slip failure | The overall wall slips forward with multi-longitudinal cracks appeared along the back of the wall, also the leading edge of surface uplifts |
| Sedimentation failure | The earthquake causes foundation instability, and the insufficient vertical bearing capacity results in subsidence of the whole wall. Usually it occurs in the soil foundation | Partial or total wall subsidence may occur, with vertical coalescence cracks, and squeezing crushing may occur in the bottom of the wall |
| Overturning damage | The increase of seismic ground acceleration leads to the increase of ground inclination moment, therefore results in the rotation about the toe of the retaining wall due to insufficient torque | The horizontal displacement of the top of the wall is greater than the bottom, the wall deforms on the basis of rotation. Crushing squeezes are prone to appear from the bottom wall |
| Wall body damage | The back wall earth pressure exceeds the ultimate bearing capacity of the wall material, so cracks, bulging and even partial collapse of the surface of wall occurs | Shear failure of wall (transverse cracks, longitudinal cracks), extrusion deformation and failure (panel off, wall bulging), partial collapse |
| Sliding failure | Under seismic shaking, the wall back slope has a landslide or collapse that leads to rock (soil) overtopping the retaining wall. Since the role of a retaining wall is to support (retain) the rock to maintain its stability, even if the retaining wall structure itself does not suffer radical damage, this is still regarded as retaining wall damage | Wall back slope landslide or avalanche occurs, the rock (soil) bodies are piled onto the road across the top of the wall and may even cover wall surfaces |

checking point method from the first-order second moment method for reliability analysis and failure probability, but its calculation only took sliding instability and overturning instability into consideration. Liu Fang et al. (2005) adopted a combination of probability theory and fuzzy mathematics to analyse the stability, but only considered the impact of the bottom friction coefficient. For existing gravity retaining walls, there are still no relevant reports, particularly for safety assessment for retaining walls damaged by seismic activity.

In 1965, L.A. Zadeh put forward the concept of fuzzy mathematics, and the fuzzy comprehensive evaluation method has been widely used for typical slope stability evaluation since then. This also provided possibilities for the application of fuzzy comprehensive evaluation methods in safety assessment for structural damage after earthquakes. In 1982, Professor Deng Julong from Huazhong University of Science and Technology founded the grey system theory, which is widely used in construction structural damage assessment, but it has not yet been applied in damage assessment for retaining walls following earthquakes. Therefore, this paper uses a combination of grey relational analysis and a fuzzy comprehensive evaluation method to build a mathematical model and conduct a comprehensive assessment of the degree of safety of post-earthquake retaining walls in the Longmen Mountain seismic zone. It also provides a reliable basis for the seismic damage assessment of retaining walls in other zones.

Seismic Failure Modes for Retaining Walls

According to the statistical data for seismic damage of geological hazard retaining engineering in the study area, the destruction of gravity retaining walls accounts for 97.1 %

of the total amount of structural damage, with wall heights mainly in the 2–8 m range, and occurring mostly in the soil foundation. The main seismic damage features in retaining walls include collapse, cut, tilt, slip, deformation cracking on surface, slope collapses and burying, wall subsidence and so on. The main retaining wall failure modes that we found in the survey are listed in Table 1.

Based on site surveys of retaining wall seismic damage and the results of early damage classifications, as well as damage from the Wenchuan earthquake, retaining-wall seismic damage can be divided into five grades: basically undamaged, slight damage, moderate damage, severe damage and destruction (see Table 2).

Construction of a Retaining Wall Safety Evaluation

Principle of Index Construction

In constructing a seismic damage index, the first step is to conduct a qualitative analysis and classification of the factors affecting seismic damage evaluation. The principles of comprehensiveness and importance, as well as scientific principles, need to be taken into consideration.

1. Principle of comprehensiveness: the safety evaluation of a retaining wall should fully reflect the damage to the retaining wall itself after seismic shaking, and should be considered by selecting from the list of failure modes of retaining walls.
2. The principle of importance: the assessment index of a retaining wall should have primary and secondary differences. When a retaining wall suffers from a strong earthquake, not only a main failure mode emerges, but

Table 2 Seismic damage level of retaining walls in the Longmen Mountain region

| Damage degrees | Assessment result |
|-----------------|--|
| Undamage | There are no seismic damage characteristics or apparent deformation and destruction of the surface of retaining wall, the retaining wall does not need to repair and can continue to be used |
| Slight damage | There is no obvious retaining wall damage or loss of retaining function. The seismic damage does not need repair and can be used temporarily |
| Moderate damage | The retaining wall damage is obvious, with significant wall cracks, dumping or displacement which requires partial repair work |
| Severe damage | The seismic damage of retaining wall is obvious, with significant wall cracks, dumping or large displacement which requires substantial repair work |
| Destruction | The seismic damage of retaining wall is severe, with the loss of retaining function. The retaining wall needs to be re-built |

multi-mode combinations should appear. Because of the extent of damage, some failure modes are fatal to the retaining wall's function, such as a direct collapse of the retaining wall. However, some damage is not as important, such as tiny cracks in the retaining wall. The scores for damage of lesser importance can be set lower to ensure the reasonableness of indices.

3. Scientific principles: the establishment of safety evaluations for retaining walls must be systematic, logical and with no duplication of information.

Index Screening

Since retaining walls are prevention engineering measures built on the surface, their seismic damage characteristics can be preliminarily assessed by eye. Then a general method of analysis is further applied. On the basis of following the principles of index construction, the failure modes of different retaining walls should be analysed to extract the appropriate evaluation factors. For example, for the sliding failure type, in which deformation is characterized by the whole wall slipping forward, the sliding distance can be the indicating factor to evaluate the overall degree of sliding. Moreover, multiple longitudinal cracks will appear in such a failure mode, with indentations and cracks appearing on the back of the wall and bulges on the front surface. For longitudinal cracks, parameters such as crack width, crack depth, etc. can be used as index factors to assess the degree of damage, while indentations and cracks on the back of wall, as well as bulges on the surface, can use indentation depth, and width, bulge height, and area and so on as evaluation factors. Thus, by analysing the retaining-wall seismic damage mode, one can obtain a number of damage assessment factors. However, the index factors extracted from varying failure modes have several disadvantages, such as information overlap, which requires qualitative analysis and classification so that the indices can be matched.

First screen out the factors that play a decisive role; if any of these factors exist, the retaining wall damage can be

considered very serious as the wall has lost its retaining function and requires a re-build. Generally speaking, such factors have a "one-vote veto" power, therefore they are known as critical factors. Through field investigation for different failure types of retaining wall, it can determine that no matter which destructive type it is, the degree of seismic damage should be an important index of the safety assessment, especially for the collapsing, burying or smashing seismic damages which should be the primary evaluation index. If the retaining wall seismic damage is determined to be over 60 % of the entire prevention engineering scope, then the retaining wall can be directly defined as destroyed and it needs no other index evaluation. If the seismic damage is more limited, then relevant quantitative indices need to be further evaluated.

After the critical factors have been determined, the remaining general factors need to be screened and determined. It is necessary to ensure that the information reflects the overall index without overestimation. Moreover, some factors are insensitive to changes in evaluation, which means that their importance is extremely low, therefore they are not included as an evaluation index. For example, the impact of depth and width of grooves on retaining wall damage are minimal, therefore may not be classified as an evaluation index. Thus, the classification and grading of all indices determines the damage level reflecting the major degree of damage to the retaining wall; these respectively are sliding degree, sedimentation degree, tilt degree, crack degree and damage degree. The determined primary indices include sliding degree, sedimentation degree, tilt degree, and crack degree of retaining wall as well as five secondary degrees including number of cracks, length, width and depth of cracks and relative dislocation distance of cracks. The destruction degree includes two secondary index as collapsing scope of retaining wall and covering scope of retaining wall by rock (soil) overtopping damage on the back of wall.

In addition, it can be seen from the statistics of seismic damage that there is no necessary relationship between the use of different materials and the damage degree in an earthquake. As long as the quality of construction is under

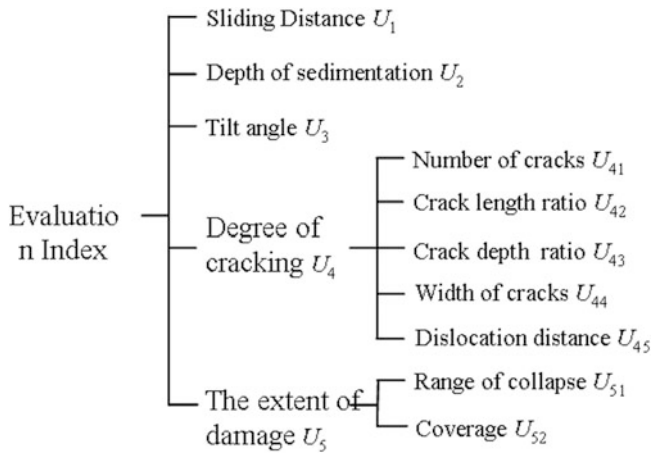


Fig. 1 Evaluation indices of retaining wall in Longmen Mountain region

reasonable control, just select an appropriate retaining wall material according to the height and importance, as well as other factors of the wall. Therefore in the seismic evaluation of retaining walls, the material is not considered in assessing the damage index.

The general index of retaining wall safety evaluation obtained from comprehensive analysis is broadly divided into two levels and 10 indexes in total. The extracted corresponding damage evaluation index is shown in Fig. 1.

Safety Assessment Model of Retaining Wall

Grey Correlation Analysis

Grey correlation analysis is a means of analysing things by establishing their internal relations, and can quantitatively analyse the different factors influencing the development of a system, calculating the weight through correlation (which is more objective than the expert-scoring method). The impact of factors on retaining wall damage can be analysed through correlation of each factor, so as to determine the weight of its importance and value.

(1) Determining the reference sequence

Damage degree D is selected for a retaining wall from the correlation analysis in the safety assessment of the retaining wall, which can comprehensively reflect the damage state of the retaining wall, also all evaluation indices have corresponding discrimination values, while the determination of damage degree D is calculated by the factor superposition integrated discrimination method:

$$Y = \sum_{j=1}^N X_j^i / N$$

Where N is the number of discriminating factor. The larger the value of N , the higher discrimination accuracy. But in retaining-wall seismic damage phenomena, there are not always 10 discriminating factors available. When there are more than 6 discriminating factors, this method can be applied, which determines the reference sequence:

$$x_0 = (x_0(1), x_0(2), \dots, x_0(n))$$

(2) Determine the comparative sequence

Apply index sequence to record various factors of retaining wall, $x_i(k)$ refers to the observational data of the k th factor, where k is the index number:

$$x_0 = (x_i(1), x_i(2), \dots, x_i(n))$$

Because of the different physical meaning of each index, the dimensions of the data are not all the same. The raw data needs to be processed into dimensionless numbers by normalization. Select the interval value operator D , $X_i D$ is the interval value image of X_i under the interval value operator D , thereby getting the sequence:

$$X_i D = (x_i(1)d, x_i(2)d, \dots, x_i(n)d)$$

Where:

$$x_i(k)d = \frac{x_i(k) - \min_k x_i(k)}{\max_k x_i(k) - \min_k x_i(k)}$$

$$k = 1, 2, \dots, n$$

(3) Correlation calculation

After data processing, the correlation coefficient sequence is obtained through a correlation coefficient calculation formula. The correlation coefficient calculation formula is:

$$r_i(x_0(k), x_i(k)) = \frac{\min_i \min_k |x_0(k) - x_i(k)| + \xi \max_i \max_k |x_0(k) - x_i(k)|}{|\min_i \min_k |x_0(k) - x_i(k)| + \xi \max_i \max_k |x_0(k) - x_i(k)|} \quad \xi(0, 1)$$

Correlation of two comparative sequences can be represented by the mean value of correlation coefficient between two sequences, calculated as:

$$r_{oi} = \frac{1}{n} \sum_{k=1}^n r_{oi}(k)$$

(4) Correlation sorting

Compare the correlations of various sequences to a reference correlation, and arrange in order of size to

Table 3 Correlation sorting

| Evaluation index | Correlation | Weight | Sorting |
|-----------------------------------|-------------|--------|---------|
| Slippage distance U_1 | 0.500 | 0.078 | 9 |
| Sedimentation depth U_2 | 0.480 | 0.075 | 10 |
| Tilt angle U_3 | 0.630 | 0.098 | 5 |
| The number of cracks U_{41} | 0.717 | 0.112 | 4 |
| Crack length ratio U_{42} | 0.611 | 0.095 | 6 |
| Crack depth ratio U_{43} | 0.833 | 0.130 | 1 |
| Crack width U_{44} | 0.771 | 0.120 | 2 |
| The dislocation distance U_{45} | 0.755 | 0.118 | 3 |
| Scope of collapse U_{51} | 0.583 | 0.091 | 7 |
| Coverage U_{52} | 0.542 | 0.084 | 8 |

form a correlation order. The correlation order directly reflects the correlation order of various correlations on a reference sequence; therefore the weight of each evaluation index is obtained (Table 3).

Fuzzy Comprehensive Assessment System

The fuzzy comprehensive evaluation method is the application of fuzzy transformation principles to consider various factors related with the things to be evaluated, to quantify the ill-defined factors which are difficult to quantify. Multiple factors are applied to conduct a comprehensive evaluation for the rank condition of things to be evaluated.

According to the fuzzy comprehensive evaluation theory evaluation model:

1. The theory set $O = \{\text{basically complete, slight damage, moderate damage, severe damage, destruction}\}$;
2. Factor set $U = \{\text{slippage distance, sedimentation depth, tilt angle, the number of cracks, crack length ratio, crack depth ratio, crack width, the dislocation distance, scope of collapse, coverage}\}$;
3. Weight set $W = \{0.078, 0.075, 0.098, 0.112, 0.095, 0.130, 0.120, 0.118, 0.091, 0.084\}$;
4. Determine the fuzzy membership degree of each factor in order to establish single factor evaluation matrix wall R for each retaining wall:

$$R = \begin{bmatrix} R_1 \\ R_2 \\ \dots \\ R_{10} \end{bmatrix} = \begin{bmatrix} r_{11} & r_{12} & \dots & r_{15} \\ r_{21} & r_{22} & \dots & r_{25} \\ \dots & \dots & \dots & \dots \\ r_{101} & r_{102} & \dots & r_{105} \end{bmatrix}$$

5. Calculate evaluation results B according to fuzzy weight set W and the evaluation matrix R:

$$B = W * R = (b_1, b_2, b_3, b_4, b_5)$$

Seismic Damage Assessment of a Typical Retaining Wall

The selected example of typical damage is located in Qinggang Village, Mao County-Beichuan New County (Longitudinal and Latitudinal: N31:51:22.3, E104:16:49.3, elevation = 854 m); it is a cast-in-site concrete retaining wall. The height of retaining wall is 1.5 m, width 4 m, and length about 100 m. In the middle of the retaining wall, a section of wall has clearly visible cracking which has about 20 cm outward displacement with a tilt angle of about 3°. The right longitudinal crack opens 5 cm with depth of 20 cm, and another transverse crack extends about 4 m with a width of 1 cm.

First carry out the sensitivity factor analysis. It is known that at the seismic damage point, its scope is about 5 %, less than 60 %, the following factor evaluation can be conducted. According to the site investigation and analysis of retaining wall damage characteristic values, the retaining evaluation matrix is:

$$R = \begin{vmatrix} 1 & 0 & 0 & 0 & 0 \\ 1 & 0 & 0 & 0 & 0 \\ 0 & 1 & 0 & 0 & 0 \\ 0 & 0.85 & 0.15 & 0 & 0 \\ 0 & 0 & 0.2 & 0.7 & 0.1 \\ 0 & 0.85 & 0.15 & 0 & 0 \\ 0.5 & 0.5 & 0 & 0 & 0 \\ 0 & 0 & 0.5 & 0.5 & 0 \\ 0.7 & 0.3 & 0 & 0 & 0 \\ 0.7 & 0.3 & 0 & 0 & 0 \end{vmatrix}$$

Consider the role of various factors on the prevention and treatment of seismic damage prevention engineering, combined with the weight of each factor given previously, the formed fuzzy vector—set of weights W, the evaluation results of W and R on seismic damage prevention engineering is:

$$B = W * R = \{0.3355, 0.4162, 0.1143, 0.1255, 0.0095\}$$

Finally, according to the principle of maximum degree of membership:

$$b_i = \max_{1 \leq k \leq 5} \{b_j\} = b_2 = 0.4162$$

It can be determined that the retaining wall has minor damage which does not need to repair and can use temporarily. However, close attention should be paid to during using to know whether the damage is further exacerbated. If there

is, then re-evaluation should be conducted to determine the degree of injury.

Conclusion

Through the analysis of retaining wall seismic damage in the study area, sum up the main failure modes of retaining wall include five categories as sliding failure, sedimentation failure, overturning damage, wall damage and overtopping destruction, and analyse failure mechanism and deformation characteristics of each failure mode.

Divide the retaining wall seismic damage in Longmen Mountain area into five levels in accordance with the retaining wall seismic damage conditions coupled with the reference of early results of early seismic damage grading, which are respectively basically complete, slight damage, moderate damage, damage and destruction, and conduct relevant description according to the evaluation results of each damage levels and initially determine its subsequent processing.

Conduct qualitative analysis and classification on the factors affecting seismic damage evaluation in accordance with comprehensiveness, importance as well as scientific principles, and comprehensively analyse the sensitivity factors and general factors of obtained safety assessment of retaining wall. Regard 60 % of the damage range as sensitive factor of retaining wall assessment, and general factors are divided into two levels with 10 indexes in total, including: sliding distance, the depth of subsidence, tilt angle, the number of cracks, crack length ratio, crack depth ratio, crack width, the dislocation distance, collapse range, coverage.

The retaining wall seismic damage assessment system proposed in this paper is based on the field investigation of seismic damage point of Longmen Mountain, adopts the grey correlation analysis to extract rules and quantify indexes through the fuzzy comprehensive evaluation method. Construct mathematical models to carry out safety assessment for retaining wall seismic damage.

The retaining wall seismic damage evaluation criteria and weights may be different, but the constructing method has universal applicability. Therefore, in practice, assessment methods can be corrected according to the specific circumstances, so as to change the post-processing into previously prevention, analyse the safety situation of retaining wall structure and conduct a comprehensive assessment of their degree of danger in order to prompt the authorities to improve such situation so as to achieve the required safety requirements.

Acknowledgments This research is financially supported by the National Natural Science Foundation of China (No. 41102191), the State Key Laboratory of Geohazard Prevention and Geoenvironment Protection Independent Research Program (No. SKLGP2011Z019) and “Twelve Five-Year” National Science and Technology Support Program of China (Key technology research about slope control in the Longmen Mountain seismic belt).

References

- Du Y, Yu Y, Li H (2008) Analysis of reliability of structural systems for stability of gravity retaining walls. *Chin J Geotech Eng* 30 (3):349–353
- Duncheng Y (2003) Retaining wall seismic failure analysis. *Eng J Wuhan Univ* 36(2):82–87
- Ji S, Tang Y, Hu D et al (2009) Analysis of typical seismic damages of highways in Wenchuan Earthquake-induced hazard areas in Sichuan Province. *Chin J Rock Mech Eng* 28(6):1250–1260
- Liu F, He B, Gao Q (2005) Analysis of fuzzy reliability for retaining wall structure. *Geotech Eng Tech* 19(5):217–219
- Richard R, Elms DG (1979) Seismic behavior of gravity retaining walls. *J Geotech Eng Div ASCE* 105(4):449–464
- Wan G (2005) Safety assessment of existing retaining walls. *Subgr Eng* 35(5):24–26
- Xu W, Jiang Z, Shi A (2003) Slope stability analysis using fuzzy sets theory. *Chin J Geotech Eng* 25(4):24–26
- Yu J, Wang X, Han S et al (2006) Adaptability appraisal for highway transportation based on weighted grey incidence degree. *J Highway Transport Res Develop* 23(5):75–78
- Zhou D, Zhang J, Tang Y (2010) Seismic damage analysis of road slopes in Wenchuan Earthquake. *Chin J Rock Mech Eng* 29 (3):565–576



Effectiveness of Hybrid Anchor Soil Nails in Stabilizing Slopes and Stability Assessment Based on Mechanics

M.J. Md. Noor, M.A. Saidin, and S.M. Tahir

Abstract

Soil nailing has been a well accepted technique for stabilizing slopes. It is particularly useful when there is a limited working area, for example on slopes along highways, where the system can be installed directly in the slope without any major earthworks. The nail shaft will tie down the potential sliding segment to the interior stable ground. Nevertheless there have been many failures in this system where creep movement of the shaft results in the loss of stabilizing friction. In passive soil nails the stabilizing effect is considered to come from the shear capacity of the nail shaft and thereby the shaft demands no initial tension force. On the other hand, for active soil nail systems, despite applying a tension force to the nail shaft, the concept of stabilizing is considered exactly as for the passive system. Apparently, based on effective stress concepts, whenever the nail shaft is subjected to tension force, the weak frontal zone will be pulled against the interior stable ground and this thereby increases the effective stress along the potential failure surface. In turn, the shear strength along the surface will be increased and thereby stabilize the slope. This is a more appropriate mechanical design and will be presented in this paper. An innovation to the conventional soil nail system is the application of hybrid anchor at the free end to provide passive pressure resistance to effectively hold down the frontal supporting wall. This involves a special drilling technique for the installation of hybrid anchors. Using this technique, creep is prevented and thus the tension in the nail shaft will provide a long-lasting effective stress along the potential failure surface and thereby effectively stabilize the slope. The design of the hybrid anchor and its in situ pullout behaviour, with and without grout will be presented.

Keywords

Soil nail • Shallow landslide • Rainfall-induced • Hybrid anchor • Effective stress

Introduction

Soil nailing was first developed as a system to improve the behaviour properties of an in situ soil mass by the inclusion of slender unstressed reinforcements as shown in Fig. 1 (Watkins and Powell 2007). The reinforcing effect is derived from the nail-soil interaction. This is a powerful method for slope stabilisation (Bruce and Jewell 1987). The zone in front of the potential slip plane tends to detach from the slope and is defined as the active zone, and the zone behind the potential slip plane remains intact and is defined as the

M.J. Md. Noor (✉)
Faculty of Civil Engineering, Institute for Infrastructure Engineering
and Sustainable Management, Universiti Teknologi MARA, Shah Alam,
Malaysia
e-mail: mohdjamaludinmdnoor@yahoo.com

M.A. Saidin • S.M. Tahir
BTS Engineering Sdn Bhd, Selangor, Malaysia

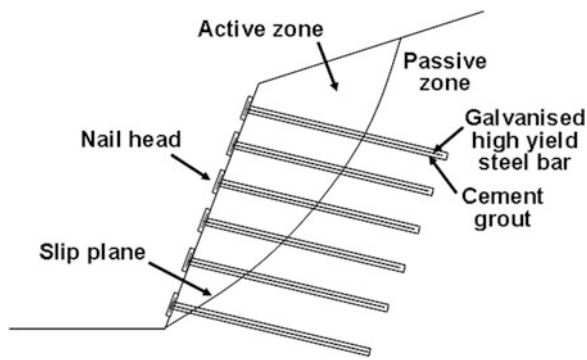


Fig. 1 Cross section of a soil nailed structure

passive zone. The failure can be in the form of the sliding of the active zone as a monolithic mass or the soil may move past the nail shaft.

In the former case the stability is provided by the shear stress exerted on the nail shaft at the potential failure plane. This provides additional shear capacity over the potential slip plane and acts to stabilise the slope. However in the latter case the shear capacity of the nail shaft has no contribution towards stabilisation since the soil just moves past the shaft.

The potential modes of failure in terms of internal instability are (1) tensile failure, which is the breakage of the reinforcement, or (2) slip of the reinforcement in the active zone, or (3) slip of the reinforcement in the passive zone. The soil nail system with the reinforcement unstressed is known as a passive system, and if the reinforcement is stressed it is known as an active system. In the passive system the resistance along the nail shaft is mobilised only when the frontal active zone starts to move.

Essentially the soil nail system consists of four types: (1) unstressed reinforcement without bearing plates (2) unstressed reinforcement with bearing plates (3) stressed reinforcement with bearing plates and (4) stressed reinforcement with bearing plates and structural surface cover, as shown in Fig. 2a, b, c and d respectively. The first and the second are not commonly used anymore but the third is commonly applied, while the fourth is beginning to gain popularity. There have been many slope failures in soil nail systems and how hybrid anchors can improve the inadequate existing system will be discussed.

Conventional Design Concepts and Failures in Soil Nail Systems

Soil nailing is thought to be a robust solution but then slope failure in this system is still inevitable. There is a need to look deeper into the mechanics in order to understand the problem. In the earlier design concept of soil nail, the stabilising effect of the nail is considered to come from the

extra shear stress of the nail shaft in addition to the shear stress of the soil along the potential slip plane. This is despite whether the nail is stressed or unstressed, i.e. irrespective of active and passive soil nails (Pappin 2007; Watkins and Powell 2007). Notably, the shear resistance of the nail shaft is very high since it comprises galvanised high tensile steel enclosed with cement grout with a composite diameter of 100 mm or 125 mm. In failures involving soil nails there has never been any case where the shaft has sheared off. Where most of them failed the active zone slipped down with the soil, moving past the nail shaft and leaving the shaft hanging down, as shown in Fig. 3. Apparently the nail shafts flex and thus cannot act as a dowel.

The shortcomings of the conventional design concept has been realised because of the many failures reported involving the conventional passive soil nail system. For example, a report by Pun and Shiu (2007) noted 31 cases of failures in Hong Kong from 1993 till 2007. Of these cases, 24 failures happened at completed slopes and 7 occurred at temporary slopes where the nail heads had not yet been constructed. The failure at the completed slopes is of shallow type, while the temporary slope failed on a bigger scale.

Note that the seven temporary slopes have no nail heads. This is a clear indication that the stabilisation, as in Fig. 2a, which is applying unstressed reinforcement without a bearing plate, has no effect on stabilising at all. The wetted frontal soil in the active zone cannot be held up by the friction between the nail shafts. Upon infiltration, where suction diminishes and apparent shear strength is lost, then the soil just flows past the nail shaft. On the other hand, for the failure in the 24 completed slopes with the nail heads where shallow failures had occurred, then the bearing plate must have already detached from the slope face. Then the system has reverted from that in Fig. 2b to that in Fig. 2a. By and large these two systems are not effective and should be avoided.

The soil nail system shown in Fig. 2c is a stressed reinforcement with independent bearing plates. In this case, the bearing plate is just pulling down the slope face at the individual points. The space between the bearing plates is subjected to erosion and if this happened close to the plate then soon the bearing plates will be left detached from the soil and the applied tension will be lost. And again this system will be reverted to the system in Fig. 2a, which is as if nothing has been done to improve stability. Some of the failures in the system, as in Fig. 2c, are shown in Fig. 4a, b, c, d, e.

Another shortcoming with the active soil nail system is the creep effect. Creep is the gradual movement of the nail shaft against the surrounding soil which causes the depletion of the applied tension to the shaft. In other words the nail shaft needs to be stressed periodically. Bear in mind that if the bearing plates have been concreted to form the nail heads, then how can the periodic stressing be done? This is another deficiency in the current system which surely needs to be corrected.

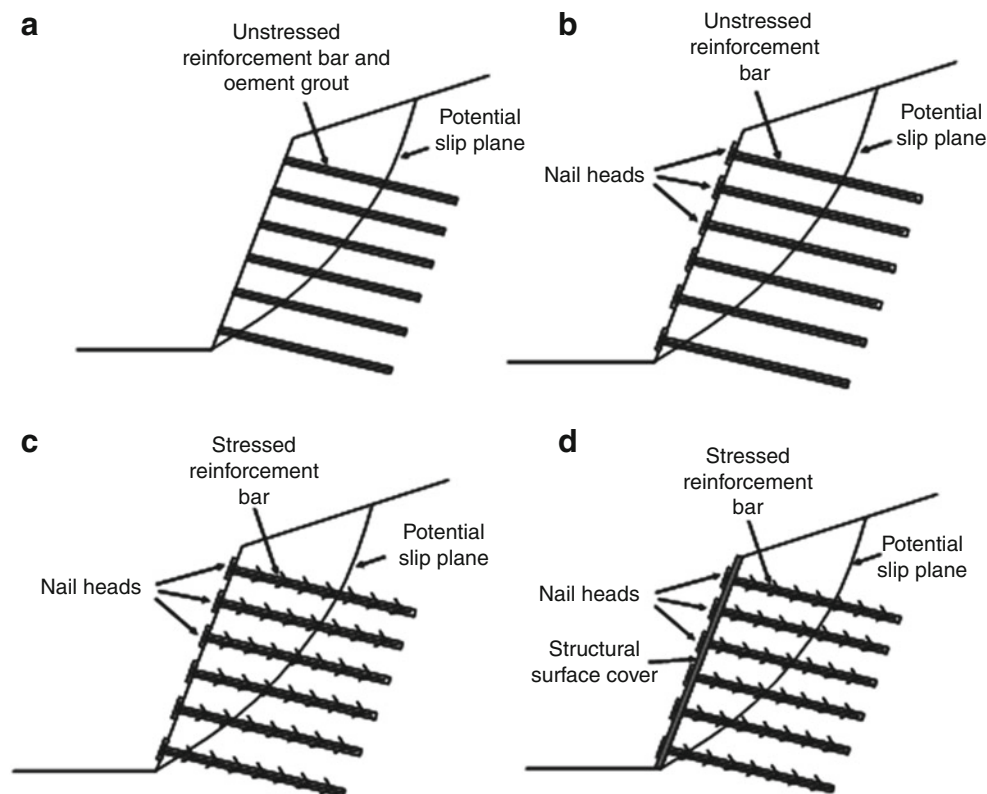


Fig. 2 Various soil nail systems. (a) Unstressed reinforcement without bearing plate, (b) Unstressed reinforcement with bearing plate, (c) Stressed reinforcement with bearing plate, (d) Stressed reinforcement with bearing plate and structural surface cover



Fig. 3 Steel reinforcement hanging down from a failed soil nail system

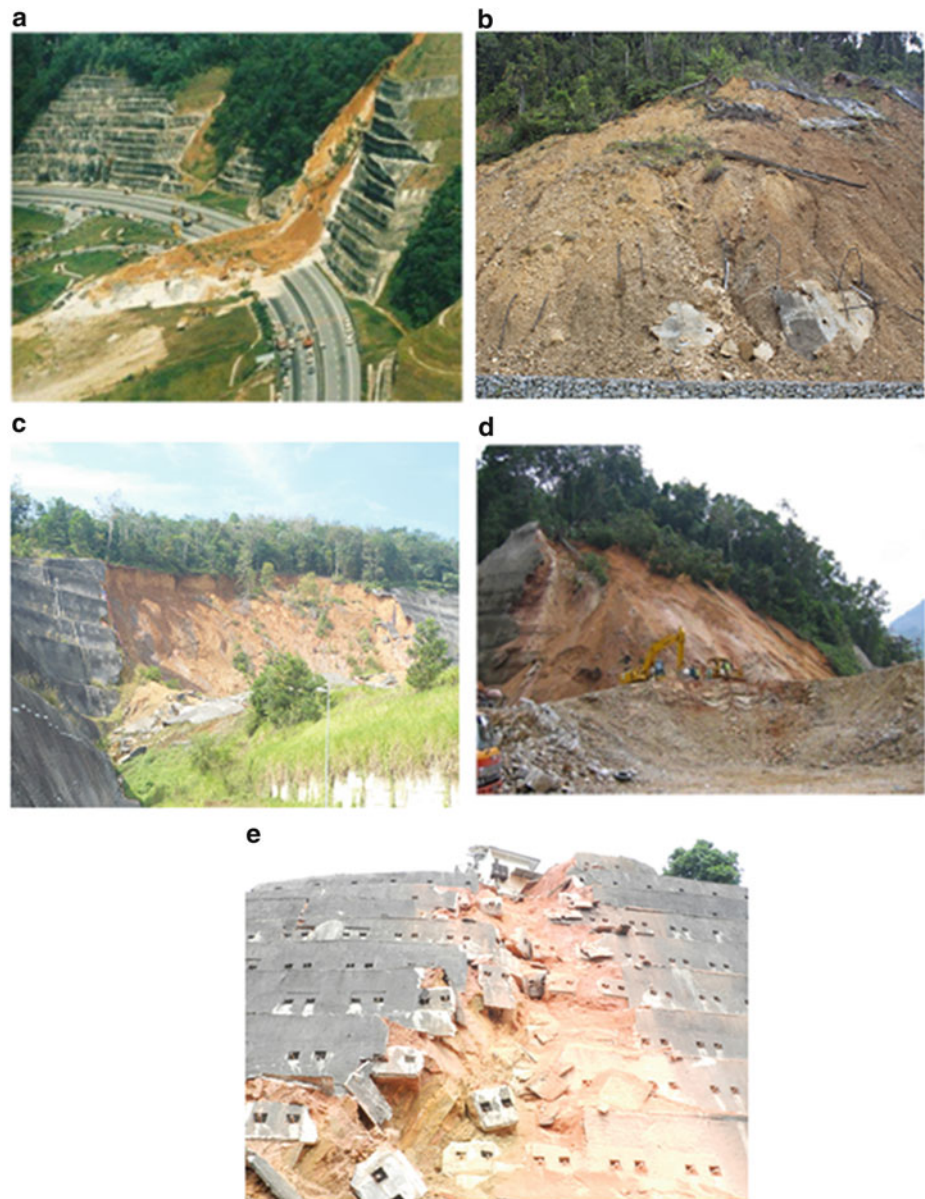
Mechanics of Stabilisation With Structural Surface Cover Tied Down by Hybrid Anchors

In active soil nail systems the idea of subjecting the nail shaft to a certain amount of tensile force is to pull down the bearing plate installed at the slope face. With nails at a

certain spacing horizontally and vertically, the effect is that the active frontal zone will be tied down against the stable passive zone. In this manner the effective stress along the potential failure plane will be elevated and thereby increase the shear strength and in turn stabilise the slope. However, the creep effect need to be eliminated, otherwise the same problem will arise due to losing the compressive effect. This is where the need for the application of the hybrid V-armed flip anchor becomes significant. The conceptual mechanics are illustrated in Fig. 5.

The installation of the hybrid V-armed flip anchor required the drilling of the bulging free end. This required a special eccentric hammer. Then the hybrid anchor is inserted with the V-arms folded against a built-in spring system using a U pin inserted at the back of the arms holding the arms together. Upon reaching the bulging end, the locking pin is pulled out via a cable to let the arms flip open and the hole is then grouted. The bulging end with the hybrid anchor provides extra passive pressure resistance and simultaneously prevents slippage between the nail shaft and the surrounding soil. The creep effect is thus completely eliminated and this leads to the maintenance-free system, ensuring the compressive effect of the frontal bearing plates over time.

Fig. 4 Slope failures in active soil nail/ground anchor systems in Malaysia. (a) Gua Tempurung, Malaysia, 1996, (b) Cameron Highland, Malaysia, 2010, (c) Bentong, Malaysia, 2009, (d) Ringlet, Cameron Highland, Malaysia, 2004, (e) Setiawangsa, Malaysia, 2013



To make the compression effect more effective there is a need for a more comprehensive system that will hold down the whole slope face to the ground, i.e. like the system illustrated in Fig. 2d. One of the options is the application of a gunite wall, as shown in Fig. 5, however this system may not be environmental friendly. Another option is to apply a cable netting system tied down at the nail points, as shown in Fig. 6. This cable netting is applied with an erosion control synthetic mat where hydroseed can be applied.

This would be a more effective and environmental friendly slope stabilising system and the effect of hydroseed is shown in Fig. 7. Another option is to apply a concrete grid beam system at the slope face and tied down to the ground at the beam intersection points using a hybrid anchor soil nail.

The grid internal surface can be turfed to make it environmental friendly.

Hybrid V-Armed Flip Anchor and the Concept Of Creep Elimination

The active soil nail suffers the gradual movement of the shaft towards the frontal bearing plate due to the tensile pull. The creep is due to the gradual shearing at the point of soil–nail interaction. Creep occurs because the tensile and the shear force are acting in the same longitudinal plane but opposite in direction (see Fig. 8). The passive pressure behind the bearing plate is providing the reaction to the pull. Creep

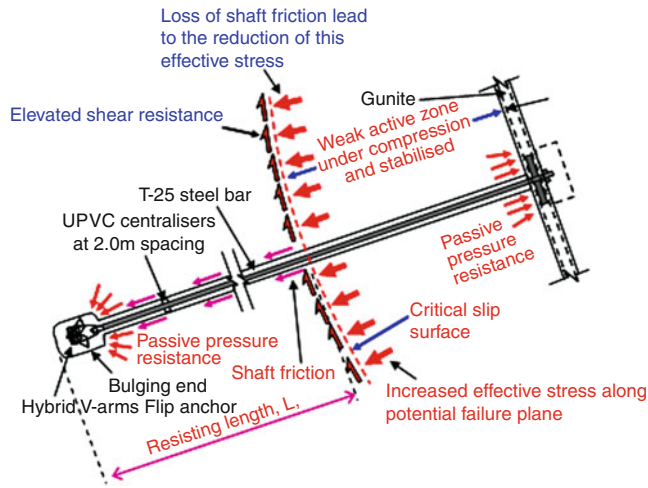


Fig. 5 Actual mechanics of stabilisation in an active soil nail system with the application of hybrid anchors at the free end



Fig. 6 Cable netting with erosion control synthetic mat tied down to the ground at the nail points

occurs due to the resisting shear force giving way to the tensile pull.

In a hybrid anchor soil nail system as shown in Fig. 5, the passive pressure exerted by the hybrid anchor is in the plane perpendicular to the nail shaft. In this system the creep would only occur in term of the compression of the soil located in between the two passive pressures at both ends. Upon the application of the tensile pull, the soil right in front of the hybrid anchor will undergo immediate compression and stop once the soil is fully compacted under the applied pressure. Once this is achieved then the chance of the soil being further compressed is minimal and hence this can stop the creep. This concept is supported by the pullout behaviour of the anchor discussed below. The movement of the nail shaft towards the frontal bearing plate is stopped by this



Fig. 7 Application of cable netting and erosion control synthetic mat before and after hydroseeding

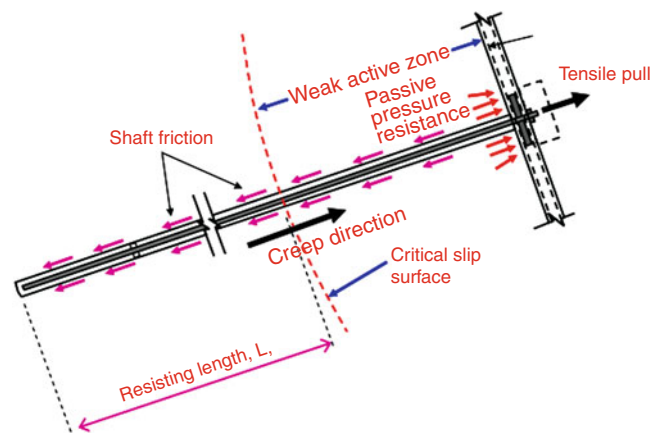


Fig. 8 Conceptual model of active soil nail system indicating the creep direction

passive pressure effect. Thence the application of hybrid anchor would be an effective solution to stop failure in an active soil nail system, besides there have been many reports on failures in passive soil nail systems.

Pullout Test on Hybrid Anchors

There are two types of pullout test conducted on this hybrid V-armed flip anchor which are: (1) a laboratory pullout test and (2) an in situ pullout test. The laboratory pullout test showed that the structural tensile strength of the anchor is 269 kN and the failure was the shearing at the coupling between the anchor and the steel reinforcement.



Fig. 9 Set up of in situ pullout test on hybrid V-armed flip anchor without grout at Dabong, Malaysia, 2012

The set up of the in situ pullout test conducted on a hybrid anchor without grout at Dabong, Kelantan, Malaysia under the supervision of the Public Work Department of Malaysia is shown in Fig. 9.

The results of two in situ pullout tests before application of grout conducted at a slope stabilisation project under the Public Work Department of Malaysia at Dabong and Gombak are shown in Fig. 10a, b, respectively. Both tests showed that the hybrid V-armed flip anchor can withstand up to a tensile strength of 150 kN. The anchors were locked in the hard layer of granitic residual soil in Gombak and sedimentary residual soil in Dabong and the anchor movements after two test cycles were 0.707 mm and 0.260 mm respectively. This shows that if the hybrid anchor is locked in a hard soil formation, the compression of the soil under test load of 150 kN is very minimal; note that this is without applying grout. If grout is applied then the passive pressure resistance would be over a bigger area and thus the resistance would be greater and this is how creep can be stopped.

Slope Stability Equation With the Compressive Effect of the Structural Surface Cover

This slope stability equation, as in (1), is developed to incorporate the increase in the effective stress along the potential failure plane due to the tensile pull by the hybrid anchor in stabilising the slope. This is according to the effective stress concept applied by Fellenius (1936) to quantify slope stability. The application for hybrid V-armed flip anchor to tie down the structural surface cover is as shown in Figs. 5 and 11. The effect of shear stress at the nail shaft that intersects the potential failure plane is neglected. The nail shaft cannot act as dowel since it is not big and stiff enough

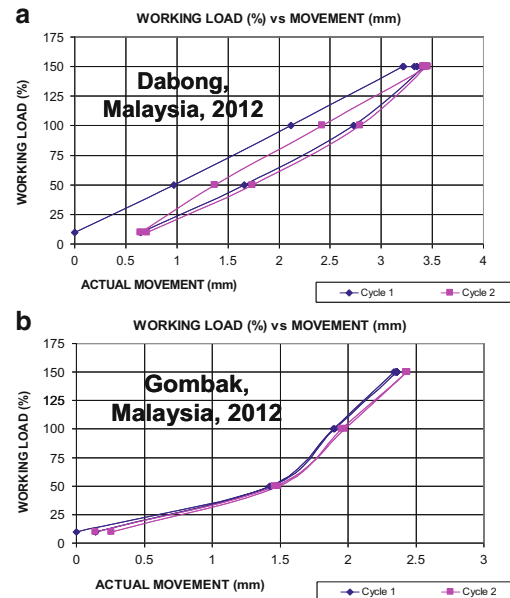


Fig. 10 In situ pullout test on hybrid V-armed flip anchor without grout at (a) Dabong, Malaysia, (b) Gombak, Malaysia, 2012

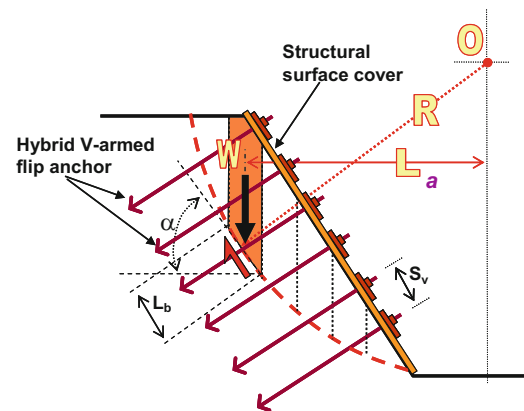


Fig. 11 Slope stabilisation using structural surface cover tied down using a hybrid anchor

to resist the shear along the potential failure plane. The distance between the nails is big enough for the soil to flow past. Equation (1) therefore quantifies the FOS according to the actual mechanics of stabilisation, incorporating the increase in effective stress due to the pull by the hybrid anchor. The efficiency factor E_f is to consider the fraction of the effective stress that has been transferred from the structural cover to the potential failure plane.

$$FOS = \frac{\sum F_{shear-soil} \times R}{\sum W \times L_a} \tag{1}$$

$$F_{shear-soil} = \tau(\sigma')_{nonlinear} \times L_b \times 1$$

$$\sigma' = \frac{W \cos \alpha}{L_b \times 1} + \frac{\text{Nail} \cdot \text{Tension}(kN)}{S_v \times S_h} \times E_f$$

where $F_{\text{shear} \cdot \text{soil}}$ = soil shear force at slice base

W = weight of typical slice

L_b = width of slice base

L_a = distance of slice to centre of rotation

R = radius of potential slip circle

S_v = vertical spacing of nails

S_h = horizontal spacing of nails

E_f = efficiency factor

$\tau(\sigma')$ = non-linear function of shear strength with respect to effective stress [i.e. according to (2) and (3)].

The non-linear function of shear strength with respect to effective stress is as shown in (2) and (3) (Md. Noor and Anderson 2006).

$$\tau = \frac{(\sigma - u_a)}{(\sigma - u_w)_t} \left[1 + \frac{(\sigma - u_w)_t - (\sigma - u_a)}{N(\sigma - u_w)_t} \right] \tau_t \quad (2)$$

valid for; $0 < (\sigma - u_a) < (\sigma - u_w)_t$

$$\tau = (\sigma - u_a) \tan \phi'_{\text{minf}} + \left[\tau_t - (\sigma - u_w)_t \tan \phi'_{\text{minf}} \right] \quad (3)$$

valid for; $(\sigma - u_a) > (\sigma - u_w)_t$

where

$$N = \frac{1}{1 - \left[(\sigma - u_w)_t \frac{\tan \phi'_{\text{minf}}}{\tau_t} \right]}$$

$(\sigma - u_a)$ = net normal stress

$(\sigma - u_w)_t$ = transition effective stress

τ_t = transition shear strength

ϕ'_{minf} = minimum soil friction angle

Conclusions

1. The application of a hybrid anchor at the free end of a soil nail managed to sustain a tensile pull of minimum 150 kN without grout with minimal displacement of less than 1.0 mm.
2. Laboratory tensile tests showed that the structural integrity of the hybrid anchor can withstand up to a tensile pull of 269 kN.
3. The application of hybrid anchor with grout would let the total structural capacity of the anchor of 269 kN to be fully mobilised.
4. The application of a hybrid anchor at the free end is an effective way to eliminate creep in active soil nails, as well as giving extra pullout capacity.
5. The application of the structural surface cover tied down using the hybrid anchor would be an effective way of stabilising slopes against shallow rainfall-induced failure.

References

- Bruce DA, Jewell RA (1987) Soil nailing application and practice – Part 2. *Ground Eng* 20(1):21–23
- Fellenius W (1936) Calculation of stability of earth dam. In: *Transactions, 2nd Congress large dams*, vol 4, Washington, DC, pp 445–462
- Md. Noor MJ, Anderson WF (2006) 'A comprehensive shear strength model for saturated and unsaturated soils'. In: *Proceedings of the 4th international conference on unsaturated soils*, ASCE Geotechnical Special Publication no. 147, vol 2, Carefree, Arizona, pp 1992–2003. ISBN: 0-7844-0802-5
- Pappin JW (2007) Soil nails in loose fill slopes. *Thirty Years of slope safety practice in Hong Kong*. Geotechnical Engineering Office, Hong Kong
- Pun WK, Shiu YK (2007) Design practice and technical developments of soil nailing in Hong Kong. *Thirty Years of slope safety practice in Hong Kong*. Geotechnical Engineering Office, Hong Kong
- Watkins AT, Powell GE (2007) Soil nailing to existing slopes as landslip preventive works. *Thirty years of slope safety practice in Hong Kong*. Geotechnical Engineering Office, Hong Kong



A Vigorous Debris-Flow Incident at Al-Hada Descent and Remedial Measures

Bahaeldin Sadagah

Abstract

Al-Hada descent lies in the western region of Saudi Arabia; it begins at an elevation of about 2,000 m, and is characterized by sharp cliffs. The Al-Hada descent road was constructed with an elevation difference of 1,500 m between the highest and lowest heights along the road. The road alignment is intersected by 14 very steep gullies of almost 60–80°. The gullies contain large quantities of consolidated and unconsolidated mud, old levees and large rock blocks. The Al-Hada descent road was hit in April 2012 by heavy rainfall lasting almost 2 h. The rainstorm initiated 11 debris flows in steep gullies, which travelled rapidly down and hit the road with speeds of 25 m/s along the gully channel. Once the debris flow dropped from a height of about 150 m elevation and reached a less confined area at the retaining wall, it partially destroyed the gabions layer, right side gabions, and edges of the retaining walls across the gullies and overflowed them, as they received more rolling, sliding and bouncing rocks from higher steep elevations along the gully. The moving debris flows spread out, lost speed and was deposited beyond the highway descent route, and dropped to the lower side of the gully towards the valley.

The study suggests a temporary solution which is removing about 150,000 m³ of the debris accumulation in the gully and to scale the remaining debris body to an angle of less than 35°. Another suggestion is to implement a permanent solution by constructing a number of high-capacity mesh barriers along the gully.

Keywords

Debris flows • Rainfall • Remedial measures

Introduction

Landslides and rockfalls frequently occur on mountain roads in rugged terrain. One of the most difficult terrains in westerly Saudi Arabia is the Al-Hada descent (Fig. 1). The famous Al-Hada descent lies at the upstream high-elevation region of Wadi Na'man in the western part of the Kingdom of Saudi Arabia (KSA). The highest elevation of the Al-Hada road reaches almost 2,000 m above mean sea level, and

its alignment lies within the sharp cliff edges of the Sarawat Mountains at the highest elevations. Before the ascent, the road starts from about 500 m elevation and reaches to more than 2,000 m.

The difference in elevation from the highest to lowest elevation is about 1,500 m. The descent lies between longitudes 40°16'8.4"E and 40°13'22.4"E and latitudes 21°22'17.3"N and 21°20'11"N (Fig. 2). Al-Hada road is 22 km long and starts west of Al-Taif city, and runs through the Al-Hada descent. The road connects the highlands where Al-Taif city is located to the lowlands at Na'man valley which leads to Makkah Al-Mokarramah city. Along this 22 km distance, natural slopes, man-made slope cuts, engineering structures, and gullies are located.

B. Sadagah (✉)
King Abdulaziz University, P.O. Box 80099, Jeddah 21589,
Saudi Arabia
e-mail: bsadagah@yahoo.com

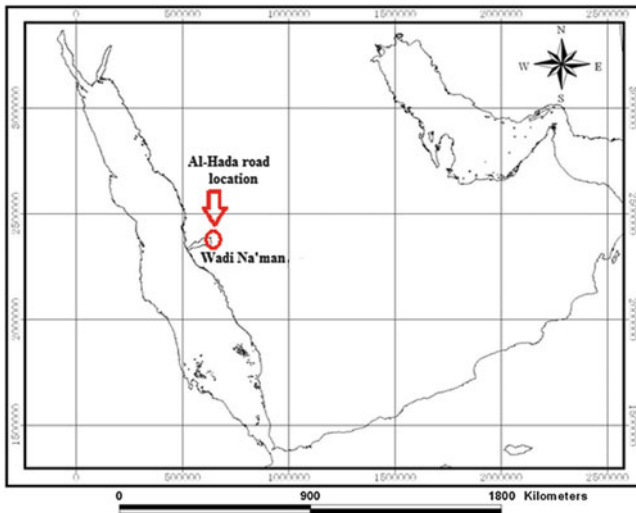


Fig. 1 Location of Al-Hada descent area in Saudi Arabia

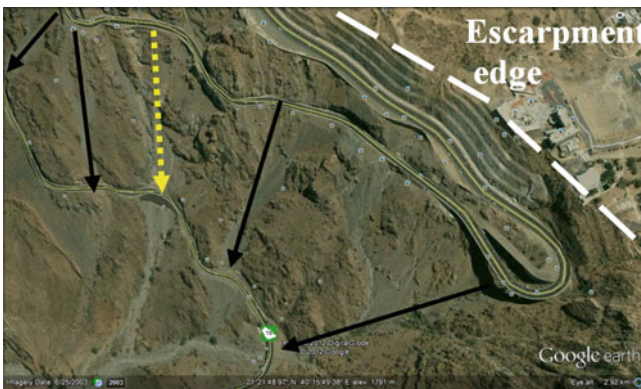


Fig. 2 Location of the debris accumulation and direction of flows (yellow dotted arrow), others in solid black lines

Brief Geomorphology and Geology

Al-Hada descent includes two distinct geomorphologic terrains: (i) a dissected upper plateau of low mountains and hills, and (ii) a precipitous escarpment. The study area is characterized by rugged, steep terrain with steeply incised drainages, and narrow crested ridges originating from a number of catchment areas. The most prominent of these features is the northwesterly trending Asir or Tihama escarpment, a structure, which is traceable for some 1,500 km.

The road alignment is intersected by 14 very steep gullies of almost 45–80° where it reaches the descent escarpment and the lowest elevations, respectively. The gullies generally contain large quantities of mud, old levees and large fallen rock blocks. The rocks in the study area are granite, granodiorite, and gabbro intersected by a large number of basic

dikes formed of diorites. Many dikes intruded through fractures with a southwest trend. The dike widths in general range between 5 to 10 m.

Field Conditions

The nature of the sediment in the gullies is (1) consolidated bodies that are a result of tens of years of sedimentation, (2) loose accumulations, which are a result of dumping the rock mass spoil from the higher levels of the road downwards onto the lower road levels, at the time of expanding the upper road. The second type usually overtopped the first type, accordingly; it is liable to move downwards in case of flow.

The gullies are scattered along and intersect the road alignment; the particular debris flow of concern is shown in Fig. 2.

Rainfall-Triggered Debris Flows

Al-Hada descent road was hit for two successive days in April 2012 by heavy rainfall lasting almost two hours. As the debris accumulation bodies are scattered along the road, as a result of rainfall (1) some of them did not move, (2) some had a small effect on the road, away from the study site, and (3) others had significant movement and caused destruction to the road and properties (Sadagah 2013).

The rainstorm initiated 11 debris flows in steep gullies, which traveled rapidly down and hit the road at a speed of 25 m/s along the gully channel. Once the debris flow dropped from a height of about 150 m elevation and reached a less confined area at the retaining wall, it partially destroyed the gabion layer, right side gabions, and edges of the concrete retaining walls retained for almost 10 m across the gullies, and destroyed most of the 1.5 m gabion above the wall and overflowed them. The debris flows received more rolling, sliding and bouncing rocks from higher steep elevations along the gully, and continued moving to cover the whole road alignments. The moving debris flows spread out, lost speed and deposited material beyond the highway descending route, and dropped to the lower side of the gully towards the valley. The height of the debris flows over the road was about 10 m high (Fig. 3). The debris flow is a combination of translational/ rotational movement, slipping above the lower layers of the old debris (Turner et al. 2012). The slide material consists of pre-existing landslide deposits, loose materials, and incised deposits in the debris accumulation. Triggering mechanisms include surface water infiltration, and toe erosion, and water inflow incision.



Fig. 3 One of the debris flows took place at the Al-Hada descent road

Field Investigation of the Debris Accumulations

At each of the 11 debris flows, the field density and moisture content of the consolidated soils were measured by a nuclear method. The technical properties of these particular debris flows is a moisture content = 3.4 %, field wet density = 1,836 kg/m³, field dry density = 1,776 kg/m³, maximum dry density 2.19 gm/cm³, optimum moisture content = 6 %, and compaction % = 83 %.

Laboratory Investigation of the Debris Accumulations

Debris accumulations samples were investigated in the laboratory, including grain size analyses (Fig. 4) and moisture-density contents relationships. A shear box test on the soil part of the debris was performed and showed that the friction angle is between 38° and 42° for the debris flows that took place.

Analysis of Debris Flow Laboratory Findings

The field density results of all debris flows show that field wet density ranges between 1,465 kg/m³ and 2,058 kg/m³, where the field dry density ranges between 1,391 kg/m³ and 1,986 kg/m³, and maximum dry density ranges between 2.147 gm/cm³ and 2.355 gm/cm³. Moisture contents range between 6 % and 8.3 %, compaction % ranges between 64.9 % and 94.3 %.

The statistical analysis shows: (1) a linear relationship between field wet density and field dry density, where the correlation coefficient is 0.99, (2) a linear relationship between field dry density and compaction %, where the correlation coefficient is 0.97, and (3) a negative relationship between moisture content % and compaction %, where the correlation coefficient is 0.12. The samples with a high field wet density have high field dry density and vice versa, but the relationship is not clear between the density and the compaction and moisture content; this is because the debris is compacted due to its own weight, and not overlaid by thick geological successions of sediments.

Modeling of the Debris Accumulations and Movement

In order to model the debris flows, DEM data is used. Digital elevation model (DEM) data consist of a sampled array of regularly spaced elevation values referenced horizontally either to a Universal Transverse Mercator (UTM) projection or to a geographic coordinate system.

In the field of natural hazards, there is an increasing demand for process models that help understand the dynamics of geophysical mass movements, from initiation to release.

Models allow engineers to predict the speed and run out of these hazardous movements in complex terrain. Such models are especially helpful when proposing mitigation measures, where knowledge of the inundated area is of critical importance. Hazard mapping, the primary application in mountainous countries, requires models that allow engineers to test different hazard scenarios. While well-tested empirical methods are available to determine run-out distances, velocities and flow heights, numerical models now allow practitioners to predict flow paths in general terrain as well as to model entrainment processes. Better mitigation strategies can result.

Remedial Measures

The DEM was used to model and to determine locations for the remedial measures for these debris flows, which are considered one of the most dangerous debris accumulations along the Al-Hada descent road. The debris is formed of many bodies scattered along the slope topography. In addition, during the rainfall, the powerful water inflow incised the debris and eroded the eastern part of it, which made possible a water passage to the contact between it and the underlying rock mass, and could soon decrease its stability.

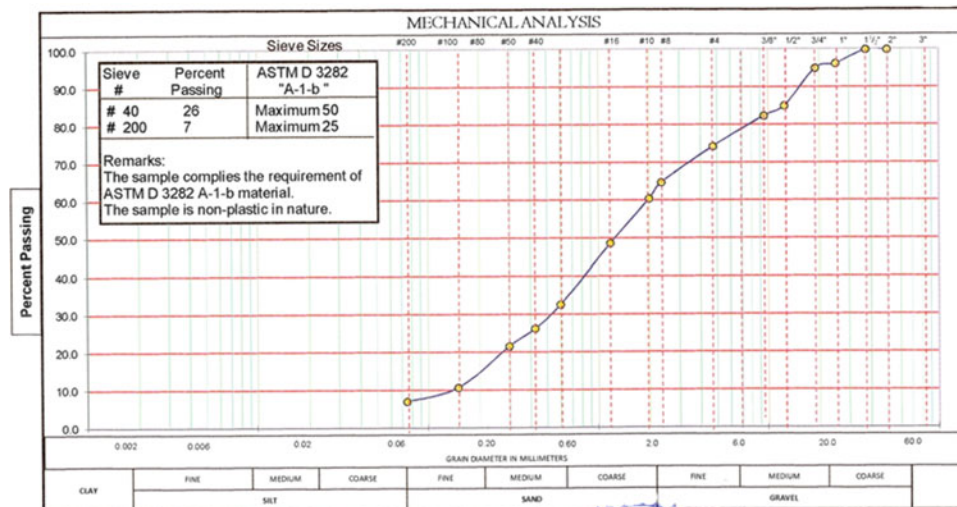


Fig. 4 Grain size analysis of the debris flows

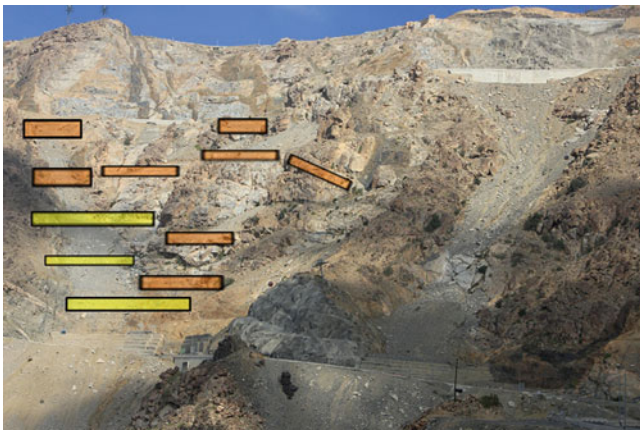


Fig. 5 The proposed locations of retaining dams (barriers, in yellow) and wire mesh draperies (brown) to stop the debris flows

The remedial measures at this station will be as follows:

1. Remove (scale) the debris accumulations starting from the upper to the lower road level.
2. Construct three retaining dams of 10 m height along the gully (Fig. 5).
3. Construct eight wires mesh draperies of 7 m height of the gully sides, where seeder rocks are located, to collect the falling and running rock blocks (Fig. 5).
4. Cover the incised sides with a welded steel mesh covered in shotcrete to block the passage of water.
5. Place soil nails in the debris accumulation to reach the underlying rock mass, if scaling is impossible using the available machinery

Conclusions on Debris Accumulation Flows

The debris accumulations are formed mainly of poorly-graded sand and gravel with minor amounts of silts (Takahashi 2007). The deposits are non-plastic.

The debris accumulations are compacted and have low values of compaction and moisture contents.

The accumulations are sitting in the gullies at angles of more than 40° , which are more than the soil friction angle ($38\text{--}42^\circ$), accordingly they are unstable.

These compacted incised debris accumulations due to rainfalls indicate that they are unstable. In addition, debris flows at these gullies took place along the debris surface slopes after the rainfall, which indicates that the cohesion is close to 0° and needs an immediate support and continuous debris monitoring.

The satellite image and DEM are necessary to show the steep slopes where the debris accumulations are formed.

References

- Sadagah BH (2013) Study of the failures, rockfalls and debris flows occurred along al-kar/al-hada descent road. King Abdulaziz University, Jeddah Saudi Arabia, 1163p
- Takahashi T (2007) Debris flow mechanism, prediction and countermeasures. Taylor & Francis, The Netherlands, 448p. ISBN 978-0-415-43552-9
- Turner JP, Duffy JD, Buell R, Zheng X (2012) Rock-socketed foundations for the bridge at Pitkins curv. In: 63rd Annual highway geology symposium, 7–10 May 2012. Redding, CA, USA.



Application of Reinforced Concrete Retaining Walls for the Rehabilitation of Landslides on Roads

Nedim Suljić

Abstract

In this study we will analyze the use of reinforced concrete retaining walls in the case of the remediation of landslide “Potoci” on a local road in Srebrenik, in the northeastern part of Bosnia and Herzegovina. This landslide occurred on the part of the road toward the Old Town of Srebrenik and due to landsliding the road was damaged over a distance of about 60 m. Deformation of the landslide is reflected in depressions, folds and fissures on the hillside terrain and two damaged facilities, one residential building and one outbuilding (garage with storage). At this location, the drainage of rainwater is completely uncontrolled, and pours from the asphalt road down the hillside terrain. The catchment area of this site covers a considerable area. During major and long-lasting precipitation most of the water flows down the slope below the road, and part infiltrates into the soil through cracks, which has led to the emergence of the landslide, and slope and road instability. In addition, unplanned construction of residential buildings resulted in an overloading of the slopes and is an additional factor that affects the occurrence of landslides. Based on the general properties determined for the landslides and the causes and mechanisms of initiation of earth masses from an engineering-geological point of view, permanent remedial measures are proposed. These permanent measures include the application of appropriate support structures and technically suitable drainage of rainwater (surface) and underground water.

Keywords

Landslide • Remediation • Retaining wall • Rainwater • Underground water

Characteristics of Terrain

Landslide “Potoci” has a length of about 60 m and covers an area of c. 0.3 ha. The moving soil mass is about 10,000 m³. The slope where the landslide occurred is quite steep, with slope of 16°. At the top of the slope there is a local road (Fig. 1) while below the road there are residential buildings.

In geological terms, the terrain is composed of a talus soil mass cover of dusty clay with a thickness of 3 to 4 m. Under the cover there is a substrate of rock marl of Miocene age.

The sliding layer is in the layer of talus dusty clay or in the contact of the talus dusty clay and the marl.

Based on geomechanical investigation it was determined that the slope does not have a steady level of groundwater. During periods of heavy precipitation and heavy rainfall, as well as during the melt of snow, underground water is created which degrades the cover layer of dusty clay and the landslide occurs. The cause of the origin of landslides is the static and dynamic effect of underground water on the steep slope of the terrain with an asphalt road on it. The sliding layer is formed at about 3 to 4 m from the surface of the slope of the terrain and at the bottom of the dusty clay cover.

Based on the determined general properties of the terrain, as well as the cause and size of the landslide, two types of

N. Suljić (✉)
The Faculty of Mining, Geology and Civil Engineering, University
Tuzla, Tuzla 75000, Bosnia and Herzegovina
e-mail: nedim.suljic@untz.ba; nsuljic@bih.net.ba



Fig. 1 Picture of the terrain slope with part of the damaged road

remediation were considered. One possibility is the application of a discontinuous retaining structure made of bored piles with spigot reinforced concrete beams, while the second variant is a reinforced concrete retaining wall. Of course, in both variants it is necessary to collect and drain surface water and groundwater outside of the sliding body.

Possible Remediation Measures

Variant With Bored Piles

The variant with a discontinuous supporting structure of bored reinforced concrete piles connected with spigot reinforced concrete beam was one of the alternatives considered for landslide remediation (Fig. 2). Besides a technically correct solution for landslide remediation, it is necessary to take into account the economic and financial side of the works. According to this scheme the bored piles would be fixed in the marl rock. The diameter of the piles would be 120 cm, and binding spigot beam size would be 100/140 cm. The bored piles and spigot beams would be made of reinforced concrete of satisfactory quality with

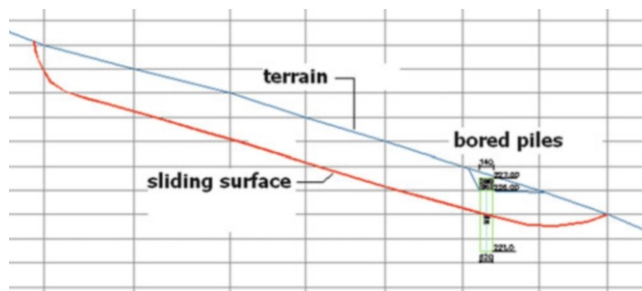


Fig. 2 Terrain slope with sliding flat area and bored piles

ribbed reinforcement. Spacing between the piles is 4 m (Fig. 3).

Besides a discontinuous retaining structure of bored piles, open channels for receiving and controlling drainage of surface water would be also made. The channels should be made of concrete resistant to frost and follow a natural slope of terrain where the slope of the channel bottom should not exceed 15 %. Surface water is drained from the open channels to a nearby local storm sewer or into the nearest natural receiving area.

It is necessary to carry out planning for the area after landslide remediation and grass planting on the surface of the landslide in order to minimize rainwater infiltration into the soil. Based on the cost estimate and the amount and type of material and the type and volume of work required, the cost of remediation of landslide by this variant would be 45,000 euros.

Variant With Reinforced Concrete Retaining Wall

A reinforced concrete retaining wall is planned for under the asphalt road, with a length of 65 m and it is based in the geological substratum or the marl. Behind the reinforced concrete retaining wall, a standard filter layer with non-woven geotextile and proper drainage pipe would be built. Drain water behind the retaining wall is taken in the gutter by the drainage system and holes in the wall (barbacanes), which are planned along the wall (in front of the wall) and from which water drains into the local storm sewer (Fig. 4).

At the top of the retaining wall (behind the wall) the concrete channel it is planned to collect the surface (rain) water from the asphalt road and take it to a planned revision concrete manhole and on to the local storm sewer (Fig. 5).

Below the reinforced concrete retaining wall, the construction of drainage ditches in the form of the letter “Y” is planned, as seen in Fig. 4. A cross-section of a drainage ditch that would be applied in remediation of the landslide is shown in Fig. 6.

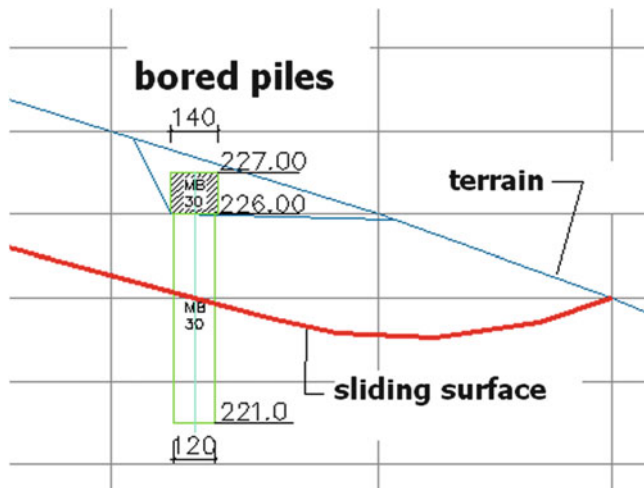


Fig. 3 Dimensions and position of bored piles in relation to the sliding area

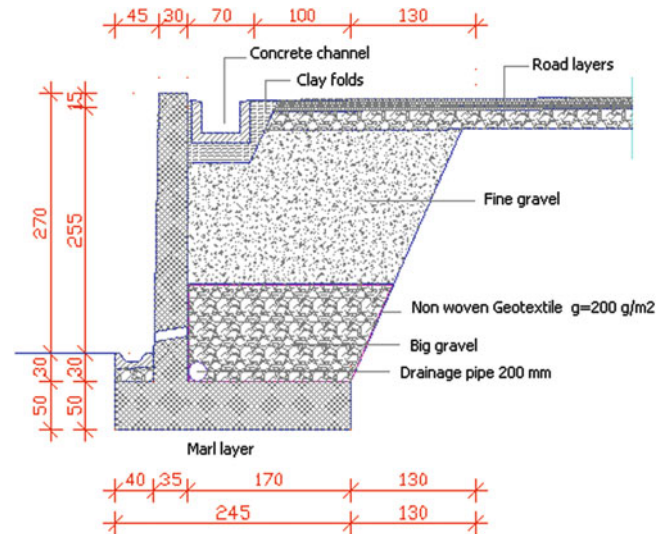


Fig. 5 The cross section of the reinforced concrete wall

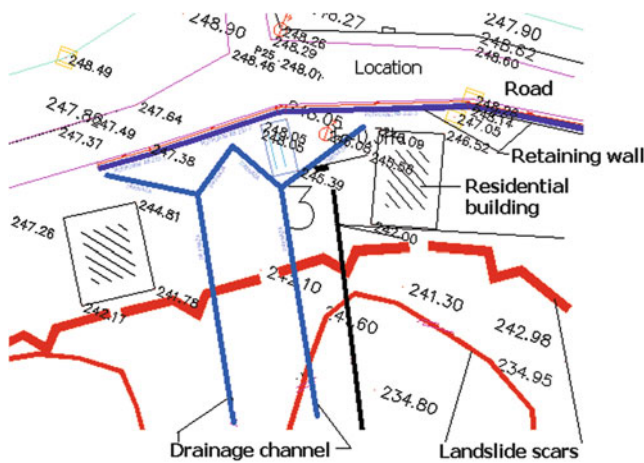


Fig. 4 Landslide situation with the position of retaining wall and drainage channels

According to the cost estimate of types of work, quantities and types of materials used, we obtained the cost of landslide remediation of 40,000 euro.

Landslide Remediation by Reinforced Concrete Retaining Wall

Based on the analysis of two variants of landslide remediation, we selected the reinforced concrete retaining wall as a cheaper solution that is a very good permanent remediation measure. In addition, because of the dynamic load of the motor vehicles on the road which was threatened by the

landslide, construction of reinforced concrete retaining wall is justified.

Also, from the top of a reinforced concrete retaining wall it is easier to build access to individual residential facilities located along the road. Remediation of the road is thus enabled by the design and construction of a permanent remediation measure using a reinforced concrete retaining wall, and by technically correct drainage of surface water and groundwater (Figs. 7 and 8).

By remediation of the landslide below the road leading to the Old Town of Srebrenik two residential buildings and an outbuilding that were directly threatened by landslide were also rescued. Infiltrated surface water is drained to the revised reinforced concrete manhole by the filter layer behind the retaining wall and by 200 mm drainage pipes, from where the pipe system drains it down the terrain slope into the existing manhole and further into the local storm sewer that runs beneath the terrain slope (Figs. 9 and 10).

Concluding Discussion

In this example, the remediation of landslides on the part of the road to the Old Town in Srebrenik in the northeastern part of Bosnia and Herzegovina proved to fully justify the construction of a reinforced concrete retaining wall with drainage channels and storm water drainage. The project was planned and executed in accordance with the technical norms and standards, and represents a good and efficient solution for landslide remediation. In fact,

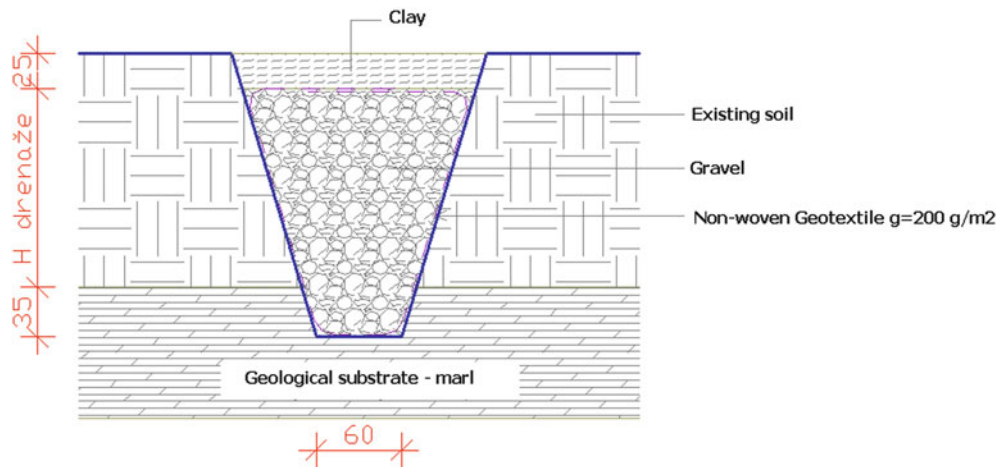


Fig. 6 Cross section of drainage ditch



Fig. 7 Concreting of one section of retaining wall

in Bosnia and Herzegovina, in many cases reinforced concrete retaining walls are used for landslide remediation. Other supporting structures, such as gabion structures, discontinuous substructures of bored piles or reinforced soil have a much less frequent application. This



Fig. 8 Construction of a retaining wall for landslide remediation

is reflected in equipment and classification of construction companies, as well as the designer's practice of using and applying reinforced concrete as a building material for the continuous measure of landslide remediation.

In Bosnia and Herzegovina, in the design and implementation of landslide remediation, one of the main indicators for selection of one of the considered alternatives is the cost price of the works. In this case, in addition to being well-chosen technical solutions, the cost of the landslide remediation had a major role.

Remediation of this landslide was completed during the month of August 2010, and until today there has been no movement of soil, which can be seen on the basis of measurements at fixed points which are used to track monitoring after completed remediation.



Fig. 9 Reinforced concrete retaining wall and revised manhole



Fig. 10 Drainage of drain water from the manhole

References

- Čačković I (2008) Stability of slopes and retaining structure, University Tuzla
- Suljić N (2005) Contemporary materials for the execution of retaining structures. IGK Planjax Tešanj
- Suljić N (2009) Study on the geomechanical investigation works for the landslide remediation on the road to the Old Town of Srebrenik. (Bijelića brdo)
- Suljić N (2010a) The main project of remediation of landslides on road heading towards the Old Town Srebrenik. "ING-PROJEKT" Doboj Jug
- Suljić N (2010b) Retaining structures. University Tuzla, University Textbook
- Suljić N, Bašić Z (2007) Analysis of the impact of deep foundation of neighboring building on the stability of the reinforced concrete retaining wall, April 2007. In: Scientific conference modern trends in construction, Banja Luka, BiH



A Simplified Analytical Model for the Design of Flexible Barriers Against Debris Flows

Andrea Segalini, Roberto Brighenti, and Gessica Umili

Abstract

A debris flow is usually represented by a mixture of solid particles of various sizes and water, flowing along a laterally confined inclined channel-shaped region; debris flow protection barriers are the focus of this research. In particular the paper presents a simplified structural model of cable-like retention barriers based upon the equation of equilibrium of wires under large displacements condition. Inputting the debris flow features, the model returns restraining forces and cable stresses that can then be used for an appropriate barrier design. Some parametrical tests were performed to analyze how the impact velocity and the mass density of the debris influence the maximum tensile force and the acting load in the cables: also the energy associated with debris flow is assessed. Results are here presented and discussed.

Keywords

Debris-flow • Retention barriers • Cable structure • Parametrical analysis

Introduction

Rapid mass movements of materials composed of a mixture of grains, water and air developing under the effect of gravitational forces are known as debris flows.

Their destructive capability is particularly severe due their high amount of energy, with movement usually taking place for several hundreds of meter along slopes, without losing kinetic energy (Takahashi 1983). This phenomenon usually takes place due to collapses of natural accumulations of material (landslides, erosion, etc.) produced by strong autumnal precipitations or rapid spring snowmelt.

Debris Flow Impacting a Flexible Surface

The effect of the debris flow impacting an obstacle is to transmit a pressure to the contact area. In the case of retention barriers, such an obstacle is deformable and its flexibility mitigates the pressures developed during the impact, allowing the flow to slow down to the point of complete arrest if the barrier strength is adequate.

Moreover, for permeable barriers, such as net-type barriers, a draining effect can take place as well, increasing the internal friction of the particles and facilitating the arrest of the flowing material. Neglecting the barrier deformation (to be on the safe side), the pressure produced by the debris flow impact can be estimated by considering both the dynamic impact pressure and the static pressure of the deposited debris (Kwan and Cheung 2012). The first one can be determined assuming the kinetic energy of the flowing material to be totally converted in a pressure load when the velocity vanishes (Bernoulli theorem). The dynamic pressure on the barrier can thus be estimated as (Fig. 1a):

A. Segalini (✉) • R. Brighenti • G. Umili
Department of Civil, Environmental and Territory Engineering,
University of Parma, V.le G.P. Usberti 181/A, 43124 Parma, Italy
e-mail: andrea.segalini@unipr.it; roberto.brighenti@unipr.it;
gessica.umili@unipr.it

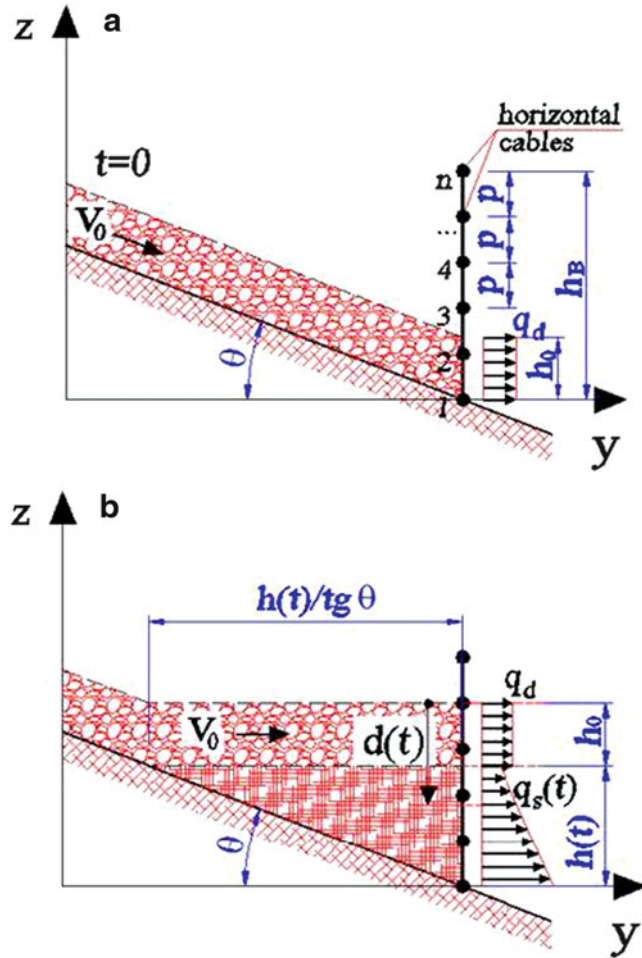


Fig. 1 Debris accumulation behind the barrier (a) and corresponding load distribution at a generic time instant (b)

$$q_d(x) = \alpha \cdot \rho_d \cdot v_0^2 \quad (1)$$

Where α is an empirical coefficient ($\alpha = 1.5\text{--}5$, Canelli et al. 2013) that can be assumed to be equal to 2.0 when the barrier is flexible and drained and the flow regime is granular, while ρ_d , v_0 are the mass density and the impact velocity of the debris, respectively. It must also be considered that after the impact, when the debris starts to accumulate behind the barrier, a static pressure develops (Fig. 1). The height of the accumulated material at the generic time t can be estimated as (Fig. 1b):

$$h(t) = \sqrt{2 \cdot v_0 \cdot t \cdot h_0 \cdot \text{tg}\theta} \quad (2)$$

where the quantities h_0 and θ (height of the debris flow and inclination of the slope behind the barrier) are assumed to be constant during the phenomenon. Note that (2) requires a positive slope, i.e. $\theta > 0$, while for $\theta = 0$, i.e. for a horizontal slope, the problem is indeterminate.

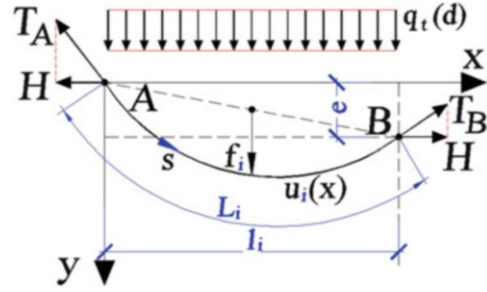


Fig. 2 Geometric and loading parameters of the single cable of a retention barrier

The static pressure acting at the depth $d(t)$, measured with respect to the current top free surface of the material, can be assessed through the trivial relation:

$$\begin{aligned} q_s(d) &= k \cdot d(t) \cdot \rho_d \cdot g \\ &= k \cdot (h_0 + h(t) - z) \cdot \rho_d \cdot g \end{aligned} \quad (3)$$

where k and g are the earth pressure coefficient and the acceleration of gravity, respectively, while z is the vertical position of the point under consideration (Fig. 1b).

Structural Model of a Cable Structure

The present model (Brighenti et al. 2013) simply assumes that the main resisting cables are loaded only in the horizontal direction, while the vertical forces transmitted by the net connecting to the cables are negligible for small vertical deformation of the barrier (Fig. 2).

The final relation between the distributed load q_i and the maximum displacement \bar{u}_i of the i -th cable occurring at its midpoint is:

$$q_i(\bar{u}_i) = \frac{64 E_i A_i}{3 l_i^4} \cdot \bar{u}_i^3 \quad (4)$$

Making use of the load-displacement relationship and considering also the effects of the brakes and of the superposed net, the equilibrium relations lead to a system of equations (Brighenti et al. 2013). Since the solution of such a system does not allow an easy analytical treatment, an iterative evolutionary algorithm belonging to the so-called Genetic Algorithm (GA) is applied (Goldberg 1989; Gen and Cheng 1996).

Parametrical Analysis

A trapezoidal barrier composed of six cables was simulated; the space between each cable was equal to 1 m. Some tests were performed to analyze how parameters influence

Table 1 Values of the correlation index between input and output parameters

| | Maximum H_{max} | Maximum u_{max} | Maximum q_{max} |
|----------|-------------------|-------------------|-------------------|
| v_0 | 0.987 | 0.988 | 0.980 |
| ρ_d | 0.108 | 0.105 | 0.111 |
| h_0 | 0.002 | 0.005 | 0.002 |
| θ | 0.002 | 0.002 | 0.002 |

Table 2 Values of the correlation index between input and output parameters

| | Maximum q_{mean} | Mean q_{max} | Mean q_{mean} |
|----------|--------------------|----------------|-----------------|
| v_0 | 0.276 | 0.980 | 0.363 |
| ρ_d | 0.467 | 0.111 | 0.320 |
| h_0 | 0.789 | 0.002 | 0.845 |
| θ | 0.123 | 0.002 | -0.008 |

maximum tensile force H , maximum displacement \bar{u} of the cables (occurring at the mid-point) and acting load q in the cables: in particular impact velocity v_0 (3–10 m/s), mass density ρ_d of the debris (1,850–2,000–2,200 kg/m³), height of the debris flow h_0 (0.2–0.4–0.6–0.8 m) and inclination of the slope behind the barrier θ (20–30–40°) have been varied and a total of 288 combinations of their values have been used as input of the barrier model.

H_{max} , u_{max} and q_{max} are the maximum values of H , \bar{u} and q , respectively, among those obtained for each considered instant. Maximum and mean values of H_{max} , u_{max} and q_{max} are obtained considering five cables, from the second one starting from the ground to the upper one. The first cable from the bottom was not considered in the analysis because its transversal section area is bigger than the others, in order to simulate the effect of anchoring it to the ground.

A correlation index was calculated between input and output data: values are reported in Tables 1 and 2.

Maximum value of H_{max} , u_{max} and q_{max} and mean value of q_{max} are strongly correlated to impact velocity (correlation index close to 1). In particular Figs. 3 and 5 show trends with exponents equal or close to 2, while Fig. 4 shows a linear trend.

The maximum value of q_{mean} and mean value of q_{mean} have an intermediate correlation index with impact velocity: Fig. 6 shows that trends in this case are influenced also by h_0 and θ . This fact must be highlighted because it proves that considering the mean value of the acting load on the cables may not always be the best choice for the design of the barriers.

Energy Assessment

The debris deposition mechanism called “run-up” (Fig. 7) is defined as follows: the fluid glides on the upper surface of a wedge of material, which is fairly stable; then continues to

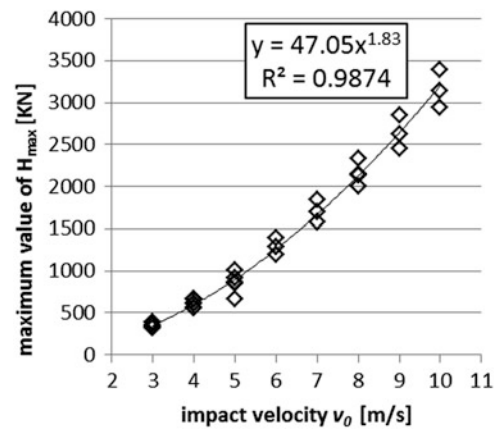


Fig. 3 Correlation between impact velocity and maximum value of H_{max}

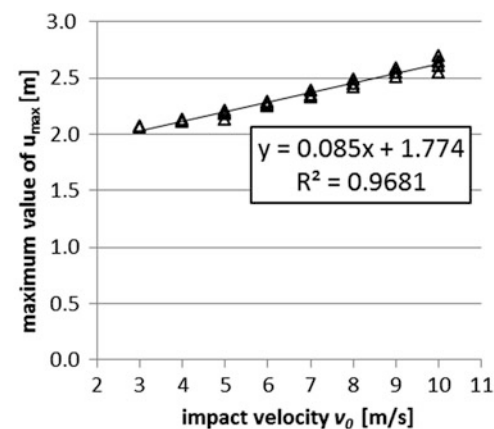


Fig. 4 Correlation between impact velocity and maximum value of u_{max}

impact the barrier until the new waves are blocked along the ramp, dissipating all the kinetic energy. The volume of debris flow involved in the interaction with the barrier is limited; a significant portion of the total kinetic energy is lost by means of inelastic deformations of debris during the impact with the barrier (Sun and Law 2012).

Sun and Law (2012) propose that, for a first approximation, the evaluation of the impact energy held up by the barrier can be related the total kinetic energy of the front portion of the flow involved in the impact. The analysis adopts the Lagrangian approach, where the reference frame is the position of the flexible barrier, that moves forward when subjected to the pressure of the debris.

Assuming $dQ/dx = 0$ (the volume of debris deposited is constant along the barrier), it is demonstrated that the dissipation of kinetic energy of the debris flow along its runout path on the material previously deposited is due to the conversion into potential energy and frictional resistance, as follows:

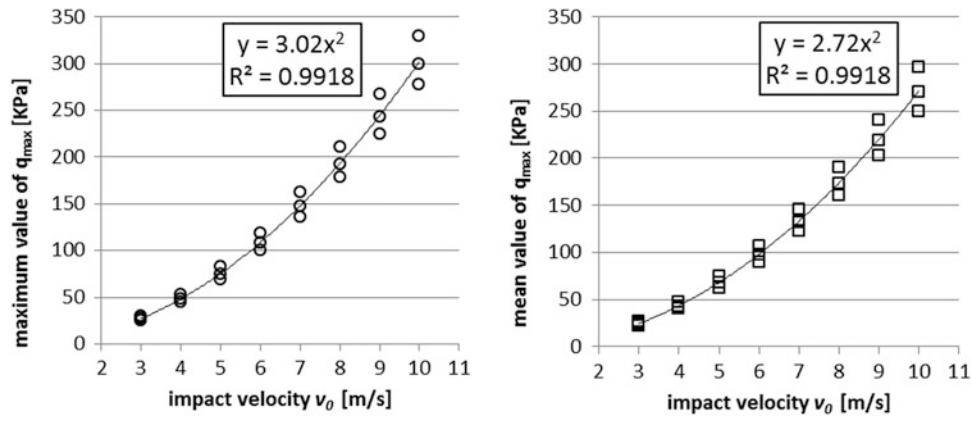


Fig. 5 Correlation between impact velocity and (a) maximum value of q_{max} , (b) mean value of q_{max}

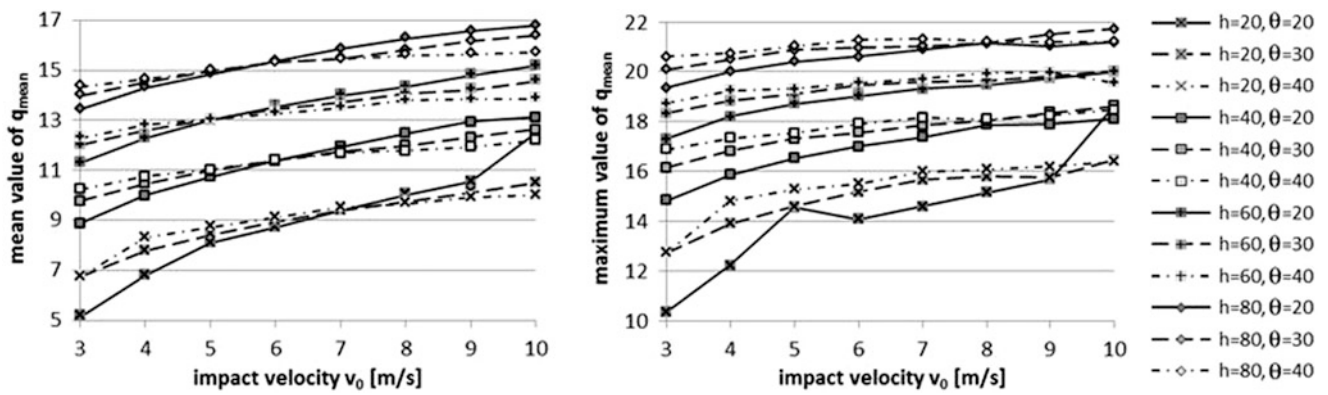


Fig. 6 Correlation between impact velocity and (a) maximum value of q_{mean} and (b) mean value of q_{mean} ; $\rho_d = 1,850 \text{ kg/m}^3$

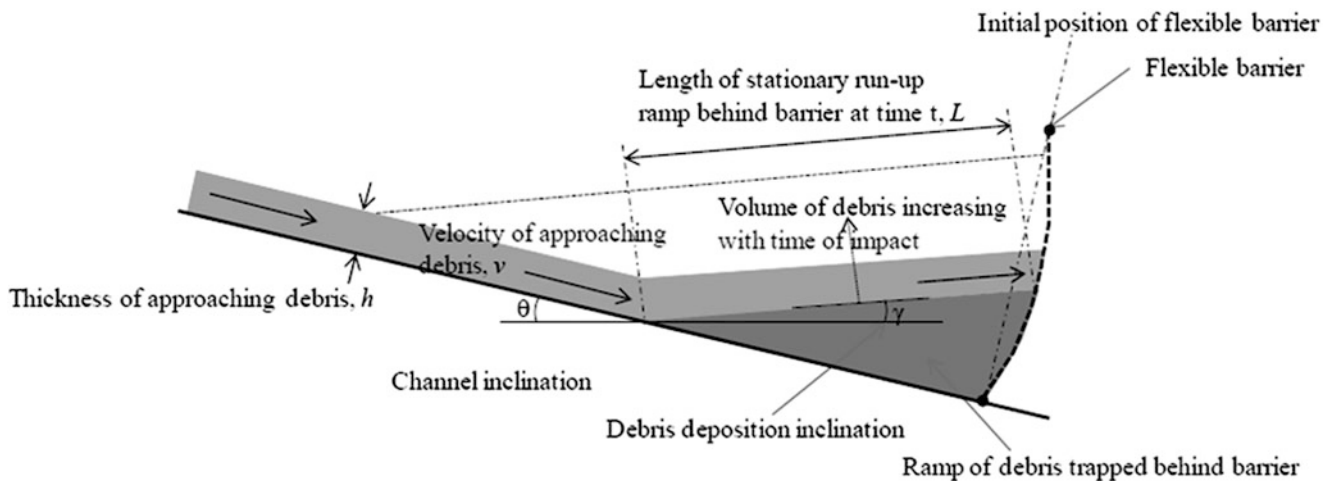


Fig. 7 Run-up deposition mechanism (Sun and Law 2012)

Table 3 Analytical solutions for the impact of a debris flow against flexible barriers (Sun and Law 2012)

| Deposition mechanism and scenario | Design impact energy of barrier (E_B) and Duration of impact (T), with $T_s \leq V/v_0$ |
|-----------------------------------|---|
| Run-up, $H_B \geq H_D$ | $E_B = \frac{\rho_d \cdot Q_0 \cdot v_0^5 \cdot \cos(\theta + \gamma) \cdot \sin(\theta + \gamma)}{48 \cdot h_0 \cdot g^2 \cdot (\mu \cdot \cos \gamma + \sin^2 \gamma)} \quad (6)$ $T_s = \frac{v_0^3 \cdot \cos(\theta + \gamma) \cdot \sin(\theta + \gamma)}{8 \cdot h_0 \cdot g^2 \cdot (\mu \cdot \cos \gamma + \sin^2 \gamma)^2} \quad (7)$ |
| Run-up, $H_B < H_D$ | $E_B = \frac{\rho_d \cdot Q_0 \cdot v_0 \cdot H_B^2}{4 \cdot h_0 \cdot \tan(\theta + \gamma)} \frac{\rho_d \cdot g \cdot Q_0 \cdot H_B^3}{3 \cdot h_0 \cdot v_0 \cdot \tan(\theta + \gamma) \cdot \sin(\theta + \gamma)} \cdot (\sin \gamma + \mu \cdot \cos \gamma) \quad (8)$ $T_f = \frac{H_B^2}{2 \cdot h_0 \cdot v_0 \cdot \tan(\theta + \gamma)} \quad (9)$ |

Table 4 Comparison of design impact energy of barrier (E_B) and duration of impact (T) calculated for ten different tests through (8) and (9) and those obtained from the analytical model (Brighenti et al. 2013)

| | Velocity v_0 (m/s) | Density ρ_d (kg/m ³) | Height h_0 (m) | Slope θ (°) | $E_{B \text{ eff}}$ (8) (KJ) | $E_{B \text{ tot}} (\mu = 0)$ (8) (KJ) | $E_{B \text{ model}}$ (KJ) | μ (-) | T_{model} (s) | T_f (9) (s) |
|--------|-------------------------|--|---------------------|-----------------------|---------------------------------|---|-------------------------------|-----------|---------------------------|------------------|
| Test 1 | 3 | 1,850 | 0.2 | 20 | 390.45 | 2189.46 | 366 | 1.5 | 52.800 | 54.273 |
| Test 2 | 4 | 1,850 | 0.2 | 40 | 336.22 | 2370.97 | 366 | 7 | 17.200 | 17.975 |
| Test 3 | 5 | 2,000 | 0.4 | 20 | 417.48 | 8879.71 | 368 | 6.5 | 17.200 | 16.282 |
| Test 4 | 6 | 2,200 | 0.6 | 30 | 271.57 | 9663.81 | 372 | 14.5 | 6.100 | 5.779 |
| Test 5 | 7 | 1,850 | 0.8 | 40 | 305.52 | 7857.68 | 371 | 24.5 | 2.700 | 2.568 |
| Test 6 | 8 | 2,000 | 0.2 | 20 | 362.61 | 99017.87 | 366 | 18.37 | 21.500 | 20.352 |
| Test 7 | 9 | 2,200 | 0.4 | 30 | 367.92 | 22535.97 | 369 | 31.4 | 6.100 | 5.779 |
| Test 8 | 10 | 1,850 | 0.6 | 40 | 334.04 | 16337.16 | 369 | 44 | 2.500 | 2.397 |

$$de_k/dx = -\rho \cdot g \cdot Q_0 \cdot [\sin \gamma + \mu \cdot \cos \gamma] \quad (5)$$

where:

ρ_d is the mass density of the deposited material;

g is the acceleration of gravity;

Q_0 is the discharge rate of the incoming debris flow;

γ is the average inclination of the debris deposited behind the barrier;

μ is the tangent of ϕ , which is the friction angle between the deposited material and incoming debris.

The height of the impacting flow is considered perpendicular to the ground surface and the debris flow velocity is much higher than the deformation velocity of the barrier due to the impact.

Table 3 shows two different equations for calculating the kinetic energy absorbed by the barrier and the duration of the impact in two different scenarios that can occur in a run-up deposition mechanism. In the first scenario the height of the barrier H_B is greater than or equal to H_D , the final thickness of the debris flow; in the second one instead H_B is smaller than H_D . In these equations v_0 is the impact velocity; h_0 is the depth of the incoming debris flow (assuming a

perpendicular impact on the barrier); θ is the average slope of the channel; V is the debris volume.

In the following, we refer to a mechanism of run-up with $H_B < H_D$ (8). For each test we assume fixed values of velocity, density, height of the flow and inclination of the slope. Knowing the geometry of the barrier, flow values are then calculated. The next step is to calculate the actual energy stored by the network, $E_{B \text{ eff}}$, through (8). In the end we obtain the value of μ for which the stored energy $E_{B \text{ eff}}$ is roughly equal to the energy value calculated by the analytical model presented here (Brighenti et al. 2013). Once the equality between the two energies is obtained, one can observe that also the two durations of impact, the first one calculated through (9) and the second one calculated by the model, are roughly equal (Table 4).

Conclusions

A simplified analytical structural model of cable-like retention barriers has been presented to assess the safety of such protection elements. A parametric study has been finally presented to show the influence of some input parameters on output data.

Also a preliminary energy assessment was performed. This work represents a starting point that will need further development and additional validation; however due to its simplicity and easy estimation of the involved parameters, it represents a promising tool to enhance the design and the verification of flexible barriers.

References

- Brighenti R, Ferrero AM, Segalini A (2013) Debris flow hazard mitigation: a simplified analytical model for the design of flexible barriers. *Comput Geotech* 54:1–15, doi: [10.1016/j.compgeo.2013.05.010](https://doi.org/10.1016/j.compgeo.2013.05.010)
- Canelli L, Ferrero AM, Migliazza M, Segalini A (2013) Debris flow risk mitigation by the means of rigid and flexible barriers – experimental tests and impact analysis. *Nat Hazards Earth Syst Sci* 12:1–7, <http://www.nat-hazards-earth-syst-sci.net/12/1/2012/>. doi: [10.5194/nhess-12-1-2012](https://doi.org/10.5194/nhess-12-1-2012)
- Gen M, Cheng R (1996) *Genetic algorithms and engineering design*, 1edn. Wiley, New York, p 40
- Goldberg DE (1989) *Genetic algorithms in search, optimization, and machine learning*. Addison-Wesley Publishing Company Inc., Massachusetts, MA, pp 1–56
- Kwan JSH, Cheung RWM (2012) Suggestion on design approaches for flexible debris-resisting barriers. Standard and testing division. Discussion note DN1/2012. The Government of Hong Kong Special Administrative Region.
- Sun HW, Law RPH (2012) A preliminary study on impact of landslide debris on flexible barriers. Geotechnical Engineering Office. Standard and testing division. Technical Note 1/2012. The Government of Hong Kong Special Administrative Region
- Takahashi T (1983) Debris flow and debris flow deposition. In: Shahinpoor M (ed) *Advances in the mechanics and flow of granular materials*, vol. II. Trans. Tech. Publ., pp 57–77



Engineering Solutions for Elimination of the Risk of Destruction of Moraine

Eduard Zaporozhchenko and Aleksandr Butenko

Abstract

In the upper reaches of the Kumtor River (Kyrgyzstan, Inner Tien Shan), behind the young end moraine, a new lake formed at approximately 3,735 m at the turn of the twentieth century. With the feeding glacier degrading, due to climate reasons, the volume of accumulated water mass has increased (up to 70 mln cu.m by 2013). The lake's natural retaining dam, composed of permafrost rocks with inclusions of buried ice blocks, is subject to thermokarst processes. Conditions for possible dam failure have formed and have been developing. Such a failure will lead to the creeping and sloughing of slopes of the developing washout channel and to a debris flow, which may be catastrophic for the infrastructure and tailings dump of the operating Kumtor gold mine. Based on analysis of the developing geotechnical situation and on multi-variate consideration of possible discharge routes and various construction designs of outlet works, a phased water level drawdown (water volume reduction) of the lake via a cascade of gabion structures during summer, in a route and mode as to achieve the best technical and economic execution and minimum engineering risk, has been accepted as a solution.

Keywords

Moraine complex • New lake formation • Permafrost section • Buried ice • Failure scenario • Spillway • Gabions

Introduction

At the beginning of 2013 the Sevkavgirovodhoz Institute presented “Pre-design Concepts” on a controlled water drawdown at a large mountain end-moraine dammed water body to a Canadian company, developing a gold mine in the upper reaches of the Kumtor River (Kyrgyzstan, Inner Tien Shan). The necessity for the drawdown had been caused by an increasing threat of water masses outbursting onto the mined area with possible disastrous consequences for the tailings pit (Fig. 1) and infrastructure facilities.

The mine of the company is situated at 3,900–4,200 m asl high, auxiliary services—at up to 4,400 m asl high. It has been in operation since 1997 and production is the second largest in the world. The gold production level, planned for 2013, is 550–600,000 ounces (with more than 300 tons produced since 1997).

The concepts, suggested by the Institute, were based on integrated data resulting from geological, hydrological and geophysical explorations and research on the issue of previous years, including those conducted in 2012 by a group of specialists from Russia, Kyrgyzstan and the Czech Republic, as well as data, received from the Customer—the Kumtor Operating Company (Chernomorets et al. 2012).

In 2012 the following work was performed: bathymetric surveys of the Petrov lake system, georadar surveys of the lateral part of the Petrov glacier; information on the moraine line structure, including geophysical data (electrosounding,

E. Zaporozhchenko (✉) • A. Butenko
Sevkavgirovodhoz Institute, pr. Kirova, 78, Pyatigorsk, Stavropol krai
357500, Russia
e-mail: skgvh@skgvh.ru



Fig. 1 July 2012. Tailings pit. Discharge of pulp (sludge) from the mineral separation plant at the Kumtor mine



Fig. 2 July 2012. Water-filled thermokarst funnel on the end-moraine line (the latter being a natural dam of Petrov Lake)

tomography, gravimetry), as well as drilling samples, was analyzed. Geo-Eye-1 space photography images were interpreted. An orthophotomap was created.

Petrov lake (Lunkin and Lunkina 1989) is located in north-east Kyrgyzstan, on the western slope of the Ak-Shiyrak mountain group. The lake waterline level is 3,733–3,734 m above sea level (asl). The lake is the source of the Kumtor River—a Bolshoy (Large) Naryn tributary. The lake is formed at the tongue of Petrov Glacier, behind young moraine. According to the 1911 survey, it had an area of 200–300,000 m³ [Erokhin (Chernomorets et al. 2012)]. Due to the climate, Petrov Glacier has been retreating (starting 1869); this process accelerated in the 1980s (15.1 m/year in 1869–1957, 24.8—in 1958–1980, 38.0—in 1981–1990, 43.3—in 1991–1999 and 61.4 m/year in 2000–2006, according to M. Cherny, B. Yansky, S. Erokhin). By 2013 (as per the bathymetric survey on 25–27 July 2012) the volume of water in the lake had reached 69 mln m³, having increased for 2009–2012 by 62,000 m³, or by c. 8.3 % of the total volume with an insignificant (by c. 2 %) increase in the area of the lake, which means it was due to ice melting and permafrost degradation at the bottom in the bowl.

Petrov Lake is formed by a young moraine complex (acting as a dam), made up of frost glacial, fluvial-glacial and limno-glacial single-grained deposits with buried ice blocks [S. Erokhin (Chernomorets et al. 2012)]. According to lichenometry dating as of 1978 (Sevestyanov 1981), this complex is c. 100 years old (according to (Serebryany and Orlov 1988), it was formed in the period of 1900–1915). It is located in the glacial deposition area of Kumtor syrts, characterized by a finely dissected, knob-and-kettle topography of the permafrost zone. The moraine surface is pecked with thermokarst funnel-shaped sinkholes and saucer-



Fig. 3 The area of the end-moraine line with Goluboy Zaliv ('Blue Bay') and Petrov Lake [space image, extracted from Chernomorets et al. (2012)]

shaped depressions, which give it a honeycomb-like look in photos and space images. During summer they are filled with water (Fig. 2). The most prominent water body is Goluboy zaliv (Blue Bay) (Fig. 3), practically connected to the main lake. Its volume as of 2012 is c. 800,000 m³.

Thermokarst processes in the last decades have been noticeably more active. This, along with the increase in the water volume in the lake, increases the risk of an outburst scenario with debris-flow formation.

Dendritic Petrov Glacier is up to 14 km in length (Sevestyanov 1981), its tongue part (Fig. 4), according to the radar sounding as of October, 2012 [D. Petrakov (Chernomorets et al. 2012)], is afloat. With water depths as low as c. 65 m at the forefront, the estimated area of the



Fig. 4 July 2012. At the front of Petrov glacier



Fig. 6 Kumtor syrt. The Tien Shan weather station. 3,654 m asl. Not operational since 1948. The building has been deformed by permafrost degradation



Fig. 5 July 2012. Mini-iceberg on the lake

floating part is 0.04 km^2 , its estimated volume is $1,700,000 \text{ m}^3$, and the estimated volume of icebergs, breaking off the glacier edge (Fig. 5), is as much as $330,000 \text{ m}^3$. The collapse of an iceberg c. $200,000 \text{ m}^3$ in volume within the period of 10–30 July 2012 (according to the space imagery) did not lead to the formation of a wave in the headwaters at the moraine dam, located c. 800 m off from the break-away point, whereas, according to the simulation in Kyrgyzstan Kumtor Mine (2012), the wave height at the dam should have reached 3 m, with a 6 m high wave splash!

The lake outflow (giving rise to the Kumtor River) is now in an area at the north part of the moraine where surface lowering has been taking place, according to S. Erokhin (Chernomorets et al. 2012), in ‘the last 10–20 years’ (with reference to 2012). Previously, for at least 70 years, it took a more northern route (‘old’ channel), which is now dry. A Tien Shan weather station (Fig. 6) recorded a discharge rate



Fig. 7 July 2012. Pulp line across the Kumtor River and a hydrometric structure of the Kumtor Operating Company on the Kumtor River c. 4 km from the source

of $66.2 \text{ m}^3/\text{s}$ on August, 2, 1943 on the Kumtor River, whereas ‘the last 10–20 years’ in the existing channel (Fig. 7) it has not exceeded $30 \text{ m}^3/\text{s}$ ($25.7 \text{ m}^3/\text{s}$ on August, 21, 2012). The Kumtor Operating Company’s waterworks have successfully managed such a discharge rate. Now the ‘dry’ source is separated from the lake with a barrier up to 2 m high.

The diversity of moraine materials—ice, frozen rocks of a wide granulometric spectrum from sands to large chunks of hard rock material, with possible presence of voids in the section—complicates both the development of forecast outburst scenarios and the assessment of the resistance of the natural dam, on average c. 30 m height, to the internal and/or surface erosion. The physical and mechanical properties and condition of the moraine complex section are exceptionally

Fig. 8 Orthophotomap from GeoEye-1 space images taken as of July, 29—August, 1, 2012 with considered section options—Petrov Lake water drawdown routes (Sections -1a, 1b, 2, 3 and 4)



problematical to determine. The preparer of “Pre-Design Concepts” did not possess the latter data and performed the work on the premise that:

- with no definite forecast of events, there is c. 70 mln.m³ of water, retained by the moraine permafrost complex, which is degrading under the warming influence of the water, above the outwash syrt on which a major hazardous production facility—a tailings pit—is located;
- there is no alternative to artificial water-level drawdown;
- a phased drawdown must start as soon as possible.

The Institute considered 5 options of outflow routes (Fig. 8) and five alternative designs of water spillways.

Section 1a The direction of release is along the ‘dry’ channel of the Kumtor River sources. It is separated from the lake by a barrier up to 2 m high (with ± 0.7 m summer fluctuations of lake water level).

Section 1b The direction is along the current channel of the Kumtor River source. As with Section 1a, it is in the youngest (northern) part of the moraine with high content of buried ice (up to 50–70 %). As with Section 1a route, the channel has a block and stone paving 3–5 m thick with a c. 0.5 m average block diameter. The estimated depth of the suprapermafrost layer under the current channel is 2–4 m. Judging by the long lifetime of the overflow path of the now ‘dry’ channel (Section 1a), the paving previously formed on its bottom should be at least 3 m thick.

Section 2 The release is carried out through the thinnest segment of the moraine complex (dam) and via Goluboy Zaliv (the distance between the Kumtor river channel and the Goluboy Zaliv shoreline is 265 m, the horizontal distance

from the shoreline to the outer slope—90 m). The moraine crest below the Goluboy Zaliv level is 13.5 m high. To achieve the lowering of the headwater level, the outfall channel depth in the permafrost section with ice inclusions should be >14 m.

Section 3 The release of water is carried out through Goluboy Zaliv, with the flow directed over a wider portion of the moraine (540 m rather than 265 m and 192 m rather than 90 m, respectively, as compared with Section 2). The maximum ‘crest/level’ height difference is 24 m. Excavation of the youngest (third) moraine sub-complex, then the second moraine sub-complex with a lower buried ice content (10–30 %) through to fluvio-glacial deposits will be required.

Section 4 The release is carried out through the downgrading part at the southern point of abutment of the moraine complex and the bedrock—a weakly defined ancient channel of the source of the Kumtor river. The maximum difference between the current water level in the lake and the highest point on the moraine surface in the section is 27 m. The initial depth of the excavation will be close to 30 m. It will penetrate heterochronous ice-containing rocks.

In the process of data analysis of the engineering and geological settings, taking into consideration the volumetrics of implementing the drawdown, Section 2, 3 and 4 options were declined (deep excavations, construction of high fills on steep outer slopes of moraine for operation of construction machinery); additionally, Sections 2 and 3 were also declined due to the risk of failure of the natural moraine dam in its thinner part, where thermokarst processes are most active.

The recent (Section 1a) and the existing (Section 1b) routes of natural water runoff from the lake were recognized as more acceptable for considering structural options for the water-drawdown task. The following conditions were satisfied:

1. minimal impact on the engineering and geological settings developed by 2013, determined by the heat exchange between the Kuntor River source surface waters, lake water masses and the rocks, composing the moraine complex;
2. a phased water-level lowering in the lake (one phase each summer runoff period);
3. release of water with a discharge rate below the maximum recorded rate in the functioning flow-through structures within the infrastructure facilities of the Customer (within $30 \text{ m}^3/\text{s}$);
4. monitoring of the functioning of the outfall route, the dynamics of processes, occurring in the lake and inside the retaining moraine, from commencement of engineering works on drawdown;
5. the implementation of the drawdown against the back-drop of a cut between Goluboy zaliv and the lake (equalization of water planes between them);
6. preferability of spillways with contraction–expansion joints, or those made as flexible units;
7. orientation towards the final lowering of the level by 15–20 m, which will make it possible to decrease the lake area by more than times times, thus increasing the base width of the natural retaining dam up to 1.8 km (it was 500–600 m in 2013);
8. exclusion of blasting in the moraine dam body;

With that:

1. large structures like regulator sluices and backwater structures [due to the danger and non-uniform deformation of foundations, subjected to thermokarst processes (such as skewing of structures and perimeter filtration, etc.)] are not expedient;
2. it is advisable to use high-definition space imagery for monitoring the effectiveness of the drawdown engineering operations (yearly—upon completion of each phase or before the commencement of the next phase);
3. in connection with the anticipated formation of separate water bodies on the above-water surface of the moraine complex (when the water level is lowered by c. 5 m), barriers between them will have to be promptly cut.

As mentioned above, five options of design of surpassing works were considered.

Option 1 As applicable to Section 1b. Cascade (Stepped spillway). The longitudinal profile requires a minimum surface cutting. The cross-section is a rectangular chute 8.0 m in

width and 2.0 m in height made of cast reinforced concrete B25 F200 W6. The chute floor thickness is 0.3 m, the thickness of walls is from 0.2 to 0.5 m. The steps are connected by means of a 1.5 m wall of cast reinforced concrete. To reduce the heat exchange between the water and buried ice in the foundation, the chute is placed over a 5 cm thick plastic foam layer set on a 10 cm thick levelling layer of sand. The backfilling is carried out using the native soil with layer-by-layer compaction, leaving 0.5 m free space to the top of the chute walls for a safe enclosure of the inner part of the spillway. On both sides of the chute a road 5 m wide is constructed for an unhindered vehicular access to any point of the water spillway by service or construction machinery. The entrance channel to the entry of the chute is cone-shaped. The discharge capacity is $34 \text{ m}^3/\text{s}$.

Option 2 As applicable to Section 1b. Cascade of gabion structures. The longitudinal profile (Fig. 9) requires a minimum surface cutting. The cross-section is a rectangular chute 8.0 m in width and 2.0 m in height (Fig. 10). The chute floor is covered with Reno mattresses $6 \times 2 \times 0.3 \text{ m}$, the walls consist of $2 \times 1 \times 1 \text{ m}$ gabions. The steps are connected by means of holding gabions $2 \times 1 \times 1 \text{ m}$ at the beginning and at the end of each step. To reduce the heat exchange between the water and buried ice in the foundation, a plastic foam layer 5 cm thick is placed over a levelling layer of sand 10 cm thick. A waterproofing construction of a 2 mm thick geomembrane, sandwiched between two layers of geotextiles, 400 g/m^2 in density, to prevent the geomembrane from being damaged, is placed above the plastic foam. The geomembrane performs the waterproofing function. The backfilling is carried out using the native soil with layer-by-layer compaction. Unfilled space to the top of the chute walls is the same as in Option 1. On both sides of the chute a road 5 m wide is constructed. The entrance is cone-shaped. The discharge capacity is the same (c. $34 \text{ m}^3/\text{s}$).

Option 3 As applicable to Section 1a. Cascade of 3d geowebs in the shape of a trapezoidal channel. The floor width is 8.0 m, the depth—2.0 m, the side slope 1:2. GW20 geowebs ($244 \times 203 \times 150$) are installed onto the floor and slopes to protect them from washout, the cells are filled with cast reinforced concrete B15 F200 W6 (a composite system, with tension strength and distributing capacity of a quasi-homogeneous layer). Geowebs are fastened to the channel slopes and floor with A-III class L-shaped reinforcement anchors, 12 mm in diameter, with 1 m spacing. The steps are connected by means of holding concrete blocks $2 \times 1 \times 1 \text{ m}$ at the end of each step. To reduce the heat exchange between the water and buried ice in the foundation, the chute is placed on a plastic foam layer 5 cm thick set

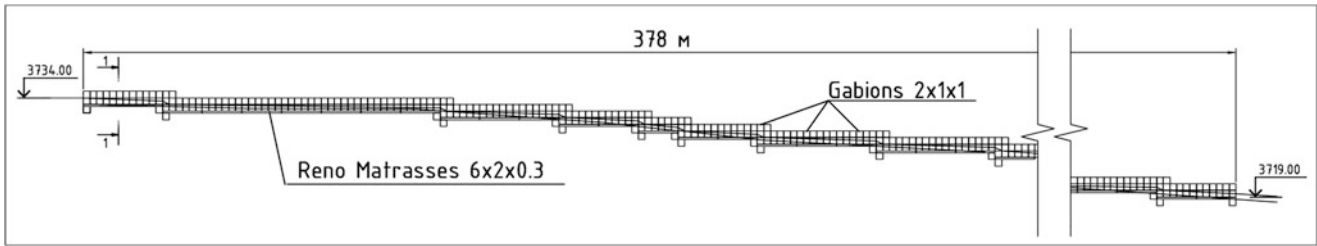


Fig. 9 Longitudinal section: Option 2 structure of the spillway on section 1b—cascade gabion ladder

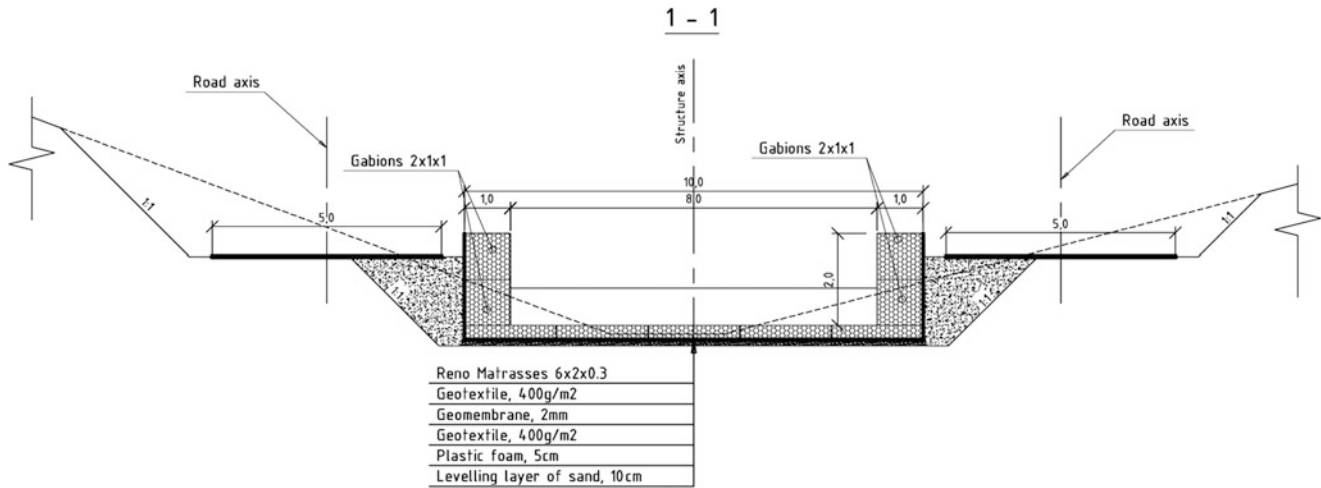


Fig. 10 Cross section of Option 2 spillway

over a levelling layer of sand 10 cm thick. A road 5 m wide is built on both sides of the chute. A cone-shaped entrance should be constructed. The discharge capacity is the same (c. $34 \text{ m}^3/\text{s}$).

Option 4 As applicable to Section 4. Battery of 8 siphons of round cross-section polyethylen pipes, 0.8 m in diameter. The discharge capacity is $25 \text{ m}^3/\text{s}$. The length of each siphon is 150 m (at Phase 1). At the beginning and in the lower part of pipes, gate valves are installed. An air evacuation valve is fitted at the highest point. An air admittance valve is fitted downstream the lower gate valve. The pipes are laid on a sand cushion 15 cm thick and are surcharged at sides and on top with native soil without large inclusions (diameter ≤ 20 mm). To render the structures immune to vibration action and to stabilize them as to prevent them from sliding down the slope, the pipes are fastened to the foundation with a U-bar #12 steel arch and ground anchors 5.5 m long, with 6 m spacing. Rubble stone riprap (a prism 300 mm in diameter) for the flow energy dissipation should be provided at the exit. On both sides of the structure a 5 m wide road is constructed.

Option 5 As applicable to Section 4. Pumping station, (Fig. 11) 13×42 m in plan, with inlet and outlet pipelines. The building is a metal framework, clad in insulated profiled-sheet. It is equipped with centrifugal type horizontal pumps (9 units of D12500-24 incl. one standby unit).

Electric motor specification: AN2-17-48-12U4. Power: 1,000 kW. The pump specification, based on the rated water transport requirement, is $25 \text{ m}^3/\text{s}$ (the maximum recorded water discharge rate at the Kumtor river over the last 15 years). The delivery rate of one pump is up to $3.47 \text{ m}^3/\text{s}$. With regard to pump inlet capability, the suction head will not exceed 2 m from the shaft centreline. There are gate valves on the inlet pipe and flow meters on the outlet pipe. There should be an overhead track crane with a load-lifting capacity of 20 ton in the equipment assembly/disassembly building. Pipe weight: 19.8 ton. Electromotor weight: 8.08 ton. The base under the pump is made of cast reinforced concrete, grade B15 F200 W6. The outlet pipeline is a steel pipe 1.0 m in diameter, 150 m in length. Rubble stone riprap (a prism 300 mm in diameter) for the flow energy dissipation should be placed at the exit. Placement location: at the same site as the currently operating pump, administering to the requirements of the Kumtor mine.

To implement Options 1, 2 or 3 of spillways, the following operating sequence and course of events (drawdown regime) are suggested:

1. at the beginning of the first year (First Phase) winter period, when natural runoff from the lake ceases, the spillway is constructed from-bottom-to-upward, with a crest, making it possible to decrease the water level by



Fig. 11 July 2012. Water intake of technical and potable water by Kumtor Operating Company near the southern shore of Petrov lake

- 1.0 m (and thus reduce the current water volume in the lake by c. 4 mln.m³);
2. the overflow from the lake starts in spring period; as the spillway crest level will be 1 m below the natural level, the overflow will start before the usual time, and though the water inflow will be happening in the same regime as before, the discharge will be taking place a longer period; the peak runoff period will also be longer. If prior to such engineering control measures the discharge with a flow rate of 25 m³/s was achieved by the end of July or August (as the lake water level rise of 1–1.2 m was required for that), when such measures are put in place this situation will presumably develop in early July already and the ending of high waters will shift to a later date (with that, the peak runoff rate of high waters will not increase: the lake water volume will be reduced not due to an increase of the runoff rate, but owing to the increase in the runoff period);
 3. as the surface runoff ceases, in winter period the upper crest of the cascade is dismantled, keeping the geotextile, geomembrane, and the foam plastic intact, if possible; the foundation is then deepened for further construction and the entrance channel to a lower crest is constructed, based on the calculation that the channel will be c. 1 m lower than the water level, established in the first phase period (the amplitude of all consequent yearly lowerings is reviewed and updated in accordance with attained level of drawdowns);
 4. the further phases are identical: the entrance channel to a spillway crest will be deepened and lengthened; the phases will be accompanied by measures for the stabilization of the dam slopes (a failure may lead to the

blockage of the section) by way of cutting shelves (benches) 4–5 m wide every 3–4 m in height;

5. ensuring a safe yield to meet the Kumtor mine's needs will call for relocations of the existing pumping station (with every 2–2.5 m level drawdown);

An achieved drawdown by c. 15 m will lead to the reduction of the lake water volume by c. 45–50 mln m³.

In view of the difficulty of forecasting the deformation behaviour of the discharge route in the permafrost section settings, it is expedient to have a reserved possibility to temporarily redirect the runoff from Section 1b system into Section 1a system (and/or vice versa).

For Option 4 the water drawdown regime will be as follows:

- in summer period a siphon spillway is constructed with the possible lowest placement of the spillway crest (preferably at the same level as the water level in the lake). The water release operation through siphons starts in autumn, when the inflow to the lake recedes abruptly; the inlet is lowered by 2 m into the water; the siphon is prepared by evacuating air with gate valves closed; after the air is evacuated, first the upper gate valve is opened and, after it is filled with water to its full capacity, the lower one, following which the water discharge takes place; the number of simultaneously operating siphons will have to be continuously determined; the water level should not go above the maximally reduced level higher than 20 cm, at which elevation the next siphon should start operating; at the beginning of the winter season the water drawdown should be stopped and the inlet section of the siphon should be dismantled so as to prevent it from being crushed by ice;
- in order to prepare for the next phase, the existing overflow crest of the lake is lowered in winter period to the level of the previously performed drawdown;
- the top section of the siphon is dismantled and mounted at a lower position; after the siphon is primed, the water is discharged;
- conditions are prepared for the next phase; each consecutive water release phase presupposes the deepening of the existing overflow crest at the source of the Kumtor river in winter period down to the level of water in the lake; the deepened part of the crest should be protected from scour, as maximum water discharges will have to pass the river channel before the spillway starts operating.

The water drawdown regime for Option 5 is presumed as follows:

- a pumping station is constructed with inlet (intake) and outlet pipelines;
- the water level in the lake is drawdowned approximately by 1 m and is maintained at this elevation during the year with the help of a required number of pumps in operation;

Table 1 Structural and technical advantages and disadvantages of suggested options

| Option | Section | Design features | Pros | Cons |
|--------|---------|---|--|---|
| 1 | 1b | Stepped spillway. Cast reinforced concrete. | Minimal earth work volume—an important factor as work will happen in winter; reinforcement cages are assembled indoors in a warm period; units are erected during construction | Concreting is carried out in winter, additional cost for concrete heating, high probability of faults; stiffness of the structure, a large number of contraction-expansion joints, it is hard to forecast in what manner the foundation-to-structure deformation will develop during runoff release |
| 2 | 1b | Stepped spillway. Gabion units | Flexibility of structures, resistance to foundation deformations (precipitation, soil heaving, etc.); structure fits well into environment (close to natural paving) | Manual work in winter; increased volume of soil works |
| 3 | 1a | Stepped spillway. 3-D geoweb | Low labour content; possibility of pre-construction work in summer period in dry channel | Concreting is carried out in winter, additional cost for concrete heating, high probability of faults |
| 4 | 4 | Battery of eight siphons (PE pipes 0.8 m in diameter) | Construction in summer | Siphon spillways designed for automatic water level control to maintain waterline at prescribed level. Not designed for permanent water level control; tilting of structure and foundation deformation are inadmissible, reliable operation is ensured by presence and deliverability of equipment for air evacuation. Permanent presence of service personnel required; large volume of soil work; incut into the moraine dam up to the waterline is required, which is highly dangerous; for securing the pipes to the moraine, ground anchors are required; vibrational impacts during work may result in loss of the moraine complex; No practical possibility to dismantle plastic pipes without defecting the latter; each phase will require new pipes in lieu of dismantled pipes (or switching to steel pipes); with each phase, following the lowering of the waterline in the lake, increasingly longer pipe columns have to be laid on soft soil surface, only previously freed from water; implementation of the siphons option is impossible without lowering of overflow crest and scour protection work (rise in cost by USD 10–12 mln) |
| 5 | 4 | Pumping station, 13 × 42 m in plan, with inlet and outlet pipes. Equipped with centrifugal horizontal pumps D12500-24 (9 units) | Possibility for construction in summer | higher cost (by 9–13 times as compared to other options); requirement for large amounts of electric power, construction of transformer house near [pumping station] building; vibrational impacts and thermal effects, which may result in loss of the moraine complex; implementation of this design is impossible without lowering of overflow crest and protection against scour (rise in cost by USD 10–12 mln) |



Fig. 12 July 2012. Source of the Kumtor river. View from the moraine crest 1—Petrov lake, 2—overflow crest

- the formed overflow crest at the source of the Kumtor river is lowered to the drawdown level, the deepened part of the crest is protected from scour.
- the pumping station is relocated (Fig. 11) onto a nearby site and is placed 1 m lower than the previous location (the lowering is adjusted based on the previous phase results); the first phase of 1 m drawdown and relocation of the pumping station will take about 1 year;
- further the consequent drawdown phases are carried out in a similar fashion.

The costs of building and installation works for the 15-phases options are as follows (estimations are in US Dollars):

Option 1—10.4 mln., Option 2—15.2 mln.; Option 3—13.0 mln., Option 4—11.8 mln.; Option 5—131.9 mln.

Structural and technical advantages and disadvantages of suggested options are given in Table 1.

Option 2—gabion spillway on Section 1b (the current Kumtor river source) route was recommended for construction as it is characterized by the lowest technological and ecological risks (Fig. 12).

Field studies of the situation developing at the site and in adjacent areas from commencement of planned drawdown works as well as an instrumental and visual monitoring program (with its makeup outlined) with methodological recommendations along with an emergency plan procedure for the personnel should indispensably be included in Design Documentation.

Acknowledgements The work was funded by CJSC Kumtor Operating Company, Bishkek, 2013.

References

- Chernomorets SS, Tutubalina OV, Doronkin Yu I, Erokhin SA, Zaginayev VV, Lavrentyev II, Petrakov DA, Usubaliyev RA, Cherny M, Shobr M, Engel Z, Yaneki B (2012) Data from engineering geological, hydro-geological and geophysical investigations for developing pre-design concepts on controlled water level drawdown in Petrov Lake (Kyrgyz Republic). Report. Moscow-Prague-Bishkek, 117p.
- Kyrgyzstan Kumtor Mine (2012) Geohazard hazard and risk assessment for potential Moraine Dam outbreak flood at Petrov Lake. Final project no. 0889-001. BGC Engineering Inc. 23, March 2012, 143p
- Lunkin YM, Lunkina TV (1989) Tourist zones of Kirgizia. Frunze Publishing House, Kyrgyzstan, 116p
- Serebryany LR, Orlov AV (1988) Tien-Shan through Glasiologist's eyes. Nauka Publishing House, Moscow, 105p
- Sevestyanov DV (1981) New data on the evolution of the high-mountain lake at Petrov glacier terminus (Tien-Shan). *Izvestiya VGO* 113(5):430–435, Nauka Publishing House, Leningrad

Part VIII

Risk Reduction Strategy



Introduction: Risk Reduction Strategy

Farrokh Nadim

Abstract

Active and passive measures for reducing the risk associated with landslides are an important part of a successful landslide risk management strategy at local, regional and national levels. The papers in this session outline various strategies for landslide risk reduction. The majority of the papers focus on non-structural measures for landslide risk reduction, in particular community preparedness, public awareness campaigns and active application of land use plans. This is in line with the latest trends in risk management for natural hazards, and demonstrates that importance of involving the affected population and other stakeholders in the decision-making process for risk reduction.

Keywords

Landslide risk mitigation • Risk management strategy • Early warning systems • Public awareness campaigns

Introduction

During the past decade, disasters caused by natural hazards were responsible for nearly one million fatalities, affecting nearly 2.5 billion people across the globe. In 2010 alone, 295,000 fatalities were recorded by the re-insurance company Munich Re (2011) and the overall economic losses were more than double those of 2009 for approximately the same number of catastrophic events.

Among the natural hazard driven by geological processes (geohazards), landslides are the most frequent one. They represent a major threat to human life, property and constructed facilities, infrastructure and natural environment in most mountainous and hilly regions of the world. In many places, the frequency and severity of landslide events seem to be rising. Some of the reasons for the increase, such as increasing population density and more infrastructure in landslide-prone areas, are obvious; others less so. However,

there is no doubt that many lives could have been saved if more had been known about the risks associated with landslides and if the risks had been managed better.

Landslide Risk Mitigation: An Important Tool for Landslide Risk Management

Landslide risk management broadly refers to coordinated activities to assess, direct and control the risk posed by various types of gravity mass flows and landslides to the society. It integrates the recognition and assessment of risk with the development of appropriate strategies for its mitigation. The risk management process is a systematic application of management policies, procedures and practices to the tasks of communicating, consulting, establishing the context, identifying, analyzing, evaluating, monitoring and implementing risk mitigation measures. Obviously active and passive risk mitigation measures are an important component of a successful risk management strategy.

An important aspect of risk management is the need to recognise that risk can rarely be eliminated completely.

F. Nadim (✉)
Norwegian Geotechnical Institute, International Centre for
Geohazards, 0806 Oslo, Norway
e-mail: Farrokh.nadim@ngi.no

However, it could be reduced below what is acceptable to the society through risk mitigation. Risk acceptability depends on several factors such as voluntary vs. involuntary situation, controllability vs. uncontrollability, familiarity vs. unfamiliarity, short/long-term effects, existence of alternatives, type and nature of consequences, gained benefits, media coverage, availability of information, personal involvement, memory, and level of trust in regulatory bodies.

The strategies for the mitigation of risks associated with landslides can broadly be classified in six categories:

- 1) land use plans,
- 2) enforcement of building codes and good construction practice,
- 3) early warning systems,
- 4) community preparedness and public awareness campaigns,
- 5) measures to pool and transfer the risks, and
- 6) construction of physical protection barriers.

The first five strategies are referred to as non-structural measures. These aim to reduce the consequences of landslides by reducing the vulnerability and exposure of the elements at risk. The last strategy comprises active intervention and engineering works, which aim to reduce the frequency and severity of landslides.

Landslide Risk Mitigation in Developing Countries

On a national scale, with regards to reducing the landslide risk in developing countries, one can observe a positive trend internationally. Preventive measures are increasingly recognized, both on the government level and among international donors. There is, however, a great need for intensified efforts, because the risk associated with all types of geohazards seem to be increasing far more rapidly than the efforts made to reduce this risk.

Three key pillars for the reduction in risk associated with natural hazards in developing countries are suggested:

1. identifying and mapping the high-risk areas, and quantifying the hazard and the risk,
2. implementing structural and non-structural risk mitigation measures, including early warning systems, and
3. strengthening the national coping capacity.

Most of the developing countries lack sufficient coping capacity to address a wide range of hazards. International cooperation and support are therefore highly desirable.

Over the last decade, a number of countries have been supportive with technical resources and financial means to assist developing countries where the risk associated with natural hazards is high. A key challenge with all projects from the donor countries is to secure that they are need-based, sustainable and well anchored in the countries' own development plans. Another challenge is coordination, which often has proven to be difficult because the agencies generally have different policies and the implementation periods of various projects do not overlap. A subject which is gaining more and more attention is the need to secure 100 % ownership of the project in the country receiving assistance.

The capacity building initiatives should focus on institutions dealing with disaster risks and disaster situations in the following four policy fields:

- Risk assessment and communication, i.e. the identification, evaluation and possibly quantification of the hazards affecting the country and their potential consequences, and exchange of information with and awareness raising among stakeholders and the general public;
- Risk mitigation, i.e. laws, rules and interventions to reduce exposure and vulnerability to hazards;
- Disaster preparedness, warning and response, i.e. procedures to help exposed persons, communities and organizations be prepared to the occurrence of a hazard; when hazard occurs, alert and rescue activities aimed at mitigating its immediate impact;
- Recovery enhancement, i.e. support to disaster-stricken populations and areas in order to mitigate the long-term impact of disasters.

In each of these fields, institutions can operate at local, regional, national or international levels.

Papers Presented in Session B8

The papers in this session outline various strategies for landslide risk reduction. Interestingly, the majority of the papers focus on non-structural measures for landslide risk reduction, in particular community preparedness, public awareness campaigns and active application of land use plans. This is in line with the latest trends in risk management for natural hazards, and demonstrates that importance of involving the affected population and other stakeholders in the decision-making process for risk reduction.



Place-Conscious Education for Disaster Prevention in Risk-Prone Areas of Sao Paulo

Erica Akemi Goto and Jefferson de Lima Picanço

Abstract

This paper outlines the importance of the use of place-conscious pedagogy in non formal education courses developed to prevent accidents and disasters in hydrological at-risk areas. In the city of São Paulo, according to the Risk Area Mapping made by the “Instituto de Pesquisas Tecnológicas—IPT” (Technological Research Institute) together with São Paulo’s City Hall, São Paulo has many at-risk areas, but the major part of them are in the city’s suburb areas. With the intention of working with non structural measures, the City Hall of São Paulo offered, during 2012 and 2013, some non formal education courses for inhabitants, technicians, and people concerned with the subject. The courses were given in many places in the city with three different focuses: “Risk Perception”, “Urban and Environmental Risk: a Prevention Approach” and “Capacity for Mapping at-Risk Areas”. Those courses used the place-conscious pedagogy by presenting the physical and social problems of the local environment, and, also, through the intention of creating in the local inhabitants attitudes that could contribute in a social and environmental mode to the community where they live. The place-conscious’ notion is an important instrument to be used in those kinds of courses. Only with an enlarge knowledge of the place where they live, those at-risk area inhabitants can integrate and participate of public politics helping to chose decisions which can contribute to decrease the inhabitants vulnerability.

Keywords

Place-conscious education • Risk areas • São Paulo • Non formal education courses • Disasters

E.A. Goto (✉)

Instituto de Geociências, Programa de Ensino e História em Ciência da Terra, Universidade de Campinas (Unicamp), 51 João Calógeras Street, 13083-870, Campinas SP, Brasil

Centro Nacional de Monitoramento e Alertas de Desastres Naturais (Cemaden), Rodovia Presidente Dutra, Km 40, SP-RJ, 12630-000 Cachoeira Paulista, SP, Brasil
e-mail: ericagoto@gmail.com

J. de Lima Picanço

Instituto de Geociências, Programa de Ensino e História em Ciência da Terra, Universidade de Campinas (Unicamp), 51 João Calógeras Street, 13083-870, Campinas SP, Brasil
e-mail: jeffppicano@gmail.com

Introduction

The city of São Paulo, as well as other cities around the world, has many singularities, which are intrinsic to the city’s formation. Each city’s community also has its singularities based on cultural influences and local environmental aspects.

After the 1960s, São Paulo has seen its number of inhabitants increase, receiving people from the whole country, especially from rural areas (Maricato 2008). However, the city didn’t have enough houses and infrastructure to receive those new inhabitants, resulting in inappropriate occupied areas, such as slopes and dales, without any basic infrastructure, like proper sanitation, safe water supply and



Fig. 1 Taken in a slum in São Paulo Metropolitan Area, the photo shows the shabby materials used at the constructions, such as wood pieces. Moreover, there are lots of garbage thrown away in the slope (Source: Erica Akemi Goto 2011)



Fig. 2 In this photo, there are many drainpipes installed by the inhabitants themselves. These pipes throw away waste water in the slope (Source: Erica Akemi Goto 2011)

running water, electricity and sewage network. These inappropriate occupied areas also lack basic public services, such as public transportation, schools and hospitals (Maricato 2008).

Besides that, many individuals have started to build their own houses by themselves in an unprepared manner, as can be seen in Figs. 1 and 2. These houses are built with precarious materials on cutting slopes and/or over earth backfills.

This urbanization process resulted in many people living in hydrological at-risk areas. According to the Risk Area Mapping mentioned earlier, there are 1.179 landslide and river bank washout risk sections, each section having a variable number of houses.

Figure 3 is a map that shows the at-risk areas' number and its geographic distribution in Sao Paulo's city districts (in Portuguese "subprefeituras"). The orange districts have

more than 20 at-risk areas; the yellow ones from 11 to 20; the light pink ones between 1 and 10; and the white ones have no at-risk areas. From the figure it can be inferred that the peripheral districts are the places with the highest number of at-risk areas.

Because of Brazilian public policies, it is well known, that it's practically impossible to relocate every at-risk areas' families. For this reason, measures that help these families live better adjusted to this reality are of utmost importance and therefore have to be taken.

There are two types of measures, the structural ones and the non structural ones. While structural measures can be engineering constructions, non structural ones can be at-risk area mapping, non formal courses, risk management and prevention plans.

This paper outlines one type of non structural measure that has an educational purpose: the non formal courses. Additionally, it will be discussed the importance of using place-conscious pedagogy when developing these types of courses. Not only the various risk sectors similarities, but also its singularities should comprise the course's content. For instance, the Parque Vila Santa Madalena community suffers with slides caused by the garbage thrown out in the slope. This topic is for this community vital and should be incorporated in the course as well, so its inhabitants can understand the reasons behind the slides formation and how to deal with this issue.

According to Gruenewald (2003a, b), the place-conscious pedagogy is a fundamental tool, which can help people develop positive attitudes toward social and environmental welfare in the place where they live. Through a multidisciplinary place analysis, it's possible to realize the difference forms in which the place is deeply pedagogical, and how the individuals as persons who live in some places have their identities and possibilities shaped by the local particularities. The culture and place are closely-related (Gruenewald 2003a, b).

Non Formal Courses Developed to Prevent Accidents and Disasters in Hydrological At-Risk Areas Offered by São Paulo's City Hall

During 2012 and 2013, the city hall offered three types of non formal courses developed to prevent accidents and disasters in hydrological at-risk areas: "Risk Perception", "Capacity for Mapping at-Risk Areas" and "Environmental and Urban Risks: a Prevention Approach". These three courses have different class loads and were developed for a distinct public.

To discuss the importance of place-conscious pedagogy, it will be used some examples of the "Risk Perception"



Fig. 4 The photo shows the amount of garbage thrown out in the slope (Source: Erica Akemi Goto 2013)

Paulo is only one city, because of its huge geographic extension and culture diversity, there are a great number of communities, each with its own traits. Some communities have just been created, while others have its origin tracked back to São Paulo's formation. On the one hand, there are communities, whose houses were constructed mainly with wood and no basic infrastructure. On the other hand, there are communities mainly with houses made of bricks and basic infrastructure. That is why the place conscious pedagogy is well suited to a city like São Paulo as well as others.

To develop a good local risk management, it is important to know the community's history and culture, as well as the area's geographic aspects and the history of natural hazard occurrences there. One of the purposes of these courses, other than helping to develop the risk perception, is to aid the community in planning and developing a hydrological risk management. Through this management, accidents and disasters related with hydrological hazards can be avoided. The place-conscious pedagogy is fundamental to help develop these courses and to help with the hydrological risk management.

To better understand the communities' issues and better structure the courses in those places, it is important to conduct a local investigation and make a diagnosis. For example, chatting with locals, leaders and institutions' representatives should not be disregarded, since they are also part of the community's history and local culture. Looking for previous reports about natural hazards in the community can also help to understand what the community has undergone.

So, before starting planning the courses, it is important to know well the place where the courses will be held, and explore the local particularities. Even though the



Fig. 5 It's possible to notice in the photo the house near the river margin. The latter has been washed away (Source: Erica Akemi Goto 2012)

“Perception Risk” courses didn't occur in the community where they were given, the city hall technicians responsible for the courses tried to approach the local risk problems, using the risk areas mapping made by the IPT (2010) and visiting risk areas before the activities to prepare the courses' activities.

At Vila Prudente-Sapopema District, they have a community named Parque Vila Santa Madalena. The place has lots of problems of planar slide, especially because of the garbage thrown out in the slope by local inhabitants, as it can be seen in Fig. 4. In this district, one of the main course discussions was about this type of problem. Another example would be the course taught at Aricanduva-Vila Formosa District. There is an area there, where flood and river washout problems are usual and frequent. During the course there, those issues were important topics. In Fig. 5, it is possible to see the course's outdoor activity.

Using the place-conscious pedagogy in these courses, students feel involved, since the course discusses things that are part of their everyday life and are important to them.

Conclusion

Considering the Brazilian reality, where some many people live in hydrological at-risk areas, it is important that they learn to cope with the everyday risk. It is believed that these courses have a fundamental role and using the place-conscious pedagogy is essential.

However, one major problem is that there are so many districts in São Paulo, and they are considerably extensive, comprehending many different kinds of hydrological risks. As it is known, hydrological risks be really different from each other. Besides that, the local culture of a community can be far different from another one in

the same district. For example, in Vila Prudente District, the problem related to the thrown out garbage in the slope can be seen at Parque Vila Santa Madalena's Community, but not necessarily in other communities of the same district. Others types of problems like river margin wash-out are not a part of Parque Vila Santa Madalena's Community reality.

So, it's understood that those courses use just in part place-conscious pedagogy. It is important that more courses are held in the community itself, where the hydrological risk is present, and not just in the district where these communities are located. A district can have more than twenty risk areas, that are different among them. With more courses, it would be possible to explore local issues better, as well as the particularities of each

community, resulting in courses that make more sense for the inhabitants.

Acknowledgments Cintia Toth Gonçalves.

References

- Gruenewald D (2003a) Foundations of place: a multidisciplinary framework for place-conscious education. *Am Educ Res J* 40(3):619–654
- Gruenewald D (2003b) The best of both worlds: a critical pedagogy of place. *Educ Res* 32(4):3–12
- Instituto de Pesquisas Tecnológicas – IPT (2010) Relatório Técnico: Prefeitura Municipal de São Paulo. São Paulo
- Maricato E (2008) *Brasil, cidades: alternativas para a crise urbana*. Vozes, Rio de Janeiro



Landslide Community Mapping and Public Awareness in the Region of Chichonal Volcano, Chiapas, Mexico

Guadalupe Hernández-Moreno, Ricardo J. Garnica-Peña, and Irasema Alcántara-Ayala

Abstract

The Chichonal is an active volcano situated in the North of Chiapas State, in the Southeast of Mexico; 60 km to the Southeast of Villahermosa, State of Tabasco and 70 km to the Northeast of Tuxtla Gutierrez, the capital of the State of Chiapas. The region comprises important areas of eight municipalities, some of them still inhabited by Zoque indigenous population.

The last eruption of Chichonal volcano occurred in 1982. Non-consolidated volcanic deposits derived from this period of activity are very susceptible to the occurrence of landslides. Landsliding frequently takes place during the rainy season (April–October) and also are associated with floods, although high seismicity is common in the region. What is more, lithological units such as sandstones, lutites and limestones are susceptible to landsliding too.

By means of participatory cartography, and based on the communities experience, residents of the municipalities situated around the Chichonal volcano developed different general landslide hazards maps. Additionally, a landslide susceptibility map was generated by means of weights of evidence using GIS. The later, considered physical variables including geological and geomorphological features.

According to the produced map, the eastern sector is the most susceptible area for landslides since slopes are high and there is a presence of ancient landslides on limestones and lutites. In the western area, there are also some strips of landslide susceptibility on high slopes formed by sandstones and lutites. Moreover, in this same area, potential lahars can also take place along the gullies on the Chichonal volcanic edifice.

In this paper, we present the experiences of landslide community mapping in the region of Chichonal volcano that took place within the context of a series of workshops that were organised in order to raise landslides public awareness.

Keywords

Mass movements • Community mapping • Chichonal volcano • Zoque indigenous population

G. Hernández-Moreno (✉)
Universidad Nacional Autónoma de México, Posgrado en Geografía,
Circuito Exterior s/n., Ciudad Universitaria, México, D.F
e-mail: zulilupiz@gmail.com

R.J. Garnica-Peña • I. Alcántara-Ayala
Universidad Nacional Autónoma de México, Instituto de Geografía,
Circuito Exterior s/n., Ciudad Universitaria, México, D.F
e-mail: garnica@igg.unam.mx; irasema@igg.unam.mx

Introduction

The Chichonal is the youngest of the Quaternary volcanoes forming the Chiapanecan Volcanic Arc (Fig. 1). Volcanism of Chichonal seems to be associated with the subduction of the Cocos plate under the North American plate. Recent studies have shown that El Chichonal volcano has produced



Fig. 1 El Chichonal volcano, Chiapas, Mexico

between eleven and sixteen eruptions during the past (De la Cruz-Reyna and Martín del Pozzo 2009; Tilling 2009).

The last eruption of Chichonal volcano took place in 1982. In just a week three eruptive episodes with Volcanic Explosion Index (VEI) of five occurred, causing one of the major disasters related to volcanic activity in Mexico (Tilling 2009).

Non-consolidated volcanic deposits derived from this period of activity are very susceptible to the occurrence of landslides. In this region, therefore, landsliding frequently takes place during the rainy season (April–October), as loose materials are widely extended.

The Chichonal volcano region comprises important areas of eight municipalities, some of them still inhabited by Zoque indigenous population (Fig. 2). Social conditions in this area are not by any means of good living standards; 74 localities are characterized by high levels of marginalization, illiteracy and poverty.

Participatory Mapping

According to Ramírez-Villarreal (2007), social cartography is a tool that involves a participatory process that is able to influence specific aspects of the territory. For FIDA (2009), participatory mapping (also called social cartography or community mapping) has been created by local communities, who have the support of organizations and sometimes public authorities.

Participatory mapping focuses on providing the tools and technical knowledge, so that community members can create their own maps which represent the knowledge that they have about where they live (FIDA 2009).

Community mapping offers the possibility that a community could increase its particular abilities to improve quality of life (FCPV 2002). Given the above, participatory maps play an important role to support marginalized groups, such

as indigenous communities, in the struggle for recognition and respect of their land (FIDA 2009).

In this sense, the construction of maps by resident population becomes a very important tool to know in a better way the characteristics of that environment. Greater impact may arise when these maps can be focused on priority topics, including disaster risk. A risk map developed by a community through a participatory approach, can be expressed as a graph, sketch or model, on which areas of the community that are likely to be affected by the impact of a natural phenomenon, like a flood, earthquake, landslides or volcanic eruption (homes or infrastructure) can be identified. Symbols, pictures and colors can be used to identify particular locations that may serve as reference, to indicate specific levels of risk (high, medium, low, none).

A risk map should include hazard and the vulnerability; the former can be understood as "... the phenomenon, substance, human activity or dangerous condition that can result in death, injury or other health impacts, also property damage, loss of livelihoods and services, social disruption and economic, or environmental damage..." (UNISDR 2009), whereas vulnerability can be defined as the "physical predisposition, economic, political or social that has a community to be affected or damaged if a destabilizing phenomenon natural or human is manifested" (Cardona 2001). Thus, risk is defined as the combination of the probability of occurrence of an event and its negative consequence (UNISDR 2009), that results from the combination of hazards and vulnerability of exposed communities.

Methodology

The methodology involved two main steps. The first one involved the generation of a landslide susceptibility map based on weights of evidence using GIS. Physical variables including geological and geomorphological features were considered for the development of that map.

In order to carry out social cartography, it was necessary to produce in advance the susceptibility map. That allowed a general knowledge of the areas likely to be affected by landslides (Fig. 3), so that efforts could be centered on specific areas. A series of participatory workshops in schools of basic education were organized in the Chapultenango town.

Susceptibility Map

The landslide susceptibility map was generated by taking into account three factors: geology, geomorphology and slope values. Specific weights were given by experts to each variable. Slopes were reclassified into five ranges.

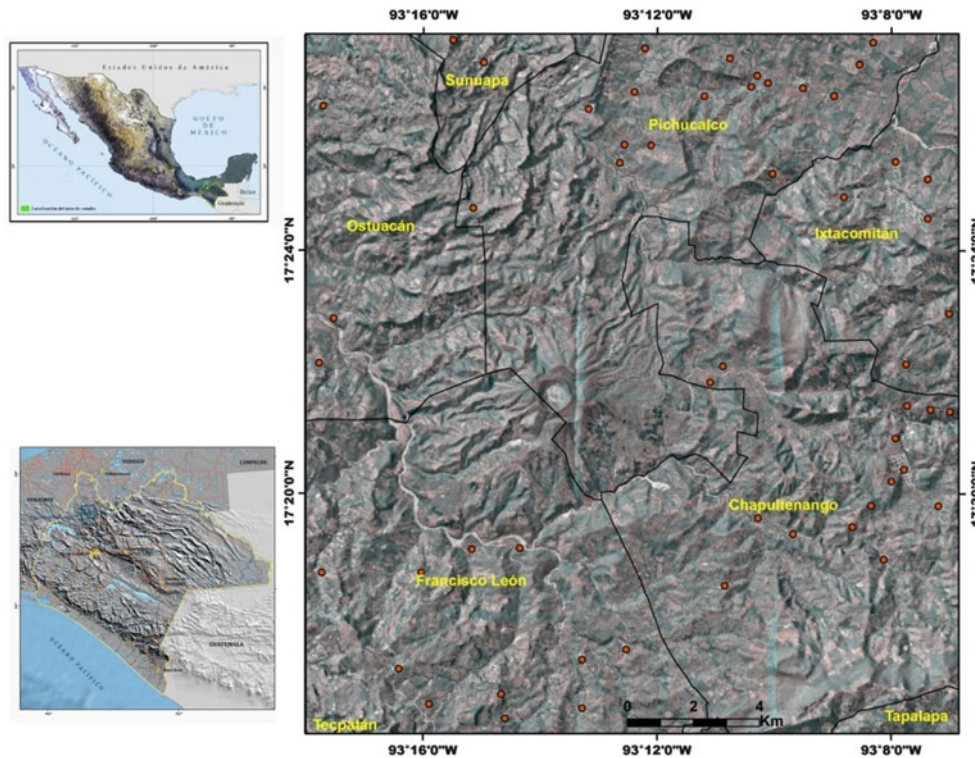


Fig. 2 Study area

Each of them was assigned a weight according to its significance to landslide susceptibility. Slopes greater than 32° were considered as the most likely to fail (very high), whereas those of $28\text{--}32^\circ$ as high, between $18\text{--}21^\circ$ were moderate, $21\text{--}15^\circ$ as low, and those with less 15° , very low.

Concerning lithological units, the highest susceptibility value (very high) corresponded to lutites, sandstones and pyroclastic flow deposits; massive limestones and sandstones were considered as high, pumicites as moderate, and the low value were andesitic and alluvial deposits.

Additionally, a geomorphology map was used to identify potential unstable features. Areas with highest probability of landslide occurrence included landslide scarps, erosion cirques, former debris flows paths, and landslides deposits. Lahar terraces, collapsed slopes, scarps and limestone anticlines were considered as areas of high susceptibility. Colluvial deposits of different origin corresponded to moderate level, whereas the units with lower susceptibility were the areas and lower slope associated with floodplains and riverbeds (Alcántara-Ayala et al. 2013).

Community Mapping

The participatory workshops were carried out at a secondary school in municipality of Chapultenango. General talks on hazard, vulnerability, and risk concepts applied to local risk

conditions were first of all given to the school community. It comprised topics on volcanic activity, flooding and landsliding.

Personnel from the local Civil Protection Unit joint the community mapping exercise and together with 65 students from third grade formed groups (Fig. 4). Interaction and feedback among participants was enhanced and was field observations and previous experiences and knowledge were used to produce different risk maps.

Results

According to the produced susceptibility map (Fig. 5), the eastern sector of the area of interest is the most predisposed area for landslides to occur; slope gradients are high and there is a presence of ancient landslides on limestones and lutites. In the western area, there are also some strips of landslide susceptibility on steep slopes formed by sandstones and lutites. Moreover, in this same area, potential lahars can also take place along the gullies on the Chichonal volcanic edifice.

Resulting from the community mapping workshop also three main areas of risk were identified. The first, no doubt, was the volcano Chichonal, which according to students, is an active volcano that may cause a lot of damage should it erupts. The second was located north of the area of study



Fig. 3 Landsliding in the area of Chichonal volcano



Fig. 4 Community mapping in Chapultenango town, Chiapas

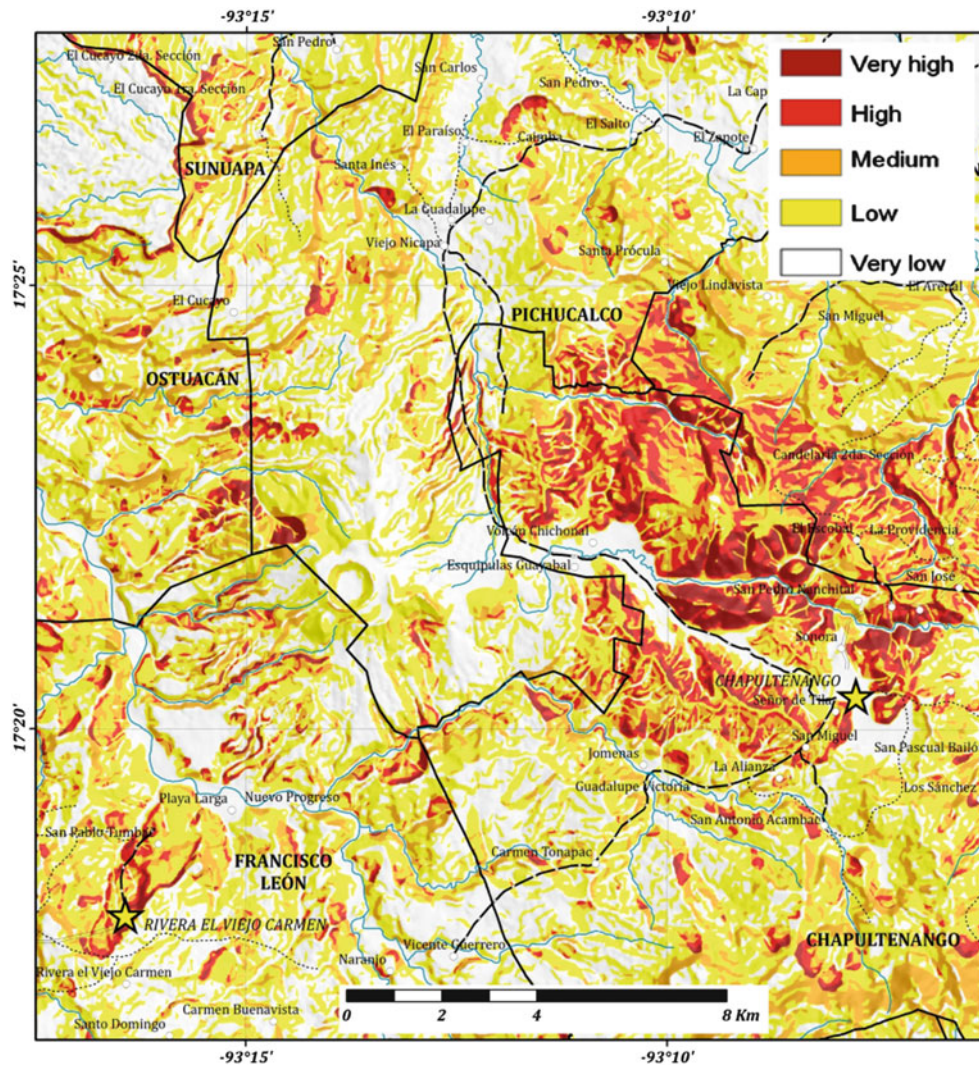


Fig. 5 Landslides susceptibility map in the area of the volcano El Chichonal 2010 (Source: Alcántara-Ayala et al. 2013)



Fig. 6 Community mapping by students of Chapultenango village

where many problems of slope instability are taking place because of the recent construction of roads that allow communication between small towns of the Chichonal region. The third area in which they all agreed, was an area that was flooded during the rainy season and interrupts communication between Chapultenango and Pichucalco, the nearest town (Fig. 6).

Conclusions

Participatory mapping is a useful tool for understanding - from the point of view of the inhabitants- the risks to which a population is exposed to. Moreover, participatory workshops can be regarded as a significant means to raise public risk awareness. However, it is also necessary to go a step further in terms of establishing particular strategies for disaster prevention on which population play a significant role in order to support capacity building at local level.

References

- Alcántara-Ayala I, Garnica R, Hernández-Moreno G (2013) Susceptibilidad a Procesos de Remoción en Masa. In: Alcántara-Ayala I, Garnica R, Coll-Hurtado A, Ramos S (eds) *La región del volcán Chichón, Chiapas: Un espacio potencial para su protección, conservación y desarrollo sustentable*. UNAM, Mexico, DF
- Cardona D (2001) *La necesidad de repensar de manera holística los conceptos de vulnerabilidad y riesgo*. “Una crítica y una revisión necesaria para la gestión”, Centro de estudios sobre desastres y riesgos (CEDERI). Universidad de Bogotá, Colombia
- De la Cruz-Reyna S, Martin del Pozzo AL (2009) The eruption of El Chichón volcano, Mexico: eyewitness of the disaster. *Geofísica Internacional* 48:21–31
- FCPV (2002) *Gestión Comunitaria de Riesgos*, Foro Ciudades para la Vida. Lima, Perú
- FIDA (2009) Buenas prácticas en cartografía participativa, Análisis preparado para el Fondo Internacional de Desarrollo Agrícola. Roma, Italia
- Ramírez-Villarreal F (2007) *Cartografía social, herramienta de indagación para la gestión territorial –desde lo local- “la primera sección de islas del delta del río Parana”*, Estudios socioterritoriales, *Revista de Geografía* – Num. 7, pp 204–220
- Tilling RI (2009) El Chichón’s “surprise” eruption in 1982: lessons for reducing volcano risk. *Geofísica Internacional* 48(1), enero-marzo, 2009:3–19
- UNISDR (2009) “Terminología sobre Reducción del Riesgo de Desastres”, Naciones Unidas, The United Nations Office for Disaster Risk Reduction. Ginebra, Suiza



Community-Based Rainfall Observation for Landslide Monitoring in Western Nepal

Yuwan Malakar

Abstract

This paper discusses community-based approach applied for observing rainfall to monitor landslide probability in Bhanu village development committee (VDC), Tanahun District, Nepal. Vulnerable communities were supported with geological study to make them understand the causes of landslides. Participatory assessment was conducted to acquire information and perceptions regarding their risks, vulnerabilities, and capacity. Participatory assessment revealed that communities perceive rainfall as a major triggering factor for landslide. Literature were reviewed to reckon rainfall-based landslide probability. Historical landslide events were correlated with rainfall data to scrutinize the relationship between rainfall and landslides. Two types of rainfall measuring systems, automatic and manual, were installed in the community for rainfall observation. Both short duration-high intensity and long duration-low intensity rainfall can trigger landslide probability. Therefore, communities are monitoring rainfall for two periods: 1-h rainfall and 24-h rainfall. Based on the literature review, past landslides events and rainfall data, communities made agreement for disseminating alert message when rainfall amount surpasses either 50 mm in 1 h or 200 mm in 24 h. The rainfall data of two monsoons (2012 and 2013) showed that the rainfall amount never reached to the identified limits. Nonetheless, communities were alert and in frequent communications with rainfall monitor during the monsoon. This case study of Bhanu VDC concludes that localized rainfall observation by communities is not only important for exploring rainfall-based empirical thresholds for landslide probability but also to assess, analyse, and act to reduce the risk associated with landslide. This approach reckons the benefit that communities are empowered and self-reliant to take their own decisions. Support on scientific knowledge, however, could be the limitation after the withdrawal of external facilitation.

Keywords

Community-based • Landslide • Rainfall observation • Capacity building • Community approach • Nepal

Introduction

The importance of involving vulnerable people in managing their own disaster risks is been highly discussed among disaster risk reduction actors and academia. Disaster is now more viewed as isolated event rather a cross cutting element in all development sectors. Disaster management is now more development oriented (Bollin and Hidajat 2006). Communities have knowledge about their own risks and

Y. Malakar (✉)

Disaster Risk Reduction and Climate Change Unit, Practical Action
South Asia Regional Office, House No. 2677, Narayan Gopal Sadak,
Maharajgunj, Kathmandu, Nepal
e-mail: yuwan.malakar@practicalaction.org.np; uanumalakar@gmail.com

have experiences of coping to disasters. Community-based disaster management (CBDM) approaches emphasize role of community in formulating risk reduction strategies. This paper contributes towards the importance of community-based approaches to disaster management. Present study exemplifies a community initiative taken to monitor landslide by observing localized rainfall in western Nepal.

Nepal possesses rugged topography, high relief, and variable climatic conditions (Hasegawa et al. 2009; Pokhrel et al. 2009). This kind of topography is prone to landslides (Hasegawa et al. 2009). It is estimated that the landslides in the Himalayan region cause annual economic loss that exceeds one billion US dollars including hundreds of human deaths (Dahal and Hasegawa 2008). According to official statistics, landslides kill more than 100 persons per year in Nepal in an average (MOHA 2009).

This community-based initiative was implemented in Bhanu Village Development Committee (VDC), Tanahun District of Nepal by Practical Action, a UK based charity organisation, with co-funding from European Commission Humanitarian Aid and Civil Protection (ECHO) under its Disaster Preparedness funding instrument for South Asia.

Project Location

Bhanu VDC is situated in the Southern and Northern slope of Mahabharat Range (also known as Middle hills) in the Western Development Region of Nepal (Fig. 1). The project site covered 3 communities of 2, 3, and 4 wards of the VDC. They are Khatithok, Ramgha and Dandagaun (Table 1).

Shallow landslides are most common in this range (Sudmeier-Rieux et al. 2011). Middle hills are formed by granite, schist and limestone (Pokhrel et al. 2009). The geology of the project site consists of low-medium-grade metamorphic rocks of the Lesser Himalaya. The Lesser Himalayan rocks consist of phyllites, slates, quartzes, limestone, and dolomites.

A geological assessment of the project site was carried out with the help of Department of Soil Conservation and Watershed Management (DSCWM), Government of Nepal (GON). Their findings were discussed with communities with a motive to raise awareness of their risks and vulnerabilities. Three types of soils are found in the project sites: alluvial, colluvial, and residual. Alluvial soil is observed along the boundary of the Bhanu VDC. The VDC is covered by colluvial soil, which is thicker near the foothills and thinner on the upper slopes. Residual soil is observed along with colluvial soils. They are red to light brown in colour and are derived mainly from phyllites.

The characteristics of all the soil types are loose and unconsolidated. These soils have poor cohesion. They are easily permeable, and highly susceptible for landslide. This

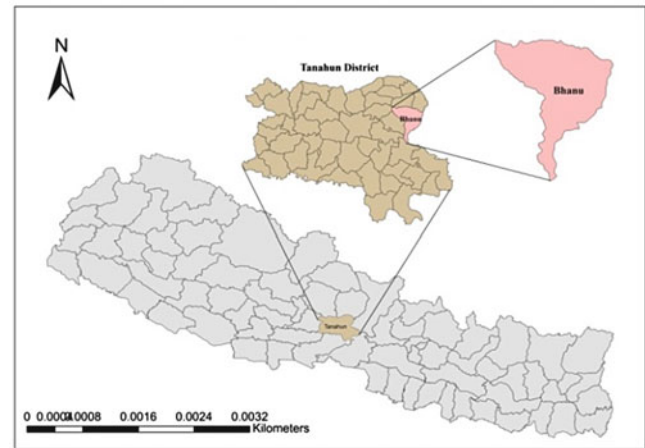


Fig. 1 Map of Nepal showing Tanahun District and Bhanu VDC

Table 1 Features of project communities

| Features | Description |
|------------------|--|
| Village location | Khatithok—N 28°02'22.6" E 084°24'47.0" |
| | Ramgha—N 28°02'31.1" E 084°23'43.1" |
| | Dandagaun—N 28°02'46.5" E 084°23'40.4" |
| Population | Khatithok—439 |
| | Ramgha—200 |
| | Dandagaun—155 (total 794) |
| Elevation | Khatithok—819 m above sea level (masl) |
| | Ramgha—845 masl |
| | Dandagaun—646 masl |

information was very much pivotal for communities to understand the causes of landslides in their vicinity.

Vulnerability Assessment

Participatory approach was applied to acquire information and perceptions regarding the risks, vulnerabilities, and capacity of the communities. Participatory approach empowers communities to discover their own means of solving their difficulties (Aalst et al. 2008). A participatory approach helps communities to reflect on necessity and direction of changes in their situation (Kumar 2002) by awakening development potential (Dovie 2003). Participatory assessment serves a basis for community based disaster management where community lead, coordinate, and execute the risk management initiatives.

Participatory tools like historical hazards timeline, social and vulnerability map, cause and effect analysis, pair wise ranking, and venn diagram were applied (Action Aid International 2005; IFRC 1999). Landslide was identified as top most ranked hazard for all the communities. Participatory assessment revealed the high trend of migration towards peri-urban area. Landslide was one of the reasons for



Fig. 2 Evidence of landslide occurred in 30 August 2008

migration. Majority of families rely on agriculture as a livelihood option. Employment to Gulf Countries and India is another good source of income.

Social and vulnerability map provided the picture of landslide vulnerable houses, comparatively safe havens, and safer evacuation routes. Community knowledge is vital to make an understanding of localized landslides (Holcombe and Anderson 2010). 7 houses in Khatithok, 7 houses in Ramgha, and 3 houses in Dandagaun were identified as most risky houses prone to landslide. The cracks on the ground and steep of the slope were considered as indicators to reckon the most vulnerable households by the community people.

Historical timeline presented three major events of landslides in the past. First event of landslide occurred in 17 June 1961, second in 19 June 1972, and third in 30 August 2008. More than 8 landslides occurred in the last event (Fig. 2). The landslides were mainly shallow type. Community averred that the latest one was the most devastating. The landslide inhumed 5.7 hectare of arable land, made cracks in houses, and swept away one livestock shed. The ready to harvest crops were all destroyed that left many of the families food insecure.

While discussing cause and effect of landslides, communities asserted that rainfall was the major triggering factor for landslide. They also shared that there was a huge down-pour when the landslide occurred in the year 2008. But nobody knew the amount of rainfall.

Rainfall Data

The rainfall data of 30 August 2008 was collected to correlate the relationship between rainfall and landslide from the

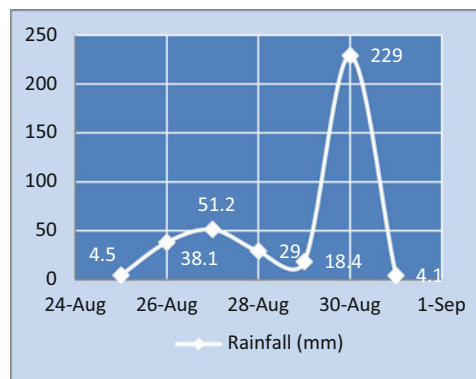


Fig. 3 Rainfall data of 25–31 August 2008

nearby rainfall station. The station was established by Department of Hydrology and Meteorology (DHM), GON in 1999. The station is situated 3 km (areal distance) far from the project site. No rainfall records of 1961 and 1972 were available. The rainfall data of 2008 exhibited that there was intense rainfall of 229 mm in 24 h on 30 August 2008 (Fig. 3). There was continuous rainfall for 5 days from 25 to 31 August 2008. The total rainfall over the 5-day period was 370.2 mm.

An interaction visit of communities was organized to rainfall station. Communities collected rainfall data and performed analysis. The analysis concluded that rainfall has to be monitored for assessing landslide probability. But nobody had answer that what intensity of rainfall has potential to trigger the landslide. This knowledge gap urged to define rainfall thresholds for landslide in that area. This process created overwhelming interest among the communities to experiment and execute landslide monitoring measures. Numerous literature suggest that participation of the vulnerable people in the process empowers them to make collective decisions (Dovie 2003; Fazey et al. 2010; Haque and Etkin 2007). In order to understand relation between rainfall and landslides, several research articles and case studies were reviewed.

Literature Review

A large anthology of literature discussed the relationship between rainfall and landslides (Baum and Godt 2010; Capparelli and Tiranti 2010; Dahal and Hasegawa 2008; Dahal et al. 2009; Ponziani et al. 2011). Dahal and Hasegawa (2008) highlights complex topography with heavy and concentrated rainfalls during monsoon periods cause severe landslides in Nepal.

There are mainly two types of rainfall thresholds found in practice for estimating landslide probability, Empirical and physical thresholds. Rainfall threshold as defined by

Capparelli and Tiranti (2010) is *critical values over which the probability of landslides occurrence becomes high*. Empirical threshold refers to relational values based on statistical analysis of the relationship between rainfall and landslide occurrence. Physical threshold is usually described with the help of hydrologic and stability models that take into account the parameters such as relationship between rainfall and pore-water pressure, suction, infiltration, slope morphology, and bedrock structure. Huggel et al. (2010) have developed a numerical modelling of landslide occurrence based on empirical threshold, which was piloted in Colombia. They have adduced following (1) to measure empirical thresholds for landslide.

$$I = aD^b \quad (1)$$

where a and b are empirical parameters, I is rainfall intensity and D is duration of rainfall. This equation derives that I intensity of rain when occurs for D duration, there is probability to trigger landslide.

Dahal and Hasegawa (2008) analyzed 193 landslide events around the Nepal to yield a threshold relationship between rainfall intensity, rainfall duration, and landslide initiation. In consistence with Huggel et al. (2010), they came up with rainfall threshold intensity for Nepal, which is expressed in following (2). Where I is hourly rainfall intensity (mm h^{-1}) and D is rainfall duration in hours.

$$I = 73.90D^{-0.79} \quad (2)$$

Tiranti and Rabuffetti (2011) have tested methods for forecasting shallow landslides using empirical thresholds. They claim rainfall based thresholds though very useful but cannot be used for prediction. Rainfall based thresholds are only “Conditional Probability”.

Rainfall Observation for Landslide Probability

All the acquired information elucidated that both intensity and duration of rainfall play substantial role in triggering landslide. An exercise for defining the rainfall thresholds was carried out applying (2) as well as taking account of previous rainfall data. The 24 h duration and intensity relationship based on the (2) is given in the table below (Table 2).

According to the Table 2, landslide may trigger with rainfall intensity of 74 mm in an hour and 10 mm/h intensity of rainfall in 12 h. The table also expresses that intensity decreases but accumulation of rainfall increases over time.

Both short duration-high intensity and long duration-low intensity rainfall are important to monitor for estimating landslide probability. Both conditions can trigger landslides.

Table 2 24-h duration and intensity relation

| Duration (h) | Intensity (mm/h) | Duration (h) | Intensity (mm/h) |
|--------------|------------------|--------------|------------------|
| 1 | 74 | 13 | 10 |
| 2 | 43 | 14 | 9 |
| 3 | 31 | 15 | 9 |
| 4 | 25 | 16 | 8 |
| 5 | 21 | 17 | 8 |
| 6 | 18 | 18 | 8 |
| 7 | 16 | 19 | 7 |
| 8 | 14 | 20 | 7 |
| 9 | 13 | 21 | 7 |
| 10 | 12 | 22 | 6 |
| 11 | 11 | 23 | 6 |
| 12 | 10 | 24 | 6 |

Therefore, communities decided to monitor rainfall of two periods at this stage. They are rainfall occurred in 1-h and 24-h.

Since 74 mm of rainfall in an hour triggers landslide probability [according to (2)], communities decided to disseminate the alert message when 50 mm of rainfall occurs in an hour in order to have preparation time for evacuation. Similarly, (2) suggests 144 mm of accumulated rainfall over the period of 24 h triggers landslide probability (intensity of 6 mm/h rainfall for 24 h). But community repudiated the calculation because in the year 2009 August 13 the 24-h-recorded rainfall was 150 mm and there was no occurrence of landslide. The exact intensity could not be known because the data recording system was 24 h. To circumvent the confusion and instigate the rainfall monitoring process, a consensus among communities was built to disseminate the alert message when 200 mm of rainfall occurs in 24 h.

There was no validation done that identified rainfall intensity and duration will trigger landslide probability. No particular study for identifying landslide triggering thresholds was done in the area. Therefore, communities wheedled to take this as an opportunity to examine the landslide triggering thresholds for their area. That is why the alert messages are only rainfall information not warning. Holcombe and Anderson (2010) also underscored that risk reduction measures be realistically developed at the local level. This invoked for establishment of rainfall stations in the project area.

Establishing Rainfall Stations and Communication Mechanisms

For the purpose of this particular intervention, two types of rainfall measuring systems, automatic and manual, were installed within the project site (Fig. 4). Rainfall observation responsibility was given to a family who gets paid by every family from the communities for the monsoon period.



Fig. 4 Automatic rain gauge (on the left), Tipping Bucket, and manual rain gauge (on the right), standard rain gauge installed in the project site for rainfall observation

Orientation training to two family members was provided. Why? Because when one person is absent another will take responsibility. The monitoring had to be done in real time so that information can be circulated very urgently with sufficient time to respond. To monitor the real time rainfall, automatic rainfall system was installed whereas manual rainfall system was installed in order to validate and calibrate the data provided by automatic system.

The automatic system records digital data into the server. The system is connected to internet for accessing the information from remote area. The automatic system was invested with mobile SIM cards. An electronic display system is also installed that displays real time rainfall information backed by solar electricity. The system is programmed in the way when rainfall reach identified levels it sends alert short message to telephone numbers of nominated persons from all the three communities.

Two persons from each community are nominated as communication focal persons. They have the responsibility to disseminate the rainfall information to every household within the community. Telephone numbers were circulated among communication focal persons and rainfall monitor. Mechanisms were identified and established to inform every household using hand-operated sirens and megaphones.

Analysing Rainfall Data

The rainfall observation system was established in July 2012. During the time of writing this paper, 152 days rainfall data from two monsoon seasons of the years 2012 (9 July 2012 to

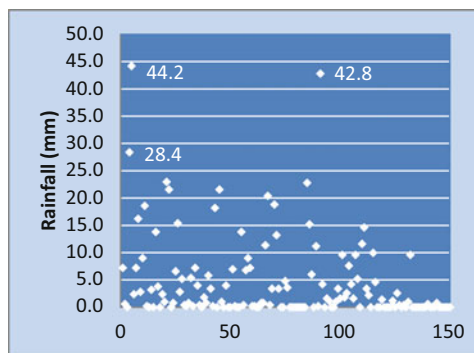


Fig. 5 1-h maximum rainfall recorded in 2012 and 2013 from July to September

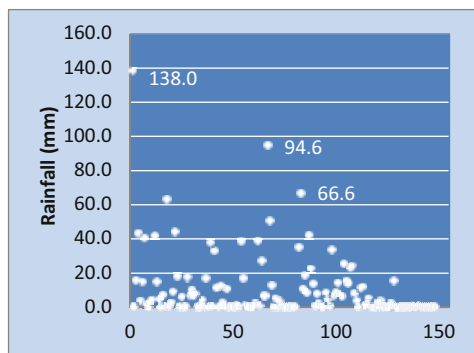


Fig. 6 24-h rainfall recorded in 2012 and 2013 from July to September

30 September 2012) and 2013 (18 July 2013 to 23 September 2013) have been recorded. The rainfall data were analysed as per the agreed two periods, 1-h rainfall and 24-h rainfall. Daily maximum 1 h recorded rainfall data of 152 days were plotted in scatter chart (Fig. 5). The top three maximum amount of rainfall occurred in the period of 1-h were 44.2 mm, 42.8 mm, and 28.4 mm recorded in the dates 13 July 2012, 24 July 2013, and 12 July 2012 respectively.

Similarly, 24-h rainfall data of 152 days were plotted in the scatter chart (Fig. 6). The top three maximum amount of rainfall occurred in the period of 24-h were 138 mm, 94.6 mm, and 66.6 mm recorded in the dates 13 July 2012, 17 September 2012, and 20 July 2013 respectively.

There was no case of landslide occurrence after the installation of rainfall observation system. The alert messages were not circulated because the rainfall did not overtop the identified limit. It seems apparent that the identified rainfall limits are valid but it would not be wise to be certain at this moment with the available rainfall data.

These rainfall data were discussed with communities. Communities apprehended that available rainfall information

did not explain specific estimation between rainfall and landslide occurrence albeit it is useful to continue rainfall observation based on identified periods and rainfall amount.

Community in Action

It is noteworthy to mention that communities were alert all the time during the monsoon whenever there is rain. There were frequent contacts between rainfall monitor and communication focal persons. Ostensibly, these frequent communications established bond of trust between rainfall monitor and communities. What's more, this process has manoeuvred the practice of being informed of rainfall for landslide probability.

When rainfall recorded 138 mm in 24 h at 11 am in 13 July 2013, rainfall monitor called communication focal persons of all the three communities. The identified limit for 24-h rainfall was 200 mm. The communication focal persons started monitoring the road banks and identified risk zones. They did not observe any signs of landslides and decided to wait until the rainfall exceeds the limit. The rainfall did not surpass the limit during that time so no alert messages were disseminated.

Similarly, the rainfall nearly reached to 50 mm in 1-h in two events: one in 13 July 2012 (44.2 mm) and another in 24 July 2013 (42.8 mm). But rainfall monitor did not call communication focal persons. Why? Because in both cases the rainfall amount recorded at 1 am in the morning and the rainfall monitor was sleeping. The automatically generated messages to telephone of communication focal persons only trigger when rainfall amount surpasses 50 mm in 1 h.

It was evident that communities were responding promptly and taking their own decision from the above event. Community-based approaches aim to enhance the capacity of communities for problem solving and managing stresses (Allen 2006). This capacity can be built by repetitive and periodic encounters to disaster and/or by external facilitation. Nevertheless, there are both advantages and limitations of this approach.

Analysing Benefits and Bottlenecks

Pelling (2007) argues that participation of local community empowers to acquire information, resources, and authorities. Present case demonstrates the involvement of communities throughout the process in implementing localized rainfall observation for landslide probability. Self-reliance of community is key factor in disaster management (preparedness, response, and recovery) (Singh 2010). It is believed that the communities are self-reliant for monitoring landslide,

identifying causes of vulnerability, and taking actions for minimizing risks.

Community knowledge and perceptions were fully utilized without subverting the scientific background. Community empowerment process accrues with the use of community knowledge in their risk reduction initiatives whereas disempowerment occurs when neglected (Allen 2006). Communities have been discussing their local issues in different public gathering to build collective actions. Allen (2006) also states that access to public forum for discussion is also community empowerment.

No further discussion required to emphasize that lack of local capacity aggravates the vulnerabilities of the people. Eakin et al. (2009) averred that the vulnerability of people living in Upper Lerma River Valley, Mexico to respond to flood risk is exacerbated due to limited capacity. Present project has underpinned the capacity of local communities through series of science based inputs like geological information and rainfall analysis. These inputs imbued to perform experiments for long-term preparedness through rainfall-based landslide monitoring.

Use of scientific knowledge, however tried to make it understandable and interpretable to the local community in the present case, may offer difficulty when external facilitation will be over. External facilitation might require for analysing rainfall information every year. Mechanisms need to be developed for establishing linkage between science-based institutions and communities. This aspect is yet to explore and will be priority for next phase. Automatic system is used and maintenance might require external experts if broken.

For smooth functioning of the system, resources are required. Communities agreed to pay to the rainfall monitor during monsoon in the present case. But households are reluctant to invest their own resources in community projects (Allen 2006). This approach has to be institutionalized within the existing institutional structure to guarantee funding availability.

Most importantly, the generated rainfall information is not warning. Communities are not legitimized to issue disaster warning. In addition to that the identified rainfall intensity and duration are not validated. Developing a rainfall-based thresholds for new areas is time-demanding that requires compiled usable records of historical landslides and spatially and temporally coincident rainfall data (Baum and Godt 2010). Misunderstanding information as warning may create exasperation among communities if the rainfall exceeds the identified limit and community put their efforts for evacuation but nothing happens.

Conclusions

This article presents a case of community-led initiative for landslide hazard monitoring. The communities of Bhanu

VDC have examined their vulnerability and analysed causes of landslides. They have actively involved in monitoring localized rainfall for landslide probability. Furthermore, vulnerable communities are analysing relationship between rainfall and landslide to define thresholds for landslide probability. Communities are interpreting the rainfall information for taking their own decision. Present case exemplified that vulnerable communities are not passive victims. They are leaders in managing their own risk if adequate capacity building is done.

Landslide is a common phenomenon in Nepal that has a negative impact on human livelihood. Landslide prediction is difficult and involves huge amount of scientific knowledge and analysis. Rainfall is one of the triggering factors of landslide. This case study of Bhanu VDC suggests that rainfall observation provides opportunity not only to explore rainfall based empirical thresholds for landslide probability but also to assess, analyse, and act to reduce the risk associated with landslide hazard.

Community-based approach for landslide monitoring exemplified empowerment and capacity building of the communities for their self-reliance. However, strong scientific backup for refinement of rainfall-based landslide probability is still required. Lack of resources for technological support is another shortfall of this approach.

In conclusion, this project is not an espistome of rainfall based landslide monitoring in Nepal. Being a new venture, this initiative entails further investigation for minimising the risk of landslide hazard led by vulnerable communities themselves.

Acknowledgments The author is grateful to ECHO for providing fund to implement this innovative intervention. Sincere acknowledgement goes to Practical Action and Nepal Red Cross Society District Chapter Tanahun for supporting the idea. The author would like to express sincere gratitude to Anup Phaiju, Jit Bahadur Gharti, Ram Kishan, Alisha Ghimire, Lok Narayan Pokhrel, and Ramesh Shreshta for their continuous support in writing this case study. Finally, Jakub Kocanda, I thank you for your constructive comments to make this paper what it is now.

References

- Aalst MKV, Cannon T, Burton I (2008) Community level adaptation to climate change: the potential role of participatory risk assessment. *Glob Environ Chang* 18:165–179
- ActionAid (2005) Participatory vulnerability analysis: a step by step guide for field staff. Action Aid International, International Emergencies Team, London
- Allen KM (2006) Community-based disaster preparedness and climate adaptation: local capacity-building in the Philippines. *Disasters* 30:81–101
- Baum RL, Godt JW (2010) Early warning of rainfall-induced shallow landslides and debris flows in the USA. *Landslides* 7:259–272
- Bollin C, Hidajat R (2006) Community-based risk index: pilot implementation in Indonesia. In: Birkmann J (ed) *Measuring vulnerability to natural hazards: towards disaster resilient societies*. United Nations University, New York, pp 271–289
- Capparelli G, Tiranti D (2010) Application of MoniFLaIR early warning system for rainfall-induced landslides in Piedmont region (Italy). *Landslides* 7:401–410
- Dahal RK, Hasegawa S (2008) Representative rainfall thresholds for landslides in the Nepal Himalaya. *Geomorphology* 100:429–443
- Dahal RK, Hasegawa S, Yamanaka M, Santosh D, Bhandary NP, Yatabe R (2009) Comparative analysis of contributing parameters for rainfall-triggered landslides in the lesser Himalaya of Nepal. *Environ Geol* 58:567–586
- Dovie DBK (2003) Whose involvement? Can hierarchical valuation scheme intercede for participatory methods for evaluating secondary forest resource use? *Forest Policy Econ* 5:265–283
- Eakin H, Lerner A, Murtinho F (2009) Adaptive capacity in evolving peri-urban spaces: responses to flood risk in the upper Lerma River Valley. *Glob Environ Chang* 20:14–22
- Fazey I, Kesby M, Evelyn A, Latham I, Wagatora D, Jude-Edward H, Reed MS, Christie M (2010) A three-tiered approach to participatory vulnerability assessment in the Solomon Islands. *Glob Environ Chang* 20(4):712–728
- Haque C, Etkin D (2007) People and community as constituent parts of hazards: the significance of societal dimensions in hazards analysis. *Nat Hazards* 41:271–282
- Hasegawa S, Dahal RK, Yamanaka M, Bhandary NP, Yatabe R, Inagaki H (2009) Causes of large-scale landslides in the lesser Himalaya of central Nepal. *Environ Geol* 57:1423–1434
- Holcombe EA, Anderson MG (2010) Implementation of community-based landslide hazard mitigation measures: the Role of stakeholder engagement in ‘Sustainable’ project scale-up. *Sustain Dev* 18:331–349
- Huggel C, Khabarov N, Obersteiner M, Ramirez JM (2010) Implementation and integrated numerical modeling of a landslide early warning system: a pilot study in Colombia. *Nat Hazards* 52:501–518
- IFRC (1999) *Vulnerability and capacity assessment: an international federation guide*. Switzerland, Geneva
- Kumar S (2002) *Methods for community participation - A complete guide for practitioners*. Practical Action Publishing, Rugby, UK
- MOHA (2009) *Nepal disaster report 2009 - the hazardscape and vulnerability*. Ministry of Home Affairs, Government of Nepal, Kathmandu
- Pelling M (2007) Learning from others: the scope and challenges for participatory disaster risk assessment. *Disasters* 31(4):373–385
- Pokhrel D, Bhandari BS, Viraraghavan T (2009) Natural hazards and environmental implications in Nepal. *Disaster Prevent Mitigat* 18(5):478–489
- Ponziani F, Pandolfo C, Stelluti M, Nicola B, Luca B, Moramarco T (2011) Assessment of rainfall thresholds and soil moisture modeling for operational hydrogeological risk prevention in the Umbria region (central Italy). *Landslides* 9(2):229–237
- Singh SK (2010) Community-based cyclone preparedness programme in Bangladesh: an overview. *Asia-Pacific J Rural Develop* XX(1):1–17
- Sudmeier-Rieux K, Jaquet S, Derron M, Jaboyedoff M, Sanjay D (2011) A case study of coping strategies and landslides in two villages of central-eastern Nepal. *Appl Geogr* 32:680–690
- Tiranti D, Rabuffetti D (2011) Estimation of rainfall thresholds triggering shallow landslides for an operational warning system implementation. *Landslides* 7:471–481



Landslide Risk Reduction in Poland: From Landslide Inventory to Improved Mitigation and Landuse Practice in Endangered Areas

Teresa Mrozek and Izabela Laskowicz

Abstract

Poland is moderately prone to natural hazards, yet floods and landslides are key threats resulting in major economic losses. Like floods, landslides here are generally triggered by precipitation. Landslides that occurred in the Flysch Carpathians and at their foreland in between 1997 and 2010 were widespread and particularly devastating. These disasters pointed to a vital need for an improved system of landslide data acquisition, hazard awareness building and developing mitigation measures. An initially developed landslide damage recovery programme evolved into a risk reduction strategy. Nowadays, the core is formed by the ongoing project named Landslide Counteracting System *LCS* (*SOPO in Polish*) combined with DBMS, meant to register landslides on a country-wide basis. However, the second streamline is focused on structural remediation measures that aim at maintaining stability and functioning of public infrastructure for foreseeable future conditions. For that, the task-oriented engineering geology documentation has to be approved by Polish Geological Survey with respect to reliability of landslide recognition and feasibility of proposed treatments. This provides technical credibility which was not present in years past.

Information on spatial distribution of landslides is, by law, to be considered in regional land use planning documents. To avoid unnecessary spending, municipal authorities draw upon previously experienced landslide threats and resultant damages, and create local management policies which impose restrictions on construction in landslide-prone terrains. Finally, risk reduction strategy involves landslide monitoring for warning purposes or remediation performance.

Keywords

Landslide damage • Landslide inventory • Risk reduction strategy • Landslide Counteracting System (SOPO) project

Introduction

By global (or even by European) standards, Poland is only moderately affected by major natural catastrophes because of its relatively stable seismic setting, gentle topographic

relief, and temperate climate. Nevertheless, floods and landslides are weather-related hazards which cannot be ignored as they result in major economic losses and even fatalities.

Whilst there is a general long-standing recognition of flood perils, landslide danger has been underrated for many years. This attitude has slowly changed, especially in the context of damages experienced since the turn of the twentieth century. The economic losses due to devastating landslides of 1997 pointed to a vital need for an improved

T. Mrozek (✉) • I. Laskowicz
Polish Geological Institute – National Research Institute, Carpathian
Branch, Skrzatow 1, 31-560 Cracow, Poland
e-mail: teresa.mrozek@pgi.gov.pl; izabela.laskowicz@pgi.gov.pl

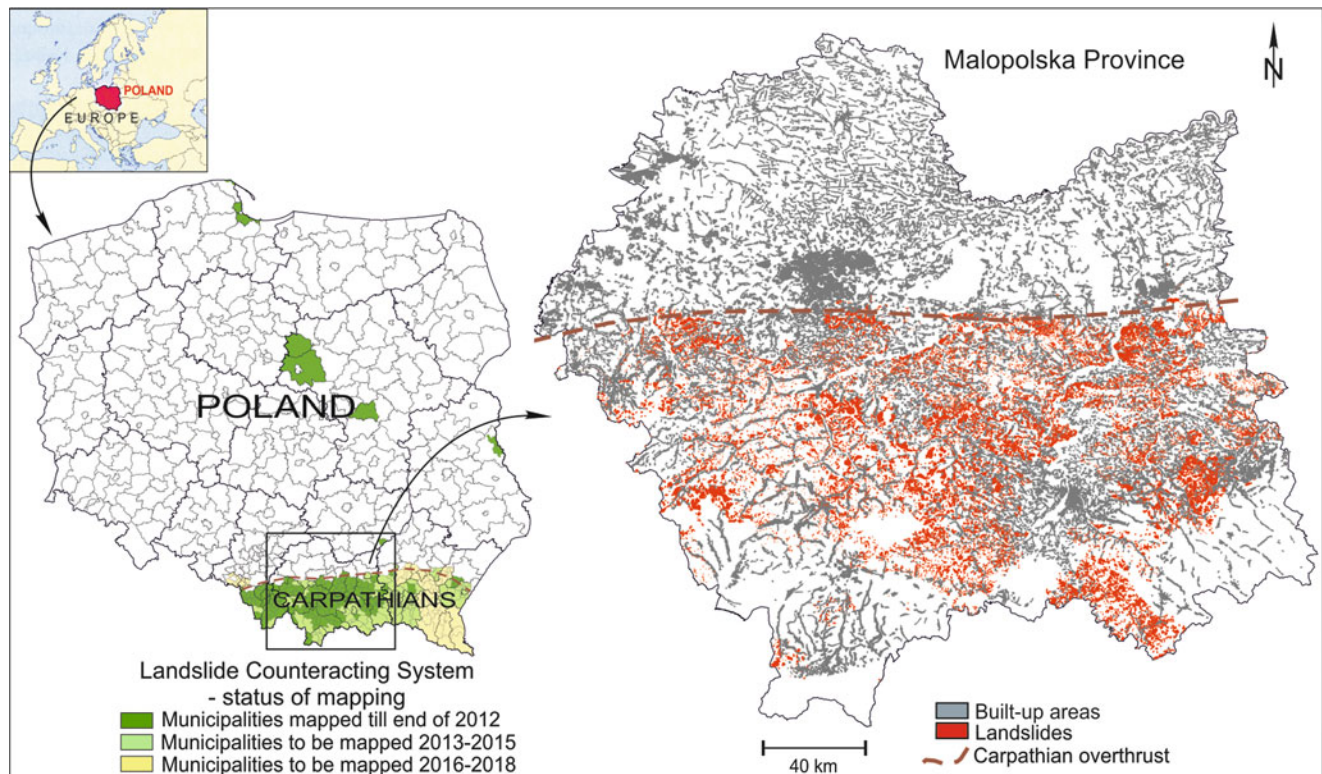


Fig. 1 Example of inventoried landslides and built-up areas in the Carpathian province of Małopolska

hazard awareness building as well as for mitigation and prevention measures. (Poprawa et al. 1998). In response to those demands, an initial landslide damage recovery scheme evolved into a risk reduction strategy.

Following current trends, the adopted strategy goes beyond landslide loss reduction by engineering treatment and incorporates also “soft” preventive methodology (Höppner et al. 2012). This two-fold approach focuses on (a) developing risk reduction strategies in site/areas already subjected to slope instability, and (b) indicating areas potentially prone to landsliding in order to provide guidance for future developments. Under such a framework, the strategy combines outcomes of landslide history with implementation of engineering solutions to areas at high risk of landslides. This results in sound land use management policies which draw upon legislation and regulations that focus on hazard mitigation.

With this publication we show accomplishments in the field of landslide risk reduction in Poland (a juvenile free-market economy country) where previously non-existent landslide mitigation and prevention policy had to come into being parallel with ongoing recovery from previous disasters.

Background on Landsliding

Landslides in Poland occur in locations which are favoured by physiogeography, where natural failures are related mainly to rainfall and meltwater triggers. In fact, landslide-prone regions are known in many parts of the country (Ostaficzuk 1999), yet they are predominant in the south—in the Flysch Carpathians (ca. 22,500 km²) and at their foreland (Fig. 1). As landslide risk indicates likelihood of experiencing financial losses, the hilly or mountainous areas are particularly at risk due to juxtaposition of weather-driven catastrophic events with widespread assets related to human activity. By Polish standards, this is a densely populated territory (of ca 221 person/km² as compared to the average in Poland of 122 person/km²) with numerous dwellings on hillsides, so the anthropogenic footprint is much stronger here than in any other part of the country. Figure 1 shows the spatial distribution of currently inventoried landslides superimposed on built-up terrain in Małopolska, one of the provinces located in the Flysch Carpathians.

Evidence of landslides date back to descriptions of the failure in the village of Duszatyn in 1907 (Zuber and Blauth

Table 1 Expenditures on recovery of public assets in the Polish Carpathians as ensured from the state budget reserve by promissory notes

| Year | Major land sliding events observed in: | Law changes | No. of tasks | Expenditures (PLN) |
|--------------|--|-------------|--------------|--------------------|
| 1997 | Summer | | | |
| 1998 | Spring | | | |
| 1999 | | | | |
| 2000 | Spring | | | |
| 2001 | Summer | + | | |
| 2002 | Spring | | | |
| 2003 | | + | | Project onset |
| 2004 | Summer | + | 27 | 23,225,000 |
| 2005 | | | 30 | 25,222,582 |
| 2006 | | | 45 | 28,046,011 |
| 2007 | | + | 53 | 40,861,816 |
| 2008 | | | 50 | 88,853,792 |
| 2009 | | | 5 | 17,627,125 |
| 2010 | Summer | | 12 | 19,873,570 |
| 2011 | | | 31 | 54,868,774 |
| 2012 | | | 37 | 85,758,020 |
| Total | | | 290 | 384,336,690 |

1907). Not only did the authors describe the mass movement process, but they also estimated the costs of resulting damages to 187,000 Kronas (Austro-Hungarian currency of that era). Moreover, they even postulated a governmental agency to revise attitude to landslide risk problems. Unfortunately, subsequent landslide studies usually neglected recovery policy issues.

As natural slope failures observed in Poland are associated mainly with rainfall triggers, they do accompany flood events to a some extent. Such flood events were observed in the Carpathians and at their foreland in: 1934, 1962, 1965–1967, 1972–1974, 1980, 1997, 2001, 2004 and 2010. Because flooding and landsliding are so closely linked, they generally occur simultaneously. Flooding, however, has commonly garnered more attention than landslide damage. Indeed, for a long time landslides used to be treated as merely localized phenomena, purely of interest to the academic community but rarely to local authorities. Such an attitude might be not surprising, given the context of the scale of individual landslides and the relatively low amount of damaged buildings or infrastructure. However, when landslides are viewed in a more spatial perspective, its catastrophic nature becomes apparent. Prolonged precipitation, often associated with storm rainfall, usually results in a “domino effect”—numerous slides become triggered sequentially in relatively close proximity. This is exemplified by the events of 1997. Extreme precipitation, with an abnormally high rainfall in July, set off 253 landslides that resulted in destruction of 137 buildings in the western Polish Carpathians (Poprawa et al. 1998). The post-event estimates of related financial losses amounted to ca. 150 million PLN. Although the landslide-related damage was widespread, the number of casualties was low

(1 debris-buried fatality and a few indirect deaths due to heart disorders). The relatively low number of casualties may be attributed to the fact that only 12 % of failures in the Polish Carpathians were catastrophic flows (Poprawa et al. 1998) transferring colluvial material at high speed, while most failures were slow or very slow movements, thereby allowing for safe evacuation of people.

Intensive landsliding triggered by rainfall in central and eastern Europe between 2000 and 2012 (Pánek et al. 2011; Klimeš and Blahůt 2012) was very destructive. In Poland, landsliding of June–July 2010 was particularly catastrophic. Cost of damage was extremely high (2.9 Billion Euro) and pointed towards a need for an improved, more holistic approach to landslide risk management (Grabowski and Przybycin 2010).

Boosting public landslide awareness required an amendment to legal regulations. Indeed, it was not until 2001 when significant changes were introduced to acts and ordinances (Table 1). Since then, landslides acquired the legal status of natural disaster (such as floods, hail, windstorms, wildfires etc.). This in turn created a setting for a more systematic approach to landslide-related emergency response, mitigation and prevention issues.

Rationale Behind Risk Reduction Strategy

The catastrophic landsliding of 1997 gave rise to an idea of developing a nation-wide strategy for landslide risk reduction. An incipient landslide remediation program comprised two major streamlines (Fig. 2): (i) recovery by restoration and reconstruction of destroyed assets in areas already

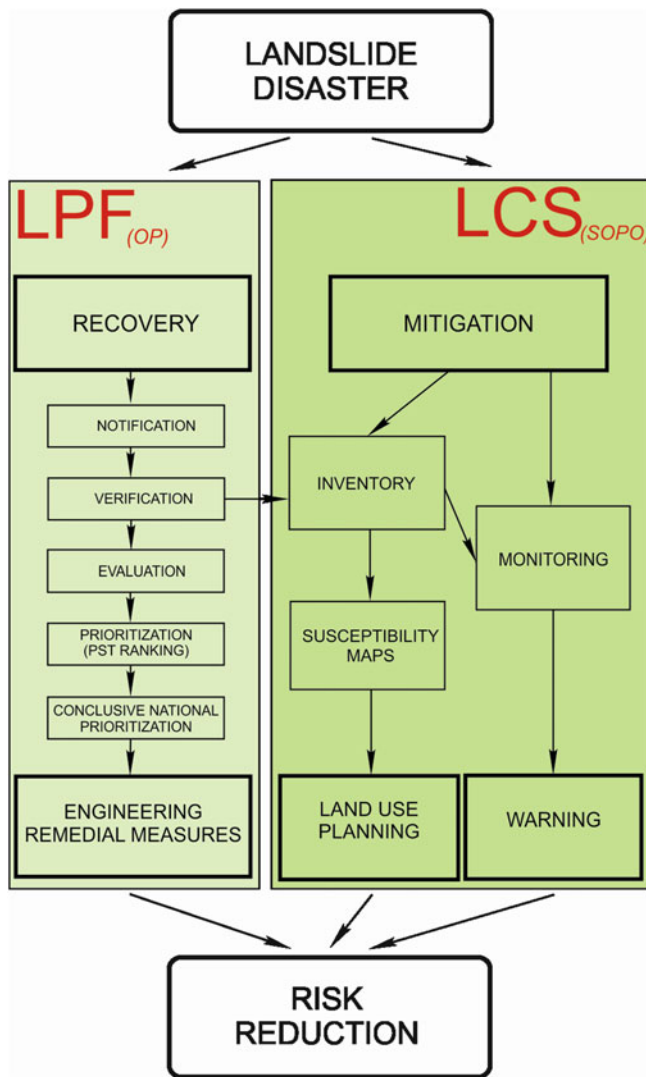


Fig. 2 Risk reduction strategy framed by LPF and LCS programmes (*OP* and *SOPO* are acronyms derived from Polish names of the projects)

affected, (ii) development of a system for mitigating and preventing losses in future.

The adopted approach generally follows risk management objectives (e.g. Crozier 2005), but obviously the emphasis initially focused on urgently needed remediation. In time, especially after subsequent landsliding events of 2000–2010, issues oriented on future risk reduction had been gradually growing in importance. Landslide inventory and mapping became an important basis of risk management (e.g. Fell et al. 2008; van Westen et al. 2009).

Thus far, there was no system in place to manage the flow of funds nor to put solutions into practice. The current national procedure has brought substantial improvements to this. Reconstruction and restoration measures are targeted for damaged sites in all of Poland. Preference is given for the sites of largest impact to the public, however. Landslide mapping and monitoring, intended to support guidance on

risk mitigation, have been initiated in the Carpathians and their foreland, the region most threatened.

Recovery Programme

Under the recovery streamline (Fig. 2), the Landslide Protection Framework programme *LPF* was launched in 2003. The *LPF* programme, currently run by the *DDPR* (Department of Disaster Prevention and Recovery under the Ministry of Administration and Digitization of Poland) is addressed to all provincial authorities. On that level, the steering is delegated to the *PST* (Provincial Supervising Teams) while the *PGS* (Polish Geological Institute—Geologic Survey of Poland) is the advisory and consulting entity. The *LPF* program forms a framework for reconstruction, relocation, and structural protection (engineering stabilization) of damaged infrastructure or civil facilities. The executive procedure in place is illustrated in Fig. 2.

Damage recovery may be accomplished in two ways: (i) by taking stabilization measures that will ensure functioning of reconstructed infrastructure/facilities located on a landslide or near it; (ii) by relocating infrastructure, facilities or housing and therefore abandoning a landslide without stabilizing it. The choice of recovery approach depends on a cost-benefit analysis taken in a social or cultural context. Based on estimates of stabilization costs relative to those of the civil facilities/infrastructure damaged or at risk, the local administrative bodies can apply for full or partial funding of remedial treatment.

As a rule, damage claims are made by local administrative bodies (municipalities), *PGS* professionals are in charge of verifying landslide recognition and approving required documentation. The feasibility of planned treatment is also evaluated. Then, the *PSTs* are required to prioritize particular tasks taking into account long-term (ca. 25 years) effectiveness of planned investments as well as socioeconomic benefits. The *DDPR* is then authorised to allocate funds based on priority. Once priorities are determined, projects are undertaken through a tender process.

As shown in Table 1, 290 tasks have been financially supported in the system described above. Since this process has been operational (2005), costs have been reduced significantly. Under the previous system, there was little control or scrutiny given to which remediation projects were to be undertaken, and many projects which were done were not very well thought out or even necessary.

Mitigation Programme

The second streamline of the adopted strategy is devoted to minimizing future landslide losses. The core is formed by the ongoing *LCS* or *SOPO* (in Polish) project (Figs. 1, 2).

Table 2 Progress in landslide inventory and mapping

| Year | No. of municipalities | Area mapped (km ²) | % of area of the Carpathians |
|------|-----------------------|--------------------------------|------------------------------|
| 2007 | 3 | 272 | 1 |
| 2008 | 4 | 372 | 2 |
| 2009 | 33 | 2,237 | 10 |
| 2010 | 78 | 5,385 | 24 |
| 2011 | 106 | 7,368 | 33 |
| 2012 | 142 | 10,903 | 47 |

The major objectives of the programme concentrate on: large-scale landslide inventory; managing a GIS-structured national landslide database; monitoring of selected landslides; and providing support for administrative bodies and land use planners (Mrozek et al. 2014). The LCS project is commissioned by the Ministry of Environment, and is supervised and managed by PGS.

A large-scale inventory (typically at a 1:10 000 scale) is carried out by integrating interpretation of aerial photographs and extensive field investigation. Rather than working under the natural constraint of individual drainage basins, the inventory is performed based on the country administrative divisions. This is because the project beneficiaries are specific municipalities, which are by law obliged to take inventory outcomes into account in their territorial planning policy.

The project also incorporates monitoring of selected landslide areas which threaten crucial civil facilities (e.g. important transportation routes). The stages of project implementation involved pilot surveying and database testing (in 2007). Subsequently a systematic landslide inventory evolved from the most threatened municipalities in the Polish Flysch Carpathians in 2008.

Landslide inventory and mapping continues to progress (Table 2; Fig. 1). Till August 2013 landslide mapping tasks had been performed in 142 municipalities, comprising 10,903 km². In the Carpathians, the number of inventoried landslides amounted to 34,036 over an area of 902 km². Of those, 60 landslides are monitored using inclinometers.

Financial Conditioning

The LPF programme was launched in 2003 with a 50 million PLN loan from EIB. The assumed budget of 165 million PLN was initially planned to cover costs of structural investments based on appropriate design proposals. Then (after 2005), funding has originated from the specific allocation of the state budget reserve. Such funds can be used only for recovery of civil (public) facilities and infrastructure, and not for private structures.

The LCS (SOPO) project is financially supported by the National Fund for Environmental Protection and Water Management. With a budget of 52 million PLN (2006–2015) it

exists to assist administrative units in handling landslide registers and in sustainable land-use planning.

Strategy Achievements and Weakness: Discussion

The adopted landslide mitigation strategy is generally in agreement with concepts of risk management (e.g. Dai et al. 2002; Crozier 2005). Unfortunately, not all phases of the risk management scheme are equally addressed or approached.

Initially, policy makers efforts focused on structural mitigation rather than on risk analysis, for example. This may be attributed to the fact that the outlined procedure developed in response to the widespread landslide disaster of 1997, which happened after a long-standing period of relative quiescence. This would appear to be more of a reactive rather than a proactive approach. Because of severe damages, rescue and reconstruction actions were given top priority. With the subsequent and repetitive landslide events in the twenty-first century (Table 1), however, the policy makers began to realize that landslide risk reduction cannot be accomplished only by relief actions, but must include and incorporate long-term prevention and hazard mitigation strategy. Therefore the development of a new regulatory and implementation framework was created.

The ongoing landslide mapping and inventory are fundamental and vital steps towards verification of the landslide risk awareness. In addition to continuous progress of a standardized mapping schedule, landslides are registered *as needed* immediately after any serious triggering event, especially when significant damages occur. With such a database, the adopted procedure is flexible and can evolve towards an event-based landslide inventory.

Methods for landslide hazard and risk zonation have to be appropriately selected (van Westen et al. 2009; Fell et al. 2008). For the country of the size of Poland, developing susceptibility maps at a small scale is of limited importance and is of a confirmational nature only. Indeed, resolution of the maps at scale 1:200,000 or 1:400,000 (Długosz 2009; Holec et al. 2013) is impractical—high susceptibility zones perfectly correlate to regions which have historical landslide

occurrence already. With that in mind, the mapping tasks of the LCS project have primarily concentrated on development of large scale maps (1:10,000). These are so-called “danger maps”, rooted in direct (expert-opinion) methods, which depict landslides and terrains prone to mass movements. They are tentative alternatives to susceptibility or hazard maps derived from an indirect or statistical approach that requires a large digital database (e.g. Guzzetti et al. 2012), but which at the time of the strategy implementation were not available.

The outlined risk mitigation strategy shows a clear procedure for civil assets remediation. Unfortunately for damaged private households, a common code of practice does not exist. The aid for victims may originate from a specific provision of state funds but is usually bound by additional terms and conditions. Under the current state policy, an insurance programme for people living in landslide endangered areas does not exist. Although this may be seen as adaptation strategy, it is only under an initial stage of consideration.

Since the legal regulations have been amended, the *starosta* (the head of the second order administrative unit) is in charge of keeping a register of landslides and monitoring them, while municipality authorities (*gminy*) are obligated to consider extents of landslides and terrains prone to future mass movements in territorial planning. Outcomes of the LCS project support these administrative entities as follows: First, the inclinometer monitoring initiated under the LCS project forms the groundwork for quality-controlling the performance of the existing remedial structural measures, as well as for forming an early warning system. Second, the danger maps developed from the inventory from the LCS project are significant tools used by municipal authorities for sustainable land-use planning and risk reduction. Unfortunately, problems arise how to translate the information from the maps into effective policy and regulations (DeGraff 2012), as there is no obligatory policy guidance. In practice, this results in imposition of certain use restrictions, although this occurs at a local level only.

Closing Remarks

Because risk is viewed as an outcome of the interplay between hazard, exposure, vulnerability and coping capacity (Roberts et al. 2009), most effective landslide mitigation strategies should involve some combination of landslide mapping, control structures, warning systems and regional planning, combined with good coordination between scientific, engineering and planning bodies (Larsen 2008). Polish risk reduction strategy is in line with such current trends, and can be even perceived as a strategic incremental approach (Anderson and Holcombe 2013). The strategy couples

ex-post mitigation with *ex-ante* risk reduction policy. In Poland, a juvenile free-market-economy country with limited funds, any task requires a consensus between policy and fiscally realistic implementation. Therefore, strategy which incrementally incorporates the best practice to risk is truly advantageous. However, more effort is needed in the domain of hazard/risk zoning and prevention, and also in developing common codes of practice. Here, there is also a room for more uniform and applied governance.

Acknowledgments The authors express their thanks to Prof. A. Wojcik for valuable discussions. Ms. M. Rzepka, Ms. A. Honza, Mr. J. Gołda, Mr. A. Nowak and Ms. J. Malec—civil servants of Provincial Administration Offices are acknowledged for their help in compiling financial data related to LPF project.

References

- Anderson M, Holcombe L (2013) Managing risk in small steps: achieving landslide risk reduction by strategic incrementalism in the Eastern Caribbean. *J Int Dev* 25:147–159
- Crozier MD (2005) Management frameworks for landslide hazard and risk: issues and options. In: Glade T, Anderson M, Crozier M (eds) *Landslide hazard and risk*. Wiley & Sons Ltd, Chichester, pp 331–350
- Dai FC, Lee CF, Ngai YY (2002) Landslide risk assessment: an overview. *Eng Geol* 64(1):65–87
- DeGraff JV (2012) Solving the dilemma of transforming landslide hazard maps into effective policy and regulations. *Nat Hazards Earth Syst Sci* 12:53–60
- Długosz M (2009) Landslide susceptibility zoning in the Polish Flysch Carpathians. *Z Geomorph* 53(3):41–48
- Fell R, Corominas J, Bonnard C, Cascini L, Leroi E, Savage WZ (2008) Guidelines for landslide susceptibility, hazard and risk zoning for land use planning. *Eng Geol* 102:85–88
- Grabowski D, Przybycin A (2010) Działania resortu środowiska w zakresie systemu osłony przeciwosuwiskowej w Polsce (*in Polish*). *Prz Geol* 58:941–945
- Guzzetti F, Mondini AC, Cardinali M, Fiorucci F, Santangelo M, Chang K-T (2012) Landslide inventory maps: New tools for an old problem. *Earth Sci Rev* 112:42–66
- Holec J, Bednarik M, Sabo M, Minar J, Yilmaz I, Marschalko M (2013) A small-scale landslide susceptibility assessment for the territory of Western Carpathians. *Nat Hazards*. doi:10.1007/s11069-013-0751-6
- Höppner C, Whittle R, Bründl M, Buchecker M (2012) Linking social capacities and risk communication in Europe: a gap between theory and practice? *Nat Hazards* 64:1753–1778
- Klimeš J, Blahůt J (2012) Landslide risk analysis and its application in regional planning: an example from highlands of the Outer Western Carpathians, Czech Republic. *Nat Hazards* 64:1779–1803
- Mrozek T, Kułak M, Grabowski D, Wójcik A (2014) Landslide counteracting system (SOPO): inventory database of landslides in Poland. In: Sassa K et al (eds) *Landslide science for a safer geo-environment*, Chap. 126. Springer, Heidelberg
- Larsen MC (2008) Rainfall-triggered landslides, anthropogenic hazards, and mitigation strategies. *Adv Geosci* 14:147–153
- Ostaficzuk S (1999) Variety of landslides in Poland, and their possible dependence on neogeodynamics. In: Griffiths JS, Stokes MR, Thomas RG (eds) *Landslides, Proceedings of the 9th International*

- Conference and Field Trip on Landslides, 5-16 September 1999. Bristol, United Kingdom, pp 111–127
- Pánek T, Brazdil R, Klimeš J, Smolkova V, Hradecky J, Zahradnicek P (2011) Rainfall-induced landslide event of May 2010 in the eastern part of the Czech Republic. *Landslides* 8:507–516
- Poprawa D, Rączkowski W, Dziepak P, Kopciowski R, Mrozek T, Nescieruk P, Zimnal Z (1998) Geologiczne skutki powodzi w 1997 roku na przykładzie osuwisk województwa nowosądeckiego (in Polish). In: Starkel L, Grela J (eds) *Powódź w dorzeczu górnej Wisły w lipcu 1997 r.* Wydawnictwa Oddziału PAN, Kraków, pp 119–132
- Roberts NJ, Nadim F, Kalsnes B (2009) Quantification of vulnerability to natural hazards. *Georisk* 3(3):164–173
- Van Westen CJ, Castellanos E, Juriakose SL (2009) Spatial data for landslide susceptibility, hazard and vulnerability assessment: an overview. *Eng Geol* 102:112–131
- Zuber R, Blauth J (1907) *Katastrofa w Duszatynie* (in Polish). *Czas Techn* 25:218–221



Quantitative Multi-risk Modelling and Management Using Bayesian Networks

Zhongqiang Liu, Farrokh Nadim, Bjørn Vidar Vangelsten, Unni Eidsvig, and Bjørn Kalsnes

Abstract

In many regions of the world, several natural hazards may act within the same time frame. Neglecting or underestimating interactions among different hazards may lead to underestimation of the overall risk and further to poor risk management. Implementation of effective and efficient risk management strategies requires that all relevant threats are assessed and considered. However, due to the differing characteristics of hazards, few quantitative models exist that can perform all the computations required for a complete multi-risk assessment. In this paper, a quantitative multi-risk management model using Bayesian networks (BaNMuR) is proposed, which could account for the assessment of cascading hazards, time-dependent vulnerability estimation and selection of optimal risk management strategies. The model was developed as part of the EU FP7 Collaborative Research Project MATRIX. An application example of the BaNMuR model for assessing the risk of tsunami triggered by rockslide is presented in the paper. The proposed multi-risk modelling evaluates the effect of interaction between single risks quantitatively, provides a more rational estimate of multiple risks and helps the decision-makers choose the best risk reduction strategy.

Keywords

Multi-risk modelling • Risk management strategy • Bayesian networks • Tsunami • Rockslide • Cascading hazards

Introduction

In many regions of the world, several natural hazards may act within the same time frame. The risks associated with different types of natural hazards such as landslides, tsunamis, and earthquakes are often estimated using different procedures and the produced results are not comparable. In addition, the hazardous events themselves could be highly correlated (e.g., floods and debris flows could be triggered by an extreme storm event), or one type of threat could be the result of another (e.g., tsunamis could be triggered by an

earthquake or landslide, even both, so-called cascade effect). Neglecting or underestimating interactions among different hazards may lead to underestimation of the overall risk and further to poor risk management. Effective multi-hazard risk reduction strategies and action plans are built on a good understanding of all relevant threats. However, due to the differing characteristics of hazards, few quantitative models exist that can perform all the computations required for a complete multi-risk assessment.

This study provides a quantitative multi-risk management model based on Bayesian networks developed as part of the EU FP7 Collaborative Research Project MATRIX (New Multi-Hazard and Multi-Risk Assessment Methods for Europe). The model addresses a number of the above issues mentioned and can be applied at any geographical level and for any multi-type hazard and risk related purpose. The

Z. Liu (✉) • F. Nadim • B.V. Vangelsten • U. Eidsvig • B. Kalsnes
Norwegian Geotechnical Institute/International Centre for Geohazards,
Oslo 0806, Norway
e-mail: zhongqiang.liu@ngi.no

proposed methodology consists of three main phases: (i) the definition of the multi-risk profile, where links between hazards and vulnerabilities are identified, (ii) multi-risk assessment, in which risks associated with each hazard are assessed and, and (iii) available risk reduction strategies are prioritized from a risk manager's perspective based on the above phases.

The Recommended Multi-risk Management Model

A new quantitative multi-risk management model based on Bayesian networks (BaNMuR) is introduced to estimate the probability of a triggering/cascade effect, model the time-dependent vulnerability of a system exposed to multi-hazard and recommend the best risk reduction strategy. The Bayesian network approach follows the probabilistic definition of risk (Ang and Tang 2007; Einstein et al. 2010):

$$E[R] = P[H]P[C|H]\mu(C) \quad (1)$$

where $P[H]$ is the probability of occurrence of a possible hazardous event; the conditional probability $P[C|H]$ is vulnerability, representing the probability of loss conditioned to certain level of intensity H ; and $\mu(C)$ is the loss of a set of consequences C .

A conceptual BaNMuR model may be built as shown in Fig. 1 (Nadim and Liu 2013). The probabilities of each hazard/vulnerability (nodes in the network) and conditional probabilities of their inter-relationships (arcs in the network) are quantified with existing empirical models, physical analyses or historical data. In addition, these probabilities and total risk can be updated quantitatively through any new information gathered on the basis of Bayes' theorem. It also helps to assess how mitigation measures influence the multi-risk consequences.

This model takes into account the potential interactions between hazards, the uncertainties in each hazard/vulnerability and their inter-relationships. Two types of hazard interactions are considered:

1. independent but threatening the same elements at risk with or without chronological coincidence (the column marked in deep orange colour in Fig. 1);
2. dependent on one another or caused by the same triggering event or hazard; this is mainly the case of 'cascading events' (the column marked in green colour in Fig. 1).

Illustrative Example

To illustrate the proposed model, an example of tsunami triggered by rockslide is studied (Lacasse et al. 2008; Eidsvig et al. 2009). In their study, three hazard event trees

were constructed: rock slide due to seismic trigger (Fig. 2); rockslide due to high pore pressure trigger (Fig. 3); tsunami against Hellesylt in Norway (Fig. 4). A more comprehensive Bayesian network for estimating the risk associated with a potential tsunamigenic rockslide is built with program Hugin Lite (Hugin Expert 7.8) in Fig. 5. There are 7 nodes and 6 arcs in the network. Each node is characterized by several discrete states as shown in Table 1.

With the prior probabilities of the basic and the conditional probabilities that represent the interrelationships between any two factors nodes in Figs. 2, 3, 4, the posterior probabilities of the medium and final nodes are calculated with Hugin Lite, as shown in Fig. 6. It is worth noting that the calculated probability distribution for tsunami run up heights is the same as that calculated by event tree approach in Fig. 4.

Mitigation Measures

The mitigation measures taken for the tsunami induced by the rockslide can be divided into two categories: hazard reducing measures and consequence reducing measures.

Hazard Reducing Measures

A brainstorming session resulted in a list of possible hazard reducing measures. The brainstorming session was followed by a discussion about the feasibility and challenges of the different solutions. A summary of the possible hazard reducing measures is given below:

1. Active drainage of water pressures;
2. Reduce water infiltration in critical locations;
3. Unload top of slide (excavation) and buttressing;
4. Piers across potential sliding surface at the toe;
5. Rock anchoring at the toe (steel cable anchors);
6. Blast down parts of the mountain;
7. Potential sliding surface strengthening (chemical, grouting) combined with drainage;
8. Hydraulic fracturing to increase permeability.

Assuming that the states of pore pressure increase were changed in light of mitigation measures that have been taken, as shown in Fig. 7, the risk for tsunami for State 1 (i.e. State >20 in Run up_1 node), after updating, decreased as expected for this specific tsunami triggered by rockslide and pore pressure increase.

Such Bayesian network could serve as an effective tool to manage tsunami risk triggered by rockslide, provided that the information for the prior is available.

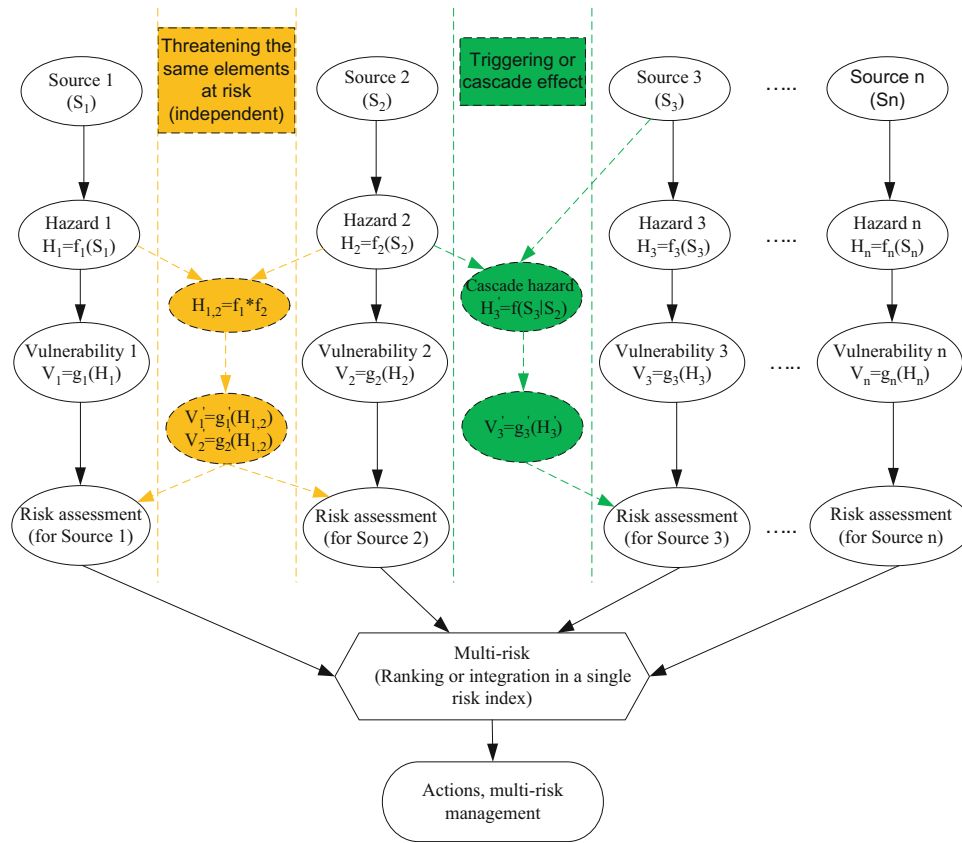


Fig. 1 Bayesian network for quantitative multi-risk assessment

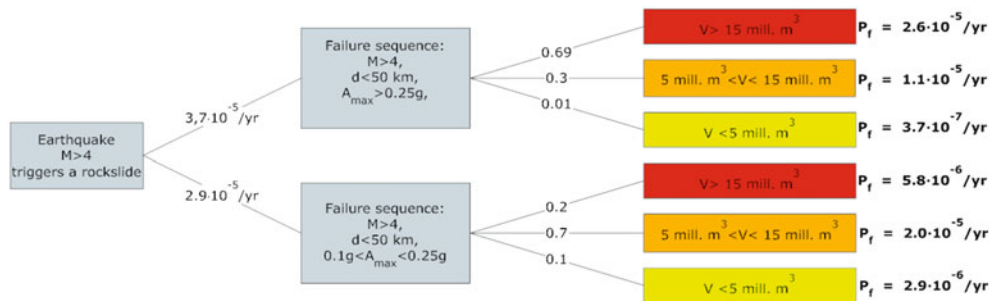


Fig. 2 Event tree for rockslide volume distribution, given that a rockslide is triggered by and earthquake with magnitude larger than 4

Consequence Reducing Measures

Once a maximum run-up height is estimated, a conservative consequence assessment is to consider all of the area at lower elevation than the maximum run-up height at the location to be inundated. Figure 8 shows a map of Hellesylt with the 50 m elevation line. The figure clearly illustrates which buildings and infrastructure could be inundated in the (assumed) worst case scenario.

A brainstorming session resulted in a list of possible consequence reducing measures. The brainstorming session

was followed by a discussion about the feasibility and challenges of the different solutions. A summary of the possible consequence reducing measures is given below:

1. Short term: Construct properly marked out safe havens and escape routes and perform drills;
2. Long term: Visual barriers on land;
3. Long term: Barriers in front of villages under sea level;
4. Long term: Relocate population and infrastructure;
5. Long term: Reinforcement of harbors and installation of brake waters.

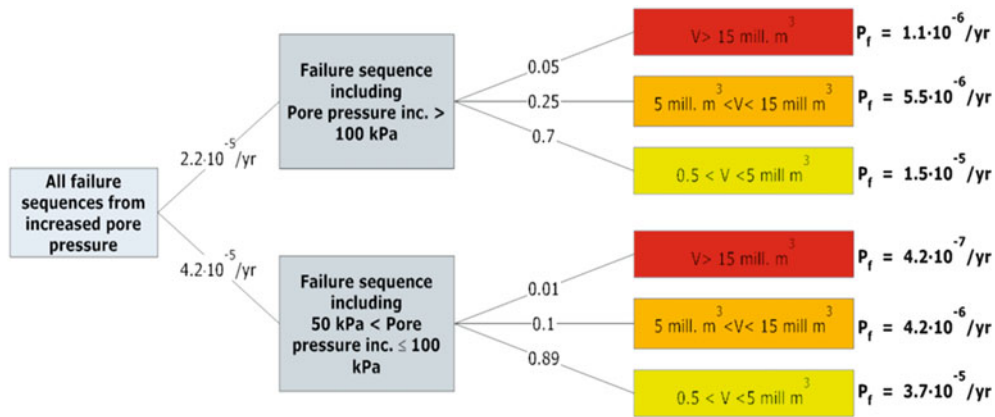


Fig. 3 Event tree for rockslide volume distribution, given that a rockslide is triggered by extreme weather conditions

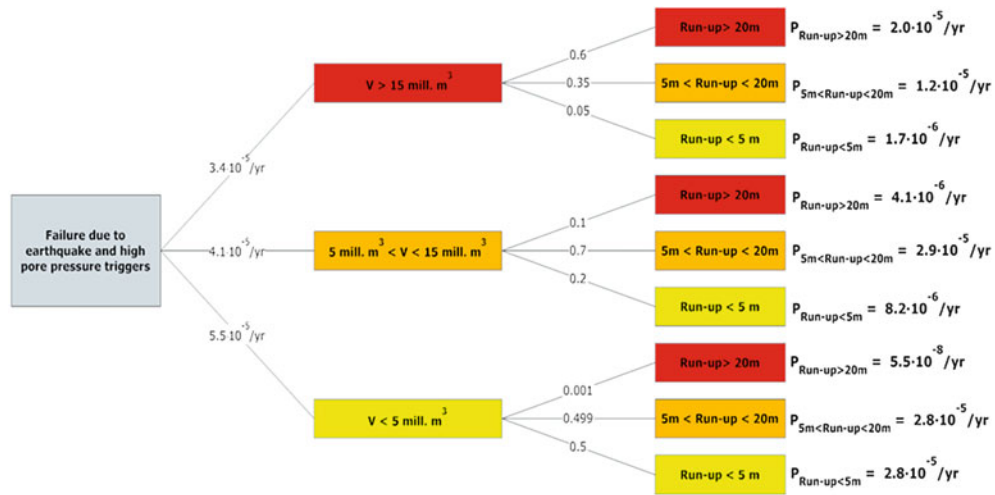


Fig. 4 Event tree for tsunami propagation, given that rockslide has occurred (v = rockslide volume)

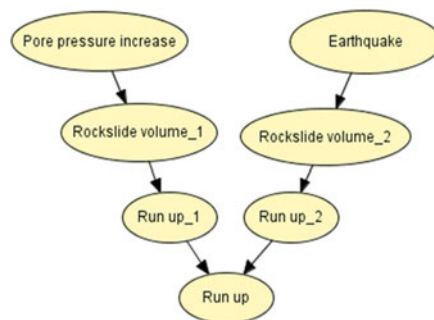


Fig. 5 A Bayesian network for estimating tsunami propagation

Table 1 Nodes and their states of the Bayesian network in Fig. 5

| Node | No. of states | States |
|---|---------------|---|
| Pore pressure increase/kPa | 3 | >100; 50–100; <50 |
| Earthquake/g | 3 | $A_{max} > 0.25$; $0.1 < A_{max} < 0.25$; $A_{max} < 0.1$ |
| Rockslide volume_1/mill. m ³ | 4 | $V > 15$; $5 < V < 15$; $0.5 < V < 5$; $V < 0.5$ |
| Rockslide volume_2/mill. m ³ | 4 | $V > 15$; $5 < V < 15$; $0.5 < V < 5$; $V < 0.5$ |
| Run up_1/m | 4 | >20; 5–15; 0.5–5; <0.5 |
| Run up_2/m | 4 | >20; 5–15; 0.5–5; <0.5 |

Note: A_{max} is peak ground acceleration; V is rockslide volume

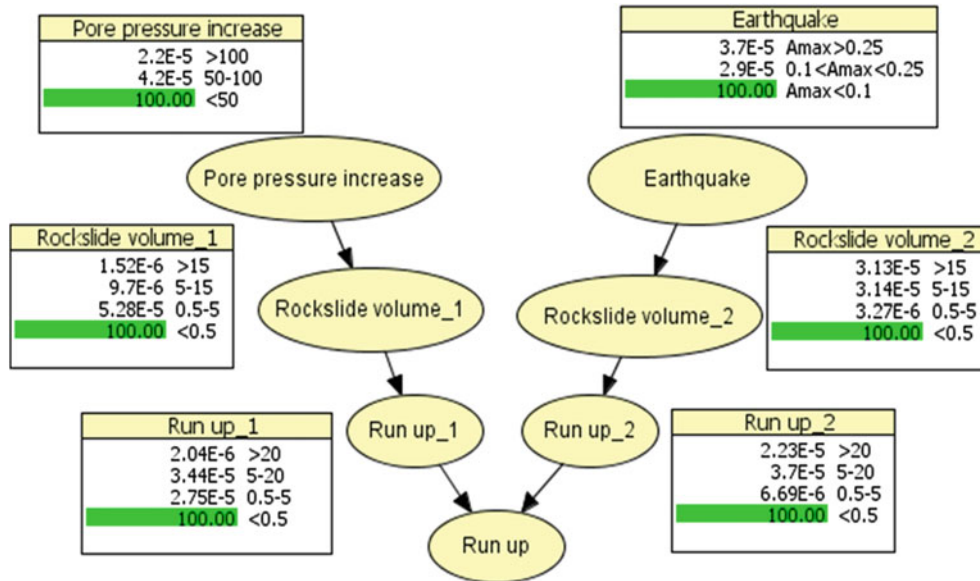


Fig. 6 Quantified Bayesian network for estimating tsunami propagation

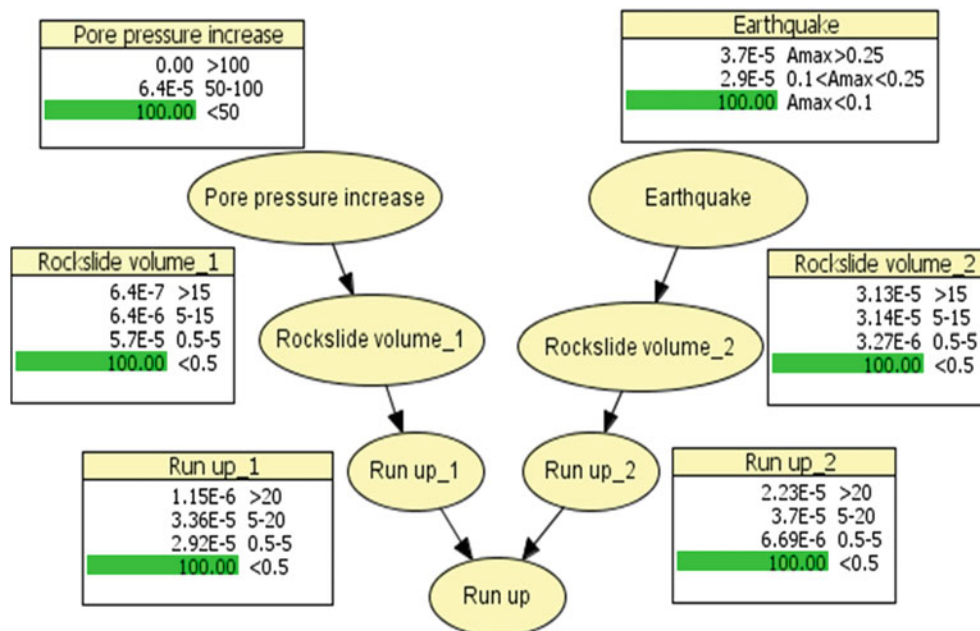
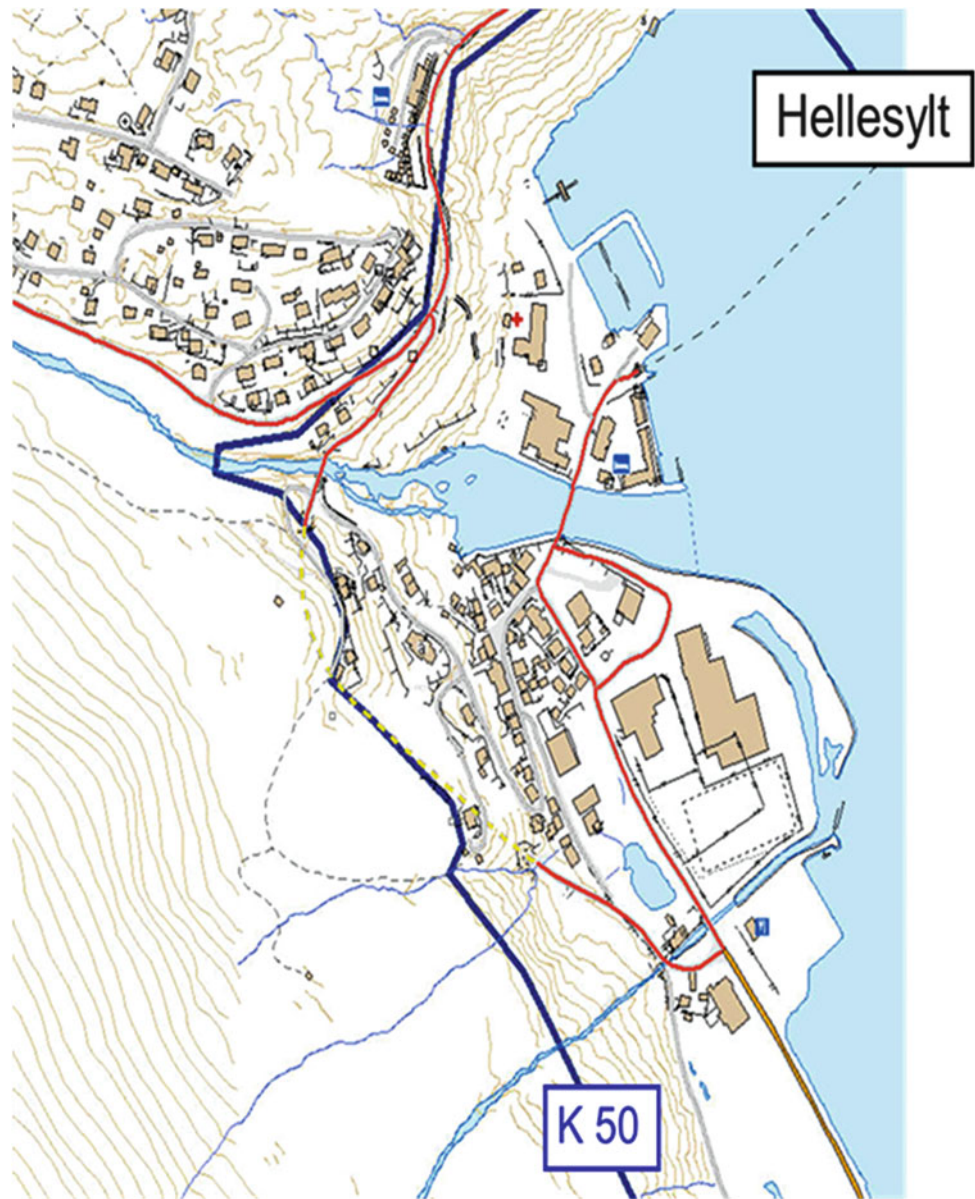


Fig. 7 Updated Bayesian network for estimating tsunami propagation after taking mitigation measures

Fig. 8 Map of Hellesylt with the 50 m elevation line



Summary

This paper presents a new model, BaNMuR, for evaluating multi-risks using Bayesian networks. A specific Bayesian network to evaluate the risk posed by a rockslide-triggered tsunami was constructed considering 7 nodes (parameters) and 6 arcs (inter-relationships) that influence the tsunami run up heights. The calculated probability distribution of run up heights using the proposed model are generally in good agreement with the results obtained by an event tree model. The present model is capable of (a) taking into account a large number of important parameters and their inter-relationships in a systematic structure and (b) including

more available information to update the total risk and manage risk effectively.

Acknowledgments The research leading to these results has received funding from the European Community's Seventh Framework Programme [FP7/2007-2013] under Grant Agreement no 265138 New Multi-Hazard and Multi-RISK Assessment MethodS for Europe (MATRIX).

References

- Ang AH-S, Tang WH (2007) Probability concepts in engineering: emphasis on applications in civil and environmental engineering. Wiley, New York

- Eidsvåg UK, Lacasse S, Nadim F (2009). Event tree analysis of hazard and risk associated with the Åknes roskslide. ICG/NGI Report 20061032-1
- Einstein HH, Sousa RL, Karam K, Manzella I, Kveldsvik V (2010) Rock slopes from mechanics to decision making. In: Jian Zhao, Vincent Labiouse, Jean-Paul Dudt, Jean-Francois Mathier (eds) Rock mechanics in civil and environmental engineering. CRC Press, London, pp 3–13
- Hugin Expert 7.8. <http://www.hugin.com/productservices/demo/hugin-lite>. Accessed 10 Sep 2013
- Lacasse S, Eidsvåg UK, Nadim F, Høeg K, Blikra LH (2008) Event tree analysis of Åknes rock slide hazard. In: Proceedings of the 4th Canadian conference on geohazards : from causes to management. Presse de l'Université Laval, Québec, 594 p
- Nadim F, Liu ZQ (2013) Quantitative risk assessment for earthquake-triggered landslides using Bayesian network. In: Proceedings of the 18th international conference on soil mechanics and geotechnical engineering, Paris

Part IX

Inventory and Database



Introduction: Landslide Inventories and Databases

Snježana Mihalić Arbanas, Marko Komac, Candan Gokceoglu,
and Gabriel Legorreta Paulin

Abstract

This is a short introduction to the Session B9 of the WLF3 entitled “Inventory and Database” with summarized overview of all contributions. Papers included in this part of the volume deals with landslide mapping and landslide identification techniques as well as with presentation of landslide inventories and data bases. There are examples of landslide identification and inventory development from Southern Kyrgyzstan, Mexico, Turkey and Croatia. Event and seasonal landslide inventories are presented in the form of Global Landslide Catalog and simple seasonal inventory from Croatia. National landslide databases encompass large archives of landslide data from Poland, Germany and Switzerland.

Keywords

Landslide identification • Event landslide inventory • National landslide database

Introduction

The Session B9 of the 3rd World Landslide Forum addresses several aspects of landslide databases. From the technical perspective, contributors use both straightforward description of simple inventories and more complex, true databases. Contributors also present different landslide data acquisition approaches—in situ data collection, aerial and satellite mapping, digitalization of topographic maps etc. Consequently databases can consist of landslide populations from local to national and global coverage. Also different

approaches to landslide coverage with reference to the temporal aspect are described, from one-time events to systematical historical coverage.

Nine contributions have been submitted to this session. They can be divided into the following broad topics according to the content:

- Landslide identification and inventory development,
- Event and seasonal landslide inventories, and
- National landslide databases.

Landslide Identification and Inventory Development

Golovko et al. (2014) present development of a regional multi-temporal landslide inventory in Southern Kyrgyzstan. The paper illustrates advantages and limitations of various data sources in the example landslide inventory developed for the Budalyk valley test site area. The regional inventory presented contains a total of over 550 landslides, which were identified from historical records and by field mapping and analysis of satellite images. Automated analysis of multi-temporal high-resolution RapidEye satellite images detected 250 landslides and it is considered as the most efficient and

S. Mihalić Arbanas (✉)
Faculty of Mining, Geology and Petroleum Engineering,
University of Zagreb, Zagreb 10000, Croatia
e-mail: smihalic@rgn.hr

M. Komac
Geological Survey of Slovenia, Ljubljana 1000, Slovenia

C. Gokceoglu
Department of Geological Engineering, Hacettepe University,
Ankara 06800, Turkey

G. Legorreta Paulin
Instituto de Geografía, Universidad Nacional Autónoma de México,
Coyoacán, México 04510, Mexico

appropriate data collection method for further updates of the inventory. Reconnaissance field mapping was also used to collect additional information about the landslides (e.g., date of failure, mechanism, estimated volume and activity). Historical records (since the 1950's) were used for dating of landslide activity. Landslide data were integrated into GIS with scanned 1:100,000 topographic base maps.

Murillo-García et al. (2014) present a geomorphological landslide inventory prepared for a 54 km² study area with different lithological settings in a temperate humid region in Pahuatlán, Puebla, Mexico, where the denudation processes are intense. A stereo-pair approach of Geoeye 1 VHR satellite images (taken on March 31, 2010) with 0.5 m of spatial resolution on the panchromatic band and 1.5 m on the multispectral bands was used for landslide identification. A PLANAR© StereoMirror system was used, combined with a Stereo Analyst ERDAS© extension for ArcGIS©, to generate the 3D view. In total, 390 landslides were identified and digitized directly, creating a digital landslide inventory. The relative age of each mass movement was inferred by geomorphological interpretation of the stereo pairs, resulting in interpretation of 385 recent landslides, 171 old landslides and 21 very old landslides. The very old and old landslides have larger areas than recent landslides. The average area for the recent landslides is 1.1×10^3 m².

Dagdelenler et al. (2014) present a comprehensive geomorphological historical landslide inventory of the eastern part of the Gallipoli Peninsula (Canakkale, Turkey) which covers an area of about 233 km² with variable geological composition. The landslide inventory was derived by using the data acquired from field work, interpretation of aerial photographs and Google Earth satellite images. Landslides were mapped by using 1:25,000 scale topographic maps. As a result of the studies, a total of 211 landslides were identified and mapped. The types of landslides observed in the field are mostly rotational. The identified landslides mostly occurred in the area where the mean slope gradient is about 10° and which are composed of Camrkdere member strata, consisting of mudstone, siltstone, sandstone, and conglomerate alternations, and the Ceylan formation, consisting of sandstone, claystone, marl, and limestone alternations. The areal extent of the smallest failure is approximately 4,837 m² while the largest one is 329,214 m².

Đomlija et al. (2014) present a preliminary detailed landslide inventory map derived by systematic landslide mapping of the 9.35 km² area of hills built of siliciclastic rocks in the Dubračina River Basin near the Adriatic coast in Croatia. A bare-earth DEM was derived from airborne LiDAR imagery scanned in March 2012 with ground-surface measurements acquired at an average density of 5 points per square meter.

Based on the visual interpretation of three different topographical maps (the hillshade map, the slope map and the contour line map), created from the 1 × 1 m bare-earth DEM and supplemented by field reconnaissance mapping of damaged roads and structures; 48 landslides were identified. According to the derived geomorphological landslide inventory map, the spatial landslide distribution is irregular and most of the landslides are associated with zones of excessive erosion. The identified landslides are shallow with an area in a range from about 7,000–40,000 m².

Event and Seasonal Landslide Inventories

Kirschbaum (2014) presents an overview of the Global Landslide Catalog (GLC), the first database which catalogs reported rapidly-moving, rainfall-triggered landslides within the recent past at the global scale. The catalog currently contains seven complete years of data (2007–2013) with continued reporting, and in the database for 2007–2012 there are 4,700 reports from 112 countries. It is compiled from online media reports, disaster databases, and other relevant information. For the landslide locations, each reported landslide includes information on several aspects of the event (e.g. landslide type and size, trigger, fatalities and impact). The paper outlines some preliminary findings for data over the years 2007–2012, evaluating the co-occurrence of GLC events with satellite precipitation, and highlighting an application of the GLC for landslide hazard model evaluation. Three study areas were chosen to evaluate the co-occurrence of landslides and rainfall for 2010: Central America, the Himalayan arc and Central China. The paper also describes evaluation of the prototype global satellite-based landslide hazard algorithm, which combines landslide susceptibility with satellite-derived rainfall estimates, for 2003 (experimental GLC database) and 2007.

Bernat et al. (2014) introduce a seasonal inventory of precipitation-induced landslides from January to April 2013 with reliable landslide records for location, initiation date and landslide area which has been developed for the hilly area in the City of Zagreb (total area of 180 km²) on the basis of field checking of reported landslides. Preliminary temporal distribution analysis of landslide occurrence showed that 63 landslide events happened during the a period of extremes: the cumulative monthly precipitation in January, February and March in 2013 was 130–190 % higher than the average monthly values for the period from 1862 to 2012; cumulative precipitation for a 3-month period in 2013 has the highest value in the last 150 years. Spatial distribution analysis shows that most of the analyzed landslide events were

triggered in engineering soils of Pontian age (approximately 1 landslide per 2 km²). The landslide inventory map presented provides a solid basis for organizing further research aimed at the analysis of landslide-triggering rainfall thresholds, as well as development of a landslide inventory map which will depict landslide contours.

National Landslide Databases

Mrozek et al. (2014) presents a Polish national landslide inventory, which has been developing from 2008 in the framework of the project Landslide Counteracting System (SOPO). The database designed and developed in the frame of SOPO project is a national archive landslide database managed by the Polish Geological Institute. Large-scale inventory map (1:10,000) has been prepared, mostly by geomorphological field mapping and partially using historical documents and visual analysis of SAR and LIDAR data. As of August 2013, the database included records of about 34,039 landslides with a mapped area of 10,903 km² in the Polish Carpathians, with detailed graphic and attribute presentations of landslide contours and landslide features, as well as accompanying information about local geological and environmental conditions, landslide hazard and risk; monitoring equipment and remedial measures. The SOPO inventory is available via Web application (<http://osuwiska.pgi.gov.pl>) and is progressively updated.

Damm and Klose (2014) present a national archive landslide database for the Federal Republic of Germany. This paper describes the structure and contents of the database and outlines its future architecture and WebGIS design. The landslide inventory is compiled from several existing landslide archives, with records about all types of mass movements which date back to 1137 AD. The database stores information on landslide types, dimensions, and processes, as well as the connection of landslides to soil and rock properties, geomorphometry, and climatic conditions. It also includes data on landslide impacts, and hazard mitigation. Today, it stores more than 5,000 data sets with over 13,000 single data files, and covers, besides the Central Uplands, several key regions of the South German Scarplands, the Alpine Foreland and the coasts of the North and Baltic Sea. Finally, examples of applying this database in trans-regional landslide impact studies are given in the paper.

Hess et al. (2014) provide a short overview of background data and dedicated landslide studies in Switzerland, which are important for establishing a national landslide inventory including shallow landslides. The Swiss Federal Office for the Environment (FOEN) launched a project in 2013 with

the objective to homogenize and merge the existing comprehensive but heterogeneous inventories into one national database that will be publicly available for researchers and practitioners. The ultimate goal of the national archive database is to provide a basis to support the generation of hazard maps and early warning systems. The paper presents a case study from the Sachseln region, where event landslide inventory was developed with 280 shallow landslides. Availability of spatial information on (hydro)geology, soil properties, soil wetness and vegetation are considered crucial for analysis of shallow landslides aimed at developing regional early warning systems.

Acknowledgments The conveners of the B9 Session would like to thank all the reviewers who have reviewed the papers submitted to this Session. The papers in the Session are significantly improved through mindful editing conducted by Eileen McSaveney and Lynn Highland. Their editorial work is highly appreciated.

References

- Bernat S, Mihalić Arbanas S, Krkač M (2014) Inventory of precipitation triggered landslides in the winter of 2013 in Zagreb (Croatia, Europe). In: Sassa K et al (eds) *Landslide science for a safer geoenvironment*, Vol. 2. Springer, Heidelberg
- Damm B, Klose M (2014) Landslide database for the Federal Republic of Germany: a tool for analysis of mass movement processes and impacts. In: Sassa K et al (eds) *Landslide science for a safer geoenvironment*, Vol. 2. Springer, Heidelberg
- Dagdelenler G, Nefeslioglu H A, Gokceoglu C (2014) Landslide inventory of the eastern part of the Gallipoli Peninsula (Canakkale, Turkey). In: Sassa K et al (eds) *Landslide science for a safer geoenvironment*, Vol. 2. Springer, Heidelberg
- Đomlija P, Bernat S, Mihalić Arbanas S, Benac Č. Landslide inventory in the area of Dubračina River Basin (Croatia). In: Sassa K et al (eds) *Landslide science for a safer geoenvironment*, Vol. 2. Springer, Heidelberg
- Golovko D, Roessner S, Behling R, Wetzel H-U, Kaufmann H (2014) GIS-based integration of heterogeneous data for multi-temporal landslide inventory. In: Sassa K et al (eds) *Landslide science for a safer geoenvironment*, Vol. 2. Springer, Heidelberg
- Hess J, Rickli C, McArdell B, Stähli M (2014) Investigating and managing shallow landslides in Switzerland. In: Sassa K et al (eds) *Landslide science for a safer geoenvironment*, Vol. 2. Springer, Heidelberg
- Kirschbaum D (2014) Global catalog of rainfall-triggered landslides for spatial and temporal hazard characterization. In: Sassa K et al (eds) *Landslide science for a safer geoenvironment*, Vol. 2. Springer, Heidelberg
- Mrozek T, Kułak M, Grabowski D, Wójcik A (2014) Landslide Counteracting System (SOPO) - inventory database of landslides in Poland. In: Sassa K et al (eds) *Landslide science for a safer geoenvironment*, Vol. 2. Springer, Heidelberg
- Murillo-García F G, Fiorucci F, Alcántara-Ayala I (2014) The development of a detailed landslide inventory for a temperate region in Mexico by using very high resolution (VHR) satellite stereo-images. In: Sassa K et al (eds) *Landslide science for a safer geoenvironment*, Vol. 2. Springer, Heidelberg



Landslide Database for the Federal Republic of Germany: A Tool for Analysis of Mass Movement Processes

Bodo Damm and Martin Klose

Abstract

This contribution deals with an initiative to develop a national landslide database for the Federal Republic of Germany. The paper highlights the structure and contents of this database and outlines its system architecture that underlies the current database transformation. With this background, the paper examines the database potential for research on landslide disaster impacts and hazard mitigation.

Due to systematic and continuous regional data compilation, the landslide database offers a differentiated data pool of more than 5,000 data sets and over 13,000 single data files. It dates back to 1137 AD and covers landslide sites throughout Germany. Besides closing an important data gap at the European level, the database has a key function in the country, as it integrates several existing landslide archives.

In seven major data blocks, the database stores information on landslide types, dimensions, and processes as well as the connection of landslides to soil and rock properties, geomorphometry, and climatic conditions. The database also includes data on land-use effects and damage impacts, disaster mitigation, and landslide costs. A useful feature is its capacity to support development of statistical data products, including time series, index and threshold values, data tables, and diagrams.

The upcoming migration to PostgreSQL/PostGIS improves data storage and geospatial data exploration. Furthermore, it enables the implementation of a WebGIS information platform for knowledge transfer.

Keywords

National landslide database • Germany • PostgreSQL/PostGIS • Data mining • Process and impact research • WebGIS

Introduction

Landslide databases are among the most important tools for scientific and applied use related to the investigation, assessment, and mitigation of landslides. Their capacity to store diverse data on past landslide occurrence plays a key role in

landslide research and disaster management. Over the last couple of years, the development of landslide databases has been pushed forward in many parts of the world (e.g. Devoli et al. 2007; Foster et al. 2012; USGS 2013; Van Den Eeckhaut and Hervás 2012).

Today, there are national landslide databases available in 22 EU member states. These databases usually show huge discrepancies in their content, integrity, format, and accessibility. In most cases, they contain a table of core attributes,

B. Damm (✉) • M. Klose
University of Vechta, ISPA, Universitätsstr. 5, Vechta 49377, Germany
e-mail: bdamm@ispa.uni-vechta.de; mklose@ispa.uni-vechta.de

different geospatial data sets, and information on landslide types and dimensions. Almost every database exists in electronic format and is part of a WebGIS application. Online access, however, is often limited, and knowledge transfer is frequently hampered by reduced data availability, technical problems, and language barriers (e.g. Van Den Eeckhaut and Hervás 2012).

Until recently, the Federal Republic of Germany was one of the few countries in the European Union that held no national landslide database. Although the development of regional data inventories has been a research focus for years, no concerted actions have been taken so far to store, organize, and manage existing landslide data sets in one centralized database system. In a current research project, the focus is therefore on data integration and the development of a national landslide database for Germany. The priority goals target not only the creation of this database, but address also its scientific exploitation for improving fundamental understanding of landslide phenomena on trans-regional levels. From the end of 2013, the key actions are focused on data exploration and analysis, including the investigation of spatiotemporal landslide patterns and recurrence frequencies as well as research on landslide types, dimensions, and dynamics, climate connections, and physical controlling factors. Further core topics concern types and costs of landslide damage, vulnerability and exposure of mobile objects and infrastructure, as well as effectiveness of disaster response and hazard mitigation. Finally, special emphasis is placed on the effects of planning or building practices and land-use activity. On the other hand, the current research project is concentrated on hazard communication and knowledge transfer. The primary objective is to develop a WebGIS information platform that provides statistical data and research findings to the science community and decision makers.

The basis of this landslide inventory initiative is the trans-regional database “*Mass Movements in German Subdued Mountains*” (Damm 2013). During recent years, this database has been permanently updated and expanded by systematic data compilation throughout Germany. Today, it stores more than 5,000 data sets with over 13,000 single data files and covers, besides the Central Uplands, several key regions of the South German Scarplands, the Alpine Foreland and the coasts of the North and Baltic Sea. The database goes back to 1137 AD and considers all types of mass movements, with a core focus on slide processes and rockfall. This study presents the structure and contents of the database and outlines its future architecture and WebGIS design. Finally, examples of applying this database in trans-regional landslide impact studies are given.

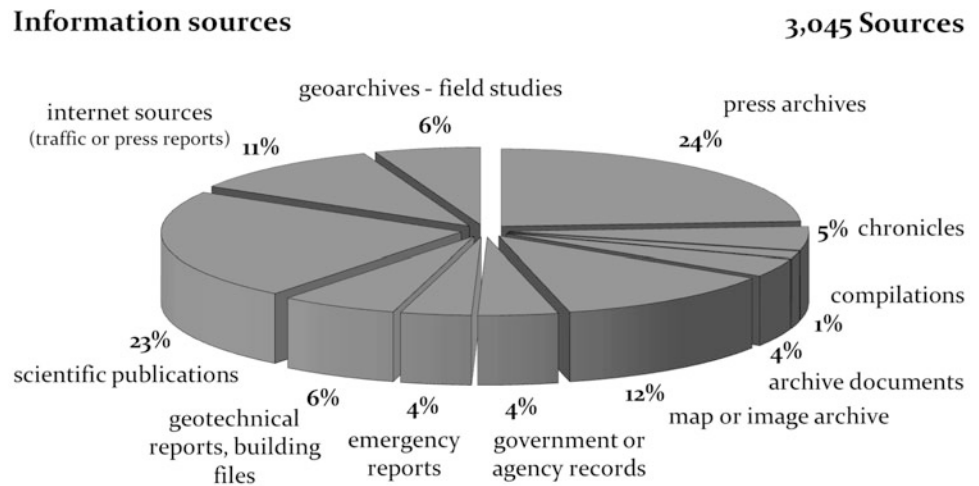
Structure of the Database and Its Current Migration

General Contents and Previous Database Model

The major purpose of the landslide database is to provide scientific data for basic and applied landslide research in Germany. At the beginning of the recent database migration and re-organization process, a MS Excel© database is still used to manage the data pool. The database structure is composed of a number of related data sheets of which one stores the basic raw data. In this data sheet, documented landslides are registered chronologically in rows and their text data sets and numerical information are compiled in seven major data blocks. Each data block represents a certain thematic area and includes a series of data tables. Besides a set of key data and storage space for general landslide documentation, there are data blocks with focus on landslide processes, landslide impacts, and hazard mitigation. The segmentation in aggregated data blocks, thematically related data tables, and special data fields is defining the database mask so far. This configuration guarantees logic and consistent data storage and provides options for profound statistical data analysis. The storage of the analysis data is managed in spread sheets connected with the database through automatized data relations and links between the single tab pages. Using customized routines and functions for statistical data exploration, the database stores different data products and research results. This information is available in form of time series, index and threshold values, data tables, and diagrams. Apart from geospatial mapping data, the database provides functionality and data capacity for a broad spectrum of scientific and practical applications.

The spatial and temporal core data collected in this database include information on occurrence date or times of movement activity, geographic coordinates and landslide location, administrative region, as well as available data sources. A general documentation stores for each landslide event all available text information and also quantitative data sets. It typically includes a process description, measurement data of landslide dimensions, site-specific soil, vegetation or lithological data sets, as well as climatic records. Furthermore, the database lists technical damage profiles, land use information, and notes on landslide costs. These thematic data sets are complemented by a validation regarding the quality of the different types of information. For the storage of numerical and statistical records, separate data tables are used. In view of landslide processes, these are ones focusing on process type, surface of rupture and volume, activity and velocity, slope gradient, as well as magnitude and slope stability. Two further data tables organize information on causes and triggers of landslides. They are

Fig. 1 Information sources of the landslide database for the Federal Republic of Germany



differentiated in natural and human factors and include amongst others data sets related to rock strength and structure, erosional activity, slope water and moisture conditions, ground shaking and vibration, artificial loads, and also human slope disturbance. Additionally, this inventory includes data tables that are geared to damage aspects and practices of hazard mitigation. The data block on landslide impacts stores information about types and levels of damage at infrastructures and mobile objects as well as evidence on personal injuries and casualties. Three data tables dealing with hazard mitigation contain technical records on slope remediation and protection and further information on site management or non-structural mitigation measures. Finally, all available economic loss data are totaled in a separate data table giving information about landslide costs.

As early as today, the contents of this database open new options for landslide process and impact research on large spatial scales. The database already supported investigations of tectonic-structural and soil physical predisposing factors, analyses of climate and soil moisture relationships (Klose et al. 2012), hazard and cost modeling (Klose et al. 2014), as well as evaluations of spatial planning practices (Damm 2006).

Information Sources and Concepts of Data Collection

The landslide database stores data sets derived from a variety of different information sources (Fig. 1). Most of them have the capacity to provide valuable data for landslide research. The most frequent information sources are scientific publications, government and agency records, geotechnical reports, as well as geoarchive and field data. An important role is also played by emergency and press reports, historical archive documents, and web information.

The concept of data collection is based on a two-tier strategy, with elements of both regional data expansion and local data specification. Usually, data collection is started with systematic web content mining and the exploration of online archives of emergency agencies, fire and police departments, and news organizations. Using web and RSS feeds and soon also a focused web crawler, this enables effective nationwide data collection for recent landslides. The acquisition of data on a national level is also supported by data sharing with different research groups, state geological surveys, departments of transportation, and spatial planning agencies. On the basis of this body of information, archive studies are performed to deepen and diversify the data pool in key landslide areas with high data density. The archive selection is guided by the data coverage in our database and the results of the prior web analyses. To get a representative view on process and damage patterns in certain case study regions, data retrieval is organized according to spatial and thematic aspects.

A major part of relevant information is usually stored in state, county, and city archives and the special records of highway, forest, and waterway departments. In some cases, there is also access to archives of construction and infrastructure companies, which often include highly valuable thematic data sets. At the beginning of archive studies, press reports and chronicles provide first pieces of information. In the next steps, data retrieval is more intensified, with key focus on exploring special data from building files, technical documentations, project accounting, or maintenance records. Finally, this text information is combined with geospatial data from topographic and geologic maps, satellite imagery, and sometimes also digital elevation models. The purpose of field studies is to prove the existing data on a case-by-case basis and to complete them if necessary. In the field, there is only time to collect basic process

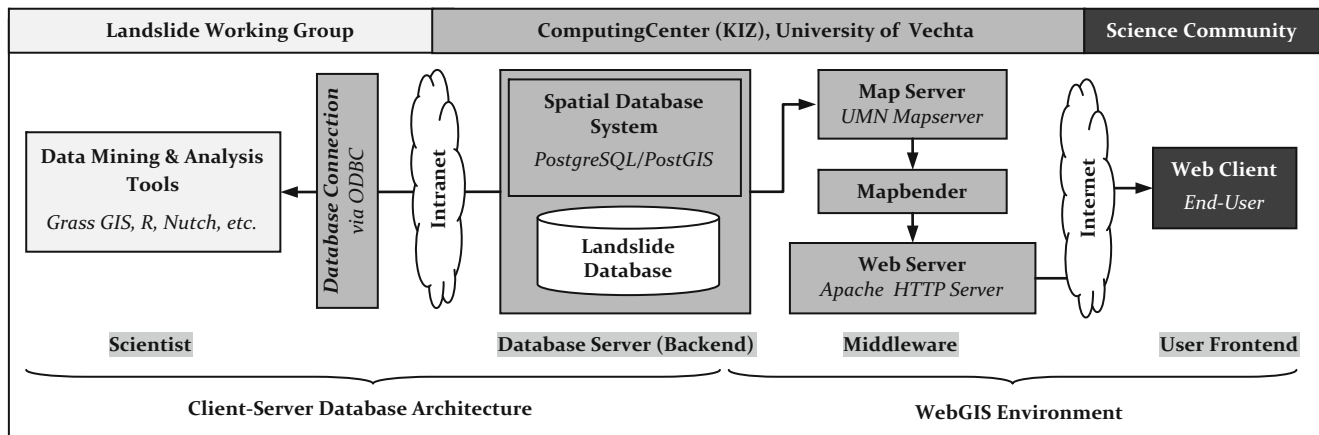


Fig. 2 Architecture of the spatial database system and the connected WebGIS application

information and site-related data; nevertheless, the database also integrates the results of periodic detail studies.

Future Database Architecture and WebGIS Design

At the moment, the landslide database undergoes a far-reaching transformation process with the overarching goal to completely modernize the ways of data storage. The key priority is to embed this inventory in a spatial data infrastructure that provides functionality to store, manage, analyze, and present the data more efficiently. Special emphasis is placed on the development of a spatial database system that expands the options in advanced data exploration and visualization while improving data persistency and integrity. Apart from this, it is a necessary step towards effective data presentation and knowledge transfer using a WebGIS application.

The spatial database system has a client-server architecture with centralized data storage on a virtual geodata server hosted by the computing center (Fig. 2). With PostgreSQL/PostGIS as the database management system, powerful open-source software is used. This software is well qualified to run optimally in an environment of Linux IBM BladeCenter© servers. After server virtualization by applying XenServer©, the database system can be installed, configured, and administrated from different workstations. PostgreSQL forms, with its spatial extension PostGIS, a high-end object-relational database engine that competes with proprietary software. It features the full range of spatial operations for geographical objects and supports connectivity to free statistical software, GIS programs, and web-based data mining tools.

On the other side of the database, an OpenGIS web service is implemented to provide data products and research

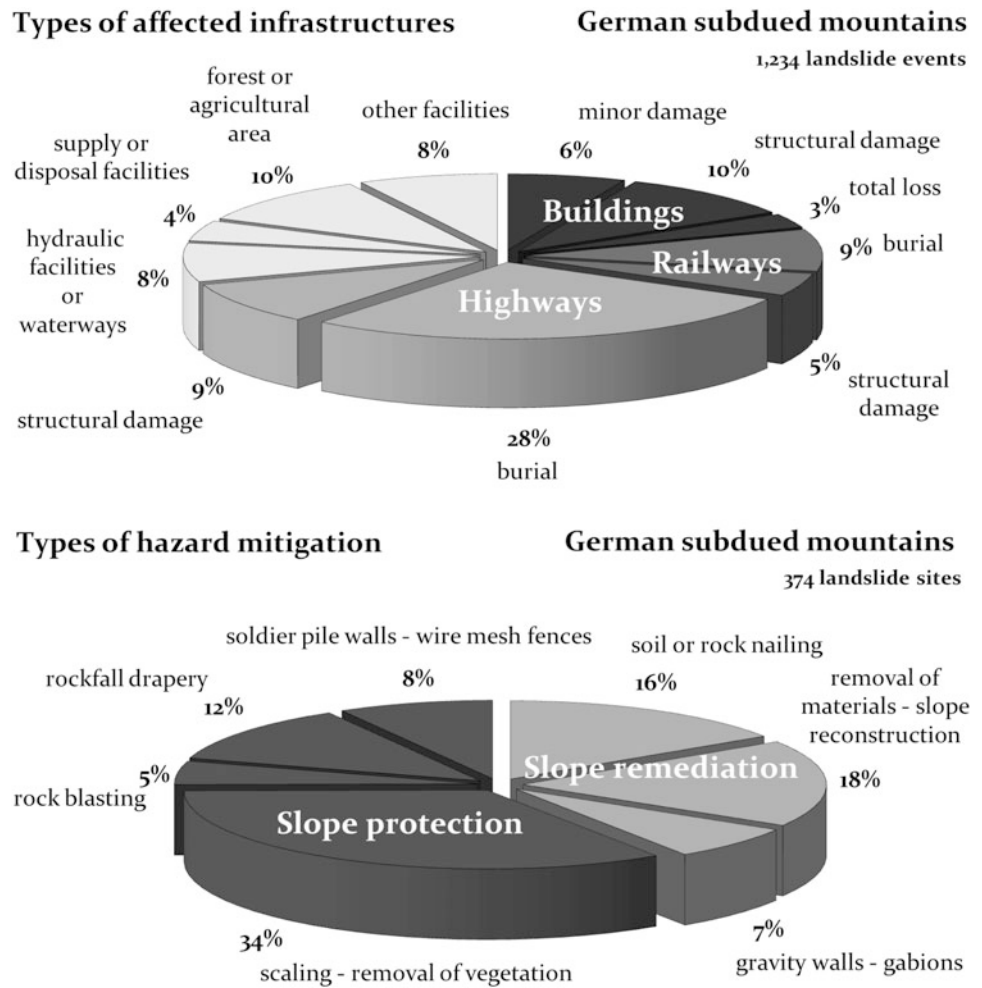
findings online. This WebGIS has a three-tier architecture, including the database server, different middleware components, and the web client. The data flow is organized on the basis of UMN MapServer, Mapbender, and Apache HTTP Server. Each of these open-source components fulfills functions in the traffic of user requests and visualized data return. Thus, Mapbender generates an interactive graphical user interface that enables querying of data contents from a standard web browser through navigating in a mapping application. The WebGIS system is fully integrated in the IT-infrastructure of the computing center.

Application in Trans-Regional Landslide Impact Studies

Overview of Disaster Impacts and Direct Damage Types

An exemplary data set for selected case study regions in the German subdued mountains containing about 1,200 landslide events shows that mass movements primarily affect traffic infrastructures in these parts of Germany (Fig. 3). About 50 % of the documented landslides took place along the highway and railroad network. The types of direct damage can be roughly subsumed under ones concerning the pure burial of facilities and ones with static-structural effects. While traffic routes are mostly hit by shallow landslides or small rockfalls, building damage refers most often to loss or reduction of structural stability as result of differential ground movement. Although with distinct lower frequency, landslides are also recorded to cause damage at hydraulic infrastructures and waterways, supply and disposal facilities, as well as forest and agricultural areas. In such damage statistics, however, it is difficult to summarize

Fig. 3 Landslide damage and hazard mitigation in case study regions of the German subdued mountains in the period 1960–2013



the relevance of insidious landslide damage. Thus, there is evidence that in many communities of the Central Uplands, creeping soil and slow slope deformation are responsible for costly disruptions of critical lifelines, especially drain and sewer systems. Finally, other facilities periodically affected by destructive landslide activity are sports fields, mining areas, graveyards, and sites of cultural heritage.

A closer look on the different types of damage at traffic infrastructures shows that, besides failures of cut and fill slopes, continuous settlement and subsidence in embankments causes frequent damage. Additionally, collapse or tilting of retaining walls and street lights, destruction of all kind of traffic safety facilities, and the high vulnerability of rail tracks are important damage aspects documented in the database. With regard to building infrastructure, landslide damage is typically related to burial of backyards and garden areas, crash or collapse of building back walls, crack formation in walls and foundations, and sometimes total structural deformation.

More importantly, landslides also have high human costs and cause considerable damage to mobile objects. In many cases, these damage events are related to car and train

accidents, which often implicate personal injuries and even death of the people involved.

Analysis of Hazard Mitigation and Its Effectiveness

Most infrastructure facilities in the German subdued mountains affected by landslide damage are further used after removal of debris or successful realization of mitigation measures. Permanent abandonment of use is primarily at private homes and other non-commercial building types of high relevance. Thus, more than 80 % of affected buildings are vacated in the long run. This high percentage mainly results of inefficient mitigation, since many times the costs of maintaining structural integrity exceed the object's market value.

For traffic routes, mitigation is mostly economically reasonable, although cases of permanent closure are documented. The protection of roads and railway lines located at the footslope of unstable soil or rock slopes is dominated by simple and cost-effective practices. Rock and

tree removal is usually the preferred solution for hazard prevention (Fig. 3). It includes, besides hand scaling of loose rock, soil, and vegetation, trimming of rock slopes and critical overhang by rock blasting. Such operations are always of temporary effectiveness and require short maintenance cycles and periodic controls. Popular alternatives to cope with risks of shallow soil slides and falling debris are soldier pile walls, wire mesh fences, and rockfall drapery. However, these simple mitigation measures are often undersized and fail under stress, causing serious accidents. The installation of slope stabilization and rockfall protection systems reduces these risks effectively. Among the most common ones are flexible catch fences, soil or rock nailing with mesh facing, and tied-back anchor walls. Many unstable soil slopes are also mitigated by concrete and masonry gravity walls. A key role in slope remediation involves in 18 % of all cases the removal of unstable soil materials and embankment fills. As long as the slope profile has to be maintained, the slope is usually reconstructed by using stable and draining gravel soils. This type of repair is typical for slope failures at road cuts and traffic embankments.

Finally, a recent trend is observed to minimize landslide and liability risks by implementing oversized and expensive protection systems. Finding the right balance in disaster mitigation is thus a crucial issue in hazard management. Knowledge transfer can help to overcome these problems in future.

Discussion

Landslide databases play a major role in the modeling of landslide susceptibility, hazard, and risk. Their data potentials in process and impact research, however, are still widely neglected. This is most likely the result of a lack of concepts to identify information sources with comprehensive, but often hidden process and damage information. On the other hand, the power and quality of available data is still underestimated or explored rudimentarily, which probably traces back to the absence of tools for being able to extract and store such data in adequate landslide databases. Furthermore, the fusion of archive and geospatial data is rare, although data integration is seen as the key for successful process and damage reconstruction. The experiences

show that in cases of systematic data retrieval and exploration as well as proper structuring of the data, the investigation of landslide processes and impacts becomes possible, even on trans-regional levels. However, some data are so complex that their nationwide compilation can only be realized incrementally, wherefore certain studies are still confined to regions with a highly differentiated data basis.

Conclusions

The development of national landslide databases is a key priority in achieving a fundamental understanding of the nature of landslide phenomena in large areas. On the basis of improved methods for data collection, it is now feasible to build comprehensive databases with the capacity to store trans-regional data sets ranging from process frequencies and intensities to landslide damage and hazard mitigation. The systematic exploitation of such databases opens a whole new window on landslide process and impact research and finally helps to improve efficiency in disaster risk reduction.

References

- Damm B (2006) Simplified planning regulations in Germany and the effects of landslides. *J Environ Plan Manag* 49(5):777–790
- Damm B (2013) Landslide database for the federal republic of Germany, previous version: database mass movements in German Subdued Mountains 1137–2013, August 2013, Univ. Vechta, Germany
- Devoli G, Strauch W, Chavez G, Høeg K (2007) A landslide database for Nicaragua: a tool for landslide-hazard management. *Landslides* 4:163–176
- Foster C, Pennington CVL, Culshaw MG, Lawrie K (2012) The national landslide database of Great Britain: development, evolution and applications. *Environ Earth Sci* 66:941–953
- Klose M, Damm B, Gerold G (2012) Analysis of landslide activity and soil moisture in hillslope sediments using a landslide database and a soil water balance model. *GEO-ÖKO* 33(3–4):204–231
- Klose M, Gruber D, Damm B, Gerold G (2014) Spatial databases and GIS as tools for regional landslide susceptibility modeling. *Zeitschrift für Geomorphologie* 58(1):1–36
- USGS (2013) Landslide inventory pilot project. <http://landslides.usgs.gov/regional/inventory/>. Last Accessed 29 Jul 2013
- Van Den Eeckhaut M, Hervás J (2012) State of the art of national landslide databases in Europe and their potential for assessing landslide susceptibility, hazard and risk. *Geomorphology* 139–140:545–558



Landslide Inventory of the Eastern Part of the Gallipoli Peninsula (Canakkale, Turkey)

Gulseren Dagdelenler, Hakan A. Nefeslioglu, and Candan Gokceoglu

Abstract

In Turkey, landslides cause several types of damage in addition to casualties in every year. Because of the losses caused by landslides, applications to reduce damage and losses require the knowledge of current and potential spatial distribution of mass movements, called a landslide inventory. For the present study, a comprehensive landslide inventory of a landslide-prone area in Turkey, a part of Canakkale, Gallipoli Peninsula, was prepared. A total of 211 landslides were identified and mapped; most are rotational. Employing the landslide inventory, the possible causative factors of the landslides, considering their types and dimensions are discussed.

Keywords

Landslide • Inventory • Gallipoli Peninsula • Canakkale • Turkey

Introduction

During the First World War, at Canakkale sea and land battles took place in the Gallipoli Peninsula. Sunken ships, cannons, trenches, castles, towers, and a broad spectrum of war artifacts, as well as more than 60,000 Turkish martyrs, and again more than 250,000 war graves of soldiers from Australia, New Zealand, British and French and memorials are located here. For this reason, the southern part of Gallipoli Peninsula, covering an area of 330 km² on the northern side of the Dardanelles, was declared as a Historical National Park, and it is currently in the United Nations list of National Parks and Protected Areas. Owing to the characteristics of some parts of the Peninsula, the eastern part of the Canakkale Gallipoli Peninsula was selected as the

study area. Despite its historical importance, there is no detailed study investigating the landslide occurrences in this region. In order to complete the landslide inventory of the study area, inspection of Google Earth satellite images and aerial photographs, as well as field checks, were carried out during the preparation of a landslide inventory of the region. As a result of the studies, a total of 211 landslides were identified and mapped. The type of landslides observed in the field are mostly rotational. The areal extent of the smallest failure is approximately 4,837 m² while the largest one is 329,214 m².

In the literature, there are different definitions of landslides. In general, landslides affected by vegetation, land use and human activities are defined as artificial, while natural slope instabilities are controlled by the frequency and intensity of rainfall and seismic events (Soeters and Van Westen 1996). Today, hundreds of people lose their lives due to landslides throughout the world, and these landslides have a substantial impact on national economies. Almost half of the loss of lives due to natural disasters in Japan are caused by landslides (Dağ 2007). In Turkey, one of the types of natural disasters that causes loss of many lives is known to be mass movements (İldrîr 1995). Because of the losses caused by landslides, planning for protection and to

G. Dagdelenler (✉) • C. Gokceoglu
Department of Geological Engineering, Hacettepe University, Beytepe
06800, Ankara, Turkey
e-mail: gdagdelenler@gmail.com; candan.gokceoglu@gmail.com

H.A. Nefeslioglu
Polatli Technical Sciences Vocational School, Hacettepe University,
06900 Polatli, Ankara, Turkey
e-mail: hanefeslioglu@hacettepe.edu.tr

reduce losses requires a spatial distribution (inventory) of the current and potential mass movements. Landslide inventory maps are prepared for different purposes, including: (i) showing the location and type of landslides in a region (Antonini et al. 1993; Cardinali et al. 2001; Antonini et al. 2002), (ii) showing the effects of single landslide triggering event, such as an earthquake (Harp and Jibson 1995, 1996), an intense rainfall event (Bucknam et al. 2001) or a rapid snowmelt event (Cardinali et al. 2000), (iii) showing the abundance of mass movements (DeGraff 1985; DeGraff and Canuti 1988; Guzzetti et al. 2000), (iv) determining the frequency-area statistics of slope failures (Hovius et al. 1997, 2000; Guzzetti et al. 2002; Brardinoni et al. 2003; Guthrie and Evans 2004a, b; Malamud et al. 2004), and (v) providing relevant information to construct models of landslide susceptibility (Soeters and Van Westen 1996; Guzzetti et al. 1999; Chung and Fabbri 1999, 2003, 2005) or hazard (Guzzetti et al. 2005, 2006a, b).

The main purpose of the present study is to document the location and the type of the landslides that have occurred in the eastern part of the Gallipoli Peninsula in Canakkale in Turkey. For this purpose, a landslide inventory was established by using the observations acquired from field work, aerial photographs and Google Earth satellite images of the study area. Landslides were mapped by using 1/25,000 scale topographic maps. Based on observations as well as the areal distributions of the failures mapped on the 1/25,000 scale topographical maps, a landslide inventory of the region was produced.

General Characteristics of the Study Area

Description of the Study Area

The eastern part of Gallipoli Peninsula (Canakkale, Turkey) was selected as the study area (Fig. 1). The study area covers an area of about 233 km² bounded by 1/25,000 scale national map border layout in the east, Saros Gulf in the north, Canakkale Strait in the south and alluvial valley bottom in the west. According to the Meteorological Station in Gallipoli, the average annual rainfall between 1958 and 2009 is 696 mm and for the last 50 years the average annual temperature is calculated to be 14.8 °C (MGM 2007).

Geology and Stratigraphy of the Study Area

The Gallipoli Peninsula is geologically bordered by the Ganos fault (Saroglu et al. 1987) in the north. An extension of the southwest portion of this fault is located in Gulf of Saros (Saroglu et al. 1987). The Peninsula is represented by a northeast-southwest-trending monoclinical fold structure.

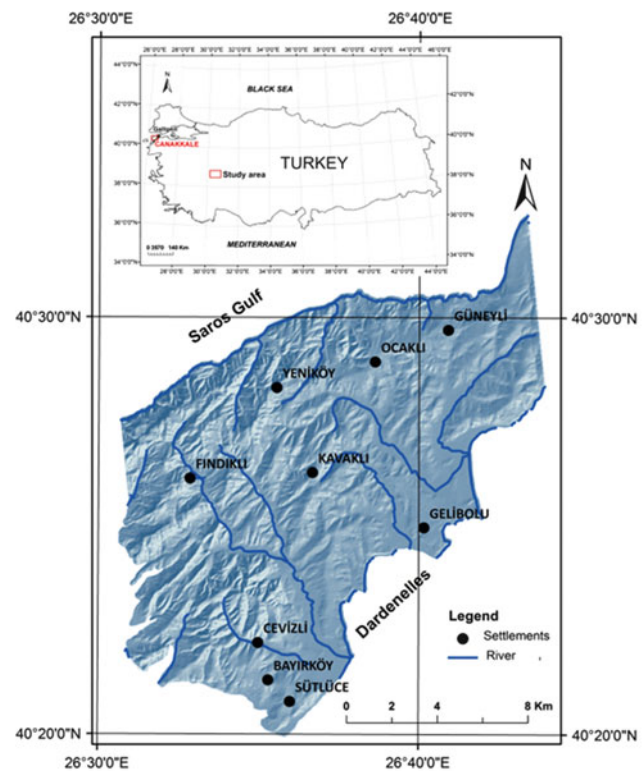


Fig. 1 Location map of the study area

The main structure of the Peninsula is a reverse fault developed by this monocline folding (Saroglu et al. 1987). Ophiolitic outcrops extend in a northeast-southwest direction in the north of Ortaköy-Şarköy-Mürefté (Dönmez et al. 2008). According to Dönmez et al. (2008), 13 different types of lithology outcropped in the study area. The stratigraphic sequence observed in the region is given in Fig. 2. These units are defined as follows: Ophiolitic series, Ficitepe Formation (pebble stone, sandstone, shale), Dededağ Volcanites (andesite, dacite, tuff, ignimbrite), Korudağ Member (sandstone, claystone), Ceylan Formation (turbidite sandstone, claystone, marl, limestone), Kanlibent Member (sandstone, mudstone, pebblestone), Kirazlı Member (pebblestone, sandstone, siltstone), Çamrakdere, Member (mudstone, siltstone, sandstone, conglomerate), Alcitepe Member (calcarene, Mactraous limestone, sandstone, marl), Bayramiç Formation (pebblestone, sandstone, claystone), Travertine, old Alluvion and Alluvion deposits.

Tectonic Settings and Seismicity of the Study Area

As mentioned above, the Gallipoli Peninsula is geologically bordered by the Ganos fault in the north and the extension of the southwest portion of this fault is in the Gulf of Saros.

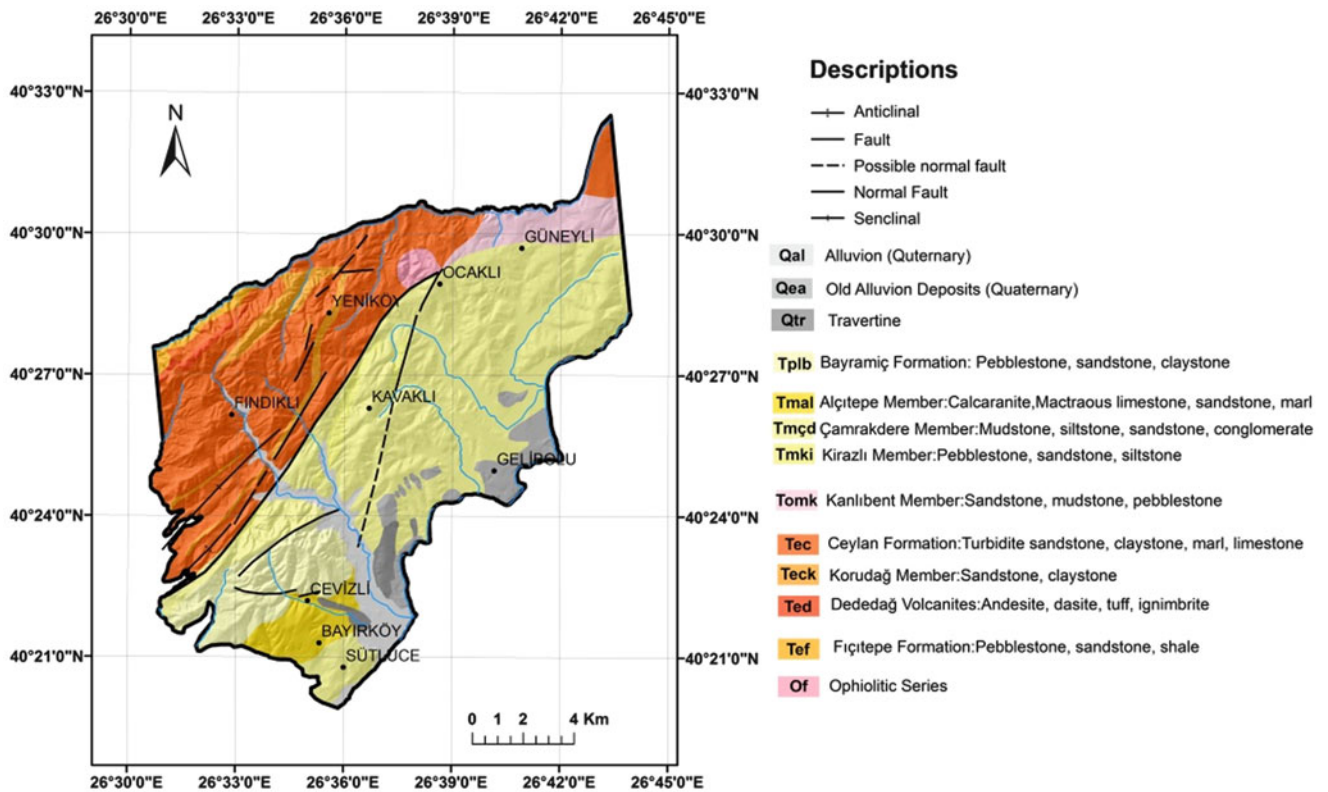


Fig. 2 Geological map of the study area (modified from Dönmez et al. 2008)

When the seismotectonic map of the region is analyzed, it indicates that earthquakes greater than 3 Mw are observed rarely in the study area (Dagdelenler 2013). However, the closest fault system to the study area is the active Ganos fault, which is located approximately 15 km away from the study area (Saroglu et al. 1987). Even though an active fault system is very close to the study area, a shear zone due to faulting in the study area is not observed.

Landslide Inventory

A landslide inventory is defined as a collection of data that contains information on topics such as location, type, activity and physical properties of landslides in a region (Fell et al. 2008). Landslide inventory maps are the terrain maps showing the areal distribution of existing landslides. In this study, the landslide inventory was prepared by considering the observations acquired from field works, aerial photographs and Google earth satellite images of the study area.

The instabilities were mapped on 1/25,000 scale topographical maps. Based on the observations, as well as the areal distributions of the failures recorded during the field and laboratory studies, a landslide inventory of the region was produced (Fig. 3). The landslides in the study area are

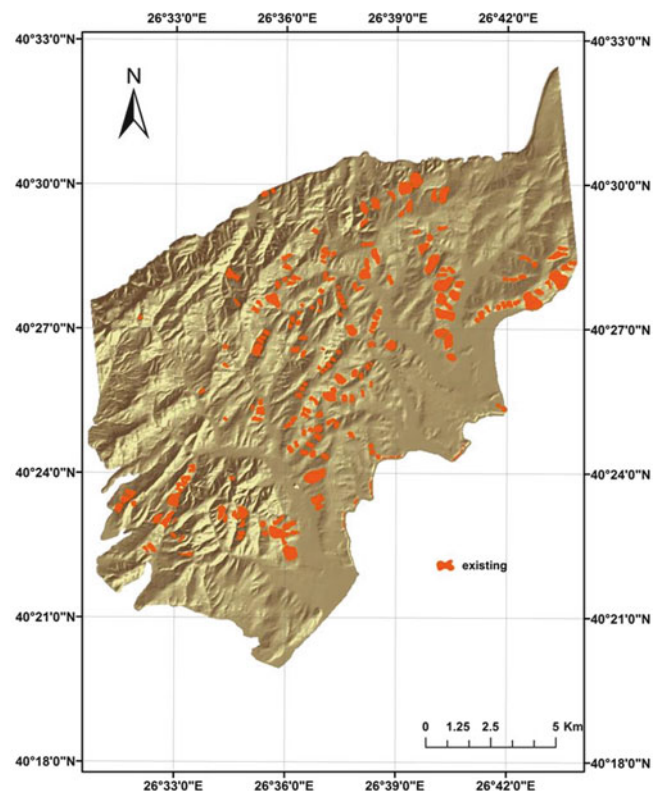


Fig. 3 Landslide inventory map of the study area



Fig. 4 Some examples of landslides in the study area

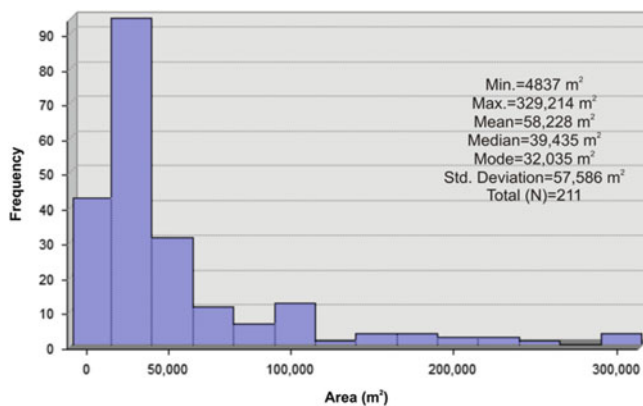


Fig. 5 Histogram showing the areal distribution of the landslide areas

mostly rotational (circular failure). Furthermore, there is no discontinuity controlled planar failures in the study area. Some example photographs of the landslides observed in the study area are given in Fig. 4. Areal statistics of the landslides are given in Fig. 5. The maximum landslide area is $329,214 \text{ m}^2$ and the minimum landslide area is $4,837 \text{ m}^2$. The mean area of the 211 landslides in the study area is determined as $58,228 \text{ m}^2$. The total area for the failures is given as $12,286,315 \text{ m}^2$ (Table 1).

Table 1 Statistics for the landslide inventory map of the study area

| Characteristics | Value/dimension |
|--|-----------------|
| The number of landslides (#) | 211 |
| Total landslide area (m^2) | 12,286,315 |
| Minimum landslide area (m^2) | 4836 |
| Maximum landslide area (m^2) | 329,213 |
| Mean of the landslide areas (m^2) | 58,228 |
| Median of the landslide areas (m^2) | 39,435 |
| Mode (m^2) | 32,035 |

Results and Discussions

Based on the results of the present study, a total of 211 landslides are defined in the region. The landslides observed in the study area mostly occurred in the Camrakdere member, consisting of mudstone, siltstone, sandstone, and conglomerate alternations, and the Ceylan formation, consisting of sandstone, claystone, marl, and limestone alternations. Since the topographic relief is not high in the area, the mean slope gradient is observed to be about 10° on the failures. Obviously, it should be noted that this statistic is given for the already failed mass. The actual pre-failure topography might be different from the recent one. In addition, considering the observation carried out during the field

studies, the landslides mapped in the inventory studies are evaluated as being active. Therefore, considering the historical importance of the region, the landslide inventory of the study area is highly crucial for further mitigation as well as planning applications.

References

- Antonini G, Cardinali M, Guzzetti F, Reichenbach P, Sorrentino A (1993) Carta Inventario dei Fenomeni Franosi della Regione Marche ed aree limitrofe, 2 sheets, scale 1:100,000. Publication no. 580, CNR-GNDICI, City, Country (in Italian)
- Antonini G, Ardizzone F, Cacciano M, Cardinali M, Castellani M, Galli M, Guzzetti F, Reichenbach P, Salvati P (2002) Rapporto Conclusivo Protocollo d'Intesa fra la Regione dell'Umbria, Direzione Politiche Territoriali Ambiente e Infrastrutture, ed il CNR-IRPI di Perugia per l'acquisizione di nuove informazioni sui fenomeni franosi nella regione dell'Umbria, la realizzazione di una nuova carta inventario dei movimenti franosi e dei siti colpiti da dissesto, l'individuazione e la perimetrazione delle aree a rischio da frana di particolare rilevanza, e l'aggiornamento delle stime sull'incidenza dei fenomeni di dissesto sul tessuto insediativo, infrastrutturale e produttivo regionale. Unpublished report, Institution, City, Country, 140p (in Italian)
- Brardinoni F, Slaymaker O, Hassan MA (2003) Landslide inventory in a rugged forested watershed: a comparison between air-photo and field survey data. *Geomorphology* 54:179–196
- Bucknam RC, Coe JA, Chavarria, MM, Godt JW, Tarr AC, Bradley L, Rafferty SA, Hancock D, Dart RL, Johnson ML (2001) Landslides triggered by Hurricane Mitch in Guatemala—Inventory and Discussion, 23 plates at 1:50,000 scale. U.S. Geological Survey Open File Report 01-443. <http://greenwood.cr.usgs.gov/pub/open-file-reports/ofr-01-0443/>
- Cardinali F, Ardizzone M, Galli F, Guzzetti P (2000) Reichenbach Landslides triggered by rapid snow melting: the December 1996–January 1997 event in Central Italy. In: Claps P, Siccardi F (eds) Proceedings of the 1st Plinius Conference on Mediterranean Storms, Bios Publisher, Cosenza, pp 439–448
- Cardinali M, Antonini G, Reichenbach P, Guzzetti F (2001) Photo—geological and landslide inventory map for the Upper Tiber River basin, scale 1:100,000. CNR Gruppo Nazionale per la Difesa dalle Catastrofi Idrogeologiche Publication n. 2154
- Chung CF, Fabbri AG (1999) Probabilistic prediction models for landslide hazard mapping. *Photogr Eng Remote Sens* 65(12):1389–1399
- Chung CF, Fabbri AG (2003) Validation of spatial prediction models for landslide hazard mapping. *Nat Hazards* 30:451–472
- Chung CJ, Fabbri AG (2005) Systematic procedures of landslide hazard mapping for risk assessment using spatial prediction models. In: Glade T et al (eds) *Landslide risk assessment*. Wiley, West Sussex, UK, pp 139–174
- Dağ S (2007) Çayeli (Rize) ve çevresinin istatistiksel yöntemlerle heyelan duyarlılık analizi. Karadeniz Teknik Üniversitesi Fen Bilimleri Enstitüsü, Trabzon, Doktora Tezi, 241s (yayımlanmamış)
- Dagdelenler G (2013) Assessment of sampling and validation strategies in production of landslide susceptibility maps (eastern part of Gallipoli Peninsula). PhD Thesis, Hacettepe University, Institute of Science, Ankara, 211 p
- DeGraff JV, Canuti P (1988) Using isopleth mapping to evaluate landslide activity in relation to agricultural practices. *Bull IAEG* 38:61–70
- Dönmez M, Akçay AE, Duru M, Ilgar A, Pehlivan Ş (2008) 1:100,000 scale Turkey Geologic Map. Section No: H-17. MTA, Ankara, 27p
- Fell R, Corominas J, Bonnard C, Cascini L, Leroi E, Savage WZ (2008) Guidelines for landslide susceptibility, hazard and risk zoning for land-use planning. *Eng Geol* 102(3–4):99–111
- Guthrie RH, Evans SG (2004a) Analysis of landslide frequencies and characteristics in a natural system, coastal British Columbia. *Earth Surf Process Landf* 29:1321–1339
- Guthrie RH, Evans SG (2004b) Magnitude and frequency of landslides triggered by a storm event, Loughborough Inlet, British Columbia. *Nat Hazards Earth Syst Sci* 4:475–483
- Guzzetti F, Carrara A, Cardinali M, Reichenbach P (1999) Landslide hazard evaluation: an aid to a sustainable development. *Geomorphology* 31:181–216
- Guzzetti F, Cardinali M, Reichenbach P, Carrara A (2000) Comparing landslide maps: a case study in the upper Tiber River Basin, central Italy. *Environ Manage* 25(3):247–363
- Guzzetti F, Malamud BD, Turcotte DL, Reichenbach P (2002) Power-law correlations of landslide areas in Central Italy. *Earth Planet Sci Lett* 195:169–183
- Guzzetti F, Reichenbach P, Cardinali M, Galli M, Ardizzone F (2005) Probabilistic landslide hazard assessment at the basin scale. *Geomorphology* 72:272–299
- Guzzetti F, Galli M, Reichenbach P, Ardizzone F, Cardinali M (2006a) Landslide hazard assessment in the Collazzone area, Umbria, central Italy. *Nat Hazards Earth Syst Sci* 6:115–131
- Guzzetti F, Reichenbach P, Ardizzone F, Cardinali M, Galli M (2006b) Estimating the quality of landslide susceptibility models. *Geomorphology* 81:166–184
- Harp EL, Jibson RW (1995) Inventory of landslides triggered by the 1994 Northridge, California earthquake: U.S. Geological Survey Open-File Report 95-213, 17p
- Harp EL, Jibson RW (1996) Landslides triggered by the 1994 Northridge, California, earthquake. *Bull Seismol Soc Am* 86(1B): S319–S332
- Hovius N, Stark CP, Allen PA (1997) Sediment flux from a mountain belt derived by landslide mapping. *Geology* 25:231–234
- Hovius N, Stark CP, Hao-Tsu C, Jinn-Chuan L (2000) Supply and removal of sediment in a landslide-dominated mountain belt: Central Range Taiwan. *J Geol* 108:73–89
- Ildır B (1995) Türkiye’de heyelanların dağılımı ve afetler yasası ile ilgili uygulamalar. 2. Ulusal Heyelan Sempozyumu Bildiriler Kitabı, Sakarya, 1–9
- Malamud BD, Turcotte DL, Guzzetti F, Reichenbach P (2004) Landslide inventories and their statistical properties. *Earth Surf Process Landf* 29(6):687–711
- MGM (2007) Meteoroloji Genel Müdürlüğü. <http://www.mgm.gov.tr/index.aspx>. Last Accessed 10 Oct 2013
- Saroglu F, Emre Ö, Boray A (1987) Türkiye’nin aktif fayları ve depremsellikleri. MTA Raporu, Rapor No. 8174, 394p
- Soeters R, Van Westen CJ (1996) Slope instability recognition, analysis, and zonation. Turner AK, Schuster RL (eds) *Landslides – Investigation and Mitigation*, National Research Council. Transportation Research Board Special Report 247. National Academy Press, Washington, DC, pp 129–177



GIS-Based Integration of Heterogeneous Data for a Multi-temporal Landslide Inventory

Darya Golovko, Sigrid Roessner, Robert Behling, Hans-Ulrich Wetzel, and Hermann Kaufmann

Abstract

Southern Kyrgyzstan is a region of high landslide activity that frequently endangers human lives and infrastructure. So far, precise spatio-temporal information on landslide activity has been limited, although landslide occurrence in this area has been investigated for the last 60 years by local authorities. The establishment of a comprehensive landslide inventory is a prerequisite for carrying out objective landslide hazard assessment. For this purpose, multiple sources of information about slope failures are analyzed with the goal of establishing a spatially and temporally consistent multi-temporal landslide inventory at a regional scale. In this context, the potential of satellite remote sensing and GIS based analysis is investigated. The paper describes the developed approach for multi-source landslide mapping and demonstrates its application to the Budalyk valley test site.

Keywords

Landslide inventory • Data integration • Kyrgyzstan

Introduction

Southern Kyrgyzstan is an area of high landslide activity that frequently results in the loss of human lives and damage to buildings and infrastructure. Landslides are especially concentrated along the Eastern rim of the Fergana Basin (Fig. 1). This area of about 12,000 km² administratively covers the Osh and Jalalabad districts (oblasts). The region belongs to the foothill zone of the adjacent high mountain areas and is situated at elevations between 700 and 2,000 m a.s.l. Large landslides occur mostly within weakly consolidated Mesozoic and Cenozoic sediments which have been subjected to ongoing tectonic deformation (Wetzel et al. 2000). The topographically high rim of the Eastern

Fergana Basin presents a barrier to the prevailing westerlies, leading to increased precipitation levels in comparison to the areas that lie further east. All of these factors create favorable conditions for the extensive development of landslides in this area. At the same time, the region represents an important human living space. Therefore, there is a big need for a spatially differentiated assessment of landslide hazard and risk. In this context, the establishment of a spatially and temporally consistent multi-temporal landslide inventory is of high importance.

A wide range of methods and approaches have already been developed in order to carry out landslide inventories. They are comprehensively discussed by Guzzetti et al. (2012), distinguishing between archive-based, historical, event-based, seasonal and multi-temporal inventories. Event-based and seasonal inventories are suitable for regions where most of the landslide activity is related to major triggering events, such as strong earthquakes, typhoons, and periods of heavy precipitation. In the landslide-affected area of Southern Kyrgyzstan, most of the slope failures are the result of complex interplays between different predisposing and triggering factors which have not been

D. Golovko (✉) • S. Roessner • R. Behling • H.-U. Wetzel • H. Kaufmann

German Center for Geosciences (GFZ) Potsdam, Section 1.4 – Remote Sensing, Telegrafenberg, 14473 Potsdam, Germany
e-mail: dgolovko@gfz-potsdam.de; roessner@gfz-potsdam.de; behling@gfz-potsdam.de; wetz@gfz-potsdam.de; charly@gfz-potsdam.de

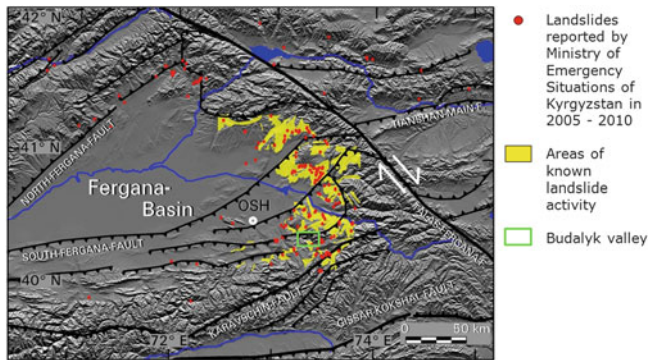


Fig. 1 Study area (yellow) and Budalyk valley (green) in Southern Kyrgyzstan

fully understood yet. Consequently, landslide occurrence cannot be related to specific triggering events. Therefore, improved understanding of landslide processes in Southern Kyrgyzstan requires regular monitoring of landslide activity in order to establish a multi-temporal landslide inventory.

Because the area affected by landslides is large (regional scale) and some of its areas are difficult to access, field-based landslide mapping is very time-consuming and difficult in the study area. Therefore, the establishment of a comprehensive landslide inventory requires incorporating information from all available sources, as well as using multi-temporal satellite remote sensing data as a consistent archive of surface conditions over large areas.

The objective of this study is the establishment of a landslide inventory for the area of high landslide activity in Southern Kyrgyzstan using satellite remote sensing and a GIS-based approach. The inventory should contain spatially and temporally explicit information about single landslide events, as well as complex landslide-prone slopes which have been subject to several phases of reactivation. The resulting GIS-based multi-temporal landslide inventory is required for deriving probabilities for probabilistic landslide hazard assessment (Guzzetti et al. 2005). Such an inventory has not been compiled yet for this region.

Data Sources of Landslide Information

The establishment of a multi-temporal landslide inventory for Southern Kyrgyzstan is a challenging task since the existing information on landslide failures is very heterogeneous. On the one hand, multiple sources of landslide data are available. They include data obtained from Kyrgyzstan's authorities, landslide mapping conducted during field campaigns, and results of manual interpretation of mono- and multi-temporal satellite images, as well as landslides which have been automatically detected from a multi-temporal satellite image database (Fig. 2). On the other

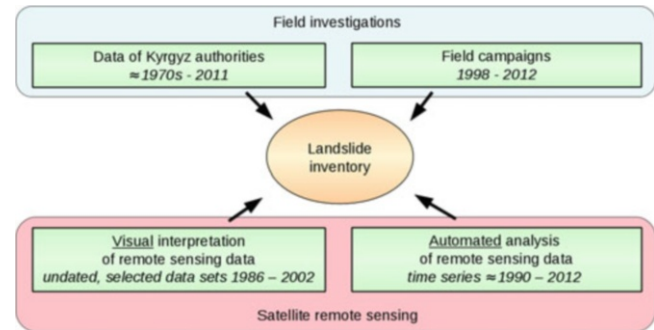


Fig. 2 Overview of main sources of data on landslide occurrence for Southern Kyrgyzstan

hand, these sources vary in the time periods they cover, their spatial and temporal completeness as well as their accuracy. Furthermore, these landslide data are of analogue and digital origin and they have different formats, such as verbal description, tabular data, and vector information (points and polygons). In the following, we give a detailed overview of the available sources of landslide information.

In the following sections, this description is illustrated by example by showing the data situation for the Budalyk valley next to the town of Gulcha in Osh district. Its location within the study region is shown in Fig. 1. However, information assessment has been carried out for the entire area of high landslide activity.

Landslide Data from Kyrgyzstan's Authorities

Since the 1950s, landslide investigations have been carried out in this region (Roessner et al. 2005). Regular monitoring of endangered areas was conducted from the 1960s until the break-up of the Soviet Union at the beginning of the 1990s. These activities also included extensive field-based mapping of landslides as well as detailed engineering geological investigations. The main goal had been the timely warning of the population and, if necessary, their evacuation and resettlement. However, after the independence of Kyrgyzstan, the possibilities for landslide investigations and monitoring have been drastically reduced. Furthermore, significant parts of the already existing data (e.g. maps and reports) are no longer available or their use is limited because of the loss of accompanying information related to methods, data sources, etc.

An important source of information on past landslide failures is the report "Monitoring of Landslides of Kyrgyzstan" (Ibatulin 2011). The report presents a description of selected landslide failures which have been observed mainly during field investigations between the 1970s and 2005. For some of the landslides, the report contains a very detailed verbal description, including results from

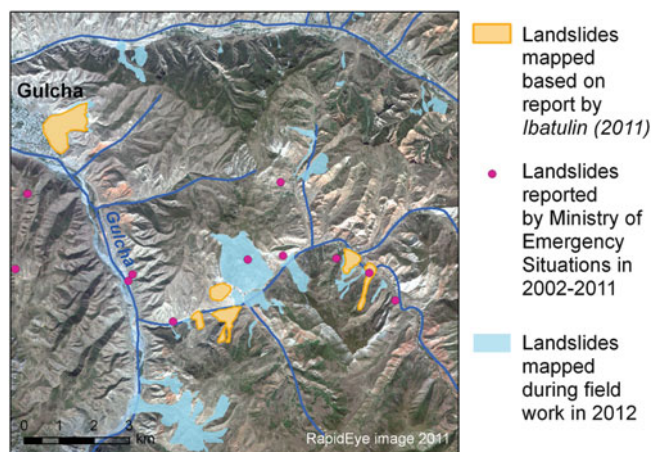


Fig. 3 Landslides reported by the Ministry of Emergency Situations of Kyrgyzstan and landslides mapped during field work

geotechnical investigations of the potentially dangerous slopes. The report also includes precise time information about landslide events; in most cases the day of failure is known, and for some events even the hour of the day. For failures occurring before 1990, the report is the only source of temporal information on slope failures, which have not been documented otherwise.

However, using data from the report is problematic because of the verbal description of the landslide information. It is difficult to find the geographic location of some of the described landslides, and in most cases it is impossible to determine the spatial extent of the slope failures. Another problem is that the report only documents large landslides, landslides in inhabited areas and areas visited by landslide experts responsible for monitoring. Therefore, the resulting landslide information is biased towards the needs of civil protection. In Fig. 3 the landslides contained in the report are outlined in orange. They represent only a subset of slope failures in this area.

Moreover, employees of the Ministry of Emergency Situations of Kyrgyzstan visited selected areas affected by landslides between the years 2002 and 2011 and recorded new landslides. The results of these surveys are available in form of tables. They represent only a small number of landslides which occurred in inhabited areas. In Fig. 3 they are shown by pink dots. Their location is represented in the table by a pair of x- and y-coordinates. However, their spatial extent is not documented. The only temporal information is the date of field mapping, whereas the time of the actual failure is mostly unknown.

Landslide Data from Field Mapping

The Remote Sensing section of the German Research Centre for Geosciences (GFZ) has been conducting field work in

Southern Kyrgyzstan since 1998 in cooperation with the Ministry of Emergency Situations of Kyrgyzstan. During this time, repetitive field work has been carried out, including selective landslide mapping. Landslide locations were recorded by GPS and documented by field photos. They have been spatially referenced by linking them to the GPS waypoints and integrated into the GIS using the extension ArcPhoto in ArcGIS. During these field investigations, additional information about the landslides, such as date of failure, mechanism, estimated volume and state of investigation were provided by the experts of the Ministry of Emergency Situations of Kyrgyzstan as well as by local residents. Field mapping was supported by satellite remote sensing data in order to map the spatial extent of the landslides, which often could not be determined in the field due to the large extent and difficult accessibility of the landslides. Because of the large area affected by landslides, each of these field campaigns could cover only selected parts. However, many landslide prone slopes have been revisited several times and thus the resulting photo documentation allows analysis of the temporal development of these slopes (e.g. revegetation).

Expert Interpretation of Satellite Images

Landslide mapping conducted during field investigations has been extended by expert interpretation of satellite remote sensing data in combination with a DEM, using the perspective visualization capabilities of a GIS (Roessner et al. 2005). As a result, landslide scarps and masses have been determined systematically for the whole area of interest (Fig. 4). The interpretation also includes information about geological structures and other landslide predisposing factors in the analysis. This method is especially suitable for mapping landslide-prone slopes which have experienced several phases of reactivation resulting in complex morphological structures. However, this integrative mapping method cannot provide differentiated information on the dates of slope failures on an event basis. They have to be added from other sources when available. Furthermore, the method is labor-intensive and mostly used for initial landslide mapping.

Multi-temporal Analysis of Satellite Images

In order to establish a dynamic landslide inventory containing the temporal evolution of landslide-prone slopes, multi-temporal analysis of satellite remote sensing data has to be carried out. For the area of high landslide activity, a multi-temporal and multi-sensor satellite remote sensing database has been established starting in 1986 (Behling et al. 2012). It enables analysis of landslide occurrence in

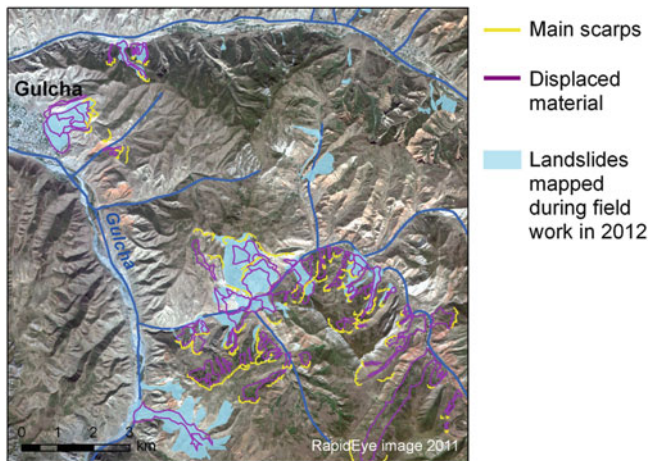


Fig. 4 Results of landslide scarps and masses interpreted from mono-temporal satellite images

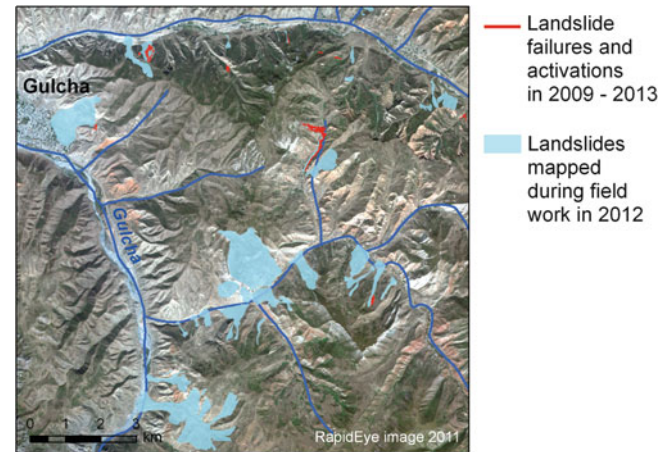


Fig. 6 Results of automated landslide detection from RapidEye data in 2009–2013

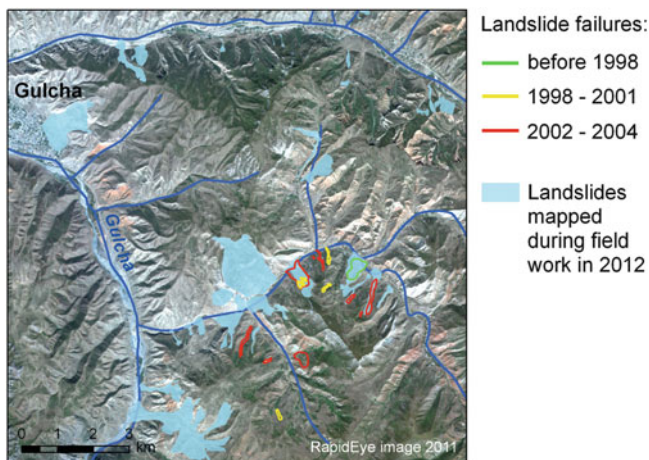


Fig. 5 Results of manual landslide mapping using multi-temporal satellite images

multiple time steps. For this purpose, images of consecutive time steps were compared visually and changes were digitized. Since this method is very labor-intensive, it has been applied only for selected subsets of the study area, such as the Budalyk valley (Fig. 5). As a result, landslide events have been mapped with higher temporal resolution and spatial precision, allowing reconstruction of the evolution of landslide-prone slopes. The temporal resolution is determined by availability of satellite images, which is better in recent years since 2000 and more limited for the years before.

However, visual interpretation of multi-temporal satellite imagery is very time-consuming and characterized by a certain degree of subjectivity. Therefore, an automated approach for landslide detection has been developed at the Remote Sensing Section of the German Centre for Geosciences using the established multi-temporal satellite

remote sensing database (Behling et al. 2013). This approach allows the analysis of large areas in multiple time steps. Figure 6 shows the results that have been obtained for the area of the Budalyk valley from high-resolution RapidEye satellite data acquired between 2009 and 2013. In this relatively small area, multiple small mass movements and one large slope failure could be detected that had not been known otherwise. Using this method for the complete study area, about 250 landslides have been detected automatically. During the same period, the Ministry of Emergency Situations only reported about 40 landslide events. Thus, the developed approach yields excellent possibilities for efficient landslide detection over large areas, allowing regular updates of existing landslide inventories as new satellite remote sensing data become available.

Approach for GIS-Based Data Integration

Integration of all of the described landslide information sources into a GIS-based system requires the establishment of a common spatial reference. In this study, the spatially adjusted multi-temporal RapidEye data stack has been used as the spatial reference (Behling et al. 2012). In case of the report by Ibatulin (2011), the verbal landslide descriptions were transformed into spatially explicit information using high-resolution RapidEye satellite imagery in combination with a scanned 1:100,000 topographic map. Some of the described slope failures were difficult to locate because distinct morphological features could not be visually interpreted from the remote sensing data, since these traces had largely been eroded. Furthermore, the names of some of the villages were changed after the collapse of the Soviet Union. For location of landslide events contained in the report we also used the results of our own field-based

mapping. Landslide location has often required careful consideration of slope failures documented in multiple data sources. In such cases, we used these repeated entries to verify the data, correct possible errors, improve locations of the landslides and determine the time of their failures with higher precision. After all data sources were converted into a spatially explicit form, they were transformed to UTM/WGS84 as the common spatial projection.

Even though multiple sources of data on landslides have been used, all of them provide information on only a subset of slope failures in the study area. The degree of completeness varies with time for different sources. For example, remote-sensing-based landslide identification can deliver data on recent slope failures, whereas the report by Ibatulin (2011) is suitable for extracting historical information. The landslide report by Ibatulin (2011) contains detailed information on the dates of slope failures in inhabited areas, but the location and spatial extent of the described landslides are often ambiguous. On the other hand, visual and automated landslide detection from satellite images offers higher spatial precision but less precise dating of landslide events, regardless of their proximity to settlements. The different landslide data sources are ambiguous in the discrimination between the spatial extent of single landslide failures and landslide-prone slopes, which are the result of multiple failures. Whereas temporal information on the landslide events typically refers to single failures within a larger slope, usually the whole landslide-prone slope is considered, because the information on landslide-prone slopes provided by Kyrgyzstan's authorities usually does not contain their spatial extent. In such cases, the spatial extent of landslides needs to be determined subsequently based on satellite imagery. To discriminate between single failures and landslide-prone slopes, adequate mapping units need to be chosen. Such mapping units are important for subsequent hazard assessment. They can comprise slope units derived from DEM-based watershed delineation, administrative units and other spatial units (Guzzetti et al. 1999; Süzen and Doyuran 2004). In this study, slope units were found to be the most suitable mapping units, since they reflect physical characteristics of the surface rather than an outcome of random sampling (Fig. 7).

Results

As a result of the GIS-based integration of the landslide data with careful consideration of temporal information and documentation of repeated landslide failures within the same slope, we have obtained a multi-temporal landslide inventory system for Southern Kyrgyzstan. Due to the use of remote sensing, it has been possible to produce an inventory of an objective and regional character. This inventory

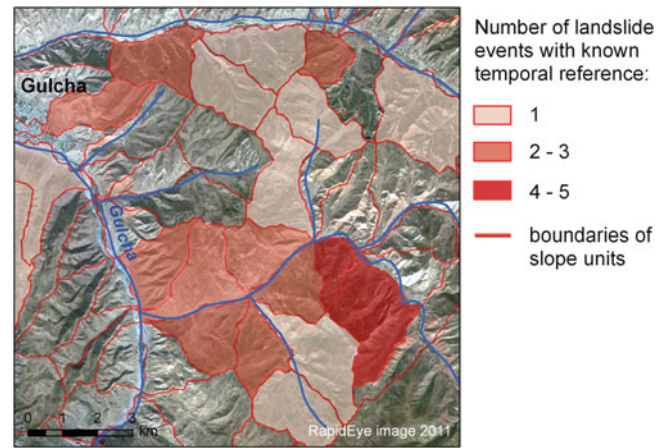


Fig. 7 Slope units derived from SRTM DEM with 30 m resolution near the settlement of Gulcha

Table 1 Components of landslide inventory obtained from different data sources and their properties

| Source | Period covered | Number of landslides | Landslide area, km ² |
|---------------------------|----------------|----------------------|---------------------------------|
| Report by Ibatulin (2011) | 1970–2005 | 72 | 25.4 |
| Ministry tables | 2002–2011 | 73 | Point data |
| Field mapping | Not dated | 263 | 105.8 |
| Expert interpretation | Not dated | n/a | 172.9 |
| Automated detection | 2009–2013 | 250 | 5.5 |

contains a total of over 550 landslides which were identified by different methods from various sources of information. Table 1 gives an overview of the detected landslides.

Besides the data on the location of a given landslide and known dates of its failure, the landslide inventory information system is capable of storing commonly assessed landslide attributes, such as area, length, slope angle and exposition, etc. Many of these values can be calculated within a GIS. Furthermore, the landslide inventory information system will include data on landslide triggering and predisposing factors within the same spatial reference. The described GIS-based system facilitates the joint analysis of the available spatial data on landslides as the basis for a regional landslide hazard assessment.

The automated method for landslide detection from multi-temporal satellite images enables updates of existing landslide inventories that are more precise and less time-consuming compared to other methods. The updated inventory is the basis for carrying out repeated hazard assessment and verifying results of previous analyses. This way it has been possible to establish a dynamic landslide inventory as a main prerequisite for dynamic landslide hazard assessment.

Discussion

The integration of landslide data in a single GIS-based system provides the capabilities for establishing a dynamic landslide inventory, including the opportunity for more efficient data access, verification and updates. In this context satellite remote sensing plays an important role in the compilation of a multi-temporal landslide inventory at a regional scale. Firstly, it is the central source of objective information on land cover change at the regional level. It is the basis for both manual and automated landslide detection and thus enables a significantly higher level of inventory completeness. Secondly, satellite images and DEMs provide the common spatial reference for adjusting heterogeneous landslide data and enable an improved spatial and temporal characterization of landslides. Thirdly, new satellite images can be acquired and serve as the source of data for updates of an already existing inventory and thus be a step towards a continuous monitoring system of landslide activity.

In our future work, we plan to use the compiled landslide inventory for landslide hazard assessment, which will include the analysis of spatial and temporal probability of landslide failures. Furthermore, we plan to continue updating the established landslide inventory using newly available satellite remote sensing data. This way, we will contribute to an improved process understanding in this area of high landslide activity which in a next step can be related to landslide predisposing and triggering factors, such as precipitation, seismic and tectonic activity as well as lithological and structural conditions.

Acknowledgments Research presented in this paper has been funded by the German Ministry of Research and Technology (BMBF) as a part of the Tienshan—Pamir Monitoring Program (TIPTIMON) and PROGRESS project.

We kindly thank our colleagues from the Ministry of Emergency Situations of Kyrgyzstan Kh. V. Ibatulin and A.K. Sarnagoev for providing information on landslide failures in the region and joint field work.

References

- Behling R, Roessner S, Segl K, Rogass C, Wetzel HU, Kaufmann H (2012) Automated geometric co-registration of multi-temporal satellite remote sensing data for landslide inventories. In: Proceedings of the 4th RESA workshop, 21–22 March 2012. Neustrelitz, Germany, pp 35–50 (in German)
- Behling R, Roessner S, Segl K, Kaufmann H (2013) Automated landslide detection using multi-temporal RapidEye data. In: Proceedings of the 5th RESA workshop, 20–21 March 2013. Neustrelitz, Germany, pp 241–257
- Guzzetti F, Carrara A, Cardinali M, Reichenbach P (1999) Landslide hazard evaluation: a review of current techniques and their application in a multi-scale study, Central Italy. *Geomorphology* 31:181–216
- Guzzetti F, Reichenbach P, Cardinali M, Galli M, Ardizzone F (2005) Probabilistic landslide hazard assessment at the basin scale. *Geomorphology* 72:272–299
- Guzzetti F, Mondini AC, Cardinali M, Fiorucci F, Santangelo M, Chang K (2012) Landslide inventory maps: new tools for an old problem. *Earth Sci Rev* 112(1–2):42–66
- Ibatulin KV (2011) Monitoring of landslides in Kyrgyzstan. Ministry of Emergency Situations of the Kyrgyz Republic, Bishkek, 145p (in Russian)
- Roessner S, Wetzel HU, Kaufmann H, Sarnagoev A (2005) Potential of satellite remote sensing and GIS for landslide hazard assessment in Southern Kyrgyzstan (Central Asia). *Nat Hazards* 35(3):395–416
- Süzen ML, Doyuran V (2004) Data driven bivariate landslide susceptibility assessment using geographical information systems: a method and application to Asarsuyu catchment, Turkey. *Eng Geol* 71:302–321
- Wetzel HU, Roessner S, Sarnagoev A (2000) Remote sensing and GIS based geological mapping for assessment of landslide hazard in Southern Kyrgyzstan (Central Asia). In: Brebbia CA, Pascolo P (eds) *Management information systems 2000 – GIS and remote sensing*. WIT-Press, pp 355–366



Investigating and Managing Shallow Landslides in Switzerland

Josef Hess, Christian Rickli, Brian McArdell, and Manfred Stähli

Abstract

During the past 40 years, shallow landslides triggered by intensive rain fall caused damage costs of >520 million Euros in Switzerland. These landslides have been mainly associated with relatively few storm events of extreme intensity. The Swiss Federal Office of the Environment, together with partners from cantons, research institutes and private companies, systematically investigated such events with regard to the occurrence and properties of shallow landslides. Comprehensive inventories of shallow landslides were collected, e.g. in the regions of Sachseln (1997), Appenzell (2002) and Emmental (2002 and 2005), resulting in a national data base that is currently being developed. This data base of observed shallow landslides will be a key-tool for future risk management in Switzerland, e.g. as a basis to support the generation of hazard maps and early warning systems. Risk management is also promoted by ongoing focused research on the triggering of shallow landslides, which is carried out within the ETH Competence Centre Environment and Sustainability (CCES).

Keywords

Shallow landslides • Switzerland • Risk management

Introduction

For Switzerland, with a large extent being located in alpine and sub-alpine areas, shallow landslides pose a substantial risk to humans and infrastructure. In the period from 1972 to 2007, total costs of 520 million Euros originating from landslides have been estimated, based on a systematic survey of natural hazard damage by the Swiss Federal Institute WSL (Hilker et al. 2009).

Typical for Switzerland, shallow landslides have been triggered during relatively rare, but very intensive rainfall events. Such events can be either very local as a consequence of concentrated short-term storm cells, such as in the case of Sachseln, central Switzerland, (area: <10 km²) in August 1997 (see below). Or they can be long-standing and affect a large part of the country as in August 2005 (Fig. 1).

Inventories of Shallow Landslides

Overview

Information related to the occurrence and to topographical, soil and vegetation attributes of shallow landslides had been sparse until in the late 1990s, when the Swiss Federal Research Institute WSL started systematic landslide monitoring after major storm events. Instead of a global Swiss-wide survey, the researchers concentrated on specific

J. Hess (✉)
Swiss Federal Office for the Environment FOEN, Vice Director, 3003 Bern, Switzerland
e-mail: josef.hess@bafu.admin.ch

C. Rickli • B. McArdell • M. Stähli
Swiss Federal Research Institute WSL, Mountain Hydrology and Mass Movements, Birmensdorf, Switzerland
e-mail: christian.rickli@wsl.ch; brian.mcardell@wsl.ch; manfred.staehli@wsl.ch

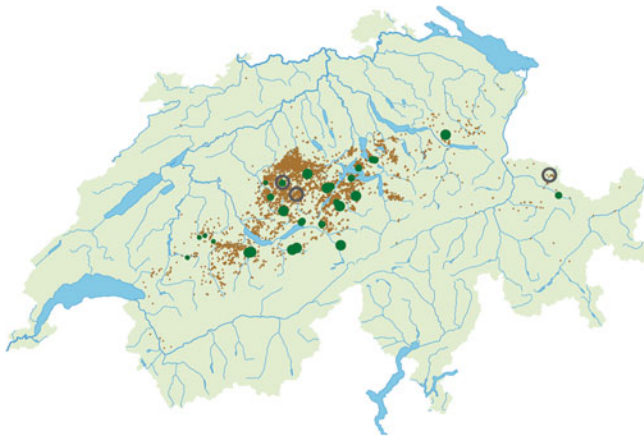


Fig. 1 Map of Switzerland indicating the locations of observed shallow (*brown dots*) and deep-seated (*green dots*) landslides after the storm event of August 2005. Locations of in-depth inventories are indicated by *green circles* (Bezzola and Hegg 2007)

watersheds of a few square kilometers size with a particularly high density of landslides, which allowed the gathering of a wide range of information on soil types, conditions, surface properties and vegetation.

The data from the focus areas Sachslen (1997; see below), Appenzell (2002), Emmental (2002 and 2005), Entlebuch (2005) and Prättigau (2005), with a total of 522 mapped shallow landslides, have been extensively used to assess the main controls of landslide occurrence (Rickli and Graf 2009), to estimate rain intensity-duration thresholds (Bezzola and Hegg 2008), and to test geostatistical methods (Von Ruetten et al. 2011), as well as to validate landslide susceptibility models (Von Ruetten et al. 2013).

Case Study Sachseln

On the 15th of August 1997 an extreme thunderstorm with heavy rainfall triggered a large number of shallow landslides in the region of Sachseln, central Switzerland (Fig. 2). A considerable part of the soil material mobilized by the landslides reached the steep torrents above the village and contributed to a massive debris flow.

This event provided an opportunity to investigate the effects of different types of forest management and land use on landslide activity. Following a systematic protocol, 280 shallow landslides were analyzed, including geological and geotechnical parameters, as well as specific aspects of soil and vegetation. The data analysis by Rickli (2001) confirmed that slope inclination and specific geological characteristics are closely related to the occurrence of



Fig. 2 Shallow landslides of several hundred m^3 size, each triggered by heavy rainfall in the area of Sachseln, Switzerland

shallow landslides. Furthermore, the data indicated that the type of vegetation and, in particular, the condition and structure of the forest, considerably influenced the stability of steep slopes (Fig. 3).

Towards a National Database

Inventories of observed shallow landslides have been assembled not only by the Swiss Federal Research Institute WSL, but also by Cantonal authorities and private engineering offices. As they were commissioned by different parties and served different specific purposes, these inventories are heterogeneous with respect to mapped parameters, database structure and geographic extent.

Recognizing the great value of these inventories for an improved national risk management of landslides, the Swiss Federal Office for the Environment (FOEN) launched a project in 2013 with the objective to homogenize and merge the different inventories into one national database that will be publicly available for researchers and practitioners. The ultimate goal of the database is to provide a basis for testing new concepts for predicting the probability of landslide occurrence, testing early-warning concepts, to evaluate if a given landslide or hillslope will produce landslides or hillslope debris flows, and to predict the resulting process intensities. In addition, such a database should be useful for dimensioning mitigation measures and identifying which areas are unusually susceptible to future landslide activity as part of hazard risk management. The database is also meant to be the framework for future inventories and may become a possible model for other countries.

Fig. 3 Number of shallow landslides per hectare (L/ha) in relation to forest conditions, observed in the Sachseln area after the storm of August 15, 1997

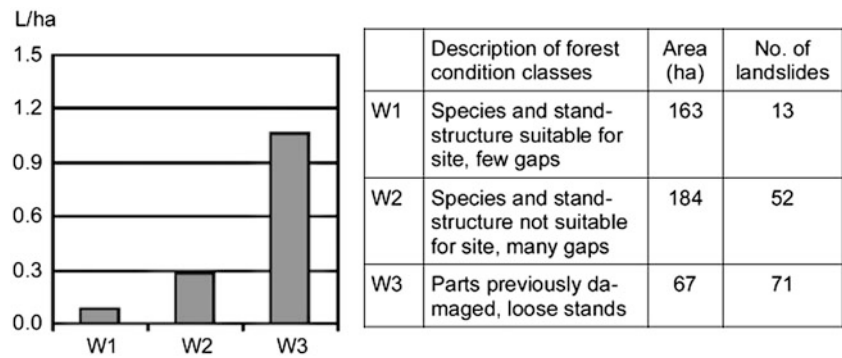


Fig. 4 Experimental landslide triggered by irrigation in the framework of the research project TRAMM (Springman et al. 2012). A comprehensive set of measurements provided insight into the wetting of the soil as well as precursors and movements prior to the release

Focused Research on the Triggering of Shallow Landslides

The Research Project TRAMM

Another important element of the Swiss risk management strategy is targeted research. For example, in 2006 eight research groups of the ETH domain joined forces to shed new light on processes controlling onset of rapid mass movements. In the frame of the project TRAMM—Triggering of Rapid Mass Movements in Steep Terrain—they developed model approaches and sensors applicable to monitoring and quantifying various forms of hazardous mass movements.

A notable achievement of TRAMM has been the performance of unique large-scale field experiments for inducing landslides that were possible only through close collaboration among the different expert groups. For example, in March 2009 an experimental landslide was closely observed

on a 8 m × 40 m large, approximately 40° inclined slope at the border of the Rhine river, which had been artificially irrigated until failure (Fig. 4). Measurements of soil wetting, pre-event soil surface movements and precursors provided new insights into the formation of such landslides.

Such experiments are a rare but very useful reference for direct validation of numerical models. In addition to classical hydromechanical models (e.g. Laloui and Nuth 2009), TRAMM developed also other physical concepts (fiber bundle models, Self-Organized Criticality) simulating material failure and mass release as progressive failure culminating in hazardous mass movement (Lehmann and Or 2012). Such models can be applied at the scale of entire watersheds and be compared with the spatial landslide inventory presented above (Von Ruetten et al. 2013).

Towards a New Generation of Early Warning Systems

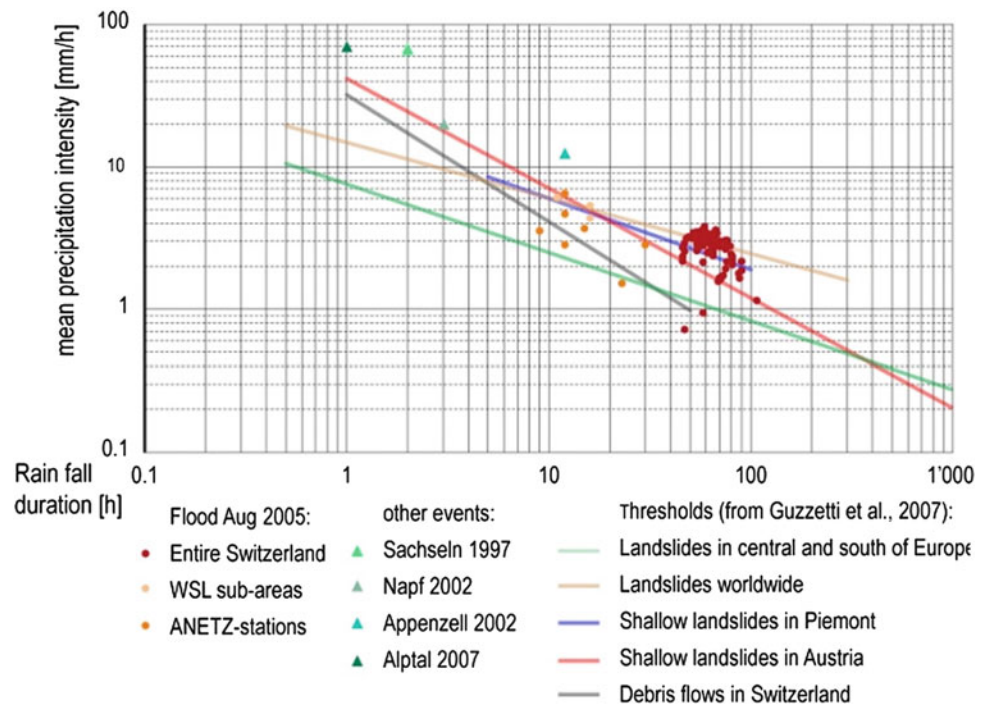
An ultimate goal of the ongoing research is the early recognition of critical situations where shallow landslides are likely to be triggered, which would allow authorities to issue warnings. While early warning systems (EWS) have been established for rock fall and debris flows at specific locations with a known risk, regional early warning systems for landslides have been very scarce worldwide.

Early warning systems based solely on precipitation thresholds have been shown to be difficult to generalize (Fig. 5). It seems quite obvious that spatial information on (hydro)geology, soil properties, soil wetness and vegetation have to be accounted for in regional early warning systems. Combinations of new sensor networks and spatial numerical models are a promising avenue toward such future warning systems. Such networks may also include new sensors for real-time monitoring of acoustic emissions associated with precursory events (Michlmayr et al. 2012).

Conclusions and Outlook

In the past few decades, Switzerland has stepped up efforts to better get insight into the mechanisms and

Fig. 5 Rain intensity–duration curves determined for various events and regions in Switzerland and neighboring countries as thresholds for the release of shallow landslides (Bezzola and Hegg 2008)



controls of shallow landslides. The inventories described in this paper, as well as dedicated research, clearly helped to advance the understanding of landslide processes as well as the management of shallow landslides. Nevertheless, we are still a great step away from accurate and reliable early warning systems for entire regions. This will be a challenge for the forthcoming years.

Acknowledgments We would like to thank numerous researchers and administrators in Switzerland who with their dedicated work have supported the systematic assembly of a data basis and knowledge for a better management of shallow landslides in Switzerland. To this end, financial support was received a.o. from the Swiss Federal Office of the Environment and from the ETH Competence Centre Environment and Sustainability.

References

- Bezzola GR, Hegg C (2007) Ereignisanalyse Hochwasser 2005, Teil 1 – Prozesse, Schäden und erste Einordnung. Bundesamt für Umwelt BAFU, Eidg. Forschungsanstalt WSL. Umwelt-Wissen Nr. 0707. 215p
- Bezzola GR, Hegg C (2008) Ereignisanalyse Hochwasser 2005, Teil 2 – Analyse von Prozessen, Massnahmen und Gefahregrundlagen. Bundesamt für Umwelt BAFU, Eidg. Forschungsanstalt WSL. Umwelt-Wissen Nr. 0825. 429p
- Hilker N, Badoux A, Hegg C (2009) The Swiss flood and landslide damage database 1972–2007. *Nat Hazards Earth Syst Sci* 9 (3):913–925
- Laloui L, Nuth M (2009) On the use of the generalised effective stress in the constitutive modelling of unsaturated soils. *Comput Geotech* 36(1–2):20–23
- Lehmann P, Or D (2012) Hydromechanical triggering of landslides: from progressive local failures to mass release. *Water Resour Res* 48, W03535. doi:10.1029/2011WR010947
- Michlmayr G, Cohen D, Or D (2012) Sources and characteristics of acoustic emissions from mechanically stressed geologic granular media – a review. *Earth Sci Rev* 112(3–4):97–114
- Rickli C (2001) Vegetationswirkungen und Rutschungen. Untersuchung zum Einfluss der Vegetation auf oberflächennahe Rutschprozesse anhand der Unwetterereignisse in Sachseln OW am 15. August 1997. Birmensdorf, Bern, Eidg. Forschungsanstalt WSL, Bundesamt für Umwelt, Wald und Landschaft. 97S
- Rickli C, Graf F (2009) Effects of forests on shallow landslides – case studies in Switzerland. *For Snow Landsc Res* 82(1):33–44
- Springman SM, Askarinejad A, Casini F, Friedel S, Kienzler P, Teyssere P, Thielen A (2012) Lessons learnt from field tests in some potentially unstable slopes in Switzerland. *Acta Slov Geotech* 1:5–29
- Von Ruette J, Papritz A, Lehmann P, Rickli C, Or D (2011) Spatial statistical modeling of shallow landslides—Validating predictions for different landslide inventories and rainfall events. *Geomorphology* 133(1–2):11–22
- Von Ruette J, Lehmann P, Or D (2013) Rainfall-triggered shallow landslides at catchment scale – threshold mechanics-based modeling for abruptness and localization. *Water Resour Res* 49 (10):6266–6285, 10.1002/wrcr.20418



Global Catalog of Rainfall-Triggered Landslides for Spatial and Temporal Hazard Characterization

Dalia Kirschbaum

Abstract

It is well known that extreme or prolonged rainfall is the dominant trigger of landslides; however, there remain large uncertainties in characterizing the distribution of these hazards and meteorological triggers at the global scale. We have developed a Global Landslide Catalog (GLC), available from 2007 to the present, which contains information on reported rainfall-triggered landslide events around the world using online media reports, disaster databases, etc. This database is being input into a map-based viewable interface. Three applications of this landslide database are outlined in this study. These applications include: (1) characterizing the spatial and temporal distribution of reported landslides and fatalities over the GLC record; (2) evaluating the co-occurrence of precipitation and rainfall-triggered landslides globally; and (3) calibrating and validating a regional landslide hazard algorithm for Mesoamerica.

Keywords

Landslide inventory • Online database • Satellite precipitation

Introduction

Despite the pervasive impacts rainfall-triggered landslides have on populations throughout the world, there remain large uncertainties in where and when these landslides occur and how they vary over space and time. In order to examine modulations in rainfall-triggered landslide activity and reporting, the Global Landslide Catalog (GLC) was created based on media reports, online disaster databases and other sources. This database has also been found valuable for evaluating regional and global landslide hazard assessment models, as well as to better understand the linkages between observed satellite precipitation and reported landslide activity. This article presents an overview of the GLC, outlining some preliminary findings for data over the years 2007–2012, evaluating the co-occurrence of

GLC events with satellite precipitation, and highlighting an application of the GLC for landslide hazard model evaluation.

Global Landslide Catalog

The GLC represents the first database of its kind to catalog reported rapidly-moving, rainfall-triggered landslides within the recent past at the global scale. The catalog currently contains seven complete years of data (2007–2013) with continued reporting through the present. The catalog is compiled from online media reports, disaster databases, and other relevant information. Each reported landslide includes information on several aspects of the event, which are documented in Kirschbaum et al. 2010. These categories include:

- Date
- Coordinates
- Country
- Nearest geographic place

D. Kirschbaum (✉)
Hydrological Sciences Laboratory (Code 617), NASA GSFC,
Greenbelt, MD 20771, USA
e-mail: dalia.b.kirschbaum@nasa.gov

- Hazard type (landslide, debris flow, rock avalanche, etc.)
- Trigger (rain, tropical cyclone, etc.)
- Fatalities and impacts
- Location accuracy (exact location, known within 1 km, known within 5 km, etc.)
- Landslide size (small, medium, large, catastrophic)
- Source

The GLC represents a minimum number of rainfall-triggered landslides around the world due to numerous reporting issues. These include reporting biases due to regional differences in reporting accuracy, missed events, and language barriers. It is often difficult to determine an accurate location for the reported event due to lack of information or difficulty in finding the cited location. At present, the GLC only contains information obtained from primarily English-speaking media, thus there are large gaps over areas where these sources are not available. Lastly, it is difficult to differentiate landslides from other triggering hazards including tropical cyclones, floods and other human impacts. Despite these challenges, this catalog provides a foundation for exploring where and when reported landslides have occurred and characterizing hotspots for both landslides and extreme rainfall activity.

Applications of the GLC

The GLC database has been used for a range of different studies. This paper presents three applications of the GLC: evaluation of spatio-temporal trends, analysing patterns of landslide reports and rainfall in 2010, and validation of a landslide hazard algorithm.

GLC Spatial and Temporal Trends

The database for 2007–2012 contains 4,700 reports from 112 countries. The GLC indicates that there is a general peak in landslide reports and fatalities during the Northern Hemisphere summer, peaking in August when the Asian monsoon and cyclone seasons are typically at a peak. Figures 1 and 2 highlight some example statistics from 2007–2012.

Landslides and Rainfall in 2010

When considering the total number of rainfall-triggered landslides by year from 2007–2012, it was apparent that 2010 had significantly more reported landslides relative to other years (Fig. 3). There were several significant events that occurred in 2010 that contributed to high fatality

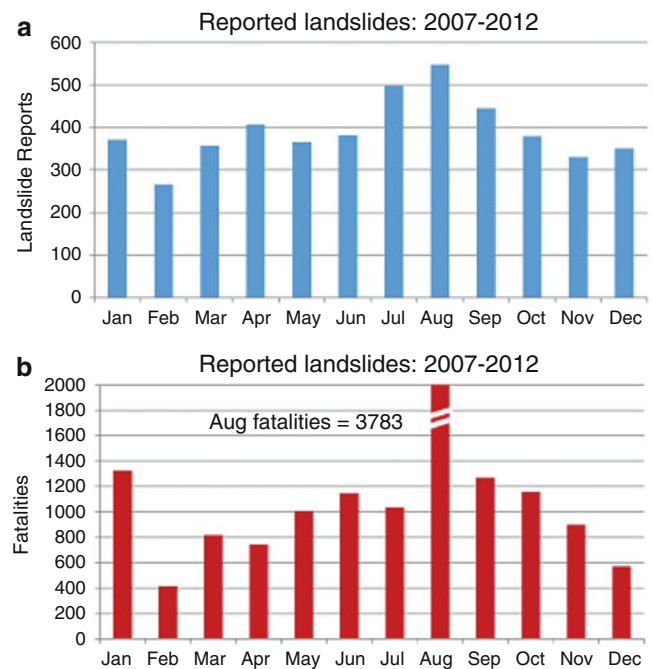


Fig. 1 Results of the GLC for 2007–2012 showing (a) reported landslides and (b) fatalities by month. The peak in August occurred as the result of two major events in August 2010 in China and India. The peak in January is due to several major events taking place near Rio de Janeiro, Brazil

estimates. For example, a catastrophic mudslide occurred in Zhouqu County in Gansu, China on August 8th, 2010 which killed 1,765 people and resulted in an estimated 759 million USD in damage (EM-DAT 2011). Additional damaging landslides occurred in Bududa, Uganda in March causing nearly 400 fatalities; Leh in Ladakh, Indian Kashmir in August, which resulted in an estimated 245 fatalities; and a series of events in eastern Brazil during January and April which killed over 700 people. Media reports identified intense rainfall as the trigger for each of these events, which mobilized large volumes of material and interacted with the local morphology to generate catastrophic landslides.

A study by Kirschbaum et al. (2012a) examines how landslide reports for selected areas in 2010 compared to accumulated and extreme precipitation. Tropical Rainfall Measuring Mission (TRMM; <http://www.trmm.nasa.gov>) Multi-satellite Precipitation Analysis (TMPA) data was extracted for 13 years from 1998–2010 and the rainfall values were compared for 2010 and previous years. Kirschbaum et al. (2012a) examined the co-occurrence of landslides in the GLC and TMPA precipitation in order to quantitatively determine how these datasets may relate to each other in terms of the spatial distribution of extreme rainfall and the occurrence of landslide “hotspots” over the globe.

Fig. 2 Distribution of triggering sources for the GLC

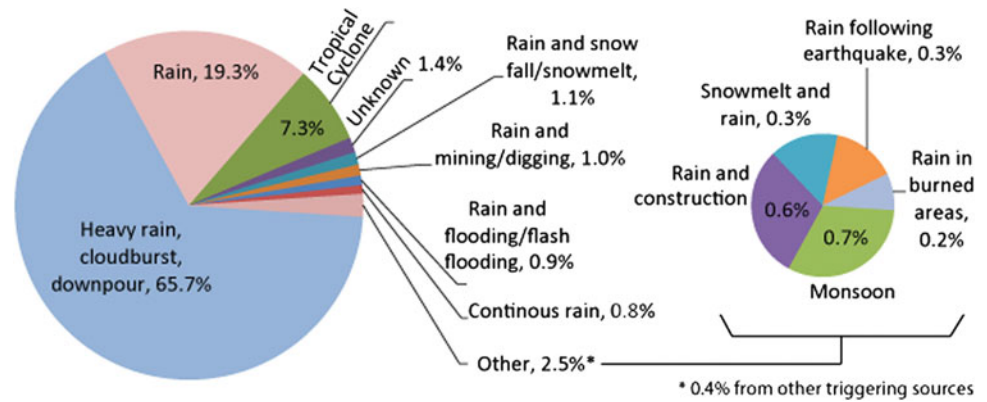
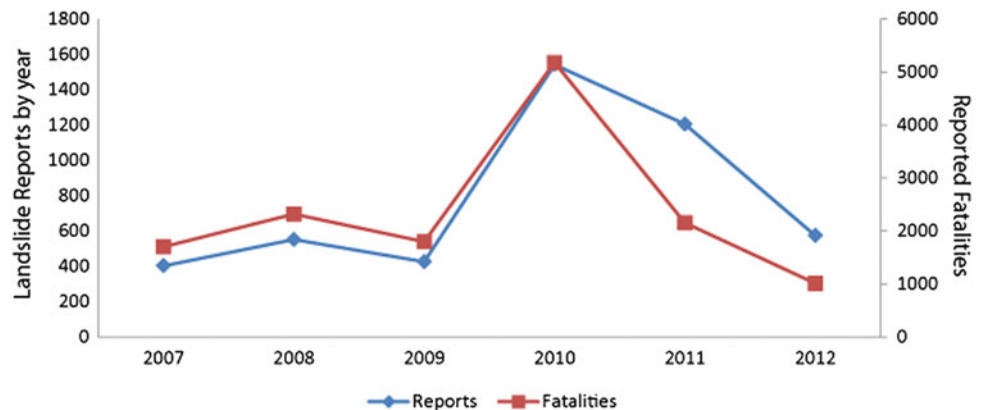


Fig. 3 Comparison of landslide reports (blue) and landslide fatalities (red) for 2007–2012



Three study areas were chosen to evaluate the co-occurrence of landslides and rainfall for 2010. Central America, the Himalayan arc and Central China were identified as regions with continuous reporting over the GLC record with above normal reporting in 2010 (Fig. 4). Other regions were identified and evaluated but are not included in this study.

Precipitation and landslide reports were compared for the three areas and to look at monthly accumulated rainfall, extreme daily rainfall and quantile estimations of daily precipitation. Figure 5 shows the results for the Central American region. Results from this study indicate that an observable signal exists between increases in reported and fatal landslide activity and increases in precipitation accumulation and daily intensity for two out of the three study areas. Findings over the China test region are less conclusive due to the limited number of landslide reports and accuracy of information for this test area.

Through this case study for 2010, evaluation of the GLC with satellite precipitation indicates that TRMM data may be used to identify locations where we may be missing landslide reports and TRMM data could be used to produce a landslide climatology over the historical record. Conversely, in areas that are considered to have reliable reporting, the GLC may be used to identify peak rainfall intensities that

may be poorly resolved by current satellite instruments. Further work is needed to characterize consistent, robust relationships between rainfall and GLC reports over time and in different regions.

Calibration and Validation of a Landslide Hazard Algorithm

A prototype global satellite-based landslide hazard algorithm has been developed to identify areas that exhibit a high potential for landslide activity. The algorithm combines a calculation of landslide susceptibility with satellite-derived rainfall estimates, which are made every 3 h based on the TMPA real time data product (Fig. 6) (Hong et al. 2006, 2007). The algorithm framework is shown in Fig. 6. The GLC was used to evaluate the global landslide algorithm for 2003 (experimental GLC database) and 2007. The algorithm was run retrospectively and algorithm outputs were compared with the spatial and temporal distribution of GLC events for their respective years (Kirschbaum et al. 2009).

Results of this evaluation indicate that while there were several areas of good model performance, there were also several challenges, including the model resolution

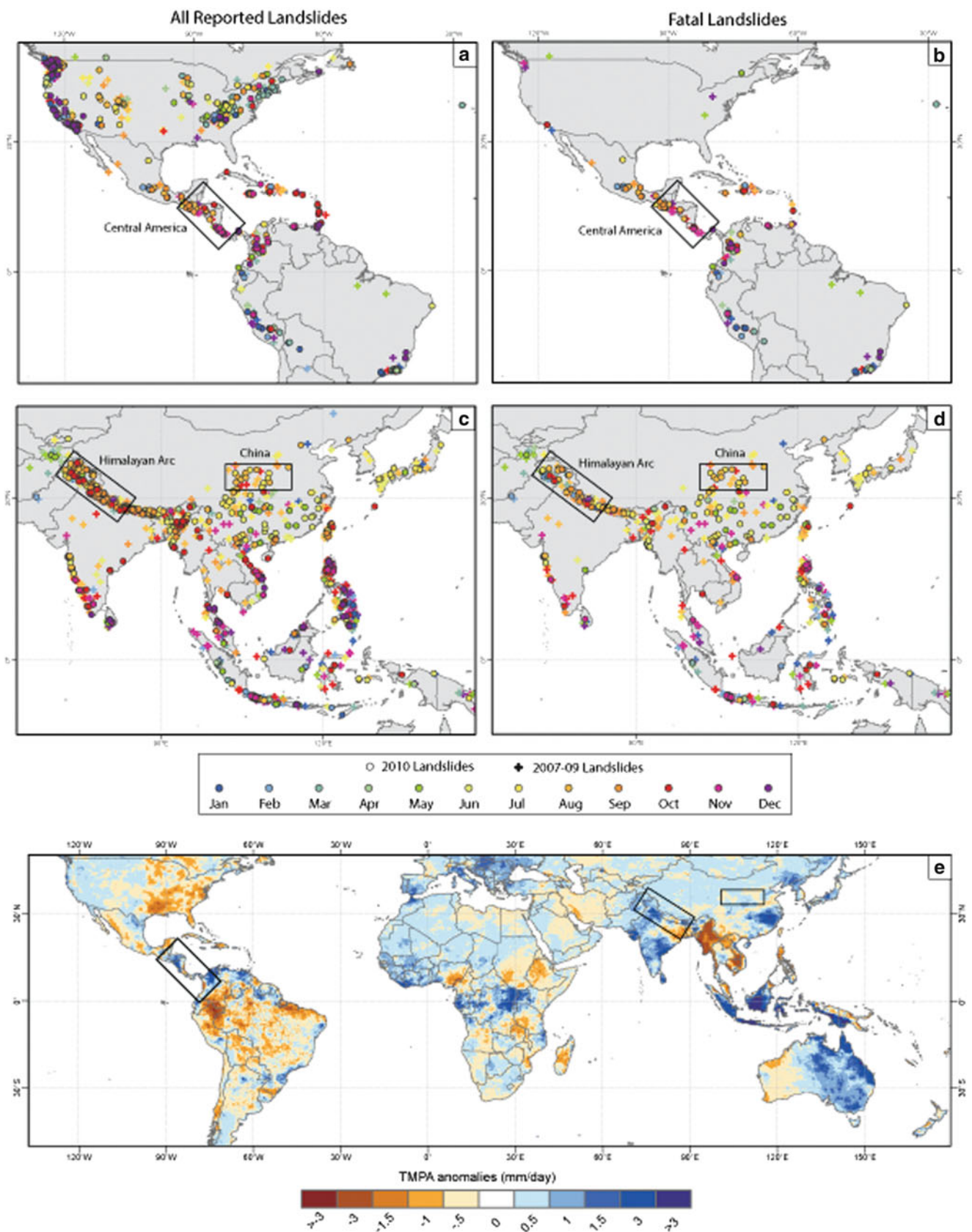
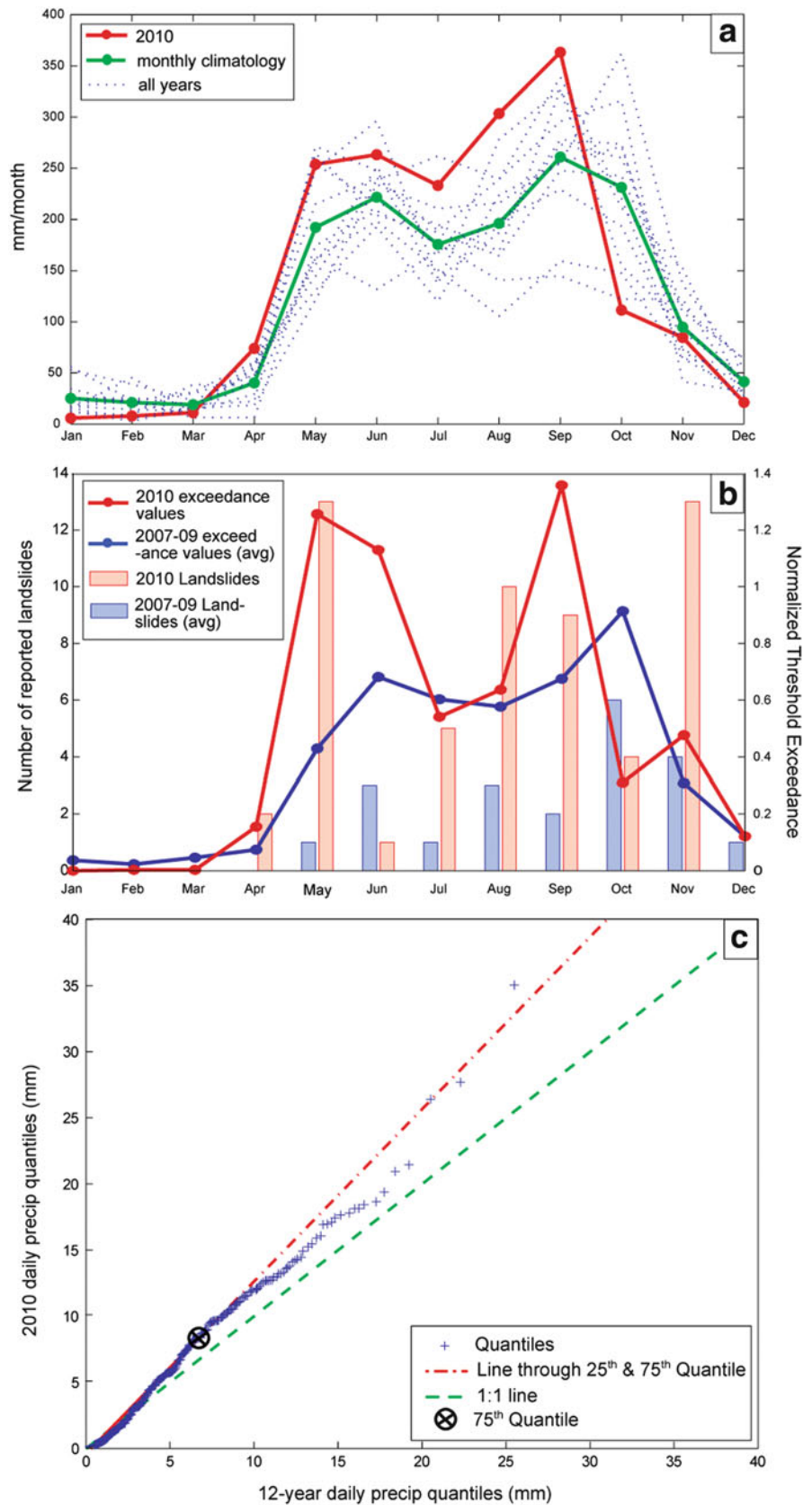


Fig. 4 Distribution of landslide reports for the years 2007–2010, showing (a) reported and (b) fatal landslides in North and South America, and (c) reported and (d) fatal landslides in Asia and Oceania. The boxes denote the three study areas: Central America, Himalayan Arc, and central-eastern China. Circles denote landslides for 2010, plus

signs display other years. The color denotes their month of occurrence. Bottom figure (e) 2010 daily precipitation anomalies computed from a TMPA daily climatology for 1998–2010 in mm/day. Figures from Kirschbaum et al. (2012a)

Fig. 5 Precipitation analysis results for Central America study area. The *upper plot (a)* highlights monthly rainfall accumulation for 2010 (*red*) with 12-year monthly climatology (*green*) calculated from the TPMA record (1998–2009). The *center plot (b)* graphs the normalized threshold exceedance values (using the regional 39 mm/day threshold—see text for details) summed for each month in 2010 (*red*) and average values for 2007–2009 (*blue*) compared to the landslide occurrence for 2010 and average number of reports from 2007–2009. The *bottom graph (c)* displays the Q–Q plot showing the distribution of daily precipitation quantiles for the 12-year TMPA record (x-axis) vs. the 2010 daily values (y-axis). The interquartile line (*red*) and 1:1 line (*green*) provide a reference to compare the distributions of quantiles for both periods. Figure from Kirschbaum et al. (2012a)



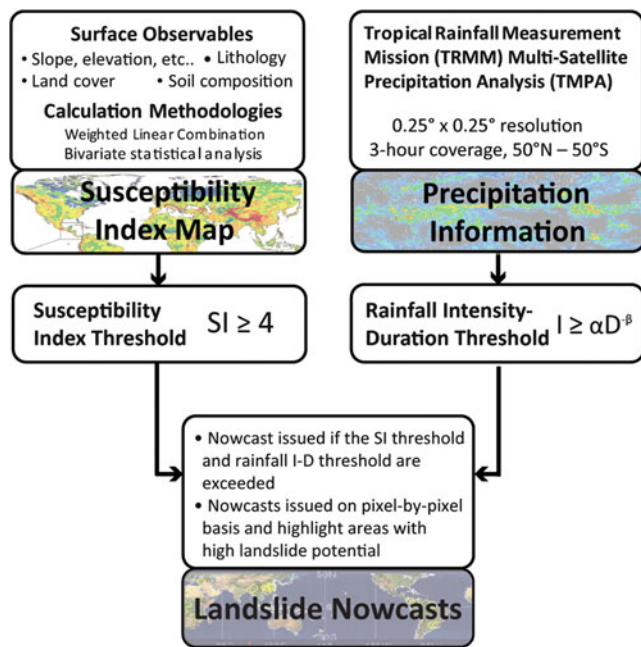


Fig. 6 Prototype Landslide Hazard Framework which includes a static susceptibility map with precipitation information from TMPA to provide a real-time “nowcast” of potential landslide activity. Figure from Kirschbaum et al. (2012b)

($0.25 \times 0.25^\circ$), improper inclusion of surface variables such as soil texture and type, and the uniformity of one intensity-duration rainfall threshold to represent landslide-triggering rainfall over the entire domain. Another challenge of the algorithm was the failure to include antecedent soil moisture as an important triggering component in the algorithm.

To improve upon the global prototype framework, a new Landslide Hazard Assessment and Forecasting System is in development which builds off of the prototype model but provides a more robust spatial representation of potential rainfall-triggered landslide activity in near-real time based on a set of static and triggering variables, including slope, geology, rainfall and soil moisture. A prototype of this system is initially being designed for use over Mesoamerica. This system will then be expanded and tested in the Himalaya region using the GLC as a validation source. Eventually, the goal is for this system to be available globally.

For both the global evaluation and regional calibration and validation, the GLC has been critical in identifying the time and location of reported landslides to better characterize susceptibility over different regions, as well as to better quantify the rainfall duration and intensities that have triggered landslides in the recent past.

Conclusions and Future Steps of the GLC

The three examples presented here demonstrate the breadth and utility of the GLC for diverse applications from statistical evaluation to slope-stability modelling. In an effort to promote the distribution and access of the GLC, a map-based interactive viewer is in development to visualize GLC data from 2007 to the present, which will allow users to view, search, query, and export landslide data. In addition to serving GLC data through this portal, users will also be able to input their own landslide event information. Both the visualization and user input tools will be open source and users will have full access to the GLC and user-provided landslide information.

Acknowledgments Compilation of the Global Landslide Catalog could not have been possible without the excellent work by Stephanie Hill, Lynne Shupp, Teddy Allen, Pradeep Adhikari, Lauren Redmond, David Adler, and Kimberly Rodgers, and Caroline Juang. This work was supported by the NASA Postdoctoral Program and SERVIR Applied Science Team grant. I would also like to acknowledge Pat Cappelaere for producing the web-based interface for the GLC and to Soni Yatheendradas for supporting this research effort.

References

- EM-DAT (2011) The OFDA/CRED International disaster database. Université Catholique de Louvain. <http://www.em-dat.net>. Last Accessed 20 Dec 2011
- Hong Y, Adler R, Huffman G (2006) Evaluation of the potential of NASA multi-satellite precipitation analysis in global landslide hazard assessment. *Geophys Res Lett* 33(L22402):1–5
- Hong Y, Adler R, Huffman G (2007) Use of satellite remote sensing data in the mapping of global landslide susceptibility. *Nat Hazards* 43(2):245–256
- Kirschbaum DB, Adler R, Hong Y, Lerner-Lam A (2009) Evaluation of a preliminary satellite-based landslide hazard algorithm using global landslide inventories. *Nat Hazards Earth Syst Sci* 9:673–686
- Kirschbaum DB, Adler R, Hong Y, Hill S, Lerner-Lam A (2010) A global landslide catalog for hazard applications: method, results, and limitations. *Nat Hazards* 52(3):561–575
- Kirschbaum DB, Adler R, Hong Y, Kumar S, Peters-Lidard C, Lerner-Lam A (2012a) Advances in landslide nowcasting: evaluation of a global and regional modeling approach. *Environ Earth Sci* 66(6):1683–1696
- Kirschbaum DB, Adler R, Adler D, Peters-Lidard C, Huffman G (2012b) Global distribution of extreme precipitation and high-impact landslides in 2010 relative to previous years. *J Hydrometeorol* 13(5):1536–1551



Landslide Counteracting System (SOPO): Inventory Database of Landslides in Poland

Teresa Mrozek, Marcin Kułak, Dariusz Grabowski, and Antoni Wójcik

Abstract

The project named the Landslide Counteracting System (SOPO in Polish) is the national landslide inventory project and was launched in 2008. The end-users of the project are administrative bodies, environmental protection inspectorates as well as non-governmental organizations. The project, commissioned by Ministry of Environment and financed by the National Fund for Environmental Protection and Water Management, is managed by Polish Geological Institute—National Research Institute in the framework of geologic survey tasks.

Information on triggering events and landslide-related damage are compiled as attributes in documentary forms. Prior to being uploaded to the database, the collected information is verified by experts with respect to data consistency and reliability. The SOPO inventory is available via Web application (<http://osuwiska.pgi.gov.pl>) and is progressively updated. The service architecture is based on Esri ArcGIS Server and uses JavaScript API. Numerous spatial data (including vector and raster data sets) are served by Oracle DB through Esri ArcSDE. In order to improve speed, most static layers have been cached and are stored locally on servers as tiles. Dynamic data are served on demand. Users are grouped into a few roles, which allows for different levels of access to the data. Till April 2014, the database handles about 39,464 landslides, covering 1031.9 km², mapped in 161 municipalities. In parallel, information on monitored landslides is stored.

Keywords

Landslide mapping • Landslide inventory • Landslide Counteracting System (SOPO) database

Introduction

In many regions of the world, landslides are important aspects of landscape evolution and causes of serious hazard. Poland is not an exception in this respect. Although landsliding has been studied here since the early 1900s (e.g. Zuber and Blauth 1907; Sawicki 1913; Teisseyre 1934), the research focused predominantly on environmental issues (e.g. Bober 1984; Starkel 1996, 2006; Alexandrowicz 1997; Margielewski 2000) while much less attention was paid to geotechnical aspects and the damaging effects of landsliding. Indeed, many Polish landslides are slow-moving, so potential terrain instability is often difficult to observe or it is easy to neglect.

T. Mrozek (✉) • A. Wójcik
Polish Geological Institute – National Research Institute, Carpathian Branch, Skrzatów 1, 31-560 Cracow, Poland
e-mail: teresa.mrozek@pgi.gov.pl; antoni.wojcik@pgi.gov.pl

M. Kułak • D. Grabowski
Polish Geological Institute – National Research Institute, Rakowiecka 4, 00-975 Warszawa, Poland
e-mail: marcin.kulak@pgi.gov.pl; dariusz.grabowski@pgi.gov.pl

The number of landslide-related fatalities is relatively low, thus, landslide hazards were generally underrated. In effect, information on failure timing and triggers, as well as on type, abundance and distribution of landslides is neither homogeneous nor collected systematically. With intensification of catastrophic landslide events since the end of 1990s, dramatically affecting hilly terrains that had been urbanized, the damage and losses experienced called for systematic mitigation and preventive measures in a framework of improved terrain management.

As stressed by Van Den Eeckhaut et al. (2012), the absence of a landslide inventory holds back the production of susceptibility or hazard maps. Bearing in mind that such maps are needed to support landslide territorial planning and landslide mitigation and recovery strategies, Polish Geological Institute (PGI) has been appointed by the Ministry of Environment as a steering party of the nation-wide project called the Landslide Counteracting System—LCS (or *SOPO in Polish*). Actually, the project was launched in 2008, with tasks of filling a gap in the landslide inventory, building-up a national database drawing upon GIS capabilities, and indicating critical sites for monitoring for warning or mitigation.

In this presentation we outline the functionality of the LCS database, which is rooted in a conventional geomorphologic landslide inventory (e.g. Guzzetti et al. 2012) and stores systematically collected data on the distribution of past landslides. It also handles data referring to current landsliding, as well as the monitoring of mass movements. Thus complementary information is compiled, which provides a background for progressing from a qualitative to a quantitative approach to landslide hazard assessment.

Landslide Inventories in Poland

Landslide-remodelled terrains and those prone to mass movements occur in many Polish districts (e.g. the Baltic coastline, steep river valley-sides, ridges mantled with glacial till or loess-covered hills), however, the most threatened regions are the Carpathians and their foreland, which occupy the southern part of the country. Unfortunately, the dangers of landsliding and its resultant detrimental effects were generally underrated for a long time. With a few exceptions, the extent and costs of landslide damage were not apparent, due to the absence of common standards for reporting and data collection. As overviewed in our earlier presentation (Mrozek et al. 2013) landslide mapping and inventory were attempted several times in the previous century, but then discontinued, so the collected data (in analogue format) are often patchy or inhomogeneous. Devastating effects related to over 400 landslides triggered in the Carpathians by storm events of July 1997 brought a general change in landslide hazard awareness. A number of different landslide

inventories with supportive databases (e.g. Ilewicz-Stefaniuk et al. 2008) that were produced afterwards pointed out the need for harmonization. With changes in legislative acts that contributed to this challenge, a new national landslide inventory was initiated. In the framework of the LCS (SOPO) project, the inventory is carried out at a scale of 1:10,000, using standardized methods (Grabowski et al. 2008). Landslide data collection is facilitated by the dedicated database.

As the LCS (SOPO) project is meant to provide support for mass movement mitigation and to improve public safety or landslide damage recovery, the end-users are administrative bodies, non-governmental organisations, environmental protection inspectorates and other enterprises acting in the areas of construction work, transportation, estate and property trade, or research and education. The Ministry of Environment as a commissioning body is the interested party as are other governmental institutions which, deal with territorial planning and management. The total endeavour is financially supported by the National Fund for Environmental Protection and Water Management on a long-term basis (Grabowski and Przybycin 2010).

Logistics and Database Structure of LCS Project

Spatial and Attribute Data Handling, Verification and User Groups

The LCS database was designed as a relational database, which consists of two schemas storing spatial and attribute data. The spatial data include not only landslide extents (areas) and activity-ranked landslide-body parts, but also inner landslide features such as main and minor scarps, toes, cracks, ridges or bulges, block/debris fields and water-logged depressions, ponds or springs, represented appropriately by polygons, lines and points (Fig. 1).

The attribute schema keeps all information gathered with registration forms for landslides (LRF) or for terrains prone to mass movements (PTRF). The fundamental attribute data comprise landslide location with reference to a drainage basin; type of movement and state of activity, morphometric parameters of a landslide, geologic units, lithology, bedding attitude, hydrogeologic aspects, age, date of occurrence and causes, land use; information on damage, expected hazard, mitigation measures, related documents; illustrative materials like geologic profiles and photos, and in the end, extra comments on potential stabilising measures and the name of the author of the data form.

Unique identification numbers allows spatial and attribute data to be connected. The attribute schema contains also all tables essential for and managed by the web application.

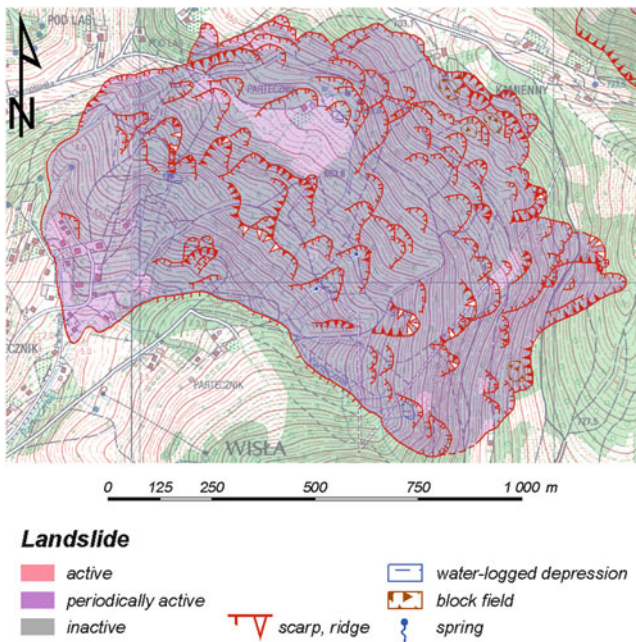


Fig. 1 Landslide features as visualized in LCS database

LCS database users (Fig. 2) are divided into a few groups according to assigned tasks and powers needed to execute them. The editor is a person entering data into the database, with an authorization for adding and modifying existing data. The verifier has substantive control and loads the data into the public part of the database. Although not allowed to modify the data, in fact the verifier is the person responsible for reliability and correctness of input registration forms. The data administrator is authorized to load, modify and manage all the data.

Information collected during geomorphologic field mapping can be entered in two manners using dedicated online or offline applications. When working in the field (without an internet connection) desktop software will be adequate, but the same functionality is implemented in the online application. In the next step, the registration forms filled offline are imported into the web system and then sent to a verifier. As mentioned before, the verifier inspects the forms and, if correct, loads them to the public database. During this operation some attributes are automatically filled using spatial data (landslide extent and reference layers).

In every stage of that process (entering, modifying, inspecting, correcting), users are supported by automatic data validation procedures. Obviously not every dependency could be checked this way, so the verifier's inspection is crucial and indispensable.

Work on the spatial data, originating mainly from the conventional landslide inventory or sometimes from SAR/LiDAR analyses (Guzzetti et al. 2012; Perski et al. 2011), is conducted in parallel. Some contractors prepare spatial data

in a digital format already during field mapping; others digitize georeferenced field maps using a predefined map composition. This, combined with a wide use of domains, allows for faster and more correct data input. Topology rules defined in the geodatabase control basic spatial relationships, e.g. separation of features belonging to the same layer, containing some inner landslide elements in a landslide polygon, or precise location of others on a landslide boundary. Examinations of complex spatial dependencies require combined sets of spatial and attribute analyses which were automated with a geoprocessing modelling. Correct spatial datasets are loaded into the aforementioned spatial schema.

Since both attribute and spatial data are available in the public database, information about landslides is available to a wide group of end-users. Some of them (mainly regional administration authorities) receive sheet-maps, both in analogue and digital formats. But the main method of accessing LCS data is a web-based map application. It has functionalities such as searching for and presenting each landslide or terrain prone to mass movements, combined with a topographic map. Moreover, users can generate a map for each landslide and print it or download it as a PDF file. Furthermore, commentary text for every municipality is also available to the public for printing or downloading. The above-mentioned can be done by every public user, it does not require registering nor logging in.

Registered users are allowed to add, modify and inspect the data—this is done by the above mentioned editors and verifiers. County administration bodies are also allowed to access both types of registration forms.

LCS IT Architecture

LCS web application and data management is organised in a three-tier, service-oriented architecture model. The public end user interacts only with the top-most tier—the presentation tier, implemented as a web application which communicates with the database (data tier) through web services (business logic tier). Obviously, all middle and back-end layer actions are unnoticeable to the users. All components are installed in a distributed environment on different servers. The software used includes, among others:

- Oracle 10g managing relational database;
- Esri ArcSDE managing spatial data in Oracle database;
- Apache Tomcat serving as a web server;
- Oracle Portal (with Oracle Identity Management) used as an application framework, content management system;
- Java-based application implementing business process;
- Esri ArcGIS Server and API for JavaScript used for displaying spatial layers, for improving viewing performance some static data are cached.

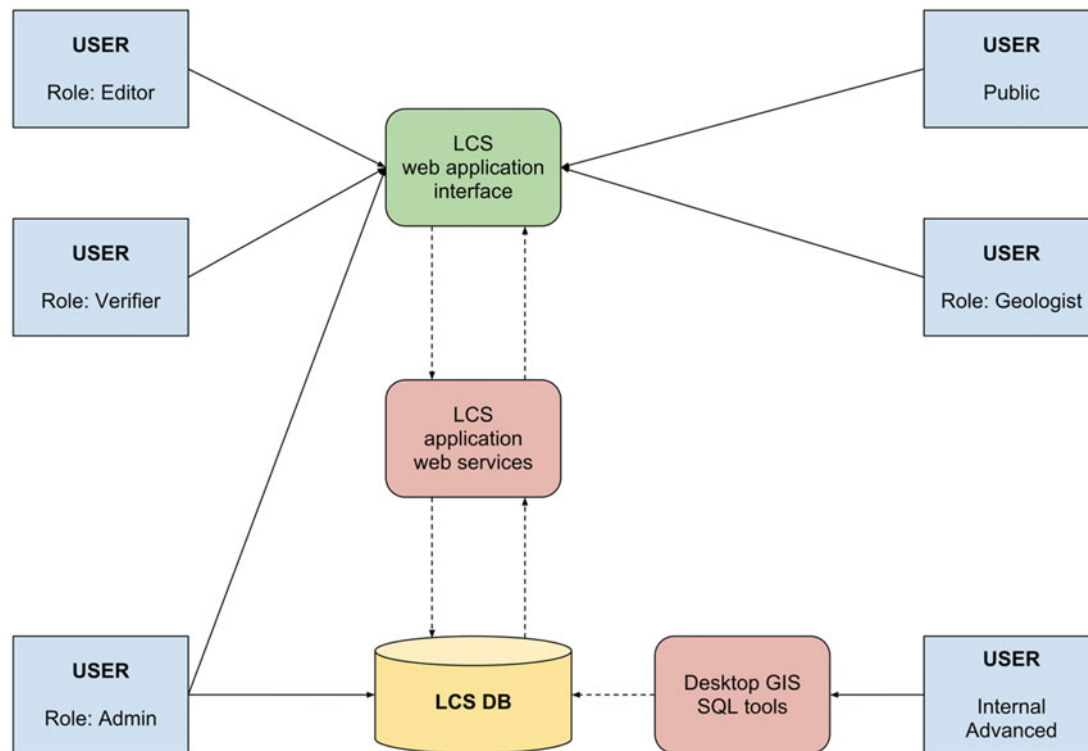


Fig. 2 LCS database architecture and roles of users

LCS Database Potential and Flexibility

The collected data are available in the framework of the above described application but, as in every database, the LCS data can be accessed with SQL language, which allows building of advanced and extended queries. For security reasons, this way is reserved only for internal PGI users. Experience gained in other projects shows that adding online user-configured reports to LCS application could significantly increase its functionality and utility.

Simultaneously, with systematic ongoing field mapping, carried out according to the adopted schedule in every municipality in the Carpathians (Mrozek et al. 2013), PGI receives notification about damage and threats posed by landslides that become active due to current triggers. Newly reported landslide events are recorded with Landslide Documentary Forms with Assessment commentary (LDFA). Preparing of such forms involves expert-based assessment to judge the amount of remediation needed to maintain the stability of the slope and to restore damaged objects (buildings or lifelines etc.) Although LDFA is an expanded version of the landslide registration form, the LCS database is ready to collect that information. Thus, by appending event-driven data on landsliding to the database storage, a more extensive background for an improved strategy on landslide risk reduction is built.

One of the parts of the LCS project is oriented toward near-real-time monitoring for early warning. During the run of the project, a hundred landslides posing threats to crucial road infrastructure are to be covered by this type of monitoring. Till August 2013, over 60 of them were already supervised using both classic (inclinometer, pluviometer and geodetic measurements) and new (GPS measurements and laser scanning) methods.

Due to unresolved legal aspects, raw data are not available to the public. However, every monitored landslide has its own documentation containing monitoring results and expert's annotation. Those documentations are constantly placed at the LCS project portal where they can be accessed as PDF files.

Inventory Results and Discussion

The database designed and developed in the framework of the LCS (SOPO) project is meant to store, manage and update information on landslides on a country-wide basis. Systematic uploading of the spatial and attributive data started with a conventional (geomorphological) landslide inventory (Malamud et al. 2004; Guzzetti et al. 2012) referring to the Polish Flysch Carpathians, the region known to be particularly susceptible to mass movements (e.g. Bober 1984; Margielewski 2006; Wójcik et al. 2006) as well as

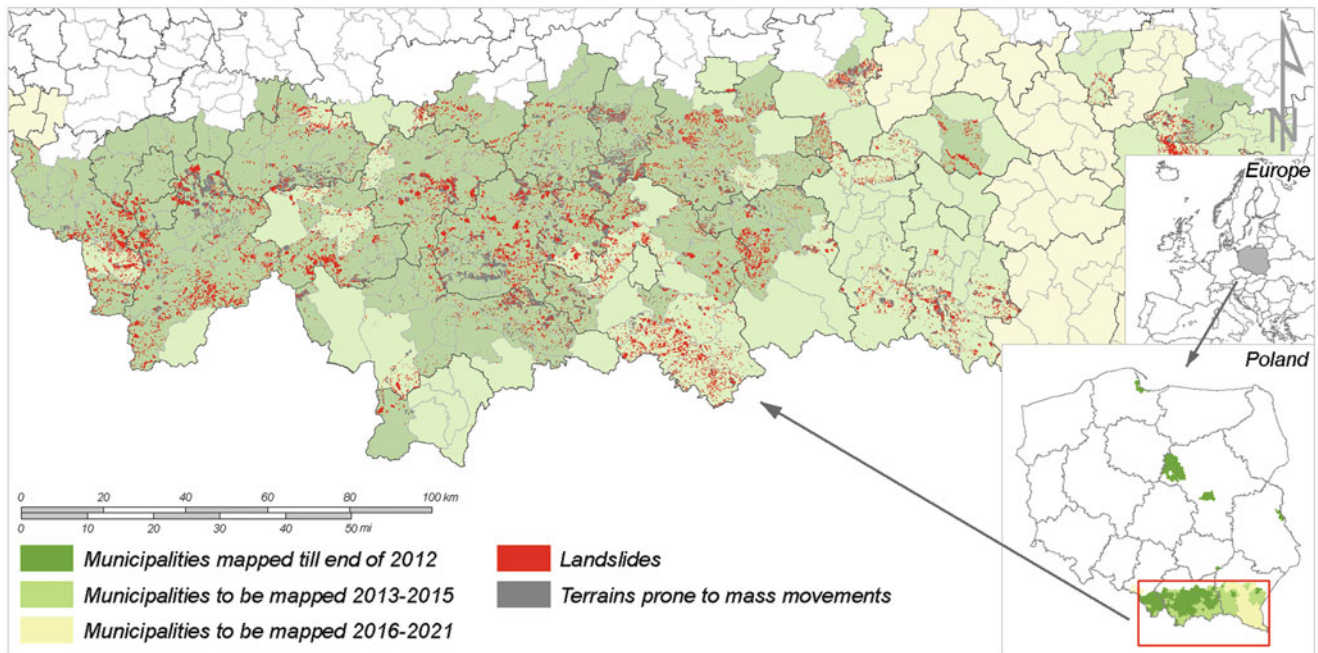


Fig. 3 Landslide inventoried in the Polish Carpathians and uploaded to LCS database

very seriously (and repeatedly) damaged due to slope failures (Rączkowski 2007; Pánek et al. 2011).

Till April 2014, landslide mapping tasks were performed in 161 municipalities comprising 12,474 km² (Fig. 3). In effect, the LCS database handles 39,464 landslides, with an area equivalent to 1031.9 km². In the case of regions designated as terrains prone to mass movements, the corresponding numbers are 3,090 and 503.8 km², respectively.

Moreover, referring to the tremendous damage caused by landslides in 2010, almost 300 LDFA forms have been already entered into the LCS database, while a next batch is under processing. With these data, the valuable information on recently observed landslides and their detrimental effects is not lost and is expected to be used for improved susceptibility assessment or for a quantitative approach to hazard and risk zonation.

Closing Remarks

For a quantitative approach to landslide susceptibility and hazard assessment, a landslide inventory is a prerequisite. According to van Westen et al. (2009) the information on the location, date and impact of past landslide events is the most important input data for such challenges. Poland had to make up for a gap in inventory tasks. Due to an adopted scheme of data acquisition, the ongoing Polish inventory keeps up with procedures used in other European countries (e.g. Trigila et al. 2010; Van Den Eeckhaut and Hervás 2012).

Research conducted by the European Commission Joint Research Centre in 2010 (Van Den Eeckhaut and Hervás 2012) delivered information which allows comparison of the LCS database to other inventory-related databases in Europe. As pointed out by the above authors, the examined national-wide databases are in the early or medium stage of collecting data (completeness <50 %), and so is the LCS database. However, with the mapping scale of 1:10,000, the Polish database is in the group of the few most detailed. Mapping techniques are also the most popular ones—a combination of field surveys, historical documents and aerial photography analyses are used in more than 75 % of the countries. But what is the most important is the scope of landslide information gathered. Compared to other databases, the Polish inventory collects almost every morphometric and geo-environmental characteristics that are collected in other countries. As in most of other inventories, because of a digital format, the LCS data is easily accessible. Making LCS data INSPIRE compliant will be a future challenge. Sharing data through web services is rather easy, which could not be said of transforming them to the Natural Risk Zones data model. Answers given to an EC JRC questionnaire (Van Den Eeckhaut and Hervás 2012) show that this is not only a Polish issue.

Acknowledgments The LCS (SOPO) programme is financially supported by the National Fund for Nature Protection and Water Management.

The authors express their gratitude to other SOPO team co-workers for their valuable critical comments.

References

- Alexandrowicz SW (1997) Holocene dated landslides in the Polish Carpathians. In: Matthews JA, Brunsten D, Frenzel B, Gläser B, Weiss MM (eds) Rapid mass movement as a source of climate evidence for the Holocene. *Paläoklimaforschung-Palaeoclimate Research* 19, pp 75–83
- Bober L (1984) Rejony osuwiskowe w polskich Karpatach fliszowych i ich związek z budową geologiczną regionu (in Polish). *Biul Inst Geol* 340:115–162
- Grabowski D, Przybycin A (2010) Działania resortu środowiska w zakresie systemu osłony przeciwsuwiskowej w Polsce (in Polish). *Przegląd Geologiczny* 58:941–945
- Grabowski D, Marciniak P, Mrozek T, Nescieruk P, Rączkowski W, Wójcik A, Zimnal Z (2008) Instrukcja opracowania Mapy osuwisk i terenów zagrożonych ruchami masowymi w skali 1:10,000 (in Polish). *Pol Geol Inst, Warszawa*
- Guzzetti F, Mondini AC, Cardinali M, Fiorucci F, Santangelo M, Chang KT (2012) Landslide inventory maps: new tools for an old problem. *Earth Sci Rev* 112:42–66
- Ilewicz-Stefaniuk D, Rybicki S, Słomka T, Stefaniuk M (2008) Surface mass movements in Poland – a review. *Pol Geol Inst Spec Pap* 24:83–92
- Malamud BD, Turcotte DL, Guzzetti F, Reichenbach P (2004) Landslide inventories and their statistical properties. *Earth Surf Process Landf* 29:687–711
- Margielewski W (2000) Landslide phases in the Polish outer Carpathians. In: Bromhead E, Nixon N, Ibsen ML (eds) *Landslides in research, theory and practice*. Thomas Telford Publishing, London, pp 1011–1016
- Margielewski W (2006) Structural control and types of movements of rock mass in anisotropic rocks: case studies in the Polish Flysch Carpathians. *Geomorphology* 77:47–68
- Mrozek T, Wójcik A, Zimnal Z, Grabowski D (2013) Landslide inventory in 1:10000 scale in Poland – benefits and dilemmas of a national project. In: Margottini C, Canuti P, Sassa K (eds) *Landslide science and practice, vol 1: Landslide inventory and susceptibility and hazard Zoning*. Springer, Heidelberg, pp 51–55
- Pánek T, Brázdil R, Klimeš J, Smolková V, Hradecký J, Zahradníček P (2011) Rainfall-induced landslide event of May 2010 in the eastern part of the Czech Republic. *Landslides* 8:507–516
- Perski Z, Borkowski A, Wojciechowski T, Wójcik A (2011) Application of persistent scatterers interferometry for landslide monitoring in the vicinity of Rożnów lake in Poland. *Acta Geodyn Geomater* 8(3 (163)): 319–323
- Rączkowski W (2007) Landslide hazard in the Polish Flysch Carpathians. *Stud Geomorph Carpatho-Balkan* 41:61–75
- Sawicki L (1913) Osuwisko ziemne w Szymbarku i inne zsuwy powstałe w r. 1913 w Galicyi zachodniej (in Polish). *Rozprawy Wydziału Matematyczno-Przyrodniczego PAU* 3(13(56)): 227–313
- Starkel L (1996) Geomorphic role of extreme rainfall in the Polish Carpathians. *Stud Geomorph Carpatho-Balkan* 30:21–38
- Starkel L (2006) Geomorphic hazards in the Polish Flysch Carpathians. *Stud Geomorph Carpatho-Balkan* 40:5–19
- Teisseyre H (1934) Osuwisko w Krasnoili (in Polish with French summary). *Czasopismo Geograficzne* 2:1–15
- Trigila A, Iadanza C, Spizzichino D (2010) Quality assessment of the Italian landslide inventory using GIS processing. *Landslides* 7:455–470
- Van Den Eeckhaut M, Hervas J (2012) Landslide inventories in Europe and policy recommendations for their interoperability and harmonization. *JRC Scientific and Policy Reports*
- Van Den Eeckhaut M, Hervas J, Jaedicke C, Malet JP, Montanarella L, Nadim F (2012) Statistical modelling of Europe-wide landslide susceptibility using limited landslide inventory data. *Landslides* 9:357–369
- van Westen CJ, Castellanos E, Juriakose SL (2009) Spatial data for landslide susceptibility, hazard and vulnerability assessment: an overview. *Eng Geol* 102:112–131
- Wójcik A, Mrozek T, Granoszewski W (2006) Lithological conditioning of landslides and climatic changes with examples from the Beskidy Mts., Western Carpathians, Poland. *Geografia Fisica e Dinamica Quaternaria* 29:197–209
- Zuber R, Blauth J (1907) Katastrofa w Duszatynie (in Polish). *Czasopismo Techniczne* 25:218–221



Development of a Landslide Inventory for a Region in Mexico Using Very High Resolution Satellite Stereo-Images

Franny G. Murillo-García, Federica Fiorucci, and Irasema Alcántara-Ayala

Abstract

In recent years, the analysis of stereo-pairs of Very High Resolution (VHR) satellite images has represented a valid alternative to aerial photographs for landslide recognition and mapping. The availability of images with even higher spatial resolution and improved digital visualization and analysis techniques have encouraged investigators to use satellite images to detect and map recent and old landslide features. In this paper we present the results of a landslide geomorphological inventory prepared for the municipality of Pahuatlan, Mexico, based on stereoscopic interpretation of GeoEye 1 VHR images.

A 54 km² study area was defined for landslide recognition. In the study area, elevations range from 450 m to 1,500 m above sea level. The study area has a mountainous terrain with deep ravines and high summits derived from orogenesis of the Sierra Madre. Mesozoic rocks, including conglomerates, shale, siltstones and limestone, outcrop in the area. The climate is temperate, with abundant precipitation all year and a mean annual rainfall of 2,500 mm. Vegetation types are rain and coniferous forest, with a high level of deforested areas also present.

According to the landslide inventory, in Pahuatlan municipality, there are 385 recent landslides, 171 old landslides and 21 very old landslides. The total landslide density is 10.5 landslides per km². The area most affected by landslides was concentrated in 34 km² and it was measured using Double Pareto analysis. In addition, stereo-images were used to generate a very high resolution Digital Elevation Model (10 m spatial resolution).

F.G. Murillo-García (✉)
Universidad Nacional Autónoma de México, Posgrado en Geografía,
Circuito Exterior s/n., Mexico, D.F., Mexico
e-mail: fran.79v@gmail.com

F. Fiorucci
Consiglio Nazionale delle Ricerche, IRPI, via Madonna Alta 126,
06128 Perugia, Italy
e-mail: Federica.Fiorucci@irpi.cnr.it

I. Alcántara-Ayala
Instituto de Geografía, Universidad Nacional Autónoma de México,
Circuito Exterior s/n., Mexico, D.F., Mexico
e-mail: irasema@igg.unam.mx

VHR satellite images are efficient for landslide identification; they reduce the time to acquire information and allow a continuous stereo-model view without changing the set of images, although the associated costs are quite high.

Keywords

Landslides • Landslides inventories • Very high resolution • Satellite images • Stereo-images

Introduction

Landslides inventories are an essential tool, and frequently are the first step for susceptibility, hazard and risk estimation and evaluation (Ardizzone et al. 2013). According to Guzzetti (2005), depending on the period of time covered, landslide inventories can be multi-temporal, seasonal or event type. The generation of these different kinds of inventories depends on the amount of resources and time available. Techniques to produce landslide inventories can be divided into traditional techniques (air-photograph stereo-pairs interpretation, field surveys and analysis of historic data) and new or recent techniques (monoscopic visual, automatic or semiautomatic analysis of satellite images, very high resolution digital elevation models—DEM, stereo-interpretation of very high resolution—VHR satellite stereo-images). In this research, we present the results of a geomorphological landslide inventory map prepared using a classification based on the relative age and depth of landslides. The study area extends over 54 km² in a temperate humid region in Pahuatlán, Puebla, Mexico. We used VHR stereo-pair images (Geo-Eye-1, with 0.5 m of spatial resolution on panchromatic band and 1.5 m on multispectral) for landslide identification and mapping.

In the first section the area of interest is described. The stereo interpretation processes and the results of the landslide inventory map are included in the second section. Finally some conclusions are also provided regarding the use of these tools for the recognition of recent, old and very old landslides.

Study Area

Pahuatlán is a municipality of Mexico located in the Sierra Norte of Puebla region, in the Sierra Madre Oriental mountain system (Fig. 1). The municipality extends 80 km², however the inventory covers an area of only 54 km² (study area). Pahuatlán municipality is affected by landslides almost every rainy season. The area is characterized by a temperate climate and the land cover is original rain forest vegetation, strongly altered by deforestation. The occurrence of hurricanes and tropical depressions is related to the climatic conditions

produced in the Gulf of Mexico, which generate extraordinary rainfall on the Sierra Norte region. These events, combined with the relief and geological features of the area, are the most important factors related to landslide occurrence. Elevations in the area range from 450 m to 1,500 m above sea level. The terrain is mountainous, with deep ravines and high summits, products of the Sierra Madre orogenesis. Terrain gradient ranges from almost zero, along the Plain of the San Marcos River, to more than 70° on the top of the mountains.

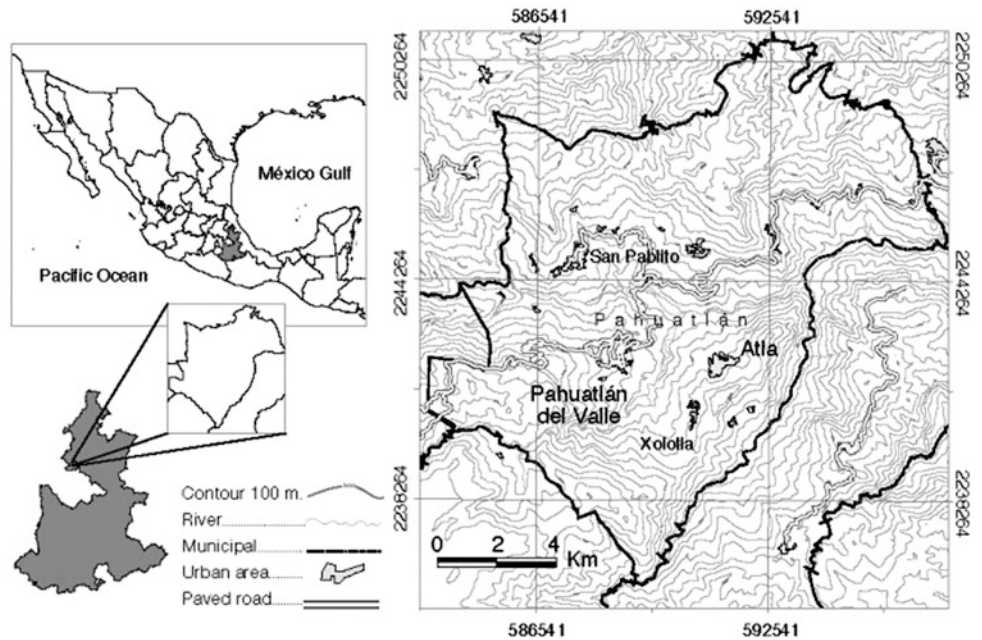
Landslide occurrence is strongly related to the arrangement of lithological units. Mesozoic rocks, and Tertiary and Quaternary volcanic deposits outcrop in the area. These units are: (i) Lower Jurassic Huayacocotla sandstone and shale sequence, (ii) Cahuas siltstone-sandstone formation, (iii) Middle Jurassic Tepéxic limestone formation, (iv) Late Jurassic Tamán clayey limestone and shale sequence, (v) Late Jurassic Pimienta black limestone-shale sequence, (vi) Lower Cretaceous Tamaulipas limestone-shale sequence, (vii) Pliocene basalt, andesite and pyroclastic deposits and recent (viii) alluvial and (ix) colluvium deposits (Sánchez Rojas et al. 2004). The rocks are mostly layered and have been altered by geotectonic processes and local metamorphism (Oliva Aguilar et al. 2011). The most important geological structures are the Huayacocotla anticline and San Pablo syncline; structural discontinuities are the Paciotla normal fault and Xolotla reverse fault (Fig. 2).

Material and Methods

This section describes the satellite images, the hardware and software visualization technology, and the interpretation criteria used to identify and map landslides.

Geo-Eye stereo pairs, panchromatic and multispectral bands were available for the area of interest. GeoEye-1 images have 0.5 m of spatial resolution on the panchromatic band and 1.64 m on multispectral bands (Table 1). The images were taken on March 31, 2010. All images were equipped with Rational Polynomial Coefficients providing the image position relative to the ground. The azimuth angles of the images are 0.19° for the first image and 359.59° for the second image of the pair. The height value of the azimuth angle allowed us to perform a stereo

Fig. 1 Location of the Pahuatlán study area



orientation with good quality, using only the Rational Polynomial Coefficient files.

Until now, successful approaches in the literature for the analysis of digital stereo images (satellite and aerial) have been limited to binocular viewing and complementary filters (Ardizzone et al. 2013).

For this research we used a complementary filter system, a PLANAR stereo-mirror. The system works with two monitors AMLCD (Active Matrix Liquid Crystal Display) oriented with 110° of angular distance. A passive beam splitter mirror bisects the angle formed between the two monitors. On one side of the glass the mirror has a reflective coating, and the other side has an anti-reflective coating. In this way, the observer can perceive the two images from each screen at the same time. The images from the two monitors can be viewed through crossed polarizing glasses which make each eye of the observer seeing only one of the two images (PLANAR 2008). The brain interprets this and the stereopsis effect is obtained.

ERDAS IMAGINE and Leica Photogrammetry Suite (LPS) software were used for the block orientation. The interior orientation of the images was obtained using the sensor model, and the exterior orientation was performed using the Rational Polynomial Coefficients files. The interior and the exterior orientation allows the generation of the 3D model. The ERDAS block image file can be exported to Stereo Analyst extension for ArcGis® to generate the 3D digital view which is perceived by using the PLANAR stereoMirror system. Using this technology, the interpreter can identify and digitize the 3D shape of the landslides directly on the images and can implement the digital data base. Figure 3 shows a 3D view based on a Very High Resolution Digital Elevation Model obtained by using the

same stereopairs. The image gives an idea of what the observer can see using the digital stereoscope.

Landslide Identification

Appropriate landslide identification on VHR satellite images improves the spatial resolution of the images. To obtain a multispectral image with the panchromatic spatial resolution (pixel size 0.5 m) a pansharpened fused technique was used. GeoEye multispectral images were fused with the panchromatic image through ENVI[©] software using the Gram-Schmidt Spectral Sharpening algorithm. The result was two multispectral images with 0.5 m of spatial resolution (Fig. 4). The treatment of the images with the pansharpening technique allowed a better visual interpretation.

Correct landslide identification depends on scale, date of acquisition, radiometric resolution, spatial resolution, cloud cover, and the quality of the available images. Moreover, the quality of the tools used for the photo-interpretation (stereoscopes, stereo-plotters or digital stereoscope systems and software and hardware elements) and the experience and skill of the interpreter are crucial for adequate landslide identification and mapping (Guzzetti et al. 2012). Other important issues are the physical conditions of the area, which can make landslide identification difficult. For example, in tropical areas such as Pahuatlán, the humid temperate climate causes rapid growth of vegetation on landslide areas, hiding the spectral evidence of recent movements.

In addition, landslide geomorphologic evidence depends on the type and velocity of movement (Pike 1988; Cruden and Varnes 1996; Dikau et al. 1996); this implies different possibilities for how a landslide can appear on the images.

Fig. 2 Geological map of the Pahuatlán study area

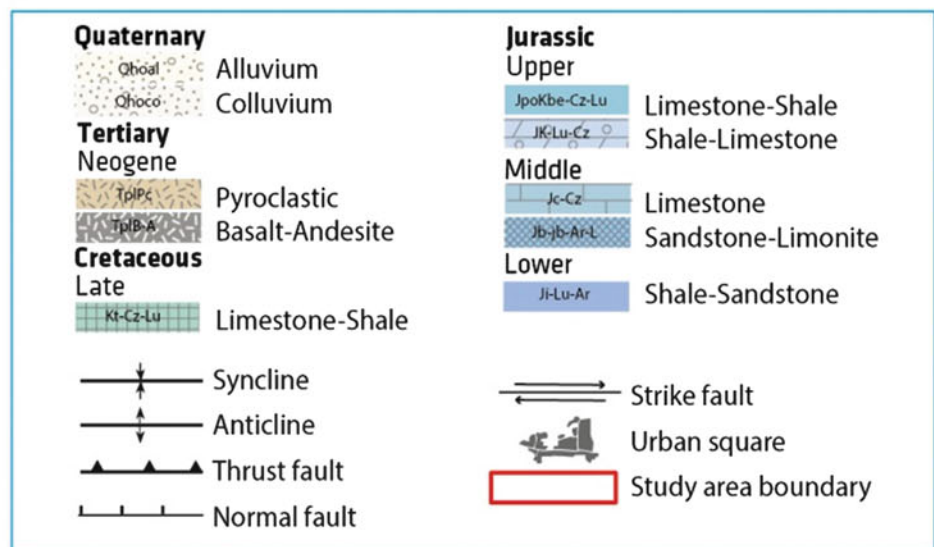
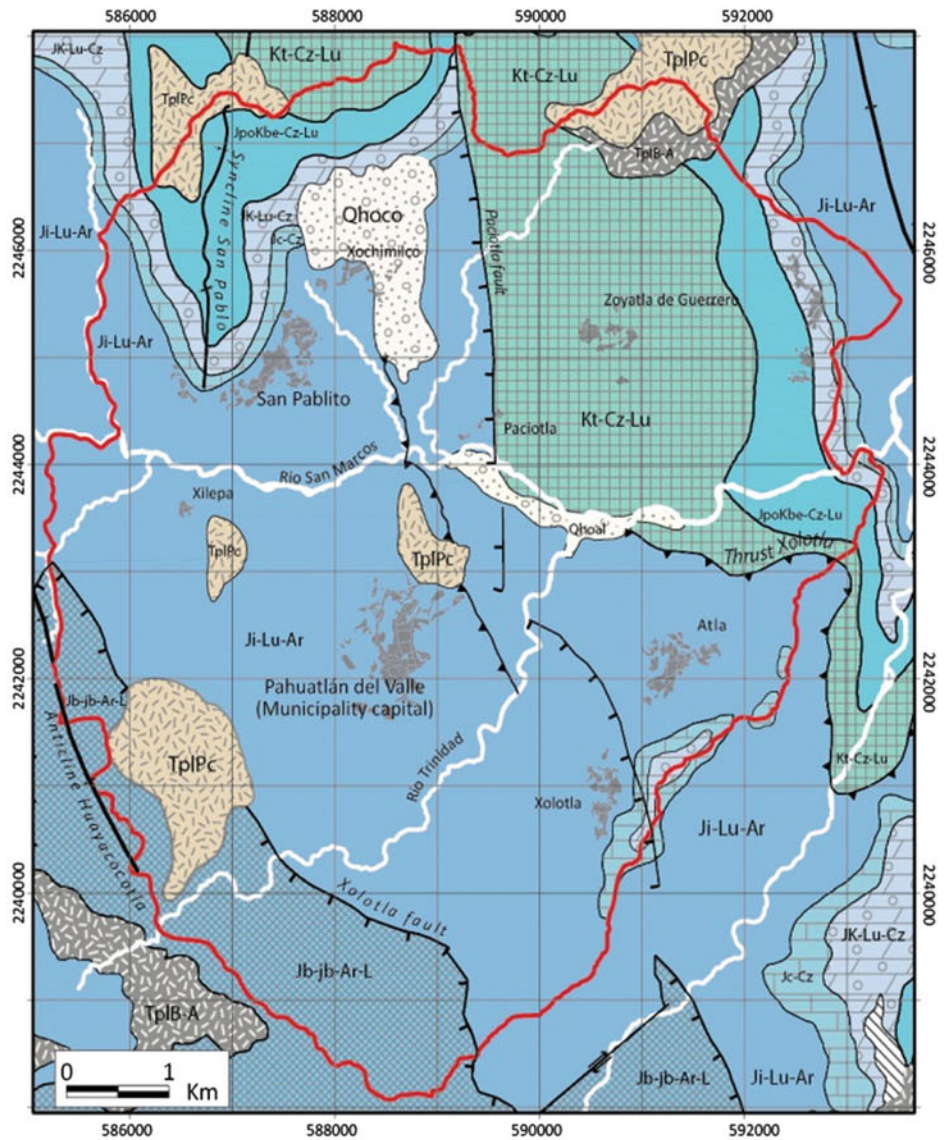


Table 1 Features of GeoEye-1 Pahuatlán, México, stereo pair images

| Satellite | Bands | Radio-metric resolution | Spatial resolution | Acquisition date |
|-----------|-------|-------------------------|-------------------------|------------------|
| GeoEye-1 | 5 | 11 bits | 0.50 m PAN 1.64 m MS | 31-03-2010 |

PAN panchromatic, ME multispectral

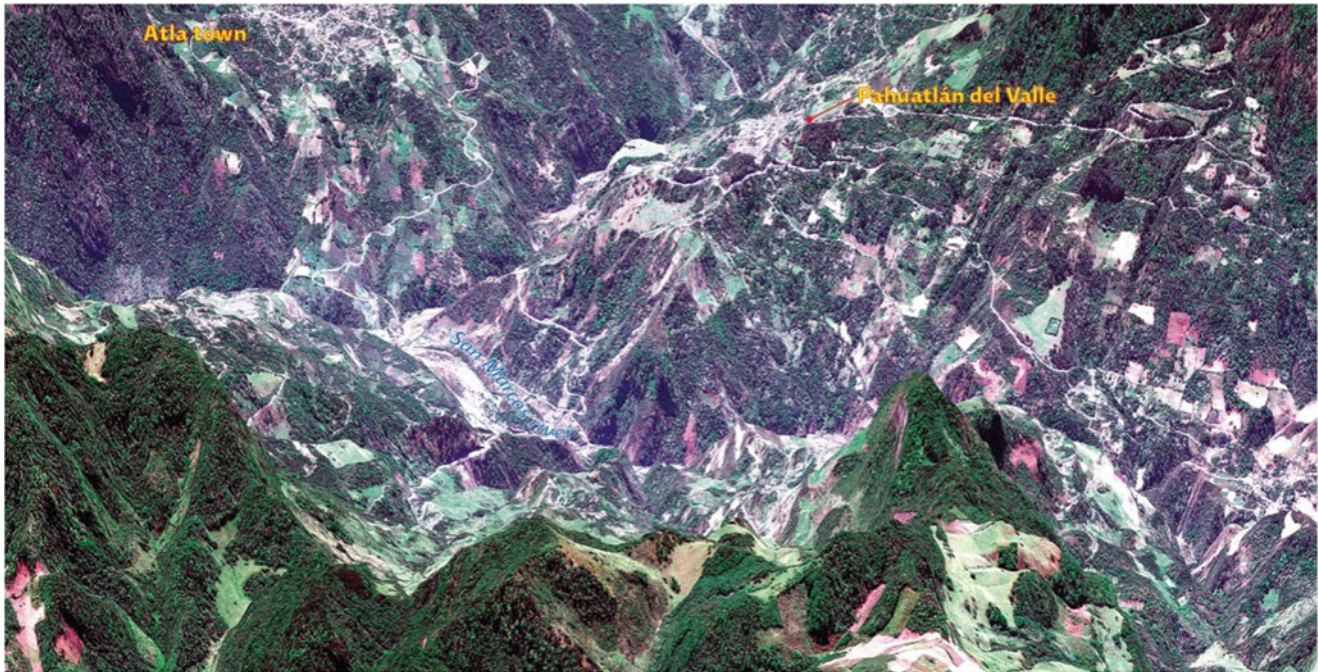


Fig. 3 Pansharpened image Geoeeye-1 drapes a DEM (vertical exaggeration = 3.0). The view is from north to south. In the *bottom left* of the image (first plane) it is possible to identify details: the shape of the trees and the borders of the field crops

The spectral firm of a landslide on a satellite image is related to: (i) the time between the occurrence of the movement and the acquisition date of the images, (ii) the hour, season and year the image was taken, (iii) the lithology and soil properties (type, humid and depth) and (iv) the land use/cover. In the 3D environment, the interpreter looks for features related to the landslide occurrence, based on basic criteria: shape, size, tone, texture, patterns, shadows, topography and environment physical conditions (Fiorucci et al. 2011). This is different for old and very old landslides (geomorphological evidence) and for recent landslides (spectral and geomorphological evidence).

Recent landslides are those which have occurred in the last year or season and are active on the date images were acquired (WP/WLI 1993). These types of landslides appear fresh on the satellite images and are recognizable by the shape and the difference of color, texture, tone and pattern of the landslide area respect to the surrounding original surface (Fig. 5).

Old landslides are those which occurred in the historical or geological past; are abandoned or movement has stabilized (Cruden and Varnes 1996).

Very old landslides are those which have occurred in the past, and other landslides (old landslides) have taken place on top of their main body. It is probable that this kind of relict landslide (very old), has taken place in different climate or environmental conditions. Very old and old landslides are recognizable by the geomorphological evidence, are mostly smoothed by erosion processes (Fig. 6).

The photo-interpretation process of VHR satellite images with digital stereo-systems is basically the same as for traditional air photographs. The advantage of the described technology is that (i) less time is involved in the identification process, (ii) the possibility of seeing a continuous stereo-model view without changing the set of images, (iii) the direct record of the information on the landslide inventory data base, and (iv) the improved accuracy of the obtained map.

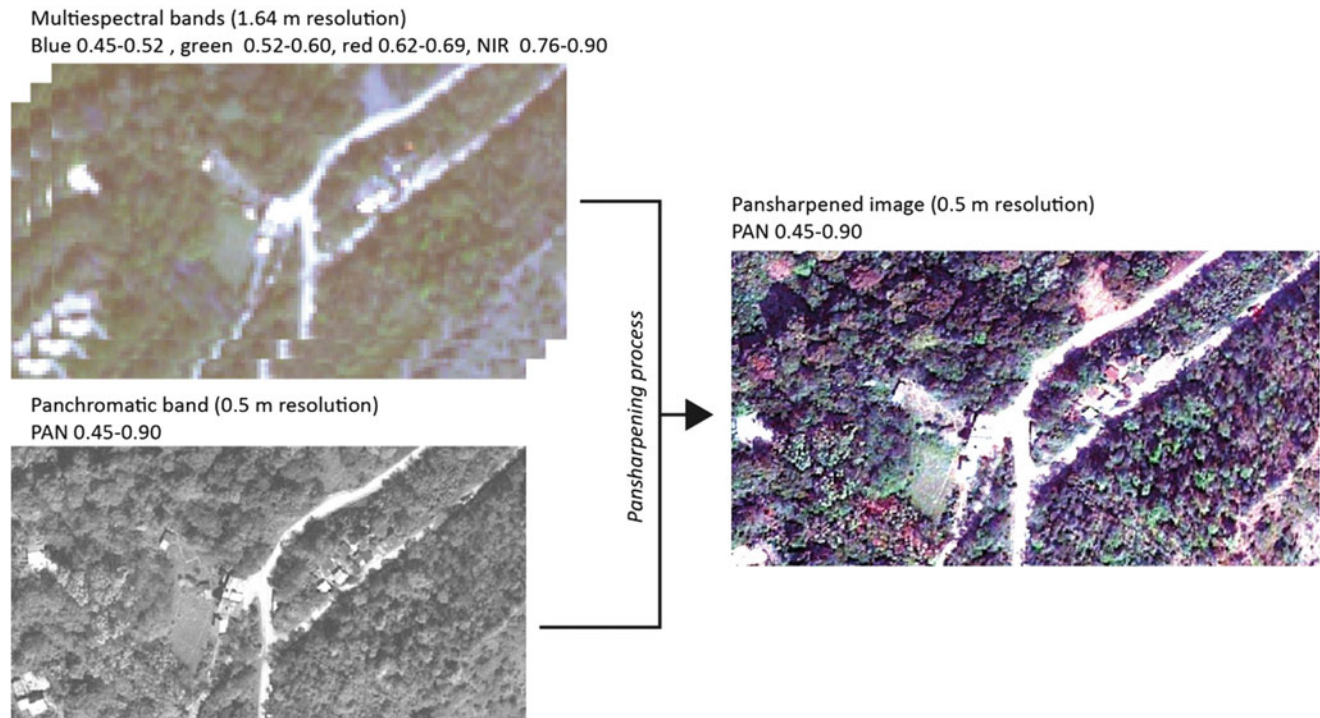


Fig. 4 Result of pansharpening process where the multispectral bands are fused with the panchromatic band. The composed *color images* obtained have the same resolution of the panchromatic band, in this case 0.5 m

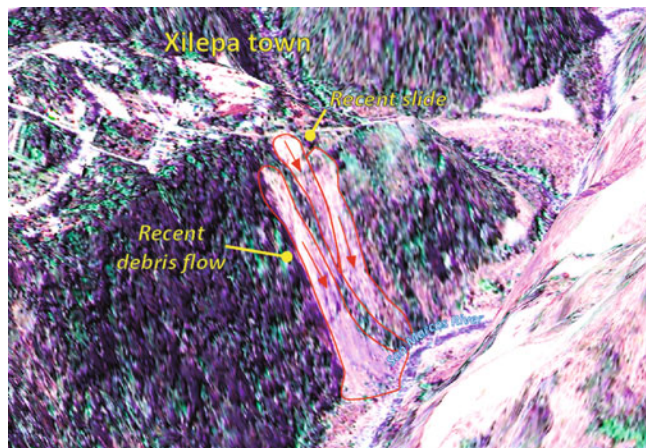


Fig. 5 Recent landslides occurred in 2010 during the rainy season (vertical exaggeration: 2). Scars of the landslides are fresh on the images, with more clear color, making contrast with the green and dark tones of the vegetation around the movements

Results

The landslide inventory of Pahuatlán included total of 557 landslides; 390 of them (67.5 %) were identified directly on the Geoeye-1 stereo-images. 171 landslides were classified as old landslides and 21 as very old landslides (Fig. 7). Landslide age and type were identified using digital stereoscopic

interpretation. 198 landslides which were classified as recent landslides occurred between 2007 and 2010; all these landslides can be considered as active landslides. Very old and old landslides were present on a larger area than those recent landslides. Mean area of the very old landslides was identified as $1.2 \times 10^6 \text{ m}^2$, the average area of the old landslides was $8.1 \times 10^5 \text{ m}^2$, and the average area for the recent landslides is $1.1 \times 10^3 \text{ m}^2$. The largest landslide identified on the study area is the Paciotla slope landslide with an area of $4.1 \times 10^6 \text{ m}^2$.

Discussions and Conclusions

By using the techniques described in this work it is possible to identify recent, old and very old landslides. For this research a geomorphological landslide inventory was prepared for a 54 km^2 study area with different lithological features in a temperate region where the denudation processes are intense. A Geoeye 1 VHR satellite images stereo-pair with 0.5 m of spatial resolution on the panchromatic band and 1.5 m on the multispectral bands was used for landslide identification. A PLANAR[©] StereoMirror system technology was used, combined with a Stereo Analyst ERDAS[©] extension for ArcGIS[©], to generate the 3D view. Using these tools, 390 landslides were identified and digitalized directly on a digital inventory data base. Furthermore, the relative age of each mass movement was inferred by geomorphological interpretation of the stereo

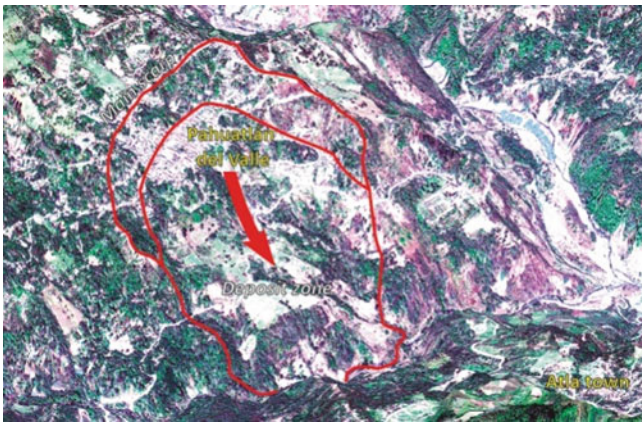
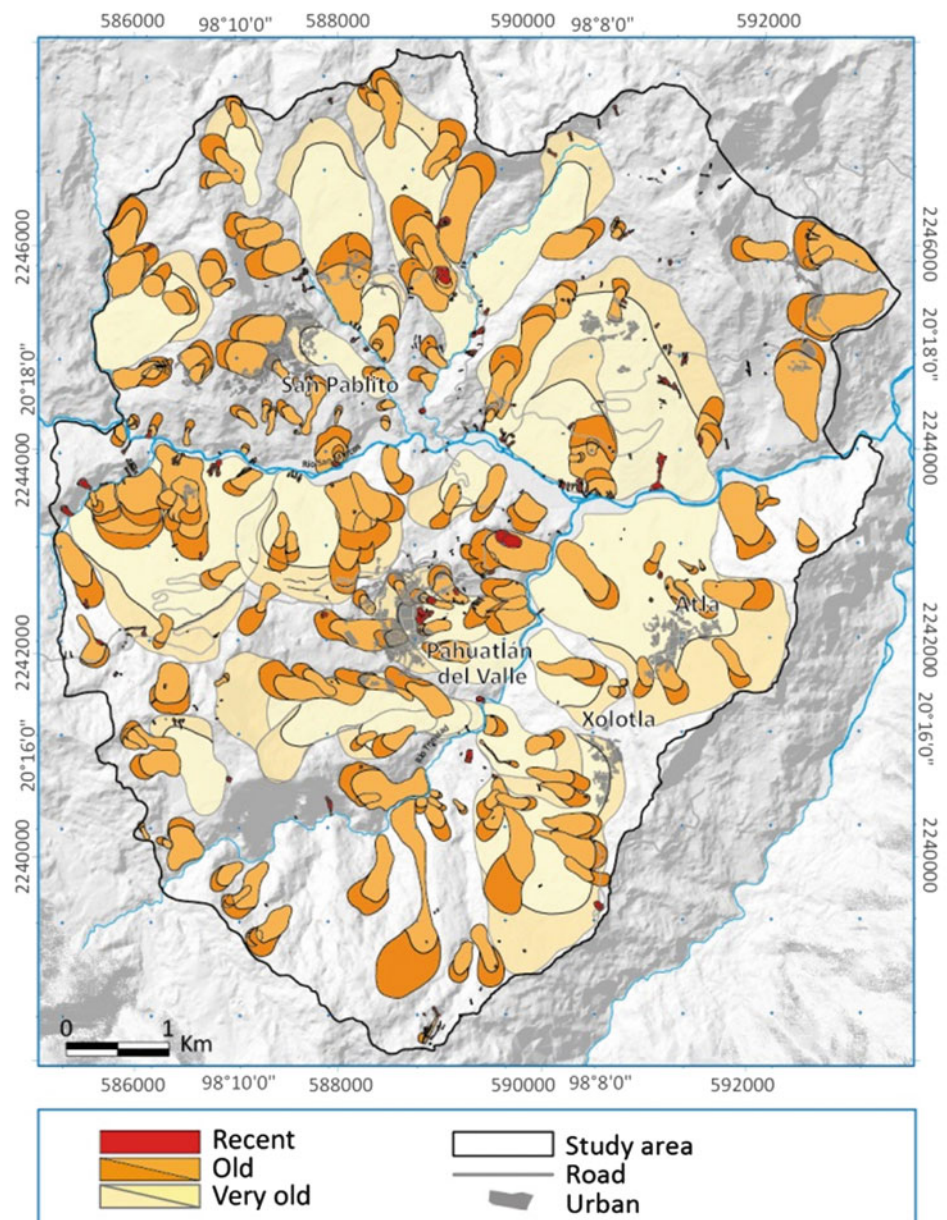


Fig. 6 Pahuatlán very old landslide. The red line outlines the landslide area, the scarp and deposit zone. The Pahuatlán village is located on the flat zone between the main scarp and the secondary scarp

pair. The very old landslides need careful analysis. Large and formerly unstable masses would need deeper investigation to understand the processes involved. Very old and old landslides can be reactivated even if these landslides are in a relict state of activity (Cruden and Varnes 1996). It is also likely that recent landslides located near the Pahuatlán Village, which have destroyed a dozen houses, two small hospitals, and one school, could be related to the reactivation of a very old landslide on which Pahuatlán del Valle is located.

Fig. 7 Pahuatlán landslide inventory map. Very old landslides are indicated in beige, old landslides in orange and recent in red. All landslide types are distributed in the study area. Pahuatlán, Xolotla, Atla and San Pablito towns are located over very old and old landslide deposits



Acknowledgments Authors are thankful to the National Autonomous University of Mexico and the CNR-IRPI from Perugia, Italy for the support given to this research, and to CONACYT post-graduated scholarship system. Thanks are also due to CONACYT for financial support for the Project 156242: MISTLI.

References

- Ardizzone F, Fiorucci F, Santangelo M, Cardinali M, Mondini A, Rossi M, Reichenbach P, Guzzetti F (2013) Very-high resolution stereoscopic satellite images for landslide mapping. In: Proceedings of 2nd world landslide forum, 19–25 September 2011. Springer, Heidelberg, pp 3–7
- Cruden DM, Varnes DJ (1996) Landslide types and processes. In: Turner AK, Schuster RL (eds) Landslides, investigation and mitigation, Transportation Research Board Special Report 247. National Academy Press, Washington, DC, pp 36–75
- Dikau R, Brunsten D, Schrott L, Ibsen M-L (eds) (1996) Landslide recognition. Identification, movement and causes. Wiley, Chichester, England, 251p
- Fiorucci F, Cardinali M, Carlà R, Rossi M, Mondini AC, Santurri L, Ardizzone F, Guzzetti F (2011) Seasonal landslides mapping and estimation of landslide mobilization rates using aerial and satellite images. *Geomorphology* 129(1–2):59–70
- Guzzetti F (2005) Landslide hazard and risk assessment. PhD thesis. Bonn University, Bonn, Germany, 373p
- Guzzetti F, Modini A, Cardinali M, Fiorucci F, Santangelo M, Chang K-T (2012) Landslide inventory maps: new tools for an old problem. *Earth Sci Rev* 112:42–66
- Oliva Aguilar VR, Garza Merodio GG, Alcántara Ayala I (2011) Configuration and temporal dimension of vulnerability: spaces and disasters in the Sierra Norte de Puebla. *Investigaciones Geográficas, Boletín del Instituto de Geografía, UNAM* 75:61–74
- Pike RJ (1988) The geometric signature: quantifying landslide-terrain types from digital elevation models. *Math Geol* 20(5): 491–511
- PLANAR (2008) SD2620W stereoscopic monitor User's Guide. Planar Systems Inc, Beaverton, OR
- Sánchez Rojas LE, De la Callejera Moctezuma AE (2004) Carta Geológico-Minera Pahuatlán F14-D73, scale 1:50,000. Servicio Geológico Mexicano, Pachuca, Hgo., México
- WP/WLI – International Geotechnical societies UNESCO Working Party on World Landslide Inventory (1993) A suggested method for describing the activity of a landslide. *Int Assoc Eng Geol Bull* 47:53–57



Inventory of Precipitation Triggered Landslides in the Winter of 2013 in Zagreb (Croatia, Europe)

Sanja Bernat, Snježana Mihalić Arbanas, and Martin Krkač

Abstract

The subject of this paper is inventory of precipitation induced landslides in Zagreb in the period of extreme weather conditions in the winter of 2013. Long-lasting heavy rainfall and a thick snow cover triggered more than 60 landslides in the hilly area of the Medvednica Mt. which belongs to the City of Zagreb. Basic data about landslide event locations, received from records of the City Office of Emergency Management (OEM), are analyzed. We present the results of preliminary temporal distribution analysis of landslide occurrence during the following extremes: cumulative monthly precipitation in January, February and March in 2013 was 130–190 % higher than the average monthly values for the period from 1862 to 2012; and cumulative precipitation for a 3-month period in 2013 has the highest value in the last 150 years. Spatial distribution analysis shows that most of the analyzed landslide events were triggered in engineering soils of Pontian age (approximately 1 landslide per 2 km²). Presented landslide inventory map provide a solid basis for organizing further research aimed at the analysis of landslide triggering rainfall thresholds as well as development of landslide inventory map which will depict landslide contours.

Keywords

Landslide inventory • Precipitation triggered landslides • City of Zagreb • Croatia • March 2013

Introduction

The winter period of 2013 in the City of Zagreb, the capital of the Republic of Croatia (in SE Europe), had extreme weather conditions that caused reactivation of 63 landslides. In the same period in the continental part of Croatia, the Croatian National Protection and Rescue Directorate (DUZS) recorded more than 900 activated landslides (Bernat et al. 2014). Figure 1 shows number of recorded landslides events per county for the period from January to April 2013. The highest number of reported landslide events

was in the NW Croatian counties. Hilly areas in the continental part of Croatia, composed of Pleistocene and Neogene sediments (i.e., engineering soils and soft rock-hard soils, e.g., marls) are prone to the development of small superficial to moderately shallow landslides (landslide volume <10⁵ m³; landslide depth <20 m). The precipitation-induced landslides caused damages to private houses and roads.

Landslide inventory data in Zagreb have been additionally collected and checked in the field by professional engineering geologists, because information about reported landslides was unreliable. It was necessary to check landslide type, locations, date of activation and landslide size. The intent of this paper is to present the importance of the development of seasonal landslide inventory for the winter of 2013 in the City of Zagreb, as well as in NW Croatia.

S. Bernat (✉) • S. Mihalić Arbanas • M. Krkač
Faculty of Mining, Geology and Petroleum Engineering, University of Zagreb, Pierottijeva 6, Zagreb 10000, Croatia
e-mail: sanja.bernat@rgn.hr; snjezana.mihalic@rgn.hr; martin.krkač@rgn.hr

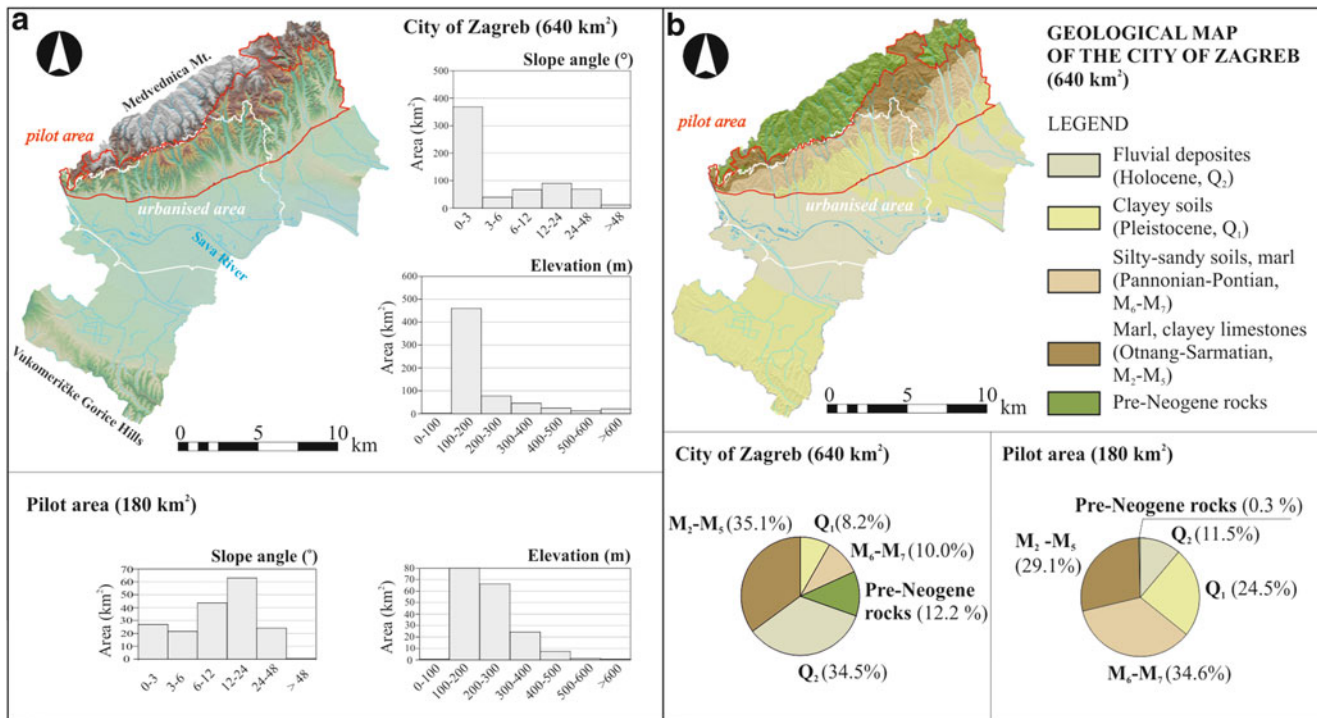


Fig. 2 City of Zagreb: (a) Histograms showing the elevation and slope angle computed from DEM for the City of Zagreb and the pilot area of the Croatian-Japanese SATREPS FY2008 project (red outline).

(b) Geological map showing the generalized stratigraphic units. Pie charts show the relative distribution of main stratigraphic units



Fig. 3 Examples of landslides endangering/damaging houses or public roads in the winter of 2013 in Zagreb

man-made processes of different types. The most frequent triggering factors are rainfall and man-made activities (Mihalić et al. 2011). The main problem with the current practice of landslide risk management in the City of Zagreb is the lack of a suitable landslide inventory and landslide hazard and risk maps.

Landslide Events in the Winter of 2013

Spatial Distribution of Landslides

Information regarding the reactivation of landslides in the winter period of 2012/2013 was received from citizens who informed City administration which is responsible for

landslide remediation or civil protection throughout that time period. Figure 3 shows three examples of landslides endangering or damaging private houses and roads. City representatives performed more than one hundred field examinations to estimate whether or not structures and/or people were at risk and to organize urgent mitigation measures. Evidence of examined landslides are recorded in the City offices only in the form of lists with the data about landslide locations and the date of activation. Figure 4 presents a landslide inventory map with 63 landslides, compiled on the basis of information collected from City administration, online media and field checking in November 2013. Additional field checking was performed to collect reliable data about landslide location and type and to collect the

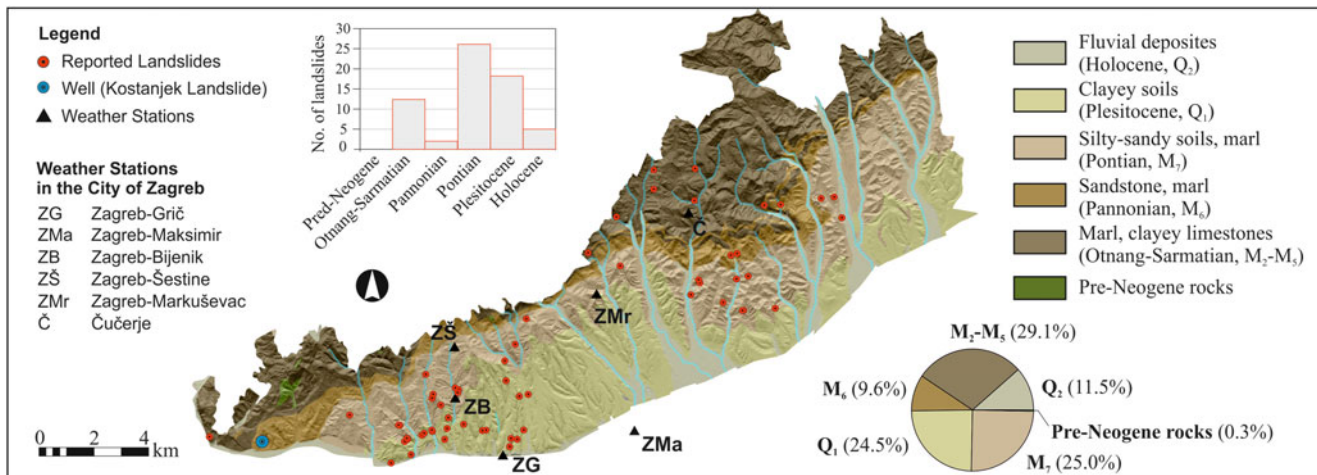


Fig. 4 Rainfall triggered landslide inventory map for the period from 1st January to 7th April 2013. Landslides are depicted by dots on generalized geological map together with weather stations and one well where continuous water level measurement is available (Krkač

et al. 2014). Pie chart shows the relative distribution of main stratigraphic units; histogram shows the number of (re)activated landslides per stratigraphic unit

descriptive information about each reported landslide by a professional engineering geologist.

Landslides are graphically depicted by dots on the landslide inventory map, because derivation of landslide contours requires additional visual or semi-automated mapping (Guzzetti et al. 2012). The main objective of the inventory compilation was to collect and achieve basic data which will enable evaluation of regional landslide hazard models. All recorded landslides have been described by the following data: landslide type (e.g., slide, flow); administrative unit; location description (street name); activation date; trigger (e.g., rain, snow melting); damages and impacts; landslide size (m²); remark on landslide size (measured, estimated); data source; and web links for media reports.

The precipitation-triggered landslide inventory (Fig. 4) was compared with landslide inventory derived on the basis of visual inspection of LiDAR imagery from 2011 given in Ferić et al. (2011). At the area of 24 km² (covered by airborne LiDAR data) 33 landslide triggered by precipitation in 2013 exist, but only 4 landslides overlap with landslide contours interpreted in 2011. This implies the possibility that a lot of reactivated landslides were not reported by citizens because they did not cause damages on houses and roads.

Precipitation and Temporal Distribution of Landslides

The City of Zagreb belongs to the NW part of Croatia, which was particularly wet at the beginning of 2013. From January to March, monthly precipitation was above the 91st and 98th percentile for the NW part of Croatia, as shown in Fig. 5 (DHMZ 2013). Measurements obtained by six meteorological

stations (Fig. 3) were used to analyze precipitation pattern at the pilot area of the Croatian-Japanese SATREPS FY2008 project in Zagreb City. General information about the meteorological stations and the mean annual precipitation (MAP) are listed in Table 1. The minimum value of MAP is 849.7 mm in lowland area at the Zagreb-Maksimir station and maximum value of 942.3 mm is at the Zagreb-Šestine station. Zagreb-Grič meteorological station was selected for further analysis of precipitation conditions, which had triggered more than 60 landslides in the analyzed period. The Zagreb-Grič station has the longest measurement period (151 years) and the amount of its cumulative precipitation for the analyzed period corresponds to the mean value of cumulative precipitation from all six stations (Fig. 6). Daily precipitation data for each weather station includes amount of rainfall and snow.

From the 1st January to the 7th April, the City of Zagreb experienced a period of intense rainfall and snow with cumulative values over the 97-day period which range from 372.4 mm (at Zagreb-Maksimir station) to 454.7 mm (at Zagreb-Markuševac station). Cumulative precipitations for the selected period at the Zagreb-Grič station exceeded 46 % of the mean annual precipitation (MAP). Figure 7a shows the cumulative precipitation for January, February and March measured at the Zagreb-Grič weather station. For the selected period, monthly precipitation in 2013 ranged from 130 % (February and March) to 190 % (January) which is higher than the average monthly values for the period from 1862 to 2012. Analysis of the available historical records at the Zagreb-Grič station indicates the following: only once (in 1984) did the monthly precipitation (173.5 mm) exceeded the monthly value measured in January 2013 (147.7 mm); four times (in 1879, 1895, 1942 and 1947) the monthly precipitations (max. value 203.5 mm) exceeded the monthly

Fig. 5 Monthly precipitation percentile calculated on the basis of data from 1961 to 1990 (DHMZ 2013) for: (a) January 2013, (b) February 2013 and (c) March 2013

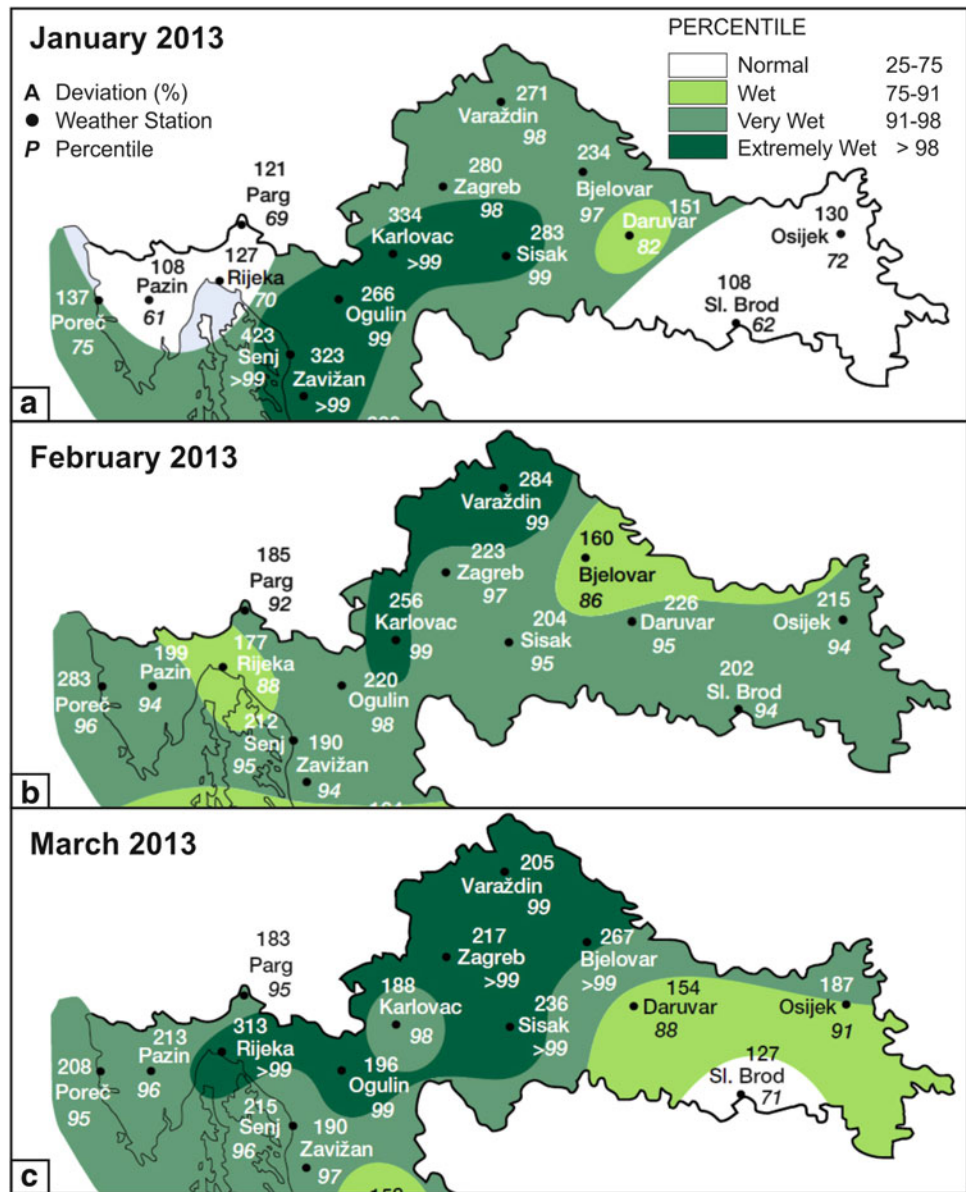


Table 1 Meteorological stations used to analyze the rainfall condition that resulted in landslides in the City of Zagreb in January to March 2013

| Meteorological station | Latitude | Longitude | Elevation (m) | MAP (mm) | Period (years) |
|-------------------------|----------|-----------|---------------|----------|----------------|
| Zagreb-Grič (ZG) | 45°48' | 15°58' | 157 | 883.6 | 151 |
| Zagreb-Maksimir (ZMa) | 45°49' | 16°02' | 123 | 849.7 | 64 |
| Zagreb-Bijenik (ZB) | 45°50' | 15°57' | 220 | 875.7 | 22 |
| Zagreb-Šestine (ZŠ) | 45°51' | 15°57' | 291 | 942.3 | 22 |
| Zagreb-Markuševac (ZMr) | 45°52' | 16°01' | 240 | 932.1 | 22 |
| Čučerje (Č) | 45°53' | 16°03' | 246 | 911.2 | 11 |

value measured in February 2013 (104.8 mm); and only two times (in 1865 and 1917) the monthly precipitations (131.9 mm and 130.9 mm) exceeded the monthly value measured in March 2013 (126.2 mm).

Based on the available historical data for the Zagreb-Grič weather station, analysis of the 3-month period from January

to March (Fig. 7b) showed that cumulative precipitation for the analyzed period in 2013 has the highest value ever measured. Analysis of the historical precipitation record in the City of Zagreb further indicates that the high intensity precipitation in the period from January to March 2013 is unique in the last 150 years. Figure 8 depicts daily

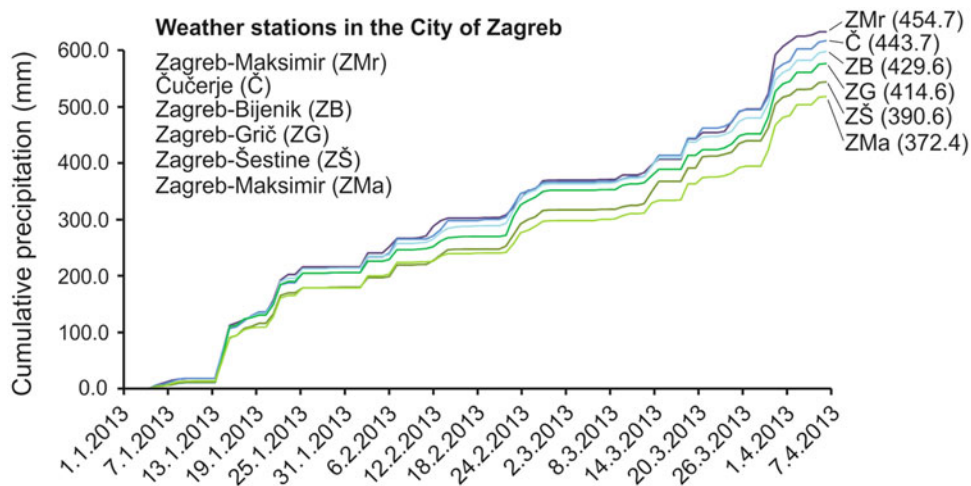


Fig. 6 Cumulative precipitation for the period from 1st January to the 7th April of six weather stations in the City of Zagreb

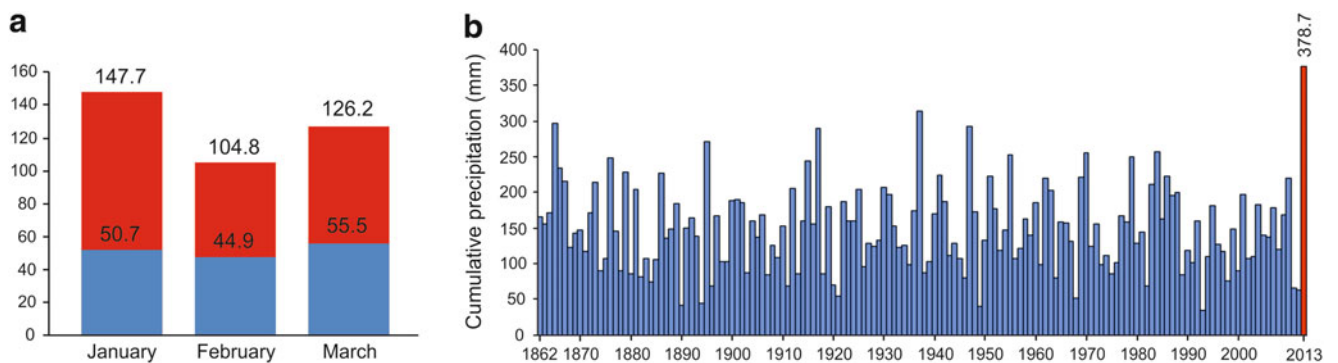


Fig. 7 Historical precipitation data at the Zagreb-Grič meteorological station: (a) Cumulative monthly precipitation for January, February and March. The red bars show quantities for 2013 and the blue bars show long-term cumulative monthly averages for the period of 150 years (1862–2012); (b) Cumulative precipitation for 3 months, from January to March, in the period between 1862 and 2013

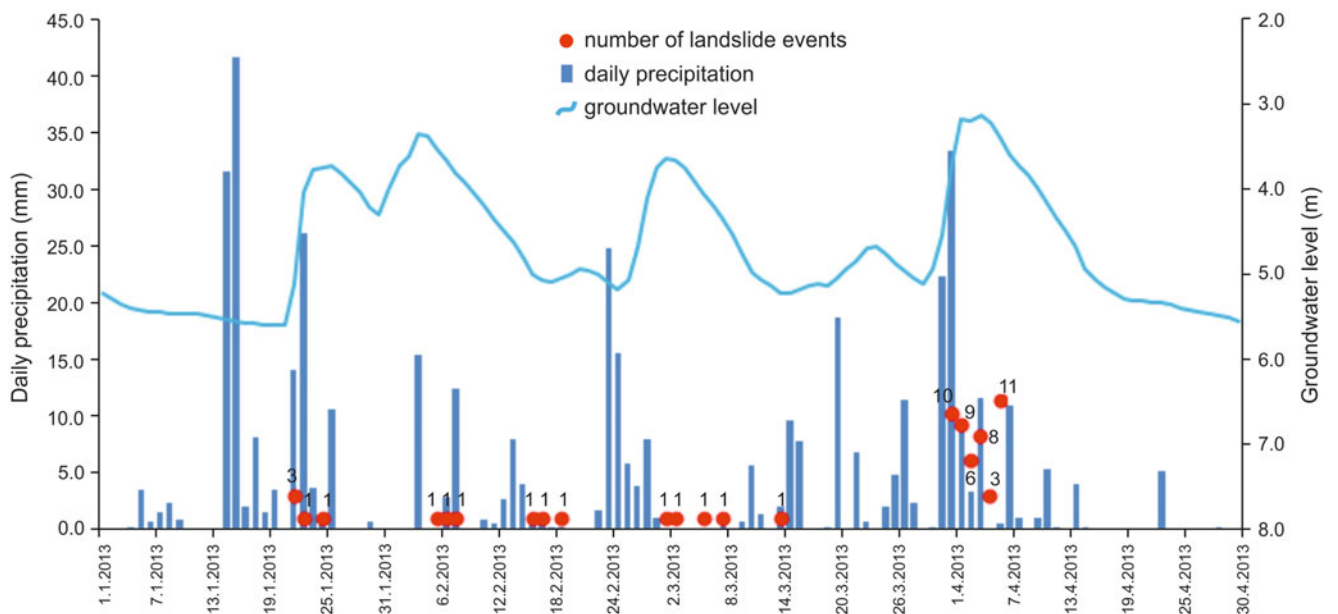


Fig. 8 Daily precipitations recorded at the Zagreb-Grič meteorological station and the number of landslide events triggered in the City of Zagreb from January to April 2013. The continuous line depicts groundwater level changes registered by a water-level gauge at the Kostanjek landslide observatory (Mihalić Arbanas et al. 2013)

precipitation data for the same period together with the number of landslide events per day. That data was also compared with the continuously measured groundwater level in one well on the Kostanjek landslide (Krkač et al. 2014) which illustrates the response of groundwater levels to precipitation. The position of the well in the western part of the city is shown in Fig. 3. In the selected period, significant rainfall occurred on the 30th of March and lasted until the 3rd of April. This 5-day event was characterized by a cumulative precipitation of 70 mm. Figure 8 shows that during this precipitation episode, 47 landslide events were (re) activated in the City of Zagreb (Bernat et al. 2014).

Discussion and Conclusion

Records from the Croatian National Protection and Rescue Directorate show about 900 landslides triggered by long-lasting heavy rainfall and a thick snow cover in the period from January to April 2013 in the NW part of Croatia and show the necessity of analysis of landslide triggering precipitation thresholds using regional approaches. The main reason lies in the fact that these events have historical importance, i.e., this period was unique in the last 150 years according to the influence of particular seasonal meteorological conditions to landslide activation in western part of Pannonian Basin in SE Europe. Simple inventory of precipitation-triggered landslides from January to April 2013 with reliable landslide records about location, initiation date and landslide area have been developed for the hilly area in the City of Zagreb on the basis of field checking of reported landslides. This inventory will enable the development of regional threshold model for the particular conditions which happened in the winter of 2013. The next step is to define minimum and maximum thresholds, using empirical bases (thresholds that combine precipitation measurements obtained for a specific precipitation event and thresholds that consider the antecedent conditions; Guzzetti et al. 2007). Data and analysis presented in this paper shows that it is also important to establish seasonal landslide inventory for the winter of 2013 for all hilly areas of six counties in NW Croatia. The most efficient methodology for landslide mapping at the area of 7,800 km², where locations of reported landslides exist, is interpretation of airborne LiDAR imagery to derive reliable landslide contours.

Acknowledgments Results presented herein have been obtained within the Japanese-Croatian JST/JICA's SATREPS FY2008 project. The authors would like to thank the DHMZ (Croatian Meteorological and Hydrological Service), the Emergency Management Office of the City and the Croatian National Protection and Rescue Directorate for providing data.

References

- Bernat S, Mihalić Arbanas S, Krkač M (2014) Landslides triggered in the continental part of Croatia by extreme rainfalls in the winter of 2013. In: Proceeding of XII IAEG Congress, 15–19 September 2014, Torino
- Bognar A (2001) Geomorphological regionalisation of Croatia. *Acta Geogr Croat* 34:7–29 (in Croatian)
- Ferić P, Mihalić S, Krkač M (2011) Visual mapping of landslides from LiDAR imagery, Zagreb, Croatia. In: Proceedings of the 2nd Japanese-Croatian Project Workshop, 15–17 December 2011. Rijeka, Croatia, pp 130–133
- Guzzetti F, Peruccacci S, Rossi M, Stark CP (2007) Rainfall thresholds for the initiation of landslides in central and southern Europe. *Meteor Atmos Phys* 98:239–267
- Guzzetti F, Mondini AC, Cardinali M, Fiorucci F, Santangelo M, Chang K-T (2012) Landslide inventory maps: new tools for an old problem. *Earth Sci Rev* 112:42–66
- DHMZ (Meteorological and Hydrological Service) (2013) *Meteorol Hydrol Bull* 1–3 (in Croatian)
- Krkač M, Rubinić J, Kalajžić J (2014) Analysis of water fluctuation dynamics in the wider area of the Kostanjek landslide. In: Landslide and flood hazard assessment. Proceedings of 1st regional symposium on landslides in the Adriatic-Balkan Region, 6–9 April 2013. Zagreb, Croatia
- Mihalić Arbanas S, Krkač M, Bernat S, Arbanas Ž (2012) Use of existing data in the City of Zagreb (Croatia, Europe) for the purpose of geo-planning. In: Proceedings of 13th World conference of ACUUS, 7–9 November 2012. Research Publishing, Singapore, pp 465–477
- Mihalić Arbanas S, Arbanas Ž, Krkač M (2013) TXT-tool 2.385-1.2 A comprehensive landslide monitoring system: The Kostanjek landslide, Croatia. In: Sassa K et al (eds) ICL landslide teaching tool. ICL, Kyoto, Japan
- Mihalić S, Arbanas Ž (2013) The Croatian–Japanese joint research project on landslides: activities and public benefits. In: Sassa K et al (eds) Landslides: global risk preparedness. Springer, Heidelberg, pp 333–349. ISBN: 978-3642220869
- Mihalić S, Bernat S, Hamasaki E, Gerber N (2011) Historical landslides in the City of Zagreb: landslide distribution analysis and 3D modeling of typical landslides in ADCALC3D. In: Proceedings of the 2nd Japanese-Croatian project workshop, 15–17 December 2011. Rijeka, Croatia, pp 122–125



Landslide Inventory in the Area of Dubračina River Basin (Croatia)

Petra Đomlija, Sanja Bernat, Snježana Arbanas Mihalić, and Čedomir Benac

Abstract

Systematic landslide mapping was performed for an area of 9.35 km² of the geomorphological unit of hills in the Dubračina River Basin. Based on the visual interpretation of LiDAR imagery, supplemented by field reconnaissance mapping of damaged roads and structures, 48 landslides were identified. In this first phase of landslide inventory preparation for the area of the Dubračina River Basin, a preliminary landslide inventory map presents data on locations of all identified landslides. Three examples of identification of landslide contours are given to show different possibilities in visual interpretation of airborne LiDAR imagery.

Keywords

Landslide topography • Airborne LiDAR • Reconnaissance mapping • Landslide inventory map

Introduction

The Dubračina River Basin is situated in the Primorsko-Goranska County in Croatia (Fig. 1). It represents a lower part of the elongated unique morpho-structural unit Rječina Valley—Bakar Bay—Vinodol Valley and covers an area of 43.5 km². This Basin is a pilot area of the Japanese-Croatian SATREPS FY2008 joint-research project with the final objective of landslide hazard mapping (Mihalić and Arbanas 2013). In order to make reliable maps that predict the landslide hazard and risks in a certain area, it is crucial to have insight into the spatial distribution and frequency of landslides. Therefore, each landslide hazard or risk study should start by making a landslide inventory that is as

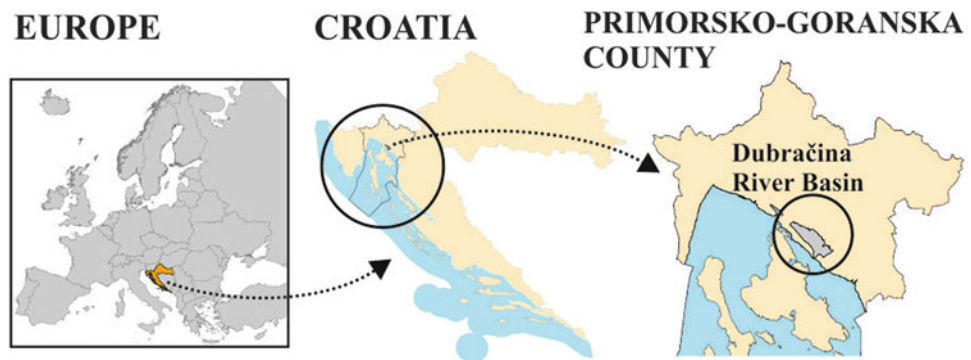
complete as possible in both space and time (Van Westen et al. 2008).

The main source of data for landslide inventory mapping in the Dubračina River Basin was airborne LiDAR (Light Detection and Ranging) data which permits an improvement in landslide identification, and more generally in geomorphological mapping (Jaboyedoff et al. 2012; Guzzetti et al. 2012). Airborne LiDAR for the study area of the 43.22 km² area was taken in March 2012, to visually identify landslides from high resolution LiDAR-derived imagery (resolution of 1 × 1 m). The first step was derivation of geomorphological units on the basis of geomorphological conditions, which reflects landslide processes. Seven geomorphological units, described in Bernat et al. (2014), are characterized by different landslide types depending on geological and morphological conditions. Most landslides in the Dubračina River Basin are in the geomorphological unit of hills built of siliciclastic rocks. The total area of this geomorphological unit is 9.33 km². This paper presents results of systematic landslide mapping in the geomorphological unit of hills in the first phase of landslide inventory preparation. Visual interpretation of LiDAR imagery was supplemented by field reconnaissance mapping of damaged roads and structures.

P. Đomlija (✉) • Č. Benac
Faculty of Civil Engineering, University of Rijeka, Radmile Matejcic 3,
Rijeka 51000, Croatia
e-mail: petra.domlija@gradri.uniri.hr; cedomir.benac@gradri.uniri.hr

S. Bernat • S. Arbanas Mihalić
Faculty of Mining, Geology and Petroleum Engineering, University of
Zagreb, Pierottijeva 6, Zagreb 10000, Croatia
e-mail: sanja.bernat@rgn.hr; snjezana.mihalic@rgn.hr

Fig. 1 Geographical position of the Dubračina River Basin



Description of the Study Area

Basic morphological and geological conditions of the Dubračina River Basin are presented in Fig. 2a, b. The elevations in this area range from 5 to 920 m a.s.l., and the prevailing slope angles (58 %) between 5° and 20° are present in the middle part of the basin. Along the northeast and southeast border, the valley is surrounded by steep cliffs whose peaks reach 922 m. The basin has an asymmetrical cross section (in the NE-SW direction) with a prominently longer northeast slope and a shorter southwest slope. The ridge peaks on the southwest side reach 357 m, and the valley bottom is 30 m a.s.l. Karstified carbonate rocks (mostly Upper Cretaceous and Paleogene limestones) are visible at the top of the slopes and cover 55 % of the basin area. The clearly marked rocky scarps represent the rim of the karstic plateau at the top of the NE slopes (Benac et al. 2010). Siliciclastic rocks of Eocene age (siltstones and sandstones interlayered with breccias and conglomerates and limestone) are situated in the lower slopes and in the bottom of the valley, but they are mostly covered by slope deposits.

Figure 2c shows seven geomorphological units distinguished in the Dubračina River Basin: alluvial plain; proluvium; terrace slope; hills; mountain slope; limestone wall; and karst plateau. Basic characteristics of the outlined landform units are given with regard to geological settings, geomorphological features and hydrological conditions in Bernat et al. (2014). The main geological hazards in the Dubračina River Basin are active geomorphological processes in the form of different types of slope movements and erosion processes. They cause significant economic losses by damaging roads, facilities, houses and watercourses.

The focus of this paper is the study area in the geomorphological unit of hills built of Upper Eocene siliciclastic rock mass, mostly covered by Quaternary slope deposits of variable thicknesses. This unit is situated between the geomorphological units of limestone walls in the NE and alluvial plain and mountain slopes in the SW. Landslide and

erosion phenomena of different types and state of activity are significant for the geomorphological unit of hills. Excessive erosion is dominant in the sub-basin area of the Salt Creek catchment (Fig. 3) resulting in badland relief (Aljinović et al. 2010), which is also one of the main landslide causal factors in the study area. There are numerous active landslides around the zones of erosion with clearly expressed landslide features. The second landslide types are generally larger, old dormant landslides, on gently inclined slopes, but they are not so clearly expressed.

Data and Methods

In the creation of the landslide inventory of the Dubračina River Basin the initial step was systematic landslide mapping of a 9.33 square kilometer area of hills. An identification of past and recent landslides was primarily based on the visual interpretation of high-resolution airborne LiDAR imagery.

LiDAR is a remote sensing technique that uses pulses of light to gather information about the surface of the Earth. For the LiDAR data used in this study, the flight took place in March 2012. Ground-surface measurements were acquired at an average density of five points per square meter. While laser scanning measures altitudes of all objects scanned, for the creation of a bare-earth DEM, post-processing is necessary to remove undesired returns from buildings and canopies (Van den Eckhaut et al. 2007). Using standard operations in ArcGIS, three different topographical maps were created from the bare-earth DEM: the hillshade map, the slope map and the contour line map. The hillshade map was generated with an azimuth angle of the illumination source of 315° and with the sun angle of 45° draped over a bare-earth DEM. The slope map characterizes the degree of terrain slope angle and is classified by categories of the slope angles, showing the areas of high slope angle in warmer (red, orange, yellow etc.) and areas of low slope angle in cooler (green) colors. The contour line map was created with 1 m contour spacing.

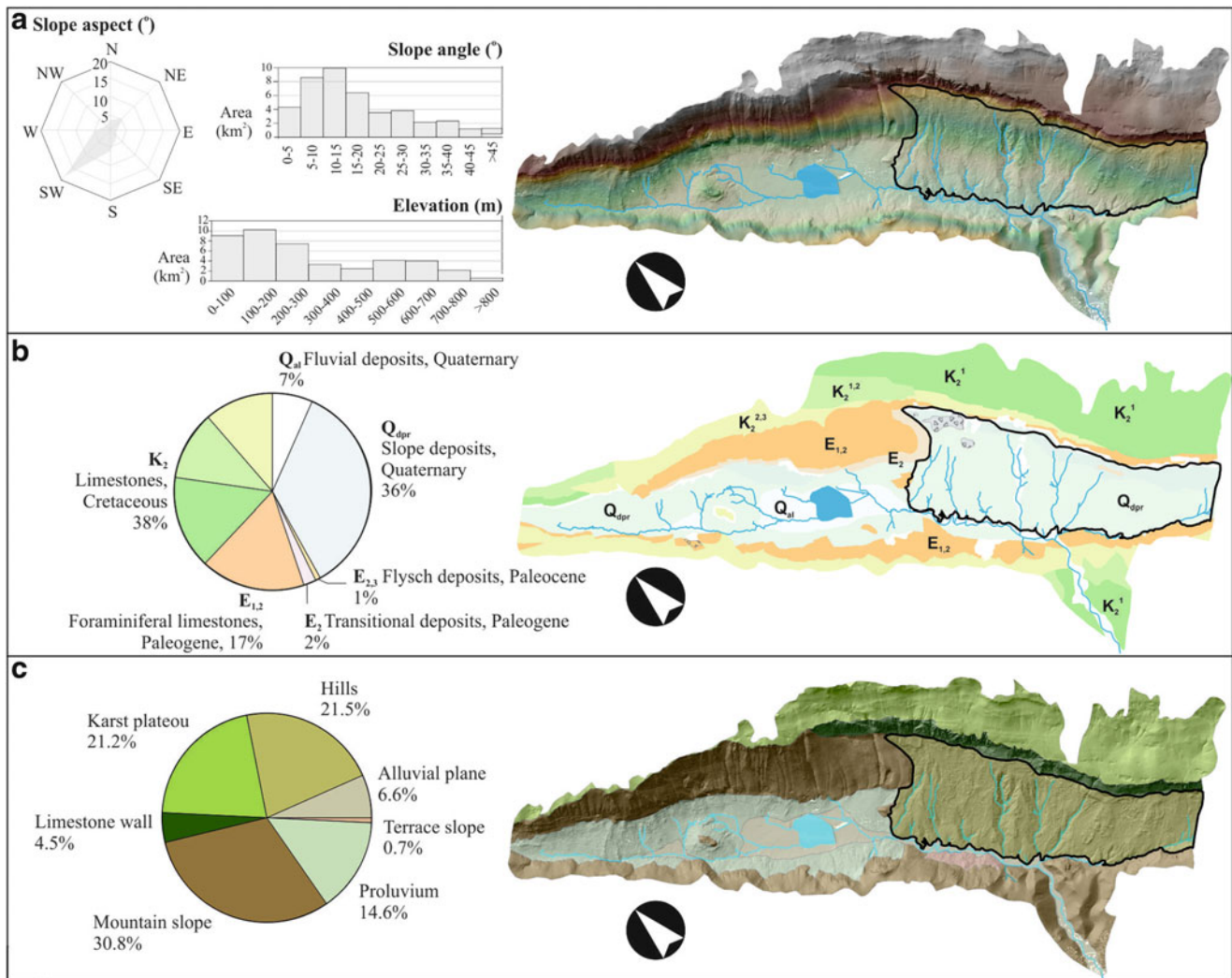


Fig. 2 Pilot area of the Japanese-Croatian project in the Dubračina River Basin (43 km²) with the geomorphological unit of hills (9.33 km²) outlined by a *thick black line*. (a) Elevation map from the 1 × 1 m DEM. Histograms show the distribution of slope angle and elevation computed

from the DEM. *Rose* diagram shows the distribution of slope aspect (in km²). (b) Generalized geological map showing the main stratigraphic units. The original scale of the geological map is 1:25,000. (c) Geomorphological map showing different landform units

All topographical maps were visually analyzed for topographical characteristics indicative of landslides, such as scarps, hummocky topography, convex and concave slope areas, midslope terraces, and offset drainages. Most of the identified landslides are visible on the LiDAR imagery. Nevertheless, some of the landslides were not easy to identify just on the basis of the visual identification of landslide features on LiDAR imagery. Such landslides were identified by additional field checking along roads. Moreover, there is one new landslide that occurred in 2013, after the flight for the collection of the LiDAR data took place in March 2012. All landslides identified by visual interpretation of the LiDAR imagery were additionally checked and evaluated in the field. A relatively dense road network in the investigated area enabled efficient field checking of most of the study area.

Results

Figure 3 presents a preliminary landslide inventory map of systematic landslide mapping of the 9.35 km² area of geomorphological unit of hills, showing data about locations of identified landslides. In total 48 landslides were identified. There are 36 landslides identified by clearly visible topographical features on the LiDAR imagery. Occurrences of 35 landslides are related to zones of excessive gully erosion. Locations of another 12 landslides were identified by field mapping of damaged roads and structures. These landslides mostly occur on much gentler inclined slopes and are in part located in urbanized areas. Their original landslide topography is almost entirely invisible on the LiDAR imagery due to

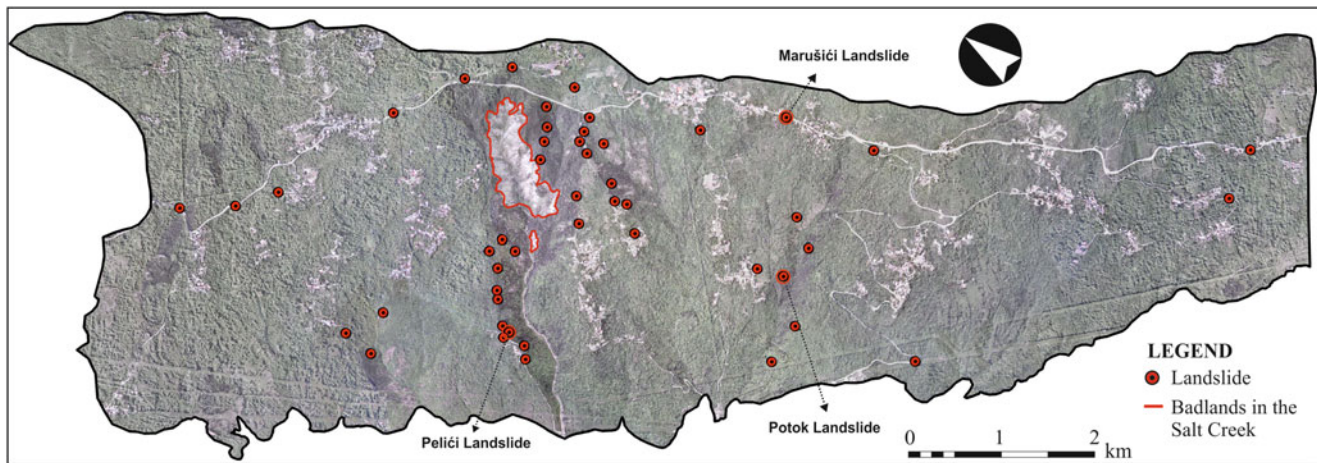


Fig. 3 Preliminary landslide inventory map of 9.35 km² area in siliciclastic rocks of the geomorphological unit of hills, showing data on locations of landslides identified by visual interpretation of LiDAR

imagery supplemented by field reconnaissance mapping of damaged roads and structures. The badlands area in the Salt Creek is outlined by a red line

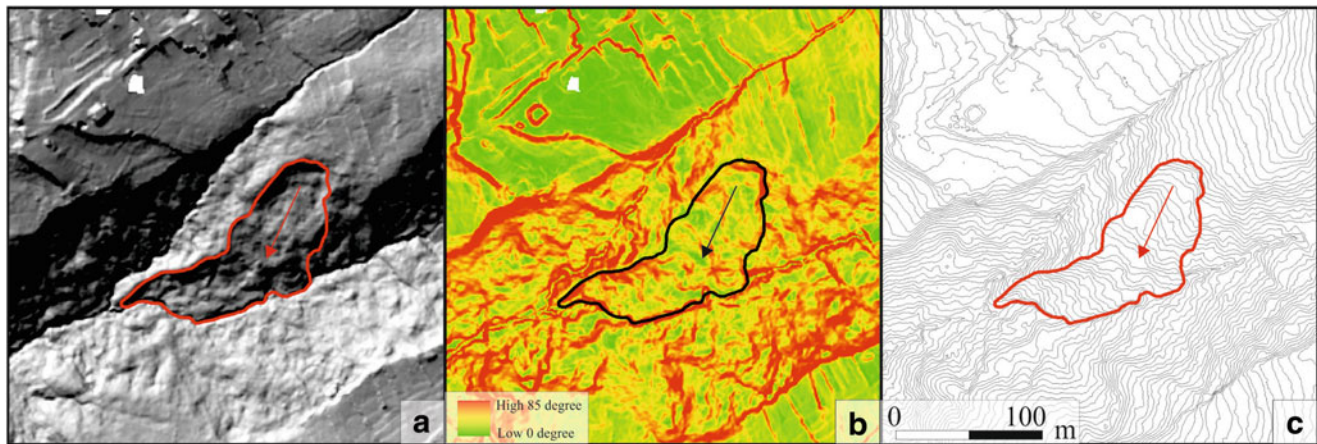


Fig. 4 Composite display of three topographic derivative maps of the Potok landslide. The estimated extent of landslide is outlined by red and black contours. (a) Hillshade map generated with an azimuth of 315° and a sun angle of 45° draped over a bare-earth DEM. (b) Slope map

showing areas of high slope angle in warmer colors (red, orange, yellow) and areas of low slope angle in cooler colors (green). (c) Contour map generated with a 1 m contour spacing

human, mostly agricultural, activities. One landslide was identified and located by mapping the most recent road damage a few days before slope collapse occurred in May 2013.

In Fig. 3 there are three highlighted landslides which are chosen as examples of significantly different landslide features and topography regarding their visibility on LiDAR imagery. Figures 4, 5 and 6 shows bare-earth LiDAR DEMs with interpreted landslide contours for Potok, Pelići and Marušići landslides.

Figure 4 presents the previously unknown Potok landslide. It was identified in the area of gully erosion and represents an example of a landslide occurring in combination with excessive erosion. The landslide topography is

clearly visible on all three topographic maps. Due to its remarkable landslide features, especially the main scarp, zone of accumulation and zone of depletion, as well as intensive hummocky topography of the landslide body, an accurate landslide contour could be outlined. The landslide area is 0.70 ha and the total length of landslide is approximately 145 m.

Figure 5 presents Pelići landslide, as an example of less clearly visible landslide topography on all three topographic maps. In the hillshade map it was recognized due to its remarkable undulating topography. The zone of accumulation is the most clearly visible among all the landslide features. The zone of depletion is also clearly visible in the hillshade map, but less clearly than the zone of accumulation.

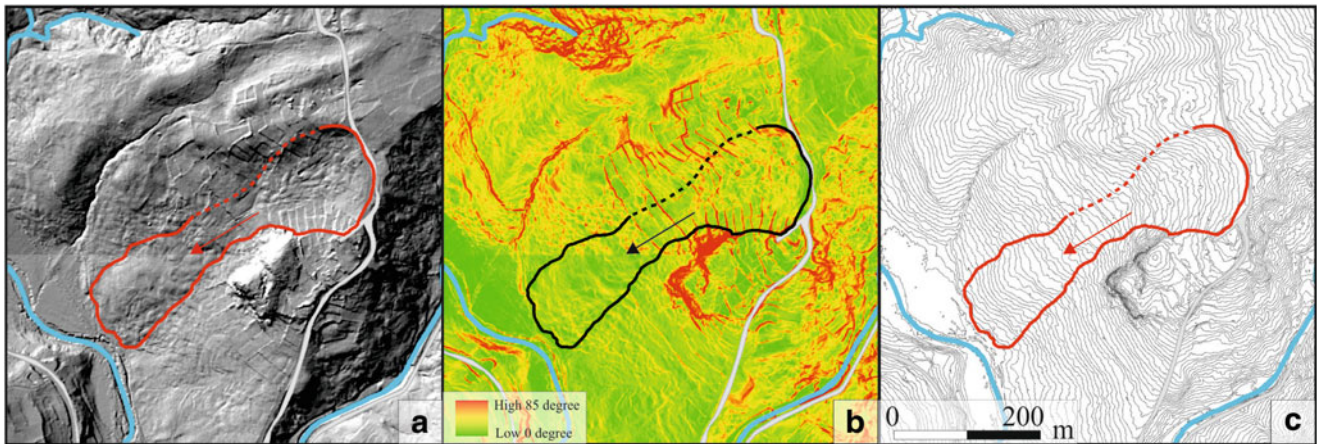


Fig. 5 Composite display of three topographic derivative maps of the Pelići landslide. The estimated extent of landslide is outlined by red and black contours. (a) Hillshade map generated with an azimuth of 315° and a sun angle of 45° draped over a bare-earth DEM. (b) Slope map

showing areas of high slope angle in warmer colors (red, orange, yellow) and areas of low slope angle in cooler colors (green). (c) Contour map generated with a 1 m contour spacing

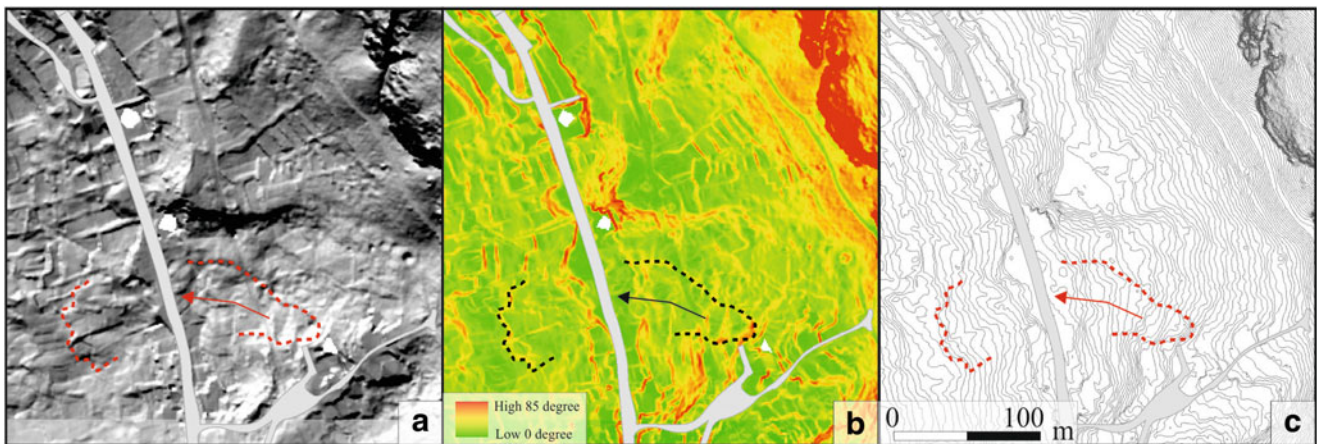


Fig. 6 Composite display of three topographic derivative maps of the Marušići landslide. The estimated extent of landslide has a red contour. (a) Hillshade map generated with an azimuth of 315° and a sun angle of 45° draped over a bare-earth DEM. (b) Slope map showing areas of

high slope angle in warmer colors (red, orange, yellow) and areas of low slope angle in cooler colors (green). (c) Contour map generated with a 1 m contour spacing

In the slope map, the zone of accumulation has characteristically lower slope angles than slope angles in the zone of depletion. Small erosional channels occur in the middle of the zone of depletion. The landslide crown is partially smoothed and thus less clearly visible in the hillshade and slope maps. The right edge of the depletion zone and middle zone of Pelići landslide is almost completely eroded. The position of right flank of the Pelići landslide body was mostly assumed, due to its invisibility. In the left side of depletion zone small agricultural terraces are situated. The landslide area is about 4 ha and the total landslide length is 430 m. Assumed landslide depth is about 15 m. Recent activity of landslide was indicated by damage to the road in the area of the landslide crown.

Figure 6 presents Marušići landslide, which was primarily identified by field reconnaissance mapping. The location of the landslide was identified on the basis of recent damage to a reconstructed road. Landslide contours were subsequently visually interpreted on the LiDAR imagery. The landslide topography is, for the most part, not clearly visible, caused in part by the highly modified original topography in the middle part of the landslides, where houses and road are located. Topographical features of the zone of accumulation are poorly visible on the hillshade map. The main scarp and the crown must be completely assumed, due to their invisibility on the DEM maps, as well as the zone of depletion. On the slope map, the slope angles are uniform over the whole landslide body and are at low angles. Due to the poorly

expressed topographical features on the LiDAR imagery, the landslide contours can be considered as less reliable, but are still useful as an indication of a potentially hazardous old landslide.

Discussion and Conclusions

A landslide inventory map was created for the part of the Dubračina Basin area with the highest landslide density, i.e., geomorphological unit of hills of 9.35 km². Based on identification of 48 landslides, it is estimated that landslide frequency is more than 5 landslides per square kilometer. According to the landslide inventory map, the spatial landslide distribution is irregular and most of the landslides are associated with zones of excessive erosion.

Most of landslides (36 landslides) were identified by visual interpretation of airborne derived bare-earth LiDAR imagery and were additionally checked in the field. There are 35 landslides characterized by clearly visible topographical features and they are mostly in zones of intensive erosion, with the highest density of landslides. They are shallow to moderate shallow (landslide depth <10 m) and small to moderate small, with landslide volumes in a range of 10³–10⁵ m³. Almost all of them are active. In total, 16 landslides are located near an urbanized area, causing continuous road and structure damage.

There are 12 landslides which were primarily identified by field mapping of damaged roads and structures. After that, it was possible to identify them visually on LiDAR imagery. These landslides occur on much gentler inclined slopes and they are very old. Moreover, long influence of anthropogenic (mostly agricultural) activities significantly changed the original landslide topography and therefore they are almost entirely invisible on the LiDAR imagery. These landslides are generally larger (landslide volume greater than 10⁵ m³) with landslide depths in a range of 10–15 m.

The applied methods of interpretation of airborne derived bare-earth LiDAR imagery from March 2012 proved to be useful for derivation of a landslide inventory map of the Dubračina River Basin with the following advantages and limitations. The high resolution of the DEM and of derivative topographic maps results in a high level of visibility of the main landslide features and accuracy in the identification of zones of depletion and accumulation, landslide contours and irregular topography of displaced masses. Hillshade maps can provide a very powerful visual aid for landslides identification, but their usefulness depends on the sun angle and the azimuth used in processing the derivative map. To utilize hillshade maps effectively requires the generation of

multiple hillshade maps with varying modeled sun angles and azimuths for the source light, since not all features share a similar aspect. Contour maps are useful to get a general insight into zones of depletion and accumulation, which are important to distinguish landslide phenomena from other geomorphological forms. Hillshade and slope maps are necessary for delineation of landslide contours.

The inventory of the Dubračina River Basin is a geomorphological historical landslide inventory, but without known time of landslide activation and/or landslide ages. It presents a solid base for further archiving of data about new or reactivated landslides. Continuous updating of the inventory is possible on the basis of data from different landslide sources (e.g., reported landslides, detailed investigation etc.)

Acknowledgments The authors acknowledge the financial support from JST/JICA's SATREP2008 Program (Science and Technology Research Partnership for Sustainable Development) for airborne LiDAR scanning.

References

- Aljinović D, Jurak V, Mileusnić M, Slovenec D, Presečki F (2010) The origin composition of flysch deposits as an attribute to the excessive erosion of the Slani Potok Valley ('Salty Creek'), Croatia. *Geol Croat* 63(3):313–322
- Benac Č, Mihalić S, Vivoda M (2010) Geological and geomorphological conditions in the area of Rječina river and Dubračina river catchments (Primorsko-Goranska County, Croatia). In: Proceedings of 1st Workshop of the Japanese-Croatian SATREPS FY2008 Project, 22–24 November 2010. JICA, Zagreb, pp 39–39
- Bernat S, Domlija P, Mihalić Arbanas S (2014) Slope movements and erosion phenomena in the Dubračina River Basin: a geomorphological approach. In: Landslide and flood hazard assessment. Proceedings of 1st regional symposium on landslides in the Adriatic-Balkan region, 6–9 April 2013. Zagreb, Croatia
- Guzzetti F, Mondini AC, Cardinali M, Fiorucci F, Santangelo M, Chang K-T (2012) Landslide inventory maps: new tools for an old problem. *Earth Sci Rev* 112:42–66
- Jaboyedoff M, Oppikofer T, Abellañ A, Derron MH, Loyer A, Metzger R, Pedrazzini A (2012) Use of LIDAR in landslide investigations: a review. *Nat Hazards* 61:5–28
- Mihalić S, Arbanas Ž (2013) The Croatian–Japanese joint research project on landslides: activities and public benefits. In: Sassa K et al (eds) Landslides: global risk preparedness. Springer, Heidelberg, pp 333–349. ISBN: 978-3642220869
- Van den Eckhaut M, Poesen J, Verstraeten G, Vanacker V, Nyssen J, Moeyersons J, Van Beek LPH, Vandekerckhove L (2007) Use of LIDAR-derived images for mapping old landslides under forest. *Earth Surf Process Landf* 32:754–769
- Van Westen CJ, Castellanos E, Kuriakose SL (2008) Spatial data for landslide susceptibility, hazard, and vulnerability assessment: an overview. *Eng Geol* 102:112–131

Landslide Technology and Engineering in Support of Landslide Science

Kyoji Sassa

The World Landslide Forum (**WLF**) is the triennial conference of the International Consortium on Landslides (**ICL**) and the International Programme on Landslides (**IPL**). The IPL is a programme of the International Consortium on Landslides, managed by ICL and its supporting organizations: UNESCO, WMO, FAO, UNISDR, UNU, ICSU, WFEO and IUGS. IPL and WLF contribute to the United Nations International Strategy for Disaster Reduction.

The World Landslide Forum provides an information and academic-exchange platform for landslide researchers and practitioners. It creates a triennial opportunity to promote worldwide cooperation and share new theories, technologies and methods in the fields of landslide survey/investigation, monitoring, early warning, prevention, and emergency management. The forum's purpose is to present achievements of landslide-risk reduction in promoting the sustainable development of society.

Advancements in landslide science and disaster-risk reduction are supported by developments in landslide technology and engineering. Here we invited ICL supporters who support the publication of the international full-color journal "Landslides: Journal of the International Consortium on Landslides", the companies advertising in the seven volumes of "Landslide Science and Practice: Proceedings of the Second World Landslide Forum 2011" and the companies exhibiting at the Third World Landslide Forum 2014 to introduce their landslide technology and engineering. Six companies applied to exhibit in this book: their names, addresses, contact information and a brief introduction are given below (in the order of receipt of application):

1. MARUI & Co. Ltd.
1-9-17 Goryo, Daito City, Osaka 574-0064, Japan
URL: <http://marui-group.co.jp/en/index.html>
Contact: hp-mail@marui-group.co.jp

MARUI & Co. Ltd is the leading manufacturing and sales company in Japan since 1920 of material testing machines for soil, rock, concrete, cement and asphalt. Marui engineers built and assisted in development of the series of stress and speed control ring-shear apparatus by DPRI and ICL to study landslides since 1982.

2. OSASI Technos, Inc.
65-3 Hongu-cho, Kochi City, Kochi 780-0945, Japan
URL: <http://www.osasi.co.jp/en/>
Contact: info-tokyo@osasi.co.jp
OSASI Technos, Inc. develops and markets the slope-disaster monitoring system called OSASI Network System (OSNET). The monitoring devices use a built-in lithium battery and operate without external electricity supply in mountainous areas. The system enables a network of up to 64 units with up to 1 km distance between units. OSNET is suitable for quickly establishing monitoring systems on landslides in emergencies.
3. Okuyama Boring Co., Ltd.
10-39 Shimei-cho, Yokote City, Akita 013-0046, Japan
URL: <http://www.okuyama.co.jp/>
Contact: info@okuyama.co.jp
The Okuyama Boring Company Ltd specializes in landslide investigation, analysis of landslide mechanisms, and design of landslide remedial measures. The company uses its own software to analyze the initiation and motion of landslides, including the tsunami generated by landslides into reservoirs.
4. Japan Conservation Engineers & Co., Ltd.
3-18-5 Toranomom, Minato-ku, Tokyo 105-0001, Japan
URL: <http://www.jce.co.jp>
Contact: hasegawa@jce.co.jp
Japan Conservation Engineers & Co, Ltd develops landslide-simulation software and shear-testing apparatus, including slip-surface direct-shear apparatus and ring-shear apparatus to measure the shear strength mobilized on the sliding surface of landslides. Japan Conservation Engineers is a consulting company for

K. Sassa (✉)
International Consortium on Landslides, Kyoto, Japan
e-mail: sassa@iclhq.org

landslide investigation, reliable monitoring, data analysis and the design of landslide-risk reduction works.

5. KOKUSAI KOGYO Co., Ltd.

2 Rokuban-cho, Chiyoda-ku, Tokyo 102-0085, Japan

URL: <http://www.kk-grp.jp/english/>

Contact: overseas@kk-grp.jp

Kokusai Kogyo has undertaken aerial surveys, infrastructure development projects for road and harbor facilities, and landslide-disaster prevention and mitigation works since its foundation in 1947. The company has recently developed remote-sensing technology using the laser profiler, satellite synthetic aperture radar, and a new monitoring system called <Shamenet> integrating GPS and other monitoring devices, all of which contribute to landslide-disaster prevention and mitigation.

6. C.S.G. S.r.l. Centro Servizi di Geingegneria

Via Cazzolini, 15A - 15010 Ricaldone (AL), Italy

URL: <http://www.csgrl.eu>

Contact: csg@csgrl.eu

C.S.G. S.r.l. Centro Servizi di Geingegneria is a leader in the production of multi-parametric in-place borehole monitoring columns called DMS (patents). DMS columns have been installed in a number of important international sites, where continuous monitoring for Early Warning,

both in shallow landslides and deep-seated rockslides requires instrumentation with high-precision, accuracy and reliability. CSG pursues a high quality standard through rigorous laboratory calibration tests, and long-term stability and alignment tests within temperature-controlled vertical and inclined boreholes in field.

Full-color presentations from these six exhibitors focusing on their landslide technology are shown in the following pages.

The progress of landslide science is supported by advances in landslide technology. The success of landslide risk-reduction measures needs effective landslide engineering. The International Consortium on Landslides seeks expressions of interest in contributing to “Landslide Technology and Engineering to Support Landslide Science” at the Fourth World Landslide Forum to be held on May 29–June 2, 2017, in Ljubljana, Slovenia. We may call for presentations on landslide technology and engineering in the proceedings, as well as through exhibitions at the site. Those interested in this initiative are requested to contact the Secretariat of the International Consortium on Landslides <secretariat@iclhq.org>. We will send invitations to interested applicants when further details become available.

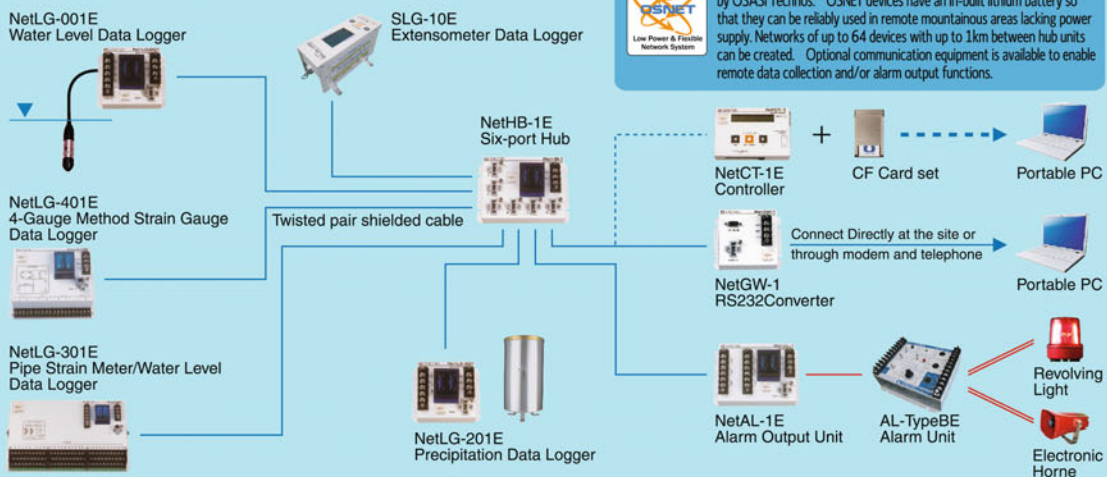


Web site : <http://www.marui-group.co.jp/en/>
E-mail : hp-mail@marui-group.co.jp
Address : 1-9-17 Goryo, Daito City, Osaka Prefecture,
574-0064, Japan
Phone : 81-72-869-3201 Fax : 81-72-869-3205

Slope Disaster Monitoring System

OSASI NETWORK System

EXAMPLE SETUP 2



OSNET is a network solution for disaster prevention monitoring developed by OSASI Technos. OSNET devices have an in-built lithium battery so that they can be reliably used in remote mountainous areas lacking power supply. Networks of up to 64 devices with up to 1km between hub units can be created. Optional communication equipment is available to enable remote data collection and/or alarm output functions.



OSASI TECHNOS INC.
We pass on voices of the earth.
OSASI Technos, Inc.



Corporate Headquarters / 65-3 Hongu-cho, Kochi-shi, Kochi 780-0945, JAPAN

Tel: +81-88-850-0535 Fax: +81-88-850-0530

Tokyo Headquarters / Sumitomoseimei Building 4F 1-10-2 nishishinbashi, minato-ku, Tokyo 105-0003, JAPAN

Tel: +81-3-5510-1391 Fax: +81-3-5510-1393

Kyushu Branch Office / Iwaho Building Ekiminami 4F 4-1-17 Hkaka Eki Minami, Hakata-ku, Fukuokashi, Fukuoka 812-0016, JAPAN

Tel: +81-92-434-9200 Fax: +81-92-434-9201

* Please note that specifications for the equipment are subject to change without notice.

* For further detailed specifications, please visit our homepage at

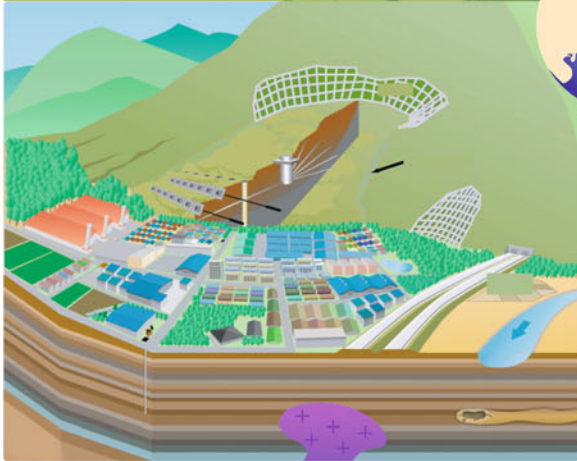
<http://www.osasi.co.jp/en/>

We keep a clean nature for the future.

Okuyama Boring Co., Ltd.

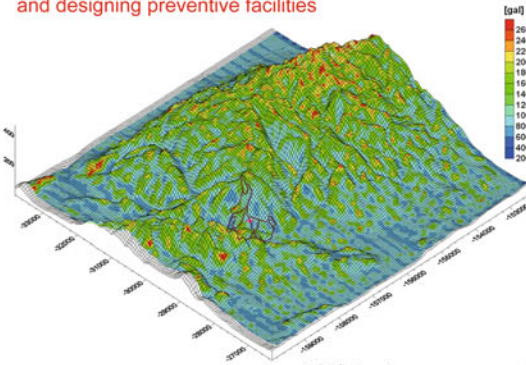


<http://www.okuyama.co.jp/>
 E-mail info@okuyama.co.jp



Landslide countermeasure works

Landslide research, analysis and designing preventive facilities



3D Seismic response analysis



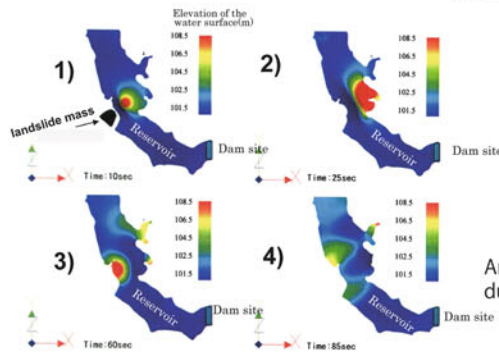
Ground anchor



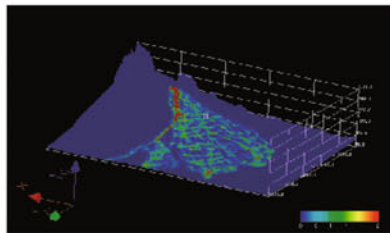
Water catchment well



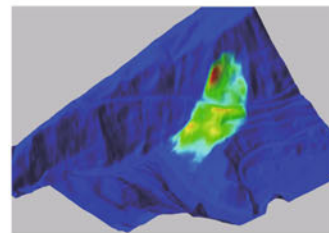
Water catchment boring



Analysis of water waves due to landslide

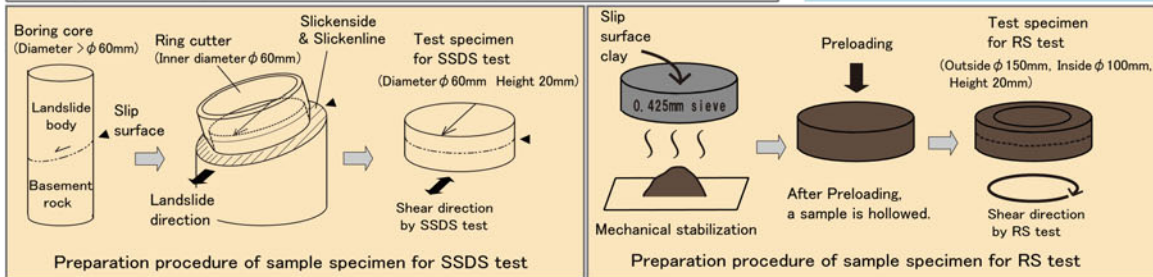
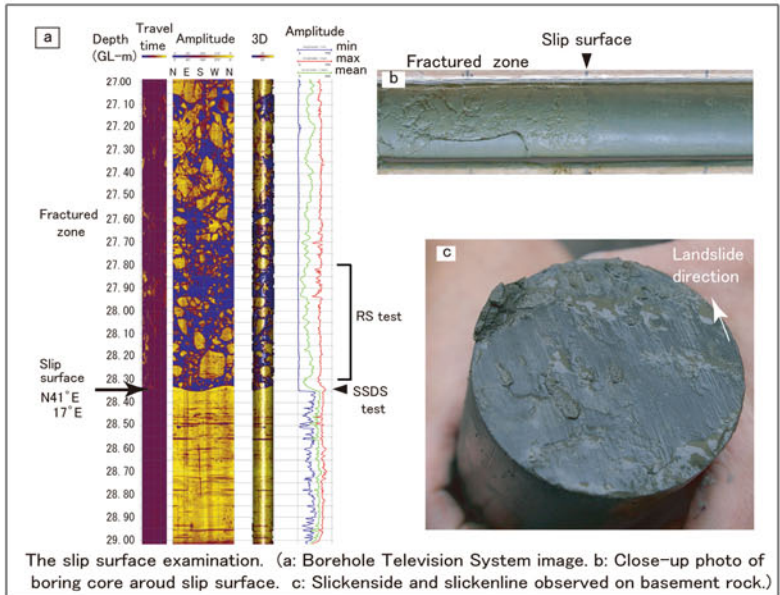


Flooding analysis in area with steep slope



Analysis of grain-fluid flow due to landslide

As for Landslide survey, we have various technologies for the slip surface examination. Slip Surface Direct Shear (SSDS) apparatus we have developed is the repeating one surface shearing testing apparatus which aims to measure the shear strength. This apparatus can exactly examine to the shear strength of the slip surface that will be demonstrated in the site. Ring Shear (RS) test is large displacement test which can obtain the fully softened strength and residual strength of the cohesive soil which constitutes a slip surface.

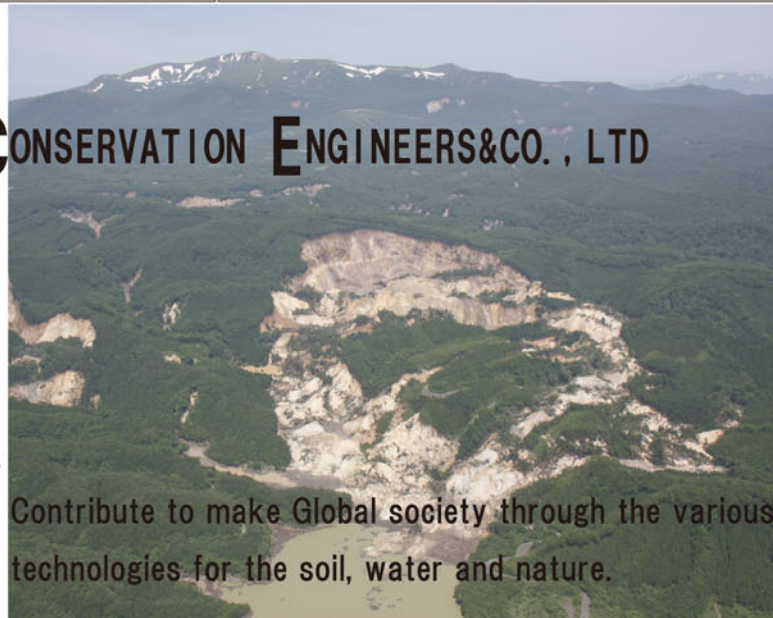


JAPAN CONSERVATION ENGINEERS&CO., LTD

URL:<http://www.jce.co.jp/>

HEAD OFFICE
 3-18-5, TORANOMON, MINATO-KU,
 TOKYO 105-0001, JAPAN
 TEL:+81.3.3436.3673
 FAX:+81.3.3432.3787

LABORATORY
 34-12, SHIMIZUMAE, MINAMIYANOME,
 FUKUSHIMA-SHI, FUKUSHIMA
 960-0112, JAPAN
 TEL:+81.24.555.0255
 FAX:+81.24.557.3966



Contribute to make Global society through the various technologies for the soil, water and nature.



Building sustainable cities of the future
Green communities

Geospatial advantage green communities

We have geospatial technology to create ever more accurate maps, essential for developing social infrastructure and nation building—the backbone of economic growth. We are providing total solutions that merge our geospatial and urban planning technologies with renewable energy sources and to create safer, disaster-resistant communities of the future.

Environment/energy



*Disaster prevention/
risk reduction*



Supporting government



Social infrastructure



Business Solutions



Our Major Fields for international development



Disaster Prevention



Solid Waste Management



Water resource development



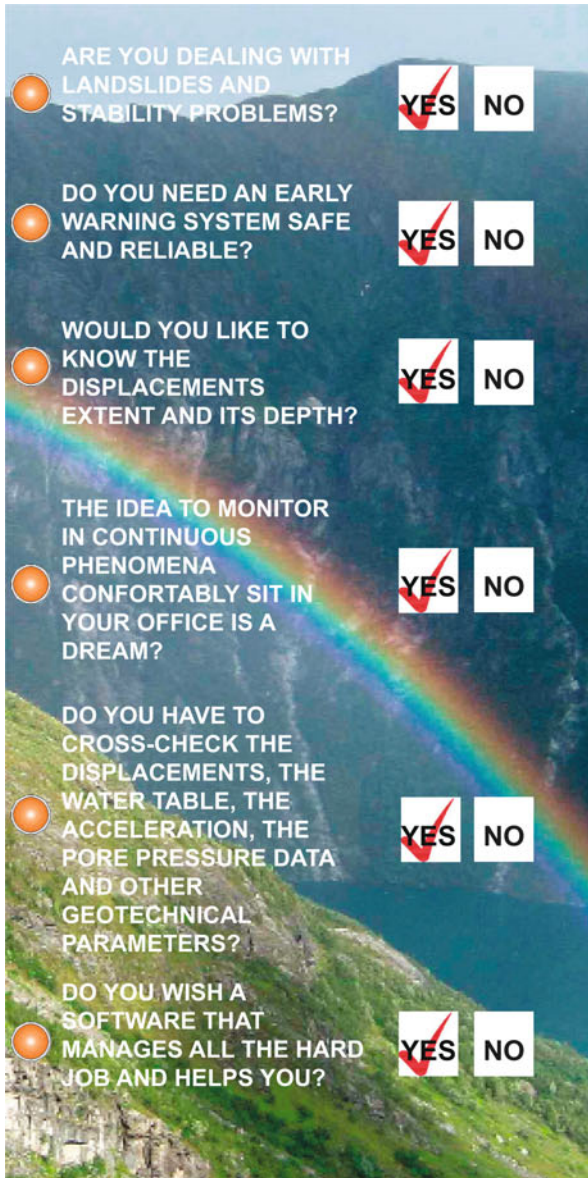
Survey and Mapping



KOKUSAI KOGYO CO.,LTD.

2 Rokubancho,Chiyoda-ku,Tokyo,Japan 102-0085

URL <http://www.kk-grp.jp/english> E-mail info_overseas@kk-grp.jp



ARE YOU DEALING WITH LANDSLIDES AND STABILITY PROBLEMS? **YES** **NO**

DO YOU NEED AN EARLY WARNING SYSTEM SAFE AND RELIABLE? **YES** **NO**

WOULD YOU LIKE TO KNOW THE DISPLACEMENTS EXTENT AND ITS DEPTH? **YES** **NO**

THE IDEA TO MONITOR IN CONTINUOUS PHENOMENA CONFORTABLY SIT IN YOUR OFFICE IS A DREAM? **YES** **NO**

DO YOU HAVE TO CROSS-CHECK THE DISPLACEMENTS, THE WATER TABLE, THE ACCELERATION, THE PORE PRESSURE DATA AND OTHER GEOTECHNICAL PARAMETERS? **YES** **NO**

DO YOU WISH A SOFTWARE THAT MANAGES ALL THE HARD JOB AND HELPS YOU? **YES** **NO**

The multiparametric column allows the measurement of the main geotechnical and mechanical parameters of soil and 2/3D structures, besides water table, temperature and acceleration in the same borehole. The column has digital sensors that transfer data to the control unit, placed on surface, which transmits data in real time to the final user and to the monitoring room.



Via Cazzulini, 15/A
 15010 RICALDONE (AL) ITALY
 Tel. +39 0144 74277
 Fax +39 0144 745914
 www.csgsrl.eu
 csg@csgsrl.eu

GEOTECHNICAL MULTIPARAMETRIC MONITORING COLUMNS

DMS column is like a "spiral cord", to be installed in place inside the borehole, composed by a sequence of hard tubular modules connected each other by special flexible joints having 2 or 3 freedom degrees that make possible to copy any deformation. These joints allow each module to perfectly fit the drilling hole and soil movements, maintaining the azimuthal direction.




**So...
 What you need is DMS**

- Continuous and multi-parametric data in the same borehole
- Fast and easy start up of the monitoring system
- Modular and retrievable system
- Advanced selection procedures
- High mechanical quality
- Advanced data processing software and graphical elaboration
- System developed for deep seated landslides and early warning
- Technical support and remote diagnostic
- After sale support and hire service
- Results and cost reduction

DMS



International Consortium on Landslides

An international non-government and non-profit scientific organization
promoting landslide research and capacity building for the benefit of society and the environment

President: Paolo Canuti (Prof. Emeritus, University of Firenze, Italy)

**Vice Presidents: Kaoru Takara (Kyoto University, Japan)/Yueping Yin (China Geological Survey)/
Claudio Margottini (National Institute for the Protection and Environmental Research (ISPRA), Italy)/
Irasema Alcantara-Ayara, (UNAM), Mexico**

Executive Director: Kyoji Sassa (Prof. Emeritus, Kyoto University, Japan)

ICL Supporting Organizations:

The United Nations Educational, Scientific and Cultural Organization (UNESCO) / The World Meteorological Organization (WMO) / The Food and Agriculture Organization of the United Nations (FAO) / The United Nations International Strategy for Disaster Reduction Secretariat (UNISDR) / The United Nations University (UNU) / International Council for Science (ICSU) / World Federation of Engineering Organizations (WFEO) / International Union of Geological Sciences (IUGS) / Government of Japan

ICL Members:

Albania Geological Survey / Federal University of Parana, CENACID-UPFR, Brazil/ Geological Survey of Canada / Chinese Academy of Sciences, Institute of Mountain Hazards and Environment / Northeast Forestry University, China / Bureau of Land and Resources of Xi'an, China / China Geological Survey / Nanjing Institute of Geography and Limnology, Chinese Academy of Sciences / Universidad Nacional de Columbia, Columbia / City of Zagreb, Emergency Management Office, Croatia /Croatian Landslide Group (Faculty of Civil Engineering, University of Rijeka and Faculty of Mining, Geology and Petroleum Engineering, University of Zagreb) / Charles University, Faculty of Science, Czech Republic / Institute of Rock Structure and Mechanics, Department of Engineering Geology, Czech Republic / Joint Research Centre (JRC), European Commission /Technische Universität Darmstadt, Institute and Laboratory of Geotechnics, Germany / Universidad Politecnica de Ingenieria, UPI, Honduras / National Institute of Disaster Management, India / University of Gadjah Mada, Indonesia / Agricultural Research and Education organization (AREO), Iran / Building & Housing Research Center, Iran / International Institute of Earthquake Engineering and Seismology (IIEES), Iran / University of Firenze, Earth Sciences Department, Italy / Italian Institute for Environmental Protection and Research (ISPRA) - Dept. Geological Survey, Italy / Forestry and Forest Product Research Institute, Japan / Japan Landslide Society / Kyoto University, Disaster Prevention Research Institute, Japan / Niigata University, Research Institute for Natural Hazards and Disaster Recovery, Japan / University of Tokyo (Institute of Industrial Science and Department of Civil Engineering, Geotechnical Engineering Group), Japan / Korea Forest Research Institute, Korea / Korea Infrastructure Safety & Technology Corporation, Korea /Korea Institute of Geoscience and Mineral Resources (KIGAM) /Korean Society of Forest Engineering / Mara University of Technology, Malaysia / Slope Engineering Branch, Public Works Department of Malaysia / Institute of Geography, National Autonomous University of Mexico (UNAM) / International Centre for Integrated Mountain Development (ICIMOD), Nepal / University of Nigeria, Department of Geology, Nigeria / International Centre for Geohazards (ICG) in Oslo, Norway /Grudec Ayar, Peru/ Moscow State University, Department of Engineering and Ecological Geology, Russia / Russian Academy of Sciences, Sergeev Institute of Environmental Geoscience (IEG RAS) / JSC "Hydroproject Institute", Russia / University of Belgrade, Faculty of Mining and Geology, Serbia / Comenius University, Faculty of Natural Sciences, Department of Engineering Geology, Slovakia / University of Ljubljana, Faculty of Civil and Geodetic Engineering (UL FGG), Slovenia / Geological Survey of Slovenia / Engineering Geoscience Unit, Council for Geoscience, South Africa / Central Engineering Consultancy Bureau (CECB), Sri Lanka / National Building Research National Organization, Sri Lanka / Taiwan University, Department of Civil Engineering, Chinese Taipei / Asian Disaster Preparedness Center, Thailand / Ministry of Agriculture and Cooperative, Land Development Department, Thailand / Institute of Telecommunication and Global Information Space, Ukraine / Institute Hydroingeo, State Committee of Geology of Uzbekistan / Institute of Transport Science and Technology, Vietnam

ICL Supporters:

Kawasaki Geological Engineering Co., Ltd., Tokyo, Japan / Marui & Co., Ltd., Osaka, Japan / Okuyama Boring Co., Ltd., Yokote, Japan / GODAI Development Corp., Kanazawa, Japan / Japan Conservation Engineers & Co., Ltd, Tokyo / Kokusai Kogyo Co., Ltd., Tokyo, Japan / Nippon Koei Co., Ltd., Tokyo, Japan / Ohta Geo-Research Co., Ltd., Nishinomiya, Japan / OSASI Technos Inc., Kochi, Japan / OYO Corporation, Tokyo, Japan / Sabo Technical Center, Tokyo, Japan / Sakata Denki Co., Ltd., Tokyo, Japan

Contact:

International Consortium on Landslides, 138-1 Tanaka Asukai-cho, Sakyo-ku, Kyoto 606-8226, Japan

Web: <http://icl.iplhq.org/>, E-mail: secretariat@iclhq.org

Tel: +81-774-38-4834, +81-75-723-0640, Fax: +81-774-38-4019, +81-75-950-0910